Lunar and Planetary Science XXIV

Abstracts of papers submitted to the Twenty-fourth Lunar and Planetary Science Conference

PART 2 G - M

National Aeronautics and Space Administration

Lyndon B. Johnson Space Center
Houston, Texas

LPI / USRA

LUNAR AND PLANETARY INSTITUTE
UNIVERSITIES SPACE RESEARCH ASSOCIATION

LUNAR AND PLANETARY SCIENCE XXIV

Abstracts of Papers Submitted to the

TWENTY-FOURTH LUNAR AND PLANETARY SCIENCE CONFERENCE

Sponsored by

National Aeronautics and Space Administration
Lunar and Planetary Institute
NASA Johnson Space Center

March 15–19, 1993

Part 2

Compiled by
Lunar and Planetary Institute
3600 Bay Area Boulevard
Houston TX 77058-1113

The Lunar and Planetary Institute is operated by the Universities Space Research Association under Contract No. NASW-4574 with the National Aeronautics and Space Administration.

CONTENTS

SPECTRAL EVIDENCE OF SIZE DEPENDENT SPACE WEATHERING PROCESSES ON ASTEROID SURFACES; M. J. Gaffey [RPI]; J. F. Bell [U. Hawaii]; R. H. Brown [JPL]; T. H. Burbine [SAO]; J. L. Piatek [ASU]; K. L. Reed, and D. A. Chaky [RPI].

Most compositional characterizations of the minor planets are derived from analysis of visible and near-infrared reflectance spectra. However, such spectra are derived from light which has only interacted with a very thin surface layer. Although regolith processes are assumed to mix all near-surface lithologic units into this layer, it has been proposed that space weathering processes can alter this surface layer to obscure the spectral signature of the bedrock lithology. It has been proposed that these spectral alteration processes are much less pronounced on asteroid surfaces than on the lunar surface [1-3], but the possibility of major spectral alteration of asteroidal optical surfaces has been invoked to reconcile S-asteroids with ordinary chondrites [4-6]. The reflectance spectra of a large subset of the S-asteroid population have been analyzed in a systematic investigation of the mineralogical diversity within the S-class [7]. In this sample, absorption band depth is a strong function of asteroid diameter. The S-asteroid band depths are relatively constant for objects larger than 100 km and increase linearly by factor of two toward smaller sizes (~40 km). Although the S-asteroid surface materials includes a diverse variety of silicate assemblages, ranging from dunites to basalts, all compositional subtypes of the S-asteroids conform to this trend. The A-, R-, and V-type asteroids which are primarily silicate assemblages (as opposed to the metal-silicate mixtures of most S-asteroids) follow a parallel but displaced trend. Some sort of textural or regolith equilibrium appears to have been attained in the optical surfaces of asteroids larger than about 100 km diameter but not on bodies below this size.

The relationships between absorption band depth, spectral slope, surface albedo and body size provide an intriguing insight into the nature of the optical surfaces of the S-asteroids and space weathering on these objects. Figure 1 plots absorption band depth versus asteroid diameter for the sample of 39 S-objects. If the two points for 354 Eleonora (near diam=160 km and depth=0.24; see below) are omitted, the S-asteroid band depths are relatively constant for objects larger than 100 km and increase steeply toward smaller sizes. For the larger S-asteroids, there is a relatively constant spectral contribution from the mafic silicate phases in the surface materials of different objects. For S-objects below 100 km diameter, the mafic spectral contribution increases with decreasing body size. The smaller S-asteroids in the Earth-approaching population exhibit stronger mafic mineral absorption features than the larger main belt S-asteroids [8], so it appears that this trend extends to even smaller sizes. The various compositional subtypes of the S-asteroids are distributed randomly within the trend, and therefore the correlation is not due to differences in silicate mineralogy between the subtypes. This behavior must arise from some systematic size-dependent differences in the regolith properties which control the optical surfaces of these objects.

An abundant metallic FeNi component has commonly been invoked to explain the relatively steep spectral slopes, the weaker absorption features and the lower albedos of the S-asteroids. Several asteroidal space weathering or regolith processes can be tested if it is assumed that regolith maturity - however incomplete - correlates with body size. This is plausible since larger bodies should more efficiently retain ejecta and on average should have older surfaces than the smaller bodies in a collisionally evolved population. These two factors combine to increase the average lifetime of a typical regolith particle on larger objects.

There is no correlation between albedo and diameter for the full set of S-asteroids or for the individual subtypes, as would be expected if simple particle comminution [9], melting and recrystallization [10,11], contamination of the surface by dark material, or shock darkening of silicates [12-15] were primary causes of these band depth differences. The full set of S-objects shows a weak negative correlation of spectral slope with diameter, but there is a strong negative correlation between spectral slope and asteroid diameter within the S(IV)-subtype which includes the possible (i.e., not excluded by silicate compositions) main-belt ordinary chondrite parent body candidates. The preferential fragmentation of metal has been proposed to produce the steep spectral slope of the S-asteroids [16,17]. It has also been

suggested that the initial development of regolith results in the increased retention or production of impact melt products [18]. Both of these processes should produce positive correlations between spectral slope (i.e., degree of metal fragmentation or agglutinate formation) and body size (i.e., regolith maturity), opposite to the observed trend. Band depth and albedo versus spectral slope do not show the expected negative correlation, nor does band depth versus albedo show the expected positive correlation that such mechanisms should produce.

Figure 1 indicates that the apparent abundance of the silicate phases on S-asteroid surfaces decreases with body size up to about 100 km diameter, and thereafter remains relatively constant. This suggests some sort of textural equilibrium has been attained in the optical surfaces of S-asteroids larger than about 100 km diameter but not on bodies below this size. It is possible that 100 km represents the transition to a fully developed regolith. However, the transition from a rocky surface to a particulate surface should increase the band depth, opposite to the observed trend. The observed relationship could be explained by some process that involves selective depletion of the silicate phase in the optical surface layer at larger body diameters to produce some equilibrium silicate/metal abundance ratio substantially lower than that in the substrate. Such a model does not explain the apparently similar (but displaced) trend exhibited by the more strongly featured mafic silicate-dominated A-, R-, and V-type asteroids plus the anomalous S-asteroid 354 Eleonora.

ACKNOWLEDGMENTS: The work carried out by M. J. Gaffey, T. H. Burbine, J. L. Piatek, K. L. Reed, and D. A. Chaky were supported by NSF Solar System Astronomy grant AST-9012180 and by NASA Planetary Geology and Geophysics grant NAGW-642. M. J. Gaffey, J. F. Bell, and R. H. Brown are Visiting Astronomers at the Infrared Telescope Facility which is operated by the University of Hawaii under contract to the National Aeronautics and Space Administration.

REFERENCES: [1] Matson D. L. *et al.* (1977) *Proc. Lunar Plant. Sci. Conf. 8th*, pp. 1001-1011. [2] Horz F. and R. B. Schaal (1981) *Icarus*, **46**, 337-353. [3] McKay D. S. and A. Basu (1983) *Proc. Lunar Planet. Sci. Conf. 14th, J. Geophys. Res. Supp.*, **89**, B193-B199. [4] Wetherill G.W. (1985) *Meteoritics*, **20**, 1-22. [5] Pellas P. (1988) *Chem. Geol.*, **70**, 32. [6] Wetherill G.W. and C.R. Chapman (1988) In *Meteorites and the Early Solar System*. U. Arizona Press, Tucson, pp. 35-67. [7] Gaffey M. J., J. F. Bell, R. H. Brown, T. H. Burbine, J. L. Piatek, K. L. Reed and D. A. Chaky (1993) *Icarus*, submitted. [8] McFadden L. A. *et al.* (1984) *Icarus*, **59**, 25-40. [9] Adams J. B. and A. L. Filice (1967) *J. Geophys. Res.*, **72**, 5705-5715. [10] Clark B. E. *et al.* (1992) *Icarus*, **97**, 288-297. [11] Fanale F. P., B. E. Clark and J. F. Bell (1992) *Icarus* submitted. [12] Bell J. F. and K. Keil (1988) *Proc. Lunar Planet. Sci. Conf. 18th*, pp. 573-580. [13] Britt D. T. *et al.* (1989) *Proc. Lunar Planet. Sci. Conf. 19th*, pp. 537-545. [14] Britt D. T. and C. M. Pieters (1992) *Geochim. Cosmochim. Acta*, submitted. [15] Keil K. *et al.* (1992) *Icarus*, **98**, 43-53. [16] Feierberg M. A. *et al.* (1982) *Astrophys. J.*, **257**, 361-372. [17] Gaffey M. J. (1986) *Icarus*, **66**, 468-486. [18] Basu A. and D.S. McKay (1985) *Proc. Lunar Planet. Sci. Conf. 16th* in *J. Geophys. Res.*, **90**, D87-D94. [19] Belton M.J.S. *et al.* (1992) *Science* **257**, 1647-1652.

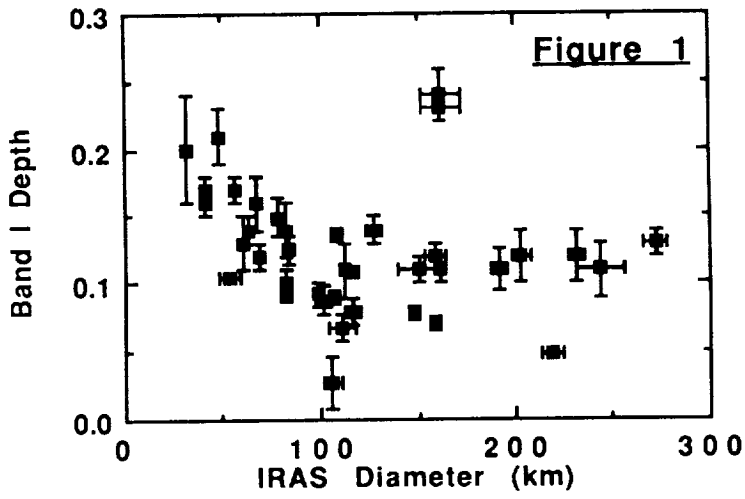

Figure 1

Fe^{2+}-Mg INTERDIFFUSION IN ORTHOPYROXENE: CONSTRAINTS FROM CATION ORDERING AND STRUCTURAL DATA AND IMPLICATIONS FOR COOLING RATES OF METEORITES: J. Ganguly, Dept. of Geosciences, University of Arizona, Tucson, AZ 85721, and V. Tazzoli, Centro di Studio per la Cristallografia Strutturale, Universita di Pavia, Via Bassi, 4, I-27100 Pavia, Italy

Orthopyroxene crystals in a number of meteorites exhibit compositional zoning of Fe and Mg, which provide important constraint on their cooling rates. However, attempts to model cooling rate of these crystals from Fe-Mg zoning profiles [1] suffer from the lack of any measured or theoretically well constrained Fe-Mg interdiffusion data in OPx. It has been assumed that Fe-Mg interdiffusion in OPx is only slightly slower than that in olivine [1]. The purpose of this paper is to (a) calculate the Fe-Mg interdiffusion coefficient (D(Fe-Mg)) in OPx from the available data on the kinetics and thermodynamics of intracrystalline Fe-Mg fractionation and (2) provide analytical formulation relating cooling rate to the length of the diffusion zone across the interface of the overgrowth of a mineral on itself with application to Mg diffusion profile across OPx overgrowth on OPx in certain mesosiderites.

Besancon [2] and Saxena et al [3] have studied the kinetics of Fe-Mg disordering and their equilibrium distributions between the non-equivalent octahedral sites, M1 and M2, at 1 bar, 600 - 800°C. Since the Fe-Mg order-disorder in OPx involves diffusion of Fe and Mg, these data permit an approximation of D(Fe-Mg), within the framework of the Absolute Reaction Rate theory [4], according to which

$$D = \lambda^2 K \qquad (1)$$

in an ideal solution, where λ is the distance between successive equilibrium positions of the diffusing species, and K is the specific rate constant governing the diffusion process. Analysis of the crystal structure of OPx suggests that the diffusion of divalent cation must be fastest parallel to c-axis and slowest parallel to a-axis. Macroscopic diffusion of Fe and Mg in OPx (in response to a compositional gradient) involves both ordering and disordering process (i.e transfer of Fe from M1 to M2 site and the reverse). Thus, in order to calculate D from K according to eqn. (1), we have taken the average of the disordering and ordering rate constants; the latter is derived from the measured values of K(disord) and K_d, using the relation K_d = K(disord)/K(ord) [5,6], where K_d is the intracrystalline distribution coefficient (=(Fe/Mg)M1/(Fe/Mg)M2). In order-disorder process in OPx, the observed effect is the result of (anisotropic) diffusive exchange of Fe and Mg along different directions, but structural considerations suggest that it should be dominated by Fe-Mg exchange parallel to the c- and b-axes. The average distance (λ) between the octahedral sites along these directions is ~3.744 Å. We, thus, obtain from eqn. (1) and the intracrystalline exchange data of [2] and [3],

$$D \approx 3.7(10^{-6})\exp(-27961/T)\ cm^2/s;\ (Q = 55.6\ kcal) \qquad (2a)$$

and

$$D \approx 7.6(10^{-4})\exp(-32{,}159/T)\ cm^2/s;\ (Q = 63.9\ kcal) \qquad (2b)$$

respectively (Q: activation energy), as average of Fe-Mg interdiffusion coefficient in OPx (Mg/(Mg+Fe) ~0.5) along c- and b-axes at fO_2 defined by WI buffer (Fig.1). Theoretical considerations suggest that the change of fO_2 should affect D according to the relation $D \propto fO^{1/6}$ [7,8]. Also the available experimental data on the compositional dependence of K [2] suggest that D should decrease with increasing Mg concentration, and would be about an order of magnitude slower at X_{Mg} ~0.15. Eqn (2) yields Fe-Mg interdiffusion coefficients of OPx, which are of the same order as those in garnet between 600°C and 1000°C [8,9], but are at least 3 orders of magnitude slower than those in olivine [10]. The similarity of Fe-Mg interdiffusion in OPx and garnet is also supported by observational data [11,12].

Assuming that the cooling rate followed an asymptotic relation $1/T = 1/T^\circ + \eta t$, where η is

a cooling time constant ($K^{-1}t^{-1}$) and T° is the initial temperature, we have derived the following relation relating η to the length of the diffusion zone (X) measured normal to the interface of an overgrowth of a mineral on itself when the core and overgrowth have different but initially homogeneous compositions, and are large compared to the length of the diffusion zone.

$$\eta = 64D(T^\circ)R/QX^2 \quad (3),$$

where $D(T^\circ)$ is the diffusion coefficient at the initial temperature T°. In order to use eqn. (3), one needs to correct the measured diffusion profile for the convolution or spatial averaging effect of the microprobe beam as discussed by Ganguly et al. [13]. However, as shown by these workers, the correction is negligible for $X \geq 15$ μm if the profile was measured by a finely focussed beam in a modern electron-microprobe. We have applied eqns. (2) and (3) to calculate the high temperature cooling rate of two mesosiderites, **Lowicz** and **Clover Springs**, on the basis of published Mg zoning profile in OPx/OPx couples and temperature of formation of the overgrowths [1]. The results yield cooling rate ($dT/dt = -nT^2$) of 1-30 K/100 year for Lowicz, and about a factor of ten less for Clover Springs between 600 -1100°C. However, the difference in the length of diffusion zoning between the two samples may be due to different crystallographic orientations of the direction of measurement of concentration profiles. These cooling rates are geologically rapid, but are 3-4 orders of magnitude slower than those estimated earlier [1].

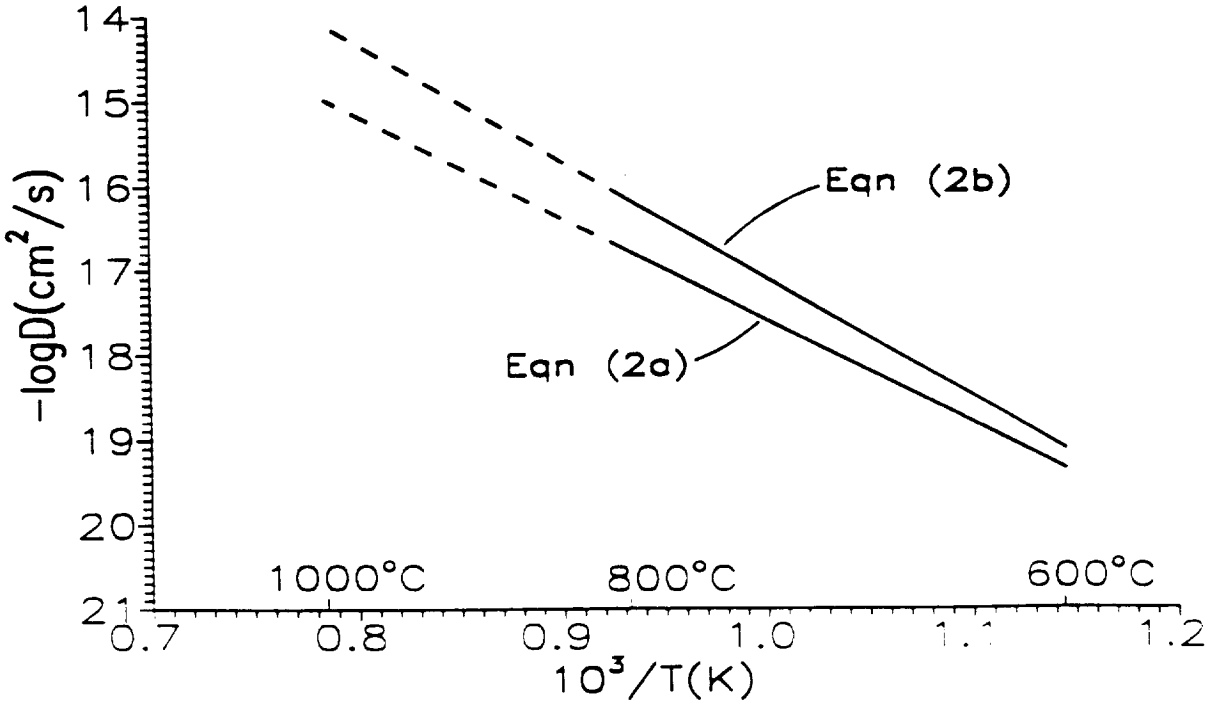

[1] Delaney J. et al. (1981) *Proc. LPS, 12B*, 1315; [2] Besancon J. R. (1981) *Amer Min 66*, 965; [3] Saxena S. K. et al. (1987) *Phys Chem Min 15*, 140; [4] Glasstone S. K. et al. (1941) *The theory of rate processes*. McGraw; [5] Mueller R. F. (1967) *Phys Chem Solids 28*, 2239; [6] Ganguly J. (1982) *Adv Phys Geochem 2*, 58; [7] Buening D. K. and Buseck P. R. (1973) *JGR 78*, 6852; [8] Chakraborty S. and Ganguly J. (1991) *in Ganguly J. ed. Adv Phys Geochem 8*, 120; [9] Chakraborty S. and Ganguly J. (1992) *CMP 111*, 74; [10] Misener D. J. (1974) *In Hoffman A. et al. ed. Geochem Transport & Kinetics. 117*; [11] Smith D. and Barron B. R. (1991) *Amer Min 76*, 1950; [12] Anovitz L. (1987) *Ph.D. Diss. U. Mich*; [13] Ganguly J. et al. (1988) *Amer Min 73*, 901.

CATION ORDERING IN ORTHOPYROXENES AND COOLING RATES OF METEORITES: LOW TEMPERATURE COOLING RATES OF ESTHERVILLE, BONDOC AND SHAW : J. Ganguly, Dept. of Geosciences, University of Arizona, Tucson, AZ 85721, H. Yang, and S. Ghose, Dept. of Geological Sciences, University of Washington, Seattle, WA 98195.

The cooling rates of meteorites provide important constraints on the size of their parent bodies, and their accretionary and evolutionary histories. However, the cooling rates obtained so far from the commonly used metallographic, radiometric and fission-track methods have been sometimes quite controversial, such as in the case of the mesosiderites and the meteorite Shaw. The metallographic method suggests extremely slow cooling rate for the mesosiderites, $\leq$1°C/Ma, which seems difficult to reconcile with the brecciated nature of the silicates in these rocks, suggesting exposure to near-surface environments [1]. For Shaw, which is an L-group chondrite consisting of three intermingled lithologies, the metallographic method suggests a relatively rapid cooling rate, ~3°C/10^3 years at 450-550°C, wherever metal occurs in this meteorite [2], which is in contrast to the very slow cooling rate, 1°C/Ma at T $\leq$ 350°C, deduced by the fission track method [3]. We have undertaken a systematic study of the cooling rates of meteorite using a different approach, which involves single crystal x-ray determination of Fe^{2+}-Mg ordering in orthopyroxenes (OPx) in meteorites, subject to bulk compositional constraints, and numerical simulation of the evolution of the ordering state as a function of cooling rate, within the framework of the thermodynamic and kinetic principles governing cation ordering [4]. In this work, we report the results obtained for OPx crystals from Shaw and two mesosiderites, Estherville and Bondoc.

Five crystals, which appeared well suited for single crystal x-ray study, were used for site occupancy refinement. These crystals did not show any exsolution either in back scattered electron imaging in a scanning electron microprobe or in single crystal x-ray precession photographs. Owing to the sensitivity of cooling rate calculations to site occupancy determinations, especially at low Fe content [5], we have carried out extremely high precision x-ray and microprobe analyses of the crystals, as briefly described below.

Each crystal was ground to nearly spherical shape to facilitate absorption correction, and x-ray intensities of a large number (~2000 - 2800) of non-equivalent reflections from each crystal were determined on an automated single crystal x-ray diffractometer (MoKα rad, 50 kv, 20 mA, scan speed 1.5°/min). Each non-equivalent reflection represents an average of the equivalent (*hkl*) and ($\bar{h}$*kl*) pair. After collection of the x-ray data, all crystals were analyzed in a JEOL electron microprobe, and found to be homogeneous within the precision of probe analysis. The standards consisted of synthetic end-member pyroxenes and garnets. The bulk composition of each crystal was first determined by averaging over 16 spot analyses and then refined by adjusting the concentration of the elements within one standard deviation of the average to meet the following crystal-chemical constraints for six oxygen per formula unit: (a) the total positive charge = 12.000, (b) the total occupancy of T(tetrahedral)-sites = the total occupancy of the M(octahedral)- sites = 2.000, and (c) the difference between the charge deficiency in the T-site (due to substitution for Si) and the charge excess in the M-site (due to substitutions for 2+ ions) = 0.000. The composition of each spot was determined by counting for 100 s at 15 kV accelerating voltage and 25 nA beam current.

The site occupancies of each crystal were refined using the proprietary program RFINE 90, which is an updated version of RFINE4 [6]. It was assumed that all Cr, Ti and Al(VI) were confined to M1 site, Ca and Na were restricted to M2 site, whereas Fe^{2+} and Mn^{2+} fractionated similarly between the two octahedral sites, M1 and M2. The closure temperature (T_c) of the observed ordering state of each crystal (which decreases with decreasing cooling rate) was determined by comparing the intracrystalline Fe(+Mn)-Mg distribution coefficient (K_d) with the

recent calibration of the variation of $\ln K_d$ vs 1/T of an OPx crystal from Johnstown meteorite of similar composition [7], as recently revised by Molin and Ganguly (lnKd = -2914/T + 0.801), following the above procedure of site occupancy refinement. The results are as follows (Fe*= Fe^{2+} + Mn^{2+}; uncertainty: ± 1 σ).

Meteorite	Bondoc		Estherville		Shaw
Crystal No.	1	2	1	2	4
M1 Site:					
Mg	.9791(17)	.9755(20)	.9730(19)	.9724(14)	.9801(16)
Fe*	.0019	.0025	.0060	.0056	.0049
Al	.002	.002	.003	.003	.000
Cr^{3+}	.016	.019	.016	.017	.015
Ti^{4+}	.001	.001	.002	.002	.000
M2 Site:					
Mg	.6495	.6415	.6491	.6516	.6384
Fe*	.3295	.3365	.3249	.3224	.3316
Ca	.020	.022	.026	.026	.027
Na	.001	.000	.000	.000	.003
Rw	.021	.023	.022	.018	.019
T_c(°C)	185	203	288	282	262

Cooling rates were calculated from the above site occupancy data, according to the method developed by Ganguly(4), using the available data on Fe-Mg order-disorder kinetics in orthopyroxene as a function of temperature and composition [8], and assuming an asymptotic cooling law, $1/T = 1/T^\circ + \eta t$, where T° is the initial temperature and η is a cooling time constant ($K^{-1}yr^{-1}$). The calculated cooling rates ($dT/dt = -\eta T^2$) are strictly valid near T_c, and are fairly insensitive to errors in the estimation of T°.

The results suggest that at 250°C, the **Bondoc** meteorite had cooled at $\leq$1 K/Ma, whereas **Estherville** had cooled at ~8 K/Ma. Although the uncertainty of the site occupancy data of the OPx crystals from Estherville permit a cooling rate of $\leq$1 K/Ma, it seems likely that it had cooled somewhat faster than Bondoc since both crystals from Estherville yield essentially the same cooling rate. The ordering state of **Shaw** yields a cooling rate of $\leq$0.3 K/Ma at 250°C and $\leq$4 K/Ma at 350°C; if the site occupancies are recalculated assuming that 50% of Cr is in the 2+ state, the cooling rate increases by a factor of 10. Thus, our result supports the slow cooling rate for Shaw obtained from the fission track method. Further work on Shaw is in progress to determine if it has silicate domains characterized by significantly faster cooling rate of OPx, similar to that deduced from metallographic methods in metal-bearing domains.

[1] Bogard D. et al. (1990) *GCA, 54,* 2549; [2] Taylor G.J. et al. (1979] *GCA, 43,* 323; [3] Pellas P. et al. *LPSC IX,* 879. [4] Ganguly J. (1982), *In Saxena S. K. (ed) Adv Phys Geochem, 2,* 58. [5] Ganguly J. et al. (1989) *LPSC XX,* 331. [6] Finger, L.W. and Prince, E. (1975) *NBS Tech Note 854*; [7] Molin G. et al. (1991) *EPSL, 105,* 261. [8] Besancon JR (1981) *Amer. Min., 66,* 965.

SCR ^{21}Ne AND ^{38}Ar IN LUNAR ROCK 68815: THE SOLAR PROTON ENERGY SPECTRUM OVER THE PAST 2 MYR;

D. H. Garrison[1], M. N. Rao[2], D. D. Bogard (NASA Johnson Space Center, Houston, TX 77058; 1-also Lockheed-ESC; 2-also Lunar & Planetary Inst.), and R. C. Reedy (Los Alamos Natl. Lab., Los Alamos, NM 87545)

Abstract: We determined concentration profiles of ^{21}Ne, ^{22}Ne, and ^{38}Ar produced by solar protons as a function of depth in oriented lunar rock 68815. A comparison with model predictions indicate a solar proton flux J(4π; E >10 MeV) of 100-125 p/cm^2/s and a rigidity R_o of 85-100 MV, assuming an erosion rate of 1-2 mm/Myr. These results for 68815 and similar results on 61016 define the integrated solar proton energy spectrum at the moon over the past ~2 Myr.

Previous Work: For oriented rock 61016, which like 68815 has a simple ~2 Myr exposure history [1], we recently resolved SCR ^{21}Ne, ^{22}Ne, and ^{38}Ar produced by nuclear interactions of energetic (~10-100 MeV) solar protons [2,3]. Concentrations of the SCR component significantly decreased with sample depth and gave the first depth profiles for stable, SCR nuclides. The ^{21}Ne/^{22}Ne ratios produced by solar (SCR) and galactic (GCR) protons were easily resolved. These SCR concentration profiles matched theoretical production profiles for a 4π proton flux above 10 MeV of J = 100 p/cm^2/s and an exponential rigidity spectral parameter [4,5], R_o, between 70 and 85 MV [3]. Several investigators have reported in 68815 the presence of SCR radionuclides [6,7,8,9] and possibly of SCR ^{3}He and ^{21}Ne [10]. The ^{26}Al and ^{53}Mn depth profiles were consistent with $J_{>10}$ = 70 p/cm^2/s and R_o = 100 MV [6]; the profile for SCR ^{14}C (in the same 68815,292 depth column as our samples) yielded $J_{>10}$ = 144 p/cm^2/s at R_o = 85 MV, or $J_{>10}$ = 91 p/cm^2/s at R_o = 100 MV [7]; depth profiles of SCR ^{81}Kr suggested $J_{>10}$ = 160 p/cm^2/s at R_o = 85 MV [8]. The nearly flat depth profile for ^{10}Be in 68815 suggested a softer proton spectral shape than previous work [9].

Experimental: From 10 carefully prepared and documented depth samples (0 to 4.3 cm) of 68815,292, gases were extracted in either two or three temperature steps of 500°C and 1600°C or 350°C, 950°C, and 1600°C. Isotopic abundances were determined by mass spectrometer, using techniques previously described [3]. Chemical composition of the samples (electron microprobe analysis by V. Yang, NASA/JSC) indicated a mixture of 80% plagioclase, 12% olivine/pyroxene, and 8% glass. The Mg concentration is 3.74%.

68815 Results: A 3-isotope correlation plot for all neon data (Fig. 1) indicate mixing between an implanted solar component with ^{20}Ne/^{22}Ne = 12.6 (determined by the surface sample) and a cosmogenic component with variable composition. (All samples released solar-implanted Ne and Ar, some at 1600°C, which we assume was incorporated into high temperature glass phases during breccia formation.) The theoretical field shown for SCR Ne was calculated using the measured major elemental concentrations, and, due to the presence of Mg, lies slightly closer to GCR Ne in 68815 than in 61016. The isotopic variation of cosmogenic Ne in 68815 is attributed to variable mixtures of solar proton-produced (SCR) Ne with galactic-produced (GCR) Ne and is shielding dependent over the range represented by these sample depths. Extrapolation of temperature data for individual samples to cosmogenic ^{20}Ne/^{22}Ne = 0.9 suggests a cosmogenic ^{21}Ne/^{22}Ne end-point for surface samples of ~0.66. This ratio is similar to the SCR + GCR value of 0.64 observed in 61016 and the predicted value of 0.65 for the composition and shielding of 68815.

Total (GCR + SCR) cosmogenic ^{21}Ne and ^{38}Ar concentrations for each sample are plotted vs. depth in Figs. 2a and 2b. Cosmogenic ^{22}Ne concentrations show a profile similar to ^{21}Ne. Surface-implanted neon and argon were removed by lever rule correction assuming trapped ^{20}Ne/^{22}Ne = 12.6 and ^{36}Ar/^{38}Ar = 5.35. Cosmogenic ^{21}Ne and ^{38}Ar comprise 84.5-99.8% and 23-84.6%, respectively, of the total isotopic releases. Since GCR production rates vary little over 0-43 mm, the systematic increase in concentrations of cosmogenic ^{21}Ne and ^{38}Ar with decreasing shielding is due to production by solar protons. These SCR production profiles are similar to the ^{21}Ne and ^{38}Ar profiles found in lunar rock 61016 [2,3] and to radionuclide profiles measured in 68815 [6-9]. Assuming the ^{21}Ne concentration of 0.184 x 10^{-8} cm^{3}STP/g in the deepest sample (42 mm) represents only GCR production, and assuming a production rate of 0.099 x10^{-8} cm^{3}STP/g/Myr [11], we obtain a GCR exposure age of 1.8 Myr. Similarly, the cosmogenic ^{38}Ar concentration of 0.195 x10^{-8} cm^{3}STP/g measured in the same sample and a production rate of 0.11 x10^{-8} cm^{3}STP/g/Myr [11] gives a GCR exposure age of 2.1 Myr. Considering uncertainties in production rates and absolute abundance, these exposure ages suggest that <10% of the ^{21}Ne and ^{38}Ar concentrations in the 42.8 mm sample are due to SCR production.

Solar Proton Energy Spectrum: We now compare the SCR depth profiles with theoretical predictions for different proton fluxes, rigidity, and surface erosion rates. Theoretical SCR + GCR production curves [4,5] are shown (Fig. 2) for a 4π proton flux J (E >10 MeV) of 100 p/cm^2/s and four values of R_o. Each theoretical

profile is normalized to the deepest sample, uses a measured rock density of 2.3 g/cm^3, and assumes a surface erosion rate (Q) of 1 mm/Myr and a depth-constant GCR component. Profile shapes are not especially sensitive to Q or sample density, but are more sensitive to J and R_o [3]. Because variations in J and R_o have opposite effects on the curve fit, only ranges and not unique values can be derived. Additional constraints are the close agreement between calculated and expected GCR exposure ages and the observation that Ne isotopic ratios from the deeper samples fall close to expected GCR values (Fig .1). Both observations indicate <10% SCR production at depths of ~42 mm, and thus provide an upper limit to R_o of ~100 MV. The values of J, R_o, and Q which give the best fit to the data were determined using a least squares technique where all parameters but one were fixed, the optimal value of the variable determined by iteration, and the process repeated for different fixed parameter values. This yielded optimal fit combinations for J = 90-140 p/cm^2/s and R_o = 85-100 MV. For a depth-variable GCR component, the optimal range of values of R_o stays the same, but the values of J and the SCR component at 42 mm depth increase somewhat, the latter usually exceeding our 10% limit. No values of R_o as low as 70 MV gave optimal fits to the data. Values of Q = 0-3 mm/Myr are all possible within these optimal fits; higher values of Q give higher values of J.

Oriented lunar rocks 68815 and 61016 provide our best evidence for the long-term flux and energy spectrum of solar protons. From Ne and Ar results, we conclude that the best parameters to describe the average solar energy spectrum over the past 2 Myr are J = 100-125 p/cm^2/s, R_o = 85-100 MV, and erosion = 1-2 mm/Myr. These ranges can be further constrained by fixing specific parameters. The 68815 and 61016 Ne and Ar profiles imply a solar proton spectrum that is less energetic than that suggested by earlier radionuclide data [6], but similar to more recent radionuclide data [7-9].

References: [1] Walker and Yuhas *Proc. LPSC 4*, 2379-23879 (1973); [2] Rao et al., *LPSC XXII* (abs), 1111 (1991); [3] Rao et al., *J. Geophys. Res., Sp. Phys.*(in press); [4] Reedy and Arnold, *J. Geophys. Res. 77*, 537-555 (1972); [5] Reedy, *LPSC XXIII* (abs), 1133 (1992); [6] Kohl et al., *Proc. LPSC 9*, 2299-2310 (1978); [7] Jull et al., *LPSC 23* (abs), 630-640 (1992); [8] Reedy & Marti, *The Sun in Time*, 260-287 (1991); [9] Nishiizumi et al., *Proc. LPSC 18*, 79-85 (1988); [10] Yaniv and Marti, *Astrophys. J. Lett. 247*, L143-146 (1981); [11] Hohenberg et al., *Proc. LPSC 9*, 2311-2344 (1978).

Fig. 1 (Below) Neon 3-isotope correlation plot for temperature extractions of depth samples of 68815. Uncertainties are ~1% and fall within the symbols. The 350°C data (not shown) represent 0.4-2% of the total release (except 0.1 mm sample). Implanted solar wind and solar flare compositions and the theoretical SCR Ne field produced *in situ* by energetic solar protons are also shown.

Fig. 2 (Right) Cosmogenic ^{21}Ne (upper) and ^{38}Ar (lower) concentrations (symbols) vs. depth from the rock surface. Uncertainties are ~±3%, or approximately twice the symbol size. Sample thickness ranged from ~1mm near the surface to ~3mm at the deepest location. Surface samples with >96% solar-implanted Ne and Ar are not shown. Lines represent theoretical SCR concentrations for the same depths, each normalized to the deepest sample.

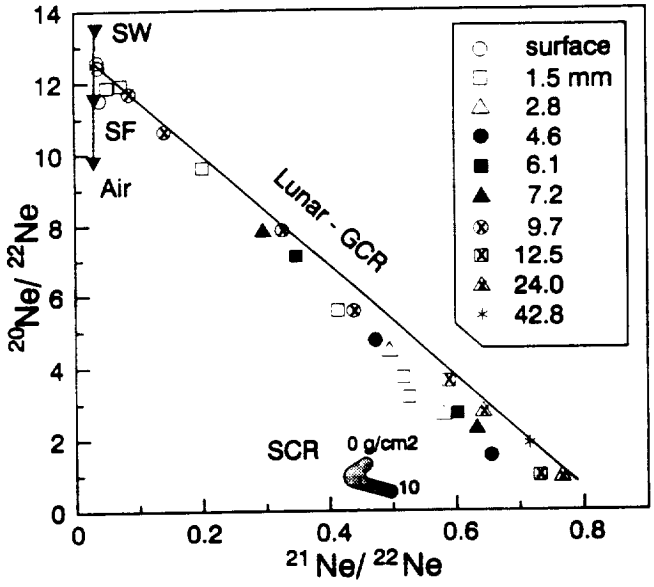

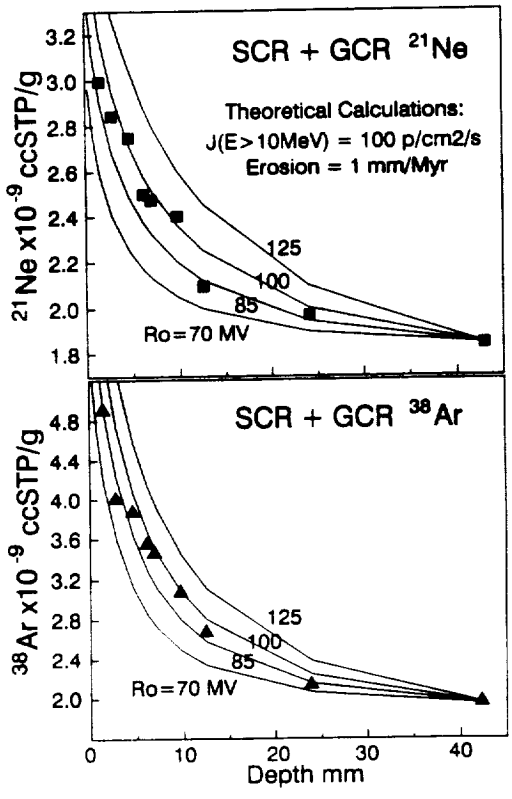

MORPHOMETRIC COMPARISON OF ICELANDIC LAVA SHIELD VOLCANOES VERSUS SELECTED VENUSIAN EDIFICES;

James B. Garvin[1] and Richard S. Williams Jr.[2]; [1]NASA/Goddard, Geodynamics, Code 921, Greenbelt, MD 20771, and [2]U. S. Geological Survey, Branch of Atlantic Marine Geology, Quissett Campus, Woods Hole, MA 02543.

INTRODUCTION: Shield volcanoes are common landforms on the silicate planets of the inner Solar System [1], and a wide variety have recently been documented on Venus by means of *Magellan* observations [2-5]. Head and colleagues [2] have compiled a comprehensive global census of discrete volcanoes on Venus, with a diameter cut-off for equidimensional, shield-like varieties of ~ 25 km. Aubele and colleagues [4] have documented the distribution of clusters of small shield-like volcanoes on Venus ("shield fields"). Most of the apparently conical landforms which define the shield fields are less than 25 km in diameter, and Garvin and Williams [5,7] have argued that many of these volcanoes (so-called "domes" in [4]) are analogous to Icelandic lava shield volcanoes on the basis of their inferred morphology. In this report, we emphasize our recently completed morphometric analysis of three representative Icelandic lava shields: the classic *Skjaldbreidur* edifice, the low-relief *Lambahraun* feature, and the monogenetic *Sandfellshaed* shield [6,8], as a basis for comparison with representative venusian edifices (> 60 km in diameter). Our detailed morphometric measurements of a representative and well-studied set of Icelandic volcanoes (Table 1) permits us to make comparisons with our measurements of a reasonable subset of shield-like edifices on Venus on the basis of Magellan global radar altimetry (i.e., GxDR). Our study has been restricted to venusian features larger than ~ 60 km in basal diameter, on the basis of the minimum intrinsic spatial resolution (8 km) of the Magellan radar altimetry data [9]. Finally, in order to examine the implications of landform scaling from terrestrial simple and composite shields to larger venusian varieties, we have considered the morphometry of the subaerial component of *Mauna Loa*, a type-locality for a composite shield edifice on Earth [1,11] (see Table 1).

THE DATA: As part of our ongoing research concerning subaerial mid-ocean ridge volcanism, we assembled 80 m spatial resolution DEM's for *Skjaldbreidur, Lambahraun, and Sandfellshaed*, as well as for *Mauna Loa* in Hawaii. These data are similar in effective resolution to the typical Magellan radar imaging resolution, but they provide quantitative topographic information at length scales inaccessible to the Magellan altimeter. From our DEM's, we have been able to objectively and systematically measure a set of morphometric parameters suggested by Pike and Clow [11], including average basal diameter D, maximum height H, mean landform volume V, average flank slope, as well as a set of ratio parameters (Table 1). For example, we have been investigating the ratio V/D, a "volume productivity per unit length of edifice" parameter or what we have called "pseudo area" in Table 1. Other ratios include V/SA, the volume to surface area index which can be related to mean landform thickness Te, "coverage" which is simple diameter-normalized thickness, and topographic "skewness" which relates the thickness to maximum volcano height. Both topographic skewness and coverage are dimensionless parameters (Table 1) which can be used to intercompare the morphometries of planetary volcanoes independent of scale. We have computed the series of morphometric statistics listed in Table 1 on the basis of two-dimensional DEM format data. However, for the three Icelandic volcanoes, we have also computed the complete set of parameters on the basis of geodetic aircraft laser altimetry profiles acquired in 1989 and 1991 with meter-scale horizontal resolution and ~ 15 cm vertical control [6]. Because our aircraft laser altimeter topographic profiles are geodetically referenced, we have been able to compare results at meter-scales with those at 100-m scales. The results differ by at most 10-15%. Thus, the values listed in Table 1 for the Icelandic features are derived by calibrating our 80 m resolution DEM data with the 1 m resolution geodetic laser altimeter topographic profiles.

ANALYSIS: In order to calibrate our comparisons of venusian shields versus Icelandic ones, we have considered the average cross-sectional "shape" of each landform (the n parameter in Table 1) by means of a dimensionless polynomial shape factor. If we consider the maximum degree n of that polynomial which best matches the mean topographic cross-section of each edifice in question, then it can be shown that : $n = \{8V\}/\{\pi HD^2 - 4V\}$, where V, H, and D are measured parameters as described above. For example, for typical conical edifices, n is ~1.0 in value, but for more dome-like forms, n increases above 2.0 (paraboloidal). When n values are less than 1.0, the flanks of the volcano are typically *concave*, as is the case for major oceanic shields such as *Mauna Loa* (n = 0.7). A brief examination of the cross-sectional shapes of terrestrial shields (Table 1) demonstrates that the larger, polygenetic varieties (*Mauna Loa, Skjaldbreidur*) have concave flanks on the basis of eruptions which oversteepen the summit at the expense of the lower-gradient flanks. Low lava shields such as *Lambahraun* are more conical, and the most pristine, monogenetic varieties (*Sandfellshaed*) tend to be

slightly paraboloidal. Of all of the *venusian edifices* we have measured (Table 1), only a few have n-values less than 1.0, and most are slightly dome-shaped like *Sandfellshaed*. Only the larger composite shield structures such as *Tepev Mons, Maat Mons, and Sapas Mons* are domical. Some of the un-named low shields (i.e., volcano at 9.4N, 29E) are sub-conical, and apparently resemble the lowest lava shields known in Iceland. In terms of the "pseudo-area" parameter (V/D), many of the sub-100-km scale Venus varieties appear to be statistically similar to *Mauna Loa*, although virtually all of the larger edifices such as *Maat Mons* are at least an order of magnitude larger. Indeed, if one were to use typical high volume eruption rate estimates [10] from terrestrial observations (i.e., from 100 m^3/s to ~ 1000 m^3/s) to investigate eruption lifetimes for the larger venusian edifices such as *Maat*, sustained eruptive activity for up to 0.1 Ma would be required. Typical Icelandic shield building volume eruption rates are probably in the 10-100 m^3/s range, suggesting that large venusian edifices such as *Maat* could be constructed over 0.1 to 1.0 Ma periods by means of essentially quiescent basaltic eruptions. Both *Maat* and *Tepev* resemble larger terrestrial shields such as *Skjaldbreidur* and *Mauna Loa* in terms of our "coverage" parameter, further suggesting that they may represent a reasonable venusian analogue to 10-100 km scale terrestrial basaltic shields. Why such large-scale venusian edifices appear more domical in cross-section than their apparent terrestrial counterparts remains to be explained, but it may be related to the long-term history of flank eruptions required to construct these features. Analysis of our preliminary morphometric results is ongoing, as is our measurement program for all identifiable venusian edifices larger than ~ 60 km in diameter.

REFERENCES: [1] BVSP (1981) *Basaltic Volcanism on the Terrestrial Planets*, Pergamon, NY, 1202 pp. [2] Head J. et al. (1992) *JGR 97*, 13153. [3] Schaber G. (1991) *Proc. LPSC XXI*, p. 3-11. [4] Aubele J. and L. Crumpler (1992) *Int'l Colloq. on Venus*, LPI Contrib. 789, p. 7-8. [5] Garvin J. and R. Williams (1990) *GRL 17*, 1381-1384. [6] Garvin J. and R. Williams (1992) *EOS Trans. AGU, Vol. 73 (43)*, p. 130. [7] Garvin J. and Williams (1991) *LPSC XXII*, p. 431-432. [8] Garvin J. and R. Williams (1992) *EOS Trans. AGU, Vol. 73 (14)*, p. 58-59. [9] Ford P. and G. Pettengill (1992) *JGR 97*, 13103. [10] Whitford-Stark J. (1982) *Earth Sci. Rev. 18*, 109-168. [11] Pike R. and G. Clow (1981) *USGS Open File Report 81-1039*, 40 pp.

TABLE 1: ICELANDIC VOLCANOES VERSUS VENUSIAN SHIELDS

VOLCANO NAME OR LOCATION	DIAMETER D (km)	MAX HEIGHT H (km)	ASPECT H/D	VOLUME V (km^3)	PSEUDO AREA V/D (km^2)	THICKNESS Te=V/SA (m)	SHAPE FACTOR n	SKEWNESS V/SA/H (x1000)	COVERAGE Te/D (x1000)	AVG FLANK SLOPE (degrees)
EARTH:										
MAUNA LOA*	51.2	2.9	0.06	1617	32	779	0.7	266	15.2	6.5
SKJALDBREIDUR	10.6	0.6	0.06	12.7	1.2	141	0.6	235	13.3	6.5
LAMBAHRAUN	7.5	0.14	0.02	2.0	0.3	44	0.9	319	5.9	2.1
SANDFELLSHAED	2.0	0.05	0.03	0.07	0.03	19	1.3	358	9.4	2.9
VENUS:										
TEPEV MONS	196.0	5.7	0.030	99618	508	2500	2.8	439	12.8	3.3
VOLC @ 2.4N, 272E	66.0	1.0	0.020	1771	27	387	2.0	376	5.9	1.7
VOLC @ 26S, 215E	77.0	1.7	0.020	3728	48	592	1.7	344	7.7	2.5
VOLC @ 36N, 21E	62.0	1.0	0.020	1400	23	533	1.6	513	8.6	1.9
VOLC @ 3.6N, 270E	87.0	3.1	0.040	4077	47	518	0.6	169	6.0	4.1
VOLC @ 21N, 91E	100.0	1.5	0.020	5077	51	494	1.6	340	4.9	1.7
VOLC @ 9.4N, 29E	320.0	2.4	0.010	59233	185	568	0.9	241	1.8	0.9
VOLC @ 11N, 174E	104.0	1.5	0.010	5542	53	496	1.5	330	4.8	1.7
VOLC @ 24N, 91E	119.0	2.1	0.020	8596	72	586	1.2	278	4.9	2.0
VOLC @ 14N, 162E	112.0	1.4	0.010	5022	45	384	1.1	272	3.4	1.4
MAAT MONS	312.0	7.5	0.024	354547	1136	3487	3.2	465	11.2	2.7
SAPAS MONS	231.0	2.3	0.010	61760	267	1128	3.6	490	4.9	1.1
SEKMET MONS	253.0	2.5	0.010	53450	211	829	1.5	332	3.3	1.1
ATIRA MONS	174.0	1.0	0.006	9326	54	307	1.3	307	1.8	0.7
VENILIA MONS	305.0	1.2	0.004	40545	133	436	1.6	352	1.4	0.5
RENPET MONS	297.0	2.2	0.007	71711	241	883	1.8	407	3.0	0.8
BACHUE	588.0	2.4	0.004	372289	633	1193	2.7	495	2.0	0.5
VOLC @ 5.7N, 269E	118.0	0.4	0.003	1647	14	116	1.2	290	1.0	0.4
VOLC @ 6.8N, 270E	64.0	0.4	0.006	565	9	135	1.9	375	2.1	0.6
VOLC @ 47S, 215E	186.0	2.4	0.013	29912	161	839	1.7	351	4.5	1.5
VOLC @ 4.6N, 274E	71.0	0.4	0.006	1164	16	227	3.8	504	3.2	0.7

NOTES:

*SUBAERIAL COMPONENT OF COMPOSITE HAWAIIAN SHIELD FROM DMA DTED DATA; ALL OTHER DATA FROM GEODETIC AIRCRAFT LASER ALTIMETER SURVEYS; VENUS DATA FROM MAGELLAN GXDR GLOBAL ALTIMETRY DATASET.

A MINERALIZED ZONE IN WESTERN CANDOR CHASMA, MARS

P.E. Geissler, R.B. Singer and G. Komatsu, Planetary Image Research Laboratory, Department of Planetary Sciences, University of Arizona, Tucson, AZ 85721

Spectral evidence from Viking and Phobos orbiting spacecraft suggests the local development of crystalline ferric oxides in a small region within Mars' equatorial Valles Marineris canyon system [1-5]. This is the same area noted for its anomalous coloration in Viking Orbiter image 583A by McEwen [6]. The unique hue of the region in Viking color data is due to a reduced green filter reflectance, relative to violet and red, in comparison to surrounding materials of similar albedo or average reflectance. For this reason the region does not appear spectrally distinctive in later Survey Mission images which were acquired without the green filter.

In high resolution, the spectral unit can be seen to correspond to two 20 km long depressions on the margins of Candor Mensa, a heavily eroded plateau-forming deposit on the canyon floor (Figure 1). Laminae (layers or erosional benches) are conspicuous in several places on the plateau (marked "L" in Figure 1), particularly within the mineralized depression at the northwestern margin of Candor Mensa where 15 to 20 cycles of alternating bright and dark laminae are exposed at approximately 200 meter vertical intervals. Laminae are also visible on the steep, vertically fluted cliffs to the south of this depression. Concentric laminae ("Lc" in Figure 1) indicate a basin in the depression on the southeastern margin of Candor Mensa at the location of the less pronounced hue anomaly (the toe of the "boot"). A distinct lineation ("F") at the base of the scarp at the western end of the canyon transects mottled canyon floor deposits believed to be among the youngest in the Valles Marineris [7].

Water is implicated in the formation of the iron oxides, since the steep surfaces of layered sediments elsewhere on Candor Mensa show no evidence of unusual coloration despite the fact that these materials were deposited concurrently with the strata exposed in the depressions. This suggests that the mineralization is secondary in nature and developed locally in association with the depressions, which could have ponded surface runoff or groundwater seepage.

References: [1] Komatsu et al., Stratigraphy and Erosional Landforms of Layered Deposits in Valles Marineris, Mars, submitted to J. Geophys. Res., 1992. [2] Geissler, P. and Singer, R., An Unusual Spectral Unit in West Candor Chasma: Evidence for Aqueous or Hydrothermal Alteration? (abs.), MSATT Workshop on Chemical Weathering on Mars, L.P.I. Tech. Rep. 92-04, p. 12-13, 1992. [3] Singer, R. and Geissler, P., An Unusual Spectral Unit in West Candor Chasma: Evidence for Aqueous or Hydrothermal Alteration? (abs.), B.A.A.S., 24, 977, 1992. [4] Geissler et al.., manuscript in prep. [5] Singer et al., this volume. [6] McEwen, A., Temporal Variability of the Surface and Atmosphere of Mars: Viking Orbiter Color Observations (abs.), L.P.S.C. XXIII, 877-878, 1992. [7] Lucchitta, B.K., Young volcanic deposits in the Valles Marineris, Mars, Icarus, 86, 476-509, 1990.

CANDOR CHASMA MINERALIZED ZONE: Geissler, P., R. Singer and G. Komatsu

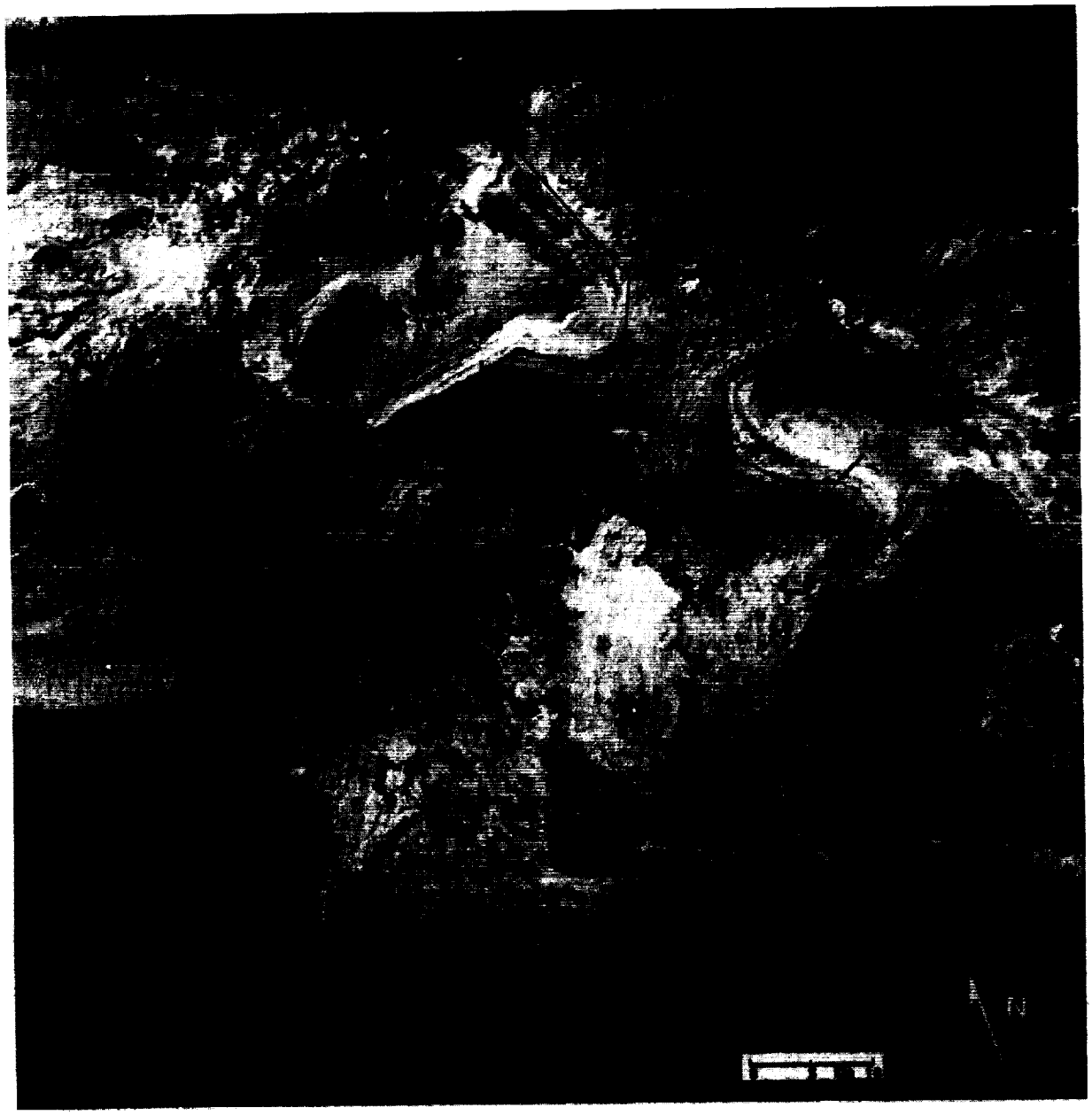

Figure 1. Candor Mensa in Western Candor Chasma.
The spatial resolution of this mosaic of Viking images 065A27, 066A20 and 066A22 is similar to Landsat MSS scenes of the Earth. Shown are the locations of spectrally anomalous regions interpreted to be zones of local enrichment of crystalline ferric oxide minerals. Also shown are the locations of laminae (L), concentric laminae (Lc), and a probable young fault at the western margin of the canyon (F).

TRAPPING OF WATER VAPOR FROM AN ATMOSPHERE BY CONDENSED SILICATE MATTER FORMED BY HIGH-TEMPERATURE PULSE VAPORIZATION.

M.V.Gerasimov (1), Yu.P.Dikov (2), O.I.Yakovlev (3), F.Wlotzka (4). Russian Academy of Sciences: 1 - Space Research Institute, 2 - Institute of Ore Deposits Geology, Petrography, Mineralogy and Geochemistry, 3 - Vernadsky Institute of Geochemistry and Analytical Chemistry; Moscow, Russia. 4- Max-Planck-Institut für Chemie, Mainz, Germany.

The origin of planetary atmospheres is thought to be the result of bombardment of a growing planet by massive planetesimals. According to some models, the accumulation of released water vapor and/or carbon dioxide can result in the formation of a dense and hot primordial atmosphere [1,2,3]. Among source and sink processes of atmospheric water vapor the formation of hydroxides was considered mainly as rehydration of dehydrated minerals (forsterite and enstatite [2]). From our point of view, the formation of hydroxides is not limited to rehydration. Condensation of small silicate particles in a spreading vapor cloud and their interaction with a wet atmosphere can also result in the origin of hydrated phases which have no genetic connections with initial water bearing minerals. Here we present results of two experiments of a simulated interaction of condensed silicate matter which originated during vaporization of dry clinopyroxene (Na- 1.95, Mg- 7.13, Al- 4.29, Si-18.00, Ca- 6.05, Ti- 0.31, Fe- 2.51 at.%) in a wet helium atmosphere.

As in our previous experiments [4,5,6] vaporization was provided by use of laser pulses of a powerful neodymium laser focused on a sample which was mounted in a hermetic cell with a volume ~500 cm^3. Parameters of the pulse are: luminous energy ~600 J, duration ~10^{-3} s, density of luminosity ~ $5x10^6$ W/cm^2. Estimated temperature of vaporization is 3000-4000 K. The cell was continuously flushed with wet He at a rate ~50 cm^3/min. In the first experiment water vapor was saturated at 22 C and in the second at ~100 C, what corresponded to about 20 mbar and 1 atm. partial water vapor pressure. A noticeable amount of condensed particles with dimensions from 50 to 1000 A originated in a spreading hot cloud [5] which interacted with the ambient atmosphere inside the cell. A certain amount of condensed material was collected on a filter which was placed at an outlet of the cell. Another part of the condensate was collected on a Ni-foil which was placed 8 cm from the sample on the path of the spreading vapor cloud. Chemical analyses of condensate was made using X-ray photoelectron spectroscopy (XPS) which provided both analyses of chemical composition and of chemical structure of the condensate. The condensate from the filter was analyzed by XPS and by transmitted electron microscopy (TEM) technic. The concentration of hydrogen was calculated from the sum of hydroxide bonds of the elements. Comparison of the amount of hydroxide groups calculated from the sum of phases of elements and from the spectral line of oxygen gives a good correlation.

XPS analyses reveal the formation of hydroxide bonds in the condensed silicates with practically all rockforming elements except Ca. Mg forms hydroxide bonds the most effectively providing ~60% of all hydroxides. About 20% of hydroxides are formed by Si and Al respectively.

Despite the large difference in partial pressure of water vapor in the two experiments the concentration of hydroxides in condensed films is practically the same in both cases. Concentration of trapped water in the bottom layers of condensed film is 10-12 wt.% and in the upper layers is 4-6 wt.%. While the front parts of the spreading vapor cloud are condensing

on the film in the bottom layers, the formation of hydroxides in the front compressed part of the vapor cloud interacting with wet atmosphere seems more effective then in the back parts of the cloud. XPS analyses of the condensate which was collected on the filter shows its identity with condensate in the upper layers of the condensed film. TEM analyses shows the presence of particles with crystal structure.

The results of these experiments are interesting to compare with results of our previous experiments in which the same sample of clinopyroxene was evapo-rated in a dry helium atmosphere and the same analytical procedure was applied to the condensed film [5]. An important difference between this two sets of experiments is the presence of noticeable amounts of reduced forms of elements (~9% of silicon in the form of Si^0 and Si^{2+}, ~15% and ~7% of metallic Al and Fe integrated through the volume of the film) in the dry experiment and their absence in experiment with water vapor. The absence of reduced forms of elements in the wet experiment demonstrates the oxidizing role of water molecules in the vapor cloud. The ratio of Fe^{3+}/Fe^{2+} is noticeably higher in the experiment with saturation of water vapor at 100 C compared with the experiment at room temperature. This observation also reveals the role of water as oxidizing component in the vapor cloud. In the dry experiment the condensed film was exposed to open air for some hours before XPS analyses and could interact with atmospheric water vapor. No detectable hydroxide phases were formed during this period. This suggests that the formation of hydroxides occurs at higher temperature conditions but probably not higher than dehydration temperature.

Another important result proving the trapping of water vapor during impact processes is the discovery of hydroxide phases in the condensed film which was produced in light-gas-gun shock experiment with serpentinite target and copper projectile (v_{imp} ~5.89 km/s) [7]. The condensate in this experiment was collected on special screens at a distance of 7-10 cm from the center of impact. Shock experiment was performed in air at 30 mbar pressure. Water vapor was injected inside the vapor cloud as a result of the dehydration of the serpentinite target. Analyses of condensed film shows uniform concentration of hydroxides through the depth of the film. Trapped water amounts to ~10 wt.% of the condensate. About 60% of Mg and 9% of Si is present as hydroxides.

These experimental results prove the possibility of effective trapping of water vapor from an atmosphere by dispersed hot silicate condensed matter. The experiment shows that trapped water can amount to ~10 wt.% of condensate mass even at rather low water vapor pressure in the atmosphere. The effectivity of the hydration process shows that it must be taken into account in evolutionary models of atmosphere formation.

REFERENCES: [1] T.Matsui, Y.Abe. Earth, Moon and Planets 34, 1986, 223. [2] M.A.Lange, T.J.Ahrens. Icarus 51, 1982, 96. [3] K.J.Zahnle, J.F.Kasting, J.B.Pollack. Icarus 74, 1988, 62. [4] L.M.Mukhin, M.V.Gerasimov, E.N.Safonova. Nature 340, 1989, 46. [5] Yu.P.Dikov, M.V.Gerasimov, L.M.Mukhin, F.Wlotzka. Lunar Planet. Sci. XXI, 1990, 289. [6] M.V.Gerasimov, L.M.Mukhin, Yu.P.Dikov, V.I.Rekharsky. Vestnik Acad. Nauk USSR, 1985, No9, p. 10 (in Russian). [7] O.I.Yakovlev, M.V.Gerasimov, Yu.P.Dikov. Geokhimiya, No 12, 1992 (in Russian).

PARGO CHASMA AND ITS RELATIONSHIP TO GLOBAL TECTONICS; R.C.Ghail, Environmental Science Div., Lancaster University, Lancaster LA1 4YQ, U.K.

Pargo Chasma was first identified on Pioneer Venus data as a 10 000 km long lineation extending from Atla Regio (3° north latitude, 200° east longitude) in the north terminating in the plains south of Phoebe Regio (latitude 40° south, longitude 290° east). More recent Magellan data have revealed this feature to be one of the longest chains of coronae so far identified on the planet. Stofan *et al.* [1] have identified 60 coronae and 2 related features associated with this chain; other estimates differ according to the classification scheme adopted, for example Head *et al.* [2] identify only 29 coronae but 43 arachnoids in the same region. This highlights one of the major probems associated with the preliminary mapping of the Magellan data: there has been an emphasis on identifying particular features on Venus without a universally accepted scheme to classify those features. Nevertheless, Pargo Chasma is clearly identified as a major tectonic belt of global significance. Together with the Artemis-Atla-Beta tectonic zone and the Beta-Phoebe rift belt, Pargo Chasma defines a region on Venus with an unusually high concentration of tectonic and volcanic features. Thus an understanding of the processes involved in the formation of Pargo Chasma may lend significant insight into the evolution of the region and the planet as a whole.

I have produced a detailed 1 to 10 million scale map of Pargo Chasma and the surrounding area from preliminary USGS controlled mosaiced image maps of Venus constructed from Magellan data. In view of the problems highlighted above in relation the efforts already made at identifying a particular set of features I have mapped the region purely on the basis of the geomorphology visible in the Magellan data without any attempt at identifying a particular set or class of features. Thus the map produced distinguishes between areas of different brightness and texture. This has the advantage of highlighting the tectonic fabric of Pargo Chasma and clearly illustrates the close inter-relationship between individual coronae and the surrounding tectonic belts. The difficulty faced in attempting to identify individual tectonic features within this belt is apparent. A useful, though much simplified, classification scheme has been identified from the geomorphological map: the ejecta deposits associated with impact craters may be identified by their bright, rough appearance; radiating bright (rough) and dark (smooth) flows locate the presence of volcanic vents, while corona may be identified by their bright lineated annuli.

More detailed mapping of specific areas of Pargo Chasma, along with several neighbouring regions that may or may not be related to it, remains to be done. The initial map has however proved useful for formulating ideas as to how Pargo Chasma formed and evolved. The topographic form, length and the fact that it lies on a great circle has led to the suggestion that the corona chain may be related to upper mantle plumes or circulation patterns akin to that associated with mid-oceanic ridges on Earth but without the significant horizontal plate motion found on Earth. These ideas require further investigation and testing but may provide an insight into the state of the upper mantle of Venus and the tectonic style of the planet.

References

[1] Stofan, E.R., Sharpton, V.L., Schubert, G., Baer, G., Bindschadler, D.L., Janes, D.M. and Squyres, S.W. (1992) J. geophys. Res., 97,13347-13378.

[2] Head, J.W., Crumpler, L.S., Aubele, J.C., Guest, J.E. and Saunders, R.S. (1992) J. geophys. Res, 97, 13153-13197.

FIRST OXYGEN FROM LUNAR BASALT

M. A. Gibson[1], C. W. Knudsen[1], D. J. Brueneman[1], H. Kanamori[2], R. O Ness[3], L. L. Sharp[3], D. W. Brekke[3], C. C. Allen[4], R. V. Morris[5], L. P. Keller[5], D. S. McKay[5]. [1]Carbotek Development Laboratories, Houston TX, [2]Shimizu Corporation, Tokyo JAPAN, [3]Energy and Environmental Research Center, Grand Forks ND, [4]Lockheed Engineering and Sciences Co., Houston TX, [5]NASA Johnson Space Center, Houston TX.

Introduction. The Carbotek/Shimizu process to produce oxygen from lunar soils has been successfully demonstrated on actual lunar samples in laboratory facilities at Carbotek with Shimizu funding and support . Apollo sample 70035 containing approximately 25 % ilmenite ($FeTiO_3$) was used in seven separate reactions with hydrogen gas varying temperature and pressure: $FeTiO_3 + H_2$ ---> $Fe + TiO_2 + H_2O$. The experiments gave extremely encouraging results as all ilmenite was reduced in every experiment. The lunar ilmenite was found to be about twice as reactive as terrestrial ilmenite samples. Analytical techniques of the lunar and terrestrial ilmenite experiments performed by NASA Johnson Space Center include iron Mossbauer spectroscopy (FeMS), optical microscopy, SEM, TEM, and XRD. The Energy and Environmental Research Center at the University of North Dakota performed three SEM techniques (point count method, morphology determination, elemental mapping), XRD, and optical microscopy.

Experimental. 10.000 grams of lunar sample 70035 were obtained from NASA for this experimental work. The sample contains pyroxene, ilmenite, plagioclase, and minor olivine. The basalt was crushed in a nitrogen blanketed glove box using a mortar and pestle and exhibited a surface/volume mean particle diameter of about 240 microns. Reduction with hydrogen proceeded in seven tests at temperatures of 900-1050°C and pressures of 1-10 atmospheres [1]. A capacitance probe, measuring the dew point of the gas stream, was used to monitor the reaction.

Reaction Kinetics and Implications. Reduction of the lunar basalt was extremely rapid, with major evolution of water occurring within minutes after the introduction of hydrogen. The data were best represented by a shrinking-core process in which both chemical reaction and diffusion play significant roles. Reaction rate showed only a 0.15-order dependence on hydrogen concentration. Rate and diffusion constants were such that, at comparable conditions of 1000°C and 10 atm., lunar ilmenites were initially about twice as reactive as the pure terrestrial ilmenites. The reduction of terrestrial MLS-1 basalt by hydrogen at 1100°C was also rapid, with major evolution of water occurring within minutes after the introduction of hydrogen.

In comparison to pure terrestrial ilmenite, the lunar sample reactivity starts out much higher than the terrestrial sample and falls much more steeply with time. This difference in reactivity behavior has important implications for both kinetic and reactor modeling as it affects both residence time and reactor sizing. It also indicates the inadequacy of relying solely on simulant materials for this type of research.

The resulting implications for a lunar oxygen plant can be determined. The predicted maximum output from a lunar oxygen plant is directly proportional to the ilmenite content of the feedstock. Most lunar rocks and soils that contain FeO and TiO_2 have essentially all titanium present as part of the ilmenite. Thus ilmenite abundance is proportional to the sample's titanium content. The expected oxygen yield is equal to 20 wt% of the feedstock's TiO_2 content assuming only FeO in ilmenite is reduced. Based on abundances of TiO_2 in representative Apollo basalt and soil samples, a lunar plant using the hydrogen reduction process would require about 40 tons of high-titanium regolith feedstock to produce each ton of oxygen [2].

Solid Sample Analysis. Ilmenite The FeMS spectrum of unreacted lunar basalt 70035 contains doublet peaks characteristic of ilmenite and pyroxene, the two major iron-bearing phases. The spectrum of the 900 °C sample (Figure 1) shows the sextet of peaks characteristic of iron metal, along with the pyroxene doublet. The ilmenite peaks are not detectable, indicating essentially complete reduction of the Fe^{2+} in this mineral. This was the case for all reacted lunar samples.

All of the reacted ilmenite grains examined by optical microscopy and SEM display characteristic phase separation textures. Ilmenite in the 900 °C sample contains generally parallel stringers of iron metal approximately 1 micrometer wide and tens of micrometers in length, in a matrix of titanium oxide

(Figure 2). The texture is uniform from the edge to the center of each grain. Samples reacted at 1000 and 1050 °C feature slightly wider and less regular stringers, along with clusters of submicrometer iron blebs. These samples commonly show iron metal concentrated on grain surfaces. From SEM photographs, the porosity of iron metal and titanium oxide from reduced ilmenite was estimated at 21%. This compares very well with values calculated from the density differences between ilmenite, Fe, and TiO_2 products.

Titanium Oxide The reduction of ilmenite yields iron metal plus a residue of TiO_2. In fact, the latter phase can also be reduced under suitable conditions. The reduction of TiO_2 involves a series of suboxides with the general formula Ti_nO_{2n-1}, known as magneli phases. The phase produced in a given reaction is a sensitive function of temperature and oxygen fugacity.

X-ray diffraction patterns of the reduced lunar samples show no detectable TiO_2, but do include peaks attributable to titanium suboxides. Phases include Ti_7O_{13}, Ti_6O_{11}, and Ti_4O_7. High-resolution TEM analysis of the 1050 °C sample confirms the epitaxial intergrowth of a disordered combination of Ti_6O_{11} and more reduced titanium oxides.

Pyroxene The major iron-bearing phases in lunar basalt 70035 are the clinopyroxenes augite ($Ca_{37}Mg_{47}Fe_{16}$) and pigeonite ($Ca_7Mg_{64}Fe_{29}$). The FeMS spectra of both the starting lunar basalt and the reacted samples are dominated by the pyroxene doublet. The majority of iron atoms in pyroxene within the reacted samples thus remain in the ferrous oxidation state, while most of the iron metal was derived from reduction of ilmenite.

Evidence of limited pyroxene reduction is present in the analytical data, however. The FeMS spectrum of unreacted lunar basalt shows 23% of the total peak area occupied by ilmenite and 77% by pyroxene. The spectrum of the 900 °C sample (Figure 1) shows 36% of the total peak area occupied by the iron metal sextet and 64% by pyroxene. This decrease in the relative total area of the pyroxene peaks is qualititative evidence that a portion of the Fe^{2+} in the pyroxene of this sample was reduced to iron metal. Again, this reduction is sensitive to temperature and hydrogen-to-water ratio.

Olivine Olivine crystals in high-Ti Apollo 17 basalts have FeO concentrations of 27-28 wt% (Fa_{30-32}). The abundance of olivine in sample 70035 is too low to permit its detection by either FeMS or XRD. The SEM images of rare olivine grains, however, show evidence of small-scale phase separation. Olivine crystals display scattered submicrometer iron blebs on exterior surfaces and narrow iron-filled veins and cracks extending tens of micrometers into the interiors.

Plagioclase Lunar anorthite generally contains less than 1 wt% FeO. No change in this mineral in any of the reacted lunar basalt samples was observed. The XRD peak positions are unchanged from those of the starting basalt. None of the SEM images shown any sign of phase separation nor decoration of plagioclase grains with iron metal.

References. [1] Ness, R. O., Jr., L. L. Sharp, D. W. Brekke, C. W. Knudsen, and M. A. Gibson (1992) in *Engineering, Construction and Operations in Space III*, Am. Soc. Civil Eng., New York, pp. 617-628. [2] Allen, C. C., M. A. Gibson, C. W. Knudsen, H. Kanamori, R. V. Morris, L. P. Keller, and D. S. McKay (1992) in *Workshop on Geology of the Apollo 17 Landing Site*, Lunar and Planetary Institute, Houston, pp. 1-2.

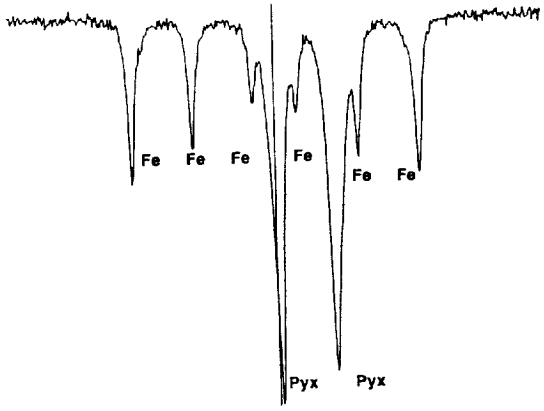

Fig. 1 FeMS spectrum of lunar basalt 70035 reacted at 900°C. Fe = iron metal Pyx = pyroxene

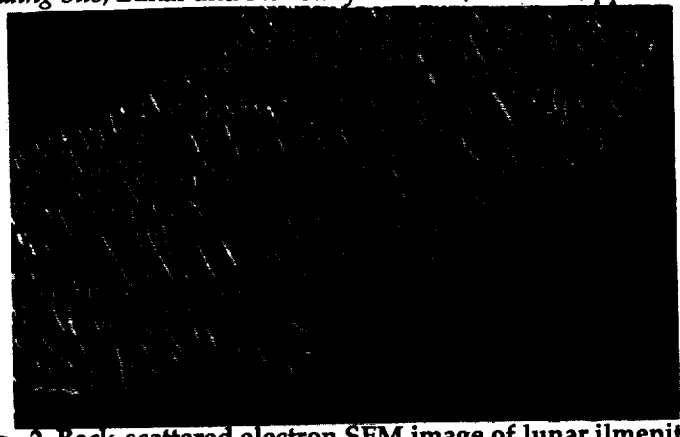

Fig. 2 Back-scattered electron SEM image of lunar ilmenite grain reacted at 900°C. Bright stringers of iron metal are set in darker titanium oxide. Frame width = 350 μm.

THE FORMATION AND EVOLUTION OF ALPHA AND TELLUS TESSERAE ON VENUS: M. S. Gilmore and J. W. Head, Department of Geological Sciences, Brown University, Providence, RI 02912.

Although tesserae comprise ≈10% of the surface of Venus, the nature of their formation and evolution is not well understood [1]. One important clue to elucidate this problem is tessera boundaries which are of two types: Type 1 are generally embayed by plains; Type II boundaries are characterized by being linear at the hundred kilometer scale and often associated with steep scarps or tectonic features [2,3]. Previous study of a distinctive Type II boundary at Alpha Regio [4] was pursued in order to characterize and assess the implications for this style in general. A model of gravitational relaxation of the tessera block was presented to explain the specific style of Type II feature seen at western Alpha [4]; however, this model cannot account for the full range of interior structures of Alpha, namely widespread compressional features overprinted by extensional features and volcanism. In order to explain the features of Alpha we have considered a three-stage model involving 1) mantle downwelling and compression of the lithosphere 2) delamination of the thickened tessera root and 3) gravitational relaxation and extension of the tessera plateau. We compare this to the characteristics of Tellus Regio in order to test its broader application.

Alpha Regio. The western (Type II) boundary of Alpha Regio contains ridges and troughs that trend northeast and extend into the adjoining plains. These are joined by a second set of extensional features that extend northwest from the tessera into the plains for several hundred kilometers. The number and spacing of these lineaments were used to define six plains units west of Alpha; the most deformed plains units were almost indistinguishable from tessera. Additionally, the tessera along western Alpha contains numerous domes, pits, and small shield volcanoes that are very similar to the array of shield volcanoes that have been mapped on the Venus plains [5]. The fractured plains units and domes are the primary clues that western Alpha Regio may consist of plains that are sequentially deformed, tilted, and uplifted, ultimately being incorporated into the tessera.

Inter-tessera plains (ITP) in Alpha comprise approximately 10% of its surface area. They range in size from 20 -200 km in length and may contain several episodes of volcanism, the oldest of which has suffered some regional deformation in many cases. The ITP are elongate to circular in shape, and most have associated concentric ridges and scarps. Small shields and fissures are also present in many of the ITP. In Alpha, no volcanism in the interior of the tessera exists outside the ITP.

Tellus Regio. Type II boundaries comprise 34% of the boundary of Tellus [6]. Six hundred kilometers of the northeast border of Tellus has features similar to the western boundary of Alpha. Large graben up to 10 km in width extend NE from the interior of Tellus into the adjoining plains unit. Many of these graben contain pit craters and seem to originate from within inter-tessera plains 200 km into the tessera. The edge of the tessera contains small domes and pits that predate and postdate graben formation. Two plains units can be distinguished, the southernmost of which has more fractures than the northern. The extensional deformation at this Type II boundary of Tellus seems to incorporate plains lavas.

Inter-tessera plains comprise perhaps up to 15% of the surface of Tellus, but this is difficult to constrain as the northern part of Tellus has been flooded by a combination of interior and exterior plains lavas. Individual ITP may range from 25 - 200 km in length and several ITP are connected into systems as large as 400 X 100 km. The ITP in Tellus are generally more rounded than those in Alpha, having a circular to oval shape. They are surrounded by concentric ridges and may also have extensional features perpendicular to their borders. Like Alpha, these plains display multiple episodes of volcanism, domes and fissures, and regional extensional features in their older flow units. Volcanism is not confined to the ITP in Tellus, however, it extends in many places to flood the graben and extensional features that are dominant in this tessera block. Plains units have encroached into the interior of Tellus; this may be due to the fact that the base of Tellus (planetary radius of 6052 km) is at a lower elevation than Alpha (6052.5 km) [7].

Models proposed to explain the characteristics at Alpha and Tellus must be consistent with several other features of both tessera: 1) the earliest deformation of the tessera block was compressional, characterized by complex thrust and strike-slip faulting; these compressional features

are overprinted by later graben and extensional faults [2]; 2) the presence of mostly undeformed inter-tessera plains up to 200 km in length; 3) the lineaments at western Alpha and northeastern Tellus have occurred relatively recently in the history of the plateau as they cross-cut all other features both in the tessera and in the plains; 4) in general, Type II boundaries do not extend over the entire margin of the tessera block.

Although both upwelling [8] and downwelling [7] have been proposed, mantle downwelling is becoming a preferable mechanism for the formation of tessera on Venus [9,10]. Downwelling would produce a topographic low initially, followed by convergence and subsequent thickening of the crust; uplift would continue until the crustal block isostatically compensates [9]. This can easily produce the compressional features seen in tessera but cannot explain as well the interior volcanism and graben.

During convergence, the mantle portion of the lithosphere should thicken along with the crust, protruding into the warmer asthenosphere [11]. This is gravitationally unstable as the mantle portion of the lithosphere is more dense than the asthenosphere below it [12]. Downward convection could delaminate the unstable upper mantle most likely at the crust-mantle boundary [11,12]. Hot asthenosphere would rise replacing the lost lithosphere, pooling at the base of the crust. This asthenosphere would undergo partial melting by adiabatic decompression and may also melt crustal material. Extension would occur because of the added heat allowing dikes to propagate perhaps to the surface or collecting in magma chambers in the upper crust. These magma chambers could then be the source for the inter-tessera plains which contain domes and small shield volcanoes as well as fissures. The rounded shape of the ITP, especially in Tellus Regio, is consistent with their being sites of diapiric upwellings of magma. The inter-tessera plains have multiple flow units; the oldest unit in the sequence is frequently overprinted with regional extensional features. This is consistent with ongoing extension and volcanism being the latest stages in tessera evolution.

As the hot mantle beneath the tesserae reequilibrates, the tessera block will subside due to gravitational relaxation which is favored under Venus conditions of high temperature and low erosion rates [13,14]. Volcanism and extensional features will become more widespread within the interior of the block. Indeed, Tellus Regio may represent this stage of tessera evolution. Compared to Alpha Regio, Tellus has more pervasive lava units within inter-tessera plains and filling most of the graben within the tessera block. Extensional features are so dominant in Tellus that few compressional structures are observable [7]. Lavas from the plains units adjacent to Tellus embay most of its boundary and have encroached upon the interior of the tessera.

Summary. Downwelling caused by mantle convection or instabilities in a depleted mantle layer could cause compression and thickening of the crust [9]. This compression would result in the thrust and strike-slip faulting seen at the surface of the tesserae [2]. Cessation of this downwelling may produce the late-stage extensional features and volcanism of Alpha and Tellus; this may be caused by a delamination event in the mantle portion of the lithosphere or along the basalt-eclogite transition in the thickened crustal root. The tessera block could then isostatically compensate and reequilibrate, and eventually gravitational relaxation becomes dominant. This relaxation is expected to produce deformation perpendicular to topographical slope at the edges of the tessera block [14]; as this relaxation continues, deformation would spread outward from the tessera into the surrounding plains.

REFERENCES: [1] Basilevsky, A. T., *et al.*. (1986) *J. Geophys. Res.*, *91*, D399. [2] Bindshadler, D. L., and Head, J. W. (1991) *J. Geophys. Res.*, *96*, 5889. [3] Ivanov, M. A., *et al.*. (1992) *LPSC XXIII*, 581. [4] Gilmore, M. S., and Head, J. W. (1992) *Abs. Int. Colloq. Venus* . [5] Aubele, J. *et al.*. (1992) *LPSC XXIII*, 47. [6] Ivanov, M. A., and Head, J. W. (1993) this volume. [7] Bindshadler, D. L. *et al.*. (1992) *J. Geophys. Res.*, *97*, 13495. [8] Philips, R. J., *et al* . (1991) *Science, 252*, 651. [9] Bindshadler, D. L., and Parmentier, E. M. (1990) *J. Geophys. Res.*, *95*, 21329. [10] Bindshadler, D. L. *et al.*. (1992) *J. Geophys. Res.*, *97*, 13563. [11] Loosveld, R. J. H., and Etheridge, M. A. (1990) *J. Metamorph. Geo.*, *8*, 257. [12] Bird, P. B. (1979) *J. Geophys. Res.*, *84*, 7561. [13] Weertman, J. (1979) *Phys. Earth. Plan. Int.*, *19*, 197. [14] Smrekar, S. E., and Solomon S. C. (1992) *J. Geophys. Res.*, *97*, 16121.

EXTRACTION AND ISOTOPIC ANALYSIS OF MEDIUM MOLECULAR WEIGHT HYDROCARBONS FROM MURCHISON USING SUPERCRITICAL CARBON DIOXIDE: Iain Gilmour and Colin Pillinger, Dept. of Earth Sciences, The Open University, Milton Keynes, UK.

The large variety of organic compounds present in carbonaceous chondrites poses particular problems in their analysis not the least of which is terrestrial contamination. Conventional analytical approaches employ simple chromatographic techniques to fractionate the extractable compounds into broad classes of similar chemical structure. However, the use of organic solvents and their subsequent removal by evaporation results in the depletion or loss of semi-volatile compounds as well as requiring considerable preparative work to assure solvent purity. Supercritical fluids have been shown to provide a powerful alternative to conventional liquid organic solvents used for analytical extractions [1]. Besides their strong solvating ability, supercritical fluids have several characteristics that make them useful for the quantitative recovery of organic compounds from carbonaceous chodrites. The solvent strength of a supercritcal fluid is directly related to its density so that modification of the extraction pressure and temperature enables species of different solubility to be extracted. The polarity of a supercritical fluid can also be controlled by the addition of solvent modifiers such as methanol. The low critical temperature of a supercritcal fluid such as carbon dioxide (31°C) can be used to avoid the decomposition of thermally labile components. Finally, although liquid when in the supercritical state fluids such as carbon dioxide retain the low viscosity and subsequent penetration of the sample matrix of a gas; after the extraction the use of a gas makes sample recovery much simpler.

A sample of Murchison from the Field Museum (courtesy E.Olsen) was used for these analysis. Two interior fragments were used; the first (2.85 g) was crushed in an agate pestel and mortar to a grain size of ca. 50-100 μm, the second (1.80 g) was broken into chips 3-8 mm in size. Each sample was loaded into a stainless steel bomb and placed in the extraction chamber of an Isco supercritical fluid extractor maintained at 35°C. High purity (99.9995%) carbon dioxide was used and was pressurised using an Isco syringe pump. The samples were extracted dynamically by flowing CO_2 under pressure through the bomb and venting via a 50 μm fused silica capillary into 5 mls of hexane used as a collection solvent. The hexane was maintained at a temperature of 0-5°C. A series of extractions were done on each sample (Table 1) using CO_2 of increasing density.

Pressure (psi)	Density CO_2 g/ml	Solubility (Hildebrand)	Time (mins)	Principal Components extracted
1927	0.801	6.828	30	Aliphatic hydrocarbons + mono and di-aromatics
3000	0.878	7.486	30	Polycyclic aromatics + S
5000	0.958	8.160	10	Trace Polycyclic aromatics
7000	1.022	8.708	90	No detectable compounds

The principal components extracted in each fraction are summarized in the table. Fig 1 shows the GCMS results for the 1927 psi fraction. The extractable organics are dominated by naphthalene and by straight chain hydrocarbons, isoprenoid hydrocarbons, and a homologous series of alkyl cyclohexanes and a broad hump due to cycloalkanes. With the excpetion of the relatively high abundance of naphthalene the results are very similar to those obtained in benzene-methanol extracts by Cronin and Pizzarello [2]. The 3000 psi extract was dominated by phenathrene, fluoranthene and pyrene, the three most abundant PAH in Murchison, and by a large peak due to S_8. The minor components were thiophene, dibenzothiophene, methyl dibenzothiophenes, methyl phenanthrenes, and methyl pyrenes. No traces of higher molecular weight PAH were found. The 5000 psi extract contained very few compounds, those that were detectable were apparently trace quantities of PAH similar to the 3000 psi extract. No compounds were found in the 7000 psi extract. In would appear that supercritical CO_2 by itself is an efficient means of separating polar from non-polar compounds.

The alkanes, isoprenoid alkanes and alkyl cyclohexanes (all common petroleum hydrocarbons) were identified by Cronin and Pizzarello [2] as terrestrial contaminants as they were found at higher abundances in exterior compared to interior samples. Their presence here in interior chips of Murchison highlights the susceptability of carbonaceous chondrites to atmospheric hydrocarbon contamination. We

have previously confirmed the indigeneity of PAH from measurements on the $\delta^{13}C$ values of individual compounds (3), however, volatile PAH like naphthalene and methyl naphthalenes are also common petroleum hydrocarbons. Isotopic measurements of these compounds will be necessary to confirm their indigeneity, however, the use of supercritical carbon dioxide at 35°C greatly reduces the possibility that these and other free PAH in Murchison are cracking products of the macromolecular material produced either during extraction with organic solvents at elevated temperatures or by rigorous ultrasonication.

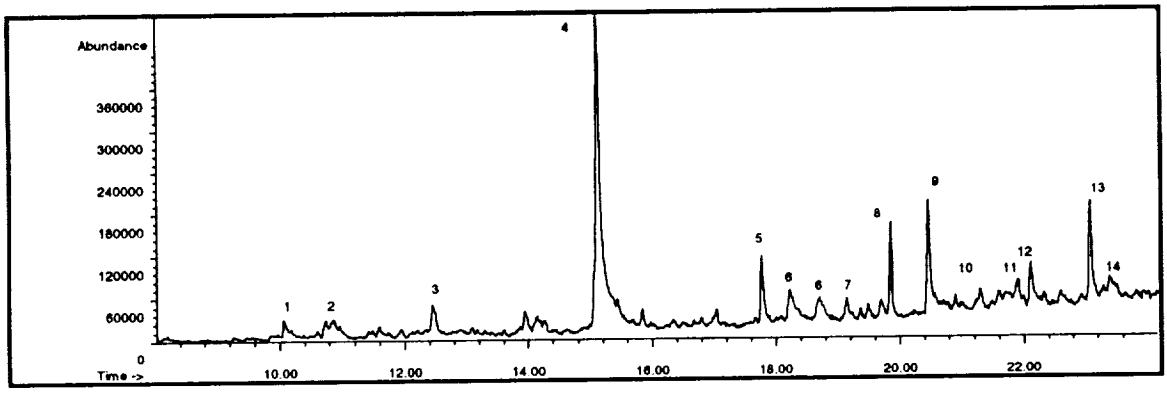

Fig 1. Partial Total Ion Chromatogram (C_{10} to C_{15} of 1972 psi supercritical CO_2 extract of 3-8 mm chips of Murchison. The numbered compounds were tentatively identified by comparison of their mass spectra with reference spectra and standards. (1) n-decane, (2) Dichlorobenzene, (3) n-undecane, (4) naphthalene, (5) n-tridecane, (6) Methyl naphthalenes, (7) Alkylcyclohexane, (8) 2,6,10-trimethyl dodecane, (9) n-tetradecane, (10) Dimethyl naphthalenes, (11) Octyl cyclohexane (?), (12) 2,6,10-trimethyl tridecane, (13) n-pentadecane, (14) Acenaphthene.

Table 2. lists the carbon isotopic compositions determined by isotope- ratio- monitoring GCMS for the hydrocarbons in the 1927 psi chip fraction. As can be seen the majority have terrestrial $\delta^{13}C$ of -26 to -33‰. However, by backflushing helium through the combustion interface of the irm-GCMS it is possible to determine the $\delta^{13}C$ value of a background hump. This was done several times in the molecular weight range C_{15} to C_{20} and gave $\delta^{13}C$ values ranging from -9 to -6‰. This confirms the indigeneity of the highly structurally diverse suite of cycloalkanes.

Compound	$\delta^{13}C$ (‰)	Compound	$\delta^{13}C$ (‰)
n-C_{13}	-28.5	cycloalkane hump C_{16}	-8.5
n-C_{14}	-33.2	cycloalkane hump C_{18}	-8.5
n-C_{15}	-28.2	cycloalkane hump C_{20}	-6.0
n-C_{16}	-30.6	cycloalkane hump C_{20}	-6.0

Supercritical carbon dioxide offers an effective low contamination risk means of separating non-polar from polar hydrocarbons in the extraction of organic compounds from meteorites. Perhaps the greatest promise of this technique comes from the ability to directly couple SFE systems to the front-end of a GCMS thereby enabling direct extraction and analysis of considerably smaller samples than conventional methods allow.

References

(1) Hawthorne S.B. and Miller D.J. (1987) J. Chromatogr. **403,** 63-76; (2) Cronin J.R. and Pizzarello S. (1990) Geochim. Cosmochim. Acta **54,** 2859-2868; (3) Gilmour I. and Pillinger C.T. (1992) Meteoritics **27,** 224-225.

EUVE OBSERVATIONS OF THE MOON; G. R. Gladstone, J. S. McDonald, and W. T. Boyd, Center for Extreme Ultraviolet Astrophysics, University of California at Berkeley, Berkeley, CA 94720

During its all-sky survey, the Extreme Ultraviolet Explorer (*EUVE*) satellite observed the Moon several times at first and last quarters, and once near the Dec. 10, 1992 lunar eclipse. We present here a preliminary reduction and analysis of this data, in the form of EUV images of the Moon and derived albedos. Extreme ultraviolet observations of the Moon are of considerable interest, since it has been speculated that lunar EUV emissions are primarily due to L- and M-shell X-ray fluorescence and may provide a useful diagnostic of surface elemental abundances [1].

The *EUVE* science payload consists of four instruments: three scanning telescopes and a deep survey and spectrometer telescope. The primary goal of *EUVE* is to carry out an all-sky survey over most of the EUV band (< 911 Å) using photometers on the three scanning telescopes [2]. The scanning telescope photometers cover four bandpasses in the EUV, using filters made of Lexan/Boron, Aluminum/Carbon, Aluminum/Titanium/Antinomy (a.k.a. "Dagwood"), and Tin for extreme ultraviolet sensitivity. The central wavelengths for the Lexan/B, Al/C, Dagwood, and Sn filters, weighted by a typical solar EUV spectrum, are 146, 230, 478 and 590 Å, and the corresponding full-widths at half maximum are 106, 138, 190, and 74 Å, respectively.

The initial results for a single scan of the first-quarter Moon suggest EUV albedos of less than 1%. The preliminary albedo for the tin photometer is ~0.5%, more than ten times smaller than a measurement made in 1973 by a 584 Å photometer on the *Mariner 10* spacecraft [3]. We are currently investigating possible sources for the discrepancy between the two measurements. Images of the first quarter, last quarter, and nearly-full Moon will be presented.

REFERENCES: [1] Edwards B. C., Priedhorsky W. C., and Smith B. W. (1991) *GRL*, 18, 2161. [2] Bowyer S. and Malina R. F. (1991) In *Extreme Ultraviolet Astronomy*, ed. R. F. Malina and S. Bowyer, pp. 397–408. Pergamon Press, New York. [3] Wu H. H. and Broadfoot A. L. (1977) *JGR*, 82, 759.

CRETACEOUS-TERTIARY BOUNDARY SPHERULES AND CENOZOIC MICROTEKTITES: SIMILARITIES AND DIFFERENCES; B. P. Glass, Geology Department, University of Delaware, Newark, DE 19716; Bruce F. Bohor and William J. Betterton, U.S. Geological Survey, Box 25046, MS 972, Denver, CO 80225

Bohor and Betterton [1] pointed out that the K-T spherules can be divided into three groups. Their Type 1 spherules appear to be found in or adjacent to North America, particularly the Western Interior and in Haiti and Mexico. The Type 1 spherules occur in the lower part of the K-T boundary clay below an Ir anomaly. It is the Type 1 spherules which are most similar to microtektites. The discovery of K-T boundary spherules in Beloc, Haiti, and Mimbral, Mexico, with residual tektite-like glass cores [2-3] supports the hypothesis that the Type 1 spherules are diagenetically altered microtektites. How similar are the Type 1 K-T boundary spherules to previously described Cenozoic microtektites and in what ways are they different?

Size and Shape. In general the Type 1 K-T spherules from the Western Interior and Haiti are similar to microtektites in size and shape. Although microtektites were originally defined as being tektites <1mm in dia., millimeter-size splash-form tektites were found in late Eocene sediments off New Jersey (DSDP Site 612). The spherical K-T spherules from the Western Interior are up to 2mm in diameter and the spherical Haitian spherules are up to 3.5 mm in size [4]. Very little data are given concerning the size distribution of the K-T spherules, but the impression is that at a given site the larger spherules are more abundant than the smaller ones. If this is the case, then the size distribution is different than for the Cenozoic microtektites which increase in number with decreasing size. Both the K-T spherules and the Cenozoic microtektites consist mostly of spheroids, with elongate forms like teardrops and dumbbells being relatively rare.

Surface Features. In contrast to the microtektites which generally exhibit a variety of surface features including pits, grooves, and mounds, the K-T spherules are generally smooth and featureless [1,3]. A few of the Western Interior K-T spherules do have pits and grooves similar those seen on Cenozoic microtektites [5], but they are rare.

Composition. The Haitian glass cores have SiO_2 contents between 60 to 68% [3,6]. This is lower SiO_2 than is generally found in tektites, but it is well within the range of SiO_2 contents observed in microtektites. In fact, all the major oxides are in the range observed for Cenozoic microtektites except for the CaO and Na_2O contents which are somewhat higher. As a group the Haitian glasses have a wide range in composition with SiO_2 between 44 and 68% [3]. The low SiO_2 (48-50%) glasses have very high CaO contents (up to 31%). Although none of the Cenozoic microtektites have this high a CaO content, some have SiO_2 contents as low as 48% and MgO as high as 24% [7]. Like Cenozoic microtektites, the more SiO_2-rich Haitian glasses are generally homogeneous; however some contain streaks of the yellow, low SiO_2, high-CaO (HCa) glass [3]. In contrast, the Cenozoic microtektites do not contain inclusions or streaks of the high MgO (HMg) glass.

K-T SPHERULES AND MICROTEKTITES: Glass, B.P. et al.

Petrography. Like most Cenozoic microtektites, the more SiO_2-rich Haitian glasses contain rare vesicles, but no crystalline inclusions. Unlike most Cenozoic microtektites, the more SiO_2-rich Haitian glasses do not appear to contain lechatelierite particles. The HCa Haitian glasses are more vesicular, and contain melilite(?) crystals and relict inclusions of what appears to be a calcium sulfate mineral. In contrast, the HMg Cenozoic microtektites are devoid of vesicles and crystalline phases. Neither the HCa K-T glasses nor the HMg Cenozoic microtektites appear to contain lechatelierite.

Association with Unmelted Impact Ejecta and Iridium. The Type 1 microtektite-like spherules occur in the lower claystone layer of the K-T boundary unit below an Ir anomaly. Shocked quartz with multiple sets of shock lamellae are found associated with the Type 1 spherules, but is most abundant in the overlying Ir-rich layer [8]. Traces of stishovite have been reported in the K-T boundary layer [9], but coesite has not. In contrast, none of the Cenozoic microtektite layers are directly associated with an Ir anomaly. Furthermore, coesite is commonly found associated with the North American microtektites and with the Australasian microtektites; but, shocked quartz with multiple sets of shock lamellae appear to be quite rare.

Discussion. Aside from the fact that the Type 1 K-T boundary spherules are mostly diagenetically altered, they have many charateristics in common with Cenozoic microtektites. There are some differences, however. In contrast with Cenozoic microtektites, the K-T spherules do not appear to increase in abundance with decreasing size, they generally do not exhibit surface sculpturing (although the relict glass cores do show sculpturing), they do not contain lechatelierite particles, and they are closely associated with an Ir anomaly and shocked quartz, but not with coesite. Most of these differences may be attributed to different parent rock, to the larger size of the K-T event, and to later diagenetic alterations. The apparent dearth of small versus large spherules at a given site may be attributed to a combination of operator bias and more complete diagenetic destruction of the small spherules. The general lack of external surface sculpturing may be due to the formation of palagonite rims as the warm spherules fell into water [10]. The lack of lechatelierite particles and the apparent lack of associated coesite may be partly related to the larger size of the K-T event which may have resulted in higher average temperatures. The lack of lechatelierite may also be related to the high CaO content of the glass. The higher lime content may have acted as a flux which resulted in greater homogenization of the Haitian K-T glass.

References. [1] Bohor, B.F. and Betterton, W.J. (1990) LPSC **XXI**, 107. [2] Smit, J. et al. (1992) Geology **20**, 99. [3] Sigurdsson, H. et al. (1991) Nature **349**, 482. [4] Izett, G.A. (1990) J. Geophys. Res. **96**, 20,879. [5] Izett, G.A. (1990) GSA Spec. Paper 249, 100p. [6] Maurrusse, F.J-M.R. and Sen, G. (1991) Science **252**, 1690. [7] Glass, B.P. (1972) J. Geophys. Res. **77**, 7057. [8] Bohor, B.F. et al. (1987) Geology **15**, 896. [9] McHone, J.F. et al. (1989) Science **243**, 1182. [10] Bohor, B.F. et al. (1993) this volume.

A TEST OF THE APPLICABILITY OF INDEPENDENT SCATTERING TO HIGH ALBEDO PLANETARY REGOLITHS;

J. D. Goguen, Jet Propulsion Laboratory, MS 183-501, California Institue of Technology, Pasadena, CA 91109

We show that "independent scattering" is a useful approximation for high albedo particles whose size and packing density are similar to typical particles in the lunar regolith. Laboratory measurements of the intensity and linear polarization of light scattered from a laboratory sample of glass spheres of known size and composition are compared to radiative transfer calculations of the same observable quantities. Mie scattering is integrated over the size distribution of the particles to determine the mean phase and polarization functions, or phase matrix, of the particles. Assuming that the particles scatter independently, the "doubling method" (1) is used to **rigorously** calculate multiple scattering in an optically thick layer of these anisotropically scattering particles. All of the major features "predicted" in the calculated intensity (double peaks at small phase angles) and polarization (negative branch at small phase angles, large positive peak near 20 degrees phase, and small polarization elsewhere) are observed in the laboratory measurements (**Fig. 1**), with good quantitative agreement indicated at phase angles <90 degrees. Even though the particles are supported by physical contact with each other in the sample, as are the particles in planetary regoliths, the independent scattering calculation yields a good approximation to both the intensity and polarization. The physical parameters input to the calculation are only the size distribution of the particles and their complex index of refraction (composition). Significant advantages of this approach are that the phase matrix is calculated from basic physical principles and both the intensity and polarization are determined simultaneously. This model may have broad applications to the interpretation of photometry, spectroscopy, and polarimetry of the icy regoliths of high albedo satellites.

The intent of this effort is to perform a *controlled* experiment that tests the utility of the independent scattering assumption for regoliths composed of high albedo particles. To accomodate this goal, the sample consists of particles whose shape, size distribution and composition are known. Soda-lime glass microspheres (Duke Scientific, Catalog #146; mean radius 4μm, FWHM 2μm; n=1.51, k$\sim$0 at λ=0.589μm) were selected for their similar size to the particles that dominate scattering in the lunar regolith. A smooth, optically thick layer $\sim$1 cm deep was formed without compacting the sample. Measurements of the intensity and linear polarization at $\lambda = 0.589\mu$m were made using the Cornell Goniometer. Measurements at very small phase angles where coherent backscatter may occur are not feasible with this experimental setup. For comparison with the measurements, Mie scattering (1) was integrated over the known particle size distribution to determine the phase matrix. The "doubling method" (1) was used to rigorously calculate multiple scattering by the anisotropically scattering particles in an optically thick layer yielding the calculated intensity and linear polarization.

A comparison of the measured and calculated intensity and linear polarization as a function of phase angle is shown in Fig. 1. Calculations are given for 2 values of the imaginary component of the index of refraction, k=0 (solid line) and k=0.0001 (dotted line). For a suitable small value of k (Duke Scientific is researching the best value of k for this sample at the time of this writing), quantitative agreement between the calculated and measured intensity and polarization is indicated for phase angles <90 degrees. At phase angles >90 degrees, the measured intensity decreases more rapidly with increasing phase angle that the calculated intensity. We conclude that at phase angles <90 degrees, the independent scattering calculation widely used in atmospheric radiative transfer calculations will give a quantitative description of both the intensity and linear polarization of visible wavelength light scattered by planetary regoliths composed of high albedo particles in the 1-10μm size range.

(1) Hansen J. E. and Travis L. D. (1974) *Space. Sci. Rev., 16,* 527.

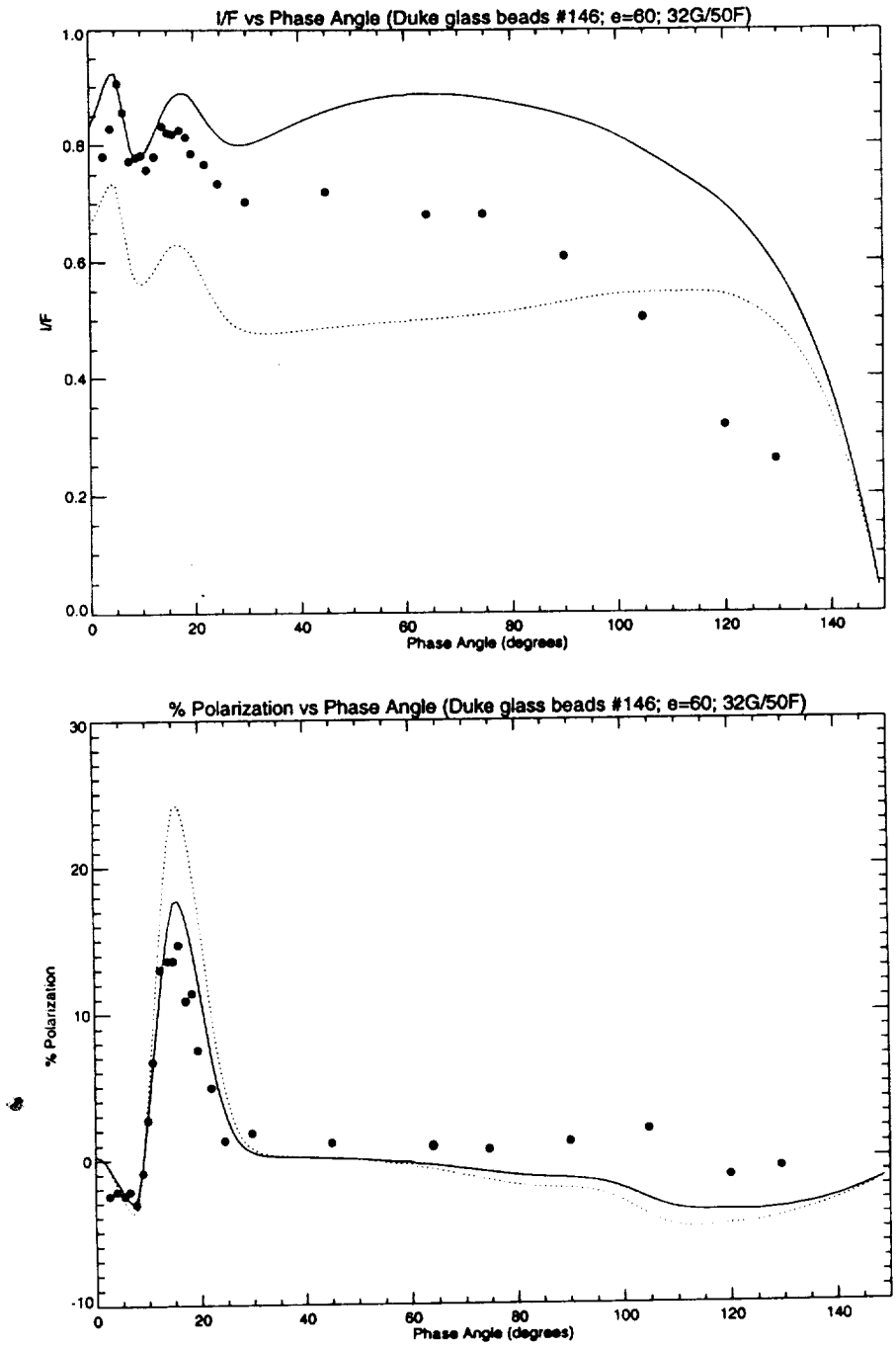

Figure 1. Comparison of laboratory measurements (dots) and rigorous calculations (lines: solid k=0, dotted k=0.0001) of the intensity (top) and linear polarization (bottom) of an optically thick sample of the glass microspheres (n=1.51) described in the text. The emission angle is fixed at 60 degrees and the incidence angle varies within the plane defined by the surface normal and emission direction. The wavelength of the measurements and calculations is λ=0.589μm. The doubling calculation uses 32 Gaussian ordinates and 50 Fourier coefficients to rigorously calculate the intensity and polarization scattered from a layer of normal optical depth τ=1024.

RHEOLOGY OF WATER AND AMMONIA-WATER ICES; D.L. Goldsby[1], D.L.Kohlstedt[1], and W.B.Durham[2], [1]Dept. of Geology and Geophysics, Univ. of Minnesota, Minneapolis, MN 55455, and [2]Lawrence Livermore National Lab, Livermore, CA 94550

Creep experiments on fine-grained water and ammonia-water ices have been performed at one atmosphere and high confining pressure P_c in order to develop constitutive relationships necessary to model tectonic processes and interpret surface features of icy moons of the outer solar system. The present series of experiments explores the effects of temperature T, strain rate $\dot{\varepsilon}$, grain size and melt fraction on creep strength. In general creep strength decreases with increasing temperature, decreasing strain rate, and increasing melt fraction. A transition from dislocation creep to diffusion creep occurs at finer grain sizes, higher temperatures and lower strain rates.

A method was developed for producing fine-grained (20-30 μm) samples to insure textural equilibrium in partially molten ammonia-water ice samples and to minimize microcracking caused by thermal and elastic anisotropies in water-ice samples. After Ice I powders were prepared by misting triply distilled water into a liquid N_2 reservoir, they were separated into the desired powder size by wet sieving in LN_2. Single-phase water-ice samples were then prepared by uniaxially hot-pressing these fine-grained Ice I powders at 12 MPa and 253 K for 24 h. Scanning electron microscopy (SEM) micrographs show that these samples have a grain size of 20-30 μm. Ammonia-water ice samples were prepared with 1, 5 and 8% NH_3 by flooding Ice I powders with an appropriate mixture of NH_3OH and water, followed by slowly cooling to and cycling through the peritectic temperature (T_p=176 K at 1 atm), using the procedure described by Durham et al. (1993).

Constant-load creep experiments at 1-atm confining pressure were performed on the single-phase water-ice samples, over the temperature range 250 to 273 K, at a differential stress of 0-2 MPa. High-pressure experiments were conducted on both pure water and ammonia-water ice samples in a gas-medium apparatus designed for cryogenic use at Lawrence Livermore National Lab under the following conditions: $3.5 \times 10^{-7} < \dot{\varepsilon} < 3.5 \times 10^{-4}$ s^{-1}, $160 < T < 220$ K, P_c=50 MPa.

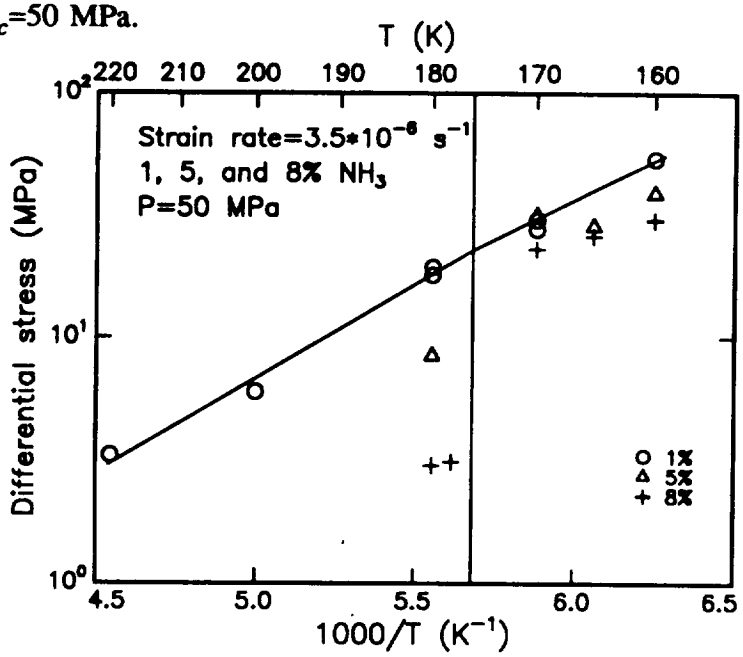

Figure 1: Differential stress versus inverse temperature for ammonia-water ice samples. Creep data for samples with 1, 5 and 8% NH_3 are plotted. Experiments were carried out at a strain rate of $3.5 \times 10^{-6} s^{-1}$ and a confining pressure of 50 MPa. The vertical line marks the peritectic temperature.

C-2

RHEOLOGY OF WATER AND AMMONIA-WATER ICES

Goldsby, D.L. et al.

For ammonia-water ice samples, the creep strength decreases with increasing NH_3 content over the entire experimental temperature range, as illustrated in Figure 1. A sharp decrease in strength occurred near the peritectic temperature for the 5 and 8% NH_3 samples, while a more gradual decrease in strength with increasing temperature occurred for the 1% NH_3 sample. The marked decrease in strength of the 5 and 8% NH_3 samples may be due to the relatively large amount of melt (>15%) that forms just above the peritectic temperature. For the 1% sample, <4% melt forms even at 220 K. Our fine-grained samples both with and without melt are weaker than coarse-grained samples (~250 μm) of the same bulk composition (Durham et al., 1993).

For the water-ice samples, the creep results for our fine-grained samples are in good agreement with those of Durham et al. (1992) for coarser-grained aggregates for $\dot{\varepsilon}=10^{-6}$ s^{-1}, as shown in Figure 2. At $\dot{\varepsilon}=10^{-7}$ s^{-1}, our fine-grained samples have slightly higher strengths than their coarse-grained samples at low temperatures. However, they are weaker than the coarse-grained samples at higher temperatures (220 K), probably reflecting a change in deformation mechanism at higher temperatures. The creep data for the fine-grained water-ice samples deformed at high confining pressure and the extrapolation of the data for the samples deformed at 1 atm at nearly identical strain rates are in good agreement with one another, suggesting that microcracking did not significantly affect the creep strength in the experiments carried out at 1 atm. The stress exponent, n, decreases systematically from ~7 at 160 K to ~2 at 260 K. This behavior is consistent with a transition from dislocation creep to diffusion creep or to grain boundary sliding accommodated creep.

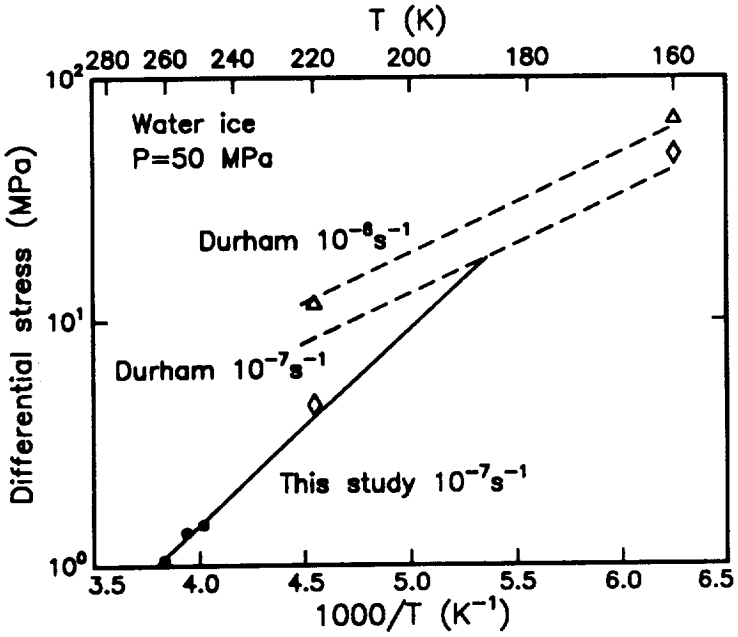

Figure 2: Differential stress versus inverse temperature for water-ice samples. The dashed lines are from Durham et al. (1992). The triangles are from this study for a strain rate of $10^{-6}s^{-1}$, while the circles and diamonds are for a strain rate of $10^{-7}s^{-1}$. The open symbols represent data obtained at P_c=50 MPa and the closed symbols represent data obtained at P_c=1 atm.

Durham, W.B., Kirby, S.H. and Stern, L.A., (1992). Effect of dispersed particles on the rheology of water ice at planetary conditions, *J. Geophys. Res.*, in press.

Durham, W.B., Kirby, S.H. and Stern, L.A., (1993). Flow of ices in the ammonia-water system, *J. Geophys. Res.*, in press.

IMPORTANCE OF EXPANSION AND CONTRACTION IN THE FORMATION OF TECTONIC FEATURES ON THE MOON

M. P. Golombek and W. B. Banerdt, Jet Propulsion Laboratory, Caltech, Pasadena, CA 91109.

The lack of globally distributed tectonic features on the lunar surface has been used to argue against significant changes in the radius of the Moon (1) since the formation of the presently observed surface, which dates to the end of heavy bombardment about 3.9 Ga. This observation has been used previously to limit the maximum stresses to ~100 MPa that could be supported by the lunar lithosphere without the formation of globally distributed tectonic features (2), which in turn limits the maximum radius change to ±1 km for a purely elastic lithosphere (3). In a previous abstract (4), limits on the elastic expansion or contraction of the Moon were reexamined with respect to realistic failure stresses necessary to produce actual lunar tectonic features. In addition, limits on the permanent (plastic) strain that could be accommodated by non-mascon grabens and wrinkle ridges were considered with more severe constraints placed on the total reasonable expansion and contraction of the Moon since 3.9 Ga. In this abstract, considerations of the distribution and mechanisms of formation of lunar tectonic features are used as an additional argument against their formation due to a planetary radius change or their accommodating much permanent plastic planetary expansion or contraction.

Grabens and wrinkle ridges are the generally accepted tectonic features on the Moon. The general approach assumed in this abstract is that the maximum elastic expansion or contraction of the Moon can be limited by application of generally accepted failure criterion (the frictional resistance to sliding on preexisting fractures [5]) to the particular structures of grabens and wrinkle ridges (4, 6, 7). Using this criterion, the maximum stresses possible before failure are about 10 MPa under extension and 30 MPa under compression, which restricts the elastic radius increase to about 100 m and the elastic radius decrease to about 300 m. Beyond this elastic limit, the surface of the Moon is everywhere on the verge of failure, so that any additional expansion or contraction will result in failure that would form structures visible on the surface. If, however, the surface of the planet is not uniformly covered by tectonic features the maximum global stress limit may be substantially lower than calculated in this manner, due to likely concentrations or inhomogeneities in the actual stresses.

Most grabens and wrinkle ridges observed on the Moon are found in and around mascon basins. Models of the flexure of the lithosphere due to mascon loading suggest that sufficient extensional stress and strain can be generated at the edges of basins to account for concentric grabens and sufficient compressional stress and strain can be generated in the interior of basins to account for wrinkle ridges (6-10). As a result, these structures should not be considered to form from global strain or stress fields. Nevertheless, there are a significant number of grabens and wrinkle ridges that are not related to mascon basin flexure and these could have formed from lunar expansion or contraction (even though these features are not globally distributed – all are on the lunar near side). In addition, only tectonic features that can be confidently assigned to extensional or compressional structural deformation are considered here (i.e., grabens and wrinkle ridges); no consideration is given to less well understood features of potential structural origin such as the lunar grid or highland scarps (11).

The total length of non-mascon related wrinkle ridges on the Moon is just short of 15,000 km and the total length of non-mascon related grabens on the Moon is just below 7400 km. Assuming these features are randomly distributed, the total radius change that can be accommodated in tectonic features is given by $\Delta R = (R^2 - \Delta A/4\pi)^{1/2} - R$ where R is the radius of the Moon and ΔA is the cumulative change in surface area, which is simply the total length of structures times their average horizontal extension or shortening (6, 7). As a result, non-mascon wrinkle ridges could have resulted from a 75 m contraction of the Moon and non-mascon grabens could have resulted from a 25 m expansion of the Moon. Nevertheless, lunar grabens and wrinkle ridges are not randomly distributed. Virtually all are found on the front side of the Moon, so that it could be argued that these results are overestimates.

If the existing non-mascon tectonic features on the Moon were indeed randomly distributed, then a simpler method could be used to determine the radius change accommodated

permanently in non-mascon grabens and wrinkle ridges. For a randomly distributed set of tectonic features any great circle traverse around the planet would encounter the same cumulative shortening or extension, for a uniformly contracting or expanding planet. If all structures within each group of features (grabens and wrinkle ridges) had the same average shortening or extension, then all great circle traverses would encounter the same number of features. If this were the case, the total shortening or extension around any particular great circle traverse is equal to the total change in circumference of the planet, which is equal to 2π times the radius change. A simple test of the above was performed on the Moon. Two equatorial great circles were chosen to maximize the number of grabens and wrinkle ridges that were crossed. (There are, of course, great circle transects that could be constructed that would not cross any tectonic features.) About 30 wrinkle ridges were crossed on one transect and 10 grabens were crossed on the other. For average shortening and extension estimates (6, 7) these transects would predict of order 1 km contraction and 300 m expansion of the Moon, respectively. These radius changes are roughly an order of magnitude greater than the estimate based on the change in surface area calculated earlier. This seems to suggest that grabens and wrinkle ridges are quite non-randomly distributed (by an order of magnitude), which could be used to infer that the previous estimates of permanent radius change are also substantial overestimates.

If, in fact, grabens and wrinkle ridges are not distributed uniformly, then any shortening or extension by tectonic features that was related to a radius change would result in a non-uniformly shrinking or expanding planet. No doubt some non-uniformity of shortening or extension can be accommodated on the Moon, but large differences implied by the above calculations seem excessive. In addition, a non-random distribution of grabens and wrinkle ridges can also be used to argue for lower elastic limits on global expansion and contraction. If large portions of a planet do not have any tectonic features, then average global stress may be lower due to concentration of stresses in particular areas, such as the lunar near side. Some limits can be placed on the amount elastic stresses could be lowered due to stress concentrations. The maximum lowering of global stresses by regional stress concentration would be attained if, for example, the stresses on the near side of the Moon were doubled, leaving no stresses imposed on the far side. Then the average global stress due to global expansion or contraction could be lower by a factor of two. If true the required radius change would be similarly decreased by a factor of two. These considerations suggest that the elastic limits on radial expansion of 300 m and 100 m for contraction and expansion derived for uniform elastic stresses may be overestimates.

Taken together, these additional arguments would suggest that a maximum expansion of the Moon of 125 m and a maximum contraction of the Moon of 375 m that were derived earlier (4) for both elastic and plastic radius change are also overestimates and that actual lunar radius changes since the end of terminal bombardment 3.9 Ga are considerably less.

These limits on the change in lunar radius during the past 3.9 Ga have important implications for models of the origin of the Moon. Previous conservative thermal models assumed a warm exterior and cool interior to minimize the change in radius (3). New models for the origin of the Moon from a giant impact imply a substantially more energetic, and correspondingly warmer (and partially melted) early history, which may be even more difficult to reconcile with such restrictive constraints on radius change (e.g., 12).

References: (1) MacDonald 1960 Planet. Space Sci. 2, 249-255. (2) Solomon 1986 in Origin of the Moon, Hartmann et al. eds., LPI, p. 435-452. (3) Solomon and Chaiken 1976 Proc. Lunar Sci. Conf. 7th, 3229-3243. (4) Golombek et al., 1992 Proc. Lunar Planet. XXII, 425-426. (5) Brace and Kohlstedt 1980 JGR 85, 6248-6252. (6) Golombek 1979 JGR 84, 4657-4666. (7) Golombek et al., 1991 Proc. Lunar Planet. Sci. 21, 679-693. (8) Solomon and Head 1980 Rev. Geophys. Space Phys. 18, 107-141. (9) Golombek and McGill 1983 JGR 88, 3563-3578. (10) Golombek and Franklin 1991 Lunar Planet. Sci. XXII, 453-454. (11) Binder 1982 Moon Planets 26, 117-133. (12) Kirk and Stevenson 1989 JGR 94, 12,233-12,144.

STALKING THE LREE-ENRICHED COMPONENT IN UREILITES. *Cyrena Anne Goodrich and **Günter W. Lugmair. *Lunar and Planetary Laboratory, University of Arizona, Tucson, AZ 85721. **Scripps Institution of Oceanography, University of California, San Diego, La Jolla, CA 92093.

Ureilites contain a LREE-enriched component whose origin and identity are unknown, but which may have been introduced into 4.55 Ga olivine + pyroxene assemblages at various times in the period 4.55->3.74 Ga [1]. This component is volumetrically minor, inhomogeneously distributed, and can be removed with concentrated HNO_3 [1,2,3], which suggests that it may be contained in minor, interstitial phases not previously recognized in ureilites. There is evidence, however, that not all of this component is leachable. Whole rock samples of Kenna, Novo Urei, and ALHA77257 form a $^{143}Nd/^{144}Nd$-$^{147}Sm/^{144}Nd$ line (Fig. 1) with a slope corresponding to an age of 3.74 Ga [1]. Although this line could be a mixing line, with one end-member being the LREE-enriched component and the other being a 4.55 Ga olivine + pyroxene assemblage, the observation that a pyroxene separate from Kenna plots on the line suggests that the LREE-enriched component at least partially equilibrated with the olivine and pyroxene and that the line is an isochron [1]. We performed a leaching experiment on Kenna, using various acids and concentrations, in an attempt to isolate the LREE-enriched component and differentiate between possible hosts for it, and to determine whether all of it is leachable. Our results suggest that most of the LREE-enriched component is surface-sited, rather than contained in a discrete mineral. However, some of it is not readily leachable because it equilibrated with Kenna olivine + pyroxene at 3.79±0.05 Ga.

EXPERIMENTAL PROCEDURES: Two new samples of Kenna ("A" and "B") were ground in a boron carbide mortar. Nd and Sm concentration determinations on small aliquots indicated that they contained significant amounts of LREE and, therefore, would be appropriate for leaching experiments. "A" was divided into a whole rock aliquot (63.4 mg) and an aliquot for leaching (66.6 mg). A whole rock aliquot of "B" (79.5 mg) was also prepared. Reagents used for the seven progressive leaches of "A" are summarized in Table 1, and were designed to progressively remove surface contaminants and various possible trace phases. All leachates, the residue, and both whole rock samples were analyzed for Nd and Sr isotopic composition and Nd, Sm and Sr concentrations (Table 2).

RESULTS: "A" is very similar in Nd and Sm concentrations and Nd isotopic composition to the previously-analyzed whole rock samples K1 and K3 [1], which plot at the LREE-enriched end of the Kenna "isochron" (Fig. 1). Samples such as these probably represent the maximum amount of LREE-enriched component in Kenna. "B" contains slightly less of this component. Addition of these samples to the Kenna line results in slight revision of the line, giving an age of 3.79±0.05 Ga (Fig. 2; note change of scale). The first three leaches did not dissolve measurable amounts of material. The 2M HNO_3 leach dissolved 11.3% by mass of the original material; since known interstitial phases soluble in HNO_3 in ureilites (carbon, sulfides, metal) generally constitute <5-7%, some olivine + pyroxene must have dissolved in this leach. The 2.5M HCl and 6M HCl leaches dissolved respectively 15.7% and 19.7% by mass of the original material, probably largely olivine. The 13M HNO_3 leach dissolved negligible mass, demonstrating that no HNO_3-soluble phases remained. The residue contained only 42.3% of the original material. If the HCl leaches dissolved principally olivine, and the sample had a typical Kenna olivine/pyroxene ratio, then the residue contains ~65% olivine and 35% pyroxene. The thoroughness of the leaching procedure and the large amount of material dissolved suggests that the residue is devoid of *leachable* LREE-enriched component. The residue is similar in Nd and Sm concentrations and Nd isotopic composition to whole rock sample K2, which plots at the LREE-depleted end of the Kenna "isochron" (Fig. 1), confirming that K2 was nearly devoid of *leachable* LREE-enriched component [1].

Progressively more aggressive leaches show progressively higher Sm/Nd ratios (Fig. 2), indicating progressive dilution of the LREE-enriched component. However, neither all of the leachates nor the residue plot strictly within error of the 3.79 Ga line, which suggests some differential leaching of Sm and Nd, as suspected in previous leaching experiments [1]. The 6M HCl leachate contained only 5%, the 13M HNO_3 leach 0.2%, and the residue 1.6% of the total Nd, indicating that most of the LREE-enriched component had dissolved in earlier leaches. The 2M HNO_3 and 2.5M HCl leachates have lower $^{147}Sm/^{144}Nd$ ratios than the whole rock and the Nd concentrations of the masses they represent (432 and 289 ppb, respectively) are higher than that of the whole rock, indicating that they are still dominated by LREE-enriched component. The 0.04M HNO_3 and 0.2M HNO_3 leachates have even lower $^{147}Sm/^{144}Nd$ (0.112) and the highest Nd concentrations. If either of these represents 1 mg of material, then the Nd concentration of that material is ~19.5 ppm. These leachates represent our best estimate of the composition of the leachable LREE-enriched component. Our previous estimate was [Nd]=8 ppm and $^{147}Sm/^{144}Nd$ =0.115 [1].

CONCLUSIONS: The concentration of LREE-enriched component in the weaker leaches coupled with its continued but progressively diminished appearance in the stronger leaches suggests that most of it is surface-sited and loosely bound, rather than contained in a discrete mineral phase. However, the possibility that minute amounts of a

phosphate host were dissolved in the 0.2M HNO_3 leach cannot be ruled out. The observation that our fully-leached residue is no more LREE-depleted than K2 strengthens the interpretation that the Kenna 3.79 Ga line is an isochron. If it were a mixing line then a sample completely devoid of leachable LREE-enriched component would be expected to have $^{147}Sm/^{144}Nd$~0.51 (the intersection of the Kenna line with the 4.55 Ga chondritic evolution line [1]). We conclude that some of the LREE-enriched component equilibrated with Kenna olivine and pyroxene at 3.79±0.05 Ga. The geologic nature of this component remains open to speculation. Investigation of what other elements may be coupled with the LREE in the leachates may shed some light on this problem.

[1] C.A. Goodrich *et al.* (1991) *Geochim. Cosmochim. Acta* **55**, 829. [2] W.V. Boynton *et al.* (1976) *Geochim. Cosmochim. Acta* **40**, 1439. [3] A.H. Spitz and W.V. Boynton (1986) *Meteoritics* **21**, 515.

Table 1: Kenna "A" leach experiment

leaching agent	conditions	mass fraction of original sample
H_2O	10 min. ultrasound.	unmeasurable
0.04M HNO_3	10 min. ultrasound, H_2O rinse.	unmeasurable
0.2M HNO_3	10 min. ultrasound, H_2O rinse.	unmeasurable
2M HNO_3	1 hr. ultrasound, 0.2M HNO_3 rinse, 0.1M HNO_3 rinse, H_2O rinse.	11.3%
2.5M HCl	1 hr. ultrasound, 0.5M HCl rinse, H_2O rinse.	15.7%
6MHCl	10 min. ultrasound, 1hr. low heat, 0.5M HCl rinse, H_2O rinse.	19.7%
13M HNO_3	45 min. ultrasound, 1M HNO_3 rinse. H_2O rinse.	<0.3%
residue		42.3%

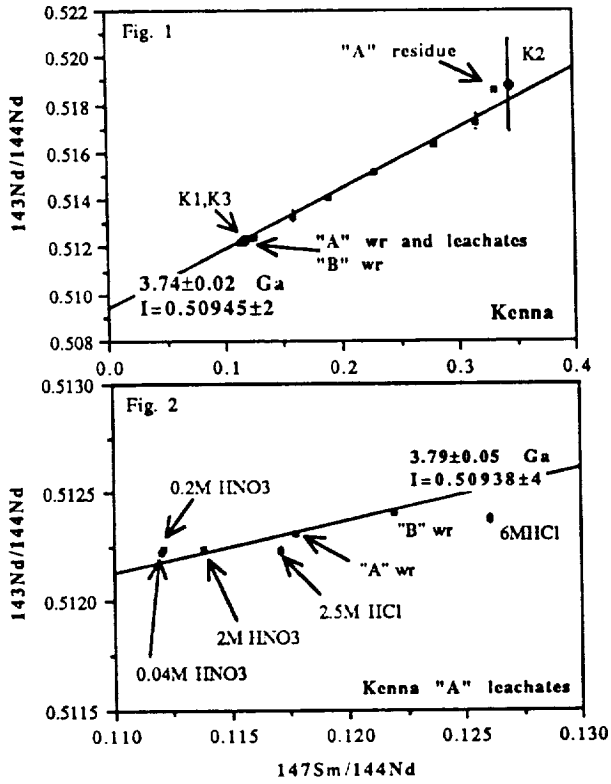

Table 2: Nd and Sr isotopic data for Kenna "A" and "B"

sample	$^{143}Nd/^{144}Nd$	$^{147}Sm/^{144}Nd$	Nd	Sm	$^{87}Sr/^{86}Sr$	Sr
"A" whole rock	0.512312±11	0.1177	222.9 ppb	43.4 ppb	0.708624±18	4.647 ppm
"B" whole rock	0.512407±11	0.1220	125.5 ppb	25.33 ppb	0.708628±17	3.834 ppm
"A" Leach Experiment						
H_2O leachate	nm	nm	nm	nm	0.708613±18 0.708590±20	80.2 ng
0.04M HNO_3 leachate	0.512225±11	0.1120	19.5 ng	3.625 ng	0.708644±22	600.8 ng
0.2M HNO_3 leachate	0.512241±10	0.1121	19.4 ng	3.586 ng	0.708637±18	397.1 ng
2M HNO_3 leachate	0.512237±17	0.1138	32.17 ng	6.055 ng	0.708600±18 0.708625±21	720.7 ng
2.5M HCl leachate	0.512232±18	0.1171	30.18 ng	5.83 ng	0.708619±26	401.0 ng
6M HCl leachate	0.512379±19	0.1261	5.469 ng	1.141 ng	0.708669±17 0.708664±15	302.7 ng
13M HNO_3 leachate	0.51242±12	nm	237 pg	nm	0.708650±32	27.8 ng
residue	0.518608±63	0.3326	1.772 ng	0.975 ng	0.708434±18	85.7 ng

GROSNAJA ABCs: MAGNESIUM ISOTOPE COMPOSITIONS. J.N.Goswami[1], G.Srinivasan[1] and A.A.Ulyanov[2]. [1]Physical Research Laboratory, Ahmedabad - 380 009, India. [2]Geological Department, Moscow State University, Moscow - 119 899, Russia.

Three CAIs from the Grosnaja CV3 chondrite were analysed for their magnesium isotopic compositions by the ion microprobe. The selected CAIs represent three distinct types: GR4(compact Type A), GR7 (Type B) and GR2(Type C). Petrographic studies indicate that all the three Grosnaja inclusions were subjected to secondary alterations.The Type A CAI GR4 is primarily composed of melilite with spinel and pyroxene occuring as minor phases. The rim of the inclusion does not exhibit distinct layered structure and secondary alteration products (garnet, Fe-rich olivine and Na-rich plagioclase) are present in some localised areas near the rim region. The average major element compositions of different mineral phases in GR4 are given in Table 1. Preliminary REE data suggest a depletion of HREE relative to LREE by about a factor of 3 without any clear indication of interelement fractionation. The CAI GR7 has textural and minerological characteristics similar to Type B inclusions. The REE data show a pattern that is similar to Group VI with enrichment in Eu and Yb. In addition, a depletion of HREE compared to LREE is also evident in this object. Melilite composition shows a broad range of akermanite content (Ak_{15-55}). Detailed petrographic study is in progress. GR2 is a anorthite-rich Type C inclusion with large plagioclase laths intergrown with Ti-rich pyroxene. The average plagioclase composition is close to pure anorthite(An99). There are however some altered

Table 1. Major element composition of mineral phases in Grosnaja CAIs†.

	GR2(Type C)					GR4 (Type A)			
	Anorthite	Pyroxene		Spinel	Garnet	Pyroxene	Melilite	Spinel	Garnet
		Core	Mantle						
SiO_2	42.46	42.02	47.18	0.07	35.07	35.86	26.81	0.04	38.99
TiO_2	0.08	5.16	2.50	0.38	0.01	9.55	0.03	0.35	0.01
Al_2O_3	36.44	14.42	9.72	70.53	0.04	21.64	28.83	71.78	22.79
Cr_2O_3	0.03	0.27	0.67	0.79	0.01	0.09	0.03	0.25	< 0.01
V_2O_3	< 0.01	0.16	0.13	0.33	< 0.01	0.15	0.01	0.41	0.01
MgO	0.11	11.76	13.31	27.36	0.17	7.53	3.20	28.02	2.45
CaO	20.04	25.59	25.49	0.08	33.43	25.28	41.10	0.16	34.93
FeO	0.10	0.16	0.21	0.53	28.26	0.02	0.08	0.08	1.35
MnO	0.01	< 0.01	0.04	0.02	0.01	< 0.01	0.01	0.03	0.02
Na_2O	0.15	0.01	0.01	–	0.01	0.01	0.03	–	0.01
K_2O	0.01	< 0.01	< 0.01	–	0.01	< 0.01	< 0.01	–	< 0.01

† All values are based on averages of 3 to 15 individual analysis

GROSNAJA ABCs: Goswami J.N. et al.

Na-rich plagioclase with lower anorthite content. Secondary phases like garnet and calcite are also present. The Ti-content of pyroxene is different in the core and in the mantle region of this inclusion(Table 1).

The magnesium isotopic studies were carried out using a Cameca IMS-4F ion microprobe. The Mg-Al data for none of the inclusions defines a well-behaved pattern. The data for the Type A inclusion GR4 is consistent with absence of of radiogenic ^{26}Mg, although the $(^{26}Mg/^{24}Mg)_i$, based on both spinel and melilite is a few permil above the normal value (0.13932). In the case of the Type B inclusion GR7 data for melilite with $^{27}Al/^{24}Mg \geq 10$ suggest the presence of radiogenic ^{26}Mg with $(^{26}Al/^{27}Al)_o$ of $\sim 2 \times 10^{-5}$, but no well behaved Mg-Al systematics could be discerened if one considers data for all the melilite with $^{27}Al/^{24}Mg$ ratio spanning the range of 2 to 16. The Type C inclusion GR2 has anorthite with $^{27}Al/^{24}Mg$ clustering around the value of 350 and along with the pyroxene data yield a normal initial magnesium isotopic composition and $(^{26}Al/^{27}Al)_o$ of $(3.3 \pm 0.8) \times 10^{-6}$. Data for anorthite near an altered zone (pyroxene, garnet and calcite assemblage) is consistent with a even lower value for $(^{26}Al/^{27}Al)_o$ of 2×10^{-6}. Intrinsic magnesium isotopic fractionation, F(Mg), of plagioclase and Ti-rich pyroxene has been measured using lake-county plagioclase and Angra-dos-Reis pyroxene as laboratory standards. The absence of positive fractionation for these phases is consistent with a lack of intense volatilization during the melting events experienced by these objects (1,2).

The Mg-Al systematics in the three different types of inclusions from the Grosnaja CV3 chondrite is a clear pointer towards the role of secondary processes leading to the disturbed Mg-Al systematics. Hutcheon et al.(3) have, however, preferred to interpret the Mg-Al systematics in another altered Grosnaja CAI (Max) in terms of heterogeneity of $^{26}Al^*$ or late formation of the object. Although the role of secondary alteration had been noted in most of the earlier magnesium isotopic studies of CAIs, its possible implications towards understanding the distribution of $^{26}Al^*$ in the solar nebula has been emphasised only recently. (4,5,6)

References: 1. Wark D., GCA **51**, 221-242(1987). 2. Beckett J.R. and Grossman L., EPSL **89**, 1-14(1988). 3. Hutcheon I.D. et al. LPSC XVII, 372-373(1986) 4. Podosek F. et al., GCA **55**, 1083-1110(1991). 5. Goswami J.N. et al. (submitted to GCA, 1992) 6. MacPherson G.J. et al., Meteoritics **27**,253-254(1992).

EUROMET UREILITE CONSORTIUM: A PRELIMINARY REPORT ON CARBON AND NITROGEN GEOCHEMISTRY; Monica M. Grady, Department of Mineralogy, The Natural History Museum, Cromwell Rd. London SW7 5BD, U. K. and C. T. Pillinger, Planetary Sciences Unit, Department of Earth Sciences, The Open University, Walton Hall, Milton Keynes MK7 6AA, U. K.

The first Euromet expedition to the Frontier Mountain in Antarctica in December 1990 recovered two ureilites, FRO 90036 (34.6g) and FRO 90054 (17.5g). Preliminary classification [1-2] indicated that the specimens had very different textures and mineral chemistries, and hence were not paired. A third ureilite, Acfer 277 (41.0g; ref. 3) has also recently been returned from the Sahara. Due to the small sample sizes of the meteorites, and the unusual mineralogy of FRO 90054, a consortium was established to ensure the most effective study of these samples; this abstract reports on the carbon and nitrogen stable isotope geochemistry of two of the three ureilites issued to the consortium.

Acfer 277. An outline of the mineralogy of Acfer 277 was presented by [3]: the meteorite is a typical ureilite, with a mean olivine core composition ca $Fa_{20.7}$. The olivine exhibits undulose extinction, implying shock facies 2 - 3, *i.e.* a moderate shock level of 5 - 10 GPa [4]. The carbon results for Acfer 277 bear out its classification as a ureilite: a carbon content of 2.4 wt. % and $\delta^{13}C$ *ca.* -2.8‰, placing the sample firmly within the field of main group ureilites defined by [5]. Interestingly, this ureilite is apparently not depleted in carbon by weathering processes, as has been found for other carbon-containing meteorites recovered from the Sahara [6], presumably a reflection of the more fixed nature of ureilite carbon. Approximately 86% of the carbon combusts between 650°C and 900°C (Fig. 1), the temperature range across which crystalline graphite generally burns, and has $\delta^{13}C$ *ca.* +0.6‰; the remainder of the carbon is released above 900°C, has a $\delta^{13}C$ *ca.* -23.5‰, and is presumably from combustion of carbides. Slightly ^{13}C-enriched carbon as graphite co-existing with ^{13}C-depleted carbides is a commonly observed assemblage in ureilites [5]. Nitrogen systematics are also typical of ureilites: a yield of 20.9 ppm nitrogen with $\delta^{15}N$ *ca.* -22.1‰. The coupled variation of carbon and nitrogen isotopic compositions is also within the spread of values shown by other ureilites (Fig. 2).

FRO 90054. Initial petrographic study of this meteorite described it as one of the few augite-bearing ureilites [2], although the modal content of 60% augite is high, even in comparison with other high Ca-pyroxene ureilites [7]. The mineral assemblage of FRO 90054 is therefore atypical, although the olivine composition of $Fa_{13.1}$ [2] falls within the range of measured values for main group ureilites. FRO 90054 is only lightly-shocked, with similar textural features to Acfer 277 in terms of olivine deformation. Carbon and nitrogen data for FRO 90054 serve to reinforce the belief that this meteorite, if it is a ureilite, is most unusual. The bulk carbon content of 0.24 wt. % is the lowest ever measured for a ureilite, with only a silicate-rich portion from Goalpara giving a similar result. Dissolution of an aliquot in HF and HCl resulted in a total weight loss of almost 100%, also implying a very low indigenous carbon content. The summed $\delta^{13}C$ of *ca.* -24.3‰ would be unique for a ureilite; all other samples analysed have $\delta^{13}C$ values between -11‰ and 0‰ [5]. Closer scrutiny of the carbon data (Fig. 1) show that 85% of the total carbon combusts below

500°C, implying that the bulk of the carbon is present as either poorly-ordered carbon or organic material. In view of its apparent solubility, the latter seems more probable. The isotopic composition of -24.4‰ implies a terrestrial, contaminant origin for this component, although such a contamination level is high for an Antarctic meteorite. A small amount of carbon combusts between 600°C and 1200°C, showing a maximum in the yield histogram at 600 - 700°C, consistent with identification of a very minor amount of poorly-crystalline graphite. However, the isotopic composition of this component is ca. -23.4‰, a value again outside the range shown by most ureilites. Nitrogen data are also unusual: the yield of 7.9 ppm is low for ureilites (range is 20 - 100 ppm), and isotopic composition is high, $\delta^{15}N$ *ca.* +64‰. Positive $\delta^{15}N$ values have been noted before, but only in brecciated ureilites [8], which generally have much higher nitrogen contents, and exhibit greater shock effects. Fig. 2 shows that FRO 90054 plots well outside the field of $\delta^{13}C/\delta^{15}N$ values exhibited by other ureilites.

Conclusions: In terms of C and N stable isotope geochemistry, Acfer 277 is a typical ureilite, containing ^{13}C-enriched and ^{15}N-depleted graphite, and ^{13}C-depleted carbides. In contrast, FRO 90054 is almost totally non-ureilitic in character, containing minimal carbon and nitrogen. Given the lightly-shocked nature of the specimen, it is unlikely that large amounts of carbon have been lost during shock-processes: FRO 90054 has the same shock classification as Acfer 277, which demonstrably has not lost its quota of volatiles. FRO 90054 is a very small specimen, only 17 g in total. It might be that the meteorite is simply a silicate-rich portion from the inhomogeneous ureilite parent, but the $\delta^{13}C$ value of the "graphite" which is present is entirely unlike that of all other ureilites. Either FRO 90054 extends the known stable isotope compositional range of ureilites, or it is not a ureilite at all. Further investigations are in progress, to include the other consortium sample, FRO 90036.

Figure 1

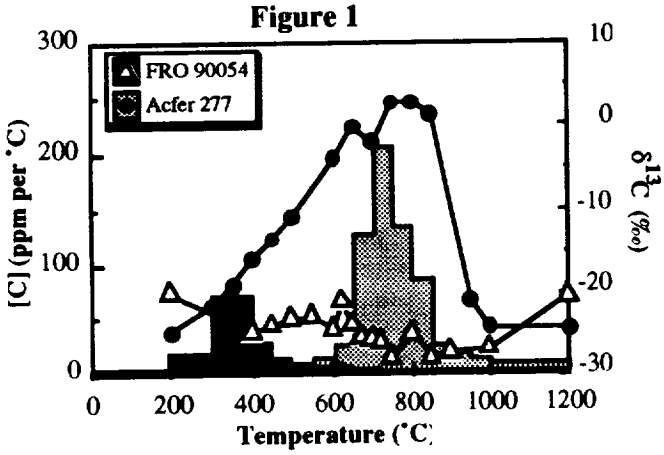

Figure 2

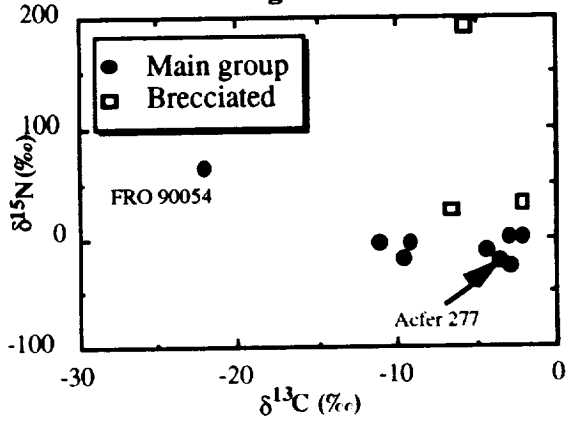

References: [1] Wlotzka, F. (1992) *Meteoritics* **27** 109-117; [2] Wlotzka, F. (1992) *Meteoritics* **27** 477-483; [3] Bland, P. *et al.* (1992) **LPSC XXIII** 119; [4] Stöffler, D. *et al.* (1991) *G.C.A.* **55** 3845-3867; [5] Grady, M. M. *et al.* (1985) *G.C.A.* **49** 903-915; [6] Ash, R. D. & Pillinger, C. T. (1992) *Meteoritics* **27** 199; [7] Takeda, H. (1989) *Meteoritics* **24** 73-81; [8] Grady, M. M. & Pillinger, C. T. (1988) *Nature* **331** 321-323.

NITRATES IN SNCS: IMPLICATIONS FOR THE NITROGEN CYCLE ON MARS; Monica M. Grady, Dept. of Mineralogy, The Natural History Museum, Cromwell Road, London SW7 5BD, U. K., I. P. Wright, I. A. Franchi and C. T. Pillinger, Planetary Sciences Unit, Dept. of Earth Sciences, The Open University, Walton Hall, Milton Keynes MK7 6AA, U. K.

Nitrogen is the second most abundant constituent of the martian atmosphere, after CO_2, present at a level of *ca.* 2.7%. Several authors have hypothesised that earlier in the planet's history, nitrogen was more abundant, but has been removed by processes such as exospheric loss from the atmosphere [*e.g.* 1]. However, an alternative sink for atmospheric nitrogen is the regolith; model calculations have predicted that, *via* the formation of NO_x, HNO_2 and HNO_3 in the lower layers of the martian atmosphere, the regolith might trap nitrite and nitrate anions, leading to the build-up of involatile nitrates [2]. Integrated over 4.5×10^9 yr, such a mechanism would contribute the equivalent of a layer of nitrates up to 0.3 cm thick distributed across the martian surface [2]. Features in thermal emission spectra of the surface of Mars have been interpreted tentatively as emanating from various anions (carbonates, bicarbonates, sulphates, *etc.*), and the presence of nitrates has also been addressed as a possibility [3]. The identification of carbonates in SNC meteorites has allowed inferences to be drawn concerning the composition and evolution of the martian atmosphere in terms of its carbon isotope systematics [4]; if nitrites, nitrates, or other nitrogen-bearing salts could be isolated from SNCs, similar conclusions might be possible for an analogous nitrogen cycle.

Nitrates are unstable, being readily soluble in water, and decomposed at temperatures between 50°C and 600°C, depending on composition. Any nitrates present in SNCs might be removed during ejection from the planet's surface, passage to Earth, or during the sample's terrestrial history, by weathering *etc.* The same might have been said for carbonates, but pockets of shock-produced glass (lithology C) from within the EET A79001 shergottite and bulk samples of other SNCs contain this mineral, which did apparently survive [5-7]. Nitrates occuring within the glassy melt pockets of lithology C in EET A79001 might likewise be protected. Lithology C glass was therfeore selected for nitrate analysis, first by non-destructive infra red spectroscopy, and then by stepped combustion.

Infra red spectroscopy: several nitrates (both AnalaR-grade chemicals and natural minerals, powdered in a matrix of KBr) were subjected to FTIR, in order to provide a calibration against which lithology C glass could be matched. In all cases, the most prominent feature in the spectrum was a very sharp singlet peak at approximately 1375 cm^{-1}. Comparison of the standard nitrate spectra with those from carbonates indicated that the two types of salt were well resolved, with the strongest carbonate feature at *ca.* 1425 - 1450 cm^{-1}. Analysis of powdered lithology C black glass yielded a spectrum with several features: a sharp peak at 1375 cm^{-1}, and a doublet between 1400 and 1450 cm^{-1}. The data imply the presence of both nitrates and carbonates in the specimen, although the technique used gave no indication of the relative concentrations of the two species.

Stepped combustion: having ascertained that nitrates might indeed be present in lithology C glass, *ca.* 5 mg of material were subjected to a high-resolution stepped combustion analysis, using FINESSE, a new gas source mass spectrometer, capable of measuring the nitrogen isotopic composition of samples as small as 100 pg; results for the combustion between 200°C and 600°C are shown in the figure. The yield histogram can be interpreted as indicating the presence of two components with discrete combustion/decomposition temperatures. The least stable component (≈ 1 ppm), labile below *ca.* 320°C, is not isotopically well-defined due to an analytical problem, but has a $\delta^{15}N$ between -8‰ and +30‰. The second component (≈ 0.25 ppm) is released between 350°C and 400°C, with $\delta^{15}N$ *ca.* -14‰. The first component might be a mixture of fractionated terrestrial atmosphere with organic material, whilst the higher temperature species, which had a lower atomic C/N ratio, could also be organic in origin or the predicted nitrates. Above 400°C, nitrogen is released in gradually decreasing quantities with generally increasing nitrogen isotopic composition.

A second sample from EET A79001, enriched in white druse (carbonates and sulphates) of postulated martian origin, also exhibited a release of nitrogen with $\delta^{15}N$ *ca.* -14‰ at temperatures below 400°C [8]. There has, however, been some discussion on the provenance of the salts, whether they are indeed martian, or simply Antarctic weathering products. The recognition of carbonates in Nakhla [6] argued against a terrestrial origin for the salts, and the same could also be applied to any nitrates present.

Implications: there appear to be two nitrogen-bearing phases in Lithology C from EET A79001 released below 400°C, either of which might be the nitrate identified by FTIR, and both of which have $\delta^{15}N$ values much lower than that estimated for the martian atmosphere [5]. It might therefore be inferred that the nitrates were not formed by direct implantation into the regolith of nitrogen (as NO_x, HNO_2 or HNO_3) from the current atmosphere. An alternative source of nitrogen for the nitrates is from recycling of martian "mantle" nitrogen into the regolith, although the mechanism for the reaction is not clear.

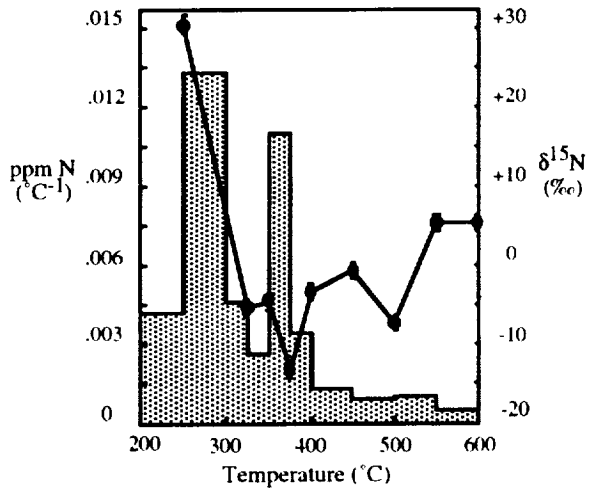

References: [1] McElroy, M. B. *et al.* (1976) *Science* **194** 70-72; [2] Yung, Y. L. *et al.* (1977) *Icarus* **30** 26-41; [3] Pollack, J. B. *et al.* (1990) *J. Geophys. Res.* **95** 14595-14627; [4] Wright, I. P. *et al.* (1990) *J. Geophys. Res.* **95** 14789-14794; [5] Becker, R. H. and Pepin, R. O. (1984) *Earth Planet. Sci. Lett.* **69** 225-242; [6] Carr, R. H. *et al.* (1985) *Nature* **314** 248-250; [7] Wright, I. P. *et al.* (1992) LPI Technical Report No. 92-05 28-29; [8] Wright, I. P. *et al.* (1988) *G. C. A.* **52** 917-924.

A CALIBRATION OF THE PRODUCTION RATE RATIO P_{21}/P_{26} BY LOW ENERGY SECONDARY NEUTRONS: IDENTIFICATION OF Ne SPALLATION COMPONENTS AT THE 10^6 ATOMS/g LEVEL IN TERRESTRIAL SAMPLES. Th. Graf, S. Niedermann[1] and K. Marti, Dept. of Chemistry, Univ. of California, San Diego, La Jolla, CA 92093-0317.

The spallation ratio $(^{22}Ne/^{21}Ne)_c$ from Si was determined as 1.243±0.022 in a terrestrial quartz sample. We carried out a calibration of the *in-situ* production rate ratio P_{21}/P_{26} in quartz samples for which ^{10}Be and ^{26}Al production rates were previously measured. A ratio P_{21}/P_{26} of 0.67±0.12 is obtained.

Recent improvements in experimental techniques make it possible to measure a number of *in-situ* produced cosmogenic radionuclides as well as ^3He and ^{21}Ne in terrestrial rock samples. Unfortunately, the potentially important applications in geomorphology and glaciology are at present limited because the production rates of stable ^{21}Ne are poorly known. This study attempts to remedy the situation by first calibrating the spallation ratio $(^{22}Ne/^{21}Ne)_c$ required for identification of *in-situ* produced cosmogenic components, and second calibrate the production rate ratio P_{21}/P_{26}.

We analyzed several splits of a quartz separate from Antarctic sandstone boulder ALH85-4 (collected in 1882m altitude in the Mawson formation). Quartz was separated according to [1]. ^{10}Be and ^{26}Al results [2] yield a minimum exposure age of 1.06±0.27 Ma and a maximum erosion rate of 0.36±0.05 m Ma^{-1}. The long exposure time accounts for a significant amount of cosmic-ray-produced ^{21}Ne (≈150x10^6 atoms/g), which is expected to outweigh any nucleogenic components in this rock. Fig. 1 shows that data from the four aliquots lie on a straight line passing through the "AIR" point, within error limits. The simplest interpretation is that Ne in ALH85-4 is a two component mixture of trapped Ne (Ne_{tr}) with essentially atmospheric composition and cosmic-ray produced Ne. ^4He can be used to constrain a possible superposition of a Ne component produced by the reaction $^{18}O(\alpha,n)^{21}Ne$: Assuming that at least 1% of ^4He is retained in the sample, less than 5% of the ^{21}Ne excess can be of nucleogenic origin. The slope of the correlation line in Fig. 1 is 1.120±0.021. For a production ratio $(^{21}Ne/^{20}Ne)_c$=0.8±0.1 adopted for Si, we obtain a ratio $(^{22}Ne/^{21}Ne)_c$=1.243±0.022. Slightly higher ratios of 1.3-1.4 were calculated by Michel et al. [3] and Hohenberg et al. [4] for meteorites and the lunar surface, respectively. This ratio should be independent of latitude and altitude of the sampling size, because the cosmic-ray energy spectrum becomes invariant at (atmospheric) depths >200g/cm^2, and negative muon captures contribute little to the Ne production from Si.

$^{21}Ne_c$ is released from quartz at very low temperatures. More then 60% of the $^{21}Ne_c$ is released below 350°C, and above 600°C less than 5% of the $^{21}Ne_c$ remain in the quartz. The stepwise extraction data can be used to estimate the activation energy for diffusion of Ne from quartz. The data ≤350°C yield activation energies of ≈100kJ mol^{-1} K^{-1}.

^{26}Al concentrations and P_{26} rates have previously been determined for quartz separates of Sierra Nevada rocks which were brought to the surface by glacial scouring during the Tioga period of the last ice age ≈11000 years ago [5]. Erosion during the last 11000 years has been less than a millimeter as evidenced by still visible glacial polish. Therefore, these samples appeared well suited for a calibration of the production rate ratio P_{21}/P_{26}. For this work, we selected two of the previously studied quartz separates W86-8, and W86-12 from 3556m and 2452m altitudes, respectively.

As it turned out, the Ne inventory in these samples is much more complicated than in the Antarctic quartz samples. Furthermore, only about 2x10^6 atoms/g $^{21}Ne_c$ are expected due to the short exposure age. The following Ne components have been identified in addition to spallation Ne:

1) Ne produced by the reaction $^{18}O(\alpha,n)^{21}Ne$. Fig. 2 shows the release pattern of excess ^{21}Ne from a density separated grain-size fraction of sample W86-12. The (α,n)-produced component is mainly released below 600°C.

2) Trapped Ne is predominantly released between 400-800°C. The higher release temperature of Ne_{tr}, if compared to $^{21}Ne_c$, indicates that it is at least in part located in different sites. This is supported by the fact that ^{20}Ne abundances show considerable variation in different splits of the same sample. Trapped Ne in density separated 38-90 and 90-125 μm grain-size fractions of sample W86-12 are lower by about a factor of 4. However, all other interfering components are still present. Trapped Ne in sample W86-12 is slightly lighter than atmospheric Ne, while Ne_{tr} in the density separated grain size fractions is within error limits consistent with an atmospheric composition.

3) At high temperatures (>800°C) an additional Ne component ($Ne_{HT,}$) is released that resembles cosmic-ray produced Ne in its isotopic composition. Based on the release profile as well as the amounts of excess ^{21}Ne, this component cannot possibly have been produced *in-situ* by cosmic-rays during the last 11000 a. Alternate

[1] Present address: Physikalisches Institut, University of Bern, Sidlerstrasse 5, CH-3012 Bern, Switzerland.

production mechanisms are (α,n)-reactions in minerals with an O/F ratio of ≈200, or reactions by fission neutrons. Using activation energies and diffusion constants estimated from the high temperature release, we corrected this component at lower temperatures. These corrections are small as can be seen from Fig. 2.

The release patterns obtained from ALH85-4 as well as W86-12 (Fig. 2), show that more than 95% of $^{21}Ne_C$ is released below 600°C. The total ^{21}Ne excess released below 600°C in two splits of sample W86-8 is 2.1±0.4 and 3.4±0.4 atoms, respectively. Therefore, the lower of these values yields an upper limit for the amount of cosmic-ray produced ^{21}Ne in sample W86-8. The corresponding production rate ratio is $P_{21}/P_{26} \leq 0.63\pm0.1$. Corrections for contributions from the high-temperature component are smaller than the stated error. Alternatively, $^{21}Ne_C$ in the density separated 38-90 and 90-125 μm grain-size fractions of sample W86-12 was determined from the Ne released below 600°C assuming that Ne in the two grain size fractions is a three component mixture of trapped, nucleogenic, and spallation Ne. Unfortunately, the calculated production rate ratio P_{21}/P_{26} depends critically on the $^{20}Ne/^{22}Ne$ ratio of the trapped component. Based on Ne three isotope diagrams of all splits from sample W86-12, we conclude that the $^{20}Ne/^{22}Ne$ ratio of the trapped component cannot be larger than atmospheric. The minimum value for P_{21}/P_{26} is 0.70±0.15, and is obtained for a trapped component of atmospheric composition.

Our P_{21}/P_{26} value is considerably larger than theoretical estimates of 0.25-0.5 for Ne produced from Si at large shielding depths [6, Reedy priv. comm.]. On the other hand, in the center of an ordinary chondrite with 65 cm radius, Michel et al. [3] calculate a production rate ratio from Si $P_{21}/P_{26} = 0.68$.

References : [1] C.P. Kohl and K. Nishiizumi (1992) *Geochim. Cosmochim. Acta* 56, 3583-3587. [2] K. Nishiizumi, C.P. Kohl, J.R. Arnold, J. Klein, D. Fink, and R. Middleton (1991) *Earth Planet. Sci. Lett.* 104, 440-454. [3] R. Michel, P. Dragovitsch, P. Cloth, G. Dagge, and D. Filges (1991) *Meteoritics* 26, 221-242. [4] C.M. Hohenberg, K. Marti, F.A. Podosek, R.C. Reedy, and J.R. Shirck (1978) *Proc. Lunar Planet. Sci. Conf.* 9, 2311-2344. [5] K. Nishiizumi, E.L. Winterer, C.P. Kohl, J. Klein, R. Middleton, D. Lal, and J.R. Arnold (1989) *J. Geophys. Res.* 94, 17,907-17,915. [6] D. Lal (1988) *Ann. Rev. Earth Planet. Sci.* 16, 355-388.

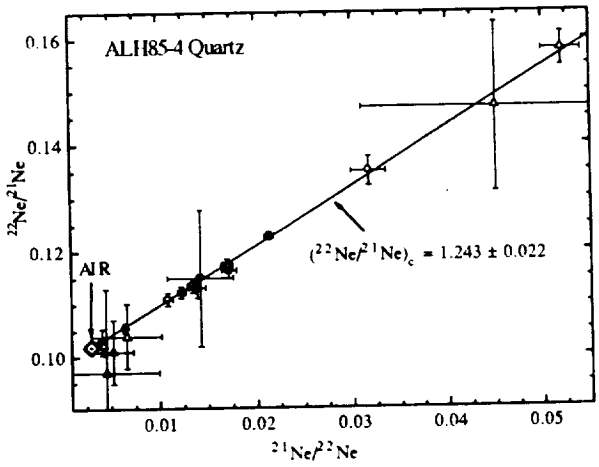

Fig. 1: Ne three-isotope diagram of data from ALH85-4. Error bars correspond to 95% confidence levels. All data lie on a straight line passing through the "AIR" point (atmospheric composition). From the best-fit line we calculate $(^{22}Ne/^{21}Ne)_c = 1.243 \pm 0.022$.

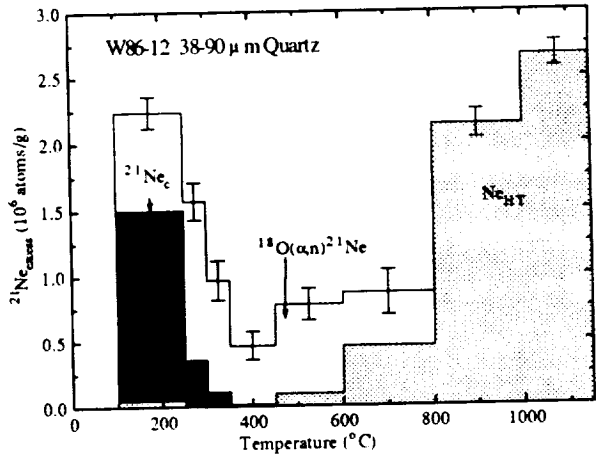

Fig. 2: Release pattern of excess ^{21}Ne from the density separated 38-90μm grain-size fraction of sample W86-12. At low temperatures, excess $^{21}Ne_c$ is of nucleogenic and cosmogenic origin. At high temperatures the release is dominated by $^{21}Ne_{HT}$ (see text). From the high temperature release we estimate an activation energy of ≈115 kJ mol^{-1} K^{-1} for this component. Due to the high activation energy, the contribution at low temperature is small.

NEW K TYPE ASTEROIDS. James C. Granahan, Greg Smith, and Jeffrey F. Bell (Planetary Geosciences, Dept. of Geology & Geophysics, SOEST, University of Hawaii, 2525 Correa Rd., Honolulu, HI 96822)

Several new K type asteroids were identified during near infrared spectral observations on July 30, 1992 at NASA's infrared telescope facility (IRTF) at Mauna Kea, Hawaii. These K asteroids are 513 Centesima, 633 Zelima, 1129 Neujmina, 1416 Renauxa, 1799 Koussevitzky, and 1883 Rauma. A K asteroid is an asteroid which possesses a S type spectra in visible wavelengths and a C type spectra visible in near-infrared wavelengths [1]. These objects are usually misclassified as S asteroids on the basis of visible spectra alone. This type was first detected by the 52 infrared color asteroid survey [2] also conducted at the IRTF . Our observations utilized a new seven color infrared asteroid filter system [3] which allows near-infrared data to be collected from asteroids as faint as 16th V magnitude.

Figures 1 & 2 illustrate the near-infrared characteristics of a newly classified K asteroid. Remember that all of the asteroids discussed in this paper have been classified as S asteroids [4] as determined by studies of their visible spectra. Figure 1 shows the spectral comparison of the new K asteroid 513 Centesima with a S asteroid 7 Iris. Figure 2 shows the spectral comparison of the new K asteroid 513 Centesima with a previously classified K asteroid [1] 221 Eos. The data for 7 Iris and 221 Eos were collected during the 52 infrared color asteroid survey [2]. The data for 513 Centesima was collected with a seven color asteroid filter system [3]. All data were normalized with respect to their 1.5 micron values.

All of the 3 previously known K asteroids were also Eos asteroid family members [1]. These objects, like 221 Eos, have a spectra analogous to that of CV and CO carbonaceous chondrites [1]. This material characterization of K asteroids is important in understanding the geology of the Eos family. In the Williams Eos asteroid family [5] and the Zappala Eos asteroid family [6] the member asteroids are predominantly a mixture of differentiated (S asteroid) materials and primitive (C asteroid) materials according to the visible spectra [7]. Such an asteroid family can not be derived from the disruption of a single parent body. The four 52 color infrared observations [2] combined with our 8 new infrared observations of Eos family asteroids indicate a different trend. These 8 new infrared observations classified the asteroids 513 Centesima, 633 Zelima, 1129 Neujmina, 1416 Renauxa, 1799 Koussevitzky, and 1883 Rauma as K asteroids and the asteroids 1148 Rarahu and 3028 1978 TA2 as S asteroids. The 52 color asteroid survey [1] collected spectra from the S asteroid 639 Latona and the K asteroids 221 Eos, 653 Bernike, and 661 Coelia. Nine of these objects are K asteroids and three are S asteroids. Hence, the Eos family is most likely to be derived from the disruption of a primitive K type parent body with a few interloping differentiated S asteroids. All other major asteroid families have been described as the result of the impact disruption of their respective singular parent bodies.

References:

[1]Bell, J.F. (1988) Meteoritics 23, pp. 256-257. [2]Bell, J.F., Owensby, P.D., Hawke, B.R., and Gaffey M.J. (1988) LPSC XIX (abstracts), pp. 57-58. [3]Granahan, J.C. and Bell, J.F. (1992) Infrared Spectroscopy of Surfaces: Capistrano Conference No.2 (San Juan Capistrano, California, August 3-6, 1992), pp. 34-35. [4]Tholen, D.J. (1989) in Asteroids II (edited by Binzel, R.P., Gehrels, T., and Matthews, M.S.), University of Arizona Press, Tucson, pp. 1139-1150. [5]Williams, J.G. (1989) in Asteroids II (edited by Binzel, R.P., Gehrels, T., and Matthews, M.S.), University of Arizona Press, Tucson, pp. 1034-1072. [6]Zappala, V. Cellino, A., Farinella, P., and Knezevic, Z. (1990) Astron. J. 100, pp. 2030-2046. [7]Granahan, J.C. and Bell, J.F. (1993) On the reality of recently proposed asteroid families, to be submitted to Icarus.

NEW K TYPE ASTEROIDS. Granahan, J.C., Smith, G., and Bell, J.F.

Figure 1

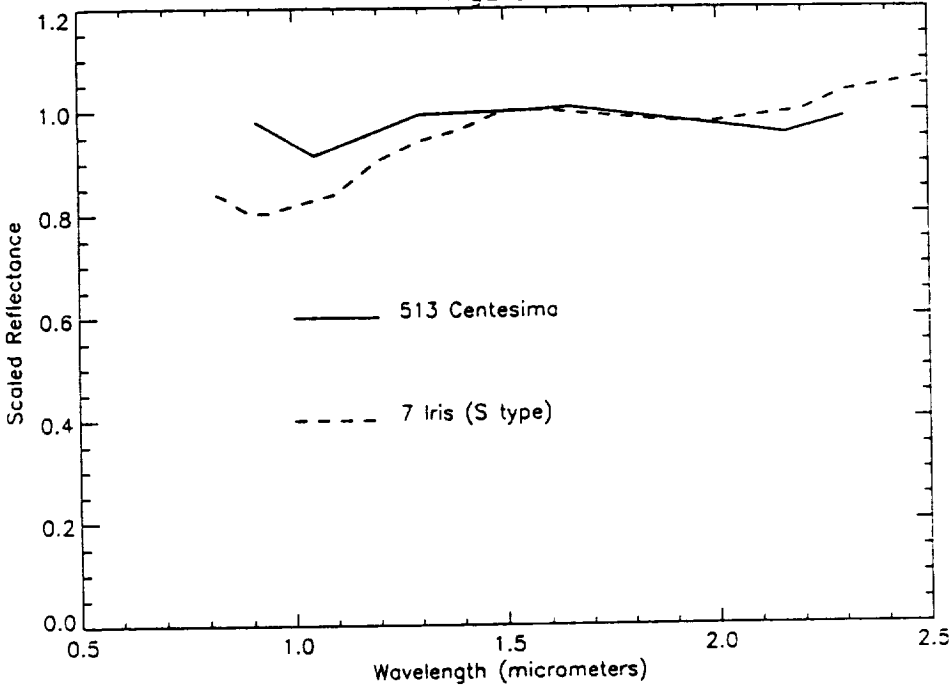

Figure 2

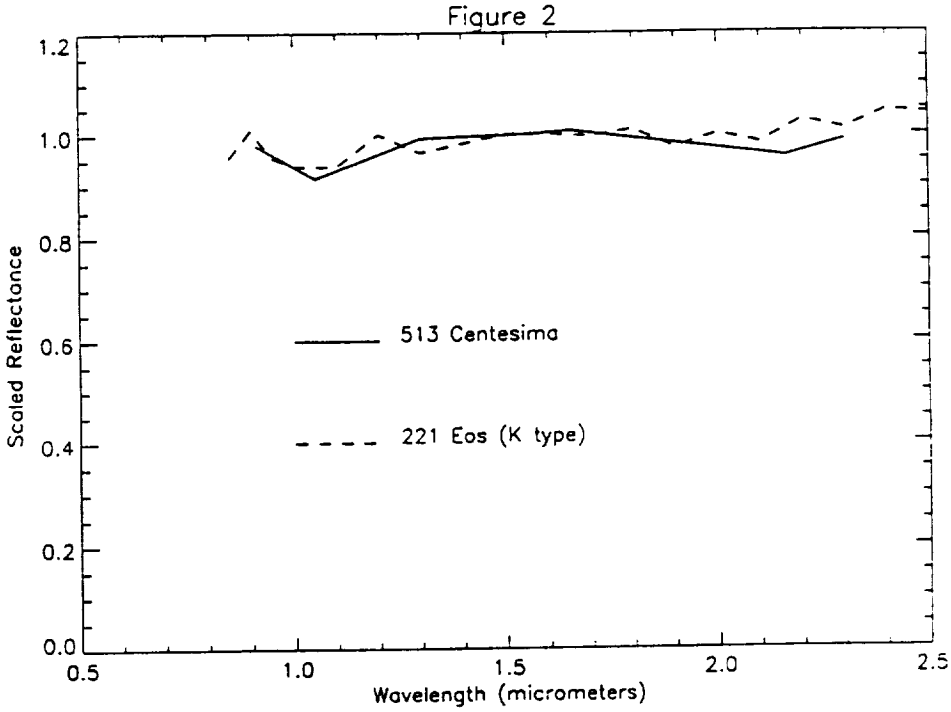

Martian Crater Degradation by Eolian Processes: Analogy with the Rio Cuarto Crater Field, Argentina; J.A. Grant and P.H. Schultz, Brown University, Providence, RI 02912.

Introduction: Numerous degraded and rimless craters occur across broad areas of the martian surface that are mantled by thick, unconformable deposits (Fig.1). These regions include Arabia, Mesogaea, Electris, Tempe, the interior and surface to the northwest of Isidis Basin, southern Ismenius Lacus, and the polar layered terrains (1–7). Occurrence of the deposits (1–7) and low regional thermal inertias (8–9) indicate that at least some accumulated fine-grained sediment (effective particle diameters of 0.1–0.5 mm or coarse silt to medium sand) to a thickness of 100's to 1000's of meters. Most unconformable deposits experienced some eolian modification (1–2, 4) that may be recent in some locales (1). Despite the presence of these deposits, simple eolian deposition appears incapable of creating the numerous degraded and rimless craters occurring within their limits (10–11). Nevertheless, terrestrial analyses of the Rio Cuarto craters formed into loessoid deposits (12–14) demonstrates that eolian redistribution of fine-grained sediment in and around craters produces degraded morphologies that are analogous to some found in mantled regions on Mars.

The Rio Cuarto Craters: The Rio Cuarto Crater Field is located at 64°15'W, 32°45'S in Argentina (12–13). Formation occurred during a low angle impact (12–13) into the Pampas plains that created ten elongate depressions extending from north to south over 30 km. Individual craters are up to 4.5 km long, 10 m deep, and all possess a 4:1 length-to-width ratio. Present expression of the craters is confined to the loessoid Pampean Formation comprised of coarse silt, very fine sand, and lesser fine sand (~0.03–0.25 mm; 14). Rim relief around the craters (Fig. 2) varies from low on upwind or north ends to more hummocky along the sides to high at downwind or south ends (12, 14). Side rims are typically mantled by eolian dunes that grade outward to the surrounding plains (Fig. 2) and side walls are alternately exposed and buried by downwind-migrating transverse dunes. Variably active longitudinal and transverse dune fields bury topography at the downwind ends of the craters (11, 14), some extending 1 km beyond the rim. Crater floors are partially stripped to expose a calcrete-like surface, especially towards downwind ends. Time of the Rio Cuarto impact remains uncertain, but was likely within the past few thousand years (11–12). Hence, degradation at Rio Cuarto is influenced by substrate and climate, thereby indicating the survival time of oblique craters in fine-grained substrates is short compared to deep craters formed by higher angle impacts (7).

Eolian Degradation at Rio Cuarto: Rapid, mostly eolian degradation predominates at Rio Cuarto based on analyses of regional sedimentology and preserved geomorphic features. Additional contributions to overall denudation are made by mass wasting and lesser fluvial processes. These conclusions are supported by: A) the large number and diversity of dunes in and around the craters that indicates a sustained, abundant sediment supply; B) the uniform, fine-grained character of the Pampean loessoid material that makes it susceptible to deflation; C) a paucity of large, lithic ejecta fragments capable of producing surface armoring lag deposits during erosion (15); D) formation of yardangs in some craters (14); E) low drainage densities in and around the craters (~0.4–2.5 km/km² and 0.3–0.5 km/km², respectively); F) rare examples of rim and wall incisement; and G) the degraded character of most mass wasting features inside the craters.

Eolian degradation is accomplished by strong prevailing winds that erode upwind rims of the Rio Cuarto craters, produce a net downwind transport of sediment, and cause backwasting of crater walls (Fig. 2). Some wind funneled into the craters escapes over side rims, decelerates, and forms deposits subsequently redistributed into dunes (Fig. 2). Eolian scouring of crater sides results in oversteepening, collapse, and significant crater enlargement via backwasting: resultant deposits are redistributed into downwind migrating transverse dunes as evidenced by the modified appearance of mass wasting debris. Most sediment stripped from crater floors is transported downwind through gaps in the impact topography (11,12) and forms longitudinal and more distal transverse dune fields. Fluvial degradation is limited by moderate hydraulic conductivity in the sandy loess (0.3–3.0 m/day) that combined with low regional gradients causes infiltration and subsurface drainage of most precipitation.

Comparisons to Mars: Analogy with Rio Cuarto indicates that eolian redistribution of sediment in areas of thick fine-grained accumulations on Mars can significantly degrade or even destroy craters. In these areas, craters may be largely confined to the fine-grained deposits, thereby creating a setting much like that at Rio Cuarto. On Mars, such craters may experience wholesale rim destruction by strong, shifting winds. Conversely, transport out of some craters could lead to near-rim deposition and formation of "false" rims. Deflation along crater walls, resultant oversteepening and mass wasting would destroy rims through backwasting and crater enlargement. Efficient eolian removal of sediment deflated from inside the Rio Cuarto craters implies that similarly derived grains could be removed from both shallow and perhaps deep martian craters by eolian activity. Therefore, eolian degradation of craters on Mars may not be self-limiting or produce obvious deposits, but may best be identified by the presence of near-rim or intra-crater dunes and a paucity of degradation signatures associated with other processes. Eolian modification of craters formed in the martian unconformable deposits may have accelerated during past epochs of more equable climate (4, 6-7). Similarities between the substrate and degradational character at Rio Cuarto and that inferred for craters in the fine-grained martian deposits implies comparative studies using high resolution Mars Observer imagery will further resolve the history of climate-controlled degradation on Mars.

References: (1) Ward, A.W., 1979: *J. Geophys. Research*, **84**, 8147. (2) Arvidson, R.E., Guinness, E. and Lee, S., 1979: Lunar and Planet. Sci. XV, 19, Lunar and Planetary Institute, Houston, Texas. (3) Scott, D.H. and Tanaka, K.L., 1982, *J. Geophys. Research*, **87**, 1179. (4) Schultz, P.H. and Lutz, A.B., 1988: *Icarus*, **73**, 91. (5) Grizzaffi, P. and Schult, P.H., 1989: *Icarus*, **77**, 358. (6) Grant, J. A. and Schultz, P. H., 1990: *Icarus*, v. **84**, 166. (7) Grant, J.A. and Schultz, P.H., 1993: *J. Geophys. Research*, in review. (8) Zimbelman, J.R., 1986: NASA Tech. Memo. 88784. (9) Christensen, P.R., 1986: *J. Geophys. Research*, **91**, 3533. (10) Zimbelman, J.R. and Greeley, R., 1981: Lunar and Planet. Sci. XII, 1233, Lunar and Planetary Institute, Houston, Texas. (11) Craddock, R.A. and Maxwell, T.A., 1990: *J. Geophys. Research*, **95**, 14,265. (12) Schultz, P.H. and Lianza, R.E., 1992: *Nature*, **355**, 234. (13) Schultz, P.H., *et al.*, 1992: Lunar and Planet. Sci. XXIII, 1237, Lunar and Planetary Institute, Houston, Texas. (14) Grant, J.A. and Schultz, 1992: Lunar and Planet. Sci. XXIII, 439, Lunar and Planetary Institute, Houston, Texas. (15) Grant, J.A., 1990: Ph.D. Dissertation: Geology, Brown University, Providence, R.I., 401p.

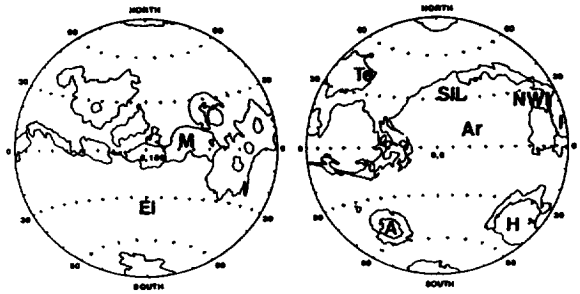

Figure 1. Regions of significant fine-grained, unconformable deposition on Mars. Letters correspond to the following locations: Mesogaea, M; Electris, El; Tempe, Te; southern Ismenius Lacus, SIL; Arabia, Ar; northwest of Isidis, NWI; Isidis basin, I; Argyre basin, A; and Hellas basin, H.

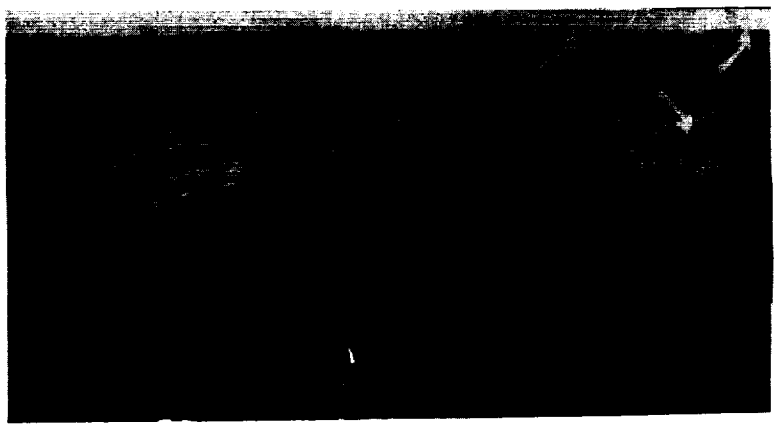

Figure 2. Prevailing wind flow (white arrows) into and through one of the smallest craters in the Rio Cuarto Field (~1 km long). These winds erode upwind sections of the rim and transport sediment eroded from along the walls out of the craters where it is deposited and redistributed into near-rim dunes. These bounding dunes grade to the level of the surrounding plains over several ~100's of m around the larger craters. Eolian degradation produces a net downwind transport of sediment.

Rover Mounted Ground Penetrating Radar as a Tool for Investigating the Near-Surface of Mars and Beyond; J.A. Grant and P.H. Schultz, Brown University, Providence, RI 02912.

Introduction: In spite of the highly successful nature of recent planetary missions to the terrestrial planets and outer satellites a number of questions concerning the evolution of their surfaces remain unresolved. For example, knowledge of many characteristics of the stratigraphy and soils comprising the near-surface on Mars remains largely unknown, but is crucial in order to accurately define the history of surface processes and near-surface sedimentary record. Similar statements can be made regarding our understanding of near-surface stratigraphy and processes on other extraterrestrial planetary bodies. Ground penetrating radar (GPR) is a proven and standard instrument capable of imaging the subsurface at high resolution to 10's of meters depth in a variety of terrestrial environments (e.g. 1-5). Moreover, GPR is portable and easily modified for rover deployment. Data collected with a rover mounted GPR could resolve a number of issues related to planetary surface evolution by defining shallow stratigraphic records and would provide context for interpreting results of other surface analyses (e.g. elemental or mineralogical). A discussion of existing GPR capabilities is followed first by examples of how GPR might be used to better define surface evolution on Mars and then by a brief description of possible GPR applications to the Moon and other planetary surfaces.

GPR on the Earth: Terrestrial experience with GPRs outfitted with transducers having frequencies of 50 to 500 MHz demonstrates the ability of instrument to define stratigraphy up to 30-40 m depth (1) and a vertical/horizontal resolution of up to ~10 cm (2,3). Moreover, successful GPR deployment in and around Meteor Crater, Arizona, Odessa Craters, Texas, and the Rio Cuarto Craters, Argentina, illustrates the capabilities of GPR in somewhat analogous planetary settings (2,3). Data collected along short transects (10-100 m) at these impact sites with an analogue GPR yielded stratigraphic markers corresponding to ejecta, alluvium, calcic soils, and *in situ* bedrock (Figs. 1 and 2), all possessing dielectric constants between 4-10. Prominent stratigraphic reflectors were identified even where calcic soils were well developed (Fig. 2). GPR data from other terrestrial settings distinguishes bedding planes in bedrock (4) and lacustrine sediments beneath a thick ice cover (5). These characteristics coupled with the probability that a planetary GPR would possess only ~2-3 kg mass, occupy less than 2000 cm^3, use ~10-15 watts, and operate at low temperatures, implies GPR could define shallow martian stratigraphy and should be considered for future rover missions.

GPR on Mars: Definition of shallow stratigraphy on Mars using a rover mounted GPR could answer a range of questions regarding surface evolution when accompanied by ground truth from penetrators or cores. Locally, GPR could define the occurrence of sulphur-enriched duricrusts (6); a varying distribution of the deposits supports a groundwater source (6) while uniform, discretely layered accumulations imply fallout of aerosols (7). GPR might also be used to identify carbonates that may have formed in the regolith (8), but are poorly detected telescopically (9). The radar would also test models of ground ice/water distribution (e.g. 10) or for the presence of near-surface brines (11-12). Even without ground truth, GPR would define shallow stratigraphic complexity, thereby providing context for interpreting data from other instruments and identifying future coring locations.

On a broader scale, GPR could be used to constrain the nature and origin of fine-grained deposits that mantle portions of the cratered uplands on Mars (e.g. 13-14) and preserve the long-term sedimentary history of surface-atmosphere exchanges. Moreover, GPR transects within the northern lowlands plains should distinguish characteristic stratigraphy and structure that would help identify whether alluvial, volcanic, eolian (e.g. 15), pelagic (16), and/or some other process(es) are responsible for their origin. For example, GPR definition of laterally discontinuous, either poorly sorted and crudely layered deposits or better sorted, more uniformly bedded bar and swale features would suggest that alluvial processes created the lowlands plains. Conversely, identification of continuously bedded, well-sorted and fine-grained deposits devoid of bedforms, but possibly interbedded with coarser turbidites is more indicative of pelagic deposition. Volcanic and eolian beds can be similarly characterized (e.g. through the presence of characteristic fracture patterns, or bedforms).

GPR on Other Planets: GPR data collected at terrestrial impact sites discriminates *in situ* bedrock, ejecta, alluvium, and soils, thereby highlighting the potential of the instrument for investigating the dry surface of the Moon as well as other satellites and planets. Inclusion of a GPR on a lunar rover would allow high resolution definition of shallow stratigraphy when interpreted using existing data on lunar dielectric properties (17) and more general results from the Apollo lunar sounder (18). In mare regions, GPR might define lava flow thicknesses, detect underlying basement topography along marginal areas, and locate lava tubes or other buried volcanic structures, some of which may be hazards to avoid during subsequent missions. Collectively, this information could verify compositional units defined by other instruments (19). On the surfaces of the icy Galilean satellites, GPR could be used to characterize any regolith, identify possible water ice dikes, further define near-surface stress patterns, or determine the near-surface distribution of ice versus rocky material (20).

References: (1) Pilon, J.A., *et al.*, 1991: *J. Geophys. Res.*, **96**, 15,563. (2) Grant, J.A. and Schultz, P.H., 1991: Lunar and Planet. Science XXII, 481, Lunar and Planetary Institute, Houston, Texas. (3) Grant, J.A. and Schultz, P.H., 1992: LPI Tech. Rept. 92-07, 5, Lunar and Planetary Institute, Houston, Texas. (4) Doolittle, J.A., 1987: Special Pub. 20, Soil Science Society of America, Madison, WI. (5) Geophysical Survey Systems, 1974: GSSI Tech. Memo, GSSI, North Salem, N.H. (6) Toulmin, P., *et al.*, 1977: *J. Geophys. Res.*, **82**, 4625. (7) Settle, M., 1979: *J. Geophys. Res.*, **84**, 8343. (8) Fanale, F.P., *et al.*, 1982, *Icarus*, **50**, 381. (9) Blaney, D.L. and McCord, T.B., 1990, Lunar and Planet. Science XXI, 97, Lunar and Planetary Institute, Houston, Texas. (10) Fanale, F.P., *et al.*, 1986: *Icarus*, **67**, 1. (11) Zent, A.P., *et al.*, 1990: *J. Geophys. Res.*, **95**, 14,531. (12) Huguenin, R.L., *et al.*, 1986: *Icarus*, **68**, 99. (13) Schultz, P.H. and Lutz, A.B., 1988: *Icarus*, **73**, 91. (14) Scott, D.H. and Tanaka, K.L., 1982: *J. Geophys. Res.*, **87**, 1179. (15) Greeley, R. and Guest, J.E., 1987: USGS Map I-1802-B. (16) Parker, T.J., *et al.*, 1989: *Icarus*, **82**, 111. (17) Olhoeft, G.R. and Strangway, D.W., 1975: *EPSL*, **24**, 394. (18) Peeples, W.J., *et al.*, 1978: *J. Geophys. Res.*, **83**, 3459. (19) LPI, 1992: Workshop on Early Robotic Missions to the Moon, Lunar and Planetary Institute, Houston, TX. (20) Morrison, D. (ed.), 1982: *Satellites of Jupiter*, U of A Press, Tucson, AZ.

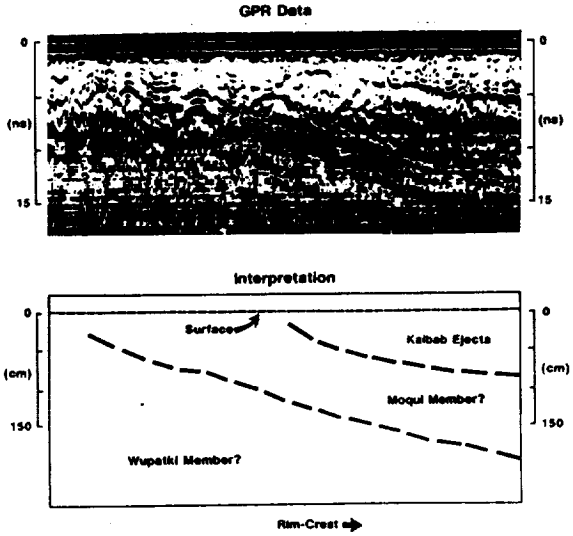

Figure 1. Analogue GPR transect from N to S across the distal edge of the continuous ejecta ~1.3 km south of Meteor Crater (GPR supplied by Geophysical Survey Systems, Inc.). Radar pulse travel time is in nanoseconds and the depth is in cm. Transducer frequency is 500 MHz. Ejecta comprised primarily of ejected Kaibab Formation fragments directly superposes *in situ* Moqui and deeper Wupatki Members of the Moenkopi Formation. Interpretations were confirmed by excavation and/or tracing reflectors to outcrop.

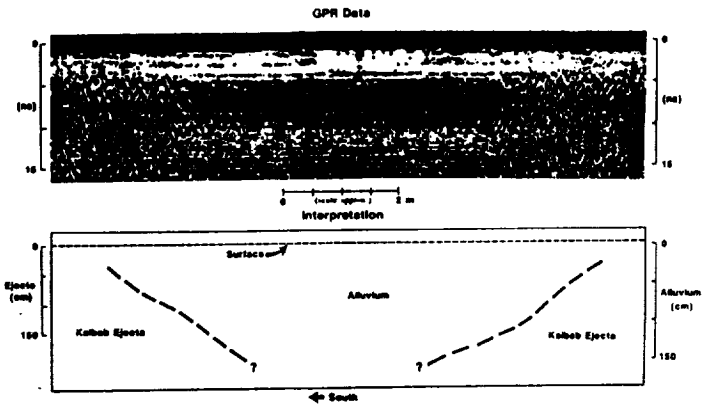

Figure 2. Analogue GPR transect from SE to NW across alluvium ~0.9 km S of Meteor Crater (GPR supplied by Geophysical Survey Systems, Inc.). Radar pulse travel time is in nanoseconds and the depth is in cm. Transducer frequency is 500 MHz. Kaibab ejecta and alluvium are clearly distinguished as is the top of a calcic soil horizon (Bk horizon) at ~50 cm depth (top of dark zone in alluvium). Discontinuous reflectors in the ejecta are caused by buried blocks. Contacts were confirmed by excavation.

SAND TRANSPORT ON MARS: PRELIMINARY RESULTS FROM MODELS;
R. Greeley, F. S. Anderson, D. Blumberg, E. Lo, P. Xu, *Arizona State University, Tempe, AZ*; and J. Pollack, *NASA-Ames Research Center, Moffett Field, CA.*

Summary:

Most studies of active aeolian processes on Mars have focused on dust [1], i.e., particles ~1 μm in diameter that are transported in suspension by wind. The presence of sand dunes on Mars [2-8] indicates that larger grains (≥60 μm, transported primarily in saltation) are also present. Although indirect evidence suggests that some dunes may be active [9], definitive evidence is lacking. Nonetheless, numerous studies [10-11] demonstrate that sand is substantially easier to transport by wind than dust, and it is reasonable to infer that sand transportation in saltation occurs under present martian conditions. In order to assess potential source regions, transportation pathways, and sites of deposition for sand on Mars, an iterative sand transport algorithm was developed that is based on the Mars General Circulation Model of Pollack et al. [12]. The results of the dust transport model are then compared with observed surface features, such as dune field locations observed on images, and surficial deposits as inferred from Viking IRTM observations. Preliminary results suggest that the north polar dune fields in the vicinity of 270°W, 70°N originated from weathered polar layered plains centered at 280°W, 85°N, and that Thaumasia Fossae, southern Hellas Planitia, and the area west of Hellespontus Montes are sand depositional sites. Examples of transportation "corridors" include a westward pathway in the latitudinal band 35°N to 45°N, and a pathway southward from Solis Planum to Thaumasia Fossae, among others.

Technique:

An algorithm was developed that enables the flux of sand as a vector-mass to be calculated for each of 960 spatial bins covering Mars, at 1.5 hour intervals of time. The program is run iteratively and displayed as a series of images portraying the net changes in sand deposits on Mars through time. Each bin is 7.5° lat. by 9° long., corresponding to the geographic cells of the GCM. The GCM provides the wind shear stress vector for each 1.5 hours under specified conditions of temperature, pressure, and atmospheric opacity (i.e., "dust-loading") appropriate for the martian season, as calibrated against measurements of the Viking landers [13]. In addition, topography to a one kilometer contour interval is taken into account. The predicted wind shear stress values on the surface are then used in the White [14] expression for sand flux on Mars. As initial conditions, we assume a layer of sand (average grain size, 100 μm) .1mm thick, spread uniformly over the entire planet. For sake of simplicity, this is the equivalent to a single 100 μm grain (the size moved by the lowest winds [11]) weathered free on the surface. The vector-mass of sand transported (for wind shears above threshold) is then partitioned to adjacent bins for the 1.5 hour period of each iteration. The output is summed over a martian year of GCM data, being careful not to move sand from bins that have become empty. This gives the net sand transport for that year, which is then converted into a color image for viewing. This result is used as the initial condition for the next year, and the process is repeated.

Discussion:

The results described in the summary represent model parameters of: a) 150 years, b) threshold stress of .04 N/m^2, c) initial sand thickness of .1 mm, and d) a sand density of 2.65 g/cm^3. In the northern hemisphere, there is westward transport of sand in saltation along a subtropic latitudinal band from 35°N to 45°N. This band extends around the planet, pinching out in the vicinity of Deuteronilus Mensae and 130°W, 50°N. Material in this band is transported to the south and west, depositing sand in Western Arcadia Planitia, in the vicinity of Cassini crater (325°W, 30°N), in the Cerberus region (190°W, 20°N), and in the vicinity of 315°W, 60°N. In the north polar area, sands are transported from 280°W, 85°N to two regions, 270°W, 70°N and 240°W, 75°N, corresponding to some of the dune fields observed around the northern pole. This result suggests that the source of the material forming these dunes are the polar layered deposits, as suggested by Thomas [5]. In addition, the model shows sand deposition in the vicinity of

315°W, 60°N, corresponding to a region of dark albedo, suggested by Edgett [15] to be sand deposits. The modeled sand deposits of western Arcadia Planitia and Cerberus correspond to regions containing bright streaks, an indication of active dust deposition [16].

The southern hemisphere is typified by four main regions of modeled sand transport. In the model, sands appear to be eroded from Solis Planum and transported to Thaumasia Fossae. In addition, sand is eroded from western Hellespontus Montes and is deposited to the west and south. Model results suggest erosion from northern Hellas Planitia and deposition to the south, possibly correlating with small dune fields observed in the area. Lastly, the model shows sand transport from the vicinity of Sirenum Fossae to the vicinity of the Mars 2 landing site (210°W, 40°S), a region associated with bright wind streaks.

Conclusion:

Preliminary results using the sand motion algorithm, suggests a pattern of erosion, transportation, and deposition on Mars that correlates well with some observed dune fields and surficial deposits. Other regions of primary deposition correlate well with areas known to contain bright streaks, although this association is poorly understood at present. Ongoing modeling is testing this relationship, exploring the effects of varying input parameters including the threshold and nonuniform initial sand distributions, and incorporating refinements to the algorithm, such as inclusion of variable surface roughness.

References:

[1] Zurek, R.W., Martian great dust storms, *Icarus, 50*, 280-310, 1982. [2] Cutts, J.A., K.R. Blasius, G.A. Briggs, M.H. Carr, R. Greeley, and H. Masursky, North polar region of Mars: Imaging results from Viking 2, *Science , 194*, 1329-1337, 1976. [3] Cutts, J.A., and R.S.U. Smith, Eolian deposits and dunes on Mars, *J. Geophys., Res., 78*, 4139-4154, 1973. [4] Breed, C.S., M.J. Grolier, and J.F. McCauley, Morphology and distribution of common 'sand' dunes on Mars: Comparison with Earth, *J. Geophys., Res., 84*, 8183-8204, 1979. [5] Thomas, P., North-south asymmetry of eolian features in Martian polar regions: Analysis based on crater-related wind markers, *Icarus, 48*, 76-90, 1981. [6] Thomas, P., Present wind activity on Mars: Relation to large latitudinally zoned sediment deposits, *J. Geophys., Res., 87*, 9,999-10,008, 1982. [7] Thomas, P., Martian intracrater splotches: Occurence, morphology, and colors, *Icarus, 57*, 205-227, 1984. [8] Peterfreund, A.R., Visual and infared observations of windstreaks on Mars, *Icarus, 45*, 447-467, 1981. [9] Tsoar, H., R. Greeley, and A.R. Peterfreund, Mars: The North Polar Sand Sea and related wind patterns, *J. Geophys., Res., 84*, 8167-8180, 1979. [10] Greeley, R., R. Leach, B. White, J. Iverson, and J. Pollack, Threshold windspeeds for sands on Mars: Wind tunnel simulations, *Geophys. Res. Lett., 7*, 121-124, 1980. [11] Iversen, J.D., and B.R. White, Saltation threshold on Earth, Mars, and Venus, *Sedimentology*, 29, 111-119, 1982. [12] Pollack, J.B., R.M. Haberle, J. Schaeffer, and H. Lee, Simulations of the General Circulation of the Martian Atmosphere, 1. Polar Processes, *J. Geophys., Res., 95*, 1447-1473, 1990. [13] Pollack, J.B., D.S. Colburn, F.M. Flaser, R. Kahn, C.E. Carlston, and D.C. Pidek, Properties and effects of dust particles suspended in the Martian atmosphere, *J. Geophys., Res., 84*, 2929-2945, 1979. [14] White, B.R, Soil Transport by Winds on Mars, *J. Geophys., Res., 84*, 4643-4651, 1979. [15] Edgett, K.S., and P.R. Christensen, The Particle Size of Martian Aeolian Dunes, *J. Geophys., Res., 96*, 22,765-22,776, 1991. [16] Skypeck, A.P., Thesis: Comparison of a Mars General Circulation Model with Aeolian Features and Deposits, Arizona State University, 1989.

GALILEO IMAGING RESULTS FROM THE SECOND EARTH-MOON FLYBY: LUNAR MARIA AND RELATED UNITS; R. Greeley[1], M.J.S. Belton[2], J.W. Head[3], A.S. McEwen[4], C.M. Pieters[3], G. Neukum[5], T.L. Becker[4], E. M. Fischer[3], S. D. Kadel[1], M.S. Robinson[6], R.J. Sullivan[1], J.M. Sunshine[3], and D.A. Williams[1]. *(1) Arizona State University, Tempe, AZ; (2) NOAO, Tucson, AZ; (3) Brown University, Providence, RI; (4) U.S. Geological Survey, Flagstaff, AZ; (5) German Aerospace Research Establishment (DLR), Inst. for Planetary Exploration, Berlin/Oberpfaffenhofen, Germany; (6) University of Hawaii, Honolulu, HI.*

The second flyby of the Earth-Moon System by Galileo occurred on December 7, 1992, on its trajectory toward Jupiter. The flyby took the spacecraft over the lunar north polar region from the dark farside and continued across the illuminated nearside. This provided the first opportunity to observe northern and northeastern limb regions with a modern, multispectral imaging system [1] with high spatial resolution (up to 1.1 km/pixel). Scientific objectives included compositional assessment of previously uncharacterized mare regions, study of various light plains materials, and assessment of dark mantle deposits (DMD) and dark halo craters (DHC). Color composite images were prepared from ratios of Galileo SSI filter data (0.76/0.41→ red; 0.76/0.99 → green; 0.41/0.76 → blue) and used for preliminary comparison of units [2]. The 0.41/0.76 ratio has been empirically correlated to Ti content of mare soils (blue is relatively high, red is relatively low) [3]. The relative strengths of the ferrous one micron absorption in mafic minerals can be compared using the 0.76/0.99 ratio. In addition, relative ages of units analyzed spectrally were determined from crater statistics using Lunar Orbiter images following the techniques of Neukum et al. [4]. Mare deposits analyzed include Mare Humboldtianum, central and eastern Mare Frigoris, Mare Crisium and other deposits in the Crisium Basin, and isolated mare patches on the northeastern lunar limb. Preliminary results show a diversity of 0.41/0.76 micron signatures, implying a wide range of titanium contents. Some light plains units are similar to units found at the Apollo 16 site; others may be ancient mare materials. Dark mantle deposits (DMD) analyzed also are variable.

Analyses of the maria show that:

1) Mare Humboldtianum contains two distinct units. The western two-thirds is composed of red (lower-Ti) mare basalts, whereas the eastern third is bluer (higher in Ti) and has a stronger 0.76/0.99 ratio.

2) Previously uncharacterized basalts in Mare Anguis are red, similar to the low-Ti Eimmart basalts [5] in Mare Crisium.

3) Previously uncharacterized basalts in Mare Undarum, Mare Spumans, and the mare patch in crater Firmicus are similar to each other and to the medium-high-Ti Alhazan basalts [5] in Mare Crisium.

4) The mare deposit in Mare Fecunditatis, which includes the Luna 16 site, appears bluer than previously mapped [6], and is composed of two distinct units.

5) A small, unusually dark mare deposit south of crater Mercurius (43.6 N, 63.8 E) is relatively blue, and is the only Ti-rich mare deposit on the northeastern limb which may not be associated with an impact basin.

6) Small areas of Ti-rich mare may be present in Mare Marginis and in craters Goddard and Neper. Both Mare Marginis and Mare Smythii have strong 0.76/0.99 micron signatures.

Dark mantle deposits (DMD) were examined in the craters Gauss, Messala, Atlas and Franklin. The DMD in Gauss and Messala are red, perhaps similar to the red deposits on the Aristarchus Plateau [7,8]. In contrast, DMD in Atlas, Franklin, and a newly discovered site in Crater Hahn (31.8 N, 74.5 E) are blue. Comparisons with previously identified DMD are currently underway.

GALILEO IMAGING RESULTS: Greeley, R. et al.

Light plains deposits are found in many regions of the Moon, as sampled at the Apollo 16 site. The largest concentration of light plains is found in the north polar region, north of Mare Frigoris [9]. In general, light plains may be of diverse origins and ages [10,11]. Galileo results show that light plains north of eastern Mare Frigoris have 0.41/0.76 micron ratios and surface morphologies comparable to those of the Apollo 16 site; impact crater frequencies indicate a cratering model age of 3.71 ± 0.05 Ga. In contrast, light plains near craters Carpenter and Philolaus have different signatures, and impact crater frequencies indicating ages from 3.9-4.0 Ga.

Some lunar surfaces appear to involve ancient mare deposits that have been thinly mantled with high albedo material such as impact crater ejecta. Dark halo craters in these regions are interpreted to represent impacts that penetrated the mantling deposits to excavate the underlying mare material [12,13]. Termed *cryptomaria* [14], such deposits extend the geographic distribution of maria and age range of volcanism on the Moon. There is evidence for an early, Ti-rich stage in the mare filling of eastern Mare Frigoris. The 8 km DHC Gärtner D (58.5 N, 33.9 E) excavated blue mare materials from beneath the light plains unit of northeastern Mare Frigoris. In addition, there is a patch of blue mare exposed at the extreme eastern end of Mare Frigoris. Another exposure of this unit may be present in the plains just north of crater Galle. SSI EM-2 data show moderate to low albedo zones over regions north of eastern Mare Frigoris, east of Mare Marginis, and southwest of Mare Smythii, which suggest the possibility of cryptomaria in these regions. Cryptomaria tentatively identified from Galileo EM-1 total ~6 x 10^5 km^2. Combined with previously known mare deposits, this makes a total of ~19% of the lunar surface involving mare volcanism. Alternatively, some of these deposits may be of other origin [15]. Cryptomaria observed in EM-1 data indicate that significant mare volcanism occurred prior to the Orientale event. Thus, lunar volcanism is seen over a wider area for a longer period of time than previous estimates.

References:

[1] Belton, M.J.S. et al. (1992) *Space Sci. Rev., 60,* 403-455.
[2] McEwen, A.S. et al. (1993) *Lunar Planet. Sci., XXIV.*
[3] Charette, M.P. et al. (1974) *J. Geophys. Res., 79,* 1605-1613.
[4] Neukum, G. et al. (1975) *The Moon 12,* 201-229.
[5] Head, J. et al. (1978) *Mare Crisium: The View from Luna 24,* 43-74.
[6] Pieters, C. (1978) *Proc. Lunar Planet. Sci. Conf. 9,* 2825-2849.
[7] Gaddis, L. et al. (1984) *NASA Tech. Memo. TM-87563,* 399-401.
[8] Lucey, P. et al. (1986) *Proc. Lunar Planet. Sci. Conf. 16,* D344-D354.
[9] Howard, K. et al. (1974) *Rev. Geophys. Space Phys. 12,* 309-327.
[10] Neukum, G. (1977) *The Moon 17,* 383-393.
[11] Greeley, R. et al. (in press) *J. Geophys. Res.*
[12] Schultz, P.H. and Spudis, P.D. (1979) *Proc. Lunar Planet. Sci. Conf. 10,* 2899-2918.
[13] Hawke, B. and Bell, J. (1981) *Proc. Lunar Planet. Sci. Conf. 12,* 665-678.
[14] Head, J.W. and L. Wilson (1992), *Geochima Cosmochima Acta 56,* 2155-2175.
[15] Head, J.W. et al. (1993) *Lunar Planet. Sci., XXIV.*

MARS ANALOG SITE STUDY (MASS); R. Greeley, *Arizona State University, Tempe, AZ*; R. Kuzmin, *Vernadsky Institute, Russia*; F. Costard, *Centre de Geomorphologie, France*; and F.S. Anderson, M.A. Geringer, R. Landheim, M.L. Wenrich, *Arizona State University, Tempe, AZ*

Many proposed missions to Mars involve landed vehicles, including the Mars 94/96 (Russia), Mars Environmental Survey (MESUR, US), and the Marsnet (ESA) missions. Most landers involve *in situ* measurements of rock and soil compositions, study of local geology by imaging, and establishment of seismic and meteorological networks. The selection of landing sites on Mars is a complex process that must meet engineering constraints and scientific objectives, using available and anticipated data. The goal of the MASS project is to conduct an "end-to-end" test of the site selection process using Earth analogs.

Approach. Criteria for landing site selection can be divided into two groups: 1) *a priori* criteria and 2) selection criteria. The first group includes factors such as elevation constraints (e.g., some landings must occur at <4 km elevation to enable sufficient atmospheric drag on parachutes) and geographic requirements (e.g., "network" science such as meteorology requires certain geographic placement of stations). The second group includes the selection of sites that have a high probability of meeting specific scientific and engineering goals. An example would be to identify a place on Mars that consists of ancient igneous rocks and has a flat, smooth surface. The MASS Project was aimed toward understanding this second group of selection criteria. The concept was to use remote sensing data of the southwest United States, apply the scientific objectives of the MESUR and Mars 94 missions, and identify analog sites in a "blind" test conducted by individuals unfamiliar with the area. This phase was followed by field work to assess the results and to collect data on rock and slope distributions and other characteristics of interest to mission engineers.

Specific types of sites included young volcanic terrains with different stages of surface modification, sedimentary deposits, aeolian terrains, sites that meet goals for exobiologic science, and others that are appropriate for most Mars landing missions. Objective criteria for the identification of these site types using remote sensing data were established. Data used in the analysis included low resolution ERTS images, higher resolution Landsat frames (color and monochromatic bands), Shuttle Large Format Camera images, conventional aerial photographs, and radar images. These data sets were selected because they are comparable to some existing and anticipated data for Mars. Data were analyzed in stages of increasing resolution, using the objective identification criteria for each type of site. In addition, site surfaces were assessed in terms of rock size and distribution, slopes, and discontinuities based on geological interpretations. At each stage, the "value added" of increased image resolution, color, and radar backscatter was assessed.

Preliminary Results. In the initial stages of study, ~45 sites were tentatively identified in Nevada and southern California. Because of limited data coverage for some sites and time constraints, the number of sites was narrowed to 10, 7 of which were examined in the field. Specific locations for field study in the general site were randomly chosen, somewhat analogous to the uncertainty in landing ellipses for Mars. The general geology was assessed and compared to the remote sensing results. A 20 by 20 m grid (2 by 2 m cells) was centered at the randomly selected target for each field site. The maximum rock size, slope, relief, and percent "bedrock" was noted for each cell as well as block size distribution (e.g., Fig. 1-3). In addition, surface characteristics at the precise "touch down" spot were noted. The collected information represented a simulated landing of a "small lander" as for the Mars 94/96 and MESUR missions, and is useful for planning operations by small rovers of limited capabilities.

Preliminary results from MASS include the development of criteria for the identification of sites by type, establishment of the potential value of specific image resolutions, and types for site identification, assessment of the ability to use geological interpretations for surface characteristics, and establishment of values for rock sizes, slopes, etc. as a function of specific terrains. Identification criteria for sites such as young volcanic terrains are relatively easy to establish, but criteria for sites such as ancient crust and exobiology are more difficult to develop. Within the context of MASS, image resolution was the single most important

parameter (in comparison to color and radar) for site identification; ~35 m/pixel resolution marked the threshold for the identification of most diagnostic features. Color, however, was important for defining unit boundaries which enabled subdivisions of materials to be identified within the site. Some of these results have been known intuitively, but MASS now documents them. Field examination showed that most sites were correctly identified by type. The qualitative assessments of surface characteristics based on geological interpretations of remote sensing data were essentially correct.

In conclusion, it must be noted that the results of MASS are limited to the analog data and terrains of Earth, and that there are significant differences in comparison to Mars. However, the general process of establishing identification criteria for each site type and recognition of the "value added" for specific remote sensing data sets are appropriate for Mars. Moreover, field measurements of surface characteristics which vary as a function of terrain provide general input for the development of engineering models.

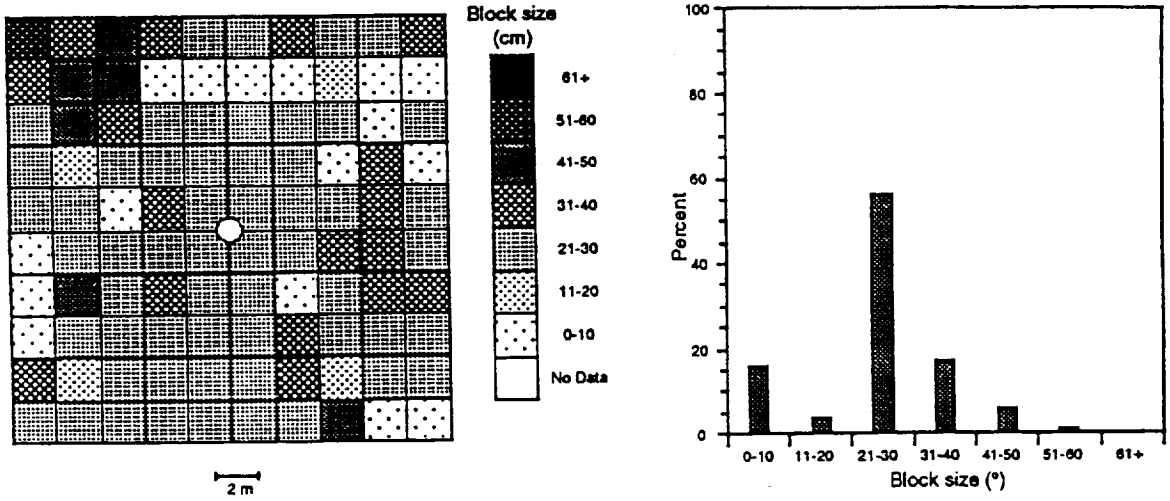

Figure 1. Block distribution and block size histogram in Site V12, Pisgah volcanic field. North is located at the top of the map. The center of the MASS landing site is located at the O.

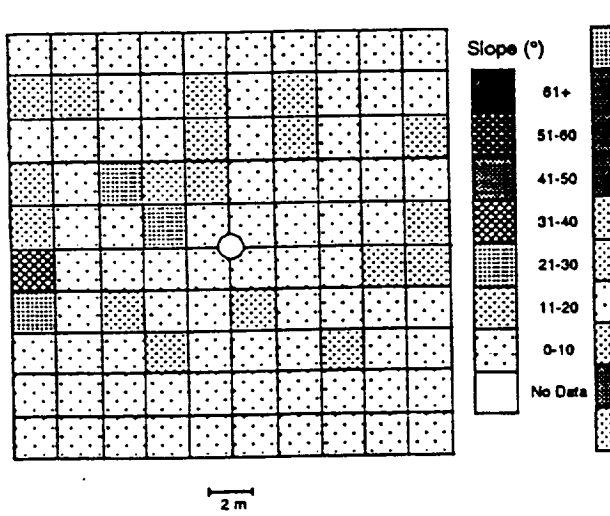

Figure 2. Slope distribution in Site A6, Kelso dunes.

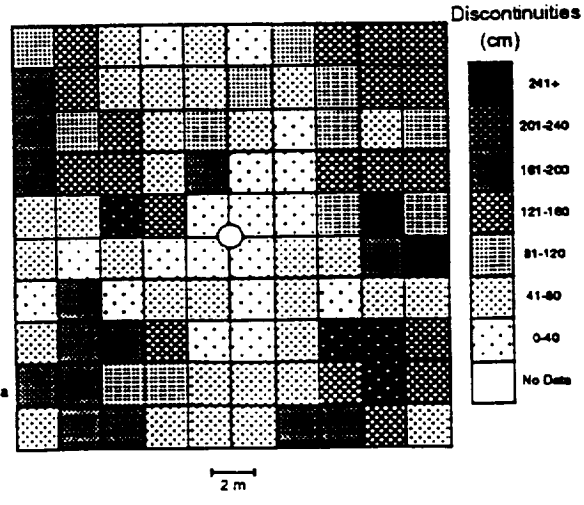

Figure 3. Relief discontinuities map in Site V11, Pisgah volcanic field.

EARTH IMAGING RESULTS FROM GALILEO'S SECOND ENCOUNTER:
R. Greenberg (U.Arizona), M. Belton (K.P.N.O.), E. DeJong (J.P.L.), A. Ingersoll (CalTech), K.Klaasen (J.P.L.), P. Geissler (U.Arizona), J. Moersch, W.R. Thompson (Cornell) and the Galileo Imaging Team

The recent flyby of the Galileo spacecraft en route to Jupiter contributes a unique perspective to our view of our home planet. Imaging activities conducted during the second Earth encounter provide an important opportunity to assess new methods and approaches on familiar territory. These include unique multispectral observations, low light-level imaging (searches for aurorae, lightning and artificial lights on the nightside) and experiments with multiple exposure times to extend the effective radiometric resolution and dynamic range of the camera system.

Galileo imaging data has the potential to make important contributions to terrestrial remote sensing. This is because the particular set of filters included in the Solid State Imaging system are not presently incorporated in any currently operating Earth-orbiting sensor system. The visible/near-infrared bandpasses of the SSI filters are well suited to remote sensing of geological, glaciological, botanical and meteorological phenomena. Data from this and the previous Earth encounter may provide an extremely valuable reference point in time for comparison with similar data expected from EOS or other systems in the future, contributing directly to our knowledge of global change.

The highest resolution imaging (0.2 km/pixel) during the December, 1992 encounter occurred over the central Andes; a five filter mosaic of visible and near infrared bands displays the remarkable spectral heterogeneity of this geologically diverse region. As Galileo departed the Earth, cooperative imaging with the Near Infrared Mapping Spectrometer (NIMS) instrument targeted Antarctica, Australia and Indonesia at 1.0 to 2.5 km/pixel resolutions in the early morning local times near the terminator. The Antarctic data are of particular interest, potentially allowing ice grain size mapping using the 889 and 968 nm filters and providing an important means of calibrating the technique for application to the Galilean satellites. As the spacecraft receded further, regional scale imaging provided data which, along with data from the previous encounter, will enable the production of global multispectral mosaics of Earth in each of the SSI filters.

COLLISIONAL AND DYNAMICAL HISTORY OF GASPRA

R. Greenberg, M.C. Nolan, W.F. Bottke Jr., and R.A. Kolvoord
Lunar and Planetary Laboratory, University of Arizona

Interpretation of the impact record on Gaspra requires understanding of the effects of collisions on a target body of Gaspra's size and shape, recognition of impact features that may have different morphologies from craters on larger planets, and models of the geological processes that erase and modify impact features.

Crater counts on the 140 km^2 of Gaspra imaged at highest resolution by the Galileo spacecraft show a steep size-frequency distribution (cumulative power-law index near -3.5) from the smallest resolvable size (150m diameter) up through the largest feature (1.5km diameter crater) of familiar crater-like morphology [1].

In addition, there appear to be as many as eight roughly circular concavities with diameters >3km visible on the asteroid. If we restrict our crater counts to features with traditionally recognized crater morphologies, these concavities would not be included. However, if we define craters to include any concave structures that may represent local or regional damage at an impact site, then the larger features on Gaspra are candidates for consideration.

Acceptance of the multi-km features as craters has been cautious for several reasons. First, scaling laws (the physically plausible algorithms for extrapolating from experimental data) indicate that Gaspra could not have sustained such large-crater-forming impacts without being disrupted; second, aside from concavity, the larger structures have no other features (e.g. rims) that can be identified with known impact craters; and, third, extrapolation of the power-law size distribution for smaller craters predicts no craters larger than 3 km over the entire surface.

On the other hand, recent hydrocode modeling of impacts [2] shows that for a given impact (albeit into a sphere), the crater size is much larger than given by scaling laws. Gaspra-size bodies can sustain formation of up to 8-km craters without disruption. Besides allowing larger impact craters, this result doubles (relative to estimates in [1]) the lifetime since the last catastrophic fragmentation event up to one billion years.

Events that create multi-km craters also globally damage the material structure, such that regolith is produced, whether or not Gaspra "initially" had a regolith, contrary to other models in which initial regolith is required in order to allow current regolith. Because the globally destructive shock wave precedes basin formation, crater size is closer to the large size extrapolated from gravity-scaling rather than the strength-scaling that had earlier been assumed for such small bodies (e.g. [1]). This mechanism may also help explain the existence of Stickney on Phobos [3].

Moreover, rejection of the large concavities as craters based on unfamiliar morphology would be premature, because (aside from Stickney) we have no other data on such large impact structures on such a small, irregular body. The eight candidate concavities cover an area greater than that counted for smaller craters, because they are most apparent where small craters cannot be seen: on low resolution images and at the limb on high resolution images. We estimate that there are at least two with diameter >4 km per 140 km^2, which would have to be accounted for in any model that claims these are impact craters.

While the existence of a few multi-km craters would imply a sharp bend in the size-distribution, which is implausible in the impacting population, such a distribution might result from geological processes that modify the surface.

One important geological process is the global jolting of surface material by large impacts, discovered by the hydrocode models [2]. When a crater of diameter 5 km is formed, for example, regolith over the entire surface jumps about 30 m, which erases topography on that scale and thus erases craters up to 150 m, while preserving compositional inhomogeneities. The large impact events are analogous to erosional and tectonic processes on terrestrial planets in terms of their ability to modify crater size distributions. The sub-km craters now counted on Gaspra may have accumulated only since the last multi-km crater was formed (a time much shorter than the asteroid's age), consistent with their relative depletion with respect to the big ones. The size distribution has been also modified by local erasure (cookie-cutting) at the site of large craters and just around them.

Such geological processes may have modified the production size-distribution of craters considerably, allowing a non-power law shape. However, the generally steep slope for sub-km craters still would require a steep asteroid size distribution, similar to that assumed in [1].

An implication of the hydrocode results is that Gaspra must be a rubble pile due to the global shock of large impacts. The elongated figure (with a somewhat pinched waist confirmed by the recently received low resolution images) probably requires the support of two or more internal solid blocks, overlain by a substantial regolith. Other observational evidence for this physical model are the surface grooves, which may be related to sinkage of regolith into the interstices between blocks after the formation event or as a result of impact jolting. Whether the required internal blocks could survive the repeated impact shock is problematical; hydrocode studies of non-spherical targets will be needed.

References:

1. Belton, M.J.S. *et al.* (1992) Galileo encounter with 951 Gaspra: First pictures of an asteroid. *Science* **257**, 1647.
2. Nolan, M.C., E. Asphaug, and R. Greenberg. (1992) Numerical simulation of impacts on small asteroids. *Bull. A.A.S.* **24**, 959.
3. Asphaug, E. and H. J. Melosh. (1993) The Stickney impact on Phobos: A dynamical model. *Icarus*, in press.

PETROGRAPHY, MINERALOGY AND MG ISOTOPE COMPOSITION OF VICTA: A VIGARANO $CaAl_4O_7$-BEARING TYPE A INCLUSION.

R.C. Greenwood[1], A. Morse[2] & J.V.P. Long[3] [1]Dept. of Mineralogy, The Natural History Museum, Cromwell Road, London SW7 5BD, UK. [2] Department of Earth Sciences, The Open University, Milton Keynes MK7 6AA, UK. [3], Department of Earth Sciences, Bullard Laboratories, University of Cambridge, Cambridge CB3 OEZ, UK.

Thermodynamic calculations [1] predict that Ca-dialuminate ($CaAl_4O_7$) condenses from a cooling gas of solar composition after hibonite and before melilite. Although Ca-dialuminate has now been recorded from Ca Al-rich inclusions (CAIs) in at least 9 meteorites [2,3,4,5,6,7,8], compared to hibonite it is a relatively rare phase. As pointed out by Michel-Levy *et al.* [2] the absence of Ca-dialuminate from most hibonite-bearing inclusions poses a serious problem for the condensation model of CAI formation. Here we describe an inclusion which contains abundant Ca-dialuminate partially altered to a hercynite-rich ($FeAl_2O_4$) assemblage. The evidence from VICTA indicates that compared to all other phases in type A inclusions, Ca-dialuminate is the most susceptible to secondary alteration; a feature which may explain its restricted occurrence. Unaltered Ca-dialuminate and melilite in VICTA display excess $^{26}Mg^*$ indicative of *in situ* decay of ^{26}Al.

Petrography and Mineralogy Measuring 7mm x 6mm, VICTA has a convoluted structure and consists of a series of distinct but interconnected regions each with a melilite-rich core enclosed by a thick rim sequence. Large matrix-filled cavities are present throughout the inclusion. Coarse-grained gehlenitic melilite (Ak0-14) forming the core regions contains local concentrations of rounded inclusions of both perovskite (up to 30μm diameter)and Fe-free spinel (5-15μm diameter). Hibonite is also present as laths up to 40μm long, forming small irregularly-shaped clumps. Ca-dialuminate occurs as densely-packed elongate grains up to 100μm long within a 300μm x 600μm zone at the centre of the largest melilite-bearing area (figure 1). The melilite-rich cores are enclosed by a 70-300μm-wide layer consisting of fine-grained hibonite laths with subordinate interstitial spinel. This layer has a high porosity with numerous 5-10μm diameter voids lined by melilite. The junction with the core region is sharp, but irregular in detail with hibonite and spinel in the outer zone apparently having formed by replacement of coarse-grained melilite. External to the hibonite-rich zone a 50-60μm-thick Wark-Lovering rim sequence is developed comprising the following layers: (from innermost out) i) spinel (FeO 1.5wt%) with minor hibonite (40μm thick), ii) melilite (Ak9.4-17.3) (5μm thick), iii) clinopyroxene zoned outwards from fassaite (Al_2O_3 16.1wt%, TiO_2 3.7wt%) to diopside (10μm thick) and iv) olivine (Fo_{99})(2-5μm thick).

Alteration The only phase in VICTA showing evidence of secondary alteration is Ca-dialuminate which has been partially altered to a fibrous material with a composition close to pure hercynite ($FeAl_2O_4$); ZnO values of up to 3 wt% were measured in some areas (figure 2). Hercynite presumably formed from Ca-dialuminate by the reaction $CaAl_4O_7 + 2FeO \rightarrow 2FeAl_2O_4 + CaO$ with the FeO being supplied by the meteorite matrix. The external surfaces of VICTA are decorated by a discontinuous 10-15μm thick layer of kirschteinite $CaFeSiO_4$, which from its morphology appears to have formed *in situ*. The CaO required to produce kirschteinite may have been supplied via breakdown of Ca-dialuminate with FeO and SiO_2 being supplied from an external source.

Mg isotopes Mg isotopes and $^{27}Al/^{24}Mg$ measurements were carried out using the P7-Concept ion microprobe designed in Cambridge [9]. Analyses were made with a 15kV, $^{16}O^-$ duoplasmatron primary beam of 0.5-1.0 nA and 5-10μm spot size. A mass resolution of >4000 was used to separate $^{24}MgH^+$ from $^{25}Mg^+$.

Both Ca-dialuminate and melilite in VICTA display $^{26}Mg^*$ excesses which correlate positively with $^{27}Al/^{24}Mg$ ratios and are therefore ascribed to *in situ* decay of ^{26}Al. Ca-dialuminate with $^{27}Al/^{24}Mg$ of 300-700 shows $^{26}Mg^*$ excesses of 114-207‰, melilite with $^{27}Al/^{24}Mg$ of 25-86 shows excesses of $^{26}Mg^*$ in the range 15-52‰.

Discussion The rarity of Ca-dialuminate relative to hibonite in CAIs has been used as an argument against a condensation origin for these inclusions [2]. However, our evidence suggests that Ca-dialuminate is highly susceptible to secondary alteration and therefore may originally have been more widespread in CAIs. The presence of up to 2.2 wt% FeO in some Leoville Ca-dialumunates was cited as evidence in favour of an igneous origin for the host CAI [2]. However, in VICTA high FeO contents in Ca-dialuminate correlate with degree of alteration and suggest that this is not a valid criterion on which to base petrogenetic models.

As pointed out by Bischoff *et al.* [7] Ca-dialuminate-bearing inclusions appear to form two distinct groups, with isolated grains such as those in Colony [6] or Acfer 182 [7] showing no detectable $^{26}Mg^*$, whereas those like VICTA which are associated with melilite display large $^{26}Mg^*$ excesses. Melilite-free Ca-dialuminate-rich inclusions from Adelaide [8] with large $^{26}Mg^*$ excesses appear to be anomalous in this respect. However, we note that so far Mg isotope measurements have been made on only a small number of Ca-dialuminate-bearing inclusions.

References. [1] Kornacki A.S. and Fegley B. (1984) *Proc. Lunar Planet. Sci. Cong.* 14th, B588-B596. [2] Michel-Levy M.C. *et al.* (1982) *Earth Planet Sci. Lett.* 61, 13-22. [3] Paque J.M. (1987) *Lunar Planet. Sci.*XVIII:762-765. [4] Davies A.M. (1987) *Lunar Planet. Sci.* XVIII:223-224. [5] Grossman J.N. *et al.* (1988) *Earth Planet. Sci. Lett.* 91, 33-54. [6] Greenwood R.C. *et al.* (1992) *Meteoritics* 27, 229. [7] Bischoff A. *et al.* (1992) *Meteoritics* 27, 204. [8] Huss G. R. and Hutcheon I.D. (1992) *Meteoritics* 27 236. [9] Long J.V.P. and Gravestock D.C. (1988) in *SIMS VI* pp.161-164.

Acknowledgements This work was supported by SERC grant GRH 13482 to Professor C.T. Pillinger and SERC grant GRF 80074 to Robert Hutchison.

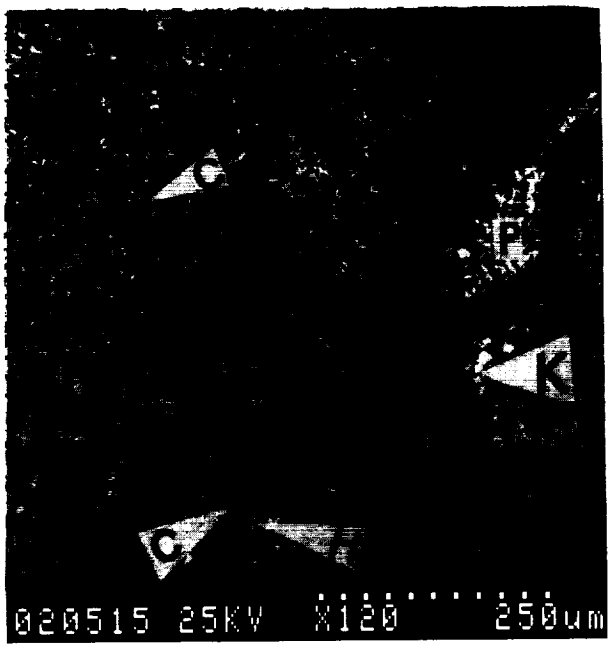

Figure 1

Figure 2

Figure 1. Melilite-rich Ca-dialuminate-bearing core of VICTA enclosed by a thick rim sequence. Coarse-grained melilite (M) contains abundant inclusions of Ca-dialuminate (C) partially replaced by a fibrous hercynite-rich alteration assemblage (H). The melilite-rich core is rimmed by a thick hibonite-rich layer (light grey) in which abundant perovskite (P) inclusions are present locally. The hibonite-rich layer is separated from the enclosing meteorite matrix (MM) by a 50μm wide wark-lovering rim sequence (see text for details). Grains of Kirschteinite (K) $CaFeSiO_4$ occur locally along the margin of the inclusion (back-scattered electron image).

Figure 2. Ca-dialuminate (C) inclusion in melilite (M) partially replaced by a fibrous hercynite-rich alteration product (H) (back-scattered electron image).

EXPLOSIVE MAFIC VOLCANISM ON EARTH AND MARS; *Tracy K.P. Gregg and Stanley N. Williams, Department of Geology, Arizona State University, Tempe, Arizona 85287-1404*

Deposits within Amazonia Planitia, Mars, have been interpreted as ignimbrite plains on the basis of their erosional characteristics [1]. The western flank of Hecates Tholus appears to be mantled by an airfall deposit, which was produced trhough magma-water interactions or exsolution of magmatic volatiles [2]. Morphologic studies, along with numerical and analytical modelling of martian plinian columns and pyroclastic flows, suggest that shield materials of Tyrrhena and Hadriaca Paterae are composed of welded pyroclastic flows [3, 4]. Terrestrial pyroclastic flows, ignimbrites and airfall deposits are typically associated with silicic volcanism [5 - 7]. Because it is unlikely that large volumes of silicic lavas have been produced on Mars [8, 9], we seek terrestrial analogs of explosive, mafic volcanism. Plinian basaltic airfall deposits have been well-documented at Masaya, Nicaragua [10], and basaltic ignimbrite and surge deposits also have been recognized there [11]. Ambrym and Yasour, both in Vanuatu, are mafic stratovolcanoes with large central calderas, and are composed of interbedded basaltic pyroclastic deposits and lava flows [12, 13]. Zavaritzki, a mafic stratovolcano in the Kurile Islands, may have also produced pyroclastic deposits, although the exact nature of these deposits is unknown [14]. Masaya, Ambrym and Yasour are known to be located above tensional zones. Hadriaca and Tyrrhena Paterae may also be located above zones of tension, resulting from the formation and evolution of Hellas basin [3, 4], and, thus, may be directly analogous to these terrestrial mafic, explosive volcanoes.

Masaya, Nicaragua, lies on a chain of Quaternary volcanoes which extends along the Pacific coast of Central America. Volcanoes within this chain are aligned in a series of *en echelon* segments, and the "segment break" which passes through Masaya Caldera is represented by an intense zone of faulting and graben formation [11, 16], and the crust beneath Masaya is anomalously thin [17]. The caldera forms a basin ~11.5 x 6km and ~100m deep; the caldera floor is covered with recent lavas. Evidence for Hawaiian and strombolian activity at Masaya is recorded in the caldera floor along eruptive fissures, and at satellite cones.

Two thick (2 - 6m), well-known, scoria airfall deposits originate at Masaya, and others are observed in the caldera walls. Both deposits are composed of Fe-rich tholeiitic to calc-alkaline basalt scoria, and are clearly plinian [11, 18, 19]. A basaltic ignimbrite, with a volume (DRE) of ~2.2 to 3.4km^3, is exposed near the top of the caldera wall. It displays a 20-35cm basal surge deposit, a co-ignimbrite lag-fall deposit near the vent, typical inverse grading of vesiculated pyroclasts, and normal grading of lithic clasts. The flow had sufficient energy to climb ~80m above the caldera rim, and to transport trees. It is capped by a 50-cm thick layer of vitric ash with occasional accretionary lapilli [11]. A pyroclastic surge deposit directly overlies the pyroclastic flow. The deposit is largely composed of shattered fragments of older lavas and plutonic rocks, and is locally massively bedded and cross-bedded. The surge apparently maintained its integrity for at least 15 - 20km from the volcano, and represents a volume (DRE) of ~4.9 - 6.5km^3. Removal of both the pyroclastic flow and surge volumes from the magma chamber beneath the caldera may have been responsible for caldera collapse [11].

Ambrym Caldera, Vanuatu, has been historically continuously active [12], but, because of its location, has been sparsely studied. Ambrym is a large, broad composite cone ~19km across, composed of basaltic lavas and basaltic ash and lapilli tuffs, with uncommon agglomerates. The large (9 x 12km x ~50m deep) central caldera contains two secondary cones, and their slopes are thickly mantled with recent ash [13]. Ambrym is located at the intersection of the Vanuatu island arc and d'Entrecasteaux Fracture Zone. A gravity gradient across the island suggests that Ambrym may straddle lower density crust to the west and higher density crust to the east [13]. Although detailed stratigraphic data is not currently available, the abundance of basaltic ash, the large, subsidence caldera, and its location above a tensional zone suggest the possibility of basaltic pyroclastic flows on Ambrym's slopes.

Less is known about Yasour, also in Vanuatu, located ~375km SE of Ambrym. It also has been continuously active historically. It is a basaltic andesite (~55% SiO_2) stratovolcano with a central crater ~400m in diameter and ~80m deep. Alternating lava flows and scoria beds are revealed in the crater walls. Historic activity has been primarily strombolian [12], but the morphology of the volcano, and its position near a fracture zone, suggest that field work may reveal evidence for extensive, mafic pyroclastic deposits.

Future work may also reveal mafic pyroclastic deposits at Zavaritzki Caldera, on Simushir Island, Kuriles. Zavaritzki is a shield-like stratovolcano with nested calderas; the external caldera is ~6km in diameter. Although recent activity has been characterized by "rare, weak eruptions" [14], there are traces of ancient plinian and strombolian eruptions in its deposits. The 1957 eruption of Zavaritzki produced several dark eruption columns up to 8km high. An eye-witness describes fallout of dark ash from the column, and walking over new "gray pumice" during an eruptive interval [15]. All known products from Zavaritzki are mafic andesites and basalts [14].

Masaya, Ambrym and Yasour are located in extensional zones. There is no direct evidence for water-magma interactions in the large ignimbrite deposits of Masaya [11] and the deposits of the other volcanoes have not been extensively studied. Rapid rise of mafic magma, facilitated by crustal extension, may allow the magma to reach the surface without degassing significantly. Rapid rise may effectively overcome the "viscosity barrier" of mafic magmas [6, 7] and allow formation of mafic plinian columns.

Deposits associated with Tyrrhena and Hadriaca Paterae are much more widespread than the terrestrial examples discussed here, largely due to environmental, and possibly compositional, differences. A basaltic column should rise 12% higher than a similar silicic column, simply because of increased eruption temperature [11, 21]; ultramafic columns would be even taller. Low atmospheric pressures on Mars should cause eruption velocities to be 50% greater than on Earth, and enable eruption clouds to rise 5 times higher on Mars [22]. Lower atmospheric pressures and temperatures on Mars allow pyroclastic flows to travel a greater distance on Mars than on Earth before falling beneath a critical welding temperature [4]. Finally, the full extent of the terrestrial deposits is unknown, because much of the deposits are submarine. It has been suggested that Hadriaca and Tyrrhena Paterae have been influenced by Hellas basin tectonics, and may be located above zones of tension [3, 4], similar to the terrestrial volcanoes discussed here. Comparison of martian highland paterae to terrestrial examples suggest that Tyrrhena and Hadriaca may have produced extensive mafic ignimbrite deposits, through violent degassing of rapidly rising mafic magma, and not through magma-groundwater interactions.

References: [1] Scott, D.H. and K.L. Tanaka, 1981, *NASA Tech. Memo., 82385*, 255-257. [2] Mouginis-Mark, P.J., L. Wilson and J.W. Head, 1982, *Jour. Geophys. Res.* **87**:9890-9904. [3] Greeley, R. and D.A. Crown, 1990, *Jour. Geophys. Res.* **95**:7133-7149. [4] Crown, D.A. and R. Greeley, 1992, *Jour. Geophys. Res. (in press).* [5] Walker, G.P.L., 1981, *Bull. Volc.* **44**:223-240. [6] Sparks, R.S.J., 1978, *J. Volc. Geotherm. Res.* **3**:1-37. [7] Smith, R.L., 1979, *GSA Sp. Paper 180*, 5-27. [8] Francis, P.W. and C.A. Wood, 1982, *Jour. Geophys. Res.* **87**:9881-9889. [9] McSween, H.Y., 1985, *Rev. Geophys.* **23**:391-416. [10] Williams, S.N., 1983, *Geology* **11**:211-214. [11] Williams, S.N., 1983, Ph.D. thesis, Dartmouth, Hanover, NH. [12] Fisher, N.H., 1957, *Active Volcanoes of the World*, International Volcanological Association, 105pp. [13] McCall, G.J., R.W. LeMaitre, A. Malahoff, G.P. Robinson and P.J. Stephenson, 1970, *Bull. Volc.* **34**:681-696. [14] Gorshkov, G.S., 1958, *Active Volcanoes of the World*, International Volcanological Association, 99pp. [15] Markhinin, Y., 1971, *Pluto's Chain*, pp. 214. [16] Stoiber, R.E. and M.J. Carr, 1974, *Bull. Volc.* **37**:304-325. [17] Wollard, G.P., 1968, *Geophys. Mono.* **13**, AGU, 320-340. [18] Irvine, T.N. and Baragar, W.R.A., 1971, *Can. Jour. Earth Sci.* **8**:523-548. [19] Walker, G.P.L., 1981, *Bull. Volc.* **44**:223-240. [20] Sparks, R.S.J., S.Self, G.P.L. Walker, 1973, *Geology* **1**:115-118. [21] Wilson, L., R.S.J. Sparks, T.C. Huang and N.O. Watkins, 1978, *Jour. Geophys. Res.* **83**:1829-1836. [22] Wilson, L. and J.W. Head, 1983, *Nature* **302**:663-669.

Heliocentric zoning of the asteroid belt by aluminum-26 heating. R. E. Grimm, Department of Geology, Arizona State University, Tempe, AZ 85287-1404, and H. Y. McSween, Jr., Department of Geological Sciences, University of Tennessee, Knoxville, TN 37996-1410.

Variations in petrology among meteorites attest to a strong heating event early in solar system history, but the heat source has remain unresolved (e.g., 1). Aluminum-26 has been considered the most likely high-energy, short-lived radionuclide (half-life 0.72 million years) since the discovery of its decay product - excess ^{26}Mg - in Allende CAIs (2). Furthermore, observation of relict ^{26}Mg in an achondritic clast and in feldspars within ordinary chondrites (3, 4) provided strong evidence for live ^{26}Al in meteorite parent bodies and not just in refractory nebular condensates. The inferred amount of ^{26}Al is consistent with constraints on the thermal evolution of both ordinary (5) and carbonaceous (6) chondrite parent objects up to a few hundred kilometers in diameter.

Meteorites can constrain the early thermal evolution of their parent body locations, provided that a link can be established between asteroid spectrophotometric signature and meteorite class (7). Asteroid compositions are heliocentrically distributed (8): Objects thought to have experienced high metamorphic or even melting temperatures are located closer to the sun, whereas apparently unaltered or mildly heated asteroids are located farther away (9).

Heliocentric zoning could be the result of ^{26}Al heating if the initial amount of the radionuclide incorporated into planetesimals was controlled by accretion time, which in turn varies with semimajor axis. Analytic expressions for planetary accretion (10) may be integrated to give the time τ required for a planetesimal to grow to a specified radius: $\tau \propto a^n$, where n = 1.5 to 3 depending on the assumptions about variations in the surface density of the planetesimal swarm. Numerical simulations of planetesimal accretion at fixed semimajor axis (11) demonstrate that variations in accretion time among small planetesimals can be strongly nonlinear depending on the initial conditions and model assumptions. The general relationship with semimajor axis remains valid because it depends only on the initial orbital properties and distribution of the planesimal swarm.

In order to demonstrate the basic dependence of thermal evolution on semimajor axis, we parameterized accretion time across the asteroid belt according to $\tau \propto a^n$ and calculated the subsequent thermal history. Objects at a specified semimajor axis were assumed to have the same accretion time, regardless of size. We set the initial $^{26}Al/^{27}Al$ ratio = 6×10^{-5} (2) and treated n and τ_0 at a_0 = 3 AU as adjustable parameters. The thermal model (6) included temperature-dependent properties of ice and rock (CM chondrite analog) and the thermodynamic effects of phase transitions.

The principal observational constraints to be met are the inferred heliocentric distances for melting of chondritic silicates and of water ice within asteroids, taken to occur at temperatures of 1100°C and 0°C, respectively. The position of the silicate melting isotherm is uncertain because of the controversy concerning the nature of S-asteroids and the origin of ordinary chondrites. One recent summary (9) considers S-types to be differentiated and divides the asteroids into igneous, metamorphic and primitive types with boundaries approximately at 2.7 and 3.4 AU. The boundary between igneous and metamorphic classes should therefore correspond roughly to the 1100 °C isotherm. Ordinary chondrites are held to originate sunward of this boundary but from smaller objects that experienced greater heat loss and were unmelted. Evidence for hydrated silicates in some low-albedo asteroids (12, 13) is now taken to support the idea that aqueous alteration occurred by melting of ice and reaction with anhydrous silicates. Such asteroids are generally dominant around 3 AU, but objects farther out show decreasing spectral signatures of hydrated silicates, suggesting that liquid water was not present there. The isotherm for ice melting is the basis for the division between metamorphic and primitive asteroid types (9) at 3.4 AU.

Incorporation of ice into planetesimals can strongly affect thermal history (6) in that ice provides a thermal buffer that substitutes low-temperature aqueous alteration (as in carbonaceous chondrites) for high-temperature metamorphic recrystallization (as in ordinary and enstatite chondrites). The distribution of ice in the asteroid belt before the heating event is uncertain.

Therefore we have performed two sets of thermal calculations: in the first (the anhydrous model) the thermal effects of ice were neglected; all model objects were assumed to be 90% rock and 10% voids. In the second set (the hydrous model) we explicitly introduced ice beyond 2.7 AU. Model objects beyond here have compositions of 60% rock, 30% ice, and 10% voids by volume.

The positions of the silicate and ice melting isotherms agree with observations for large diameters for the anhydrous model with $\tau_0 = 3.5$ million years and for the hydrous model with $\tau_0 = 3.0$ million years (Fig. 1). A shorter accretion time is required for the hydrous model because a larger complement of ^{26}Al is necessary to achieve the specified threshold temperatures when ice is present. Both of these times are upper limits because objects will radioactively heat during formation and reach limiting temperatures more rapidly than in our model where full-grown objects start cold. In both the anhydrous and hydrous models the best fit was achieved with $n = 3$, although $n = 2.5$ gave comparable results if τ_0 was increased slightly. The large value of n is required to accommodate the strong variation in temperature over < 1 AU and is in agreement with suggestions that the surface density of the planetesimal swarm varied as a^{-1} to $a^{-3/2}$ (14, 15). Such values of n lead to variations in accretion time of several half-lives of ^{26}Al across the asteroid belt (Fig. 1).

These calculations demonstrate that heliocentric zoning of the asteroid belt can be achieved by ^{26}Al heating with reasonable assumptions about the variation of accretion time with semimajor axis (16). Although solar electromagnetic induction heating has gained favor with the recognition of a sun-centered heating pattern in the asteroid belt, that model is highly simplified and contains considerable uncertainties in parameter choices (17). We cannot reject this hypothesis with present data, but we favor ^{26}Al heating because it can explain the observed data with fewer assumptions and because ^{26}Al is known to have been present in significant quantities in newly accreted meteorite parent bodies (3).

References (1) Wood and Pellas, in *The Sun in Time* (Univ. of Arizona Press, Tucson, 1991) pp. 740-760. (2) Lee et al., *GRL 3*, 109-112 (1976). (3) Hutcheon et al., *Nature 337*, 238-241 (1989). (4) Zinner and Gopel, *Meteoritics 27*, 311-312 (1992). (5) Miyamoto et al., *Proc. Lunar Planet. Sci. Conf.* 12B, 1145-1152 (1981). (6) Grimm and McSween, *Icarus 82*, 244-280 (1989). (7) Gaffey and McCord, *Space Sci. Rev. 21*, 555-628 (1978). (8) Gradie and Tedesco, *Nature 216*, 1405-1407 (1982). (9) Bell et al., in *Asteroids II* (Univ. of Ariz. Press, Tucson, 1989) pp. 921-945. (10) Wetherill, *Ann. Rev. Astron. Astrophys. 18*, 77-113 (1980). (11) Wetherill and Stewart, *Icarus 77*, 330-357 (1989). (12) Lebofsky et al., *Icarus 48*, 453-459 (1981). (13) Jones et al., *Icarus 88*, 172-192 (1990). (14) Weidenschilling, *Astrophys. Space. Sci.* 51, 153-158 (1977). (15) Wetherill and Chapman, in *Meteorites and the Early Solar System* (Univ. of Ariz. Press, Tucson, 1988). (16) Grimm and McSween, *Science*, in press, 1993. (17) Sonett et al., *Astrophys. Space Sci 7*, 446-488 (1970).

Fig. 1. Peak temperatures in model objects as functions of size and semimajor axis for hydrous and anhydrous models. Dependence of accretion time on semimajor axis described in text. Shaded bands mark major divisions of the asteroid belt based on spectrophotometric data (9).

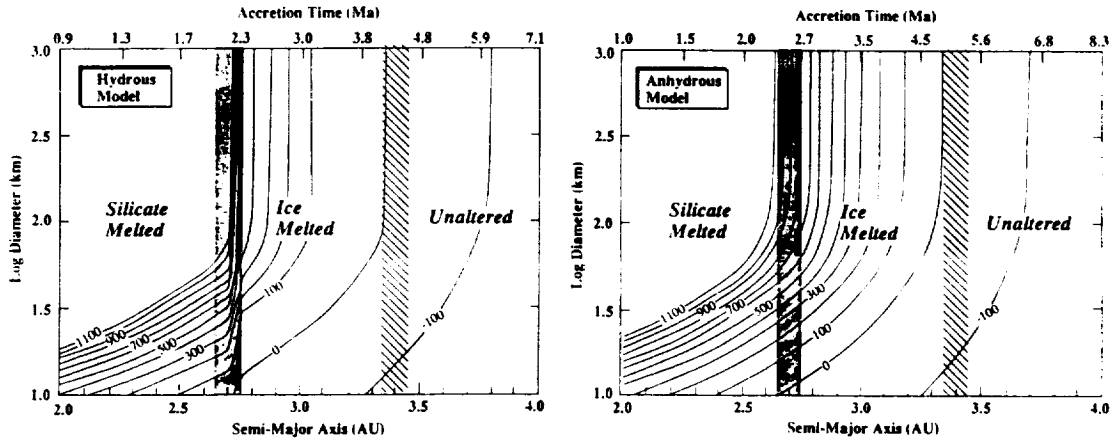

EVOLUTIONARY IMPLICATIONS OF A STEADY-STATE WATER ABUNDANCE ON VENUS;
David H. Grinspoon, Laboratory for Atmospheric and Space Physics, University of Colorado, Box 392, Boulder, CO 80309

In 1987 Grinspoon proposed that the data on hydrogen abundance, isotopic composition and escape rate were consistent with the hypothesis that water on Venus might be in steady-state rather than monotonic decline since the dawn of time [1-3]. This conclusion was partially based on a derived water lifetime against nonthermal escape of approximately 10^8 years. Others have questioned this conclusion. De Bergh *et al.* [4] found H_2O lifetimes of > 10^9 years. Donahue and Hodges[5], derived H_2O lifetimes of 0.4 - 5 x 10^9 years. The most sophisticated analysis to date of near-IR radiation from Venus' nightside reveals a water mixing ratio of approximately 30 ppm [6]. Recent re-analysis of Pioneer Venus Mass Spectrometer Data are consistent with a water abundance of 30 ppm [7].

Hodges and Tinsley [8] found an escape flux due to charge exchange with hot H^+ of 2.8 x 10^7 cm^{-2} s^{-1}. Gurwell and Yung [9] estimated an escape flux of 3.5 x 10^6 cm^{-2} s^{-1} from collisions with hot O produced by dissociative recombination of O_2^+. Brace *et al.* [10] estimated an escape flux of 5 x 10^6 cm^{-2} s^{-1} from ion escape from the ionotail of Venus. The combined estimated escape flux from all of these processes is 3.7 x 10^7 cm^{-2} s^{-1}, suggesting a lifetime against escape for water of less than 10^8 years. A recent estimate of H escape flux employing a different ionospheric model and using Pioneer Venus reentry data to estimate the response of the escape flux to the solar cycle finds a somewhat lower escape flux of 1.4 x 10^7 cm^{-2} s^{-1}[11], suggesting a water lifetime closer to 2 x 10^8 years, significantly less than the age of the planet. Large uncertainties remain in these quantities, yet the data suggest that a source of water more recent than primordial sources is required and that a steady-state is likely. Two obvious candidates for this source water are cometary impact and volcanic outgassing.

If water on Venus is in steady-state, then the escape flux of hydrogen provides an upper limit on the outgassing flux of hydrogen containing compounds averaged over the last 10^8 years. If the source hydrogen is dominated by outgassed water and the recent cometary contribution is unimportant, then the escape flux is a direct measure of the time-averaged outgassing flux.

Gurwell and Yung [9] have reanalyzed the collisional ejection escape process, yielding improved values for the efficiency of H and D escape. This process was previously thought to be extremely inefficient at causing D to escape, but is now found to be the dominant escape mechanism for deuterium. This leads to an estimated fractionation factor (a measure of the efficiency of D escape relative to H) of f = 0.13, an order of magnitude higher than previous estimates. This change has a paradoxical effect on the interpretation of the observed high D/H ratio on Venus: The timescale to reach a "mature" steady-state - where the D/H ratio has relaxed to the limiting steady-state value and the signature of the "primordial" D/H is erased - is reduced by an order of magnitude, making it quite likely that such a state has been reached. Yet, the change in f also means that a mature steady state is only consistent with the observed high D/H ratio if the source hydrogen is enhanced over terrestrial by a factor of 10 or 15. This may rule out comets as a source if the observations of D/H on Comet Halley [12] are representative of average cometary hydrogen.

The escape fluxes given above could be supported by an outgassing flux of approximately 6 x 10^{10} grams of water per year. Magellan mapping of volcanic features, combined with

STEADY-STATE WATER ON VENUS: Grinspoon, D.H.

simulations of the crater population[13,14] have allowed preliminary estimates of volcanic resurfacing rates of around 0.5 km^3/yr, yielding a rate of magma production (RMP) of approximately 1.5 x 10^{15} grams/yr. This rate may be combined with the outgassing flux derived above to estimate the average water content by weight of Venusian magmas:

$$\text{magma water content} = \frac{\phi_{OG}}{RMP} + \beta \qquad (1)$$

where β is a parameter representing the efficiency of outgassing which equals 1 for complete outgassing. There are many complex factors which have not been fully modeled which determine the efficiency of volcanic degassing under the thick, hot atmosphere of Venus [15]. These include considerations of solubility and diffusion. If β is close to 1, perhaps reasonable for thin, voluminous flows, then Eq. 1 yields a magma water content of 40 ppm by weight. This is more than 1000 times drier than typical basaltic magmas on Earth [16]. Thus even if β is much lower than this, Venusian magmas are apparently extremely desiccated, perhaps implying a desiccated mantle as well. Such a desiccated mantle could be the result of continuous outgassing over the planet's history, with no recycling of water in the absence of a surface reservoir and possible absence of subduction. Could this mantle reservoir be the source of the fractionated hydrogen necessary to reconcile the observed D/H ratio with the expected value for a mature steady state? Such processes as differential diffusion and bond-breaking could lead to preferential outgassing of H over D, yet the expected fractionation factor for mantle degassing has not been modeled, and is probably near unity. However large fractionation effects are found in severely depleted reservoirs. If water in the mantle has been depleted by a factor of 10^5 (the approximate difference in the known water reservoirs of Venus and Earth), then an outgassing fractionation factor of f = 0.8 could have produced an enhancement of D/H in the mantle by a factor of 10. Alternatively, an enhanced mantle D/H ratio could reflect massive hydrogen escape which occurred very early in the planet's history and was then frozen into the mantle when an early magma ocean solidified. In this scenario, the observed D/H may indeed be the result of primordial water loss, but this signature would have been preserved in the mantle reservoir, not in the atmosphere.

Another resolution of the paradox described above is that the observed high D/H ratio could be the isotopic signature of massive outgassing associated with catastrophic resurfacing of the planet in the last one-billion years.

REFERENCES [1] Grinspoon, D.H. (1987). *Science*, 238, 1702-1704. [2] Grinspoon, D. H. (1988). Ph. D. thesis, University of Arizona. [3] Grinspoon, D. H. and J. S. Lewis (1988). *Icarus*, 74, 21-35. [4] de Bergh, C., B. Bezard, T. Owen, C. Crisp, J-P. Maillard and B.L. Lutz (1991). *Science*, 251, 547-549. [5] Donahue, T.M. and R.R. Hodges (1992). *JGR* 97, 6083-6091. [6] Pollack, J.B., D.H. Grinspoon, J.B. Dalton, R. Wattson, R. Freedman, D. Crisp, D.A. Allen, B. Bezard, C. deBergh, L.P. giver, Q. Ma, and R. Tipping (1992). *Icarus*. in press. [7] Donahue, T.M. & Hodges, R.R. (1992)*International Colloquium on Venus, LPI Contrib.# 789*. [8] Hodges, R.R. and B. Tinsley (1986). *JGR* 91 13649-13658. [9] Gurwell, M.A. & Yung, Y.L. (1992)*Planet. Space Sci.* In press. [10] Brace, L.H.,W.T.Kasprzak, H.A. Taylor, R.F. Theis, C.T. Russel, A. Barnes, J.D. Mihalov,and D.M.Hunten. (1987) *JGR* 92, 15-26. [11] Donahue, T.M. & Hartle, R.E. (1992) *Geophys. Res. Lett.* In press. [12] Eberhardt, P., Dolder, U., Schulte, W., Krankowsky, D., Lammerzahl, P., Hoffman, J.H., Hodges, R.R., Berthelier, J.J. & Illiano, J.M. (1987)*Astron. Astrophys.* **187**, 435-437. [13] Head, J.W., Crumpler, L., Aubele, J., Guest, J. & Saunders, R.S. (1992)*JGR***97**,13,153-13,197. [14] Bullock, M.A. Grinspoon, D.H., & Head, J.W. (1992) *International Colloquium on Venus, LPI Contrib. # 789*. [15] Holloway, J.R. (1992) abstracts of the 23rd LPSC, 545. [16] J.G. Moore, *Contrib. Mineral. Petrol.* **28**, 272(1970)

N94-16207

SPATIALLY EXTENSIVE UNIFORM STRESS FIELDS ON VENUS INFERRED FROM RADIAL DIKE SWARM GEOMETRIES: THE APHRODITE TERRA EXAMPLE.

Eric B. Grosfils & James W. Head, Dept. Geological Sciences, Brown University, Providence, R.I. 02906

Overview: The high resolution and near global coverage of Magellan radar images is facilitating attempts to systematically investigate the stresses that have deformed the venusian crust. Here we continue earlier efforts[1] to utilize ~170 large, radially lineated structures interpreted as dike swarms to assess the orientation of the regional maximum horizontal compressive stress (MHCS) which existed in their vicinities during emplacement. Examination of swarms near the equator reveals a link to broad scale regional structures, such as Aphrodite Terra, across distances in excess of 1000 km, suggesting the existence of first order stress fields which affect areas of more than 10^6 km^2 in a uniform fashion. Focusing further upon the Aphrodite Terra region, the MHCS field in the surrounding lowlands inferred from radial swarms is oriented approximately normal to the slope of the highland topography. This stress configuration appears, at a simple level, to be incompatible with that expected during either upwelling or downwelling construction of the highlands. In addition, the relatively undeformed geometry of the radial structures within the highlands implies that these dike swarm features formed more recently than their highly deformed surroundings. We therefore conclude that the differential stresses which existed during emplacement of the dike swarms within and adjacent to the Aphrodite Terra highlands are related to the gravitational relaxation of pre-existing topography.

Basic Principles: Application of continuum mechanical principles has shown that terrestrial dikes propagate perpendicular to the least compressive stress direction[2]. Thus, when intruded laterally at shallow levels within the crust, dikes are expected to align with the direction of MHCS. Given geologically contemporaneous formation or a temporally persistent far field stress configuration, therefore, dikes will orient perpendicular to folds and other structures formed by compressive buckling and parallel to extensional features such as rift zones. This kind of behavior has provided data for recent attempts to characterize the global organization of shallow stress fields on Earth at a continental scale[3]. The success of this paleostress analysis suggests that a similar approach can be utilized for other terrestrial planets as well.

Application to Venus: Ongoing consideration of radial dike swarms[1, 4] and wrinkle ridges[5, 6] suggests that Venus is a good candidate for spatially extensive shallow stress analyses. Across equatorial domains many 10^6 km^2 in area the behavior of radially lineated swarms indicates that sequential stress fields are recorded in the geologic record, and that careful structural mapping may provide insight into their origin at the regional level. One interesting example, discussed in further detail below, occurs within and adjacent to the Aphrodite Terra highlands.

Aphrodite Terra: Radial dike swarms associated with Aphrodite Terra (Figure 1) adopt two general geometric configurations. The first is comprised of swarms with almost purely radial geometries. From this configuration, dominant within the highland areas and along their southern margin, we infer that the swarms were emplaced in the presence of a low differential far field stress. In addition, these swarms appear to have undergone far less strain than their highly deformed surroundings, and thus are interpreted to have formed subsequent to construction of the highland areas. The second geometric configuration is one in which swarms that are radial near their focus gradually become unidirectional at greater radial distances. From this we infer that, as the dikes increase in length, the influence of the local intrusive stresses at the swarm's focus gradually diminishes, causing the dikes' orientations to realign with the far field MHCS direction. This type of geometry dominates in a broad, stratigraphically indeterminate swath north of Aphrodite Terra which curls around to the east of Atla and then terminates along its southern border. For all swarms within this swath, as well as one isolated example south of and intermediate to Ovda and Thetis Regiones, the direction of MHCS indicated is oriented nearly perpendicular to the highland topography.

At present there is an ongoing debate about whether hotspot upwelling or coldspot downwelling, each described briefly below, is the more likely explanation for formation of the Aphrodite Terra highlands. One obvious course of action is to compare the stress states recorded by the radial swarms with those predicted by the two models. The hotspot model predicts uplift, rifting, and shield volcanism followed by intrusion and continued extrusive volcanism that thicken the crust[7]. The coldspot model predicts downward flexure and small strains followed by thickening of the lower crust through inwardly directed ductile flow[8]. The post-constructional stages of both models involve gravitational relaxation of the highland topography, producing increasingly extensional stresses in the interior portions of the plateau and radially directed compressional stresses near the margins.

Ascent of molten material through the thickened crust and formation of dike swarms will be aided by the extensional stresses developed in the interior as the topography relaxes. The abundance of swarms in Thetis Regio relative to Ovda Regio suggests, therefore, that Ovda is the younger and least relaxed of the

STRESS STATES ON VENUS FROM DIKE SWARMS; Eric B. Grosfils & James W. Head

two regions, in agreement with predictions based upon the superposition of graben upon older compressional structures[9]. In addition, the overall strain predicted to accumulate in the highlands through relaxation is minor[10]; combined with the swarms' lack of structural disruption relative to their surroundings, this further supports the contention that the radial dikes were emplaced preferentially during the post-constructional phase of the highland's evolution. If, as suggested, the highland's construction is essentially complete at the present time, this may help explain the lack of a distinguishing correlation between Ovda and Thetis Regiones and either upwelling or downwelling plumes[11].

As deduced for the highlands, neither model's constructional phases appear to account for the behavior of swarms in the surrounding lowlands. Stresses resulting from dynamic uplift, such as that produced by impingement of a mantle plume, should not extend any significant distance beyond the resultant rise[12]. Similarly, at a simplistic level the inward flow of material and compression caused by downwelling must, at some distance, disperse through strain induced by compensating extensional stress oriented normal to the highland topography, producing unidirectional swarm orientations perpendicular to their current alignment. Stress orientations induced in the surrounding lowlands by gravitational relaxation, however, are similar to those inferred from the dike swarms' behavior and should pass from highland to lowland. Thus we postulate that topographic relaxation is currently controlling the differential stress state in the lowland areas, and that tessera formation within the highlands has effectively ceased.

Conclusion: The geometry of radial dike swarms within and adjacent to the Aphrodite Terra highlands appear to record differential stress fields controlled primarily by the gravitational relaxation of pre-existing topography. Similar to the results from mapping of wrinkle ridges across broad regions[5, 6], the MHCS direction recorded by the dike swarms surrounding Aphrodite Terra implies that shallow stress fields on Venus, as on Earth, are capable of uniformly affecting areas of more than 10^6 km^2. We are presently examining other portions of Venus to assess the extent and character of the differential stress fields recorded by radial dike swarms in order to decipher their relationship to regional structure and stratigraphy.

References: *1*) Grosfils, E.B. & Head, J.W. LPSC XXIII, 457-458 (1992). *2*) Pollard, D.D. Geol. Assoc. Can. Sp Pap. 34, 5-24 (1987). *3*) Zoback, M.L. JGR 97, 11703-11728 (1992). *4*) Parfitt, E.A. & Head, J.W. LPSC XXIII, 1029-1030 (1992). *5*) Bilotti, F. & Suppe, J. LPSC XXIII, 101-102 (1992). *6*) McGill, G.E. Eos 73, 330 (1992). *7*) Solomon, S.C., et al. JGR 97, 13199-13225 (1992). *8*) Bindschadler, D.L., et al. JGR 97, 13563-13577 (1992). *9*) Bindschadler, D.L., et al. JGR 97, 13495-13532 (1992). *10*) Smrekar, S.E. & Solomon, S.C. JGR 97, 16121-16148 (1992). *11*) Herrick, R.R. & Phillips, R.J. JGR 97, 16017-16034 (1992). *12*) Withjack, M.O. & Scheiner, C. Am. Assoc. Pet. Geol. Bull. 66, 302-316 (1982).

This material is based upon work supported under an NSF Graduate Fellowship.

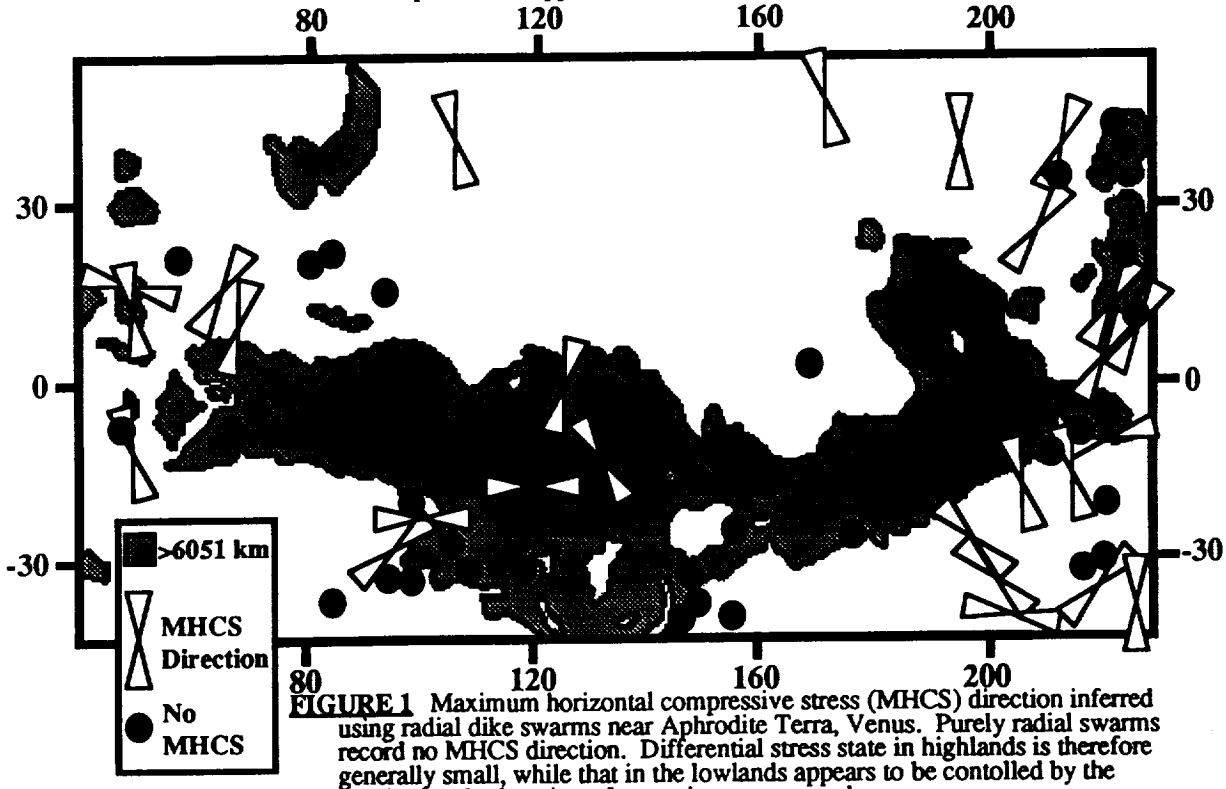

FIGURE 1 Maximum horizontal compressive stress (MHCS) direction inferred using radial dike swarms near Aphrodite Terra, Venus. Purely radial swarms record no MHCS direction. Differential stress state in highlands is therefore generally small, while that in the lowlands appears to be contolled by the gravitational relaxation of pre-existent topography.

PETROLOGIC CONSTRAINTS ON THE SURFACE PROCESSES ON ASTEROID 4 VESTA AND ON EXCAVATION DEPTHS OF DIOGENITE FRAGMENTS; T. L. Grove, Department of Earth, Atmospheric and Planetary Sciences, Massachusetts Institute of Technology, Cambridge, MA 02139

The eucrite-howardite-diogenite meteorite groups are thought to be related by magmatic processes [1,2]. Asteroid 4 Vesta has been proposed as the parent body for the these basaltic achondrite meteorites [3]. The similarity of the planetesimal's surface composition to eucrite and diogenite meteorites and the large size of the asteroid (r = 250 km) make it an attractive source, but its position in the asteroid belt far from the known resonances from which meteorites originate make a relation between Vesta and eucrite-howardite-diogenite group problematic. It has been proposed that diogenites are low-Ca pyroxene-rich cumulates that crystallized from a magnesian parent (identified in howardite breccias [4]), and this crystallization process led to evolved eucrite derivative magmas. This eucrite-diogenite genetic relationship places constraints on the physical conditions under which crystallization occurred. Elevated pressure melting experiments on magnesian eucrite parent compositions [5,6] show that the minimum pressure at which pyroxene crystallization could lead to the observed compositions of main series eucrites is 500 bars, equivalent to a depth of 135 km in a 4 Vesta-sized eucrite parent body. Therefore, the observation of diogenite on the surface of 4 Vesta [7] requires a post-crystallization process that excavates diogenite cumulate from depth. The discovery of diogenite asteroidal fragments [8] is consistent with an impact event on 4 Vesta that penetrated the deep interior of this planetesimal.

Models for eucrite formation Based on experiments carried out at 1-atm, Stolper [9] concluded that eucrite basalts could be generated by small extents of partial melting of a chondritic olivine-rich composition at shallow depths in the eucrite parent body. Consolmagno and Drake [10] reached a similar conclusion from an analysis of rare-earth element systematics. These shallow level partial melting models do not provide a mechanism for generating diogenite cumulates; rather, they would generate lherzolite residues. Although higher extent partial melts could undergo fractional crystallization of low-Ca pyroxene under near-surface conditions, the relation of the olivine-low-Ca-pyroxene reaction boundary to the partial melt composition is such that pyroxene crystallization would lead to derivative melt compositions that do not resemble any sampled eucrite lavas. Bartels and Grove [5,6] carried out experiments at elevated pressures and showed that magnesian eucrite parent magmas could generate diogenite cumulates and main series eucrite lavas by fractional crystallization at pressures achieved in the interior of a Vesta-sized parent body (> 500 bars).

Advantages of a major impact A major impact on the surface of 4 Vesta therefore reconciles several issues concerning the origin of eucrites and diogenites. Binzel and Xu [8] have observed numerous small asteroids of eucrite and diogenite material between 4 Vesta and the 3:1 resonance. These fragments have orbital elements similar to those of Vesta, and they propose that these fragments are excavated from Vesta and suggest that it is now dynamically possible for the eucrite-howardite-diogenite meteorite group to be linked to Vesta. A large impact on Vesta also allows the observation of diogenite [6] on the surface to be reconciled with petrologic constraints. The observed presence of diogenite-rich areas on the surface of Vesta requires an event that disturbed the interior. Petrologic constraints indicate that diogenite is

excavated material from a depth of at least 135 km, placing some constraints on dynamic modeling of the impactor. Higher resolution imaging studies of Vesta might focus on determining whether the asteroid has experienced a few large impacts that have excavated deeply or whether the planetesimal is chaotically reassembled like Miranda, the Uranian moon.

References [1] B. Mason, 1962, *Meteorites*, Wiley, New York. [2] B. Mason, 1963, Am. Mus. Novit. 2155, 1-13. [3] T. B. McCord et al., 1970, Science 168, 1445. [4] Dymek et al , 1976, Geochim Cosmochim Acta 40, 1115-1130. [5] K. S. Bartels and T. L. Grove, 1991, Proc. Lunar Planet. Sci. 21, 351-365. [6] T. L. Grove and K. S. Bartels, 1992, Proc. Lunar Planet. Sci. 22, 437-445. [7] M. J. Gaffey, 1983, Lunar Planet. Sci. XIV, 231-232. [8] R. P. Binzel and S. Xu, Science (submitted). [9] E. M. Stolper, 1977, Geochim Cosmochim Acta, 41, 587-611. [10] G. C. Consolmagno and M. J. Drake, 1977, Geochim Cosmochim Acta, 41, 1271-1282.

THE PLANETARY DATA SYSTEM EDUCATIONAL CD-ROM; E. A. Guinness and R. E. Arvidson, Dept. of Earth and Planetary Sci., McDonnell Center for the Space Sci., Washington University, St. Louis, MO 63130; M. Martin and S. Dueck, Jet Propulsion Laboratory, 4800 Oak Grove Dr., Pasadena, CA, 91109.

The Planetary Data System (PDS) is producing a special educational CD-ROM that contains samples of PDS datasets and is expected to be released in 1993. The CD-ROM will provide university-level instructors with PDS-compatible materials and information that can be used to construct student problem sets using real datasets. The main purposes of the CD-ROM are to facilitate wide use of planetary data and to introduce a large community to the PDS. To meet these objectives the Educational CD-ROM will also contain software to manipulate the data, background discussions about scientific questions that can be addressed with the data, and a suite of exercises that illustrate analysis techniques. Students will also be introduced to the SPICE concept, which is a new way of maintaining geometry and instrument information. The exercises will be presented at the freshman through graduate student levels. With simplification, some of the material should also be of use at the high school level.

The nine datasets to be included on the Educational CD-ROM are listed in Table 1, along with the individuals who are producing the datasets, documentation, and exercises. The Planetary Image dataset consists of approximately 200 of the best color and black and white images from the U.S. planetary exploration program and captions for each image. The comet dataset includes spectra of sublimating gases from comet Halley, with exercises focussed on determining the production rate of water at different points in the comet's orbit. The meteorite and asteroid dataset consists of several multispectral datasets with an exercise to identify the signature of specific minerals. The Titania dataset consists of radiometrically calibrated Voyager images acquired at different geometries. The exercise associated with the Titania dataset explores the moon's bi-directional reflectance function in terms of the composition and texture of the surface. The Viking Orbiter Infrared Thermal Mapper dataset includes temperature, thermal inertia, and elevation maps of Valles Marineris with an exercise dealing with the control of temperature variations. The Viking Lander dataset contains Viking Lander 2 color images and temperature and pressure measurements acquired over the course of two Mars years. The exercise associated with this dataset explores visual and meteorological observations of frost at the Viking 2 site. The Viking Orbiter gravity and topography dataset includes gravity, topography, and image data over Olympus Mons with an exercise to test models explaining the gravity observations. The Apollo 17 dataset includes chemical analyses of Apollo 17 soils and possible endmember materials. The exercise will involve using mixing models to explain the composition of the soils. Finally, the Magellan dataset consists of synthetic aperture radar, elevation, and emissivity data over Sapas Mons and Maat Mons. The purpose of the exercise is to explore how terrain type, relative age, and elevation control microwave properties.

The information on the CD-ROM is organized by directories, of which there is one for each dataset, documentation, indices, and software. The documentation directory contains a text file, VOLINFO.TXT, which includes background discussions of the datasets and descriptions of the exercises and software. Students can access the datasets and exercises through this directory structure using several popular operating systems,

including DOS, VAX/VMS, Unix, and MacOS. An alternate access capability is the Journey to the Planets program included on the CD-ROM, which will run on Macintosh and PC computers (Windows 3.1) with a 256 color display. The program will allow users to browse through the images or display them as a slide show. Image captions and descriptions of the planets, missions, and spacecraft are also included as well as descriptions of the exercises on the CD-ROM.

The PDS Educational CD-ROM is dedicated to Dr. William Quaide, former chief scientist, Office of Solar System Exploration, NASA Headquarters. Before his retirement in 1992, Dr. Quaide was instrumental in launching the Planetary Data System. Further, he has influenced in very positive ways each of the missions or projects that produced data included on this CD-ROM. With Dr. Quaide's strong interest in education, it is entirely appropriate that publication and dissemination of the Educational CD-ROM be done in honor of his many contributions to the planetary sciences.

TABLE 1

Dataset	Lead Persons	Institution
Planetary Images	M. Martin, S. Dueck	Jet Propulsion Laboratory
Comet Spectra	M. A'Hearn, E. Grayzeck	U. of Maryland
Meteorite and asteroid spectra	C. Pieters	Brown U.
Photometry of Titania from Voyager images	B. Brackett C. Acton	Washington U. Jet Propulsion Laboratory
Viking Orbiter Infrared Thermal Mapper data	T. Martin	Jet Propulsion Laboratory
Viking Lander image and meteorology data	E. Guinness, R. Becker S. Lee	Washington U. U. of Colorado
Viking Orbiter gravity and topography data	R. Phillips	Washington U.
Chemical data for Apollo 17 samples	R. Korotev	Washington U.
Magellan SAR, elevation, and emissivity data	R. Arvidson, N. Izenberg	Washington U.

FLUVIAL EROSION ON MARS: IMPLICATIONS FOR PALEOCLIMATIC CHANGE; Virginia C. Gulick and Victor R. Baker, Department of Geosciences and the Lunar and Planetary Laboratory, University of Arizona, Tucson, AZ 85721; email address: gulick@convx1.ccit.arizona.edu.

Fluvial erosion on Mars has been nonuniform in both time and space. Viking orbiter images reveal a variety of different aged terrains exhibiting widely different degrees of erosion. Based on our terrestrial analog studies, rates of fluvial erosion associated with the formation of many of the valleys on Mars is probably on the order of hundreds of meters per million years, while rates of erosion associated with the formation of the outflow channels probably ranged from tens to hundreds of meters in several weeks to months. However, estimated rates of erosion of the Martian surface at the Viking Lander sites are extremely low, on the order of 1 μm/yr or less. At most this would result in a meter of material removed per million years, and it is unlikely that such an erosion rate would be able to produce the degree of geomorphic work required to form the fluvial features present elsewhere on the surface. In addition, single terrain units are not eroded uniformly by fluvial processes. Instead fluvial valleys, particularly in the cratered highlands, typically are situated in clusters surrounded by vast expanses of uneroded surfaces of the same apparent lithologic, structural, and hydrological setting. Clearly throughout its geologic history, Mars has experienced a nonuniformity in erosion rates. By estimating the amount of fluvial erosion on dissected terrains and by studying the spatial distribution of those locations which have experienced above normal erosion rates, it should be possible to place further constraints on Mars' paleoclimatic history.

In the heavily cratered terrains, evidence for fluvial erosion is found on the ejecta blankets of impact craters, on some volcanoes, and in intercrater plains regions. Many of the valleys in the intercrater plains appear to be associated with dark units which have been interpreted as igneous sill intrusions [1]. An asymmetric distribution of valleys around impact craters is common on Mars, unlike drainages situated around terrestrial impact craters which tends to be more uniform. While most of the Martian valley networks are attributed to formation by ground-water outflow processes [2,3,4], the distribution of these networks is unlike valley systems formed by ground-water sapping on Earth.

On Mars, valleys exhibiting a runoff-dominated morphology are rare; sapping valleys form as isolated systems. On Earth, sapping valleys almost always form with runoff dominated systems, regardless of lithologic or climatic conditions. In Hawaii, sapping valleys develop when the larger runoff valleys tap into the underlying ground-water reservoir. The addition of ground water to the fluvial system increases overall stream power and accelerates erosion at valley heads and along walls. Oversteepening of relief and removal of support for the overlying material causes subsequent collapse in these areas and results in the characteristic sapping morphology of theater-headed tributaries and either U-shaped or broad flat-floored valleys with steep walls. Sapping valleys form in a variety of climatic regimes and lithology. On the Colorado Plateau, under semi-arid conditions, sapping valleys have formed in sedimentary deposits of highly permeable, jointed sandstone which is underlain by a relatively impervious rock unit composed of mudstones, siltstones and sandstones. Runoff-dominated systems are also present and form under the same lithologic, stratigraphic, and climatic conditions as the sapping valleys; morphologic differences are attributed to structural constraints that determine the effectiveness of surface and ground-water flow [5]. In the permafrost region along the eastern North Slope of Alaska the ground is frozen to depths of several hundred meters. Here spring-fed valleys and gullies flow year-round while runoff-fed streams flow only in the warmer months. The average precipitation is only a few centimeters of snow per year [6].

The heavily cratered terrains contain numerous valley systems. We have selected two of the best developed valleys in the heavily cratered terrains for comparison with our estimates of valley erosion on martian volcanoes. A particularly well-formed drainage network is located along the highlands-lowlands boundary at 42.5°S, 92.6°. Although at first glance this valley system exhibits a high degree of integration, which led many to cite as evidence for an early warm climate on Mars, detailed study of this valley system indicates less morphological similarity to terrestrial runoff valleys than previously thought. The system lacks a hierarchial network of tributaries (see also [2]), unlike the runoff dominated systems on Earth. The estimated volume of valley erosion (assuming valley side slopes of between 10° and 30°) yields between 10^{11} and 10^{12} m^3 of material removed to form the valley network. The estimated eroded volume in the Parana valley system, at 22°S, 8.5° in the Margaritier Sinus region, also lies within this range. These eroded volumes are remarkably similar to those estimated for the volcanoes Alba Patera, Hecates Patera, and Ceraunius Tholus. Hadriaca and Tyrrhena Paterae have estimated eroded volumes 1 to 2 orders of magnitude larger. Results are shown in Figure 1. Assuming a particular lithologic environment, estimates of Martian valley erosion can be combined with terrestrial fluvial erosion rates scaled to the gravity of Mars in order to obtain estimates of the total volume of water required to form each set of Martian valleys. Some estimates of the ratios of water volume to eroded volume for Mars are as low as 2 or 3 to 1 [7]. Based upon our own study of fluvial erosion on volcanic landscapes, we find ratios as large as 1000 to 1. The total water volume using each estimated ratio is shown for each valley group in Figure 2. For each locality the lower bar represents the uncertainty due to valley side wall slopes while using a water to eroded volume ratio of 3:1, the upper bar using a ratio of 1000:1.

As Figure 2 indicates, while the uncertainty in absolute quantity of water required to erode these valleys is large,

the quantity of water passing through the two selected valley systems on the heavily cratered terrain does not drastically differ from that on the martian volcanoes, barring major differences in lithology. Since the valleys on some volcanoes were formed much later than the heavily cratered terrain valleys, we conclude that the climatic controls on valley formation must have been similar for the various valleys.

Whether the formation of the martian valley networks provide unequivocal evidence for drastically different climatic conditions remains debatable. Recent theoretical climate modeling seems to preclude the existence of a temperate climate early in Mars' geological history [8], but such a climate may have been possible later when the sun's luminosity was close to today's value. An alternative hypothesis [9] suggests that Mars had a globally higher heat flow early in its geological history which would bring water tables to within 350 meters of the surface. While this would allow liquid water to exist closer to the surface and initiate circulation of subsurface water at depth, most of the valley networks would have probably required ground water to be much closer to the surface. However, the addition of persistent, vigorous, localized hydrothermal circulation such as those associated with igneous intrusions, volcano formation, and large impact craters could circulate ground water into the surface environment and may be able to initiate and maintain hydraulic gradients sufficient for valley formation. The horizontal lines in Figure 2 illustrate the cumulative discharge of hydrothermal systems associated with 50, 500, and 5000 km^3 igneous intrusions.

The valley characteristics discussed above suggest a scenario involving both precipitation and hydrothermal activity. Directly adjacent to the hydrothermal system, heat flow can be sufficient to entirely melt through the permafrost zone. Snow falling in the vicinity would be melted from the rising thermal energy as well. Alternatively, water vapor emitted by the hydrothermal system might produce enhanced precipitation along the perimeter of the zone. In areas away from an active hydrothermal system snowfall would not melt because of the lack of significant geothermal energy; this snow would sublimate and produce little or no significant erosion of the surface. Thus the formation of locally vigorous hydrothermal systems may explain why valley development tends to be clustered and why some fairly well developed fluvial valleys are adjacent to regions of similar age and apparently similar lithology with little to no valley development.

References: [1] Wilhelms, D.E. and Baldwin, R.J. (1989) *Proc. 19th LPSC*, 355-365. [2] Pieri, D. (1980) NASA TM-81979, 1. [3] Carr, M.H. (1981) The Surface of Mars. [4] Baker, V.R. (1982) The Channels of Mars. [5] Laity, J.E. and Malin, M.C. (1985) GSA Bull., **96**, 203-217. [6] Sellmann, P.V. et al. (1972) Artic Environmental Data Package Suppl. 1, U.S. Army CRREL Document. [7] Goldspiel, J.M. and Squyres, S.W. (1991) *Icarus* **89**, 392. [8] Kasting, J. (1991) *Icarus*. [9] Squyres, S.W. (1989) *LPSC XX*, 1044-1045.

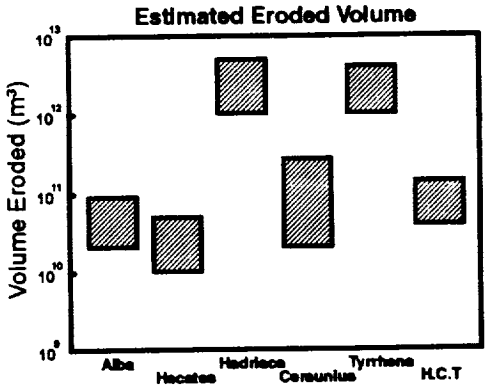

Figure 1.

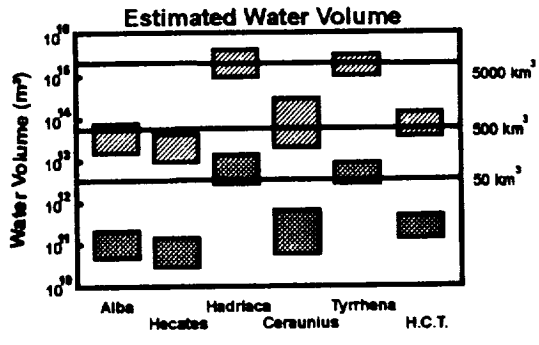

Figure 2.

THE ACRAMAN IMPACT STRUCTURE: ESTIMATION OF THE DIAMETER BY THE EJECTA LAYER THICKNESS

E. P. Gurov, Institute of Geological Sciences, Ukrainian Academy of Sciences, Chkalov str., 55-b, Kiev, Ukraine, 252054.

The big role of gigantic craters formation in geological history of the Earth was established by the example of the K/T boundary event. The discovery of the iridium anomaly in the sedimentary rocks of Vendian in the western part of Ukrainian shield (1) allows to suppose its origin in connection with the great impact of that time. The only one big impact structure of that age is the Acraman Crater in south-eastern part of Australia (2).

The Acraman Crater is presented by deeply eroded structure, original diameter of which it is difficult to determine. By geological and morphological data the Acraman Crater is presented by an inner ring 30 km in diameter, an intermediate ring 90 km in diameter and an outer ring about 150-160 km in diameter (2). In (3), the diameter of the collapse crater was determined as 85 km. If the original diameter of the crater was equal to the diameter of outer ring, it may be estimated as 160 km. The formation of such impact structure was accompanied with not only regional consequences, but with global fenomenon such as deposition of the material of the fireball on the considerable part of the Earth surface.

The ejecta layer of the Acraman Crater is exposed in the Adelaide Geosyncline at the distance about 300 km from its center. At the same time the situation of the ejecta in the folded structure of Adelaide Geosyncline may reduce the original distence of their exposures from the center of the crater by some tens of kilometers (3,4). The thickness of the ejecta ranges from 0 to 40 cm, mainly less than 10 cm. The sequence of the sediments including ejecta layer detects its good preservation. As the thickness of the ejecta of the Acraman Crater is known, it is possible to estimate its original diameter with the formulae in (5,6) for determination of the thickness of the ejecta by the data of the crater diameter and the distance from its center.

DIAMETER OF THE ACRAMAN CRATER

E.P.Gurov

In the table 1 the thickness of the ejecta was determined for several possible radii of the Acramen Crater. If the radius of the crater was about 80 km, the thickness of the ejecta was about some tens meters at the distance of 300-350 m. If the radius was about 42.5-45 km, the thickness of ejecta layer was about some meters, that was 10 times greater, that was observed. The data of the table 1 allows to estimate the radius of the crater as about 15-20 km, but less than 42.5 km. The reduction of the distance of the ejecta by 50 km insignificantly changed its thickness.

Table 1. The ejecta thickness t (m) as a function of the crater radius R (km)and the distance from its center, r_1=300 km, r_2= 350 km.

R	$t=0.04R(\frac{r}{R})^{-3.0}$ (5)		$t=0.06R(\frac{r}{R})^{-3.26}$ (6)	
	r_1	r_2	r_1	r_2
15	0.07	0.05	0.05	0.03
20	0.24	0.15	0.18	0.10
30	1.20	0.74	1.00	0.58
42.5	4.9	3.0	4.4	2.6
45	6.1	3.7	5.6	3.4
80	60.1	38.1	64.8	39.3

As the original diameter of the Acraman Crater was less than 85-90 km, its formation caused only regional, but no global consequences. So the iridium anomaly in the sediments of Vendian in the Ukrainian shield cannot be connected with the Acraman crater.

References

(1) Felicin S.B., Sochava A.V., Vaganov P.A., Meyer V.A., 1989, Dokl. AN USSR, v.309, N 5, p.1200-1203 (in russian).

(2) Williams G.E., 1986, Science, v.233, N 4760, p.200-203.

(3) Gostin V.A., Keays R.R., Wallace M.W., 1989, Nature, v.340, N 6243, p.542-544.

(4) Gostin V.A., Haines P.W., Jenkins R.J.F., Compston W., Williams I.S., 1986, Science, v.233, N 4760, p.198-200.

(5) McGetchin T.R., Settle M., Head J.W., 1973, Earth Planet. Sci.Lett., v.20, p.226-236.

(6) Stöffler D., Gault D.E., Wedekind J., Polkowski G., 1975, Journ. Geophys. Res., v.80, N 29, p.4062-4077.

THE KARAKUL DEPRESSION IN PAMIRS - THE FIRST IMPACT STRUCTURE IN CENTRAL ASIA

Gurov E.P., Gurova H.P., Rakitskaya R.B., Yamnichenko A.Yu., Institute of Geol. Sciences Ukrainian Academy of Sciences, Kiev, Ukraine, 252054.

The Karakul depression was picked out as the possible impact structure by the study of space images of Tadjikistan. Its striking similarity with some complex impact craters such as Dellen and Gosses Bluff is evident. Our investigations of the Karakul depression in 1987 and 1989-1991 years allowed to determine it as the impact crater with the central uplift (1,2).

The target of the crater is presented by slightly metamorphosed sedimentary rocks of Paleozoic, intensively folded and intruded with granites during the Gercynian orogeny. The modern structure of north-eastern Pamirs was formed by Alpinian orogeny; the raise of the area in Neogene was about 4000-7000 m (3,4).

The Karakul crater is presented by the circular depression with the flat floor and uplifted rim. The rim-rim diameter is about 52 km. The bottom of the depression 30 km in diameter is occupied by the Karakul Lake and unconsolidated lakustrine deposites. The central uplift forms an island and peninsula in the lake in the middle part of the depression (fig. 1). The height of the uplift is to 250-300 m above the lake level. The elevation of the rim is about 1000 m above the floor of the depression and about 120-200 m above the surrounding area.

The rocks of the central uplift and of inner slopes of the rim are disturbed. Breccia, brecciated rocks and cataclasites are widespread in the central uplift.The limestones with the gries structures and granites converted to the rock meal were observed in that area. The shock metamorphic effects are distributed in some rock types. In brecciated quartz mosaicism and undulatory extinction are abundant. The planar elements in shocked quartz are represented by the systems $\{10\bar{1}3\}$, $\{10\bar{1}4\}$, $\{10\bar{1}1\}$ and some others (fig.2,3). The system of $\{10\bar{1}2\}$ rare was observed in the biggest part of examined samples. The kink bands are represented in biotite and quartz. The shock pressures determined in quartz are to 15-17 GPa.

The impactites, suevites and allochtonous breccia were newer observed in the depression, but they might be preserved in its deepest part around the base of the central uplift under the Quaternary deposites and below the lake level.

The youngest rocks of the target of the crater are granites with the K-Ar age of about 230-190 m.y. The oldest sediments formed in the depression are represented by the lakustrine deposites of Pliocene-Pleistocene (?). The age of the crater was preliminary estimated as Neogene, probably, Pliocene.

KARAKUL IMPACT CRATER

Gurov E.P. et al.

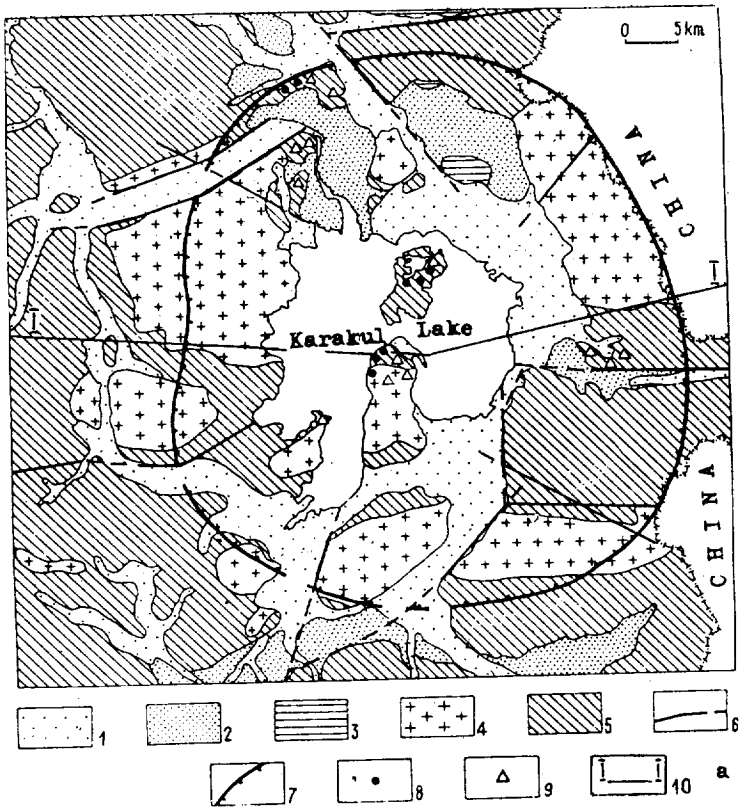

Fig.1. Simplified geological map of the Karakul impact structure (after E.F.Romanko and autors' data)/a/ and its morphological crossection /b/. 1.Quaternary lakustrine and alluvial deposites; 2. Glacial deposites; 3.Pliocene-Pleistocene (?) lakustrine deposites; 4.Karakul granites; 5.Paleozoic sedimentery rocks; 6.Faults; 7.Crater rim; 8. Shock metamorphosed rocks; 9. Breccia, megabreccia; 10.Position of crossection.

Fig.2. Photomicrograph (crossed nicols) of quartz in breccia exposed in the island in the Karalul Lake.

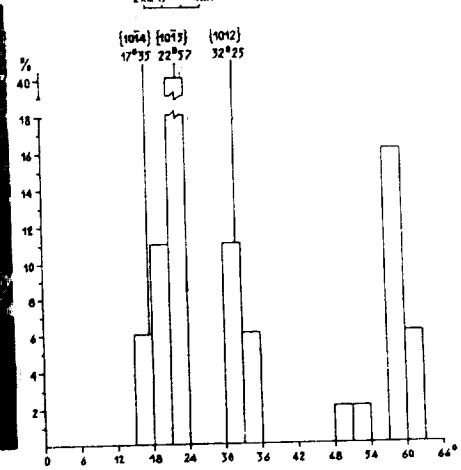

Fig.3. Histogram of the planar elements orientation in quartz from the north-western part of the Karakul depression. 26 measurements of 14 grains.

REFERENCES. 1. Gurov E.P.,Gurova H.P., Rakitskaya R.B., Yamnichenko A.Yu. (1988). Abstr.Eight Sov.-Amer.symp. Comparat. Planet., Moscow, Vernadsky Inst. Geochim.and Analyt. Chem.Press, p.37. 2. Gurov E.P., Gurova H.P., Rakitskaya R.B., Yamnichenko A.Yu. (1992). Preprint 92-8 Inst. Geol. Sci. Ukr.Acad.Sci., Kiev, 42 p. 3. Belousov T.P. The tectonik movements of Pamirs in Pleistocene-Golocene and its seismity.(1976). Moskow:Nauka Press,119 p. (in russian). 4. Schvolman V.A.The tectonic development of of Pamirs in Cretaceous and Paleogene periods. (1977). Moskow: Nauka Press, 160 p.(in russian).

SYSTEMATIC CHEMICAL VARIATIONS IN LARGE IIIAB IRON METEORITES: CLUES TO CORE CRYSTALLIZATION; H. Haack, E.R.D. Scott; Planetary Geosciences, University of Hawaii, USA; G. S. Rubio, D.F. Gutierrez, Institute of Geology and Institute of Astronomy, Universidad Nacional Autonoma de Mexico, Mexico, D.F., Mexico; C.F. Lewis, Center for Meteorite Studies, Arizona State University, Tempe, USA; J.T. Wasson, Institute for Geophysics and Planetary Physics, UCLA, USA; R.R. Brooks, X. Guo, Dept. of Chemistry and Biochemistry, Massey University, Palmerston North, New Zealand; D.E. Ryan, and J. Holzbecher, Dept. of Chemistry, Dalhouse University, Halifax, N.S., Canada

Abstract. Analysis of numerous individual iron meteorites have shown that fractional crystallization of iron cores results in variations in chemical concentration of the solid core which span several orders of magnitude. The magnitude and direction of the resulting spatial gradients in the core can provide clues to the physical nature of the core crystallization process [1,2]. We have analyzed suites of samples from three large IIIAB irons (Cape York, 58t; Chupaderos, 24t; Morito, 10t) in order to estimate local chemical gradients. Initial results for the concentrations of Ge, Pd, Pt (Massey group), Ir, Au, As, Co, Os, and Rh (Dalhouse group), and P (Arizona group) show significant ranges among the Cape York and Chupaderos samples and marginally significant ranges among the Morito samples. Measurements of Au, Ir, Co, Ni, Cu, Ga, As, W, Re (from UCLA) and Ni and Co (Arizona group) are in progress. We find a spatial Ir gradient in Chupaderos with a magnitude similar to the one reported for Agpalilik (Cape York iron) by Esbensen et al.[1].

Introduction. Prior to the remarkable discoveries of chemical variations in Cape York by Esbensen et al. [1] it was generally believed that core crystallization process did not result in chemical gradients which could be detected in even large iron meteorites. Previous workers have either argued that the iron cores crystallized by dominantly outwards concentric growth [1,3] or inward dendritic growth [2,4]. Pure concentric growth would result in spatial chemical gradients within a single meteorite below the detection limit, whereas dendritic crystallization would produce gradients which are generally above the detection limit. One possible way to discriminate between the two scenarios is therefore to measure typical spatial gradients in large iron meteorites.

Purpose of study. In the current study we have sampled two more large IIIAB iron meteorites (the 24-ton Chupaderos and the 10-ton Morito) and expanded the study of Cape York in order to provide more constraints on the crystallization of the IIIAB core. We have tried to answer 3 important questions about chemical variations in iron cores: a) Are the observations from the Cape York shower a normal or a rare feature of iron cores. b) What is the average magnitude of chemical gradients? c) Do the compositional variations within large iron meteorites differ from the trends defined by individual analyses of small iron meteorites?

Method. We hacksawed 10 samples from Chupaderos and 4 from Morito, each sample weighing 10-20 g. The spatial coordinates of each sample was measured and the relative orientation of the two main Chupaderos masses prior to break-up was determined. Au, As, Pd, Rh, Os, Ir, and Pt were determined using the methods described in Hoashi et al. [5].

Results: *Cape York.* Esbensen et al. [1] found a chemical gradient in Ir within the 20-ton Cape York Iron, Agpalilik. They also found a variation in chemical composition among the Cape York irons with Thule (2.68 ppm Ir) and Savik II (5.13 ppm Ir) as end-members. Haack and Scott [2] suggested a correlation between scatter in IIIAB and the deviation between the Cape York trend and the main IIIAB trend. This could indicate that the scatter in the IIIAB compositional trends are in part due to deviating local trends like the Cape York trend. In order to further test this idea we have expanded the data set to include the elements P, Pt, Ge, Rh, and Os for the meteorites Savik I, Agpalilik, and Thule. These data are consistent with the idea that part of the scatter is due to deviating local trends. We find a correlation between Au and Pd, an inverse correlation between Au and Pt, Rh, Ir, and Os, and a correlation between our new Ge data and the previously reported Ga data [1]. The Ir concentrations span the largest range (a factor 2.1).

Of particular interest is the distribution of P, since it has a much higher diffusion rate (2 orders of magnitude higher than Ni) than the other elements. Our data shows that the P variation among the Cape York iron meteorites follows the variation defined by data on other IIIAB iron

meteorites (e.g. there is no evidence for solid state equilibration of P). This observation suggests that the compositional gradients through the Cape York meteorites extended over tens of meters.

Chupaderos. This meteorite is the second largest IIIAB iron meteorite and therefore a prime candidate for a study of chemical gradients in the IIIAB core. With a Ni concentration of 9.7 wt % [6], Chupaderos crystallized much later than Cape York (≈ 8 wt% Ni) and may possibly provide clues to the state of the core at a time were it was largely solid. The three Chupaderos fragments can be reassembled to form a mass with dimensions of 4.0 x 2.65 x 0.9 m [7]. Abundant troilite nodules can be seen on the surface of these fragments with the larger nodules being aligned within and among the three masses.

9 out of the 10 analyzed samples from Chupaderos seem to define a spatial gradient. One sample had a very unusual composition, possibly due to the proximity of a troilite nodule [1]. In the remaining 9 samples Au showed a correlation with Ge, Pd, Rh, and Ir, an inverse correlation with Pt, and no correlation with Co. Discarding the anomalous sample we obtained the following ratios between the highest and lowest measured concentrations: Co: 1.1, Ge: 1.1, As: 1.2, Au: 1.4, Pd: 1.7, Ir: 1.8, Rh: 2.2. Compositional variations show relatively well defined trends along a direction which coincides with the direction defined by the troilite nodules in the XY-plane. The limited vertical dimensions of the meteorites does, however, make it difficult to constrain the Z-component of the compositional gradient vector.

We found that the P concentrations of the Chupaderos samples varied by a factor of 2 consistent with previous measurements of P in the Chupaderos fragment Adargas (0.47 wt% P) [8] and 0.16 wt% P in Chupaderos [9]. These numbers are lower by approximately a factor of 2 compared to other IIIAB irons with similar Ni concentrations. The lack of correlation of the P data with our other analyses does, however, suggest that sample heterogeneity is partially responsible for the variation.

Morito. Morito has the same average composition as Cape York and did therefore crystallize around the same time. Due to the beautifully sculptured shape of this large meteorite we were only allowed to take 4 samples spaced approximately 1 m from each other. We found significant compositional variations for the following elements: Co: 1.1, Ge: 1.2, As: 1.4, Au: 1.1, Pd: 1.1, Ir: 1.1, Rh: 1.4. The small number of samples made it impossible to estimate a spatial gradient, although the compositions of the samples seem to correlate with position. Positive correlations between Au and As and Os, Pt, and Ir suggest that the variations are real, although we cannot draw any conclusions before the full data set is available.

Conclusions: Our new compositional data from three large IIIAB iron meteorites suggest that at least the IIIAB core had large spatial gradients in chemical composition. Comparison of our data with literature data on IIIAB iron meteorite compositions suggests that local compositional trends in the parent core may deviate from the general IIIAB trends. The magnitude of the Ir gradient inferred for Chupaderos is close to the previously reported Ir gradient in the Cape York mass Agpalilik.

Acknowledgements: Ignacio Casanova's help to initiate this project is greatly appreciated. V.F. Buchwald, F. Ulff-Møller, and K.L. Rasmussen are thanked for providing the Cape York samples. This work was partially supported by NASA grant NAG 9-454 and NAGW - 3281 (K. Keil).

References: [1] Esbensen K.H., V.F. Buchwald, D.J. Malvin, and J.T. Wasson (1982) *Geochim. Cosmochim. Acta*, **46**, 1913-1920. [2] Haack H. and Scott E.R.D. (1993)*Geochim. Cosmochim. Acta*, submitted. [3] Pernicka, E, and J.T. Wasson, (1987) *Geochim. Cosmochim. Acta*, **51**, 1717-1726. [4] Haack H. and Scott E.R.D. (1992) *J. Geophys. Res*, **97**, 14727-14734. [5] Hoashi, M., H. Varela-Alvarez, R.R. Brooks, R.D. Reeves, D.E. Ryan, and J. Holzbecher (1992) *Chem. Geol.*, **98**, 1-10. [6] Scott, E.R.D., J.T.Wasson, and V.F. Buchwald (1973)*Geochim. Cosmochim. Acta*, **37**, 1957-1983. [7] Buchwald, V.F. (1975) Handbook of Iron Meteorites, University of California Press. [8] Moore, C.B., C.F. Lewis, and D., Nava (1969) In *Meteorite Research* (ed. P.M. Millman) 738-748. [9] Lewis, C.F. and C.B. Moore (1971) *Meteoritics*, **6**, 195-205.

ASSIMILATION OF SOLIDS DURING ASCENT OF MAGMAS FROM THE BARTOY FIELD OF THE BAIKAL REGION, SIBERIA Johnson R. Haas[1], Larry A. Haskin[1], James Luhr[2], and Sergei Rasskazov[3], 1 Department of Earth and Planetary Sciences and McDonnell Center for the Space Sciences, Washington University, St. Louis, MO 63130; 2 Dept. of Mineral Sciences, Smithsonian Institution, Washington D. C., 20560; 3 Institute of the Earth's Crust, Irkutsk, Russia.

Most investigators ascribe mare basalt magma genesis to partial melting at depths of ~130 - >400 km [e.g., 1-4] within the cumulate pile deposited from a lunar magma ocean. Mare basalts share with mid-ocean ridge basalts the characteristic of relative depletion in LREE and other incompatible trace elements that arises from melting within "used" mantle, from which crust-forming elements have already been separated. Some mare basalt types do not show the classical, La-Nd depleted mare basalt REE distributions, however, and some types are isotopically heterogeneous. These differences have been ascribed to assimilation, mainly AFC-style [5], of KREEPy highland material overlying the source region [e.g., 6-9 and references therein]. Might such assimilation occur during magma ascent through the KREEPy material? To gain information from a terrestrial setting on possible assimilation during ascent, we have studied a suite of Quaternary nepheline-hawaiites and nepheline-mugearites from the Bartoy cinder cone complex of the Baikal Rift, Siberia. The Bartoy magmas originated from >80 km deep, and erupted through thick Archean crust [10]. We find evidence for assimilation of ~31 wt% xenocrysts of garnet, aluminous clinopyroxene, kaersutite, and olivine, all presumably from the basalt source region, but no appreciable assimilation of overlying crust, consistent with isotopic constraints [11]. Magmatic superheat made available by rapid ascent and decompression accounts adequately for the energy of assimilation; no accompanying fractional crystallization is required or evident.

Compositional models for mare basalt genesis from magma ocean cumulates account intriguingly well for gross features of major element composition and REE distribution, but usually fall short of quantitative descriptions of basalts of a given type or from a given region, and particularly fail to account for high-Al (HA) basalts and very high-K (VHK) basalts from Apollo 14 [e.g., 12], and type B2 basalts from Apollo 17 [13]. Assimilation of KREEPy material has been proposed to account for the differences.

The deep source region of the Bartoy magmas (22-25 kb [10]), coupled with the overlying thick, Archean crust, facilitate detection of crustal assimilation within the ascended, mantle-derived magmas. Unlike lunar lavas, the Bartoy suite contains abundant mafic xenoliths, cm-sized megacrysts, and fine- to coarse-grained xenocrysts. Principal xenocrystic minerals are garnet, clinopyroxene, and kaersutite [10]. Basalt samples analyzed were aphanitic fragments free of obvious macroscopic contamination by xenoliths, xenocrysts, and megacrysts.

Chondrite-normalized REE distributions are shown in Fig. 1. The lavas are notable for their systematic decrease in HREE concentrations with increasing LREE concentrations, with all REE patterns "rotating" about the position of Dy-Ho on the diagram. These variations in REE concentration preclude low-pressure fractionation, which would produce a stack of roughly parallel REE patterns. Petrogenesis involving garnet is indicated by these crossing REE patterns.

The compositions of the lavas are accounted for precisely by a chemical mixing model as mixtures of BK-134 (the most evolved lava) and megacrystic garnet, clinopyroxene, kaersutite, and minor olivine, all of constant compositions. The mixing results are so precise that, although the lava compositions vary substantially (Max/Min of 1.9 for MgO, 2.1 for Sc, 1.3 for Co, 1.4-1.5 for LREE and other incompatible elements, and 1.6 for HREE), small errors in mixing-model fits are significantly independent of the estimated proportions of BK-134 and xenocrysts in the mixtures; i.e., constant composition of mixing end members is required by the precise fits. Analyzed xenocrysts show little compositional variation. Concentration ranges of major elements are inconsistent with fractional crystallization of high-pressure, equilibrium clinopyroxene and garnet. Observed concentration ranges of compatible trace elements are too large to be consistent with the extents of partial melting of a single source estimated from concentration ranges of incompatible trace elements (e.g., Fig. 2).

ASSIMILATION OF SOLIDS: Haas J.R., *et al.*

Petrographic observations of the Bartoy lavas support the assimilation model. Small xenocrysts are absent. Larger garnet xenocrysts are corroded, suggesting that assimilation occurred for as long as excess heat was available. Larger clinopyroxene xenocrysts are corroded, but subsequently armored with augite of low-pressure composition, suggesting that assimilation occurred until clinopyroxene reappeared on the liquidus during or just prior to eruption. Olivine occurs as two populations -- compositions of Fo85, interpreted to be xenocrysts, and compositions as low as Fo60, interpreted to be phenocrysts. Kaersutite appears as xenocrysts. We estimate the quantity of heat available from pressure release to be roughly 260 J/g, enough to supply the ~230 J/g needed for assimilation of ~30 wt% of xenocrystic material.

The compositions of the garnet, clinopyroxene, and olivine xenocrysts are those expected for high-pressure equilibrium with the most evolved lava, BK-134 [14], suggesting that the xenocrysts might have been part of the source system. The ferroan, alkalic composition of BK-134 constrains the mineralogy of its source-rock to be essentially olivine- and orthopyroxene-free. The source rock was probably a metasomatized garnet clinopyroxenite. The isotopic data indicate that no appreciable assimilation of Archean crust could have occurred [11]. Thus, despite apparent excess heat, portions of the ascending magmas in the crust must have chilled against their conduits, rather than removing and assimilating ancient crust from them. This suggests that magmas rising rapidly from depth within the Moon could also have avoided significant assimilation at higher levels, consistent with conclusions of [15] for ascending magma. Some physical arrangement other than mere ascent through a KREEPy layer may be required if significant incorporation of KREEPy material occurred.

Acknowledgments. This work was supported in part by NASA grant NAG-9-56.

Figure 1

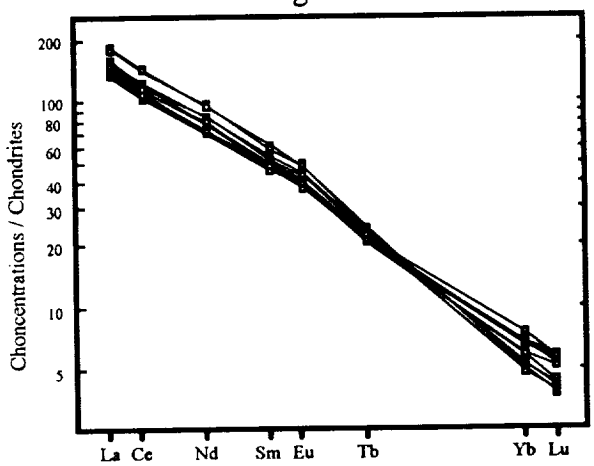

Figure 2

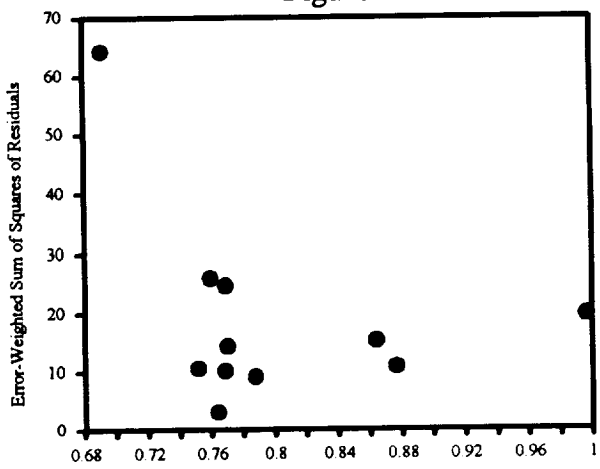

[1] Walker *et al.* (1975) *Geochim. Cosmochim. Acta* 39, 1219-1235 [2] Binder (1982) *Proc. Lunar Planet. Sci. Conf.* 13, A37-A53. [3] Hughes *et al.* (1989) *Proc. Lunar Planet. Sci. Conf.* 19, 175-188 [4] Neal and Taylor (1992) Apollo 17 Workshop, LPI [5] DePaulo (1981) *Earth Planet. Sci. Lett.* 53, 189-202. [6] Binder (1985) *Proc. Lunar Planet. Sci. Conf.* 16, D19-D30 [7] Shervais *et al.* (1985) *Proc. Lunar Planet. Sci. Conf.* 16, D3-D18 [8] *Proc. Lunar Planet. Sci. Conf.* 18, 139-153. [9] Neal & Taylor, (1990) *Proc. Lunar Planet. Sci. Conf.* 20, 101-108. [10] Rasskazov *et al.* (1990) Volc. Seis. 11, 337-353. [11] Luhr *et al.* (1992) EOS, Trans. Am. Geophys. Un. 72, 266. [12] Neal *et al.* (1989) *Proc. Lunar Planet. Sci. Conf.* 19, 147-161 [13] Paces et al. (1991) *Geochim. Cosmochim. Acta* 55, 2025-2043 [14] Kushiro *et al.* (1972) *Earth Planet. Sci. Lett.* 14, 19-25. [15] Irving (1980) *Am. J. Sci.* 280-A, 389-426.

MORPHOLOGY AND MODELS FOR THE EVOLUTION OF EASTERN HECATE CHASMA, VENUS, Victoria E. Hamilton, Department of Geology, Occidental College, Los Angeles, CA 90041; Ellen R. Stofan, Jet Propulsion Laboratory, California Institute of Technology, Pasadena, CA 91109.

Introduction: Hecate Chasma is a deep trough characterized by a chain-like concentration of coronae and corona-like features trending approximately southwest-northeast between approximately 200 and 260 degrees east longitude (terminating at Beta Regio). The section of Hecate in which we have concentrated our study is centered at 15N, 249, where the trough is especially well-defined. Nearby, a smaller chain of eight coronae lies along a minor trough parallel to the general trend of the greater chain. The trough itself is unusual in this area because it has a highly asymmetric profile. Using Magellan radar and topography data, we have examined the morphology of this area in order to assess the tectonic and volcanic history of the area. After examining the most important types of features (linear, arcuate and circular) in eastern Hecate, we present two possible models of origin. A companion abstract [1] presents an overview of the Hecate and Parga linear deformation zones.

Linear Features: Hecate Chasma is primarily characterized by linear features. For the most part, these features trend east-west and are generally located within 300 km of the main trough. Approximately 70% are typically characterized by long, straight, paired lineaments which are interpreted to be graben. The remaining lineaments generally trend east-west as well, but are usually more irregular and are interpreted to be wrinkle ridges. The graben are chiefly concentrated on the topographically lower southern side of the main trough and are associated with digitate flows extending to the north and south. It is difficult to distinguish the extreme variation in the topography of this area as the lineaments to not display any appreciable displacement or curvature consistent with the topography. The few ridges associated with the small chain follow topographic highs, as they are concentrated at the rims and outer rises of the coronae.

Arcuate Ridges: Broad arcuate ridges are visible around the large corona located at 16N, 252. These are 15 km across axis, and of probable compressional origin. These ridges are unusual in this area and require more in depth examination. More prominent are the slightly less arcuate ridges which typically define the coronae of the smaller eight-corona chain. These ridges maintain the generally east-west trend of the linear features, and may even run through the center of a corona and continue past to the next corona. While the arcuate ridges all partially define the rims of coronae, they only make up a small portion of the annulus and tend to extend beyond the corona.

Circular Features: Coronae are the dominant type of circular structure studied in this region, with average diameters of about 225 km, and circular to highly angular shapes. The 10-12 coronae in this area display morphologies typical of others on Venus, and are in a range of developmental stages [2-4].

EVOLUTION OF EASTERN HECATE CHASMA, VENUS, cont.,

However, only the 525 km diameter corona at 16N, 252 is bounded by the extremely asymmetric west-southwest to east-northeast trending main trough. To the west of this large corona, the north side of the chasm is considerably higher than the south side, but to the east of the corona, the higher topography is on the southern side of the trough. The relationship between the coronae and the linear features varies with location; the above described corona superposes nearby linear features while in the smaller chain, corona formation and compressional deformation overlapped in time.

Models of Formation: Based on the types and relationships between the features in this region, two possible models of evolution are assessed. A hotspot-type origin is not considered here as there is little evidence for a time progression of the features [1]. A model like that of Sandwell and Schubert [5] proposes limited retrograde subduction and/or delamination along the arcuate troughs around large coronae. One large corona does exist along the trace of the main trough, and it is ringed by many concentric fractures. The extreme asymmetry of the chasm is also very similar to profiles of terrestrial trenches [5]. Nonetheless, there is substantial evidence which opposes this model for this area. The evidence includes: the abundance of extensional features and the general lack of compressional features along a dominantly linear trough, and the lack of coronae along the trace of the main chasm which presents a problem for the initiation of subduction-like activity. In addition, in places, the deformation is not restricted to the trough. Lastly, this model cannot account for the radical switch in topography across the chasm as described above. The final model proposes an extensional rift system with coronae related to diapiric upwellings [3]. Some terrestrial rifts are known to have deep troughs with asymmetrical profiles due to uneven normal faulting. The switch in profile topography may be accounted for by a change in the pattern of normal faulting, also encountered terrestrially. At this time, we feel that the structural, volcanic and topographic characteristics are best explained by a rift zone and diapiric upwellings. This is consistent with the observed abundant graben, associated flows, and sequence of events in the eastern Hecate region. Future research will be directed at examining the rest of the Hecate and Parga regions, their relationship to each other, and comparisons to similar regions such as the Dali and Diana Chasmata.

REFERENCES [1] E.R. Stofan et al., LPSC XXIV, this volume.; [2] E.R. Stofan and J.W. Head, Icarus, 83, 216, 1990.; [3] E.R. Stofan et al., JGR, 97, 13, 347, 1992.; [4] S.W. Squyres et al., JGR, 97, 13, 611, 1992.; [5] D.T. Sandwell and G. Schubert, JGR, 97, 16,069, 1992.

A PLUTO THERMAL MODEL; C. J. Hansen[1] and D. A. Paige[2], ([1] Jet Propulsion Laboratory, [2] Dept. of Earth and Space Sciences, UCLA).

The recent discovery of nitrogen on Pluto [1] suggests that Pluto's volatile cycles may be similar to those on Neptune's moon Triton. Here, we report the first results of our efforts to apply a thermal model that we developed to study the seasonal nitrogen cycle on Triton[2] to the case of Pluto. The model predicts volatile behavior as a function of time to calculate frost deposit depth, polar cap boundaries, temperature of the frost and substrate, and atmospheric pressure, assuming nitrogen frost deposits in solid-vapor equilibrium with nitrogen in the atmosphere.

The thermal model is based on the Leighton and Murray diurnal and seasonal formulation for heat balance of the polar caps on Mars. This model solves the frost energy balance equation, incorporating solar insolation, thermal emission, heat conduction between layers in the substrate and between the substrate and the frost deposit, the heat capacity of the frost deposit, and the latent heat of condensation and sublimation. The primary input parameters are the albedo and emissivity of the frost, the albedo and thermal inertia of the substrate, and the total nitrogen inventory. Pluto and Triton's similar sizes, densities, and diurnal periods. These bodies also have similar insolation rates when Pluto is at Perihelion. Consequently, very few changes were required to transform our Triton model into a Pluto model.

On Triton we learned that the thermal inertia of the substrate plays an important role in the partitioning of volatiles between the polar cap deposits and the atmosphere, thus significantly affecting atmospheric pressure. As with Triton, assuming bright, dark, or transparent seasonal frost deposits on Pluto results in significant variations in the locations of seasonal and permanent polar caps. This sensitivity may be advantageous for clearing up ambiguities in the properties and behavior of polar caps on both bodies. One early Pluto conclusion is that although the nitrogen atmospheric pressure may vary by orders of magnitude over the course of a Pluto year, nitrogen is not likely to freeze out completely at any season.

The output of our thermal model calculations can be compared to a number of Pluto observations, including: maps of albedo features observed during a series of Pluto - Charon mutual events[4,3], atmospheric pressure measured from the stellar occultation[5] can be compared to predicted atmospheric pressure, and the disk-integrated albedo may be compared to long-term observations of the variability of Pluto's brightness as seen from the earth[6].

1. Owen et al, BAAS 24, No. 3, 961, 1992.
2. Hansen and Paige, Icarus 99, 273-288, 1992.
3. Buie, Tholen, and Horne, Icarus 7, 211, 1992.
4. Young and Binzel, Icarus in press, 1993.
5. Mills, Hubbart and Elliot, 1988.
6. Buie and Tholen, Icarus 79, 23-37, 1989.

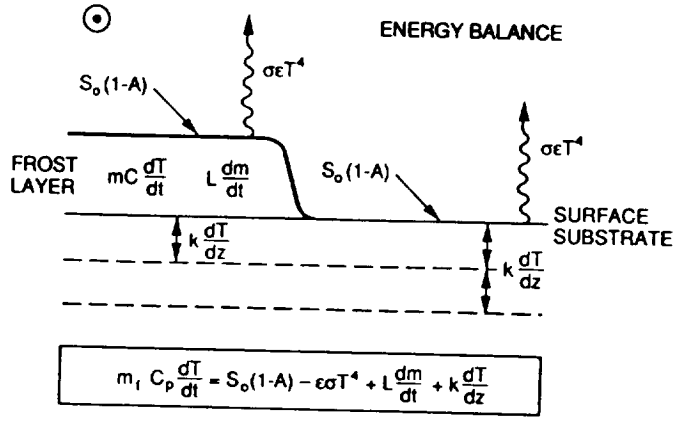

Fig. 1 This diagram illustrates the terms in the heat balance equation for seasonal N_2 frost and bare soil in the Pluto and Triton thermal models.

MODELING THE REFLECTANCE OF CO_2 FROST WITH NEW OPTICAL CONSTANTS: APPLICATION TO MARTIAN SOUTH POLAR CAP SPECTRA; Gary B. Hansen, Univ. of Wash./Jet Propulsion Lab 183-601, Pasadena, CA 91109; Terry Z. Martin, Jet Propulsion Lab 169-237, Pasadena, CA 91109

New measurements of the absorption coefficients of CO_2 ice, in most of the spectral range 0.2 to 3.9 μm where absorption coefficients are below 1.5 per cm, have recently been made [1]. Although these measurements are preliminary, they contain spectral detail not seen previously in the literature. Therefore, it is useful to combine these new data with older data from spectral regions of stronger absorption [2] and reformulate models of the albedo [3] or reflectance [4] of CO_2 frost. These models can then be adjusted in an attempt to match measurements of Martian polar deposits, such as the set of spectra returned by the IRS instrument on Mariner 7 (1969) [5,6].

The new absorption coefficients of CO_2 ice were measured on several samples of 41-mm thickness at 150-155 K. A portion of the spectrum from 1.9 to 3.9 μm wavelength is shown in Figure 1 in the form of imaginary coefficient of refraction (= linear absorption × wavelength / 4π). The data above about 3×10^{-5} are obtained from [2], except for the absorption line at 3.32 μm, which is extrapolated in a way that is consistent with laboratory frost measurements [7], but the peak level is still highly uncertain.

This new imaginary coefficient, combined with the real coefficient from [2], can be immediately applied to the models for hemispherical albedo used in [3], resulting in markedly different results from those in that study. The results for an infinite optical depth layer and solar incidence of 60° are plotted in Figure 2 for a range of mean particle radii from 0.03 to 3 mm.

Although this is an albedo model and not a bidirectional reflectance model, it can still be qualitatively compared to measured spectra of the Martian polar cap, such as the set of near- to middle-infrared spectra taken of the south polar cap in spring (L_S = 200°) by the IRS instrument on Mariner 7. The albedo model degraded to the resolution of the IRS is compared to two of these spectra in Figure 3. They are scaled to 1.0 at their maximum reflectance near 2.2 μm. The regions from 2.2 to 2.6 and from 3.0 to 3.9 μm are substantially free of atmospheric gas absorptions and can be compared directly. Note the coincidence of the characteristic absorption features of the ice at 2.28, 2.34, 3.00, 3.32, and 3.67 μm, and the albedo/reflectance maximum at 3.57 μm. (The wavelength calibration used for the IRS spectra is not yet accurate for the 2.2-2.6 μm region.)

Fig. 1: New CO_2 imaginary index of refraction

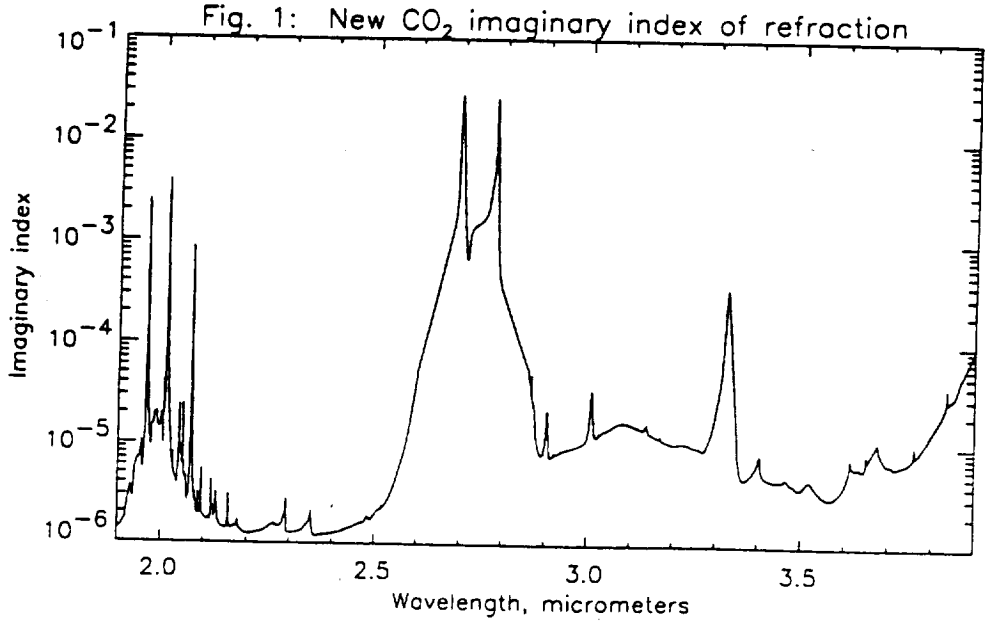

NEW MODEL REFLECTANCE OF CO_2 FROST: Hansen, G.B., and T.Z. Martin

Fig. 2: CO_2 frost albedo, infinite optical depth, 60° incidence

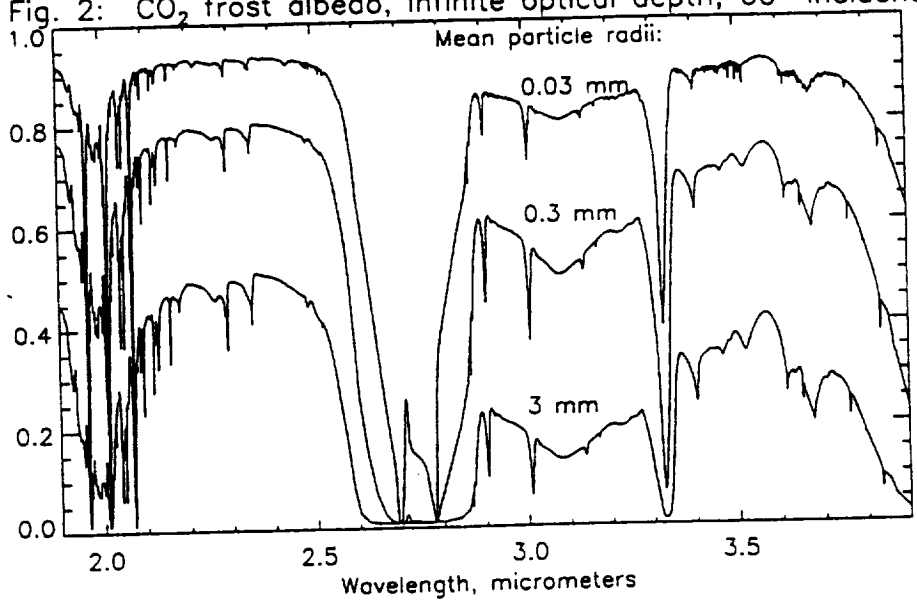

Fig. 3: Model albedo of CO_2 frost and two IRS spectra

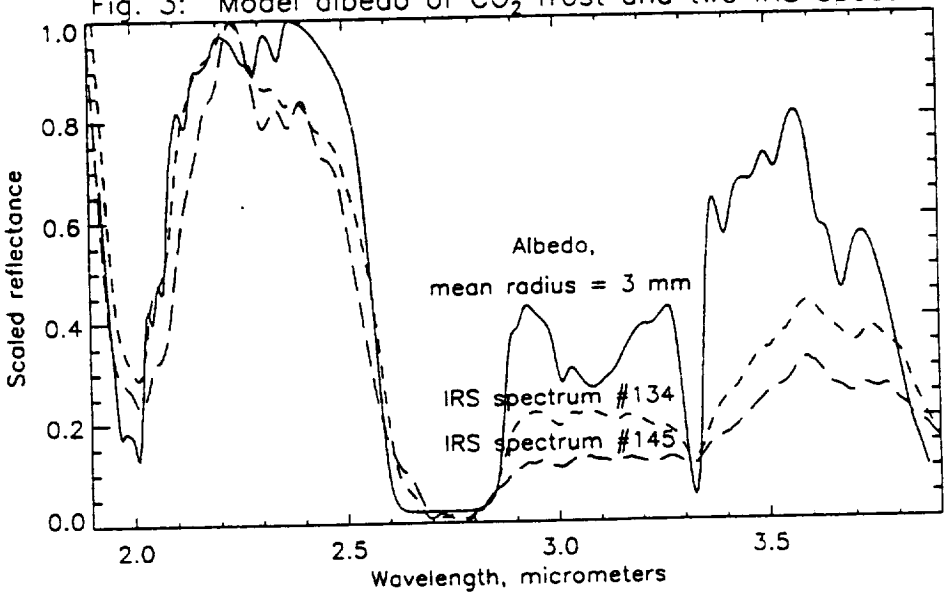

The use of a reflectance model as well as the addition of water ice and/or dust contamination will be addressed in an effort to better match the observed spectra in this data set. In particular, the maximum at 2.2 μm, the slope from 2.3-2.6 μm, and the depression and muting of features at wavelengths longer than 2.9 μm are characteristic of water ice contamination as illustrated in [3].

This is a cooperative project of the University of Washington, Seattle, WA, and the Jet Propulsion Laboratory, Pasadena, CA, and is supported partly by a grant from NASA and partly by the Caltech President's Fund.

REFERENCES: [1] Hansen, G.B. (1992), *BAAS*, **24**, 978. [2] Warren, S.G. (1986), *Appl. Opt.*, **25**, 2650. [3] Warren, S.G. et al. (1990), *JGR*, **95**, 14717. [4] Calvin, W.M. (1990), *JGR*, **95**, 14743. [5] Pimentel, G.C. et al. (1974), *JGR*, **79**, 1623. [6] Martin, T.Z. (1993), *JGR*, in press. [7] Fink, U. and G.T. Sill (1982), in *Comets*, L.L. Wilkening, ed., U. of Arizona Press, Tucson, 164.

ISHTAR DEFORMED BELTS: EVIDENCE FOR DEFORMATION FROM BELOW?; V.L. Hansen[1] and R.J. Phillips[2]; 1. Dept. of Geological Sciences, SMU, Dallas, TX 75275. 2. McDonnell Center for the Space Sciences and Dept. of Earth and Planetary Sciences, Washington University, St. Louis, MO 63130

The mountain belts of Ishtar Terra are unique on Venus. Models for their formation include mantle upwelling [1-2], mantle downwelling [3-4], and horizontal convergence [5-6]. The present forms of these models are too simple to predict surface strain, topography, or gravity. More detailed models will require specific constraints as imposed by geologic relations. In order to develop specific constraints for geodynamic models we examine the geology of Ishtar Terra as viewed in Magellan SAR imagery in an attempt to interpret regional surface strain patterns. In this paper we present geologic and structural relations that leads us to postulate that Ishtar deformed belts result from shear forces within the mantle acting on the lithosphere, and not by horizontal forces from colliding plates. We propose that the surface strains result from differential strain and displacement of domains within the upper mantle, and that further analysis of Ishtar deformation may allow us to identify individual domains within the mantle, and to constrain displacement trajectories between domains.

Introduction. Ishtar mountain belts, which surround Lakshmi Planum (4 km above mean planetary radius, MPR), are defined on the basis of deformation and topography (3.5-10 km MPR). Ishtar tessera terrains, which are also deformed, sit at lower elevations (1-4.5 km MPR) and lie outboard of the mountain belts. Fortuna tessera lies east of Maxwell Montes, Clotho tessera south of Danu, Atropos tessera west of Akna, and Iztpapalolt tessera lies north of western Freyja Montes. In the case of Maxwell and western Fortuna, Danu and Clotho, and Akna and eastern Atropos, the dominate structural trend of the mountain belt is mimicked by parallel structures in the adjacent tessera. In these cases the major difference between the mountain belt and neighboring tessera is topographic relief. Ridges, interpreted as contractional features [7-10], define each mountain belt and adjacent tessera. Extensional structures are preserved locally and indicate that gravity spreading accompanied crustal shortening [11].

Observations. In addition to high elevations, models for Ishtar deformed belts must explain numerous geologic and structural relations derived from Venera and Magellan imagery. 1. Lakshmi Planum is relatively free of deformation. 2. Each deformed belt is defined by a characteristic structural fabric that is developed across the width of the deformed belt; temporal relations across each belt are difficult to discern. 3. This structural fabric ends abruptly along strike without evidence of truncating faults; the termination typically corresponds with a change in slope (e.g. southern and northern Maxwell Montes). 4. The structural fabric is dominantly contractional in origin [7-14]. Limits of crustal strain can be estimated assuming ridges are continuous folds. Wavelengths of 6-10 km with amplitudes of 1, and 2 km (almost certainly a gross exaggeration), yield 2-5%, and 8-20% shortening, respectively. 5. Within Akna, and locally in Freyja and Maxwell, extensional fractures trend normal to the fold axes which define the ridges [e.g., 14]. Folds and fractures formed synchronously, and are consistent with shortening perpendicular to the ridge trends. This character of deformation is rheologically akin to that of viscous lava [14]. 6. Volcanism is present in most of the deformed belts, and occurred late in the deformation history. Lava fills structural valleys, yet local small-scale ridges that deform the valley fill parallel adjacent fold ridges, and are therefore indicative of local late-stage shortening that continued after flooding [10-11]. 7. Lava filled valleys cover 100's of thousands of square km (e.g. Akna and Atropos), yet few, if any, obvious vents or channels are identified. 8. In plan view the mountain belts and their tessera are short and squat, they each have length (measured parallel to the trend of dominant structural fabric) to width (measured normal to the trend of structural fabric) ratios < 2, with the exception of Danu Montes with length:width of 15 (Clotho tessera has length:width of 1.9) and Iztpapalotl tessera with length:width of 5. In comparison, terrestrial mountain belts typically have length:width values > 7, and values > 10 are common (e.g. the Appalachian and Andean belts). Terrestrial belts mark present or ancient plate boundaries.

Model. In modeling Ishtar deformation we follow premises outlined by Solomon et al. [13], the most pertinent of which are: 1. The elastic lithosphere is only a few tens of km thick due to high surface temperature [15]. 2. A 10-30 km thick crust has two elastic lithospheres, one in the upper crust, and one in the upper mantle [16-19]. 3. The weak lower crust can detach along a ductile decollement [20]. 4. Viscous mantle flow can induce horizontal stresses in the lithosphere and cause intense tectonic deformation [21]. 5. Lithosphere is limited in its ability to move horizontally due to a lack of a low-viscosity zone [21].

The very small aspect ratios of Ishtar deformed belts (they are, in fact, not true belts, but rather deformed domains) distinguishes them from their terrestrial counterparts, and holds a key to their formation. This, taken together with the relatively uniform distribution of strain over extremely large areas (300 to 1,000 km normal to structural trend), the lack of obvious temporal development of the structures, and modest values of shortening (2-20%) which can be accommodated by the structural fabric, argues for deformation from below, rather than horizontally across the deformed domains. If, as in the case of terrestrial mountain belts, deformation resulted from horizontal transmission of stress, the development of structures normal to strike should be time transgressive, should

exhibit differences in structural styles, such as foreland and hinterland deformation, and would not be distributed over a region 1,000 km normal to the structural trend. Therefore, the distribution of relatively uniform deformation that records modest strain over large regions with small aspect ratios suggests Ishtar deformation results from forces transmitted from below the crust, rather than from forces transmitted horizontally as in plane forces.

Furthermore, the observation that characteristic structural fabrics continues, in a direction normal to structural trend, from mountain belt to adjacent tessera, across changes in elevation of 2-6 km, indicates that these structures are not specifically related to topography. Similarly, the abrupt termination of structural fabric along strike with no obvious truncating faults, and the coincidence of this termination with topographic slopes suggests that mountain belt topography is defined by something other than the structural fabric. In addition, the modest shortening which can be accommodated by the ridges of Ishtar mountain belts and tessera terrains (<25%) is not sufficient to support the elevated topography of these regions. Each of these observations argues, therefore, that the structures themselves are not responsible for the elevation of the deformed belt. The simplest explanation then, is that the topography of the deformed belts results from below.

On a related point, the regionally distributed (passive) volcanism seems paradoxical to the high topography of the deformed belts if the deformed belts result from thickened crust [10-11].

We propose a model for Ishtar deformation in which the surface strain results from stresses below the crust rather than from horizontal forces of colliding plates. Basilevsky et al. [22] suggested that sub-lithospheric flow might be responsible for large regions of deformation given the lack of plate tectonic features interpretable from Venera images. Phillips [21,23] modeled viscous flow in the interior of Venus and illustrated flow can induce horizontal stresses capable of intense lithospheric deformation. Our model follows this original suggestion.

In the model, domains within the upper elastic mantle transmit stresses to the overlying crust, which deform in tablecloth fashion. The observations require that the crust be partly decoupled from the mantle such that it can deform, yet coupled to the elastic mantle such that shear strain acting on the elastic mantle (presumably in response to mantle convection) can be transmitted to the upper crust. The two layer crust deforms in parasitic structures over the elastic mantle; the upper, strong crust deforms in folds with local extensional fractures. The lower crust deforms in a ductile fashion, and provides a source of partial melt, which given the appropriate tectonic conditions (pressure release melting) could be leaked to the surface. Each structural and topographic domain within Ishtar Terra could be underlain by a discreet domain, or by transitions between domains, within the upper mantle. Differences in viscosity, thickness, and displacements define individual domains. For example, Lakshmi Planum may be underlain by a strong, immobile mantle, and the uncharacteristically large aspect ratio of Danu and Itzpapalotl might indicate their locations above domain boundaries. Danu would lie above a transition between Lakshmi upper mantle, and that of Clotho tessera. Itzpapalotl may lie above a broad transitional domain between plains mantle and strained mantle of Freyja Montes, and its apparent structural asymmetry [24] may record northeast translation of the plains block relative to the mantle domain which underlies Freyja.

In this model the evolution of Ishtar deformed belts is very different from that of terrestrial mountain belts, which result from horizontal forces of colliding plates. The closest terrestrial analog is that of the Tertiary Laramide orogeny that affected western North America from Montana to Texas, and Nevada to Colorado. Laramide deformation was due to extremely low angle subduction of the Farallon plate beneath North America, and resulted from stresses transmitted from below across the horizontal plate boundary [25-26].

In summary, we propose that Ishtar deformation results from stresses below the crust rather than from horizontal forces of colliding plates. Individual deformed belts within Ishtar Terra might be underlain by discreet domains within the upper mantle. Domains could be defined by changes in viscosity, thickness, and displacement rates and trajectories. Detailed structural and kinematic mapping of Ishtar deformation may allow us to identify individual domains, and to constrain spatial and temporal displacement trajectories between domains. Such results would place important constraints on geodynamic models.

References. [1] A.A Pronin (1986) Geotec. **20**, 271; [2] R.E. Grimm and R.J. Phillips (1991) GJR **96**, 8305; [3] D.L. Bindschadler and E.M. Parmentier (1990) JGR **95**, 21,329;[4] A.W. Lenardic et al., (1991) GRL **18**, 2209; [5] J.W. Head (1990) Geol. **18**, 99; [6] K.M. Roberts and J.W. Head (1990) GRL **17**, 1341; [7] D.B. Campbell, et al. (1983) Sci. **221**, 644; [8] V.L. Basukov, et al. (1986) JGR **91**, D378; [9] L.S. Crumpler, et al. (1986) Geol. **14**, 1031; [10] W.M. Kaula, et al. (1992) JGR **97**, 16,085; [11] S.E. Smrekar and S.C. Solomon (1992) JGR **97**, 16,120; [12] S.C. Solomon, et al. (1991) Sci. **252**, 297; [13] S.C. Solomon, et al. (1992) JGR **97**, 13199; [14] M. Keep and V.L. Hansen (1993) this volume; [15] S.C. Solomon and J.W. Head (1984) JGR **89**, 6,885; [16] R.E. Grimm and S.C. Solomon (1988) JGR **94**, 12,103; [17] W.B. Banerdt and M.P. Golombek (1988) JGR **93**, 4,759; [18] M.T. Zuber (1987) JGR **92**, E541.; [19] M. T. Zuber and E. M. Parmentier (1990) Icarus **85**, 290; [20] S. Smrekar and R.J. Phillips (1988) GRL **15**, 693; [21] R.J. Phillips (1986) GRL **13**, 1141; [22] A.T.A. Basilevsky, et al. (1986) JGR **91**, D399; [23] R.J. Phillips (1990) JGR **95**, 1301; [24] V.L. Hansen (1992) LPSC XXIII, 479; [25] P. Bird (1984) Tectonics **3**, 741; [26] P. Bird (1988) Sci. **210**, 1,501.

WHY IS THE MOON DARK?: B. Hapke, Univ. of Pittsburgh, Pittsburgh, PA 15260.

This paper reports the results of attempts to model the spectral properties of the lunar regolith as consisting of crystalline rocks, glass and submicroscopic metallic iron (SMFe), produced by a process involving vapor phase differentiation. The models differ in the location of the SMFe.

The lunar regolith differs from crystalline rocks and glasses of similar composition in having a lower albedo, redder continuum spectrum and more subdued absorption bands. Early melting experiments [1,2,3] seemed to indicate that these properties could be accounted for by simple vitrification. However, the oxygen fugacities in these experiments were below the Fe-wustite boundary, so that they do not simulate lunar impact vitrification. Glasses made at low fugacities have high albedos and strong absorption bands [4,5,6,7], so that some other component of the soil must be responsible for its optical properties.

It has been suggested [5,7] that SMFe is the cause of the low albedo of the moon, and that the SMFe is made by chemical differentiation accompanying the deposition of vapors within the regolith created by solar wind sputtering and impact vaporization. The rates at which vapor and melt glass are generated on the lunar surface are not significantly different, and most of this vapor is trapped in the soil, rather than escaping from the moon. Although the differentiation has been verified by laboratory experiments [5 6,7], it has not been widely accepted because of the apparent lack of vapor condensates in lunar soil. However, Keller and McKay [8,9] have detected vapor deposited coatings ~ 100 nm thick on soil particles. As predicted from laboratory simulations [5], these coatings are enriched in Si and Fe, much of the latter being SMFe, although whether they are present in sufficient amounts to cause the darkening is not yet clear.

I have attempted to determine whether the SMFe can indeed account for the lunar optical properties, as hypothesized. Several theoretical models were calculated in which the SMFe was assumed to be in different locations in the soil, including (1) bare SMFe on the surfaces of the grains, (2) SMFe-containing silicate coatings on all grains, (3) SMFe inside the glass particles only, and (4) SMFe distributed throughout the glass and also coating the crystalline grains. The models all had 50% crystalline rock, 50% vitrified rock and 0.5% SMFe. The best match to the actual soil spectrum was model 4, as shown in the figure.

Based on these results, it is proposed that on the luanr surface soil particles, consisting of both crystalline and vitrified material, become partially coated with vapor-deposited glass containing SMFe. Subsequent impacts partially fuse the coated particles together, forming agglutinates in which the SMFe is distributed throughout the particle. This process would be important on the moon and Mercury, but not in the asteroid belt.

[1] Conel J. and Nash D. (1970) *Proc. Apollo 11 Lun. Sci. Conf.*, 2013. [2] Adams J. and McCord T. (1971) *Proc. Lun. Sci. Conf.* 2nd, 2183. [3] Nash D. and Conel J. (1973) *Moon* **8**, 246. [4] Wells E. and Hapke B. (1977) *Science* **195**, 977. [5] Hapke B., Cassidy W. and Wells E (1975) *Moon* **13**, 339. [6] Cassidy W. and Hapke B. (1975) *Icarus* **25**, 371. [7] Hapke B. (1977) *Phys. Earth Planet. Int.* **15**, 264. [8] Keller L. and McKay D. (1992) *Proc. Lun. Planet. Sci. Conf 22nd*, pp. 137. [9] Keller L. and McKay D. (1992) *Lunar and Planetary Science XXVIII*, pp. 673.

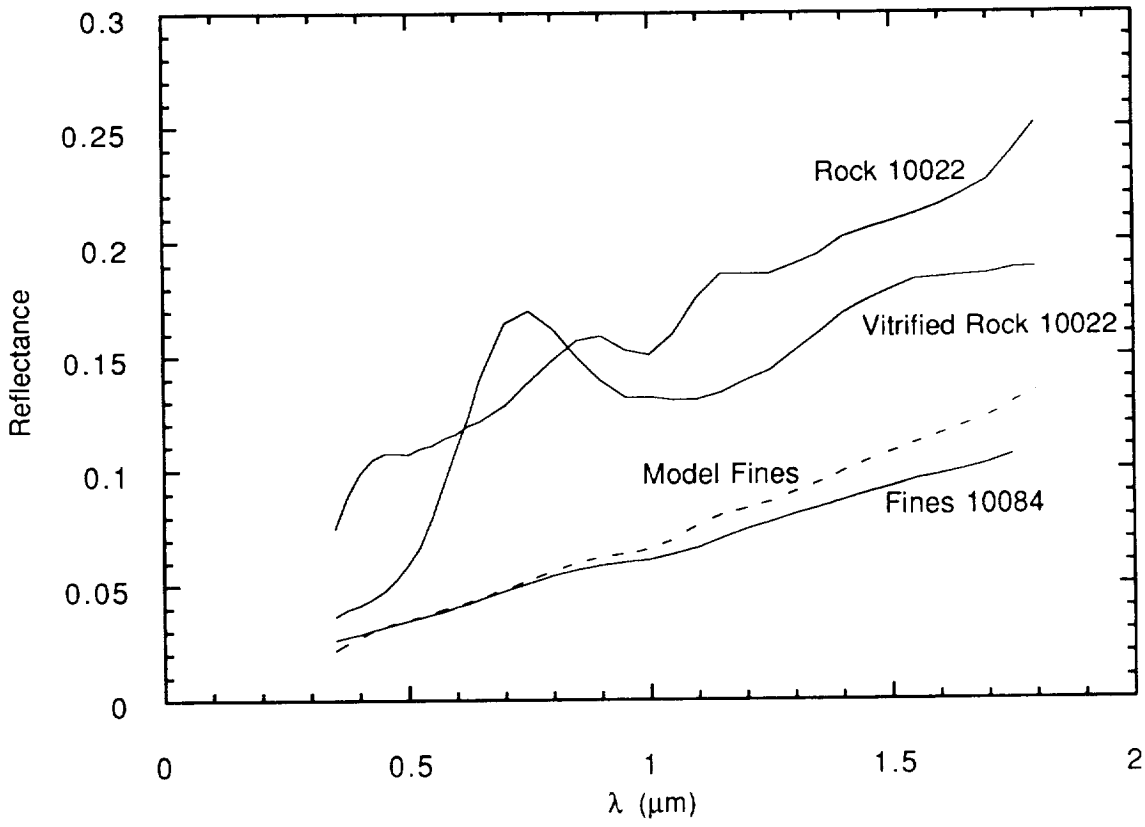

$^{142}Nd/^{144}Nd$ IN BULK PLANETARY RESERVOIRS, THE PROBLEM OF INCOMPLETE MIXING OF INTERSTELLAR COMPONENTS AND SIGNIFICANCE OF VERY HIGH PRECISION $^{145}Nd/^{144}Nd$ MEASUREMENTS

C. L. Harper Jr. & S. B. Jacobsen, Department of Earth and Planetary Sciences, Harvard University, 20 Oxford St., Cambridge, MA 02138 USA

Introduction: Apart from the challenge of very high precision $^{142}Nd/^{144}Nd$ ratio measurement, accurate applications of the coupled $^{146,147}Sm$-$^{142,143}Nd$ systematics [1] in planetary differentiation studies require very precise knowledge of the present-day (post-^{146}Sm decay) $^{142}Nd/^{144}Nd$ ratios of bulk planetary objects (BP). The coupled systematics yield model ages for the time of formation of Sm/Nd-fractionated reservoirs by differentiation of Sm/Nd-unfractionated bulk planetary reservoirs [1,2,3,4]. Estimates of $(^{142}Nd/^{144}Nd)_{BP}$ and $(^{143}Nd/^{144}Nd)_{BP}$ therefore provide the critical baseline relative to which these model ages are referenced. In the ^{147}Sm-^{143}Nd systematics, $^{143}Nd/^{144}Nd$ variations are mostly large (>200 ppm), and therefore small (*viz.*, <20 ppm) variations in initial $^{143}Nd/^{144}Nd$ ratios generally can be ignored. However, in the case of ^{146}Sm-^{142}Nd, the range of $^{142}Nd/^{144}Nd$ divergence for differentiated planetary reservoirs is much smaller (<~100 ppm). Consequently $^{146,147}Sm$-$^{142,143}Nd$ model ages are sensitive to small variations in bulk planetary $^{142}Nd/^{144}Nd$ (both present-day and initial). One major unanswered question is whether or not Nd shelf standards (CIT Ndβ/Ames metal, La Jolla, NASA-JSC/Ames metal) have $^{142}Nd/^{144}Nd$ identical to the bulk Earth or otherwise might record some degree of radiogenic evolution in an early-fractionated reservoir. Our discussions of early Earth differentiation based on $^{142}Nd/^{144}Nd$ in Isua and Acasta samples [1,5] have employed a working assumption: $(^{142}Nd/^{144}Nd)_{Nd\beta} = (^{142}Nd/^{144}Nd)_{Bulk\ Earth}$. This requires experimental justification and is apparently contradicted by chondrite $^{142}Nd/^{144}Nd$ measurements [3,4], which have been interpreted to indicate: $(^{142}Nd/^{144}Nd)_{JSC/Ames\ metal} = ((^{142}Nd/^{144}Nd)_{CHUR} + 35\pm8$ ppm) [4]. At present, interpretations of the early Earth and Moon hinge largely on this issue. Because Ba in bulk chondrite samples exhibits similar magnitude nuclear anomalies [6], attributable to incomplete mixing of interstellar components, a critical question is whether or not nuclear effects are also present in $^{142}Nd/^{144}Nd$, both in bulk chondrites and between planetary objects. In general, $^{142}Nd/^{144}Nd$ variations between bulk planetary reservoirs could result from four possibilities: (i) *ab initio* ("nuclear") variation of initial $^{142}Nd/^{144}Nd$; (ii) *ab initio* variation of $(^{146}Sm/^{144}Sm)_{BP}$; (iii) variation in $(Sm/Nd)_{BP}$; and (iv) radiogenic evolution of $^{142}Nd/^{144}Nd$ in an Sm/Nd-fractionated "parental" reservoir prior to formation of the Moon putatively by giant impact. The first two possibilities result from incomplete mixing of interstellar components and the third from cosmochemical fractionation of the rare earths. Possibility (ii) is an unlikely problem because isotopic variability on the planetary scale due to incomplete mixing is a small effect---apparently <100 ppm in the Ba-REE region. At this level, initial $^{146}Sm/^{144}Sm$ heterogeneity will not be significant, either as a chronometric bias (from error in the $^{146}Sm/^{144}Sm$ ratio) or via the post-decay shift in bulk planetary $^{142}Nd/^{144}Nd$. (A 100 ppm shift in initial $^{146}Sm/^{144}Sm$ amounts to only a 28 ppb shift in $^{142}Nd/^{144}Nd$). A larger nebular heterogeneity scale in $^{146}Sm/^{144}Sm$ would be expected if ^{146}Sm was synthesized "locally" by protosolar flare spallation, but the low abundances of ^{53}Mn and ^{92}Nb in the early solar system preclude more than ~2% local spallogenic production of the *ab initio* ^{146}Sm budget [7]. By an indirect argument, planetary-scale Sm/Nd variability (possibility iii) also appears not to be a significant problem. The degree of moderately volatile/refractory element fraction between the Earth, Moon, Mars, EPB, bulk solar system and EPB, can be gauged from inferred bulk Mn/Cr ratios [*cf.*, 8]. The bulk Earth and Moon exhibit the strongest inferred Mn/Cr fractionations---about equal to bulk Allende. High precision measurements of $^{147}Sm/^{144}Nd$ in large homogenized samples of Allende [9,10] differ from the "CHUR" average ($^{147}Sm/^{144}Nd = 0.1967$ [9]) only by a very small fractionation factor ($^{147}Sm/^{144}Nd = 0.1964$; $f_{Sm/Nd} = -0.0015$). Assuming Sm/Nd variation between bulk planetary reservoirs to be limited to the range $f_{Sm/Nd} = \pm0.0020$, bias relative to CHUR will be less than a total range of 46 ppm and 1.1 ppm in ε_{143Nd} and ε_{142Nd}, respectively---which is not significant. Discussions of (iv) are critically dependent on a satisfactory evaluation of (i) and determination of an appropriate $^{142}Nd/^{144}Nd$ bulk Earth value from Sm/Nd-unfractionated meteorites, adjusted for nuclear effects. Here we show that the problem of planetary-scale nuclear effects can be satisfactorily addressed by coupling high precision $^{142}Nd/^{144}Nd$ measurements with $^{145}Nd/^{144}Nd$ measurements using the decomposition of Nd into s- and r-process components obtained from SiC studies [11].

Nuclear Effects in Ba and Nd due to Incomplete Nebular Mixing: R-excess type anomalies in Ba, Nd and Sm isotopes are well-known from studies of the highly anomalous "FUN" inclusion EK1-4-1 [12]. More recently, similar effects at <50 ppm levels have been resolved in Ba in large bulk samples of Orgueil and Allende, and a strong hint of an anomaly at the ~8±6 (2σ) ppm level was observed in 4 high quality runs of the LEW 86010 angrite [6; Fig. 1]. The presence of isotopic anomalies in Ba in bulk chondrites and an achondrite indicates that similar effects are probably also present in Nd. Measurements of $^{142}Nd/^{144}Nd$ in Sm/Nd-unfractionated meteorites, therefore, probably do not provide an accurate measure of the CHUR/bulk Earth value without correction for nuclear differences relative to the bulk Earth. The data required for these corrections are: (a) a measure of nuclear effects in Nd and (b) the relative proportions of the r- and s-process contributions across the Nd masses. Modelling of r/s-type nuclear anomalies begins with a determination of the r-process excess parameters: $\eta_{r,i} = \varepsilon_i(N_{\Sigma\ r+s}/N_r)_i$, where ε_i is the

abundance anomaly in the nuclide i (due to an excess in its r-process component) and N refers to atom number proportions [13]. It can be seen that abundance anomalies are demagnified in proportion to the fraction of s-process component in any nuclide for a given r-process excess. For self consistency, $\eta_{r,i}$ should agree for all masses of the same element. (Excesses may agree between nuclides of different elements, but this is not necessarily the case.) In practice, anomalies are determined in normalized ratios which involve a cumulate of the effects at 3 or 4 masses. However for Ba, an s-only mass-136 index and $^{134}Ba/^{136}Ba$ normalization can be utilized, and the magnitudes of the r-excesses are then obtained simply from the $^{135}Ba/^{136}Ba$ and $^{137}Ba/^{136}Ba$ ratio anomalies multiplied by $(N_{\Sigma\, r+s}/N_r)_i$ for masses 135 and 137. From the Mainz Murchison SiC s-process decomposition [11], we obtain multipliers of 1.2 and 2.0 for masses 135 and 137, respectively. The product of these and the measured anomalies yield self consistent r-excesses of 48±~10 ppm and 44±~14 ppm for the Allende $^{135}Ba/^{136}Ba$ and $^{137}Ba/^{136}Ba$ anomalies, and 28±~8 ppm and 32±~11 ppm for Orgueil (Fig. 1). An r-excess of 10±8 ppm is inferred from the LEW 80610 $^{135}Ba/^{136}Ba$ data. Figures 2a and 2b show the expected anomaly patterns in $^{i}Nd/^{144}Nd$ for r-excesses of 10, 20 and 30 ppm, normalized to $^{146}Nd/^{144}Nd$ and $^{148}Nd/^{144}Nd$, respectively, using the Mainz Nd decomposition: $\{(N_{\Sigma\, r+s}/N_r)_i$: (142, 143, 144, 145, 146, 148, 150) = (1.00/0.00, 1.44±0.01, 2.15±0.09, 1.33±0.01, 2.21±0.03, 1.07±0.01, 1.00)$\}$ [11]. It can be seen that the signs of the $^{142}Nd/^{144}Nd$ anomalies are negative for both normalizations and that their magnitudes are reduced by factors of 2.2 and 4.5, respectively, w.r.t. the r-excess. The -35±8 ppm deviation in $^{142}Nd/^{144}Nd$ relative to the NASA standard (identical to Ndβ) reported by [4] for bulk chondrites corresponds to excesses of 77 ppm relative to $^{146}Nd/^{144}Nd$ and 1.6 ε-units relative to $^{148}Nd/^{144}Nd$.

Monitoring Nuclear Effects with Very High Precision $^{145}Nd/^{144}Nd$ Measurements: Figure 2 also shows that r-excesses in the 10-30 ppm range produce small anomalies of 3-9 ppm in $^{145}Nd/^{144}Nd$. If these small effects can be resolved, appropriate corrections can be applied to $^{142}Nd/^{144}Nd$. Larger effects will be present in $^{148}Nd/^{144}Nd$ and $^{150}Nd/^{144}Nd$ for the $^{146}Nd/^{144}Nd$ normalization, but these ratios are difficult to measure to high precision. Figure 3 shows reproducibility for 17 dynamic mode $^{145}Nd/^{144}Nd$ measurements of Ndβ (7) and terrestrial samples (10), exponentially normalized to $^{146}Nd/^{144}Nd = 0.724134$. $2\sigma_p$ of these data is ±3.9 ppm ($2\sigma_m$ = ±0.95 ppm, about a mean value of $^{145}Nd/^{144}Nd = 0.34894096$), demonstrating a capability for resolving shifts in $^{145}Nd/^{144}Nd$ down to 2 ppm, 2σ, with quadruplicate measurements. This corresponds to a ±3 ppm control on r *vs.* s polarization-type anomalies in $^{146}Nd/^{144}Nd$-normalized $^{142}Nd/^{144}Nd$ ratios due to incomplete nebular mixing. Applications of this method to chondrites, eucrites, lunar rocks and SNC meteorites will provide strong constraints on the bulk planetary $^{142}Nd/^{144}Nd$ values and contribute significantly towards understanding early planetary differentiation processes.

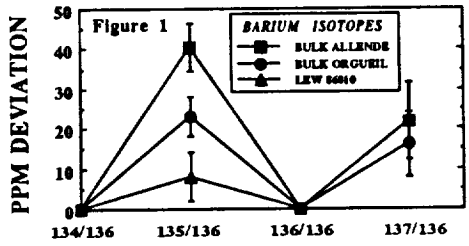

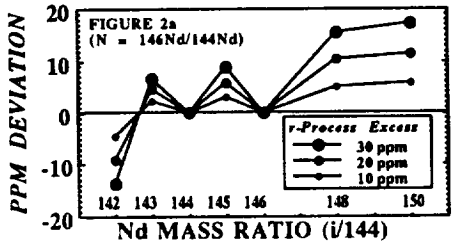

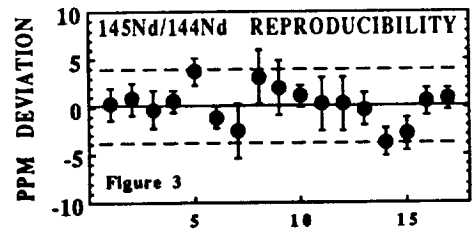

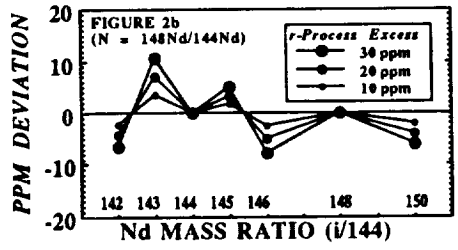

REFERENCES: [1] Harper C. L. Jr. and Jacobsen S. B. (1992). *LPS XXIII*, 487; --- (1992). *Nature*, 360: 728; [2] Nyquist L. E., Harper C. L., Wiesmann H., Bansal B. and Shih C.-Y. (1991). *Meteoritics*, 26: 381; [3] Harper C. L. Jr., Nyquist L. E., Bansal B., Wiesmann H. and Shih C.-Y. (submitted to *Science*); [4] Nyquist L. E., Bansal B., Wiesmann H., Shih C.-Y. and Harper C. L. Jr. (submitted to *GCA*); [5] Harper C. L. Jr. and Jacobsen S. B. (1992). *EOS*, 73: 622; Jacobsen S. B. and Harper C. L. Jr. (1992). *EOS*, 73: 622; [6] Harper C. L., Wiesmann H. and Nyquist L. E. (1991). *Meteoritics*, 26: 341; --- (1992). *Meteoritics*, 27: 230; [7] Harper C. L. *et al.* (1991). *LPS XXII:* 519; [8] Harper C. L. and Wiesmann H. (1992). *LPS XXIII*, 489; [9] Jacobsen S. B and Wasserburg G. J. (1980). *EPSL*, 50: 139; --- (1984). *EPSL*, 67: 137; [10] Nakamura N. and Masuda A. (1987). *Smithson. Contrib. Earth Sci.*, 27: 38; [11] Richter S., Ott U. and Begemann F. (1992). *LPS XXIII*, 1147; Ott U., Richter S. and Begemann F. (preprint, Hubert Reeves Festschrift Meeting, Paris 1992); [12] McCulloch M. T. and Wasserburg G. J. (1978). *Ap. J.*, 220: L15; Lugmair G. W. (1978). *USGS Open File Rpt.* 78-701: 262; [13] Mathews G. J. and Fowler W. A. (1981). *Ap. J.*, 251: L45.

THE PHYSICAL MECHANISM OF COMET OUTBURSTS: AN EXPERIMENT; William K. Hartmann, Planetary Science Institute, Tucson AZ 95719

During a series of impact experiments into regolith-like powders at the NASA Ames Research Center Vertical Gun Facility in 1976, I observed and filmed a unique anomalous even that may illuminate outburst mechanisms in comets.

During one test, a new batch of basalt powder (half the mass in particles less than 800 μm in diameter) retained some air pressure while the vacuum chamber was being evacuated. As a result, the projectile impacted into gas-charged regolith. Instead of ejecting the normal , relatively negligible amount of debris, the disturbance triggered a major eruption that lasted for at least 17 seconds. The experimental results have been recently re-analyzed with reference to cometary phenomena.

Figure 1 shows a series of frames from this eruption experiment. The ejecta velocities of 150 to 300 cm/s would have been sufficient to drive debris into the coma of a comet nucleus smaller than a few kilometers diameter.

The event suggests a mechanism for comet outbursts, discussed briefly by Hartmann *et al.* [1]: The pore space in a layer of regolith, possibly with weak effective tensile strength, becomes gas charged as ice slowly sublimates. Once the effective tensile strength is exceeded by the gas pressure, the surface fails locally, triggering an eruption such as photographed here.

This model is consistent with the emerging view of regolith materials on comets [2, 3, 4], and is closest to the recent model of Rickman *et al.* [5]. The earlier models generally picture a more uniform flow of debris off the comet, not outbursts. Rickman *et al.* allow gas pressure to build until it matches the overburden pressure, followed by "instantaneous blow-off." They note that "...as soon as the mantle is found to be unstable, we consider it to be instantaneously swept away by the gas pressure."

The main new points made here are that the experiment gives a more realistic view of the blow-off process after surface failure occurs, and the present model gives a recharge mechanism that can explain recurrent outbursts on comets such as P/Schwassmann-Wachmann 1 and 2060 Chiron. In fact, the resulting jets resemble distinct jet structures in high-resolution comet comae, as seen in Figure 2.

These results are described in more detail in a paper submitted to *Icarus*. The work was supported by the NASA Planetary Astronomy and Planetary Geology and Geophysics programs.

References: [1] Hartmann, W.K., Cruikshank, D., and Degewji, J. (1982) *Icarus* 52, 377; [2] Brin, G.D. and Mendis, D.A. (1979) *Astrophys. Journ.* 229, 402; [3] Brin, G.D. (1980) *Astrophys. Journ.* 237, 265; [4] Fanale, F. and Salvail, J.R. (1984) *Icarus* 60, 476; [5] Rickman, H., Fernandez, J., and Gustafson, B. (1990) *Astron. Astrophys.* 237, 524.

COMET OUTBURST MECHANISM: Hartmann, W.K.

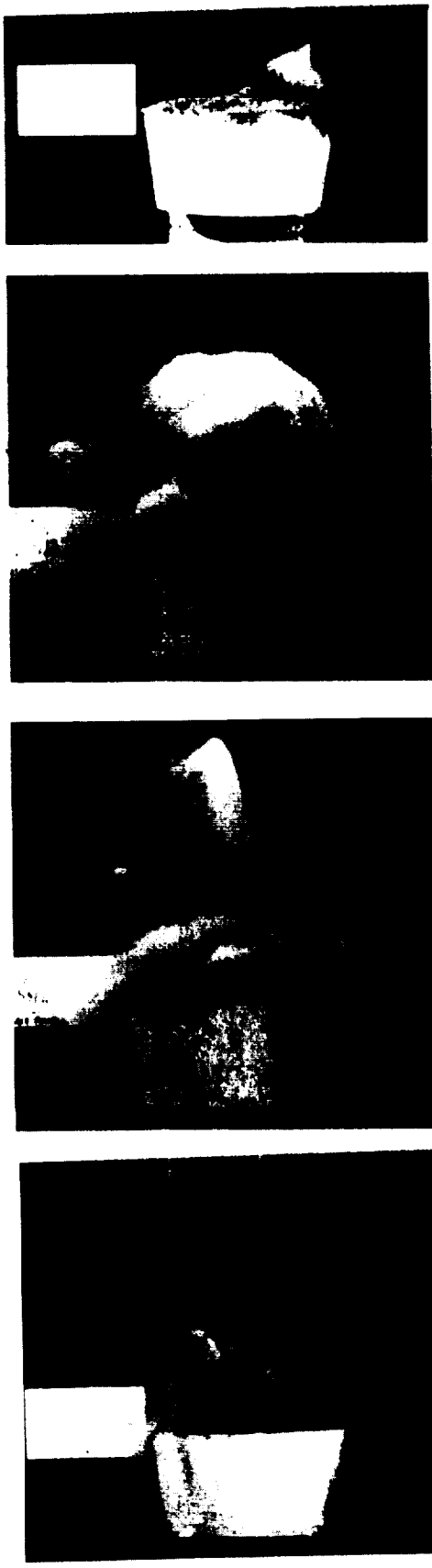

Figure 1 (left). Four frames from the film of the experimental eruption of gas-charged regolith powder *in vacuo*. Frame times are .07, .66, 1.32, and 3.32 seconds after impact. First frame shows jet of gas-driven debris (white) just emerging from impact site (impacts without gas jetting produced ejecta spray clouds of about this size). Last three frames show different states of continuing surges of gas-driven debris.

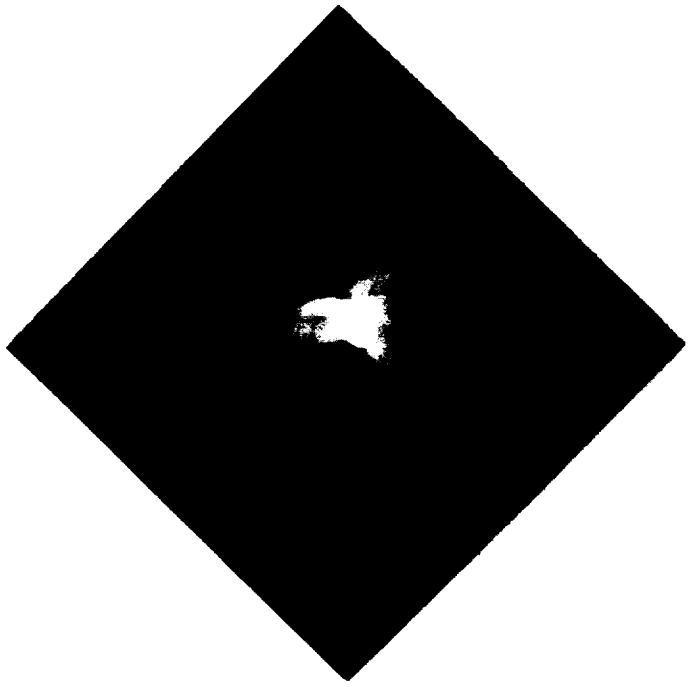

Figure 2 (above). Contrast enhanced view of Comet Halley, showing distinct jet structure in nucleus reminiscent of distinct jets generated by eruptive event in gas-charged regolith (Figure 1). (1986 March 15 image by Tapia and Senay, Boyden Observatory, processing by S. M. Larson; courtesy S.M. Larson, University of Arizona).

CONFIRMATION OF SATURATION EQUILIBRIUM CONDITIONS IN CRATER POPULATIONS; William K. Hartmann, PSI, Tucson AZ 85719, Robert W. Gaskell, JPL, Cal Tech, Pasadena CA 091009

We have continued work on realistic numerical models of cratered surfaces, as first reported at last year's LPSC. We confirm the saturation equilibrium level with a new, independent test.

One of us (RWG) has developed a realistic computer simulation of a cratered surface. The model starts with a smooth surface or fractal topography, and adds primary craters according to the cumulative (or log-incremental) power law with exponent -1.83, as observed on lunar maria and martian plains. Each crater has an ejecta blanket with the volume of the crater, feathering out to a distance of 4 crater radii.

We use the model to test the levels of saturation equilibrium reached in naturally occurring systems, by increasing crater density and observing its dependence on various parameters. In particular we have tested to see if these artificial systems reach the level found by Hartmann [1] on heavily cratered planetary surfaces, hypothesized to be the natural saturation equilibrium level. (On the plot of relative crater densities, Figure 1, this is the horizontal line referred to as $N/N_{HC} = 1$.)

Last year we reported that when we allowed input crater densities to rise to nearly 10 times that level, the observed numbers of craters stabilizes near the level $N/N_{HC} = 1$, supporting the hypothesis that this is the saturation level [2, 3].

These tests are important because the Voyager team predicated its interpretation of all outer planet satellites on the assumption that saturation equilibrium has never been achieved, and thus that all impacts that ever occurred are recorded in the crater diameter distribution. This appears to be incorrect, in which case the interpretations change significantly [2].

This year's work gives the first results of a crater population that includes secondaries. Our model "Gaskell-4" (September, 1992) includes primaries as described above, but also includes a secondary population, defined by exponent -4. We allowed the largest secondary from each primary to be 0.10 times the size of the primary. These parameters will be changed to test their effects in future models (being run as this abstract is written).

The model gives realistic images of a cratered surface (Figure 1), although it appears richer in secondaries than real surfaces are. The effect of running the model toward saturation gives interesting results for the diameter distribution. Our most heavily cratered surface had the input number of primary craters reach about 0.65 times the hypothesized saturation equilibrium, but the input number rises to more than 100 times that level for secondaries below 1.4 km in size, i.e., $N/N_{HC} > 100$ (Figure 2).

In spite of the extremely high input crater densities among the secondaries, the observed crater densities cluster in the region $N/N_{HC} = 0.4$ to 2, the same range observed in the most heavily cratered terrains in the solar system. Among the primaries, the observed crater density averages about half the input density, implying that saturation is beginning, partly due to obliteration and suppression of large craters by the large numbers of small secondaries.

SATURATION OF CRATER MODELING, Hartmann, W.K. & Gaskell, R.W.

In conclusion, even with a very steep power law representing secondaries, it is hard to drive the observed size distribution more than a few times higher than $N/N_{HC} = 1$. This tends to confirm the earlier conclusions that natural saturation equilibrium sets in near $N/N_{HC} = 1$. The natural populations may show some structure above and below that line.

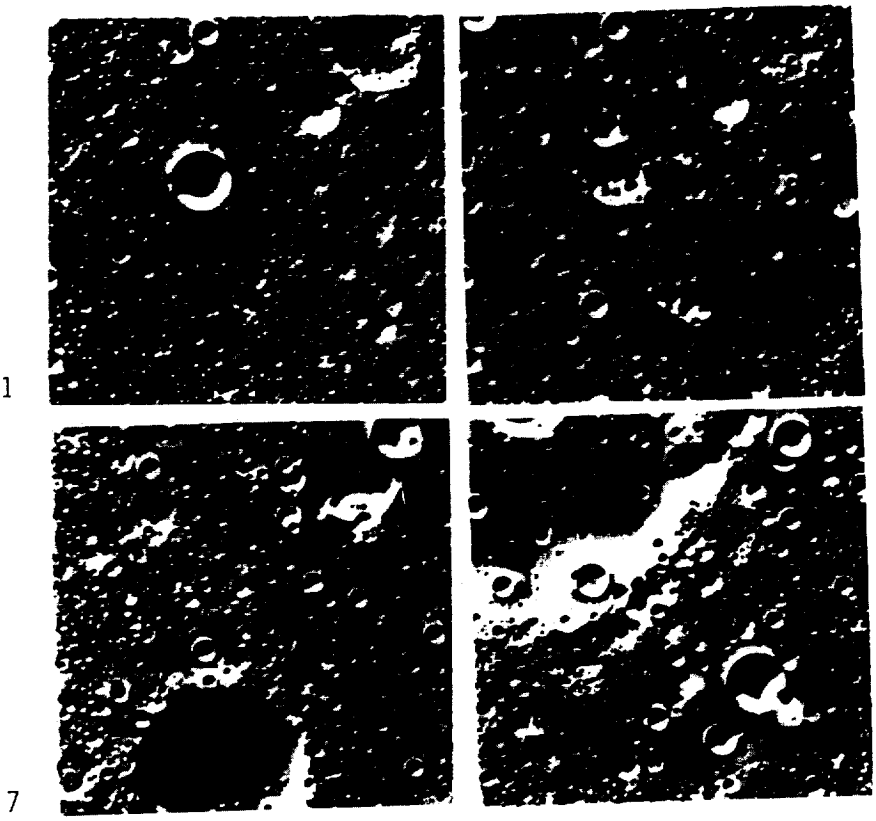

Figure 1. Artificial cratered terrain created by Gaskell program, planet "Gaskell-04." Images are 522x522 km. They show 1st, 3rd, 7th and 9th stages of cratering in a 9-stage sequence.

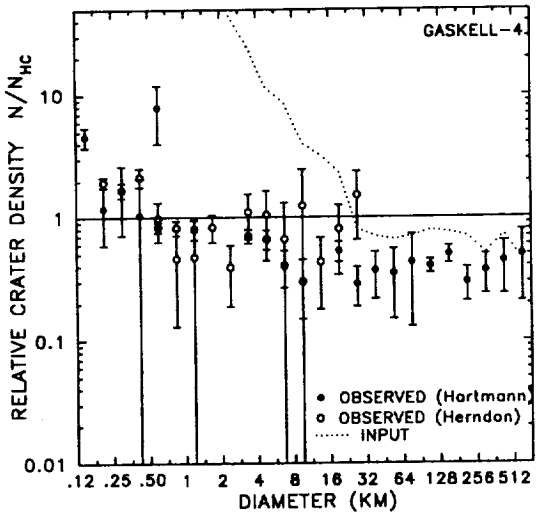

Figure 2. Relative diameter distribution observed on Gaskell-4" surface. Points with error bars are observed. Dotted line gives input number density of craters.

REFERENCES

[1] Hartmann, W.K. 1984. *Icarus* **60,** 56-74.
[2] Hartmann, W.K. 1992. *LPSC XXIII Abstracts.*
[3] Hartmann, W.K., and Gaskell, R.W. 1992. *LPSC XXIII Abstracts.*

CORVID METEOROIDS AND A GIORDANO BRUNO RAY ARE GENETICALLY RELATED. Jack B. Hartung.
9108 Potomac Ridge Road, Great Falls, Virginia 22066, U.S.A.

Summary

Both Corvid meteoroids and the Giordano Bruno (GB) crater are products of recent events. On June 25, or 26, 1178, Corvid meteoroids and a portion of GB ejecta were at the same place in the Solar System and moved in the same direction (right ascension = 12° and declination = $+19^{\circ}$). The ground track of this direction is the same as that of the most prominant GB ray (azimuth = 237°). These "coincidences" could not have occurred by chance and, therefore, support the conclusions that the GB impact occurred on June 26, 1178, and that Corvid meteoroids are high-velocity ejecta fragments from that impact. Finally, those fragments ejected with somewhat lower velocities failed to escape from the Earth-Moon system and produced the prominant ray extending southwest from the GB crater.

Abstract

Between June 25 and July 2, 1937, a Corvid meteor shower was observed (1). The apparent lack of Corvid showers in other years suggests that Corvids are the product of a recent break-up event. The right ascension and declination, corrected for zenith attraction, of 192° and -19° were reported for the radiant of this shower (2). This corresponds to a right ascension and declination of the direction of motion of Corvid meteoroids of 12° and $+19^{\circ}$. In ecliptic coordinates the celestial longitude and latitude of this direction are 18° and $+13^{\circ}$.

In the medieval chronicles of Gervase of Canterbury for June 25 (26), 1178, it is reported that "...there was a bright new moon...and suddenly the upper horn split in two. From the midpoint of this division a flaming torch sprang up, spewing out, over a considerable distance, fire, hot coals, and sparks" (3). This report is interpreted as an eyewitness account of events surrounding the formation of the 20-km-diameter crater, GB (4). In selenographic coordinates the location of GB is given by a lunar longitude and latitude of 103° E and 36° N. On June 25 (26), 1178, the ecliptic longitude of the Sun was 93° (94°) (5), the phase of the Moon was $19^{\circ}.5$ (32°) past new moon, and the geometric libration of the Moon in longitude was $1^{\circ}.5$ ($1^{\circ}.5$). It follows that the ecliptic longitude of the lunar prime meridian was 294° (306°), and the ecliptic longitude of the zenith direction at the GB impact site was 37° (49°). The corresponding latitude was approximately $+36^{\circ}$ ($+36^{\circ}$). The resulting elevation angle of the direction of Corvid motion above the local horizontal plane at the GB impact site was 61° (54°). The values given in parentheses correspond to conditions that prevailed exactly one day after June 25, 1178.

Experimental results show that for ejection velocities near the lunar escape velocity, 2.7 km/sec, the ejection elevation angle ranges up to about 60° (6,7). Therefore, the observed direction of Corvid motion and the direction of motion expected independently for some GB ejecta are essentially the same. In addition, the

selenographic azimuth of this direction, with the origin of the coordinate system at the GB crater, is 221° (238°). The azimuth of the most prominant, 1000-km-long, ray emanating from the GB crater is 237° (8).

It has been argued recently that on June 25, 1178, the Moon was not visible from the Earth because just after sunset it would have been too near both the Sun and the local horizon (9,10). However, one day later, not only would the crescent Moon have been visible, but the resulting ejection elevation angle would be lower (more in line with expectation), and the ejection azimuth would be essentially the same as that of the most prominant GB ray. This agreement lends support to the idea that June 26, 1178, is more likely the actual date of the GB impact.

Conclusions

1. The GB impact crater was formed on June 26, 1178.
2. Corvid meteoroids are high-velocity (>2.7 km/sec) members of the GB (azimuth = 237°) ejecta family.
3. The GB ray at an azimuth of 237° was formed by lower-velocity (<2.4 km/sec) members of the same ejecta family.

References

1. Hoffmeister C. (1948) Meteorstrome. Johann Ambrosius Barth, Leipzig.
2. Cook A.F. (1973) in Evolutionary and Physical Properties of Meteoroids, NASA SP 319, 183-191.
3. Stubbs W., ed. (1879) The Historical Works of Gervase of Canterbury, Vol. I, Her Majesty's Stationery Office, London. (Reprinted by Kraus Reprint Ltd., 1965.)
4. Hartung J.B. (1976) Meteoritics, 11, 187-194.
5. Tuckerman B. (1964) Planetary, Lunar, and Solar Positions A.D. 2 to A.D. 1649. The Am. Philosoph. Soc., Philadelphia.
6. Gault D.E. and Heitowit E. D. (1963) Proc. 6th Hypervelocity Symp., 2, 419. Firestone Rubber Co., Cleveland, Ohio.
7. Fechtig H., Grun E. and Kissel J. (1978) in Cosmic Dust, J.A.M. McDonnell, ed. 607-669. John Wiley & Sons.
8. Rand McNally 12-inch lunar globe.
9. Meeus J. (1990) J. Br. Astron. Assoc., 100, 2, 59.
10. Schaefer B. E. (1990) J. Br. Astron. Assoc., 100, 5, 211.

PYROXENE EQUILIBRATION TEMPERATURES IN METAMORPHOSED ORDINARY CHONDRITES. R.P. Harvey, M. L. Bennett, and H.Y. McSween Jr. Department of Geological Sciences, University of Tennessee, Knoxville, TN 37996-1410.

Ordinary chondrites are divided into petrographic types based on observed mineralogical and textural properties consistent with progressive thermal metamorphism from low grade (type 3) to high (type 7). Regardless of the exact cause of the metamorphism, higher-type chondrites should retain information concerning peak temperatures reached and for what duration. Using the two-pyroxene geothermometer of Lindsley [1], we have calculated the equilibration temperatures for 26 H, L and LL type 5 and 6 ordinary chondrites, to investigate the relative peak temperatures and equilibration-states reached by these various meteorite classes.

The Lindsley thermometer relies on a detailed accounting of non-quadrilateral components in pyroxenes, whose recalculated compositions are then plotted onto an empirically-derived polythermal diagram from which temperatures can be interpolated. The reported uncertainty of this method is ± 50°C; in addition, close spacing of isotherms on the graph (particularly for orthopyroxene compositions) increase this uncertainty. We have parameterized the Lindsley polythermal quadrilateral for 1 atm pressure (< 2 bar), and interpreted recalculated coordinates directly in terms of 25°C temperature intervals. Meteorites selected for this study include both relatively shocked and unshocked specimens; heavily weathered or visibly brecciated specimens were avoided. Temperatures were calculated from orthopyroxene (opx) and clinopyroxene (cpx) analyses within one relative percent of ideal sums and stoichiometry.

Histograms summarizing the calculated temperatures for type 5 and 6 ordinary chondrites are shown in Fig. 1. The uncertainty mentioned above corresponds roughly to one 25°C-wide bin in either direction. Temperatures indicated to be >1200°C, corresponding to chondrule crystallization temperatures rather than metamorphism, were not included in the summary statistics. Antarctic and non-Antarctic H chondrites were treated as separate groups to investigate the possibility that they have had different thermal histories. Cpx temperatures for all classes of type 6 ordinary chondrites show a mean temperature of 919°C (Fisher, an L6 showing anomalously low cpx temperatures, was not included in the cpx statistics). Similarly, opx in type 6 show a mean of 799°C. Cpx shows temperatures consistently higher than opx, as noted by [2]. Type 5 ordinary chondrites show a mean temperature of 946°C for cpx and 786°C for opx. The cpx temperature distributions all show a spread of values around a central peak; in addition, these peaks occur within 1 σ of each other and thus are consistent with equilibration to a single temperature for both type 5 and 6 near 925°C. Opx temperature distributions show a similar relationship at lower temperatures. Our temperatures are consistently higher than those previously reported for cpx in L6, LL6 and H6 meteorites by [3]. No significant difference between the Antarctic and non-Antarctic groups was noted.

Chondrule crystallization temperatures for pyroxenes are generally quite high; cpx in type 3 ordinary chondrites rarely give temperatures below 1200°C. Therefore the temperatures given by pyroxenes represent attempts to equilibrate downward to lower temperatures. The resulting temperature distribution reflects the rapidity of cooling and the duration of exposure to peak temperatures. The type 6 temperature distributions have lower σ's and are more symmetrical than those shown by type 5, suggesting that type 6's experienced a longer time at peak temperature and less time at lower temperatures; i.e., faster cooling. Similarly, the higher σ shown by type 5 ordinary chondrites may represent the same peak temperature, but with less time spent at the peak and more gradual cooling, allowing equilibration to lower temperatures. This apparent relationship between petrographic type and cooling rate (higher petrographic types experiencing faster cooling) is contrary to that predicted by standard onion-shell models for ordinary chondrite parent bodies. Type 6 meteorites also do not appear to have reached a higher temperature than type 5, as predicted by onion-shell models. The concordance of the peak temperature across compositionally distinct classes suggests that metamorphism affected all types of parent bodies to the same level. Future expansion of our database, studies of equilibration in opx and cpx, and application of independent thermometers and cooling rate speedometers will all have a strong bearing on these hypotheses.

References: [1] D.H. Lindsley (1983) *Am.. Mineralogist* **68**, 477-493. [2] H.Y McSween, Jr. and A.D. Patchen (1989) *Meteoritics* **24**, 219-226. [3] E.J. Olsen and T.E. Bunch (1984) *Geochim.. Cosmochim. Acta* **48**, 1363-1365.

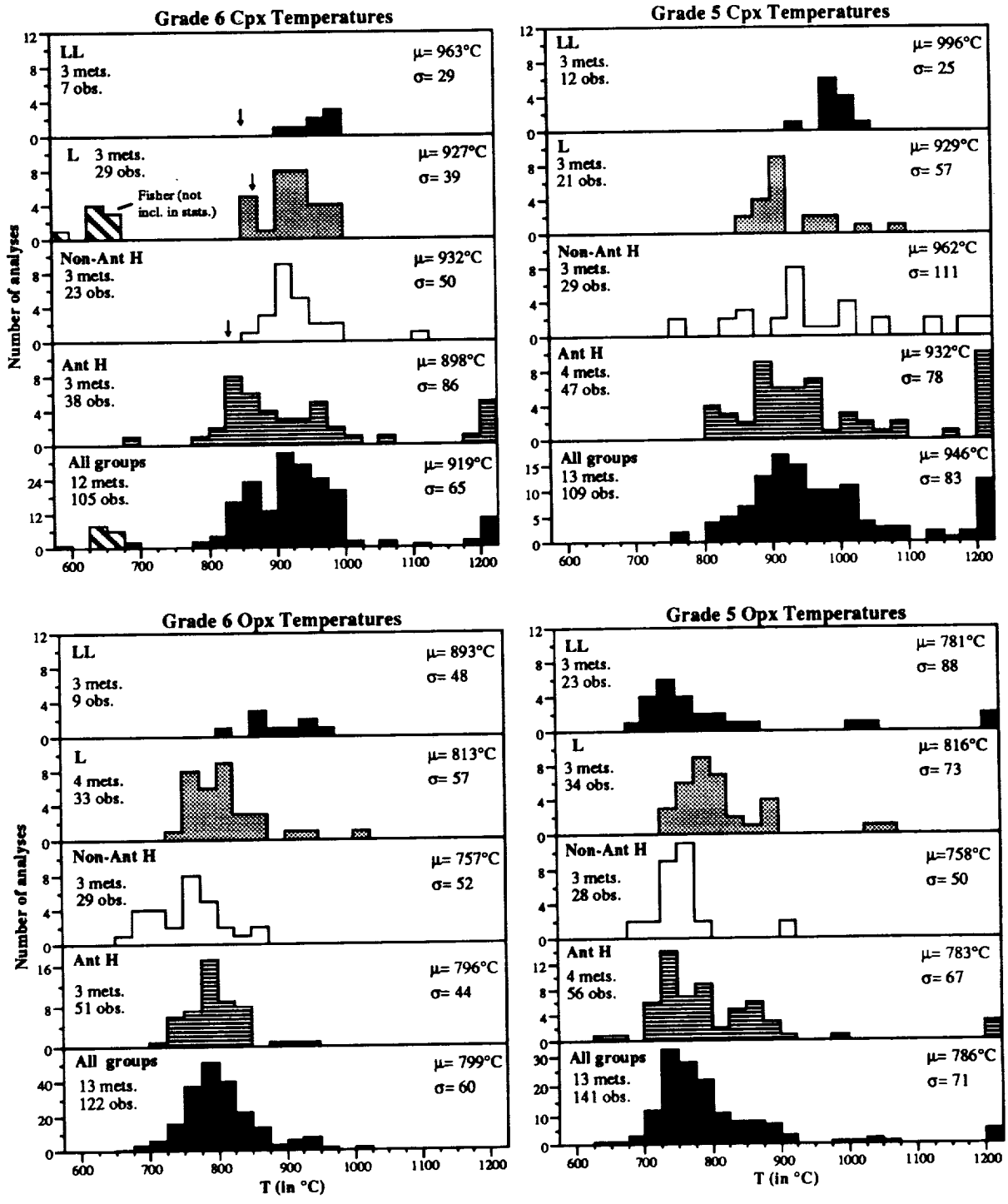

Figure 1. Temperature distribution histograms for petrographic grade 5 and 6 LL, L and H ordinary chondrites. Each bin along the X-axis represents a 25°C temperature interval. Arrows show mean temperatures for LL6, L6 and H6 groups reported by [3].

REMOTE SENSING STUDIES OF THE NORTHEASTERN PORTION OF THE LUNAR NEARSIDE

B.R. Hawke, D.T. Blewett, P.G. Lucey, G.J. Taylor, C.A. Peterson, J.F. Bell, M.S. Robinson, Planetary Geosciences, SOEST, Univ. of Hawaii, Honolulu, HI 96822; J.F. Bell III, NASA-ARC , Moffet Field, CA 940355; C.R. Coombs, POD Associates, Albuquerque, NM 87106; R. Jaumann, H. Hiesinger, G. Neukum, DLR-Planetary Remote Sensing, Oberpfaffenhofen, FRG; P.D. Spudis, Lunar and Planetary Inst., Houston, TX 77058

During the Galileo spacecraft encounter with the Earth-Moon system in December, 1992, a variety of spectral data and imagery were obtained for the eastern limb region as well as much of the lunar nearside. In order to support this encounter, we have been collecting near-infrared spectra and other remote sensing data for that portion of the northeastern nearside (NEN region) for which the highest resolution Galileo data were obtained. Analysis of spectra obtained for highlands units in the NEN region indicates that most surface units are dominated by anorthositic norite. To date, no pure anorthosites have been identified in the region. Several dark-haloed impact craters have exposed mare material from beneath highlands-rich surface units. Hence, ancient mare volcanism occurred in at least a portion of the NEN region. Endogenic dark-haloed craters in the region are the sources of localized dark mantle deposits (LDMD) of pyroclastic origin and at least two compositional groups are present.

INTRODUCTION. The Galileo spacecraft obtained very high-resolution remote sensing data for the northeastern part of the nearside of the Moon. In order to prepare for and support this encounter, we have collected and analyzed a variety of spectral data for the NEN region. Numerous unanswered questions exist for this region. These include: 1) the composition and stratigraphy of the local highlands crust, 2) the nature and mode of formation of regional light plains, 3) the composition of localized pyroclastic deposits, and 4) the distribution of possible cryptomare in the region. The purpose of this paper is to present the preliminary results of our analyses of remote sensing data of remote sensing data obtained for the NEN region.

METHOD. Near-infrared reflectance spectra (0.6-2.5μm) were obtained at the 2.24-m telescope of the Mauna Kea Observatory during a series of observing runs using the Planetary Geosciences indium antimonide spectrometer. The lunar standard area at the Apollo 16 landing site was frequently observed during the course of each evening, and these observations were used to monitor atmospheric extinction throughout each night. Extinction corrections were made using the methods described by McCord and Clark [1], and spectral analyses were made using the techniques described by McCord *et al.* [2]. The Earth-based multispectral images used in this study were described by McCord *et al.* [3], Bell and Hawke [4], and Neukum *et al.* [5]. Information concerning the reduction and calibration of Mariner 10 images for this portion of the Moon were described by Robinson *et al.* [6].

RESULTS AND DISCUSSION: In order to investigate the existence of cryptomare in the NEN region, near-IR spectra were collected for a series of features near the

eastern edge of Mare Frigoris. Baily K (diameter=3 km) and a small mare crater immediately west of the mare/highlands contact exhibit spectral parameters characteristic of fresh mare basalt deposits. Both spectra have relatively deep "1μm" absorption features centered longward of 0.95μm. The spectrum for a light plains unit just east of the mare/highlands contact [7,8] indicates that this area is dominated by mare basalt with a minor component of highlands material. Apparently, this is a mare basalt deposit that has been contaminated with a small amount of highlands debris.

Gartner D is a small crater (diameter=8 km) with a partial dark halo which excavates material from beneath the surface of a light plains deposit in the floor of Gartner crater. Two spectra were obtained for Gartner D and both exhibit characteristics which clearly indicate that mare basalt was exposed by this impact event. Two other dark-haloed impact craters have exposed mare basalt from beneath highlands-rich material in the NEN region. One is located south of Hercules crater and the other is southeast of Chacornac. The DHC south of Hercules appears to have excavated mare basalt from beneath the highlands-rich ejecta blanket emplaced by the Hercules impact event. Additional analysis of multispectral imagery of the NEN region should clarify these stratigraphic relationships and provide more information concerning the distribution of cryptomare.

Endogenic dark-haloed craters in the region are the sources of localized dark mantle deposits (LDMD) of pyroclastic origin. Although LDMD exhibit many morphologic similarities, spectral reflectance studies indicate that two compositional groups are present in the region [9,10]. The first group includes spectra from the two dark-haloed craters on the floor of Atlas as well as the Franklin dark floor deposits. The spectral parameters determined for this group indicate the presence of feldspar-bearing mafic assemblages dominated by orthopyroxene and containing glass-rich juvenile material. The second group includes spectra obtained for two LDMD east of Aristoteles. These spectra closely resemble those obtained for mature mare areas, and the deposits in this group contain very large amounts of mare basalt. As part of this study, a previously unmapped LDMD has been identified on the floor of Gauss crater. Galileo data may provide compositional information for this endogenic dark-haloed crater as well as other LDMD on the floor of Gauss.

Analysis of spectra obtained for a variety of highlands materials in the NEN region indicates that most surface units are dominated by anorthositic norite. The most anorthositic material in the NEN region is exposed by Thales crater. To date, no pure anorthosites have been identified in the region.

REFERENCES. [1] McCord T.B. and Clark R.N. (1979) *Publ. Astron. Soc. Pac., 91,* 571. [2] McCord T.B. *et al.* (1981) *J. Geophys. Res., 86, no. B11,* 10883. [3] McCord T.B. *et al.* (1976) *Icarus, 29,* 1. [4] Bell III J.F. and Hawke B.R. (1992) *LPSC XXIII,* 123. [5] Neukum G. *et al.* (1991) *LPSC XXII,* 971. [6] Robinson M.S. *et al.* (1992) *J. Geophys. Res., 97, no. E11,* 18,265. [7] Lucchitta B.K. (1972) U.S.G.S. Map I-725. [8] Lucchitta B.K. (1978) U.S.G.S. Map I-1062.

TESSERA TERRAIN ON VENUS: IMPLICATIONS OF TESSERA FLOODING MODELS AND BOUNDARY CHARACTERISTICS FOR GLOBAL DISTRIBUTION AND MODE OF FORMATION; James W. Head[1] and Mikhail Ivanov[1,2]. [1]Department of Geological Sciences, Brown University, Providence RI 02912; [2]V. I. Vernadsky Institute of the Russian Academy of Sciences, Moscow, Russia.

Introduction: Mapping of tessera terrain using Magellan global high-resolution data has shown that it comprises about 10% of the surface area of Venus, is not randomly distributed, is extremely highly deformed relative to intervening plains, lies at a wide range of elevations, is embayed by and largely predates adjacent volcanic plains, is generally negatively correlated with broad lowlands and volcanic rises, may underlie a considerable percentage of the superposed volcanic plains, and has linear/tectonic margins for about 27% of its boundaries (1,2). In this paper we investigate further the distribution and origin of tessera through analysis of the changing nature of tessera occurrences during sequential flooding, and assessment of the nature and distribution of Type II (linear/tectonic) tessera boundaries (2,3).

Models of Sequential Flooding of Tessera Terrain: Global mapping of tessera shows that the number of small tessera patches far exceeds those of medium and large size, although small tessera patches make up only a small part of the total tessera population by area. These observations, together with the volcanically embayed nature of about 73% of the boundaries of tesserae, the wide areal distribution of small patches (1), and the common presence of small patches adjacent to larger ones, has led to the hypothesis that tessera terrain may underlie larger portions of the surface than the ~10% presently exposed. In order to test this hypothesis and to assess quantitatively the amount of volcanic cover that may overlie such a tessera basement, we developed a series of volcanic flooding models to study volumes, thicknesses, and outcrop patterns of tesserae flooded by volcanic deposits. We report here on the first stage of this analysis, in which we take known major areas of presently exposed tessera (Alpha, Tellus, Laima, Fortuna, Thetis, and Ovda), flood them evenly to specific contours above MPR, and track the relationship between lava thickness and changing outcrop patterns (Fig. 1). Alpha Regio Tessera: Flooding of the Alpha region to 0.5 km above MPR removes all outliers of tessera and reduces the area of the main occurrence by less than about 20% but does not modify its coherence. Flooding an additional 1 km to 1.5 km reduces the outcrop pattern by more than 50% and results in five outliers, each with a different shape and orientation and less than about 500 km in mean width, replacing the coherent Alpha tessera. Flooding to 2.5 km removes all trace of Alpha tessera. Tellus Regio Tessera: Flooding to 0.5 km results in loss of virtually all outliers, in the reduction of the northern arc and outlier to several small patches, and reduction of the main occurence area by about 10%, although it retains its coherence. Flooding to 1.5 km reduces the outcrop pattern by more than 50% and results in six outliers, two large ones and four small ones, replacing the coherent main Tellus tessera. Flooding to 2.5 km removes all trace of Tellus tessera (Fig. 1). Laima Tessera: Flooding to 0.5 km removes outliers and begins to embay the southern and eastern margin of Laima. Because Laima is on a regional slope leading northwestward to Ishtar Terra, flooding to 1.5 km causes systematic embayment for 500-1000 km in a NW direction, forming about ten outliers of tessera SE of the main body, now reduced to less than 50% of its original extent. Flooding to 2.5 km reduces the total tessera outcrop to a single 250 x 500 km patch. Fortuna Tessera: Flooding to 0.5 km causes large-scale embayment and breakup of northern Fortuna. Because of the E-W trending large-scale topographic fabric, flooding to 1.5 km causes systematic breakup of the main tessera body into a highly embayed southern block and a northern outlier. Total outcrop is now reduced to less than ~70% of its original extent. Flooding to 2.5 km reduces the total tessera outcrop to a series of about six patches extending in an E-W direction. Thetis Tessera: Thetis consists of a northern highly embayed and segmented portion, and a southern highly embayed but more coherent portion. Flooding to 0.5 km causes virtually no modification, while flooding to 1.5 km removes much of the northern segments of tessera. Because of the steep sides of the southern segment, flooding to 3.5 is required to seriously alter the outcrop pattern, and even then the outcrop pattern is coherent and arc-like. Ovda Tessera: Flooding to 0.5 km removes a few outliers but has no major effect on the main tessera distribution. Flooding to 1.5 km removes a large portion along the western end (~15-20% of the total), but has little influence elsewhere. Increasing levels of flooding remove portions of the western end and isolate the high region to the east until at 3.5 km thickness, there is one major (~2000 x 3000 km) outcropping that still is coherent. Summary: Flooding of presently exposed tessera terrains such as Alpha and Tellus to 1.5 km above MPR produces outcrop patterns similar to the widely distributed clusters of small tessera patches common on Venus (1), and flooding to 2.5 km totally obliterates all tessera patches. Flooding of Fortuna to 2.5 km would yield a patchy distribution of tessera similar to the present outcrop patterns of Ananke or Meshkenet tesserae. Flooding of Ovda and Thetis to 3.5 km would produce tessera outcrops which had an areal extent only 1-2 times that of present-day Alpha tessera. This simple exercise supports the idea that the widespread areas presently characterized by tessera patches and clusters (1) may have tessera terrain underlying the plains at depths of several hundred meters to 1-3 km. It also

demonstrates that all traces of tessera terrain for significant regional occurrences (e.g., Alpha, Tellus) can be removed from sight by as little as 2-4 km thickness of volcanic plains.

Characteristics of Tectonic Boundaries of Tessera Terrain: Abundance: Classification of tessera boundaries has shown that 27% are Type II, more linear at the tens to hundred kilometer scale and usually associated with large-scale tectonic features bounding tessera massifs. Association with tessera topography and structure: For large tesserae the linear boundary often coincides with the high elevated edges of the tessera, and ridges and troughs inside the tessera are in general oriented subparallel to this boundary. Continuity: Some Type II boundaries occur locally (interrupting regional Type I embayed boundaries), but many form regionally continuous parts of boundaries that extend for hundreds to thousands of km (e.g., along the northern edge of Itzpapalotl and Fortuna). Boundary Shapes: One of the modes of occurrence for tesserae boundaries and tesserae patches is in arc-like arrangements which may extend for thousands of km: examples are the northern boundaries of Itzpapalotl-Fortuna Tessera and Itzpapalotl Tessera; Kutue-Ananke tessera chain at the edge of Akkruva Colles Region; Dekla tessera; tesserae at the northern margin of Beta Regio and at Phoebe Regio. In most cases, Type II linear/tectonic boundaries dominate at these arcuate patch/boundary occurrences. Symmetry: Type II boundaries are generally asymmetrical in large tessera occurrences, existing on one side but commonly not on the other (e.g., Fortuna, Ovda). In some smaller linear cases (e.g., Tethus) the boundaries occur on both sides. Age: In some cases, border deformation has extended over a period of time and has involved adjacent plains (4) while in others the boundary has been embayed by plains which are not clearly deformed; in still others, the slopes are sufficiently steep as to suggest geologically recent activity (5). Associations with convection patterns: Comparison of these boundaries to interpreted present patterns of mantle convection (6) show very little correlation. Arcuate Type II boundaries are commonly not closely associated with or oriented appropriately to suggest a relationship to regions interpreted to represent present patterns of upwelling and downwelling. Summary and interpretation: The linearity of Type II boundaries and the association with large scarps or tectonic features suggest that these boundaries formed at tectonically active edges of tesserae. The common asymmetry of occurrence of many of these boundaries would suggest that processes responsible for their formation are dynamic and not just passive gravitational relaxation. The regional arcuate nature of many Type II boundaries suggests that they may mark the location of large-scale flexure and overthrusting and/or underthrusting. Lack of correlation with present mantle convection patterns suggests that many Type II tesserae boundaries may be the product of previous convective activity or other processes, such as relicts of large-scale overturn processes (7).

Summary: Flooding models suggest that tessera may be much more widespread beneath the plains than is represented by the ~10% surface exposure. Embayment and lack of correlation of tectonic tessera boundaries with present convection patterns suggest tessera formation largely predates the plains. We are presently assessing two end-member models for the tessera formation: 1) that it represents continuing stages of downwelling following initial stages like the current Lavinia and Atalanta lowlands (3), and 2) that it represents the results of near-global catastrophic downwelling linked to processes such as depleted mantle layer instabilities (7) or catastrophic plate tectonics (8).

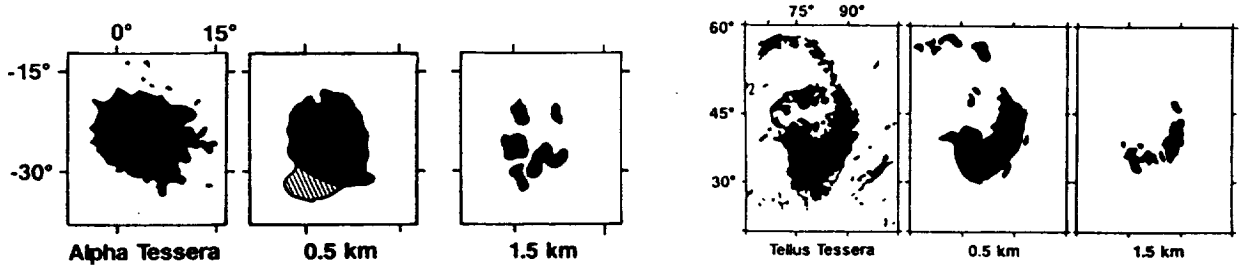

References: 1) M. Ivanov *et al.* (1992) *LPSC 23*, 581; 2) M. Ivanov and J. Head (1993), *LPSC 24*, this volume; 3) D. Bindschadler *et al.* (1992) *JGR, 97*, 13495; 4) M. Gilmore and J. Head (1992); 5) S. Smrekar and S. Solomon (1992) *JGR, 97*, 16121; 6) D. Bindschadler, *et al.* (1992) *JGR, 97*, 13495; 7) E. Parmentier and P. Hess (1992) *GRL, 19*, 2015; 8) D. Turcotte (1992) *LPI 789*, 127.

MODE OF EMPLACEMENT OF LUNAR MARE VOLCANIC DEPOSITS: GRABEN FORMATION DUE TO NEAR SURFACE DEFORMATION ACCOMPANYING DIKE EMPLACEMENT AT RIMA PARRY V;

J. W. Head[1] and L. Wilson[1,2]. [1] Dept. Geol. Sci., Brown Univ., Providence, RI 02912 USA, [2] Environ. Sci. Div., Inst. of Environ. and Biol. Sci., Lancaster Univ., Lancaster LA1 4YQ, UK.

Abstract: Theoretical analyses, together with the observed style of emplacement of lunar mare volcanic deposits, strongly suggest that mare volcanic eruptions are fed by dikes from source regions at the base of the crust or deeper in the lunar mantle (1). Some dikes intrude into the lower crust, while others penetrate to the surface and are the sources for voluminous outpourings of lava. Still others stall near the surface generating a near-surface extensional stress field. We have investigated the hypothesis that some lunar linear rilles (graben) are the near-surface manifestations of dikes intruded to shallow depths. For a specific example (Rima Parry V) we show that the geometry of the faults implies a mean dike width of about 150 m and depth to the dike top of about 500 m, values consistent with other theoretical and observational data on lunar dike geometry. Localized pyroclastic deposits along Rima Parry V are evidence for the presence of near-surface magma, and are interpreted to be the result of degassing and pyroclastic eruption subsequent to the emplacement of the dike.

Dike Emplacement in the Lunar Crust: Linear and arcuate rilles (simple graben) have been interpreted to be linked to impact basin structure, and to the emplacement of mare deposits in the basins via flexural deformation related to the mare deposit load (2). Linear rilles are generally thought to represent deformation confined to the upper layers of the crust (3) where stresses are concentrated as rocks at deeper levels adjust viscously to long-term applied loads (4). Several linear rilles, however, have volcanic (commonly pyroclastic) deposits associated with them over at least parts of their horizontal extent. A likely situation is that these graben are themselves the surface expressions of stress fields generated by dikes approaching the surface from great depths (5). The surface manifestation of dike emplacement in the crust may be quite different depending on the depth below the surface to which the dike penetrates as it rises. In general, if the dike propagates to the surface and erupts lava, the stress field immediately surrounding the propagating dike will be compressional all the way to the surface and the surface manifestation will be a fracture. If the dike does not propagate to the vicinity of the surface (perhaps stalling at depths greater than several km), then the strain associated with dike emplacement will be insufficient to cause any dislocation in the near surface rocks. On the other hand, there exists a range of intermediate depths of dike penetration at which eruption does not occur, but at which strain associated with dike emplacement influences rocks near enough to the surface that extensional deformation will take place and graben will form.

During the period of mare basalt emplacement, the anorthositic highland crust was underlain by zones of mantle partial melt (6). Buoyant diapirs ascended through the ductile portions of the mantle and become trapped at the base of the crust (a buoyancy trap; 7) or at later times at the base of the thickening lithosphere (a strength trap). For the case of the buoyancy trap, magma stalled at depths averaging ~65 km on the nearside and ~85 km on the farside. Magma remained in bodies at these depths until excess pressure had built up sufficiently to propagate a dike toward the surface. Buildup of excess pressure resulted in dike propagation into the crust, or to the surface producing volcanic eruptions, depending on total excess pressure, volume of magma available, and local crustal thickness (1). The minimum driving pressures needed to propagate dikes to the surface from magma source depths in the range 64 to 100 km is in the range 14 to 20 MPa. The mean width of dikes with these driving pressures and heights lies in the range 150 to 200 m. A value close to 25 MPa may be the most plausible for the driving pressure in dikes leading to actual surface eruptions (1). For dikes propagating from deeper parent magma bodies such as might be related to strength traps at depths close to 300 km, pressures up to 50 MPa and dike widths in the range 600 to 800 m are inferred. The maximum horizontal extent (length) of a dike which propagates through a great vertical distance is likely to be comparable to its vertical

height (8), though the disc-like shape of such a dike will mean that the surface outcrop length is likely to be much less than the maximum length at depth.

Lunar Linear Rille - Rima Parry V Example: Rima Parry V, about 50 km in length and 730m-1.8 km wide, cuts the floor and rim of the craters Fra Mauro and Bonpland and has mantling material and a row of small cones along its western margin about midway along its strike. The general surface and subsurface deformation expected as a result of shallow dike intrusion has been investigated (5,9,10). A combination of these theoretical and experimental investigations shows that the location of the boundary faults of any graben formed is dictated by a combination of elastic and anelastic processes. Using the empirical result (10) that the total horizontal extension produced by a dike which extends vertically from a shallow depth to a very great depth is close to 2/3 of the mean dike width, we can use the strain associated with the linear rille graben to estimate dike widths. The typical depth of Rima Parry V is ~54 m, the total extension is ~62 m and the implied average dike width is (1/[2/3]) = 1.5 times this, i.e. ~93 m. An additional estimate of the dike width can be obtained from assessment of the horizontal surface strain per meter of dike width as a function of horizontal position above a shallow dike for various depths to the dike top (10). The distance between the strain maxima is inferred to be similar to the width of the graben, and for Rima Parry V, where the graben width is 1800 m, the implied depth to dike top is ~750 m, and the typical strain per meter width of dike is close to 0.0002. Using a graben width of 1800 m and the horizontal extension of 62 m deduced above, the strain is 62/1800 = 0.034 and so the implied dike width is 0.034/0.0002 = 172 m. Thus, from the two approaches to finding the dike width we have a lower limit of 93 m and an estimate of 172 m. We adopt a final estimate of 150 m from these values. This value is at the lower end of the 150-200 m mean dike widths estimated for dikes with sufficient driving pressure to cause near-surface dike intrusions from magma parent bodies at depths of 64-100 km (1). On the basis of the hypothesis that the length of a dike which propagates through a great vertical distance is likely to be comparable to its vertical height (8), the length of Rima Parry V (about 50 km) and its tendency to narrow at both ends suggests that the parent magma body may lie at a minimum depth of 50 km.

Rima Parry V also displays a row of volcanic cones aligned parallel to the western margin of the graben. These, and associated deposits that mantle the rille topography, occur in a 10 km long segment located about midway along the rille extent (Figure 1). We interpret these to indicate the presence of magma just below the surface in the vicinity of the rille. A combination of chemical evolution due to cooling of magma in the top of a dike and the migration of exsolved volatiles to shallow depths (11,12) could lead to positive buoyancy of part of the melt at the top of the dike, the propagation of fractures to the surface, and the eruption of pyroclastic materials.

Conclusions: On the basis of these considerations, the presence of associated pyroclastic deposits, and the lack of significant effusive eruptions, we conclude that the characteristics of Rima Parry V are consistent with formation by a dike which propagated from great depth to near the lunar surface. Several other linear rilles (e.g., Hevelius, Rima Bode) share some of the characteristics of these two examples and may also represent the surface manifestation of shallow dikes emplaced from parent magma bodies at depth.

References:
(1) Head, J.W. and Wilson, L., *Geochim. Cosmochim. Acta.*, 56, 2155-2175, 1992. (2) Solomon, S. and Head, J., *Rev. Geophys. Space Phys, 18*, 107-141, 1980. (3) Golombek, M. *J. Geophys. Res., 84*, 4657-4666, 1979. (4) Melosh, H., *Proc. Lunar Planet. Sci. Conf. VII*, 2967-2982, 1976. (5) Pollard, D. *et al.*, *Tectonophys., 94*, 541-584, 1983. (6) Longhi, J., *Geochim. Cosmochim. Acta., 56*, 2235-2252, 1992; Neal, C. and Taylor, L., *ibid.*, 2177-2212, 1992. (7) Solomon, S., *Proc. 6th Lunar Sci. Conf.*, 1021-1042, 1975. (8) Takeda, A., *J. Geophys. Res., 95*, 8471-8481, 1990. (9) Pollard. D. and Holzhausen, G., *Tectonophysics, 53*, 27-57, 1979. (10) Mastin, L. and Pollard, D., *J. Geophys. Res., 93*, 13221-13235, 1988. (11) Wilson, L. and Head, J., *J. Geophys. Res., 86*, 2971-3001, 1981. (12) Head, J. and Wilson, L., *Proc. Lunar Planet. Sci. Conf. 10th*, 2861-2897, 1979.

LUNAR IMPACT BASINS: NEW DATA FOR THE NEARSIDE NORTHERN HIGH LATITUDES AND EASTERN LIMB FROM THE SECOND GALILEO FLYBY.

J. W. Head[1], M. Belton[2], R. Greeley[3], C. Pieters[1], E. Fischer[1], J. Sunshine[1], K. Klaasen[4], A. McEwen[5], T. Becker[5], G. Neukum[6], J. Oberst[6], C. Pilcher[7], J. Plutchak[1], M. Robinson[8], T. Johnson[4], D. Williams[3], S. Kadel[3], R. Sullivan[3], I. Antonenko[1], N. Bridges[9] and the Galileo Imaging Team. [1]Brown University, Providence RI; [2]Kitt Peak National Observatory, Tucson AZ; [3]Ariz. State Univ., Tempe AZ; [4]JPL, Pasadena CA; [5]USGS, Flagstaff AZ; [6]DLR, Oberpfaffenhofen FRG; [7]NASA HQ, Washington DC; [8]Univ. Hawaii, Honolulu HI; [9]USGS, Menlo Park CA.

During the December 1992 Galileo Earth/Moon encounter the northern half of the nearside, the eastern limb, and parts of the western farside of the Moon were illuminated and in view, a geometry that was complementary to the first lunar encounter in December, 1990, which obtained images of the western limb and eastern farside.[1] The Galileo Solid State Imaging system[2] (SSI) obtained multispectral images for these regions during the second encounter and color ratio composite images were compiled using combinations of band ratios chosen on the basis of telescopic spectra and laboratory spectra of lunar samples.[1] Ratios of images taken at 0.41 and 0.76μm are sensitive to changes in the slope in the visible portion of the spectrum, and ratios of 0.99 and 0.76μm relate to the strength of near-infrared absorptions due to iron-rich mafic minerals (0.76/0.99 ratio) such as olivine and pyroxene. Results of the analyses of the compositional diversity of the crust[3], maria[4], and Copernican craters[5] are presented elsewhere.

Primary objectives for lunar basin analysis for the second encounter include analysis of: the north polar region and the Humboldtianum basin; the characteristics of the Imbrium basin along its northern border and the symmetry of associated deposits; the origin of light plains north of Mare Frigoris and associated with several other basins; the nature and significance of pre-basin substrate; the utilization of the stereo capability to assess subtle basin structure; the identification of previously unrecognized ancient basins; basin deposits and structure for limb and farside basins (e.g., Crisium, Marginis, Smythii, Lomonosov-Fleming); and assessment of evidence for proposed ancient basins (e.g., Procellarum). These data and results will be applied to addressing general problems of evaluation of the nature and origin of basin deposits, investigation of mode of ejecta emplacement and ejecta mixing, analysis of the origin of light plains deposits, analysis of basin deposit symmetry/asymmetry, investigation of basin depth of excavation and crustal stratigraphy, and assessment of models for basin formation and evolution. Here we discuss some preliminary results concerning lunar impact basins, their deposits, and prebasin substrates, using the same approaches that we employed for the Orientale and South Pole-Aitken basins using the data from the first encounter.[6]

The Humboldtianum basin (61N 84E; 650 km diameter; middle Nectarian) has been described as a possible double or triple impact basin[7,8], with the crater Bel'kovich as the possible inner structure or an independent crater. Humboldtianum basin deposits do not show anomalous characteristics relative to typical highlands. Galileo data distinctly show a markedly linear and angular structure of the outer (second) ring in the SE quadrant of the basin. In addition, the illumination geometry clearly highlights the radial texture of the deposits between the second and first ring, providing additional evidence that the inner ring is equivalent to the initial crater rim crest. Preliminary analyses suggests that the Bel'kovich structure is most likely a separate crater unrelated to the complex Humboldtianum western ring structure. Initial analyses show little evidence for a strong 0.76/0.99 signature for pre-mare Imbrian-aged light plains within the basin and within Bel'kovich, but many of the patches are small and will require further analysis.

The northern rim and ejecta deposits of the Imbrium basin (33N 18W; ~1200 km diameter; Lower Imbrian) are well illustrated in the Galileo SSI data. Along the northern rim the Alpes and Fra Mauro formations are generally similar to typical mature highland soils, but detailed analysis of the global mosaics is necessary to establish more specific affinities. Impact craters which have formed astride the northern part of the basin ring most likely to represent the transient crater rim crest (Plato, 101 km diameter and Iridum, 200 km diameter) display anomalously red rims. One

possible interpretation is that these deposits represent material of a different composition excavated from depth (probably deepest crust[9]).

Extensive areas to the north of Imbrium and Mare Frigoris are characterized by radial Imbrium sculpture, deposits of the Fra Mauro Formation, and Imbrian-aged light plains. Indeed, this region has one of the highest concentrations of light plains on the Moon[8]. On the basis of our initial analysis, much of the area mapped as Fra Mauro Formation and equivalent aged plains (Ip1) north of western and central Mare Frigoris show highland spectral characteristics; however, a small number of the fresh (bright-halo) craters in the plains have stronger 0.76/0.99 ratio signatures (indicative of iron-bearing minerals, but not necessarily of basalts). Thus, much of the bright plains in this region are apparently of highland composition, but there may be some mafic and possibly cryptomaria components locally. A series of younger (Orientale basin age[10]) Imbrian light plains are extensively exposed north of eastern Mare Frigoris; these have been interpreted to be thin Orientale ejecta overlying old mare materials.[7] SSI data indicate that much of the younger Ip2 plains also show typical highlands signatures, for example in the Arnold/Kane area; however, a small number of the fresh bright-halo craters have relatively more intense one-micron signatures. A dark halo crater with mare basalt affinities has been reported inside the crater Gärtner, within about 100 km of the basalts of Mare Frigoris[11]. The area in general has a mature highland soil spectral signature, and only a few hints of possible mafic fresh craters. Our analysis of the SSI data indicate that the ejecta of the dark-halo crater inside Gärtner does have a distinctly mare-like signature comparable to the medium-titanium basalts in the Imbrium interior and the younger Frigoris basalts.[12] At the present time, this is the most conclusive evidence for the presence of cryptomare deposits beneath the light plains, but it does not provide information on how widespread the deposit might be. Thus, although there is some evidence for locally more mafic material excavated by some fresh craters, and the one dark-halo crater with mare affinities, there is at present no comprehensive and extensive evidence of the presence of a cryptomaria deposit under either or both (Ip1 or Ip2) light plains deposits of the distinctiveness and extent that was observed in the Schiller-Schickard area southeast of Orientale on the first encounter.[1] This may mean that the light plains are predominantly ejecta, or that there is more extensive cryptomaria, but that: a) the ejecta is too thick here to see evidence of cryptomaria (the radial position of the dark halo crater in Gärtner is closer to the rim of the larger Imbrium basin than that of the Schiller-Schickard deposits to the smaller Orientale), b) the cryptomaria are in tiny patches only and so we see only a few impact craters with a more mafic signature, c) we are dealing with a "non-traditional" cryptomare[13] (basalt with non-distinct 1μm band depth similar to some western limb basalts seen in the first encounter [14]), d) the Ip2 are post-Imbrium lavas with a veneer of later ejecta, and/or e) we are dealing with a different type of lava (non-mare basalt, and relatively high albedo).

Earth-based spectra show an olivine-bearing fresh crater ejecta deposit on the northeastern rim of the Crisium basin[15] (17.5N 58.5E; 1060 km diameter; Nectarian); this crater is observed in the SSI data, but so far we see no evidence for an extensive deposit of similar composition on the north rim or elsewhere on the basin rim. We are presently analyzing data for the eastern limb highland basins such as Marginis basin (20N 84E; 580 km diameter; pre-Nectarian), Smythii basin (840 km diameter; pre-Nectarian) and Lomonosov-Fleming basin (19N 105E; 620 km diameter; pre-Nectarian).

References: 1) M. Belton *et al.* (1992) *Science*, 255, 505; 2) M. Belton *et al.* (1992) *Space Sci. Rev.*, 60, 413; 3) C. Pieters *et al.*, this volume; 4) R. Greeley *et al.*, this volume; 5) A. McEwen *et al.*, this volume; 6) J. Head *et al.* (1992) Lunar Impact Basins: New Data for the Western Limb and Farside (Orientale and South Pole-Aitken Basins) from the first Galileo flyby, *JGR*, in review; 7) B. Lucchitta (1978) *USGS MI*-1062; 8) D. Wilhelms (1987) *USGS PP*-1348; 9) C. Pieters *et al.* (1992) Crustal and mantle diversity: Compositional analysis of SSI Moon data, *JGR*, in review; 10) J. Boyce *et al.* (1974) *PLSC 5*, 11; 11) B. R. Hawke *et al.* (1992) *LPI TR 92-09*, 14; 12) J. Whitford-Stark (1990) *PLPSC 20*, 174; 13) J. Head *et al.* (1992) this volume; 14) R. Greeley *et al.* (1992) Galileo imaging observations of lunar maria and related deposits, *JGR*, in review; 15) C. Pieters (1986) *Rev. Geophys.*, 24, 557.

LUNAR SCOUT MISSIONS: GALILEO ENCOUNTER RESULTS AND APPLICATION TO SCIENTIFIC PROBLEMS AND EXPLORATION REQUIREMENTS: J. W. Head[1], M. Belton[2], R. Greeley[3], C. Pieters[1], A. McEwen[4], G. Neukum[5], T. McCord[6]. [1]Brown Univ., Providence RI; [2]Kitt Peak National Observatory, Tucson AZ; [3]Ariz. State Univ., Tempe AZ; [4]USGS, Flagstaff AZ; [5]DLR, Berlin, Germany; [6]Univ. Hawaii, Honolulu, HI.

On the basis of US and Soviet orbital and surface exploration and results from Earth-based observations, we have a first-order understanding of the major stages in the formation and evolution of the Moon[1]. The Moon is known to have formed an initial lunar highland primary crust[2], and a secondary basaltic crust due to mantle partial melting. Impact craters at all scales have modified the crust and the largest basins may have excavated through the crust into the mantle. Exploration of Mercury and Mars has shown many similarities to the Moon, indicating that the Moon is a key to the understanding of the evolution of one-plate planets[3]. The Moon may have formed from the impact of a Mars-sized object into a proto-Earth[4]. These factors indicate that the Moon is a baseline and a cornerstone in planetary exploration in reference to such fundamental questions as planetary origin, the impact record, and the formation and evolution of primary and secondary planetary crusts. In addition, some of our most fundamental information about the Moon was collected during the Apollo human exploration expeditions and many questions and issues will only be resolved by future long visits and extended exploration traverses.

Although Apollo sites are known in relative detail, and we have important Apollo orbital geochemical data for about 20% of the Moon, we lack significant geochemical and mineralogic information for much of the rest of the Moon, particularly the farside. Ironically, there is better systematic image coverage for Mars and Venus than for the Moon, the topography of Venus is better known than that of the Moon, and the majority of lunar exploration was completed more than two decades ago with old technology. Prior to the Galileo encounters, the only spacecraft digital image data for the Moon[5] was obtained by Mariner 10 on its way to Mercury in 1974!

The Lunar Scout Missions (payload: x-ray fluorescence spectrometer, high-resolution stereo camera, neutron spectrometer, gamma-ray spectrometer, imaging spectrometer, gravity experiment) will provide a global data set for the chemistry, mineralogy, geology, topography, and gravity of the Moon. These data will in turn provide an important baseline for the further scientific exploration of the Moon by all-purpose landers and micro-rovers, and sample return missions from sites shown to be of primary interest from the global orbital data. These data would clearly provide the basis for intelligent selection of sites for the establishment of lunar base sites for long-term scientific and resource exploration and engineering studies.

The two recent Galileo encounters with the Moon (December, 1990 and December, 1992) illustrate how modern technology (e.g., instruments such as the Galileo SSI-Solid State Imaging System, M. Belton, PI, with high spatial resolution and relatively low spectral resolution, and the Galileo NIMS-Near-Infrared Mapping Spectrometer, R. Carlson, PI, with high spectral resolution and relatively low spatial resolution) can be applied to significant lunar problems. Here we emphasize the regional results of the Galileo SSI to show the promise of geologic unit definition and characterization as an example of what can be done with the global coverage to be obtained by the Lunar Scout Missions.

During the first encounter the SSI System obtained multispectral imaging data for the western part of the nearside, the western limb including the Orientale basin region, and parts of the farside including the South Pole-Aitken Basin[6]. These data, although of limited resolution (several up to about 20 km at Orientale and the farside), provided important new information on questions of the homogeneity and heterogeneity of the highland and mare crust and the depth of excavation of lunar basins. The affinity of limb and farside mare basalts to those on the nearside and at the Apollo and Luna sites is poorly known. SSI multispectral image data have permitted a census of mare deposits along the western margins of Oceanus Procellarum, in the patches along the western limb of the nearside, in the Orientale Basin, and in the farside South Pole-Aitken Basin, and the establishment of the affinities of these deposits to mare basalts on the nearside. These data show that no mare basalts with Ti abundances approaching those of the high-Ti Apollo 11 basalts or of the high-Ti regions of central Oceanus Procellarum are observed on the western limb and eastern farside; the basalts exposed there are remarkably uniform in composition, being characterized by intermediate Ti content and a relatively weak 1 μm absorption band[7]. Mare volcanism began prior to the end of heavy bombardment, in pre-Nectarian times (the period of cryptomare formation[8]). The SSI data confirmed the presence of the Schiller-Shickard cryptomare and permitted the more detailed mapping of its configuration beneath the Orientale ejecta deposit. This, together with the documentation of an additional cryptomare in the Mendel-Rydberg region, contributes to an understanding of the areal significance of mare-like volcanism in the period of basin formation[7,9]. Global assessments and stratigraphic analyses will provide additional important information on the volumetric significance of early mare volcanism. In

addition, mixing models of Orientale ejecta and cryptomaria provided tests on ejecta emplacement dynamics[9], a technique that will be extremely useful globally. The compositional data on mare diversity is also providing additional insight into the existence of planet-wide mantle heterogeneity and the development of diversity and trends in single regions. Fundamental issues remain in understanding the lateral and vertical homogeneity and heterogeneity of the lunar highlands crust and its implications for models of initial crustal formation and evolution. Comparison of the deposits of major impact basins provides evidence for vertical crustal heterogeneity and depth of excavation; Galileo data show the distribution of highland and ejecta units of the 900 km diameter Orientale basin and suggest that excavation largely came from upper to middle crustal levels[9]. Data for the farside lunar crust show a major and widespread mafic anomaly primarily within the ~2000 km diameter South Pole-Aitken basin region[9,10]; the entire region has a much lower albedo than surrounding highlands. The inner, darker region has optical properties indistinguishable from low-Ti basalts, and deposits in the southern basin interior have a strong and broad ferrous 1 μm absorption, most consistent with abundant olivine. These data suggest that the South Pole-Aitken has excavated mafic-rich lower crust, and that part of its interior is characterized by cryptomaria[9,10]. Fresh impact craters show additional regional compositional diversity below the megaregolith[10] and their characteristics can be used to map the ages of craters and the impact flux[11]. Correlation of the Galileo SSI multispectral image data and Apollo x-ray spectrometer data permits the extension of Al/Si ratios over broader parts of the farside[12]. This illustrates the synergism that will be possible with complementary Lunar Scout global data sets.

The second Galileo encounter of the Moon provided higher spatial resolution SSI data (~1.1 km pixel) over the north polar and northeastern limb regions, and favorable illumination geometry for the acquisition of NIMS data, which will permit high spectral resolution characterization of broad units defined by the SSI data. Preliminary analysis of the SSI data shows that the maria (e.g., Humboldtanium, Frigoris, Crisium, eastern limb and other patches) are more diverse than those seen on the western limb and farside during EM1[13], and that several craters on basin rims have anomalous compositional characteristics relative to typical rim deposits[14]. One of the highest abundances of light plains on the Moon occurs north of Mare Frigoris[1] and SSI data suggest that some of these plains are predominantly Imbrium ejecta, while others have a cryptomare signature[13,14]. The large number of Copernican-aged craters permits further assessment of their albedo and age of emplacement[15]. Much of the highlands and plains north of Mare Frigoris are generally similar to mature highlands soils with a distinctly feldspathic composition but there are local anomalies that suggest diversity[16].

These examples of the scientific return from Galileo regional low spatial resolution coverage demonstrate that global high-resolution data from the Lunar Scout scientific payload would provide fundamental scientific return. These data in turn provide the foundation for lunar base site selection and traverse planning, as well as resource assessment (e.g., Ti, Fe, Al, soil maturity and surface correlated gases, etc.)[17]. These examples further underline the importance and synergism of global data sets (e.g., chemistry, mineralogy, geology, topography, gravity) in order to properly utilize the unique and accessible lunar laboratory and prepare for further exploration of the Moon.

References: 1) D. Wilhelms (1987) USGS. *PP1348*; 2) S. R. Taylor (1989) *Tectonophys.*, 161, 147; 3) J. Head and S. Solomon (1981) *Science*, 213, 62; 4) W. Hartmann and D. Davis (1975) *Icarus*, 24, 504; 5) M. Robinson *et al.* (1992) *JGR*, 97, 18265; 6) M. Belton *et al.* (1992) *Science*, 255, 505; 7) R. Greeley *et al.* (1992) Galileo imaging observations of lunar maria and related deposits, *JGR*, in press; 8) J. Head and L. Wilson (1992) *G&CA*, 56, 2155; 9) J. Head *et al.* (1992) Lunar impact basins: New data for the western limb and farside (Orientale and South Pole-Aitken basins) from the first Galileo flyby, *JGR*, in press; 10) C. Pieters *et al.* (1992) Crustal and mantle diverstiy of the Moon: Compositional analyses of Galileo SSI data, *JGR*, in review; 11) A. McEwen *et al.* (1992) Galileo observations of post-Imbrian lunar craters during the first Earth-Moon flyby, *JGR*, in review; 12) E. Fischer *et al.* (1992) *LPSC 23*, 361; 13) R. Greeley *et al.* (1992) this volume; 14) J. Head *et al.* (1992) this volume; 15) A. McEwen *et al.* (1992) this volume; 16) C. Pieters *et al.* (1992) this volume; 17) G. Heiken *et al.*, eds. (1991) *Lunar Sourcebook*, Cambridge, NY, 736 pp.

LAVA FLOW-FIELD MORPHOLOGICAL CLASSIFICATION AND INTERPRETATION: EXAMPLES FROM VENUS.

J. W. Head[1], K. Magee Roberts[1], L. Wilson[1,2] and H. Pinkerton[1]. [1]Dept. Geological Sci., Brown Univ., Providence RI 02912 USA, [2]Environmental Sci. Div., Lancaster Univ., Lancaster LA1 4YQ, U.K.

Introduction: Recent analyses[1] suggest that thermal constraints will act to limit the maximum length of an advancing lava flow being fed at a given volume or mass effusion rate from a vent. These constraints can be characterized through the Grätz number[2], which has a large value at the vent and decreases down flow; under a wide range of conditions, motion apparently ceases when the Grätz number has decreased[1] to a value close to 300. In cooling-limited flows, effusion from the vent should be steady; the flow front thickens, eventually stops due to this cooling, and the central channel does not drain (Fig. 1). If the vent remains active, a break-out flow will form from some point on the margin of the initial flow unit. If flows on planetary surfaces can be shown to be cooling limited, eruption rates can be estimated[1]. In this analysis, we illustrate the morphological characteristics of various flow configurations, and we describe the application of these concepts to a flow length histogram for a hypothetical flow field and then apply this to an example on Venus.

Variations on the cooling limited theme: A variety of factors may prevent a flow from reaching its maximum potential cooling-limited length (Fig. 1): In volume-limited flows, the front stops when effusion stops; the flow is shorter than a cooling-limited flow formed at the same effusion rate. The central channel of the flow unit may drain to form a thinner and narrower flow unit; no break-out flows will occur. Accidentally-breached flows will form a break-out somewhere upstream of the blockage; the parent flow will be shorter than if it had not been breached. Break-out flows form in cooling-limited flows if effusion at the vent continues after the flow front stops due to cooling, or from the sides of accidentally breached flows. Flows captured by pre-existing topography often show confinement to a narrower channel; these flows reach a greater cooling-limited length than if they had not been captured. For non-captured flows, the total flow width, central channel width and flow thickness will all increase systematically with decreasing substrate slope. Tube-fed flows are flows fed by a roofed-over tube system; once magma has emerged from the roofed-over tube system, the flow units formed obey the same rules as those given above for flows fed from a primary vent.

Typical histogram: These morphological factors can be applied to examples of mapped planetary flow fields in the following manner[1]: In a compound flow field consisting of many flow units which have been produced by long-lived eruptions, most of the flow units will be cooling limited. Mapping of compound flow fields allows one to identify discrete units and to determine superposition and continuity relationships between units or groups of units. A histogram of the lengths of the units should show a distinctive peak corresponding to the length, L, of a single cooling-limited flow unit; significant peaks at lengths which are integer multiples of this basic length (2L) may correspond to unrecognized break-out flows from the front of an earlier unit (Fig. 2). Peak sharpness will depend on effusion rate constancy: a declining effusion rate yields shorter cooling-limited flows and a skewing of the peak towards lengths shorter than L. Superimposed on the simple pattern due to cooling-limited flows will be a distribution of lengths arising from volume limited and accidentally breached flows (lengths shorter than L by various amounts) and of captured flows (lengths greater than L). If it is possible to distinguish these variations, the main peak due to cooling-limited flows, at the flow length, L, can be used to estimate the mean effusion rate feeding the flow field[1].

Application to Venus: Measurement of the lengths of 41 of the most distinctive flows surrounding a volcanic edifice about 375 km in diameter in Imdr Regio (214°; -46.5°) (Fig. 3) shows a broad peak between 140 and 220 km, slightly skewed toward greater lengths, and minor peaks at 250 and 330 km. If the flows were cooling-limited and emplaced with the longest flows first, than the 250 km lengths imply effusion rates of 3400 m^3/s (8.8 x 10^6 kg/s) and the 330 km lengths imply effusion rates[1] of 5300 m^3/s (14 x 10^6 kg/s). The two peaks in the shorter

flow sequence (150 km and 190 km; Fig. 3) imply effusion rates of 1500 m^3/s (4 x 10^6 kg/s) and 2200 m^3/s (6 x 10^6 kg/s) respectively. A simple interpretation of this would be that the different lengths represent differing phases in the evolution of the edifice, with the longer ones representing early high-effusion rate eruptions, and the shorter ones, later lower effusion rate eruptions as the source region evolved. Alternatively, the presence of numerous lateral and distal break-out flows and the lack of a clear superposition stratigraphy between units of different lengths suggests that the basic broad peak between 150-190 km may represent the typical range of flow lengths for a single cooling-limited flow unit (mean effusion rate of 1850 m^3/s, 5 x 10^6 kg/s). The other peaks might then represent break-out flows emerging from the front of previous flows, with lengths at multiples of L of the short and long end of the range. In contrast, Sif Mons[3] is characterized by a series of five flow units which have fairly distinctive flow lengths over large parts of the volcano (for example, the SE quadrant). This distinctive stratigraphy suggests that the flow units are not multiples of L (the cooling-limited flow length), but that they may represent sequential periods of evolution representing decreasing volume-limited stages, or cooling-limited flows representing phases of decreasing effusion rates. We are presently undertaking detailed mapping of several other examples to assess these factors.

Figure 1.

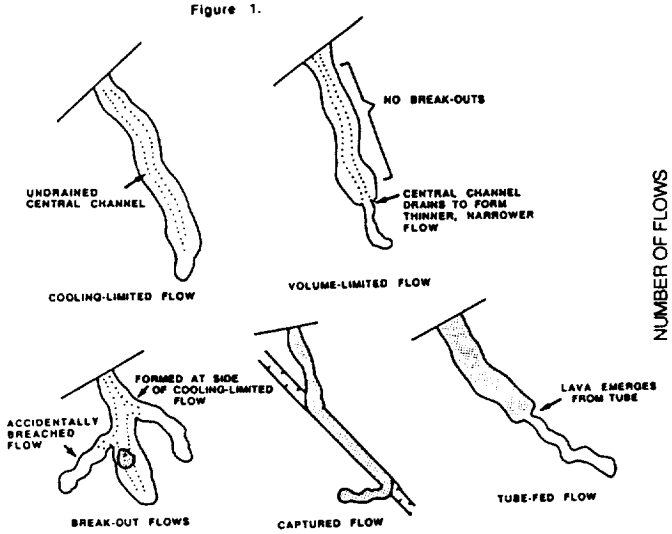

Figure 2. Hypothetical histogram of flow lengths

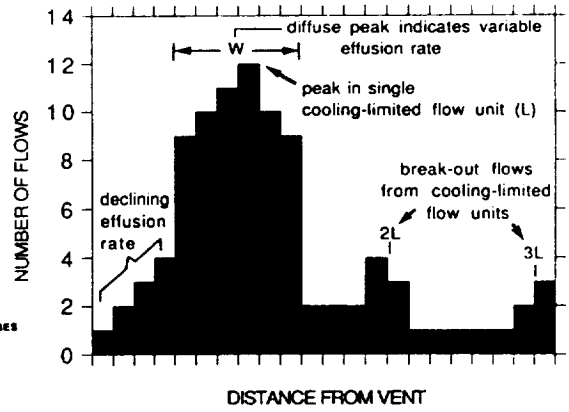

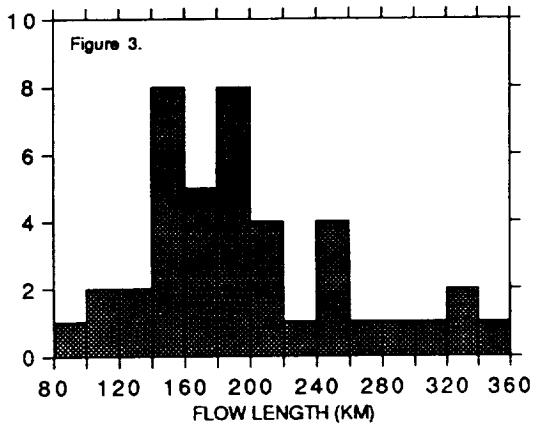

References: 1) Pinkerton, H. and Wilson, L. (1992) Factors controlling the lengths of channel-fed lava flows, submitted to *Bull. Volcanol.*; Wilson, L. *et al.* (1993) A classification scheme for the morphology of lava flow fields, *LPSC XXIV*, this volume; 2) Knudsen, J.G. and Katz, D.L. (1958) *Fluid dynamics and heat transfer*. McGraw Hill; 3) Keddie, S. and Head, J. (1992) *LPSC XXIII*, 669.

MODES OF FORMATION OF LUNAR LIGHT PLAINS AND THE DETECTION OF CRYPTOMARIA DEPOSITS; James W. Head, John Mustard, Irene Antonenko, Dept. of Geol. Sci., Brown Univ. Providence RI 02912 and B. Ray Hawke, SOEST, Univ. Hawaii, Honolulu, HI 96822.

Introduction: The early volcanic and impact histories of the Moon are closely linked and the record preserved in surface morphology and samples is tightly convolved because of the interaction of the two processes. The deconvolution of the record is an important goal in order to assess early volcanic flux (1) and the mode of emplacement of large crater and basin deposits. For example, lunar light plains have been variously interpreted as volcanic (2), impact (3), and volcanic covered by impact deposits (4) [e.g., cryptomare (1)]. The development of criteria for the determination of the origin of light plains and the detection of cryptomaria is thus a key to the deconvolution of this early record. In this paper we outline the various hypotheses for the origin of, and potential modes of occurrence of light plains and cryptomaria, and develop criteria for their recognition and documentation. We use the example of the Schiller-Schickard (5) and Balmer (6) cryptomaria to illustrate the application of these techniques to the problem of light plains interpretation and cryptomaria documentation.

Modes of Occurrence and Origin of Light Plains and Cryptomaria: Prior to the Apollo 16 mission, the Cayley light plains were thought to be of volcanic origin (Fig. 1) because of their smooth nature, their filling of highland craters, and their stratigraphic and crater age placing them between the latest impact events and the earliest maria (2); thus, a significant phase of highland (high-albedo) volcanism was thought to characterize the early Imbrian history of the Moon. Astronauts John Young and Charles Duke immediately recognized that the plains at the Apollo 16 site consisted of impact breccias. Analysis of returned samples and reassessment of the impact cratering process (3,7) led to the conclusion that light plains could be produced by ballistic erosion and sedimentation processes associated with large cratering events. However, the wide range of crater ages shown by light plains led some to continue to favor a volcanic origin for many light plains deposits (8). Analysis of dark-halo craters on basin ejecta and light plains provided evidence for mare deposits that had been covered by and mixed with later basin ejecta (4). Multispectral imaging provided evidence for the regional extent of some cryptomaria and the percentage of underlying maria incorporated into the overlying ejecta deposit (5). It also showed that in cryptomaria regions proximal to basins, the contribution of primary ejecta may be so great or the vertical mixing is not thorough enough so that the percentage of underlying cryptomaria incorporated is below the detection level, and is only obvious from the direct excavation and exposure in dark halo craters (4). In addition, this study, together with crater ages (9), has shown that light plains overlying cryptomaria may form from a thin dusting of post-basin crater ejecta. Recent identification of mare basalts with a weak absorption band at 1 μm (9,10) has led to a new possibility, "non-traditional" cryptomaria (Fig. 1), where the lack of the characteristic absorption band could hinder distinction of mare contributions to mixtures with highland basin and crater ejecta. Although albedo could still be an important factor in the recognition of these types of cryptomaria, extrusive volcanic deposits (including some maria) may also exist which have relatively higher initial (mature soil) albedos. We now use the example of the Schiller-Schickard (5) and Balmer (6) cryptomaria to illustrate the application of these techniques to the problem of light plains interpretation and cryptomaria documentation.

The Schiller-Schickard Example: This cryptomaria (4,5) is located about 900 km to the southeast of the Orientale basin in the transition zone of radially textured ejecta, plains, and secondary craters; its presence is shown by dark-halo craters with mare basalt-like spectra (4) and its extent is indicated by mixing-model calculations (5). A mare fraction image (5) shows the details of cryptomare distribution; abundance values are density-sliced into discrete levels, with a lower bound of 25% chosen to mark the lower limit of confidence for an unambiguous mare signal. Patches of cryptomaria that are smaller, thinner, or closer to the basin might not be detected with this lower bound. The two zones of high abundance on the floor of the Schickard impact crater correspond to the previously known small patches of post-Orientale mare; the rest of the floor shows moderate to low abundance. The east, south, and west walls of Shickard show an absence of mare indicating a surface dominated by highland components. This illustrates the fact that many cryptomaria will be difficult to detect because they are patchy and infilling crater floors. Most of the light plains and discontinuous facies of the Hevelius Formation within and between the Schickard and Schiller craters, and in the northern half of the Schiller-Zucchius Basin, also exhibit moderate to low mare abundances. On the basis of crater counts (5) some of the light plains within Schiller-Zucchius apparently post-date the emplacement of the Hevelius Formation and may be post-Orientale maria that have been covered by bright ejecta from nearby craters such as Zucchius. This shows that dusting by post-basin crater ejecta can at least locally produce higher albedo plains. The mare fraction map (5) shows that a minimum areal extent of pre-Orientale mare is $\approx 3\text{-}4 \times 10^5$ km^2. However, evidence from dark halo craters suggests that additional mare patches are buried by the continuous facies of the Hevelius formation west of this main area (4). These areas are not detected in this analysis (because they have mare abundances less than the 25% cutoff) and may be covered by a greater thickness of ejecta, or be smaller than the spatial resolution of the instrument. Thus, in this case, crater probes (dark-halo craters) help to detect the presence of cryptomaria where

they are being swamped by basin ejecta. The sizes of the cryptomare outlined here are comparable to several post-basin maria (e.g., Humorum, Nectaris, Vaporum, Orientale); however, it is also clear that additional deposits exist closer to the basin but are swamped by ejecta deposits.

The Balmer Basin Example: The interior of this basin is the site of geochemically anomalous (11) light plains of Imbrian-Nectarian age interpreted to be mare basalts underlying a veneer of bright material (5,11); however, no major basin in the vicinity appears to be capable of providing a substantial post-plains ejecta deposit. Instead, the bright veneer is interpreted to be due to the presence of five large impact craters within a distance of 250 km from the plains (5) providing a veneer of highlands crater ejecta to obscure the cryptomare (Fig. 1). Another possible explanation, potentially supported by the geochemical data (11), is that these plains represent volcanic deposits that have an initially higher albedo than typical mare deposits (Fig. 1).

Conclusions: On the basis of these analyses, it is clear that multiple approaches and data sets must be used to determine the potential modes of origin of light plains and cryptomaria. In some cases, ancient cryptomaria deposits may never be detected if they are beneath proximal basin ejecta, while in other cases, it is clear that the judicious use of global orbital spectral reflectance, imaging, and geochemical data will reveal a range of anomalies and occurrences well beyond our current knowledge. In this analysis, we are continuing to develop criteria for their recognition and documentation.

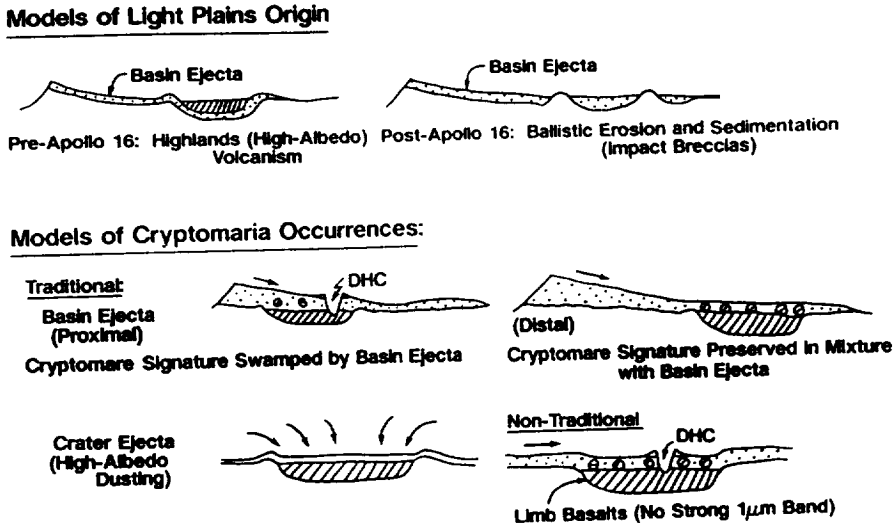

References: 1) J. Head and L. Wilson (1992) *G&CA*, 56, 2155; 2) D. Wilhelms (1970) *USGS PP 599F*; 3) V. Oberbeck *et al.* (1974) *PLSC 5*, 111; (1975) *Moon*, 12, 19; 4) P. Schultz and P. Spudis (1979) *PLPSC 10*, 2899; B. Hawke and J. Bell (1981) *PLPSC 12*, 665; 5) J. Mustard *et al.* (1992) *LPSC 23*, 957; J. Head *et al.* (1992) Lunar impact basins: New data for the western limb and farside (Orientale and South Pole-Aitken basins) from the first Galileo flyby, subm. to *JGR*; 6) B. Hawke *et al.* (1985) *EMP*, 32, 257; 7) V. Oberbeck (1975) *RGSP*, 13, 337; 8) G. Neukum (1977) *Moon*, 17, 383; 9) R. Greeley *et al.* (1992) Galileo imaging observations of lunar maria and related deposits, *JGR*, in review; 10) C. Pieters *et al.* (1992) Crustal and mantle diversity: Compositional analysis of SSI Moon data, *JGR*, in review; 11) T. Maxwell and C. Andre (1981) *PLPSC 12*, 715.

CHEMICAL DIFFERENTIATION, THERMAL EVOLUTION, AND CATASTROPHIC OVERTURN ON VENUS: PREDICTIONS AND GEOLOGIC OBSERVATIONS

J. W. Head, E. M. Parmentier, and P. C. Hess, Dept. of Geol. Scis., Brown University, Providence RI 02912 USA.

Observations from Magellan show that: 1) the surface of Venus is generally geologically young[1,2]; 2) there is no evidence for widespread recent crustal spreading or subduction[3]; 3) the crater population permits the hypothesis that the surface is in production[1,2], and 4) relatively few impact craters appear to be embayed by volcanic deposits suggesting that the volcanic flux has drastically decreased as a function of time[1]. These observations have led to consideration of hypotheses suggesting that the geological history of Venus may have changed dramatically as a function of time due to general thermal evolution[4,5] and/or thermal and chemical evolution of a depleted mantle layer[6], perhaps punctuated by catastrophic overturn of upper layers[6] or episodic plate tectonics[5]. We have previously examined the geological implications of some of these models[7]; here we review the predictions associated with two periods of Venus history (1. Stationary thick lithosphere and depleted mantle layer, and 2. Development of regional to global instabilities) and compare these predictions to the geological characteristics of Venus revealed by Magellan.

Presence of a stationary thick lithosphere and/or depleted mantle layer: In these scenarios, the crust has thickened to several tens of km (less than the depth of the basalt/eclogite transition) and overlies a thick depleted mantle layer[6] and/or the lithosphere has greatly thickened[4-6]. Rates of surface volcanic extrusion should have decreased with time due to evolving lithospheric thickness and increase in depleted layer thickness and should be low; present rates of volcanism are apparently low (<0.5 km^3/a), comparable to terrestrial intraplate volcanism rates[8]. Plumes ascending from depth would not penetrate to shallow depths and thus should undergo less pressure-release melting; coronae apparently represent plumes[9] and the bimodal distribution of associated flow fields may be related to time-dependent variations[10]. Plumes undergoing pressure-release melting at the base of this layer would produce MgO-rich melts which should yield very voluminous, low-viscosity surface flows[11], perhaps related to abundant large-volume lava flows and sinuous rille-like features observed[8,12]. Volcanism should be concentrated in regions above the largest upwellings; this could be consistent with the observation that much of the volcanic activity is associated with large rises such as Beta, Atla, Themis[8]. The apparent depth of compensation of many regional-scale features is much greater on Venus than on Earth[13]; these could be related to the presence of a thick lithosphere or depleted layer[5,6].

Implications of instabilities developing in a thick lithosphere and/or depleted mantle layer: Two scenarios for instabilities and surface deformation and volcanism seem plausible. In one, the residual layer becomes negatively buoyant[6] and diapirism is widespread, but the diapirs, while widespread, are not laterally or vertically coupled with the uppermost mantle and crust, and surface deformation is limited and localized to the region above the negative diapir. In this scenario, fertile mantle material would flow in to replace the lost diapir region and pressure-release melting at depths previously occupied by the depleted layer would cause extensive regional volcanism. Resurfacing would take place focused on these regional centers of diapirism. In another scenario, lithospheric instability would cause large-scale downwelling and subduction[5,6] and local crustal thickening, and rifting and the initiation of crustal spreading to create new crust in distal regions. Crustal spreading could be a major part of the renewal process, with old crust being thickened, deformed, underthrust, and possibly subducted over regions of downwelling; crustal thinning, large-scale pressure-release melting, and crustal spreading would occur over the complementary regions of the planet. Such scenarios may be consistent with many aspects of the crater population which can be interpreted to be in production and superposed on a substrate that was produced over a very short period of time about 500 m.y. ago[1]. In the process of development and evolution of instabilities in either of the two scenarios, crustal shortening, thickening, and surface deformation is likely to occur. The scales and styles will be related to the scale of the instabilities and the rheology of the crust and upper mantle material. We consider the possibility that the tessera regions represent relict sites of downwelling

associated with such instabilities[7]. Tesserae are highly deformed[14], represent regions of thickened crust[15], make up about 10% of the planet[16], often have borders suggesting deformation and underthrusting[17], and show crater densities suggesting ages somewhat older than surrounding plains[18]. Tessera borders often extend for many hundreds to thousands of km, indicating that the underthrusting events were large-scale[17]. Thus, these regions could be linked to large-scale downwelling events associated with depleted layer instabilities. For example, the major tessera occurrences (Western Ishtar, Fortuna, Laima, Tellus, Ovda, Thetis, and Alpha) could mark the sites of the individual downwellings and the collection of thickened and deformed crust; the arcuate nature of many of the borders of these tessera would indicate the regions where downwelling or underthrusting was most prominent[17]. There is good evidence that tessera extends beneath the volcanic plains in many areas, particularly in the intervening regions between the major tessera occurrences[17,20]. In addition, these major occurrence are localized in a large region centered at about 45°N, 45°, and most of the arcuate boundaries are convex away from this region. Thus, this large region is a candidate for the location of concentrated downwelling during a catastrophic event. In the subduction and catastrophic plate tectonics hypothesis[5], an organized array of spreading ridges and new crustal formation would be anticipated in regions complementary to the downwelling. Modest crustal spreading rates (similar to those on the Earth, e.g. ~5 cm/a) for a total ridge length equivalent to a planetary circumference could result in creation of new crust for between one-third and one-half of the planet in 100 million years[19]. So far, evidence for such regions has not been recognized, although some of the linear planitiae (e.g., Aino, Niobe, Sedna) flanking the tessera regions could be candidates. Alternatively, broader complementary regions of upwelling might be anticipated. Candidates for these include the Beta-Atla-Themis region, a concentration of volcanic features, extensional tectonism, broad rises, and positive gravity anomalies that makes up about 20% of the surface of Venus[8,21]. In addition, a second less well-developed region occurs in the Eistla-Bell area[22]. Thus, geologic evidence exists for both broad regions of downwelling and upwelling that might be characteristic of, or a result of, catastrophic overturn events.

Further development and tests of these scenarios: No one observation can be shown to uniquely confirm these models and scenarios, but many of the features predicted are consistent with the observed characteristics of Venus geology and geophysics. These models therefore merit further consideration; some of the things that are required to permit further analysis and testing are: 1) Better definition of the growth, stability and style of renewal of the crust, depleted layer, and lithosphere. 2) Analysis of the scale and nature of instabilities; are they characterized by catastrophic surface turnover and crustal spreading, or deeper negative diapirs and resurfacing of a relatively stable veneer? 3) If crustal spreading occurred, what geometries and rates are compatible with the cratering record. 4) What resurfacing rates are required to be consistent with the crater record and is this reasonable from a magma generation point of view?

References: 1) G. Schaber *et al.*(1992) *JGR*, 97, 13257; 2) R. Phillips *et al.* (1992) *JGR*, 97, 15921; 3) S. Solomon *et al.* (1992) *JGR*, 97, 13199; 4) J. Arkani-Hamed & N. Toksoz (1984) *PEPI*, 34, 232; J. Arkani-Hamed *et al.* (1992) *LPI Pub. 789*, 5; 5) D. Turcotte (1992) *LPI Pub. 789*, 127; 6) E. Parmentier & P. Hess (1992) *GRL*, 19, 2015; 7) J. Head et al. (1992) *LPI Pub. 789*, 45; 8) J. Head *et al.* (1992) *JGR*, 97, 13153; 9) E. Stofan *et al.* (1992) *JGR*, 97, 13347; 10) K. Magee-Roberts & J. Head (1992) this volume; 11) P. Hess & J. Head (1990) *EMP*, 50/51, 57; 12) V. Baker *et al.* (1992) *JGR*, 97, 13421; 13) R. Phillips *et al.* (1991) *Science*, 252, 651; 14) D. Bindschadler & J. Head (1991) *JGR*, 96, 5889; 15) S. Smrekar and R. Phillips (1991) *EPSL*, 107, 582; 16) M. Ivanov *et al.* (1992) *LPSC 23*, 581; 17) M. Ivanov & J. Head (1993) *LPSC 24*, this vol.; J. Head & M. Ivanov, *ibid.*; 18) A. Basilevsky & M. Ivanov (1993) *LPSC 24*, this vol.; 19) J. Head (1990) *EMP*, 50/51, 25; 20) A. Sukhanov (1986) *Geotectonics*, 20, 294; 21) L. Crumpler *et al.* (1992) *LPI Pub. 789*, 25; (1993) *LPSC 24*, this vol.; J. Head *et al.* (1992) *LPSC 23*,, 515; 22) L. Crumpler & J. Aubele (1992) *LPSC 23*, 275.

N94-16233

A MÖSSBAUER SPECTROMETER FOR THE MINERALOGICAL ANALYSIS OF THE MARS SURFACE: FIRST TEMPERATURE DEPENDENT TESTS OF THE DETECTOR AND DRIVE SYSTEM

P. Held, R. Teucher, G. Klingelhöfer, J. Foh, H. Jäger, E. Kankeleit, Institut für Kernphysik, Technical University Darmstadt, 6100 Darmstadt, Germany

Introduction: Part of the scientific payload of the Mars-96 mission is a ^{57}Fe-Mössbauer (MB) spectrometer installed on a small rover to be placed on the surface of Mars [3, 5]. The instrument is under development at the University of Darmstadt. This instrument, with some modifications, is also included in the scientific payload of the proposed MARSNET mission of the European Space Agency (ESA). A similar instrument is currently under development in the US [4].
The reason for developing a Mössbauer spectrometer for space applications is the high abundance of the element iron, especially on the surface of Mars. The elemental composition of Martian soil was determined during the Viking mission in 1976 but not it's mineralogical composition. One believes that it is composed mainly of iron-rich clay minerals, with an iron content of about 14(±2) wt-%, partly magnetic. Of extremely great interest are the oxidation state of the iron, the magnetic phases, and the mineral composition of the Mars surface. To these questions MB spectroscopy can provide important information [1, 2], which are not available by other methods. We report on first tests of parts of the experimental setup in the temperature range +20°C to -70°C, roughly corresponding to the temperature range on the surface of Mars. Also questions concerning the signal/noise ratio (s/n) are discussed.

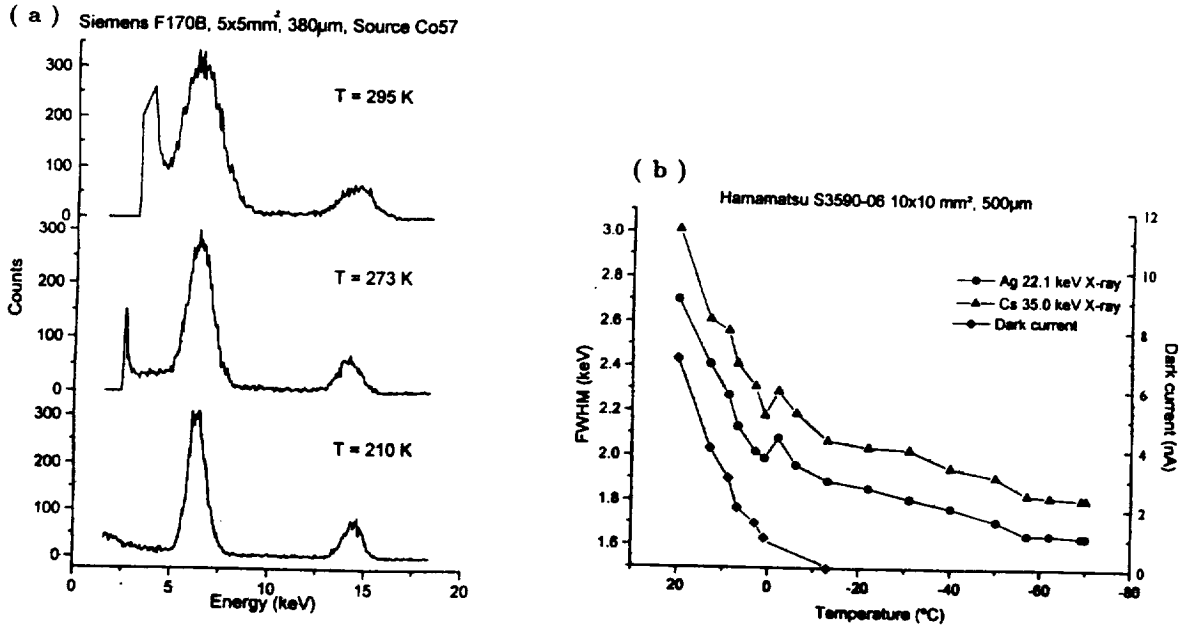

Figure 1: Temperature dependence of the energy resolution of Si-PIN-diodes: (a) 5 x 5 mm^2; 380 μm thick: 6.4 and 14.4 keV; (b) 10 x 10 mm^2; 500 μm thick: 22.1 and 35 keV;

The main parts of the **Experimental Setup**, which has been described previously [3], are the electromechanical vibrator, the detector system consisting of silicon-PIN-diodes, the electronics for the drive and the detectors, the ^{57}Co MB-source with an activity up to 1 Ci [3, 6], a multilayered

radiation shield, and a γ- and x-ray window. The total weight of the system is less than 400g, with a maximum power consumption < 2 W. The total volume will be below 700 cm^3 (comparable to a coca-cola can). Backscattering geometry was choosen, to study the rocks and soil as found.

Detector system: Our detector system for Mössbauer spectroscopy consists of at least 4 Silicon-PIN-diodes [3], with active areas of about 1 cm^2. The operating voltage is (30-100)V. The energy resolution, influencing the s/n ratio of the MB spectrum, has been measured as function of temperature (see fig.1), within a temperature range comparable to Mars ambient temperatures. As seen in fig.1, the energy resolution is improved significantly by cooling only to about 0°C. Using smaller diodes (5x5 mm^2) with low capacitance, an energy resolution of about 1 keV (at 6.4 keV) was achieved at -60°C. This shows that x-ray fluorescence measurements should be possible by using small Si-PIN-diodes, cooled to the Mars surface temperature via heat exchange.

Drive system: An electromechanical velocity transducer is chosen [3], with a diameter and length of about 20mm and 45mm, respectively. It weighs about 50g. The accuracy of the drive is found to be better than 0.3% for a triangular wave form. Velocity calibration and control of linearity will be done by recording simultaneously a calibration spectrum using a second source and a combination of reference absorbers [3]. The temperature dependence of the drive system (magnets, springs, etc.) was investigated in the range +20°C to -70°C. The strength of the magnetic field in the gap of the magnetic system, and therefore the maximal velocity, changed according to the temperature coefficient of the magnetization of the SmCo-magnets. Also the main resonance frequency increased a few percent with decreasing temperature, due to the temperature coefficient of the spring constant. Both effects have to be taken into account when planing and performing measurements on Mars.

The signal/noise ratio of Mössbauer spectra will be influenced not only by temperature effects, as discussed above, but also by other parameters as for instance (i) surface roughness of the sample (Mössbauer Albedo), (ii) width of selected energy window, (iii) shielding of the source, etc.. Also the s/n ratio will be different for MB spectra recorded with the 6.4 keV x-rays and the 14.4 keV γ-rays, respectively. Due to the different escape depth of the 6.4 and 14.4 keV radiation the corresponding MB spectra can give us information on the depth profile of Fe phases.

The detector system, including its electronic part, as well as the drive system withstand a few temperature cycles (+20°C to -70°C) without damage. Nevertheless we are planing to use (may be partly) the technique of *Hybridisation* to improve the reliability of the system. Also these technique allows further reduction in volume and weight, which is important in the case of the MARSNET, and also the MESUR mission.

References: [1] J.M.Knudsen, Hyp. Int. 47(1989)3. [2] J.M.Knudsen et.al., *Mössbauer spectroscopy on the surface of the planet Mars. Why?*, Hyp. Int. 68 (1992) 83. [3] G.Klingelhöfer, J.Foh, P.Held, H.Jäger, R.Teucher, and E.Kankeleit, *Development of a Mössbauer Backscatterring Spectrometer, including x-ray Fluorescence Spectroscopy, for the in-situ Mineralogical Analysis of the Mars Surface*, in: Fegley B. Jr. and Wänke H., eds. (1992) *Workshop on Innovative Instrumentation for the In Situ Study of Atmosphere-Surface Interactions on Mars.* LPI Tech. Rpt. 92-07, part 1, Lunar and Planetary Institute, Houston. 19pp. [4] D.G.Agresti, R.V.Morris, E.L.Wills, T.D.Shelfer, M.M.Pimperl, M.-H.Shen, and T.Nguyen, *A Backscatter Mössbauer Spectrometer (BaMS) for Use on Mars*, in: see ref. [3]. [5] E.N.Evlanov, L.M.Mukhin, O.F.Prilutski, G.V.Smirnov, J.Juchniewicz, E.Kankeleit, G.Klingelhöfer, J.M.Knudsen, C.d'Uston, In *Lunar and Planetary Science XXII*(1991), pp. 361-362. Lunar and Planetary Institute, Houston. [6] E.N. Evlanov, V.A. Frolov, O.F. Prilutskii, G.V. Veselova, A.M. Rodin, G. Klingelhöfer, In *Lunar and Planetary Science 24* (1993).

GALILEO PHOTOMETRY OF APOLLO LANDING SITES. P. Helfenstein[1], J. Veverka[1], J.W. Head[2], C. Pieters[2], S. Pratt[2], J. Mustard[2], K. Klaasen[3], G. Neukum[4], H. Hoffmann[4], R. Jaumann[4], H. Rebhan[4], A.S. McEwen[5], M. Belton[6], [1]Cornell University, Ithaca, NY 14853, [2]Brown University, Providence RI 02912, [3]Jet Propulsion Laboratory, Pasadena CA 91109. [4]Deutsche Luft und Raumfahrt, 8031 Oberpfaffenhofen, FRG, [5]U.S.Geological Survey, Flagstaff, AZ, [6]Kitt Peak National Observatory, NOAO, Tucson AZ 85719

As of December 1992, the Galileo spacecraft performed its second and final flyby (EM2) of the Earth-Moon system, during which it acquired Solid State Imaging (SSI) camera images of the lunar surface suitable for photometric analysis using Hapke's [1,2,3] photometric model. These images, together with those from the first flyby (EM1) in December 1989, provide observations of all of the Apollo landing sites over a wide range of photometric geometries and at eight broadband filter wavelengths ranging from 0.41 μm to 0.99 μm. We have completed a preliminary photometric analysis of Apollo landing sites visible in EM1 images and developed a new strategy for a more complete analysis of the combined EM1 and EM2 data sets in conjunction with telescopic observations and spectrogoniometric measurements of returned lunar samples.

No existing single data set, whether from spacecraft flyby, telescopic observation, or laboratory analysis of returned samples, describes completely the light scattering behavior of a particular location on the Moon at all angles of incidence (i), emission (e), and phase angles (α). Earthbased telescopic observations of particular lunar sites provide good coverage of incidence and phase angles, but their range in emission angle is limited to only a few degrees because of the Moon's synchronous rotation. Spacecraft flyby observations from Galileo are now available for specific lunar features at many photometric geometries unobtainable from Earth; however, this data set lacks coverage at very small phase angles ($\alpha < 13°$) important for distinguishing the well-known "opposition effect" [3]. Spectrogoniometric measurements from returned lunar samples can provide photometric coverage at almost any geometry; however, mechanical properties of prepared particulate laboratory samples, such as particle compaction and macroscopic roughness, likely differ from those of those on the lunar surface. In this study, we have developed methods for the simultaneous analysis of all three types of data: We combine Galileo and telescopic observations to obtain the most complete coverage with photometric geometry, and use spectrogoniometric observations of lunar soils to help distinguish the photometric effects of macroscopic roughness from those caused by particle phase function behavior (i.e., the directional scattering properties of regolith particles).

DATA SOURCES AND CALIBRATION:

Galileo SSI Images: Radiometric calibration of the EM2 frames is described elsewhere in this volume [4]. The calibration of the EM1 frames differ from the EM2 calibration in that the flat-field correction was accomplished with preflight data. In addition, EM1 frames were corrected for the spectral transmission, aperture, and ghost images introduced by the SSI's deployable quartz dust cover (removed shortly after EM-1). Dust particles accumulating on the cover introduced removable blemishes in the EM1 images that are not present in the EM2 frames. The relative spectral sensitivity of the SSI is currently still under study; however, calibrated SSI images of Venus, Jupiter, the Moon, 951 Gaspra, and standard calibration stars suggest the relative spectral response of the camera differs from predicted by less than 5% through most filters, but perhaps as much as 11% to 49% at violet (0.41 μm), methane-2 (0.89 μm), and 1-micron (0.99 μm) bandpasses. The SSI's absolute radiometric accuracy has not yet been fully checked so that, in this study, we have used Galileo measurements only in a relative photometric sense and used spectrogoniometry of returned lunar samples to fix reflectance values on an absolute scale.

EM1 frames provide useful coverage only for Apollo 12, 14, and 15 sites, with Apollo 12 and 14 having the most complete phase angle coverage from 19° to 130°, at spatial resolution of 4 km/pixel or better. Broadband SSI spectral coverage using most SSI filters was consistently obtained throughout the encounter. Clear filter (CLR) images were acquired only in the early stages of the encounter at large phase angles ($\alpha > 90°$) while methane-1 filter (0.73 μm) was obtained later in the encounter ($\alpha < 90°$). EM2 coverage will provide data for all of the Apollo sites $14° \le \alpha \le 123°$. In this preliminary study we have focused only on EM1 coverage of Apollo 12 and 14.

RELAB Spectra of Apollo Soil Samples: Reflectance spectra of four Apollo soil samples (Apollo 11, 10084; Apollo 12, 12070; Apollo 14, 14259; Apollo 16, 62231) were obtained relative to a Halon reflectance standard using the RELAB [5] spectrogoniometer at Brown University (Pieters et al. 1991). High-resolution spectra ($\Delta\lambda = 0.01$ μm) of each sample [6] were acquired over $0.35 \le \lambda \le 2.5$ μm. All spectra were obtained within the scattering plane over a wide range of incidence ($0° \le i \le 60°$), emission ($0° \le e \le 60°$), and phase angles ($10° \le \alpha \le 110°$). In order to scale the

sample/halon reflectance ratios to absolute radiance factors, we evaluated the absolute reflectance of Halon at all laboratory photometric geometries from a best-fit of Hapke's photometric model to National Bureau of Standards Halon reflectance data [7] ($\tilde{\omega}_0$=0.999997, h=0.79, B_0=1.51, g=0.415, where $\tilde{\omega}_0$ is single scattering albedo, h and B_0 are parameters of Hapke's opposition surge function, and g is the asymmetry factor in the well-known Henyey-Greenstein particle phase function). The high-resolution RELAB spectra were convolved with the Galileo camera and aperture cover transmission functions for each filter bandpass [8] and a solar spectrum to derive "Galileo equivalent" spectral radiance factors.

Earthbased Telescopic Data: We employed two separate sources of telescopic observations. For the Apollo 12, we used data of Shorthill et al.[9]. The effective wavelength of these data is about 0.45 μm, making it most similar to the violet (0.411 μm) Galileo observations. Their spatial resolution is about 2 km. over phase angles from 2.3° to 112°. There are no observations from Shorthill et al. (1969) near Apollo 14. Anticipating the need for such data, work was undertaken at the Deutsche Forschungsanstalt für Luft-und Raumfahrt (hereafter referred to as DLR) to acquire Earthbased telescopic CCD observations of various lunar terrains at Galileo broadband wavelengths. We have used preliminary data [10] from this source for the Apollo 14 site at a single wavelength (0.40 μm), and over phase angles from 3°-50°.

PRELIMINARY RESULTS: Our purpose in this study is to obtain well-constrained fits of Hapke's photometric parameters for the Apollo 12 and 14 sites at all SSI bandpasses. For each site, our most complete photometric angle coverage is at violet wavelengths. We began by obtaining violet-filter fits for all of the Hapke parameters with the non-linear least squares method described in Helfenstein and Veverka [10]. Since Hapke's θ and h parameters represent mechanical properties of the regolith (macroscopic roughness and regolith compaction) they should be the same at all wavelengths. Thus, for the remaining filters, we fixed θ and h at their best-fit violet-filter values and need only seek optimal values of $\tilde{\omega}_0$, B_0, and b and c parameters of the particle phase function.

Our preliminary best-fit parameters allow us to predict how the spectral properties of lunar materials change with phase and, more importantly, why these changes occur. For both areas studied, the phase functions of average particles become more strongly backward and less strongly forward scattering with increasing wavelength. The colors of lunar soils change with photometric geometry: lunar materials become "redder" with increasing phase angles for 0° to 90°, but the trend reverses and materials become "bluer" as phase angles increase beyond 90°. This effect has long been known from telescopic observations; however, we now understand that it is caused by the fact that the particle phase function behavior changes with wavelength. In addition, RELAB data for Apollo 16 samples indicate that the effect is more pronounced for highland soils than for mare soils. We expect that the addition of EM2 coverage will not only refine our fits for Apollo 12 and 14, but will provide observations for Apollo 11, 15 and 16, and 17 as well.

REFERENCES: [1] Hapke, B. (1981), **JGR 86**, 3039-3054. [2] Hapke, B. (1984) **Icarus 59**, 41-59. [3] Hapke, B.(1986), **Icarus 67**, 264-280. [4] McEwen, A. et al. (1993), this volume. [5] Pieters, C.M. (1983) **JGR 88**, 9534-9544. [6] Pieters, C.M., et al. (1991), LPSC XXII, 1069-1070. [7] Weidner, V.R. and J.J. Hsia (1981), J. Opt. Soc. Am. **71**, 856-861. [8] Breneman, H. and K. Klaasen (1988), JPL Technical Report JPL D-5880, Jet Propulsion Laboratory, Pasadena, CA 213 pp. [9]Shorthill, R. et al. (1969). NASA Contractor Report CR-1429, 405 pp. [10] Rebhan et al. (in preparation). [11] Helfenstein, P. and J. Veverka (1989), In **Asteroids**, Univ. Ariz. Press.

EMPLACEMENT OF MULTIPLE FLOW UNITS ON VERY SHALLOW SLOPES, EAST KAWELU PLANITIA FLOW FIELD, VENUS. Michael B. Helgerud (Carleton College, Northfield, MN 55057), and James R. Zimbelman (CEPS/NASM, Smithsonian Institution, Washington, DC 20560)

Lobate flows with variable radar brightness occur at several locations on Venus (1). Here we present preliminary mapping results for a lava flow field on the eastern side of Kawelu Planitia, centered at approximately 41° N, 251° E. Numerous individual flows of varying brightness can be traced for up to 400 km at this location. Magellan image F-MIDRP.40N251;1 (Fig. 1) contains two major flow complexes as well as a distinct minor flow field associated with a volcanic dome (Fig. 3). The southern flow field (unit F) changes from radar dark to radar bright in a convex arc from west to east. The flow path is diverted (see below) by a ridge system (unit B) and associated N-S faulted zone (unit A) evident in the Magellan altimetry data (2;Fig. 2). The 130-km-long radar-bright flow field located at 41.5°N and 249-250°E is comprised of a narrow, channeled flow (unit E) overlying an intermediate brightness flow (unit D), all of which appears to emanate from a solitary dome at 249°E. The southern lobe of unit E disappears under a broad leveed channel (41.3°N, 250.1°E) in unit 5 (discussed below), only to reappear south of the unit 5 boundary. The source of this largest flow field is not evident, but could be associated with the region of small domes west of the F-MIDRP image (centered at 41°N, 246°E). Another possible source is the fractured area south of unit C. The flow complex is clearly a conglomeration of many flow episodes, not necessarily from a single source. For this reason, individual flows within unit 6 are not traceable, except for the radar dark region at 40.8°N. The northern edge of the dark region is superposed on unit 6 flows while the southern margin is superposed by unit 6 flows. East of 250° longitude the relationships of flow termini provide evidence for the stratigraphy of 5 flow units. Unit 1 is the oldest, and it is covered by all other distinguishable flows. Unit 2 is the extensive radar-dark region which forms a broad "foot" on top of the eastern portion of unit 1 and which underlies units 3 and 4. Unit 3 is the partially exposed remnant of a multi-lobed, radar-bright flow east of 250° longitude. On top of this was emplaced a radar-dark flow (unit 4) traceable to approximately 250°E, where the flow has been breached by a thin lobe associated with unit 5, the youngest distinguishable flow unit. Units 3 and 4 cover and therefore postdate the graben which run north-south at 253°E, but the graben in the southwest corner formed after unit 6 had been emplaced, as evidenced by graben that crosscut the flows.

The captivating feature in this image is the distinct bend which the northern flow field undergoes at approximately 250°E. Before this investigation, it was assumed that the cause of such a pattern would be due to either topography or tectonic processes. Topography is clearly the explanation in the case of the southern flow field (unit F). The arc of the northern boundary of this flow field precisely follows the ridge belt. Altimetry data (Fig. 2) show that the slope in this region does not exceed 1-2°, and is considerably less in most places. For the northern flow field (units 1-6), the average slope is only .05°, less than the .1-.2° associated with very fluid lunar flows (3,4). Despite the minute slope, the flow field extends for nearly 500km. We suggest that these flows could have had viscosities considerably less than that generally postulated for either Venusian (6) or lunar flows (3). The only explanation for the bend in the northern flow field is found in the presence of a ridge belt (unit B) located at 40.4°N, 250°E (Fig. 1) with < 100 m relief (Fig. 3). This ridge belt is located in the correct position to deflect the flow pattern to the north and is embayed on the west by lava, clearly demonstrating it's older age with respect to the flow field. In addition the northern edge of this ridge terminates at precisely the point where the flow makes it's sharp angle, as it would if it were just clearing a deflecting obstacle. The lack of a radar bright boundary for the flow complex suggests that the boundary lacks a high degree of relief, despite the clear evidence of multiple flow episodes. Alternatively, a combination of higher eruption temperatures on Venus (6) and reduced cooling of an active flow under venusian conditions may be sufficient to explain the long flows. Computer simulations are in progress to investigate these possibilities (7).

KAWELU PLANITIA FLOW FIELD, VENUS: M. B. Helgerud and J. R. Zimbelman

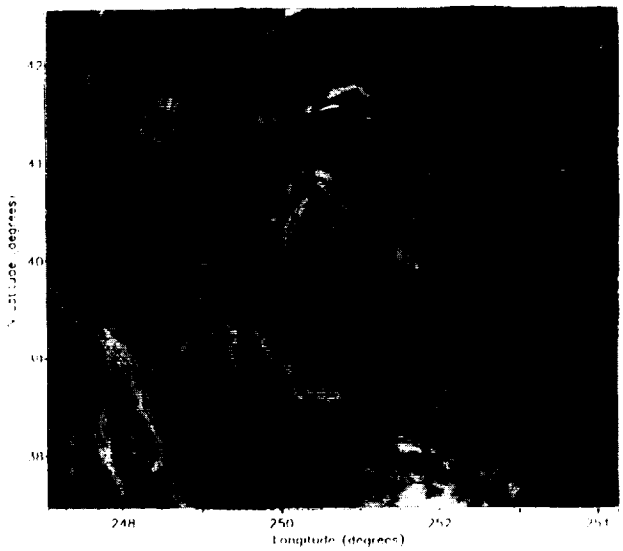

Figure 1. Magellan radar mosaic F-MIDRP.40N25;1 (see ref. 5), showing the lava flow field in eastern Kawelu Planitia.

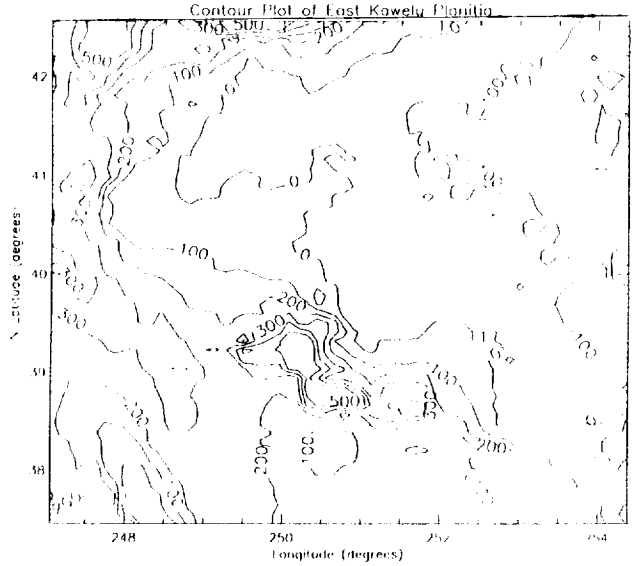

Figure 2. Contoured Magellan radar altimetry (see ref. 2) for the area shown in Fig. 1. The zero contour corresponds to the mean Venusian radius of 6051km adopted by the altimetry team.

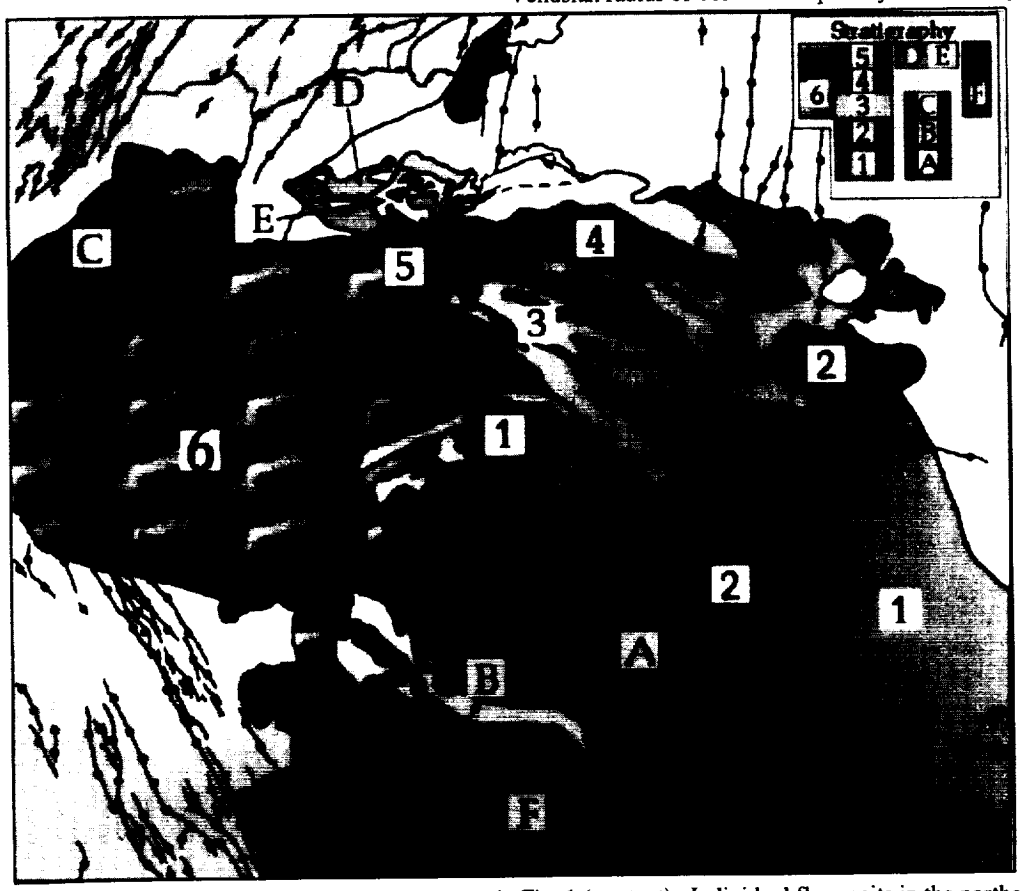

Figure 3. Simplified geological sketch map for the area shown in Fig. 1 (see text). Individual flow units in the northernmost portion of the flow field are divided into 6 units based on the stratigraphic relationships in the image. Additional units in the area are labeled A through F.

REFERENCES: 1) Head, J. W. et al., 1992, J. Geophys. Res 97, 13153-13197. 2) Magellan Altimetry, GxDR CD, MG3001 V1. 3) Schaber, G. G., 1973, Proc. LPSC 4th, 73-92. 4) LTO maps 39C2, 40A1, 40A4 (250). 5) Magellan F-Mosaics CD, MG 0044 V1. 6) Head, J.W., and Wilson, L., 1986, J. Geophys. Res. 91, 9407-9446. 7) Zimbelman, J.R., et al., 1993, LPS XXIV, this volume. [This work was carried out while M. Helgerud was an Undergraduate Intern at NASM.]

NEAR-SURFACE TEMPERATURE GRADIENTS AND THEIR EFFECTS ON THERMAL-INFRARED EMISSION SPECTRA OF PARTICULATE PLANETARY SURFACES; B.G. Henderson* and B.M. Jakosky**, Laboratory for Atmospheric and Space Physics, University of Colorado, Boulder, CO 80309-0392 (* also Department of APAS, ** also Department of Geological Sciences).

Introduction: The infrared energy emitted from a planetary surface is generated within a finite depth determined by the material's absorption skin depth. This parameter varies significantly with wavelength in the infrared but has an average value of around 50 μm for most geologic materials. In solid rock, heat transfer is efficient enough so that this 50 μm zone of the near surface from which the radiation emanates will be more or less isothermal. In particulate materials, however, heat transfer is more complicated and occurs via a combination of mechanisms, including solid conduction within grains and across grain contacts, conduction through the interstitial gas, and thermal radiation within individual particles and across the void spaces in between grains [1]. On planets with substantial atmospheres, the gas component dominates the heat transfer and tends to mitigate near-surface thermal gradients. However, on airless bodies, the gas component is absent and heat transfer occurs via solid conduction and radiation. If the particles are small relative to the average absorption skin depth, then the top 50 - 100 μm or so of the surface will be cooled by radiation to space allowing the creation of significant near-surface thermal gradients. In those regions of the spectrum where the absorption coefficient is low, the emission will come from the deeper, warmer parts of the medium, whereas in regions of high absorption, the emission will emanate from shallower, cooler parts of the medium. The resulting emission spectrum will show non-compositional features as a result of the thermal structure in the material.

We have modeled the heat transfer in a particulate medium in order to determine the magnitude of near-surface thermal gradients for surfaces on airless bodies and on Mars. We use the calculated thermal structure to determine the effects it has on the infrared emission spectrum of the surface.

Model Description: We have constructed a layered thermal model to calculate the heat exchange within a particulate planetary surface. At present, our model treats the medium as a homogeneous material in which heat is transferred between layers via conduction (solid and gas components) and radiation (radiative component).

We have assumed that the medium is purely emitting and absorbing (no scattering) which would be the case for a material consisting of particles very small relative to the wavelength of emission. Layer opacities at each wavelength are calculated by scaling the optical constants to the appropriate density using the Rayleigh scaling law [2]. The model layers are heated from below and the medium is allowed to cool until a steady-state temperature profile is reached at which point we calculate a spectrum by determining the brightness temperature of the medium at each wavelength.

Results: Preliminary results indicate that spectra from our modeled surfaces (for both Mars and airless bodies) show significant differences from spectra of isothermal surfaces. These differences are attributed to near-surface thermal gradients over the range of depths from which the emission is generated. Our results demonstrate the importance of calculating the effects of near-surface temperature gradients in interpreting thermal emission spectra for both Mars and the Moon.

References: [1] Wechsler, A.E., P.E. Glaser, and J.A. Fountain, in *Thermal Characteristics of the Moon*, J. Lucas, ed., MIT press, 1972. [2] Campbell, M.J. and J. Ulrichs, *J. Geophys. Res.*, **74**, 5867-5881, 1969.

BUBBLE COALESCENCE IN MAGMAS

Richard A Herd & Harry Pinkerton
Environmental Sciences Division, Lancaster University, Lancaster, LA1 4YQ, U.K.

Summary: The most important factors governing the nature of volcanic eruptions are the primary volatile contents, the ways in which volatiles exsolve, and how the resulting bubbles grow and interact. In this contribution we assess the importance of bubble coalescence. The degree of coalescence in alkali basalts has been measured using Image Analysis techniques and it is suggested to be a process of considerable importance. Binary coalescence events occur every few minutes in basaltic melts with vesicularities greater than around 35%.

Introduction Several processes influence the bubble size distribution (BSD) in a solidified volcanic rock, *e.g.* nucleation, diffusional growth, decompressional growth, coalescence and loss by dissolution, ascent or fracturing. Sparks [1] described the major controls on the growth of bubbles in supersaturated melts, but did not incorporate the effect of bubble coalescence. Coalescence is important because it is a spontaneous process leading to a reduction in the free energy of the gas, and it has three major consequences: *Physical and rheological properties.* Coarsening of the mean bubble size affects the tensile strength, permeability and viscosity of a vesiculated magma, altering its behaviour during ascent and eruption. Binary coalescence in a foam halves its tensile strength and increases its permeability to gas flow by 60%. *Gas separation.* Coalescence facilitates the separation of gas from magma due to the improved collection of gas and the increased ascent velocity of bubbles. This is particularly important in shallow, long-lived magma bodies undergoing continuous degassing and influences eruption dynamics. High degrees of coalescence control the spasmodic style of Strombolian explosive activity [2–4]. *Volumetric changes.* In low pressure environments, significant gas expansion accompanies coalescence, increasing the vesicularity of lavas and bombs. The amount of inflation is obtained by considering the pressures inside bubbles in magmas. The internal pressure, P_b in a non-growing bubble is given by:

$$P_b = h\rho g + \frac{2\sigma}{r} + P_{atm}$$

The number of moles of gas is constant before and after coalescence, *i.e.*: $PV_n = nPV$, where n is the number of bubbles that coalesce and V_n is the volume of the resulting bubble, or specifically:

$$\left(h\rho g + \frac{2\sigma}{r_n} + P_{atm}\right) r_n^3 = n\left(h\rho g + \frac{2\sigma}{r} + P_{atm}\right) r^3$$

where r_n is the new bubble radius, r the initial radius, and the other symbols have their standard meanings. If the pressure generated due to surface tension (σ) is significant relative to the other pressure terms, then there is a noticeable net expansion of the new bubble. Solutions are given in Fig. 1 for coalescence on the surface of Earth and Mars for bubbles of 1 mm diameter. The expansion of the gas phase on Earth would be only 1.5%, but on Mars it is 16%.

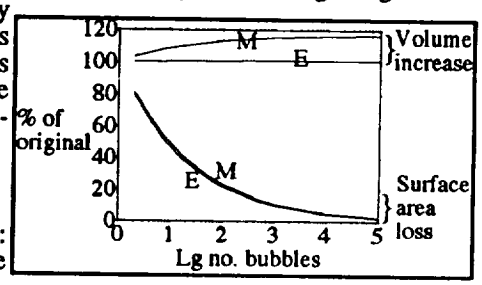

Fig. 1. Plot showing changes in volume of the gas phase and total surface area as a function of no. of bubbles, during coalescence on Earth (E) and Mars (M).

Unambiguous evidence of coalescence can be seen in samples when the common wall between two bubbles has failed and partially coalesced bubbles are observed. However, the septum of the common wall will retract due to surface tension, leaving a single, larger bubble with no evidence of coalescence. Consequently, visual inspection of the samples cannot be used to determine the e tent of coalescence. We have used image analysis techniques to model the degree (*i.e.* values of n) and rate of coalescence in vesiculated samples. The lower cooling rate of the interiors allows a greater time for vesiculation and interaction of bubbles, resulting in strong zonation with respect to vesicularity and bubble size, both increasing towards the centre of the sample. Bombs, lava crusts and aa blocks from Mt. Etna have been used in this study.

Methods Ten samples of alkali basalts were sawn perpendicular to their crusts. Vesicles on their polished surfaces were filled with a white matrix of alumina to produce a strong colour contrast between rock and vesicles. The samples were scanned using a Hewlett Packard ScanJet Plus at a resolution of 85 μm/pixel and the 8-bit images processed on a Macintosh IIci. Image analysis software (*NIH Image*) was used to measure raw properties (areas, perimeters, orientations and axial lengths) of bubble intersects on binary images. Stereological theory [5,6] was used to convert raw properties measured on 2-D images to the related properties of 3-D samples. These included bubble size analyses and morphological properties, *i.e.* bubble number density (N_v, the number of bubbles per unit volume), porosity (ϕ), mean radius (r) and specific surface area (S_v, surface area per unit volume). Models have been developed to follow the evolution of bubbles in related samples (related by, cooling time in a zoned sample, position in a lava flow, *etc.*). Vesiculation expands a melt and can be dominated by nucleation or diffusion. Coalescence, which reduces S_v but does not affect the value of ϕ, may be superimposed on these processes. Point A on Fig. 2 represents the vesicularity of a clot of magma erupted with a given ϕ and S_v. During protracted cooling, if sufficient volatiles are available for continued degassing, the sample could evolve along the nucleation, diffusion or coalescence paths. The final path taken is potentially a combination of all three processes.

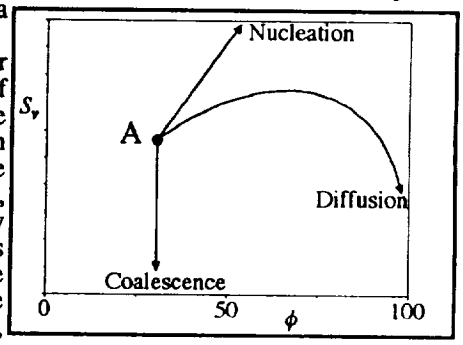

Fig. 2. Paths taken by a magma erupted at A depending upon the dominant vesiculation process on an S_v v. ϕ plot.

BUBBLE COALESCENCE IN MAGMAS

Richard A Herd & Harry Pinkerton

The margins of each sample we have studied are dense relative to their interiors and they are assumed to represent the state of the melt on eruption (*i.e.* point A on Fig. 2). It is further assumed that the interiors have followed a growth path from this point. In order to evaluate the contribution of the three processes, growth curves have been fitted to the measurements made on the margins of each sample.

Results Results for sample RH/E8 are shown (Fig. 3) as a profile of ϕ and S_v as functions of position and then as S_v against ϕ to estimate the degree of coalescence by comparison with a diffusional growth curve. *Bombs and aa blocks.* All samples show an increase in ϕ as the interior of a sample is approached, with an equivalent fall in S_v. This is due to the combined effects of diffusional growth and coalescence. RH/E8 has been used to show how the number of coalescence events is calculated (Fig. 3b). A single binary coalescence event produces a 21% reduction in S_v. For RH/E8, the bubbles in the interior grew as a result of diffusion, taking ϕ from 50% to over 80% coupled with 6–7 binary coalescence events, giving an S_v which is 22% of that predicted by the growth curve. *Lava crusts.* Data obtained from lava crusts is complicated by the possibility of additional bubbles ascending from the hotter interior of the flow. One sample shows extensive coalescence. Bubbles in the upper part of its crust fit exactly on the growth curve; lower in the crust, at high porosities, coalescence has been extensive and the measurements are displaced below the growth curve. Our other lavas have low porosities (<30%) and show a positive correlation between ϕ and S_v as they are on the early part of a growth curve and few bubbles have interacted.

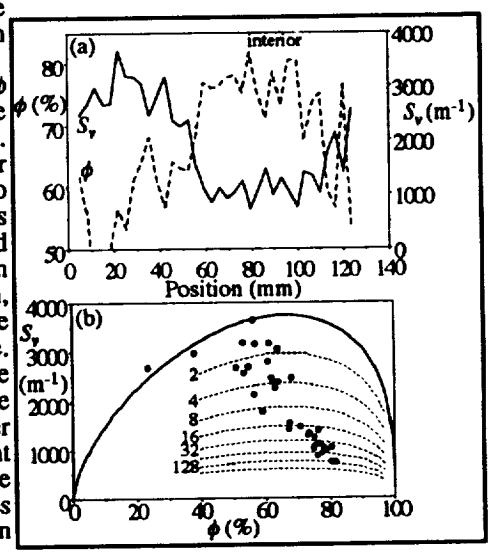

Fig. 3. (a) Profile of ϕ and S_v through RH/E8. Note that the inflated interior has the lowest S_v, (b) Plot of S_v against ϕ. Top curve is path taken for diffusion only, underlying curves indicate reduced S_v due to coalescence. The number of bubbles involved is shown to the left of each curve.

Discussion Field measurements [7] and theoretical studies (Kent, pers. comm) indicate that a 5 cm thick crust can form on the top of a basalt flow in about 30 min. In view of the small sample size, this has been taken as the maximum time for bubble growth and interaction after eruption, indicating binary coalescence events every few minutes. If magmatic foams can form at the tops of shallow magma chambers [8,9], their lifetimes should be carefully evaluated as the speed of coalescence suggested here would indicate collapse to dense melt and free gas in a few hours. This would result in free gas at the top of a chamber, overlying a zone of frothy melt undergoing coalescence and film drainage above melt whose vesicularity decreases with depth.

Aubele *et al.* [10] describe a model for the vesiculation of lavas, based on diffusional growth and ascent of bubbles. If their model was obeyed by all our samples, ϕ and S_v would both increase downwards at all values of ϕ. This is seen in our low porosity samples. At higher porosities, the effect of coalescence becomes significant reducing S_v. Walker [11] and Sahaigan *et al.* [12] observed significant bubble coalescence in basaltic flows. At porosities greater than 30–35%, the Aubele *et al.* model should be modified to include this effect.

Limitations of this study. It is stressed that this method underestimates both the degree and rate of coalescence because: (i) the samples are compared with the diffusion growth curve which predicts a minimum number of events compared to nucleation; and (ii) the cooling rates assume a dense rock equivalent. They do not include radiative heat loss across bubble walls or forced convective heat loss from the bombs during passage through the atmosphere. The models assume spherical geometry and so have limitations at high vesicularities, due to close packing. At all gas fractions a range of bubble sizes is observed, rather than a single size as modelled.

Conclusions We have put forward a simple method for measuring the degree of nucleation, diffusional growth and coalescence of bubbles in vesicular, volcanic rocks. The technique has been applied to a series of alkali basalts from which we conclude the following: (i) Bubble coalescence is detectable in vesicular rocks at porosities as low as 35%. Above this porosity, coalescence is extensive and S_v is inversely correlated with ϕ; (ii) Binary coalescence events occur on timescales of a few minutes, suggesting that basaltic foams will collapse and separate to melt + free gas in a few hours; and (iii) Given the degree of coalescence measured in our samples, products erupted into a low pressure atmosphere will suffer a marked expansion and increase in vesicularity solely due to coalescence of bubbles. Foams of more viscous magma will be longer-lived [8] but still undergo steady coalescence, which aids degassing. Coalescence is a general process that should be considered in the late stages of magmatic evolution when gas may coexist with the magma, and during the vesiculation history of lavas and pyroclastics.

Acknowledgements Many thanks to Russell Kent for the provision of two samples and discussions about cooling rates and to the NERC for studentship GT4/90/GS/53.

References [1] Sparks RSJ (1978) J. Volcanol. Geotherm. Res., 3:1–37. [2] Blackburn EA, Wilson L & Sparks RSJ (1976) J. Geol. Soc. Lond., 132:429–440. [3] Wilson L & Head JW III (1981) J. G. R., 86 B4:2971–3001. [4] Vergniolle S & Jaupart C (1986) J. G. R., 91(B12):12842–12860. [5] Cruz Orive L-M (1976) J. Micros., 107:1–18. [6] Russ JC (1986) Practical Stereology. Plenum Press, New York. [7] Jones AC (1992) (Unpub. PhD Thesis, Uni. Lancaster). [8] Jaupart C & Vergniolle S (1989) J. fluid. Mech., 203, 347–380. [9] Parfitt EA, Wilson L & Head JW III. (1992) J. Volcanol. Geotherm. Res., in review. [10] Aubele JC, Crumpler LS & Elston WG (1988) J. Volcanol. Geotherm. Res., 35:349–374. [11] Walker GPL (1989) Bull. Volcanol., 51:199–209. [12] Sahaigan DL, Anderson AT & Ward B (1989) Bull. Volcanol., 52:49–56.

THERMAL INERTIA AND RADAR REFLECTIVITY OF THE MARTIAN NORTH POLAR ERG: LOW-DENSITY AGGREGATES; K. E. Herkenhoff, Geology and Planetology Section, Jet Propulsion Laboratory, California Institute of Technology, Pasadena, CA 91109

The north polar layered deposits on Mars appear to be the source of the dark material that comprises the north polar erg [1]. The physical properties and chemical composition of the erg material therefore have important implications for the origin and evolution of the Martian layered deposits. Viking bistatic radar and infrared thermal mapping (IRTM) data indicate that the bulk density of the erg material is lower than that of the average Martian surface [2,3]. These data are consistent with hypotheses involving formation of filamentary sublimation residue (FSR) particles from erosion of the layered deposits [4,5]. The color and albedo of the erg and of the layered deposits, and the presence of magnetic material on Mars, suggest that the dark material is composed of low-density aggregates of magnetic dust grains, perhaps similar to FSR particles created in laboratory experiments.

Magnetic FSR Particles

Sublimation of dust/ice mixtures has been shown to result in the formation of FSR particles of various sizes [6]. Such particles can saltate along the Martian surface, and may therefore create dunes [4,7]. In order to form saltating material that is at least 3 times darker (in red light) than the bright dust that mantles much of Mars, dark dust grains must preferentially form FSR particles. Magnetic dust grains would be expected to form FSR more easily than non-magnetic dust, and are probably much darker. Experimental formation of FSR with magnetic material has not been attempted, and should be the subject of future research.

There is direct evidence for 1-7% magnetic material (magnetite or maghemite) in the surface fines at the Viking lander sites [8]. In addition, analysis of Viking lander sky brightness data indicates that suspended dust over the landing sites contains about 1% opaque phase, perhaps of the same composition as the magnetic material on the surface [8,9]. Within the uncertainties in these measurements, the percentages of magnetic material given above are identical to the volume of dark dune deposits in the polar regions expressed as a percentage of the estimated volume of eroded layered deposits [10-12]. This comparison indicates that the presence of magnetic dust in the layered deposits is likely, and that formation of dunes from dark FSR particles is plausible. Eventual destruction of the particles could allow recycling of the dark dust into the layered deposits via atmospheric suspension. Under the assumption that FSR can be formed by sublimation of mixtures of water ice and magnetic dust, the thermal properties of this material have been estimated and compared with observational data, as detailed below.

Thermal Inertias

A recent study using Viking IRTM observations of an area completely covered by dunes within the north polar erg [11] shows that the dunes have thermal inertias of less than 100 J m^{-2} $sec^{-1/2}$ K^{-1} [2]. Previous interpretations of Martian thermal inertia data in terms of particle sizes have utilized the relationship between these quantities presented by Kieffer *et al.* [13], which is based primarily upon measurements of the thermal properties of quartz sands [14]. The low albedos of Martian dunes are inconsistent with a siliceous composition, so basalt grains and magnetite FSR are considered here. The thermal conductivities of the materials considered here are only weakly dependent on temperature between 200 and 300 K, so values measured near 300 K have been used in all cases.

The thermal conductivity of basaltic sands is about 1.2 x 10^{-2} W m^{-1} K^{-1} (~40%) less than that of pure quartz sands of the same size (~100 microns). If the polar dunes are composed purely of basaltic grains, their effective particle size is no greater than about 50 microns (40% porosity). Particles in this size range will be transported by atmospheric

suspension [15], and are therefore not likely to form dunes. Hence, low-inertia materials that are capable of saltation must be examined as possible dune-forming materials on Mars. The thermal properties of FSR particles are therefore estimated below.

The density of magnetite is 5200 kg m^{-3}, almost twice that of quartz (2650 kg m^{-3}) or basalt (2680-2830 kg m^{-3}). The specific heat of magnetite is 544 J kg^{-1} K^{-1} at 220 K [16], only slightly less than the specific heat of various silicates [17]. The porosity of clay FSR formed in laboratory experiments is 99% [6]. Magnetite FSR would therefore have a bulk density of only 52 kg m^{-3}. The thermal conductivity of porous clay at 313 K, 740 torr ranges from 0.477 to 2.05 W m^{-1} K^{-1}, depending on water content [16]. The lowest value is identical to that of clay FSR [6]. When this dry clay was placed in a high vacuum, its thermal conductivity decreased only 7%. Therefore, the conductivity of clay FSR at 6 mbar is probably no greater than 0.47 W m^{-1} K^{-1}. The thermal conductivity of clay *minerals* is probably similar to that of most silicates, about 2.8 times less than the conductivity of magnetite. Hence, magnetite FSR should have a thermal conductivity of 1.2 W m^{-1} K^{-1} or less, implying a thermal inertia of no more than 187 J m^{-2} $sec^{-1/2}$ K^{-1}. The thermal inertia of ensembles of FSR particles may be lower still, and is compatible with the north polar erg thermal inertias derived from Viking data.

Radar Reflectivity

Viking bistatic radar data show that the north polar erg is rougher and less reflective (and therefore less dense) than surrounding terrains [3]. Increased radar roughness is expected for dune fields, and their low apparent density is consistent with the presence of FSR particles. Although magnetite is a conductor, experiments involving low-density suspensions of conductors in dielectrics [18,19] suggest that the index of refraction (and therefore reflectivity) of magnetite FSR might be very low. The results of further analysis of theoretical and experimental work on loaded dielectrics will be discussed at the conference.

REFERENCES:

[1] Thomas, P. C., and C. Weitz (1989). *Icarus* **81**, 185-215.
[2] Paige, D. A. *et al.* (1992). "Thermal and albedo mapping of the polar regions of Mars using Viking thermal mapper observations: 1. North polar region. Submitted to *J. Geophys. Res.*
[3] Simpson, R. A., and G. L. Tyler (1981). *Icarus* **46**, 361-389.
[4] Saunders, R. S., *et al.* (1985). *NASA Tech. Mem.* **87563**, 300-302.
[5] Herkenhoff, K. E., and B. C. Murray (1990). *J. Geophys. Res.* **95**, 1343-1358.
[6] Storrs, A. D., *et al.* (1988). *Icarus* **76**, 493-512.
[7] Saunders, R. S., and D. T. Blewett (1987). *Astron. Vestnik* **21**, 181-188.
[8] Hargraves, R. B., *et al.* (1979). *J. Geophys. Res.* **84**, 8379-8384.
[9] Pollack, J. B., *et al.* (1979). *J. Geophys. Res.* **84**, 4479-4496.
[10] Thomas, P. (1982). *J. Geophys. Res.* **87**, 9999-10008.
[11] Lancaster, N., and R. Greeley (1991). *J. Geophys. Res.* **95**, 10921-10927.
[12] Herkenhoff, K. E. (1990). *Lunar Planet. Sci.* **XXI**, 495-496.
[13] Kieffer, H. H., *et al.* (1973). *J. Geophys. Res.* **78**, 4291-4312.
[14] Wechsler, A. E., and P. E. Glaser (1965). *Icarus* **4**, 335-352.
[15] Edgett, K. S., and P. R. Christensen (1991). *J. Geophys. Res.* **96**, 22,765-22,776.
[16] Touloukian, Y. S., *et al.* (1970). In "Thermophysical Properties of Matter," vols. 2 and 5, IFI/Plenum, New York.
[17] Winter, D. F., and J. M. Saari (1969). *Astrophys. J.* **156**, 1135-1151.
[18] Kelley, J. M., *et al.* (1953). *J. Appl. Phys.* **24**, 258-262.
[19] Pettengill, G. H., *et al.* (1988). *J. Geophys. Res.* **93**, 14,881-14,892.

THE THREE AGES OF VENUS: A HYPOTHESIS BASED ON THE CRATERING RECORD;

R. R. Herrick, Lunar & Planetary Institute, 3600 Bay Area Blvd, Houston, TX 77058

The elevation range of 6051.9 - 6053.9 km on Venus is deficient in craters but has a high proportion of embayed and tectonically deformed craters. On the basis of this data and previous work, I propose that Venus has experienced three distinct geologic ages: pseudo-plate tectonics until 1 - 2 Ga, volcanic flooding of low-lying areas, and currently hot spot tectonics.

THE CRATERING RECORD. Previous work [1] showed that the global areal distribution of impact craters cannot by itself be distinguished from a spatially random population, but embayed (by volcanism exterior to the crater) and tectonized (fractured or faulted floor) craters are in areas with lower-than-normal crater density and high crater density is associated with areas of low radar backscatter. However, the crater distribution is distinctly nonrandom with elevation. Figure 1 shows elevation histograms (% of craters in 500-m elevation bins) for the observed crater population and 100 Monte Carlo simulations of randomly placed crater populations. The observed crater population is deficient relative to the mean of the simulations in the 6051.9 - 6053.9 km elevation range, and below the minimum of the simulations in the 6051.9 - 6052.9 km range. Similarly, an excess in the observed data exists in the 6049.9 - 6051.4 km range, and this excess is above the maximum of the simulations for 6050.4 - 6051.4 km. Thirty-two percent of the planet's surface area resides in the 6051.9 - 6053.9 km range, which contains only 22% of the craters. Thirty-five percent of the surface is in the 6049.9 - 6051.4 km range, which contains 45% of the craters.

Figure 1. Histograms of impact craters vs. elevation. Connected squares are observed data and vertical line seqments are maximum, minimum, and mean of 100 Monte Carlo simulations of a random distribution.

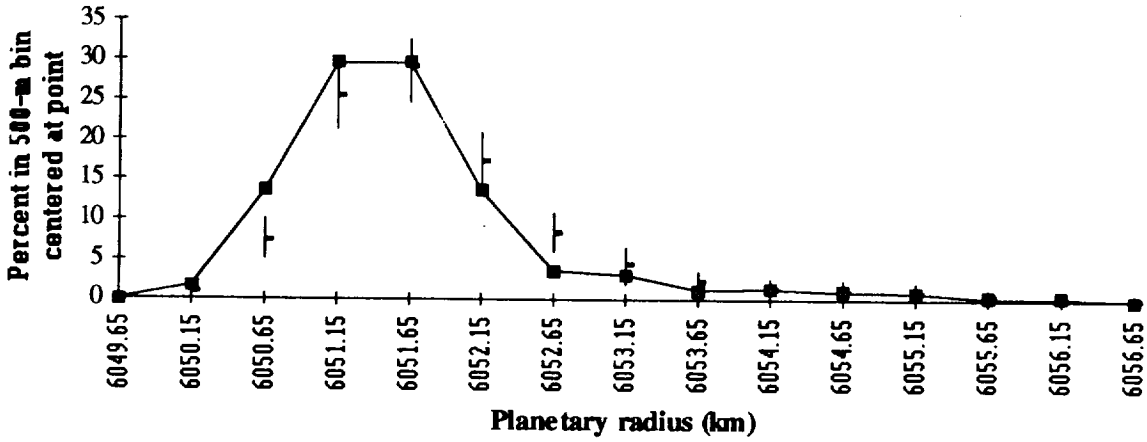

For the scenario of a near-global resurfacing followed by a constant rate of limited resurfacing, Figure 1 implies that the limited resurfacing has covered 40 - 50% of the planet since the global event. If all elevation ranges are undergoing resurfacing, the rate in the 6051.9 - 6053.9 km range must be double the rate for the 6049.9 - 6051.4 km range. The idea that resurfacing has been concentrated in the 6051.9 - 6053.9 km range is supported by the fact that the mean elevation of unmodified craters is 6051.6 ± 0.8 km, but the mean for embayed craters is 6052.8 ± 1.3 km and the mean for tectonically deformed craters is 6052.3 ± 1.1 km. Furthermore, 33% of the craters in the 6051.9 - 6053.9 km range are either embayed or tectonized, as opposed to only 5% of the craters in the 6049.9 - 6051.4 km range and 18% of the entire crater population.

THE THREE AGES OF VENUS: Herrick R. R.

GEOLOGICAL AND GEOPHYSICAL OBSERVATIONS. Of course, differences in resurfacing with elevation actually correspond to differences in resurfacing rates for different geologic settings. Elevations below mean planetary radius (6051.9 km) are dominated by largely featureless plains, whereas the highest elevations are composed of mountain belts, tesserae, or volcanic summits. The middle elevations (6051.9 - 6053.9 km) are populated by rifts, coronae, and volcanic swells. Initial analysis of the terrain type that an impact crater is located in indicates that embayed craters occur preferentially on or near volcanoes and tesserae terrains but generally are not found in the plains. Tectonically deformed craters occur preferentially in rift/coronae systems and tesserae and also are usually not in the plains.

Before using the above observations to speculate on the resurfacing history of Venus, it is important to note some of the properties of the different geologic settings on Venus. Tesserae regions are the only areas on Venus that show large-scale horizontal movement of the crust, as evidenced by linear compressive mountain belts [2], large-offset strike slip faults [3], and indenter zones [3]. Tesserae are generally embayed by plains and may be "basement" material for a large percentage of the planet's surface [4]. Large volcanoes are often connected by systems of rifts and coronae and frequently have numerous flows that extend out onto otherwise featureless plains. The long-wavelength geoid is strongly correlated with the locations of large volcanoes on Venus, suggesting that these regions are currently active [5]. However, no correlation exists between the geoid and locations of large tesserae regions [5].

THE THREE AGES OF VENUS HYPOTHESIS. On the basis of the above observations, I propose that Venus has undergone three distinct geologic episodes:

1. Some form of pseudo-plate tectonics existed until 1 - 2 Ga. Pseudo-plate tectonics ceased when mantle cooling reduced the surface-mantle temperature differential enough to make the lithosphere too bouyant to subduct. Tesserae represent the remnants of this age. The term "pseudo-plate tectonics" does not necessarily imply a well-organized set of distinct plates as on Earth but does imply crustal formation through lithospheric spreading, crustal recycling through subduction, and large-scale horizontal movement of surface material.
2. Cessation of crustal recycling effectively changed the mantle convection boundary condition from free-slip to no-slip. Consequently, the mantle temperature rose enough to induce a brief period of partial melting in the uppermost mantle that caused global volcanic fooding of low-lying areas.
3. Since the time of global volcanic flooding, the style of volcanism and tectonism on Venus has been dominated by "hot spot" tectonics [6], heat release through lithospheric thinning over upwelling plumes. The upwelling plumes and their associated lithospheric stresses cause large volcanoes and limited horizontal movement of the lithosphere and is manifested as rifts and associated coronae.

The relatively rapid and synchronous formation of the plains accounts for the mostly pristine and uniform crater population. Active crustal recycling and deformation prevented the tesserae regions from being more than a few hundred Ma older than the plains. The deficit of craters at 6051.9 - 6053.9 km is a consequence of hot spot tectonics.

FUTURE WORK. Much work needs to be done before the above hypothesis can be considered a viable theory. The proposed cooling history for the Venusian mantle needs to be tested for plausibility through convection modeling. Traditional stratigraphic analysis of Venus needs to be done, particularly with regard to whether any major regions of tesserae are stratigraphically young. The cratering record for different terrain types, or even different geologic units, needs to be carefully analyzed. Detailed analysis of existing and future gravity data sets may yield further insight on which surface features are geologically active.

REFERENCES. [1] Phillips R. J. *et al.* (1992) *JGR, 97,* 15923. [2] Suppe J. and Connors C. (1992) *JGR, 97,* 13545. [3] Pohn H. A. and Schaber G. G. (1992) *LPSC XXIII,* 1095. [4] Ivanov M. A. *et al.* (1992) *LPSC XXIII,* 581. [5] Herrick R. R. and Phillips R. J. (1992) *JGR, 97,* 16017. [6] Phillips R. J. and Malin M. (1983) *Venus,* 159.

N94-16240

^{26}Al-^{26}Mg AGES OF IRON METEORITES: G.F. Herzog[1], A.E. Souzis[2], S. Xue[1], J. Klein[3], D. Juenemann[3], and R. Middleton[3]. 1) Dept. Chemistry, Rutgers Univ., New Brunswick, NJ 08903; 2) US Army Research Lab., EPSD, Fort Monmouth, NJ 07703-5601; 3) Dept. Physics, Univ. Pennsylvania, Philadelphia, PA 19104.

Introduction. An exposure age for an iron meteorite can be calculated from measurements of a radioactive nuclide and a stable nuclide that are produced by similar sets of nuclear reactions, provided that the stable nuclide is present with low initial abundance. The standard methods rely on either ^{40}K ($t_{1/2}$ = 1.26 Gy), ^{39}K, and ^{41}K (e.g., [1,2]) or on a shorter-lived radionuclide and a stable, noble gas isotope. Widely used pairs of this type include ^{36}Cl/^{36}Ar and ^{26}Al /^{21}Ne (e.g., [3] and [4]). Other pairs may serve the purpose for iron meteorites contain many stable isotopes besides those of K and the noble gases that are produced partly by cosmic rays [5-8]. We consider here the calculation of exposure ages, t_{26}, from measurements of ^{26}Al ($t_{1/2}$ = 0.7 My) and (stable) ^{26}Mg. Ages based on ^{26}Al/^{26}Mg ratios, like those based on ^{36}Cl/^{36}Ar ratios, are "buffered" against changes in relative production rates due to shielding because decay of the radioactive nuclide accounts for a good part of the inventory of the stable nuclide.

Experimental Methods. Encouraged by the work of [7] and [8], we decided to apply the method of glow-discharge mass spectrometry to the analysis of stable isotopes in iron meteorites. This method is capable of part-per-trillion (ppt) detection limits at high mass resolution (> 4000). Samples were introduced into the VG 9000 spectrometer as "pins," i.e., rectangular solids ~ 20 x 2 x 2 mm trimmed to size with a diamond-studded saw. The sample of Tlacotepec was taken adjacent to the one analyzed by Smith and Huneke [7]. Before data acquisition began, the samples were subjected to 0.5-1 h of sputtering at 1 kV and 5 mA (Ar^+) in order to remove surface contamination. Data were then acquired using discharge conditions of 1 kV and 3 mA. Initially, a broad elemental survey requiring ~3 h and covering the mass range from 6 to 59 AMU was taken for each sample. This survey was followed by longer (4 h) and more detailed measurements of the isotopic magnesium concentrations (24-26 AMU). Each mass window was scanned 200 times and the resulting signals were summed and averaged. Each window consisted of 100 channels with a dwelltime/channel of 100 ms. In separate experiments, the ^{26}Al activities of 4 iron meteorites were measured by accelerator mass spectrometry [9].

Results. Figure 1 shows the results obtained for minor and trace elements from the elemental scan for Tlacotepec. Concentrations were calculated from the raw data using *R*elative *S*ensitivity *F*actors (RSFs) developed from previous analyses using NBS standards. For those elements for which we had no standard, the RSFs supplied by VG with their software were used. The uncertainties estimated from the reproducibility of the measurements for Tlacotepec and the other irons vary considerably: from ~2% for the major elements Fe and Ni, to ~10% for the minor elements, to 30-100% for the trace elements. Also shown in Figure 1 are the results of Smith and Huneke [7] for Tlacotepec. Agreement is good for the major elements (Fe = 84.0% vs. 82% and Ni = 15.9% vs. 17%). For the other elements, the concentrations of ref. [7] typically exceed ours by 5% to 100%, perhaps because a different library of RSFs was used. Table 1 and Figure 2 show the

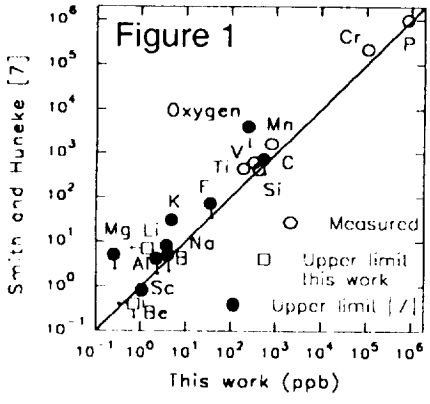

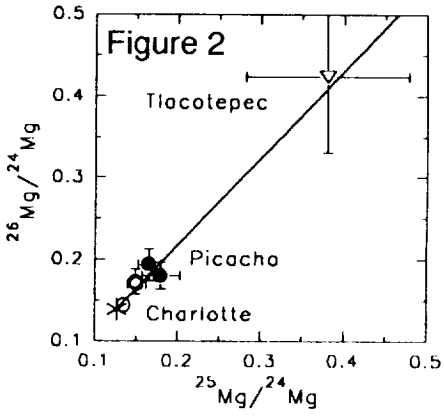

magnesium isotopic data for Charlotte, Picacho, and Tlacotepec. The errors plotted in Figure 2 are conservative. The isotopic ratios for Tlacotepec agree well with those of ref. [7]. The experimental points plot (within error) on a line defined by terrestial Mg and cosmogenic Mg, taken here to have the composition $^{24}Mg/^{26}Mg$ = 0.90 and $^{25}Mg/^{26}Mg$=0.95 in analogy with cosmogenic neon. The irons studied contain between 2% and 30% of cosmogenic ^{26}Mg ($^{26}Mg_c$). The ^{26}Al activities, which are only in fair agreement with results reported previously [4] are given in Table 2.

Table 1. Mg (ppt) in iron meteorites.

Sample	^{24}Mg	^{25}Mg	^{26}Mg	$^{26}Mg_c$	$^{24}Mg_p$
Charlotte (4A)	1533± 20	231 ± 17	261 ± 10	47 ± 12	1488 ± 23
	2041 ± 26	304 ± 15	353 ± 30	69 ± 35	1975 ± 42
	3385 ± 67	458 ± 23	487 ± 25	1 ± 31	3383 ± 73
Picacho (3A)	1242 ± 44	207 ± 15	239 ± 22	70 ± 26	1175 ± 50
	1074 ± 37	193 ± 24	193 ± 16	45 ± 20	1031 ± 42
Tlacotepec (4B)	257 ± 41	98 ± 20	109 ± 16	83 ± 20	178 ± 45

$^{26}Al/^{26}Mg$ Ages. To calculate $^{26}Al/^{26}Mg$ ages, t_{26} (Table 2), we assume single-stage irradiations at production rates, P(^{26}Mg) and P(^{26}Al) [atom/My], that are constant for each meteorite. In addition, we can plausibly assume that the exposure ages and the terrestrial ages of the iron meteorites are long and short, respectively with respect to the half-life of ^{26}Al so that the measured ^{26}Al activity equals P(^{26}Al) in each case. Under these conditions it can shown that

$$t_{26} = \frac{44.1 \times {}^{26}Mg(ppt)/{}^{26}Al(dpm/kg)}{[1 + P({}^{26}Mg)/P({}^{26}Al)]}$$

Table 2. $^{26}Al/^{26}Mg$ ages of four iron meteorites.

Meteorite	^{26}Al (dpm/kg)	$^{26}Mg_c$ (ppt)	t_{26} (My)	$t_{K\text{-}K}$ (My)
Cape of Good Hope	1.6	138[7]	1360	775±70[1]
Charlotte	4.4	41±12	148±45	365±80[1]
Picacho	3.2	56±16	273±81	635±50[2]
Tlacotepec	2.1	83±20	622±157	945±55[1]
		250[7]	1130[7]	

where the factor 44.1 converts the ratio of measurement units in the numerator to My. The term in brackets allows for the fact that ^{26}Al decays to give ^{26}Mg. A production rate ratio P(^{26}Mg)/P(^{26}Al) = 1.79 (atom/atom) was calculated from the work of Silberberg and Tsao [10], assuming production rates for iron and nickel are the same; for comparison we note that P(^{21}Ne)/P(^{26}Al), the ratio needed for the calculation of $^{26}Al/^{21}Ne$ ages, is 2.70 [4]. Our $^{26}Al/^{26}Mg$ ages are 35-60% smaller than the ^{40}K-K ages. A discrepancy in this direction and of this approximate magnitude is expected based on short-lived radionuclides (see [4]). We note, however, that the $^{26}Al/^{26}Mg$ ages calculated from the $^{26}Mg_c$ concentrations given by Smith and Huneke [7] are appreciably larger.

Conclusions $^{26}Al/^{26}Mg$ ages are in fair agreement with ages for iron meteorites based on noble gases and other short-lived radionuclides. The largest uncertainty in the $^{26}Al/^{26}Mg$ ages, now about 30%, is associated with the the determination of the cosmogenic ^{26}Mg. The uncertainty arises partly because cosmogenic Mg comprises at most 30% of the total Mg observed and partly because the calibration factors for Mg are not well known. The variations in the observed concentrations of non-cosmogenic Mg are large and appear to be associated with the samples. The Mg may occur in crystallites or as contamination. It would be of interest to investigate the Mg systematics in iron meteorites.

Acknowledgment: A.E. Souzis would like to acknowledge that this work was done while the author held a National. Research Council Research Associateship.

References: [1] Voshage H. and Feldmann H. (1979) *Earth Planet. Sci. Lett. 45*, 293-308. [2] Voshage H. et al. (1982) *Z. Naturforsch. 38*, 273-280. [3] Lavielle B. et al. S. (1985) In: *Isotopic Ratios in the Solar System*, Centre Nat'l. d'Etudes Spatiales, 15-20. [4] Aylmer D. et al. (1988) *Earth Planet. Sci. Lett. 88*, 107-118. [5] Birck J.L. et al. (1982) Abstract in: *5th Intl. Conf. Geochronology, Cosmochronology and Isotope Geology*, 27-28. [6] Fink D. et al. (1991) *Earth Planet. Sci. Lett. 107*, 115-128. [7] Smith S.P. and Huneke J.C. (1991) *Meteoritics 26*, 396-397. [8] Shimamura T. et al. (1986) *Lunar Planet. Sci. XVII*, 795-796. [9] Middleton R. and Klein J. (1987) *Phil. Trans. Roy. Soc. London A323*, 121-143. [10] Silberberg R. and Tsao C.H. (1973) *Astrophys. J., Suppl. 25*, 315-333.

THE ILMENITE LIQUIDUS AND DEPTHS OF SEGREGATION FOR HIGH-TI PICRITE GLASSES:

P.C. Hess, Department of Geological Sciences, Brown University, Providence, RI 02912

Lunar picrite glasses represent primitive and perhaps near primary liquids which have suffered only minor degrees of crystallization or near crustal modification (1). These glasses are multisaturated with olivine and othopyroxene at pressures from 20-25kb. I argue below that high TiO_2 mare glasses were indeed equilibrated with orthopyroxene and were segregated from the lunar mantle at mean depths of 400-500 km.

The glasses are typically modelled as products of relatively low degrees of melting of an hybridized source resulting from the overturn and mixing of the gravitationally unstable cumulate pile. But the models are neither unique nor, in some cases, correct.

Hughes et al (2), for example found that the trace element characteristics of Apollo 17 74220 orange glass could be obtained by melting 4-7% of an hybridized source formed of 95.8% early cumulate olivine and 4.2% late stage cumulates containing 24% augite, 40% plagioclase and 36% ilmenite plus much smaller amounts of apatite and highly evolved trapped KREEPy liquid. These results, however, are unacceptable if major elements are considered. A very powerful constraint is that ilmenite, augite, and plagioclase (or garnet) are not found near the high pressure liquidus of the orange glass 74220 (3). Thus melting must eliminate these phases from the source. The liquid produced by 4% melting and leaving only olivine in the residue must have about 20% TiO_2 , and 13% Al_2O_3 and 11% CaO! Compare this liquid to the orange glass which has about 9% TiO_2, 6% Al_2O_3 and 7% CaO. The liquid produced by 7% melting is closer to the mark (11% TiO_2, 7% Al_2O_3, 6% CaO) but is not a good match for orange glass. It is clear from this example that the major and trace elements must be considered together in petrogenetic modelling. This abstract focuses on the constraints imposed by the TiO_2 content of high TiO_2 mare basalts.

Delano (4) determined the high pressure phase relations and the chemical composition of near liquidus minerals and melts of Apollo 15 red picrite glass. The results include the chemical compositions of ilmenite-saturated melts obtained from 1 bar to 20 kb. These compositions are now used to calculate the ilmenite saturation surface of Apollo 15 red glass over a wide range of pressures and temperatures

The solubility of ilmenite varies with pressure at fixed T°C as

$$(1)\ \ln x(T,P) = \ln x'(T,P') + \frac{\Delta\bar{V}}{RT}\Delta P$$

where X (T,P) is the normative $FeTiO_3$ content of the melt at the T,P of interest, X' is the normative $FeTiO_3$ content of ilmenite saturated liquids (4) at $T,P',\Delta V$ is equal to the difference in the molar volume of ilmenite and pure $FeTiO_3$ liquid and ΔP is equal to $P-P'$. Equation [1] ignores the variation in concentration of the $MgTiO_3$ component in ilmenite and assumes that the liquid activity coefficient, γ_{FeTiO_3}, is independent of pressure and $FeTiO_3$ content. The molar volume of ilmenite, the coefficient of thermal expansion and compressibility are from (5). The partial molar volumes, the partial molar coefficients of thermal expansion and compressibility of liquid TiO_2 and FeO are taken from (6,7). and are used to calculate the liquid molar volume of $FeTiO_3$.

Once the TiO_2 contents of ilmenite-saturated liquids are contoured with respect to pressure, the results are used to obtain the ilmenite saturated surface as a function of temperature at constant pressure. The TiO_2 contents of ilmenite-saturated picrite glasses are found for pressures up to 35 kb and temperatures from 1200-1500°C.

Table 1 gives the TiO_2 (wt%) contents of three picrite glasses under P-T conditions obtained at their liquidi. The liquidus of the Apollo 14 yellow glass was estimated using the empircal 1 bar liquidus (9) and a slope of 7°/ kb. Table 2 gives the TiO_2 contents of melts along the ilmenite-lherzolite solidus ($Mg^*\approx80$). The solidus is estimated using $dT/d(Mg^*)=9$ °C/Mg^* and the constraint that the lherzolite solidus should occur at a higher temperature than that of mare basalt solidi. Note that the TiO_2 contents of ilmenite-saturated near solidus melts remain constant near 12% TiO2 for P=15-30kb.

The three picrite glasses, TiO_2 contents from 4.6 to 13.5 wt%, (table 1) are strongly under-saturated with respect to ilmenite as confirmed by phase equilibria. Indeed, none of the picrite glasses (maximum TiO_2= 16.4%) listed in (1) are in equilibrium with ilmenite under lunar conditions. Of even more significance, as discussed below, is that the TiO_2 contents of ilmenite saturated liquids at the lherzolite solidus, are greater than all but the most TiO_2-rich picrite glasses.

IILMENITE LIQUIDUS: Hess, P.C.

Consider the melting of an Apollo 15 Red glass source. The near- solidus melt of ilmenite-lherzolite contains about 12% TiO_2. Melting must continue to temperatures to at least 30°C above the solidus to reproduce the TiO_2 contents of the red glass. But to produce a melt which is undersaturated with respect to ilmenite even higher super-solidus temperatures are required. For example, ilmenite saturated melts 60-70°C above the solidus contain about 16% TiO_2at 20-25 kb. The melt mass must be increased by about 15% by melting olivine ± orthopyroxene beyond the ilmenite-out curve in order to reduce the TiO_2 content of this melt to 13.5% TiO_2 and to undersaturate the melt with respect to ilmenite. The total amount of melting is determined by the modal content of ilmenite. If, for example, the mode of ilmenite is 2 wt% (≡ 1.1 % TiO_2) then about 6% melting is required to reach the ilmenite-out curve and an additional 1% to attain the Red glass composition. Doubling the ilmenite mode doubles the amount of melting.

Using the same arguments, the melt mass must be increased another 2.5 times beyond that at the ilmenite-out curve to reproduce the observed TiO_2 (4.6) contents of the Apollo 14 Yellow glass. If the mode of ilmenite in the source was 1%, the total amount of melting was about 14%, 71% of which from melting TiO_2-poor phase(s). If the TiO_2-poor phase melted was olivine, then the CaO and Al_2O_3 contents of the ilmenite-saturated melts would be 26% and 20% respectively. Melts with such high CaO contents are not obtained from lherzolite. If the TiO_2-poor phases are olivine and diopside, then CaO contents of ilmenite saturated melts are buffered at much lower values. But no known mare picrite glass has diopside within 100° of the liquidus. The most reasonable model is that the CaO and Al_2O_3 contents are buffered by an olivine and orthopyroxene residuum, as permitted by the phase equilibria. It is concluded that the mare glasses were equilibrated with orthopyroxene and probably olivine and that the mean depths of segregation are 400-500 km.

Table 1

P(Kb)	(1)	(2)	(3)
10	22%	30%	38%
20	20	25	29
25	19	-	

TiO_2 (wt%) contents of ilmenite saturated liquidus for Apollo (1) 15 Red (13.5% TiO_2); (2) 17 Orange (9% TiO_2); (3) 14 Yellow Glasses (4.6% TiO_2)

Table 2

P(kb)/T(°C)	10/1180	20/1280	30/1380
	10%	12%	12%

TiO_2 contents (wt%) of the mare basalts along the ilmenite "lherzolite" solidus

References

1) Delano, J.W. (1986) Proc Lunar Planet. Sci. Conf, 16, JGR, 91, D201-215
2) Hughes,S.S., Delano, J.W., and Schmitt, R.A. (1989) Proc 19th Lunar and Planet. Sci. Conf., 175-184
3) Green, D.H., A.E., Ringwood, W.O Hibberson, N.G. Ware (1975) Proc. Lunar Sci, Conf., 19, 175-188
4) Delano, J.W., (1980) Proc. Lunar Planet Sci. Conf. 11, 251-288
5) Saxena, S.K., and Shen, G. (1992), *JGR*, 97, 19813-198227
6 Lange, R.A., I.S.E., Carmichael, (1987), GCA, 51, 2931-2946
7) Dingwell, D.B., (1992) GCA, 56, 3403-3408
8) Delano, J.W., (1990) Proc 20th Lunar Sci. Conf. 3-22

OVERTURN OF MAGMA OCEAN ILMENITE CUMULATE LAYER: IMPLICATIONS FOR LUNAR MAGMATIC EVOLUTION AND FORMATION OF A LUNAR CORE. P.C. Hess and E.M. Parmentier , Department of Geological Sciences, Brown University, Providence, RI, 02906

We explore a model for the chemical evolution of the lunar interior that explains the origin and evolution of lunar magmatism and possibly the existence of a lunar core. A magma ocean formed during accretion differentiates into the anorthositic crust and chemically stratified cumulate mantle. The cumulate mantle is gravitationally unstable with dense ilmenite cumulate layers overlying olivine-orthopyroxene cumulates with Fe/Mg that decreases with depth. The dense ilmenite layer sinks to the center of the moon forming the core. The remainder of the gravitationally unstable cumulate pile also overturns. Any remaining primitive lunar mantle rises to its level of neutral buoyancy in the cumulate pile. Perhaps melting of primitive lunar mantle due to this decompression results in early lunar Mg-rich magmatism. Because of its high concentration of incompatible heat producing elements, the ilmenite core heats the overlying orthopyroxene-bearing cumulates. As a conductively thickening thermal boundary layer becomes unstable, the resulting mantle plumes rise, decompress and partially melt to generate the mare basalts. This model explains both the timing and chemical characteristics of lunar magmatism.

Solidification of an 800 km deep magma ocean creates 60 km of anorthosite crust, 40 km of an ilmenite enriched residuum beneath the crust, a 700 km cumulate pile that has relatively dense orthopyroxene-olivine (low Mg*) layers near the top and less dense dunite (high Mg*) layers at the base, overlying about 940 km of primitive moon. The chemical stratification is gravitationally unstable; an estimate of the time needed to develop a Rayleigh-Taylor instablity of the ilmenite layer is given by (1)

$$t = \frac{4\,\mu_2^{2/3}\mu_1^{1/3}}{\Delta\rho g h}$$

where μ_1 and μ_2 are the viscosity of the ilmenite and underlying cumulate, respectively (10^{18}-10^{19} Pa-s for mantle silicates near their melting temperature would be a minimum value), $\Delta\rho$ (0.35×10^3 kg/m^3) is the density difference between them, and h is the layer thickness. Given the uncertainty in a number of the variables, particularly the viscosities, this time ranges from 10-100 Myr .

Part of the ilmenite-rich cumulate layer may mix with the mantle (2), but a large fraction of it sinks through the magma ocean cumulates and primitive moon. A 40 km ilmenite layer formed near the top of a cumulate pile 740 km thick would form a dense 600 km radius lunar core. Provided that the cumulates contain sufficient heat producing elements, the ilmenite core could supply the heat necessary to mobilize and melt the overlying mantle. This mantle, the sources for the picrite mare glasses, is formed from orthophyroxene-olivine cumulate layers (Mg* 75-80) that have small amounts of added ilmenite crystallization products.

Heating of the overlying olivine-orthopyroxene cumulates by the ilmenite core will generate mantle plumes that rise through the cumulates and undergo decompression melting. The ilmenite core will be highly radioactive compared to the overlying cumulates. An estimate of the radiogenic heat production H in the ilmenite core is about 10 times that of the primitive moon. About 4 Byr ago we take heat production in the primitive moon to have been about 4 times the presentday heat production rate in the Earth's mantle (~6×10^{-12} W/kg-s). The conductive thermal boundary layer will thicken with time t as $2\sqrt{\kappa t}$, and the temperature difference across it will increase as Ht/c_p where c_p is the specific heat at constant pressure. When the Rayleigh number based on the boundary layer

LUNAR MAGMATIC EVOLUTION AND CORE FORMATION

P.C. Hess and E.M. Parmentier

thickness exceeds a critical value Ra_c (~1000), instability will lead to the formation of mantle plumes. The time for plumes to form, corresponding to the time between overturn and the beginning of mare basalt formation, is given by

$$t = \left(\frac{Ra_c \, \mu_1^{1/3} \mu_2^{2/3} c_p}{8 \rho_o \alpha H g \kappa^{1/2}} \right)^{2/5}$$

where ρ_o is a reference density (3.3×10^3 kg/m^3), α is the coefficient of thermal expansion (3×10^{-5} °C^{-1}), and κ is the thermal diffusivity (10^{-6} m^2/s). The average temperature difference between the plumes and surrounding mantle, roughly one-half the temperature difference across the thermal boundary layer, is simply $Ht/2c_p$. Here μ_1 is the viscosity in the thermal boundary layer (which we take to be mantle silicate near its melting temperature ~10^{18} Pa-s) and μ_2 is the viscosity in the overlying mantle. After overturn, the base of the olivine-orthopyroxene cumulates will be near their low pressure melting temperature (~1100-1200°C). For a melting temperature which increases 10°K/kbar, the melting temperature of the cumulates at a depth of 1000-1100 km, corresponding to the core-mantle boundary in our model, will be 1400-1500°C. The cumulates must therefore be at least 300°C cooler than their melting temperature. If the viscosity increases by a factor of 6 for each 100°C below the melting temperature, $\mu_2 = 2 \times 10^{20}$ Pa-s. With these values and g about 1/3 of the surface value at this 1000 km depth, the time estimated for plume formation is about 100 Myr. After this time the boundary layer thickness is about 100 km and the temperature difference across the thermal boundary layer is 600°C. This would predict temperatures exceeding 1700-1800°C in the ilmenite core, suggesting that it would be largely molten at this time. The viscosites used in this estimate are minimum values. Increasing the viscosities by an order of magnitude would increase the time between overturn and the beginning of mare basalt magmatism to 250 Myr. Decreasing the rate of heat production in the ilmenite core by a factor of 2 would increase this time by about 30%.

High TiO_2 picrite mare glasses are near primary melts segregated from mean depths of 400-500 km and generated from an olivine-orthopyroxene source (2,3). If the ages of the picrite glasses overlap those of mare basalts, then picrite volcanism began at least 3.9 Byr ago (4). Thus a time of at least several hundred Myr between overturn and the beginning of mare volcanism is required. The potential temperature within mantle plumes must be in the range of 1450-1550°C, assuming about 10% melting (2). With an initial temperature of the olivine-orthopyroxene cumulates to be 1100-1200°C and an average temperature increase in the thermal boundary layer of 300°C at the time that plumes begin to form, our model predicts temperatures in this range. Thus, both the age of volcanism and the temperatures required for melting are consistent with the model described above. If this model is correct, the heat source for high TiO_2 mare basalt volcanism is ilmenite cumulate. But these cumulates exist deep within the moon and may form part or all of a lunar core.

References: (1) Whitehead, J.A., Ann. Rev. Fluid Mech. 20, 61, 1988. (2) Hess, P.C., GRL 18, 2069, 1991. (3) Delano, J.W., Proc. 16th Lunar Planet. Sci. Conf., JGR 91, D201, 1986. (4) Nyquist, L.E., and C.-Y. Shih, Geochm. Cosmochm. Acta 56, 2213, 1992.

GEOCHEMISTRY AND COSMOCHEMISTRY OF FULLERENES III : REACTION OF C_{60} AND C_{70} WITH OZONE. D. Heymann and L.P.F. Chibante. Department of Geology and Geophysics and of Chemistry. Rice University, Houston 77251, USA. (713) 527 4890.

C_{60} and C_{70} dissolved in toluene were treated with O_2 gas containing 2.6 volume% ozone and with O_3-free oxygen. No reaction products were detected for 0.1 mole of O_2 passed through the solution, but destruction of C_{60} was clearly detectable for a dose of 10^{-6} moles of O_3. C_{70} was destroyed more slowly than C_{60}. Among the substances remaining in solution, we identified $C_{60}O$, $C_{70}O$, $C_{60}O_2$, $C_{60}O_3$, and $C_{60}O_4$. C_{60} crystals exposed to O_3 at room temperature became less soluble in toluene in a matter of days, but oxides were apparently not formed.

The discovery of C_{60} and C_{70} on the Earth (1) has stimulated interest in the geochemistry of these compounds. We found earlier that these substances decomposed so swiftly when heated in ambient air (2,3) that their survival in a Precambrian rock (1) seemed puzzling. Acting, as we did, on a hunch that O_3 rather than O_2 might be the dangerous chemical in air, we exposed C_{60} and C_{70} in solution to O_2 gas containing 2.6 volume % O_3. The gas mixture was bubbled through the solutions. Figure 1 shows the decrease of C_{60} concentration as a function of ozone dose. Within about 3 minutes, C_{60} is essentially destroyed and a buff colored precipitate has formed. Treatment with ozone-free O_2 (a total of 0.1 mole) showed no decomposition of the C_{60}. The reaction with ozone is at least five orders of magnitude faster than with oxygen.

Figure 2 shows the results of the ozonation of both fullerenes in toluene solution. The deduced rate of C_{70} to $C_{70}O$ is about 0.7 that of C_{60} to $C_{60}O$. Figure 3 is an HPLC chromatogram of the solution in which 0.66% and 2.10% of the original C_{60} and C_{70} had remained. The substance labels are certain except for $C_{60}O_4$ and $C_{70}O_2$. The oxides are well-soluble in toluene. Figure 4 shows the areas of the $C_{60}O$ and $C_{60}O_2$ peaks determined spectroscopically at 290 nm, during the ozonation. Since we have not yet determined the molar extinction coefficients at any wavelength, the area ratios are only closely equal to the molar ratios. However, these results are consistent with the hypothesis that the transformation of the fullerenes to (toluene) insoluble matter proceeds along chains such as C_{60} to $C_{60}O$ to $C_{60}O_2$ to $C_{60}O_3$, etc to insoluble matter. We cannot deduce for which value of n in $C_{60}O_n$ the cage ruptures. Our results are not in conflict with a report (4) that n = 5 when oxygen is adducted electrochemically.

A crystalline sample of C_{60} was exposed to oxygen/ozone at room temperature. After 24 hours, about 95% of the original mass was still soluble in toluene. After seven days, only about 20% went into solution. However, no oxides were detected in the solutions.

A sample of C_{60} in toluene was completely transformed to insoluble matter with ozone. The weight of the recovered precipitate was 2.2 times that of the untreated sample. The precipitates are obviosly highly polar substances such as ketones, aldehydes, and/or carboxylic acids with an over-all C : O ratio close to unity!

A major requirement for fullerene survival in nature is that the environment must be essentially free of ozone. The survival of fullerenes in coal or graphite might be aided by the catalytic conversion of ozone

to oxygen by the matrix (coal, graphite).

References. (1) Buseck, P.R., Tsipurski, S.J. and Hettich R. (1992) Science 257, 215-217. (2) Heymann, D. in Lunar and Planetary Science XXIII (1992), pp. 531-532. (3) Chibante, L.P.F. and Heymann, D. (1992/93) Carbon (in print). (4) Kalsbeck, W.A. and Thorp, H.H. (1991) J. Electroanal. Chem. 314, 363-370.

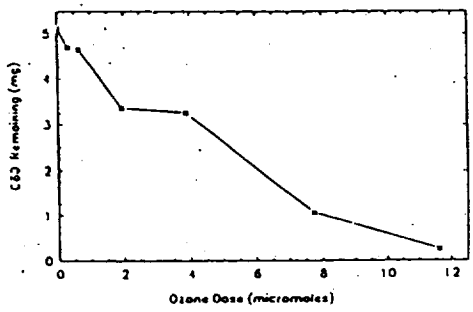

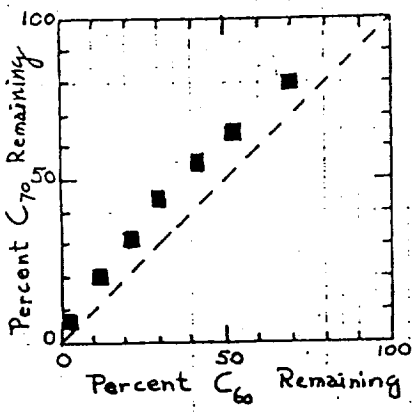

Figure 2

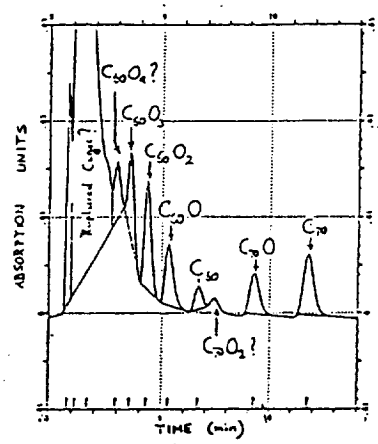

Figure 3

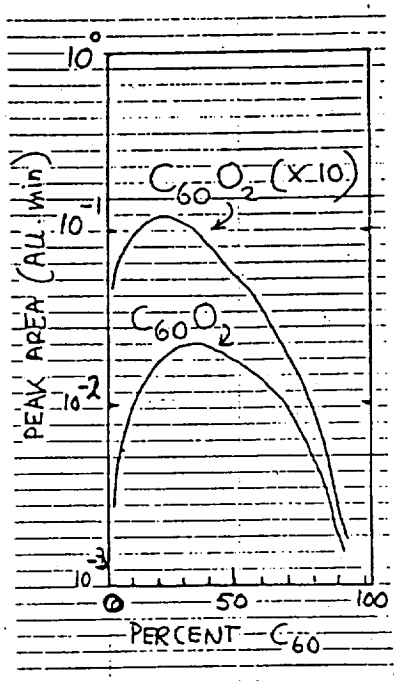

Figure 4

SOME CHEMISTRY. It is generally believed that the O-atoms bridge C-C bonds between two adjacent 6-membered C-rings. For C_{70} it has been postulated that the O occurs in a bridged annulene-like structure. For C_{60}, an epoxide structure has been proposed. In principle, $C_{60}O$ can have two isomers and $C_{70}O$ can have eight; in each case equal to the number of different C-C bonds. $C_{60}O_2$ will have nine structural isomers if O bridges are (6-6) types. The number of isomers of the higher oxides is even larger. There are indications that the oxides are less thermally stable than their respective parent molecules. The C_{60} oxides decompose on dry neutral alumina, which can, therefore, not be used as a substrate for their separation by liquid chromatography.

EARTH-BASED AND GALILEO SSI MULTISPECTRAL OBSERVATIONS OF EASTERN MARE SERENITATIS AND THE APOLLO 17 LANDING SITE

H. Hiesinger, R. Jaumann, G. Neukum, GLL Imaging Team. German Aerospace Research Establishment (DLR), Inst. for Planetary Exploration, Berlin/Oberpfaffenhofen, Germany.

Introduction: Both the Apollo 17 and the Mare Serenitatis region have been observed by Galileo during its fly-by in December 1992. We used earth-based multispectral data to define mare units which then can be compared with the results of the Galileo SSI data evaluation.

Remotely sensed spectral and photometric data are highly indicative of the composition and the physical state of the lunar surface. In 1989 we started a program of telescopic lunar observations to achieve a new multispectral and photometric data base. The observations were made at the Mauna Kea Observatory/Hawaii using the DLR CCD camera equipped with 12 narrow band filters (bandwidth = 20 nm) from 0.38 μm - 1.0 μm. The spatial resolution is 2 km / pixel. In our data reduction the Apollo 16 landing site is used as calibration area and a differentiated photometric correction based on the model of Hapke (1, 2) has been applied to the data in order to remove effects induced by different viewing conditions.The determination of spectral-chemical correlations through laboratory measurements of lunar samples (3) enabled us to calculate the geochemical composition of the spectrally defined basalt units for Fe, Ti, Al, and Ca. Both Apollo 17 and Mare Serenitatis/Tranquillitatis are covered by our earth-based data and by the Galileo EM-2 data (LUNMOS 05). This allows us to compare these data sets directly. The Galileo data have a spatial resolution which is better by a factor of ≈2 compared to the earth-based data. The Galileo data set consists of 6 color channels in the visible light and the near IR (409nm - 993nm). This in combination with our earth-based filter set increases the spectral resolution. Galileo multispectral data of the moon are without any atmospheric distortions. Using the new Galileo data it is also possible to investigate areas which are not visible from Earth. The Galileo data are in good agreement with the earth-based data and allow a more detailed differentiation of spectral units. This all led to the conclusion that the Galileo EM-2 images are now the best available data to define spectral units on the lunar surface.

Previous multispectral imaging data (4) show a well defined compositional differentiation between the basalts of Mare Tranquillitatis and Mare Serenitatis. Mare Tranquillitatis basalts in general have higher contents of TiO_2 and FeO (TiO_2: 4-6wt%; FeO: >16wt%) than basalts from the center of the Serenitatis basin (TiO_2: 2-4wt%; FeO: 14-16wt%). Inside the Serenitatis basin we found several mare units which are different in albedo, TiO_2 content and spectral properties. Using color ratios we are able to distinguish at least 6 units including the dark mantle deposits west of crater Littrow and the ejecta of crater Dawes.

Unit I is a very titanium rich basalt located at the boundary region of Mare Tranquillitatis and Mare Serenitatis. We expect this oldest unit to be the base of the Mare Tranquillitatis basalt filling. Unit II consists of Tranquillitatis ilmenite basalts which are also exposed in the boundary region of Mare Tranquillitatis and Mare Serenitatis. This unit is superimposed by the mare basalts of the center of Mare Serenitatis (Unit III). At the eastern border of Mare Serenitatis we found a younger basalt unit IV inside and west of crater Le Monnier. Basalts of the eastern edge of Mare Serenitatis exhibit higher TiO_2 contents compared to the central basalts of Mare Serenitatis. Dark mantle deposits west of crater Littrow are characterized by high amounts of agglutinate (low 720/990 ratio) suggesting that this unit V has a pyroclastic origin. It seems that the dark mantle deposits have the highest contents of TiO_2 (6-8wt%) of all spectrally defined units. The dark mantle deposits are older than the mare units. In the Serenitatis/Tranquillitatis region the titanium content of the basalts increases with age. North of this area like in the western lunar hemisphere there are again overlying titanium rich basalts (Unit IV) which are the youngest of all investigated mare basalts of the eastern part of the Mare Serenitatis basin. Northwest of crater Dawes we found a unit which is depleted in titanium.. We interpret this unit VI to be ejecta material consisting of fragments of titanium basalt, Tranquillitatis ilmenite basalt, and a third component which is depleted in TiO_2. Dawes, a Copernican impact crater (5) probably penetrated the Tranquillitatis ilmenite basalts and excavated the underlying substrate.

unit	Normalized difference	400/720 ratio	720/990 ratio	FeO (wt%)	TiO_2 (wt%)	Al_2O_3 (wt%)	CaO (wt%)
I	very dark	bright	dark	>14	6-8	<9	<11
II	dark	bright	dark	>14	4-6	<9	<11
III	bright	dark	bright	14-16	2-6	9-13	11-12
IV	intermediate	intermediate	intermediate	14-16	4-6	<9	<11
V	very dark	bright	very dark	14-16	6-8	9-13	11-12
VI	intermediate	dark	bright	14-16	2-4	<9	9-11

Table 1: Summarized results of the spectral units

References:
(1) Hapke, B., (1981), J. Geophys. Res. **86** B4, 3039-3054
(2) Helfenstein, P., Veverka, J., (1987), Icarus **72**, 342-357
(3) Jaumann, R., (1991), J. Geophys. Res. **96** E5, 22793-22807
(4) Jaumann, R., (1989), DLR Forschungsbericht DLR-FB 89-40
(5) Neukum, G. et al., (1975), The Moon **12**, 201-229

TRACE-ELEMENT COMPOSITION OF CHICXULUB CRATER MELT ROCK, K/T TEKTITES AND YUCATAN BASEMENT; A.R. Hildebrand, D.C. Grégoire, Geological Survey of Canada, 1 Observatory Crescent, Bldg. 3, Ottawa, Canada K1A 0Y3; M. Attrep, Jr., Los Alamos National Laboratory, Los Alamos, NM 87545; P. Claeys, Department of Geology, University of California, Davis, CA 95616; C.M. Thompson and W.V. Boynton, Department of Planetary Sciences, University of Arizona, Tucson, AZ 85721

The Cretaceous/Tertiary (K/T) boundary Chicxulub impact is the best preserved large impact in the geologic record. The Chicxulub crater has been buried with no apparent erosion of its intracrater deposits and its ejecta blanket is known and is well preserved at hundreds of localities globally. Although most of the molten material ejected from the crater has been largely altered, a few localities still preserve tektite glass. Availability of intra- and extracrater impact products as well as plausible matches to the targeted rocks allows the comparison of compositions of the different classes of impact products to those of the impacted lithologies.

Determination of trace-element compositions of the K/T tektites, Chicxulub melt rock and the targeted Yucatán silicate basement and carbonate/evaporite lithologies have been made using instrumental neutron activation analysis (INAA) and inductively coupled plasma mass spectrometry (ICP-MS). Some sample splits were studied with both techniques to ensure that inter-laboratory variation was not significant or could be corrected. The concentration of a few major and minor elements was also was also checked against microprobe results. Radiochemical neutron activation analysis (RNAA) was used to determine Ir abundances in some samples.

Beloc, Haiti K/T localities: Trace-element concentrations obtained for the Haitian tektites were in fair agreement with those of two previous studies (1, 2) but were substantially different from those of a third (3) suggesting that the latter study's results are invalid. The distinction of green vs. yellow glasses has been previously reported for the Haitian localities and 1 grain of lechatelierite-bearing glass has also been described (2). In this study two different types of green glasses with different trace-element compositions were found among the 6 grains analyzed. The most common glass type is a light to moderately dark green glass that alters forming a coarsely fluted surface. However, occasional grains of darker green glass have greater degrees of sphericity and a "wormy" surface texture similar to that found on tektites from other strewnfields. Although the rare-earth element (REE) pattern exhibited by the less common glass type is similar to that of the other Haitian tektites it is of slightly lower abundance. Relative to the typical glass the dark green grain had incompatible elements Na, K, Rb, Sr, Cs, Ba, and U depleted by up to 3 times, the chalcophiles Zn and Sb also strongly depleted, and the siderophile elements Cr, Co and Ni variably enriched although the Fe concentration is typical of Haitian glasses. In general, W displays the most variable concentrations (up to 4 times variation) of any element analyzed in the green glasses. The Ir concentration of the Haitian tektites is reported as <30 ppt (4).

Mimbral, Mexico K/T locality: The 6 grains of Mimbral green glass analyzed show greater variations in trace-element concentrations than the Haitian examples and, despite their similar appearance, define a different trace-element signature. Their REE pattern is lower and flatter than that of the Haitian tektites. The Mimbral glasses display lower Zn, Rb, Zr, Hf, Ta and Th concentrations, greater Sc, Cr, and Co concentrations and highly variable Sr, Cs, and Ba concentrations (up to 10 times variation). The Mimbral locality has occasional grains with the "wormy" texture as found at Beloc but none of these grains were analyzed in this study. On some grains it appears that the channels are controlled by compositional banding (manifested as slight colour variations) within the glass.

Chicxulub crater melt rock: The 6 chips analyzed from the Y6 N17 core sample of the Chicxulub crater show minor compositional variability which presumably reflects varying compositions and proportions of entrained inclusions. The REE pattern is slightly steeper than that of the Beloc and Mimbral tektites although the abundances are similar. The melt rock displays higher Na, Ca, W,

Th and U than the tektites, and lower Fe, Sc, Ni, As, and Cs. All other trace-element concentrations are similar to those of the tektites and the chips show relatively consistent concentrations as expected for chips from a single core sample. No Ir was found in the melt rock to an INAA detection limit of ~1 ppb so the result of (5) was not confirmed, but Au was found in concentrations varying from 1 to 7 ppb. Whether the varying Au concentrations reflect contamination of the samples from previous handling is unknown. In this context we note that a concentration of only 1 ppt Ir was determined (by RNAA) for a sample of the proximal ejecta blanket from the Y2 N6 core (composed of carbonate and evaporite fragments) suggesting that in addition to the Haitian tektites at least some proximal impact products do not contain anomalous quantities of Ir.

Yucatán basement: The Quintana Roo-1 well bottomed in the silicate basement of the Yucatán peninsula ~200 km south of the Chicxulub crater. The QR1 N4 sample (from 2390-2394 m depth) is a coarse-grained equigranular metamorphic rock. Its REE abundances are roughly similar to those of the Chicxulub melt rock but the pattern is different indicating that this rock is not representative of the bulk of the lithologies impacted at Chicxulub. Other trace-element abundances are generally different from those of the melt rock and tektites indicating that at least some significant variation in upper crustal composition occurs across the Yucatán platform. This rock contains 71 ppt Ir, a typical background value for continental crust.

Discussion: Despite the obvious geochemical similarities of the Haitian and Mimbral glasses, they display distinct signatures that would allow separation in a blind test. The trace-element patterns are typical of the upper continental crust as was apparently excavated at the Chicxulub crater. The differences presumably reflect crustal compositional variations from opposite sides of the crater. The "Mimbral" side of the crater sampled more variable silicate crust than the "Beloc" side based on the modest number of samples analyzed although a distinct general character is also exhibited. Because the Chicxulub crater's transient cavity, the crater of excavation, was 90 to 100 km in diameter, it is not surprising that compositional variation occurs between impact products thrown out from opposite sides of the crater. (This transient crater size is derived from the size of the thick melt pool as inferred from the magnetic field anomaly associated with the crater (6).) In fact, given the large size of the transient cavity, the upper crust targeted by the Chicxulub impact must have been relatively homogenous or more dramatic compositional variations in tektite compositions would be observed. Alternatively, the alteration process could preferentially replace all but a certain class of compositions. More completely preserved samples will be required to explore this possibility. The different types of green glass may reflect a layering in the crust or a mixture of lithologies regionally.

Chalcophile element anomaly origin: The K/T fireball layer, as preserved in both marine and nonmarine environments, has an associated chalcophile-element (e.g. Zn, As, Se, Sb) anomaly of an as yet unknown origin. The low abundances of the chalcophile elements in the tektites relative to those expected in typical marine sediments allow the possibility that the fireball-layer chalcophile anomalies were produced by impact devolatization of the impacted lithologies (7). The problem with this mechanism is the requirement that a large volume of rock need be outgassed to produce the observed fluence of chalcophiles. In this scenario the chalcophile elements' subsequent condensation and precipitation would have led to their association with the fireball layer rather than the ejecta layer.

Acknowledgements: We are grateful to G. Penfield, A. Camargo, A. Montanari and Petróleos Méxicanos for supplying some of the samples used in this study.

References: (1) Sigurdsson et al., 1991, Nature, 353: 839-842; (2) Koeberl and Sigurdsson, 1992, GCA, 56: 2113-2129; (3) Izett, 1991, JGR, 96: 20,879-20,905; ((4) Jéhanno et al., 1992, EPSL, 109: 229-241; (5) Sharpton et al., 1992, Nature, 359: 819-821; (6) Ortiz Aleman et al., this volume; (7) Hildebrand, 1992, Ph.D. dissertation.

COMPARISON OF REFLECTANCE SPECTRA OF C ASTEROIDS AND UNIQUE C CHONDRITES Y86720, Y82162, AND B7904;

T. Hiroi, SN3, NASA Johnson Space Center, Houston, TX 77058, C. M. Pieters, Dept. of Geological Sciences, Brown University, Providence, RI 02912, and M. E. Zolensky, SN2, NASA Johnson Space Center, Houston, TX 77058.

Reflectance spectra (0.3-2.6μm) of 11 carbonaceous (C) chondrite powders (<100 or <125μm) including "unique" ones Y86720, Y82162, and B7904, have been measured and compared with those of 14 C asteroids. Among those C chondrites, only three "unique" ones had close counterparts among C asteroids (Y86720 and 1 Ceres, Y82162 and 704 Interamnia, and B7904 and 31 Euphrosyne). Mixing calculations of those C chondrites by Hapke's isotropic model were also performed to improve fits of reflectance spectra of all the 14 C asteroids. If the grain-size distributions of those asteroid surfaces are similar to those C chondrite powders, the result suggests that all tested C asteroids contain a high amount of heated C chondrite material, such as Y86720, Y82162, and B7904.

The C asteroids have been believed to be the counterparts of C chondrites based on their reflectance spectra around visible wavelength range. However, not many studies have been done using longer near-infrared wavelengths ranging up to 2.6μm, which contain important mineralogical information. In this paper, reflectance spectra (0.3-2.6μm) of 14 C asteroids [1,2] have been compared with those of 11 C chondrites including "unique" ones that have characteristics of both CI and CM groups and show evidence of thermal metamorphism [3].

Shown in Fig. 1 are bidirectional reflectance spectra (30° incidence and 0° emergence angles) of C chondrites grouped according to their spectral characteristics. Those meteorites were ground and dry-sieved into size fractions of <100μm except for Ivuna and three "unique" ones (<125μm). Every care was taken to avoid any samples with weathering effects. Orgueil and Ivuna (CI1) have characteristic absorption bands around 0.47 and 1.95μm, ALH83100, Murray, and ALHA81002 (CM2) have a common band around 0.75μm, Renazzo (CR2) has a featureless red spectral profile, Vigarano (CV3) has some extremely shallow and broad absorption bands, and Bells (CM2) has an intermediate reflectance spectrum of CI1, CM2, and CR2 groups measured in this study. These results are consistent with previous studies [4,5] except for the possible differences in standard materials, spectrometer configurations, and sample mineral assemblages. B7904, Y82162, and Y86720 ("unique") have a characteristic absorption edge around 0.3-0.45μm. Their reflectances decrease to only 55-80% at 0.3μm (scaled to 100% at 0.55μm) while all the others decrease to 25-45%. Those spectral features can greatly change if the smaller grain-size portions of the samples are removed [5].

After comparing reflectance spectra of these 11 C chondrite powders and 14 C asteroids, only three asteroids had close counterparts among these C chondrites, which are all "unique" ones. These fits are shown in Fig. 2. Scaled asteroid spectra of 1 Ceres, 31 Euphrosyne, and 704 Interamnia have good fits with Y86720, B7904, and Y82162, respectively. Reflectances at 0.55μm of those scaled asteroid spectra, have the same order with the IRAS albedoes [6] plotted after being scaled by 0.65. In order to get better fits for the other asteroids, mixing calculations were performed using Hapke's isotropic model [7]. The results of the spectral fits are shown in Fig. 3, and the calculated volume abundances of C chondrite groups on all the tested C asteroids are plotted versus their average distances from the sun (semimajor axis) in Fig. 4. Unique C chondrites are abundant on these C asteroids, based on their spectral characteristics, which suggests the C asteroid surfaces may be thermally metamorphosed as was suggested based on mineralogical evidences in those "unique" C chondrites. There seems to be no clear correlation between the distance from the sun and the abundance of the "unique" C chondrites.

This modeling analysis necessarily assumes that there is a direct relation between meteorite and asteroid spectra and that alteration in the terrestrial or asteroid environment is minimal. The fact that the largest asteroid 1 Ceres is included among the C asteroids well-fit with unique C chondrites supports the validity of this kind of approach for C asteroid reflectance spectra. If this kind of analysis is also valid for other C asteroids, the results suggest that the most abundant (as falls) C chondrites do not really represent the surface material of the tested C asteroids. The large difference of the size-range between C asteroids tested (100-900km) and most C chondrites that fall to the earth (<1m), may be the reason for such a situation.

Acknowledgments: We thank the National Institute of Polar Research for Y86720, Y82162, and B7904 studied as a part of the consortium study. We also thank the Meteorite Working Group for ALH83100 and ALHA81002. Reflectance spectra of meteorite powders were measured at RELAB in Brown University. We thank Steve Pratt for those measurements. RELAB is a multiuser facility operated under NASA grant NAGW-748. This work was done while one of the authors (T. Hiroi) held a National Research Council-NASA/JSC Research Associateship.

COMPARISON OF C ASTEROIDS AND UNIQUE C CHONDRITES: Hiroi T. et al.

References: [1] Chapman C. R. and Gaffey M. J. (1979) In Asteroids, pp. 1064-1089. [2] Bell J. F. *et al.* (1988) Lunar Planet. Sci. XIX, 57-58. [3] Ikeda Y. (1992) *Proc. NIPR Symp. Antarct. Meteorites, 5*, 49-73. [4] Gaffey M. J. (1976) *JGR, 81*, 905-920. [5] Johnson T. V. and Fanale F. P. (1973) *JGR, 78*, 8507-8518. [6] Tedesco E. F. (1989) In Asteroids II, pp. 1090-1138. [7] Hapke B. (1981) *JGR, 86*, 3039-3054.

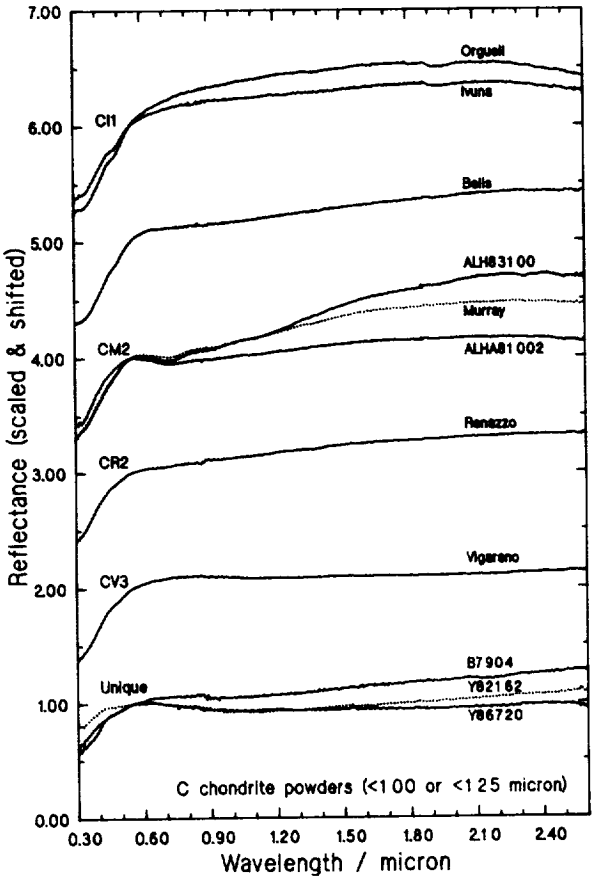

Fig. 1. Reflectance spectra of C chondrite powders.

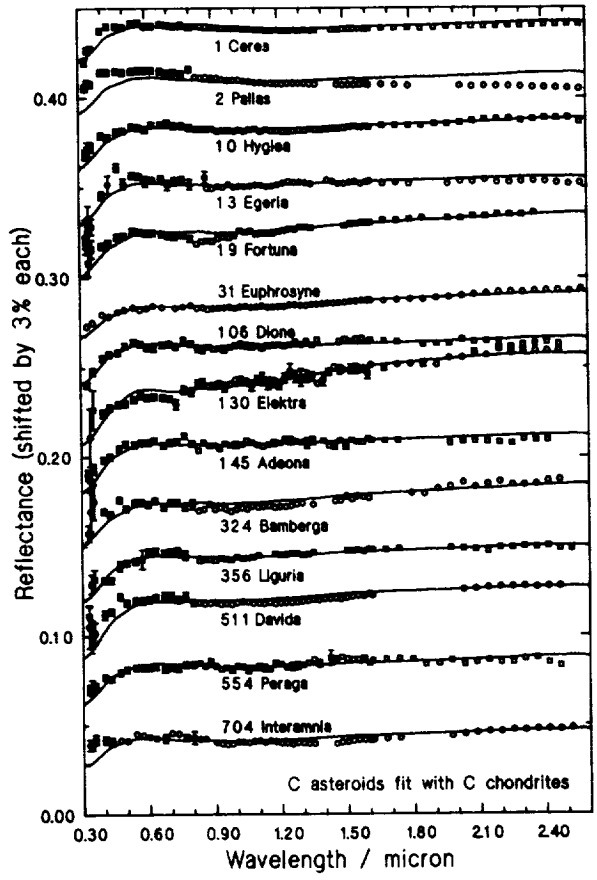

Fig. 3. Reflectance spectra of C asteroids [1,2] fit with those of C chondrite powders by Hapke's isotropic model.

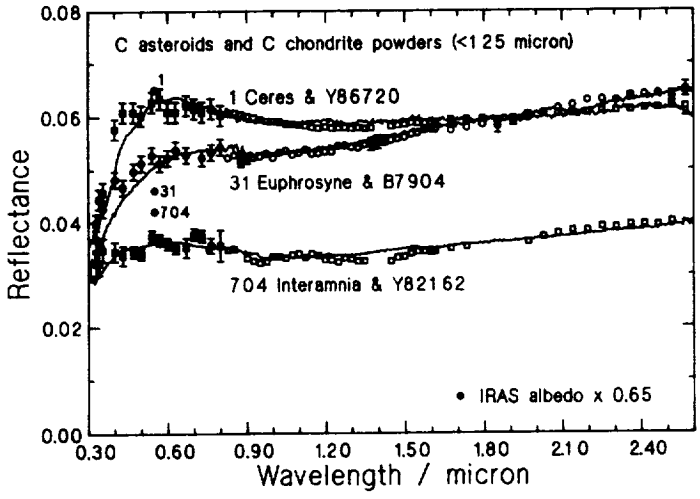

Fig. 2. Counterparts found between C asteroids and C chondrites.

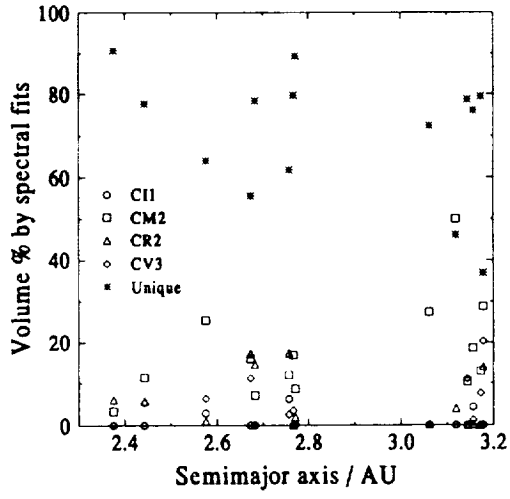

Fig. 4. Calculated C-chondrite volume % vs. semimajor axes of C asteroids.

PHASE EQUILIBRIA OF THE MAGNESIUM SULFATE-WATER SYSTEM TO 4 KBARS

D.L. Hogenboom[1], J.S. Kargel[2], J.P. Ganasan[1], and L. Lee[1], [1] Department of Physics, Lafayette College, Easton, PA 18042, [2] University of Arizona, Tucson, AZ 85721 (now at USGS, Flagstaff)

Introduction. Magnesium sulfate is the most abundant salt in carbonaceous chondrites [1], and may be important in the low-temperature igneous evolution and aqueous differentiation of icy satellites and large chondritic asteroids [2]. Accordingly, we are investigating high-pressure phase equilibria in $MgSO_4$-H_2O solutions under pressures up to four kbars. An initial report was presented two years ago [3]. This abstract summarizes our results to date including studies of solutions containing 15.3%, 17%, and 22% $MgSO_4$. Briefly, these results demonstrate (1) that increasing pressure causes the eutectic and peritectic compositions to shift to much lower concentrations of magnesium sulfate, and (2) the existence of a new low-density phase of magnesium sulfate hydrate.

Experimental. The experiment was conducted with the same apparatus and techniques described previously [3]. The pressure vessel and ~ 2.6 ml of enclosed sample were pressurized by additional sample through small-bore tubing which connected the vessel to a mercury u-tube maintained at 30°C. The sample was cooled to the desired temperatures using a liquid nitrogen bath. Volume changes of the sample were measured by a sensitive transducer that produced a voltage proportional to the displacement of mercury in the u-tube. The temperature of the sample was measured by a thermometer strapped to the outside of the vessel. Recent improvements in the experiment will allow the subsolidus region to be explored in future runs. A deformable sample cell has been developed to go inside a new pressure vessel surrounded by a pressure transmitting fluid. This should eliminate the problem of the vessel "locking up" when the sample freezes [3]. A new thermometer in an armored probe will permit the temperature of the sample to be measured directly with greater sensitivity and more rapid response.

Results. Fig. 1 illustrates the phase diagram of the system H_2O-$MgSO_4$ system at 1 atm (from [2]). This system exhibits four magnesium sulfate hydrates, of which dodecahydrate (hereafter, MS12) and epsomite (MS7), plus an unidentified new hydrate, occur in these experiments. These experiments also have encountered a eutectic and a peritectic which, at 1 atm, occur near 17% and 21.1% $MgSO_4$, respectively. Our earlier report showed two examples of experimental runs, one for a 15.3% solution at 2000 bars (below the ice transition pressure) and the other for a 17% solution at 3460 bars (above the transition). Figs. 2 and 3 of this report show two more runs, including a 17% mixture at 3800 bars and a 22% mixture at 2950 bars. The voltages plotted in these figures are almost linearly related to sample volume. The runs shown in Figs. 2 and 3 were conducted above the ice I / ice II transition pressure, so that the frozen samples apparently consist of ice II and MS12. Both frozen mixtures are denser than their equivalent liquids, as indicated in Figs. 2 and 3.

The 17% sample melts in four stages at 3800 bars including two nearly temperature-invariant transitions and two univariant stages (Fig. 2). The invariant transitions are equated with the eutectic and peritectic, designated 'E' and 'P1', respectively, in Fig. 1. The fact that the 17% sample seems to undergo peritectic melting indicates that the peritectic shifts to the water-rich side of 17% $MgSO_4$ at 3800 bars. In [3] we indicated a similar compositional shift for the eutectic. These compositional shifts result from pressure-induced depression of the ice liquidus temperature and an elevation of the liquidi of the denser phases, MS12 and MS7. The sloping curve between the eutectic and peritectic in Fig. 2 apparently corresponds to MS12 melting along the liquidus between 'E' and 'P1' in Fig. 1. MS 7 appears to be the final, high-temperature liquidus phase.

Fig. 3, in addition to showing the eutectic, also shows that the last solid to melt has a density lower than the liquid's density. This phase cannot be ice II because it completely melts above 275 K. A hitherto unknown magnesium sulfate hydrate, containing over twelve molecules of water, is the only alternative because MS7 and MS12 are denser than the liquid. This phase has been observed on several runs. There are indications that this phase either is metastable or has a very restricted stability.

Fig. 4 shows the eutectic and peritectic temperatures for $MgSO_4$ solutions. The eutectic curve apparently represents pressure melting of mixtures of MS12 and ice I or ice II. The short-dashed curve represents the peritectic reaction (P1 in Fig. 1), and the long-dashed 'metaeutectic' curve probably represents melting of metastable mixtures of MS7 and ice; the metaeutectic often is encountered at 1 atm when melting rapidly-frozen $MgSO_4$ solutions.

Conclusions. The eutectic and peritectic ('E' and 'P1' in Fig. 1) shift to substantially lower salinities under increasing pressures up to four kbars. This indicates that magnesium sulfate would be more likely to

remain as a residual solid in the interiors of icy satellites, contrary to predictions of models based on phase equilibria at 1 atm [2]. Therefore, all briny lavas should be saturated with $MgSO_4$. These experiments have also detected a relatively low density magnesium sulfate hydrate, but the stoichiometry, stability limits, and other properties of this phase have not yet been determined.

References. [1] Fredriksson, K. and J.F. Kerridge 1988, *Meteoritics* **23**, 35-44. [2] Kargel, J.S. 1991, *Icarus* **94**, 368-390. [3] Hogenboom, D.L. et al., 1991, *Lun. Planet. Sci.* **XXII**, 581-582.

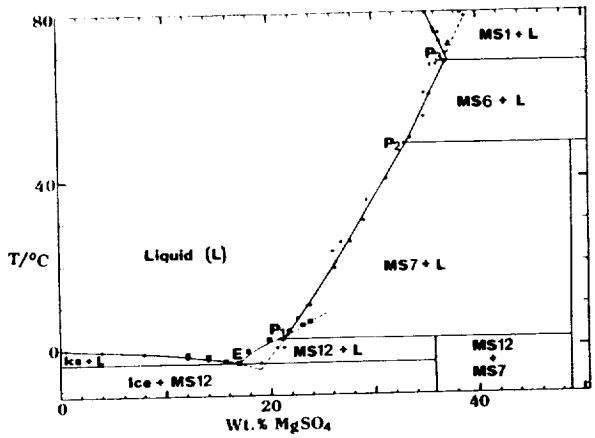

Figure 1. Phase diagram of the magnesium sulfate-water system at 1 atm (from [2]). MS1 refers to $MgSO_4.1H_2O$; MS6, $MgSO_4.6H_2O$; MS7, $MgSO_4.7H_2O$; and MS12, $MgSO_4.12H_2O$.

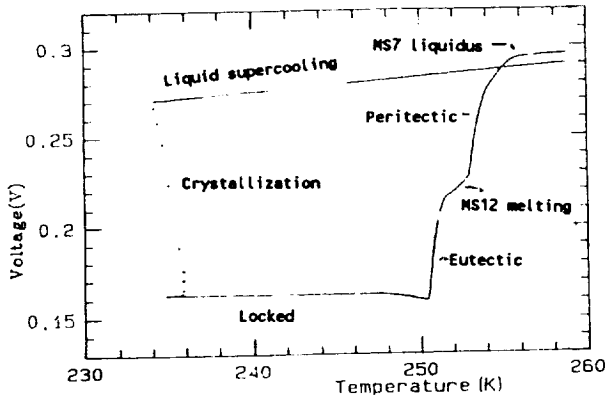

Figure 2. Experimental run at 3800 bars and 17% $MgSO_4$ solution.

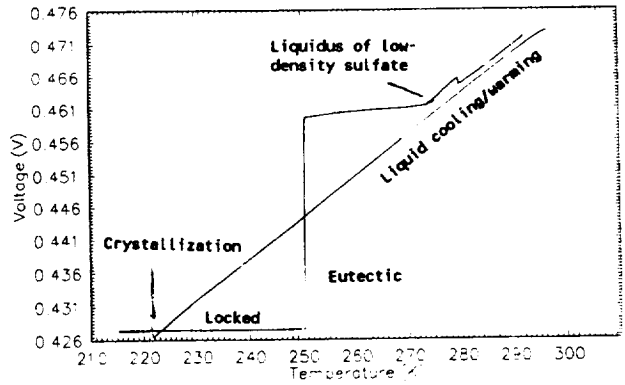

Figure 3. Experimental run at 2950 bars and 22% $MgSO_4$ solution.

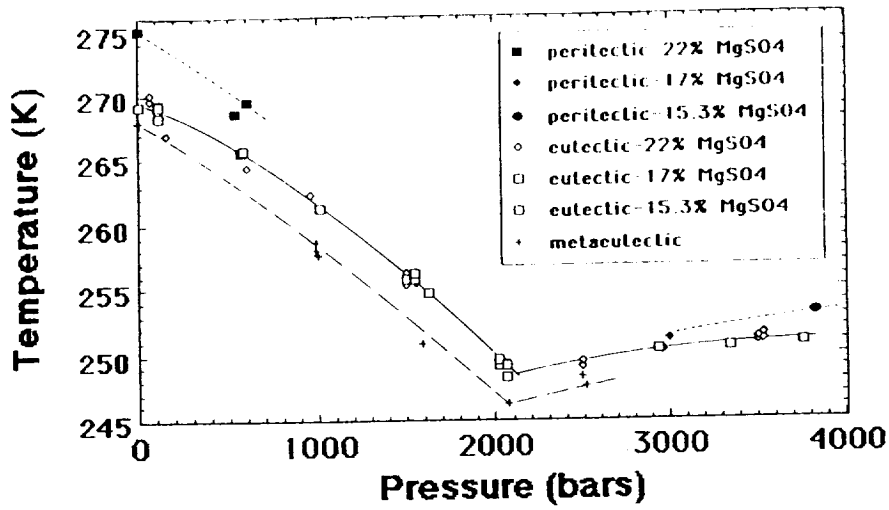

Figure 4. Melting points of magnesium sulfate mixtures.

EXPERIMENTAL CONSTRAINTS ON CO_2 AND H_2O IN THE MARTIAN MANTLE AND PRIMARY MAGMAS; John R. Holloway, Kenneth J. Domanik, and Peter A. Cocheo, Department of Geology, Arizona State University, Tempe, AZ 85281 USA

We present new data on the stability of hornblende in a martian mantle composition, on CO_2 solubility in iron-rich basaltic magmas, and on the solubility of H_2O in an alkalic basaltic magma. These new data are combined with a summary of data from the literature to present a summary of the current state of our estimates of solubilities of H_2O and CO_2 in probable martian magmas and the stability of hornblende in a slightly hydrous mantle. The new results suggest that hornblende stability is not sensitive to the Mg/(Mg+Fe) ratio (mg#) of the mantle, that is the results for terrestrial mantle compositions are similar to the more iron-rich martian composition. Likewise CO_2 solubility in iron-rich tholeiitic basaltic magmas is similar to iron-poor terrestrial compositions, the solubility of H_2O has been measured in an alkalic basaltic (basanite) composition for the first time and it is significantly lower than predicted for models of water solubility in magmas. The lack of mg# dependence observed in hornblende stability and on CO_2 solubility means that in many cases terrestrial results can be applied to martian compositions. This conclusion does not apply to other phenomena such as primary magma compositions and major mantle mineral mineralogy.

An iron-rich martian mantle composition (DW) based on the calculations of Dreibus and Wanke (1985) was prepared by sintering at 1 bar at an oxygen fugacity equivalent to the quartz-fayalite-magnetite buffer reaction (QFM). In order to synthesize amphibole peridotite, the DW mixture was sealed in $Ag_{70}Pd_{30}$ capsules with 10 wt% H_2O and run in an IHPV at 4 kb, 900 °C, QFM for one week. Experiments to determine amphibole stability and amphibole peridotite melting relations were performed in a non-end loaded, solid media piston-cylinder assembly with a 0.5" diameter cell assembly. Synthetic amphibole peridotite was loaded in Fe-saturated Pt capsules and run at 13, 18, 22, 26 and 28 kb at temperatures of 900-1500 °C. Oxygen fugacity in the piston cylinder runs was not controlled but was monitored using the Pt and Pd wire method and found to range from QFM at 13 kb to four $\log_{10}$ units below QFM at 22 kb. Run products were characterized by X-ray diffraction and electron microprobe at an accelerating voltage of 15 kV and 10 nA beam current. Analyses were corrected using the Bence-Albee method. The results show that hornblende disappears under the following conditions: 13 kb, 1000-1100 °C; 18 kb, 1100-1200 °C; 22 kb 1000-1100 °C; and 1000 °C, 26 -28 kb. These results are consistent with recent studies of hornblende stability in terrestrial mantle compositions, eg. Wallace and Green (1991).

The solubility of CO_2 was determined by Pan and Holloway (1990) in the melt composition Eg derived by Longhi and Pan (1989). The solubilities determined are very close to those found in a terrestrial tholeiitic basalt with much higher mg# (Pan, et al., 1991) and we conclude that there is little, if any effect of mg# on CO_2 solubility.

The solubility of H_2O in a basanite magma was determined to evaluate the existing solubility models for alkalic compositions as these have never previously been measured. All experiments were conducted in an internally heated rapid-quench pressure vessel (Holloway, et al., 1992). Experimental charges were contained in Fe pre-saturated platinum capsules. Powdered natural basanite was loaded into each capsule along with

known quantities of distilled or deionized water. Capsules were sealed by use of a arc welder. Oxygen fugacity was controlled by use of hydrogen-argon gas mixtures which also served as the pressure medium. Experimental charges were mounted in epoxy and polished for electron and ion microprobe analyses. Electron microprobe analyses of silicate glasses were run at an accelerating voltage of 15kV, a beam current of 10nA, and a 10μm beam size using Bence-Albee correction factors. Analyses of the platinum capsule material for iron were run at an accelerating voltage of 20kV, a beam current of 20nA with a 2μm beam size using ZAF correction factors. Doubly polished thin sections were made for some of the samples with thicknesses ranging from 20 to 70 μm for use on a FTIR spectrometer. Mid-infrared spectra were gathered to determine water concentrations using the method of Stolper (1982). The results for 1200 °C and 200 bars pressure are 1.09±0.9 wt % and for 1250 °C, 200 bars, 0.8 ±0.3 wt %. These results are significantly lower than predicted by the model of Burnham (1975) and the results of Dixon, et al. (1991) for tholeiitic basalt.

References:
Burnham, C.W. *Geochim. Cosmochim. Acta* **39**, 1077-1084 (1975).
Dixon, J.E., Stolper, E.M. & Holloway, J.R. *EOS* **73**, 348 (1992).
Dreibus, G. & Wanke, H. *Meteoritics* **20**, 367-382 (1985).
Holloway, J.R., Dixon, J.E. & Pawley, A.R. *American Mineralogist* **77**, 643-646 (1992).
Longhi, J. & Pan, V. *Proc. Lunar Planet. Sci. Conf. 19th* **19**, 451-464 (1989).
Pan, V. & Holloway, J.R. *LPI Tech. Rept.* **90-04**, 46-47 (1990).
Pan, V., Holloway, J.R. & Hervig, R.L. *Geochim. Cosmochim. Acta* **55**, 1587-1595 (1991).
Stolper, E.M. *Contrib. Mineral. Petrol.* **81**, 1-17 (1982).
Wallace, M.E. & Green, D.H. *Contrib. Mineral. Petrol.***44**, 1-19 (1991).

THE SIZE OF COMPLEX CRATERS; K.A. Holsapple, University of Washington FS-10 Seattle, WA 98195

Lunar craters larger than about *15 km* and terrestrial craters larger than about *3 km* in diameter presumably underwent gravity-driven, "late-stage" collapse that modified an initial transient bowl-shaped "simple" crater into the flat-floored complex craters observed. These same mechanisms were operative for the larger craters on other solar system bodies, at a threshold size inversely proportional to gravity. This paper presents a new look at the scaling relations for these complex craters.

There have been significant advances in the understanding of simple crater scaling relations over the past decade, those can be attributed to the combination of new experimental techniques, especially the centrifuge gravity methods Schmidt and Holsapple [1], to advances in the understanding of the theoretical basis for scaling Holsapple [2], and to the improvement in calculation techniques, e.g., O'Keefe and Ahrens [3]. It is now possible to predict with some degree of confidence and accuracy the crater that will result in a given geology from the impact of a relatively small body with given size, velocity and composition; or, from observations of a resulting crater, to ascertain combinations of conditions that would have created it. However, these advances apply only to the so-called simple craters characterized by the bowl shapes characteristic of small laboratory craters and not to the complex craters.

In addition to strength scaling for small craters, and gravity scaling for larger, there is a final complex crater regime for very large craters. The complete scaling relations are then as shown in figure 1. This complex crater regime has not been successfully calculated with codes, and require much larger combinations of gravity-scaled size than possible for experiments.

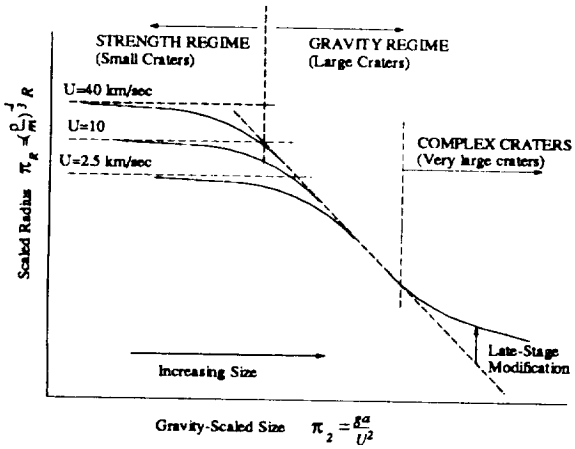

Figure 1. Scaling for crater radius, showing strength, gravity and complex crater regimes.

Previous researchers have studied the relations between a transient bowl-shaped crater and a final large complex crater, most notably Croft [4] and Melosh [5]. Both assumed that the gravitational-driven collapse of a transient bowl-shaped crater is a process that preserves volume. As a consequence, the relations for the volume scaling of simple craters should be extendible well into the regime of complex craters and basins, but the relations for crater depth and radius need significant modification.

If the slumping and rebound phenomena are effectively separate from the transient crater stages of the formation, then usual scaling relations for the gravity regime (e.g. Holsapple [2]) can be used for a maximum transient crater rim radius R_t. The subsequent crater modification stage does not depend at all on the impactor conditions but only on this transient crater size, on gravity g, on the mass density ρ of the material and on some material strength Y, so that the final rim radius is given by

$$R = f(R_t, \rho, g, Y) \tag{1}$$

This has the dimensionless form

$$\frac{R}{R_t} = f\left(\frac{\rho g R_t}{Y}\right) \tag{2}$$

and there is a single unknown function to be determined.

This relation will hold only when the crater radius is greater than some transitional crater radius R_*. At that transition $R_t = R_*$ and also $R = R_*$ so that the function must be unity when $R_t = R_*$. Thus (2) gives that

COMPLEX CRATER SIZES: Holsapple K.A.

$$R_* \propto \frac{Y}{\rho g} \tag{3}$$

and the transition radius must be proportional to some strength measure and inversely to the gravity. Using (3) gives a useful form of (2) eliminating the unknown crustal strength in terms of the observable transition radius as

$$\frac{R}{R_t} = f\left(\frac{R}{R_*}\right) \tag{4}$$

as given by Croft [4]. While it is tempting to introduce the usual power laws for this function, there is no known theoretical reason to do so. It is clear though that the function must be unity for craters below the transition size R_* and an increasing function above that threshold.

Here the function was determined from a comparison of the measured crater shapes for simple craters, and those observed for the complex craters on the Moon. The simple crater morphometry is based on laboratory craters by Schmidt et al [6] and Schmidt and Housen [7] rather than the simple analytical power law model used by Melosh [5]. The data of Pike [8] for lunar craters gives their volume as a function of the final radius R. Then the extent of the crater slumping can be determined, and a particular function determined.

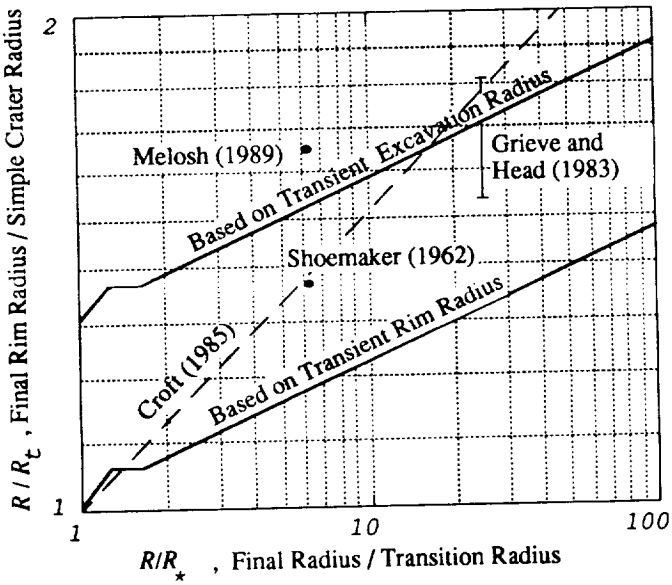

Figure 2. The radius enhancement due to late-stage modification.

The final results of this analysis are as shown in *Figure 2*. There are two curves shown, one the ratio of the final rim radius R to the transient rim radius R_r and one the ratio of the final rim radius to the transient excavation radius R_e. Previous studies have not distinguished between these, and there is a factor of *1.3* difference. Either curve is essentially a power law over most of the domain of interest. These results seem to be as consistent with the large variety of observed features given by Croft [4] as is his power-law estimate. The Shoemaker [9] estimate for Copernicus seems to be for the ratio of rim radii, so the present result is definitely below it. The Melosh [10] estimate for Copernicus is based on a model that has no difference in the two radii. The Grieve and Head [11] estimate for the *100 km* diameter terrestrial crater Manicouagan is applicable to the ratio using the transient excavation radius, and the present result agrees well.

REFERENCES

[1] Schmidt, R.M. and K.A. Holsapple *Geo. Soc. Am., Special Paper No. 190*, 1982.
[2] Holsapple, K.A. Annu. Rev. Earth Planet. Sci. 21:333-73, 1993.
[3] O'Keefe, J.D. and T.J. Ahrens *Lunar and Planetary Science XXIII*, pp 1017-1018, Houston, TX, 1992.
[4] Croft, S.K. Proc. Lunar Science Conf. 15th, *J. Geophys Res.* **90** (Supplement) pp 828-842 1985.
[5] Melosh, H.J. in Impact and Explosive Cratering, ed by Roddy, D.J. and others, Pergamon Press, N. Y., 1977.
[6] Schmidt, R.M., K.A. Holsapple, and K.R. Housen Defense Nuclear Agency Report DNA-TR-86-182, 1986.
[7] Schmidt, R.M. and K.R.Housen *Intl. J. Impact Engr.5*, 543-560, 1987.
[8] Pike, R.J. in Impact and Explosive Cratering, p 489, ed by Roddy, D.J. and others, Pergamon Press, N. Y. 1977.
[9] Shoemaker, E.M. in Physics and Astronomy of the Moon, ed. Z. Kopal, pp. 283-359, Academic, N. Y 1962.
[10] Melosh, H.J. Impact Cratering, A Geological Process, Oxford University Press, New York, 1989.
[11] Grieve, R.A.F. and J.W. Head Proc. Lunar Planet. Sci. Conf. 13th, *J. Geophys. Res.* **88**, A807- 818, 1983.

SIDEROPHILE ELEMENTS IN THE UPPER MANTLE OF THE EARTH: NEW CLUES FROM METAL-SILICATE PARTITION COEFFICIENTS: A. Holzheid, A. Borisov, H. Palme. MPI für Chemie, Saarstrasse 23, D- 6500 Mainz, Germany

New, precise data on the solubilities of Ni, Co and Mo in silicate melts at 1400°C and fO_2 from IW to IW-2 are presented. The results suggest NiO, CoO as stable species in the melt. No evidence for metallic Ni or Co was found. Equilibrium was ensured by reversals with initially high Ni and Co in the glass. Mo appears to change oxidation state at IW-1, from MoO_3 to MoO_2. Metal-silicate partition coefficients calculated from these data and recent data on Pd [1] indicate similar partition coefficients for Pd and Mo at the conditions of core formation. This unexpected result constrains models of core formation in the Earth.

EXPERIMENTAL METHODS. All experiments were conducted in a gas mixing furnace. A PtRh-Pt thermocouple and a ZrO_2 solid electrolyte oxygen sensor were employed for measuring temperature and oxygen fugacities. $CO_2/H_2/N_2$ gas mixtures were used for most of the experiments.

Silicate starting materials close to anorthite- diopside eutectic composition (48.8 wt% SiO_2, 22.7% CaO, 14.4% MgO, 14.1% Al_2O_3) were inserted into loops of pure Co, Ni and Mo- metal with a maximum diameter of 2.5 mm. Samples were equilibrated at constant temperature (1400°C) and constant run duration (50 h). Ni, Co and Mo- loops were simultaneously included in the run. Samples were quenched by withdrawal from the furnace. After separation from the loops glass samples were polished to remove possible metal contamination and were then analysed by instrumental neutron activation analysis (INAA). Repeated analyses of bulk samples and several individual pieces showed homogeneity of Co, Ni and Mo- distribution in silicate melt. A reversed experiment (AD 14*) with initially high Co and Ni content in the glass confirmed the attainment of equilibrium.

RESULTS AND DISCUSSION. Experimental conditions and results of measurements are presented in Table 1. Analytical uncertainties are below 10%. Figure 1 shows the dependence of Ni, Co and Mo solubilities on oxygen fugacity. Slopes for Ni and Co are close to 0.5 (Ni=0.48±0.02, Co=0.54±0.01), implying NiO and CoO as stable species in silicate melt. From olivine/melt partition data [4] inferred a significant fraction of metallic Ni below IW-0.3 and metallic Co below IW-2. Metallic Ni in silicate melts below IW was also postulated by [3]. No evidence for the presence of metallic Ni and Co was found in the silicate melt within the range of conditions of the present experiments (at least as low as IW-2.2). The Mo species in the silicate melt appear to change from MoO_2 at reducing conditions to MoO_3 at oxidizing conditions, alternatively a significant change of the activity coefficient of MoO_2 (γ_{MoO2}) must be considered.

In Fig. 1 we have also plotted recent data on the solubility of Pd in silicate melt of the same composition as that used here [1]. These data were obtained at 1350°C. Extrapolation to 1400°C would result in a 5% increase of solubilities [1]. The Pd-results and the partition data on Ni, Co and Mo reported here are extrapolated to lower oxygen fugacities into a region were planetary core formation is expected to occur (FeO in silicate from 20% to 1%). The two lines for the extrapolated Mo and Pd data in Fig. 1 intersect in this region. Metal/silicate partition coefficients derived from solubilities probably show a similar behaviour, as the activity coefficient of Pd in Fe-metal (γ_{Pd} = 0.4, see [1]) is only about a factor of two lower than that of Mo (γ_{Mo} in Fe- metal is assumed to be one). Since D_{Pd} is decreasing with increasing temperature [1] and D_{Mo} probably increasing (expected from MoO_2 in melt) the Pd and Mo- metal/silicate partition coefficients could be similar at even higher fO_2 than indicated in Fig. 1. In a global mantel/core equilibrium such as envisioned by [5], the residual silicate mantle would have similar, or even higher CI- normalized abundances of Mo compared to Pd, depending on the temperature extrapolation. Mo is generally considered a moderately siderophile element (together with W, P and Ge) and Pd a highly siderophile element (similar to Ir, Os and Au). Upper mantle abundances of moderately siderophile elements (Mo) are, however, more than a factor of ten above the abundances of highly siderophile elements (Pd). In the inhomogeneous accretion model [7] upper mantle abundances of moderately siderophile elements are established by addition of oxidized material that is later affected by removal of a small amount of Ni-rich metal modifying moderately siderophile elements and removing, more or less completely, the highly siderophile elements. This would occur at rather oxidizing conditions where the difference between D_{Pd} and D_{Mo} is much higher (Fig. 1). The late veneer (late accretional spike) would then provide the required amount of highly siderophile elements in the upper mantle. The amount of Mo associated with the late veneer is low, 7 ppb vs. 59 ppb in the present upper mantle [6].

REFERENCES. [1] Borisov, A. et al. (1993) *GCA* (submitted). [2] Capobianco, C.J. and Amelin, A.A. (1993) *GCA* (to be submitted). [3] Colson, R.O. (1992) *Nature* 357,65-68. [4] Ehlers, K. et al (1992) *GCA* 56,3733-3743. [5] Murthy, V.R. (1991) *Science* 253,303-306. [6] Newsom, H.E. and Palme, H. (1984) *EPSL* 69,354-364. [7] Wänke, H. et al. (1984), in *Archean Geochemistry*, 1-24.

SIDEROPHILE ELEMENTS IN THE UPPER MANTLE OF THE EARTH: Holzheid, A. et al.

Table 1. Experimental results of solubility of Ni, Co and Mo in silicate melts and calculated Fe-metal/liquid silicate partition coefficients at T=1400°C and variable oxygen fugacities

Run	#	log pO2	IW	Ni solub. [ppm]	Ni s.d. [%]	Ni D (M/S) [w.r.]	Co solub. [ppm]	Co s.d. [%]	Co D (M/S) [w.r.]	Mo solub. [ppm]	Mo s.d. [%]	Mo D (M/S) [w.r.]
AD 13	1	-9.4	IW+0.1	1699	8	840	26677	5	35			
AD 12	2	-9.6	IW-0.1	1615	5	884	21990	5	43	4183	5	411
AD 7	3	-10.0	IW-0.5	841	7	1697	12673	5	74	1129	5	1522
AD 10	4	-10.3	IW-0.8	672	5	2124	9322	5	101	548	5	3135
AD 6	5	-10.6	IW-1.1	434	5	3288	6206	5	151	223	5	7705
AD 1	6	-10.6	IW-1.1	410	5	3481	6179	5	152	196	5	8766
AD 8	7	-10.8	IW-1.3	350	5	4078	4728	5	198	83.2	5	20659
AD 11	8	-10.9	IW-1.4	337	6	4235	4243	5	221	69.2	5	24830
AD 5	9	-11.1	IW-1.6	279	7	5115	3392	5	277	40.0	6	42923
AD 9	10	-11.3	IW-1.8	224	5	6371	2709	5	346	34.5	5	49746
AD 14	11	-11.4	IW-1.9	160	9	8920	2377	5	395	21.6	6	79694
AD 14 *	12	-11.4	IW-1.9	178	6	8018	2430	5	386			
AD 2	13	-11.6	IW-2.1	156	6	9149	1850	5	507	15.2	9	113115
AD 3	14	-11.7	IW-2.2	164	7	8702	1535	5	611	11.3	7	151920

*-reversal; solub.-solubility; s.d.-standard deviation; w.r.-weight ratio; D(M/S) are calculated from D(M/S)=1/[X(metal)×γ(metal, in Fe-metal alloy)], X(metal)= mole fraction of the total amount of metal in silicate melt, γ_{Ni} =0.736 (see [2]), γ_{Co} =1.124 (see [2]), γ_{Mo} =1 (assumed)

Fig.1: Solubilities of siderophile elements in silicate melt

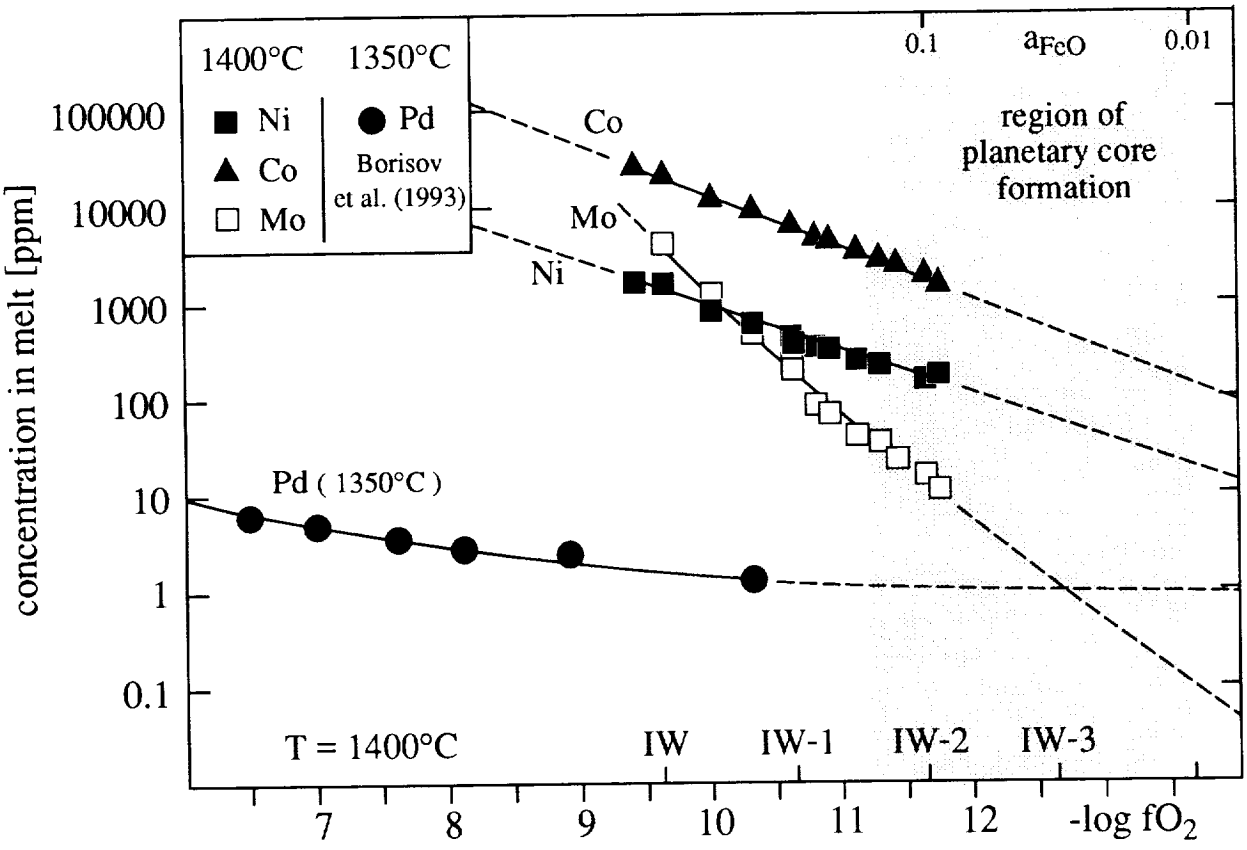

GAS-GRAIN ENERGY TRANSFER IN SOLAR NEBULA SHOCK WAVES: IMPLICATIONS FOR THE ORIGIN OF CHONDRULES; L. L. Hood, Lunar and Planetary Laboratory, University of Arizona, Tucson, AZ 85721; and M. Horanyi, Laboratory for Atmospheric and Space Physics, University of Colorado, Boulder, CO 80309.

Meteoritic chondrules provide evidence for the occurrence of rapid transient heating events in the protoplanetary nebula (1,2,3). Astronomical evidence suggests that gas dynamic shock waves are likely to be excited in protostellar accretion disks by processes such as protosolar mass ejections, nonaxisymmetric structures in an evolving disk, and impact on the nebula surface of infalling "clumps" of circumstellar gas (4,5). Previous detailed calculations of gas-grain energy and momentum transfer have supported the possibility that such shock waves could have melted pre-existing chondrule-sized grains (4). The main requirement for grains to reach melting temperatures in shock waves with plausibly low Mach numbers is that grains existed in dust-rich zones (optical depth > 1) where radiative cooling of a given grain can be nearly balanced by radiation from surrounding grains. Localized dust-rich zones also provide a means of explaining the apparent small spatial scale of heating events. For example, the scale size of at least some optically thick dust-rich zones must have been relatively small (< 10 kilometers) to be consistent with petrologic evidence for accretion of hot material onto cold chondrules (6,7). The implied number density of mm-sized grains for these zones would be > 30 m^{-3}. In this paper, we make several improvements of our earlier calculations to (i) include radiation self-consistently in the shock jump conditions; and (ii) include heating of grains due to radiation from the shocked gas. In addition, we estimate the importance of momentum feedback of dust concentrations onto the shocked gas which would tend to reduce the efficiency of gas dynamic heating of grains in the center of the dust cloud.

To account for radiative losses of the shocked nebular gas in one dimension, radiative loss terms were added to the energy conservation equation of the ordinary gas dynamic shock jump conditions (8). Assuming that hydrogen in the nebula can be approximated as a polytropic gas (constant ratio of specific heats), we have used the ideal gas law and polytropic relations for enthalpy in terms of temperature and pressure. The resulting system of equations was solved numerically to calculate post-shock parameters such as temperature, mass density, and relative velocity. As expected, the post-shock temperature is reduced at a given Mach number compared to that calculated from the ordinary gas dynamic relations and is also a function of initial number density. For plausible Mach numbers (< 6), the nebula number density must exceed $\sim 10^{14}$ cm^{-3} for post-shock temperatures to reach levels of at least 850 K as needed (see below) to bring grain temperatures up to silicate melting temperatures in dust-rich zones.

Using the calculated post-shock gas physical parameters for a given Mach number, we have numerically integrated the gas-grain energy and momentum transfer equations as in ref. 4. The pre-shock gas number density was chosen as 10^{14} cm^{-3} and temperature as 500 K. Radiative energy transfer from gas to grain was accounted for by adding an appropriate T^4 term where T is the gas temperature. The grain emissivity was chosen as 0.75 and the grain absorption coefficient was chosen as 0.9 (albedo 0.1). The grain was assumed to be surrounded by an optically thick cloud of other grains with the same temperature as

GAS-GRAIN ENERGY TRANSFER: Hood, L.L. and Horanyi, M.

the grain of interest. Results show that complete melting of 1 mm radius silicate grains within a time of $\sim$ 1 minute requires Mach numbers of at least 3.5 under these assumed conditions. An example calculation is shown in Figure 1 for a Mach 4 shock (post-shock gas temperature 920 K and relative velocity 5.7 km/s). The solid fraction (SF) is reduced to zero within 15 seconds. In contrast, an isolated grain exposed to a Mach 4 shock wave reaches a maximum temperature of only 1250 K. One significant contributor to the heating is drag heating due to the translational velocity of the shocked gas relative to an individual grain as the shock wave passes. In reality, grains near the center of a dust-rich zone will experience lower gas relative velocities due to interaction of the up-stream gas with other grains. As an approximate way of gauging the significance of this momentum feedback effect on the shocked gas, we have carried out additional calculations with the gas relative velocity set equal to zero. The shocked gas is assumed to diffuse to the interior of the dust cloud so that heating of grains via radiation and molecular collisions can still occur. Results show that somewhat higher minimum Mach numbers of about 4 are required to melt grains. Of course, dust concentrations that are sufficiently dense as to completely shield their interiors from the shocked gas will not be efficiently heated by this mechanism.

REFERENCES. (1) Taylor, G. J. et al., in *Chondrules and Their Origins*, (E. A. King, ed.), pp. 262-278, Lunar and Planetary Institute, Houston, 1983; (2) Grossman, J. N. et al., in *Meteorites and the Early Solar System* (J. F. Kerridge and M. S. Matthews, eds.), pp. 619-659, Univ. of Arizona Press, Tucson, 1988; (3) Hewins, R. H., *ibid.*, pp. 660-679; (4) Hood, L. L. and M. Horanyi, *Icarus, 93*, 259-269, 1991; (5) Boss, A. and J. A. Graham, *Icarus*, submitted, 1993; (6) Kring, D. A., *Earth Planet. Sci. Lett., 105*, 65-80, 1991; (7) Wood, J. A., *Earth Planet. Sci. Lett., 70*, 11-26, 1984; (8) Landau, L. D., and E. M. Lifshitz, *Fluid Mechanics*, Pergamon, New York, 1987.

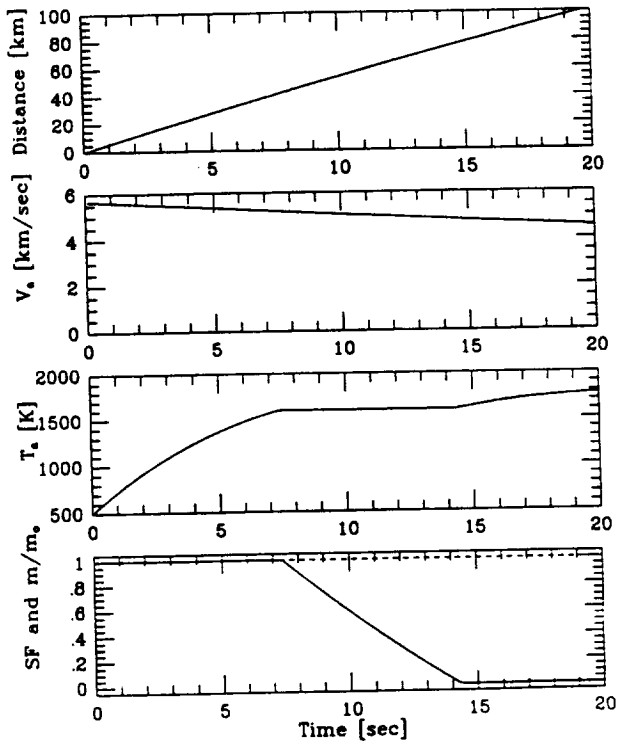

Fig. 1

MASS OF SATURN'S A RING

L.J. Horn, Jet Propulsion Laboratory, Pasadena, CA 91109; C.T. Russell, Institute of Geophysics and Planetary Physics, University of California, Los Angeles, CA 90024

The mass of Saturn's A ring is reestimated using the behavior of spiral density waves embedded in the ring. The Voyager photopolarimeter (PPS) observed the star δ Scorpii as it was occulted by Saturn's rings during the Voyager 2 flyby of Saturn in 1981 [1] (see Figure 1), producing a radial profile of the rings. We examined forty spiral density waves in the Voyager PPS data of the A ring, including 10 weaker waves that have not been previously analyzed, using an autoregressive power spectral technique called Burg. The strengths of this new method for ring studies are that weaker, less extended waves are easily detected and characterized. This method is also the first one which does not require precise knowledge of the resonance location and phase of the wave in order to calculate the surface mass density [2]. Uncertainties of up to 3 km are present in the currently available radial scales for Saturn's rings.

Spiral density waves are gravitational perturbations in the ring produced by discrete, non-overlapping orbital resonances with satellites orbiting just outside the ring. The material in these waves is alternately compressed then rarefied producing horizontal oscillations in ring opacity. This changing pattern of ring particle density transfers energy and angular momentum to the satellite until the wave is damped. The behavior of the wave as it disperses is one tool for probing the physical characteristics of the ring. Key ring properties, including surface mass density, are determined from the dispersion of the waves. Surface mass density, the mass of ring particles per unit area, is then used to estimate the total ring mass.

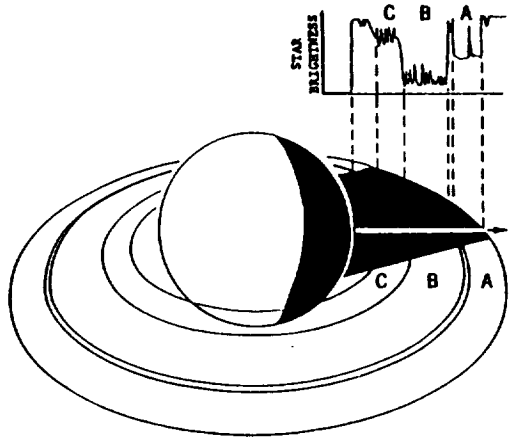

Figure 1: Voyager 2 PPS Occultation Scan.

The bulk of the density waves disperse in a linear fashion. This dispersion behavior is used to calculate the local surface mass density in the vicinity of each wave. We assume that the surface mass density in a spiral density wave is representative of more extended ring regions around the wave. For purposes of comparison, the A ring is divided into three sections, using the Encke and Keeler gaps as boundaries. Average surface mass densities were calculated for each of these regions. The region inward from the Encke gap has an average surface mass density of 44.6 gm/cm^2. The region between the Encke and Keeler gaps has an average surface mass density of 28.9 gm/cm^2 and the region from the outer Keeler gap edge to the edge of the A ring has an average surface mass density of 30.3 gm/cm^2. The mass of each section of the A ring was then computed from these average values.

The reestimated mass for the A ring is 5 x 10^{21} gm, equivalent to the mass of a satellite (composed of ice) with a radius of 110 km. This new mass estimate is about 15% smaller than estimates from previous studies. Those studies attempted to perform linear fits to some of the density waves that we found to disperse non-linearly in this study. Those earlier estimates of surface mass density may have been a factor of 2 to 4 too high for some of the strongest density waves, leading to a slight overestimate in A ring mass.

MASS OF SATURN'S A RING: L.J. Horn and C.T. Russell

The total Saturn ring mass was initially estimated by Esposito [3] using 13 waves from the PPS data and by Holberg [4] using fewer and lower resolution waves from the Voyager ultraviolet data. Each group assumed that the ratio of mean optical depth near the first wave crest to the surface mass density was more or less constant. Then, assuming a constant particle size distribution across the ring system, the mass was estimated. Our results indicate that the ratio of optical depth to surface mass density is not constant, especially in the outer A ring.

The A ring surface mass density generally tends to decrease with increasing radial distance from Saturn. The region, from the beginning of the A ring to the Encke gap, has typical surface mass densities of 40 to 60 gm/cm^2. The typical surface mass densities for the region outside the Encke gap are 20 to 30 gm/cm^2, a significant decrease given that the average optical depth is roughly 10% greater for the region outside the Encke gap than for the region interior to the Encke gap. This behavior indicates that the ring particle size and composition are not uniform throughout the A ring. If they were similar the surface mass density and optical depth would increase or decrease concurrently.

Surface mass densities were calculated for the weak waves outside the Keeler gap for the first time. Surface mass densities in this region are also uncorrelated with optical depth, indicating that particle size and composition are not uniform in this region of the A ring. These measurements are significant because the photometric properties of the particles in this ring region are quite different from those in the remainder of the A ring [5].

One notable exception to the general trend is the Prometheus 9:8 density wave in the inner portion of Saturn's A ring. This density wave is driven by the satellite Prometheus where the ratio between the ring particle mean motion and Prometheus mean motion is 9/8. This wave has a surface mass density of 70.5 ± 6.1 gm/cm^2, the largest surface mass density of any of the density waves we studied. Even with the large error bars, the Prometheus 9:8 surface mass density does not fall within the error bars of other measured density waves in this study. The only published surface mass density for this wave is from Rosen [6], using the Voyager radio occultation data taken one year earlier. Rosen's value is more than a factor of 2 smaller for this wave. No other known density waves or wakes lie close to this region. The large disparity between results in this study and Rosen's calculated surface mass density is in need of an explanation. Perhaps an azimuthal variation within the ring or a temporal effect within the wave over the one year which separates the measurements might explain the large difference in surface mass density measurements. Both the rings of Uranus and Neptune display azimuthal variability so such variability should not be ruled out for Saturn's rings.

REFERENCES

[1] Lane, A. L. *et al.* (1982) *Science* **215,** 537-543.
[2] Horn, L.J., Hui, J., Lane, A.L., and Nelson, R.M. (1993) Saturn A ring surface mass densities from spiral density wave dispersion behavior. submitted to *Icarus.*
[3] Esposito, L.W., O'Callaghan, M. and West, R.A. (1983) *Icarus* **56,** 439-452.
[4] Holberg, J.B., Forester, W. and Lissauer,J.J. (1982) *Nature* **297,** 115-120.
[5] Dones, L., Cuzzi, J.N., and Showalter, M.R. (1993) Voyager photometry of Saturn's A ring. submitted to *Icarus.*
[6] Rosen, P.A., Tyler, G.L., Marouf, E.A., Lissauer, J.J. (1991) *Icarus* **93,** 25-44.

IMPACT PENETRATION EXPERIMENTS IN TEFLON TARGETS OF VARIABLE THICKNESS; F. Hörz[1], M.J. Cintala[1], R.P. Bernhard[2] and T.H. See[2], [1]Solar System Exploration Division, SN4, NASA-Johnson Space Center, Houston, TX 77058, [2]Lockheed-ESC, C23, 2400 NASA Road 1, Houston, TX 77058.

INTRODUCTION - Approximately 20.4 m^2 of Teflon thermal blankets on the non-spinning Long Duration Exposure Facility (LDEF) were exposed to the orbital debris and micrometeoroid environment in low-Earth orbit (LEO) for ~5.7 years. Each blanket consisted of an outer layer (~125 μm thick) of FEP Teflon that was backed by a vapor-deposited metal mirror (Inconel; <1 μm thick). The inner surface consisted of organic binders and Chemglaze thermal protective paint (~50 μm thick) resulting in a somewhat variable, total blanket thickness of ~180 to 200 μm. There was at least one of these blankets, each exposing ~1.2 m^2 of surface area, on nine of LDEF's 12 principal pointing directions, the exceptions being Rows 3, 9 and 12. As a consequence, these blankets represent a significant opportunity for micrometeoroid and debris studies, in general, and specifically they provide an opportunity to address those issues that require information about pointing direction [1] (*i.e.*, spatial density of impact events as a function of instrument orientation). During deintegration of the LDEF spacecraft at the Kennedy Space Center, all penetration holes ≥300 μm in diameter were documented [2] and were recently synthesized in terms of spatial density as a function of LDEF viewing direction by [3]. The present report describes ongoing cratering and penetration experiments in pure Teflon targets, which are intended to establish the relationships between crater or penetration-hole diameters and the associated projectile dimensions at laboratory velocities (*i.e.*, 6 km/s). The ultimate objective of these efforts is to extract reliable mass-frequencies and associated fluxes of hypervelocity particles in LEO.

IMPACT EXPERIMENTS - A single piece of round stock (~80 mm in diameter) of Teflon[FEP] was machined into targets of variable thickness, with T ranging from "infinite halfspace" (≥ 25 mm) to 0.5 mm; targets <0.5 mm in thickness were cut from commercially available Teflon sheets. All targets were impacted with 3175 μm diameter (D_p) soda-lime glass spheres at 6.2 to 6.4 km/s; a few experiments were conducted with glass projectiles 150 and 1000 μm in diameter at modestly lower velocities of 5.9 to 6.1 km/s. We refer to all experiments as being representative for nominal encounter velocities of ~6 km/s.

RESULTS - Figure 1 illustrates some

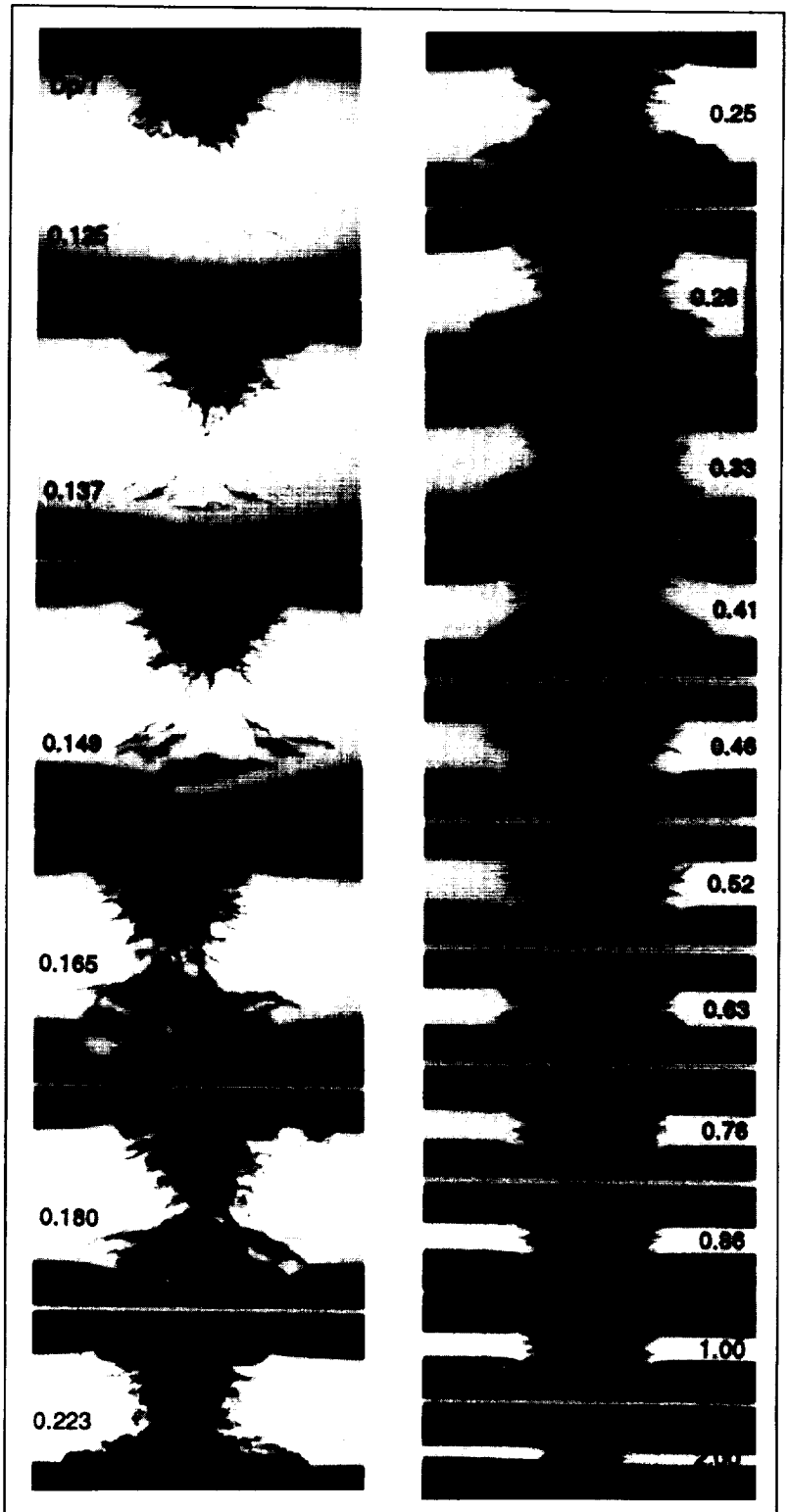

Figure 1. Typical cross-sections of craters and penetrations for Teflon target where D_p=3175 μm and V=6 km/s. Note D_p/T=1.0 for uniform scale.

Q-4

N

IMPACT PENETRATION EXPERIMENTS IN TEFLON TARGETS; Hörz, Cintala, Bernhard and See

representative cross-sections of penetrations of relatively massive Teflon targets, systematically arranged with increasingly larger relative projectile size (D_p/T). Note that Teflon fails largely in a brittle fashion, giving rise to sizeable, highly scalloped spall zones surrounding a central crater on the target's front side, and surrounding the exit hole at the target's rear in the case of penetrations. The poorly defined central craters posses average diameters of 3.6 D_p, while the morphologically dominant spall diameters (D_s) average 6.1 D_p at 6.3 km/s using the 3175 μm projectiles. As previously described from similar experiments employing aluminum targets of variable thickness [4], penetrations of massive Teflon targets (at $D_p/T<0.75$) must be viewed as truncated craters, because their surface expressions on the front side remain relatively uniform, unlike the spall features at the target's rear. Note that the cross-sections in Figure 1 are totally dominated by spallation phenomena at the rear surface. Foil thicknesses below 1.0 D_p are required for production of penetration-hole diameters that are significantly smaller than the crater diameter (D_c) in the "infinite halfspace" Teflon targets. Actual measurements of the penetration-hole diameters for all experiments are summarized in Figure 2. Note that unique solutions for D_p result from any measurement of D_h and T, at least at constant velocity. The delineation between "cratering" and incipient penetration (*i.e.*, the ballistic limit) for Teflon is at $D_p/T=0.17$ under the prevailing conditions, while the ballistic limit for aluminum 1100 occurred at $D_p/T=0.29$ [4]. The condition where $D_h=D_p$ in Teflon is met only at T of ~1/100 D_p. The transition from the pure cratering regime in the massive targets to the condition of $D_h=D_p$ is very gradual and encompasses approximately three orders of magnitude in target thickness. This gradual transition illustrates the great care needed when extracting projectile sizes from the LDEF thermal blankets. Figure 3 illustrates the size distribution, normalized to target thickness, of all penetration holes ≥300 μm in diameter that were documented for the LDEF thermal blankets. Note that most penetrations are characterized by $D_p/T<5$. On the basis of Figure 2 it must be concluded that neither pure cratering formulas, much less the assumption of $D_h=D_p$, are suitable to solve for the diameters of the respective projectiles for most LDEF penetrations.

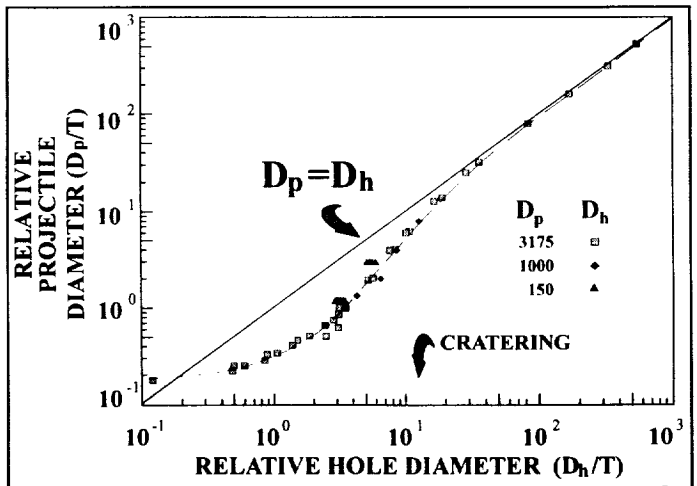

Figure 2. Diameter of penetration hole (D_h) versus projectile (D_p) for Teflon targets of thickness (T) at an encounter velocity of 6 km/s for soda-lime glass projectiles 3175, 1000 and 150 μm in diameter. Solid line represents the case of $D_p = D_h$.

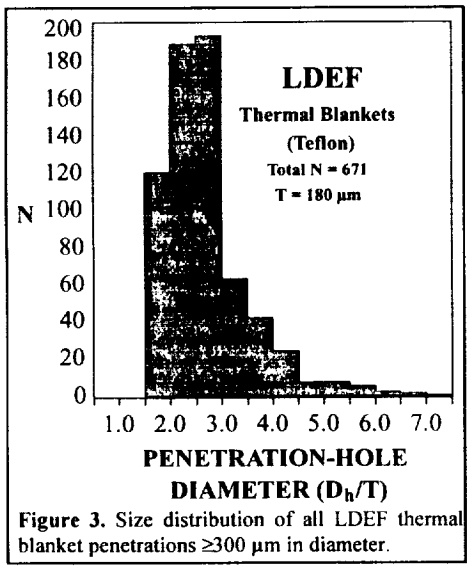

Figure 3. Size distribution of all LDEF thermal blanket penetrations ≥300 μm in diameter.

A variety of curve-fitting techniques were applied to the data points in Figure 2, with the best fit resulting from the polynomial equation of the form

$$\log_{10} y = a_0 + a_1 (\log_{10} x)^2 + a_2 (\log_{10} x)^3 + a_n (\log_{10} x)^n$$

where $y = D_p/T$ and $x = D_h/T$; for Teflon, the following coefficients apply: a_0 = -0.485, a_1 = 0.667; a_2 = 0.562 ; a_3 = -0.230; a_4 = 0.518, a_5 = 0.021, a_6= -0.661, a_7 = 0.415, and a_8 = -0.075.

CONCLUSIONS - Calibration curves for the relationship between the projectile diameter, target thickness, and penetration-hole size were established for pure Teflon targets and spherical glass projectiles traveling at ~6 km/s. These experiments and those of [4] indicate a gradual yet systematic transition from the cratering regime in infinite halfspace targets to penetration(s) of increasingly thinner targets. This continuum is best described by a polynomial fit. This approach eliminates the previous difficulties encountered when converting measured populations of crater and penetration-hole diameters, all derived from a single, space-exposed target, into projectile-size and mass-frequency distributions. Such conversions typically resulted in substantial mass discontinuities, depending on the specific cratering or penetration formula used [*e.g.*, 5 and 6]. Clearly, additional and substantial experimental efforts at higher and lower impact speeds are needed to establish the velocity dependence of the current results. Once this is accomplished, one may apply the mean encounter velocities of [1] for any given viewing direction on LDEF to extract, in principle, a unique projectile size from every penetration hole, making the additional assumption of uniform projectile materials. This seems to be an improvement over traditional ballistic-limit considerations that produced a single, cumulative datum only for all impactors larger than a specified threshold size (for otherwise identical, general assumptions).

REFERENCES - [1] Zook. H.A. (1991), in *LDEF-69 Months in Space, First Post Retrieval Symposium, NASA CP-3134*, p. 569-579. [2] See, T.H., *et al.*, (1990), *NASA Johnson Space Center Publication # 24608*, pp. 583. [3] See, T.H. *et al.*, (1992), in *LDEF-69 Months in Space, Second Post Retrieval Symposium*, in press. [4] Hörz, F. *et al.*, (1993), *Int. J. Impact Eng.*, submitted. [5] Warren, J. *et al.*, (1989), Proc. Lunar Planet. Sci. Conf. 19th, p. 641-657. [6] Humes, D.H. (1991), in *LDEF-69 Months in Space, First Post Retrieval Symposium, NASA CP-3134*, p. 399-418.

SIMULATION OF COLLISIONAL FRAGMENTATION WITH EXPLOSIVES

Kevin Housen, Shock Physics Group, The Boeing Company MS 87-60, Seattle, WA, 98124.

For practical reasons, experimental studies of collisional fragmentation must at times rely on explosives to fragment a target body. For example, Housen *et al.* (1991) described experiments in which spheres were fragmented in a pressurized atmosphere. Explosives were used because impacts could not be performed in the pressure chamber. Explosives can also be used to study targets much larger than those which can be disrupted by conventional light-gas guns, thereby allowing size- and rate-effects to be investigated. The purpose of this study is to determine the charge burial depth required to simulate various aspects of collisions.

Explosions have long been used as analogues of impact cratering events (e.g. Shoemaker, 1963; Roddy *et al.*, 1975; Oberbeck, 1977). Although one cannot expect an explosion to reproduce all of the details of an impact, experiments have shown that, with a suitable choice of the explosive burial depth, various aspects of the problem, such as crater size or shape, can be simulated quite well. For example, Holsapple (1981) showed that, for an impact and explosion of equal energies, the impact crater volume could be reproduced by burying the explosive at a depth of 1 to 2 charge diameters, depending on the energy and velocity of the impact in question.

Various measures can be used to gauge the equivalence between impacts and explosions, such as the size distribution of fragments, fragment velocities, etc. As an example, consider the mass, M_L, of the largest target fragment. For a collision with a strength dominated target, M_L depends on the impactor mass, m, density δ, and specific energy q (i.e. velocity^2/2), and the target's density ρ, strength Y, and mass M. To simulate an impact, an explosive charge is used whose mass, specific energy and density are given by m', q', δ'. The center of the charge is buried a distance d beneath the target surface.

Housen *et al.* (1991) derived a nondimensional scaling law based on a point-source approximation for the impactor or explosive. In the point-source limit, the source variables are replaced by the single quantity $m\,q^{3\mu/2}$. Housen *et al.* showed that the scaling exponent μ for the weakly-cemented basalt used in their experiments is about 0.55, distinctly below the energy scaling value of 2/3. The point-source limit provides a relatively simple scaling form in which, for impact, the mass of the largest fragment is a function of a single parameter, π_Y, which is a measure of the intensity of the collision. For explosions, the largest fragment is a function of this same parameter, along with the nondimensional burial depth of the charge. That is,

$$\text{Impact: } \frac{M_L}{M} = F[\pi_Y]; \qquad \text{Explosion: } \frac{M'_L}{M} = F\left[\pi'_Y,\ \frac{d}{a'}\left(\frac{Y}{\rho q'}\right)^{\mu/2}\right] \quad \text{where} \quad \pi_Y = \frac{Q}{q}\left(\frac{Y}{\rho q}\right)^{-3\mu/2}$$

and where Q is the source energy per unit target mass, mq/M, a' is the radius of the explosive charge, and π'_Y is the value of π_Y for the explosion. The equivalent burial depth is defined here as that depth which, for equal values of π_Y and π'_Y, results in equal masses of the largest fragment from an impact and an explosion.

A series of fragmentation tests were performed using spherical targets, 14.7 cm in diameter, constructed from the weakly cemented basalt described by Housen *et al.* (1991). The spheres rested on a foam pedestal inside a chamber which was lined with foam rubber to prevent breakage of fragments which struck the chamber wall. The impact tests used aluminum cylinders launched horizontally at velocities ranging from 2 to 3.5 km/s. The explosion tests used cylindrical charges made from green deta sheet. The events were filmed with a Fastax camera running at 6000 frames/sec. The masses of the largest fragments are shown in the accompanying figures and table.

Three identical impacts were performed to determine the experimental scatter in the largest fragment mass (see Fig. 1). Four explosion tests were then performed at the same value of π_Y as the three impacts. The burial depth was varied over a range of 2 to 4.2 charge radii. As shown in Fig. 1, the explosives buried at depths of 2 and 2.4 radii agreed well with the impact results, while the two tests at 3.4 and 4.2 radii produced largest fragments smaller than the impacts. This is also illustrated in Fig. 2, which shows the variation of the largest fragment mass with burial depth, for a value of $\pi_Y \approx 2.4$. As might be expected, the mass of the largest fragment steadily decreased as the charge was buried

deeper in the target. Figure 2 suggests that a burial depth near 2.5 charge radii gives a largest fragment comparable to that of the impact tests (shown on the left axis of the figure).

Other measures can be used to assess the equivalence between explosive and collisional fragmentation. As an example, Table 1 shows the velocity of the largest fragment, as measured from films of the events. The three collision tests gave velocities in the range of 1.4 to 1.6 m/sec. For comparison, the explosion at a depth of 2.4 radii gave a velocity of 1.4 m/sec. The velocity for the deepest charge (4.2 radii) was only slightly higher (1.6 m/sec). Therefore, although the velocities from the explosions are in general agreement with the impact results, the velocity of the largest fragment is a relatively insensitive measure of equivalence.

These tests give a preliminary measure of equivalence between collisional and explosive fragmentation. For the value of π_Y studied here, which gives largest fragments close to the usual definition of the threshold for catastrophic fragmentation ($M_L/M \approx 0.5$), equivalence in the largest fragment is obtained if the center of the charge is buried at roughly 2.5 charge radii. This value may depend on the value of π_Y. Additional tests are planned to study this question.

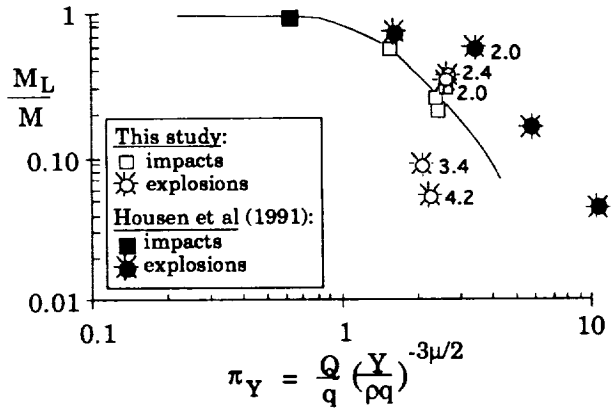

Fig. 1. Comparison of the mass of the largest fragment from impacts and explosions at various burial depths. The numbers next to the explosion points give the burial depth of the charge normalized by the charge radius.

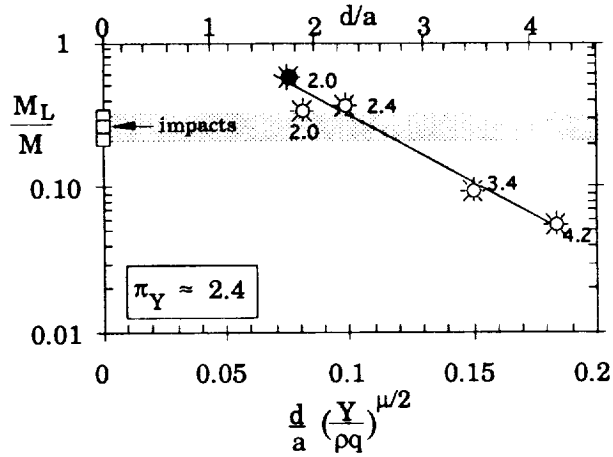

Fig. 2. The mass of the largest fragment from an explosion as a function of charge burial depth. Agreement with the impact results is obtained when the explosive is placed about 2.5 charge radii beneath the target surface.

Table 1. Summary of results of impact and explosive fragmentation tests.

#	Y		q	m	δ	d	d/a	M	ML	Q	πY	ML/M	vL
shot	tensile	source	specific	source	source	burial	depth/	target	largest	energy/		frag/	vel of
no.	strength	type	energy	mass	density	depth	radius	mass	frag	targ mass		total	ML
-	(dyn/cm^2)	-	(ergs/gm)	(gm)	(gm/cc)	(cm)	-	(gm)	(gm)	-	-	-	cm/s
1185	9.23E+05	imp	6.02E+10	0.537	2.8	-	0.00	4457	1405	7.26E+06	2.56	0.32	143
1186	9.56E+05	imp	5.99E+10	0.537	2.8	-	0.00	4434	933	7.25E+06	2.46	0.21	162
1187	9.94E+05	imp	5.92E+10	0.540	2.8	-	0.00	4451	1159	7.17E+06	2.37	0.26	160
1188	9.47E+05	imp	3.38E+10	0.537	2.8	-	0.00	4443	2536	4.09E+06	1.55	0.57	
1190	9.27E+05	expl.	3.85E+10	0.800	1.48	1.00	1.98	4499	1511	6.85E+06	2.57	0.34	120
1191	1.13E+06	expl.	3.85E+10	0.800	1.48	2.15	4.24	4456	244	6.91E+06	2.20	0.05	161
1192	1.21E+06	expl.	3.85E+10	0.800	1.48	1.72	3.40	4481	413	6.87E+06	2.08	0.09	141
1193	9.27E+05	expl.	3.85E+10	0.800	1.48	1.21	2.39	4427	1629	6.96E+06	2.63	0.37	136

References: (1) Holsapple K.A. (1981) *Proc. Lunar Planet. Sci. Conf. 11th*, 2379-2401. (2) Housen *et al.* (1991) *ICARUS* **9 4** 180-190. (3) Oberbeck V.R. (1977) *Impact and Explosion Cratering*, Pergamon (New York), 45-65. (4) Roddy *et al.* (1975) *Proc. Lunar Sci. Conf. 6th*, 2621-2644. (5) Shoemaker E.M. (1963) *The Moon, Meteorites and Comets*, Univ. Chicago Press, 301-306.

OLIVINES IN THE KABA CARBONACEOUS CHONDRITE AND CONSTRAINTS ON THEIR FORMATION

X. Hua[1,2] and P. R. Buseck[1], [1]Depts. of Geology & Chemistry, Arizona State University, Tempe, AZ 85287 USA. [2]Central Laboratory, China University of Geosciences, Wuhan, PRC.

INTRODUCTION Kaba is unique in containing almost pure fayalitic olivine ($Fo_{0.1}$) [1]. Its coexistence with pure forsterite (up to $Fo_{99.6}$) and normal (Fo_{92} to Fo_{59}) and reversely ($Fo_{0.4}$ to $Fo_{4.7}$) zoned olivines suggests that the Kaba olivines are in thermodynamic disequilibrium and experienced a complicated history. The fayalite is sufficiently pure that it is unlikely that it could have been produced by fractional crystallization. A gas-solid reaction under oxidizing conditions (H_2O/H_2 ratio ~10) is probably responsible for its formation.

OBSERVATIONS Kaba fayalite occurs in matrix, chondrules, and rims around CAIs. The fayalite in matrix occurs (a) as isolated euhedral crystals up to 85 μm across (Fig. 1), (b) grouped around cores of troilite and pentlandite with or without magnetite, and (c) "sandwiched" between sulfides. The zoned olivines also occur within matrix. The fayalite in chondrules and chondrule-like objects is more abundant than in matrix. It occurs within enstatite and barred forsterite chondrules and in thin (< 10 μm) rims surrounding some chondrules (Fig. 2). It is found in a rim (65 μm wide) around a chondrule-like object with a 200-μm core consisting of magnetite and dispersed troilite. Fayalite crystals also occur in accretionary dust mantles around type-A Ca-Al-rich inclusions. Pure forsterite occurs in chondrules, and some spindle-like fayalitic halos surround the Ni-rich metal inclusions within the forsterite [2].

Minor elements such as Mg, Mn, and Ni in the fayalite are of special interest because they provide information relevant to its origin. The Kaba fayalites contain from 0.02 wt % to 2.5 wt % MgO, but can reach up to 4.7 wt % MgO where the grains are smaller than 5 μm or sandwiched between sulfides. They contain 0.5 to 1 wt % MnO. In the fayalites with reversed zoning, MnO shows a positive correlation with MgO. NiO is close to the minimum detection limit of 0.05 wt %.

DISCUSSION Olivine of such high fayalite content is unknown in other meteorites. A major problem exists in understanding its formation and subsequent persistence without reequilibration with the coexisting forsterite. The presence of forsterite adjacent to fayalite indicates that Kaba could not have experienced high-temperature metamorphism subsequent to the development of the olivine assemblage; the low temperature is confirmed by the presence of phyllosilicates [3]. The occurrence of zoned olivines in the matrix is also in agreement with the above conclusion, because otherwise homogeneous compositional profiles would have developed. Coexisting forsterite and fayalite is a disequilibrium assemblage that could not have formed in place and retained the end-member compositions. The questions are where and how could these olivines have formed? Forsterite could easily have crystallized from a melt or by condensation, as is widely observed in, respectively, terrestrial rocks and other meteorites. The fayalite is more puzzling. It is difficult to conceive of a melt that is sufficiently free of Mg, Mn, Ni, and perhaps other divalent cations to allow almost pure fayalite to crystallize. Similarly, normal condensation processes in the solar nebula invariably produce forsteritic olivines [4,5]. The answer to this problem is not clear, but minor-element chemistry can provide useful information.

If the fayalite formed from a melt, as is typical of terrestrial olivines, then it would almost invariably contain appreciable quantities (several percent or more) of MgO and MnO. If the parent melt had been in equilibrium with metal or a sulfide such as pentlandite, then Ni would have entered the fayalite structure. Lack of appreciable Mg, Mn, and Ni in the fayalite indicates that it formed by another mechanism. Based on its low Ni content, we conclude that it is unlikely that the fayalite formed by reaction between metal and silicate. We also conclude that it is unlikely that the fayalite formed from a melt; condensation remains a viable alternative.

OLIVINES IN KABA: Hua X. and Buseck P. R.

A possible mechanism for the formation of fayalite is the reaction of a Si-bearing gas such as SiO with an Fe oxide such as magnetite. We therefore propose the following as a possible model for olivine formation within Kaba.

(1) According to the normal condensation sequence in the solar nebula, forsterite, enstatite, sulfides, and magnetite formed at low temperatures (<400 K) [4,5].

(2) Forsterite and enstatite moved to a dust-rich region such as possibly the mid-plane of the asteroid belt, where the temperature and fO_2 were high as a result of the high density and the evaporation of some O-rich dust [6].

(3) Enstatite was reheated enough to partially evaporate, releasing SiO gas. A possible reaction is:

$$2\ MgSiO_3\ (s) + H_2 = Mg_2SiO_4\ (s) + SiO\ (g) + H_2O$$

At this stage, metal inclusions within the forsterite began to be oxidized, producing Fe^{2+} and leaving the metal enriched in Ni. The Fe^{2+} diffused into the surrounding forsterite to form the spindle-like halos [2].

(4) Magnetite and sulfides reacted with SiO gas to form fayalite. A possible reaction is:

$$2\ Fe_3O_4\ (s) + 3\ SiO\ (g) + H_2O = 3\ Fe_2SiO_4\ (s) + H_2$$

(5) Fayalite then moved into a cooler region shortly after its formation, where it remained.

(6) Accretion of the Kaba meteorite took place at a rather low temperature (~400 K?), which gave different olivines no chance to react with one another.

Thermodynamic calculations indicate that in the absence of Mg, pure fayalite coexisting with magnetite and sulfides will form in an environment that has an H_2O/H_2 ratio equal to 10 [7] at a temperature of around 1200 K [5].

REFERENCES: (1) Hua X. and Buseck P. R. (1992) Meteoritics 27, 236, (2) Hua X. et al. (1991) Meteoritics 26, 347, (3) Keller L. P. and Buseck P. R. (1990) GCA 54, 2113-2120, (4) Grossman L. and Larimer J. W. (1974) Reviews of Geophysics and Space Physics 12, 71-101, (5) Larimer J. W. (1967) GCA 31, 1215-1238, (6) Wood J. A. (1985) Protostars & Planets II, 687-702, (7) JANAF thermochemical tables (1971)

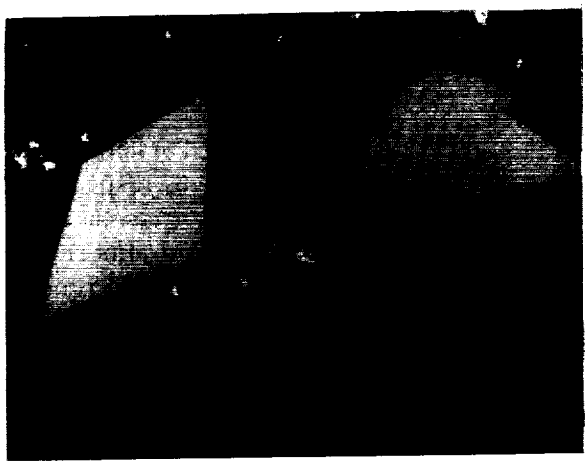

Fig. 1 Diamond shaped fayalite crystals embedded in the matrix.

Fig. 2 Fayalite grains associated with sulfides and magnetite within a thin rim and wrapped in a chondrule.

REMOVAL OF CARBONACEOUS CONTAMINANTS FROM SILICA AEROGEL. Hui-Ping Huang, I .Gilmour and C.T. Pillinger, Planetary Sciences Unit, Department of Earth Sciences, Open University, Milton Keynes, UK. M.E. Zolensky, Johnson Space Center, Houston, Texas, USA.

Capture of micrometeorite material from low Earth orbit or dust grains around active comets for return to terrestrial laboratories, capable of praticing the most up to date techniques of chemical isotopic and mineralogical analysis, will greatly enhance our knowledge of primitive material in the solar system. The next generation of space launched cosmic dust collectors will undoubtedly include extremely low density target materials such a silica aerogel as the decelerating and arresting medium. This material has been found to be clean from the point of view of inorganic elements (1, 2) and is thus acceptable for the purpose of harvesting grains to be studied by, for example PIXE, INAA or SXRF. On the contrary however the process used in making aerogel leaves substantial carbon and hydrogen containing residues (3, 4) which would negate their suitability for collection and subsequent investigation of the very important CHON particles. Attempts to precondition aerogel by solvent extraction or heating at 500°C and 750°C in air for 24 hours or under a vacuum of 2×10^{-7} torr at 260°C were largely ineffective except that pyrolysis did reduce volatile species. In this investigation we have examined the use of supercritical fluids for the purpose of extracting organic residues. The logic of the new approach is that beyond the supercritical point a substance has the solvating properties of a liquid but the viscosity characteristics of a gas. For example carbon dioxide becomes supercritical at a pressure of 73 atmospheres and a temperature of 31°C; in consequence it can transform to a very powerful and ultraclean solvent. It can dissolve organic matter from low molecular weight up to molecules containing 90 carbon atoms. On release of pressure the fluid reverts to a gas which can easily be pumped away and removed from the substrate being extracted.

Preliminary trials using supercritical carbon dioxide conducted with $0.12 g/cm^3$ aerogel (the lowest density material and hence presumably the most open structured available) show considerable promise. Our previous analyses (4) of this substrate and more recent results by both bulk and stepped combustion suggest a relatively low but still unacceptable carbon content of 0.18 to 0.27 wt %. Approximately 85% of this contamination is liberated by burning aerogel at 600°C attesting to the organic nature of the contaminant carbon. The Table shows carbon yields following various treatments with supercritical CO_2. It can easily be seen that the total carbon can be reduced without too much effort by at least a factor of ten.

In two analyses we tried modifying the supercritical CO_2 by the addition of methanol, a standard technique to increase polarity. As can be seen in the Table this greatly added to the carbon content demonstrating how difficult it is to eliminate solvents from the aerogel structure. During the most successful experiment (#5) we monitored the weight loss of the aerogel during temperature increase (Fig.). A total reduction in sample mass of nearly 6% was observed, much of it (75%) at the minimum temperature used. It appears that CO_2 at pressure is able to flush the sample of water at practically ambient temperatures assuming that the weight loss is not simply attributable to particulate matter becoming suspended in the mobile fluid phase. The latter interpretation does not seem likely otherwise capillaries in the pressure cell of the extraction apparatus would inevitably become blocked.

REMOVAL OF CARBONACEOUS....Hui-Ping Huang, I. Gilmour, C.T. Pillinger.

Table.

Carbon yields from 0.12 g/cm^3 silica aerogel following various treatments with supercritical CO_2.

Ex. No.	P(psi)	T(°C)	Modifier	Sample Wt(mg)	Carbon (%)
1	-	-	-	27.8	0.27
2	3000	50	-	48.4	0.20
3	4000	46	-	38.0	0.080
4	4000	85	-	27.6	0.095
5	4000	150	-	32.2	0.014
6	4000	46	1% MeOH	70.4	0.70
7	3000	55	5% MeOH	56.3	2.80

In this initial investigation it is quite likely that we have not yet identified the optimum conditions for cleansing aerogel. We wish to explore the efficacy of SFE with the more dense forms of the substrate richer in carbon. Non-carbon containing supercritical fluids need to be tried. For the method to be suitable for preparing aerogel targets for space launch, a facility capable of accommodating relatively large slabs of the material will need to be constructed.

We thank Jenny Gibson for laboratory assistance, SERC and the Royal Society for support.

References:

1. G. Flynn and S.R. Sutton (1990) LPSC **XXI**, 371 - 372.
2. M.E. Zolensky *et al.* (1990) LPSC **XXI**, 1381 - 1382.
3. C.P. Hartmetz *et al.* (1990) LPSC **XXI**, 463 - 464.
4. J.E. Gibson *et al.* (1991). LPSC **XXII**, 441 - 442.

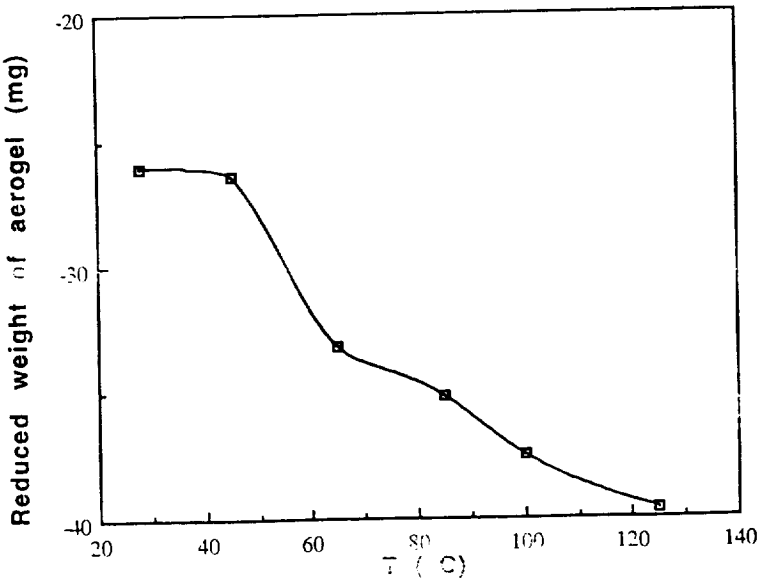

SFE operation: CO2 as mobile phase, 4000 psi, 125 - 23 C.
The initial weight of aerogel for extraction: 595.75 mg.
The final reduction of weight after SFE: 4.38%.
The carbon composition in the final extract: 0.014%.

N94-16257

THE GROUP A3 CHONDRULES OF KRYMKA: FURTHER EVIDENCE FOR MAJOR EVAPORATIVE LOSS DURING THE FORMATION OF CHONDRULES. S.Huang, P.H. Benoit and D.W.G. Sears. Cosmochemistry Group, Department of Chemistry and Biochemistry, University of Arkansas, Fayetteville, AR 72701, USA

Like Semarkona (type 3.0), Krymka (type 3.1) contains two distinct types of chondrule (namely groups A and B) which differ in their bulk compositions, phase compositions and CL properties. The group A chondrules in both meteorites show evidence for major loss of material by evaporation; i.e. elemental abundance patterns, size, redox state, olivine-pyroxene abundances. Group A and B chondrules probably formed from common or very similar precursors by the same processes acting with different intensities, group A suffering greater mass-loss by evaporation and reduction of FeO and SiO_2. While Krymka chondrules share many primary mineralogical and compositional properties with Semarkona chondrules, the minimal metamorphism it has suffered has also had a significant effect on its chondrules.

A new comprehensive classification for chondrules based on the composition of their phenocrysts and mesostases has been proposed[1,2]. The most primitive (type 3.0) ordinary chondrite, Semarkona, contains chondrule groups, A1, A2, A5 and B1, while Krymka (type 3.1), contains groups, A3, B2 and A5. Group A1-3 chondrules contain CaO-rich mesostases and FeO-poor olivine, and sometimes pyroxene, while group B1,2 chondrules are composed of SiO_2-rich mesostases, FeO-rich olivine and are generally pyroxene-free. Group A5 chondrules contain Na_2O-rich mesostases and FeO-rich olivine, and similar to those in equilibrated chondrites. The proportions and abundances of these groups are listed in Table 1, which includes cathodoluminescence data which may also be used for chondrule classification. Here we report our continuing studies of primitive chondrules. We emphasize the A groups[3,4], whose significance in ordinary chondrites has only recently been realized[5,6]. Because of their smaller size and extreme friability[7], we use photographs of the CL of polished sections to select chondrules which are then removed by chiselling[3]. The present report concerns chondrules from Krymka.

The CI-normalized INAA data for each chondrule group are plotted in Fig. 1. Clear compositional differences are seen between the A3 and B2 groups, which resemble those previously observed between group A1,2 and B1 chondrules in Semarkona[3]. Group A3 chondrules are enriched in refractory lithophile elements and depleted in volatile elements with the depletion increasing steadily with volatility along the series Mn-Na. In contrast, group B2 chondrules show a flat pattern of lithophile elements. Both group A3 and group B2 chondrules show depletions in siderophile and chalcophile elements relative to CI, although group A3 chondrules may be slightly enriched in refractory siderophile elements (such as Ir, Co and Ni) relative to group B2 chondrules.

Group A chondrules in both Semarkona[8] and Krymka are generally smaller than group B chondrules, in addition to being depleted in Na and other volatiles (Fig. 2). This is consistent with evaporative loss during chondrule formation. On the basis of many laboratory experiments[9-11], considerable Na loss is to be expected during chondrule formation. The Na contents we now measure are, of course, upper limits for the Na in the chondrule at peak temperature during formation because (1) mesostasis profiles indicate Na recondensation[2,12], (2) our chondrules may have matrix attached to them, (3) aqueous alteration[13] and (4) metamorphism[1] may have redistributed Na. We suggest that the stronger correlation in Fig. 2 displayed by Krymka results from metamorphic mobilization of Na. If the size difference between group A and group B chondrules is due to evaporative loss (assuming 35% mass loss), then about 40% loss of Si (and somewhat less Mg) and 60% loss of Fe are indicated. The relevant reactions, which also involve reduction of FeO and SiO_2, are of the sort[3,4,14-17]:

$$2Fe_2SiO_{4(l)} + Mg_2SiO_{4(l)} + 5H_{2(g)} \rightarrow 2MgSiO_{3(l)} + 4Fe_{(g)} + SiO_{(g)} + 5H_2O_{(g)}$$

$$FeSiO_{3(l)} + 2MgSiO_{3(l)} + 3H_{2(g)} \rightarrow Mg_2SiO_{4(l)} + Fe_{(g)} + 2SiO_{(g)} + 3H_2O_{(g)}$$

and since the first reaction is the most important there is a net increase in pyroxene, as observed experimentally[4-6,18,19]. It seems unlikely to us that olivine and pyroxene reduction, volatile-loss, size, and the olivine-pyroxene abundance trends could all be due to random fluctuations in precursors[20,21]. Rather, we think that A and B chondrule groups probably had very similar precursor materials and were formed by the same processes acting with different intensities, so that while group A chondrules suffered volatile-loss, group B did not. Jones also suggested that type IA chondrules (a subset of group A) can be derived from type II chondrules (a subset of group B) by reduction and volatilization of major elements such as Si, Fe and Na[22].

The small sample size has made it impossible to obtain oxygen isotope data for group A chondrules, but we can predict that group A1-3 chondrules should show greater mass-fractionated patterns and greater

isotope exchange with the surrounding gases than B2 chondrules. However, it is unclear whether the surrounding gas was ^{16}O-rich, as inferred by the inverse correlation between ^{16}O and size for Dhajala (H3.8) chondrules[23], or ^{16}O-poor as inferred by an ^{16}O-depleted Mezö Madaras (L3 breccia) glass fragment[24].

The A1 chondrules of Semarkona differ from the equivalent A3 chondrules of Krymka in the CL of the mesostases, probably due to metamorphism-driven changes in Mn or major structural changes[12,25]. Olivine and mesostasis compositions of A1 and A3 chondrules also differ[1,2], and Krymka lacks the extremely volatile-poor chondrules observed in Semarkona (< 0.2% Na_2O), apparently because of diffusion during Krymka's extremely mild metamorphic episode. While mesostasis compositions of Semarkona B1 chondrules differ significantly from those of Krymka B2, bulk chondrule and phenocryst compositions are similar, presumably because of their relatively sluggish response to metamorphism.

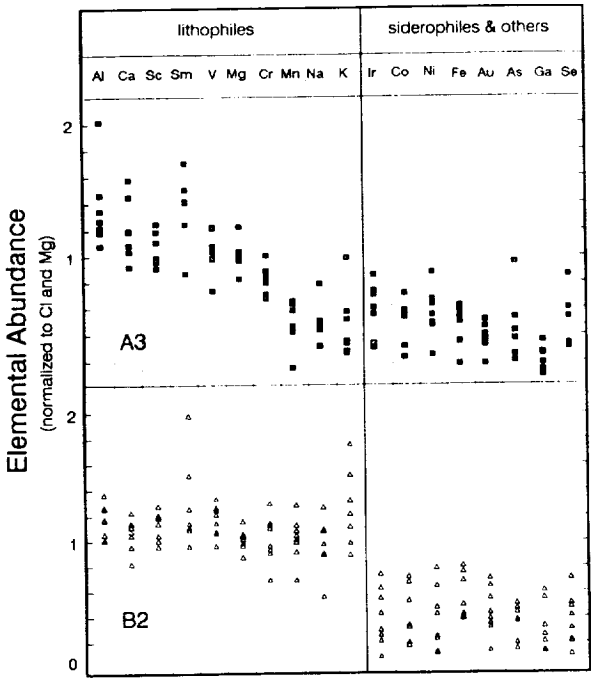

Fig. 1 (above) CI- and Mg- normalized INAA data for chondrules from Krymka. Fig. 2 (upper right) Na vs. diameter for Semarkona and Krymka chondrules.

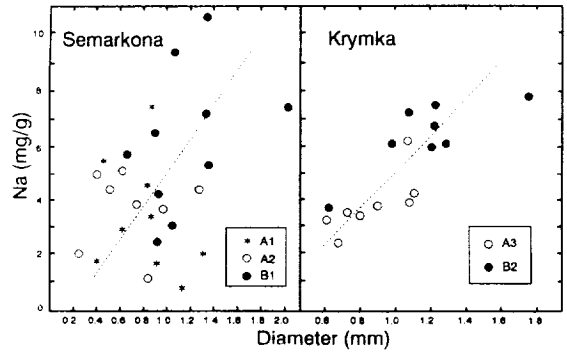

TABLE 1. Cathodoluminescence (CL), mesostasis and olivine compositions and frequency (Freq., %) of chondrule groups in Krymka and Semarkona*.

	Mesos. CL	Mesos. Norm	Ol CL	Ol %FeO	Ol %CaO	Freq. Kry.	Freq. Sem.
A1	yellow	pl(An>50%)	red	<2	>0.17	3.6	10.5
A2	yellow	pl(An>50%)	none/dull red	2-10	0.1-0.2	0.0	25.0
A3	blue	pl(An>50%)	red	<4	>0.2	33.3(9)	0.0
A4	blue	pl(An>50%)	none/dull red	>4	0.16-0.3	7.3	0.0
A5	blue	pl(An<50%)	none	>10	<0.16	14.5(1)	5.0
B1	none	>30% Qtz	none	7-25	0.08-0.3	0.0	56.9
B2	none	30-50% Qtz	none/dull red	10-25	0.08-0.3	36.4(8)	0.0
B3	purple	15-30% Qtz	none	15-20	<0.08	0.0	2.6

*The compositional fields are not rectangular, see ref. 1,2. pl = plagioclase.

In summary, group A3 chondrules in Krymka resemble the group A1,2 chondrules in Semarkona in many respects. They are equally abundant, being ~35% by number, with similar phase and bulk compositions. Semarkona B1 and Krymka B2 chondrules also closely resemble each other. However differences are present which reflect a very mild metamorphic overprint in Krymka, which is especially true for group A chondrules which are more responsive to metamorphism. For both meteorites, the differences between group A and B chondrules suggest to us that they formed from similar starting materials, but that group A chondrules suffered greater evaporative loss of mass, and reduction, during chondrule formation.

1. Sears D.W.G. *et al* (1992) *Nature* **357**, 207. 2. DeHart J.M. *et al* (1992) *GCA* **56**, 3791. 3.Lu J. *et al* (1990) *LPSC* **XIII**, 720. 4. Lu J. *et al* (1992) *LPSC* **XXIII**, 813. 5. Scott E.R.D. & Taylor G.J (1983) *LPSC* **XIV**, 680. 6. Jones R.H. & Scott E.R.D. (1989) *Proc. 19th LPSC* 523. 7. Sears D.W.G. & DeHart J.M.(1989) *Meteoritics* **24**, 325. 8. Lu J. (1992) Ph.D thesis. 9. Tsuchiyama A. *et al* (1981) *GCA* **45**, 1357. 10. Notsu K. *et al* (1978) *GCA* **42**, 903. 11. Gooding J.L. & Muenow D.W. (1977) *Meteoritics* **12**, 401. 12. Matsunami S. *et al* (1992) *GCA* submitted. 13. Hutchison R. *et al* (1987) *GCA* **51**, 1875. 14. Wood J.A. (1985) In "*Protostars and Planets II*" (ed. Black D.C. & Matthews M.S.), 682. 15. Johnson M.C. (1985) *LPSC* **XVI** 402. 16. Kracher A. (1985) *LPSC* **XVI** 467. 17. Rubin A.E. *et al* (1988) In "*Meteorites and the early solar system*" (ed. Kerridge J.F. & Matthews M.S.), 488. 18. Walter L.S. and Dodd R.T. (1972) *Meteoritics* 7, 341. 19. Hashimoto A. (1983) *Geochem. J.* **17**, 111. 20.Grossman J.N. & Wasson J.T. (1983) In "*Chondrules and their Origins*" (ed. King E.A.), 88. 21. Hewins R.H. (1991) *GCA* **55**, 935. 22. Jones R.H. (1990) *GCA* **54**, 893. 23. Clayton R.N. *et al* (1991) *GCA* **55**, 2317. 24. Mayeda T.K. *et al* (1989) *Meteoritics* **24**, 301. 25.DeHart J.M. (1989) Ph.D thesis. Supported by NASA grant NAG 9-81.

PETROLOGIC MODELS OF 15388, A UNIQUE APOLLO 15 MARE BASALT; **S.S. Hughes,** Dept. of Geology, Idaho State University, Pocatello, ID 83209; **E.J. Dasch,** FEH, NASA Headquarters, Washington, DC 20546; and **L.E. Nyquist,** SN4, NASA/Johnson Space Center, Houston, TX 77058.

Mare basalt 15388, a feldspathic microgabbro [1] from the Apennine Front, is chemically and petrographically distinct from Apollo 15 picritic, olivine-normative (ON) and quartz-normative basalts [2]. The evolved chemistry, coarse texture, lack of olivine, and occurrence of cristobalite in 15388 argue for derivation by a late-stage magmatic process that is significantly removed from parental magma. It either crystallized from a magma evolved from the more mafic Apollo 15 basalts, or it crystallized from a currently unrepresented magma. Rb-Sr and Sm-Nd isotopic systematics [3] yield isochron ages of 3.391 ± 0.036 and 3.42 ± 0.07 Ga, respectively, and ε_{Nd} = 8.6 ± 2.4, which is relatively high for Apollo 15 mare basalts. In contrast to chemical patterns of average Apollo 15 ON basalts and Apollo 15 picritic basalt (Figure 1), 15388 has a strongly positive LREE slope, high Ti, shallower HREE slope and a slightly positive Eu anomaly. These features argue against 15388 evolution by simple olivine fractionation of a parental ON or picritic basalt magma although olivine is a dominant liquidus phase in both potential parents.

Figure 1

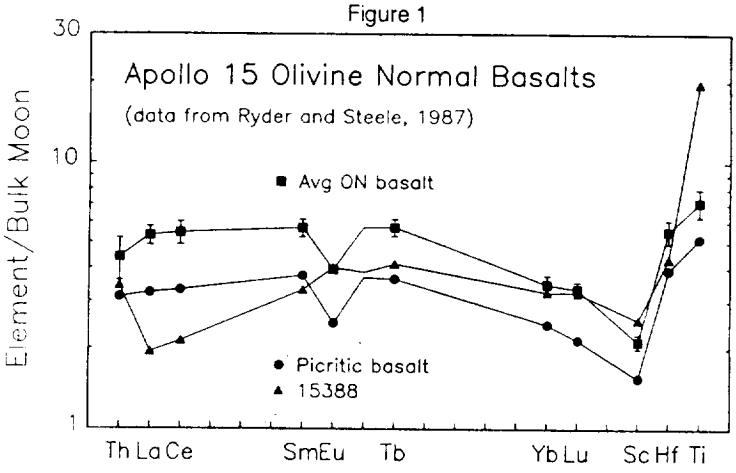

Modal mineralogy suggests that the chemistry may be explained by accumulation of observed minerals pyroxene ("bow" shaped REE), ilmenite (high Fe, Ti), and plagioclase (Eu anomaly) from an evolved ON magma [4]. In this scenario, elevated trace element abundances would require at least 88% crystallization prior to 15388 accumulation, but 15388 is not significantly depleted in Mg, Cr, Co, etc., as would be expected after much evolution by mafic mineral (and plag) fractionation. This discrepancy could be related to successive batches of ON magma reintroduced into, and mixing with, the evolving 15388 parental magma; however, enrichments of LILE would become diluted by low-LILE magma. One possibility is to assume that crystallization prior to 15388 cumulate deposition was essentially an equilibrium process throughout the crystallization history. Extensive fractionation of LILE in the original magma would be allowed, yet compatible elements would not be severely depleted. Alternatively, extensive fractionation of the primary magma may not be required such that elevated LILE in the 15388 cumulate can be related to entrapment of small amounts of the evolving liquid into the crystalline mush.

In order to demonstrate the possibility of 15388 being non-exotic relative to other Apollo 15 basalts, petrologic models assume that later stage cumulate phases contributed to the bulk chemical signature and the most likely parental magma was equivalent to an Apollo 15 ONB, the compositions of which span a fairly restricted range controlled by ~10 percent olivine fractionation [2]. The actual precursor magma composition could be any of the ON basalts, the only difference being amount of olivine crystallization. Other potential models, including any that depict 15388 as a primary magma or a cumulate from some unknown Apollo 15 magmatic composition, introduce complexities that are possibly nonessential to 15388 petrogenesis. Source hybridization models, using technique of [5], yielded no viable mechanisms by which the trace element pattern of 15388 could be derived as a primary mafic magma, albeit a normative olivine-free one. Models (Table 1) predict the major element composition by accumulation of 15388 mineralogy from an evolved ON composition using crystal/liquid molar partition coefficients appropriate to low alkali systems [6]. Trace element partition coefficients are those used by [5], except for pyroxene [7].

In model #1 (Figure 2), an ON magma first evolves by 75% equilibrium crystallization of 12% ol + 62% px + 26% pl, the normative mineralogy of an average ON basalt. From this liquid, accumulation of 59% px + 31% pl + 10% ilm closely reproduces the observed 15388 major element composition in Table 1. Within errors associated with the average ON composition used as a primary magma, trace element abundances are not predicted by this scenario. Also, precursor crystallization using an equilibrium process involving normative mineralogy is excessive and presents an unlikely petrologic scenario.

Model #2 yields a better prediction of 15388 chemistry and a more reasonable amount of precursor crystallization of the primary magma. Because the 15388 composition lies very close to the olivine control line [2] for the ON series, evolution of the primary magma was probably related to olivine-only crystallization. After 24% olivine (stepwise equilibrium) crystallization of the ON basalt magma, a modeled accumulation of 59% px + 30% pl + 11% ilm closely predicts the major element composition of 15388 but fails to yield an appropriate trace element signature. Addition of 6% trapped liquid to this cumulate does not appreciably change major element abundances, yet provides a reasonable approximation, within observed uncertainties, of the trace element signature.

Table 1.

			Model #1		Model #2		
	15388	Average ONB	75% Crystall.	Px-Pl-Ilm Cumulate	24% Ol Crystall.	Px-Pl-Ilm Cumulate	Cumulate + TL
SiO_2 (%)	44.2	45.9	42.4	43.4	48.6	42.8	43.3
TiO_2	5.9	2.1	7.7	5.9	2.8	5.8	5.5
Al_2O_3	11.1	8.9	4.3	11.8	11.7	11.4	11.5
FeO	19.8	21.8	27.5	20.4	19.3	20.9	20.7
MnO	0.35	0.35	0.44	0.33	0.31	0.34	0.34
MgO	8.0	10.9	4.1	7.8	4.0	7.9	7.6
CaO	10.2	9.5	12.3	10.0	12.3	9.8	10.1
Na_2O	0.32	0.26	1.01	0.20	0.34	0.07	0.20
K_2O	—	(est.) 0.04	0.16	0.06	0.05	0.01	0.07
Cr_2O_3	0.34	0.59	0.09	0.11	0.62	0.78	0.77
Sc (ppm)	48.6	40.4	40.0	43.8	49.3	48.4	47.8
Co	41.9	52.5	45.6	55.9	35.5	35.3	35.1
Hf	1.82	2.32	8.11	1.15	3.04	1.14	1.54
Th	0.43	0.55	2.18	0.07	0.72	0.07	0.19
La	1.75	4.8	18.3	0.98	6.32	0.73	1.8
Ce	5.0	12.8	48.6	2.8	16.9	2.3	5.1
Sm	1.89	3.25	11.30	1.44	4.68	1.60	2.16
Eu	0.84	0.83	1.61	0.84	1.15	0.90	0.96
Tb	0.58	0.80	2.68	0.42	1.15	0.48	0.60
Yb	1.98	2.12	6.58	1.57	3.01	1.62	1.90
Lu	0.30	0.31	0.95	0.25	0.44	0.24	0.28

Drawbacks to model #2 are unpredicted Th and Cr abundances. Trace element signatures (Figure 1) suggest that Th in 15388 cannot be related to any process of closed system evolution of ON magma unless a phase compatible to Th and incompatible to LREE is present. Assuming the reported value of Th is correct, the only possible alternatives would have to include contamination by an unrepresented composition. Cr values may be less difficult to predict by assuming either a small amount of chromite was included in the initial ol crystallization or that Cr partitioning in ol was higher. Modeling supports a cumulate scenario; however, the depleted nature of the LREE is consistent with direction but not the degree of ε_{Nd}. The chemical model suggests that an open system is not a significant requirement for 15388 evolution, but the discrepancy in Th prediction, high ε_{Nd}, and the trapped liquid requirement argue for a possible exotic component.

Figure 2

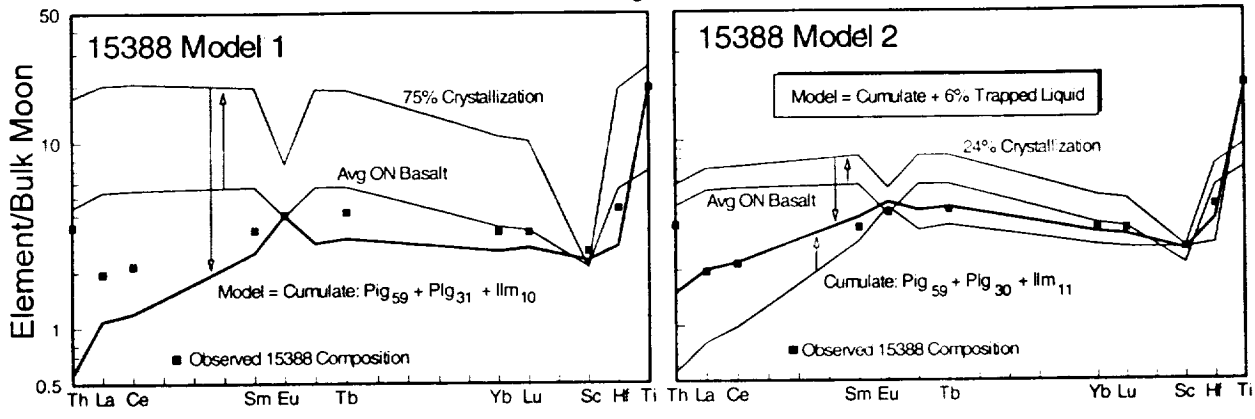

REFERENCES: [1] Dowty E. et al. (1973) PLPSC-4, 423-444. [2] Ryder G. and Steele A. (1987) LPSC-18, 862-863. [3] Dasch E.J. et al. (1989) LPSC-20, 218-219. [4] Ryder G. (1989) PLPSC-19, 43-50. [5] Hughes S.S. et al. (1988) GCA 52, 2379-2391. [6] Longhi J. and Pan V. (1988) J. Petrol. 29, 115-147. [7] McKay G. et al. (1986) GCA 50, 927-937.

POTASSIUM ISOTOPE COSMOCHEMISTRY, VOLATILE DEPLETION AND THE ORIGIN OF THE EARTH; M. Humayun[1] and R. N. Clayton[1,2], [1] Dept. of Geophysical Sciences, [2]Enrico Fermi Institute and Dept. of Chemistry, University of Chicago, Chicago, IL 60637, USA.

We report the first results obtained by our techniques for the precise and accurate determination of the isotopic composition of potassium [1] to constrain the mechanism of volatile element depletion in the formation of the Earth, Moon and meteorites. Our measurements of $\delta^{41}K$ for six chondrites and ten terrestrial rocks attained an average precision of the individual measurement of ±0.4 ‰ (2σ; ±0.2 ‰/ a.m.u.) and yield a net chondrite-Earth difference unresolved at the 99% confidence limit, $\Delta^{41}K$ = -0.32± 0.35 ‰ (3σ). This sets a firm upper limit of 1.3±1.4 % Rayleigh evaporation of terrestrial potassium (using $\alpha=\sqrt{41/39}$), compared with an observed ≈85% chemical depletion of K relative to C1 chondrites. Similar conclusions are reached for the SNC meteorites, Shergotty and Zagami, for 15495 (lunar mare gabbro), and for the eucrite Juvinas. Our conclusion is that direct evaporation of volatile elements from planets (e.g. from silicate vapor atmospheres following giant impact [2]) can be ruled out, and the cause of volatile loss must be sought elsewhere, e.g. nebular processes [3]. Our present findings do not support the conclusions of Hinton *et al.* [4,5], the discrepancy to be resolved at a later date. We also find lunar soil 64801, $\delta^{41}K$ = +4.99±0.53 ‰, to be distinctly heavy in accord with Garner et al. [6].

Planets and planetesimals have been subjected to high temperature processing evidenced by the systematically lower abundances of volatile elements compared with Mg, Si, and Fe, and a complementary enrichment of refractory elements [3]. Recent models of planetary accretion have emphasized the role of large impacts in planetary growth, and volatile element depletion has been proposed as a cosmochemical signature of vaporization accompanying such impacts [2]. Volatile element depletion has previously been attributed to nebular processes, e.g. incomplete condensation. The processes of partial evaporation can be distinguished from incomplete condensation by the production of large mass-dependent isotopic fractionation (Rayleigh distillation) in elements that otherwise lack stable isotopic variations in nature. It has been our ambition to determine which of these processes was principally active in the formation of planets by searching for such isotopic fractionation in bulk planetary compositions. Candidate elements must be moderately volatile, preferably light in mass, and not be subject to equilibrium or kinetic isotopic effects due to geological processes (e.g. Li, B, Cl, S). Additionally, incompatible lithophile elements are preferable to chalcophile elements as the extent of lithophile element depletion is easily ascertainable from volatile/refractory ratios (K/La, K/U, Rb/Sr, Cs/Ba, etc.). This is a very restrictive criterion, and would not be satisfied by any element if we required that the element be conveniently determined by routine mass spectrometric techniques. The choice of K over Rb and Zn is obvious, and a suitable mass spectrometric procedure had to be developed. An early attempt utilizing ion microprobe measurements of K-rich minerals indicated some interesting results [4,5] but was limited in scope by both the rarity of suitable minerals in chondrites, and by the ability to convincingly demonstrate the precision and accuracy of the ion probe technique.

Experimental Techniques: We have previously detailed most of our experimental techniques [1]. We separate K by ion exchange and mount it in 2% K Ba-borate glass prepared by fusion from Suprapur® reagent $Ba(NO_3)_2$ and H_3BO_3. Six sample beads are mounted on a glass slide with an equal number of standard beads, prepared from Suprapur® KNO_3 (our in-house standard). The K isotopes, 39 and 41, are measured using the Chicago AEI IM-20 ion microprobe at $M/\Delta M \approx 300$. All instrumental tunings are set at the beginning of each day, except repeller and MS7 Z focus controls, which are tuned separately for each point to give maximum intensity. Isotopic ratios are found to be independent of the applied voltage settings. Internal precision of a single point is ≈ ±1 ‰ (±0.75 ‰ counting statistics), and external precision of a block of 10 to 16 points is ≈ ± 0.6 ‰. Instrumental fractionation is removed by determining the isotopic difference between the sample and the standard, with error propagation,

$$\delta^{41}K = [\,(41/39)_x\,/(41/39)_{std} - 1\,] \times 1000 \pm 2\sigma_N, \text{ and}$$

$$\Delta^{41}K = \delta^{41}K_A - \delta^{41}K_{Earth} \pm \{(3\sigma_A)^2 + (3\sigma_{Earth})^2\}^{1/2}$$

The precision obtained is in large part due to the good point to point reproducibility of the K secondary ion intensity, and the ability to alternate standard and unknown points on the same thin section, with equivalent tuning adjustments. To demonstrate both precision and accuracy, we prepared enriched

POTASSIUM ISOTOPE COSMOCHEMISTRY: Humayun M. and Clayton R.N.

standards in the range -10 to +30 ‰ using ORNL separated isotopes, the results of which are shown in Fig.1, and obtain good agreement between gravimetric and ion probe determined $\delta^{41}K$. Fractionation during ion exchange chromatographic separation is limited by effectively complete recovery of K from the column (> 99.8 %). This is hardest to obtain for samples with low K and high Mg contents where recovery is ≈ 97 %. Blank contributions of K are kept below 10^{-3}.

Results (a selection of which is shown in Fig. 2) obtained on ten terrestrial samples spanning a wide compositional range indicate that individual measurements of $\delta^{41}K$ do not deviate by more than the mass spectrometric error from the terrestrial mean. A similar result can be obtained by comparing the six measurements on L and LL chondrites. Replicate analyses have been carried out on separate aliquots of BCR-1, and on Krähenberg [courtesy H. Palme, 7], with excellent agreement obtained. It can also be seen that the mean of all L/LL chondrites and Orgueil C1 is separated from mean terrestrial K by less than $3\sigma_{mean}$. Similarly, Shergotty, Zagami, and mare gabbro 15495 are within error of terrestrial K. Results for Juvinas, and the CV chondrites Leoville and Vigarano differ by ≥ 4σ, which we are cautious to interpret as intrinsic fractionations, given that all the distinct samples share the lowest recovery obtained. Further experiments are being carried out on separated components of CV chondrites. Lunar soil 64801 is distinctly heavier, $\delta^{41}K$ = +4.99±0.53 ‰, and our values for 64801 and 15495 agree within error with [6]. The value of 15556 mare basalt is being redetermined, and additional measurements of lunar mare basalts and highlands samples are in progress.

Cosmochemical interpretations: First we note that our main result, the absence of significant fractionation between chondrites and terrestrial, lunar and achondritic samples based on direct measurement, stands in stark contrast to the observations of Hinton et al. [4,5]. Further, the presence of large effects, on the order of the square root of the masses of ^{41}K and ^{39}K, is a necessary consequence of any partial evaporation hypothesis for volatile element depletion in planets, e.g. Jeans escape from a silicate vapor atmosphere, where the residual vapor is enriched in the heavy isotope. We note that, although a silicate vapor atmosphere is a likely consequence of any model for the origin of the Earth involving large impacts (including the Moon-forming Giant Impact), such models do not all require that the vapor escape from the Earth's gravity field [8]. Given the large escape velocity of the Earth (11.2 km/s for 1.0 Earth mass), significant escape of vapor species with m≈ 40 a.m.u. only takes place if the silicate vapor atmosphere has an exobase T≈ 10^5 K, compared with model derived surface T≈ 10^4 K. We also observe that such fractionation must have embarrassing chemical implications, because at T≈ 10^4 K the distinction between volatile and refractory elements is lost, as the entire portion of the planet affected will be in the vapor phase. Thermal loss from this phase in a mass dependent manner should significantly deplete ***light*** species (e.g. Li, Mg, Al) over ***heavy*** species (e.g. Cs, Yb, Pb). We do not find any support for models [2, 9] that allow thermal vaporization accompanying the Moon-forming giant impact (or impacts) to shape the Earth's chemical characteristics (including the Mg/Si, Fe/Si ratios of the mantle).

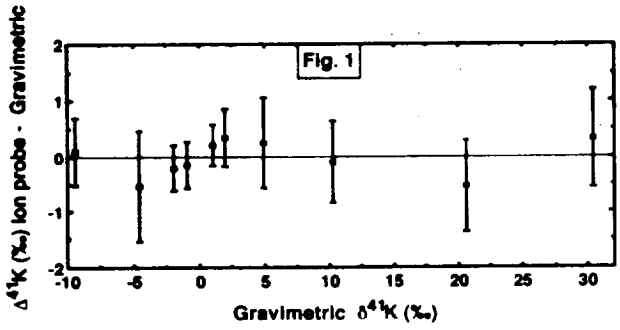

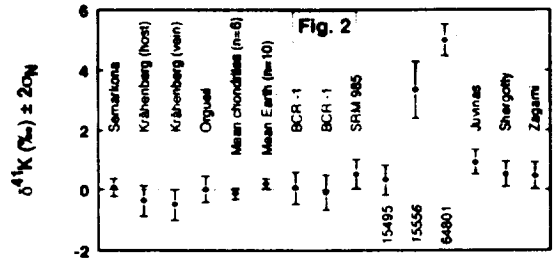

[1] Humayun *et al.* (1991) LPS XXII, 597. [2] Cameron and Benz (1991) Icarus 92, 204. [3] Palme *et al.* (1988) Meteorites and the Early Solar System, Arizona, 436. [4] Hinton *et al.* (1987) LPS XVIII, 429. [5] Hinton *et al.* (1988) LPS XIX, 497. [6] Garner *et al.* (1975) PLSC 6, 1845. [7] Wlotzka *et al.* (1983) GCA 47, 743. [8] Stevenson (1987) Ann. Rev. Earth Planet. Sci. 15, 271. [9] Ringwood (1992) EPSL 111, 537. [10] Taylor (1991) Meteoritics 26, 267-77.

DO SiC GRAINS IN ORGUEIL DIFFER FROM THOSE IN MURCHISON?

Gary R. Huss, Ian D. Hutcheon, and G. J. Wasserburg, Lunatic Asylum, Div. of Geol. and Planet. Sci., Caltech, Pasadena, CA 91125, USA.

Studies of individual presolar SiC grains have shown that most are enriched in ^{29}Si, ^{30}Si, and ^{13}C, and depleted in ^{15}N, compared to solar-system abundances, and that many have large excesses of ^{26}Mg, most plausibly from *in situ* decay of ^{26}Al [1–5]. Stone *et al.* [2,3] observed that Si from a family of platy SiC grains define a linear array on a 3-isotope plot that does not pass through normal solar-system Si. In contrast, Si-isotope data from over 100 3–4 μm SiC grains from Murchison form an elongate ellipse enclosing the Stone *et al.* linear array but also including 'normal' solar-system Si [6]. To investigate whether this difference in Si isotopes indicates different populations of SiC in the two meteorites and to improve the characterization of Orgueil SiC, we used the PANURGE ion microprobe to measure Si, C, N, and Mg isotopes and Al and Na concentrations in a suite of 2–5 μm SiC grains from a new sample of Orgueil.

With the exception of one grain, the combined Si-isotope data from this study and that of Stone *et al.* lie within three standard deviations of a single array indistinguishable from that defined by the Stone *et al.* data alone. Fig. 1 shows the regression through our data and a slope 1/2 line passing through normal Si. This behavior contrasts with the ellipse of data obtained by Amari *et al.* [6] for Murchison SiC of similar size (KJG+KJH) and demonstrates that the adherence of the Stone *et al.* data to a single array was not an artifact of the relatively small sample size. Relative to this array, one Orgueil grain is enriched in ^{29}Si with a Si isotope composition more typical of sub-micron SiC [3]. Orgueil data are distributed uniformly along the linear array, as are the Murchison KJG and KJH data [6]. This contrasts with the clustering exhibited by larger (>6 μm) Murchison SiC grains (LS, LU) measured by Virag *et al.* [4]. We found no SiC with 'normal' Si, whereas both Murchison KJG+KJH and LS+LU populations included 'normal' grains [4, 6].

All measured Orgueil SiC grains are enriched in ^{13}C and highly depleted in ^{15}N relative to solar-system abundances (Figs. 2, 3), in general agreement with Murchison data [4, 6]. The distributions of C, N, and Si isotopes among the Orgueil SiC are generally uncorrelated and exhibit none of the clustering of C and Si isotopic compositions observed for the larger Murchison LS+LU grains [4]. Among Orgueil grains, ^{13}C-rich C tends to accompany ^{30}Si-rich Si (Fig. 2). No Orgueil SiC was found with 'normal' C, in contrast to SiC from Murchison [4,6]. Orgueil SiC is, on average, more ^{15}N-poor. Murchison KJG+KJH grains have a continuous distribution of $^{15}N/^{14}N$ ratios ranging from about 0.0045 to 0.0002 ($\delta\,^{15}N$ = +200 to -950‰) [6] ('normal' is 0.0037). We found no grains with $^{15}N/^{14}N$ higher than 0.0015 ($\delta\,^{15}N$ = -590‰) (Fig. 3), and any correction for multiplier background or extraneous N would serve to lower the ratios.

Three Orgueil SiC grains had resolvable $^{26}Mg^*$ excesses, corresponding to $^{26}Al/^{27}Al$ ratios of $(5.0\pm0.4)\times10^{-4}$ to $(1.8\pm0.2)\times10^{-3}$. $^{26}Mg^*$ was detected in grains with the highest Al contents. Other grains gave upper limits roughly comparable to the amounts detected in our resolved grains, so failure to resolve $^{26}Mg^*$ does not demonstrate the absence of $^{26}Mg^*$. The three grains with detectable $^{26}Mg^*$ also have the three most extreme ^{15}N depletions and the grain with the highest $^{26}Al/^{27}Al$ ratio has the heaviest Si. Murchison KJG+KJH grains show a rough correlation between the $^{26}Al/^{27}Al$ ratio and $^{12}C/^{13}C$ ratios [6], but our limited data cannot confirm this trend.

The Orgueil SiC exhibit a striking correlation between the abundance of Al (as Al^+/Si^+) and N (as CN^-/Si^-) (Fig.4), similar to that reported for Murchison SiC [5] but with much less scatter. This correlation is consistent with the suggestion that Al and N are present in SiC as AlN, either in solid solution or inclusions, but the low condensation temperature of AlN, ≥350 K below that of SiC, makes it difficult to understand how AlN is incorporated into SiC.

Brown and Clayton [7,8] proposed a model to explain the Si correlation line (Fig. 1) in which ^{29}Si is over-produced by $^{26}Mg(\alpha,\gamma)\,^{29}Si$ in hot-bottom burning at 450×10^6 K. A side effect of this mechanism is almost complete destruction of ^{22}Ne, which, along with other noble

gases, is abundant in SiC. They suggest that ^{22}Ne was trapped as ^{22}Na and require a Na/Si ratio in SiC of ~$5x10^{-3}$ to produce the observed ^{22}Ne [8]. Na measurements were made to test this hypothesis, but because Na is an ubiquitous contaminant, only upper limits were established. Measured Na^+/Si^+ ratios ranged from $5x10^{-3}$ to $2x10^{-1}$. However, Na^+ forms much more efficiently than Si^+ and, using an ion-yield ratio of ~20, we calculate Na/Si ratios of $3x10^{-4}$ to $1x10^{-2}$. But most of the measured Na did not come from the grains, as determined by ion imaging before and after the measurements. Thus our preliminary data appear to limit the Na/Si ratios of Orgueil SiC to $\leq 5x10^{-3}$, with the Na contents of most grains 10 to 50 times lower.

In summary, we have more than doubled the number of grains measured by Stone *et al.* and find that their Si-isotope correlation does not dissolve into an ellipse as observed for similar-sized Murchison SiC. N in Orgueil SiC seems to be more ^{15}N-poor than in similar-sized Murchison SiC. No X or Y grains have been found, but our numbers are still small. These observations tentatively suggest that 2–5 μm Orgueil SiC may have a more limited range of compositions than similar SiC from Murchison.

[1] Zinner *et al.* (1989) *GCA* **53**, 3273–3290. [2] Stone *et al.* (1991) In (Taylor, O'Neil, and Kaplan, eds) Stable Isotope Geochemistry: A tribute to Samuel Epstein, 487–504. [3] Stone *et al.* (1991) *EPSL* **107**, 570–581. [4] Virag *et al.* (1992) *GCA* **56**, 1715–1733. [5] Zinner *et al.* (1991) *Nature* **349**, 51–53. [6] Amari *et al.* (1992) *Ap. J.* **394**, L43–L46. [7] Brown and Clayton (1992) *Ap. J.* **392**, L79–L82. [8] Brown and Clayton (1992) *Science* **258**, 970–972. Supported by NASA, NAGW 3040. Division contribution #5234 (798).

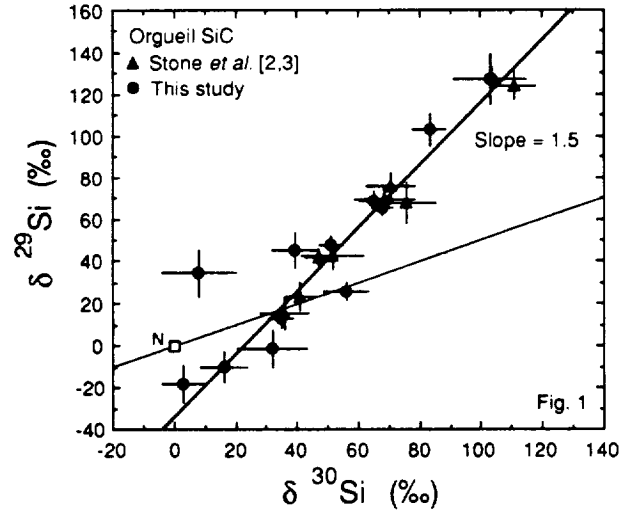

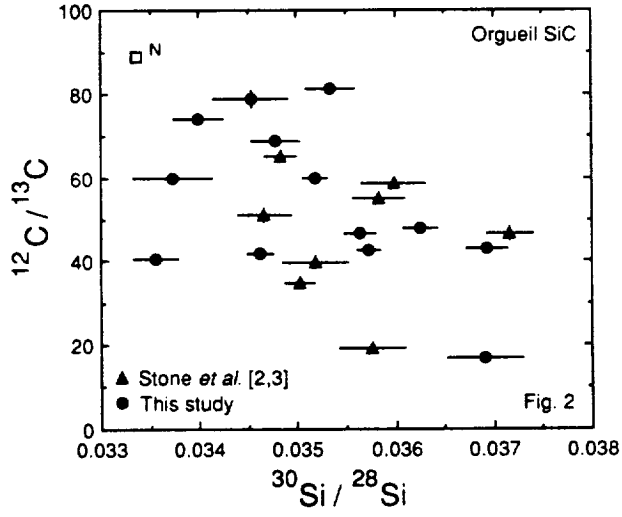

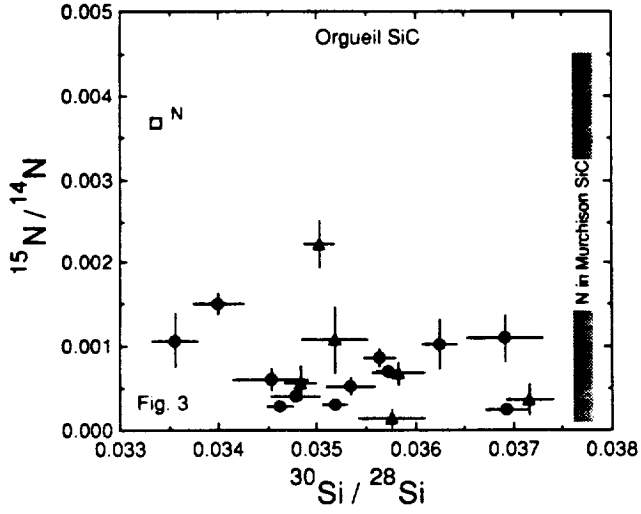

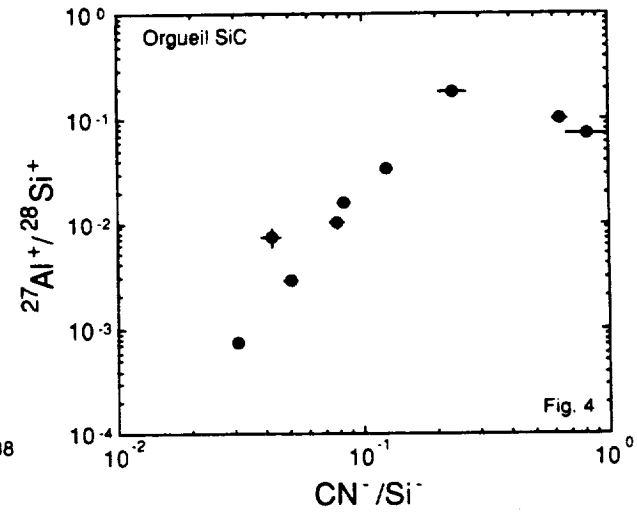

THE DEPTHS OF THE LARGEST IMPACT CRATERS ON VENUS; B. A. Ivanov, Institute for Dynamics of Geospheres, Russian Academy of Sciences, Moscow
P. G. Ford, Center for Space Research, Massachusetts Institute of Technology

The largest impact craters on Venus may be used as witnesses of various geological processes within the Venusian crust. We seek to continue the task (1), of constructing a data base for the further investigation of large craters on Venus (LCV), hoping to find evidence of crater relaxation that might constrain the thickness and thermal gradient of the crust, as proposed in (2). The current work concentrates on 27 impact craters with diameters (d) larger than 70 km, i.e., large enough that the footprint of the Magellan altimeter (3) has a good chance of sampling the true crater bottom. All altimeter echoes from points located within (d/2)+70 km from the crater center have been inspected.

In practice, many of the footprints studied contain multiple echoes. For this reason, the data for each crater were first arranged as a table containing the coordinates of each footprint, a main echo altitude, and, in cases where multiple echoes exist, two leading echo altitudes (preceding the main echo) and two trailing echo altitudes (following the main echo). The data were then analyzed by hand, locating the altimeter footprints on radar images of the craters. In many cases, this technique was useful in the interpretation of multiple-echo altimeter data. For instance, a leading echo might be identified as coming from the near-crater terrain and a delayed echo from the deeper crater floor.

n	*latitude (deg)*	*longitude (deg)*	*cycle 1 points*	*cycle 2 points*	*Official IAU crater name*	*d (km)*	*h (km)*
1	12.50	57.20	707	N/A	Mead	280	1.0
2	-29.70	204.10	400	398	Isabella	174	1.2
3	-55.90	321.80	N/A	140	Meitner	152	-
4	78.16	104.20	N/A	46	Klenova	139	-
5	-23.20	199.30	300	301	Stanton	110	0.9
6	9.80	288.80	279	N/A	Bonheur	100	0.9
7	51.90	143.30	513	N/A	Cochran	100	0.85
8	-1.60	62.40	230	N/A	Joliet Curie	100	0.75
9	23.40	140.30	320	N/A	Marie Celeste	99	0.8
10	65.90	7.00	516	N/A	Cleopatra	97	-
11	22.90	145.10	288	N/A	Greenaway	94	0.95
12	-36.10	127.00	366	47	Bonnevie	92	0.95
13	31.60	53.10	255	N/A	Potanina	90	0.85
14	-56.10	98.60	132	267	Addams	89	0.8
15	25.60	25.20	275	N/A	Mona Lisa	87	0.65
16	33.80	288.50	248	N/A	Sanger	86	0.7
17	24.50	228.80	217	N/A	O'Keeffe	82	0.75
18	-43.20	233.20	292	284	Stowe	80	0.8
19	61.40	223.00	195	N/A	Barsova	79	0.8
20	16.60	268.05	193	N/A	Wheatley	77	0.7
21	-51.90	145.90	127	258	Henie	78	0.7
22	-3.00	68.80	227	167	Andreianova	74	0.65
23	-26.50	99.30	77	197	Boulanger	73	0.8
24	-4.10	155.50	221	188	Franklin	72	0.75
25	-30.76	20.20	233	N/A	Stuart	71	0.8
26	24.40	220.05	133	N/A	Boleyn	70	0.9
27	48.30	195.30	235	N/A	Yablochkina	70	0.8

N/A = Not Available. Data for Meitner, Klenova, and Cleopatra are missing or ambiguous.

The measured crater depths (h), i.e., the average depths of their floors beneath the surrounding terrain, are shown in the rightmost column of the above Table. The depths shown here are generally smaller than those reported in (4). It appears that the Magellan altimeter cannot resolve either the crater rims themselves or any areas of deeper floor close to the inner rims—it may be necessary to use a stereo technique to locate them. Our preliminary results show that crater floors are typically horizontal, even when the surrounding terrain is very irregular or has some regional tilt. The measured RMS height variation of crater floors is typically 50 to 100 m—in only 5 cases

DEPTHS OF THE LARGEST IMPACT CRATERS ON VENUS: Ivanov, B. A. and Ford, P. G.

(Mead, Cochran, Marie Celeste, Mona Lisa and Sanger) is it higher—from 200 to 300 m. A general least-squares fit yields a depth-diameter relationship (h and d in km) of

$$h = 0.25\pm0.07\ d^{0.26\pm0.06}. \quad (1)$$

Using the exponent found earlier (5,6) for crater diameters of 8–60 km, we get the relationship

$$h = 0.17\pm0.04\ d^{0.34}, \quad (2)$$

in comparison with a rim-bottom depth relationship (5,6) of

$$h = 0.2\ d^{0.34}. \quad (3)$$

All craters in this study come within 100 m of obeying equation (1), and the residuals show no correlation with the emissivity of the crater interiors, a property which has been proposed to be related to crater age (7). At this time, it is hard to identify a parameter that can be used to search for crater relaxation on Venus.

(1) Ivanov, B. A., Weitz, C. M., and Basilevsky, A. T., "Largest impact craters on Venus," in "Abstracts of the International Colloquium on Venus," Pasadena, 1992.

(2) Grimm, R. E. and Solomon, S. C., "Viscous relaxation of impact crater relief on Venus: Constraints on crustal thickness and thermal gradient," *J. Geophys. Res.*, **93**, 11,911–11,929, 1988.

(3) Ford, P. G., and Pettengill, G. H., "Venus Topography and Kilometer–Scale Slopes," *J. Geophys. Res.*, **97**, 13103-13114, 1992.

(4) Garvin, J. B. and Schaber, G. G., "Morphometry of large impact craters on Venus: Comparisons with terrestrial and lunar examples," LPSC XXIII abstract, 399–400, 1992.

(5) Ivanov, B. A., "Morphometry of impact crates on Venus," *Solar System Research,* V **23**, No. 1, 1989.

(6) Ivanov, B. A., "Impact craters," chapter 1.6 in "Venus Geology, Geochemistry, Geophysics...," V. L. Barsukov *et al.*, eds., Univ. of Arizona Press, 1992.

(7) Weitz, C. M., Moore, H. J., and Schaber G.G., "Low-emissivity impact craters on Venus," LPSC XXIII abstract, 1511–1512, 1992.

TESSERA TERRAIN ON VENUS: GLOBAL CHARACTERIZATION FROM MAGELLAN DATA; Mikhail Ivanov[1,2] and James W. Head[2]. [1]V. I. Vernadsky Inst., Russian Academy of Scis., Moscow, Russia; [2]Dept. Geol. Scis., Brown Univ., Providence RI 02912.

Introduction: Tessera terrain is characterized by relatively high elevations and complex tectonic patterns (1,2); analysis of Venera 15/16 data showed that large (up to thousands of km across) and small (up to hundreds of km across) occurrences of tesserae are widespread and non-randomly distributed and make up about 10-15% of the surface of Venus north of ~30°N (3). In a previous analysis (4), we used the Magellan Cycle 1 and 2 data to map the global distribution of tesserae on the basis of: 1) complex deformational patterns (two or more trends), 2) relatively high radar backscatter, and 3) relatively high elevation. Here we report on the quantitative aspects of tesserae areal, size, and shape distribution, and on the characterisitcs and distribution of tesserae boundaries. Experiments on volcanic flooding of tessera and implications for tessera presence beneath the plains (5) and analysis of the distribution of impact craters on tesserae and the plains (6) are reported elsewhere.

Tesserae Areal and Size Distribution: Using the global map of tessera terrain derived from Cycle 1 and 2 data (4), we have estimated the total area of all tesserae mapped to be about 10% of the total surface area of Venus. The size of individual tessera occurrences varies over a wide range from a few km to a few thousands of km. The largest tesserae have areas of about 3-4 x 10^6 km^2, each slightly less than 1% of the surface area of the planet. The cumulative distribution of tessera areas (Fig. 1) suggests three subdivisions separated by two breaks at about 30,000 km^2 and 200,000 km^2: Large Tesserae: (Fortuna, Ovda, Alpha, etc.) are regions of slightly elongated (aspect ratio of about 2:1) or equidimensional shape with a typical area about 1 - 2 x 10^6 km^2. Although only 9% of all tessera occurrences belong to this size class, their total area comprises about 82.5% of the tessera terrain on Venus. Medium-Sized Tesserae: (Shimti, Lachesis, etc.) are massifs with a typical area of about 100,000 km^2 and aspect ratios of about 3:1. Twenty-one percent of all tesserae belong to this size class and make up about 13.1% of the tessera terrain surface. Small Tesserae: (Nemesis, individual parts of Manzan-Gurme tesserae, etc.) are the most numerous and have typical areas of about 10,000 km^2 and aspect ratios of about 3:1. However, the total area of the small tesserae comprises only about 4.4% of the whole tessera population.

Three modes of occurrence are observed for tessera patches: 1) *arc-like* arrangements of equidimensional and elongated tessera patches. These arc-like bands may extend for thousands of km: examples are Kutue-Ananke tessera chain at the edge of Akkruva Colles Region; Dekla tessera; tesserae at the northern margin of Beta Regio and at Phoebe Regio. 2) *diffuse clusters* of tesserae. One large cluster begins at Atropos tessera and continues toward the southeast, including Fortuna, Laima, and Tellus tesserae to Thetis Regio. There the broad band of tesserae turns to the west and runs along Western Aphrodite extending to Alpha Regio where again the trend changes and continues to the southern margin of the mapped area. Another cluster of tesserae begins at Phoebe Regio and extends northward through Beta Regio to Virilis tesserae. Both these clusters contain all of the large and most of the medium-sized tesserae. Within the clusters, at their diffuse edges, and outside, there is a large number of individual small tessera patches and groups of them. 3) areas where tesserae are *rare or absent*; these regions occur in two contrasting environments: a) vast, low-lying plains like Guinevere, Sedna, Lavinia, Helen, Atalanta, and Navka Planitiae, and b) several of the broad volcanic rises (7) including Atla and Eistla Regiones where linear graben and volcanoes are the most important structures.

Tesserae Elevation Distribution: In terms of number of occurrences, tesserae do not display a strong correlation with elevation at the global scale. Although some large tessera massifs are at higher elevations (Fortuna, Ovda, Thetis) and dominate any terrain/altitude correlation, an abundance of small tessera patches commonly occupy low-lying regions. For example, small tesserae inside Atalanta and Lavinia planitiae are below the level of mean planetary radius. However, the greatest portion of tesserae of all size classes are concentrated at intermediate elevations.

Tesserae Boundaries: Tesserae are known to have two types of boundaries with surrounding plains (3,8). Type I boundaries have very sinuous outlines due to deep embayment of lava plains into tessera massifs. This type of boundary (sinuous/ embayment) is the most common; 73% of the total boundaries measured are of this type. The sinuosity of the shoreline and its similarity to the the lunar highlands-mare boundary suggest that Type I boundaries are also characterized by a shallow angle of dip under the plains. Small tessera patches and clusters of patches display sinuous boundaries almost everywhere on the Venus surface where they occur. This, in turn, suggests that in these areas, tessera material may underlie the lava plains between the tessera massifs. On the basis of these relationships, many of the clusters of small tesserae may represent outcrops of a single larger tessera

massif almost completely flooded by lava plains (5). The predominance of Type I boundaries suggests that tesserae, taken as a type of terrain, are commonly the relatively older geological complexes on Venus, an observation supported by detailed crater counts (6). Type II boundaries are more linear at the tens to hundred kilometer scale but also often show plains embayment at the finer scale. This type of boundary (linear/tectonic) is less abundant and usually associated with large-scale tectonic features bounding tessera massifs; 27% of the total boundaries measured are of this type. For large tessera the linear boundary often coincides with the high elevated edges of the tessera. Ridges and troughs inside the tessera are in general oriented subparallel to this boundary. The linearity of Type II boundaries by themselves, the usual association of the boundaries with large scarps or tectonic features, and the sporadic occurrences of this boundary type, together suggest that Type II boundaries formed at tectonically active edges of tesserae.

Conclusions: Mapping of tessera terrain using Magellan global high-resolution data show that it: 1) comprises about 10% of the surface area of Venus, 2) is widespread but not randomly distributed, 3) is extremely highly deformed relative to intervening plains and is commonly characterized by initial compression followed by extensional deformation (2,3), 4) lies at a wide range of elevations, 5) largely predates adjacent volcanic plains which embay tessera for almost three-fourths of its boundaries, 6) may underlie a considerable percentage of the superposed volcanic plains, 7) has linear/tectonic margins for about 27% of its boundaries, and 8) is generally negatively correlated with broad lowlands and volcanic rises. Other studies show or suggest that: 1) there is a paucity of volcanism associated with the tessera (9), 2) there is a statistically significant greater number of large craters on the tesserae than the plains (6), 3) tesserae are associated with negative density anomalies in the lithosphere interpreted to be thickened crust (10), 4) tesserae show no distinctive relationship to recent mantle convection patterns (10, 11) and 5) tesserae may be the consequence of crustal thickening during mature stages of mantle downwelling following initial stages characterized by lowland formation (11). These characteristics tend to favor cold spot (11) over hot spot (12) models for the origin of tesserae, but these data, together with the potentially widespread distribution of tesserae below the volcanic substrate, also permit hypotheses favoring a global chemically evolved layer (13), or the catastrophic formation of a near-global highly deformed layer due, for example, to geologically recent instabilities in a depleted mantle layer (14) or lithosphere (15).

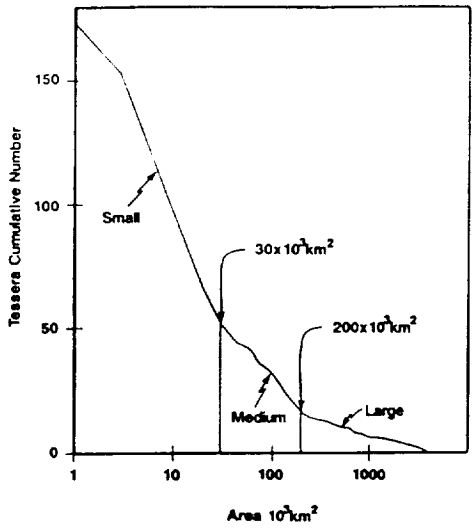

References: (1) V. Barsukov *et al.* (1986) *JGR, 91*, D378; (2) D. Bindschadler and J. Head (1989) *Icarus, 77*, 3; (3) A. Sukhanov (1986) *Geotectonics, 20*, 294; (4) M. Ivanov *et al.* (1992) *LPSC 23*, 581; (5) J. Head and M. Ivanov (1993), *LPSC 24*, this volume; (6) M. Ivanov and A. Basilevsky (1993) Density of Impact Craters on Tessera Terrain, Venus, submitted to *GRL*; (7) D. Senske et al. (1992) *JGR, 97*, 13395; (8) D. Bindschadler and J. Head (1991) *JGR, 96*, 5889; (9) J. Head, *et al.* (1992) *JGR, 97*, 13153; (10) R. Herrick and R. Phillips (1992) *JGR, 97*, 16017; (11) D. Bindschadler, *et al.* (1992) *JGR, 97*, 13495; (12) R. Phillips *et al.* (1991) *Science, 252*, 651; (13) O. Nikolayeva *et al.* (1988) *LPSC XIX*, 864; (14) E. Parmentier and P. Hess (1992) *GRL, 19*, 2015; 15) D. Turcotte (1992) *LPI 789*, 127.

DENSITY OF IMPACT CRATERS ON TESSERA, VENUS; M.A. Ivanov[1], A. T. Basilevsky[2]; 1) Vernadsky Institute, Moscow, 11975 Russia; 2) Brown University, Providence, RI 02912; permanent affiliation is with the Vernadsky Institute, Moscow, 117975 Russia.

Introduction. After the plains, tessera is the most abundant terrain on Venus. It occupies about 10% of Venus' surface, forming the continent-like blocks and small islands above the adjacent plains. Tessera is a result of tectonic deformations of some precursor terrain. However, the nature of that precursor, as well as the causes and mechanisms of its deformations, are under debate. Any models considering tessera terrain involve estimation of tessera age, either relative or absolute. It is well known that the important information on the age of a planetary surface comes from impact crater statistics. The Magellan global overview of Venus with improved resolution provides an opportunity to gather data on impact craters in amounts large enough for statistically reliable estimations of crater density for different terrains. Our study of impact crater density on tesserae compared to the surrounding terrains has a goal to determine whether it is higher, lower, or the same, and to interpret it in terms of the tessera age and processes involved.

Results. We have counted impact craters and measured their diameters using C1-MIDR images which have lower spatial resolution compared to F-MIDRs but have much more areal coverage. Because of the lower resolution of the images used, we have overlooked the amount of the smallest craters (a few km across). However, we checked our results with the crater catalogue of Schaber *et al.* [1] for which compilation of the full resolution imagery was used, and corrected our figures. We studied the images for a significant part of the surface between 30° S and 45° N. The area under study is about 230 million km^2 (about a half of Venus surface) and 11% of it (26 million km^2) is occupied by tessera terrain.

In our study, we distinguished only two categories of terrain: tessera and non-tessera. The latter includes many varieties of terrain such as plains, ridge belts, coronae and so on, but the majority of it is a volcanic plain, and in future considerations, we will refer to it as the plains. We present the results of our study in the form of a table:

Diameter	*Craters outside tessera*			*Craters inside tessera*		
interval, km	No.	Density	Standard	No.	Density	Standard
<16	206	1.00E-06	6.97E-08	15	5.77E-07	1.49E-07
16-128	170	8.26E-07	6.33E-08	29	1.11E-06	2.07E-07
32-128	53	2.57E-07	3.54E-08	12	4.62E-07	1.30E-07
>128	2	9.72E-09	6.87E-09	0	0	0

From the table it is evident that the density of small impact craters (D<16 km) on tessera is lower than on the plains while the density of large craters (D>16 km) on tessera is higher than on the plains.

Discussion. Higher density of larger craters on tesserae means that tesserae on the whole are older than the plains. If we assume that average crater retention age for a venusian surface (which practically means for the plains), is about 500 m.y. [1,2,3] and take into account the tessera and plain crater density error bars for 16-128 and 32-128 km size intervals, the crater retention age for tessera is estimated as 670 +365/-165 m.y. and 900 +430/-330 m.y. Following Schaber *et al.* [1] who used D>35 km crater subpopulation for estimating the age of the venusian surface, we favor the second of these estimations.

Lower density or deficit of small impact craters (D<16 km) for tesserae compared to their density on the plains, combined with the fact that for larger

craters the density is higher, may be interpreted either as observational effect or, if this is not the case, as evidence that the smaller craters on tesserae were affected by some resurfacing which was significantly more efficient than the resurfacing on the plains.

The observational effect was the first thing we tried to check because it is obvious that it is more difficult to recognize craters on the rough surface of tessera than on the plains. But after comparing our data with the catalog [1] which had been compiled based on a special search for craters using full resolution imagery, we recognized that either we and [1] had overlooked a significant number of small craters on tessera, or both of us did not overlook them. So let us assume as a hypothesis that the deficit of craters on tessera is real.

If the hypothesis is correct, this means that a portion of the small craters on tesserae were destroyed by some process(es). Processes supposedly destroying craters are downslope mass wasting, aeolian erosion/deposition, volcanism, and tectonic deformations. To test all these possible causes of the deficit we have studied the morphology of the largest on-tessera craters, which we used for estimation of the tessera age. The logic of this study is: If there were some processes which destroyed a significant amount of craters from a few to 16 km in diameter, these processes also had to modify the bigger craters. We have studied these 12 craters, which vary in diameter from 36 to 85 km. Their morphology shows no evidence of significant downslope mass wasting or aeolian activity which might be considered a reason for the deficit of small craters on tessera. There is also no evidence of heavy volcanic flooding, which seems to exclude volcanism as a reason for the deficit. Tectonic deformation is seen only in two of twelve studied craters. The other ten craters show no evidence of tectonic deformation. So tectonic deformations also have to be ruled out as a reason for the small crater deficit. This forces us to return to the idea that both we and (4) could not recognize a significant amount of small craters on tessera terrain.

Conclusions. Our study has shown that for craters of 16-128 km and especially 32-128 km diameter size intervals, the on-tessera density is significantly higher than on the plains. If we use statistics for 32-128 km interval and assume that the average crater retention age for the plains is about 500 m.y., the average age for the tessera is estimated to be 900 +430/-330 m.y.

The density of craters < 16 km in diameter on tessera is significantly lower than on the plains. A study of the morphology of the largest on-tessera craters has shown that neither downslope mass wasting, aeolian activity, volcanism, nor tectonic deformations were the processes effective enough to significantly modify these large craters and therefore to destroy a significant amount of small ones. Therefore, the deficit of small craters on tessera is evidently an observational effect caused by difficulty in recognizing the small craters on rough terrain.

Absence of recognizable tectonic deformations in most of the large on-tessera craters means that during most of the accumulation time of the craters' subpopulation, most of the studied tesserae were tectonically stable and did not undergo gravitational spreading [4,5]. If this process was involved in the tessera formation it ceased before that time had come.

References: [1] Schaber G. *et al.*, *JGR*, 97, 13,257-13,302, 1992. [2] Ivanov B.A. and A.T. Basilevsky, *Astronom. Vestnik*, 21,136-143, 1987 (in Russian). [3] Neukum G., LPSC XIX (Abstract), 850-851, 1988. [4] Bindschandler D.L. and J.W. Head, *JGR*, 96, 5889-5907, 1991. [5] Smrekar S. E. and S.C. Solomon, *JGR*, 97, 16,121-16,148, 1992.

N94-16264

FIRST INVESTIGATION OF NOBLE GASES IN THE DENGLI H3,8 CHONDRITE

M.A. Ivanova, S.S. Assonov, Yu.A. Shukolyukov. Vernadsky Inst. Geochem. Anal. Chem., Russian Acad. Sci.

The Dengli (H3,8) meteorite weighting 243,5 g is a find from the Karakum desert. It' s a complex microbreccia contaned unusual clasts which are more typical for regolithic breccias than for H-chondrites. Based on Xe and Kr contents and their isotopic composition, the Dengli doesn't differ significantly from other H-chondrites. Its exposure age is 7,6 Ma. That's near to common possible data of exposure age (6,2+0,2 Ma) of 350 H-chondrites. Dengli's K/Ar age (4,01 Ga) coincides with the same ages of many other H-chondrites. Thus the Dengli isn't regolithic breccia and it probably formed during accretion of its parent body.

Based on features of texture and chemical composition of olivine and low-Ca pyroxene he has been classified as H3,8 chondrite [1]. The meteorite has a chondritic texture, but irregular achondritic clasts and isometric SiO_2-bearing inclusions distinguished on composition from the meteorite-host were discovered. Therefore this meteorite can consider a complex breccia, for example, a regolithic breccia.

The purpose of this investigation was a verification of this assumption using isotopic peculiariteis of noble gases. The concentration of solar wind gases which are characterized by typical solar isotopic composition, should be much more in the regolithic breccia than in the ordinary chondrites.

The contents of Ar, Kr and Xe are very similar to other ordinary chondrites of petrologycal types 3-5 [2-5] (Tabl.1). Xe isotopic composition on any temperature step distinguishs from solar Xe (Fig.1) and resembles Xe of ordinary chondrites (there are average results for 16 H-chondrites [3-9]). Kr isotopic composition is within a rande of other H-chondrites (Fig. 2) and it differs as strongly from solar Kr as Xe. Distinct features of cosmogenic $^{38}Ar_c$ (Tabl. 1) were founded in isotopic composition of Ar_c. The majority of Ar_c was isolated at 900°. The consentration of $^{38}Ar_c$ is $4,18*10^{-9}$ sm^3/g, exposure age is 7,6 Ma ($P_{38}=0,055*10^{-8}$ sm^3/g) that is near to the maximum (6,3+0,2 Ma) of exposure age spread for 350 H-chondrites [10]. K/Ar age was estimated using the consentration of K=805+8 ppm and radiogenic $^{40}Ar=(2,94+5)*10^{-5}$ sm^3/g. The age is 3,73+0,10 Ga which is near to the ages of some H-chondrites: Zaoyang (H5)-4,13+0,10 Ga, Lunan (H6)-4,15+0,10 Ga [3], Gueni (H4)-4,20 Ga, 474192 (H6)-4,10 Ga, 474418 (H6)-4,20 Ga [11], but the ages of other H-chondrites are older or younger.

Though the Dengli has some specifically petrological features different from most of the H-chondrites, it has no evidence of solar wind exposure as confirmed by our investigations of noble gase . That suggests that Dengli should not be interpreted as a regolithic breccia.

References: (1) Ivanova M.A. et al.(1992) Meteoritics v.27, N 4, c. 463-465, (2) Shultz L., Kruse H. (1983) Meteoritenforschung, p. 88, (3) Engster O. et al. (1987) EPSL, 84, p. 42-50, (4) Begemann F. et al. (1985) EPSL, 72, p. 247-262, (5) Takaoka N. et al. (1989), 44a, p.935-944, (6) Engster O. et al. (1968) (preprint), (7) Heymann D., Mazor E. (1968), GCA 32, p.1-19, (8) Ozima M., Podosek F. A. (1983) Cambridge University Press, (9) Freundel M. et al. (1986) GCA, 50, p.2663-2673, (10) Alekseev V. (1991) Astrologichesky vestnik (in Russian) 25, N 2, p.233-244, (11) Weber H.W. et al. (1982), 38a, p.262-272

FIRST INVESTIGATION OF NOBLE GASES IN THE DENGLI H3.8 CHONDRITE: Ivanova et al

Tabl.1

Isotopic composition (^{130}Xe=1.000, ^{86}Kr=1.000) and concentration of Xe, Kr, and Ar in the Dengli (H3.8), 365.1 mg.

T°C	^{136}Xe	^{134}Xe	^{132}Xe	^{131}Xe	^{129}Xe	^{128}Xe	^{126}Xe	^{124}Xe
800	2.24±4	2.63±7	6.47±13	5.18±10	7.11±14	0.472±20	0.0277±20	0.0222±20
900	2.20±8	2.40±10	6.63±25	5.43±22	7.25±30	0.504±40	0.0237±35	0.0247±35
1100	2.11±8	2.60±12	6.44±20	5.21±16	7.10±35	0.483±25	0.0232±30	0.0225±30
1300	2.01±3	2.38±3	6.24±7	5.08±5	8.34±8	0.507±10	0.0282±7	0.0272±7
1600	2.01±3	2.40±5	6.11±9	4.90±8	8.35±12	0.503±10	0.0293±12	0.0286±11
Total	2.04	2.41	6.24	5.06	8.17	0.502	0.0280	0.0269

T°C	^{84}Kr	^{83}Kr	^{82}Kr	^{80}Kr	^{130}Xe $sm^3/g*10^{-12}$ STP	^{86}Kr $sm^3/g*10^{-7}$ STP	^{40}Ar	$^{38}Ar/^{36}Ar$	$^{40}Ar/^{36}Ar$
600							0.5	0.225	1522±10
800	3.22±13	0.594	0.677±40	0.139±10	1.7	11.5	38.9	0.285	1755±28
900	3.17±16	0.653	0.550±44	0.136±14	0.9	5.1	54.5	0.451	5050±200
1100	3.12±15	0.662	0.659±33	0.148±14	1.7	6.0	81.6	0.410	5988±156
1300	3.23±7	0.707	0.664±20	0.164±6	19.2	35.6	153.0	0.340	1443±15
1600	3.27±7	0.695	0.694±20	0.145±6	7.3	22.5	52.9	0.271	369±4
Total	3.23	0.681	0.667	0.152	30.8	80.5	381.9	0.310	1287±12

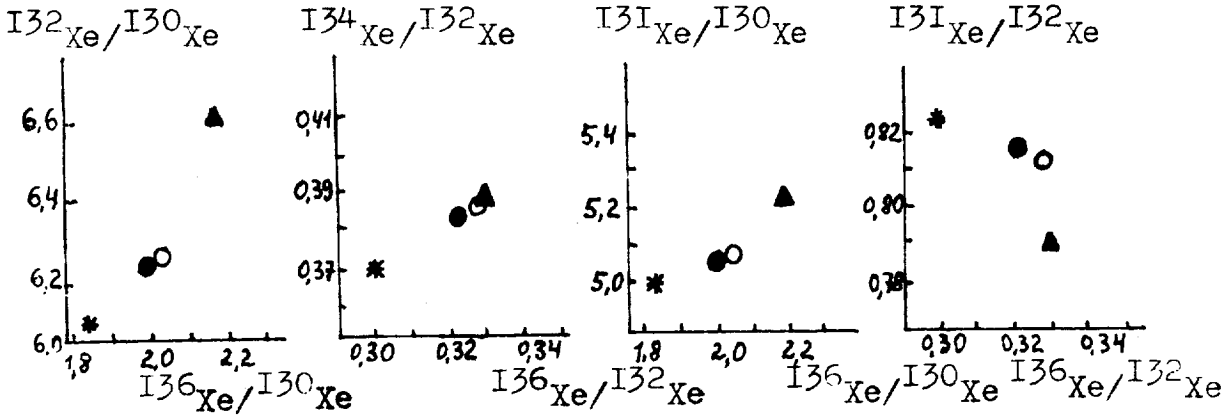

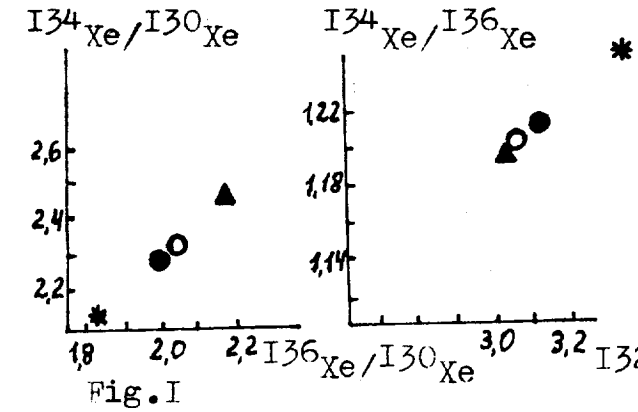

Fig.I

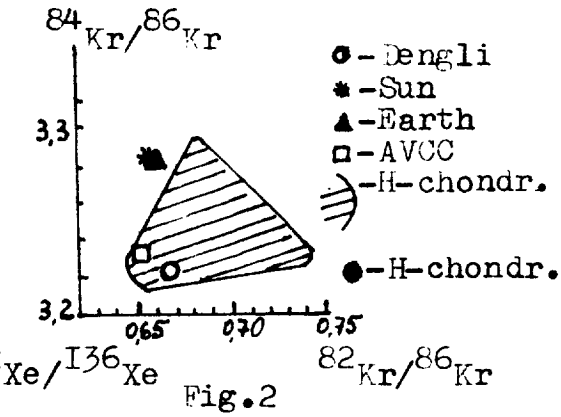

Fig.2

SILICA-BEARING OBJECTS IN THE DENGLI H3.8 AND GORLOVKA H3-4 CHONDRITES

Ivanova M.A.[1], Kononkova N.N.[1], Petaev M.I. [1,2] 1 - Vernadsky Inst. Geochem. Analyt. Chem. RAN, Moscow, Russia; 2 - Harvard-Smithsonian Center for Astrophysics, Cambridge, MA, USA

Silica-bearing objects are enigmatic components of the olivine-normative ordinary chondrites. Several papers [1,2 and references therein] has been devoted to the study of these objects in various chondrite types. While a relatively large body of information has been collected, the origin of these objects is still controversial. Here we report new data on silica-bearing objects in the unequilibrated H-chondrites Dengli and Gorlovka. The crystallization history of these objects could be explained on the basis of the phase diagram of the Q-Ol-Pl (Al_2O_3) system, but the origin of the silica-rich liquids remains unclear.

STRUCTURE AND MINERALOGY. The clast in (Fig. 1a), from the Dengli H3.8 chondrite [3] is irregular in shape and ~ 160 μm in size. It has a granular mosaic structure and consists of relatively large grains of a silica (65 vol.%) and low-Ca pyroxene (25 %), with interstitial sub-calcic augite (1.6 %) and bitownite (3 %). Terrestrial oxides filling cracks in the clast make up 6.1 % of it. Because of its fluorescence, the silica mineral has been identified as crystobalite. This clast appears to be the most silica-rich of all such objects studied so far.

Silica-bearing objects in the Gorlovka H3-4 chondrite include clasts and chondrules. Major phases in these objects are low-Ca clinopyroxene and Si,Al-rich glass, often saturated with tiny skeletal crystals of high-Ca pyroxene. Many other chondrules and clasts lacking a silica mineral have such a glass as a principal constituent.

One of the silica-bearing objects in Gorlovka (Fig. 1b), #M-1, an ellipsoidal clast ~ 1.8x1.1 mm, has microporphyritic structure and consists of zoned euhedral and subhedral pyroxene grains and small amount of mesostasis. The central part of the clast contains anhedral silica grain of about 50 μm dimension. The boundaries between pyroxene and mesostasis or silica are decorated by high-Ca pyroxene rims of varying thickness. The clast contains rare veinlet-like or rounded grains of metal and troilite.

Another clast, #B2-1, almost rectangular with rounded corners (Fig. 1c), ~ 0.8x0.3 mm in size, also has microporphyritic structure and consists of the same phases, but in roughly 1:1 ratio. The clast contains two clusters of euhedral silica laths up to 250 μm in length. The mesostasis of the clast is saturated with tiny skeletal crystals of high-Ca pyroxene and separated from the other phases by μm-thick rim of high-Ca pyroxene. Rare thin veins of the same composition cross the silica laths.

The third clast, #B1-2 (Fig. 1d), is ~ 260x100 μm rectangular granoblastic aggregate consisting mainly of blocky grains of silica mineral separated by low-Ca pyroxene with subordinate olivine in vein-like geometry.

The fourth object, #B1-3, an ~ 0.8x0.6 mm ellipsoidal complex chondrule (Fig. 1e), contains a continuous concentric internal layer of silica mineral varying in thickness from ~ 10 to ~ 30 μm. The major phases, again, are subhedral grains of low-Ca pyroxene and mesostasis in roughly 5:1 ratio. Pyroxene in the interior of the chondrule occurs as subparallel laths, and in its outer part as equidimensional grains. The domains with differently oriented pyroxene grains are separated by the layer of silica mineral. The low-Ca pyroxene grains are decorated by thin rims of high-Ca pyroxene along boundaries with other phases.

MINERAL CHEMISTRY. Mineral compositions in the Dengli clast shows only minor variability; mean values are listed in Table 1. Also in Table 1 is the mean composition of Gorlovka's siliceous mesostasis. The glass can be characterized by the approximate formula (Mg,Fe,Mn,Ca,Na,K,Ti,Cr,Al)[$Al_2Si_7O_{18}$] with minor deviations from this "stoichiometry". The compositions of pyroxenes, especially high-Ca Px, vary considerably within and between objects (Fig. 2). In glass-bearing objects, orthopyroxene also shows intragrain variations; an example is shown in Fig. 3. In clast #B1-2 orthopyroxene is more ferrous and even more variable in composition than in other objects and in the meteorite as a whole, and it coexists with rare grains of ferroan olivine (Fa_{25-32}).

DISCUSSION. All of the objects studied, except #B1-2, have clear igneous textures, and their origin can be explained by the crystallization of silica-rich melts in the system Q-Ol-Pl (Al_2O_3) [1,2]. The bulk compositions of all the objects plot inside silica crystallization field: silica is the first liquidus phase, followed by low-Ca pyroxene. The crystallization sequence thereafter depends upon the primary composition and cooling history. In the Dengli clast slow crystallization of residual liquid formed high-Ca pyroxene and bitownitic plagioclase in interstices between the major minerals (silica and low-Ca pyroxene). The Gorlovka objects experienced fast cooling, and residual liquids were quenched to glassy mesostases. The precipitation of tiny skeletal grains of high-Ca pyroxene from these mesostases appears to have occurred later, probably during a shock reheating event on the parent body.

The most difficult question is, how were liquids so rich in silica produced in the first place? Several mechanisms have been proposed [1,2], but none of them seem to be totally satisfactory. In principle, alumina- and silica-rich and alkali-poor melt could be produced by the partial melting of H-chondrite precursor, followed by the

removal of alkalies, for instance by volatilization. The observed enrichment of glassy mesostases in K relative to Na seems to support such a suggestion. However, details of the composition and texture of silica-bearing objects, especially in Gorlovka, are inconsistent with such a simple story. A multistage crystallization history seems to be needed to explain the origin of the internal silica-mineral layer in Gorlovka chondrule.

REFERENCES: [1] Brigham C.A. et al.(1986) *GCA*, **50**, 1655-1666 [2] Ruzicka A., Boynton W.V. (1992) *Meteoritics*, **27**, 284 [3] Ivanova M.A. et al. (1992), *Meteoritics*, **27**, 463-464

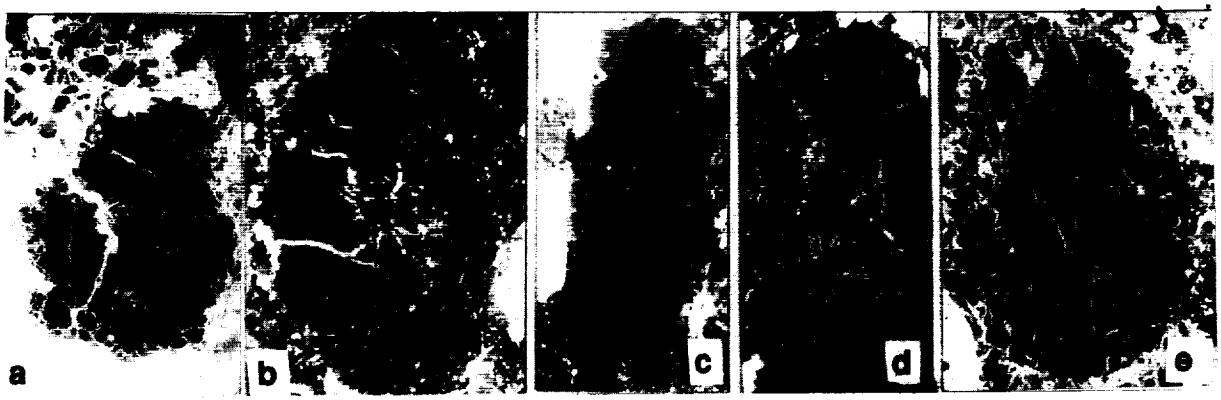

Fig. 1. BSE images of silica-bearing clasts. Silica (black), pyroxenes (light-grey), plagioclase or glass (medium grey). A - Dengli(~160 μm); b - e - Gorlovka; b - #M-1(~1.8x1.1 mm), c - #B2-1(~0.8x0.3 mm), d - #B1-2(~0.26x0.1 mm), e - #B1-3(0.8x0.6 mm).

Table 1. Mineral chemistry

	Dengli			Gorlovka
	Opx	Cpx	Pl	Glass
SiO2	56.38	52.80	49.45	72.77
TiO2	0.09	0.74	0.10	0.38
Al2O3	1.09	4.35	33.48	17.99
Cr2O3	1.02	1.67	n.d.	0.29
FeO	11.17	10.09	0.34	1.39
MnO	0.40	0.45	0.35	0.04
MgO	27.33	18.53	n.d.	2.60
CaO	3.08	12.96	15.39	1.56
Na2O	0.18	0.27	2.59	0.78
K2O	<0.05	<0.05	<0.05	0.69
Total	100.69	101.91	101.75	98.49

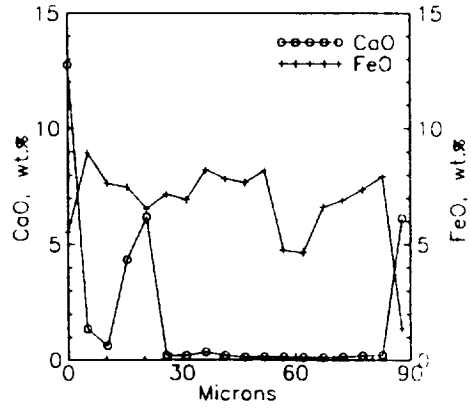

Fig. 3. Intragrain variations in Gorlovka Px.

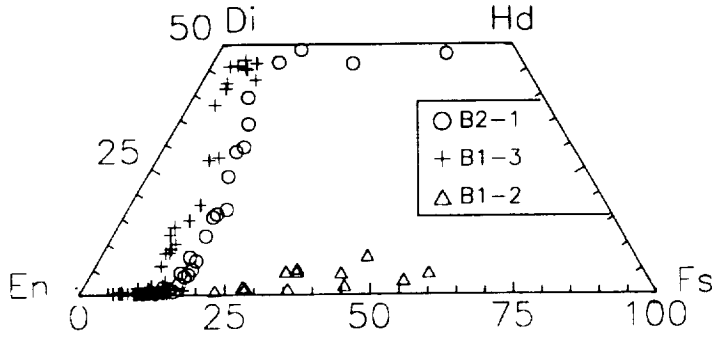

Fig. 2. Intergrain variations in Gorlovka Px.

INDUCED THERMOLUMINESCENCE STUDY OF EXPERIMENTALLY SHOCK-LOADED OLIGOCLASE

A.I. Ivliev, L.L. Kashkarov, and D.D. Badjukov.
V.I. Vernadsky Institute of Geochem. and Analyt. Chemistry,
Russian Academy of Sciences, Moscow, Russia

Artificially induced thermoluminescence (TL) in the oligoclase samples which were shock-loaded up to 27 GPa was measured. Essential increase of the TL sensitivity in relation to the total gamma-ray irradiation dose was observed only in the sample at the 27 GPa pressure. This result can be explained by the initiation of the additional radiation damages in the so high shocked oligoclace crystal lattice.

The study of artificial TL of feldspars shock-loaded in a wide pressure range shows that the method is very sensitive to lattice damages caused by shock /1-4/. However the reason for change of such TL characteristics as the TL sensitivity, the peak temperature, and full width of the peak at half the maximum of the peak (FWHM) is not quite clear. Consequently it causes troubles at quantitative interpretation of the TL data for shocked feldspar.

Earlier we have demonstrated the anomal increase of TL sensitivity for oligoclase experimentally shock-loaded at 13 and 27 GPa /4/. (The TL sensitivity is luminescence intensity per one mass unit of sample aliquot relative to one unit of radiation dose.) The aim of this work is further study of the TL behaviour of the oligoclase samples under their different irradiation dose.

The oligoclase samples experimentally shocked up to 27 GPa were irradiated by gamma-rays of ^{60}Co. The dose of irradiation varied from 50 to 350 krad. After each irratiattion the artificial TL was measured. According to the measurements at the dose of irradiation as high as 350 krad the intensity of TL does not reach saturation. The TL sensitivity of the oligoclase shocked at 27 GPa has a tendency to some increase with increase of the cumulative absorbed dose (see Fig). For this sample the increase of the cumulative dose by 1 Mrad causes increase of TL sensitivity calculated for 230-380 ^{o}C temperature interval by a factor 1.4 . The rise of the TL sensitivity for the oligoclase shocked at 27 GPa can be connected with increase of lattice defects concentration. The defects can be formed not only by

irradiation of the sample but also by its annealing during the measurements of glow curves. For the check of the last assumption we performed a number of experiments. All unshocked and shocked samples were heated up to 500 °C 10 times. Before each heating the samples were irradiated by relatively low dose of about 8 krad and TL sensitivities of the samples were measured. According to the data the repeated anneling does not lead to formation of new glow centers. Also we can conclude that the irradiation of the shocked at 9-25.5 GPa and unshocked oligoclases does not cause the appearance of the some additional lattice defects.

Thus, the obtained preliminary results give the possibility to explain the increase of TL sensitivity in the oligoclase which was shocked at 27 GPa. This effect can be explained by the increase of concentration of the defects in the oligoclase crystal lattice. At the same time the anomal growth of TL sensitivity in the oligoclase sample influenced by 13 GPa must have another nature. We assume that the results on high gamma-rays doses irradiation of shocked oligoclase samples allow us identify the shock event pressures lower or higher than the value of 27 GPa.

References.

1. Sears, D. (1980) Icarus **44**, 190.
2. Sears, D. et al. (1984) GCA **48**, 2265.
3. Hartmetz, C. et al. (1986) JGR **91**, E263.
4. Ivliev, A.I. et al. (1992) LPS XXIII, 589.

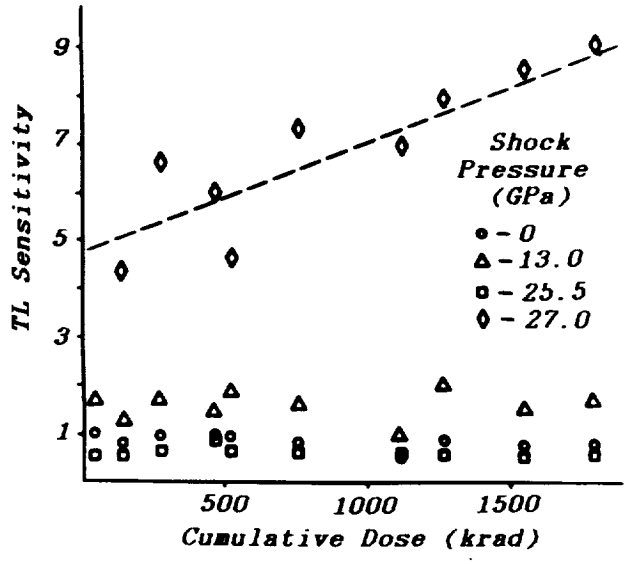

Fig. Plot of TL sensitivity against cumulative dose, by which oligoclase samples were irradiated before the TL measurement. The samples shocked up to 9.0 and 22.5 GPa have trends analogous to that for 25.5 GPa. The 1 σ uncertainty for the shock pressure data in all the cases is +- 30%.

SHOCK-THERMAL HISTORY OF KAPOETA HOWARDITE MATTER ON DATA OF THERMOLUMINESCENCE ANALYSIS OF INDIVIDUAL MINERAL GRAINS

A.I. Ivliev[1], L.L. Kashkarov[1], and Yu.Yu. Korotkova[2]. [1]V.I. Vernadsky Institute of Geochem. and Analyt. Chemistry, Russian Academy of Sciences. [2]Moscow State University, Faculty of Geology, Moscow, Russia

The artificially induced thermoluminescence (TL) was measured in OPx grains from Kapoeta howardite. TL glow curves for individual OPx grains are significantly distinguished from each other both by their shape and TL sensitivity: 5 groups of OPx grains were characterized. The observed variety of glow curves of OPx grains could be caused by their distinct shock-thermal events at the regolith stage of meteorite parent body formation.

Now TL method is widely applied to the study of formation history of meteorite parent bodies [1-3] because of its very high sensitivity. At the same time the complex relation between TL parameters and a number of factors such as chemical composition as well as microinclusions, and defects in mineral grains was reported. Devitrification of meteorite glasses resulting in plagioclase formation [4] could take place both at the shock-thermal events and at the thermal ones only. Therefore it is very important to find a possibility to use the TL characteristics for study the shock-thermal influence only. In this case we suggest that under the same thermal conditions any alterations in crystals will be far less manifested than in glasses.

In the present work the TL characteristics of OPx have been determined in order to elucidate a possibility of TL method application to study of its shock-thermal history. The Kapoeta howardite was chosen as a polimict breccia affected by multiple shock-thermal treatment in the parent body regolith [5]. About 100 transparent monomineral OPx grains were picked out from the bulk meteorite sample weighing ~ 100 mg. All these ~ 50-100 μm-sized grains were divided into 7 groups on the base of their chemical, microstructure and colour analyses. The transparent light yellowish OPx fragments compose the dominant part of grains in all groups. The chemical composition of this OPx ranges within very narrow values according to microprobe analysis data: $Mg_{1.38-1.68}$ $Fe_{0.32-0.58}$ $Si_{1.98-1.99}$ O_8.

The natural TL was measured in crushed samples as small as ~ 10 μm in size. Then these samples were irradiated by ^{137}Cs source gamma-rays up to dose of 160 krad. The artificially induced TL was measured twice in each sample. The glow curves were graphically treated to reveal peaks in Gaussian distribution of TL intensity. Mathematical treatment of OPx TL spectra showed the following results. 1. Among all the crystals under study at least five groups were found (see Fig.) distinguishing both by the different numbers of selected TL peaks and TL intensity change observed after the first TL measurement in low <(180-200 °C) as well as in high >(180-200 °C) temperature intervals. The examples of the most typical cases are given in the table. It is evident that the ratio value of $R=I_{TL(>200)}/I_{TL(<200)}$ can be both more than 1 (samples 1f, 5f) and less than 1. 2. The peak (T_{PEAK}) temperature selected in low-temperature part of glow curve is

within the range of (172-184 °C) for all samples, and the full width of peaks at half the maximum (FWHM) ranges from 48 to 78 °C. 3. The TL measurements after reirradiation of the same samples show that: a) the lower T_{PEAK} (145-155 °C) were revealed in some samples; b) the several-times rise of TL sensitivity for the same samples (5b) was observed whereas it remained practically constant for the other ones; c) the TL intensity relation in different temperature intervals was significantly affected for some samples: the increase of TL in high-temperature region for the sample 3d by a factor of several times and decrease of that by a factor of ~ 2 for other fragments (e.g. 5f) were observed; d) there is no correlation between the TL parameters and the contents of the main rockforming elements.

On the base of obtained data we can suggest that the observed variety of TL characteristics for Kapoeta howardite individual OPx grains can reflect the peculiarities of their microstructure caused by distinct shock-thermal history at the regolith stage of meteorite parent body formation. The diversity of changes of TL parameters obtained under reirradiation leading both to increase and decrease of TL storage probability in different samples confirms this supposition.

References. 1. Sears, D.W.G. et al. (1980) Nature, **287**, 791. 2. Guimon, R.K. and Sears, D.W.G. (1986) Meteoritics, **21**, 381. 3. Kashkarov, L.L. and Kashkarova V.G. (1989) Meteoritics, **24**,284. 4. Guimon, R.K. et al. (1985) GCA, **49**, 1515. 5. Wilkening, L.L. (1973) GCA, **37**, 1985.

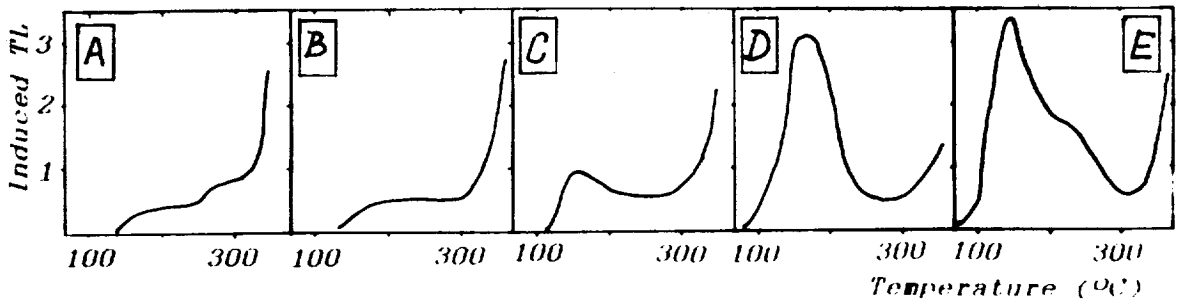

Fig. Induced TL glow curves from the orthopyroxene grains.

Table. TL glow curve parameters for Kapoeta OPx grains.

Group	Sample	First irradiation T_{PEAK}	FWHM	R	Second irradiation T_{PEAK}	FWHM	R
A	1f	184	57	1			
		230	48	1.58:			
		285	38	1.14			
		320	42	1.14			
B	5c	184	75	1	189	71	1
		230	23	0.20	247	30	0.35
		282	38	0.28	285	44	0.44
		280	25	0.23	323	19	0.45
C	3d	184	65	1	148	64	1
		243	54	0.4	200	54	0.67
		286	49	0.23	247	38	0.35
		>324	-	0.18	>263	-	0.80
D	5b	184	73	1	148	59	1
		>220	-	0.78	188	72	1.30
E	5f	178	52	1	180	82	1
		232	39	0.38	221	33	0.26
		273	43	0.31	255	35	0.15D
		308	31	0.32	277	23	0.08
		347	41	0.18	300	21	0.07

A FIRST-ORDER MODEL FOR IMPACT CRATER DEGRADATION ON VENUS

Noam R. Izenberg, Raymond E. Arvidson, and Roger J. Phillips, McDonnell Center for the Space Sciences, Department of Earth and Planetary Sciences, Washington University, St. Louis, MO 63130
Internet: izenberg@wunder.wustl.edu

A first-order impact crater aging model is presented based on observations of the global crater population of Venus. The total population consists of 879 craters found over the ~98% of the planet that has been mapped by the Magellan spacecraft during the first three cycles of its mission. The model is based upon three primary aspects of venusian impact craters: 1) extended ejecta deposits (EEDs); 2) crater rims and continuous ejecta deposits; and 3) crater interiors and floors.

Assumptions

The primary assumptions of the model are: 1) all or most impact crater events on Venus generate EEDs during their formation. 2) parabolic EEDs are thin deposits (several cm thick) of fine-grained particles [1,2]; 3) halo-like components of EEDs are composed of larger ejecta particles and/or ground blasted or otherwise affected by the shock of impact [3,4,5]; and 4) Craters form with continuous ejecta and crater floors with a high radar backscatter cross section due to the large size (meter scale and larger) and blocky character of their materials [3,5]. Crater floors may start out with low emissivities relative to the surrounding terrains perhaps due to excavated materials not being at chemical equilibrium with the atmosphere. Figure 1a is a sketch of a typical impact crater at time = 0, defined as the initial time where modification of the crater occurs primarily at the geologic timescale.

Observations

A global survey of the total crater population was conducted to identify craters with EEDs and the superpositional relationships of EEDs with respect to surrounding materials. Craters were also examined for tectonism, exterior modification (embayment by external volcanic sources), and interior modification of crater floors (e.g., dark floors of indeterminate origin). Results are as follows:

EEDs: 1) Between 61% and 73% of all craters have EEDs. The spread is due to craters for which SAR data are not clear enough to confirm the presence of an EED.

2) The occurrence of EEDs decreases to 40% for craters above the 6053km planetary radius (1.2 km above the mean planetary radius), to 34% for tectonized craters, and to 23% for volcanically embayed craters. Simple binomial distribution tests indicate a low probability (<.01) that these lower percentages are random.

3) The occurrence of EEDs also decreases for the population of craters with dark floors (i.e., floors with low radar backscatter relative to the rim and continuous ejecta). This part of the survey is still incomplete and reliable statistics are not yet available.

4) Parabolic EEDs are found around less than 10% of the crater population.

5) Partial parabolic and halo-like EEDs have been observed. About 17% of EEDs have been modified by tectonic activity, embayed by lavas from sources outside the crater, or by subsequent nearby impacts. Mottled EEDs, and EEDs modified by wind and possibly affected by high altitude atmosphere surface chemistry have been observed, but not yet quantified.

Rims and Continuous Ejecta: Backscatter properties of crater rims and continuous ejecta do not appear to vary as a function of preservation state, except for severely tectonized craters or craters that have been embayed by external volcanic sources. That is, extraction of backscatter cross sections of continuous ejecta materials for a number of craters of different sizes and characteristics reveal no significant or systematic variations.

Crater Interiors and Floors: 1) About 54% of all impact craters have floors with lower backscatter cross sections than their continuous ejecta. Differences of 5-10 dB are common.

2) Only 36% of craters with parabolic EEDs have at least some dark material on their floors.

3) Of the 95 craters with modified EEDs (i.e., craters whose EEDs have been clearly modified by tectonism, volcanism, or subsequent impact events) as many as 70 have dark floors. This occurrence is 10% to 20% above the planetary average.

Implications

The observations imply that impact craters and associated ejecta deposits degrade in a characteristic way. Figure 1b-e shows sketches of the hypothesized process. Parabolic EEDs are interpreted to be easily removable by surface winds over a geologic timescale (figure 1b), so the 8-10% of craters with parabolas are likely to be the youngest 8-10% of the crater population [1,2]. This possibility is supported by association of wind streaks with many parabolas, the relative paucity of dark floors in craters with parabolic EEDs, and examples of partial parabolic EEDs, which may show parabolas in the process of disappearing. The halo-like components of EEDs are interpreted to be harder to remove by wind. As halos age, they may become mottled, degraded in appearance (losing backscatter contrast with surroundings), or become tectonized or embayed by lavas. Heavily modified impact craters may have

their EEDs totally obliterated, but some will remain observable even at this stage (figure 1c - 1e).

Crater rims and continuous ejecta remain pristine in SAR appearance until heavy modification by tectonism and/or embayment by lava flows (figure 1e). While a crater may be tectonized or embayed early in its lifetime, the likelihood and degree of the modification increase with time.

Crater interiors may be darkened by several processes, which are not necessarily mutually exclusive. Impact melt ponding and cooling may darken some craters' floors at the outset. Infilling of the crater floor by volcanic material originating beneath the crater may occur over the crater's lifetime. As the crater ages, the likelihood of lava infilling may increase (figure 1d). It is unlikely that dark interiors are the result of a surface/atmosphere chemical reaction, since rims and continuous ejecta are not likewise darkened over time. Low emissivity signatures of craters may be removed by infilling and/or possibly by equllibration of excavated materials with the atmosphere.

References

[1] R. E. Arvidson et al. (1991) *Science* 252, 270-275. [2] D. B. Campbell et al. (1992) *JGR* 97 E10, 16,249-16,278. [3] R. J. Phillips et al. (1991) *Science* 252, 288-297. [4] R.J. Phillips et al. (1992) *JGR* 97 E10, 15,923-15,948. [5] G. G. Schaber et al. (1992) *JGR* 97 E8, 13,257-13,302.

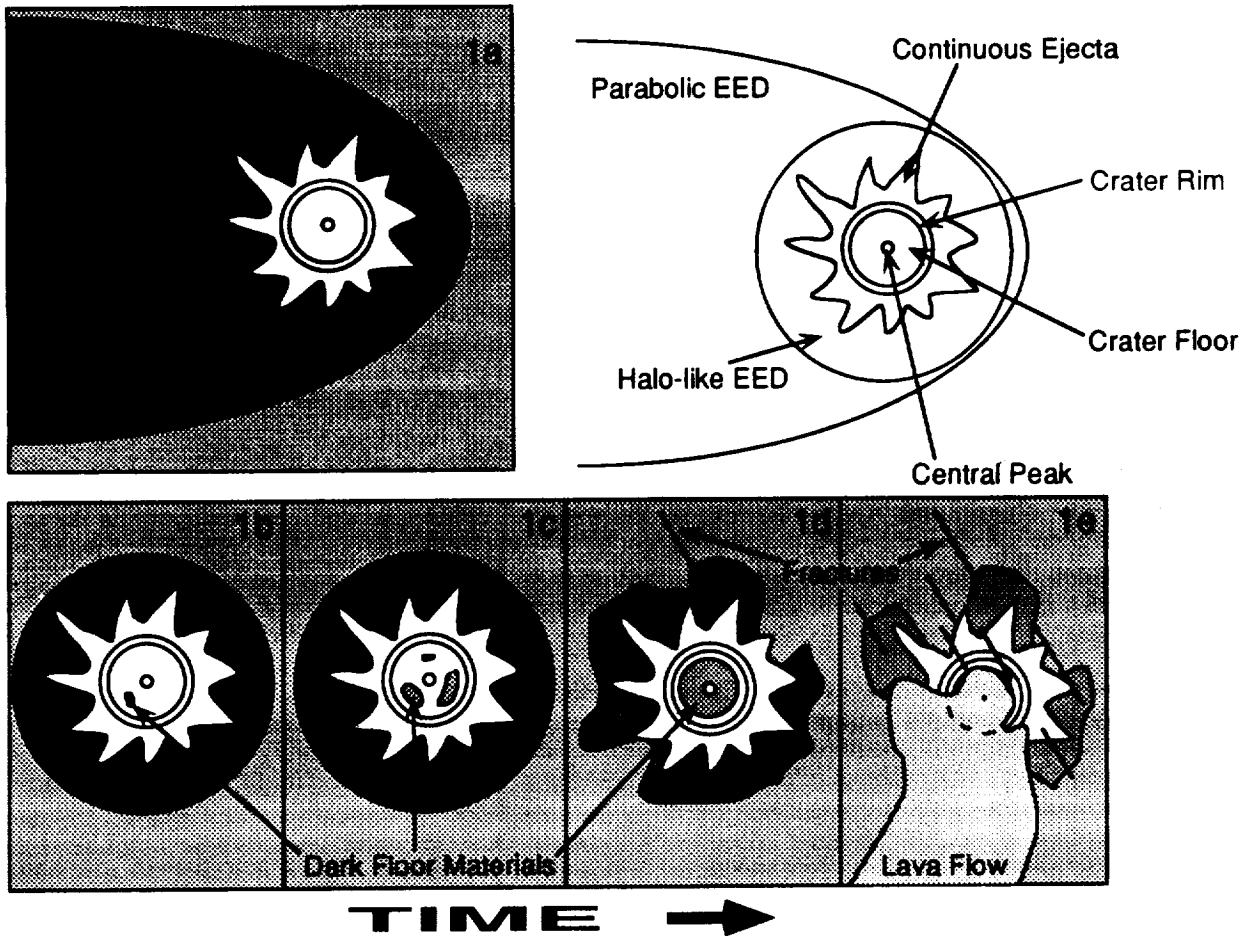

Figure 1. A simplified schematic of crater degradation on Venus. A central peak crater (20-40 km diameter on average) is used. Letters **a** to **e** denote increasing time.

A DISCONTINUOUS MELT SHEET IN THE MANSON IMPACT STRUCTURE

G.A. Izett, R.L. Reynolds, J.G. Rosenbaum, and J.M. Nishi, U.S. Geological Survey, Denver Federal Center, Denver, CO 80225

Petrologic studies of core recovered from holes drilled in the Manson, Iowa, buried impact structure may unravel the thermal history of the crater-fill debris. We made a cursory examination of about 200 m of core recovered from the M-1 bore hole, which was the first of 12 holes drilled as part of a cooperative drilling program between the U.S. Geological Survey and the Iowa Geological Survey Bureau [1]. The M-1 core hole is about 6 km northeast of the center of the impact structure, apparently on the flank of its central peak [1]. We developed a working hypothesis that a 30-m-thick breccia unit within a 53-m-thick unit previously termed the "crystalline clast breccia with glassy matrix" [1] is part of a discontinuous melt sheet in the crater-fill impact debris. The 30-m-thick breccia unit reached temperatures sufficient to partially melt some small breccia clasts and convert the fine-grained breccia matrix into a silicate melt that cooled to a greenish-black, flinty, microcrystalline rock.

Large clasts in the 30-m-thick breccia unit consist of Precambrian crystalline rocks (granite, gneiss, and mafic rocks), most of which are 5-10 cm long. Smaller clasts 0.5-1.0 cm include quartz, quartzite, and feldspar. Microcline clasts are pink and fresh appearing from the bottom of the core (~700 ft depth) up to ~500 ft depth. Above this level, especially in the 30-m-thick breccia unit, microcline and other feldpsar clasts are chalky white and show various effects of melting or partial melting, including feldspar masses consisting of radially oriented crystals and sheaf-like masses (spinifex? texture). Some microcline clasts, which contain shock lamellae, were thermally converted to potassium feldspar (sanidine?) having a very small optic angle ($2V_X$). A conspicuous type of small clast consists of yellowish-brown dusty-appearing quartz cores containing shock lamellae surrounded by haloes of quartz that are in optical continuity with the shocked quartz cores (fig. 1). Coronas of clinopyroxene crystals (<40 μm) are concentrated near the margins of the quartz haloes with the surrounding matrix. The former presence of shocked quartz clasts is indicated by centimeter size polycrystalline quartz masses surrounded by coronas of clinopyroxene crystals. EDS-SEM analysis of the clinopyroxene crystals shows that they are augite ($Mg_{48}Ca_{37}Fe_{15}$). Biotite (100 μm), skeletal ilmenite (fig. 2), and titanomagnetite crystals (<50 μm) also occur in the quartz coronas. The above described mineralogic relations suggest to us that the small shocked quartz clasts were partly to wholly melted and that clinopyroxene, biotite, titanomagnetite, and ilmenite crystallized in the associated quartz coronas.

Optical microscopic and SEM study of the matrix of the 30-m-thick breccia unit shows that it is composed of a microcrystalline intergrowth of quartz and feldspar. Previously, the matrix was thought to be glassy[1], but we found no mineralogic evidence to support this idea. The matrix contains conspicuous amounts of disseminated titanomagnetite and ilmenite crystals, and shocked zircon and apatite crystals were recovered from the matrix using standard mineral separation methods.

Measurements of the intact M-1 core showed that a 30-m-thick interval from 380 to 480 ft depth (116-146 m) is characterized by high magnetic susceptibility (fig. 3). Microscopic and thermomagnetic study of a few samples (421 and 423 ft depths) in the core revealed that the source of the high magnetic susceptibility is disseminated 5-50 μm euhedral crystals of unaltered titanomagnetite. In addition, the breccia matrix contains unaltered ilmenite crystals 10-100 μm in diameter. An important morphological feature of some ilmenite crystals is their skeletal habit typical of crystals whose growth in a liquid has been arrested (fig. 2). Another crucial observation is that the ilmenite and titanomagnetite crystals are in some places intimately associated. Small areas of titanomagnetite within, or adjacent to, large ilmenite crystals were observed with an SEM. EDS-SEM analyses of 10 spots within 10 crystals of titanomagnetite and ilmenite in the breccia matrix show that the crystals are fairly uniform in composition. The titanomagnetite (Usp 30%) has the following average weight % composition: Fe as FeO, 84.7; TiO_2, 10.6; Al_2O_3, 2.7; MgO, O.2; and MnO, 1.0. The ilmenite (Hm 13%) has the following average weight % composition: Fe as FeO, 50.5; TiO_2, 46.6; Al_2O_3, 0.5; MgO, 1.4; and MnO, 0.8.

Assuming that (1) our observational and chemical data for titanomagnetite and ilmenite are representative of the 30-m-thick breccia interval and (2) the titanomagnetite and ilmenite are an equilibrium pair, the temperature and oxygen fugacity can be estimated using the computer program of Andersen et al. [2]. Application of their computer program indicates that the titanomagnetite and ilmenite crystallized at about 760° C at an oxygen fugacity of log fo_2 -10^{14}. It should be stressed that the above observational and chemical data for the 30-m-thick breccia unit are based on only a few samples and confirmation of our preliminary results awaits complete characterization of the core.

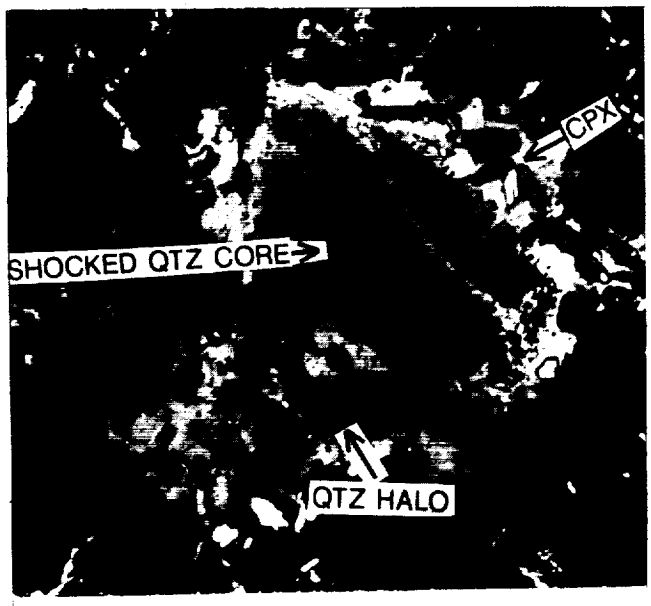

Figure 1

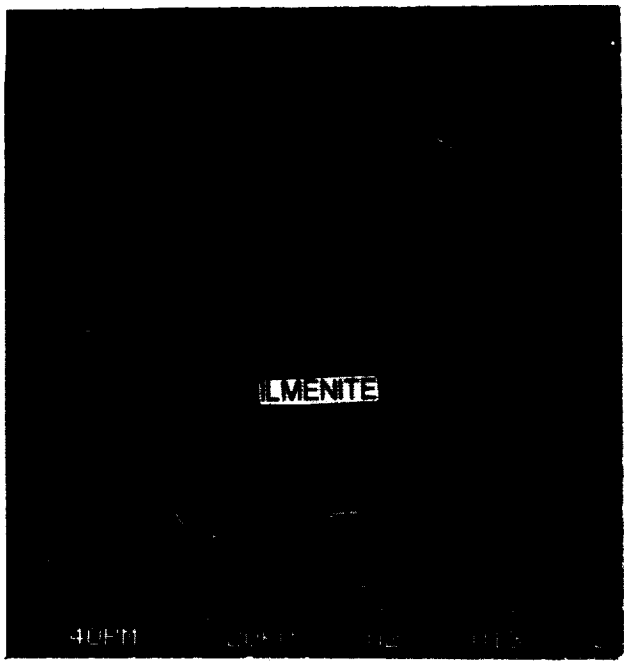

Figure 2

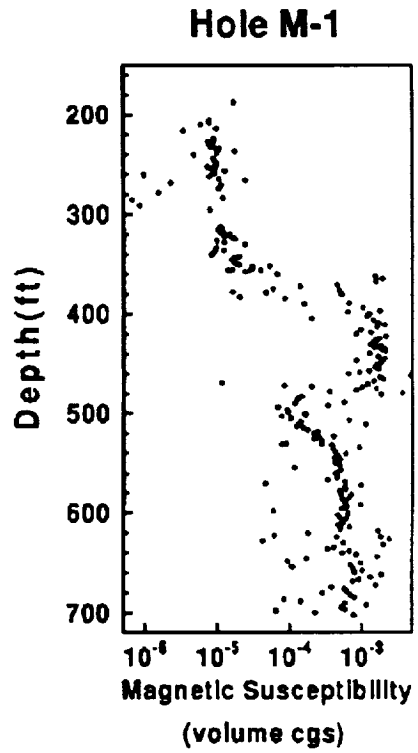

Figure 3

References: [1] Anderson, R.R., Hartung, J.B., Roddy, D.J., and Shoemaker, E.M., 1992, LPI Contribution 790, 2-3; [2] Andersen, D.J., Lindsley, D.H., and Davidson, P.M., 1992, QUILF: A Pascal program to assess equilibria among Fe-Mg-Ti oxides, pyroxenes, olivine, and quartz [In Press}.

ORBITAL EVOLUTION OF DUST FROM COMET SCHWASSMANN-WACHMANN 1: A CASE OF ONE-TO-ONE RESONANCE TRAPPING.

A. A. Jackson, Lockheed Engineering and Science Co., Houston, Texas
H. A. Zook, NASA Johnson Space Center, Houston, Texas

In a recent study [1] we have modeled the orbital evolution of dust particles released from comets and asteroids in the solar system. The source bodies were either asteroids inside Jupiter's orbit or comets from the Jupiter family of comets. However there are other dust producing parent bodies in the solar system of interest, one of these is comet P/Schwassman-Wachmann 1. Since comet Schwassman-Wachmann 1 has an orbit outside of Jupiter's orbit, is an active dust producer and has low eccentricity, dust particle evolution from it is of interest. We report on a particular 2 micron radius particle that captured into a 1 to 1 mean motion resonance orbit with Saturn.

Our method was to numerically integrate the equations of motion of dust particles evolving from comet Schwassman-Wachmann 1. The particles were released at perihelion and are modeled as ideal black bodies of density 1 gm/cc. The forces are those of the Sun and eight planets, radiation pressure and Poynting-Robertson (PR) and solar wind drag. The planets are all moved in their correct n-body orbits. Dust evolving from comets follow complicated orbital evolution histories in the solar system. Radiation forces can bring dust particles into various gravitational configurations with respect to the planets that include scattering, and capture into exterior and interior mean motion resonances. We discuss the motion of a particular 2 micron particle.

Comet Schwassman-Wachmann 1's orbital elements [2] are semimajor axis , a= 6.041, eccentricity, e = .0445 and inclination i= 9.4 degrees. Upon release a 2 micron particle suffers a large change in a and e [1] going to a new a of 10.7 AU and e of .461. With a aphelion of 15.6 AU the particle crosses the orbit of Saturn at 9.5 AU by an ample margin.

Fig. 1 shows the first 80,000 years of orbit evolution of a 2 micron particle released from Schwassman-Wachmann 1. This time history of semimajor axis shows early irregular motion the particle being scattered to nearly 20 AU before decaying under drag forces to a region near Saturn. There are a couple of ragged possible orbit resonances at about 10 AU before a finally scattering causes the particle to settle into 35,000 year 1 to 1 resonance capture at an interior point with Saturn. This interior resonance has semimajor axis a_i located by $a_i = (1 - \beta)^{1/3} a_p$, where β is the ratio of gravitational to radiation force and a_p is the planetary semimajor axis. This one to one resonance is located at a= 8.53 AU for the 2 micron particle. Fig 2. shows detail of the time history of capture of semimajor axis during resonance capture. We see a quasi-saw-tooth pattern of co-rotation resonance.

In Fig. 3 we plot the motion of the dust particle in a rotating frame with respect to Saturn. Early on the particle is captured into a region around the L5 Lagrange point. (The location of this Lagrange point is however modified by radiation pressure [3].) However it librates about this point with an unusual amplitude finally migrating around to another quasi-stable libration about the L4 Lagrange point Fig 4. The trapping resonance is stable for about 35,000 years before breaking out. These instabilities in the trapping location and amplitude are probably due perturbations by Jupiter and weak instability of this 1:1 resonance cause by the Poynting-Roberston drag [3].

[1] Jackson, A and Zook, H., Icarus, 97 , 70 - 84 (1992), [2] Marsden, B, Catalog of Cometary Orbits, 1989. [3] Schuerman, D , Ap. J., 337-342 (1980.

ORBITAL EVOLUTION OF DUST: Jackson A. A. and Zook H. A.

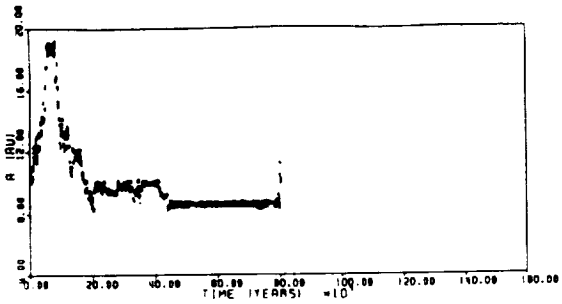

Figure 1. Time history of semimajor axis of a 2 micron particle released from Comet Schwassman-Wachmann 1. Time in thousands of years and semimajor axis in AU.

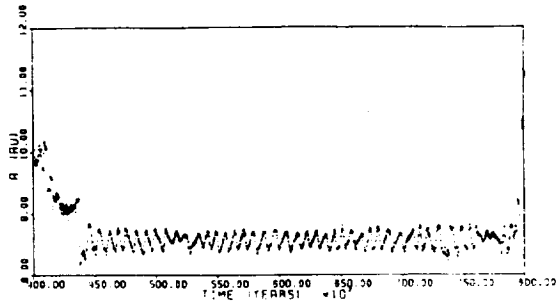

Figure 2. Detail from Figure 1 of orbital evolution of 2 micron dust particle at and during capture into a 1 to 1 mean motion resonance w.r.t. Saturn.

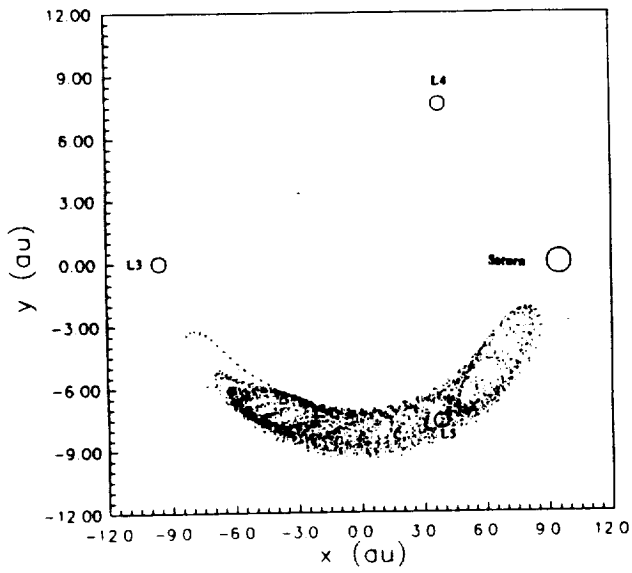

Figure 3. Early time history, about 4000 years into resonance, of orbit of 2 micron particle in a frame rotating with Saturn. There are wide quasi-librations about L5.

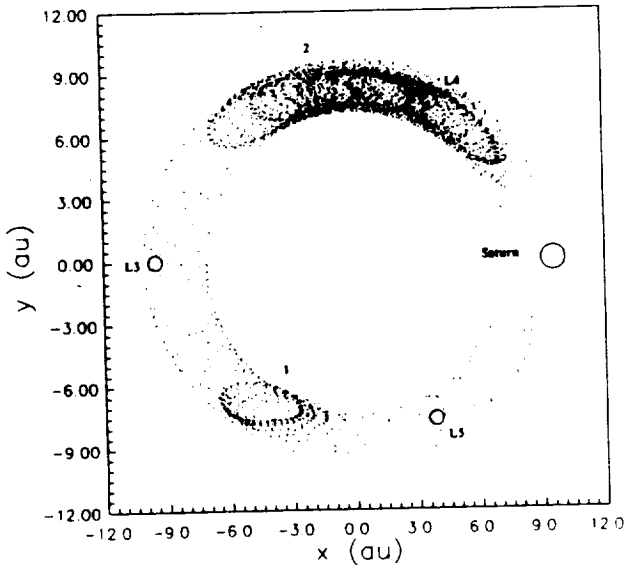

Figure 4. Subsequent history of particle evolution of Saturn rotating frame. The starts at point (1) and moves in a librating orbit towards Saturn then back towards (1) all the way around to near Saturn before settling down into quasi-libration around L4.

CONSTRAINTS ON THE DIFFERENTIATION OF THE EARTH FROM THE COUPLED ^{146,147}Sm-^{142,143}Nd SYSTEMATICS, **S. B. Jacobsen and C. L. Harper Jr.,** Department of Earth and Planetary Sciences, Harvard University, 20 Oxford Street, Cambridge, MA 02138, USA.

The coupled Sm-Nd systematics are a powerful (albeit analytically challenging) tool for investigating the geodynamic history of the Earth. We have previously reported evidence for a 33 ppm difference of an Isua sample relative to our terrestrial standard [1]. Interpretation yields a formation age range for the depleted mantle (DM) source reservoir of 4.45-4.55 Ga. This is consistent with an epoch of LREE-enriched melt extraction from the mantle (proto-crust formation), soon after magma ocean freeze-up following the putative Moon forming giant impact.

The rate of crustal recycling inferred from $^{143}Nd/^{144}Nd$ evolution in DM over Earth history using a two-reservoir recycling model [2,3] can be evaluated from the following equation:

$$\frac{d\epsilon_{143Nd}}{dt} = -\left(\frac{\varphi}{Y_{Nd}}\right)\epsilon_{143Nd} + Q_{143Nd} f^{Sm/Nd}$$

Here φ is the fractional rate of recycling, Y_{Nd} is the mass fraction of Nd in the depleted mantle, Q_{143Nd} = 25.13 Ga^{-1} and $f^{Sm/Nd}$ is the Sm/Nd fractionation factor in the DM. The constraints from the ^{143}Nd evolution may be used to calculate the average $^{142}Nd/^{144}Nd$ evolution of DM. As shown in Fig. 1 such a continuous model (with both growth and recycling) would not allow the survival of $^{142}Nd/^{144}Nd$ >+10 ppm (w.r.t. bulk Earth) in bulk DM at any time. Use of the above equation, however, requires detailed knowledge of the $f^{Sm/Nd}$ evolution of the depleted mantle. The mantle source of Isua 715-28, however, can be interpreted with a two-stage model with an initial time of differentiation of 4.45-4.54 Ga, as shown by the two-stage evolution curves in Fig. 1. The survival of a +33 ppm ^{142}Nd enrichment in the mantle source region of the Isua 715-28 at 3.8 Ga indicates an isolation with respect to geodynamic remixing. The survival of the effect in the mantle as late as 3.8 Ga also suggests that crustal recycling (and therefore contemporary style plate tectonics) may not have been active in the Hadean. If the Isua 715-28 source reservoir represents bulk DM, then our results suggest that contemporary-style crustal recycling was not active prior to ~ 3.9 Ga and that the 'lost' ancient cratered terrains survived on the Earth's surface at least until the epoch of 'heavy bombardment' at this time.

The oldest (~4.0 Ga) known terrestrial crustal rocks are found in the Acasta region of the Northwest Territories [4]. Sam Bowring kindly provided powder aliquots of some of his oldest samples (SB91-37 and SB89-39), for which he obtained initial ϵ_{143Nd} of +2.9 and +3.5 respectively using ~4.0 Ga U-Pb zircon ages. We measured $^{142}Nd/^{144}Nd$ for these samples by both static and dynamic multicollection methods. The deviations (in ppm) relative to the Ndβ standard are shown in Fig. 2. It appears that these samples are within 5 ppm of the Ndβ value and within error of our inferred bulk Earth value (based on Ndβ and a young flood basalt sample BCR-1). If Ndβ is representative of the present bulk Earth value of $^{142}Nd/^{144}Nd$, this implies an extreme LREE depletion at a relatively late time (<4.3 Ga) in the source region(s) of the Acasta gneisses, in contrast to that of the Isua 715-28 source where the depletion appears to have taken place very early in the Hadean (~4.5 Ga).

^{142}Nd heterogeneity is generated only as a result of early differentiation (plausibly protocrust formation). The primary step in exploring the utility of the ^{142}Nd tracer is to determine the magnitude of the 'initial' post-^{146}Sm-decay (*viz.*, ~4.3 Ga) $^{142}Nd/^{144}Nd$ of DM. Subsequent measurements of younger samples will allow a first order estimate of the progressive 'erasure' of the initial heterogeneity in the average DM by geodynamic remixing of the complementary reservoir (the protocrust). For the post-^{146}Sm-decay we have

$$\frac{d\epsilon_{142Nd}}{dt} = -\left(\frac{\varphi}{Y_{Nd}}\right)\epsilon_{142Nd}$$

and thus the recycling rate may be obtained directly from the ϵ_{142Nd} evolution in DM without any estimate of the Sm/Nd fractionation in the source region. After ~4.3 Ga, therefore, the evolution of $^{142}Nd/^{144}Nd$ in the Earth's depleted mantle reservoir becomes a tracer for geodynamic mixing and can be employed to quantify the 'global' geodynamic history of the crust-mantle system throughout geological time. Figure 3 shows the general properties of the coupled Sm-Nd systematics in relation to investigations of global-scale history of geodynamic mixing in the Earth. Here the lowermost panel diagram has been scaled to fit the boundaries

^{146}Sm-^{142}Nd IN THE EARTH, Jacobsen S. B. and Harper C. L.

of the Isua 715-28 result (+33±4 ppm) at 3.8 Ga. Initiation of (plate tectonic) recycling, shown here in the second panel as a step function in the recycling rate at 3.75 Ga, leads to progressive diminution of the initial anomaly in the average DM by remixing of the complementary reservoir (the protocrust). Companion plots of time evolution in ϵ_{143Nd} and in the total mass of the crust are also shown.

The above considerations demonstrate the potential utility of the coupled chronometer as a tracer of geodynamic mixing. However, our new results on the Acasta samples as well as other reports [5,6,7,8] do not support ^{142}Nd enrichments to be a widespread effect in early crustal rocks derived from inferred high ϵ_{143Nd} sources. The most critical aspect of continuing these studies is to firmly establish the bulk Earth value for $^{142}Nd/^{144}Nd$ [see our companion abstract]. It is possible that Ndβ could itself have been derived from an early-formed depleted mantle reservoir. At present we are only beginning to explore the potential of the coupled Sm-Nd systematics and our efforts are mostly focused on the challenges of very high precision Nd mass spectrometry. We emphasize, however, that all of the measurement problems are solvable by development of better techniques and mass spectrometers and consequently that there is very great promise for the eventual exploitation of $^{142}Nd/^{144}Nd$ measurements in addressing a range of fundamental issues in global geodynamics.

REFERENCES. [1] Harper C.L. & Jacobsen S.B. (1992) *Nature*, **360**, 728. [2] Jacobsen S.B. (1988) *GCA*, **52**, 1341. [3] Jacobsen, S.B. *EPSL* **90**, 315 (1988). [4] Bowring, S.A., Williams, I.S. & Compston, W. (1989) *Geology*, **17**, 971. [5] Galer, S.J.G. & Goldstein S.L. (1992) *EOS*, **73**, 622. [6] Bennett V.C. & McCulloch M.T. (1992) *EOS*, **73**, 621. [7] Jacobsen S.B. & Harper C.L. (1992) *EOS*, **73**, 622. [8] Harper C.L. & Jacobsen S.B. (1992) *EOS*, **73**, 622.

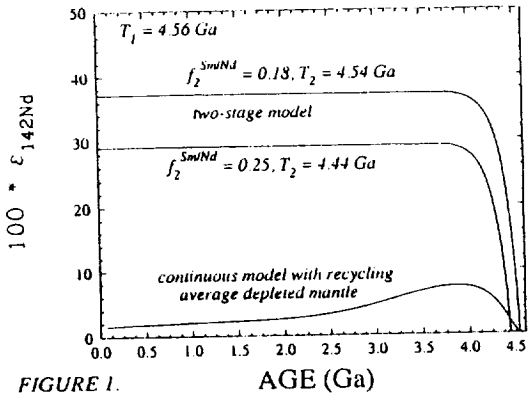

FIGURE 1.

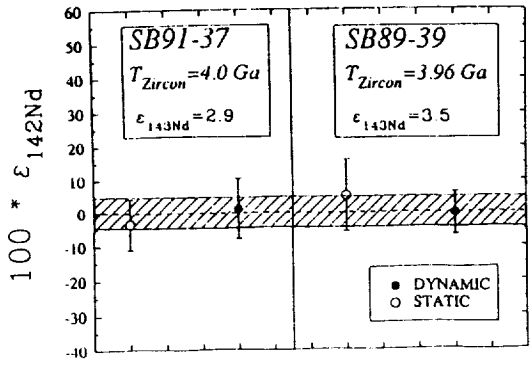

FIGURE 2

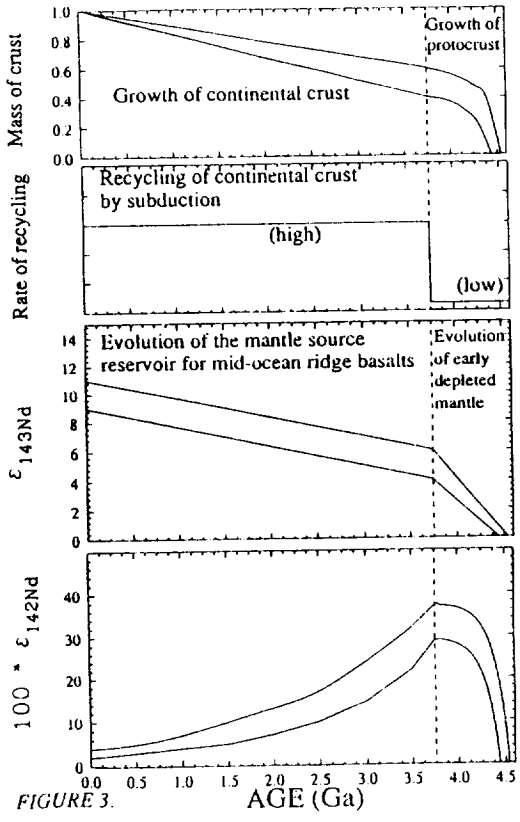

FIGURE 3.

OS ISOTOPES IN SNC METEORITES AND THEIR IMPLICATIONS TO THE EARLY EVOLUTION OF MARS AND EARTH:

E.Jagoutz [1], J.M.Luck [2], D. Ben Othman [2] and H. Wänke[1] [1] MPI f. Chemie, Saarstr. 23, 65 Mainz, Germany; [2] Lab. d. Géochimie Isotopique, 34095 Montpellier, France

A new development on the measurement of the Os isotopic composition by mass spectrometry using negative ions opened a wide field of applications. The Re-Os systematic provides time information on the differentiation of the nobel metals. The nobel metals are strongly partitioned into metal and sulphide phases, but also the generation of silicate melts might fractionate the Re-Os system. Compared to the other isotopic systems which are mainly dating the fractionation of the alkalis and alkaliearth elements, the Re-Os system is expected to disclose entirely new information to the geochemistry. Especially the differentiation and early evolution of the planets such as the formation of the core will be elucidated with this method.

We are measuring Os isotopes in SNC meteorites, which may represent samples from the planet Mars, and compare this with the general isotopic systematic as observed on Earth.

The highly siderophile elements in the Earth`s mantle are depleted when compared to chondrites, but occur in chondritic abundance ratios as firstly pointed out by Jagoutz et al., 1979. Allegre and Luck (1980) demonstrated that the Os isotopic composition of the Earth`s mantle evolved along the chondritic evolution line. This strongly suggests that the Re/Os ratio of the mantle was chondritic throughout the evolution of the Earth. Since each of the highly siderophile elements has divers affinity to metal and sulphide phases, an equilibrium with the core contradicts the observed chondritic abundance pattern.

The moderately siderophile elements like Co, Ni, Ga, and Cu have mantle abundances close to 0.1 (relative to Si and CI), while the abundance of the highly siderophiles like Ir, Os, Re, Au are 0.002. However the Ni/Co and the Re/Os ratios are identical to the chondritic ratios. The budget of highly siderophile elements in the Earth's mantle was attributed to a late veneer of about 0.5% CI material mixed into the terrestrial mantle (Wänke, 1981).

From the SNC meteorites there is some indications on the siderophile element pattern on Mars. Since the SNC`s are magmatic rocks and the particular melting conditions are not known the determination of the element abundances in Mars' mantle is problematic. Wänke`s method of the correlated elements provided the first insight in the composition of Mars' mantle. From this it was evident that the chemical composition of Mars' mantle is unlike the mantle on Earth. The moderately siderophile elements are considerably more variable in their abundances on Mars. The Ni/Co ratio is about be 5-6 on Mars compared with 21 in the Earth's mantle. Co is slightly and Ni is strongly depleted in Martian mantle when compared to Earth. Also it appears that Zn, Cu, and In have also been depleted in Martian mantle. Wänke and Dreibus (1988) attributed these observations to extraction of a sulphide phase at the formation of the Martian core.

The highly siderophile elements are also not in chondritic abundances on Mars. Chassigny, an olivine-rich SNC meteorite, has a Re/Os ratio which is about half the chondritic ratio. While the Os isotopic composition of Chassigny is considerably higher than the general range of the chondritic Os isotopes. It is evident that the Os isotopes are not supported by Re in Chassigny.

An Os evolution model for Chassigny might be embedded in a general isotopic model for the SNC meteorites. The crystallisation age (around 1.3 Ga) and the Sr isotopic composition as well as the Rb/Sr ratio of Chassigny might coincide with Nakhla, another SNC meteorite (Nakamura et al., 1982).

Most attempts to model the evolution for the SNC meteorites could not integrate the old Rb-Sr and Pb model ages with the young Nd systematic. In order to illustrate some of the problems some implications of the Nd isotopes will be discussed. In Fig. 1, a Sm - Nd isochron diagram is shown. The chondritic point which contains all bulk samples of normal stony meteorites is shown. A corresponding plagioclase-pyroxene isochron, like the isochron of Juvinas, is also indicated. The shaded areas mark in a simplified form the Earth`s samples. The oceanic mantle represented by selected lherzolitic xenoliths is indicated. Shifted to the left there is the area of oceanic floor basalts. These basalts have the same isotopic composition as the oceanic mantle, but the melting process shifts these basalts to the left to lower Sm/Nd ratios. Although this melting process is not entirely understood yet, but we are able to model in an innocent first order this shift. The SNC meteorites, however, are basaltic and mainly plot on the right side of the meteoritic isochron (except Nakhla). A source for these basalts might be postulated on the far right side, but such a depleted reservoir might be very radiogenic in relatively short time. An unspecified multistage model is usually postulated for such cases. The Rb-Sr isotopic systematic as well as the Pb-Pb and U-Pb systematic of the SNC meteorites clearly show that complicated multistage models can be excluded. In the Rb-Sr system the SNC meteorites plot close to the 4.55 Ga isochron. The Pb isotopes measured in maskelinite plot close to the geochron. In an concordia diagram the trend of the data also

suggests that a two stage model might comply with the data. An early differentiation and a late one. Whereas at the late differentiation the Rb/Sr ratio should not be changed drastically.

To model the Os evolution,we therefore use a two stage evolution for good reasoning. In Fig. 2 the measured Os isotopic composition is plotted on the y-axes, the slope of the line through this measured point is determinated by the Re/Os ratio. At 1.3 Ga this evolution stopped and a straight line leads to the initial differentiation of Mars. The interesting result of our investigation is the slope of this line. This slope tells us with good reason that the Re/Os ratio in the source of Chassigny was a factor of 10 higher than chondritic. There might be less Re in the Martian mantle than in the mantle of the Earth as a consequence Os must be more than

Fig. 1

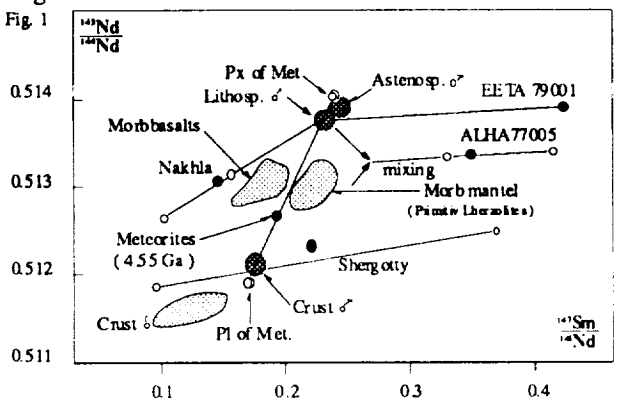

Fig. 2

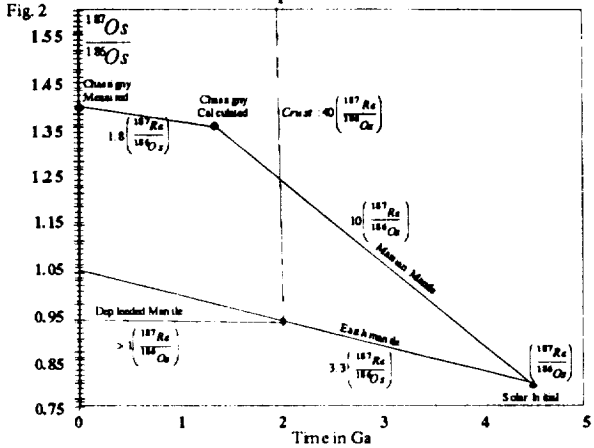

a factor of 10 less.This seems to be the fingerprint of the core formation on Mars.The contrasting evolution of the Earth`s mantle is also indicated in Fig 2.

From the relative unradiogenic Sr isotopic composition of Chassigny we consider that Chassigny comes isotopically from a similar source as Nakhla. There are 3 groups of Sr isotopic composition in SNC`s : 1) Nakhlites (0.704); 2) ALHA 77005 and EETA 79001 (0.71-0,715); 3) Shergotty and Zagami.(0,72-0,73). These 3 groups are formed early in the Martian history which is in line with the Pb isotopes. The isotopic reservoirs formed by the early differentiation were not remixed by convection. For a number of reasons we can attribute the isotopic signature of Nakhla and Chassigny to the Martian asthenosphere.(Jagoutz, 1991).

As pointed out above, the inventory of highly siderophile elements in the Earth's mantle is thought to be dominated by a late veneer. Why did the late veneer not hit Mars? It is possible that this late veneer is on Mars, but since Mars was not homogenized after the first differentiation this veneer might not be mixed in to the Martian mantle yet. Therefore we might be able to study the remnants of the highly siderphile elements in the Martian mantle just after core segregation.

References: 1) Jagoutz E., Palme H., Baddenhausen H. et al. Proc. Lunar Planet. Sci. Conf. 10th, 2031-2050, 1979. 2.) Allègre C.J. and Luck J.M., Earth Planet. Sci. Lett. **48**, 148-154, 1980. 3.) Wänke, H. Phil. Trans. R. Soc. Lond. A **303**, 287-302, 1981. 4.) Wänke, H. and Dreibus G., Phil. Trans. R. Soc. Lond. A **325**, 545-557, 1988. 5.) Nakamura N., Unruh D.M., Tatsumoto M. and Hutchison R., Geochim. Cosmochim. Acta **46**, 1555-1573, 1982. 6.) Jagoutz E., Space Sci. Rev. **56**, 13-22, 1991.

TRANSITION METALS IN SUPERHEAT MELTS. Petr JAKES (Faculty of Sciences, Charles University, Albertov 6, 128 43 Praha 2, Czech Republic) and Michael-Patrick WOLFBAUER (Bemidji State University, Bemidji MN)

A series of experiments with silicate melts doped with transition element oxides was carried out at atmospheric pressures of inert gas at temperatures exceeding liquidus. As predicted from the shape of fO_2 buffer curves in T-fO_2 diagrams the reducing conditions for a particular oxide-metal pair can be achieved through the T increase if the released oxygen is continuously removed. Experimental studies suggest that transition metals such as Cr or V behave as siderophile elements at temperatures exceeding liquidus temperatures if the system is not buffered by the presence of other oxide of more siderophile element. For example the presence of FeO prevents the reduction of Cr_2O_3. The sequence of decreasing siderophility of transition elements at superheat conditions (Mo, Ni, Fe, Cr) matches the decreasing degree of depletion of siderophile elements in mantle rocks as compared to chondrites.

The partition of elements between the metal and silicate phases is of importancce in the study of Earth's and other planetary cores and the behavior of iron and moderately siderophile elements, i.e., elements that may occur in natural minerals in both oxidic and metallic form provide constraints on the mantle-core relationship. We have been interested in the behavior of those siderophile elements that are moderately depleted in the upper mantle of the Earth since the observations of natural objects, i.e., tektites, meteoritic ablation spherules, lunar glasses (e.g., Jakes et al., 1992) indicate that very high temperatures of silicate melts may involve structural changes (due to breaking bonds between oxygen and metal) of the melts and may ultimatively lead to siderophile behavior of transition elements (Mo, Cr, V) as well as Si.

In order to assess the behavior of elements in the metal/silicate system in relation to increasing temperature (superheat melts) we have carried out a series of experiments in which we studied the behavior of transition elements, especially their partition between the metal and silicate phases at superheat conditions.

Three significantly different compositions were studied:

(1) JAP represents a composition with extremely high contents of refractory elements and it is close in composition to eutectic of $CaMgSi_2O_6$–$CaAl_2SiO_6$–$CaTiAl_2O_6$. This composition is similar to refractory "igneous" inclusions in carbonaceous meteorites. We have synthesized two derivative compositions by doping JAP with Cr_2O_3 and MoO_3.

(2) LBI represents a composition of potential lunar "oxygen" ore composed of 50% Apollo 11 basalt simulant and 50% ilmenite. Whereas the JAP compostion has zero content Fe, this (LBI) is extremely Fe rich.

(3) Indochinite composition represents high Si melts (terrestrial-type superheated melt) with relatively low Fe contents.

Indochinite composition was prepared from natural indochinite; JAP and LBI compositions were mixed from chemicals.

Experiments were run in a Deltech vertical furnace in a nitrogen atmosphere. The samples were run in platinum or alumina crucibles at 1300°, 1425°, and 1550°C each for a period of three hours. Carbon sleeve was positioned around the experimental charges to act as a buffer and to prevent oxidation of the system. We believe that both oxygen brought to the system with the nitrogen gas and oxygen released from melts due to high-temperature-induced reduction were reacted with carbon sleeve. No physical contact between the carbon and capsule containing the

melt was allowed. At the end of the run, the compositions in platinum were quenched in liquid nitrogen, the aluminum crucibles were cooled on switching the furnace. The experimental charges were examined optically and using the electron microprobe. In an analytical procedures platinum was used as a representative of metallic phase and concentrations of metals were measured at the boundary of silicate and metal phases. None of the experiments could be considered to have reached equilibrium.

Generally, the reaction of metal oxide with the metallic phase (represented) by the Pt capsule is dependent on temperature and hence fO_2. There is a positive correlation between temperature and the amount of particular metallic oxide entering a metallic state. As temperature increased more FeO to Fe took place, apparently releasing oxygen as a byproduct of superheating (in high-silica highly viscous melts, for example, more boubles are observed). In alumina crucibles a few metallic grains of Fe were precipitated from melt in LBI composition run for period of three hours (LBI composition was mixed from trivalent iron oxide reactants). In a superheat melt less siderophile element enters a metallic state only in the absence of an oxide of more siderophile element (e.g., the presence of FeO prevents reduction of Cr_2O_3. Interesting results were obtained in an experiments where superheated (LBI) melt was seeded with metallic seeds containing the (87%) and Cr (13%). After quenching, all precipitated metal at the bottom of the alumina capsule was Fe and had less than 0.1% Cr, whereas quenched silicates were Cr, Al, and Ti rich. In experiments with no Fe present (JAP), Cr and Mo were noted to enter the metallic (platinum) phase, though in the experiments with no Cr and Mo, minute amounts of Ti entered the Pt capsule.

The formation of metallic species from silicate melts is definitely temperature controlled and metal formation (i.e., high-temperature-induced reduction) strictly buffered by the presence or absence of other transitional-siderophile metals or their oxides.

There are two major implications of these experiments: (1) superheating (temperature-induced reduction) itself could be used for the production of oxygen in the lunar environment through the thermal decomposition of Fe silicates and oxides and (2) it is very difficult to envisage the formation of a siderophile depletion pattern characteristic of the upper mantle of the Earth by simply mixing two components, one reduced the other oxidized. The sequence of T- or fO_2-controlled events or mixing of components with different degrees of reduction must be sought.

IRON OXIDE BANDS IN THE VISIBLE AND NEAR-INFRARED REFLECTANCE SPECTRA OF PRIMITIVE ASTEROIDS; Kandy S. Jarvis, Dept. of Geology, Wright State Univ., Dayton, OH 45417; Faith Vilas, NASA Johnson Space Center/SN3, Houston, TX 77058; Michael J. Gaffey, Dept. of Earth and Environmental Sciences, Rensselaer Polytechnic Institute, Troy NY 12181.

High resolution reflectance spectra of primitive asteroids (C, P and D class and associated subclasses) have commonly revealed an absorption feature centered at 0.7 μm attributed to an Fe^{2+} - Fe^{3+} charge transfer transition in iron oxides and/or oxidized iron in phyllosilicates [1,2]. A smaller feature identified at 0.43 μm has been attributed to an Fe^{3+} spin-forbidden transition in iron oxides [3]. In the spectra of the two main-belt primitive asteroids 368 Haidea (D) and 877 Walkure (F), weak absorption features which were centered near the location of 0.60 - 0.65 μm and 0.80 - 0.90 μm [1] prompted a search for features at these wavelengths and an attempt to identify their origin(s).

CCD reflectance spectra obtained between 1982 - 1992 were reviewed for similar absorption features located near these wavelengths [1, 2, 4, 5, 6]. Figures 1, 2, 3 show the spectra of asteroids in which these absorption features have been identified. These spectra are plotted in order of increasing heliocentric distance. No division of the asteroids by class has been attempted here (although the absence of these features in the anhydrous S-class asteroids, many of which have presumably undergone full heating and differentiation should be noted). For this study, each spectrum was treated as a continuum with discrete absorption features superimposed on it. For each object, a linear least squares fit to the data points defined a simple linear continuum. The linear continuum was then divided into each spectrum, thus removing the sloped continuum and permitting the intercomparison of residual spectral features.

The most discernible feature is an absorption band centered at 0.65 μm of width ranging from 140 - 245 Å. Analogues for this feature are seen in spectra of the CM2 carbonaceous chondrites Cold Bokkeveld and Murray [1]. The depth, spectral placement of the beginning and end of the feature, width and area of the feature were all checked for correlations with properties of the asteroids such as albedo [7], distance [8,9] and classification [10]. No correlations were observed except for a weak trend of decreasing depth of feature with increasing heliocentric distance. Several minerals possess this 0.65-μm absorption feature, which has been associated with charge-transfer bands or spin-forbidden bands of transition metal elements. The source of this band is most likely Fe^{2+} or Fe^{3+} or both. Other possible elements such as Cr^{3+} and Ti^{3+} are much rarer than iron in most meteorites. (There is also a solar absorption band at 0.6563 μm, but it is unlikely to generate such a comparatively broad feature.) Based upon spectral shape, the most probable sources of this feature are goethite or hematite. These are strong possibilities due to their association with aqueous alteration of iron-bearing minerals (the assumed cause of the 0.7-μm absorption feature[1,2]), their absorption band locations, and their association with jarosite (a proposed cause for the 0.43-μm feature [3]). Many of these spectra also have a feature located near 0.8 - 0.9 μm. Goethite has an absorption feature at 0.65 μm and at 0.90 μm, while hematite, the anhydrous version of goethite, has bands located at 0.66 and 0.85 μm. Townsend [11] has proposed that the spectral placement of the longer wavelength feature could be used as a discriminator between the two minerals for terrestrial remote sensing. Presumably, the same may be true for asteroid spectra. Extreme care must be exercised, however, as telluric water absorption features become prominent near 0.9 μm and, if not fully compensated during the data reduction, will affect the identification and interpretation of these features.

A third feature found nested in the broader 0.65-μm feature in some of the asteroid spectra is a small peak located at ~0.63 μm. The apparent double absorption feature at 0.60 μm and 0.66 μm is presently unexplained. The variations in height of the feature in both spectra of 1 Ceres suggests surface mineralogical variations evident throughout its rotational period.

IRON OXIDES IN PRIMITIVE ASTEROID SPECTRA; K. S. Jarvis et al.

In some spectra displaying the prominent 0.70-μm absorption feature, a shoulder occurs at ~0.63 μm (Fig. 4). This shoulder may be the result of the 0.65-μm feature superimposed on the 0.70-μm feature, and represent a change in the aqueous alteration event sequence in solar system history between those asteroids that have spectra showing only the 0.65-μm feature and those also showing the 0.7–μm feature. Laboratory spectra of CM2 meteorites Cold Bokkeveld, Murray, Mighei, Murchison and Nogoya [12] also show this shoulder.

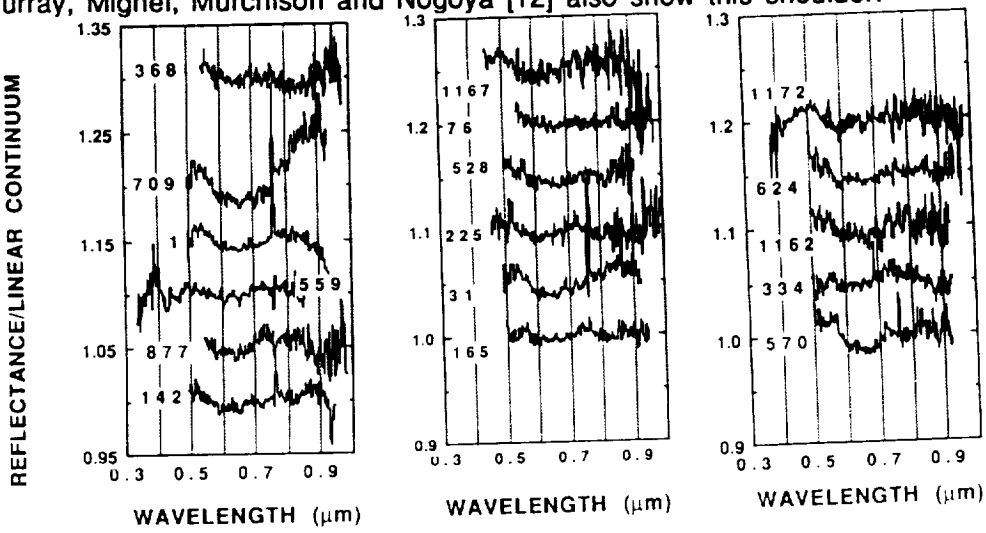

Figs. 1, 2, 3 Reflectance spectra with ascending heliocentric distance.

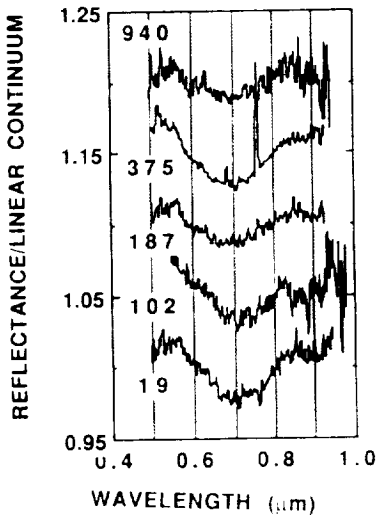

Fig. 4 0.7-μm Feature with 0.63-μm Shoulder

Acknowledgements: This work is supported by the NASA Planetary Astronomy program, the Lunar and Planetary Institute Summer Internship Program, and NASA grant NAGW-642.

References: [1]Vilas and Gaffey, Science *246*, p. 790- 792, 1989; [2]Sawyer, S., Ph.D. Thesis, U. Texas, 1991; [3]Vilas et al., submitted to Icarus; [4]Vilas and Smith, Icarus *64*, p. 503-516, 1985; [5]Vilas and McFadden, Icarus *100*, p. 85 - 94, 1992; [6]Vilas et al., submitted to Icarus; [7]Matson, D. L., JPL Doc D-3698, 1986; [8]Milani and Knesevic, Asteroids II (Binzel et al., Eds), p. 1073 - 1090, 1989; [9]Williams, Asteroids II (Binzel et al, Eds) 1989, p. 1034 - 1072, 1989; [10]Tholen, Asteroids II (Binzel et al, Eds) 1989; p. 1139 - 1150[11]Townsend, JGR *92*, 1441 - 1454, 1987; [12] Gaffey, M. J.LPSC XI, p. 312 - 315, 1980.

SEARCHING FOR *neu*KREEP: AN EMP STUDY OF APOLLO 11 GROUP A BASALTS

Eric A. JERDE and Lawrence A. TAYLOR, Dept. of Geol. Sci., University of Tennessee, Knoxville, TN 37996

The Apollo 11 and 17 landing sites are characterized by the presence of high-Ti basalts (TiO2 > 6%). The Group A basalts of Apollo 11 have elevated K compositions (> 2000 ppm; [1]) and are enriched in incompatible trace elements relative to the other types of high-Ti basalt found in the region (Fig. 1). These unique basalts also are the youngest of all high-Ti basalts, with an age of 3.56 ± 0.02 Ga [2]. Recent modelling of the Apollo 11 Group A basalts by Jerde et al. [3] has demonstrated that this unique variety of high-Ti basalt may have formed through fractionation of a liquid with the composition of the Apollo 11 orange glass, coupled with assimilation of evolved material (dubbed *neu*KREEP, and having similarities to lunar quartz monzodiorite). Assimilation of this material would impart its REE signature on the liquid, resulting in the elevated REE abundances observed. Minerals such as whitlockite which contain a large portion of the REE budget can be expected to reflect the REE characteristics of the assimilant. To this end, an examination of the whitlockite present in the Apollo 11 Group A basalts was undertaken to search for evidence of the *neu*KREEP material assimilated.

THE NATURE OF *neu*KREEP

The evolved *neu*KREEP component must have been generated after complete crystallization of the LMO and represents the late-stage crystallization product of a magma melted from the depleted "adcumulate" mantle. Assuming that this melt, indeed, was originally derived from the depleted cumulate mantle and that it crystallized with a $^{147}Sm/^{144}Nd$ greater than, but similar to, KREEP (= 0.168), an **age of 4.15 Ga can be calculated** [4]. This calculated model age is similar to the measured age (4.08 ± 0.07 Ga) of a KREEP basalt from Apollo 17 [5]. Furthermore, Shih et al. [5] suggested that other KREEPy rocks (including basalts, granites, troctolites, and norites) from various landing sites also may be cogenetic with this Apollo 17 KREEP basalt.

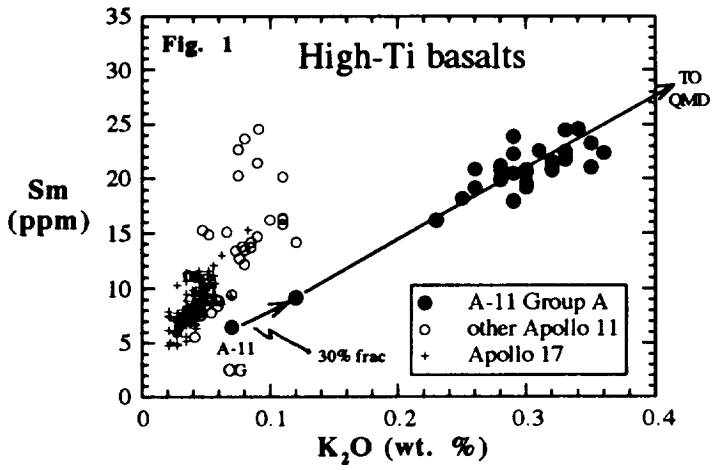

Table 1. neuKREEP.

SiO_2	60.0
TiO_2	2.6
Al_2O_3	11.9
Cr_2O_3	2.04
FeO	---
MnO	0.03
MgO	---
CaO	11.9
Na_2O	0.9
K_2O	1.7
La	164 ± 10
Ce	504 ± 34
Nd	377 ± 21
Sm	110 ± 6
Eu	
Gd	134 ± 8
Tb	21.0 ± 1.1
Dy	167 ± 8
Yb	114 ± 7
Lu	17.6 ± 0.9
Hf	96.0 ± 6.5
Ba	1375 ± 128

Oxides in percent, all others are in ppm.

QMD values are from [5].

The composition calculated for this evolved component [3] is similar to that of the quartz monzodiorites (QMD) summarized by Marvin et al. [6] from Apollo 15 (Table 1), although with a chondrite-normalized REE slope that is shallower than that of the previously described QMD's. It is envisaged that such material was assimilated into a magma of Apollo 11 orange glass composition undergoing fractionation. Approximately 7.5% assimilation of *neu*KREEP is required to produce the baseline Group A basalt, and the entire array of Group A compositions can be generated by 7.5 - 15% assimilation of *neu*KREEP with the composition in Table 1. The major-element composition (Table 1) was determined through mass-balance using the assimilation values obtained from the REE.

However, no rocks akin to QMD have been recognized in the material returned from the Apollo 11 site. Assimilation of QMD-like material with the composition of *neu*KREEP would greatly increase the REE abundances in the liquid, imparting the REE signature of *neu*KREEP to the magma. We have undertaken a search for REE-rich phases (namely whitlockite and apatite; no zircons were found) in the Apollo 11 Group A basalts. Since whitlockite will hold the majority of the REE, the chondrite-normalized patterns can be expected to reflect those of the liquid in which it crystallized.

For this search, Apollo 11 Group A basalts with high abundances of REE were chosen since these would likely harbor the greatest amounts of whitlockite. The mesostases of these rocks were examined for the presence of phosphates using the electron microprobe (EMP), which was also used to analyze the observed grains. Counting times of 60 seconds were used for the REE during analysis to enhance the counting statistics. REE oxides analyzed in the whitlockites are all present in amounts >0.3 wt.%. In apatite, the most abundant REE analyzed (Ce) was present in amounts only ~0.3 wt.%. Due to the low REE abundances in apatite, we concentrated mainly on whitlockite in our analyses.

WHITLOCKITE CHARACTERISTICS

The majority of the phosphates are small and irregular, with the greatest dimension being approximately 50 μm. However, the grains are seldom more than 10 μm wide. In many cases, the grains are composite with both whitlockite and apatite forming portions with sharp interfaces

SEARCHING FOR *neu*KREEP: Jerde E.A. and Taylor L.A.

between the two minerals. Examples of apatite rods with whilockite ends and whitlockite rods with apatite ends both exist. Zoning is also common, with some grains exhibiting order-of-magnitude variations in REE abundance, essentially varying from apatite to whitlockite. Where strong zoning exists, we utilized the high-REE analyses from the zoned grains for our discussion.

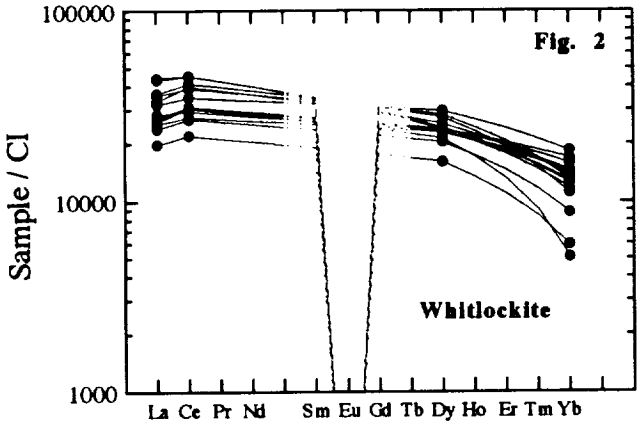

Whitlockite REE patterns obtained for three Apollo 11 Group A basalts are shown in Fig. 2. While outwardly similar to REE patterns for whitlockite from other lunar basalts, the whitlockite in Apollo 11 Group A basalts generally has a shallower chondrite-normalized REE pattern. Chondrite-normalized Ce/Dy ratios in whitlockites from lunar basalts tend to be >1.7 (data in Neal and Taylor [7]), while in our "Group A" whitlockites, the normalized Ce/Dy ratios are usually <1.6. This suggests that the liquid from which the Apollo 11 whitlockite crystallized had a shallower slope as well, relative to other lunar basalts. Indeed, the calculated *neu*KREEP composition (Table 1; [3]) has a shallower REE slope than other evolved materials such as KREEP. Assimilation of *neu*KREEP would dominate the REE budget and, presuming constant partition coefficients, whitlockite forming from the *neu*KREEP-dominated liquid would be expected to have a shallower REE slope than that crystallizing from a KREEP-dominated liquid.

An additional feature present in the whitlockites analyzed from the Apollo 11 Group A basalts is the "kink" (reversed slope) in the pattern at Ce (Fig. 2), the result of a slight depletion in La. A pronounced kink is not characteristic of whitlockites in basalts from other missions (e.g., [7]), or in other whitlockite analyzed by our group (e.g., [8]), but is present in all analyzed to date from Apollo 11 Group A basalts. The calculated ***neu*KREEP** material (Fig. 3) is slightly depleted in La, resulting in a **similar kink in the REE pattern at Ce**. This suggests a link between the supposed *neu*KREEP composition and the whitlockites actually observed in the basalts. This high point at Ce is akin to, although smaller than, the positive Ce anomalies observed in some zircons due to preferential takeup of Ce^{4+} in the mineral (e.g., [9]). However, no similar Ce peak is seen in other lunar whitlockites, and it is unlikely that sufficient oxidizing conditions existed in the lunar environment to create significant amounts of Ce^{4+}.

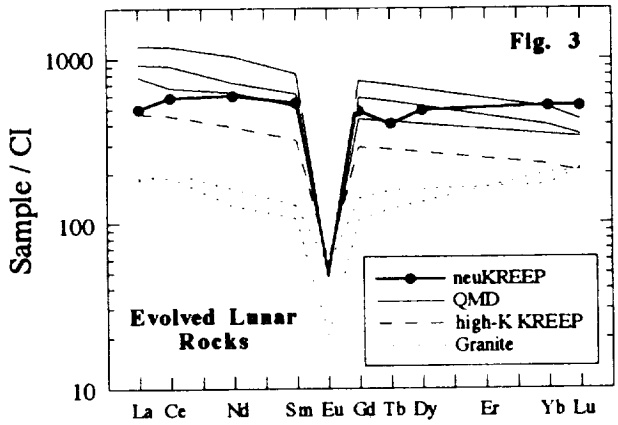

***neu*KREEP is more evolved than the postulated high-K KREEP composition** given by Warren [10], with the major-elements similar to those of quartz monzodiorites from Apollo 15 (e.g., [6]). The chondrite-normalized REE slope is less than that of both high-K KREEP and the quartz monzodiorites, however, pointing to slightly different material. The subtle differences in whitlockite compositions in the Apollo 11 Group A basalts relative to whitlockites from other lunar basalts suggest a connection to the calculated *neu*KREEP component, additional evidence for the existence on this new lunar component.

References:

[1] Neal C. R. and Taylor L. A. (1992) GCA, 56, 2177-2211; [2] Snyder G. A., Lee D.-C., Taylor L. A., Jerde E. A., and Halliday A. N. (1992) LPS XXIII, 1321-1322; [3] Jerde E. A., Snyder G. A., and Taylor L. A. (1993) LPS XXIII (this volume); [4] Jerde E. A., Snyder G. A., and Taylor L. A. (1992) In: Workshop on Geology of the Apollo 11 landing site, [G. Ryder, H. H. Schmitt and P. D. Spudis, ed.], LPI, Technical Report 92-09, part 1, 21-24; [5] Shih C.-Y., Nyquist L. E., Bansal B. M., and Wiesmann H. (1992) EPSL, 108, 203-215; [6] Marvin U. B., Lindstrom M. M., Holmberg B. B., and Martinez R. R. (1991) Proc., LPSC, 21, 119-135; [7] Neal C. R. and Taylor L. A. (1991) GCA, 55, 2965-2980; [8] Snyder G. A., Taylor L. A., Liu Y-G., Schmitt R. A. (1992) LPSC, 22, 399-416; [9] Hinton R. W. and Upton B. G. J. (1991) GCA, 55, 3287-3302; [10] Warren P. H. (1989) In: Workshop on Moon in transition: Apollo 14 KREEP, and evolved lunar rocks, [G. J. Taylor and P. H. Warren, ed.], LPI, Technical Report 89-03, 149-153.

ON THE COMPOSITION OF *neu*KREEP: QMD CONTAMINATION AT APOLLO 11?

Eric A. JERDE, Gregory A. SNYDER, and Lawrence A. TAYLOR, Dept. of Geol. Sciences, University of Tennessee, Knoxville, TN 37996

APOLLO 11 GROUP A BASALTS: AN ANOMALOUS HIGH-Ti GROUP

The Group A basalts of Apollo 11 differ in many respects from other high-Ti basalts of the region. Chemically, they are the only high-K (> 2000 ppm K; [1]) variety of high-Ti basalt and are enriched in incompatible trace elements relative to other basalts from both the Apollo 11 and Apollo 17 sites (Fig. 1). In addition, Group A basalts are the youngest of all high-Ti basalts, with an age of 3.56 ± 0.02 Ga [2]. The cluster of compositions is consistent with the Apollo 11 Group A basalts representing a single flow (e.g., [3,4]). Papanastassiou et al. [5] have also indicated the uniqueness of these basalts, based particularly on relatively young Rb-Sr model ages (3.8 - 3.9 Ga). A model for the formation of the Group A basalts was presented by Jerde et al. [3,6], wherein the Apollo 17 orange volcanic glass is the parent liquid. Fractionation of this composition, coupled with the assimilation of incompatible-element-rich material, results in compositions akin to those of the Apollo 11 Group A basalt population. Orange glass of similar major-element composition is present at the Apollo 11 site as well [7], although complete trace element analyses are not available. New modelling results using the Apollo 11 orange glass major elements are grossly similar to those obtained using the Apollo 17 orange glass [e.g., 6], indicating ~30% fractionation (Table 1).

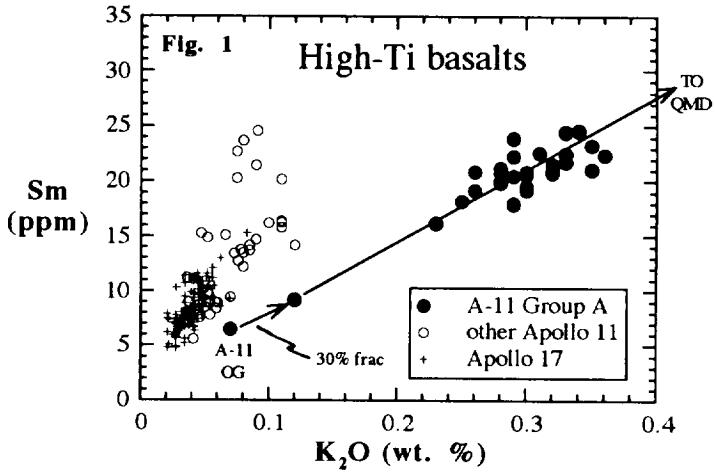

EVIDENCE OF KREEPy CONTAMINATION

Incompatible trace elements in Group A basalts were modelled by Jerde et al. [3], utilizing bulk partition coefficients calculated from the mineral assemblages indicated by fractionation calculations. The lack of trace-element data for the Apollo 11 orange glass precludes its use in modelling. However, the similarity in major-element composition of the Apollo 11 orange glass to that from Apollo 17 suggests that the trace elements follow suit (Delano, pers. comm.), and for the purposes of calculation, the Apollo 17 orange glass trace-element composition was used.

It is evident from the results (Table 1) that the incompatible-element abundances in Group A basalts are much too high (e.g., La = 26.5 ppm) to be explained by simple Rayleigh fractionation of the orange volcanic glass, which only leads to La = 8.8 ppm after 30% fractionation. The fact that K, P, and the REE are low in the calculated liquids suggests the addition of a KREEP component to obtain the basalts observed. In order to match the trace elements, ~20% of such a component (the high-K KREEP of Warren [8]) must be added, which would imply that the Apollo 11 Group A basalts are a young type of KREEP basalt. However, while this works chemically, isotopic considerations preclude it.

Table 1. Fractionation calculations.

	A11 OG	32% xtall'zd	10017
SiO_2	37.3	38.3	40.9
TiO_2	10.0	12.6	11.4
Al_2O_3	5.68	7.3	7.85
Cr_2O_3	0.63	0.12	0.35
FeO	23.7	23.9(21.3)	19.2
MnO	0.28	0.28	0.25
MgO	14.3	6.7(7.7)	7.78
CaO	7.62	10.2	10.4
Na_2O	0.31	0.43	0.49
K_2O	0.07	0.10	0.29
Total	99.89	99.93	98.91
La	6.2	8.8	26.7
Ce	19.0	26.9	80.1
Nd	17.8	25.2	65.6
Sm	6.5	9.2	21.0
Eu	1.8	2.55	2.26
Gd	8.5	12.1	(26.8)
Tb	1.65	2.34	4.63
Dy	9.4	13.3	30.9
Er	5.1	7.2	18.9
Yb	4.43	6.13	17.0
Lu	0.61	0.86	2.46

Oxides are in %, REE in ppm.
A-11 OG from [7].

Addition of 20% of an old KREEP component (~4.4 Ga with ε_{Nd} = -3 at 3.56 Ga) would overwhelm the LILE in the magma, yielding basalts with ε_{Nd} values <0. However, ε_{Nd} values of the Group A basalts of Apollo 11 fall in the range of +3 to +4. Therefore, any KREEPy assimilant could not have had an ε_{Nd} much less than +2 to +3. This KREEPy component must have been generated **after** complete crystallization of the LMO and represents the late-stage crystallization products of a magma melted from the depleted "adcumulate" mantle. However, such a late melting event must have occurred prior to the initiation of high-Ti basalt volcanism. We have termed the **post-LMO KREEPy component** which fits these parameters *neu*KREEP (new-KREEP) because of its young age relative to postulated *ur*KREEP (dregs of the LMO).

Table 2. neuKREEP.

		σ
La	164	10
Ce	504	34
Nd	377	21
Sm	110	6
Eu		
Gd	134	8
Tb	21.0	1.1
Dy	167	8
Yb	114	7
Lu	17.6	0.9
Hf	96.0	6.5
Ba	1375	128

All concentrations are in ppm.

Mass-balance calculations were employed to determine a composition for *neu*KREEP from a set of twelve samples chosen from the suite of Group A basalts. These samples lie

along an assimilation line from the fractionated Apollo 11 orange glass composition through the array of Group A basalts (Fig. 1). Details of these calculations are given in Jerde et al. [6]. The results for some REE and other trace elements are given in Table 2. Approximately 7.5% (7.59 ± 0.18%) assimilation of *neu*KREEP is required to produce the baseline Group A basalt, and the entire array of Group A compositions can be generated by ~30% fractionation of the Apollo 11 orange glass coupled with 7.5 - 15% assimilation of *neu*KREEP with the composition in Table 2.

The major-element composition was determined through mass-balance using the assimilation values obtained from the REE. Sample 10017 was chosen as the target composition since it is a well-characterized Group A basalt. The trace-element abundances in 10017 indicate ~13% assimilation of the *neu*KREEP component, and the major elements were determined for *neu*KREEP using the mass-balance equation given above (Table 3).

COMPARISON OF *neu*KREEP WITH KNOWN LUNAR MATERIALS

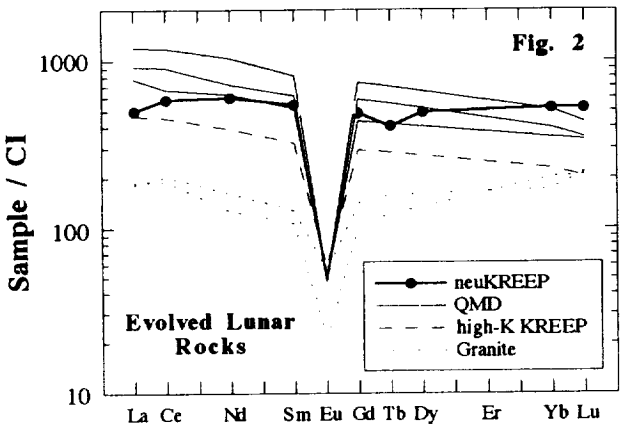

The *neu*KREEP composition given in Table 2 and shown in Fig. 2 is more evolved than the postulated high-K KREEP composition given by Warren [8]. The major-elements are similar to those of the quartz monzodiorites (QMD) from Apollo 15 (e.g., [9]), although the chondrite-normalized REE slope is less than that of both high-K KREEP and QMD, more akin to some lunar granites (e.g., 73215c, 14321,1027 in [10]). The major-element composition given for *neu*KREEP is similar to that of QMD, suggesting that the Apollo 11 Group A basalts represent the fractionation product of a picritic glass along with the assimilation of a quartz monzodiorite component. The modelling is not as successful for Fe and Mg, with Fe overestimated and Mg underestimated in the fractionated orange glass, and not falling in the range of known lunar QMD. The fractionation program used for the calculations (MAGFOX; J. Longhi, pers. comm.) underestimates the K_d for olivine crystallization, using 0.26. If a more realistic K_d is used (i.e., 0.3), the Fe and Mg results match more closely (see the values in parentheses in Tables 1 and 3). Taking into account incomplete fractional crystallization and perhaps crystallization of some native iron and chromite may resolve remaining discrepancies in the composition of *neu*KREEP.

Warren et al. [10] noted the possibility that some lunar granites may be the late-stage remnants of younger, smaller intrusions formed through partial melting of the deep interior, which is essentially what we envisage as the origin of *neu*KREEP. Assuming that this melt, indeed, was originally derived from the depleted cumulate mantle and that it crystallized with a $^{147}Sm/^{144}Nd$ greater than, but similar to, KREEP (= 0.168), an age of 4.15 Ga can be calculated. This calculated model age is similar to the measured age (4.08 ± 0.07 Ga) of a KREEP basalt from Apollo 17 [11]. Furthermore, Shih et al. [11] suggested that other KREEPy rocks (including basalts, granites, troctolites, and norites) from various landing sites also may be cogenetic with this Apollo 17 KREEP basalt. This could further indicate that a Moon-wide melting event occurred at this time which fused only the most evolved rocks. Internal isochrons for granite 14321,1027 give ages of 4.09 ± 0.11 Ga and 4.11 ± 0.20 Ga from Rb-Sr and Sm-Nd, respectively [12], coinciding with our estimated age of *neu*KREEP of 4.15 Ga.

Table 3. neuKREEP major-elements.

	neuKREEP	QMD
SiO_2	60.0	(55)
TiO_2	2.6	2.6
Al_2O_3	11.9	11.9
Cr_2O_3	2.04	0.1-0.2
FeO	(3.8)	10.8-15.1
MnO	0.03	---
MgO	(8.4)	3.8
CaO	11.9	8.6- 11.3
Na_2O	0.9	0.79-1.01
K_2O	1.7	1.4-2.1

QMD values are from [9].

References:

[1] Neal C. R. and Taylor L. A. (1992) GCA, 56, 2177-2211; [2] Snyder G. A., Lee D.-C., Taylor L. A., Jerde E. A., and Halliday A. N. (1992) LPS XXIII, 1321-1322; [3] Jerde E. A., Snyder G. A., and Taylor L. A. (1992) LPS XXIII, 609-610; [4] Beaty D. W. and Albee A. L. (1980) Proc., LPSC, 11, 23-35; [5] Papanastassiou D. A., DePaolo D. J., and Wasserburg G. J. (1977) Proc., LPSC, 8, 1639-1672; [6] Jerde E.A., Snyder G.A., and Taylor L.A. (1992) In: Workshop on geology of the Apollo 17 landing site, [G. Ryder, H. H. Schmitt, and P. D. Spudis, ed.], LPI, Technical Report 92-09, 21-24; [7] Delano J.W. (1986) Proc., LPSC, 16, D201-D213; [8] Warren P. H. (1989) In: Workshop on Moon in transition: Apollo 14 KREEP, and evolved lunar rocks, [G. J. Taylor and P. H. Warren, ed.], LPI, Technical Report 89-03, 149-153; [9] Marvin U. B., Lindstrom M. M., Holmberg B. B., and Martinez R. R. (1991) Proc., LPSC, 21, 119-135; [10] Warren P. H., Taylor G. J., Keil K., Shirley D. N., and Wasson J. T. (1983) EPSL, 64, 175-185; [11] Shih C.-Y., Nyquist L. E., Bansal B. M., and Wiesmann H. (1992) EPSL, 108, 203-215; [12] Nyquist L., Shih C.-Y., Bansal B., Weismann H., and Wooden J. (1983) LPS XIV, 576-577.

ESTIMATES OF LITHOSPHERIC THICKNESS ON VENUS: C. L. Johnson and D. T. Sandwell, Scripps Institution of Oceanography, La Jolla, CA 92093 - 0215

Summary

Magellan altimetry data have revealed many examples of topographic flexure on Venus. Modeling of flexural features is of interest as it provides information on spatial (and for the earth, temporal) variations in lithospheric thickness. Lithospheric thickness may be determined solely from modeling topographic flexure or by combining gravity and topography data. On Venus even the highest resolution gravity is insufficient for modeling all but the very longest wavelength flexural features, so we rely heavily on altimetry data for information about lithospheric thickness. Sandwell and Schubert [1] modeled flexure around four coronae and found lithospheric thicknesses h, in the range 35 - 70 km. Studies of several more flexural features [2] suggests that these are typical of Aphrodite Terra and other chasmata regions on Venus [2]. However lithospheric thicknesses associated with other regions are in the range 15 - 30 km [2]. McKenzie et al.[3] noted that part of Aphrodite Terra appeared similar in planform and morphology to the subduction zones of the East Indies on Earth. Other flexure studies using Magellan data have looked at smaller coronae [4] (h = 5-30 km), and rifts [5] (h = 8-20 km). It can be seen that the range of thicknessses suggested by studies to date is extremely large and it is difficult to establish whether their mean is in agreement with that predicted by heat flow scaling arguments (h ~ 18km) [6]. Here we present results from a global study of flexure on Venus, with particular emphasis on the variation in our results with different tectonic settings.

Analysis and Results

Initially 12 flexural features were modeled assuming a 2-D loading geometry applied to a thin elastic plate [1]. This approximation is valid for any features with a sufficiently large ratio of radius of curvature to flexural wavelength. The model predicts lithospheric thickness, surface stresses (which can be compared with deformation patterns seen in the SAR images) and a bending moment associated with the flexure. The mechanical thickness of the lithosphere can be estimated once a yield strength envelope for the lithosphere is assumed. Preliminary results for the 12 features are shown in figure 1. The distinction between the much larger thicknesses associated with Aphrodite Terra and the smaller values obtained for other areas can be clearly seen.

Modeling of terrestrial gravity - topography admittance has shown that approximating a 3-dimensional feature by a 2-dimensional feature can lead to an overestimate of elastic thickness [7]. On Venus most flexural signatures are associated with either linear loads (e.g. chasmata) or axisymmetric loads (coronae). If we consider flexure due to a ring load, width Δa, (e.g. coronae), then the important parameter is the ratio of the (planform) radius of curvature (a) to the flexural

LITHOSPHERIC THICKNESSES ON VENUS, C. L. Johnson & D.T. Sandwell

parameter (α). As a/α exceeds a critical value the load can be approximated by a 2-D load of width Δa. We have investigated the validity of a 2-D approximation to an axisymmetric geometry in the following way. Synthetic flexure profiles were generated for ring loads with increasing a/α for a given $\Delta a/\alpha$ (0.1). Our 2-D flexure code was then used to retrieve the best fitting flexural parameter. When a/α exceeds about 2 the 2-D model provides a good fit to the synthetic profile and it also yields a correct estimate of the true flexural parameter (Figure 2). However, for a/α less than about 2, the 2-D model overestimates the true flexural parameter by up to 10%. While this overestimate may appear acceptable, the fits of the 2-D model to the synthetic profile is quite poor, especially on the outer rise. This type of approach allows a quantitative discrimination between features requiring an axisymmetric model and those for which a 2-D approximation is valid. For example, the radius of Latona is 340 km and the estimated flexural parameter is 70 km so it is appropriate to use a 2-D model in this case. Smaller features require axisymmetric modeling. Estimates of lithospheric thickness for such features will be presented.

It has been suggested that viscous models for lithospheric bending on Venus are more appropriate than purely elastic models. We have investigated bending of a viscous lithosphere at Latona Corona using the approach of DeBremaecker [8]. This allows the quantity $h^3\eta U$ to be established where h is the sheet thickness, η is the viscosity of the sheet and U is the bending rate. To estimate the elastic thickness we need to make some assumption about the viscosity and the horizontal velocity. Preliminary results for Latona indicate that a viscous model requires a thick lithosphere unless the horizontal strain rate is very high. Stresses predicted by the viscous model are much lower than those predicted by thin elastic plate theory as expected.

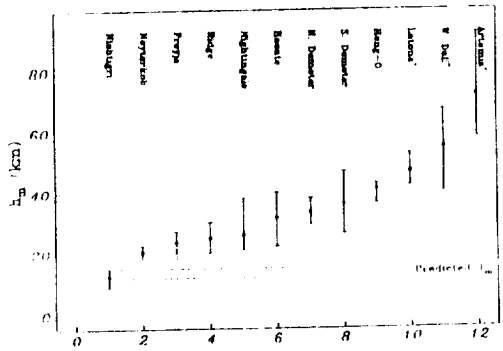

Figure 1: Mechanical thicknesses for 12 features on Venus. Features within Aphrodite are denoted by an asterisk. Dashed lines give predicted range [6].

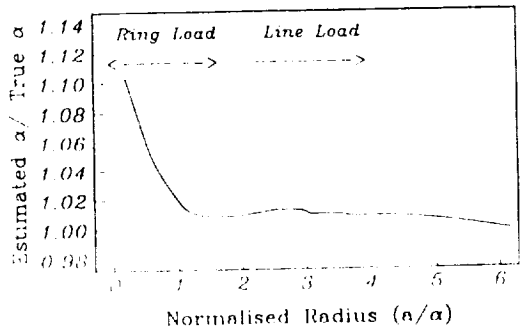

Figure 2: Ratio of estimated flexural parameter (2-D model) to true flexural parameter (3-D axisymmetric geometry) for increasing a/α.

[1] Sandwell, D. & G. Schubert, J. Geophys. Res., 97, 16,069-16,083, 1992; [2] Johnson, C. & D. Sandwell, LPSC XXII, 619-620, 1992; [3] McKenzie et al., J. Geophys. Res., 97, 13,533-13,544, 1992; [4] Moore et al., International Colloqium on Venus, 72-73, 1992; [5] Evans et al., International Colloqium on Venus, 30-32, 1992; [6] Phillips, R. & M. Malin, In *Venus* , Univ. Arizona Press, 1983; [7] Watts, A. et al., J. Geophys. Res., 93, 3051-3077, 1988; [8] DeBremaecker, J., J. Geophys. Res., 82, 2001-2004, 1977

RADAR PROPERTIES OF SEVERAL FLUIDIZED EJECTA BLANKETS ON VENUS; J.R. Johnson and V.R. Baker, Lunar and Planetary Laboratory and Department of Geosciences, Space Sciences Bldg., University of Arizona, Tucson, AZ, 85721.

Magellan SAR imagery, altimetry, and radiometry are being analyzed to characterize the radar properties of the fluidized ejecta blankets (FEBs) that are associated with over 40% of the impact craters on Venus [1,2,3]. The FEB flows and plains units surrounding the craters Isabella (175 km), Addams* (90 km), Seymore (65 km), and a crater located at 4°S, 155.5°E (70 km) are examined here using the MIT-produced ARCDR and GxDR data. Individual orbital footprints obtained from the ARCDRs have been classified according to their dominant simple geologic unit (e.g., plains, FEB flows). This permits average values of reflectivity (corrected for diffuse scattering), rms meter-scale slopes, emissivity, and SAR backscatter to be calculated for each unit. GxDR images provide a means of visualizing the spatial relations between the various data sets. Variability of radar properties within the FEBs and relative to surrounding regions may have implications concerning the genesis and possible emplacement mechanisms of fluidized ejecta.

Method. GxDR images of the corrected reflectivity, emissivity, rms slopes and topography data sets were displayed and analyzed with MGMDQE software [4] to provide an overview of the relations between these data. More rigorous treatment of the available radar properties requires use of the individual orbital footprint data available in the ARCDRs. Cycle 1 altimetric and radiometric orbital footprints were overlain onto SAR images of the four craters using the MGMDQE software [4]. The regions selected for analysis encompassed all crater materials and were bounded north-south by lines of latitude and east-west by orbit tracks. Individual footprints were manually classified according to their dominant simple geologic unit (plains and FEB flow materials are presented here). For each footprint the ARCDR data provided values of corrected reflectivity and its formal error, rms slope and its formal error, average radar backscatter values, emissivity, and the non-range-sharpened goodness-of-fit between the radar echo profiles and the MIT templates derived from Hagfors' function [5,6]. Average values and standard deviations about the mean of these parameters were then calculated for each unit. The results are shown for the FEB flows in Table 1 and surrounding plains in Table 2.

Obervations. The GxDR images show that the paths of the FEB flow materials for these four craters appear to follow topography, with distal flows often ponded in depressions. While most flows are often distinguished by their relatively high rms slopes (especially in their more distal portions and terminal ponded units), the correlation is not entirely consistent. For example, high rms slope values (5-7°) in the medial portion of the Addams' flow are followed distally by lower values (1-3°) which are in turn followed by high values (6-9°) at the ponded ends of the flow [3]. FEB flows appear as low corrected reflectivity units (e.g., < 0.1) but are less easily distinguished than in the rms slope images. This is again especially noticeable for Addams (although it should be noted that the high latitude location of Addams (56°S) may affect the rms slope and reflectivity Cycle 1 data, [pers. comm., P.Ford, 1992; [7]). High emissivities (up to 0.94 for 4S-155.5) distinguish the FEB flows except for Isabella, which shows highest values in the crater interior and intermediate values in the distal flows.

The average radar property values of the plains and FEB flows associated with the four craters presented here (Tables 1 and 2) exhibit several consistent trends. The corrected reflectivities are higher for the plains units in all cases, while the emissivities, average radar backscatter, and rms slopes and their associated formal errors are higher for the flows. In addition, the standard deviations of the rms slopes and their errors are higher for the flows than the plains. The goodness-of-fit parameter is also consistently higher for the FEB flows (i.e., the fit of the observed echo to a Hagfors' function is better).

Discussion. The radar property data suggest that the FEB flows are rougher on both the meter-scale (rms slope) and wavelength-scale (SAR backscatter and emissivity) than the surrounding plains. The flows also have a higher variability of roughness relative to the plains as evidenced by their higher rms slope standard deviations. This variability within the flows might have implications concerning the genesis and deposition of the flow materials. For example, the pattern of roughness variations could provide information concerning the rheologic state(s) of the flow materials during transport. Asimow and Wood [2] point out that the viscosity and yield strength of lava-like flows (melt rock, acoustically fluidized materials [8]) increase with distance from the source (e.g., the distal pahoehoe to aa transition observed for terrestrial lavas [9]), while debris-like flows (pyroclastic flows, debris avalanches) can exhibit the opposite behavior due to sorting of flow components. Detailed analysis of radar property variations within individual FEB flows might provide a means to constrain the type of flow regime and/or rheology that was dominant during emplacement of a flow unit.

Future work. Altimetry and radiometry from subsequent Cycles of the Magellan mission will provide a more comprehensive analysis of FEB materials, with emphasis on variability of radar properties downflow and correlations between different properties. Software is currently being developed to automate the synthesis of the radar property data sets using ARCDR data. This will permit quicker and more accurate analysis of the radar properties of all FEB craters. Comparison of backscatter data at two or more look angles to different scattering functions will also be done to assist in FEB classifications.

Table 1. FEB Flows: Preliminary average values from Cycle 1 altimetry and radiometry.

Crater	Corr. ρ	(Error)	Slope °	(Error)	Fit	σ (dB)	Emissiv.	N(alt)	N(rad)
Addams	.17 ± .05	.02 ± .02	3.4 ± 1.4	0.3 ± 0.2	.58 ± .22	3.2 ± 0.9	.879 ± .007	203	302
Isabella	.11 ± .02	.01 ± .00	2.5 ± 1.0	0.2 ± 0.1	.53 ± .27	2.0 ± 1.7	.864 ± .011	580	692
Seymore	.08 ± .01	.01 ± .01	3.3 ± 0.7	0.3 ± 0.2	.75 ± .19	0.0 ± 1.6	.855 ± .011	188	381
4S-155.5	.08 ± .02	.01 ± .01	4.1 ± 2.1	0.5 ± 0.8	.68 ± .21	4.2 ± 1.3	.908 ± .017	307	612

Table 2. Plains: Preliminary average values from Cycle 1 altimetry and radiometry.

Crater	Corr. ρ	(Error)	Slope °	(Error)	Fit	σ (dB)	Emissiv.	N(alt)	N(rad)
Addams	.20 ± .05	.02 ± .02	2.6 ± 0.9	0.2 ± 0.1	.55 ± .20	0.8 ± 0.7	.869 ± .007	517	947
Isabella	.14 ± .03	.01 ± .00	1.4 ± 0.1	0.1 ± 0.0	.47 ± .23	-0.8±1.4	.862 ± .148	2112	2331
Seymore	.09 ± .02	.01 ± .00	2.4 ± 0.7	0.2 ± 0.1	.66 ± .23	-1.7±1.0	.836 ± .010	653	1534
4S-155.5	.11 ± .02	.01 ± .00	2.0 ± 0.7	0.2 ± 0.1	.61 ± .23	0.1 ± 1.2	.873 ± .023	527	950

*Note: Addams is a provisional name, while 4S-155.5 was formerly named Franklin [1]. ± values are standard deviations about the mean. **Corr. ρ** is the corrected reflectivity. **Slope** is the rms meter-scale slope of the surface (expressed in degrees). **Error** is formal error from ARCDR data (ar_error parameter). **Fit** represents non-range-sharpened goodness-of-fit between the observed echo profile and the MIT-derived Hagfors' function template (ar_fit parameter in ARCDRs). σ is the average SAR backscatter value (expressed in decibels) obtained from the ARCDRs (rr_sar parameters) [5]. **Emiss.** is the emissivity obtained from the radiometer data on the ARCDRs. **N(alt)** and **N(rad)** are the number of altimeter and radiometer footprints, respectively, that were used in the analyses (altimeter footprints provide the corrected reflectivity and rms slopes, while the radiometer footprints provide the emissivity and running-average backscatter [5]).

ACKNOWLEDGEMENTS: We thank P. Ford (MIT) and R. Simpson (Stanford) for assistance with use and interpretation of the altimetry and radiometry data.

REFERENCES: [1] Schaber G.G. et al. (1992) *JGR, 97,* 13257; [2] Asimow P.D. and Wood J.A. (1992) *JGR, 97,* 13643; [3] Johnson, J.R. and Baker, V.R., (1992) EOS, Trans. AGU, 73, 332; [4] Liu, F., and Ford, P.G. (1992), MGMDQE Users Guide, Version 2.13, MIT; [5] Ford, P.G. (1992), in USA_NASA_JPL_MG_2010 V1 (ARCDRCD.010;1); [6] Ford, P.G. and Pettengill, G.H. (1992), *JGR, 97,* 13103; [7] USA_NASA_JPL_MG_3001 V1 (GxDRCD.001;1), 1992; [8] Melosh, H.J., *JGR, 84,* 7513, 1979; [9] Head, J.W., and Wilson, H.,(1986) , *JGR, 91,* 9407.

A MONAZITE-BEARING CLAST IN APOLLO 17 MELT BRECCIA. BRADLEY L. JOLLIFF, DEPARTMENT OF EARTH AND PLANETARY SCIENCES & MCDONNELL CENTER FOR THE SPACE SCIENCES, WASHINGTON UNIVERSITY, ST. LOUIS, MO 63130.

A phosphate-rich clast in a pigeonite-plagioclase mineral assemblage occurs in Apollo 17 impact-melt breccia 76503,7025. The clast, measuring 0.9 × 0.4 mm in thin section, contains 3.3% (volume) apatite [$Ca_5P_3O_{12}(F,Cl)$], 0.8% whitlockite [$Ca_{16}(Mg,Fe)_2REE_2P_{14}O_{56}$], and trace monazite [$(LREE)PO_4$]. Major minerals include 26% pigeonite, $En_{53-57}Fs_{34-35}Wo_{8-13}$, and 69% plagioclase, $An_{84-92}Ab_{7-15}Or_{0.6-1.1}$. Troilite, ilmenite, and other accessory minerals constitute <1% of the assemblage and Fe-metal occurs along fractures. Also present in the melt breccia as a separate clast is a fragment of felsite (K,Ba-feldspar, "ternary" plagioclase, and a silica phase - quartz[?]). Based on the association of these clasts and their assemblages, a parent lithology of alkali-anorthositic monzogabbro is postulated. Monazite occurs in the phosphate-bearing clast as two <10 μm grains intergrown with whitlockite. The concentration of combined REE oxides in monazite is 63.5% and the chondrite-normalized REE pattern is strongly enriched in LREE (Figure 1a), similar to lunar monazite in 10047,68 [1] and terrestrial monazite [e.g., 2]. Thorium concentration was not measured in monazite, but based on oxide analyses of ~100% (including interpolated values for REE not measured), substantial Th concentration is not indicated, similar to monazite in 10047,68. Measured monazite/whitlockite REE ratios are La: 11, Ce: 8, Sm: 3.6, Y: 0.9, Yb: 0.5. Compositions of monazite and coexisting whitlockite and apatite are given in Table 1.

Analytical methods. Mineral analyses were done using a JEOL 733 electron microprobe, operating at an accelerating voltage of 15 KeV and a beam current of 30 nA. Synthetic glass standards were used for the REE [3] and natural apatite was used as the standard for P and Ca. Mineral standards were used for other elements in the phosphates and for all elements in the silicates. The data were reduced according to the method of [4].

Petrographic description. The texture of the phosphate-bearing clast is generally subophitic and fractured. Blocky plagioclase laths range in size up to 100 μm and pyroxenes range up to 150 μm. Pigeonites contain very fine exsolution lamellae and the larger crystals contain blocky, prismatic plagioclase inclusions. The forms of apatite crystals range from small, euhedral prisms (narrow, 2 × 30 μm, to squat, 10 × 20 μm) to subhedral, somewhat poikilitic masses up to 80 μm across. Whitlockite occurs as irregular overgrowths and extensions of the large apatite crystals, up to 30 μm in maximum dimension, and as smaller, rare, isolated grains. Monazite is intergrown with whitlockite as small masses of maximum dimension ~8 μm. Textures suggest the following crystallization sequence for the phosphates: apatite → whitlockite → monazite → whitlockite. Early, euhedral apatite, mantled by plagioclase, has relatively high Mg' [atomic Mg/(Mg+Fe)] and Cl concentration, and low REE concentrations. Coarser apatite overgrown by whitlockite has lower Mg', lower Cl concentration, and 2 × higher REE concentrations than early apatite (Table 1). Apatite adjacent a whitlockite overgrowth has the lowest measured Mg' (0.18) and highest REE concentrations (e.g., 0.71 % Ce_2O_3). There is *no* systematic zoning in whitlockite in a traverse from a contact with apatite → monazite inclusion → edge of whitlockite crystal.

Discussion. According to the model developed by [5] based mainly on experimental work by [6], DREE (whit/melt) values of whitlockite in this assemblage are strongly suppressed due to partial saturation of the dominant REE substitution mechanism, ranging from 6-7 for the LREE to 4 for Y (treated as a proxy for Ho) and 2 for Yb. These compare to DREE values 2-4× higher (dependant on Fe/Mg) in whitlockite at low REE concentrations [5,6,7]. As a result, whole-rock DREE (solid/melt) for late-stage crystallizing assemblages having 3-10% whitlockite range from ~0.2 to 0.8, but do not exceed unity, suggesting that the melt concentrations of REE did not decrease once whitlockite began to crystallize, but increased only moderately. If the final residual liquid equilibrated with 0.75% whitlockite (volume % in the assemblage), then a bulk or starting composition (REE) of about 2 × high-K KREEP [8] is sufficient to yield whitlockite of the observed composition. Due to nonsaturating REE substitutions at this concentration level, the whitlockite structure can

accommodate REE in excess of 2 atoms per 56 oxygens [5,7], thus it is not necessarily high REE concentration in residual melt that led to monazite saturation. Rather, a decrease in the activity of Ca relative to that of P is suggested as the cause of monazite stability.

The ratios of REE in whitlockite to those in apatite in an REE-rich zone adjacent to a whitlockite crystal are 4.8 (La) and 4.7 (Ce) (Table 2), indicating apatite/melt DREE values of 1.2 and 1.3, respectively, if the apatite and whitlockite are in equilibrium. These compare to values of half that magnitude or less inferred by [5] from coexisting apatite-whitlockite pairs in Apollo 14 samples.

Acknowledgements. Funding for this work was through NASA grant NAG 9-56.

References. [1] Lovering J.F., Wark D.A., Gleadow A.J.W., and Britten R. (1974) EPSL 21, 164-168. [2] Fleischer M. and Altschuler Z.S. (1969) GCA 33, 725-732. [3] Drake M.J. and Weill D.F. (1972) Chem. Geol. 10, 179-181. [4] Bence A.E. and Albee A.L. (1968) J. Geol. 76, 382-403. [5] Jolliff B.L., Colson R.O., and Haskin L.A. (1993) The distribution of REE between lunar apatite and whitlockite from Apollo 14 and implications for the evolution of residual liquids of lunar magmas, GCA (accepted). [6] McKay G., Wagstaff J., Le L., Lindstrom D., and Colson R. (1987) LPS XVIII, 625-626. [7] Colson R.O. and Jolliff B.L. (1993) this vol. [8] Warren P.H. (1989) in Workshop on Moon in Transition: Apollo 14, KREEP, and evolved lunar rocks. LPI Tech. Rpt. 89-03, p.153.

Table 1. Phosphate compositions in 76503,7025c.

	Apt (1) n=1	Apt (2) n=4	Whit n=8	Monazite n=2
P2O5	41.92	41.37	42.10	32.21
SiO2	0.35	0.48	0.33	0.18
Al2O3	na	na	0.04	0.02
FeO	0.71	0.39	1.59	0.45
MnO	0.06	0.04	na	na
MgO	0.23	0.07	2.61	0.32
CaO	54.42	54.66	39.69	3.99 (3)
Na2O	<0.02	0.07	0.02	<0.02
Y2O3	na	na	3.56	3.08
La2O3	0.06	0.17	1.24	13.30
Ce2O3	0.12	0.42	3.36	27.45
Nd2O3	na	na	2.28	11.97
Sm2O3	na	na	0.60	2.13
Yb2O3	na	na	0.16	0.08
Other REE (4)	--	--	[2.2]	[5.5]
F	3.90	3.83	na	na
Cl	0.35	0.17	na	na
oxide sum	102.1	101.7	99.7	100.6
- O = F	1.64	1.61	--	--
- O = Cl	0.08	0.04	--	--
corrected sum	100.4	100.0	99.7	100.6
No. of cations based on following negative charges:	25	25	112	8
Tetrahedral cations				
P	2.98	2.96	13.70	1.00
Si	0.03	0.04	0.13	0.01
Sum (tet)	3.01	3.00	13.83	1.01
Non-tetrahedral cations				
sum REE	0.01	0.02	2.07	0.86
sum others (5)	4.98	5.00	18.39	0.19
Sum non-tet	4.99	5.02	20.45	1.05
Mg/(Fe+Mg)	0.36	0.24	0.75	0.56

na = not analyzed
(1) Fine-grained, euhedral, enclosed in plagioclase, early-forming.
(2) Coarser, subhedral, intergrown with whitlockite, late-forming.
(3) Possibly some contribution from whitlockite.
(4) Other REE by interpolation or extrapolation.
(5) "Others" include Al, Fe, Mn, Mg, Ca, Na.

Table 2. REE ratios.

	Mon/ Whit	Whit/ Apt(1)
Y2O3	0.9	
La2O3	10.7	4.8
Ce2O3	8.2	4.7
Nd2O3	5.2	
Sm2O3	3.6	
Yb2O3	0.5	

(1) Apatite in "REE-rich" zone adjacent contact with whitlockite.

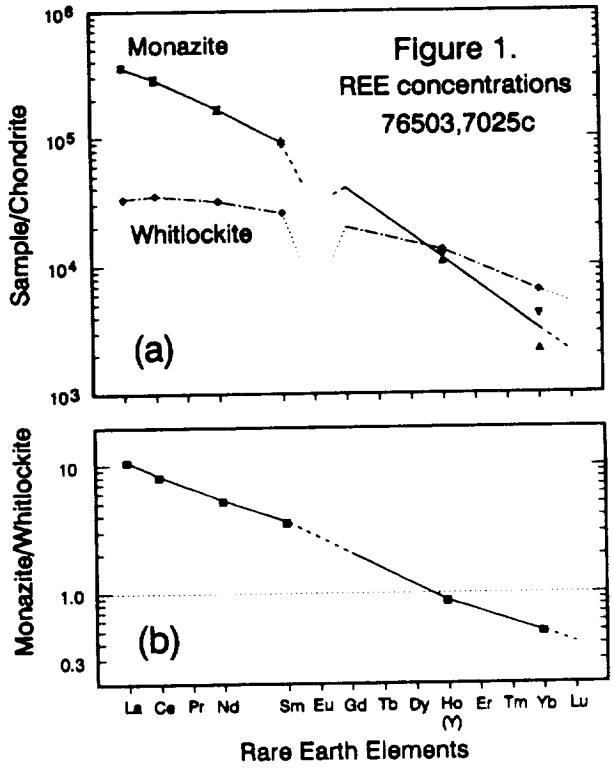

Figure 1. REE concentrations 76503,7025c

APOLLO 17 MATERIALS VIEWED FROM 2-4 MM SOIL PARTICLES: PRE-SERENITATIS HIGHLANDS COMPONENTS. BRADLEY L. JOLLIFF AND KAYLYNN M. BISHOP, DEPARTMENT OF EARTH AND PLANETARY SCIENCES & MCDONNELL CENTER FOR THE SPACE SCIENCES, WASHINGTON UNIVERSITY, ST. LOUIS, MO 63130.

Among the highlands lithologies of 2-4 mm rock fragments in North Massif soil 76503, we have found a compositional group, low in incompatible element concentrations, that we interpret as representing the pre-Serenitatis surface. A component of these materials is an igneous-textured lithology that we believe formed in large impact melts. These are compositionally similar to, and possibly precursors of, many of the granulitic breccias that appear to be mixtures of ferroan and magnesian-suite rocks. The polymict, or *old, upper-crustal breccias*, along with granulitic breccias and the endogenous igneous lithologies found particularly at the North Massif stations, constitute the poorly consolidated portions of North Massif. Highland samples from the South Massif, on the other hand, are enriched in materials of the competent, impact-melt breccias formed by the Serenitatis impact. The competent melt-breccias contain clasts of most of the pre-existing surface materials, but they also contain components not found in the rocks of the poorly consolidated massif materials.

Although the breccia boulders from the North and South Massifs are in many ways similar, the soils collected at the South Massif stations differ substantially from those of the North Massif [1]. We believe that the soil and rake samples collected away from the boulders [2], including 76503, sample, in part, poorly consolidated Massif materials which are distinct from materials constituting the Station 6 boulders, i.e., Serenitatis impact-melt breccia. Soils from North Massif stations, particularly Station 6, have a combination of highlands components distinctly different from South Massif [1]. A combination of an anorthositic-norite component and very magnesian norite and troctolite components is relatively abundant in the North Massif soils, yet the very magnesian components are minor or absent from South Massif soils based on mixing-model results [1]. This leads to the interpretation that the Massifs are stratified such that South Massif soils contain a high proportion of melt-breccia debris rich in incompatible trace elements (ITE) from upper levels of the massif, brought to the sampling site by landslide or ejecta surge following secondary impacts of Tycho [3], whereas the higher proportion of ITE-poor highlands components in the North Massif soils might mean that they sample, in part, a lower level free of Serenitatis impact melt.

Highlands lithologies and pre-Serenitatis upper-crustal breccias. The ITE-poor highlands lithologies of rock particles in 76503, sampled away from the Station 6 boulders [3] are mainly: (1) igneous fragments of troctolitic anorthosite and cataclastic noritic and gabbroic-anorthosite breccias; (2) several groups of granulitic breccias, and compositionally equivalent, but lithologically diverse variants; and (3) a lithologically diverse group of feldspathic, old, upper-crustal breccias [4,5]. Of special interest are the complex, polymict breccias of group (3). These breccias are uncontaminated by mare materials and low in incompatible trace element concentrations (Figure 1). Mineral clasts include very magnesian olivine and orthopyroxene and very calcic plagioclase, indicating magnesian-suite igneous precursors. In addition to magnesian-suite assemblages and granulitic breccias, lithic fragments include ferroan gabbroic anorthosite, with coarsely exsolved, ferroan pyroxenes. Some of these breccias have regolith components such as rounded, glassy melt clasts, similar to the lunar highlands meteorites, which are considered to be regolith breccias [e.g., 6]. Fine-grained melt clasts have compositions ranging from 16 to 22 wt.% alumina ("LKFM"), but these constitute only about 10% of the breccias. We suggest that these regolith breccias reflect the pre-Serenitatis upper crust in this region of the Moon.

Pre-Serenitatis aluminous impact melts. Some lithic clasts within the 2-4 mm highlands rock fragments have anorthositic-gabbro assemblages and textures ranging from cataclastic, relict igneous to granulitic breccia. These have mineral compositions that plot in the gap between magnesian and ferroan-suite rocks on An-Mg' diagrams. These we interpret as having originally crystallized in an impact-melt of magnesian and ferroan-suite igneous lithologies such as occur as clasts in the same rocks. Evidence of generally shallow "melt"

origin is that pyroxenes are not exsolved, and olivine CaO concentrations are intermediate between deep, slowly cooled plutonic values and basaltic, rapidly cooled values, i.e., 0.1-0.3 wt.%. Compositions of these aluminous impact melts are relatively feldspathic, e.g., 25% alumina (Table 1). The composition shown in Table 1 is similar to a typical moderately magnesian granulitic breccia and to Allan Hills 81005 magnesian lunar-highlands meteorite [7]. If we cast this composition in terms of known, endogenously igneous lithologies, the following proportions are indicated: 35% gabbroic anorthosite, 30% anorthositic norite, 20% troctolitic anorthosite, and 10-15% ferroan anorthosite or ferroan gabbroic-anorthosite. This composition is dominated by magnesian-suite lithologies, but a substantial ferroan component is suggested, more than is indicated by the scant representation in the Apollo 17 sample collection. We interpret the breccias that contain these clasts as having formed atop a large impact melt or group of impact melts. The minerals of many granulitic breccias and basaltic-textured, impact-melt lithologies also plot in the gap on An-Mg' diagrams. These, too, are members of the suite of impact-melt derivation older than Serenitatis.

The crust in the pre-Serenitatis region was dominated by Mg-suite plutonic rocks, but also contained minor ferroan-suite rocks; these were very well mixed by pre-Serenitatis impacts. We see evidence in these small breccia fragments of the regolith which developed on this surface before the Taurus-Littrow Valley was created. The friable massif material, as sampled by the Station 6 soils, is rich in these older crustal components. The competent melt-breccias of the massifs contain these materials as clasts, but they also contain more mafic and compositionally evolved lithologies, perhaps derived deeper, not seen among clasts in the older breccias.

Acknowledgements. Funding for this work was through NASA grant NAG 9-56.

References [1] Korotev R.L. and Kremser D.T. (1992) PLPS 22, 275-301. [2] Wolfe E. and others (1981) USGS Prof. Paper 1080, p. 125. [3] Luchitta B. (1992) in Workshop on Geology of the Apollo 17 Landing Site. LPI Tech. Rpt. 92-09, p.31. [4] Bishop K.M. et al. (1992) in Workshop on Geology of the Apollo 17 Landing Site. LPI Tech. Rpt. 92-09, p.2-4. [5] in Workshop on Geology of the Apollo 17 Landing Site. LPI Tech. Rpt. 92-09, p. 24-26. [6] Warren P.H. and Kallemeyn G.W. (1991) in the MacAlpine Hills Lunar Meteorite Consortium, GCA 55, 3123-3138. [7] Warren P.H. and Kallemeyn G.W. (1987) in NIPR Spec. Issue 46, 3-20.

Table 1. Comparison of compositions of pre-Serenitatis impact melt, magnesian granulitic breccia, and ALHA 81005 lunar-highlands meteorite.

	76503 ,7109 Melt	Avg Magn Granulitic Breccia	Highlands meteorite ALHA81005
SiO2	45.2	44.9	45.8
TiO2	0.5	0.4	0.3
Al2O3	25.6	25.8	25.7
FeO	4.7	5.5	5.5
MgO	7.5	8.1	8.2
CaO	15.0	14.5	15.0
Na2O	0.41	0.46	0.30
Mg'	74.0	72.4	72.7
Cr	906	841	890
Sc	8.9	7.8	9.1
La	5.1	4.4	2.0
Eu	0.99	0.82	0.69
	this work	Lit. Average	[7]

Precursors of 76503,7109:

Gabbroic Anorthosite	- 35%
Anorthositic Norite	- 30%
Troctolitic Anorthosite	- 20%
Ferroan "Anorthositic"	- 10-15%

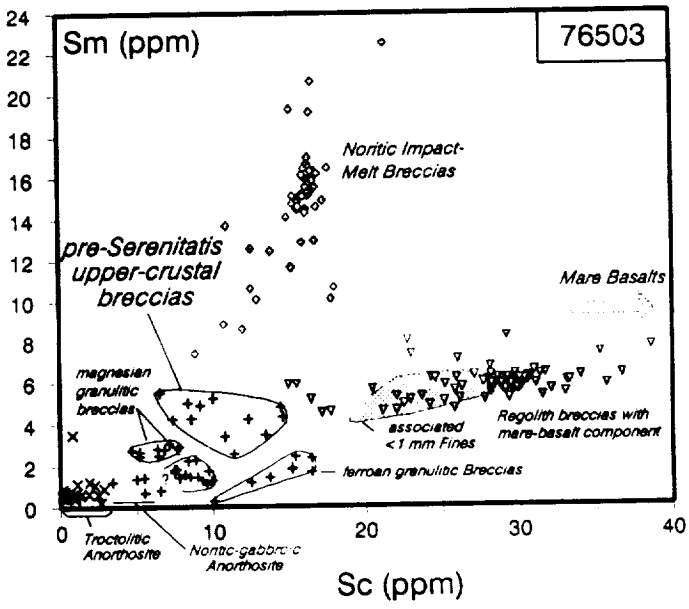

Figure 1. Plot of Sc versus Sm concentrations of 2-4 mm soil particles from 76503, North Massif. Mare basalts not shown. Samples whose compositions lie in fields labelled granulitic breccias are texturally diverse.

AN IRIDIUM-RICH IRON MICROMETEORITE WITH SILICATE INCLUSIONS FROM THE MOON. BRADLEY L. JOLLIFF, RANDY L. KOROTEV, AND LARRY A. HASKIN, DEPARTMENT OF EARTH AND PLANETARY SCIENCES & MCDONNELL CENTER FOR THE SPACE SCIENCES, WASHINGTON UNIVERSITY, ST. LOUIS, MO 63130.

We have found a 0.1 mg iron micrometeorite containing meteoritic silicate inclusions in an agglutinate from 2-2.5 cm deep in regolith core 60014. The metal is 93% iron, 6.5% nickel, 0.5% cobalt, ~150 ppm iridium, and <2 ppm gold. Although the Ir concentration is higher than that reported previously for any iron meteorite group, it lies on the extrapolation to low Ni and high Ir concentrations of several meteorite groups on Ni,Ir plots (groups IIC,D,E, and IIIAB,E,F) [1,2]. Tiny, subrounded silicate inclusions comprise low-Ca pyroxene (En_{83}), olivine (Fo_{80}), and albitic and potassic feldspars, as mixtures of minerals or glasses. Minor phases include oldhamite (CaS) and, tentatively, hercynite ($FeAl_2O_4$). The inclusions have pyroxene FeO/MnO of ~25 and olivine FeO/MnO of 40-60. In comparison with known iron meteorites, the inclusions are most similar to those in type IIE, e.g., Weekeroo Station, Colomera, and Kodaikanal [3-7]. As far as we know, this is the first observation of an iron meteorite with silicate inclusions from a lunar sample. No metal fragments with meteoritic, nonmetallic inclusions were reported in several previous, exhaustive studies of soil particles [8-10].

Observations. We isolated the particle from an anomalously Ir-rich split of 60014,19 [11]. The metal fragment is ~0.3 x 0.4 mm in cross section and appears to be compositionally uniform under electron backscatter. It constitutes ~67 wt.% of its enclosing particle of typical agglutinatic glass with fine-grained, entrained soil. The bulk metal composition is typical of meteoritic metal particles in Apollo 16 polymict samples [e.g., 8,9]; i.e., it is similar to the Fe-Ni metal in Apollo 16 soils (avg 94% Fe, 5.6% Ni, 0.36% Co) [9,10,12,13] and mafic melt breccias (5.2-6.8% Ni, 0.32-0.43% Co) [14]. Its Ir concentration, however, is 150 ppm as determined by INAA on the isolated particle, ~100× higher than that of typical Apollo 16 metal. We find by EMPA that the Ir is uniformly distributed in the metal (Fig. 1). Electron microprobe scans failed to detect Pt and Os (detection limit ~50 ppm).

Nonmetallic inclusions within the micrometeorite are 1 to 30 μm long and have rounded to cuspate morphologies. They are disseminated irregularly throughout the metal, constituting <5% of the volume. We interpret their compositions to mean that distinct mineral grains and polycrystalline aggregates were present in the meteorite before its collision with the Moon (as in Weekeroo-Station types, [5-7]) and that these were subsequently melted or shocked into their present, presumably glassy state; however, we have seen the particle only in reflected light in thick section and do not know whether any of the silicates retain crystalline structure. The most common inclusions have bronzite composition (Table 1). Next most common are mixtures dominated by sodic feldspar and olivine compositions as tiny, separate "phases" that are difficult to resolve individually by EMP (e.g., Table 1, Incl. 1) (as in Kodaikanal, [5]). Isolated inclusions with olivine composition are rare (Table 1, Incl. 7). Most analyses of the alkali-feldspar composition include some Fe and Mg, (beam overlap onto olivine?) or excess Fe (beam overlap onto the host metal or hercynite). The "purest" sodic-feldspar phase has 8.3% Na_2O and 2.5% K_2O (Table 2); the highest K_2O concentration is 3.82%. Alkali-rich spots yield variable Na_2O/K_2O, suggesting that the original material contained both K-feldspar and albite (cf. Colomera and Kodaikanal [5]). Only one inclusion (Table 2, Incl. 5) has high CaO and Al_2O_3 concentrations suggestive of plagioclase feldspar (Table 2, Incl 5). Oldhamite and hercynite (tentative) occur singly in one isolated inclusion each. No augite, Cr and Ti oxides, or whitlockite were found in the exposed inclusions.

Implications. We do not know whether the micrometeorite, when it fell, caused the enclosing agglutinate to form or whether the metal is a surviving chunk of a larger impactor and became incorporated into the agglutinate during a later impact. The metal fragment may be part of a small, recently fallen iron meteorite, unrelated to the general geology of the Apollo 16 site. Nevertheless, because its Fe-Ni-Co composition is dissimilar to metal in ordinary chondrites, but typical of metal found in ancient Apollo 16 melt rocks, it is

tempting to speculate that, despite its high Ir concentration, it might be an artifact of the impactors [13,14] that shaped the Apollo 16 region, and that its silicate inclusions provide information about those impactors. Silicate inclusions of similar mineralogy within an iron meteorite have been dated at 3.8 and 4.5 Ga [3,4]. We infer that silicate inclusions of meteoritic origin were somehow incorporated into the metal as the meteorite parent body formed and differentiated, but not by impact at the time of fall. Perhaps their isotopic clocks would be reset by shock heating so that age measurements on such inclusions would indicate the time of lunar impact. No intercommunication between lunar and meteoritic silicate is evident from our analyses. The search for, and characterization of, such micrometeorites may be a fruitful avenue of future investigations.

Acknowledgements. We thank Dan Kremser for assistance with the electron microprobe. This work was supported in part by NASA under grant NAG 9-56.

References. [1] Wasson J.T. (1985) Meteorites: Their Record of Early Solar-System History. W.H. Freeman and Company, New York [2] McSween, H.Y., Jr. (1987) Meteorites and Their Parent Planets. Cambridge Univ. Press. [3] Burnett D.S. and Wasserburg G.J. (1967) EPSL 2, 137-147. [4] Burnett D.S. and Wasserburg G.J. (1967) EPSL 2, 397-408. [5] Bunch T.E. and Olsen E. (1968) Science 160, 1223-1225. [6] Wasserburg G.J., Sanz H.G., and Bence A.E. (1968) Science 161, 684-687. [7] Bunch T.E., Keil K., and Olsen E. (1970) Contr. Mineral. Petrol. 25, 297-340. [8] Goldstein J.I. and Axon H.J. (1973) PLSC 4th, 751-775. [9] Reed S.J.B. and Taylor S.R. (1974) Meteoritics 9, 23-34. [10] Misra K.C. and Taylor L.A. (1975) PLSC 6th, 615-639. [11] Korotev R.L., Morris, R.V. and Lauer H.V.Jr. (1993) this volume. [12] Hewins R.H., Goldstein J.I., and Axon H.J. (1976) PLSC 7th, 819-836. [13] Korotev R.L. (1987) PLPSC 17, E491-E512. [14] Korotev R.L. (1993) submitted, GCA.

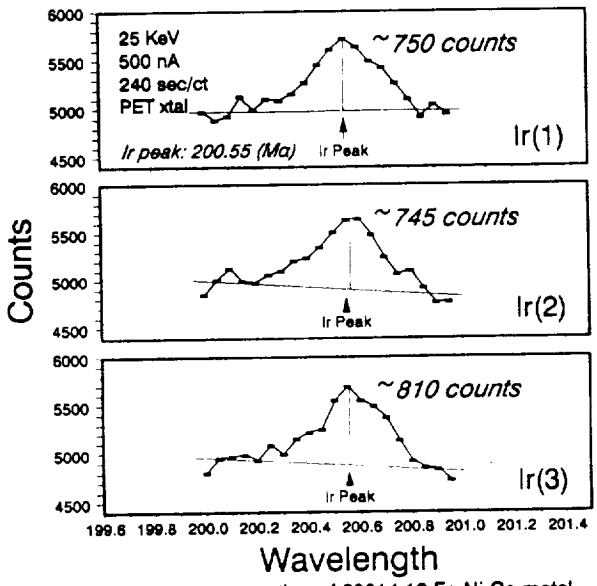

Figure 1. Ir concentration of 60014,19 Fe-Ni-Co metal. The average concentration obtained by comparison to a pure Ir metal standard is 160 ppm. Beam: 10 microns.

Table 1. Silicate inclusions in iron micrometeorite in 60014,19 (,133).

	Low-Ca Px average n=4	Oliv Incl 7	Oliv Inc 1-7	Albite Incl 16-1	Hercynite see note Incl 6	Oliv+ Herc Incl 8	Alk Fs plus ? Incl 1B	Alk Fs plus ? Incl 2	Mix/Gls Av (n=5) Incl 1	Glass? Incl 5	Glass? Incl 5-5
SiO2	56.60	39.13	39.5	66.37	0.23	35.24	66.09	62.24	52.16	35.02	40.75
TiO2	0.10	0.00	0.00	0.09	0.00	0.01	0.06	0.01	0.03	0.19	0.39
Al2O3	0.11	0.04	0.25	18.93	64.86	1.51	18.53	18.11	9.90	21.84	24.31
Cr2O3	0.09	0.40	0.00	0.00	0.00	0.00	0.00	0.02	0.00	0.03	0.04
FeO	11.47	18.25	17.90	2.50	35.96	22.19	4.90	5.34	11.36	26.16	13.75
MnO	0.48	0.47	0.31	0.00	0.00	0.42	0.02	0.03	0.26	0.10	0.09
MgO	30.87	42.16	42.12	0.00	0.02	39.12	4.35	3.67	23.47	6.09	5.19
CaO	0.52	0.00	0.05	0.69	0.07	0.02	0.57	0.69	0.27	9.56	14.08
Na2O	0.01	0.01	0.04	8.27	0.01	0.00	5.56	5.22	2.06	0.94	0.44
K2O	0.00	0.01	0.00	2.46	0.00	0.00	0.46	2.32	0.50	0.07	0.11
Sum	100.25	100.47	100.17	99.32	101.15	98.51	100.54	97.65	100.00	100.00	99.15
Mg'	83	80	81			76	61	55	79	29	40
FeO/MnO	24	39	58			53			43	260	153

Notes: CaS (oldhamite) also observed (one inclusion), but not quantitatively analyzed.
Ca-rich phase or glass is present in one inclusion, but analysis was compromised apparently by beam overlap on Fe-metal.
Inclusion 5 glass appears to be a mixture of plagioclase, olivine, bronzite, hercynite, and metal. Analysis normalized to 100% after compensation for metal overlap.
Identification of hercynite is tentative due to small inclusion size.

THE COOLING RATES OF PAHOEHOE FLOWS : THE IMPORTANCE OF LAVA POROSITY.

Alun C Jones, Institute of Environmental& Biological Sciences, Lancaster University , Lancaster LA1 4YQ, U.K.

Many theoretical models have been put forward to account for the cooling history of a lava flow (1, 2, 3, 4), however only limited detailed field data exist (5, 6, 7, 8) to validate these models. To model accurately the cooling of lava flows, data are required, not only on the heat loss mechanisms, but also on the surface skin development and the causes of differing cooling rates. This paper argues that the cause of such variations in the cooling rates are attributed, primarily, to the vesicle content and degassing history of the lava.

The cooling rates of 20 pahoehoe lobes on the slopes of Kilauea's South East Rift were obtained using two Minolta hand held Cyclops thermal infrared thermometers. The instruments, C330 and C52, obtained surface temperatures by recording emitted radiation from the flow surface in the wavelength ranges of 0.8 to 1.1 μm and 8 to 13 μm; temperatures were obtained at 0.5 s intervals and both instrument view angle resulted in surface target diameters of < 2 cm.

There are two parts to each curve (Fig 1): a high temperature part characterised by a steep, smooth profile and a low temperature part characterised by a shallower, uneven profile. The best fit equation between surface temperature (T / °C) and time (t /s), for all flows monitored, where the surface temperature was > 600 °C was exponential; e.g. $T = 1154 * 10^{(-2.7e-3t)}$, (Correlation coefficient, C_C = 0.76). For surface temperatures < 600°C the best fit equation was logarithmic, e.g. T =773.5+(-157 Log t) (C_C = 0.84). When the whole flow profile is considered the best fit equation is again logarithmic, e.g. T = 1099 + (- 165 Log t), (C_C = 0.94). From the time of lobe extrusion to the time where the surface cooled to 600°C, the lava was incandescent and heat was lost predominantly by radiation, and therefore the relationship between temperature and time is exponential. After the formation of the crust between 600 and 550°C, conduction through the thickening crust and convection away from the surface becomes the dominant heat transfer processes (2), and the relationship between temperature and time becomes logarithmic. The development of such a crust is a significant factor in controlling the final dimensions of the lava lobes. The cooling profiles obtained from the surfaces of pahoehoe lobes (Fig 1), with similar dimensions (flow thicknesses between 10 and 45 cm), show that flows cool at differing rates, and as they solidify the differences between their cooling profiles become exaggerated. A number of parameters which may influence the cooling rates, e.g. flow effusion and stagnation rates; flow field topography; distance from source; lobe position on flow field; residence time of lava within a tube system; and weather conditions, (chemical differences are ignored as these lavas can be considered as chemically homogeneous) have been studied and discounted (9). The one parameter which differed significantly in all flows monitored was the lava porosity.

Three distinct types of pahoehoe have been recognised on the basis of their porosity: (i) vesicle-rich lava termed spongy pahoehoe (S-type), (ii) vesicle-poor lava termed pipe pahoehoe (P-type) (10) and (iii) dense pahoehoe (D-type) (9). D - Type pahoehoe (porosity <29%) has a vesicle content lower than P-type (30 - 39%) and S - Type (>40%), cools noticeably slower than the other lava types and has a higher surface temperature upon extrusion from the tube system (9).

As radiative heat transfer across the vesicles is more effective than conduction through the surrounding solid basalt, the presence or absence of vesicles will affect the rate at which heat is lost from the interior of the lobe. This leads to the conclusion that the cooling rates of lobes are sensitive to their vesicle population and this is reflected in the gradient of the cooling profiles (Fig 1).

The relationship between these cooling profiles however cannot be quantified as each have different initial temperatures and it is uncertain as to amount of cooling the lobe has undergone prior to the start of monitoring. Cooling profiles obtained from the surface of Kupaianaha lava pond (11), during its eruptive periods provided a near complete cooling profile of lava between 1153 and 280 °C. This cooling profile is used as a base line against which the incomplete cooling profiles obtained from pahoehoe lobes can be matched against (Fig 2). For this method it is assumed that the cooling history of a lobe, prior to being recorded, cooled from an initial temperature of 1153 °C along the pond profile, to the temperature at which the thermometer started recording the lobe. Thereafter the cooling profile deviated from the pond profile, due to differences in the volatile content of the lava.

The cooling rates of Pahoehoe Flows : Jones A.C.

Although the vesicle population of lava in the pond and the lava extruded on to the flow field are extremely different (9), the differences in the gradient of each profile only becomes significant during the later stages of the cooling history of the lobe. Using the profiles for which the lobe porosities are already known (from field samples of lobes monitored) the remaining unknown porosities were determined by calculating the relationship between the various profiles (3).

The above however, may not be the case for larger flows, i.e. channelised pahoehoe and a'a, where the flow dimensions can be an order of magnitude greater than those of pahoehoe lobes, and an increase in flow thickness will, almost certainly, influence the cooling rate of the flow. This work shows how remotely sensed thermal data can provide an insight to the mechanisms of flow cooling and highlights the significance that lava porosity has on the cooling rates of such bodies. When modelling the cooling and morphology of terrestrial or planetary sheet and lobate flows, the porosity and degassing history must therefore be considered and accounted for.

References: (1) Baloga, S.M. & Pieri, D.C (1986). J. Geophys. Res. 91, 9543-9552. (2) Head, J.W. & Wilson, L. (1986). J. Geophys. Res. 91, 9407-9446. (3) Pieri, D.C. & Baloga, S.M. (1986). J. Volcanol. Geotherm. Res. 30, 29-45. (4) Crisp, J. & Baloga, S.M. (1990). J. Geophys. Res. 95, 1255-1270. (5) Pinkerton, H & Sparks, R.S.J. (1978). Nature. 276, 383-384. (6) Lipman, P.W. & Banks, N.G. (1987). U.S.G.S. Prof. Paper 1350, 1527-1568. (7) Neal, C.A. et al., (1988). U.S.G.S. Prof. Paper 1463, 99-127. (8) Flynn, L.P. & Mouginis-Mark, P.J. (1992). Geophys. Res. Lett. 19, 1783-1786. (9) Jones, A.C. (1992). Ph.D. Thesis, Lancaster. (10) Walker, G.P.L. (1989). Bull. Volcanol. 51, 199-209. (11) Jones, A.C. et al. (1990). IAVCEI absts, Mainz.

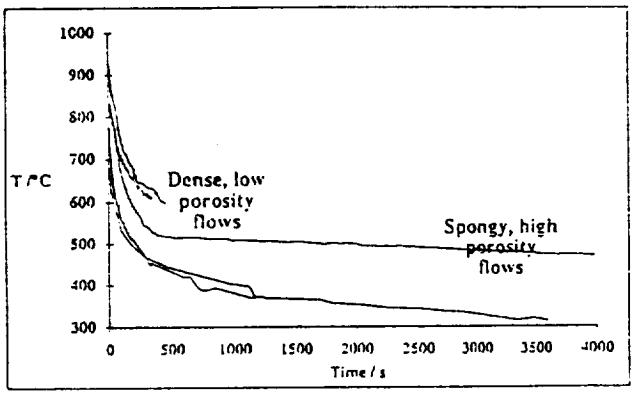

Fig. 1 Cooling profiles from the surfaces of pahoehoe lobes. The dense flows begin to flatten out before the spongy flows.

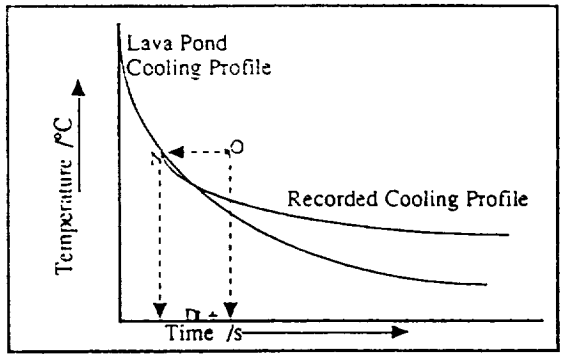

Fig. 2 Method of correcting the cooling profiles of flows against the pond profile The origin of the flow profile (O) is moved to the corresponding temperature on the pond curve(N), and the time difference (Dt) is added to the original flow data.

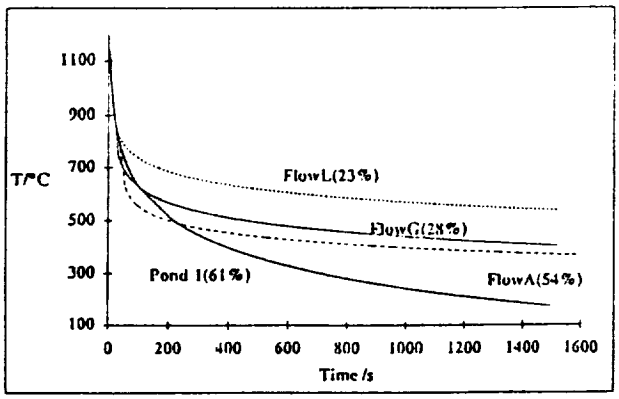

Fig. 3 Importance of porosity (%) on the cooling rate of flows is shown, using best fit equations for flows whose porosity is known.

PARTITIONING OF Nb, Mo, Ba, Ce, Pb, Th and U BETWEEN IMMISCIBLE CARBONATE AND SILICATE LIQUIDS: EVALUATING THE EFFECTS OF P_2O_5, F, AND CARBONATE COMPOSITION. J.H. Jones* and D. Walker+. *SN4, NASA/JSC, Houston, TX 77058. +Lamont-Doherty Earth Observatory, Palisades, NY 10964.

Introduction. Previously we have reported carbonate liq./silicate liq. partition coefficients (D) for a standard suite of trace elements (Nb, Mo, Ba, Ce, Pb, Th, and U), and Ra and Pa as well [1]. In brief, we have found that immiscible liquid partitioning is a strong function of temperature. As the critical temperature of the carbonate-silicate solvus is approached, all partition coefficients approach unity. Additionally, for the overwhelming majority of the partitioning elements, lnD is a linear function of "ionic field strength," z/r, where z is the charge of the partitioned cation and r is its ionic radius.

The system in which our previous experiments were performed was a relatively simple one, CMAS + Na + Fe +CO_2. The silicate portion was initially a synthetic MORB and the carbonate was a 1:1 mixture of Na_2CO_3 and $CaCO_3$. The silicate:carbonate mixture was then prepared in proportions of either 1:1 or 1:2.

We considered it highly likely that additional components such as phosphorus or halogens might strongly influence partitioning behavior, especially for the actinides Th and U. Actinides are known to readily form complexes in aqueous solutions, and large changes in $D^{cpx/liq}$ which correlate with the addition of phosphate have been attributed to phosphate complexation of actinides in the silicate liquid [2]. Consequently, we have carried out a series of experiments to evaluate the effects of potential complexing agents on trace element partitioning between immiscible liquids.

In addition, the Soret effect in liquids provides an index of expected changes in trace element partitioning behavior deriving from changes in major element composition. This has been demonstrated in both silicate [3] and polymetallic sulfide liquids [4] which show strong Soret activity. We attempted to use the Soret effect in a predominantly carbonate liquid (with a small fraction of dissolved silicate) to anticipate the sensitivity of our partitioning results to such chemical parameters as the Na/Ca/Mg ratio of the carbonate liquid.

Experimental and analytical. Experimental procedures and preparation of starting materials have been described previously [1]. Briefly, starting materials consisted of reagent oxides, carbonates, phosphates and fluorides, which were mixed by grinding under acetone. Trace elements were spiked as reagent oxides or carbonates or as natural minerals. Three starting compositions of MORB+carbonate were prepared that also contained 2, 5 and 14.5 wt.% of $Ca_3(PO_4)_2$, and three other mixtures were prepared that contained 5, 10, and 14.5 wt.% CaF_2. Runs were performed in graphite capsules in a piston cylinder. Our standard run conditions were 4-24 hours at 1250°C and 10 kbar. Charges were analyzed by electron microprobe using standard techniques.

We note that our experimental charges have some tendency for the carbonate liquid to disperse onto the grain boundaries of the graphite capsule, presumably by a combination of reaction and capillary migration. Consequently, we have reduced our experimental run times to maximize our chances of finding two liquids. However, even in those cases where the carbonate liquid has been sequestered into the graphite, the remaining silicate liquid appears to have equilibrated with the carbonate. Thus, we infer that equilibrium is approached quickly [1] and that the chemical characteristics of our immiscible liquids are established early in the experiment. The difficulty that we have had in containing the carbonate is testimony to the mobility of carbonate liquids and may have implications for the extraction of carbonate-rich partial melts from planetary mantles.

To investigate possible Soret activity, Na/Ca and Mg/Na/Ca carbonate charges, with ~5% silicate and doped with our standard tracers, were placed in graphite capsules in a thermal gradient of ~200°C/4 mm according to our routine procedures [5]. The Na/Ca charge precipitated

immiscible silicate at the cold end (~1250°C) allowing an additional consistency check on partitioning information at a different Na/Ca/Mg ratio than previously investigated.

Results. The primary result of adding P or F to our MORB+carbonate system is to expand the carbonate liquid stability at the expense of the silicate. As more phosphate and fluoride were added, the silicate became less modally abundant. At least one reason for the expansion of the carbonate field is that P and F are both strongly partitioned into the carbonate phase. D(P) is about 4 and D(F) is 2-4, in favor of the carbonate. Consequently, as more phosphate and fluoride components are added to the system, the amount of carbonate should increase. In addition, however, the SiO_2 concentration of the carbonate liquid increases as the total amount of P or F increases, suggesting that the addition of these components promotes miscibility. For example, in the case of the 14.5 wt.% CaF_2 composition, there appeared to be complete miscibility, as only one phase was found.

The addition of P and F to our MORB+carbonate system apparently has only a minor effect on partitioning (Figures 1 and 2). While there does appear to be some modest change in D's at low P and F contents, we cannot rule out that this is due to small differences in bulk chemical composition. In most cases the partition coefficients in the P- and F-bearing systems are within 30% of those in the P- and F-free system.

Surprisingly, the liquids of both our Soret experiments were quite homogeneous, showing no Soret effect. In addition, the immiscible liquid at the cold end of the Na/Ca carbonate Soret experiment showed carbonate/silicate partitioning entirely consistent with our previous results, although the linear trend of lnD with field strength may be marginally less steep. This result is consistent with our previous results being insensitive to the Mg/Na/Ca ratio in the carbonate system. This conclusion is reinforced by the surprising result that no measurable Soret activity was detected for any element.

Conclusions. On the basis of these new experiments, we conclude that our previous results are not strong functions of carbonate composition. We also conclude that our original partition coefficients are not strong functions of the abundances of minor, high-field strength components or of complexing agents. We therefore believe that our earlier results are likely to have greater application than would initially have been predicted.

References: [1] Jones J.H. et al. (1992) *Lunar and Planet. Sci. XXIII.* pp. 627-228. [2] Jones J.H. and Burnett D.S. (1987) *Geochim. Cosmochim. Acta* **51**, 769-782. [3] Lesher C.E. (1986) *J. Geophys. Res.* **91**, 6123-6141. [4] Jones J.H. and Walker D. (1991) *Proc. Lunar Planet. Sci. Conf. 21st.*, 367-373. [5] Lesher C.E. and Walker D. (1991) *Adv. Phys. Geochem.* **8**, pp. 396-451.

Figure 1

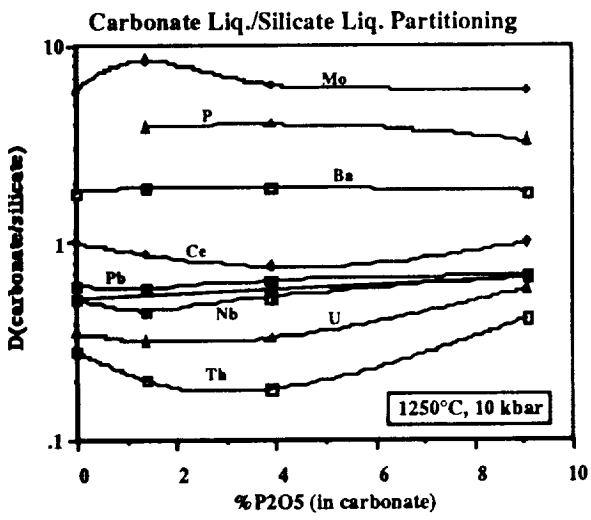

Figure 2

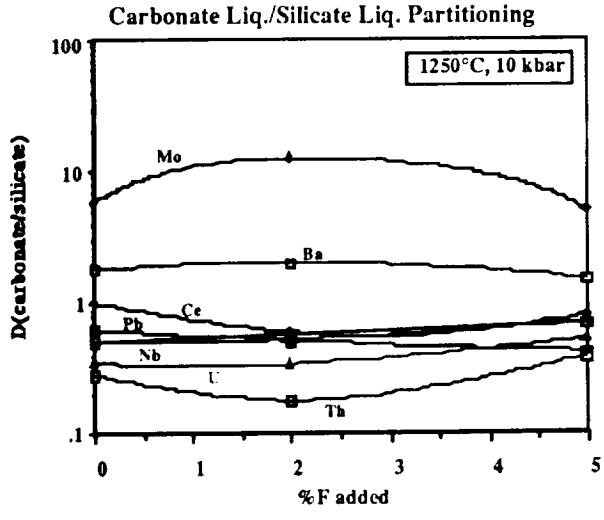

COMPLEX ZONING BEHAVIOR IN PYROXENE IN FEO-RICH CHONDRULES IN THE SEMARKONA ORDINARY CHONDRITE. Rhian H. Jones, Institute of Meteoritics, Department of Earth and Planetary Sciences, University of New Mexico, Albuquerque, New Mexico 87131, USA.

A detailed understanding of the properties of silicate minerals in chondrules is essential to the interpretation of chondrule formation conditions. This study is further work in a series of petrologic studies of chondrules in the least equilibrated LL chondrite, Semarkona (LL3.0). The objectives of this work are a) to understand chondrule formation conditions and nebular processes and b) to use the data as a basis for understanding the effects of metamorphism in more equilibrated chondrites. FeO-rich pyroxene in the chondrules described shows complex zoning behavior. Low-Ca clinopyroxene, orthopyroxene, pigeonite and augite are all observed, in various associations with one another. Coexisting olivine phenocrysts are also FeO-rich and strongly zoned. Compositional and zoning properties are similar to those observed in boninites and are interpreted as resulting from rapid cooling of individual chondrules.

Textures. A textural description of FeO-rich, porphyritic, pyroxene-rich chondrules in Semarkona has been given previously [1]. The chondrules described here are those classified as types IIAB and IIB: type IIAB chondrules contain both olivine and pyroxene phenocrysts, and type IIB contain no olivine. Large phenocrysts of olivine and pyroxene may be intergrown and are euhedral or hopper-shaped in morphology. Mesostasis in these chondrules is relatively abundant (up to about 30 vol%) and usually glassy, with quench crystals of pyroxene. Some of the chondrules contain coarse (up to 150 μm wide) parallel bars of pyroxene rather than isolated, randomly-oriented phenocrysts. Nine chondrules from Semarkona that fit the textural descriptions above have been studied in detail. Low-Ca pyroxene compositions in this suite of chondrules are in the range Fs_{10-24}.

Pyroxenes. Four distinct categories of pyroxenes are observed in the chondrules studied: low-Ca pyroxene (twinned clinoenstatite), orthopyroxene, pigeonite and augite. The most common association is low-Ca pyroxene with rims of augite, similar to the pyroxene observed in the type I, FeO-poor, series of porphyritic chondrules [2,3]. Augite rims are common but do not rim all low-Ca pyroxene grains. Pigeonite is less common, and when present occurs as a distinct layer between low-Ca pyroxene and augite. Orthopyroxene has been observed in only one chondrule, and in this case occurs as complete, individual, euhedral grains with a small amount of augite overgrowth. These observations are similar to those made by [4].

Low-Ca pyroxene. Complex zoning behavior is observed within low-Ca pyroxenes. In contrast to FeO-poor PP chondrules [3], the more FeO-rich, low-Ca pyroxene grains commonly contain skeletal cores of more Fe-rich compositions that are observed clearly in BSE images. An example is illustrated in Fig. 1. Optically, this grain shows continuous twinning characteristic of clinoenstatite along its length. A microprobe traverse across the zones indicated in the sketch shows the compositional variation typical of these grains. FeO content is 1-2 wt% higher in the skeletal Fe-rich portion than in the core and adjacent overgrowth. There is an overall increase in FeO content from the core to the edge of the grain. The point on the traverse at the outer edge of the grain is a Ca-rich (augite) rim containing 14 wt% CaO (data for CaO > 2 wt% are not indicated on Fig. 1). Cr, Mn, Ca and Al contents also vary with Fe: in the low-Ca pyroxene, zoning behavior of all these minor elements follows that of FeO. In the Ca-rich rim, Al and Cr are also strongly enriched and Mn follows the decrease seen in Fe.

Orthopyroxene. In one chondrule two distinct types of low-Ca pyroxene are recognised: i) low-Ca pyroxene showing characteristic clinoenstatite twinning, and ii) two large, euhedral grains of orthopyroxene that show no optical twinning. Although concentrations of most elements in the two types are not distinguishable, there is a distinct difference in CaO contents. The clinopyroxene has CaO = 0.2 wt% and the orthopyroxene has CaO = 0.6 wt%. Clinopyroxene grains contain Fe-rich skeletal cores similar to those described above (Fig. 1). The two grains of

orthopyroxene show concentric oscillatory zoning, with at least 8 zones between core and rim of each grain (Fig. 2). Oscillations correspond to compositional changes in FeO, as illustrated, and there is an overall increase in FeO towards the edge of the grain. These changes are accompanied by changes in Cr, Ca, Mn and Al contents which all vary sympathetically with Fe in similar degrees to the variations observed in clinopyroxene.

Olivine. Olivine phenocrysts in the chondrules studied are Fe-rich and strongly zoned with increasing FeO from core to rim. Mean Fe/(Fe+Mg) ratios of olivine phenocrysts in individual chondrules are similar to mean compositions of coexisting low-Ca pyroxene phenocrysts (Fa_{10-18}). Typical zoning properties of olivine grains show FeO profiles that are flat in the core and increase sharply in the rim regions, similar to profiles observed in olivine in type IIA (olivine-rich) chondrules in the same chondrite [5]. Cr and Mn profiles are similar to Fe and increase in the rim region. Ca profiles are generally flat, or show only very minor increases towards the rims.

Discussion. Cooling rates of porphyritic, pyroxene-rich chondrules lie in the range 5 to >100°C /hr [6]. The presence of twinned low-Ca pyroxene, resulting from inversion from protoenstatite, is also an indication of rapid cooling. Zoning properties of pyroxenes in the chondrules studied are similar to those observed in terrestrial boninites [7] and may be understood in a similar framework of rapid cooling of the parent liquids. The complex zoning observed in the Fe-rich chondrules is likely to result from significant effects of disequilibrium during the rapid cooling interval. The origin of skeletal cores with slightly elevated Fe contents commonly observed in low-Ca clinopyroxene may be attributable to a small degree of undercooling in the initial stages of nucleation. Pyroxene and olivine compositions in each chondrule have similar Fe/(Fe+Mg) indicating that they grew from a common liquid. There is also a correlation between FeO contents of mesostases and mean FeO contents of coexisting pyroxenes and olivines which is additional evidence for closed system crystallization. Oscillatory zoning in orthopyroxene is likely to be the result of disequilibrium boundary layer effects in the adjacent liquid (e.g. [8]). The complexities described need to be fully understood before the effects of metamorphism on pyroxene can be interpreted.

References: [1] Jones RH (1992) LPSC XXIII, 629-630 [2] Jones RH and Scott ERD (1989) Proc 19th Lunar Planet Sci Conf, 523-536 [3] Jones RH (1992) LPSC XXIII, 631-632 [4] Noguchi T (1989) Proc NIPR Symp Antarctic Met 2, 169-199 [5] Jones RH (1990) GCA 54, 1785-1802 [6] Lofgren G and Russell WJ (1986) GCA 50, 1715-1726 [7] Ohnenstetter D and Brown WL (1992) J Petrol 33, 231-271 [8] Downes MJ (1974) Contrib Mineral Petrol 47, 187-196.
Acknowlegdement: Funded by NASA grant NAG9-497, J.J. Papike, P.I.

FIG 1

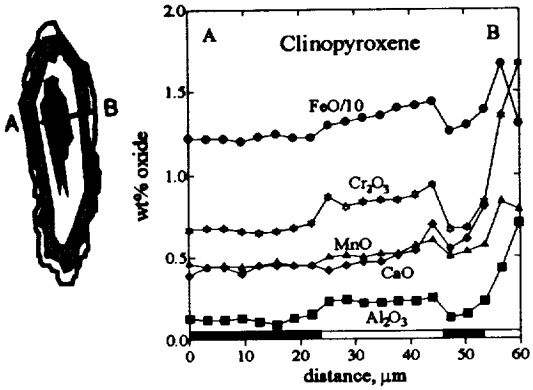

FIG 2

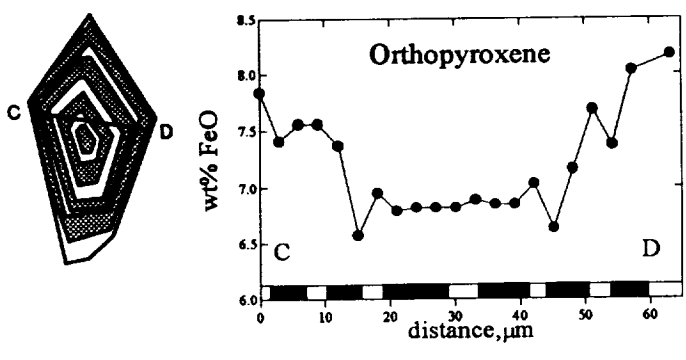

Figures: Zoning in pyroxene. Sketches show general appearance in BSE image. White zones are more Fe-rich than adjacent shaded zones. Fig. 1: Low-Ca clinopyroxene grain with a skeletal Fe-rich zone (white). Fig. 2: Orthopyroxene grain showing multiple oscillatory growth zones.

ANGRITE LEW87051: ARE THE OLIVINES PHENO'S OR XENO'S? A CONTINUING STORY.

A.J.G Jurewicz (LESC C23, P.O. Box 58561, Houston TX 77258) and G.A. McKay (NASA SN4, Johnson Space Center, Houston TX 77058).

INTRODUCTION: The achondrite LEW87051 is a porphyritic basalt consisting of large subhedral to euhedral zoned olivines in a finer-grained groundmass. The texture of this groundmass looks remarkably like a quenched melt. However, although the rock is clearly igneous, its exact origins and history are under dispute. From petrographic observations, Prinz *[1]* felt that the large olivines were xenocrysts and that the zoning reflected interaction with an unrelated, CAI-enriched melt. McKay *et. al [2,3,4]* was able to model the olivines as phenocrysts, whose zoning was the result of a parent melt that changed in composition as material crystallized, eg., fractional crystallization in a closed system, and calculated a parent melt composition. Jurewicz and McKay *[5]* compared the calculated parent melt composition with actual partial melts from CV and CM chondrites. They showed that the calculated melt was substantially different from equilibrium melts of these chondrites; however, the LEW87051 groundmass composition *[3]* was similar to some of the low temperature partial melts, although slightly enriched in AN (or depleted in OL) components.

This study presents the results of an independent petrologic look at other olivines in LEW87051, and the preliminary results of a quantitative model for the major zoning in these olivines as diffusive-exchange with an olivine-saturated, low temperature angritic melt.

PETROGRAPHY: Figure 1 shows a photomicrograph of the euhedral grain which is the focus of this study. The long axis is nearly parallel to the c-axis of the crystal. The zoning is most developed along the long axis, and less developed perpendicular to that axis. EPMA analysis shows that this zoning is primarily in Fe, Mg and Mn, and that it transverses the "rim" and "main grain" sections of *[4]*, as defined by molar FeO/(FeO+MgO) ratios. Figure 2 gives details of the FeO gradient parallel to the c-axis, as determined by several EPMA traverses near the center of the grain. No high Cr central core equivalent to that observed by McKay *et. al [4]* was found in this particular cross-section. The Cr and Ca in the olivine was weakly zoned. Also, the Cr and Ca contents were higher and lower, respectively, than would be expected from equilibration with a low-temperature angritic groundmass (*[4]*, this study).

EXPERIMENTAL: A 16 hour isothermal diffusive-exchange experiment *[6]* was slowly quenched (1185^{o}C to 1000^{o}C in ~20 minutes), and is shown in Figure 3. This charge qualitatively reproduces some of the general textural and chemical features (ie, gradients in Fe, Mg and Mn but not Ca or Cr) of olivine in LEW87051. The source melt for this experiment was chosen (based upon previous work in angritic systems *[4],[7]*) to simulate the groundmass of LEW87051 in that plagioclase was on the liquidus (~1195^{o}C) but olivine was present at run conditions (1185^{o}C, IW+1). A charge of this source melt was run for 7-days, and results from this equilibrium experiment were used to constrain the initial conditions needed for a diffusion model of the zoning in the LEW87051 olivines.

THE MODEL: The zoning in LEW87051 parallel to the c-axis was modeled assuming isothermal, composition-independent diffusion of cations from an infinite source (a melt of constant composition *[6]*) as a first approximation. Implicit to this model is that a compositional profile can be linearized by inversion through an error function. Accordingly, the FeO gradient of Figure 2 is shown inverted through an error function in Figure 4. In order to quantify this result, diffusion rates for Fe in olivine at the appropriate temperature and oxygen fugacity (first guess, ~1185^{o}C, IW+1) were obtained from *[6]* and *[8]* and plugged into the model to obtain a residence time of ≤10 days for the olivine in the low temperature melt. This short residence time can also be shown to account for the observed Mg and Mn profiles, and the lack of Ca-rich and Cr-poor rims.

DISCUSSION AND CONCLUSIONS: The strong Fe, Mg, and Mn zoning in the olivines from LEW87051 are consistent with the rapid diffusional-exchange of cations with a low-temperature, angritic melt. The lack of strong zoning in Cr and Ca near the edge of the olivine that might otherwise be expected from contact with a low temperature angritic melt can be explained by slower Ca and Cr diffusion. Accordingly, the observed, weak gradients in Cr and Ca may be relict growth phenomenon from a higher temperature process such as that

suggested by McKay *et. al [2,4]*. In fact, we note that, if the blocky crystal studied in *[4]* was cut perpendicualr to the c-axis, the diffusion profiles may have been so short that they became inconsequential to modeling the Fe/Mg profiles using fractional crystallization. (Although we are checking, it seems unlikely that the model of *[4]* becomes strikingly linear during inversion through the error function). Perhaps the large olivines are xenocrysts, equilibrating with a low-temperature angritic melt. Another possibility is that LEW87051 underwent two periods of melting: one where euhedral olivine crystallized and settled from a melt, followed by a second, short, low temperature melting event during which the strong Fe, Mg and Mn zoning was produced. A third possibility is that the crystals recall a single melting event with a nonlinear cooling history.

REFERENCES: [1] Prinz et at (1990) LPSC XXI 979-980; [2] McKay et. al (1990) LPSC XXI 771-772; [3] G.A. McKay (1989) 52th Met. Soc. Annual Meeting (oral presentation); [4] McKay et. al (1991) Meteoritics 26 370; [5] Jurewicz and McKay (1992) LPSC XXIII 643-644; [6] Jurewicz and Watson (1988) CMP 99 186-201; [7] McKay et. al (1988) LPSC XIX 760-761; [8] Buening and Buseck (1973) JGR 78:29 6852-6862.

Fig.1. SEM photomicrograph of LEW87051 showing the crystal being modeled (long axis //c) with major-element zoning, and "quench" texture of groundmass.

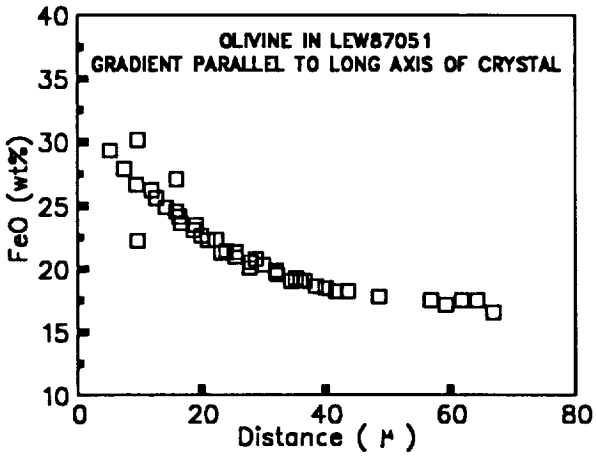

Fig.2. Change in FeO //c axis. The position of the Crystal-melt interface was determined visually. Data <5 μ from interface was excluded.

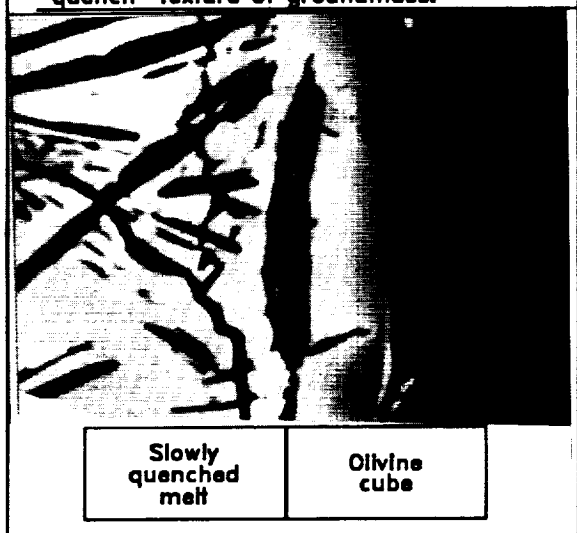

Fig.3. BEI photomicrograph of the diffusive-exchange experiment showing texture of the groundmass and zining in the olivine cube.

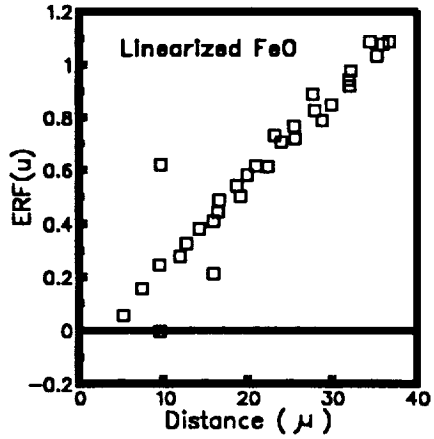

Fig. 4. Data from Fig. 1 inverted through the error function. The Y-intercept less than 0 indicates either an incorrect estimate of initial composition (<2% FeO) or a systematic error in position (~8 microns). In the system of [2,4], the olivine changes ~2wt% FeO in 10-20°C.

C-5

PARTIAL MELTING OF ORDINARY CHONDRITES: LOST CITY (H) AND ST. SEVERIN (LL). Amy J. G. Jurewicz[+], John H. Jones[#], Egon T. Weber[*], David W. Mittlefehldt[+]: [+]Mail Code C23, Lockheed ESC, 2400 NASA Rd. 1, Houston, TX 77058; [#]SN4, NASA/Johnson Space Center, Houston, TX 77058; [*]Dept. of Geology, Univ. of Michigan, Ann Arbor, MI 48109.

Eucrites and diogenites are examples of asteroidal basalts and orthopyroxenites, respectively. As they are found intermingled in howardites, which are inferred to be regolith breccias, eucrites and diogenites are thought to be genetically related. But the details of this relationship and of their individual origins remain controversial.

Work by Jurewicz *et. al [1]* showed that 1170-1180°C partial melts of the (anhydrous) Murchison (CM) chondrite have major element compositions extremely similar to primitive eucrites, such as Sioux County. However, the MnO contents of these melts were about half that of Sioux County, a problem for the simple partial melting model. In addition, partial melting of Murchison could not produce diogenites, because residual pyroxenes in the Murchison experiments were too Fe- and Ca-rich and were minor phases at all but the lowest temperatures *[1]*. A parent magma for diogenites needs an expanded low-calcium pyroxene field. In their partial melting study of an L6 chondrite, Kushiro and Mysen *[2]* found that ordinary chondrites did have an expanded low-Ca pyroxene field over that of CV chondrites (i.e., Allende), probably because ordinary chondrites have lower Mg/Si ratios.

This study expands that of both Kushiro and Mysen *[2]* and Jurewicz *et. al [1]* to the Lost City (H) and St. Severin (LL) chondrites at temperatures ranging from 1170 to 1325°C, at an f_{O2} of one log unit below the iron-wüstite buffer (IW-1).

EXPERIMENTAL: Chemically-characterized, silicate-rich and metal-rich separates of Lost City and St. Severin (obtained from E. Jarosewich) were used as starting materials. Initially, the silicate and metal fractions were mixed, pre-annealed at higher oxygen fugacity, and then re-ground to eliminate large metal flakes which might be distributed inhomogeneously among the small (100 mg) charges. Unfortunately, nucleation problems forced a change to a mix of the silicate-rich separate with an Fe_2O_3-NiO powder that duplicated the Fe/Ni ratio of the natural metal fraction. Flowing CO/CO_2 was used to control f_{O2}. For experiments run at or below 1220°C, charges were placed in re-usable Pt-wire baskets; for higher temperature experiments, charges were spot-welded onto Pt-wire loops. Runs ranged from 4 to 7 days, depending on the temperature, and were drop-quenched into water. Chemical analyses were performed at NASA/JSC by EPMA.

RESULTS: Melt, olivine, low-calcium pyroxene, and minor Fe-Ni metal (Fe>80%) ±sulfides were present in all St. Severin and Lost City charges. Representative melt and pyroxene analyses are given in Tables 1 and 2. In Table 1, melts from CM and CV chondrites *[1]* are given for comparison. There was always less melt in the H and LL chondrites than in the CM or CV chondrites run under corresponding conditions *[1]*.

At 1170°C, the lowest temperature run to date, ~10-15% melt was present in both St. Severin and Lost City charges. Chromite (<1%) was also observed. By analogy with Murchison and Allende charges run under the same conditions *[1]*, the solidi are probably ~1150-1160°C. In examination of the 1170°C charges, plagioclase was not observed, but both melt compositions plot near the peritectic point of Stolper *[3]*.

In the charges run at high temperatures, melt fractions are again less than that observed in Murchison or Allende at equivalent conditions: ~22-28% for St. Severin at 1275°C; and ~25-30% for Lost City at 1325°C. Pyroxene is still a major phase (≥10%) in both. Chromite was not observed, although mass balance suggests that it may be present in the St. Severin charge in trace amounts.

DISCUSSION: This study, combined with *[1,4]*, gives preliminary data for partial melting in chondrites bracketing a wide range of likely compositions (refractory element/Si by ~2x; Fe/Si ratios by 30-50%). Partial melting of anhydrous CV and CM chondrites leaves a residue that is dominated by olivine, so there is little chance that diogenites could be formed from such materials. On the other hand, melts of Murchison at 1170°C had major element contents within 3% of those measured for the Sioux County eucrite, and melts of Allende at 1180°C were similarly close to Ibitira *[1]*. In contrast, partial melting of H and LL chondrites results in either a pyroxene-enriched residue or, at higher degrees of partial melting, a pyroxene-enriched melt, which has potential for producing large amounts of pyroxene cumulates. On the other hand, although the major elements in partial melts from St. Severin and Lost City are broadly eucritic (±10% of Sioux County; Table 1), they do not specifically match any known eucrite.

Eucrites. Although partial melts of ordinary chondrites at 1170°C and IW-1 are broadly eucritic, their MnO/FeO ratios are much too low (as are those from Murchison), their TiO_2 concentrations are 20% low, and their CaO/Al_2O_3 ratios are 5-10% lower than those of Sioux County. Fractional crystallization of higher

temperature, pyroxene-saturated partial melts might alleviate some of these discrepancies. However, considering the low values of pyroxene/melt partition coefficients for CaO, Al_2O_3 and TiO_2, fractional crystallization of these higher temperature melts would probably help the CaO/Al_2O_3 problem somewhat, but not the discrepancy in TiO_2. Thus, we do not have a satisfactory model that uses a known chondrite as a protolith that will exactly produce eucrites, although the refractory lithophile major and minor elements (Si, Ti, Al, Cr, Fe, Mg, Ca) of the Murchison 1170-1180°C partial melts most closely match those of Sioux County.

Diogenites. The pyroxenes of our St. Severin and Lost City experiments seem to bracket the range of diogenitic pyroxenes in major element composition (Table 2). Even so, the complex processes that have produced diogenites are difficult to unravel. In diogenitic pyroxenes, large variations in Ti, Al and REE without commensurate changes in Mg# suggest that different cations have diffusively equilibrated at different rates *[5]*. However, we note that the TiO_2/Al_2O_3 and CaO/Al_2O_3 ratios of our experimental pyroxenes are similar to those of pyroxenes in diogenites. We take this similarity to indicate that most diogenites crystallized from melts that had ~chondritic relative proportions of Ca, Al and Ti. Exceptions are Y-75032, ALHA84001, and Manegaon *[5]*.

CONCLUSIONS: If not for the howardites, the simplest solution to the eucrite-diogenite problem would be to decouple their petrogenetic histories (e.g., formation on different parent bodies). If eucrites and diogenites truly are cogenetic, then one solution is to postulate an unknown type of chondrite source region, resembling an ordinary chondrite, but enriched in refractory lithophiles and MnO.

REFERENCES: [1] Jurewicz *et. al* (1993) *GCA* in press; [2] Kushiro and Mysen (1979) *Mem. NIPR, Sp. Issue 15*, p.165; [3] Stolper (1977) *GCA* 41 p.587; [4] Jurewicz *et. al* (1992) *Science* 252(5) p.695; [5] Mittlefehldt (1993) *LPSC* XXIV, submitted.

Table 1. Example experimental melts: This study and [1] compared to Sioux County

	All. 1170	Murch. 1170	LC 1170	SS 1170	LC 1275	SS 1275	SC bulk
SiO_2	49.4	49.22	49.61	48.63	50.79	50.59	49.50
TiO_2	0.93	0.63	0.48	0.49	0.39	0.38	0.60
Al_2O_3	13.0	13.67	13.62	14.19	11.02	8.50	13.40
FeO	17.4	18.90	19.71	17.72	17.33	23.43	18.80
MnO	0.18	0.26	0.21	0.29	0.42	0.41	0.55
MgO	7.26	7.09	6.73	6.80	11.27	10.43	7.20
CaO	11.8	10.56	9.32	10.16	8.07	6.85	10.30
Cr_2O_3	0.31	0.31	0.30	0.25	0.67	0.72	0.32
Total	100.4	100.9	100.5	99.2	100.0	101.4	101.2
FeO/SC	0.93	1.01	1.05	0.94	0.92	1.25	
MgO/SC	1.01	0.98	0.93	0.94	1.57	1.45	
CaO/SC	1.15	1.03	0.90	0.99	0.78	0.66	
Al_2O_3/SC	0.97	1.02	1.02	1.06	0.82	0.63	
MnO/SC	0.33	0.47	0.39	0.53	0.76	0.74	

Table 2. Pyroxenes in the experimental charges *versus* those in diogenites.

	SS 1275	SS 1220	SS 1170	LC 1325	LC 1275	LC 1170	diogenites typical	diogenites magnesian	diogenites ferroan
SiO_2	55.09	54.32	52.98	55.62	54.92	53.91	54.22	54.9	53.98
TiO_2	0.04	0.04	0.11	0.02	0.03	0.08	0.1	0.09	0.09
Al_2O_3	0.48	0.66	2.20	0.38	0.48	0.95	0.82	0.97	0.49
Cr_2O_3	0.79	0.69	0.72	0.68	0.75	0.76	0.62	0.6	0.47
FeO	17.42	18.18	17.67	12.99	14.43	18.66	15.37	13.05	18.16
MnO	0.33	0.35	0.33	0.30	0.34	0.35	0.51	0.45	0.59
MgO	27.41	25.54	25.07	29.74	28.56	24.44	26.68	28.09	24.93
CaO	0.78	1.38	1.42	0.43	0.73	2.17	1.16	1.26	1.17
total	102.34	101.17	100.51	100.16	100.26	101.32	99.48	99.41	99.88
wo	1.5	2.70	2.84	0.83	1.42	4.27	2.3	2.5	2.3
en	72.6	69.53	69.63	79.65	76.81	67.02	73.8	77.3	69.3
fs	25.9	27.76	27.53	19.51	21.77	28.71	23.9	20.2	28.3

EXPERIMENTAL PARTITIONING OF Zr, Ti, AND Nb BETWEEN SILICATE LIQUID AND A COMPLEX NOBLE METAL ALLOY AND THE PARTITIONING OF Ti BETWEEN PEROVSKITE AND PLATINUM METAL. Stephen R. Jurewicz and John H. Jones, Code SN4, NASA Johnson Space Center, Houston, TX 77058

INTRODUCTION: El Goresy et al.'s [1] observation of Nb, Zr, and Ta in refractory platinum metal nuggets (RPMNs) from Ca-Al-rich inclusions (CAIs) in the Allende meteorite led them to propose that these lithophile elements alloyed in the metallic state with noble metals in the early solar nebula. However, Grossman [2] pointed out that the thermodynamic stability of Zr in the oxide phase is vastly greater than metallic Zr at estimated solar nebula conditions.

Jones and Burnett [3] suggested this discrepancy may be explained by the very non-ideal behavior of some lithophile transition elements in noble metal solutions and/or intermetallic compounds. Subsequently, Fegley and Kornacki [4] used thermodynamic data taken from the literature to predict the stability of several of these intermetallic compounds at estimated solar nebula conditions.

Palme and Schmitt [5] and Treiman et al. [6], conducted experiments to quantify the partitioning behavior of certain lithophile elements between silicate liquid and Pt-metal. Although there results were somewhat variable, they did suggest that Zr partition coefficients were too small to explain the observed "percent" levels in some RPMNs. Palme and Schmitt also observed large partition coefficients for Nb and Ta. No intermetallic phases were identified.

Following the work of Treiman et al. [6], Jurewicz and Jones [7] performed experiments to examine Zr, Nb, and Ti partitioning near solar nebula conditions. Their results showed that Zr, Nb, and Ti all have an affinity for the platinum metal, with Nb and Ti having a very strong preference for the metal. The intermetallic phases $(Zr,Fe)Pt_3$, $(Nb,Fe)Pt_3$, and $(Ti,Fe)Pt_3$ were identified.

Curiously, although both experiments and calculations indicate that Ti should partition strongly into Pt-metal (possibly as $TiPt_3$), no Ti has ever been observed in any RPMNs. Fegley and Kornacki [4] also noticed this discrepancy and hypothesized that the Ti was stabilized in perovskite which is a common phase in Allende CAIs.

EXPERIMENTAL: The current experiments were undertaken to determine: 1) the transition element partitioning behavior in a Fe-free system, 2) the effect of a complex Pt-Ir-Os-Ru alloy on transition metal partitioning, and 3) the partitioning behavior of Ti into Pt-metal in the presence of perovskite.

The Fe-free system experiments were performed using the technique described in Jurewicz and Jones [7]. The "CAI-like" liquid composition from our previous experiments was used except that FeO was deleted from the starting mix. The starting glass composition was spiked at the 1.0 wt.% level with the transition element oxide to be studied. Two micron platinum powder was blended into the doped mix as described by Jurewicz and Jones[7]. The experimental charge was then loaded into an alumina capsule and sealed in an evacuated silica glass tube with an additional crucible containing 100 mg of Cr-metal. The oxygen fugacity of the $Cr\text{-}Cr_2O_3$ buffer is about one log unit greater than solar (10^{-16}) at the run temperature of 1548K. The sealed silica tubes were run in a controlled atmosphere furnace with flowing CO/CO_2 providing a log fo_2 of -9.63 on the outside of the capsule. The charges were run for 48 hours.

The complex alloy experiments were similar to the above except that the original Fe-bearing CAI oxide mix and a metal mix of Pt, Os, Ir, and Ru in roughly equal atomic percentages, were used.

A mixed oxide "CAI-like" composition for the perovskite experiment was selected from Beckett [8] and was expected to crystallize substantial perovskite at the run temperature of 1548K. The initial oxide mix was melted in air at 1743K for 24 hours and then crystallized at 1548K for 150 hours. The resulting starting material contained about 20% vol. perovskite with olivine, fassaite, and spinel. The material was ground to a fine powder, blended with 2 micron Pt-powder, and loaded into an alumina capsule and run as per the previous experiments.

PARTITIONING OF Zr, Nb, AND Ti: Jurewicz S.R. and Jones J.H.

RESULTS: The partitioning results are shown in Table 1 in addition to the previous results of Jurewicz and Jones [7] and Palme and Schmitt [5]. The results indicate that although Zr does partition into Fe-free Pt-metal, it's partition coefficient is about the same as in the Fe-bearing system. Also, Zr does not appear to partition into the complex noble metal mix at all. Nb and Ti on the other hand, strongly partition into the metal in both the Fe-free and complex systems. Because Nb partitioned so strongly into the metal, only minimum D values were determined. The actual values are probably much higher, as suggested by Palme and Schmitt's [5] results.

Significantly, substantial Ti (5.8 +/- 0.6wt.%) was observed in the Pt-metal phase from the perovskite experiment and modal perovskite dropped to a few percent. Thus, perovskite decomposes in the presence of Pt-metal at solar oxygen fugacities and 1548K.

DISCUSSION: The observed Fe-free Zr partition coefficient, while similar to those previously observed, is still too small to account for "percent levels" of Zr in RPMNs. In addition, Zr does not tend to partition at all into a complex Os-Ru-Pt-Ir alloy, which more closely resembles natural RPMNs. Titanium appears to partition into Pt-metal even when the Ti is initially contained in perovskite. Our results suggest that the observed transition elements in RPMNs are not the result of a simple silicate/metal equilibration process and/or the RPMNs formed in a more oxidizing environment than that of solar composition.

TABLE 1. Partitioning results for all the experiments. Numbers in parentheses are two sigma deviations.

Tracer Wt%	$D_{Zr}^{Me/liquid}$	$D_{Nb}^{Me/liquid}$	$D_{Ti}^{Me/liquid}$
	Jurewicz and Jones (1992)		
0.5	2.09(0.47)		
1.0	3.82(0.52)	>10	151(60)
2.5	4.55(0.51)		
5.0	3.91(0.38)	>55	5.94(4.93)
8.0	2.06(0.33)		
10.0		77(30)	1.49(0.10)
	Complex Noble Metal		
1.0	nd[1]	>40	14(5)
	Fe-free System		
1.0	3.25(1.24)	>22	400(145)
	Palme and Schmitt (1984)		
	0.3-2.3	588-2700	

[1] Zr in the metal phase is below the detection limit of the electron probe.

References: [1] El Goresy A. et al. (1978) *Proc. Lunar Planet. Sci. Conf. 9th.*, 1279-1303. [2] Grossman L. (1980) *Ann. Rev. Earth Planet. Sci.* **8**, 559-608. [3] Jones J.H. and Burnett D.S. (1980) *Proc. Lunar Planet. Sci. Conf. 11th.*, 995-1001. [4] Fegley B. ,Jr. and Kornacki A.S. (1984) *Earth Planet. Sci. Lett.* **68**, 181-197. [5] Palme H. and Schmitt W. (1984) *Lunar and Planetary Science XV*, 623-624. [6] Treiman A.H. et al. (1991) *Lunar and Planetary Science XXII*, 1413-1415. [7] Jurewicz S.R. and Jones J.H. (1992) *Lunar and Planetary Science XXIII*, 645-646.[8] Beckett J.R. (1986) Ph.D. Thesis, Univ. of Chicago.

EXPERIMENTAL SEGREGATION OF IRON-NICKEL METAL, IRON-SULFIDE , AND OLIVINE IN A THERMAL GRADIENT: PRELIMINARY RESULTS. Stephen R. Jurewicz and J.H. Jones, Mail Code SN4, NASA Johnson Space Center, Houston, Texas 77058

INTRODUCTION: Speculation about the possible mechanisms for core formation in small asteroids raises more questions than answers. Petrologic evidence from iron meteorites, pallasites, and astronomical observations of M asteroids suggests that many small bodies were capable of core formation. Recent work by Taylor [1] reviews the geochemical evidence and examines the possible physical/mechanical constraints on segregation processes. Taylor's evaluation suggests that extensive silicate partial melting (preferably 50 vol.% or greater) is required before metal can segregate from the surrounding silicate and form a metal core. The arguments for large degrees of silicate partial melting are two-fold: 1) elemental trends in iron meteorites require that the metal was at its liquidus, and 2) experimental observations of metal/sulfide inclusions in partially molten silicate meteorites show that the metal/sulfide tends to form spherules in the liquid silicate due to surface tension effects (Takahashi [2], Walker and Agee [3], Dickinson and Lofgren [4]). Taylor points out that for these metal spherules to sink through a silicate mush, high degrees of silicate partial melting are required to lower the silicate yield strength.

Although some qualitative experimental data exists, little is actually known about the behavior of metals and liquid sulfides dispersed in silicate systems. In addition, we have been impressed with the ability of cumulative olivine to expel trapped liquid when placed in a thermal gradient (Walker et al. [5]). Consequently, we undertook to: 1) experimentally evaluate the potential for metal/sulfide/silicate segregation in a thermal gradient; and 2) obtain quantitative data of the wetting parameters of metal-sulfide melts among silicate grains.

EXPERIMENTAL: San Carlos olivine was selected as the silicate starting material because of its abundance and because olivine is the dominant silicate mineral in planetary mantles. Iron and nickel metal powders were used for the metal fraction and powdered pyrite was used for the sulfide. The starting composition was selected to be 60 wt.% olivine (76.1 vol.%), 25 wt.% Fe (13.3 vol.%), 5 wt.% Ni (2.3 vol.%), and 10 wt% FeS_2 (8.3 vol.%). Thus, the total volume fraction of metal + sulfide in the system was 24%. Both olivine and pyrite were ground to fine powders before being blended in an agate mortar with the iron and nickel powders until uniform.

The starting mix was loaded into a fired pyrophyllite capsule with a 10mm long by 2mm diameter sample chamber. The capsule was then loaded into a piston cylinder assembly such that the top of the capsule was next to the control thermocouple. Based on thermal gradient measurements of the piston cylinder assembly employed, we estimate the bottom of the charge to be about 100-150 degrees colder than the thermocouple reading. The assembly was loaded into the piston-cylinder apparatus and run at 10kb pressure and 1200°C for 8 days. Runs were quenched to near room temperature within 10 seconds. After quenching, the runs were sectioned parallel to the long axis and polished for microstructural analysis. Chemical compositions were obtained using standard WDS analysis techniques on the CAMECA microprobe at JSC.

RESULTS: Figure 1 is a reflected-light photograph of the 8 day run. Figure 1 only shows the bottom 4mm of the charge. The total length of the sample after the run is 6-7mm. The abrupt change in reflectivity in the center of the photograph marks the boundary between two distinct regions of the charge. The higher reflectivity lower region is composed of Fe-Ni-metal and olivine and the upper darker region is composed of Fe-Ni sulfide and olivine. The segregation of sulfide and metal into the two regions is complete. The bright band at the bottom of the charge is Fe-Ni-metal.

Microstructural examination shows that the uppermost portion of the sulfide-olivine region appears to have approached textural equilibrium (as shown in the SEM photograph in Fig. 2), and contains about 10 vol.% sulfide by visual estimate. The volume fraction of sulfide increases down the thermal gradient and near the sulfide/metal interface the volume fraction of sulfide is estimated at 15-20%. On the olivine/metal side of the boundary, the Fe-Ni-metal fraction is estimated at 30-40 vol.%. The volume fraction of metal in the rest of olivine/metal region varies between 30-50 vol.%. Thus, the metal + sulfide component at the hot end of the charge has decreased, whereas the metal fraction at the cold end has increased.

The equilibrated-looking texture of the uppermost olivine/sulfide region permitted the measurement of wetting angles between the sulfide (liquid at run temperature) and the olivine. One hundred angles were measured and processed as described in Jurewicz and Jurewicz [6]. The olivine/sulfide liquid wetting angle was

determined to be 92°. This wetting angle value implies that a critical melt fraction must be exceeded to establish interconnectivity.

DISCUSSION: Our experiments demonstrate essentially complete metal/sulfide segregation in a thermal gradient and the beginnings of olivine/metal-sulfide segregation in a period of 8 days at relatively moderate temperature. This segregation occurred with 0% silicate partial melting and < 40% (by weight) melting of the metal+sulfide assemblage. Consequently, the total volume fraction of melting within the system is constrained to be $< 13 \pm 3\%$. It is especially interesting to note that sulfide did not simply melt and migrate to the top of the charge, but all the solid Fe-Ni metal moved to the bottom. Obviously, this is a complicated experiment and the exact segregation mechanisms and their respective contributions are debatable. Gravitational segregation is difficult to invoke because only about 13 vol.% of the sample is liquid at run conditions. However, the observation that the Fe-metal moves to the cold end of the charge is consistent with the results of Jones and Walker [7] for thermal diffusion of Fe in metal-sulfide systems. Given that diffusivities in liquid metals are generally on the order of $1x10^{-5}$ cm^2/sec [8], thermal diffusion cannot be ruled out. On the time scale of our experiments, the diffusive scale length is approximately 2.5 cm, considerably longer than the experimental charge. Our tentative conclusion is that solid metal dissolved at the hot end and precipitated at the cold end. Given the inevitability of boundary layers and thermal gradients in natural systems, we believe that this mechanism should be considered in discussions of core formation.

REFERENCES: [1] Taylor G.J. (1992) *J. Geophys. Res.* **97**, 14717-14726. [2] Takahashi E. (1983) *Mem. Nal. Inst. Polar Res. Spec. Issue Jpn.* **30**, 168-180. [3] Walker D. and Agee C.B. (1988) *Meteoritics*, **23**, 81-91. [4] Dickinson T.L. and Lofgren G.E.(1992) *Lunar and Planetary Science XXIII*, 307-308. [5] Walker D., Jurewicz S.R., And Watson E.B. (1988) *Conrib. Mineral. Petrol.* **99**, 306-319. [6] Jurewicz S.R. and Jurewicz A.J.G. (1986) *J. Geophys. Res.* **91**, 9277-9282. [7] Jones J.H. and Walker D. (1991) *Proc. Lunar Planet. Sci. Conf. 21st.*, 367-373. [8] Leymonie C. (1963) Radio Tracers in Physical Metallurgy, Wiley, NY.

FIG. 1

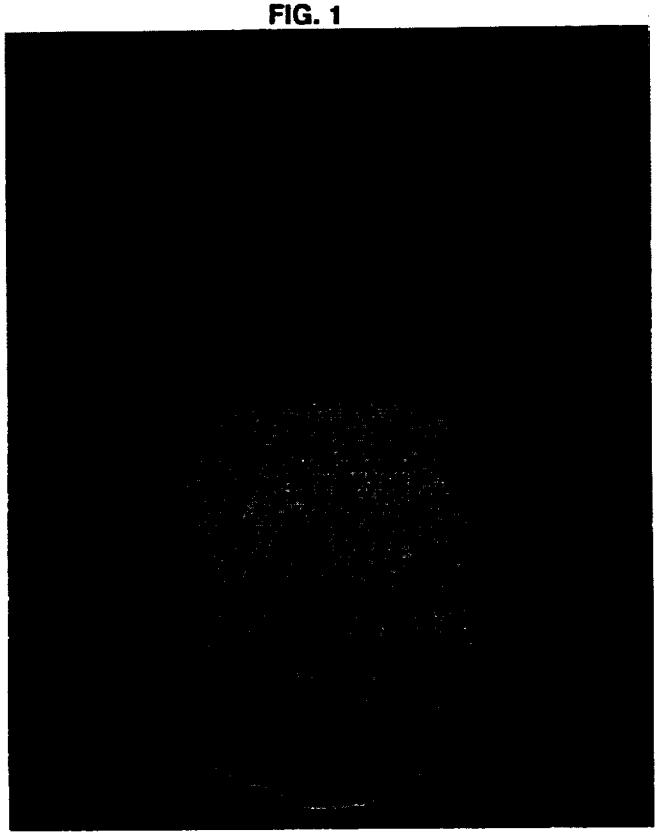

FIG 2.

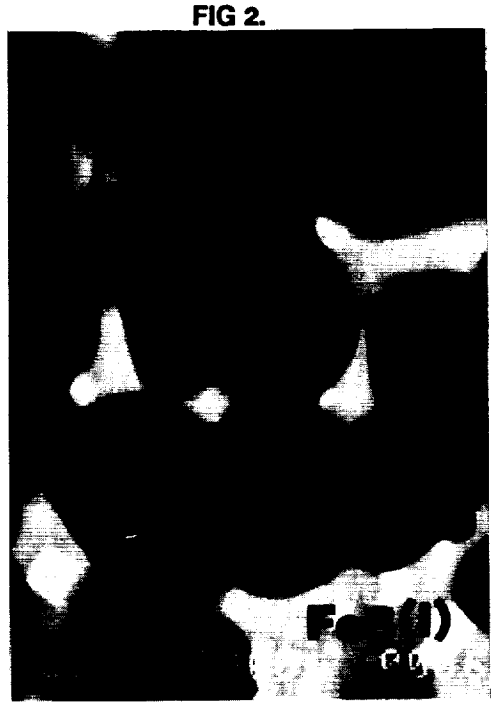

THE HISTORY OF MARE VOLCANISM IN THE ORIENTALE BASIN: MARE DEPOSIT AGES, COMPOSITIONS AND MORPHOLOGIES S.D. Kadel and R. Greeley, *Department of Geology, Arizona State University, Tempe, Arizona 85287*; G. Neukum and R. Wagner, *German Aerospace Research Establishment (DLR), Institute for Planetary Exploration, Berlin/Oberpfaffenhofen, Germany.*

The eruptive history of mare basalts in the Orientale Basin has been studied, using Lunar Orbiter IV high-resolution photographs, Zond 8 photographs, and recently acquired Galileo EM-1 multispectral images [1,2]. This work represents a refined set of compositional data, incorporating the use of a linear mixing model for mare compositions, crater count data, and a comprehensive morphologic analysis of Orientale Basin mare deposits. Evidence for multiple eruptive episodes has been found, with compositions ranging from medium- to high-Ti basalt (<4 to >6 wt. % TiO_2). Eruptive styles included flood, rille-forming and shield-forming eruptions. Impact crater densities of mare units in the Orientale Basin enable determination of the ages of these deposits, using the method of Neukum et al. [3]. Earliest eruptions of mare basalt in the basin occurred at ≥3.70 Ga and the latest eruptions occurred at about 2.3-2.5 Ga. Hence, mare volcanism occurred over a period of nearly 1.5 Ga.

The spectral slope between 0.40 μm and 0.56 μm can be used to obtain estimates of the Ti content (expressed as wt. % TiO_2) of mature mare soils [4,5]. Galileo 0.41/0.56 μm spectral reflectance ratio images indicate that medium-Ti (<4 wt. % TiO_2) basalt signatures are present in the northern and west-central regions of Mare Orientale, in a narrow bench around its southern and western margins, and in a mare patch just offshore to the southwest. Medium-high-Ti (3-7 wt. % TiO_2) basalt signatures are present throughout most of southern and eastern Mare Orientale. Small areas of high-Ti (>6 wt. % TiO_2) basalt are present in southeastern Mare Orientale, although these deposits do not approach the TiO_2.contents (>10 wt. %) of the high-Ti Apollo 11 or Apollo 17 basalts. Medium-Ti (<4 wt. % TiO_2) basalt signatures are present in the northern and northeastern mare deposits of Lacus Veris, whereas medium-high-Ti (3-7 wt. % TiO_2) signatures dominate the central and southern deposits. Medium-high-Ti (3-7 wt. % TiO_2) signatures are observed for the northern mare deposit of Lacus Autumni, and medium-Ti (<4 wt. % TiO_2) signatures are present in the central and southern Lacus Autumni mare deposits.

In order to distinguish between medium-Ti mare and medium-high-Ti mare contaminated with Ti-poor highlands material, it is necessary to "unmix" the components present in the mare surface soils. A three-component linear mixing model has been applied to the Galileo spectral reflectance data for the Orientale Basin. The resulting endmember fraction data, when combined with a survey of possible sources of contamination, suggest that the medium-Ti signatures in northern Mare Orientale and northern Lacus Veris are a result of contamination of medium-high-Ti basalt with highland ejecta from craters Maunder and Lowell. In addition, there are localized areas of contamination caused by smaller fresh highland craters adjacent to southeastern Lacus Veris and northwestern Mare Orientale. The medium-Ti signatures in west-central Mare Orientale, the nearby mare bench, the offshore mare patch to the southwest, northeastern Lacus Veris, and central Lacus Autumni represent uncontaminated medium-Ti basalt compositions for these mare deposits.

A morphologic survey of mare deposits in the Orientale Basin gives an indication of the styles of volcanism involved during their emplacement, as the surface features of lava flows are related to eruptive style [6,7]. Mare Orientale was emplaced primarily by flood eruptions, as evidenced by the presence of several large collapse depressions and a paucity of sinuous rilles. Lacus Veris was emplaced primarily by moderate effusion rate eruptions, as sinuous rilles are abundant. The most recent eruptions in central Lacus Veris were of low effusion rate, producing numerous mare domes. Northern and southern Lacus Autumni were emplaced at moderate

effusion rates, as evidenced by prominent sinuous rilles, and the northern mare deposit lavas (which are very thin and have small dark-mantle-like deposits associated with them) appear to have had a higher volatile content than others in the basin. Central Lacus Autumni was emplaced as a flood basalt, as indicated by numerous small collapse features.

Synthesis of all the above information suggests the following emplacement and modification history of mare deposits in the Orientale Basin:

1) Medium-Ti basalt flood eruptions fill much of the center of the Orientale Basin (≥3.70 Ga).
2) Initial eruptions occur in northeastern Lacus Veris, and are medium-Ti basalts emplaced at moderate effusion rates (3.58 + 0.05/-0.06 Ga).
3) Northern Lacus Veris is emplaced as rille-forming eruptions of medium-high-Ti basalt (~3.45 Ga).
4) Much of Mare Orientale is again flooded (≤3.45 Ga), this time with medium-high-Ti basalts. Subsidence of Mare Orientale occurs before, during and after emplacement of this basalt, leaving the older medium-Ti basalt exposed only in west-central Mare Orientale and as a shelf along its southern and western margins. The last eruptions in southeastern Mare Orientale are of Ti-rich basalts.
5) Thin northern Lacus Autumni unit is emplaced (~3.40 Ga) by volatile-rich, rille-forming eruptions of medium-high-Ti basalt. Southern Lacus Autumni mare patches are emplaced as rille-forming eruptions at about the same time.
6) Central Lacus Autumni is emplaced (2.85 +0.28/-0.57 Ga) as flood eruptions of medium-Ti basalt.
7) Central Lacus Veris is emplaced (2.29 +0.51/-0.55 Ga) as rille-forming eruptions of medium-high-Ti basalts. Late-stage eruptions have sufficiently low effusion rates to produce numerous mare domes.
8) Craters Lowell and Maunder are formed, blanketing northern Lacus Veris and northern Mare Orientale with extensive amounts of highland ejecta.
9) Various small Copernican impact craters form in highlands adjacent to mare deposits causing localized contamination of mare surfaces with highlands materials.

A more refined compositional study of the Orientale mare deposits will be possible as a result of a high-resolution (both spectral and spatial) Lunar Scout mission. However, more precise dating of the eruptive events will have to await direct analysis of sample materials from the mare deposits.

[1] M.J.S. Belton et al. (1992) *Science, 255*, 570-576. [2] S.D. Kadel and R. Greeley, (1992) *LPSC XXIII*, 647-648. [3] G. Neukum et al. (1975) *The Moon, 12*, 201-229. [4] C.M. Pieters (1978) *Proc. Lunar Planet. Sci. Conf., 9th*, 2825-2849. [5] M.P. Charette et al. (1974) *J. Geophys. Res., 79*, 1605-1613. [6] R. Greeley (1976) *Proc. Lunar Planet. Sci. Conf., 7th*, 2747-2759. [7] J.W. Head et al. (1981) *BVSP*, 753.

N94-10290

THE AL RAIS METEORITE: A CR CHONDRITE OR CLOSE RELATIVE?; G.W. Kallemeyn, Institute of Geophysics and Planetary Physics, University of California, Los Angeles, CA 90024, USA.

Although the classificational group 'CR' was first put forth by McSween (1979) more than 10 years ago, it included only the Al Rais and Renazzo meteorites. It has only been the relatively recent discovery of several CR-related chondrites in Antarctica and the Sahara that has provided the necessary research material for an extensive group description and classification (Weisberg et al., 1993); Bischoff et al., 1993). Some 22 separate specimens representing at least 6 falls are now purportedly members of the CR group. In light of all this new data, an old question can once again be raised as to whether or not Al Rais should be classified in the same distinct group as Renazzo.

A previous compositional study by Kallemeyn and Wasson (1982) showed that Al Rais and Renazzo are probable members of the same clan, possibly related to the CI clan, based on similarities in refractory lithophile element abundances. They concluded, though, that the low volatile abundances of Renazzo (≤CV chondrites) relative to Al Rais (mid CM-CV range) precluded their placement in the same distinct group. Recently, Weisberg et al. (1993) presented petrographic evidence supporting the inclusion of Al Rais in the CR group, claiming that the volatile differences are the result of differences in abundances of matrix and/or dark inclusions.

We now have compositional data on five CR chondrites in addition to data on Al Rais and Renazzo. CI-normalized refractory (Al, Sc, Ca, REE, V) and common nonvolatile (Mg) lithophile abundances are very similar among all the chondrites studied, close to CI levels. Refractory siderophile (Os, Ir, Ru) and common siderophile (Fe, Ni, Co) abundances are also very similar amoung all the chondrites. Volatile lithophile abundances (Mn, Na, K) show small differences between the different chondrites, but the abundances in Al Rais are always highest. Among the volatile siderophiles and chalcophiles, abundances in Al Rais are distinctly higher than those in Renazzo and the Antarctic chondrites which cluster together. These differences in volatile abundances cannot simply be attributed to differences in abundances of matrix and dark inclusions. Abundance data for nine volatile elements (including data for El Djouf from Bischff et. al (1993)) shows no distinct correlation with matrix and dark inclusion abundances among the CR chondrites studied.

A very useful method for distinguishing between all known chondrite groups is a comparison of Zn/Mn and Al/Mn atom ratios. On such a plot the Antarctic CR chondrites and Renazzo group together closest to the CO chondrites (to which they have no petrographic similarity) and are quite distinct from Al Rais which plots close to the CM group. The carbonaceous chondrite groups also show a strong correlation between Ga and Sb abundaces. Al Rais plots between the CM and CO groups on such a plot, distinctly separate from Renazzo and the other CR chondrites which plot together in the CK-CV range.

Whole-rock oxygen isotope data for Al Rais (Weisberg et. al, 1993) also show it different from Renazzo and the other CR chondrites. The $\delta^{18}O$ value for Al Rais is nearly 5‰ higher than the closest CR chondrite (Renazzo). This is as

THE AL RAIS METEORITE: G.W. Kallemeyn

great as the range shown by all of the CR chondrites. The Al Rais whole-rock oxygen isotope data does not fall on a line fit through Renazzo and the other CR chondrite whole-rock data. But the Al Rais data does fall on an extention of a line fit through CK-CO-CV whole-rock data.

The petrographic data for Al Rais and the CR chondrites (Weisberg et. al, 1993) also show distinct differences. The metallic Fe-Ni in Renazzo the other CR chondrites (~0.7) is twice that in Al Rais. The difference in the (matrix+dark inclusion)/chondrule ratio between Al Rais (1.85) and the nearest CR (1.06) is nearly twice the range shown by Renazzo and the other CR chondrites.

In nearly every case of differences in taxonomic properties, the new CR chondrites from the Antarctic and Sahara, tend to either cluster around Renazzo. None cluster around Al Rais, or even fall in the hiatus between Al Rais and Renazzo. It would appear that Al Rais should not strictly be classified as a CR. Although it is closely related to the CR chondrites in some ways, this relationship is probably no more than that between an LL chondrite and an L chondrite.

References: Bischoff et. al (1993) Geochim. Cosmochim. Acta., in press. Weisberg et. al (1993) Geochim. Cosmochim. Acta., in press.

CHEMICAL AND ISOTOPIC COMPOSITIONS IN ACID RESIDUES FROM VARIOUS METEORITES

N. Kano[1], K. Yamakoshi[1], H. Matsuzaki[1] and K. Nogami[2]
1) Institute for Cosmic Ray research, University of Tokyo, Tanashi, Tokyo 188, Japan
2) Department of Physics, Dokkyo University School of Medicine, Tochigi 321-02, Japan

To study the pre-history of the solar system such as possible direct evidences for processes of nucleosynthesis in the pre-solar stage and detection of extinct radioactive nuclide, we are planning to carry out systematic isotopic investigations on Ru, Mg and so on in primordial samples. In this paper, we present the results of chemical compositions of acid residues obtained from three types of meteorites [1) Canyon Diablo (IA), 2) Allende (CV3), 3) Nuevo Mercuro (H5)] and the preliminary results of Ru isotopic compositions.

Many studies on isotopic anomalies of elements, specially noble gases, in acid residues from primitive meteorites have been done[e.g. 1-3]. Particularly, Zinner et al. have recently recovered silicon carbide from therein, and detected isotopic anomalies of noble gases, C, N, Si, Mg, Ba etc. [4-7]. Therefore, these samples are considered to be of precursor origins which have survived the pre-solar nebula stages.

The method to recover acid residues from meteorites in our work are as follows; After removing fusion crusts with a ceramics blade grinder, the three types of meteorites were disaggregated by using the freeze-thaw method and were dissolved by repeated alternating treatments with HCl, HF, and aqua regia at room temperature. The acid residues were concentrated by centrifuging and then dried up. The weight of the acid residues we obtained are listed in Table 1 with the total weight of the bulk meteorite.

Elemental analyses were carried out by combustion method, INAA and AAS. The typical results of elemental analyses are shown in Table 2 and Fig. 1. Fig. 1 show that refractory elements are generally enriched in acid residues regardless of the kind of meteorites. It matches the features that acid residues contain primary condensates from the cooling solar gas as well as extra-solar grains. Particularly, in acid residue of Allende, enrichment factors for refractory siderophiles are generally higher (7-20 times/CI), however in the cases of W and Mo, they are slightly depleted compared with those of Canyon Diablo. Since both elements would be the first metals to be oxidized under high oxygen fugacity[e.g. 8,9], acid residue of Allende should contain fractions that were produced under oxidising conditions. And the considerable diverse chemical compositions of acid residues between these meteorites deserves our attention. It may arise from the diference of generative environmental conditions of these meteorites in space.

The samples were decomposed in sealed teflon vessels by a microwave dissolution method and then Ru was separated by distillation[10]. The total procedural Ru blank was measured by isotope dilution method using ^{104}Ru enriched spike, and only a few ng were detected. Ru isotopic analyses have been performed by a VG 354 thermal ionization mass spectrometer. Ru ion beams in each samples were so faint because of its high ionization potential(7.36eV) and small sizes of samples that they were detected by the Daly Photomultiplier detector equipped with an ion counting assembly. In mass spectrometric technipues of Ru, the zone-refined (99.995%) outgassed V-shaped Re single filament with silica gel and phosphoic acid was employed.

Fig. 2 shows preliminary results for Ru isotopic analyses. In these measurements, all ratios of Ru were corrected for mass fractionation by normalization to ^{99}Ru/^{102}Ru=0.4042 (exponential law) provisionally [11]. And Mo ion beam from Re filaments were not negligible as the filament temperature increases, so Mo isobaric interference was corrected by the monitoring of ^{97}Mo based on recent precise measurements of Mo isotopes[12]. In the measurement of acid residue of Allende, all ratios were not found to be distinguishable from terrestrial values within the experimental errors, though errors were rather high because of the intererence of molecular ion peaks and small Ru ion beam intensities. Poths et al.[13] also reported that in two aliquants of acid residue of Allende, all isotopic ratios of Ru are indistinguishable from the terrestral values within the experimental errors.

The fact that Ru isotopic anomalies have been not yet detected even in Allende acid residue, which is considered to be the one of the most primordial and exotic samples, suggests as follows; Ru components originate from interstellar medium might be very rare and/or the diffusion of Ru might be unexpectedly rapid due to high temperatures and shock waves or something during the condensation stage of the solar system.

However, judging from fration % of acid residue in Allende and Fe contens (~1%) in these acid residues, it could be said that the acid treatments in this work were relatively moderate and/or incomplete. We are, therefore, going on with acid treatments still more. In other words, the acid residues we obtained here are not so definite samples. So, the chemical compositions of the acid residues differ with the kinds of acids, and the conditions

under acid treatments.

Unfortunately, we could not identify what kind of minerals were there in these acid residues by our SEM (HORIBA EMAX-8000) this time. We are now preparing to check these acid residues by high resolution transmission electron microscopy (TEM) to identify what kind of minerals contained there. And much more precise and reliable isotopic data will be obtained, then more detailed discussions on the prehistory of the solar system, and the origin of acid residues could be done, too.

^{104}Ru enriched spike used in this work were kindly supplied by Dr. H.Hidaka. We are grateful to Dr. T. Seki in Org. Anal. Center (Dept. of Chem., Fac. of Science, Univ. of Tokyo) for analyzing C,N,H and S in acid residues we used in this work by combustion method. We also would like to thank Prof. K.Tomura and staff of Inst. for Atom. Energy Res. in Rikkyo Univ. for neutron irradiations of the samples and use of the counter facilities.

References [1] Lewis, R. S. et al. (1983) Science, **222**, 1013; [2] Lugmair, G. W. et al. (1983) Science, **222**, 1015; [3] Loss, R. D. et al. (1990) GCA, **54**, 3525; [4] Zinner, E. et al. (1989) GCA, **53**, 3273; [5] Zinner, E. et al. (1991) Nature, **349**, 51; [6] Zinner, E. et al. (1991) LPS, **22**,1553; [7] Amari, S. et al. (1992) LPS, **23**, 27; [8] Palme, H. et al. (1982) EPSL, **61**, 1; [9] Fegley, B. and Palme, H. (1985) EPSL, **72**, 311; [10] Terada, K. et al. (1975) Bull. Chem. Soc. Jpn., **48**, 2567 [11] Hutcheon, I. D. et al. (1987) GCA, **51**, 3175; [12] Qi-Lu and Masuda,A (1992) J. Am. Soc. Mass Spec., **3**,10; [13] Poths, H. et al. (1987) GCA, **51**, 1143

Table 1 The weight and fraction % of acid residues

Sample Name	Sample weight (g)	Acid Residue weight (g)	Acid Residue fraction(wt.%)
Canyon Diablo	587.50	3.6425	0.62
Allende	62.379	1.8975	3.04
Nuevo Mercurio	45.104	0.4631	1.03

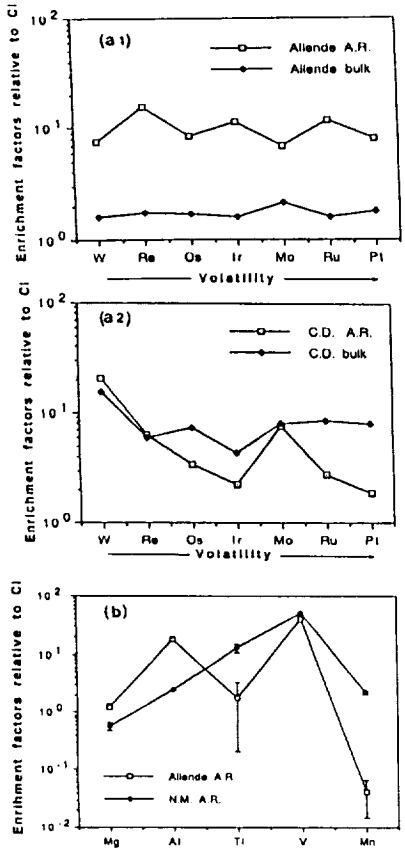

Fig. 1 Enrichment factors in acid residues relative to CI. 1σ error bars are shown when they are larger than the symbols. A.R. stands for "Acid Residue". 3(a1),3(a2): Refractory Siderophile 3(b): Refractory Lithophile (N.M. stands for Nuevo Mercurio)

Table 2 Elemet concentration in acid residues (%) (combustion method)

	C	N	H	S
Canyon Diablo	42.86	2.82	2.72	-----
Allende	9.70	1.80	0.51	0.60
Nuevo Mercurio	-----	0.29	-----	2.22

----- stands for below detection limit.

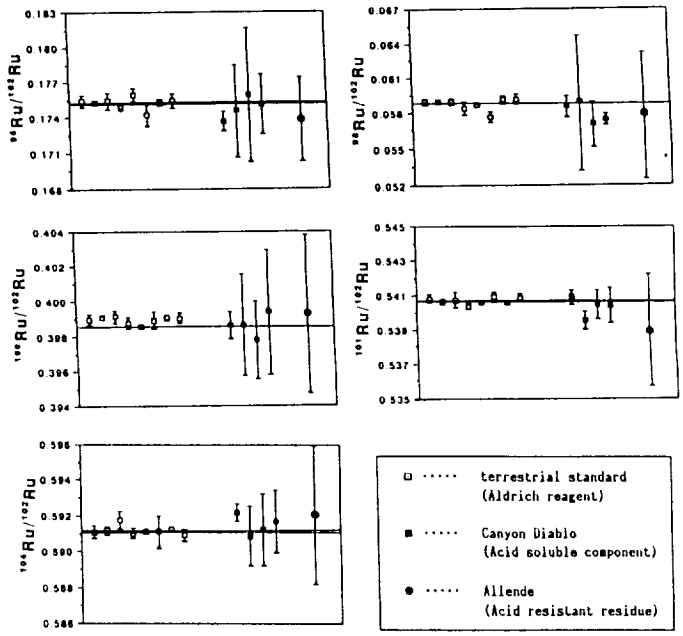

Fig. 2 Preliminary results for Ru isotopic analyses: All isotope ratios are collected for mass fractionation by normalization to $^{99}Ru/^{102}Ru=0.4042$ (exponential law). Errors are 2σ of the mean. The solid lines represent the range of weight means in terrestrial standard.

CRUSTAL STRUCTURE AND IGNEOUS PROCESSES IN A CHONDRITIC IO;

J.S. Kargel, U.S. Geological Survey, Flagstaff, AZ 86001

Liquid sulfur can form when metal-free C1 or C2 chondrites are heated [1]. It may be obtained either by direct melting of native sulfur in disequilibrated C1 or C2 chondrites or by incongruent melting of pyrite and other sulfides in thermodynamically equilibrated rocks of the same composition. Hence, Lewis [1] considered C2 chondrites to be the best meteoritic analog for Io's bulk composition. Metal-bearing C3 and ordinary chondrites are too chemically reduced to yield liquid sulfur and are not thought to represent plausible analogs of Io's bulk composition. An important aspect of Lewis' work [1] is that $CaSO_4$ and $MgSO_4$ are predicted to be important in Io. Real C1 and C2 chondrites contain averages of, respectively, 11% and 3% by mass of salts (plus water of hydration) [2]. The most abundant chondritic salts are magnesium and calcium sulfates, but other important components include sulfates of sodium, potassium, and nickel and carbonates of magnesium, calcium, and iron. It is widely accepted that chondritic salts formed by low-temperature aqueous alteration. Even if Io originally did not contain salts, it is likely that aqueous alteration would have yielded several percent sulfates and carbonates. In any event, Io probably contains sulfates and carbonates.

This report presents the results of a model of differentiation of a simplified C2 chondrite-like composition that includes 1.92% $MgSO_4$, 0.56% $CaSO_4$, 0.53% $CaCO_3$, and 0.094% elemental sulfur [2]. The temperature of the model is gradually increased; ensuing fractional melting results in these components extruding or intruding at gravitationally stable levels in Io's crust. Relevant phase equilibria were reviewed by [3]. A deficiency of high-pressure phase equilibria renders the present model qualitative.

Figure 1 shows the modeled evolution of Io's crust. The most abundant chondritic sulfate, epsomite ($MgSO_4.7H_2O$), melts incongruently in several stages, leaving progressively more dehydrated residua. During stage 1, occurring near 321 K, epsomite yields an aqueous solution containing 33% $MgSO_4$ plus solid hexahydrite ($MgSO_4.6H_2O$). During stage 2, hexahydrite decomposes at 341 K to an aqueous solution of 37% $MgSO_4$ plus residual kieserite ($MgSO_4.1H_2O$). This liquid is denser than the stage 1 crust, so it presumably intrudes beneath the early formed stage 1 crust. During stage 3, elemental sulfur melts at 392 K and intrudes beneath the stage 2 sulfate layer. During stage 4, kieserite melts and produces a very dense solution containing up to 87% $MgSO_4$; this liquid intrudes beneath the sulfur layer. After stage 4 is complete, Io's mostly anhydrous silicate-rich mantle still contains anhydrite ($CaSO_4$) and carbonates (mainly $CaCO_3$). During stage 5, a dense carbonate-anhydrite melt intrudes and possibly mixes with the stage 4 layer.

After stage 5, the layered sulfate-carbonate crust contains 42% water, including some water ice in the surface layer, and pure sulfur resides at a depth of nearly 50 km. To produce an object resembling Io, some process is required to thoroughly desiccate Io's crust. As the crust dries, the sulfate-rich residual solids become denser than sulfur and consequently sink. Sinking sulfates eventually displace sulfur, which rises to the surface. After stage 6, anhydrous carbonates and sulfates reside beneath the sulfur in a layer averaging 25 km thick. Presumably the sulfate-carbonate layer is differentiated, but for simplicity it is depicted in Fig. 1 as a homogeneous layer. Stage 6 might reflect Io's present crustal structure. The modeled thickness of pure sulfur on Io is about 1 km. This layer might be substantially thicker than modeled, perhaps several kilometers, if incongruent fusion of sulfides contributed additional sulfur or if Io was initially composed of C1 chondrite-like material.

While the quantitative aspects of this scenario are very sensitive to the exact types of material accreted by Io, the qualitative aspects are not so sensitive. Qualitatively, the model depends on accretion by Io of material containing salts (such as C1 or C2 chondrites) or on post-accretion formation of salts by aqueous alteration. The model also depends on a workable mechanism to remove water from Io, because all likely salt-rich planetesimals are expected to contain also at least several percent water. If Io initially had accreted a significant amount of water ice, this water would have to be removed. One possible mechanism involves impact erosion by comets, which could account for loss of as much water as occurs in the icy mantles of Ganymede and Callisto (Eugene Shoemaker, personal communication, 1992). Smaller amounts of water may have been sputtered by charged particles. If water loss occurred primarily by impact erosion, then the current prevalence of sulfur volcanism on Io imposes a time constraint on impact erosion. While water was extruded, sulfur may have been "protected" in a rocky core and then lost; only after impact erosion had subsided might sulfur have been extruded and still have remained on Io's surface. According to a scenario modified from that illustrated by Figure 1, Io underwent

early low-temperature aqueous differentiation to form layers B and C; then impact erosion stripped these briny ice layers; then a higher temperature phase of differentiation occurred, when sulfur extruded onto an impact-battered surface; then, finally, molten carbonates and sulfates intruded beneath the sulfur.

Io's sulfur volcanism may be driven by magmatic processes in the sulfate-carbonate layer. The peritectic temperature for $MgSO_4$-rich compositions in the system $MgSO_4$-Na_2SO_4-$CaSO_4$ is 696 K [4]. Addition of carbonates and minor sulfate components probably reduces the peritectic to ~ 450-550 K. Intrusion of molten salts could cause extensive melting of Io's sulfurous upper crust. The temperatures are high enough that a wide range of liquid sulfur allotropes could be erupted, thus accounting for the yellow, orange, red, and black flows photographed by the Voyager spacecraft [5]. It is also possible that high mountain peaks on Io are composed of carbonate-sulfates rather than silicates, as is commonly supposed.

References. [1] Lewis, J.S., 1982, *Icarus*, 50, 103-114. [2] Burgess, R., I.P. Wright, and P.T. Pillinger, 1991, *Meteoritics*, 26, 55-64. [3] Kargel, J.S., 1991, *Icarus*, 94, 368-390. [4] Mukimov, S.M. and Z.I. Filipova, 1949, *Trudy Inst. Khim., Akad. Nauk Uzbek. SSSR, Inst. Khim., No. 2, Obshchaya i Neorg. Khim.*, 1949, 123-132. [5] Sagan, C., 1979, *Nature*, 280, 750-753.

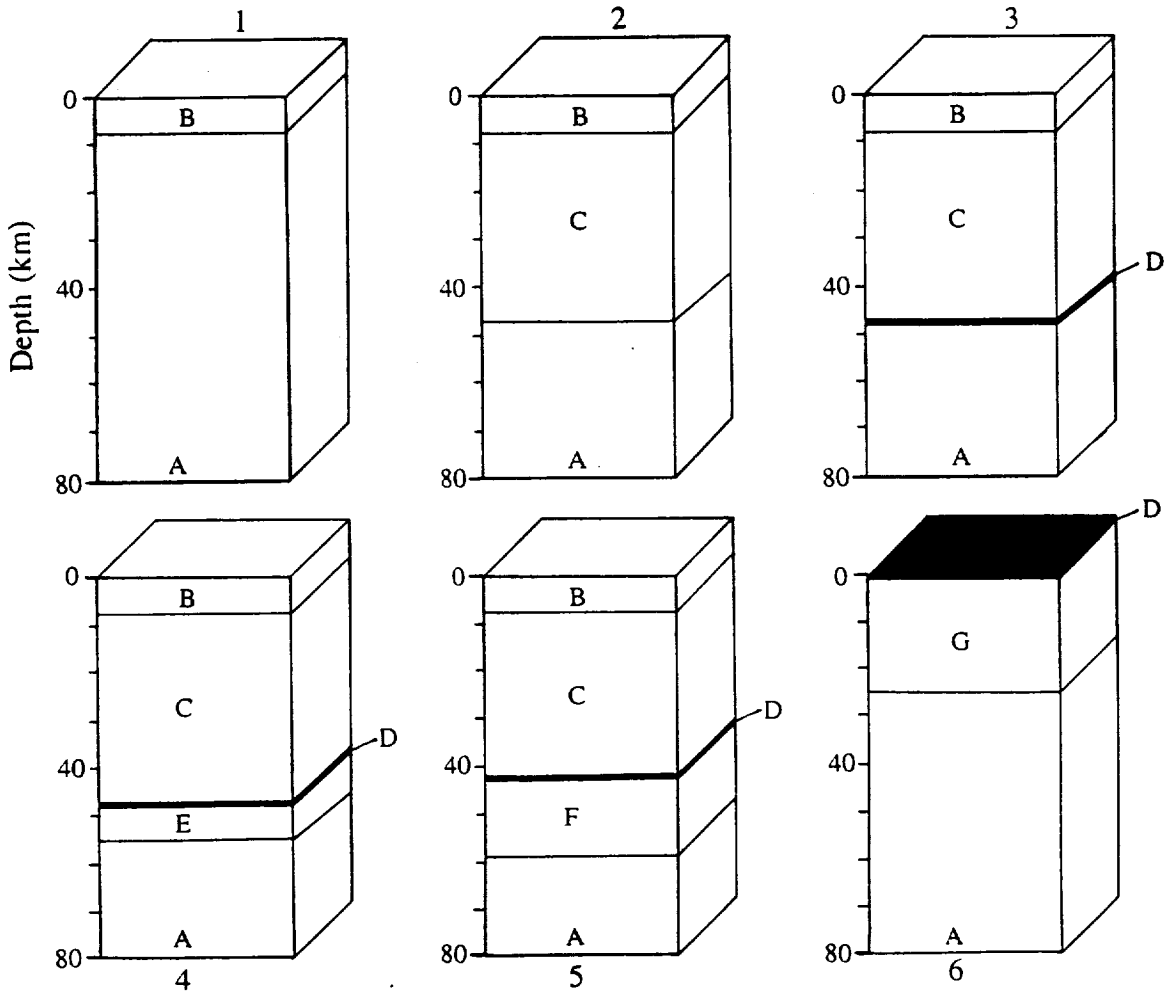

Figure 1. Model showing the evolution of Io's crust during melting stages 1-6. Properties and compositions of rock units are as follows: A, Silicate-rich mantle. B, 33% $MgSO_4$ + 67% H_2O, density = 1.44 g cm^{-3}, melting temperature = 321 K. C, 37% $MgSO_4$ + 63% H_2O, density = 1.53 g cm^{-3}, melting temperature = 341 K. D, Sulfur, density = 2.07 g cm^{-3}, melting temperature = 392 K. E, 87% $MgSO_4$ + 13% H_2O, density = 2.46 g cm^{-3}. F, $MgSO_4$ + $CaSO_4$ + $CaCO_3$ + H_2O. G, Anhydrous sulfate-carbonate layer, density ~ 2.7 g cm^{-3}, melting point < 696 K.

GEOMORPHIC PROCESSES IN THE ARGYRE-DORSA ARGENTEA REGION OF MARS; J.S. Kargel, U.S. Geological Survey, 2255 N. Gemini Dr., Flagstaff, AZ 86001

Introduction. Among many indications of possible ancient Martian glaciation are sinuous eskerlike ridges in southern Argyre Planitia and the Dorsa Argentea region [1, 2]. But, in photogeology, other interpretations are always possible, and what appears eskerlike to one set of eyes may appear quite different to another. Interpretations of these ridges are about as numerous as observers, who collectively have suggested nine distinct hypotheses! Martian sinuous ridges have been interpreted as wrinkle ridges, lava flows, igneous dikes, clastic dikes, linear sand dunes, spits or bars, examples of inverted stream topography, or glacial crevasse fill [3-8]. With Mars Observer en route to Mars the prospects for a narrowing of the debate are bright. The esker hypothesis will gain support if Mars Observer images show that the ridges contain boulders, that the ridges are layered and contain channel structures, that the ridges are modified by thermokarst, or that the ridges occur in close, logical associations with other glacial landforms such as flutes, oriented grooves, and moraines. In the meantime, the evidence presented below bolsters the esker hypothesis, challenges certain alternative ideas, and draws a tentative geomorphic connection between the sinuous ridges of Argyre and those of Dorsa Argentea.

Data. Sinuosity is a key aspect of Martian sinuous ridges. This characteristic of the Martian ridges is compared with sinuosities of suggested terrestrial analogs in Figs. 1-4. These comparisons confirm that, in scale and sinuosity, Martian sinuous ridges resemble many terrestrial river channels and eskers and may be distinguished from terrestrial linear dunes. The data for wrinkle ridges and sinuous ridges overlap considerably, but wrinkle ridges tend to be less sinuous than sinuous ridges; other morphologic aspects of wrinkle ridges clearly distinguish them from sinuous ridges, including the tendency of wrinkle ridges to form en echelon patterns and to have asymmetric cross profiles. One cannot easily rule out the existence of conditions unique to Mars or to these regions of Mars that might have contributed to formation of unusual wrinkle ridges or sand dunes or some other feature. However, a simpler explanation is that the patterns of Martian sinuous ridges resemble terrestrial channels and eskers because all these features were deposited by channelized water flows. This explanation is also consistent with the hypothesis of inverted stream topography, but the occurrence of other possible glacial landforms in the Argyre and Dorsa Argentea regions favors the esker analog.

Figure 5 shows a longitudinal topographic profile from a mountainous region (near 79° S lat, 350° long) to what is believed to be the proximal end of Dorsa Argentea ridges, to the distal end, along a deep channel incised through the Charitum Montes, and into the area of sinuous ridges in Argyre Planitia. Although topographic uncertainties are large, the data are consistent with a continuous down-gradient from the mountainous region (where peaks probably exceed 7000 m in elevation) to the floor of Argyre. If the Mars Observer laser altimeter confirms this gradient, it will be a powerful argument favoring a gravitationally driven fluid-flow origin of the sinuous ridges. Such a gradient also is consistent with an integrated interpretation of sinuous ridges and other landforms of possible glacial origin in the Dorsa Argentea and Argyre regions.

Conclusions. The sinuosities of Martian sinuous ridges are comparable with those of terrestrial rivers and eskers. The esker hypothesis is favored because other plausible glacial landforms occur in the Argyre and Dorsa Argentea regions. Glacial features in these two regions may well have been related to the movement of an ice sheet from the south polar area across Dorsa Argentea and into Argyre Planitia.

References. [1] Kargel, J.S. and R.G. Strom (1992) *Geology*, **20**, 3-8. [2] Kargel, J.S. and R.G. Strom (1991) *Lun. Planet. Sci.*, **XXII**, 683-684. [3] Carr, M.H. and 12 others (1980) *Viking Orbiter Views of Mars*, Washington, D.C., U.S. Government Printing Office, p. 136. [4] Howard, A.D. (1981) *Repts. Planet. Geol. Prog.*, NASA TM-84211, 286-288. [5] Parker, T.J., D.C. Pieri, and R.S. Saunders (1986) *Repts. Planet. Geol. Prog.*, NASA TM-88383, 468-470. [6] Tanaka, K.L. and D.H. Scott (1987) Geologic map of the polar regions of Mars, *U.S. Geol. Surv. Misc. Inv. Ser. Map I-1802-C*. [7] Ruff, S.W. and R. Greeley (1990) *Lun. Planet. Sci.*, **XXI**, 1047-1048. [8] Metzger, S.M. (1991) *Lun. Planet. Sci.*, **XXII**, 891-892.

Figure captions. Figure 1. Sinuosities of Martian sinuous ridges in Argyre region (solid circles) and Dorsa Argentea region (solid squares) and of Canadian eskers (open squares).

Figure 2. Sinuosities of Argyre's ridges (solid squares) and terrestrial eskers (large circles) and rivers (Yangtze, small circles; Niger, triangles; middle Porcupine, diamonds; and lower Porcupine, open squares).

Figure 3. Sinuosities of sinuous ridges in Argyre region (solid diamonds) and Dorsa Argentea region (solid squares), and of terrestrial linear sand dunes (Simpson Desert, Australia, open circles; Namib Desert, southern Africa, open squares; and Erg Chech, North Africa, open diamonds).

ARGYRE - DORSA ARGENTEA REGION OF MARS: Kargel, J.S.

Figure 4. Sinuosities of sinuous ridges in Argyre and Dorsa Argentea regions (solid symbols) and wrinkle ridges in Lunae Planum (open circles).

Figure 5. Longitudinal topographic gradient in Dorsa Argentea and Argyre regions (see text).

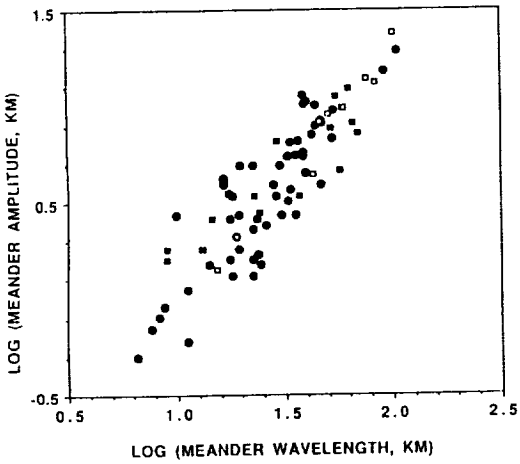

Figure 1.

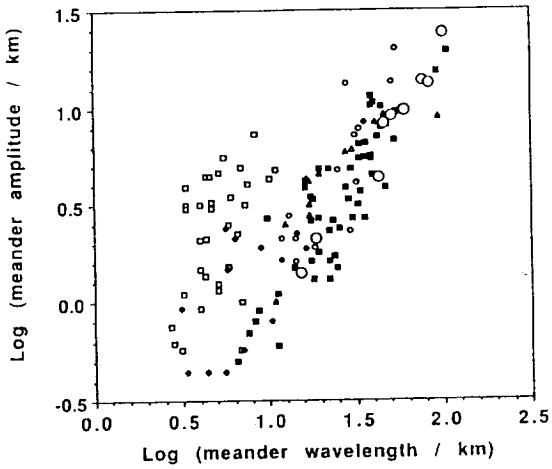

Figure 2.

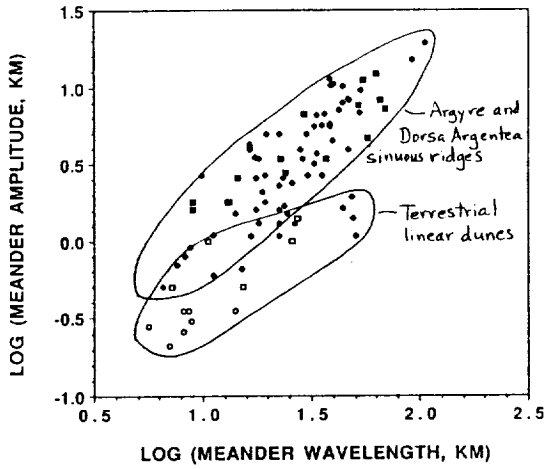

Figure 3.

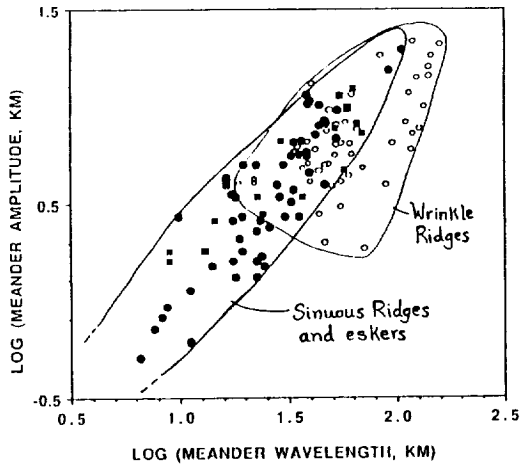

Figure 4.

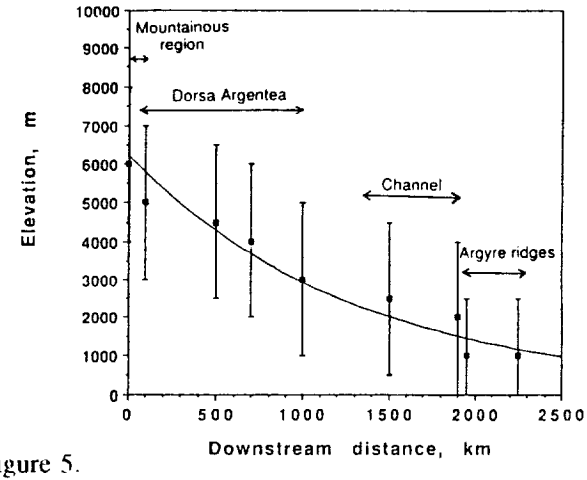

Figure 5.

THE RHEOLOGY AND COMPOSITION OF CRYOVOLCANIC FLOWS ON ICY SATELLITES;
Jeffrey S. Kargel, U.S. Geological Survey, 2255 Gemini Dr., Flagstaff, AZ 86001

The rheologic properties of terrestrial lavas have been related to morphologic features of their flows, such as levees, banked surfaces, multilobate structures, and compressional folds. These features also have been used to determine rheologies and constrain the compositions of extraterrestrial flows. However, with rare exceptions, such features are not resolvable in Voyager images of the satellites of outer planets. Often only flow length and edge thickness of cryovolcanic flows can be measured reasonably accurately from Voyager images. The semiempirical lava-flow model presented below is a renewed effort to extract useful information from such measurements.

The model supposes that a flow moves downslope until its chilled crust attains a critical fraction of flow thickness. The solidifying crust is assumed to thicken at a rate proportional to the inverse square root of time, analogous to the solidification of the crust on a lava lake. The model does not explicitly account for fracturing and foundering of crust, for suspension of crystallized solids in the liquid underlying the crust, nor for extrusion of fresh, hot slurry at the leading edges of lava flows. Therefore, this model does not accurately portray the behavior of real lava flows. Despite this simplistic approach, the model successfully relates the Newtonian viscosities of pure phase liquid lavas to actual flow thicknesses and lengths on Earth and the Moon, as shown below. An accurate analytical solution to the problem of the freezing crust (the Stefan problem) was presented by [1]. The time, t_c, for the crust to thicken to the critical fraction of flow thickness defines a flow emplacement time. A characteristic flow speed, **u**, is defined as $u = L/t_c$, where L is the length of the flow. No unique critical ratio of crust thickness to flow thickness, T_c/T_f, has been defined by actual measurement or by analytical methods. Setting $T_c/T_f = 1/6$ forces the model of one particularly well documented lava flow, Kilauea's Royal Gardens flow of 1983, to reproduce the observed characteristic flow speeds and the same effective viscosities as given by [2]. Henceforth, it is assumed that this ratio holds for all other flows. The applicability of this assumption to icy flow is supported by laboratory data for ammonia-water slurries [3]. Although the exact physical significance of this ratio is unclear, it might relate to existing concepts of threshold values such as the Bingham yield strength.

An effective viscosity (the 'morphologic viscosity') is estimated by combining the flow speed calculated in the manner just described with the analytical solution presented by [1], relating the viscosity of a fluid flowing down an inclined plane to other parameters, including flow speed:

$$\mu_{morp} = (\rho_l g \sin\alpha T_f^4 \rho_c C) / (288 L \lambda^2 k) \quad (1)$$

where μ_{morph} is morphologic viscosity, ρ_l is the density of liquid, α is surface slope, T_f is flow thickness, ρ_c is the density of the solidified crust, **C** is the heat capacity of the crust, **L** is the length of the lava flow, **k** is the thermal conductivity of the crust, and λ is a term given by iteration of the transcendental equation (from [1]:

$$e^{-\lambda 2}/\lambda erf\lambda = Q\sqrt{\pi}/C(T_m - T_o) \quad (2)$$

where **Q** is the heat of fusion of the lava, T_m is its liquidus temperature, and T_0 is the ambient surface temperature. All temperature-dependent material properties of the crust are averages over the temperature interval T_0 to T_m.

Figure 1 shows the morphologic viscosities of 97 flows plotted against measured or estimated viscosities of these lavas at their liquidus temperatures. Morphologic data for these flows and other relevant information were obtained from literature sources [2,4-11]. These flows include a wide range of terrestrial silicate flows, two sulfur flows, one carbonatite flow, and a lunar flow. They range in length from 5 m to 300 km and in thickness from 3.5 cm to 300 m. The least-squares fit has a slope of unity and an intercept of about 10^5. The modeled morphologic viscosity correctly tracks the actual liquidus viscosity (Fig. 1) even though the mechanics of real lava flows are far more complex than modeled. The dispersion of data about the correlation line indicates a 1σ uncertainty of 1.25 log units in the liquidus viscosity thus determined. A great deal of important physics probably accounts for the dispersion, but for present purposes these effects may probably be ignored.

Calculated viscosities of three flows on Triton and one on Ariel are listed in Table 1. Both viscosities calculated for the flow on Ariel are several orders of magnitude less than calculated by [12]. The liquidus viscosities of Triton's and Ariel's flows are in the range exhibited by multi-component ammonia-water liquids [3,13]. The liquidus viscosities are also much greater than the viscosities of water (10^{-3} Pa-s) and brines (10^{-3} to 10^{-1} Pa-s), and they are much less than the viscosity of ice (warm ice viscosity $\sim 10^3$ Pa-s). These

viscosity comparisons do not necessarily imply that flows on Ariel and Triton are composed of ammonia-water liquids, but such a composition is cosmochemically reasonable.

References. [1] Turcotte, D.L. and G. Schubert, 1982, *Geodynamics*, John Wiley & Sons, New York, 450 pp. [2] Fink, J.H. and J.R. Zimbelman, 1986, *Bull. Volcanol.* **48**, 87-96. [3] Kargel, J.S., S.K. Croft, J.I. Lunine, and J.S. Lewis, 1991, *Icarus*, **89**, 93-112. [4] Moore, H.J. and G.G. Schaber, 1975, *Proc. Lunar Sci. Conf., 6th*, 101-118. [5] Swanson, D.A., T.L. Wright, and R.T. Helz, 1975, *Amer. J. Sci.*, **275**, 877-905. [6] Tazieff, H., 1977, *Bull. Volcanol.*, **40-3**, 189-200. [7] Frazzetta, G. and R. Romano, 1984, *Bull. Volcanol.*, **47-4**, 1079-1096. [8] Murase, T., A.R. McBirney, and W.G. Melson, 1985, *J. Volcanol. Geotherm. Res.*, **24**, 193-204. [9] Duffield, W.A. and G.B. Dalrymple, 1990, *Bull. Volcanol.*, **52**, 475-487. [10] Wadge, G. and R.M.C. Lopes, 1991, *Bull. Volcanol.*, **54**, 10-24. [11] Gadmundsson, A., et al., 1992, *Bull. Volcanol.*, **54**, 238-246. [12] Jankowski, D.G. and S.W. Squyres, 1988, *Science*, **241**, 1322-1325. [13] Kargel, J.S. 1993, *Icarus* (in press).

TABLE 1. Calculated flow viscosities.

Flow name	Satellite	Morphologic viscosity	Liquidus viscosity (Pa-s)	Possible lava compositions (Pa-s)	Unlikely lava compositions
Crater dome flow lat 14N long 39	Triton	1.7×10^{10}	1.7×10^{5}	H2O-NH3-GKWE*	Pure water, brine, pure ammonia-water, or pure ice
Lobate flow lat 9S long 57	Triton	3.1×10^{8}	3.1×10^{3}	H2O-NH3-GKWE*	Pure water, brine, pure ammonia-water, or pure ice
Lake spill flow lat 20N long 20	Triton	1.8×10^{7}	1.8×10^{2}	H2O-NH3 or H2O-NH3-GKWE*	Pure water, brine, or pure ice
Kewpie-Brownie flow**	Ariel	2.3×10^{9}	2.4×10^{4}	H_2O-NH_3-GKWE*	Pure water, brine, or pure ice
		or 4.6×10^{6}	49	H_2O-NH_3 or H_2O-NH_3-GKWE*	

* GKWE = God-Knows-What-Else. Might include methanol, ammonium sulfide, sodium chloride, or other substances providing substantial added freezing-point depression and increased viscosity [3, 4].

**First entry based on assumption of axial eruption; second entry, on assumption of longitudinal flow.

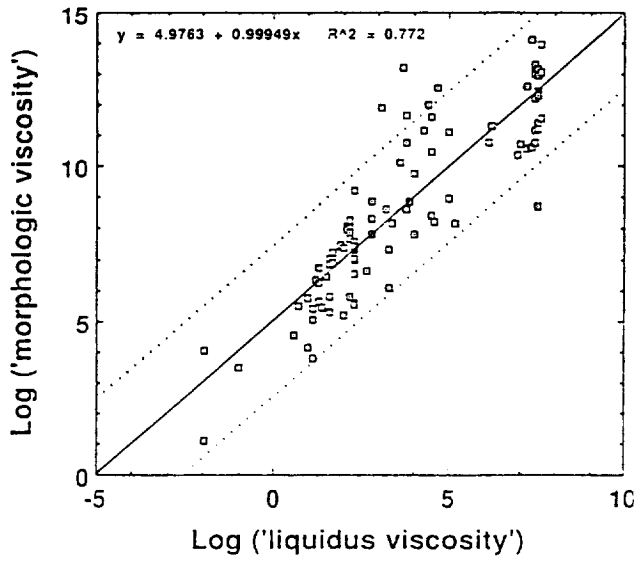

Figure 1. Calculated morphologic viscosities and estimated liquidus viscosities of 97 lava flows.

MARTIAN CARBON DIOXIDE: CLUES FROM ISOTOPES IN SNC METEORITES;

H. R. Karlsson[1], R. N. Clayton[2], T. K. Mayeda[2], A. J. T. Jull[3] and E. K. Gibson Jr.[4].
[1]Dept.. of Geosciences and Dept. of Chemistry and Biochemistry, Texas Tech Univ., Lubbock, TX, 79409. [2]Enrico Fermi Inst., Univ. of Chicago, Chicago, Il 60637. [3]NSF Facility of Radioisotope Analysis, Univ. of Arizona, Tucson, AZ 85721. [4]SN2, NASA/JSC, Houston, TX 77058.

INTRODUCTION. Attempts to unravel the origin and evolution of the atmosphere and hydrosphere on Mars from isotopic data have been hampered by the impreciseness of the measurements made by the Viking Lander and by Earth-based telescopes. The SNC meteorites which are possibly pieces of the Martian surface offer a unique opportunity to obtain more precise estimates of the planet's volatile inventory and isotopic composition. Recently, we reported results on oxygen isotopes of water extracted by pyrolysis from samples of Shergotty, Zagami, Nakhla, Chassigny, Lafayette and EETA-79001 [1]. Now we describe complementary results on the stable isotopic composition of carbon dioxide extracted simultaneously from those same samples. We will also report on ^{14}C abundances obtained by accelerator mass spectrometry (AMS) for some of these CO_2 samples.

METHODS. After overnight evacuation at room temperature, powdered samples of Chassigny (2.0 g), EETA-79001 (lith A: 3.1 g; lith B: 3.2 g), Lafayette (3.0 g), Nakhla (2.1 g), Shergotty (3.1 g) and Zagami (2.9 g, 3.4 g) were heated under high vacuum and the volatiles evolved condensed into a cold-trap at -209°C. Non-condensable gases were discarded. Each sample was heated step-wise to 150°C, 350°C, 600°C and 1000°C, and held at those temperatures for 1 hr. Carbon dioxide was cryogenically separated from water by warming the cold-trap up to -79°C. The CO_2 was purified by exposing it to silver phosphate and by repeated passes through a cold-trap at -130°C. Finally it was isotopically analyzed on a triple-collecting ratio mass spectrometer.

RESULTS. Total carbon dioxide yields (wt%) were: Chas., 0.082; EETA-79001A, 0.036; EETA-79001B, 0.046; Laf., 0.211; Nak., 0.125; Sher. 0.088; Zag., 0.064, 0.049. The shergottites (EETA-79001A, B, Shergotty, Zagami) were generally lower in total carbon contents than the nakhlites (Lafayette, Nakhla) and Chassigny. In contrast to water, carbon dioxide yields for individual samples increased at higher extraction temperatures. The quantity of gas collected per temperature step ranged from 0.2 to 50 μmol CO_2 - well above blank levels (0.007 to 0.021).

Isotopic results for CO_2 analyses, as a function of pyrolysis temperature, are summarized in Figs. 1 and 2. Fig. 1 shows the variation in $\delta^{18}O$ values of the SNC. The oxygen isotopic composition varies from 1 to 45‰, and there is a wide variation within individual meteorites. $\delta^{18}O$ values generally decrease with increasing temperature.

Fig. 2 shows the variation in $\delta^{13}C$ values of the SNC. Carbon isotopic ratios range from -31‰ to +11.4‰. Although there is considerable variation in $\delta^{13}C$ values at each temperature cut, the largest variation is clearly in the 350-600°C step. In Chassigny, Shergotty and the nakhlites the $\delta^{13}C$ values peak in 350-600°C step. This peak is most pronounced in Nakhla and appears to be a charateristic feature of this meteorite since it has been observed in a similar temperature range by most workers [3, 4, 5, 6]. Except for 350-600°C step in Nakhla all the $\delta^{13}C$ values are negative. With the exception of EETA-79001 the highest temperature cuts have $\delta^{13}C$ values of -25±1‰. Comparison of our yield or isotopic results with those of other workers are not straight forward since they either used smaller samples or combustion techniques. The only studies that allow direct comparison are those of Watson et al. who studied Nakhla [3, 4]. Our data for Nakhla are in reasonable agreement with theirs.

DISCUSSION. It is clear from Fig. 1 that the $\delta^{18}O$ of CO_2 decreases with temperature because it approaches oxygen isotopic equilibrium with the bulk rock (+4 to 5‰). Similar results were obtained for a terrestrial control sample. The shergottites have suffered greater exchange than Chassigny and the nakhlites possibly reflecting the lower volatile content of the shergottites. Karlsson et al [1], reported that $\delta^{18}O$ values of some SNC water decrease with temperature and attributed this behavior to kinetic isotope effects. However, in light of the $\delta^{18}O$ data for the CO_2 it is evident that the $\delta^{18}O$ of the water is affected by isotopic exchange with the carbon dioxide that evolves simultaneously. Thus, we find that for each SNC meteorite the $\Delta^{18}O(CO_2\text{-}H_2O)$ systematically decreases as a function of temperature. The observed $\Delta^{18}O$ values are generally higher than theoretical equilibrium values for the same temperature range. The most plausible explanation is that the two gases equilibrated to a lower temperature once they evolved out of the hot region of the sample tube before they were quenched in the cold-trap. Since the molar CO_2/H_2O ratio per cut (0.002 to 10.6) increases with increasing temperature the water is most affected at higher tempertures. Because of the oxygen isotope exchange among CO_2, H_2O and residual silicates during

extraction, information on values of the Martian atmospheric gases is lost. However, $\Delta^{17}O$ values may be retained as discussed in Karlsson et al. [1].

The simplest interpretation of the carbon isotope data (Fig. 2) is that they represent contributions of carbon from four distinct sources: the terrestrial atmosphere, the terrestrial biosphere, the Martian atmosphere and the Martian mantle. Carbon extracted in the two lowest temperature steps (24-350°C) is thus mostly likely to a mixture of adsorbed terrestrial CO_2(-7‰) and terrestrial organic matter (-26‰), whereas the highest temperature step (600-1000°C) is most likely to be dissolved Martian magmatic carbon which according to Wright et al. [5] has a $\delta^{13}C$ between -20 and -30‰. Our data show a tight cluster around -25±1‰ suggesting a more uniform $\delta^{13}C$ for the Martian mantle. The 350-600°C step may represent a mixture of a Martian atmospheric carbon and terrestrial sources. Carbonates decrepitate in this temperature range under vacuum. The high Nakhla $\delta^{13}C$ value, +11.4 ‰, is most likely associated with the breakdown of carbonate which is known to be abundant in the meteorite [6]. Wright et al. [5] reported slightly lower $\delta^{13}C$ values of +6 to +9‰ for Nakhla carbonate. ^{14}C data obtained by AMS on Nakhla carbonate suggest a preterrestrial origin. If the 11.4‰ value for Nakhla is due to carbonate, then it is possible to estimate a $\delta^{13}C$ value for the Martian atmosphere. Assuming that the carbonate was calcite and formed in equilibrium at 0°C with Martian CO_2 then the $\delta^{13}C$ value of Martian CO_2 would have to be at about 0‰. This result suggests that the atmosphere may be more enriched in ^{13}C than the Martian mantle. As in the case of the oxygen isotope results for SNC waters reported by Karlsson et al. [1], this difference in carbon isotopes may be due to lack of interaction between the atmosphere and lithosphere on Mars because of the absence of plate tectonics on the planet and might imply either an extraplanetary origin for the atmospheric CO_2 or heavy-isotope enrichment of the atmosphere due to preferential exscape of ^{12}C compounds to space [7].

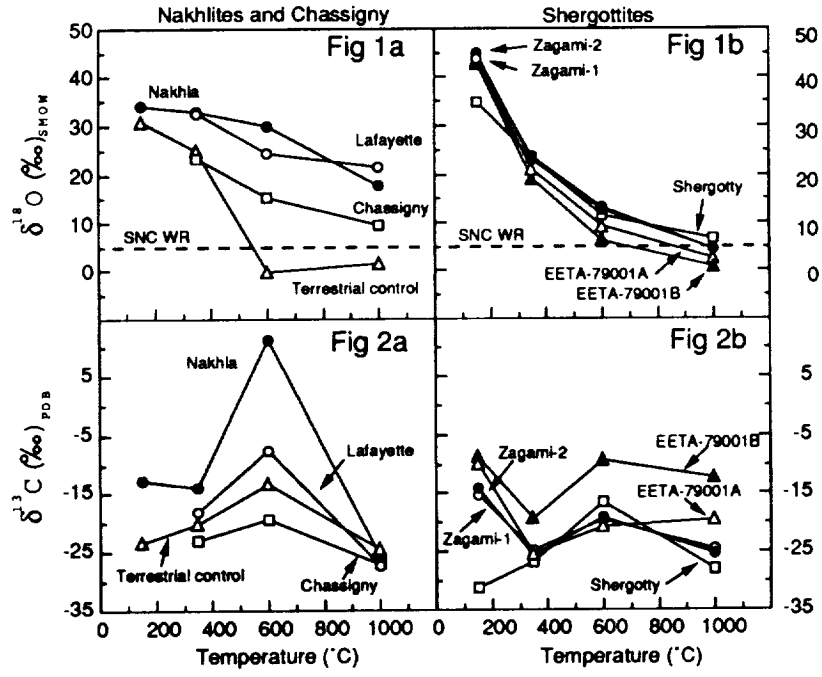

CONCLUSIONS. During pyrolysis of SNC meteorites, CO_2 may experience considerable oxygen isotopic exchange with the host rock, particularly at high temperatures. As CO_2 and H_2O evolve out of the samples they also exchange oxygen isotopes. Great care must therefore be taken in interpreting oxygen isotope values for these gases when using pyrolysis. Shergottites are intrinsically lower in H_2O and CO_2 than Chassigny and the Nakhlites and hence the oxygen isotopic composition of these gases in shergottites are more likely to be altered by isotopic exchange with the host rock. This may explain why the ^{17}O anomalies reported by Karlsson et al [1] are absent or less pronounced in the shergottites.

The carbon isotopic data are probably unaffected by the pyrolysis process and may thus give undisturbed $\delta^{13}C$ values for the various carbon reserviors within the samples. Our data suggest that the Martian atmosphere is enriched in ^{13}C relative to the Martian mantle. This isotopic difference may be entirely of inorganic origin and not due to biological processes such as photosynthesis.

REFERENCES. [1] Karlsson H. R. et al. (1992) *Science*, 255, 1409. [2] Fallick A. E. et al. (1985) In *Lunar and Planet. Sci. XIV*, 183-184. [3] Watson L. L. et al. (1991) In *Lunar and Planet. Sci. XXII*, 1473-1473. [4] Watson L. L. et al. (1992) In *Workshop on the Martian Surface and Atmosphere Through Time*, 165-166, LPI Tech. Rpt. 92-02. [5] Wright I. P. et al. (1992), *GCA*, 56, 817. [6] Gooding J. L. et al. (1991) *Meteoritics*, 26, 135. [7] Jakosky B. (1991) *Icarus*, 14,

DIFFERENT RADIATION AND METAMORPHIC HISTORY OF THE KAINSAZ CO 3.2 CHONDRULES

Kashkarov L.L., Kalinina G.V. V.I.Vernadsky Institute of Geochem. and Analyt. Chem., Russian Acad. Science, Moscow, Russia

Track and thermoluminescence parameters in chondrules from the Kainsaz CO 3.2 chondrite have been studied. Obtained results indicate on their individual shock-thermal history on the early pre-accretion stage of the meteorite parent body formation.

The pre-accretion stage of the chondrite formation is ane of the mostly important in the history of these meteorites. A wide variaty of the last years investigations (for example [1-3]) indicate that in this early stage not only the chondrules and the mineral grain aglomeration processes occured, but the principal metamorphic processes are related to this period. It is possible that the last processes can be due to the local cases of the shock-thermal reworking of the initial chondrite matter. Mostly significant in so doing is proved that during the whole subsequent history of the chondrite existence the thermal conditions were not so critical that can to result in the total flattening of the quite of a number of parameters which indicate the heterogeneous character of the chondrite matter. To these parameters in particular track and thermoluminescence (TL) characteristics are related. The investigations of the identity and difference of these parameters for the ordinary and the carbonaceous chondrites acquire a great importance at present [4].

The aim of this work is the study of the radiation-thermal history of the carbonaceous chondrite matter with help of the complex measuring of the nuclear track and TL-parameters in the chondrules of the low-metamorphic chondrite Kainsaz CO 3.2. The chief objective in this case was the elucidation of the essential siqns which give possibility to consider the radiation and thermal conditions existed at the pre-accretion stage of these meteorite parent body formation.

The track results obtained for the about 500 olivine grains (higher than 30 μm in size) which were separated from 98 chondrules of the microgranular and porphiritic types are the following: 1)The total spread of the track density values (ρ) is in the interval of three orders of magnitude $(0.003\text{-}2)10^{6}cm^{-2}$ 2)The track density due to the fission fragments of the uranium nuclei, concentration of which for the searched olivine crystals is in the interval $(0.2\text{-}2.3)\ 10^{-8}$ g/g, is not higher than $5\cdot10^{3}cm^{-2}$. 3)The part of the crystals with $\rho \geq 10^{5}cm^{-2}$ amounts to smaller than 10%. 4)Only in two crystals $\rho \geq 10^{6}cm^{-2}$ was obsered. 5)The gradient O from the surface to inside of the individual grains was detected in nine cases. These track results indicate, that in the part of the carbonaceous chondrite Kainsaz matter the traces of the early pre-accretion irradiation were storaged. The fraction of this matter as compared to the total crystal number under investigation is equal to a few percentages and the integral irradiation dose is smaller by 2-3 orders of magnitude than for brecciated ordinary chondrites

matter, which was influenced by the intensive irradiation during the regolith stage of their parent bodies formation.

The results of TL-investigations for the 50 individual chondrules of the Kainsaz CO 3.2 in relation with the same TL-parameters for chondrules of the Dhajala H 3.8 chondrite are presented in Figure 1a,b. The character of the relationship between TL-parameters - FWHM and the temperature peak maximum T_{peak} - indicate that the chondrules under investigation represent at least two different groups: for the first group the both TL-parameters are in the very narrow interval (FWHM about (27+7)°C and T_{peak} (150+12)°C); however the second chondrule group is characterised by the directly proportional relationship of these TL-parameters. In this case FWHM values are increased by more then two-fold that can be due to different dislocations and electron trap level concentrations depending on the different shock-thermal local events.

A correlation between track and TL-parameters for the investigated chondrules was not observed that is in accordance with a concept of local character of the relatively weak shock-thermal processes,presented in the pre-accretion solar nebula conditions.

References. 1.Fredriksson K. (1983) - Chondrules and their origins ed. by E.A.King, Houston,44. 2.Kurat G. (1988) -Phil. Trans. R. Soc.Lond., **A325**, 459-482. 3.Ninagawa K. et al. (1991) - Proc. NIPR Symp. Antarct. Meteorites, **4**, 344-351. 4. Sears D.W.G. et al. (1991) - Ibid, 319-343.

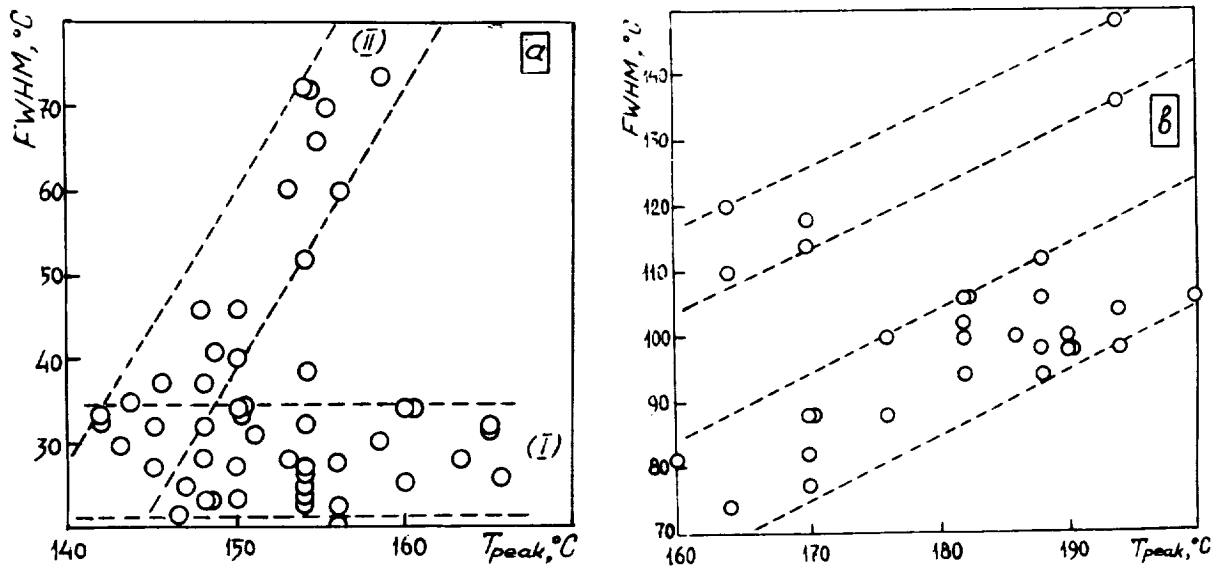

Fig.1. TL-parameters FWHM and Tpeak relations in the individual chondrules for the Kainsaz CO 3.2 (a) and Dhajala H 3.8 (b) chondrites.

COMPLEX RADIATION-THERMAL HISTORY OF KAIDUN METEORITE ON DATA OF TRACK STUDY OF SILICATE MINERALS

L.L. Kashkarov, N.N. Korotkova, and A.Ya. Skripnik
V.I. Vernadsky Institute of Geochem. and Analyt. Chemistry, Russian Acad. of Science, Moscow, Russia.

The results of track study of ~80 individual silicate mineral crystals (ol, px, plag) picked out from Kaidun meteorite are presented. A wide range of observed ρ_{VH} value distributions indicate the complex irradiation history of Kaidun minerals. In one anortite crystal having two track groups with different parameters the pre-accretion irradiation traces were observed in all probability.

In the earlier track and thermoluminescense (TL) studies of Kaidun unique heterogeneous breccia /1-3/ we have obtained some TL-parameters and ancient natural track characteristics for the glass fragments (~tens-hundreds μm in size) picked out from the individual glass inclusions in the Kaidun carbonaceous matrix. These data indicate the absence or the very low degree of heating influence and strong heterogenity of track and TL-parameter distributions for the investigated glass samples.

Now we present the results of track study of ~80 individual silicate mineral crystals (ol,px,plag) picked out both from the crushed bulk sample and from Kaidun carbonaceous matrix. The most part of olivine grains (~85%) is characterized by extremely low track density of $\rho \lesssim 10^3$ cm^{-2} (see fig.1), which is caused by uranium fission fragments. The other mineral grain percentages having the same ρ value are lower, from 15 to 70%. Part of crystals (10-60%) with $\rho \simeq 10^4$-10^5 cm^{-2} and those with $\rho \gtrsim 10^6$ cm^{-2} are considered to irradiate by low-energy VH-nuclei cosmic rays at the pre-accretion stage. The presence of grains with $\rho > 10^8$ cm^{-2} is characteristic of all minerals (apart from En). Their percentages among total quantity of crystals under study are differents: 6, 10, 15, and 25% for ol, an, ab and Ca-px respectively. Track density gradients were not observed in these crystals. The wide range of ρ_{VH} values (more than 3 orders of magnitude) indicate complex irradiation history of Kaidun minerals. In the fig.1 the ρ_{VH} value distributions for Kaidun glasses are presented for comparison with those in crystals. It can be seen that there are no glass samples having $\rho < 0.4 \cdot 10^5$ cm^{-2}. This heterogenity of track characteristics indicate the differences of radiation-thermal conditions for individual grains of tens-hundreds μm in size.

The observation of two track groups in an anorthite crystal with different values of lengths and densities is of particular interest (see Table). This individual anorthite grain was picked out from the black meteorite matrix. It contains the matrix contamination traces on the one of its faces. The I group tracks with higher track densities are characterized by much less lengths as compared to II group tracks. The I group track lengths shortening is caused by heating influence unlike the unannealed II group tracks. We observe the tracks stored during

Table. Characteristics of group I and II tracks in the anorthite crystal K.10.2.11 from Kaidun meteorite.

Track group	Track number	Track density, cm^{-2}	Track* length intervals, μm
I	459	$(1.4+-0.07)\cdot10^{8}$	1 - 3
II	86	$(2.6+-0.3)\cdot10^{5}$	4 - 13

* Track lengths were measured on the crystal surface.

two-stage irradiation: 1) the first pre-accretion irradiation stage has taken place very early in the Kaidun breccia formation in all probability; 2) the following second irradiation stage has taken place after I group track annealing.

References. 1. L.L.Kashkarov, N.N.Korotkova et al. XXI, LPSC,1990,p.611. 2. L.L.Kashkarov, N.N.Korotkova et al. XXII LPSC,1991, p.695. 3. L.L.Kashkarov, N.N.Korotkova et al. XXIII LPSC, 1992, p.665.

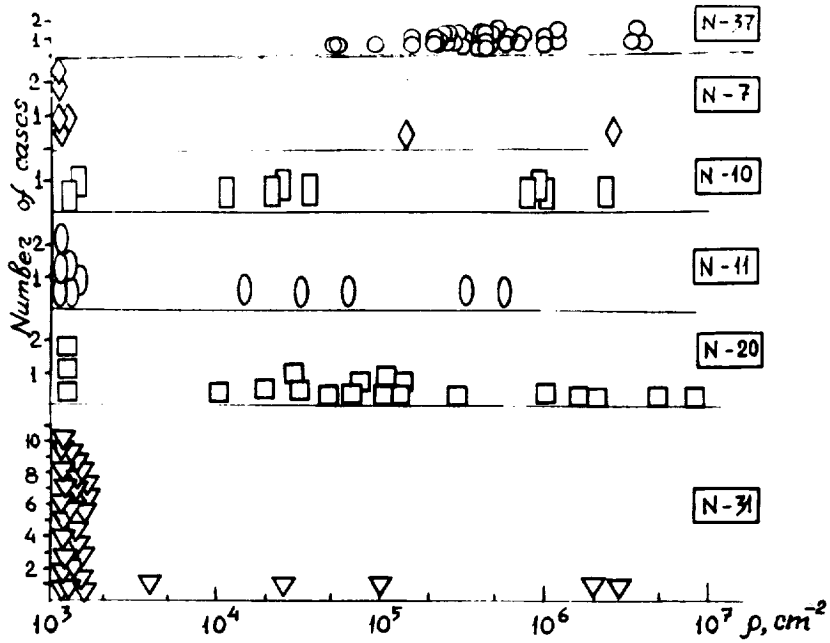

Fig.1. Track density distributions in different mineral phases of Kaidun meteorite: ○ - glass, ◊ - albite, ▯ - anorthite, 0 - enstatite, □ - Ca-px, ▽ - olivine. N is the number of mineral fragments under study.

FRACTAL GEOMETRY OF SOME MARTIAN LAVA FLOW MARGINS: ALBA PATERA.

K. Kauhanen, Dept. of Astronomy, Univ. of Oulu, SF-90570 Oulu, Finland

Fractal dimension for a few lava flow margins on the gently sloping flanks of Alba Patera were measured using the structured walk method. Fractal behaviour was observed at scales ranging from 20 to 100 pixels. The upper limit of the linear part of log(margin length) vs. log(scale) profile correlated well to the margin length. The lower limit depended on resolution and flow properties.

Fractals are objects that look similar on all scales [1]. Many geological (as well as other natural) phenomena show fractal behaviour through a limited range of scales. Lava flow margin is one example of a fractal curve in nature. Recent work by Bruno et. al. [2] has confirmed that lava flow margins are fractals and the range of scales extend from tens of centimeters to a few kilometres for terrestrial flows and tens of kilometres for flows on other planetary bodies. They also found that lava flows on terrestrial planets can be roughly divided in two groups according to their fractal dimension indicating either pahoehoe or a'a type lava flows. Fractal dimensions were between 1.05 and 1.09 for a'a and between 1.13 and 1.23 for pahoehoe. This leads to an interesting question: what kind of constraints are needed to apply fractal behaviour on lava flows.

We calculated the fractal dimension for some lava flow margins at Alba Patera, Mars. Seven lava flow margins were drawn and measured on flanks of the volcano (fig. 1) using the structured walk method [3]and varying the scale, i.e. the yardstick length (r), from 1 to 100 pixels (appr. 100 m to 10 km). The lava flow margins were at least ten times longer than the largest scale. Two fractal dimensions were calculated by a linear regression procedure from log(margin length) vs. log(scale) plot, one for all data and another for the most linear part of the plot, which also gave the range, that is the upper and lower limit of scales where the most self-similar behaviour was observed.

A typical margin length curve (fig. 2) shows a rapid increase of length for small scale sizes, a slightly curved part of values which is gradually distorted and eventually scalloped as the scale length approaches the margin length. The lower limit of the linear part was determined by the beginning of upward curvature for small scales and the upper limit was put before the scalloped pattern in the length curve.

Results. 1.) A fractal behaviour of flow margins was observed at a range of scales. Lower limit was restricted by pixel size and precision of margin drawing. The upper limit correlated well to the margin length especially within flows of similar fractal dimension (fig. 3). In one occasion (A) the length curve showed two linear patterns with different slopes. This could be due to a change in the lava flow type caused by topography or change in the material properties. One lava flow (F) expressed no distinct linear part in the length curve causing difficulties in setting the lower limit for the linear part and decreasing the goodness of fit for the regression line.

2.) The lava flows were of type a'a except a short and wide one (B) clearly expressing pahoehoe behaviour (fig. 4). Fractal dimensions for of all data were considerably lower than those for the linear part of data (fig. 5), except for one curious lava flow margin (E) showing similar values for both all of the data and the linear part. This could indicate that the flow stopped on a slope or due to cessation of lava extrusion and only a few flow lobes formed.

3.) Narrow a'a type lava flows (A, E) seem to differ from the group of wide a'a flows and the pahoehoe flow in the previous fractal dimension comparison (fig. 5). This may indicate that a'a flow properties were quite similar when the flows stopped.

Discussion. The goodness of fit estimates (R^2) for the regression lines were of the order 0.75, which seems to be too low in a statistical sense. The larger scales were weighted because measurements were made linearly at two-pixel intervals.

References: [1] Mandelbrot B. B. (1977) Fractals. W.H. Freeman and Company. San Francisco. [2] Bruno B.C., Taylor G.J., Rowland S.K., Lucey P.G. and Self S. (1992) LPSC, XXIII, 171-172. [3] Longley P.A. and Batty M. (1989) Computers & Geosciences, 15, 167-183.

FRACTAL DIMENSION OF ALBA PATERA FLOWS: K. Kauhanen

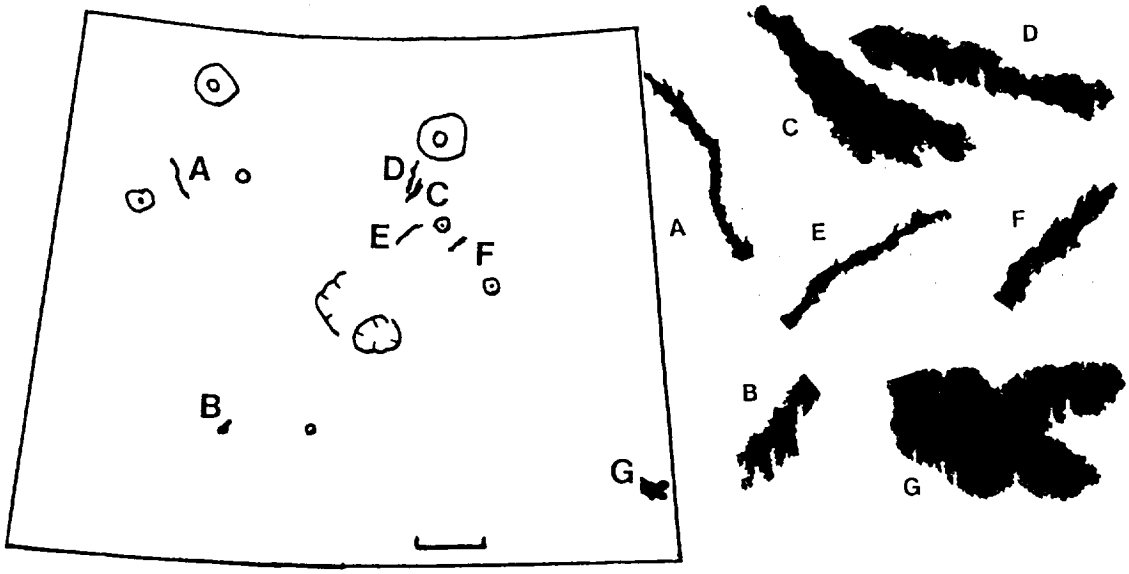

Figure 1. Location and outlines of the measured lava flows. Scale bar is 100 km.

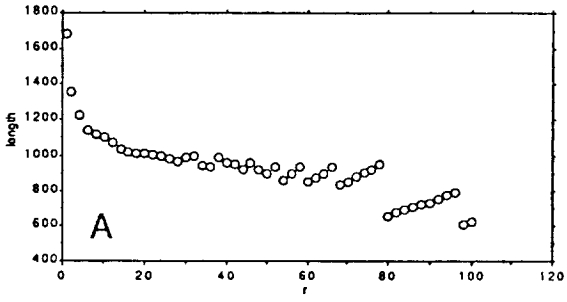

Figure 2. Lava flow margin lengths with increasing scale length.

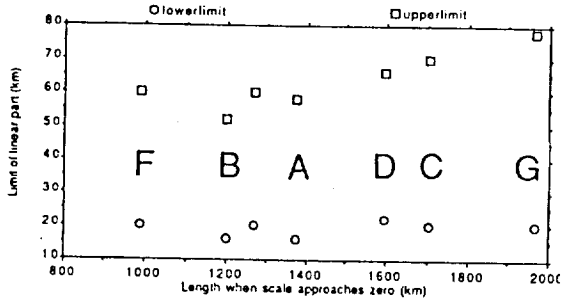

Figure 3. Upper and lower limits for the linear part of the margin length curve.

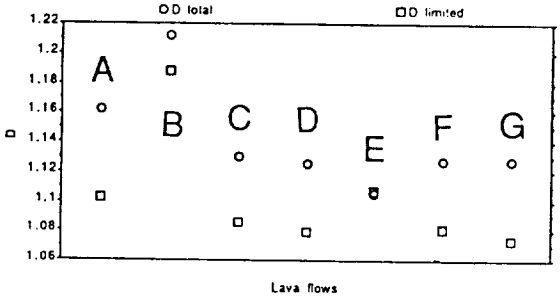

Figure 4. Fractal dimension for the flow margins. Square marks all data, sphere the linear part.

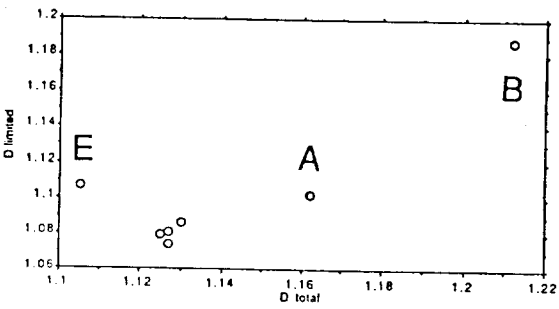

Figure 5. Fractal dimension comparison, the linear part vs. all data.

TECTONICS OF NEYTERKOB CORONA ON VENUS; K. Kauhanen, Department of Astronomy, University of Oulu, SF-90570 Oulu, Finland

Neyterkob double corona (50°N 202°) presents an area of corona-related interfering tectonic patterns which are formed in different phases of evolution of the corona and modified by regional stresses. Analyzing the patterns can reveal us something about the coronal formation. Tectonic features form distinct units on topographic depressions, slopes and volcanic flows extending over one radius of the corona. A remarkable amount of compressional features were found near the rim and related to interaction between adjacent coronae. Radial extension was manly observed on a peculiar NE-SW trending high crossing the corona. Concentric fractures were found to the east partly connected to the lithospheric flexure. Tectonic features indicate movements of volcanic activity and modification of the area by more regional stresses.

Coronae are circular or elongate surface features characterized by concentric belt(s) of ridges or fractures and/or a raised rim. Central region is usually higher than outside plains. The width of the annulus varies from 10 to over 200 km and diameters from 60 to over 2000 km [1]. Many of the individual coronae are asymmetric or multiple indicating movements of activity with time. Coronae in clusters or chains do not indicate formation by lithospheric movement over hotspots [1]. Origin of a corona by an upwelling mantle plume explains its general evolution by sequence of initial updoming of the lithosphere followed by a flattening of the diapir and gravitational relaxation due to cooling of the diapir [2].

Neyterkob Corona is located on Ganiki Planitia centered near latitude 50°N and longitude 202°. It consists of two subcircular components both 200 km by diameter and surrounded by a fresh-looking rim and radial and concentric lineaments extending over 200 km outwards of the rim. Some features can be traced as far as 350 km away from the rim. The eastern subcorona is nearly circular and the western subcorona with a heavily fractured and partly degraded rim is an older one.

Two major ridge belts, Pandrosos Dorsa in the east and Ahsonnutli Dorsa in the west border the corona longitudinally. Pandrosos Dorsa is cut by a satellite corona on the northeastern corner of Neyterkob. Ahsonnutli Dorsa branches and deflects slightly to form a subconcentric pattern. A ridge belt runs south from the Neyterkob through a faint circular feature, possibly a corona. Neyterkob cannot be located in the middle or at the junction of major ridge belts as other coronae in this area [3]. Instead, it is a rather distinct feature and perhaps induced ridge belts of its own.

Topographic data reveals a trough both outside and inside the coronal rim. The trough disappears in the north and southwest and instead, a wide topographic high can be seen extending across the corona from SW to NE. This bulge is characterized by long, narrow fractures connecting the corona to Razia Patera and Pandrosos Dorsa. Central plains of the eastern subcorona are slightly below the surrounding terrain.

Lava flows have covered areas inside and outside the corona destroying tectonic features. Flow fronts are best seen outside the southeastern rim, where flood-like radar-dark flows cover the earlier radar-bright flows. To the north of the corona small volcanic edifices and pits are located on NE-SW trending fractures. Markings of late volcanic activity are also found on the bottom of both of the components and the satellite corona.

The rim shows a well-preserved topography around the corona Radial grabens cut the rim where lineaments join nearby coronae or deformation belts to Neyterkob. The top of the rim rises about 2 km above the trough in the southeastern side. Morphology of the rim suggests two phases in the main activity included by minor volcanic events in both of the components or perhaps movements or scattering of the decreasing activity by time. A number of features indicate later modification of the rim by more global forces.

TECTONICS OF NEYTERKOB CORONA: K. Kauhanen

Tectonic patterns of the corona components are different although similarities can also be found. Particularly near the rim, distinct tectonic units relate to lava flow units or topography. To the east the long concentric fractures are located on a slope caused by the flexure of the lithosphere. Wrinkle ridges are found near the rim forming two different patterns close together, one parallel to the rim and another inclined. More compressional features are located on the trough overlying an older radial/concentric fracture net. The area to the west of the corona is covered by a massive subradial ridges extending to the Ahsonnutli Dorsa. The pattern changes into a net between Razia Patera and Neyterkob. Wrinkle ridges and thrusts are found on narrow zones near the rim and on a wider zone extending to the northwest. Extensional features are concentrated on the slopes of the rim supporting the idea of deformation of the rim by horizontal forces. Young radial features include short grabens to the south and long narrow fractures mainly in the NE-SW direction and resembling dike swarms discussed by MacKenzie [4]. On the eastern side, compressional features are located on the trough while extension is marked by narrow grabens on a slope indicating lithospheric flexure.

Conclusions. Though the eastern corona is clearly younger, it is not a different formation just overlying the western one. Two phases in the main activity were followed by minor volcanic events. Flexural response of the lithosphere is clearly evident near the rim. Tectonic features related to the initial stage are nearly all destroyed because of volcanic and tectonic resurfacing. The central topographic rise may have formed by volcanic reworking in NE-SW direction. This could be favoured by the long narrow fractures if they are interpreted to be surface expressions of dikes. Tectonic features in different phases of the coronal formation are strongly related to topography and continuously destroyed and deformed by volcanic and later tectonic activity. Regional stresses have contributed to the deformation.

References: [1] Stofan E.R, Sharpton V.L., Schubert G., Baer G., Bindschadler D.L., Janes D.M. and Squyres S.W. (1992) JGR, 97, 13347-13378. [2] Squyres S.W. Janes D.M., Baer G., Bindschadler D.L., Schubert G., Sharpton V.L. and Stofan E.R. (1992) JGR, 97, 13611-13634. [3] Raitala J. and Kauhanen K. (1991) Earth, Moon and Planets, 53, 127-148. [4] MacKenzie D., MacKenzie J. M. and Saunders R. S. (1992) JGR, 97, 15977-15990

Figure. Magellan SAR image of Neyterkob Corona. Razia Patera is shown to the SW of Neyterkob.

IMPLICATIONS OF CRATER DISTRIBUTIONS ON VENUS. W. M. Kaula, University of California, Los Angeles.

The horizontal locations of craters on Venus are consistent with randomness. However, (1) randomness does not make crater counts useless for age indications; (2) *consistency* does not imply necessity or optimality; and (3) horizontal location is not the only reference frame against which to test models. Re (1), the apparent smallness of resurfacing areas means that a region on the order of one percent of the planet with a typical number of craters, 5-15, will have a range of feature ages of several 100 My. Re (2), models of resurfacing somewhat similar to Earth's can be found that are also consistent and more optimal than random: i.e., resurfacing occurring in clusters, that arise and die away in time intervals on the order of 50 My. These agree with the observation that there are more areas of high crater density, and fewer of moderate density, than optimal for random. Re (3), 799 crater elevations were tested; there are more at low elevations and fewer at high elevations than optimal for random: i.e., 54.6% below the median. Only one of 40 random sets of 799 was as extreme.

1. An evident inference of both catastrophic and equilibrium models [1,2] is that crater density is not useful as a measure of relative ages of different areas: only for areas at the extremes of the distribution are there found evidences of features such as recent uplifts and volcanic flows with low crater density and of degradation and discordant fractures with high crater density. If actuality is closer to the equilibrium random resurfacing model [2], the reason for this is apparently that the typical scale of tectonic and volcanic activity is comparable to the patch area $a < 0.0003$, or 150,000 km^2. If meaningful statistical discrimination requires about 5 to 15 craters, then the areas must be about $| 10 / 763 | \times 0.875 \times 460 \times 10^6 = 5 \times 10^6$ km^2: about 30 Phillips "patch" [2] areas. Within most areas of 5 million km^2 on Venus there typically is a wide range of geomorphic features, implying a wide range of tectonic and volcanic activity. If the scale of events is comparable to the patch area of 0.15×10^6 km^2 or smaller, then normally an area of 5×10^6 km^2 will contain a great range in age among its features, up to 1.5 Gy or more. Inference of a kinematic sequence from imagery then implies appreciable age differences between earlier and later patterns. Such temporal differences are constraints on physical models; for example, a feature of high gravity: topography ratio, implying dynamic support, should be expected to be late in the kinematic sequence for its area, while a fractured and relaxed geomorphic unit should be several 100 My old.

Counts were therefore made of the distribution in age of surviving craters within blocks of $a = 0.01$, or areas about 5×10^6 km^2, generated by the ER model of random occurrence of craters at a rate of 888 per resurfacing time (1.78/My), and random volcanic patches of $a = 0.0003$. Sixty runs of 5.4 resurfacing times (2.7 Gy) were made; in each run, 4800 craters and 18,000 volcanic patches were generated.

Thus, for example, the 75% quartile for an area with five craters is about equal to the 25% quartile for an area with fifteen craters, so there is about a 6% probability that the area with five craters still has a crater older than the oldest in the area with fifteen craters. But even with as few as five craters, there is a rather high probability that a 5 million square kilometer area contains features as old as 500 My. At the other extreme, the probability of a youngest crater under 50 My is greatly enhanced for areas with more than 10 craters.

2. To test the consistency of the crater distribution with cluster occurrence, Monte Carlo models were computed in which craters occur randomly in location x, y and time t over a planet lifetime T, and in which clusters occur randomly with respect to other clusters, and have a Gaussian distributions of specified rms radius σ of resurfacing events about their centers. The rate of occurrence of clusters relative to cratering was assumed proportional to $\exp(-t/\lambda)$. To save computer time, the planet was assumed flat and square, and wrap around to the opposite side made for resurfacing patches located less than their radii from the edge. Counts of surviving craters in areas 0.01 of the total area were kept, to test against crater counts in 5×10^6 km^2 areas on Venus, by sampling with multiple circles [2]. Fits to this Venus data appreciably *better* than random distribution were obtained with a range of cluster sigmas σ 0.1 to 0.2 of planet dimension (areas 3 to 12 percent of the total); decay constants λ T/3 to T, and probability

CRATER DISTRIBUTIONS: Kaula W.M.

intervals on the order of $T\sigma^2/4$: i.e., sufficient to be well-distributed over the planet in a time $T/4\pi$, close to the canonical resurfacing time.

3. The distribution of 799 crater elevations on Venus was compared to that of 3720 points at uniform intervals (pi/54=3.33°). All elevations were calculated from the 120-degree harmonic expansion of Borderies [3], which interpolates smoothly across gaps in the altimetry. A distinct bias toward lower elevations was found; thus, 54.6% of craters are at elevations below the median (178 meters below the mean). Such an extreme distribution was obtained in only one of 40 random selections of 799 elevations. The bias toward lower elevations is consistent with resurfacing events being associated with higher areas, but not markedly so.

[1] Schaber et al (1992) *JGR, 97,* 13,257; [2] Phillips et al (1992) *JGR, 97,* 15,923; [3] Borderies, N. (1992) informal communication.

MEGAPLUMES ON VENUS. W. M. Kaula, University of California, Los Angeles.

The geoid and topography heights of Atla Regio and Beta Regio, both peaks and slopes, appear explicable as steady-state plumes, if non-linear viscosity $\eta(T, \dot{\epsilon})$ is taken into account. Strongly constrained by the data are an effective plume depth of about 700 km, with a temperature anomaly thereat of about 30°, leading to more than 400° at the plumehead. Also well constrained is the combination $Q\eta/s_0^4$ =(volume flow rate)Xviscosity/(plume radius)^4: about 11 Pa/m/sec. The topographic slopes dh/dsconstrain the combination Q/A , where A is the thickness of the spreading layer, since the slope varies inversely with velocity. The geoid slopes dN/ds require enhancement of the deeper flow, as expected from non-linear viscosity. The Beta data are best fit by Q =500 m^3/sec and A = 140 km; the Atla, by Q =440 m^3/sec and A =260 km. The dynamic contribution to the topographic slope is minor.

A major controversy about solid Venus is whether its contemporary rate-of-heat-loss (on a 100 My timescale), and thence its level of volcanism & tectonism, is (1) much less than the rate averaged over about 1 Gy, due to an oscillatory character arising from material properties– most obviously, density differences of constituents– or (2) near this averaged rate (within a factor of two), as appears to be true for the Earth. Rather moot between hypotheses (1) and (2) is the important finding of Pioneer Venus, confirmed by Magellan, of a much higher ratio of gravity-to-topography than Earth's, which requires a much stiffer upper mantle. Supporting hypothesis (1) are (a) a considerably smaller rms variation in topographic elevation about the mean than exists on Earth; (b) the absence of the topographic signature of a plate tectonic spreading system [1]; and (c) a consistency of the horizontal distribution of craters with randomness [2]. To claim hypothesis (2) against property (a) is to say that Venus's averaged level of activity is lower than Earth's in recent Gy; against property (b), to say that convective heat transfer on Venus is appreciably more regional than Earth's. Property (c) is discussed in another abstract to the effect that consistency does not entail necessity [3]. Supporting hypothesis (2) more directly is the extraordinary magnitude of some extremes in the topography and gravity of Venus, such as (d) the steep slopes of the western front of Maxwell Montes, and (e) the great geoid highs over Beta Regio and Atla Regio: 20 percent higher than the Earth's maximum. We explore whether the data (e) are compatible with hypothesis (2): are Atla and Beta explicable as steady-state flow features? For this, it is probably necessary to take into account the greater stiffness of Venus's upper mantle, mentioned above.

The model is stimulated by Sleep's for sub-oceanic plumes on Earth [4] . A significant difference from Sleep's concern is that the Venus plume is a primary phenomenon in its heat transfer, rather than being secondary to lithospheric spreading from a rise elsewhere. Hence in a Venus-relevant model the overlayer is a passive crust, through which heat transfer is conductive, and the axisymmetric flow from the plume is analogous to to the bilateral flow from the rise, in that the topography and geoid are controlled by conductive cooling. However, an important difference of the spreading from a plume is that conservation of volume flow leads to an inverse correlation of velocity with distance from the rise, and hence, in the simplest case of a steady-state cooling half-space, a decrease in height linear with distance, rather than with the square-root thereof. The reduction in strain-rate with velocity as well as the cooling act to increase the effective viscosity. Hence there may be a dynamic contribution to the topographic and geoidal slopes. To drive this horizontal flow there must be a pressure generated by the buoyancy of the plume, $P = \rho g \alpha \int_0^K \Delta T dz$, where K is the depth of the plume and the other symbols have their usual meanings.

MEGAPLUMES ON VENUS: Kaula W.M.

In an actual planet, the density anomaly ΔT will vary with depth z, since the plume will have a temperature gradient dT/dz closer to adiabatic than its surroundings. We divide the problem in two parts. Firstly, from the peaks in geoid height N and topographic height h we can infer, as an inverse problem, the temperature anomaly ΔT and the depth of the plume K. These lead to the pressure P and its gradient. Then the product $Q\eta/s_0^4$, as defined in the first paragraph, can be inferred from the Poiseuille formula [5]: $Q\eta/s_0^4 = \pi(dP/dz)/8 = \pi\rho g\alpha\Delta T/8$. To separate $Q\eta$ from the plume radius s_0, an assumption about the ratio s_0/K must be made. But the high power to which s_0 appears in the constrained combination limits it plausible range. The product $Q\eta$ has the dimensions of energy, like the flexural ridigity: first-order tectonic geometry and dimensions can always be fit by steady state viscous flow as well as by elastic flexure. To separate Q from η, a rheology must be assumed. A form $\eta = B\exp(CT_M/T)/\dot{\epsilon}^m$ is used; values corresponding to the results of Karato et al [6] are B =24200, C =8.91, m =0.71. This is a weak point not only in the extrapolation from the laboratory, but also in the effective temperature– or corresponding depth $z(\eta)$– which probably is near the plume head within the spreading layer, but must be assumed.

However, from the radial topographic slope $dh/ds = (dh/dt)/v$, due to cooling, there is a different constraint from conservation of the volume flow rate: $Q = 2\pi sAv$. To compute the thermal decrease dh_T/dt, the conductive formula for $dT(z)/dt$ for one boundary at a fixed temperature and the other at zero heat flow [7] was used. For the dynamic slope dh_D/ds, we need the pressure gradient $dP/ds = -\Psi Q\eta/\pi A^3 s$, where Ψ is 6 for a fixed boundary and 2 for a free boundary: more realistic, and always used. After a complete set of temperatures and topographic heights are calculated, the geoid heights $N(s)$ are obtained by a two-dimensional FFT: the most time-consuming step. To get geoid slopes dN/ds as steep as observed, it was necessary to assume that the nonlinear rheology led to a deeper skewing and confinement of the velocity: i.e., terms proportionate to $z^3$and z^4 in $v(z)$.

The principal defining parameters, and values explored, were thus the observed peaks of 3.5 km in topography and 110 m in geoid height, and slopes $dh/ds = 0.0017$ and $dN/ds = 0.03 - 0.04m/km$; the viscosity parameter B : $24200 - 242000$; plus ratios A/K : $0.2 - 0.5$; s_o/K : $0.1 - 0.2$; $z(\eta)/K$: $.05 - 0.2$; v_3/v : $0 - 1$; v_4/v : $0 - 2$;, C/K : $.02 - .03$; and D/K : $0 - 0.25$. C is the thickness of the passive crust, and D is the "dynamic" part of the plume, leading to an apron around the peak, $h(s)$, $s < s_0$, which must be included in the mass balance. Values corresponding to a best fits were B= 80000, v_3/v =1, v_4/v =4, $z(\eta)/K$ =.05, C/K =.03, D/K =0 for both plumes; $A/K = 0.2$ and $S_0/K = 0.175$ for Beta; $A/K = 0.4$ and $S_0/K = 0.2$ for Atla.

The steepness of the dropoffs is the main constraint on the volume flows Q. The total of about 950 m^3/sec is about one-third the *minimum*for the Earth's spreading rises (from area/year X crustal thickness X cumulate factor = 3 X 7 X 4 km^3/yr).

[1] Kaula, W.M. & Phillips, R.G. (1981) *GRL, 8,* 1187; [2] Phillips, R.G. , et al (1992) JGR, 97, 15,923; [3] Kaula, W.M. (1993) *LPSC XXIV;* [4] Sleep, N. H. (1990) *JGR, 95,* 6715; [5] Batchelor, G.K. (1967) *Fluid Dynamics,* Cambridge, p. 180; [6] Karato et al (1986) *JGR, 91,* 8151; [7] Carslaw, H.S. & Jaeger, J.C. (1959) *Conduction of Heat in Solids,* Oxford, p. 104.

PRELIMINARY ANALYSIS OF DIONE REGIO, VENUS: THE FINAL MAGELLAN REGIONAL IMAGING GAP.; S.T. Keddie, Dept. of Geological Sciences, Brown University, Providence, RI, 02912.

Introduction: In September, 1992, the Magellan spacecraft filled the final large gap in its coverage of Venus when it imaged an area west of Alpha Regio. F-BIDR's and some test MIDR's of parts of this area were available as of late December. Dione Regio had been imaged by the Arecibo observatory and a preliminary investigation of Magellan images supports the interpretations made based on these earlier images (Keddie et al., 1990; Senske et al., 1991): Dione Regio is a regional highland on which is superposed three large, very distinct volcanic edifices. The superior resolution and different viewing geometry of the Magellan images has also clarified some uncertainties and revealed fascinating details about this region.

Observations: Dione Regio extends from approximately 20°S to 45°S and from 315° to 335°, covering an area of about 2700 x 1200 km. Superposed on this 1-1.5 km region of elevated plains are numerous small shields and three volcanic edifices: Ushas Mons (≈500 km diameter) in the north; Innini Mons (≈600 km diameter) 1050 km to the SSE; and Hathor Mons (≈500 km diameter) 600 km SW of Innini. These edifices have been described elsewhere (Senske et al., 1991) and, interestingly, the major characteristics of the volcanoes are unchanged. Ushas Mons is radar-bright with many distinct, overlapping flow units and a dark summit region. Innini Mons is radar-dark with a few well-defined flows distally and a diffuse summit. Hathor Mons has a diffuse, radar-bright summit region and poorly defined flanks. Many details of these edifices revealed by Magellan give a new perspective on the nature and development of these volcanoes.

Ushas Mons in many ways is similar to Sif Mons; it has numerous flow episodes, overlapping bright and dark flows near the summit, distal flows which surround and partly bury small cones on the flanks of the volcano, and possible capture of distal flows by pre-existing fractures to the northwest of the summit. Unlike Sif, there is no summit caldera, although images of possible small cones observed in Arecibo data on the eastern half of the summit have not yet been processed. Two zones of narrow fractures tens of kilometers long extend away from the summit to the north and south. The southern set fans slightly and makes a small angle with the northern set.

Innini Mons also has a set of fractures extending to the south of the volcano and arcing in towards Hathor Mons. This fracture set, however, is comprised of shorter and less distinct fractures than those at Ushas. Lava flows extend away from the summit region, particularly to the north and northwest. These flows are generally radar-dark, though distally many have relatively brighter edges, suggesting rougher flow margins. The summit of Innini is complex, with a mesa-like dome surrounded by bright deposits, a tick-like feature, and an irregular dome.

To the south of Innini is a 50 km diameter impact crater with bright crater flows extending down the regional slope to the northeast. The flows appear to be confined by narrow ridges in

the plains, suggesting that they are relatively thin. Although this feature was observed in the Arecibo images, poor resolution of the rim and the association with apparent lava flows made its identification as an impact crater ambiguous.

Hathor Mons has a well-developed rift zone cutting through it in a northwest-southeast orientation. The fractures of this zone are obscured at the summit by bright diffuse deposits and a variety of structures. A large tick (20-25 km) dominates the summit at the southwestern side. Further north and east are several small pits ranging in diameter from 2 to 12 km and a nested caldera-like depression with bright flow deposits surrounding it. A fan of graben extend south from this caldera and appear to be superposed by deposits associated with the tick at their western edge. Other graben degrade into chains of pits. The summit graben form an arc which extends discontinuously to the southwest, forming a third arm of the rift zone cutting the edifice. A more complete picture of Hathor Mons is needed to determine more precisely the relative ages of rifting and volcanism.

Conclusions: On the basis of the Arecibo images it was suggested that the differences in major characteristics of the three volcanoes may be indicating different styles of eruption with the bright well-defined flows of Ushas Mons pointing to a relatively effusive nature and the diffuse deposits of the other two, particularly Hathor Mons, suggestive of possible explosive activity. Although it was considered that the variation in incidence angle (26° at Ushas to 37° at Hathor) might be contributing to apparent differences in major characteristics of individual volcanoes, the complimentary nature of the Magellan incidence angles (35° at Ushas to 28° at Hathor), as well as a nearly 90° change in look direction, suggests that these variations are in fact real. A detailed look at the summit regions supports this suggestion: Innini and Hathor both have steep dome and tick-like features associated with bright diffuse deposits whereas the only summit features on the western half of Ushas Mons observed at the time of writing are a few small (<2 km) pits and cones. The relative development of fractures and rifts at the three volcanoes also indicates that they have had different histories. Preliminary interpretations suggest that this region is most similar to Western Eistla Regio in that it is a broad regional rise with superposed focused volcanism and rifting and fracturing that has not developed as fully as it has at Beta Regio. Both areas have experienced minor distributed volcanism on the plains surrounding the major edifices in the form of shield fields and mid-sized volcanic centers and there are indications of variations in style at the major edifices, although this is probably better developed at Dione. At Western Eistla a detailed chronology as been established (Senske et al.., 1992) but it does not appear that overlapping flow units are present at Dione to give the relative ages of the three edifices. A more complete picture of the region, particularly a detailed analysis of the fractures, may provide the needed evidence to build a stratigraphic history of the region which will serve as a basis for a more detailed comparison with similar rises.

References: Keddie, S.T., et al., 1990, LPSC XXI, pp. 615-616; Senske, D.A., et al., 1991, EMP 55, pp. 97-161; Senske, D.A., et al., 1992, JGR 97 E8, pp. 13395-13420.

THE DISTRIBUTION OF LARGE VOLCANOES ON VENUS AS A FUNCTION OF HEIGHT AND ALTITUDE;

S.T. Keddie and J.W. Head, Brown University

Introduction: Theory predicts that the slower cooling of lava flows on Venus should result in lava flows that are typically 20% longer than their terrestrial counterparts [1] and that the development of neutral buoyancy zones (NBZ) on Venus may be strongly influenced by altitude-controlled variations in surface pressure [2]. Observations that support these predictions would include relatively low heights for Venus volcanoes (discussed with pre-Magellan data by [3]), and an increase in both the number and development of large edifices with increasing basal altitude. We present the results of an analysis of the height and altitude distribution of 123 large (diameter >100 km) volcanoes made using Magellan image and altimetry data and we use these results to begin to test the predications of the above theories.

Height of large volcanoes: The height of a volcano was determined by taking the difference between the altitude of the highest point on the edifice and the average altitude of the plains at the distal reaches of flows from the edifice. The mean height of 123 large volcanoes on Venus was found to be 1.42 km (Figure 1), less than the heights of many terrestrial volcanoes, which are often a few kilometers high [4] and, in the case of Hawaii, as much as 8 km high [3] This low height results in a low mean slope for these volcanoes of less than one degree.

Altitude distribution of large volcanoes: If the bases of large volcanoes were evenly distributed as a function of elevation, they would be found in the skewed, unimodal distribution shown by the dark columns ('expected') in Figure 2. The actual distribution, however, shown in the observed category, shows a slight paucity of volcanoes at the extreme elevations and an enhancement in the number of edifices in the mid-altitudes. Chi-square tests of the data reveal that the two data sets are different at the 95% confidence level and that the deviations from the expected distribution are most pronounced in the mid-altitudes (more volcanoes than expected) and, to a lesser degree, in the lowlands (fewer volcanoes).

Height as a function of altitude: Although the majority of volcanoes cluster between basal altitudes of 6051-6053 km and at heights of <3 km, there is a weak correlation (R=0.55) of volcano height with basal altitude. Volcanoes that occur at the greatest elevations in general reach the greatest heights.

Discussion: The generally low heights of venusian volcanoes are consistent with the prediction that lava flows on Venus would be relatively long; the further a given volume of lava flows from its source, the thinner the flow will be and thus the less height it will contribute to a growing shield. Calculations of flow volumes may make it possible to estimate the degree to which this lengthening of flows has influenced volcano heights. There is a weak correlation of edifice height with basal altitude; the highest volcanoes occur at the greatest altitudes. These tall volcanoes, such as Maat Mons, are also quite well-developed; many flow episodes, of often significantly variable radar properties, hint at a long and complex history of volcanism [5]. Thus to a first order, there appears to be some evidence for the positive correlation of edifice development and topography predicted by Head and Wilson [2]. The distribution of large volcanoes as a function of altitude also supports these predictions. Poor or no development of a NBZ in the lowlands would inhibit edifice growth and promote flood and channel-type eruptions (illustrated by the paucity of low-altitude volcanoes in figure 2 and the prevalence of flood deposits and channels at this altitude range [6,7]). Early development of NBZ's at relatively shallow depths and enhanced magma production associated with local mantle upwelling at small regional rises would encourage growth and development of edifices at the mid-altitudes (illustrated by the greater-than-expected number of volcanoes in this altitude range in figure 2). The predicted

deepening of magma reservoirs with altitude suggests that larger magma reservoirs should form and that edifices should be common and well developed (illustrated by the relatively greater heights reached by volcanoes at high basal altitudes in figure 2 and the complexity of high-altitude volcanoes like Maat Mons).

Although to a first order the observed distribution of volcanoes on Venus as a function of altitude and height can be quite nicely explained by theoretical considerations, there are many factors that will influence the location of volcanoes on the above figures: age of a volcano; magma supply; thermal gradient and mantle dynamics; terrain type; burial by large flows; and possible changes in the intrusion to extrusion ratio of magma. Further consideration of these and other factors will result in a better understanding of the reasons for the distribution of large volcanoes on Venus.

References: [1] Head, J.W., and Wilson, L., 1986, JGR, 91, pp. 9407-9446; [2] Head, J.W., and Wilson, L., 1992, JGR, 97, pp. 3877-3903; [3] Schaber, G.G., 1991, PLPSC XXI, pp. 3-11; [4] McClelland, L., et al. (Ed.), 1989, Global Volcanism 1975-1985, 655 p.; [5] Keddie, S.T., and Head, J.W., 1992, LPSC XXIII, pp. 669-670; [6] Baker, V.R., et al., 1992, JGR, 97 E8 pp. 13421-13444; [7] Head J.W., et al., 1992, JGR, 97 E8, pp. 13153-13197.

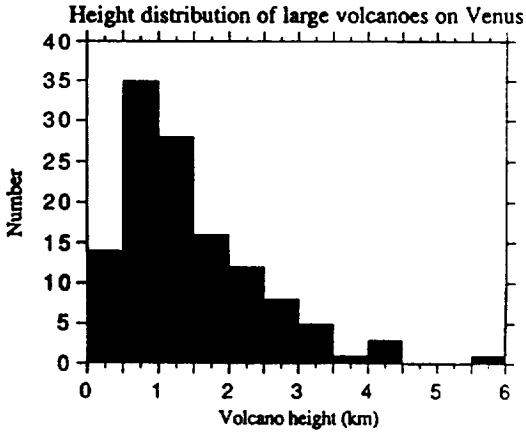

Fig. 1: Histogram of heights of large volcanoes on Venus. See text for method of calculating heights.

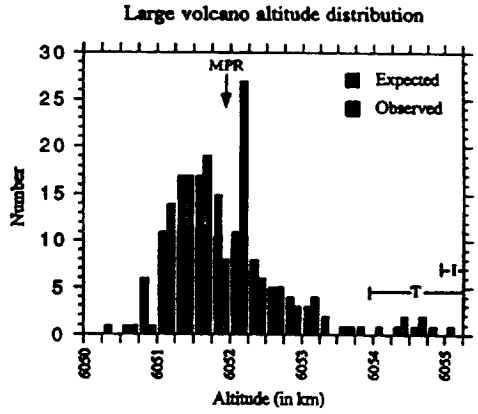

Fig. 2: Histogram showing location of the base of large volcanoes. 250 m altitude bins. 'MPR' is mean planetary radius, 'T' and 'I' indicate approximate altitude range for tessera and Ishtar Terra respectively. See text for a discussion of 'expected' vs. 'observed' categories.

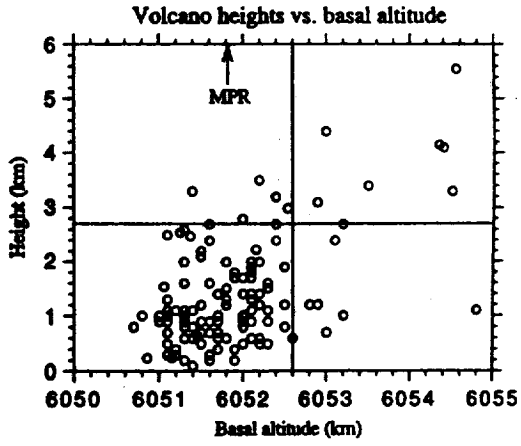

Fig. 3: Height of large volcanoes as a function of the altitude of the base of the volcano. Mean planetary radius (MPR) is indicated.

STRUCTURAL MAPPING OF MAXWELL MONTES; Myra Keep and Vicki L. Hansen, Southern Methodist University, Dallas, Texas, 75275.

Introduction. Four sets of structures have been mapped in the western and southern portions of Maxwell Montes. An early north-trending set of penetrative lineaments is cut by dominant, spaced ridges and paired valleys that trend northwest. To the south the ridges and valleys splay and graben form in the valleys. The spaced ridges and graben are cut by northeast-trending graben. The northwest-trending graben formed synchronously with or slightly later than the spaced ridges. Formation of the northeast-trending graben may have overlapped with that of the northwest-trending graben, but occurred in a spatially distinct area (regions of 2° slope). Graben formation, with northwest-southeast extension, may be related to gravity-sliding. Individually and collectively these structures are too small to support the immense topography of Maxwell, and are interpreted as parasitic features above a larger mass that supports the mountain belt.

Observations. Maxwell Montes comprises several physiographic provinces including; the northwest arm, the modified area associated with the impact crater Cleopatra, eastern and western ridges and the southern slope. Similar provinces are described by Kaula et al. [1]. This work addresses structural styles observed in the western ridges and southern slope. Structures in this area are mapped with confidence as they are relatively unaffected by flooding or ejecta-type modification from the impact crater Cleopatra. Structures with similar trends and timing relationships exist in other parts of the mountain belt.

Structural mapping of Magellan SAR images (C- and F-MIDR's) and framelets reveals the existence of four families of structures on the western ridges and southern slope of Maxwell Montes. Northwest-trending ridges, which dominate the structural fabric, extend from the northwest arm down to the southern slope (~ 700 km). Individual ridges vary in length from 150 to 500 km, have an average spacing of 8 to 10 km, and are relatively straight. Some of the ridges appear to anastomose, but this may be the effect of interaction with other lineament sets. Right-looking SAR images reveal radar-bright, west-facing slopes, enhanced by their contrast to a band of radar-dark material that runs the length of the western ridged area. To the east, spaced ridges continue through the modified, radar-bright bands associated with the impact crater Cleopatra, into the eastern flooded area, where ridge crests separate flooded valleys. To the west, ridges become increasingly radar-bright toward the steep western boundary with Lakshmi planum, and the spacing of ridges changes slightly, to ~ 6 km. On the southern slopes of Maxwell Montes ridge spacing increases and graben appear along the trace of the valleys. These graben are straight, parallel, paired lineaments which extend to the southern terminus of the mountain range and record northeast-southwest extension [2].

The third set of structures, which trend northeast, occur predominantly on the southern slope of the mountain range. This set contains a series of narrow, straight, paired, parallel-sided lineaments, with an average length of 20 km. We interpret these features as extensional because the area between lineaments is commonly filled with radar smooth material, both dark and bright, apparently filling topographic lows. These northeast to east-northeast trending graben occur mainly south of latitude 63N, in areas of 2° regional slope [2].

A fourth, weaker set of lineaments lies within the ridge-dominated area of central and western Maxwell Montes. This third set of structures contains closely spaced (6 to 12 km), wispy, north-trending, penetrative lineaments, which are especially well-developed between 3E and 5E, 64N. These lineaments interact with the spaced ridges, causing variations in strike direction and length that make their length and continuity difficult to ascertain. However, their penetrative nature readily distinguishes them from the spaced ridges. These penetrative lineaments continue into the crater-modified area, and the flooded area further east. They do not occur on the steep western slope.

Timing. As mentioned above, where the penetrative lineaments interact with the spaced ridges, their strike is modified. As a north-trending lineament approaches a ridge, the strike changes, becoming parallel to the ridge. Away from the ridge, the strike reverts to north. This modification occurs everywhere the penetrative lineaments encounter a ridge. The same effect is seen wherever penetrative lineaments encounter northwest-trending graben on the southern slope, but the relationships are obscured by flooding in the graben. The overall effect is that the penetrative lineaments snake their way north in a sigmoidal fashion. This suggests that the spaced ridges and northwest-trending graben postdate formation of the penetrative lineaments. Northeast-trending graben on the southern slope are interpreted as the youngest of the four sets of structures as they crosscut the ridges and northwest-trending graben. In places, these northeast-trending graben also clip the ends of the penetrative lineaments, causing irregularly-shaped depressions that have the tips of the penetrative lineaments and parts of the ridges preserved as "islands"(e.g., 63N, 6E). Their orientation, perpendicular to the trace of the spaced ridges, is consistent with a single strain regime in which the trend of the spaced ridges parallels the maximum principal strain axis and the trace of the grabens parallels the direction of maximum shortening. The orientation

STRUCTURE OF MAXWELL MONTES: Keep, M. and Hansen V.L.

of the northwest-trending graben is additionally controlled by the abrupt decrease in topography. In summary, the penetrative lineaments are the oldest structures, crosscut and modified by the spaced ridges and northwest-trending graben, which are themselves cut at their downslope extremities by northeast-trending graben. The periods of formation of these sets of structures may have overlapped with each other within the given temporal framework.

Interpretation.. The sigmoidal nature of the interference of the spaced ridges and the penetrative lineaments is similar to S-C shear geometries [3]. However, S-C geometries require specific angular relationships (0-45°) between the S (penetrative) and C (spaced ridges) planes. Although these relationships are seen for most of the interactions, to the south the spaced ridges change orientation slightly toward west-northwest, whereas the penetrative lineaments keep a northerly trend, and the angular relationship between these two sets of structures changes from acute to perpendicular. These observations are not compatible with S-C geometry, but are common with the development of crenulation cleavage [4], which simply records evidence of two sequential deformation events. We believe that the two sequential events on Maxwell Montes are the formation of the penetrative lineaments and the formation of the ridges. The short wavelengths and close spacing of the penetrative lineaments resemble surface deformation in a thin layer, such as wrinkles on a lava flow [5]. We therefore interpret the penetrative lineaments to be the result of contraction of a thin cover (over Maxwell Montes), forming "wrinkles". Continuing contraction, with a rotation of the principal axes of the strain ellipse, or later contraction in response to a new stimulus, produced the spaced ridges. The downslope splaying and extension of the spaced ridges in southern Maxwell indicates that contraction was stronger in the central part of Maxwell than on the southern slope. A good analogy to this downslope extension of spaced ridges would be that of stretching a thin or weak layer over a block. The thin or weak layer is extended both parallel and perpendicular to the slope. In areas of high topography on Earth, e.g., the Himalayas, extensional collapse parallel to the direction of maximum contraction accompanies contraction [5]. No such extension occurs on Maxwell, as evidenced by the lack of extensional overprint of the penetrative lineaments. This indicates that the highest points of Maxwell, away from areas of 2° regional slope, are stable. During formation of the spaced ridges, extensional features with traces parallel to the direction of maximum shortening developed on the flanks of the ridges in areas of 2° regional slope. As contraction progressed, extension was ongoing, perhaps as a result of gravity-sliding on the slopes of Maxwell Montes [2]. Although northeast-trending extension occurs only on the southern slope, the other lineament sets are seen throughout the modified area in the center of Maxwell, and in the flooded region to the east. Extensional faults may be present but obscured by flooding. We therefore extrapolate our interpretations to the modified area and the flooded eastern ridges.

These timing relationships allow us some insight as to the processes operating on Maxwell Montes. However, we interpret these processes to be surface processes only. The nature of the deformation (penetrative ridges, spaced ridges) is inconsistent with the great height of the mountain range; these structures are not responsible for the great elevation. Rather, the small scale features have the character of parasitic structures developed over a larger mass. We propose that the surface structural features on Maxwell Montes are the equivalent of "cover" deformation, and that Maxwell Montes is underlain by a rigid block of strong material. The shape and elevation of the underlying block controls the type, wavelength and orientation of features at the surface. Evidence in favor of this theory include: 1) the small scale of structures at the surface; 2) extension only in areas of 2° slope (i.e. defining the margins of the block; extension is downslope; 3) lack of extension parallel to contraction in the main part of the spaced ridges (the highest points of the mountain belt are not collapsing); and 4) the splaying of ridges and graben formation after a critical slope angle is reached. The more complexly deformed northwest arm of Maxwell Montes also has ridge structures parallel to those of the western ridges. Additional deformation in this area is largely parallel to the discontinuity separating the arm from the rest of Maxwell. This discontinuity may also represent a boundary to the underlying block.

[1] W.M. Kaula et al. (1992) JGR **97**, 16085; [2] S. E. Smrekar and S. C. Solomon (1992) JGR, **97**, 16121; [3] D. Berthe et al. (1979) J. Struct. Geol. **1**, 31; [4] J. G. Ramsay and M. I. Huber (1983) The Techniques of Modern Structural Geology, Academic Press, London, 307 pp.; [5] J. Green and N. M. Short (1971) Volcanic landforms and surface features, Springer-Verlag, New York. 519 pp., plate 143A; [6] B. C. Burchfiel et al. (1989) Geology **17**, 748.

I-Xe STRUCTURE OF ILAFEGH 009 AND SHALLOWATER: EVIDENCE FOR EARLY FORMATION AND RAPID COOLING OF IMPACT-DERIVED ENSTATITE METEORITES: K. Kehm, R.H. Nichols, Jr. and C.M. Hohenberg, McDonnell Center for Space Sciences, Washington Univ., St. Louis, MO 63130 USA; T.J. McCoy and K. Keil, Planetary Geosciences, Dept. of Geology and Geophysics, SOEST, Univ. of Hawaii at Manoa, Honolulu, HI 96822, USA.

Introduction. Enstatite meteorites have proven to be ideal samples for past studies of the I-Xe system [1,2,8]. This work focuses on two enstatite meteorites that were formed by impact processes. Ilafegh 009 is a clast-free impact melt rock from the EL chondrite parent body [3]. The Shallowater aubrite likely formed when a fully molten planetesimal collided with a solid planetesimal, mixing fragments of the solid planetesimal into the enstatite mantle of the molten planetesimal. A complex three-stage cooling history resulted from this mixing and later break-up and reassembly of the parent body [4]. The present study indicates that the I-Xe structure of these two meteorites resulted from *in situ* decay of live ^{129}I and that both experienced xenon closure of the iodine host phase at approximately the same time. I-Xe cooling rates are consistent with the cooling rates derived from mineralogic and petrologic studies of these objects [3,4]. The similarities in ages suggest that the region of the nebula in which enstatite parent bodies formed must have experienced an intense early bombardment.

Results. We have extracted Xe from neutron-irradiated samples of Shallowater and Ilafegh 009 by stepwise heating (Fig. 1a,b). The released gas included trapped xenon of normal composition and minor amounts of fission xenon, but the major contributions to ^{129}Xe and ^{128}Xe were due to the decay of extinct ^{129}I ($t_{1/2}$ = 17 Ma) and ^{128}Xe produced by neutron capture on stable ^{127}I. The radiogenic ^{129}Xe ordinate in Figs. 1a,b is shifted 10% to prevent overlap of the release patterns. Release of both iodine-derived isotopes in concert demonstrates that essentially all of the iodine in the meteorite remains associated (in fixed proportion) with radiogenic ^{129}Xe.

Linear isochrons (Figs. 2a,b) also illustrate the intimate association between radiogenic ^{129}Xe and ^{127}I. These isochrons plot the higher temperature extractions, which represent 96% of the radiogenic ^{129}Xe in Shallowater and >98% for Ilafegh 009. The precision of the slopes of these isochrons (defined by 27 temperature steps for Ilafegh 009 and 17 for Shallowater) corresponds to an uncertainty of about 80,000 years for each with xenon closure occurring in Ilafegh 009 about 400,000 years earlier than in Shallowater (about 1.6 Ma earlier than Bjurbole).

We have obtained cooling rates (Table 1) from the approach to the isochron, assuming that differences in closure temperatures were proportional to differences in extraction temperatures. These cooling rates are qualitatively consistent with cooling rates derived from petrologic studies [3,4]. The impact melt rock Ilafegh 009 cooled at hundreds of °C/Ma at high temperatures, decreasing asymptotically to a few °C/Ma at lower temperatures. The more limited temperature range for Shallowater reflects its narrow release pattern (Fig. 1b). I-Xe cooling rates, which suggest rapid cooling at high temperature with a sharp decrease in the cooling rate at lower temperatures, are consistent with the three-stage cooling history derived from petrological studies [4]. I-Xe does not maintain a reliable record at very low temperatures (~600 °C), at which very fast cooling is indicated by the kamacite-taenite system.

Chronological Significance. Variations in the observed ratio of ^{129}I to stable ^{127}I in the host minerals can, in principle, be due to isotopic heterogeneity instead of radioactive decay. However, the release patterns (Figs. 1a,b), which demonstrate that the ^{129}Xe comes from *in situ* decay of live ^{129}I, and the regular variations of initial iodine with release temperature, interpreted here in terms of cooling rates, both favor chronometric interpretation. The observation that the I-Xe chronometer seldom seems to agree with other chronometers [5] does not invalidate the I-Xe chronometer. In fact, we might not expect similar results from other chronometers which are dominated by other host phases. Instead, we should focus on the meaning of the I-Xe chronometer, especially for the enstatite meteorites.

The interpretation of the I-Xe structure depends critically on the siting of iodine in the meteorite. In many cases iodine is predominately located in secondary phases such as sodalite and apatite [6,7], and the I-Xe system reflects the chronometry of *secondary* processes (explaining, to a large extent, the discordancy with other chronometers). In the enstatite meteorites, the host phase is probably the major mineral enstatite [5,8] and here the I-Xe structure reflects crystallization and closure of this mineral.

Implications. Although Ilafegh 009 and Shallowater formed in different ways and on different parent bodies, impact played a role in the formation of both meteorites. It is interesting that the iodine-bearing phases of both meteorites closed for xenon within 400,000 years of each other. Even if isotopic heterogeneity should play some role in establishing the initial isotopic ratio, ^{129}I *does* decay to ^{129}Xe and the inferred time differences can then only *overstate* the actual differences in xenon closure times. Further, I-Xe studies of Happy Canyon [2], another impact melt form the EL parent body [3], indicates formation at essentially the same time, midway between Shallowater and Ilafegh 009. Thus, the impact events which formed Shallowater, Ilafegh 009 and Happy Canyon must have occurred essentially simultaneously, suggesting an early epoch of bombardment that was intense and terminated abruptly in the region of the solar nebula in which the enstatite meteorites formed.

References. [1] Hohenberg (1967) *EPSL* **3**, 357-362. [2] Kennedy *et al.* (1988) *GCA* **52**, 101-111. [3] McCoy *et al.* (1992) *LPSC XXIII*, 869-870. [4] Keil *et al.* (1989) *GCA* **53**, 3291-3307. [5] Swindle and Podosek (1990) In *Meteoritics and the Early Solar System* (eds. Kerridge and Matthews), 1127-1146. [6] Nichols *et al.* (1992) *Meteoritics* **27**, 268. [7] Swindle *et al.* (1988) *GCA* **52**, 2215-2227. [8] Kennedy (1981) Ph.D. Thesis, Washington Univ., St. Louis.

Table 1. Inferred I-Xe Cooling Rates (°C/Ma)

Temperature (°C)	Ilafegh 9	Shallowater
800	7.5 ± 1.2	
1000	3.5 ± 0.3	
1200	4.7 ± 0.2	
1400	43.6 ± 2.3	5.5 ± 0.3
1600	908 ± 500	4.7 ± 0.1
1800	~infinite	1500 ± 1500

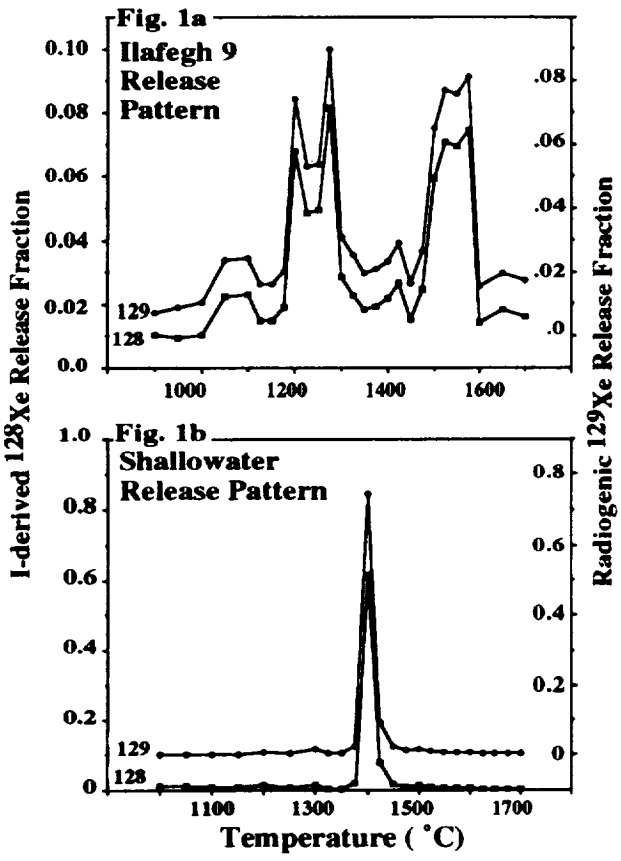

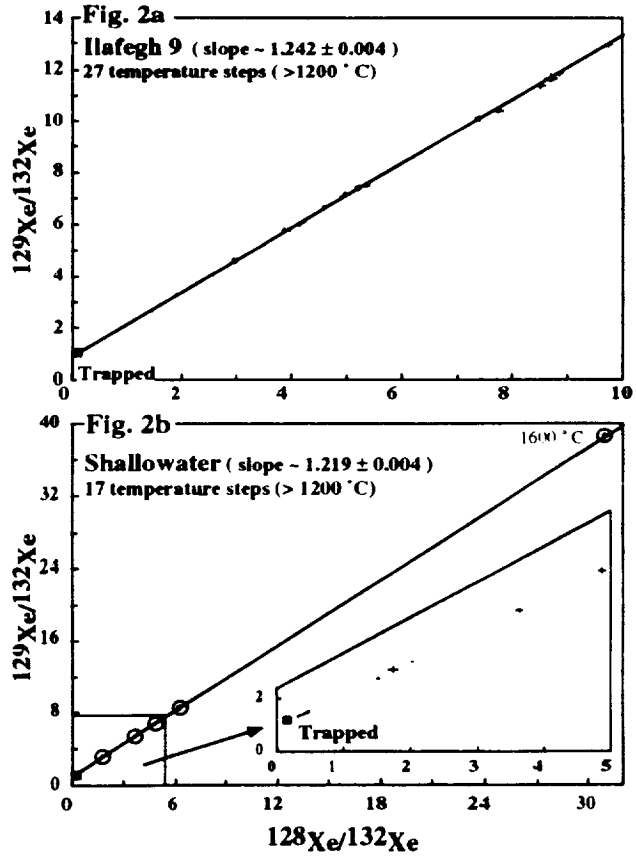

EXPLOSIVE VOLCANISM AND THE COMPOSITIONS OF THE CORES OF DIFFERENTIATED ASTEROIDS;

Klaus Keil[1] and Lionel Wilson[1,2] [1]Planetary Geosciences, Dept. of Geology and Geophysics, School of Ocean and Earth Science and Technology, University of Hawaii at Manoa, Honolulu, Hawaii 96822, USA [2]Environmental Science Div., Institute of Environmental and Biological Sciences, Lancaster University, Lancaster LA1 4YQ, UK

Abstract: Eleven iron meteorite groups showing correlations between Ni and siderophile trace elements that are predictable by distribution coefficients between liquid and solid metal of fractionally crystallizing metal magmas, are interpreted to be fragments of the fractionally crystallized cores of 11 differentiated asteroids. Many of these groups crystallized from S-depleted magmas which we propose resulted from removal of the first partial melt (a Fe,Ni-FeS cotectic) by explosive pyroclastic volcanism. We show that these dense, negatively buoyant melts can be driven to asteroidal surfaces by the combination of an excess pressure in the melt and the presence of buoyant bubbles of gas which decrease the bulk density of the melt. We also show that in typical asteroidal materials, veins will form which grow into dikes and serve as pathways for migration of melt and gas to asteroidal surfaces. Since cotectic Fe,Ni-FeS melt consists of about 85 wt.% FeS and 15 wt. % Fe,Ni, removal of small volumes of eutectic melts results in major loss of S but only minor loss of Fe,Ni, thus leaving sufficient Fe,Ni to form sizeable asteroidal cores.

The abundances of siderophile trace elements of 11 of the 13 known iron meteorite groups are correlated with Ni contents [1] and trace element/Ni ratios can be explained by the distribution coefficients between liquid and solid metal of fractionally crystallizing metal magmas [2-4]. These groups, called the magmatic iron meteorite groups, appear to be fragments of the fractionally crystallized cores of 11 differentiated asteroidal parent bodies. The initial S contents of the magmas from which these meteorites crystallized have been estimated from the abundance patterns of siderophile trace elements and the effects that S has on the distribution coefficients of these elements [2-5]. Many of these groups must have crystallized from magmas that were depleted in initial S contents by factors of up to about 6 from those of reasonable precursor materials, such as ordinary chondrites. Table 1 lists the magmatic iron meteorite groups for which estimates of initial S contents are available [3-5], the ranges of their metallographic cooling rates, their parent body radii calculated from those rates, and the best estimates of the specific radii, using the most plausible cooling rates and parent body models (H. Haack, pers. comm.; [6]). With decreasing S content, meteorite cooling rates increase and, hence, parent body radii decrease.

Hypotheses proposed to explain the S depletions of magmas of magmatic iron meteorite groups include loss by volatilization, by continuous removal as an immiscible liquid, and by removal of metastable liquid layers produced by episodic melting [7]. We propose a new model to account for the S depletions of a number of the magmatic iron meteorite groups, involving explosive volcanism such as that postulated to explain the loss of partial melts from the aubrite parent body [8]. A few hundred ppm of expanding volatiles present in early partial (basaltic) melts on the aubrite parent body (or other differentiated asteroids less than about 100 km in radius), upon ascent of the magma to the surface of the body, would have caused disruption into a spray of droplets moving with velocities in excess of the local escape velocities of small asteroidal-sized bodies. The droplets would thus escape and be lost into space 4.55 Ga ago. As a result, no such basaltic rocks exist as individual meteorites nor as clasts in brecciated aubrites. This concept of pyroclastic volcanism has also been applied to explain the lack of complementary basaltic rocks to the ureilites [9-11], and Muenow et al. [12] have shown how pressure rises in asteroids of at least 10s of MPa due to partial melting cause the growth of pathways (fractures, connecting into dikes) which can deliver these early partial melts to the surfaces of asteroids. We suggest that the depletion in initial S contents of the magmas of some of the magmatic iron meteorites is the result of removal from the parent bodies and loss into space of cotectic Fe,Ni-FeS melts by explosive pyroclastic volcanism. This process is expected to be more effective the smaller the bodies and, thus, could explain the decrease in initial S contents of Fe,Ni magmas with decreasing parent body radii (Table 1) [13].

EXPLOSIVE VOLCANISM AND ASTEROID CORES: Keil K. and Wilson L.

If the precursor material of the magmatic iron meteorite groups was roughly similar in composition to ordinary chondrites such as those of the H group, as seems reasonable, then it contained 16.8 wt. % Fe,Ni and 5.1 wt. % FeS [14], and an unfractionated Fe,Ni-FeS magma derived from such material should have 76.7 wt. % Fe,Ni and 23.3 wt. % FeS. However, upon heating of an asteroid of H group composition, the first partial melt would form at the Fe,Ni-FeS cotectic temperature of about 980°C and consist of about 85 wt. % FeS and 15 wt. % Fe,Ni [15,16]. When all of the FeS in the asteroid has been incorporated into such a melt, the melt represents 6.0 wt. % of the asteroid; because of its high density (5000 kg m^{-3}), the melt occupies about 4.2 % of the volume of the asteroid.

The negative buoyancy of this melt can be entirely compensated by the presence of a few hundred to thousand ppm volatiles at pressures up to several tens of MPa. These pressures are produced by the density change on partial melting, and can cause growth and interconnection of cavities occupied by gas and liquid to form dikes which eventually connect to the surface. The rate at which the pathways are formed can be greater than the rate at which gas bubbles rise through the dense liquid, thus ensuring fairly uniform dispersion of the bubbles throughout the liquid. The subsequent expansion of the pressurized volatiles then drives pyroclastic volcanism [8]. Removal of about 88 wt. % of the Fe,Ni-FeS cotectic liquid from an average H group precursor material would deplete the residue in S content to approximately that of the IVB iron meteorite group, which is the group most highly depleted (Table 1). The percentages are even lower for the magmatic iron meteorite groups with higher initial S contents (Table 1). However, because the cotectic melt is relatively poor in Fe,Ni (15 wt. %) and rich in sulfide (85 wt. %), removal of even 88 wt. % of this melt would result in removal of only about 3.5 wt. % metallic Fe,Ni and leave about 96 wt. % of the original Fe,Ni to form a sizeable core.

Table 1: Estimated initial S contents of magmas of magmatic iron meteorite groups, their metallographic cooling rates (MCR), parent body radii (R), and percentage required loss of cotectic Fe,Ni-FeS liquid (LCL).

GROUP	S(%)	MCR (K/Ma)	R (km)	LCL(%)
II AB	10-17	6-12	100-73; avg.87	0
IIIAB	4-5	3-75	138-31; avg. 85	41
IV A	1.0-1.8	11-500	75-13; avg. 44	82
IV B	0.6-1.2	30-260	47-17; avg. 32	88
H chondrites*	8.6			

* This is the S content of the metallic Fe,Ni-FeS portion of H chondrites.

References: [1] Malvin D.J., Wang D. and Wasson J.T. (1984) GCA 48, 785. [2] Willis J. and Goldstein J.I. (1982) JGR 87, A435. [3] Jones J.H. and Drake M.J. (1983) GCA 47, 1199. [4] Sellamuthu R. and Goldstein J.I. (1985) JGR 90, C677. [5] Rasmussen K.L., Malvin D.J., Buchwald V.F. and Wasson J.T. (1984) GCA 48, 805. [6] Haack H., Rasmussen K.L. and Warren P.H. (1990) JGR 95, 5111. [7] Kracher A. and Wasson J.T. (1982) GCA 46, 2419. [8] Wilson L. and Keil K. (1991) EPSL 104, 505. [9] Warren P.H. and Kallemeyn G.W. (1991) EOS 72, 281. [10] Scott E.R.D., Keil K. and Taylor G.J. (1992) LPS XXIII, 1253. [11] Scott E.R.D., Taylor G.J. and Keil K. (1993) GRL (submitted). [12] Muenow D.W., Keil K. and Wilson L. (1992) GCA 56 (in press). [13] Keil K. and Wilson L. (1992) Meteoritics 27, 241. [14] Keil K. (1962) JGR 67, 4055. [15] Kullerud G. (1963) Ann. Rep. Geophys. Lab. Washington D.C. 1412, 175 [16] Kubaschewski O. (1982) Iron-Binary Phase Diagrams, 185 pp. Springer Verlag.

HIGH-RESOLUTION SEISMIC REFLECTION SURVEY AT THE MANSON CRATER, IOWA

KEISWETTER, D.A.[1], BLACK, R.[1], STEEPLES, D.W.[1], and ANDERSON, R.R.[2],
[1] Univ. of Kansas, 120 Lindley Hall, Lawrence, Kansas 66045; [2] Iowa Dept. Nat. Res., Geol. Survey Bureau, 123 N. Capitol St., Iowa City, Iowa 52242.

Approximately 17.4 km of high-resolution reflection data were acquired along an east-west radius of the Manson Impact Structure (MIS) to delineate the shallow (upper 300 m) subsurface structural configuration. The geometry of the shallow structure is poorly known due to a 30-90 m thick Pleistocene till cover. The resolution of the new seismic data is roughly 5-10 times that of existing Vibroseis data. Data quality varies rapidly along the line from exceptional to poor, due primarily to velocity variations associated with the geological complexity of the area. Preliminary results indicate subsurface structural blocks previously envisioned to be several hundreds of meters in size are actually an order of magnitude smaller and more complex. A seismogram-by-seismogram analysis is necessary to confidently identify intricate stratigraphic and structural relationships seen on preliminary CDP sections, as numerous faults, diffractions, and complicated reflection patterns create potential pitfalls.

Two existing industry Vibroseis lines ([1], [5]) have been used to help define the deep structure of the MIS. The lines intersect near the central uplift, extend radially to the east and to the south, and indicate the structure is approximately symmetric. Based on the Vibroseis lines, water well cuttings, cores, and geophysical logs, the structure can be broken into three general structural domains ([1], [5]); an outermost, 5 km wide ring fracture zone, a 7 km wide moat, and an apparent central uplift. The seismic signature of the ring fracture zone is characterized by subparallel sets of discontinuous events interpreted to be down-dropped blocks of Paleozoic and Cretaceous strata. A strong reflection event occurs at approximately 2 s (about 4 km depth) and is interpreted to represent the top of the Proterozoic crystalline basement rocks. Numerous normal faults are observed in the upper 500 ms of data within the ring-fracture domain. Within the moat domain the basement reflector shallows rapidly, the Paleozoic strata reflections are absent, and a series of discontinuous, flat-lying events may represent either a melt layer [3] or lake bed deposits [2]. Along the edge of the central uplift, Proterozoic gneissic and granitic basement rocks have been encountered as shallow 30 m below the land surface. The shallow portion of the uplift is not well imaged by the Vibroseis data but the data seem to indicate that the structure is fairly symmetric. Preliminary reprocessing of existing gravity [4] and magnetic data suggest a more complex central uplift. The potential field data indicate the central uplift may be saddle-shaped. Alternatively there may possibly be two distinct uplifts, positioned slightly off the currently believed location [5].

While the Vibroseis data provide critical constraints on the gross structural components, poor near surface (less than 300 m) resolution renders it useless for correlation of well information. For this reason, new high-resolution seismic data was acquired to allow new drilling information to be tied together and correlated with the existing seismic information. In July of 1992, walkaway noise tests were conducted prior to production to determine optimum recording parameters. Parameters varied during the tests included the 50 Caliber rifle, 30.06 rifle (both fired downhole), and the 8- and 12-gauge auger guns [6] as sources, and 0, 50, 100, 140, and 280 Hz low cut filters. The receiver arrays consisted of three 40-Hz geophones equally spaced over approximately 1 m and centered on 2.5 m stations, with source-to-receiver offsets ranging from 2.5 m to 345 m. A 48 channel, 2401-X EG&G seismograph recorded the data in a modified SEG-Y format. Distinct wave types can be identified on the walkaway profiles (Figure 1). After analysis of the walkaway data in the lab, production parameters were chosen: 1) an end-on shooting geometry, 2) the 50 Caliber rifle was (based on relative energy levels and data bandwidth), 3) 50 Hz low-cut filters, 4) 1/2 ms sample interval, and 5) a record length of 750 ms. Over 1,700 shot points of high-resolution shallow reflection seismic data were subsequently acquired along the route of the east-west radial Vibroseis line. A total of 17.4 km of seismic line was acquired with a station spacing of 5 meters and a shot point interval of 10 meters. The data quality of the resulting nominal 12 fold CDP data varies from excellent to poor along the transect.

Preliminary interpretations of the seismic data suggest that the structural blocks originally assumed to be hundreds of meters in size are actually on the order of tens of meters in size. Many of the shot records have multiple faults, and/or diffractions interpretable on the field files (Figure 2). Because of the geologically complex structures and lateral as well as vertical velocity variations the subtle stratigraphic and structural details present require essentially a seismogram-by-seismogram analysis for interpretation.

References

[1] Anderson R. R. and Hartung J. B. (1992) *Proceeding of Lunar and Planetary Science*, 22, 101-110.
[2] Anderson R. R. and Ludvigson G. A. (1989) Geological Society of Iowa, Guidebook 50.
[3] Sharpton B. L. and Grieve R. A. (1990) Geological Society of America Special Paper 247, 301-318.
[4] Holtzman A. F. (1970) Unpublished masters thesis, University of Iowa.
[5] Black R. A., Anderson R. R., Keiswetter D. A., and Steeples D. W. (1992) [abstr.], EOS, 73, 43, 354.
[6] Healey J., Anderson J., Miller R. D., Keiswetter D. A., Steeples D. W. and Bennett B. (1991) SEG Expanded Abstracts, 1, 588-591.

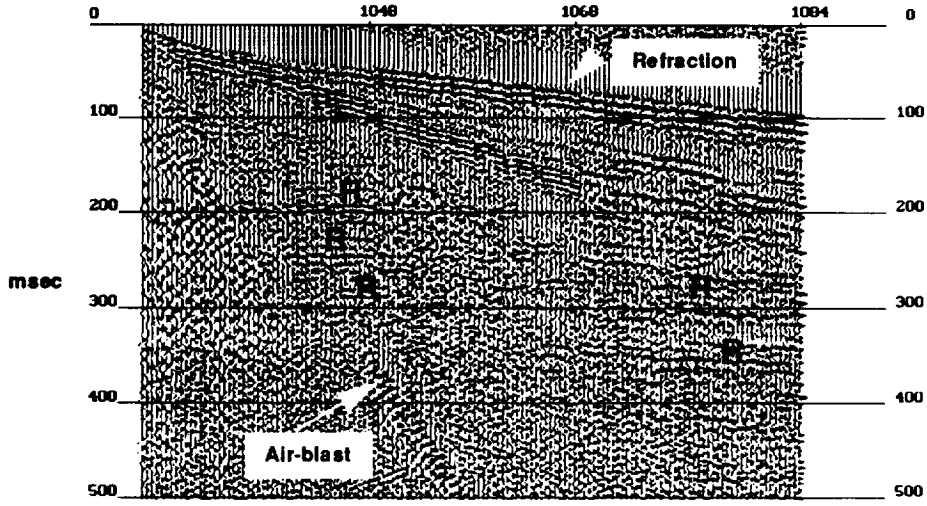

Figure 1. Walkaway noise test, AGC scale and digitally filtered, acquired with the 50 Cal. rifle. Reflections can be interpreted from 30 ms to 500 ms in these data (marked by an R).

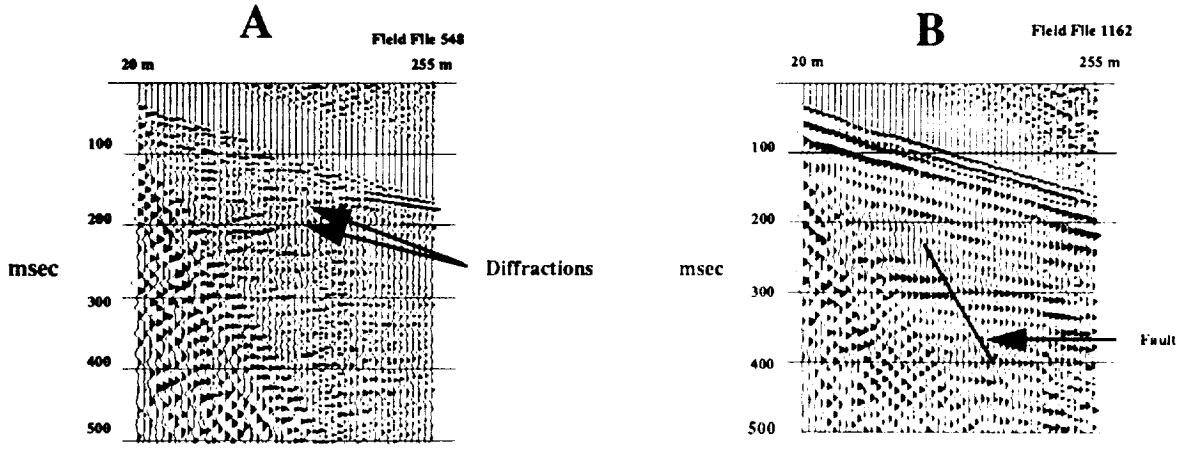

Figure 2. Field files, AGC scaled and digitally filtered, showing easily identifiable diffractions (A) and a fault (B).

HETEROGENEOUS PLAGIOCLASE COMPOSITIONS IN THE MARALINGA CK4 CHONDRITE. Lindsay P. Keller, SN4 NASA Johnson Space Center, Houston, TX 77058.

Introduction. One of the characterisitic features of CK chondrites is the wide compositional range displayed by feldspar grains in matrix relative to the narrow range of compositions exhibited by the highly equilibrated olivines and pyroxenes [e.g. 1, 2]. Recently, it was suggested that these heterogeneous feldspar compositions may have been strongly influenced by shock metamorphism [3]. In this report, it is shown that the apparent range of feldspar compostions in Maralinga probably results from annealing during parent body thermal metamorphism rather than shock.

The majority of matrix feldspars in Maralinga are typically 50 um in size and are compositionally zoned, with oligoclase cores (~An40) and bytownite rims (~An80). The contact between core and rim is sharp and abrupt and is readily observed in backscattered SEM images (Fig 1).

Experimental. Over 40 plagioclase grains with distinct rims were analyzed from three polished thin sections of Maralinga. Quantitative electron microprobe analyses were obtained using a rastered beam over a 4 um X 4 um square region in order to minimize Na loss. Analyses were collected so that the errors associated with counting statistics were <1% for Na, Al, Si, and Ca.

Regions of matrix were extracted from the polished thin sections and ion-thinned to electron transparency for transmission electron microscope study of the feldspar microstructures.

Results and Discussion. Figure 2 is a histogram showing the frequency distribution of matrix plagioclase compositions from Maralinga. The cores of the plagioclase grains cluster around An44, but range from An34 to An52. The rim compositions range from An76 to nearly end member anorthite (An98), but are strongly peaked at An84. These preferred compositions are consistent with the inferred subsolidus relations in the plagioclase solid solution series proposed by [4]. Grove et al. [4] suggested that at equilibrium, a miscibility gap occurs between ~An40 and ~An90 in the temperature range 400 to ~575C. Within this gap, intermediate plagioclase compositions probably result from metastable spinodal decomposition within either the Boggild or Huttenlocher gaps [4]. The overgrowth relation of An84 on more sodic cores is consistent with the production of the calcic rims by prograde reactions during thermal metamorphism on the Maralinga parent body. Equilibrium has not been completely attained however. The initial TEM examination of the matrix plagioclase shows that the calcic rims display the distinctive diffraction effects (i.e. the presence of *e*- and *b*-reflections in [001] electron diffraction patterns) associated with the presence of Huttenlocher intergrowths.

Conclusions. An equilibration temperature of 720 C was calculated for Maralinga using the Lindsley two-pyroxene geothermometer [1]. The presence of "equilibrated" plagioclase compositions coupled with the high degree of Fe-Mg-Ni equilibration of Maralinga olivines suggests that the thermal metamorphic event was of long duration. This conclusion is also supported by measurements of trace elements, particularly Zn [5].

Detailed analysis of the compositions of matrix plagioclase grains in Maralinga indicates that the heterogeneous compositions result from subsolidus equilibration during thermal metamorphism. The formation of the heterogeneous plagioclase compositions in Maralinga matrix by shock metamorphism as proposed by [3] is not consistent with the observed level of shock effects in Maralinga.

References. [1] Geiger, T. and Bischoff, A. (1991) *Meteoritics* 26, 337. [2] Kallemeyn, G. W. *et al.* (1991) *GCA* 55, 881. [3] Rubin, A. E. (1992) *GCA* 56, 1705. [4] Grove, T. L. *et al.* (1983) *Amer. Min.* 68, 41. [5] Lindstom, D. J. et al. (1993) *LPSC XXIV*, this volume.

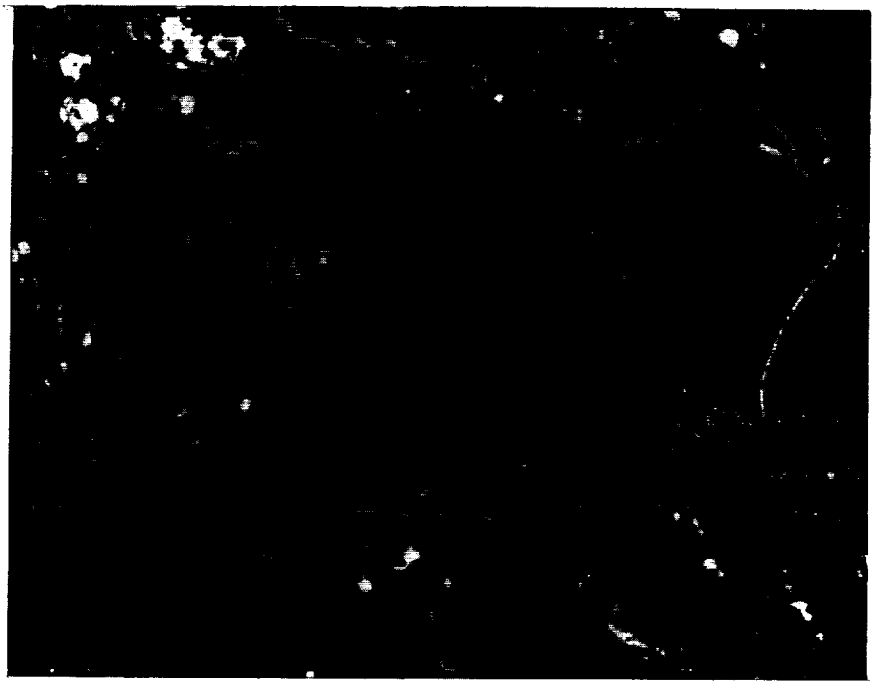

FIGURE 1. Backscattered SEM image of a typical matrix plagioclase grain in Maralinga

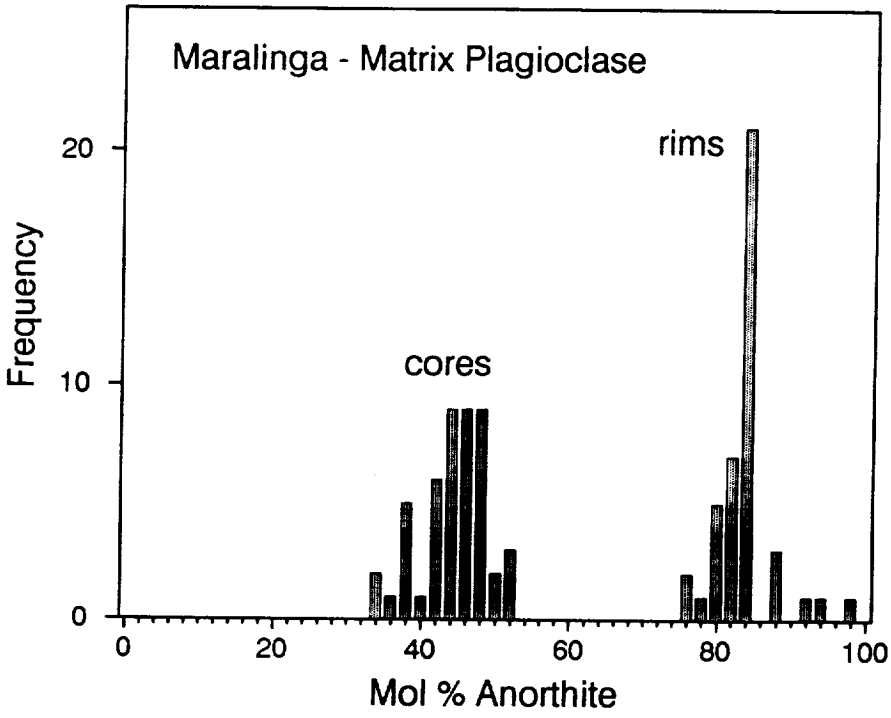

FIGURE 2. Distribution of compositions for Maralinga matrix plagioclase grains.

CARBON ABUNDANCES, MAJOR ELEMENT CHEMISTRY, AND MINERALOGY OF HYDRATED INTERPLANETARY DUST PARTICLES. L. P. Keller, K. L. Thomas, and D. S. McKay, SN4 and SN, NASA Johnson Space Center, Houston, TX 77058 and C23, Lockheed, 2400 NASA Rd. 1, Houston, TX 77058.

Introduction. Hydrated interplanetary dust particles (IDPs) comprise a major fraction of the interplanetary dust particles collected in the stratosphere. While much is known about the mineralogy and chemistry of hydrated IDPs, little is known about the C abundance in this class of IDPs, the nature of the C-bearing phases, and how the C abundance is related to other physical properties of hydrated IDPs. Here we report bulk compositional data (including C and O) for 11 hydrated IDPs that were subsequently examined in the TEM to determine their mineralogy and mineral chemistry. Our analysis indicates that these hydrated IDPs are strongly enriched in C relative to the most C-rich meteorites. The average abundance of C in these hydrated IDPs is 4X CI chondrite values.

We determined the bulk compositions (including C and O) of 11 hydrated IDPs by thin-window, energy-dispersive x-ray (EDX) spectroscopy of the uncoated IDPs on Be substrates in the SEM (procedures described in detail in [1]). As a check on our C measurements, one of the IDPs (L2006H5) was embedded in glassy S, and microtome thin sections were prepared and placed onto Be substrates (see [2], this volume). Thin-film EDX analyses of multiple thin sections of L2006H5 show good agreement with the bulk value determined in the SEM [2]. Following EDX analysis, the mineralogy and mineral chemistry of each IDP was determined by analyzing ultramircotome thin sections in a TEM equipped with an EDX spectrometer.

Mineralogy. Table 1 summarizes the major mineralogy and mineral chemistry of the 11 hydrated IDPs analyzed in this study. All of our hydrated IDPS are low porosity objects that are dominated by abundant phyllosilicates (from ~30 to 80% by volume) and fine-grained Fe-Ni sulfides. The phyllosilicates are usually Fe-bearing saponites with Mg/Mg+Fe > 0.5, but in two of the IDPs, serpentine is the phyllosilicate phase. Generally, there is detectable Al in the saponites as well, so that the saponites contain a small component of dioctahedral smectite (montmorillonite). Fine-grained sulfides are ubiquitous in hydrated IDPs. Electron diffraction patterns show that the sulfides are mainly pyrrhottite or pentlandite. Pentlandites show a range of Ni contents extending up to 30 wt.% Ni. Typically, sulfide grains in hydrated IDPs show a range of Fe/Ni.

Minor phases in our hydrated IDPs include anhydrous silicates (olivine, enstatite, high-Ca cpx), Mg-Fe carbonates, kamacite, chromite, and magnetite. The anhydrous silicates such as pyroxenes and olivines are generally a minor component or are entirely absent in our set of hydrated particles. Olivine and pyroxene compositions vary over a wide range of Mg/Mg+Fe but most are concentrated near very magnesian compositions. Distinct Mg-Fe carbonates occur in only 3 of the 11 analyzed IDPs. Their compositions span a wide range of Mg/Mg+Fe values from 0.3 to 1. Ca and Mn are detectable in the carbonates, but are uniformly low in abundance (typically <0.5 wt.%). In the heated IDPs, magnetite commonly occurs as discontinuous or complete polycrystalline rims up to 200 nm thick surrounding the particles.

Bulk Compositions. Element abundances for major elements (including C and O) in the 11 hydrated IDPs are given in Table 2. Several other elements not listed in Tab. 2 (e.g. P, K, Ti, Cr, and Mn) were analyzed for and detected in most of the particles, but at concentrations below 0.5 wt.%. As a group, our IDPs are well within a factor of 2 of CI abundances for all elements with the exception of C which is systematically enriched by 2 to 6X CI levels. L2005P13 is the only particle in this study which does not show the strong depletion in Ca that has been used as a diagnostic feature of hydrated IDPs [3].

Heating effects during atmospheric entry. The 11 IDPs show a range of mineralogical and chemical changes in response to atmospheric entry heating, ranging from prominent magnetite rims, degraded crystallinity of phyllosilicates, and Zn depletions [4] in strongly heated IDPs; to pristine particles that lack mineralogical evidence for any significant heating during atmospheric entry and show chondritic Zn levels. Moderately heated IDPs exhibit thin, discontinuous magnetite rims yet retain well-crystalline phyllosilicates. In Table 1, the IDPs are classified as unheated, mildly heated with discontinuous magnetite rims, or strongly heated with continuous magnetite rims. The strong heating experienced by some of the hydrated IDPs may result from relatively high entry velocities [5].

The lack of a correlation between C and S abundance and the degree of entry heating suggests that there was no appreciable loss of these elements during the transit of the IDPs through the atmosphere.

The nature of carbon in hydrated IDPs. Our measured bulk carbon abundances for the group of 11 IDPs ranges from 6 to 22 wt.% (Table 1), with an average of ~13 wt.% C (nearly 4X CI levels). With the exception

of the few cases where distinct carbonate grains are observed, other discrete carbon-rich phases have not been identified. Fine-grained carbonates could account for some but not all of the measured C abundances. Thus, we believe that C-rich materials such as poorly-graphitized or amorphous C must be finely dispersed throughout the hydrated IDPs.

Hydrated IDPs are generally believed to be derived from asteroidal sources that have undegone some degree of aqueous alteration. However, the high C contents of hydrated IDPs determined in this study indicate that they are probably not derived from asteroidal sources sampled by the known chondritic meteorites.

References. [1] Thomas, K. L. *et al.* (1993) *GCA*, in press. [2] Bradley, J. P. *et al.* (1993) *LPSC XXIV*, this volume. [3] Schramm L. S. *et al.* (1990) *Meteoritics* 24, 99. [4] Flynn, G. J. *et al.* (1992) *LPSC XXIII*, 375. [5] Flynn, G. J. (1990) *Proc. 20th LPSC*, 363. [6] Anders, E. and Grevesse, N. (1989) *GCA* 53, 197.

Table 1. Mineralogical data for 11 hydrated IDPs.

IDP	phyllo type1	Mg# of phyllos	Ni in sulfide	heated ?	Mt rim2	Other phases
L2005L6	sap	0.5	22-28	Y	D	chromite, no anhydrous silicates
L2005P9	serp	-	2-28	Y	W	low-Ca pyx, extremely heated
L2005P13	serp	-	4-6	Y	W	olivine, low-Ca & high-Ca pyx
L2006H5	sap	0.5-0.8	~5	N	U	enstatite, magnetite, Mg-carbonates
L2005R7	sap	0.5-0.6	0-25	N	U	no anhydrous silicates
L2006C12	sap	-	variable	Y	D	Ni-rich sulfides
L2006E10	sap	0.2-0.5	5-50	N	U	kamacite
L2006F10	sap	0.5	4	Y	D	no anhydrous silicates, Mg-Fe carbonates
L2006F12	sap	-	4-7	Y	W	kamacite, no anhydrous silicates
L2006G1	sap	0.4	3-23	N	U	distinct carbonate grains
L2006J14	sap	0.4-0.6	1-14	Y	D	no anhydrous silicates

1 sap = saponite, serp = sepentine.
2 U=unheated, D=discontinuous magnetite rim, W=well-developed mt rim

Table 2. Element abundances in 11 hydrated IDPs.
Orgueil data from [6].

	Element Abundances (in wt.%)									
IDP	C	O	Na	Mg	Al	Si	S	Ca	Fe	Ni
L2005L6	12	29	0.8	10.2	0.9	12	3.1	1.4	27	2.5
L2005P9	20	29	0.8	8.0	1.3	10	2.1	0.1	28	0.7
L2005P13	11	28	0.5	11.4	1.0	14	3.2	2.4	25	1.4
L2006H5	8	36	0.9	8.5	1.2	17	7.3	0.2	18	1.1
L2005R7	9	35	0.9	12	1.4	19	2.9	0.1	19	0.8
L2006C12	6	33	0.8	6.2	1.2	8.8	3.2	0.1	40	0.3
L2006E10	11	37	1.3	11	1.3	15	2.1	0.5	18	1.6
L2006F10	15	40	1.5	10	1.0	14	3.9	0.1	13	0.8
L2006F12	7	36	1.5	9	1.3	13	2.3	0.4	27	1.1
L2006G1	20	38	1.5	9.6	0.8	13	4.0	0.7	12	0.8
L2006J14	22	38	1.4	12	1.1	13	1.6	0.2	10	0.6
Average	13	34	1.1	9.8	1.1	14	3.2	0.6	22	1.1
Orgueil	3.5	46	0.5	9.5	0.9	10.7	5.2	0.9	18.5	0.6

AN INITIAL PERSPECTIVE OF S-ASTEROID SUBTYPES WITHIN ASTEROID FAMILIES; M. S. Kelley and M. J. Gaffey, Dept. of Earth & Env. Sci., Rensselaer Polytechnic Institute, Troy, NY 12180-3590

Many main belt asteroids cluster around certain values of semi-major axis (a), inclination (i), and eccentricity (e). Hirayama [1,2] was the first to notice these concentrations which he interpreted as evidence of disruptions of larger parent bodies. He called these clusters "asteroid families". The term "families" is increasingly reserved for genetic associations to distinguish them from clusters of unknown or purely dynamical origin (e.g. the Phocaea cluster [3]). Members of a genetic asteroid family represent fragments derived from various depths within the original parent planetesimal. Thus, family members offer the potential for direct examination of the interiors of parent bodies which have undergone metamorphism and differentiation similar to that occuring in the inaccessible interiors of terrestrial planets. The condition that genetic family members represent the fragments of a parent object provides a critical test of whether an association (cluster in proper element space) is a genetic family. Compositions (types and relative abundances of materials) of family members must permit the reconstruction of a compositionally plausible parent body. The compositions of proposed family members can be utilized to test the genetic reality of the family and to determine the type and degree of internal differentiation within the parent planetesimal. The interpretation of the S-class mineralogy provides a preliminary evaluation of family memberships.

To date no detailed investigation of proposed genetic relationships using the specific mineralogy and petrology of family members has been published. The closest approximations to a genetic relationship study have been attempts to confirm logical family groups based upon taxonomic types of family members primarily from existing survey data [4-9]. While a valuable first step, such taxonomy-based approaches do not have the sensitivity nor the discriminability of a mineralogy-based approach. In particular, it is generally accepted that each asteroid started with some initial composition similar to one of the chondritic groups. The composition of the mafic silicates in a differentiated parent body can be related to the chondritic group from which it was derived. For example, any genetic affinity between two fragments in a nominal family would be precluded if their compositions differed in a manner which did not conform to some part of the chemical evolutionary sequence from a single initial composition.

Since Hirayama's pioneering work, the number of known asteroids has increased greatly, improved methods of calculating orbital elements have been devised [e.g. 10-13], and new methods of distinguishing statistically significant clusters have been utilized [e.g. 11, 12, 14-17]. All subsequent surveys have confirmed Hirayama's six original families, with additional members added as the known asteroid population has increased. However, there has been considerable disagreement among recent studies regarding the total number of families and the family memberships, including additions to the original six. The various approaches have different criteria for identifying a family and for including or excluding potential members. The detection of small families against high backgrounds is a particularly contested issue, with some investigators identifying large numbers of such families while others find few. The validity of such families could be tested by determining the compositions of members and establishing whether they represent plausible compositions for a single parent body.

Detailed mineralogical and petrological analysis has been done based on the reflectance spectra of 39 S-type asteroids [18]. The result is a division of the S-asteroid class into seven subtypes based on compositional differences. These subtypes, designated S(I) to S(VII), correspond to surface silicate assemblages ranging from monomineralic olivine (dunites) through olivine-pyroxene mixtures to pure pyroxene or pyroxene-feldspar mixtures (basalts). The most general conclusion of this study is that the S-asteroids cannot be treated as a single group of objects without greatly oversimplifying their properties. Each S-subtype needs to be treated as an independent group with a distinct evolutionary history.

Half of the objects in the Gaffey et al. [18] survey fall into Williams [12] families and 8 of the asteroids (4 pairs) fall into 4 families. 39 Laetitia, subtype S(II), and 264 Libussa, subtype S(V), are in family 67. Two subtype S(V) objects, 101 Helena and 389 Industria, are

in family 144. Asteroid 115 Thyra is a borderline subtype S(III-IV) object and 584 Semiramis is a subtype S(IV), both fall within the family 163. Family 170 only contains two numbered objects, 9 Metis and 113 Amalthea, both of which are S-type asteroids. 113 Amalthea is a subtype S(I) object and 9 Metis is presently ungrouped, but appears to be related to the S(II) subtype. All of these pairings make compositional or petrographic sense based on current meteoritic and igneous petrogenic models. The probability of any of these compositional family pairings occurring in the surveyed S-asteroid population is on the order of only a few percent. The probability of all of these pairs occurring in this sample population is much less than one percent.

This study by Gaffey et al. [18] has provided tentative support for the Williams [12,16] family classifications.

ACKNOWLEDGEMENTS: Portions of this work were supported by NSF Solar System Astronomy grant AST-9012180 and by NASA Planetary Geology and Geophysics grant NAGW-642. M. J. Gaffey and M. S. Kelley are Visiting Astronomers at the Infrared Telescope Facility which is operated by the University of Hawaii under contract to the National Aeronautics and Space Administration.

REFERENCES: [1] Hirayama K. (1918) *Proc. Phys. Math. Soc. Japan, Ser. 2, No. 9*, 354-361. [2] Hirayama K. (1919) *Proc. Phys. Math. Soc. Japan, Ser. 3, No. 1*, 236-240. [3] Williams J.G. (1971) in *Physical Studies of Minor Planets*, NASA SP-267, pp. 177-181. [4] Gradie J.C., et al., (1979) in *Asteroids*, U. Arizona Press, pp. 359-390. [5] Tedesco E.F. (1979) *Icarus, 40*, 375-382. [6] Chapman C.R. (1987) *Meteoritics, 22*, 353-354. [7] Bell J.F. (1989) *Icarus, 78*, 311-322. [8] Chapman C.R., et al. (1989) in *Asteroids II*, U. Arizona Press, pp. 386-415. [9] Granahan J.C. and Bell J.F. (1991) *Lunar and Planet. Sci. XXII*, 477-478. [10] Brouwer D. (1951) *Astron. J., 56*, 9-32. [11] Williams J.G. (1979) in *Asteroids*, U. Arizona Press, pp. 1040-1063. [12] Williams J.G. (1989) in *Asteroids II*, U. Arizona Press, pp. 1034-1072. [13] Knezevic Z. and Milani A. (1989) in *Asteroids II*, U. Arizona Press, pp. 1073-1089. [14] Arnold J.R. (1969) *Astron. J., 74*, 1235-1242. [15] Carusi A. and Massaro E. (1978) *Astron. Astrophys. Suppl., 34*, 81-90. [16] Williams J.G. (1992) *Icarus, 96*, 251-280. [17] Zappala V., et al. (1990) *Astron. J., 100*, 2030-2046. [18] Gaffey M.J., et al. (1992) *Icarus*, submitted.

TIDAL INTERACTION: A POSSIBLE EXPLANATION FOR GEYSERS AND OTHER FLUID PHENOMENA IN THE NEPTUNE-TRITON SYSTEM;

W.D. Kelly, C. L. Wood, MS B12 Lockheed Engineering and Sciences Company, Houston, Texas 77058-3711

Discovery of geyser-like plumes on the surface of Triton was a highlight of Voyager 2's passage through the Neptune planetary system [1-4]. Remarkable as these observations were, they were not entirely without precedent. Considering the confirmed predictions [5] for the 1979 Voyager Jovian passage, it was logical to consider other solar system bodies beside Io where tidal effects could be a significant factor in surface processes. It was our intuition [6] that the Neptune-Triton gravitational bond acting at high inclination to the Neptune equator and the fact that Neptune was a fluid body with significant oblateness would produce tidal and mechanical forces that could be transformed into thermal energy vented on Triton's surface. Prior to the Voyager flyby, others have noted that capture and evolution of Triton's orbit from extreme eccentricity to near circular state today would have resulted in significant tidal heating [7], but these analysts disregard current day forces. Our calculations indicate that the time varying forces between Neptune-Triton fall midway between those exerted in the Earth-moon and Jupiter-Io systems, and considering the low level of other energy inputs, this source of internal energy should not be ignored when seeking an explanation for surface activity. In each planet-satellite case, residual or steady-state eccentricity causes time-varying stresses on internal satellite strata. In the case of Jupiter the residual eccentricity is due largely to Galilean satellite interactions, particularly Io-Europa, but in the case of Neptune-Triton, it is the effect of Triton's inclined orbit about an oblate primary.

Since the Neptune flyby, two candidate explanations for geyser-like plumes have been offered:

1) a subsurface nitrogen greenhouse process in which heated nitrogen surface ices are evaporated and boiled off through vents [2,8,9] ; and,

2) a less widely accepted dust-devil hypothesis [10], vortices forming in the rarefied Triton atmosphere.

The first theory has at least one shortcoming in so far as the mechanism suggested is limited to surface regions of a few meters depth in crystalline nitrogen. Considering the magnitude of the releases and their frequency of occurrence, it is possible that solar heating would not provide an adequate fluid reservoir. Such objections are reasons to re-examine tidal mechanisms. Tidal effects were studied using a method developed for analyzing time varying effects of the micro-gravity contours located about the center of mass of a spacecraft [11] (e.g., the Space Station Freedom Laboratory). Ellipsoidal contours of constant micro-g levels were identified as a function of satellite or spacecraft orbit true anomaly. Fluctuations in contour semi-axes and orientation with orbital motion were taken as tidal force indicators.

Secondary effects also considered were the effects of the tidal bore on the Neptune planetary ocean. Tidal bores in this system [12] would be 8 times higher than corresponding terrestrial tides, displacing mass perhaps tens of thousands of kilometers into the planetary interior since there is no clear demarcation between atmosphere and "surface". Perhaps it is only a circumstantial connection, but it is worth noting that large Neptune atmospheric features observed in low latitudes as deep as several bars pressure are carried east to west [13-14] up to 325 mps, roughly synchronous with Triton's retrograde rotation about Neptune (301 mps). Without doubt the Neptune-Triton tidal bond is significant for Neptune "meteorology", but our calculation of bore height as a gravitational potential perturbation is significantly smaller than the observed effect of the rotationally induced re-distribution of Neptunian mass that probably dominates the J_2 gravity term. Still, this "off-axis" tidal distribution could contribute to a residual forced eccentricity for Triton not included in our tidal stress calculations.

When comparing the relations [15] below (summarized in table-1),

$$\sigma_{obl} = 12/\pi \; J_2 \, (r_{pl}/r_{sat}) \, \mu_{pl} \; m_{sat}/a^4 . \qquad \sigma_{ecc} = 2/\pi \, e \, \mu_{pl} \; m_{sat} / (a^3 \; r_{sat})$$

NEPTUNE-TRITON TIDAL INTERACTION: W.D. Kelly, C. L.Wood

where subscripts sat and pl designate satellite and planet, (m) the mass, (r) the surface radius and (a) the mean distance of the two bodies, it can be seen that tidal stresses for the earth's moon based on eccentricity ($\sigma_{ecc\text{-}1}$) are about 2.6 times larger than those for Triton based on oblateness (σ_{obl}), but the rotational rate of Triton about its primary is about five times more rapid.

Table -1 Relative Satellite Physical Factors

	$\sigma_{obl} / \sigma_{ecc\text{-}1}$	$\sigma_{ecc} / \sigma_{ecc\text{-}1}$	ω / ω_1	$(\omega/\omega_1)^2$	Tidal bore (scale)
Luna	-	1.0	1.0	1.0	1.0
Triton	1 / 2.666	-	4.65	21.6	8.07
Io	-	36.69	15.44	238.5	45.23
Europa	-	8.49	7.67	58.8	6.12

The effect of tidal forces perturbing a spherical mass of uniform density (analogous to a satellite with a solid or icy surface) can be derived with a correction to the equation of hydrostatic equilibrium. Superimposed on these equilibrium forces are those of the time varying tidal forces exerted by the gravitational field of Neptune. The magnitude of these forces can be mapped out into time varying ellipsoidal contours[11] of constant micro-g contours. Revising the hydrostatic equations accordingly

$$d P'/dr = - \rho [g(r) + \Delta g_t (r)] = -\rho [4/3 \pi \rho G r + r^2 k_1 (1 + k_2 \sin \omega_0 t)]$$

where the time varying tidal pressure exerted in the satellite interior is

$$\Delta P'(r) = - \rho / 3 \; r^3 \; k_1 \; k_2 \sin \omega_0 t + \text{constant} = \rho / 3 \; k_1 \; k_2 \sin \omega_0 t \, (r_0^3 - r^3)$$

with k_1 and k_2 scaling factors for the planet-satellite system, ρ the density, r distance from the satellite center of mass, ω_0 orbital angular rate, g for gravitational accelerations, and P' combined hydrostatic and tidal pressures.

REFERENCES

[1.] Kerr, R., Science, Vol. 245, pp. 928-930.
[2.] Smith, B. A. et al., Science, Vol. 246, pp. 1422-1449.
[3.] Soderblom, L. A. et al, Science, Vol. 250, 410-415, 19 October 90.
[4.] Hansen, C. J., et al. , ibid., pp. 421- 424.
[5.] Peale, S. J., Cassen, P. , Reynolds, R. T., Science, Vol. 203, pp. 892-894, March 79.
[6.] Kelly,W., Letter to AAAS/Science, 27 July 92 (unpublished).
[7.] Chyba, C. F. et al., Astronomy and Astrophysics - Letters, Vol. 219, L23, l26 (1989).
[8.] Kirk, R. L., Brown , R. H., Soderblom, L. A., Science, Vol. 250, pp 424- 429, 19 October 90.
[9.] Brown, R. L., et al. " Energy Sources for Triton's Geyser-Like Plumes", Ibid. pp. 431- 435.
[10.] Ingersoll, A. P., Tryka, K. A. "Triton's Plumes: the Dust Devil Hypothesis", Ibid., pp. 435- 437.
[11.] Kelly, W. D., Lockheed Engineering and Sciences Company, Technical Report 30224, April 92.
[12.] Lamb, H., "Hydrodynamics", Dover Press, 6th edition, New York.
[13.] Hammel, H. B., et al., Science, Vol. 245, pp. 1367-1369.
[14.] Suomi, V. E., et al., Science, Vol. 251, pp. 929-932, 22 Feb. 91.
[15.] Ojakangas, G, private communication, 29 June 92.

INTERNATIONAL TESTING OF A MARS ROVER PROTOTYPE;
A. Kemurjian, Mobile Vehicle Engineering Institute, St. Petersburg, Russia: V. Linkin, Space Research Institute, Moscow, Russia; L. Friedman, The Planetary Society, Pasadena, Ca, USA

Tests on a prototype engineering model of the Russian Mars 96 Rover were conducted by an international team in and near Death Valley in the United States in late May, 1992. These tests were part of a comprehensive design and testing program initiated by the three Russian groups responsible for the rover development. The specific objectives of the May tests were: (1) Evaluate rover performance over different Mars-like terrains, specifically a Viking 1-site-like boulder field, and sand dunes; (2) Evaluate state-of-the-art teleoperation and autonomy development for Mars rover command, control and navigation; (3) Organize an international team to contribute expertise and capability on the rover development for the flight project.

The test team included representatives from the three Russian space organizations: Space Research Institute, Babakin Center, Mobile Vehicle Engineering Institute; France; Hungary; and The Planetary Society, Ball Aerospace and ISX in the United States. Each of the test objectives were met through a series of tests at two sites: Dumont Dunes, and "Mars Hill."

The range and performance that can be planned for the Mars mission is dependent on the degree of autonomy that will be possible to implement on the mission. Current plans are for limited autonomy, with Earth-based teleoperation for the nominal navigation system. Several types of television systems are being investigated for inclusion in the navigation system including panoramic camera, stereo, and framing cameras. The tests used each of these in teleoperation experiments. Experiments were included to consider use of such TV data in autonomy algorithms. Image processing and some aspects of closed-loop control software were also tested.

A micro-rover was tested to help consider the value of such a device as a payload supplement to the main rover. The concept is for the micro-rover to serve like a mobile hand, with its own sensors including a television camera.

AN EXPERIMENTAL STUDY OF TRACE ELEMENT PARTITIONING BETWEEN PEROVSKITE, HIBONITE AND MELT: EQUILIBRIUM VALUES;

A.K. Kennedy[1], G.E. Lofgren[2] and G.J. Wasserburg[1] ,[1]Lunatic Asylum, Div. of Geol. and Planet. Sci. 170-25, C.I.T., Pasadena, CA 91125, [2]SN2 NASA, Johnson Space Center, Houston, TX 77058.

Introduction: The presence of perovskite ($CATiO_3$) and hibonite ($Ca\ Al_{12}O_{19}$) within different regions of Calcium-, Aluminum-rich Inclusions (CAI) and the trace element concentrations of these minerals in each circumstance, constrain models of precursor formation [1], nebular condensation [2], the thermal history of inclusions with relict perovskite and hibonite[2,3] and the formation of the Wark-Lovering rim [4]. At present mineral/melt partition coefficient (D) data for hibonite are limited to a few elements in simple experimental systems [5], or to those derived from hibonite-glass pairs in hibonite/glass microspherules [6]. Similarly, there is only limited data on perovskite D that are applicable to meteorite compositions [7,8]. Apart from the importance of partitioning studies to meteorite research, D values also are invaluable in the development of thermodynamic models [9], especially when data is available for a large number of elements that have different ionic charge and radii. In addition, study of the effect of rapid cooling on partitioning is crucial to our understanding of meteorite inclusions [3,10]. To expand our knowledge of mineral/melt D for perovskite and hibonite, we have instituted a study similar to that of [10], where D values are obtained in both equilibrium and dynamic cooling experiments. As an initial phase of this study we have measured mineral/melt D for major elements (Ca, Mg, Al, Ti and Si), 15 rare earth elements (La-Lu) and 8 other elements (Ba, Sr, U, Th, Nb, Zr, Hf and Ge) in perovskite and hibonite grown under equilibrium conditions, in bulk compositions that are respectively similar to Compact Type A (CTA) CAI and to a hibonite/glass microspherule [6]. Experimental mixes (Table 1) were doped with REE at 20-50x chondritic (ch) abundances, Ba at 50 ppm, Sr, Hf, Nb and Zr at 100 ppm and, U and Th at 200 ppm.Trace element abundances were measured with the PANURGE ion microprobe using the techniques and standards of [11]. Major element compositions were obtained by electron microprobe analysis.

Experimental Technique: Experiments were performed in 1 atmosphere gas-mixing furnaces. The oxygen fugacity was fixed at -1.5 log units below the Iron-Wustite (IW) buffer curve. The temperature and cooling rate were controlled with a Eurotherm controller. Perovskite experiments were held at temperatures within the range 1525°C to 1545°C for 4 hours, then cooled at 2°C/hour to either 1500°C or 1450°C and then allowed to equilibrate at this temperature for 24 hours. Complex cooling and heating paths were used to reduce the number of crystal nuclei in the hibonite experiments. Experiments were held at a temperature of 1500°C for 8 hours, then cooled to, and held at, either, 1300°C or 1350°C for 24 to 36 hours, then heated to, and held at, 1450°C for 9 to 24 hours. The experiments were then either quenched, or cooled at 2°C/hour to either 1400°C or 1300°C and equilibrated at this temperature for 24 hours. In both perovskite and hibonite experiments large (up to 200 um wide) individual crystals adjacent to the main mass of melt were selected for analysis. Points from the core, rim and adjacent glass were analysed and for hibonite analyses were performed adjacent to the different crystal faces. Melt inclusions, which were common in experiments on olivine and orthopyroxene[10], were not observed in the analysed crystals.

Results: Figure 1 shows representative D patterns for perovskite and hibonite for the complete set of elements analysed, with the elements grouped by ionic charge and arranged in descending order from left to right according to ionic radii. The data shown is for hibonite equilibrated with the melt at 1350°C and 1400°C. Pattern #2 is from the 1400°C experiment and patterns #6 and #7 are from a single crystal in the 1350°C experiment. The pattern for perovskite is from an experiment with a final temperature of 1450°C. D range from 10^{-2} to >10 for both minerals and there is a strong similarity between the patterns. Perovskite and hibonite D are almost identical for the divalent cations Ba (respectively 0.02 and 0.03) and Sr (respectively 1.1 and 0.8) in our

experiments. D_{Ca} is as expected, with respective values of 1.2 and 0.32 in perovskite and hibonite. Our D are similar to those of other experimental studies[5,8]. D_{Mg} for perovskite is low, 0.03 when compared with the value for hibonite, 0.5. Mineral/melt D for the REE decrease continuously from D_{La}=6 to D_{Lu}=0.03 in hibonite. For perovskite, REE Ds increase slightly from D_{La}=10 to D_{Nd}=15 and then decrease continuously to D_{Lu}=1.0, and Ds for trivalent cations with smaller ionic radii than the REE are lower, with D_{Al}=0.08 and D_{Sc}=0.15 lower than D_{Cr}=0.8 and D_V=1.0. D values for Cr, Sc and V were not measured in hibonite due to interferences [1]. With the exception of D_{Th} and D_{Si} in perovskite and D_{Si} in hibonite, the D values for tetravalent cations and Nb, the only pentavalent element fall within the range of Ds for the REE (Fig. 1). D_{Th}/D_U equals 3 in perovskite and approximately 15 in hibonite.

Example applications: (1) Low Ba relative to other refractory elements, such as Hf, Zr, La etc, in hibonite has been explained by increased volatility of Ba under oxidising conditions during condensation [2]. $D_{Ba} << D_{Hf}$, D_{Zr} and D_{La} in our experiments suggests an alternate explanation; that low Ba results from the incompatibility of Ba in hibonite. (2) High REE abundances (500-1000xch) and Th/U ratios of 3-4 in perovskite from the outer region of Type B1 CAI [3,12] are inconsistent with equilibrium partitioning between perovskite and a melt that contains ~20xch REE and that probably has Th/U >3 [13], and the perovskite is a relict. (3) Since D_{LREE}/D_{HREE} is ~200 for hibonite, LREE/HREE ratios of 1 indicate that in hibonite in L575, a Leoville CTA CAI, and 2 in hibonite in Linus Jr., an Allende CTA CAI, [14] are inconsistent with hibonite equilibrating with the melts that formed these inclusions, and hibonite is a relict.

Summary: We have measured mineral/melt D for 31 elements in perovskite and hibonite in equilibrium crystallization experiments on compositions that are applicable to meteorite inclusions. Our data includes elements not previously studied and provide a self consistent set of D. Use of these D will provide additional constraints for CAI research and for crystal fractionation models and partial melting in terrestrial igneous systems that contain perovskite.

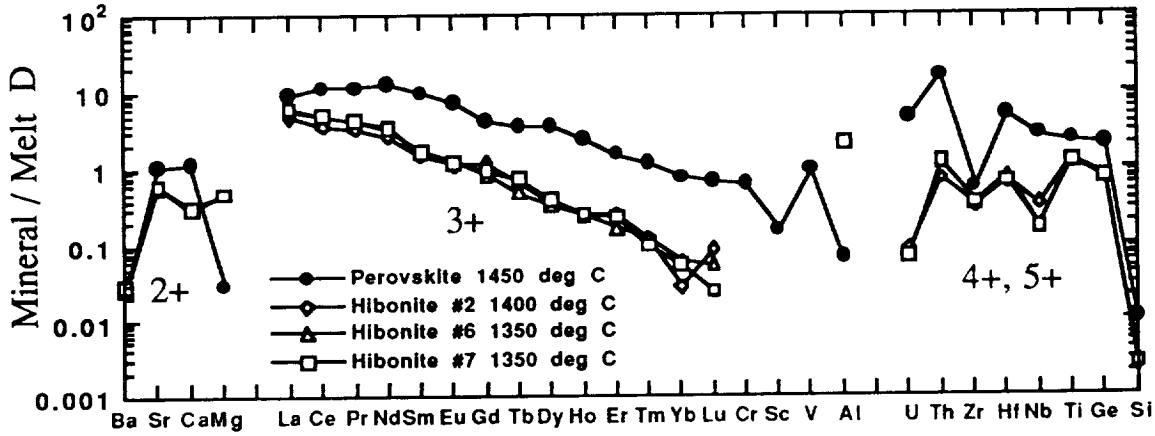

Table 1 Composition of starting mixes

	SiO2	Al2O3	MgO	CaO	TiO2	FeO	Total
Perovskite	25.61	14.27	6.26	31.55	20.72	0.01	98.41
Hibonite	28.23	38.22	1.99	26.94	4.94	0.01	100.32

References:[1] Hinton et al. (1988) GCA 52 p2573; [2] Ireland et al. (1992) GCA 56 p2503; [3] Kennedy et al. (1990) LPSXXI p621; [4] Wark (1986) EPSL 77 p129;[5] Drake and Boynton (1988) Meteoritics 23 p75;[6] Ireland et al. (1991) GCA .55.p367;[7] Nagasawa et al. (1980) EPSL 46 p431;[8] Simon et al. (1993) submitted;[9] Colson et al. (1988) GCA 52 p539; [10] Kennedy et al. (1993) EPSL in press; [11] Kennedy and Hutcheon (1992) Meteoritics 27 p ;[12] Ireland et al. EPSL 101 p379;[13] Chen and Wasserburg (1981) EPSL 52 p1;[14] Kennedy et al. (1991) LPSXXII p 709. [Div. Contib. 5235 (799)].

NITROGEN ISOTOPIC SIGNATURES IN AGGLUTINATES FROM BRECCIA 79035

John F.Kerridge, Yoosook Kim, Jin S.Kim & Kurt Marti, Dept.Chemistry, UCSD, La Jolla, CA 92093-0317.

Agglutinates in the size range 125-175μm from regolith breccia 79035 are substantially depleted in N compared with bulk 79035. Isotopically, agglutinate N closely resembles that found previously in ilmenite separates. The minimum $\delta^{15}N$ value found during stepwise pyrolysis of agglutinates is significantly heavier than that observed for bulk 79035. The major host phase for trapped N in 79035, and the host phase of the lightest isotopic component(s), remain unidentified.

Although the cause of the long-term variation in isotopic composition of regolith N is recognised as one of the outstanding problems in lunar surface science, it is less commonly appreciated that several other aspects of lunar N isotope systematics are also poorly understood. Thus, the reason for the difference in release temperature of the two (or more) isotopically distinct components of trapped N [1] is not known with any certainty, and neither are the sources of those components, or the underlying cause of the isotopic differences between them. In addition, as first pointed out by Norris *et al.* [2], the distribution of N isotopic components among different lithic units in the regolith is not well understood. That issue is the focus of the present study.

Norris *et al.* [2] showed that agglutinates separated from soil 12023 contained trapped N that was not significantly lighter than that in the bulk sample. This was surprising because, within the context of a secular increase in $^{15}N/^{14}N$ of regolith N [3], agglutinates, which should contain material with an earlier surface exposure, on average, than mineral grains in the same regolith sample, would be expected to contain N relatively depleted in ^{15}N compared with the bulk-sample composition [4]. Put another way, since bulk 12023 was known to release ^{15}N-depleted N during stepwise pyrolysis, the question becomes: What is the host phase of that isotopically light N?

We decided to revisit this problem when we found that ilmenite from regolith breccia 79035, which during stepwise pyrolysis releases some of the lightest N yet observed in lunar regolith (-243‰ at high resolution [5] and -210‰ at lower resolution [6]), yielded a minimum $\delta^{15}N$ during stepwise release of only -180‰ [1], as found also by Becker & Pepin [7]. A coarse pyroxene separate (175-250μm) yielded somewhat lighter N during stepwise pyrolysis (-212‰ [1]), which is close to the minimum $\delta^{15}N$ value observed in bulk 79035 by Clayton & Thiemens [6], but the host of the -243‰ component remained unidentified.

For several reasons we decided to follow up on the results of Norris *et al.* [2] by analysing agglutinates in 79035. First, the earlier study did not rule out possible release of light N from agglutinates within some restricted temperature interval. Second, although bulk 12023 yields a relatively light N component during stepwise pyrolysis, its $\delta^{15}N$ is not particularly light (-32,-61 [2]; -15[8]), with the stepwise release spanning a range of about 100‰ [2,8]. By contrast, the minimum value for bulk 79035 is -243‰ [5], with a range of about 200‰ [6,9]. (This latter factor may be somewhat exaggerated by the possible influence of terrestrial N at the lowest release temperatures.) Third, the constituents of 79035 were exposed on the lunar surface much earlier, on average, than those of 12023, raising the possibility of a long-term change in the style with which trapped N is distributed among lithic units in the regolith. Finally, although the agglutinate content of 79035 has apparently not been quantified, its bulk N content of about 100ppm [6,9] suggests, by comparison with other regolith samples, that it likely contains >50% agglutinates, i.e., agglutinates probably represent the dominant lithic constituent in 79035 and must therefore be included in any study of the distribution of N within this breccia.

We therefore handpicked two agglutinate fractions from a nominally "agglutinate" (i.e., magnetic) separate (125-175μm) prepared by J.P.Benkert at ETH, Zurich. One consisted of irregular particles with a relatively dull surface, the other of spheroidal particles characterised by a lustrous, glassy surface. These were wrapped in Au foil, combusted in pure O_2 at 400°C to minimise terrestrial contamination and then analysed by stepwise pyrolysis to 1040°C. Following pyrolysis, the first (irregular) sample was combusted at 700°C and repyrolysed at 1040°C. The second (spheroidal) sample was pyrolysed to 850°C, then combusted at 700°C, followed by pyrolysis to 1040°C.

Residues from these pyrolyses were kept for subsequent transfer to another system for further pyrolysis to 1700°C to extract spallogenic N.

Results are illustrated in Fig. 1. Comparison of that figure with the analogous one for 79035 ilmenite [1] shows that they are very similar, though the amounts of N released by agglutinates exceed, by a factor of about five, those released by ilmenites, presumably due to a volume-correlated component. Clearly, agglutinates in this size range are not responsible for the -243‰ component. Furthermore, the N contents of these agglutinates (20 and 26ppm), compared with whole-rock values (93ppm [6]; 114ppm[9]), are surprisingly low. For comparison, soil sample 12023 yielded 127ppmN in agglutinates and 70ppmN for the whole rock [2]. (Note, however, that our 79035 ilmenite data [1] agree closely with those from Minnesota [7] in both abundance and isotopic composition.) Either agglutinates in the size range studied here are not representative of agglutinates as a whole, or agglutinates in regolith breccias are depleted in N relative to those in soils. Size fractions of mature soil 69941, with a bulk agglutinate content probably close to that of 79035, showed only a slight lowering of $\delta^{15}N$ with decreasing grain size [4], though a <38μm fraction of submature soil 79261 yielded $\delta^{15}N$ values during stepwise pyrolysis that were systematically lighter than those for the >38μm fraction by some tens per mil [6].

We therefore conclude that our study of 79035 separates gives no indication that N components in agglutinates are either older than those in ilmenites or pyroxenes, or have sampled a lighter N reservoir. In fact, our data are consistent with 79035 agglutinates having incorporated N identical in abundance and isotopic composition to that trapped in ilmenites. The host phase of the lightest N component(s), and indeed the major host phase of N in 79035, remain unidentified.

[1] Kerridge J.F. *et al.* (1992) *Proc.Lunar Planet.Sci.Conf.22*, 215. [2] Norris S.J. *et al.* (1983) *Proc.Lunar Planet.Sci.Conf.14*, B200. [3] Kerridge J.F. (1980) In:*The Ancient Sun*, p.475. [4] Becker R.H. & Clayton R.N. (1975) *Proc.Lunar Sci.Conf.6*, 2131. [5] Carr. L.P. *et al.* (1985) *Meteoritics* 20, 622. [6] Clayton R.N. & Thiemens M.H. (1980) In:*The Ancient Sun*, p.463. [7] Becker R.H. & Pepin R.O. (1989) *Geochim.Cosmochim.Acta* 53, 1135. [8] Becker R.H. & Clayton R.N. (1978) *Proc.Lunar Planet.Sci.Conf.9*, 1619. [9] Frick U. *et al.* (1988) *Proc. Lunar Planet.Sci.Conf.18*, 87.

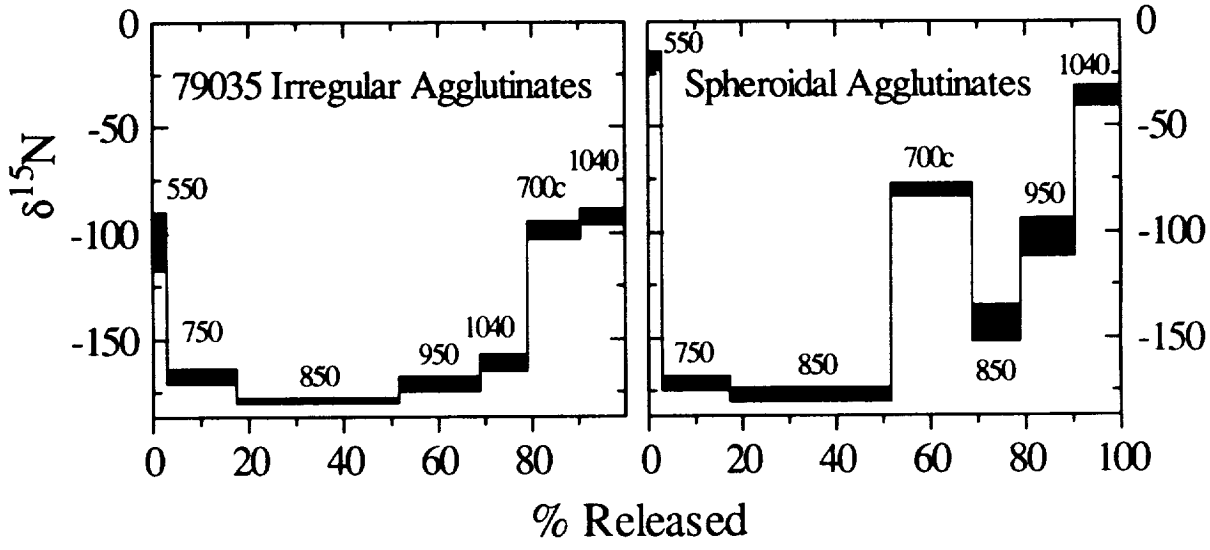

Figure 1. Isotopic composition of agglutinates separated from regolith breccia 79035. as a function of percentage of N released. Note that N released during combustion at 400°C is not included and that 1040°C was the maximum pyrolysis temperature. All steps were by pyrolysis except those marked with a "c" which employed combustion.

AN INVERSION OF GEOID AND TOPOGRAPHY FOR MANTLE AND CRUSTAL STRUCTURE ON MARS

Walter Kiefer[1,4], Bruce Bills[1], Herb Frey[1], Steve Nerem[2], Jim Roark[1], and Maria Zuber[1,3]

[1] Geodynamics Branch, Code 921, Goddard Space Flight Center, Greenbelt MD 20771

[2] Space Geodesy Branch, Code 926, Goddard Space Flight Center, Greenbelt MD 20771

[3] Dept. Earth and Planetary Sciences, Johns Hopkins Univ., Baltimore MD 21218

[4] Now at: Lunar and Planetary Institute, Houston TX 77058

Mars has the largest amplitude geoid anomalies and surface topography known on the terrestrial planets. A number of prior studies have analyzed Martian gravity anomalies and topography in terms of isostasy and flexure of the crust and lithosphere [e.g., 1, 2]. Other studies have emphasized the role of mantle convection in producing gravity anomalies and topography in some regions of Mars [3, 4]. In this study, we invert geoid and topography observations for simultaneous estimates of density anomalies in the crust and mantle of Mars. In performing this study, we make use of a recent degree 50 spherical harmonic expansion of the Martian gravity field (GMM-1) [5] and a corresponding resolution expansion of the USGS Mars topography model [6]. However, our analysis is restricted to harmonic degrees up to $L=25$, which are better determined than the higher harmonics. This provides a half-wavelength horizontal resolution of 425 km.

If density anomalies are allowed to exist at two different depths, it is always possible to solve for densities which exactly (but non-uniquely) reproduce the observed geoid and topography. Calculations of this sort were performed in several recent studies of Venus [7-9] on either a global or regional basis. In those studies, the density anomalies in the uppermost layer were interpreted as crustal thickness variations and the density anomalies in the lower layer were interpreted as due to mantle temperature variations. Our approach to the problem most closely resembles the global Venus model of Herrick and Phillips [7], although our model parameterization is somewhat different than theirs. In particular, we assume that density anomalies are distributed vertically throughout the mantle, whereas Herrick and Phillips [7] considered loading at a single interface in the mantle. It is important to allow for vertically distributed density anomalies, because different harmonic degrees are most sensitive to loading at different depths [10]. With only gravity and topography data as constraints, it is only possible to estimate two density contrasts at each spherical harmonic coefficient. However, it is possible to assume a functional form for the radial distribution of the density anomalies and simply solve for a multiplicative scaling factor. As a first approximation, we assume that the density anomalies in the mantle outside the thermal boundary layers are uniformly distributed with depth. This is a reasonable approximation of features such as mantle plumes, but it undoubtedly oversimplifies the details of the density distribution. Our results should therefore be regarded as an estimate of the vertically averaged mantle structure. We convolve this density distribution with response functions for a Newtonian viscous mantle [10] to estimate the geoid and topography produced by mantle convection.

Because the distribution of density anomalies as a function of wavelength is different in the thermal boundary layer than it is in the non-boundary layer part of the mantle [11], we parameterize the boundary layer separately from the rest of the mantle. The treatment of the lower thermal boundary layer is unimportant, because both the geoid and topography response functions go to zero at the base of the mantle [10]. At the long wavelengths considered here, the geoid and topography produced by viscous flow in the upper thermal boundary layer approaches that predicted by Pratt isostasy. Presuming that crustal thickness variations are also isostatically compensated, we are unable to distinguish the effects of thermal boundary layer structure from crustal structure. We therefore combine both effects into our parameterization of the upper density layer. The effects of lithospheric flexure are not included in our calculations.

Model results are sensitive to a number of poorly constrained parameters, particularly the thickness of the mantle and the variation of viscosity with depth in the mantle. A broad range of structural models have been proposed for the interior of Mars [12], with mantle thicknesses ranging between about 925 and 1850 km. We consider these as limiting cases and also consider an intermediate model with a mantle depth of 1550 km. The intermediate case has a ratio of core radius to planetary radius which is the same as the earth. For viscosity models, we are guided by recent estimates of the viscosity stratification in the mantles of Earth and Venus [13, 14]. Because the pressure at the base of the Martian mantle is comparable to the pressure at the base of the upper mantle on Earth and Venus, we consider only the upper mantle portions of those viscosity models. We therefore consider an isoviscous mantle and a mantle with a factor of 30 increase in viscosity at the mid-depth of the mantle. Both models include a high viscosity layer in the upper 150 km to represent the thermal boundary layer.

For an isoviscous mantle and an intermediate size core, our results indicate pronounced hot upwellings beneath Tharsis and Elysium (temperature several hundred K higher than average), along with moderate crustal thinning. Substantial crustal thinning is predicted beneath the Hellas and Isidis impact basins. Lesser amounts of crustal thinning are required beneath the Argyre, Chryse, and Utopia basins. In the spectral domain, the deeper density layer dominates the observed geoid power at all modeled wavelengths, although the shallow layer becomes increasingly important at shorter wavelengths. Except for the lowest harmonic degrees, the shallow density anomaly typically supports 50 to 70% of the observed topography power. Changing the mantle viscosity profile or the size of the core does not substantially alter the predicted spatial patterns but does alter the required density amplitudes. Decreasing the core size slightly decreases the required range of thermal anomalies and crustal thicknesses. Including a low viscosity upper mantle significantly increases the required range of thermal variations and also requires considerable crustal thinning beneath Tharsis.

References

[1] Sjogren and Wimberly, Icarus, 45, 331-338, 1981. [2] Phillips et al., JGR, 95, 5089-5100, 1990. [3] Kiefer and Hager, LPI Tech. Report 89-04, 49-50, 1989. [4] Schubert et al., JGR, 95, 14105-14129, 1990. [5] D.E. Smith et al., this volume. [6] USGS, Misc. Investigations Map I-2030, 1989. [7] Herrick and Phillips, JGR, 97, 16017-16034, 1992. [8] Grimm and Phillips, JGR, 97, 16035-16054, 1992. [9] Bills and Fischer, JGR, 97, 18285-18294, 1992. [10] Richards and Hager, JGR, 89, 5987-6002, 1984. [11] Jarvis and Peltier, JGR, 91, 435-451, 1986. [12] Schubert and Spohn, JGR, 95, 14095-14104, 1990. [13] Hager and Richards, Phil. Trans. R. Soc. London, A328, 309-327, 1989. [14] Kiefer and Hager, JGR, 96, 20947-20966, 1991.

LAVA CRUSTS AND FLOW DYNAMICS. C.R.J. Kilburn, Environmental Science Division, Lancaster University, Lancaster, LA1 4YQ, U.K, and Osservatorio Vesuviano, Napoli, Italy.

Lava flows can be considered as hot viscous cores within thinner, solidified crusts. Interaction between crust and core determines a flow's morphological and dynamical evolution. When the lava core dominates, flow advance approaches a steady state. When crusts are the limiting factor, advance is more irregular. These two conditions can be distinguished by a timescale ratio comparing rates of core deformation and crustal formation. Aa and budding pahoehoe lavas are used as examples of core- and crustal-dominated flows respectively. A simple model describes the transition between pahoehoe and aa flow in terms of lava discharge rate, underlying slope and either the thickness or velocity of the flow front. The model shows that aa morphologies are characterized by higher discharge rates and frontal velocities and yields good quantitative agreement with empirical relations distinguishing pahoehoe and aa emplacement on Hawaii.

Interaction between the core and crust of a lava produces a variety of surface morphologies [1,2], cooling regimes [3] and modes of flow advance [4,5]. Such variations are especially evident comparing the main categories of subaerial basaltic lava, *pahoehoe* and *aa* [6]. Pahoehoe lavas have smooth crusts, typically thicker than 1-3 cm, which break locally across a flow front; advance occurs unevenly by the extension of numerous small tongues [6,7,8]. Aa lavas have irregular surfaces, usually hidden beneath loose debris; crustal failure is widespread and fronts tend to advance steadily as single units [8,9,10]. The clearest quantitative data distinguishing pahoehoe and aa emplacement concern flow discharge rate (Q), higher values of Q being associated with aa morphology [7,11].

It is proposed that such a discharge-rate control reflects a critical condition for lava crusting. Lava crusts are important because of their high tensile strength [8,9]. Nevertheless, it is normal for crusts to be disrupted during the early stages of flow growth. Crustal restraint thus depends on how quickly broken crust can heal compared with how quickly it continues to be deformed by movement of the lava interior. When healing is slow, emplacement is governed by the lava core; when healing is fast, emplacement is dominated by crustal resistance. Transitional conditions occur when the rates of core deformation and of crustal healing are comparable. In terms of process timescales, core-dominated flow occurs when the timescale of core deformation (t_{def}) is smaller than the timescale of crustal healing (t_h); crustal-dominated flow is described by $t_h/t_{def} < 1$; and transitional conditions coincide with $t_h/t_{def} = 1$.

A recent model which treats lava fronts as newtonian fluids within brittle crusts [9], and which accounts for the final planimetric shapes of aa flow fields [9], as well as the positive dependence of aa flow length on discharge rate [8], indicates that, for core-dominated advance: (a) the mean frontal velocity u depends on Q and slope angle ß through the relation $u^3 = (Q \sin ß)(t_h/t_{def})^2/(3\, t_h^2)$, and (b) Q and mean frontal thickness h are linked by $Q = 3h^3 (t_h/t_{def})/(t_h \sin ß)$. Observed minimum thicknesses of pahoehoe crust are consistent with values of $t_h \sim t_{ch}$, the timescale of initial surface chilling [3,8,9; nominally 200 s for basalt]. Since $(t_h/t_{def}) < 1$ for crustal-dominated flow, the equations above yield for the emplacement of pahoehoe lavas ($t_h = t_{ch}$):

$$u^3 < (Q \sin ß)/(3\, t_{ch}^2) \quad (1)$$

and

$$Q < 3h^3/(t_{ch} \sin ß) \quad (2)$$

Core-dominated, aa lavas are thus expected when equations (1) and (2) are not satisfied. Knowing the slope angle and flow front thickness (a surrogate measure for the lava's physical properties [8]), equations (1) and (2) can be used to describe conditions for aa and pahoehoe development in terms of Q and u. Using Hawaiian lavas as an example (ß between 3^o and 5^o; maximum transitional values of h between 3 and 5 m [8]), equations (1) and (2) suggest that (a) pahoehoe must occur for $Q < 4\ m^3s^{-1}$ and $u < 0.01\ ms^{-1}$, and (b) aa must occur for $Q > 40\ m^3s^{-1}$ and $u > 0.03\ ms^{-1}$; at intermediate values of Q and u, the preferred flow morphology depends on the specific combination of ß and h. These limits compare extremely well with those determined empirically for historical lavas on Mauna Loa and Kilauea [7]: pahoehoe exclusively when $Q < 5\ m^3s^{-1}$ and $u < 0.007\ ms^{-1}$, and aa exclusively when $Q > 20\ m^3s^{-1}$ and $u > 0.02\ ms^{-1}$. Such agreement confirms the importance of crusts on lava flow development. It also suggests that equations (3) and (4) may be used to place upper limits on the mean discharge rate and frontal velocity of a pahoehoe lava once its frontal thickness and the mean underlying slope are known.

REFERENCES [1] Fink J.H. and Griffiths R.W. (1990) *J. Fluid Mech., 221*, 485. [2] Kilburn C.R.J. (1990) *IAVCEI Proc. Volcanol. 2*, 129. [3] Crisp J.A. and Baloga S.M. (1990) *J. Geophys. Res., 95*, 1255. [4] Kilburn C.R.J. and Lopes R.M.C. (1988) *J. Geophys. Res., 93*, 14759. [5] Whitehead J.A. and Helfrich K.R. (1991) *J. Geophys. Res., 96*, 4145. [6] Macdonald G.A. (1953) *Am. J. Sci., 251*, 169. [7] Rowland S.K. and Walker G.P.L. (1990) *Bull. Volcanol., 52*, 615. [8] Kilburn C.R.J. (1993) *Active lavas*, Chap. 10, UCL Press, London. [9] Kilburn C.R.J. and Lopes R.M.C. (1991) *J. Geophys. Res., 96*, 19721. [10] Kilburn C.R.J. and Guest J.E. (1993) *Active lavas*, Chap. 3, UCL Press, London. [11] Pinkerton H. and Sparks R.S.J. (1978) *Nature, 276*, 383.

ISOTOPIC SIGNATURES AND DISTRIBUTION OF NITROGEN AND TRAPPED AND RADIOGENIC XENON IN THE ACAPULCO AND FRO90011 METEORITES; Y. Kim and K. Marti, Department of Chemistry, University of California, San Diego, La Jolla, CA 92093-0317.

Acapulco metal and silicate show distinct N isotopic signatures. Trapped heavy noble gases are carried by "magnetic" opx and radiogenic ^{129}Xe excesses are observed in phosphate and in minor surficial phases on metal grains. N and Xe isotopic signatures in FRO90011 do not agree with those observed in Acapulco.

The Acapulco meteorite is unique in having achondritic texture and chondritic composition. Its mineralogical study shows the record of high temperature (1100°C) recrystallization (1). However, this meteorite shows abundances of volatile elements close to the levels observed in carbonaceous chondrites and concentrations of heavy noble gases comparable to those observed in type 4 ordinary chondrites, not expected for a presumed highly equilibrated object. Nitrogen measurements in bulk Acapulco (2) revealed two different isotopic signatures, in apparent conflict with evidence for a high degree of recrystallization. We have studied N and Xe in separated mineral phases to search for the carriers in order to better understand the formation and thermal history of the Acapulco parent body.

Nitrogen: Our nitrogen measurements of metal revealed two distinct isotopic signatures ($\delta^{15}N$= +20 and -130‰) (3), indicating that nitrogen carrier phases are not equilibrated. Very light nitrogen ($\delta^{15}N \leq$ -130‰) was found only in metal, while heavy nitrogen (+20‰) was observed both in silicates and in the low-temperature release from metal. The complex nitrogen release patterns during stepwise heating of metal and during oxidation suggested a heterogeneous distribution of nitrogen in metal. Since Acapulco metal is composed of taenite and kamacite, and taenite is known to have a higher nitrogen solubility than kamacite, we prepared concentrates of low Ni (6.4%) and high Ni (>11%) phases by etching with 2N H_2SO_4. Nitrogen measurements show that taenite (28ppm) is enriched in nitrogen relative to kamacite (4.5ppm). Taenite exhibits the signature of very light nitrogen ($\delta^{15}N$= -150± 3‰) (Fig. 1) while the isotopic signature of kamacite ($\delta^{15}N$~ -130‰) has a large uncertainty because of a small amount of nitrogen in the concentrate. Heterogeneous distribution of taenite in metal may explain the complex release pattern, but the possibility of a nitrogen-rich phase in the taenite cannot be excluded. Further measurements on an acid residue of taenite shows enrichment of nitrogen (>50ppm) with less negative isotopic signature ($\delta^{15}N$= -125‰). The etched taenite, kamacite and the acid residue of taenite released a smaller amount of heavy nitrogen, which is characteristically released at low temperature. This result suggests that the metal initially carried light nitrogen ($\delta^{15}N \leq$ -150‰), and that the signature of heavy nitrogen is a later overprint due to a partial equilibration of metal with silicates. An unusual feature in the Acapulco mineralogy is the frequent occurrence of swarms of metal blebs in orthopyroxene (opx). The study of these metal blebs may help to better understand the formation history of the Acapulco parent body. Our results show that the signature ($\delta^{15}N$= -68‰) of "magnetic"opx (with metal blebs) (Fig. 1) is different from that of opx itself (+15‰). The negative values are observed in the higher temperature steps. Further measurement of a metal-bleb "concentrate" reveals two different nitrogen isotopic signatures ($\delta^{15}N$= +10 and -120‰). This result and the fact that metal blebs in opx grains show variable Ni/Fe ratio suggest that metal blebs did not form by the reduction of ferrous iron in opx, but had different origin. The formation of metal blebs and the mechanism of introduction into opx without equilibration of nitrogen components represent important constraints on the history of Acapulco.

Trapped noble gases: The heavy noble gases measured in a bulk sample (^{132}Xe= 0.62×10^{-9} cm^3STPg^{-1}), and in magnetic (0.84×10^{-9} cm^3STPg^{-1}), and nonmagnetic (0.16×10^{-9} cm^3STPg^{-1}) separates were interesting because the enrichment in the magnetic fraction was unexpected, since magnetic fractions of ordinary chondrites are strongly depleted in noble gases. Our results show

that the metal phase and the troilite are very minor carriers while "magnetic" opx carries four times the Xe concentration of the bulk sample (2.4×10^{-9} cm^3STPg^{-1}). Further studies of this material reveal that the noble gases are enriched two times at the site of swarms of metal blebs, but their concentrations are low in metal blebs. The specific carrier of heavy noble gases is not revealed yet. Options are inclusions in addition to metal blebs in opx or microbubbles in opx that may have trapped the gas at the time when the metal was incorporated into opx. We conclude that the trapped heavy noble gas and nitrogen carriers are distinct phases.

Extinct ^{129}I: The records of extinct ^{129}I in Acapulco yield interesting chronological information. We reported two characteristic release patterns of radiogenic ^{129}Xe carried by two different carriers (3). Radiogenic ^{129}Xe released at high temperature ($\geq 1200^{\circ}C$) is correlated with fission Xe ($^{136}Xe = 6 \times 10^{-12}$ cm^3STPg^{-1}) from ^{244}Pu and the carrier is identified as phosphate. The low temperature ($\leq 600^{\circ}C$) ^{129}Xe component carried by a minor phase on the metal surface has important implications regarding the thermal history of Acapulco. It appears that this phase contains most of the radiogenic ^{129}Xe. Concentrates of this phase substantially enriched the ^{129}Xe (730×10^{-12} cm^3STPg^{-1}) in low-temperature fraction, relative to ^{129}Xe in bulk Acapulco (50×10^{-12} cm^3STPg^{-1}), but identification is only preliminary. EDS analyses of some metal surfaces show weak peaks of sulfur and chlorine, which may suggest minor S- and/or Cl-bearing compounds. While working for the signature of extinct ^{129}I, it was found that a hand-picked troilite fraction (13mg) contains significant amounts of ^{129}Xe (100×10^{-12} cm^3STPg^{-1}). This ^{129}Xe was released mainly at $950^{\circ}C$, but the isotopic systematics of troilite Xe indicate a relationship to that discussed above as the low temperature release. On the other hand, troilite does not appear to be the main carrier of ^{129}Xe since three other small separates of troilite do not release much ^{129}Xe. Possibly the carrier of ^{129}Xe is heterogeneously distributed in inclusions in some troilite.

Antarctic meteorite FRO90011 (Acapulcoite?): The petrological study of this meteorite suggests a possible relationship to Acapulco because of its high metal content and well-crystallized silicate structure. The isotopic signatures of nitrogen and of Xe were expected to be useful in this regard since Acapulco has a unique nitrogen isotopic signature. Our nitrogen measurements for magnetic ($\delta^{15}N = +10‰$) and nonmagnetic ($\delta^{15}N \sim 0‰$) separates of FRO90011 are different from those in Acapulco and do not show the signature of light nitrogen. The ratio of radiogenic ^{129}Xe (70×10^{-12} cm^3STPg^{-1}) and of fission $^{136}Xe_f$ ($<1 \times 10^{-12}$ cm^3STPg^{-1}) differs significantly from those in Acapulco.

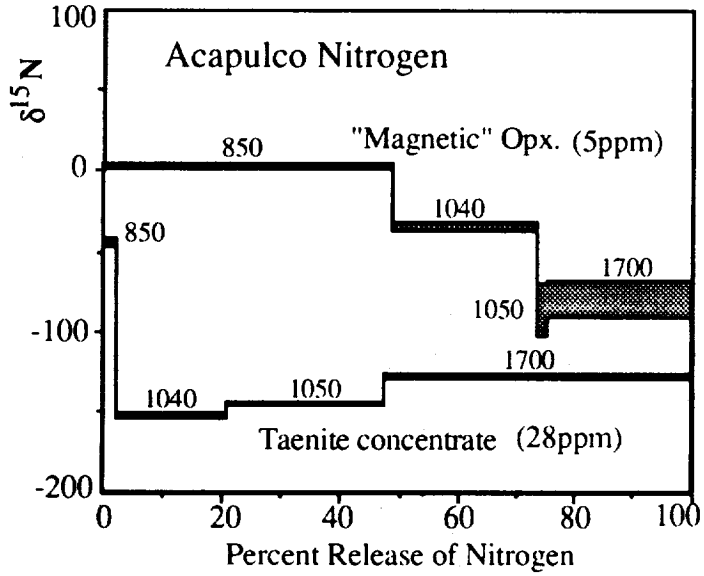

Fig. 1. Isotopic data from step-wise release of nitrogen from Acapulco.

References: (1) Palme H., Schultz L., Spettel B., Weber H. W., Wänke H., Michel-Levy C. M. and Lorin J. C. (1981) Geochim. Cosmochim. Acta 45, 727-752. (2) Sturgeon G. and Marti K. (1991) Proc. Lunar Planet. Sci. Conf. 21th, 523-525. (3) Kim Y., Kim J. S. and Marti K. (1992) Lunar and Planet. Science XXIII, 691-692.

SEPARATION OF TOPOGRAPHIC AND INTRINSIC BACKSCATTER VARIATIONS IN BISCOPIC RADAR IMAGES: A "MAGIC AIRBRUSH"

R. L. KIRK, U.S. Geological Survey, Flagstaff, AZ 86001

Introduction Shaded-relief maps portraying landforms as they would appear in the absence of variations in the intrinsic brightness of the surface are a venerable and extremely useful tool in planetary geology. Such maps have traditionally been produced by a highly labor intensive manual process. Skilled cartographer-artists develop detailed mental images of landforms by meticulous scrutiny of all available data, and are able to use an airbrush and electric eraser to draw these images on a map [1]. This process becomes increasingly time-consuming or even impossible if—as is true for radar data in general and Magellan data in particular—the effects on image brightness of varying scattering properties greatly outweigh those of slope variations. Because of the difficulty of interpreting relief in the Magellan images, the airbrush technique is being used only to remove obvious artifacts from low-resolution, shaded-relief images computed digitally from altimetric data [2]. The purpose of this abstract is to describe a novel and surprisingly simple digital-processing technique that can be applied to pairs of radar images to produce shaded-relief-like results at the full image resolution. These shaded-relief images can be used not only as base maps, but to improve the accuracy of quantitative topographic mapping by radarclinometry and stereoanalysis.

Approach The concept underlying the technique described here is extremely simple. Consider a pair of radar images obtained with illumination from opposite or nearly opposite sides, as, for example, Magellan images from the first and second mapping cycles. If the average incidence angles of the two images are not too dissimilar, then features that have an intrinsically strong backscatter will appear bright in both images, whereas a slope that faces the illumination and therefore appears bright in one image will face away and appear dark in the other. Therefore, the sum or average of the two images will display primarily intrinsic backscatter variations, while the difference will display primarily slope-related modulation. (I am assuming that the image data consist of the logarithm of the backscatter cross-section σ_0, so that differencing the images removes *multiplicative* factors common to both σ_0 measurements. The Fresnel reflectivity of the surface is one such factor. At the large incidence angles used by Magellan, the effects of differing surface roughness are also nearly multiplicative.)

To put this simple observation into practice, two refinements are needed. First, *weighted* sums and differences of the images must be used to achieve the best cancellation of slope and intrinsic backscatter effects, respectively. The appropriate weights may be calculated by using a parametric model of the backscatter properties of the surface, as follows. I have utilized the scattering model of Hagfors [3]; very similar results would be obtained with that of Muhleman [4] (with the surface roughness left as a free parameter, rather than assigned its global average value, as the function is used by the Magellan project for image normalization). Let $B^k = \log(\sigma_0^k)$ denote the data value in the two images ($k = 1, 2$) at a given point. Further, let $\overline{i}^k$ be the mean incidence angles in the two images, i^k the local incidence angles at the point of interest, $\overline{C}$ the average roughness parameter for the surface, and C the roughness at the given point. Then we can write down the following first-order expansions for the image brightnesses about their mean values:

$$B^k \simeq B(\overline{I}^k, \overline{C}) + \frac{dB^k}{di} \cdot (i^k - \overline{i}^k) + \frac{dB^k}{dC} \cdot (C - \overline{C}), \qquad k = 1, 2 \tag{1}$$

The observations B^1 and B^2 provide two constraints on the three unknowns i^1, i^2, and C. To proceed we must therefore make the further assumption that the slope of the surface is entirely in the direction of illumination. This is not an unreasonable assumption, given that slopes in the transverse direction will have a much weaker effect on image brightness. Then we have the further constraint that $(i^1 - \overline{i}^1) = -(i^2 - \overline{i}^2)$. With this third constraint we can solve for the unknowns, and, more importantly, form the following "topographic" and "roughness" images:

$$a_0^k + a_1^k B^k + a_2^k B^{3-k} \simeq B(\overline{I}^k, \overline{C}) + \frac{dB^k}{di} \cdot (i^k - \overline{i}^k), \qquad k = 1, 2 \tag{2a}$$

and

$$b_0^k + b_1^k B^k + b_2^k B^{3-k} \simeq B(\overline{I}^k, \overline{C}) + \frac{dB^k}{dC} \cdot (C - \overline{C}), \qquad k = 1, 2 \tag{2b}$$

The required coefficients are readily calculated in terms of the derivatives of the model backscatter function:

$$a_0^k = B(\overline{I}^k, \overline{C}) \cdot (1 - a_1^k - a_2^k), \qquad k = 1, 2 \tag{3a}$$

$$a_1^k = -\left(\frac{dB^k}{di} \cdot \frac{dB^{3-k}}{dC}\right) / \left(\frac{dB^{3-k}}{di} \cdot \frac{dB^k}{dC} - \frac{dB^k}{di} \cdot \frac{dB^{3-k}}{dC}\right), \qquad k = 1, 2 \tag{3b}$$

$$a_2^k = +\left(\frac{dB^k}{dC} \cdot \frac{dB^k}{di}\right) / \left(\frac{dB^{3-k}}{di} \cdot \frac{dB^k}{dC} - \frac{dB^k}{di} \cdot \frac{dB^{3-k}}{dC}\right), \qquad k = 1, 2 \tag{3c}$$

MAGIC AIRBRUSH: R. L. Kirk

The b coefficients are identical in form to the corresponding a coefficients, except that derivatives with respect to i and C are exchanged. Note that the coefficients will vary (weakly) with incidence angle. I have therefore developed software that recalculates them for each line of the image, taking into account the variation of the Magellan incidence angles with latitude. If the images are not too extensive in latitude, however, a successful result can be obtained by calculating the coefficients by hand for a representative incidence angle and adding the entire images with these weights.

The second important refinement to the technique addresses the fact that forming the "topographic" image $a_0^k + a_1^k B^k + a_2^k B^{3-k}$ directly does *not* lead to an acceptable result. Intrinsic backscatter variations will have cancelled, but each topographic feature will be doubled. This is the inevitable consequence of parallax between the two images. The following three-step process can be used to generate an acceptable result in the presence of parallax:

1) Form the "roughness" image $b_0^k + b_1^k B^k + b_2^k B^{3-k}$. In this image, topographic shading from the two inputs will have cancelled in magnitude, but, because of parallax, will be present in the form of offset bright and dark "fringes."
2) Lowpass-filter the "roughness" image to remove the fringes. A one-dimensional median filter elongated in the illumination (range) direction is preferable to a conventional, linear boxcar filter. Either filter will remove the fringes if it is wider than the maximum parallactic displacement between conjugate points in the images. The median filter has the advantage that it will not blur sharp discontinuities in the "roughness" image [5].
3) The result of the second step is a "mask" image that should show only intrinsic backscatter variations. Subtraction of this mask from the original image gives the desired result: a shaded-relief-like image containing only topographic modulation.

Applications The shaded-relief-like images produced by the method described here have several intriguing applications. First, like airbrush maps, they can serve as grist for the process of photogeologic interpretation. The USGS is therefore including the "magic airbrush" image in the support materials for the Venus Geologic Mapping program for each quadrangle that contains a significant amount of two-side image coverage. Such overlapping coverage is available for only about 30% of the planet. Some care must be used in interpreting the images, of course; there is a strong component of topographic modulation, but there are also artifacts caused by residual misregistration of the images and by departures of the surface from the assumed backscatter function. A second application for the technique makes positive use of these artifacts: the examination of the "topographic" image is a rapid way to screen large areas for unusual backscatter behavior, including non-Hagforsian (diffuse) scattering and even anisotropic scattering [6]. Third, to the extent that the processing succeeds in removing intrinsic σ_0 variations, the processed image will be preferable to the raw image as an input to radarclinometry or shape-from-shading techniques. Finally, there is reason to hope that the biscopic processing will facilitate stereoanalysis of opposite-side images. Once the intrinsic backscatter variations have been removed from both images, one can make a negative of one of them. The result is a stereopair in which the brightness of features in the two images is everywhere positively correlated, whereas the raw-image pair contains both positively and negatively correlated features, confounding attempts at both manual and automatic stereocompilation.

References Cited

[1] INGE, J. L. AND P. M. BRIDGES, (1976) Applied photointerpretation for airbrush cartography, *Photogram. Eng. Remote Sens.*, **42**, 749–760; BATSON, R. M. (1978) Planetary mapping with the airbrush, *Sky and Telescope*, **55**, 109–112. [2] KIRK, R. L., *et al.* (1993) The cartography of Venus with Magellan data, this volume. [3] HAGFORS, T. (1964) Backscattering from an undulating surface with applications to radar returns from the Moon, *J. Geophys. Res.*, **69**, 3779–3784. [4] MUHLEMAN, D. O. (1964) Radar scattering from Venus and the Moon, *Astron. J.*, **69**, 34–41. [5] PRATT, W. K. (1978) Digital image processing, Wiley-Interscience, 330–332. [6] PLAUT, J. J., *et al.* (1992) Anomalous scattering behavior of selected impact "parabola" features: Magellan cycle-to-cycle comparisons. *Papers Presented at the International Colloquium on Venus*, 92.

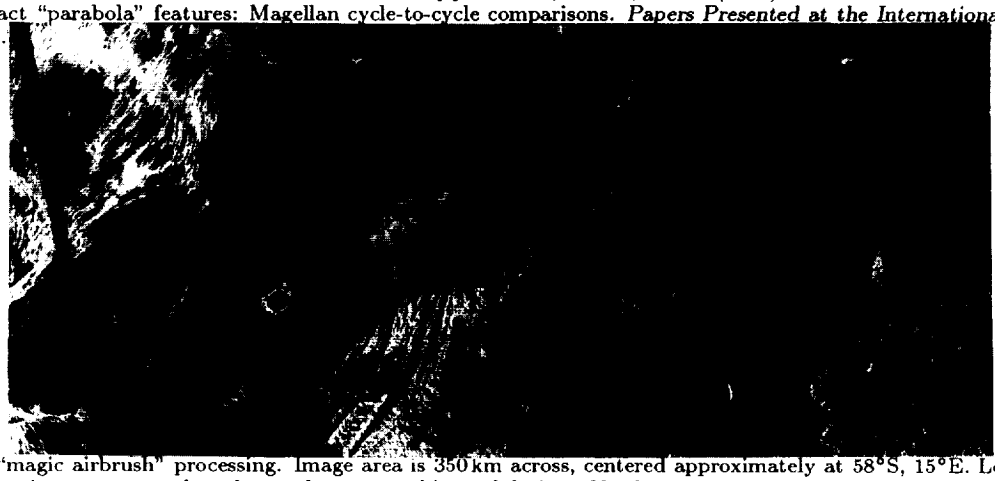

Example of "magic airbrush" processing. Image area is 350 km across, centered approximately at 58°S, 15°E. Left: raw cycle 1 image Right: image processed to show only topographic modulation of backscatter.

C-6

GLOBAL MAGELLAN-IMAGE MAP OF VENUS AT FULL RESOLUTION;

R. L. KIRK, K. B. EDWARDS, H. F. MORGAN, L. A. SODERBLOM, AND T. L. STOEWE, U.S. Geological Survey, Flagstaff, AZ 86001

Introduction During its first 243-day mapping cycle, the Magellan spacecraft succeeded in imaging 84% of the surface of Venus at resolutions on the order of 100 meters; subsequent cycles have increased the total coverage to over 97% and provided redundant coverage of much of the planet with differing viewing geometries [1]. Unfortunately, this full-resolution global dataset is in the form of thousands of individual orbit tracks (F-BIDRs) whose length-to-width ratio of nearly 1000 : 1 makes them minimally useful unless mosaicked. The Magellan project has produced full-resolution mosaics (F-MIDRs) only for selected regions on the planet, whereas a global set of mosaics has been made only at threefold degraded resolution (C1-MIDRs). Furthermore, although the F-MIDRs, which are approximately equidimensional, are much better suited for scientific interpretation than the F-BIDRs, they are still an unwieldy dataset: over 1500 quadrangles, each showing a region only about 600 km on a side, would be required to cover the entire planet. The USGS has therefore undertaken to produce and distribute a global, full-resolution set of mosaics of the Magellan image data in a format that will be efficient for both hardcopy and digital use.

The initial motivation for this project was that it would provide an efficient means of verifying the integrity of the F-BIDRs to be archived on computer-compatible tape at the USGS Flagstaff facility. However, the resulting product, known as the FMAP, should also serve as an important resource for future scientific interpretation. It will offer several advantages beyond global coverage at full resolution. The first, alluded to above, is its division of the planet's surface to minimize the number of quadrangles and maximize their area, subject to the limits on the number of pixels imposed by state-of-the-art digital recording media and hardcopy output devices. The second, the use of improved "cosmetic" processing techniques, will greatly reduce tonal discontinuities between component F-BIDRs in the FMAP compared to the standard Magellan mosaic products. Finally, wherever possible, the FMAP will incorporate data that were unavailable (*e.g.*, because of processing delays) when the standard MIDR products were created, as well as data that have been reprocessed to improve their radiometric or geometric quality.

Quadrangle Scheme The FMAP, like the standard Magellan image products, will be compiled in Sinusoidal projection. Each of the 340 quadrangles will have a projection longitude in the center of its area of coverage. The accompanying figure shows the quadrangle scheme to be used for the FMAP. (Note that, because of the convergence of meridians in Sinusoidal projection, adjacent FMAP quadrangles will overlap slightly. The figure shows the midlines of the areas of overlap.) The quadrangles span approximately 12° in latitude except for those nearest the poles, which extend from ±84° to ±90°. Near the equator, the quadrangles also span approximately 12° in longitude, but the longitude range is increased at high latitudes to keep the width in pixels approximately constant. Data near the poles will also be reprojected and distributed in Polar Stereographic projection.

Quadrangles at different latitudes will differ slightly in their dimensions, but all will consist of approximately 17,000 lines and 17,000 samples, or slightly under 300 megabytes of data. It will therefore be possible to store one quadrangle on each side of an erasable magneto-optical disk during processing, and to distribute the digital FMAP on compact disk (CD-ROM) with two quadrangles per disk. To facilitate access to the data on CD-ROM, each quadrangle will be divided into sub-quadrangles or tiles approximately 2° (3000 pixels) on a side. All tiles in a given quadrangle will have a common projection longitude, making them easy to assemble into larger areas.

The hardcopy version of the FMAP will be output on Optronix 5040 large-format filmwriter at a resolution of 50 μm per pixel. At this pixel size, the images are approximately 0.85 m on a side, well within the 1 m × 1.25 m capability of the filmwriter. The resulting negatives will be printed without enlargement, resulting in a map scale of 1 : 1,500,000.

Cosmetics Considerable effort has been devoted to the development of cosmetic techniques to suppress the artifacts—tonal gradients across the BIDR strips and tonal discontinuities between strips—that lead to mosaics with a "stripy" appearance. First, we have developed a fairly complicated scheme for trimming the edges of the F-BIDRs before mosaicking. This scheme uses both *a priori* information (arrived at by trial and error) about the variation of the signal-to-noise ratio and the extent of overlap between BIDRs with latitude, and statistical testing of the data quality. The object is to trim away noisy image data that would lead to artifacts when the images are mosaicked, without trimming so deeply as to introduce gaps in the data. Second, after trimming the BIDRs, we highpass-filter them with a boxcar filter 1 sample wide by 701 lines (~50 km) tall. This process is relatively fast and removes systematic gradients in intensity across the BIDR (caused, for example, by misestimation of the antenna sensitivity pattern) without introducing significant artifacts even in areas where the surface displays strong backscatter contrasts. Finally, once the BIDRs are reprojected to a common center longitude, we blend the data in the area of overlap by using a

slightly refined version of the feathering algorithm that was originally developed by Michael Girard of JPL and used in creating the Magellan MIDRs.

Production and Distribution The gray area in the figure below shows progress on the FMAP to date. Data are read in one BIDR at a time and incorporated into all quadrangles crossed by that BIDR; because of the roughly north-south alignment of Magellan's orbit, groups of about 10 quads tend to be completed simultaneously. Compilation of the FMAP is currently proceeding at a rate of roughly 10 orbits per day, which corresponds to an average output of eight quadrangles per week. Completed quadrangles are immediately output as continuous-tone negatives, and contact prints are generated and supplied to the Magellan project, the NSSDC, and the Regional Planetary Image Facilities (RPIFs).

Digital versions of the FMAP quadrangles are, for the moment, being archived in Flagstaff. Distribution of the data in digital form will be delayed in order to incorporate further improvements of the dataset (within reason). We anticipate that, by the end of FY93, some fraction of the quadrangles will have to be recompiled in order to incorporate currently unavailable or reprocessed BIDR data, or to correct unforseen errors in the compilation process. In addition, efforts are currently underway to greatly improve the geodetic accuracy of the Magellan dataset by refining the spacecraft ephemeris through a combination of inter-orbit tiepointing and an improved model of the Venusian gravity field. Incorporation of the refined ephemeris would greatly increase the utility of the FMAP for future stereogrammetric studies (at present, navigation errors lead to artifactual "cliffs" up to several kilometers high in stereomodels of the surface). However, it is not yet clear whether the new navigation data will be available soon enough to be incorporated in the FMAP. Whatever the schedule, the FMAP CD-ROMs will be premastered by the Data Distribution Laboratory at JPL, produced by SONY, and distributed by the USGS to the RPIFs and all former Magellan investigators. Additional distribution will be handled by the Planetary Data System. Once the final data are compiled, they will also be published by the USGS as printed maps. The possibility for widespread distribution of such maps will greatly offset the loss of resolution inherent in the halftone printing process.

References Cited [1] R. S. SAUNDERS, *et al.* (1992) Magellan Mission Summary, *J. Geophys. Res.*, **97**, 13067–13090.

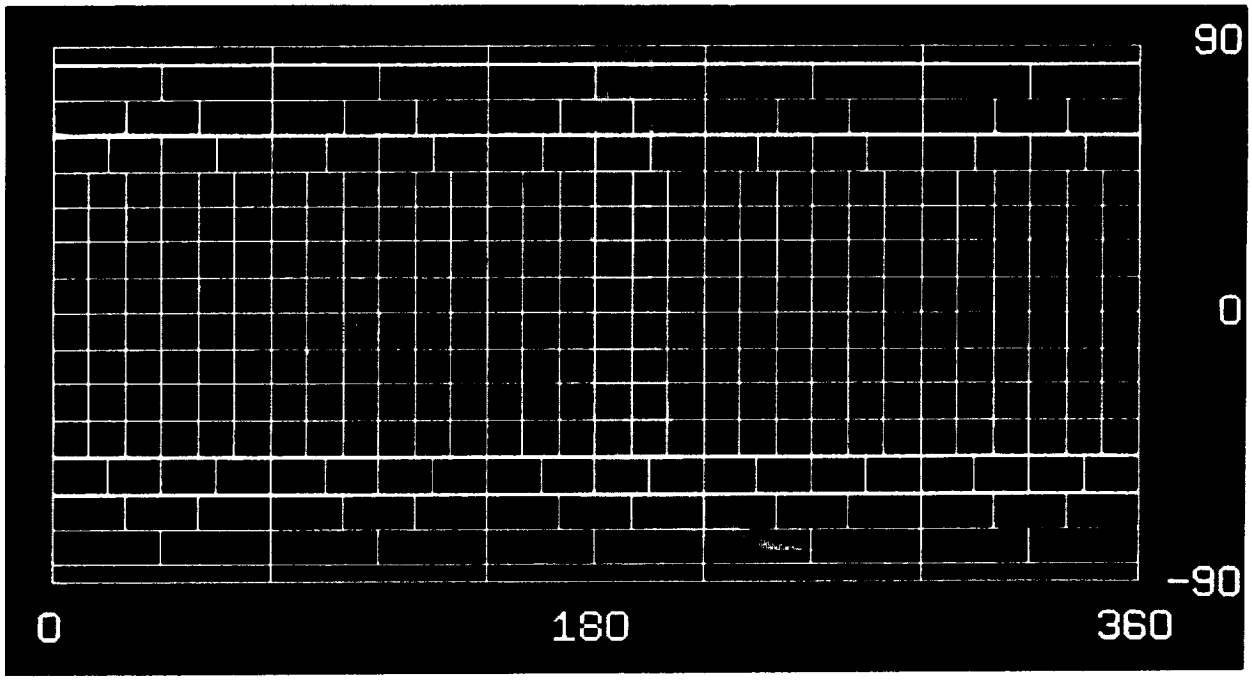

Global map of Venus in Simple Cylindrical projection, showing the division of the planet into 340 FMAP quadrangles. FMAP will be in Sinusoidal projection; overlap of quadrangles caused by convergence of meridians is not shown. Gray area shows data processed to date.

THE CARTOGRAPHY OF VENUS WITH MAGELLAN DATA;

R. L. KIRK, H. F. MORGAN, AND J. F. RUSSELL, U.S. Geological Survey, Flagstaff, AZ 86001

Maps of Venus based on Magellan data are being compiled at 1 : 50,000,000, 1 : 5,000,000 and 1 : 1,500,000 scales. Topographic contour lines based on radar altimetry data are overprinted on the image maps, along with feature nomenclature. Map controls are based on existing knowledge of the spacecraft orbit; photogrammetric triangulation, a traditional basis for geodetic control for bodies where framing cameras were used, is not feasible with the radar images of Venus. Preliminary synthetic aperture radar (SAR) image maps have some data gaps and cosmetic inconsistencies, which will be corrected on final compilations. Eventual revision of geodetic controls and of the adopted Venusian spin-axis location will result in geometric adjustments, particularly on large-scale maps.

The first set of maps, being compiled on eight sheets, consists of radar image mosaics. Mercator and Polar Stereographic projections are used for this series; map scales are 1 : 10,000,000 at the poles and at latitudes ±52°305. A shaded relief version of each map in the set, derived from the Magellan radar altimetry, is being compiled by manual airbrushing, which restores an impression of topographic relief that is lost in the image mosaics. Base maps for systematic geologic mapping will be made at 1 : 5,000,000 scale; this series consists of 62 quadrangles in Mercator, Lambert Conformal, and Polar Stereographic projections. In addition to the SAR mosaics and the altimetric shaded relief and contour maps, this series includes a novel type of high-resolution, shaded relief image created by digital processing of oppositely illuminated SAR image pairs. This technique is described in an accompanying abstract [1]. Full-resolution SAR image mosaics are being compiled digitally and reproduced photographically at 1 : 1,500,000 scale in Sinusoidal projection. This map series is further described in an accompanying abstract [2].

Sets of synthetic stereograms of SAR images of the entire planet are being made by introducing parallax derived from altimetry measurements into the images [3]. Each stereo set comprises a Magellan C1-MIDR mosaic (~ 15° square in Sinusoidal projection) and two stereo companions with different degrees of vertical exaggeration. Thematic maps in which the Magellan altimetry, emissivity, normal reflectivity, and RMS-slope datasets are color coded and merged with the SAR image are also being produced and can be viewed stereoscopically in combination with the gray-scale synthetic stereo images. The stereo and thematic images are being distributed as 25 cm x 25 cm photographic products with 225 m per pixel and 675 m per pixel resolutions, respectively. Special-purpose, non-cartographic products, including oblique perspective views of the Venusian surface, are also being produced for scientific analysis [4]. Finally, a 16-inch-diameter globe of Venus (approximate scale 1 : 3,000,000) has been produced. The image data for this globe is a combination of the Magellan SAR and digitally produced shaded relief.

A regional network of feature names is being prepared to support scientific communication, and is described in an accompanying abstract [5]. Experience with the typical number of named features per unit area on other planets indicates that names for 4000 or more features on Venus are likely to be required in the coming decade.

References Cited [1] KIRK, R. L. (1993) Separation of topographic and intrinsic backscatter variations in biscopic radar images: A "magic airbrush," this volume. [2] KIRK, R. L. *et al.* (1993) Global Magellan image map of Venus at full resolution, this volume. [3] BATSON, R. M., *et al.* (1978) Synthetic stereo and LANDSAT pictures, *Photogramm. Eng. Remote Sens.*, **42**, 1279–1284. [4] KIRK, R. L., *et al.*, (1992) Enhanced visualization for interpretation of Magellan radar data: Supplement to the Magellan special issue, J. Geophys. Res., **97**, 16371–16380. [5] RUSSELL, J. F., AND G. G. SCHABER (1993) Named Venusian craters, this volume.

OSMIUM ISOTOPES IN IVORY COAST TEKTITES: CONFIRMATION OF A METEORITIC COMPONENT AND RHENIUM DEPLETION.

Christian Koeberl[1,2] and Steven B. Shirey[2]. [1]*Institute of Geochemistry, University of Vienna, Dr.-Karl-Lueger-Ring 1, A-1010 Vienna, Austria;* [2]*Department of Terrestrial Magnetism, Carnegie Institution, 5241 Broad Branch Road, N.W., Washington, D.C. 20015, USA.*

We used the sensitive negative thermal ionization mass spectrometry method for the measurement of concentrations and isotopic ratios of osmium and rhenium in four Ivory Coast tektites. These tektites have crustal major and trace element compositon, as well as large negative ε_{Nd} (-20) and positive ε_{Sr} (+260 to +300) which are characteristic for old continental crust. We have found Os concentrations ranging from 0.09 to 0.30 ppb, clearly much higher than average crustal values, $^{187}Os/^{186}Os$ ratios of about 1.2-1.7, and low $^{187}Re/^{186}Os$ ratios. These results show unambiguously the existence of a meteoritic component (on the order of 0.06%) in the Ivory Coast tektites. Low Re abundances are the result of fractionation of Re during the impact.

Tektites are natural glasses occurring on earth in several strewn fields. Geochemical arguments have shown that tektites have been derived by hypervelocity impact melting from terrestrial upper crustal rocks (e.g., [1,2]). For two of the four tektite strewn fields (Ivory Coast, moldavite), a connection to impact craters (Bosumtwi, and Ries, respectively) has been suggested on the basis of chemical, isotopic, and age data. Even though the geochemistry of tektites is in unequivocal favor of an origin by impact melting of terrestrial rocks, the absence of definitive crater identifications as well as the absence of a clear demonstration of the presence of an extraterrestrial contribution to the chemistry of most tektites remains a problem. Tektites consist predominantly of terrestrial material, because the impacting body ("projectile") is vaporized upon impact. Taking into account the complexity of the mixing processes occurring during impact, and the small contribution of the projectile to the total mass of the melt, it is extremely difficult to discover any extraterrestrial contamination of impact glasses and tektites. The only elements that seem to be useful in such an identification are some siderophile elements, especially the platinum-group elements (PGEs). Their abundances and interelement ratios in meteorites are considerably different from terrestrial upper crustal rocks. Studies of PGE abundances in melt rocks and breccias from several impact craters yielded some estimates of the composition of the projectiles (e.g., [3,4]).

These projectile identifications are, however, few and often uncertain. The method has been more successful for melt rocks and impact glasses, but no conclusive results were obtained for any tektite group. Only few tektites have been analyzed for their PGE contents, mainly due to analytical problems at the very low abundance levels present in tektites. Only one H-Mg australite (out of 6 analyzed) showed a distinct PGE enrichment over the typical abundances in upper crustal rocks [5]. Analyses of two Ivory Coast tektites yielded Ir abundances of 0.24 and 0.33 ppb [4,6]. The low abundances precluded the measurement of all PGEs in the Ivory Coast tektites, but Palme et al. [6] suspected that an iron projectile might have been responsible for the Bosumtwi crater. However, no unambiguous identification of an extraterrestrial component has been confirmed for any tektite group, and no definite meteorite group could be allocated to any of the reported PGE enrichments. Part of the problem seems to be the possibility of irregular fractionation between the PGEs and other siderophile elements during impact [7,8].

We suggest that the study of Os isotopes is able to provide unambiguous proof for the presence of an extraterrestrial component in impact glasses and tektites because the ratio of $^{187}Os/^{186}Os$ in meteorites is distinctly different from the ratio in old continental crustal rocks that make up the target material for tektites. It is also unlikely that there is a significant fractionation of Os isotopes during impact. Only one earlier study [9] tried to determine Os isotopes in impact melts; it succeeded only partly because the analytical methods were not yet sensitive enough.

We used the highly sensitive negative thermal ionization technique for the determination of Os isotopes and the abundances of Os and Re (e.g., [10]) in four Ivory Cost tektites. Improved laboratory procedures yielded total procedural blanks of 2 pg for Os and 12 pg for Re for the acid digestion-distillation-anion exchange procedures used to dissolve the sample and purify Re and Os. We found Os concentrations of about 0.09-0.30 ppb, which are clearly elevated over normal crustal values (Fig. 1). Re, on the other hand, having concentrations of only 0.004-0.020 ppb, is strongly depleted relative to both continental crust (Fig. 1) and meteorites. The $^{187}Os/^{186}Os$ ratios are shown in Fig. 2. The ratios are low for all four tektite samples, and are inconsistent with crustal values. Also plotted in Fig. 2 are carbonaceous chondrites and iron meteorites, which define the meteoritic (4.56 Ga) isochron [11,12]. The tektites plot to the left of the meteorite isochron, while crustal contamination would have caused an elevated $^{187}Re/^{186}Os$

METEORITIC OSMIUM ISOTOPES IN IVORY COAST TEKTITES: Koeberl C. and Shirey S.B.

ratio. Laboratory procedures can be excluded as a source for the low Re contents (see [13] for details). In contrast, the low Re values indicate loss of Re during the impact, in agreement with earlier suggestions [5].

Our model is shown in Fig. 3. The impact occurred about 1.1 Ma ago, into old crustal target rocks having ε_{Nd} of -20 and mantle extraction Sm-Nd model ages of about 1.9 Ga [14]. Crustal rocks of that age should define a mixing line with meteoritic material (Fig. 3). The $^{187}Re/^{186}Os$ ratio for typical crustal rocks can vary between about 300-600; we use a conservative estimate of about 300. If the Os in the tektites would be of crustal origin, it would plot far to the right and above the borders of Fig. 3. The low $^{187}Os/^{186}Os$ ratios in the tektites are therefore unambiguous proof that almost all the Os is meteoritic. During impact, crustal rocks are mixed with the meteoritic component (represented by the intercept of the mixing line with the meteorite isochron), and through concurrent Re loss they move to the left of the meteorite line. The $^{187}Os/^{186}Os$ ratios in the Ivory Coast tektites are compatible with an iron projectile, although that distinction is not unambiguous.

Acknowledgements: C.K. wishes to thank the Carnegie Institution/DTM for hospitality. This work is supported by the Austrian FWF, Project No. P9026-GEO, and the National Science Foundation, Project EAR-9218847.

References: [1] Taylor, S.R., Earth Sci. Rev. 9, 101.123, 1973. [2] Koeberl, C., Annu. Rev. Earth Planet. Sci. 14, 323-350, 1986. [3] Morgan, J.W., Higuchi, H., Ganapathy, R., and Anders, E., Proc. 6th Lunar Sci. Conf., 1609-1623, 1975. [4] Palme, H., Geol. Soc. Am. Spec. Paper 190, 223-233. [5] Morgan, J.W., Proc. 9th Lunar Planet. Sci. Conf., 2713-2730, 1978. [6] Palme, H., Grieve, R.A.F., and Wolf, R., Geochim. Cosmochim. Acta 45, 2417-2424, 1981. [7] Attrep, M., Orth, C.J., Quintana, L.R., Shoemaker, C.S., Shoemaker, E.M., and Taylor, S.R., Lunar Planet. Sci. XXII, 39-40, 1991. [8] Mittlefehldt, D.W., See, T.H., and Hörz, F., Meteoritics 27, 361-370, 1992. [9] Ellam, R.M., Carlson, R.W., and Shirey, S.B., Nature 359, 718-721, 1992. [10] Fehn, U., Teng, R., Elmore, D., and Kubik, P.W., Nature 323, 707-710, 1986. [11] Walker, R.J., and Morgan, J.W., Science 243, 519-522, 1989. [12] Horan, M.F., Morgan, J.W., Walker, R.J., and Grossman, J.N., Science 255, 1118-1121, 1992. [13] Koeberl, C. and Shirey, S.B., Science, submitted, 1993. [14] Shaw, H.F., and Wasserburg, G.J., Earth Planet. Sci. Lett. 60, 155-177, 1982. [15] Walker, R.J., Morgan, J.W., Naldrett, A.J., Li, C., and Fassett, J.D., Earth Planet. Sci. Lett. 105, 416-429, 1991.

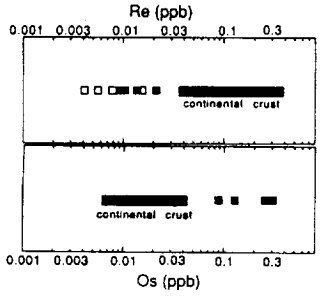

↑Fig. 1: Range of Os and Re concentrations in Ivory Coast tektites compared to crustal values (from [15]). Solid symbols are maximum possible Re values assuming no blank correction for Re. Open symbols are corrected for average laboratory blank.

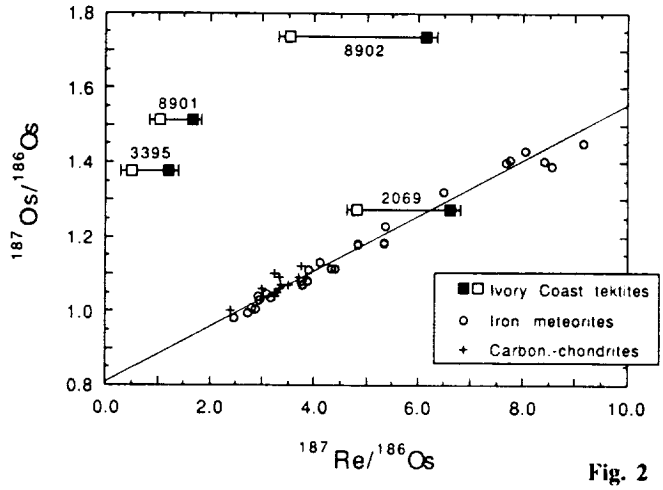

Fig. 2

→Fig. 2: $^{187}Re/^{186}Os$ vs. $^{187}Os/^{186}Os$ for 4 Ivory Coast tektite samples, compared to carbonaceous chondrites [11] and iron meteorites [12]. The error bars are defined by uncertainties in the level of the Re blank. The error bars for Os are smaller than the symbols. Symbols see Fig. 1.

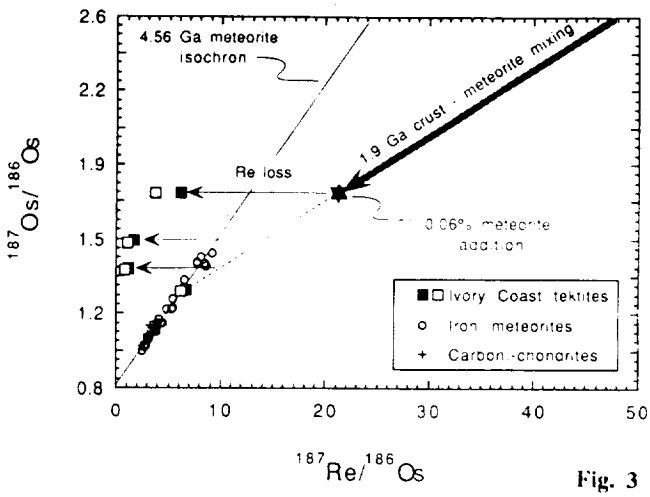

Fig. 3

→Fig. 3: Mixing model between 1.9 Ga old crustal rocks (having $^{187}Re/^{186}Os$ ratios of about 300) with a meteoritic component, and subsequent loss of Re.

MANSON IMPACT STRUCTURE, IOWA: FIRST GEOCHEMICAL RESULTS FOR DRILL CORE M-1.

Christian Koeberl[1], Raymond R. Anderson[2], Jack B. Hartung[2], and Wolf Uwe Reimold[3]. [1]*Institute of Geochemistry, University of Vienna, A-1010 Vienna, Austria;* [2]*Iowa Geological Survey Bureau, 109 Trowbridge Hall, Iowa City, IA 52242-1319, USA;* [3]*Economic Geology Research Unit, Department of Geology, University of the Witwatersrand, Johannesburg 2050, South Africa.*

The Manson Impact Structure is a large complex impact crater centered ca. 5 km north of the town of Manson, Iowa [1,2]. It is the largest intact impact structure recognized in the United States (35 km in diameter). Its $^{40}Ar/^{39}Ar$ age is indistinguishable from that of the Cretaceous-Tertiary (K-T) boundary [3]. The Manson structure may be one element of the events at the K-T boundary. The crater is completely covered by Quaternary glacial sedimentary deposits that are normally underlain by Cretaceous clastic sediments and flat-lying carbonate sediments of Phanerozoic age, as well as Proterozoic red clastic, metamorphic, volcanic, and plutonic rock sequences (e.g., [1,2,4]. The study of a reflection seismic profile, provided by Amoco, was critical in interpreting the structure [4]. In the 35 km diameter zone that marks the extension of the crater the normal rock sequence is disturbed due to the impact, and at the center of the structure granitic basement rocks are present that have been uplifted from about 4 km depth.

In 1953, two drill holes yielded core samples at locations on the central uplift (Fig. 1). The lithologies encountered in these cores are described by [1]. Recently, 12 new holes (M-2 and M-2A at the same location) were drilled (for locations see Fig. 1). A total of 4019 feet of core was obtained. The goal of the drilling was to understand the structure of the crater (in comparison to geophysical data), to find clues regarding the nature of the projectile, obtain more precise age data, and to determine the properties and distribution of the lithologies present at the crater. Our studies consist of detailed petrological and geochemical characterization of all cores, with emphasis on a detailed description of all rock types found in the core samples and their relationship to target rocks. In addition we try to study possible connections between the Manson crater and events at the K-T boundary. After completion of the geochemical analyses, we will calculate which mixtures of known target rocks provide a good match for the composition of impact melts and impact derived breccias at the crater. Some earlier work was based on samples obtained from well cuttings and provided some first estimates of the breccia and melt rock compositions [5,6].

Here we present first geochemical data on samples from the Manson M-1 core (Pierson). The drilling for this core was completed on May 8, 1991, at a depth of 703 feet. The interval from 186-703 feet was cored. The drill hole was placed on the flanks of the central uplift (Fig. 2). The major lithologies encountered in this drill hole are, in order of increasing depth, glacial till, followed by thick sequences of sedimentary clast breccia, and igneous clast breccia (with "glassy" and sandy matrices; see Fig. 2). For the geochemical and petrological studies we have obtained samples from 42 different depths, representing all major lithologies. The sedimentary clast breccia contains numerous shale clasts which may be of Cretaceous age and could be part of the pre-impact target lithology. The samples were powdered and analyzed by XRF. The results given in Table 1 show the relatively wide variations present in the shale composition as compared to more restricted compositions of the matrices of both the sedimentary and the crystalline rock breccia. Figs. 3a-c show the variation of some major elements with depth for the three main lithologies. It is obvious that the matrix compositions show only a limited variation, with the exception of one sample (660.6 ft) which contains a partly altered mafic rock clast.

Acknowledgements: We are grateful to the U.S. Geological Survey and the Iowa Geological Survey Bureau for the core samples and for logistical support. B. Träxler and A. Vormaier assisted with the sample preparation. Supported by the Austrian FWF, Proj. No. P8794-GEO.

References: [1] Hartung, J.B.; and Anderson, R.R., LPI Tech. Rept. 88-08, 32 pp, 1988. [2] Hartung, J.B., Kunk, M.J., and Anderson, R.R., Geol. Soc. Am. Spec. Paper 247, pp. 297-222, 1990. [3] Kunk, M.J., Izett, G.A., Haugerud, R.A., and Sutter, J.F., Science 244, 1565-1568, 1989. [4] Anderson, R.R., and Hartung, J.B., Proc. Lunar Planet. Sci. 22, 101-110, 1992. [5] Koeberl, C., and Hartung, J.B., Lunar Planet. Sci. XXII, 733-734, 1991. [6] Koeberl, C., and Hartung, J.B., Proc. Lunar Planet. Sci. 22, 111-126.

MANSON IMPACT STRUCTURE

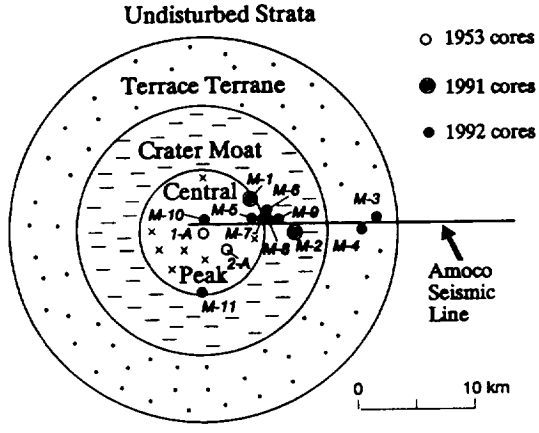

Fig. 1: Location of Manson drill holes. →

MANSON CRATER DRILL CORE M-1: FIRST GEOCHEMICAL DATA: Koeberl C. et al.

Table 1: Major element compositions (average and range) for selected rock types encountered in Manson Core M-1 (in wt%)

	M-1 Avg Sh/C	M-1 Min Sh/C	M-1 Max Sh/C	M-1 Avg SCB-M	M-1 Min SCB-M	M-1 Max SCB-M	M-1 Avg CRB-GM	M-1 Min CRB-GM	M-1 Max CRB-GM	M-1 Avg CRB-SM	M-1 Min CRB-SM	M-1 Max CRB-SM
SiO2	59.55	45.63	74.41	63.71	59.88	68.32	63.75	59.73	65.26	60.15	51.53	62.10
TiO2	1.00	0.63	1.25	0.58	0.53	0.65	0.96	0.84	1.40	0.86	0.74	1.03
Al2O3	16.84	10.75	21.08	8.77	7.82	10.73	13.96	13.18	14.86	14.94	10.15	15.80
Fe2O3	5.04	1.92	9.97	4.13	3.37	4.77	5.51	4.62	7.60	7.04	6.13	11.13
MnO	0.03	0.01	0.08	0.06	0.04	0.07	0.09	0.07	0.11	0.11	0.07	0.23
MgO	1.52	0.78	2.14	4.39	3.18	6.00	2.90	2.11	3.73	4.14	3.11	11.94
CaO	2.22	0.24	16.56	6.80	3.17	10.27	2.35	1.81	3.04	4.73	3.16	9.12
Na2O	0.40	0.11	0.70	1.07	0.07	2.43	3.78	3.41	4.44	4.74	2.22	5.50
K2O	3.38	2.13	4.50	1.09	0.65	1.72	3.41	3.02	3.87	2.13	1.19	2.66
P2O5	0.11	0.03	0.19	0.18	0.12	0.31	0.20	0.18	0.26	0.19	0.08	0.22
LOI	9.21	3.55	17.17	8.39	5.78	11.88	2.40	1.58	3.62	1.20	0.69	2.20
Total	99.30			99.18			99.30			100.22		

Note: Sh/C + (Creteaceous?) Shale; SCB-M = Sedimentary Clast Breccia (Matrix); CRB-GM = Glassy Matrix, Crystalline Rock Breccia CRB-SM = Crystalline Rock Breccia, Sandy Matrix

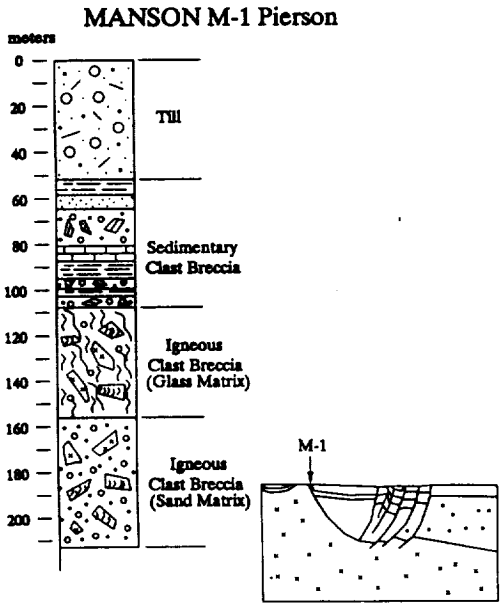

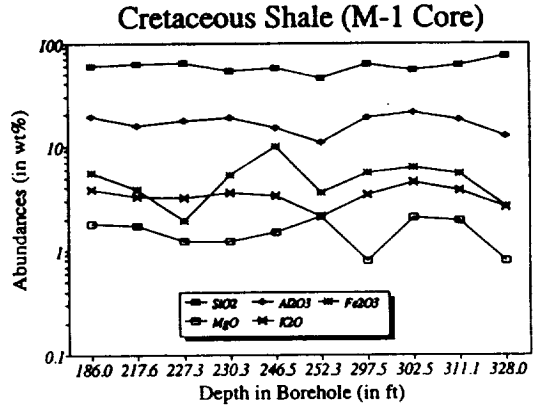

← Fig. 2: General M-1 core stratigraphy.

↕ Fig. 3a-c: Major element variation with depth in individual samples of three major rock types from the Manson M-1 core.

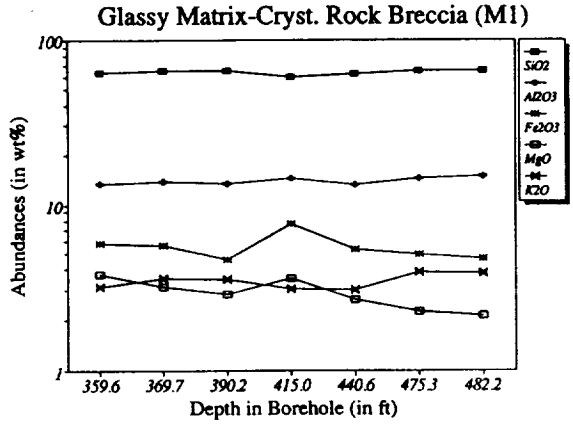

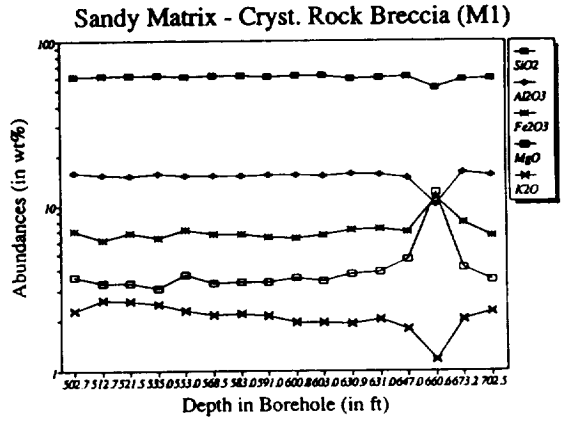

AGE DETERMINATIONS AND EARTH-BASED MULTISPECTRAL OBSERVATIONS OF LUNAR LIGHT PLAINS;

U. Koehler, R. Jaumann, G. Neukum; German Aerospace Research Establishment (DLR), Inst. for Planetary Exploration, Berlin/Oberpfaffenhofen, Germany.

Introduction: The history of Light plains still remains doubtful, but there are good arguments – mainly obtained by age determinations and supported by multispectral observations – for an endogenic (magmatic) instead of an (exclusively) impact related origin.

Light plains are characterised by smooth areas with an albedo lower than the surrounding highlands (12 - 13 %), but significantly higher than maria (5 - 6 %). Before Apollo 16 a volcanic source has been supposed, but analysis of returned samples (highly brecciated and metamorphosed rocks) favoured an impact ejecta related origin. Among the currently discussed models are (a) formation by ejecta sedimentation from multi-ringed basins [1], (b) formation by secondary and tertiary cratering action of balistically ejected material during the formation of multi-ringed basins [2], (c) in situ formation by impact melt of large events [3], and (d) premare (crypto-) volcanism basalts covered by a thin ejecta cover [4, 5]; younger impacts penetrated the ejecta surface to create the dark haloed craters. To find arguments in favour or against these ideas the chronology of light plains is of major importance. Obviously a genetic relationship between the evolution of light plains and the basin forming impacts can be possible only if the events of emplacement features happened simultaneously.

Age determinations can be performed by interpreting lunar crater size-frequency distribution measurements. Earlier investigations [6] led to the conclusion that some light plains in the surroundings of the Orientale and Imbrium basin are neither of same age nor can their origin be exclusively attributed to two specific epochs (i. e. Orientale and Imbrium events). Another important observation are variations in age even in the very vicinity of the basins. For example, in the NE rim of the Imbrium basin light plains decrease in age from N to NE; plains near the Apollo 16 landing site (3.8 - 3.9 * 10^9 a) are older than those 10° more to the W (3.6 - 3.8 * 10^9 a), followed again by older plains in and around crater Ptolemaeus and the Fra Mauro area (3.8 - 3.9 * 10^9 a; [7]). We have performed more age determinations of lunar light plains, and the results seem to reconfirm that a) there are plains certainly younger than the last basin forming event of the Orientale impact – thus making it impossible to explain their origin by impact ejecta –, and b) many ages show no or only weak correlation with the Orientale or Imbrium event.

Another aim was to investigate possible dependences between the age of light plains and their chemical-mineralogical composition to get hints about the evolution of the plains' surfaces. To extend the Apollo 16 spectral informations we used these data as a calibration standard for our earth based spectral and photometrical data. We performed telescopic lunar observations at the Mauna Kea Observatory/Hawaii in 1983 in six and 1989 with the DLR CCD camera in

12 narrow band filters (bandwidth = 20 nm) in the visible and near IR wavelenghts. Data underwent reduction, and effects induced by the athmosphere have been eliminated. To remove effects caused by different viewing angles we applied a differentiated photometric correction based on the model of Hapke [8] for bright, intermediate and dark areas respectively [9].

The data have been correlated with a spectral-chemical model derived from laboratory measurements. This model enables us to define spectral surface units and their respective geochemical composition in terms of wt% of Ti-, Fe-, Al- and Ca-oxides [10]. One result of our first observation campaign are different FeO-contents with values between 3 and 12 wt%, showing us mineralogical variations of light plains. Even a tendency towards decreasing FeO-numbers from W to E in the central nearside terrae can be observed, but no definite geographical correlation with the age variations of the respective plains mentioned above. The data obtained with 12 filters in 1989 reconfirmed these results by analysing the content of TiO_2.

We can summarise that an impact related origin of light plains cannot be denied, but it certainly was not the only involved process. There are arguments in favour of a magmatic origin of light plains. Most convincing for a volcanic source is the fact, that there are light plains clearly dated younger than the Orientale event. If it's true that light plains are of magmatic origin, this would imply dark mare volcanism occurring over a period of time parallel to the less mafic volcanism of the terrae-like light plains, and that there existed regional variations in magma composition. More detailed spectral information and more age determinations are needed to obtain arguments for further discussions. Galileo Earth/Moon-2 encounter data include high resolution multispectral information of areas poorly covered by earth based observations. These data may be helpful in answering questions about light plains.

References:

[1] Eggleton, R. E. and Schaber, G. G., (1972), *Apollo 16 Prel. Sci. Rep.* **NASA SP-315**, 29-7 to 29-15

[2] Oberbeck, V. R., Hörz, F., Morrison, R. H., Quaide, W. L., Gault, D. E., (1974), *Lun. Sci. Conf.*, **V**, 111-136

[3] Head, J. W., (1974), *The Moon* **11**, 327-356

[4] Spudis, P. D. and Hawke B. R., (1981), *Lun. Plan. Sci. Conf.* **XII**, 1028-1029

[5] Head, J. W., Murchie, S. L., Mustard, J. F., Peters, C. M., Neukum, G., McEwen, A., Greeley, R., Belton, M. S., (1992), *J. Geophys. Res.* -subm.-

[6] Neukum, G., (1977), *The Moon* **17**, 383-393

[7] Engel, S., (1986), Diplomarbeit, *University of Munich*, 75 pp.

[8] Hapke, G., (1977), *J. Geophys. Res.* **68**B4, 3039-33054

[9] Helfenstein, P. and Veverka, J. (1987), *Icarus* **72** 342-357

[10] Jaumann, R., (1992), *Journ. Geophy. Res.*, **96E5**. 22.793-22.807

MEANDER PROPERTIES OF VENUSIAN CHANNELS; G. Komatsu and V. R. Baker, Lunar and Planetary Laboratory, University of Arizona, Tucson, AZ 85721

Venusian lava channels have meander dimensions that relate to their mode of formation. Their meander properties generally follow terrestrial river trends of wavelength (L) to width (W) ratios, suggesting an equilibrium adjustment of channel form. Slightly higher L/W for many Venusian channels in comparison to terrestrial rivers may relate to nonaqueous flow processes. The unusually low L/W values for some Venusian and lunar sinuous rilles probably indicate modification of original meander patterns by lava-erosional channel widening.

Terrestrial river channels use their meander development to adjust channel slope through the interaction of erosion and deposition [1]. Consistent scaling of meander wavelength (L) and width (W) occur in typical rivers [2] as well as in glacier melt water channels [2], ocean currents [2] and submarine channels [3]. Meander wavelength (L) also trends to be proportional to discharge. We plotted ranges of L and W for Venusian channels (canali, sinuous rilles, channels with flow margins, classified according to our previous studies[4, 5]), and compared these values to those for lunar sinuous rilles and terrestrial lava channels, and to empirical lines [2, 6] representing terrestrial river meanders (Fig. 1). Several implications can be derived from the plot:

(1) Venusian channels generally follow terrestrial river meander patterns. Wavelength-to-width ratios are generally within 5-30, although there are channels exhibiting large deviations from the standard values. The similar scaling implies similar dynamical behavior between the channel-forming lavas and water flow in rivers.

(2) Canali-type channels tend to have slightly higher L/W ratios than terrestrial rivers. Canali-type channels often have poorly defined low wavelength meanders superposed on long wavelength meanders. The long wavelength components may locally have L/W greater than 100, which expands the plot range of canali to high L/W (Fig. 1). This may be a result of topographic or structural control rather than flow dynamics.

(3) Terrestrial lava channels and Venusian channels with flow margins (channels occurring on well-defined flow deposits) tend to have slightly higher L/W ratios for the measured samples. Their range of L/W is similar to that of canali-type channels.

(4) Venusian sinuous rilles and lunar sinuous rilles have similar meander properties (Fig. 1), as well as other similar qualitative morphological characteristics [4]. At least some of them tend to be wider for a given wavelength than other channel types (L/W ratios in the range 2-10). An experiment conducted with hot water flowing on polyethylene glycol indicates that the meander sinuosity is determined by initial flow discharge (higher the discharge, lower the sinuosity), but the hot water thermally widens and deepens the channel while retaining the original meander sinuosity [7]. Thus, L/W ratios decrease with time. Since both Venusian and lunar sinuous rilles have unusually low L/W ratios (Fig. 1), it is likely that they are eroded, probably thermally, and thereby widened and deepened [8, 9] (Fig. 2)

REFERENCES: [1] Chang, H.H. (1988), *Fluvial processes in river engineering*, John Wiley & Sons. [2] Leopold, L.B., and Wolman, M.G. (1960), *Bull. Geol. Soc. Amer.*, **71**, 769-794. [3] Clark, J.D., Kenyon, N.H., and Pickering, K.T. (1992), *Geology*, **20**, 633-636. [4] Baker, V.R., Komatsu, G., Parker, T.J., Gulick, V.C., Kargel, J.S., and Lewis, J.S. (1992), *J. Geophys. Res.*, **97**, 13,421-13,444. [5] Komatsu, G., Baker, V.R., Gulick, V.C., and Parker, T.J. (1992), *Icarus*, in press. [6] Leopold, L.B., Wolman, M.G., and Millar, J.P. (1964), *Fluvial Processes in Geomorphology*, W.H. Freeman and Company. [7] Huppert, H.E., and Sparks, S.J. (1985), *Jour. Petrology*, **26**, 694-725. [8] Komatsu, G., and Baker, V.R. (1992), *Lunar and Planet. Sci. Conf.*, **XXIII**, 715-716. [9] Hulme, G. (1973), *Modern Geology*, **4**, 107-117.

MEANDERS OF VENUSIAN CHANNEL: G. Komatsu and V.R. Baker

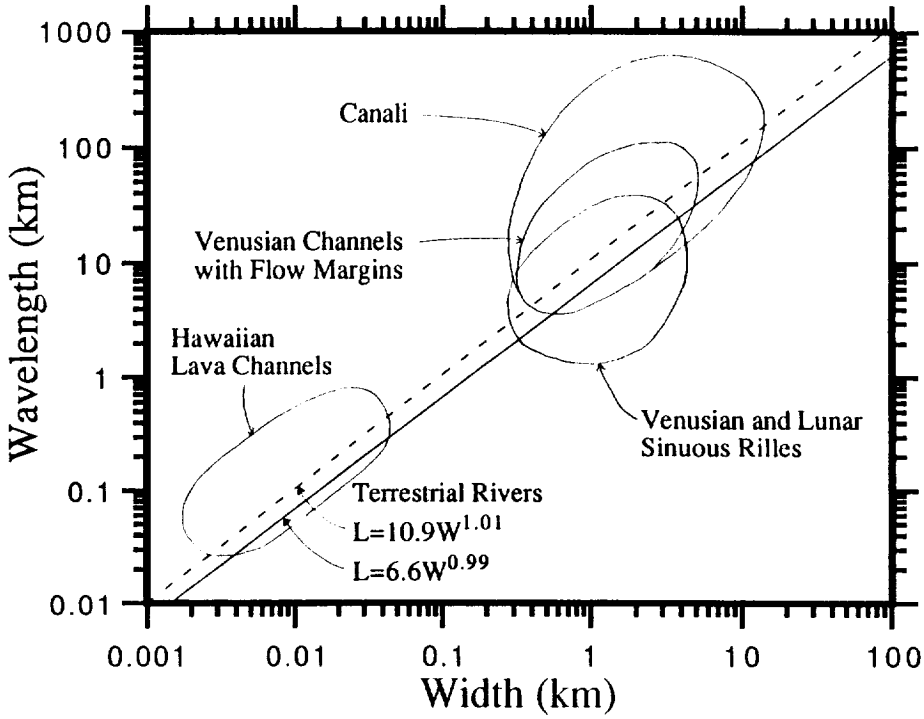

Fig. 1 Meander Wavelength (L)/Channel Width(W) plot of Venusian, lunar, terrestrial channels. Ranges of data points are shown.

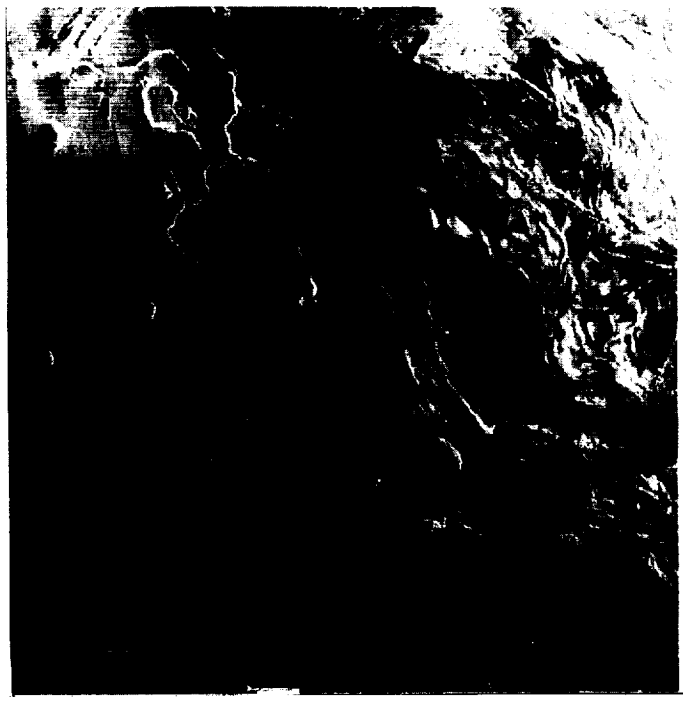

Fig. 2 Venusian sinuous rilles cutting through massifs in highland plains of Aphrodite Terra. These are examples of erosional processes involved in the channel formation.

TERRESTRIAL BITUMEN ANALOGUE OF ORGUEIL ORGANIC MATERIAL DEMOSTRATES HIGH SENSITIVITY TO USUAL HF-HCl TREATMENT.

A.V.Korochantsev and O.V.Nikolaeva; Vernadsky Institute, Russian Academy of Science, 117975 Moscow, Russia.

The relationship between the chemical composition and the interlayer spacing (d002) of organic materials (OMs) is known for various terrestrial OMs (see, for example, [1,2]). We improved this general trend by correlation with corresponding trend of natural solid bitumens (asphaltite-kerite-anthraxolite) up to graphite. Using the improved trend we identified bitumen analogues of carbonaceous chondrite OMs residued after HF-HCl treatment (as proposed in [3,4]). Our laboratory experiment revealed that these analogues and, hence, structure and chemical composition of carbonaceous chondrite OMs are very sensitive to the HF-HCl treatment. So, usual extraction of OM from carbonaceous chondrites may change significantly structural and chemical composition of extracted OM.

BITUMEN ANALOGUES OF CARBONACEOUS CHONDRITE OM RESIDUES. Rietmeijer [5] constructed a diagram of d002 vs. C/(C+H+N+O)(at.) for various natural OMs and received a rough trend which gave him a possibility to determine the bulk chemical composition of a CP IDP [6]. We plotted on the diagram more recent data and correlated with the trend for all natural solid bitumens (asphaltite-kerite-anthraxolite) up to graphite. The H/C ratio for this continuous series is gradually decreasing from asphaltite to graphite. The d002 values of acid residues of carbonaceous chondrites, measured by HRTEM [7], and chemical compositions of these residues [8] allowed to evaluate the validity of the obtained trend as applied to chondrite OMs (Fig.). Orgueil (CI) residues have the prominent d002 value of 3.8A [7] and the C/(C+H+N+O)(at.) ratio of 0.505 [8], which is within the range of C/(C+H+N+O)(at.) ratios (0.45-0.65) given by the trend. Murchison (CM) residues have the prominent d002 value of 3.57A [7] and the C/(C+H+N+O)(at.) ratio of 0.53 [8], i.e. again within our range of C/(C+H+N+O)(at.) ratios (0.50-0.71). Thus the diagram can be used successfully to estimate compositions of OMs in carbonaceous chondrites. For example, Allende (CV) residues show the prominent d002=3.50A [7], and hence, they should have the C/(C+H+N+O)(at.) ratio of about (0.56-0.78). Our plot (Fig.) indicates that CI residues correspond mainly to the kerite field, CM residue lies on the kerite-anthraxolite interface, and CV residues belongs mostly to the anthraxolite field.

SIMULATION OF HF-HCl TREATMENT OF ORGUEIL. However, the HF-HCl residues of carbonaseous chondrites are products of heating and chemical treatment. Therefore the OMs of the residues may not reflect the true composition and structure of meteorite OMs. In order to estimate possible chemical and structural changes of OMs in carbonaseous chondrites after the acid treatment we carried out an experimental study. A sample of kerite [9], which can be inferred above as an analogue of the Orgueil residue, was powdered and mixed with a serpentine powder

in a proportion to obtain 6 wt.% of carbon in the mixture for a rough simulation of the Orgueil composition. The mixture was demineralized by repeated soft HF-HCl treatment. The obtained organic residue was analysed for C, H, N, O, S and studied by X-ray diffraction. Results show that the HF-HCl treatment of the kerite-serpentine mixture led to a considerable change the H/C atomic ratio of the kerite from 0.99 before to 0.62 after treatment and a great change of d002 from 4.0A before to 3.65A after. The direction of the observed shift permits to conclude that the true composition of Orgueil OM, before HF-HCl treatment could be richer in H and less ordered than OM in Orgueil acid residue. In order to define the true chemical composition and structure of OMs in carbonaceous chondrites it is necessary either to introduce some corrections in analyses of acid residues or to study the OMs in situ as it was done by [6] for CP IDP.

CONCLUSIONS: As shown by our laboratory experiment on serpentine+bitumen analogue of Orgueil, the chemical composition and structure of carbonaceous chondrite OM could be subject to significant alteration by HF-HCl treatment.

REFERENCES: [1]Yen T.F. et al. (1961), Anal.Chem., 33, 1587-1594. [2]Korolev Yu.M. (1989), Chemistry of solid fuel., 6, 11-19, (in Rus.). [3]Nikolaeva O.V. (1988), LPSC X1X, Abstr., 862-863. [4]Nikolaeva O.V. (1991), XV1 Gen.Assembly of EGS, Wiesbaden,383-384. [5]Rietmeijer F.J.M. (1991), Carbon, 29, 669-675. [6]Rietmeijer F.J.M. (1992), Geochim.Cosmochim.Acta, vol.56, 1665-1671. [7]Lumpkin G.R. (1986), LPSC XV11, Abstr., 502-503. [8]Hayatsu R. (1977), Geoch.Cosm.Asta, 41, N-9, 1325-1339. [9]Luk'yanova V.T. et al.(1989), New date on minerals, Moscow: Nauka, 83-91 (in Rus.).

Fig. Summary of C/(C+H+N+O)(at.) versus d002(A) for naturally occurring carbonaceous materials

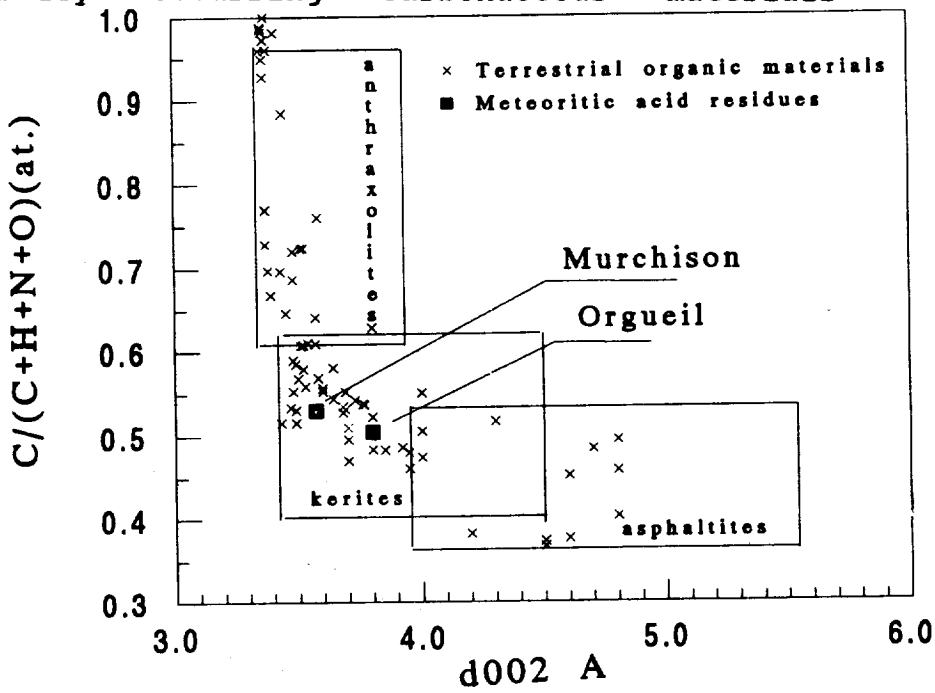

COMPOSITION OF APOLLO 17 CORE 76001; RANDY L. KOROTEV and KAYLYNN M. BISHOP, Department of Earth & Planetary Sciences, Washington Univ., St. Louis, MO.

Core 76001 is a single drive tube containing a column of regolith taken at the base of the North Massif, station 6, Apollo 17 (Fig. 1). The core material is believed to have accumulated through slow downslope mass wasting from the massif [1,2,3]. As a consequence, the core soil is mature throughout its length [2]. Results of INAA for samples taken every half centimeter along the length of the core indicate that there is only minor systematic compositional variation with depth (Figs. 2,3). Concentrations of elements primarily associated with mare basalt (Sc, Fe) and noritic impact melt breccia (Sm) [4,5] decrease slightly with depth, particularly between 20 cm and the bottom of the core at ~32 cm depth. This is consistent with petrographic studies that indicate a greater proportion of basalt and melt breccia in the top part of the core [3]. However, Sm/Sc and La/Sm ratios are remarkably constant with depth, indicating no variation in the ratio of mare material to Sm-rich highlands material with depth. Other than these subtle changes, there is no compositional evidence for the two stratigraphic units (0-20 cm and 20-32 cm) defined on the basis of modal petrography [3], although all samples with anomalously high Ni concentrations (Fe-Ni metal nuggets) occur above 20 cm depth (Fig. 3b).

All surface and trench soils from station 6 are very similar to each other in composition, but those samples collected on (76321) or near (76241, 76261, 76281) boulders tend to be richer in ITEs (incompatible trace elements) such as Sm than samples collected away from boulders (76031, 76221, 76501) (Figs. 1,4). This is because noritic melt breccia, which is the principal carrier of ITEs at the site, is a principal component of the boulders, and these soils contain a large component of material derived from the boulders ("blocks" of Fig. 4). Core 76001 was collected several meters from a boulder and, on average, it is compositionally indistinguishable from surface and trench soils also collected away from boulders. The Sc- and Sm-poor soil at the bottom of the core, however, is poorer in ITEs than any of the surface and trench soils from station 6 or any other part of the site. In terms of the mixing model used to account for compositional variation in Apollo 17 soils [4], the low-Sm soil at the bottom of 76001 has the greatest ratio of anorthositic norite (gabbro) component to noritic melt breccia component of any known Apollo 17 soil.

The slight compositional variation within the core leads to a weak correlation between Sm and Sc concentrations (Fig. 4; $R^2 = 0.37$, or 0.49 if the two high-Sc samples are excluded; these samples probably contain large fragments of mare basalt). A linear trend on a 2-element plot of related lunar soil samples usually represents a binary mixing relationship, either between a soil and a rock lithology or between two soils. For the 76001 samples, the identity of the two mixing components is not obvious. In the high-Sm direction the trend does not extrapolate toward any of the lithologic components of the site, but instead to a point between the fields for mare basalt and noritic melt breccia. As noted above, the ratio of these two components remains constant throughout the core. Similarly, extrapolation of the trend in the low-Sm direction also does not intersect the field of any single station-6 lithology [6]. Thus, if the trend represents a mixing line, both components must be soils. In the high-Sm direction the trend extrapolates to soil 76131 from LRV stop 10 ("Turning Point Rock"). This soil has the highest concentrations of ITEs among soils from the North Massif area and may represent an end-member composition.

As is typically seen in small samples of lunar soil, a few individual samples (each 120 mg in mass) have anomalously high concentrations of Ni that are accompanied by high concentrations of FeO (total Fe as FeO; Fig. 3) as well as Ir and Au (not shown). These usually result from 'nuggets' of Fe-Ni metal of meteoritic origin, or possibly fragments of chondrites. However, the sample at 8 cm depth is anomalously enriched in Fe and Co with respect to Cr, Ni, Ir, and Au. This probably reflects contamination with a fragment of terrestrial metal. The uppermost two samples are clearly contaminated with Au (Fig. 3d). The low Au/Ni ratios of Fig. 3d, e.g., at 8 and 24 cm depth, are highly imprecise as a result of low absolute concentrations of Au (<1 ng/g).

This work was funded by NASA grant NAG 9-56 to L. A. Haskin.

References. [1] Nagle J. S. (1979) *PLPSC10*, 1385-1399. [2] Morris R. V. and Lauer H. V. Jr. (1979) In *Lunar and Planetary Science XX*, pp. 861-863. [3] Papike J. J. and Wyszynski J. (1980) *PLPSC11*, 1609-1621. [4] Korotev R. L. and Kremser D. T. (1992) *PLPS, Vol. 22*, 275-301. [5] Korotev R. L. (1992) *Workshop on Geology of the Apollo 17 Landing Site*, pp. 26-29, LPI Tech Rpt. 92-06. [6] Bishop K. M., Jolliff B. L., Korotev R. L., & Haskin L. A. (1992) *Workshop on Geology of the Apollo 17 Landing Site*, pp. 2-4, LPI Tech Rpt. 92-06.

COMPOSITION OF APOLLO 17 CORE 76001; KOROTEV R. L. & BISHOP K. M.

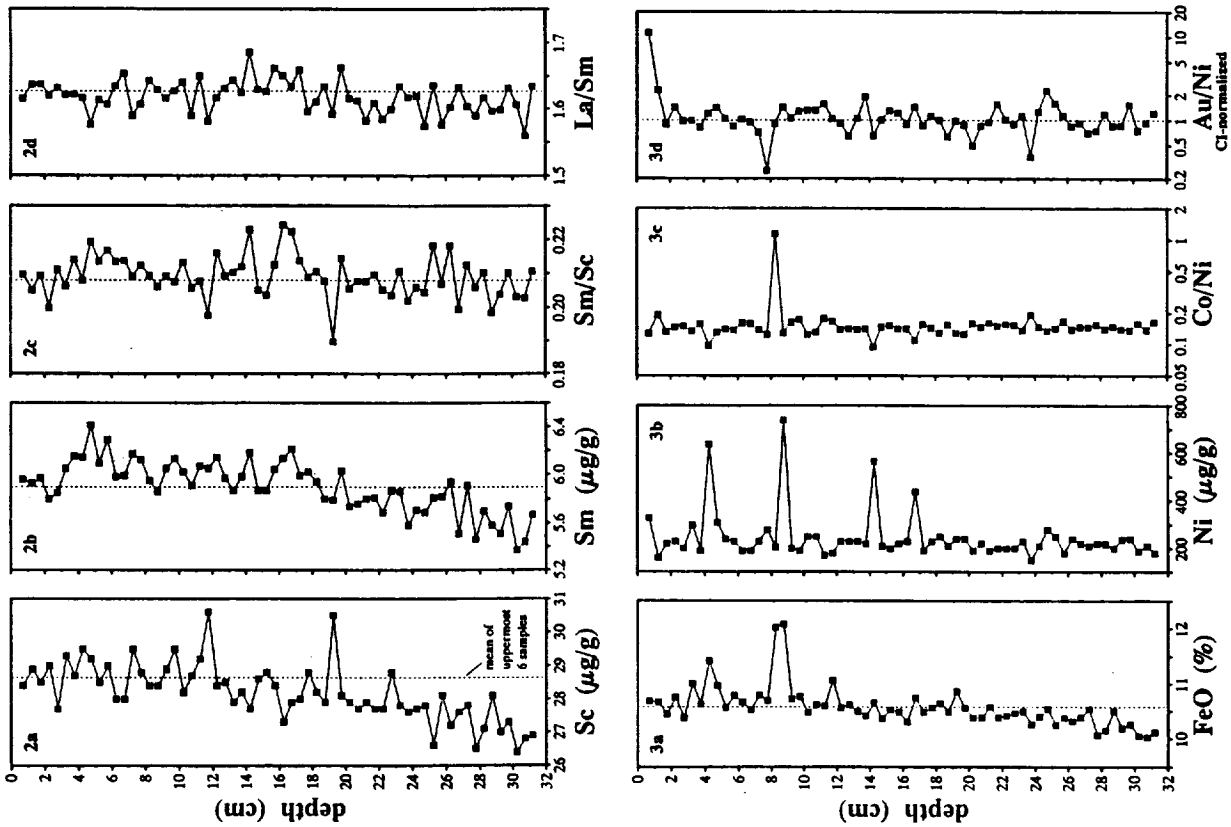

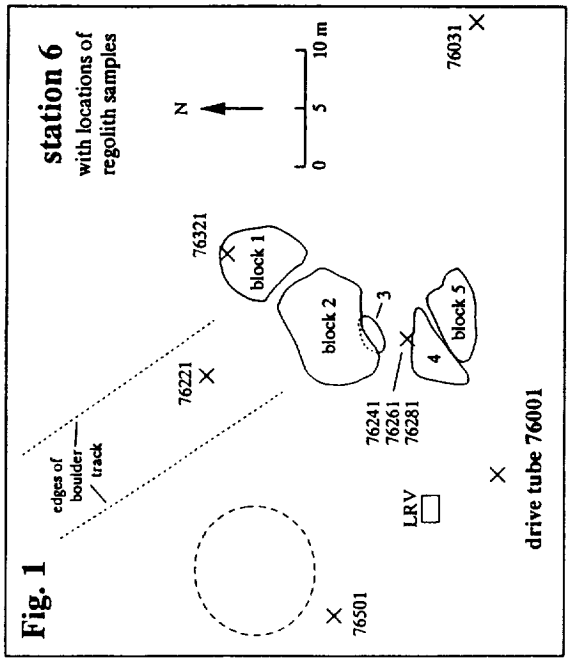

Fig. 1

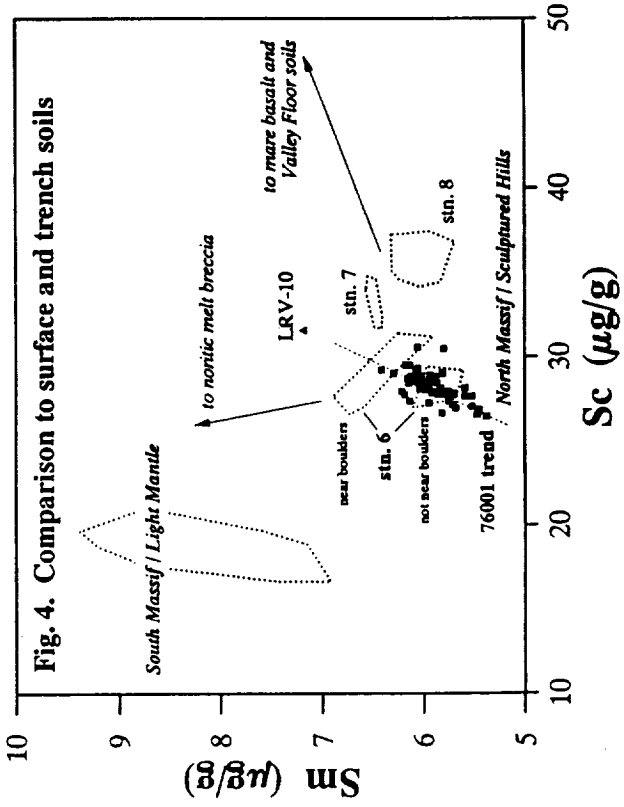

Fig. 4. Comparison to surface and trench soils

COMPOSITION AND MATURITY OF THE 60013/14 CORE; RANDY L. KOROTEV, Dept. of Earth & Planetary Sciences, Washington Univ., St. Louis, MO, RICHARD V. MORRIS, NASA Johnson Space Center, Houston, TX, and HOWARD V. LAUER, JR., Lockheed Engineering & Sciences Co., Houston, TX.

The 60013/14 double drive tube (62 cm deep) is one of three regolith cores taken 35-40 m apart in a triangular array on the Cayley plains at station 10' (LM/ALSEP), Apollo 16 (Fig. 1). This trio, which includes double drive tube 60009/10 (59 cm deep) and deep drill core 60001-7 (220 cm), is the only such array of cores returned from the Moon [1,2]. The top 45 cm of 60013/14 is mature (Fig. 2a), as is surface reference soil 60601 taken nearby. Maturity generally decreases with depth, with soil below 45 cm being submature. The zone of lowest maturity ($34 \le I_s/FeO < 50$) extends from 46 to 58 cm depth, and corresponds to the distinct region of light-colored soil observed during core processing [3]. In the other two cores, most of the compositional variation results from mixing between fine-grained, mature soil with 10-11 μg/g Sc and coarse-grained ferroan anorthosite consisting of >99% plagioclase with <0.5 μg/g Sc [1]. This is most evident in 60009/10 which contains a high abundance of plagioclase at about 54 cm depth (minimum Sc: 3-4 μg/g; Fig. 3); a similar zone occurs in 60001-7 at 17-22 cm (MPU-C [1]), although it is not as rich in plagioclase (minimum Sc: 6-7 μg/g). Compositional variations are less in 60013/14 than in the other two cores (range: 7.9-10.0 μg/g Sc; Figs. 4,5a), but are generally consistent with the "plagioclase dilution" effect seen in 60009/10, i.e., most 60013/14 samples plot along the mixing line of 60009/10 (Fig. 4). However, a plagioclase component is not the cause of the lower maturity and lighter color of the unit at 46-58 cm depth in 60013/14. Many of the samples in this zone (hollow symbols in figures) have distinctly lower Sm/Sc ratios than typical LM-area soils and plot off the mixing trend defined by 60009/10 (Figs. 4,5c). This requires a component with moderately high Sc, but low-Sm/Sc, such as feldspathic fragmental breccia (FFB) or granulitic breccia [4]. A component of Descartes regolith, such as occurs at North Ray crater (NRC) and which is rich in FFB, could account for the composition of these soils (i.e., a 3:1 mixture of 60601 and NRC soil; Fig. 3). It seems unlikely that NRC ejecta would occur half a meter deep at the LM station [5], thus this low-Sm/Sc component may result from an older, local crater that penetrated the Cayley surface layer and excavated underlying Descartes material, as did North Ray crater. There is no evidence for such a unit or component in the other two cores. Soil below the light-colored unit (58-62) cm has 'typical' Sm/Sc ratios, but the lowest absolute Sc concentrations (Figs. 4,5), i.e., it is compositionally equivalent to a mixture of surface soil and plagioclase such as that in ferroan anorthosite. This is the only soil that might be related to the plagioclase-rich units in the other two cores. Except for the mature soil at the top of each core and, perhaps, the plagioclase-rich layers, there is little compositional evidence for any common unit among the three cores. Soil corresponding to the mare-glass-bearing unit (MPU-B) and regolith-breccia-bearing unit (MPU-A) of 60001-7 do not occur in 60013/14 or 60009/10 [1].

Metal nuggets. Concentrations of metallic iron (Fe^0) are highly correlated with those of Ni ($R^2 = 0.983$) because Fe-Ni metal containing about 6% Ni is the major carrier of both constituents in samples with high metal concentration (Fig. 2) [1]. Some samples (50-60 mg each) contain 'nuggets' of metal grains, leading to anomalously high concentrations of Fe^0, Ni, and FeO (total Fe as FeO). With 6.4% Fe^0 and 4740 μg/g Ni, the sample at 35 cm depth has the greatest concentration of metal we have observed in more than 1000 lunar soil samples (i.e., a 4-mg nugget). In Apollo 16 soils, Ni, Ir, and Au are carried subequally by a chondritic micrometeorite component and by the Fe-Ni metal, which derives from ancient impact-melt breccias that are a major constituent of the soil. The Ir/Ni ratio of the metal is low compared to chondritic meteorites [6]. Thus, most soil samples have Ir/Ni ratios intermediate to those of the metal and chondrites, and samples with high Fe^0 and Ni concentrations (Figs. 2c,d) typically have anomalously low Ir/Ni ratios (Fig. 5d). The Ni-rich sample at 4 cm depth has approximately chondritic Ir/Ni (Fig. 5d) and Co/Ni (not shown) ratios, thus this sample probably contains a fragment of metal from an ordinary chondrite.

Iron micrometeorite. The sample at 2.0-2.5 cm depth (split of 60014,19) is highly unusual in having 427 ng/g Ir, but normal concentrations of Fe, Ni, Co, and Au. This leads to an exceedingly high chondrite-normalized Ir/Ni ratio of 17 (Fig. 5d). The cause of this anomaly is an iron micrometeorite containing *148 μg/g Ir* which is discussed more fully in a companion abstract [7].

References. [1] Korotev R. L. (1991) PLSC21, 229-289. [2] Gose W. A. and Morris R. V. (1977) *PLSC8*, 2909-2928. [3] Schwarz C. (1992) In *Lunar and Planetary Science XXIII*, pp. 1249-1250. [4] Korotev R. L. (1992) In *Lunar and Planetary Science XXIII*, pp.721-722. [5] Stöffler D., Ostertag R., Reimold W. U., Borchardt R., Malley J., and Rehfeldt A. (1981) *PLPSC12B*, 185-207. [6] Korotev R. L. (1987) *PLSC17*, E447-E461. [7] Jolliff B. L., Korotev R. L., and Haskin L. A. This volume.

CORE 60013/14; KOROTEV R. L., MORRIS R. V. & LAUER H. V., JR.

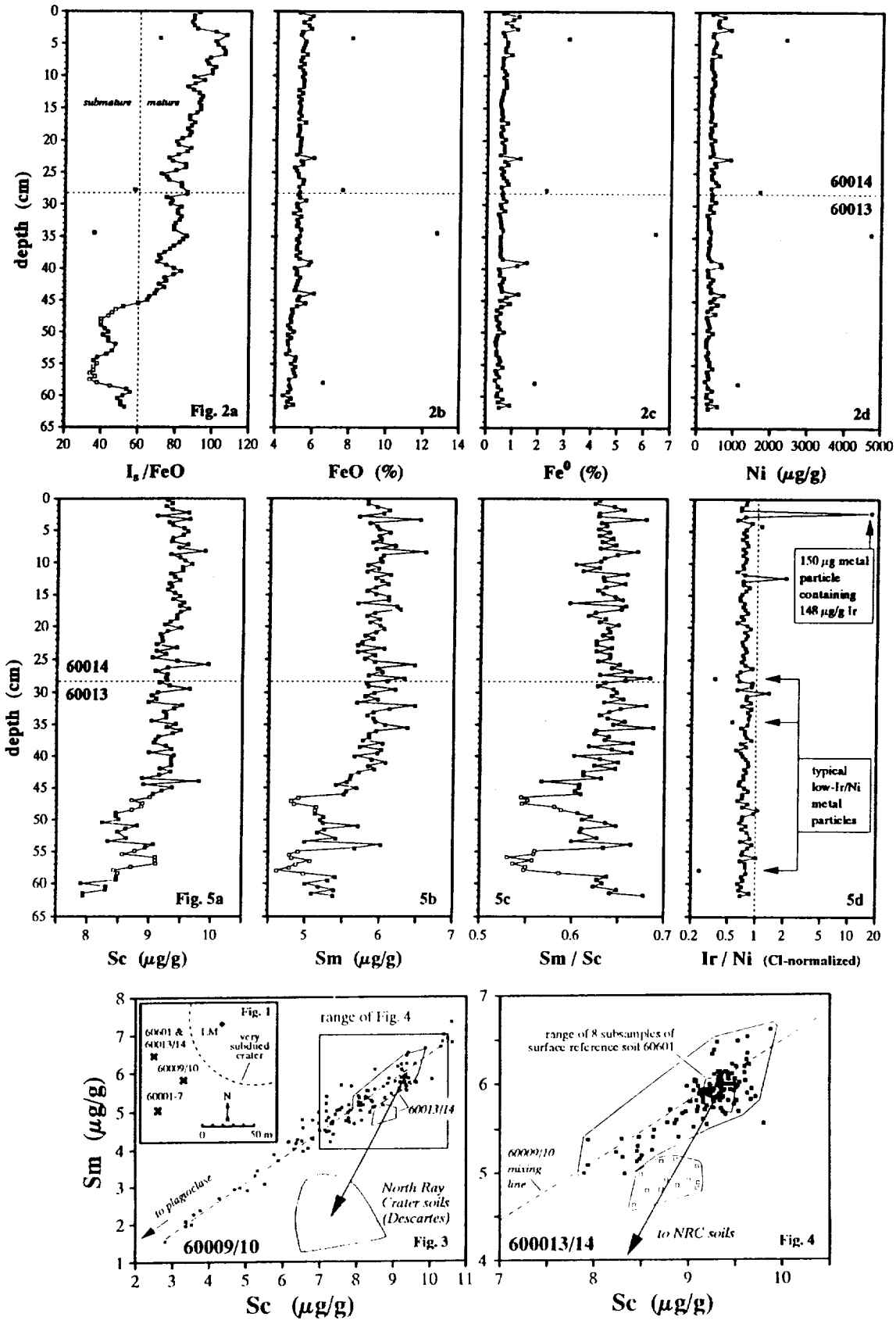

CAT MOUNTAIN: A METEORITIC SAMPLE OF AN IMPACT-MELTED CHONDRITIC ASTEROID

-- David A. Kring, Lunar and Planetary Laboratory, University of Arizona, Tucson, AZ 85721 USA.

Although impact cratering and collisional disruption are the dominant geologic processes affecting asteroids, samples of impact melt breccias comprise <1% of ordinary chondritic material and none exist among enstatite and carbonaceous chondrite groups [1]. Because the average collisional velocity among asteroids is sufficiently large to produce impact melts [*e.g.*, 2], this paucity of impact-melted material is generally believed to be a sampling bias, making it difficult to determine the evolutionary history of chondritic bodies and how impact processes may have affected the physical properties of asteroids (*e.g.*, their structural integrity and reflectance spectra). To help address these and related issues, the first petrographic description of a new chondritic impact melt breccia sample, tentatively named Cat Mountain, is presented below.

Cat Mountain is a 2.7 kg stone containing large dark gray elliptical chondrule-bearing clasts in a medium dark gray vesicular matrix, with silver metal scattered throughout both areas (Fig. 1). In sawn surfaces (120 cm^2), these phases represent 49% of the stone each, while the remaining 2% consists of smaller vesicular and dark clasts. The larger clasts, ranging in size from 0.8 to at least 7.4 cm, are shocked and partially melted L5 material. They contain barred olivine and radial pyroxene chondrules and ghosts of porphyritic chondrules. Olivine (Fo_{75}) and pyroxene ($Wo_1En_{77}Fs_{21}$) are equilibrated and accompanied by lesser amounts of augite ($Wo_{44}En_{47}Fs_8$), chromite (Mg/(Mg+Fe) = 0.16, Cr/(Cr+Al) = 0.86), apatite, whitlockite, martensite, kamacite (0.86 wt.% Co), and troilite. Feldspathic material associated with olivine and pyroxene is either turbid or birefringent and contains spindly to radiating feldspar.

These clasts are crosscut by isotropic polycrystalline dikes of micron-sized silicate phases which are thoroughly mixed with similarly-sized opaque phases (Fig. 2). These dikes often surround unmelted islands or rafts of birefringent (but sometimes recrystallized) olivine and pyroxene. Melt pockets are common at the junctions of multiple dikes. Opaque metal-sulfide veins also crosscut the clasts and sometimes occur along the margins of silicate-rich dikes. While most opaque veins are devoid of silicates, one of them contains small pockets of quenched feldspar laths and skeletal pyroxene crystals. Olivine grains adjacent to the dikes and veins have been variously deformed; they have undulatory extinction, irregular fractures, multiple planar

Fig. 1. Sawn face of Cat Mountain which consists of elliptical L5 clasts in an igneous-textured matrix. The white specks in both the clasts and the melt matrix are Fe,Ni-metal alloys. The width of the stone is ~11 cm.

Fig. 2. Transmitted-light image of a clast in thin-section. Dark polycrystalline dikes and opaque veins crosscut a large portion of the clast. The width of this slice of the clast is 1.8 cm.

fractures, Fe,Ni-metal and sulfide fillings in fractures, and some have been recrystallized. Other deformation features include fractured pyroxene and disrupted chromite, both of which also have Fe,Ni-metal and sulfide fillings.

In contrast to the partially-melted shock-metamorphosed clasts, the matrix is a total melt with a relatively uncomplicated igneous texture. The silicate portion consists of subhedral to euhedral olivine (Fo_{75}), subhedral pyroxene laths ($Wo_2En_{78}Fs_{20}$), some of which poikilitically enclose olivine chadacrysts, and an interstitial feldspathic mesostasis (CIPW normative composition of 48% quartz, 38% feldspar, 11% corundum, 1% hypersthene, 1% ilmenite, and 1% apatite.). A few pyroxene laths have thin (calcic?) rims. One bronzite overgrowth was seen surrounding a partially resorbed relict pyroxene grain; both have similar major element compositions, although the overgrowth contains more Cr_2O_3 (0.95 *vs.* 0.11 wt.%) and less TiO_2 (0.04 *vs.* 0.19 wt.%). The melt assemblage is very fine-grained, typically <50 μm in size, although olivine sometimes nucleated or aggregated into submillimeter-sized polycrystalline clots, producing a fine-grained glomeroporphyritic texture.

The opaque portion of the melt is dominated by Fe,Ni-metal and sulfides, although it also includes chromite (Mg/(Mg+Fe) = 0.18, Cr/(Cr+Al) = 0.86). Some of the metal and sulfide occur in large millimeter- to centimeter-sized distended particles which produce a sense of flow in hand-specimens. Metal-sulfide assemblages are often associated with vesicles, suggesting that sulfur was being volatilized or, alternatively, that the gas vesicles, trapped in a rapidly solidifying silicate melt, associated themselves with more plastic metal-sulfide assemblages. The metal is dominantly martensite (8.8 to 19.3 wt.% Ni) and occurs in ellipsoidal orbs that are embedded in troilite. Thin rims of kamacite (7.1 wt.% Ni), associated with small phosphide patches (probably schreibersite), have crystallized at the interface between the martensite and troilite. Occasional skeletal laths have also crystallized inside the martensitic orbs. Troilite, in addition to being associated with the orbicular metal assemblages, is finely-disseminated in some areas of the melt.

Because the melt fraction of Cat Mountain appears to be total melt and mixed with shock-metamorphosed clasts, it was probably produced by impact processes and is not a plutonic intrusion of melt into a chondritic crust or a volcanic extrusion with crustal xenoliths. To produce the partial and total melts in Cat Mountain, the impact event must have been sufficiently energetic to produce peak temperatures in excess of 1000 °C. As indicated by the vesicles in the melt matrix, these temperatures allowed the breccia to begin degassing. The hot melt was rapidly cooled against the relatively cold clastic material, producing zones of cryptocrystalline (and sometimes isotropic) assemblage of silicates and metal-sulfide droplets around the margins of the clasts. The cooling induced by the rapid thermal equilibration of the clasts and melt, as well as conduction to the melt breccia's surroundings, also quenched the cores in metal-sulfide assemblages to martensite, producing a texture similar to that in Ramsdorf, Rose City, and Orvinio [3,4,5]. However, since the metal orbs in Cat Mountain, like those in Rose City, also have kamacite rims, Cat Mountain probably cooled at a slower rate than Ramsdorf and Orvinio [5], and most likely represents a melt breccia lens or melt dike that was partially insulated by the overburden of fragmental and fallback breccias inside or near the rim of an impact crater.

Acknowledgements: Cat Mountain was found by William Goldups (now deceased). I thank his friend, George Bakutis, for pursuing the stone's origins and Shirley Wetmore for directing him to me.

References: [1] Scott E.R.D., Taylor G.J., Newsom H.E., Herbert F., Zolensky M., and Kerridge J.F. (1989) in Asteroids II, R.P. Binzel, T. Gehrels, and M.S. Matthews (eds.), University of Arizona Press, Tucson, 701-739. [2] Vickery A.M. and Melosh H.J. (1983) Icarus 56, 299-318. [3] Begemann F. and Wlotzka F. (1969) Geochim. Cosmochim. Acta 33, 1351-1370. [4] Taylor G.J. and Heymann D. (1971) J. Geophys. Res. 76, 1879-1893. [5] Smith B.A. and Goldstein J.I. (1977) Geochim. Cosmochim. Acta 41, 1061-1072.

COMPARATIVE MAGNETIC AND THERMOANALYTICAL STUDY OF TWO ENSTATITE CHONDRITES : ADHI KOT AND ATLANTA, Elizabeth Król (Institute of Geophysics of the Polish Academy of Sciences, Ks. Janusza 64, 01-452 Warsaw) and Bruno Lang (Warsaw University, Department of Chemistry, Żwirki i Wigury 101, 02-089 Warsaw)

With allowance for the discussion of classification of enstatite chondrites and their relation to aubrites we submit the obtained by us magnetic and thermoanalytical data to be considered as additive arguments. Our study covered the Adhi Kot (EH4) and Atlanta (EL6). meteorites belonging to two distinct groups of enstatite chondrites. Applying AF demagnetization we measured the intensity of natural remanent magnetization (NRM) and determined the mean magnetic susceptibility of the samples. We obtained too the differentialthermal (DTA) and thermogravimetric (TG) curves for meteorites understudy. For measurements of the intensity of NRM a superconducting cryomagnetometer SQUID (2 G Enterprise, USA), while of magnetic susceptibility Kappabridge KLY-2(Czechoslovakia) were used.
The abbreviated magnetic data sheets are given in Fig.1 and 2.
The values 786 x 10^{-4}A/mkg and 196.1 x 10^{-4}A/mkg were obtained as NRM intensities for Atlanta and Adhi Kot respectively, while 17.4x10^{-6} SIu/kg and 43.4x10^{-6} SIu/kg for their susceptibilities. Both meteorites proved to be strongly magnetized. The demagnetization down to 3.2 % of NMR was received for Atlanta at AF field intensity of 250 Oe. For Adhi Kot at this level rested 13.2 % of NRM intensity, this sample being demagnetized without change of direction till 750 Oe field.

The demagnetization curves are similar to those obtained for Abee (EL4) chondrite by Sugiura and Strangway (1981). Against Abee the Adhi Kot exhibited a little bit steeper downfall. In both cases dominate one component of magnetization.

The DTA and TG curves were obtained with Rigaku-Denki thermoanalytical instrument. The DTA curves in Fig. 3 and 4 exhibit striking similarity in their shape and relativily close temperature values for various features. The same is valid for TG curves. The higher values for TG for Adhi Kot express its higher content of oxydable (Fe,Ni) whose oxidation in air is reached at 1000°-1020 °C.

The above study will be continued.

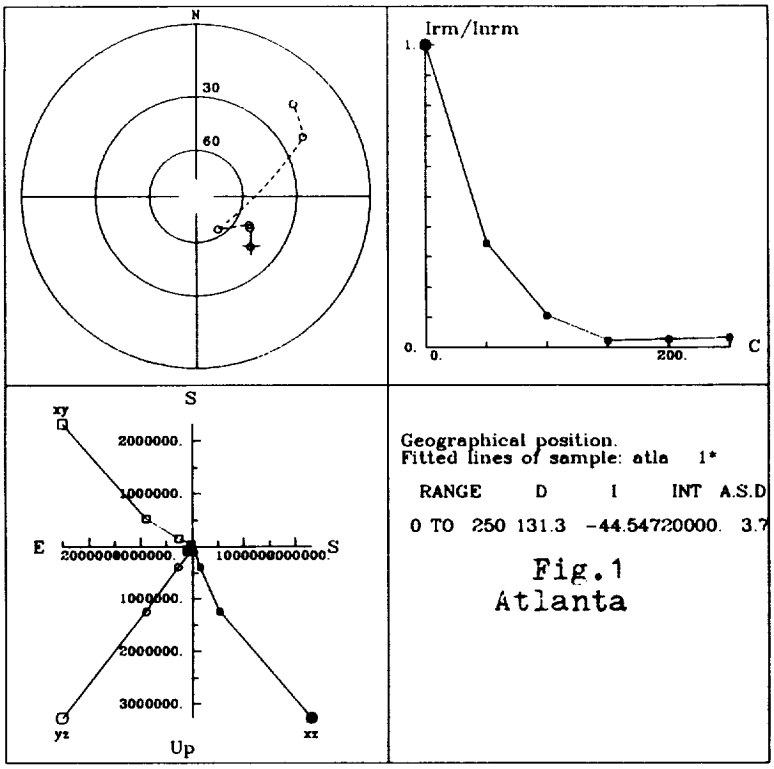

Fig.1
Atlanta

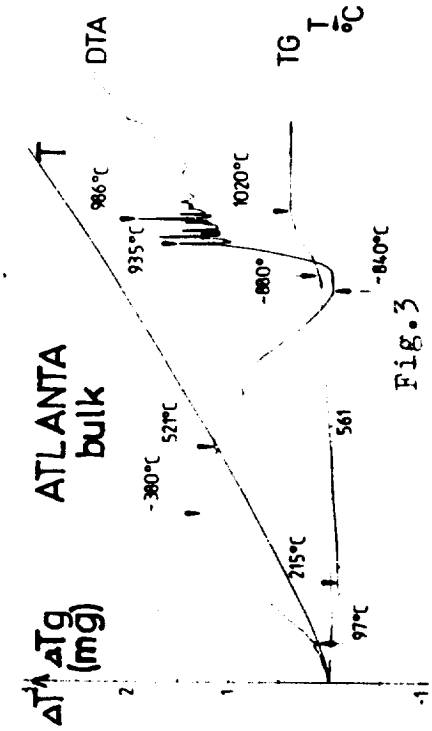

Fig.3

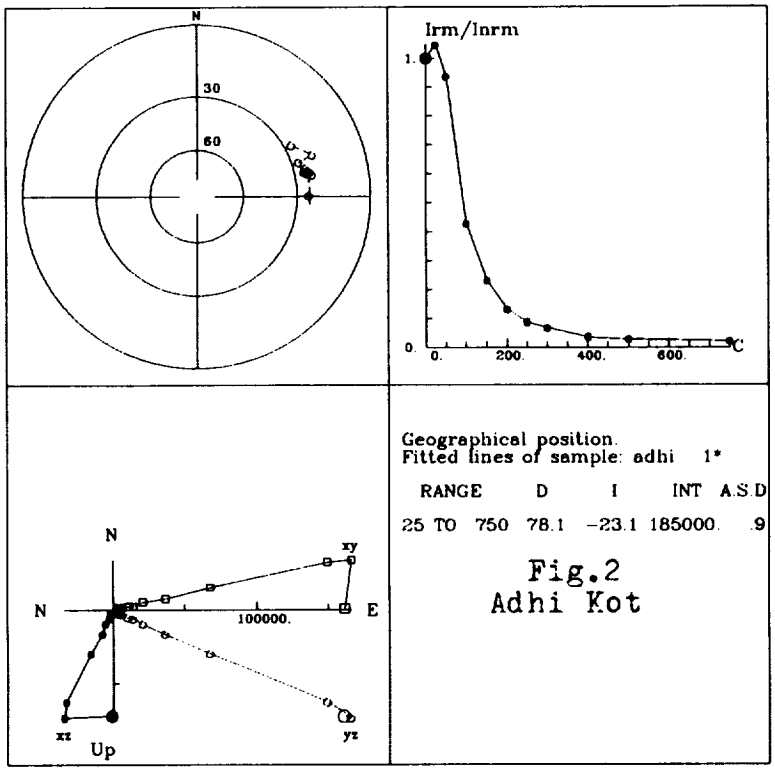

Fig.2
Adhi Kot

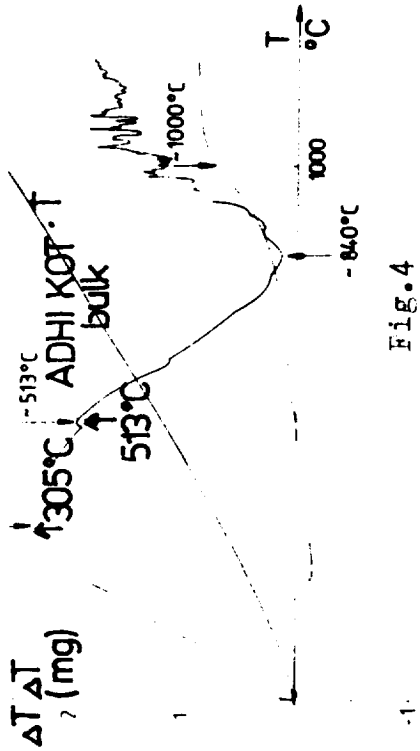

Fig.4

CHROMITE-RICH MAFIC SILICATE CHONDRULES IN ORDINARY CHONDRITES: FORMATION BY IMPACT MELTING. Alexander N. Krot and Alan E. Rubin, Institute of Geophysics and Planetary Physics, University of California, Los Angeles, CA 90024, USA.

Chromium-rich chondrules constitute <0.1% of all ordinary chondrite (OC) chondrules and comprise three groups: chromian-spinel chondrules, chromian-spinel inclusions and chromite-rich mafic silicate (CRMS) chondrules. Chromian-spinel chondrules (typically 100-300 μm in apparent diameter) exhibit granular, porphyritic and unusual textures and occur mainly in H chondrites. Their morphologies are distinct from the irregularly shaped chromian-spinel inclusions of similar mineralogy. Chromian-spinel chondrules and inclusions consist of grains of chromian-spinel embedded in plagioclase (Pl) or mesostasis of Pl composition. Many also contain accessory ilmenite (Ilm), high-Ca pyroxene (Px), merrillite (Mer) and rare olivine (Ol); some exhibit concentric mineral and chemical zoning. CRMS chondrules (300-1100 μm in apparent diameter) are generally larger than chromian-spinel chondrules and occur in all metamorphosed OC groups. Most CRMS chondrules are nearly spherical although a few are ellipsoidal with a/b aspect ratios ranging up to 1.7. Textures include cryptocrystalline, granular, radial, barred and porphyritic varieties; some contain apparently relict grains. The chondrules consist of chromite (Chr), Ol and Pl, along with accessory Mer, troilite (Tr), metallic Fe-Ni (Met), Px and Ilm. The mesostasis in CRMS chondrules is nearly opaque in transmitted light; thus, they can be easily recognized in the optical microscope. Based on the similarity of mineralogy and chemistry between CRMS chondrules of different textures (opaque chromite-rich mesostasis, skeletal morphology of Ol grains, similar bulk compositions) we suggest that these chondrules form a genetically related population.

Chromite occurs as tiny (<1-5 μm) euhedral grains or larger (~200 μm) porphyritic and subhedral grains embedded in Pl-normative mesostasis. Chondrules Mg1 from H6 Magombedze and R1 from LL5 Richmond contain anhedral Chr grains intergrown with Tr, Met and Ilm embedded in albitic Pl; these intergrowths are probably relict. These relict Chr and Ilm grains have compositions similar to that of matrix Chr (Cr/(Cr+Al)=0.80-0.81; [1]) and Ilm [2]. Plagioclase surrounding Chr-Tr-Met±Ilm intergrowths in these two chondrules has a uniform sodic composition similar to that of matrix Pl in equilibrated OC (Ab 79-85). The other Chr grains in the CRMS chondrules consist of compositionally uniform or slightly zoned grains, although there is significant grain-to-grain compositional variation (Cr/(Cr+Al)=0.41-0.86). Olivine in the CRMS chondrules occurs as anhedral or skeletal grains. Its composition is similar to that of the host chondrites. High-Ca Px with ≤10.2 wt.% Al_2O_3 and ≤3.3 wt.% TiO_2 forms anhedral grains in interstitial areas between Chr grains. Three of the CRMS chondrules also contain large grains of Mer surrounded by Chr. Because the mesostasis of CRMS chondrules is highly enriched in tiny Chr and Ilm grains it is nearly opaque in transmitted light. The mesostases are Pl-normative; some are uniform and others are variable in composition (Ab 20-85 Or 0-6). In some cases mesostasis exhibits flow structure, i.e., differently oriented domains of aligned crystallites of Ol and Chr. Bulk compositions of CRMS chondrules are similar to the Na-Al-Cr-rich chondrules described by Bischoff and Keil [3].

There are two classes of models for the formation of CRMS chondrules. In *nebular models*, the high Cr/Mg ratios of CRMS chondrules (20-500xCI) indicate that their precursor materials contained chromian-spinel or chromite. However, nebular Cr condenses mainly as a metal alloyed with metallic Fe-Ni at $pH_2 \geq 10^{-3}$ atm [4,5] or as magnesiochromite dissolved in spinel or forsterite at $pH_2 \leq 10^{-4}$ atm [6]; it does not condense as chromite. Because 3 (of 20) CRMS chondrules contain large Mer grains that crystallized from the chondrule melt, it is apparent that P-rich precursor material was also present in the region where some of these chondrules formed. However, P does not form its own mineral phases in the most primitive OC (LL3.0 Semarkona; [7]); instead it occurs in solid solution in metallic Fe-Ni and sulfide grains. This is consistent with the siderophile and chalcophile behavior of P during condensation in the solar nebula [5]. Tiny phosphate grains (<1 μm) occur in association with metallic Fe-Ni and

sulfide in the slightly metamorphosed OC, LL3.1 Bishunpur and Krymka [8,9]; it thus seems likely that phosphate grains were formed by oxidation of P-bearing metal during parent-body metamorphism. It seems impossible to produce Cr- and P-rich precursor material by condensation or by a mechanical process such as size sorting, selective adherence or stochastic sampling of fragments from previous chondrule generations. Although Krot et al. [10] suggested a solid-vapor fractionation at high nebular temperatures as a possible mechanism for enriching chondrules in Cr, ion probe bulk analyses of chromian-spinel chondrules and inclusions in OC by A.M. Davis (unpublished data) show no signs of high-temperature nebular fractionation effects in their rare earth patterns.

Another nebular model [11] maintains that Al-rich chondrules (a group that would include CRMS chondrules) formed from mesostases lost from normal mafic silicate chondrules during collisions. This model implies that mesostases in type-3 OC chondrules are Na- and Cr-rich; however, this is not the case [12-14]. Thus, both nebular models appear implausible.

In *impact-melting models* CRMS chondrules formed by impact melting pre-existing target rocks exposed at the surface of the host parent body. Chondrules that formed by such a process may exhibit various characteristics including relict chunks of target material, flow structures in the mesostasis, unequilibrated minerals and low modal abundances. We suggest that the CRMS chondrules were formed by preferential impact melting of Chr- and Pl-rich precursor material on the surface of metamorphosed parent bodies because: (1) they are present only in metamorphosed OC, (2) they have Chr and Pl of variable composition, (3) some of them contain coarse relict grains of minerals formed only during parent body metamorphism (e.g., Chr, Mer and Ilm), (4) they exhibit characteristic features of fast cooling (i.e., skeletal Ol grains and mesostasis with flow structure), (5) they constitute only ~0.08% of all OC chondrules, and (6) some melt pockets in shocked OC are similar to CRMS chondrules in mineralogy and texture. Although the impact-melting model is most probable for the CRMS chondrules containing relict grains of metamorphosed chondritic material, it is also applicable to the other CRMS chondrules because these chondrules differ only in being more completely melted. Because CRMS chondrules are rare in OC and some of them are rich in mafic silicates, we suggest that some mafic silicate chondrules (perhaps 3-5% of all OC chondrules) could also have been formed by impact melting. Potential criteria for recognizing them include (a) the presence of unmelted relicts of metamorphosed chondritic material such as Chr, Ilm and Pl, (b) the occurrence of coarse spherules of phosphate, (c) enrichment in a Pl component, and (d) mesostases containing flow structures. Ordinary chondrite regolith breccias are the most likely rocks to contain such chondrules.

References: [1] Bunch *et al.* (1967) Geochim. Cosmochim. Acta 31, 1569-1582; [2] Snetsinger and Keil (1969) Amer. Mineral. 54, 780-786; [3] Bischoff and Keil (1984) Geochim. Cosmochim. Acta 48, 693-709; [4] Grossman (1972), Geochim. Cosmochim. Acta 36, 597-619; [5] Wai and Wasson (1977) Earth Planet. Sci. Lett. 36, 1-13; [6] Wasson and Krot (1992) Lunar Planet. Sci. 23, 1499; [7] Perron and Boourot-Denise (1992) Lunar Planet. Sci. 23, 1055-1056; [8] Rubin and Grossman (1985) Meteoritics 20, 479-489; [9] Perron *et al.* (1992) Meteoritics 27, 275-276; [10] Krot et al. (1992) Earth Planet. Sci. Lett. (submitted); [11] Bischoff *et al.* (1989) Earth Planet. Sci. Lett. 93, 170-180; [12] Gooding (1979) Ph.D. dissertation, Univ. New Mexico; [13] Jones (1990) Geochim. Cosmochim. Acta 54, 1785-1802; [14] DeHart *et al.* (1992) Geochim. Cosmochim. Acta 56, 3791-3807.

EVAPORATION KINETICS OF Mg_2SiO_4 CRYSTALS AND MELTS FROM MOLECULAR DYNAMICS SIMULATIONS;

J. D. Kubicki and E. M. Stolper, Division of Geological and Planetary Sciences, California Institute of Technology, 170-25 Pasadena, CA 91125

Abstract. Computer simulations based on the molecular dynamics (MD) technique have been used to study the mechanisms and kinetics of free evaporation from crystalline and molten forsterite (i. e., Mg_2SiO_4) on an atomic level. The interatomic potential employed for these simulations reproduces the energetics of bonding in forsterite and in gas-phase MgO and SiO_2 reasonably accurately. Results of the simulation include predicted evaporation rates, diffusion rates, and reaction mechanisms for $Mg_2SiO_4(s \text{ or } l) \rightarrow 2Mg(g) + 2O(g) + SiO_2(g)$.

Introduction. Hashimoto [1] showed that evaporation and condensation kinetics played a role in the cosmochemistry of the early solar nebula. Davis et al. [2] demonstrated based on the results of evaporation experiments on forsterite crystals and melt that the so-called FUN CAI's (fractionated and unknown nuclear effect; calcium-, aluminum-rich refractory inclusions) in carbonaceous chondrites could have obtained anomalous isotopic signatures from kinetic isotope effects during non-equilibrium evaporation. In their experiments, however, isotope fractionations were significant only for molten Mg_2SiO_4 and not crystalline forsterite. They explained this as due to the fact that the rate of evaporation from the solid is much faster than the rate of diffusion, so no isotopic fractionation is possible. In contrast, diffusion and evaporation rates operate on similar time scales in the molten phase, so a significant vapor-liquid isotopic fractionation occurs because light isotopes from the interior of the melt diffuse to the surface as fast as they are evaporated. This study was conducted to investigate possible mechanisms of evaporation from forsterite crystals and melts. Such simulations can lead to insights into the main evaporating species (i.e., SiO(g) vs. SiO_2(g)) and into the factors influencing the magnitude of kinetic isotope effects accompanying evaporation.

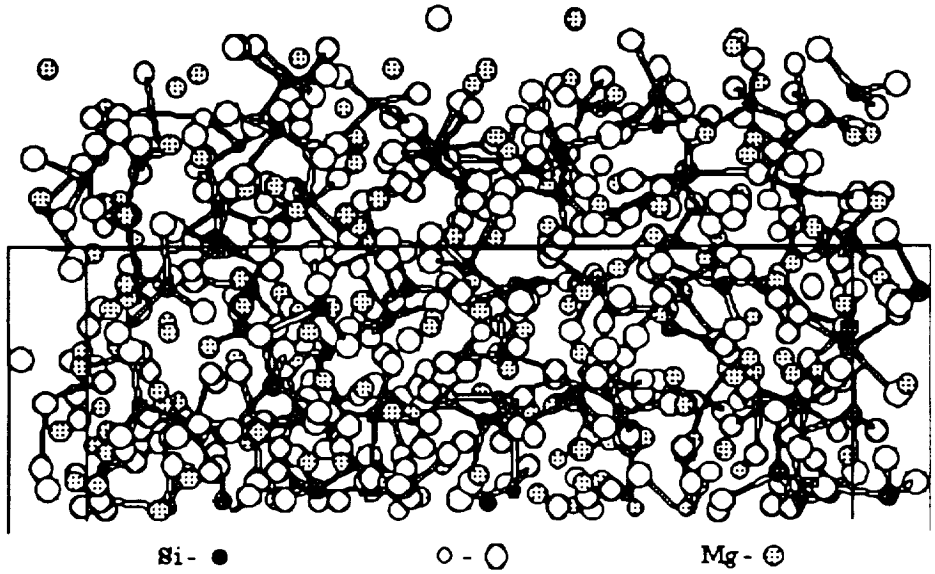

Figure 1 - Edge view of forsterite crystal evaporating. Lines denote boundaries of MD cell.

Methodology. MD simulations calculate the motion of particles in an atomic system with Newton's equations of motion employed over small time increments, usually 10^{-15} s. The extremely small time steps are required to conserve the energy of the system but this causes the real time duration of the simulation to be short (i. e., 10^{-10} to 10^{-12} seconds). Structural, thermodynamic, and kinetic properties of the system can be calculated with the MD technique. (For a review, see [3, 4]). The MD system in this study consisted of 1680 atoms (240 Mg_2SiO_4 formula units) with initial crystal positions determined from the experimental crystal coordinates. Mg_2SiO_4 melts were generated from the simulations of [5] with 1280 atoms in the MD cell. Two-dimensional periodic boundary conditions were employed along the a- and b-axes, approximating an infinite layer with a thickness along the c-axis of 24 Å in the crystalline phase (Fig. 1) and 16 Å in the molten phase (Fig. 2). The potential of Leinenweber and Navrotsky [6] was used to model the interactions of Si^{4+}, Mg^{2+}, and O^{2-} ions within the evaporating forsterite. We chose this potential because it accurately reproduces mineral structures in the Mg - Si - O system [6], and also

EVAPORATION OF FORSTERITE FROM MD SIMULATIONS: J.D. Kubicki and E.M. Stolper

does an accurate job of fitting the energetics of neutral gas phase molecules [7]. Evaporation rates were determined from simulations at 3000, 4000 and 5000 K in the crystalline phase and 4000, 5000, and 6000 K in the molten phase. The positions of all particles are known as a function of time, so the evaporation rate is the number of ions leaving the mineral surface per unit time per unit surface area. Atomic masses are read in as part of the input data set; hence, it is possible to isotopically "dope" the simulated mineral with ^{18}O, ^{26}Mg, and ^{30}Si. Relative rates of evaporation versus diffusion (calculated with the Einstein equation) can be compared in the crystalline and melt phases.

Results and Discussion. Due to the short durations of the MD simulations, the evaporation and diffusion rates are most accurately determined at temperatures much higher than normally employed in the laboratory. However, the short time duration also allows crystalline systems to be studied at temperatures far above the melting point because the system remains crystalline metastably [8]. Evaporation rates predicted from the simulations are on the order of 1 to 10 mol/cm^2/sec at 3000 to 6000 K in both crystalline and molten Mg_2SiO_4 similar to values obtained from extrapolation of the experimental data [1]. Evaporation from crystals occurs more rapidly than from melts at the same temperature in these simulations, but diffusion is more rapid in the melt phase. This is also evidenced in the melt simulation by mixing of isotopes initially placed in separate regions of the cell (Fig. 2); whereas, in the simulations of crystalline Mg_2SiO_4, the isotopes do not mix significantly from one crystal plane to the next (Fig. 1). These results are consistent with Hashimoto's [1] interpretation of the experimental data.

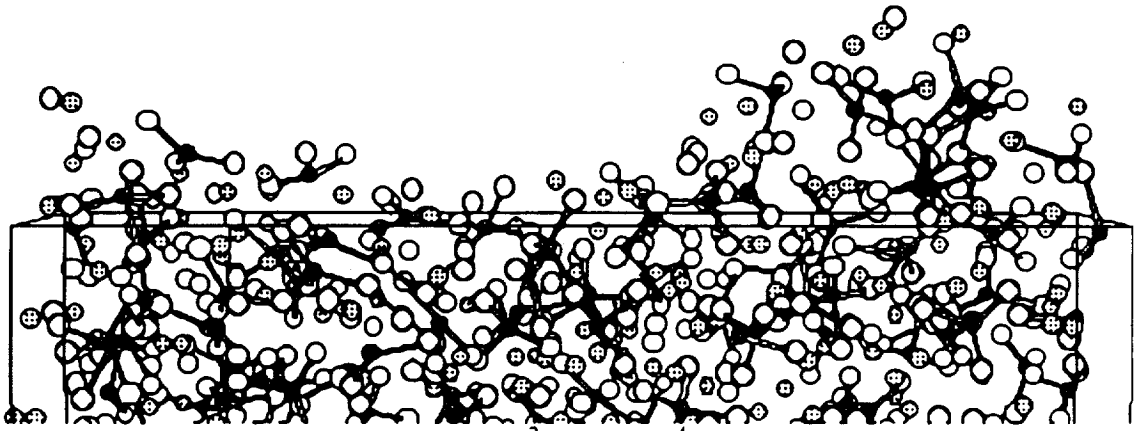

Figure 2 - Surface of molten Mg_2SiO_4 shows Mg^{2+} and $[SiO_4]^{4-}$ anions evaporating and diffusion in the melt as heavy isotopes (^{18}O, ^{26}Mg, and ^{30}Si), initially in the right-hand side of the cell, mix with light isotopes on the left. (Key in Fig. 1).

The reaction mechanism predicted in the MD simulations is somewhat different from the experimental interpretation, however. Although the ionic nature of the interatomic potential may be somewhat inaccurate for modelling neutral atoms,The species leaving the surface are dominated by Mg^{2+} and $[SiO_4]^{4-}$ ions rather than Mg and O atoms and SiO_2 molecules. Such speciation may contribute to the larger isotopic fractionation of Mg during evaporation of Mg_2SiO_4 melts compared to O and Si [2] because the larger $[SiO_4]^{4-}$ anion will be less affected by small mass differences due to isotopic substitutions compared to the atoms and molecular SiO_2. Gas-phase reactions could subsequently lead to conversion of $2Mg^{2+} + [SiO_4]^{4-} \rightarrow SiO_2 + 2O + 2Mg$.

References [1] Hashimoto A, 1990, *Nature*, **347**, 53-55. [2] Davis AM, A Hashimoto, RN Clayton, and TK Mayeda, 1990, *Nature*, **347**, 655-658. [3] Kubicki JD and AC Lasaga, 1990, Advances in Physical Geochemistry,Vol. 8, Springer-Verlag, New York, pp. 1-50. [4] Ciccotti G, D. Frenkel, and IR MacDonald, eds. 1987, Simulation of Liquids and Solids, North-Holland, Amsterdam. [5] Kubicki, JD and AC Lasaga, 1991, *Phys. Chem. Min.* **17**, 661-673. [6] Leinenweber K and A Navrotsky, 1988, *Phys. Chem. Min.* **15**, 588-596. [7] Kubicki JD, 1991, *Eos, Trans. Am. Geophys. Union*, **72**, 144. [8] GD Price and Matsui M and 1991, *Nature*, **351**, 735-737.

SPECTRAL STUDY OF VENUS GLOBAL TOPOGRAPHY AND GEOID FROM MAGELLAN AND PVO DATA; A.B. Kucinskas and N.J. Borderies, Jet Propulsion Laboratory/ California Institute of Technology, Pasadena, CA 91109; D.L. Turcotte, Department of Geological Sciences, Cornell University, Ithaca, NY 14853.

We have conducted an analysis of newly available global harmonic models for topography and geoid on Venus. We find that the power spectral density for Venus topography has a power - law dependence on wave-number characteristic of Brown Noise, similar to what is found for the Earth. However, the Venus topography spectrum presents a rollover at lower degree (l=3) than is observed for the Earth spectrum and has smaller amplitudes than that of the Earth's. The Venus geoid also obeys a power-law relationship, at least for small values of l, but with a smaller slope and more power (for l> 3) than the Earth geoid.

With the gravity data gathering phase (cycle 4) of the Magellan mission well under way and the Venus altimetry data from Magellan being complete new, higher degree and order, spherical harmonic models of Venus gravity and topography have been produced. It is worthwhile to analyze these harmonic fields which have improved coefficient estimates and incorporate data from the Pioneer Venus Orbiter (PVO) and higher resolution data from the Magellan spacecraft. However, it is also important to note that the application of an a priori constraint (namely Kaula's law) to the estimation of the gravity harmonic coefficients makes any quantitative analysis of the higher degree parts of the resulting gravity power spectra unreliable at this point. In this work we thus performed a spectral study of the power spectrum resulting from a new spherical harmonic model for Venus topography and of the lower degree part of the spectrum from a harmonic model of the Venus geoid (equipotential surface) comparing the results to that obtained for Earth spectra.

For the gravity field we used a 60th degree and order spherical harmonic model (1) recently produced at the Jet Propulsion Laboratory and combining PVO and recent Magellan Doppler tracking data. We deliberately restricted our analysis of the geoid spectrum derived from this field to lower degrees ($l \leq 18$). The topography model we used was also produced at JPL (1); its spherical harmonic coefficients were computed by numerical quadrature from a grid of planetary radii derived from the complete set of PVO and Magellan altimetry data (2).

One standard practice is to expand global data sets on a planetary surface in terms of spherical harmonics; examples include geoid and topography (3,4). We define the degree variances of these spectra by:

$V_l^t = R_o^2 \sum_{m=o}^{l} (A_{lm}^2 + B_{lm}^2)$, for the topography and: $V_l^n = R_o^2 \sum_{m=o}^{l} (C_{lm}^2 + S_{lm}^2)$ for the geoid,

where R_o is a reference radius (mean equatorial radius for Venus), A_{lm}, B_{lm} and C_{lm}, S_{lm} are the non dimensional and normalized coefficients (of degree l, order m) for the spherical harmonic expansions of topography and geoid respectively. The C_{lm}, S_{lm} are the same as for the gravity potential and the geoid spectrum is obtained from the perturbing potential via Brun's formula (3). We can then define a power spectral density (PSD) for these expansions as: $P_l^t = 1/k_o \; V_l^t = \lambda_o V_l^t$ for the topography and $P_l^n = 1/k_o \; V_l^n = \lambda_o \; V_l^n$ for the geoid, where $\lambda_o = 2\pi R_o$ is the wavelength over which data are included in the expansions and $k_l = 1/\lambda_l = 1/2\pi R_o$ is the wave number. Such spherical harmonic representations are said to be statistically scale invariant over a given range in wavelength if the PSD has a power-law dependence on wave number (4): $P_l \sim k_l^{-\beta}$, $-\beta$ being the slope.

In Figure 1 we show the PSD for global Venus topography corresponding to the spherical harmonic model we used, plotted against k_l in a log-log scale. We

can see that the Venus data agrees quite well with a power-law spectral correlation, over a range $50 \geq l \geq 3$ (760 km $\leq \lambda_l \leq$ 12, 675 km), with $\beta = 2$ (dashed correlation line in Figure 1). This correlation is characteristic of Brown noise, with the amplitudes directly proportional to the wavelengths. Such a $\sim l^{-2}$ dependence of the PSD is also observed for Earth topography (5), where the height to width (ie aspect) ratios of mountains and hills are the same. For $l < 3$, the Venus topography spectrum shows a rollover. This is also observed on the Earth although the power deficiency starts at a higher degree ($l \sim 5$). Furthermore, when compared to Earth data (6,7), the Venus spectrum has significantly lower amplitude values which could be attributed to a weaker lithosphere over most of Venus (4).

The PSD for the Venus geoid data analyzed here also obeys a power-law, at least for $l \leq 18$. However, terrestrial geoid data (8), displays a larger slope consistent with Kaula's law ($P_l^n \sim k_l^{-3}$). Smaller geoid spectra slopes on Venus have been attributed to shallower gravity sources (9). Also, for $l > 3$, the PSD for Venus geoid shows larger amplitudes than for Earth data, a possible consequence of the significant correlation seen on Venus between gravity and topography (10).

Comparisons between the spherical harmonic expansions of gravity and topography on Venus can prove useful in probing the internal structure of the planet and testing evolution models predictions. However, Magellan data from the planned circularized orbit phase should greatly reduce the burden of an a-priori bias required to produce current high degree and order gravity harmonic models, thus significantly increasing the reliability of quantitative analysis of these data sets.

References: (1) Konopliv, A.S., N.J. Borderies, P.W. Chodas, E.J. Christensen, W.L. Sjogren, and B.G. Williams, 1993, in preparation. (2) Ford, P.G. and G.H. Pettengill, JGR 97, 13,103-13,114, 1992. (3) Heiskanen, W.A. and H. Moritz, Physical Geodesy, W.H. Freeman, New York, 1967. (4) Turcotte, D.L. Proc. Lunar Planet. Sci. Conf. 17th, Part 2, JGR, 92, suppl., E597-E601, 1987 (5) Vening-Meinesz, F.A., Proc. K. Ned. Akad. Wet. Ser. B. Phys. Sci., 54, 212-228, 1951. (6) Balmino, G.K., K. Lambeck, and W.M. Kaula, JGR, 78, 478-481, 1973. (7) Rapp, R.H., Geophys. J. Interna., V. 99, 449-455, 1989. (8) Reigber, C. G. Balmino, H. Muller, W. Bosch, and B. Moynot, JGR, 90, 9285-9299, 1985. (9) Kaula, W. M. in Proceedings IAG Symposium "Determination of the Gravity Field", O. Colombo, Ed. Springer-Verlag, 1992, in press. (10) Phillips, R.J., and Malin, M. C., in Venus, edited by D.M. Hunten, L. Colin, T.M. Donahue, and V.I. Moroz, University of Arizona Press, Tucson, 1983.

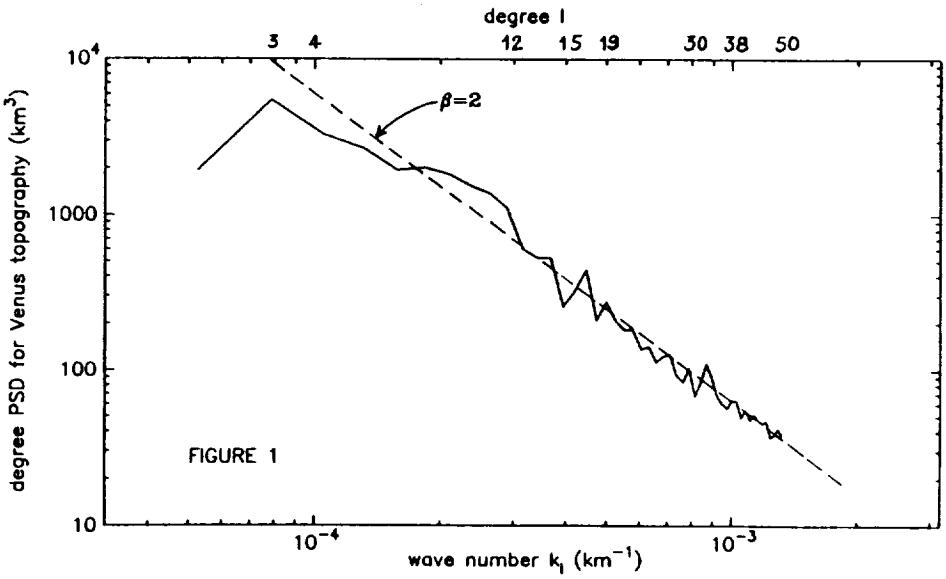

Figure 1. Power spectral density of Venus' topography as a function of wave number. The dashed line illustrates a correlation with a power-law for $\beta = 2$.

VERTICAL STRUCTURE MODELS OF THE 1990 EQUATORIAL DISTURBANCE ON SATURN; D.M. Kuehn, Pittsburg St. U., C. D. Barnet, ISTS, and R. F. Beebe, NMSU

In September 1990, an atmospheric disturbance in the form of an abnormally high albedo area developed in the equatorial region of Saturn. Events of this nature are exceeding rare for this planet as they have been detected in the equatorial region on only two other occasions in over a century [1]. In ongoing monitoring of the atmospheres of the outer planets, CCD imaging observations of Saturn by New Mexico State University's Tortugas Mountain Station were made before, during, and after the disturbance's formation through both broad-band filters and narrow-band visible/near-IR filters centered in methane absorption bands. Also, multispectral Hubble Space Telescope observations were made within weeks of the event and later in 1991 [2, 3]. These observations have been calibrated and scans of reflectivity at constant latitude are being modeled with a vertically inhomogeneous, multiple scattering model previously used to model Jupiter's South Equatorial Belt brightening event in 1989 [4]. In addition, the reflectivity of the disturbance as a function of the scattering angles is being obtained so as to model this feature's vertical structure in particular. A preliminary report of the modeling results will be presented.

[1] Sanchez-Lavega, A. (1989) *Sky and Telescope* **78**, 141-143
[2] Westphal, J. A. *et al.*(1991) *Astrophys. J.*, **349**, L51-L53.
[3] Barnet, C. D., Westphal J. A., Beebe R. F., and Huber L. F. (1992) *Icarus*, **100**
[4] Kuehn, D. M., (1990) Ph.D. thesis, New Mexico State University.

PRELIMINARY $^{40}Ar/^{39}Ar$ AGE SPECTRUM AND LASER PROBE DATING OF THE M1 CORE OF THE MANSON IMPACT STRUCTURE, IOWA: A K-T BOUNDARY CRATER CANDIDATE: Kunk, M.J.,USGS, Reston, VA 22092, Snee, L.W., USGS, Denver, Co 80225, French, B.M., NASA HQ, Washington DC 20546, Harlan, S.S., USGS, Denver, CO 80225, and McGee, J.J., USGS, Reston, VA 22092

Preliminary $^{40}Ar/^{39}Ar$ age spectrum and laser probe dating results from new drill core from the 35-km-diameter Manson Impact Structure (MIS), Iowa indicates a reasonable possibility that the MIS is a Cretaceous-Tertiary (K-T) boundary impact event. Several different types of samples from a melt-matrix breccia, a unit of apparent crater fill intersected by the M1 core, have been analyzed. $^{40}Ar/^{39}Ar$ results from these samples indicate a maximum age for the MIS of about 65.4 ± 0.4(2σ) Ma. Petrographic analyses of the samples indicate a high probability that all the dated samples from the melt-matrix breccia contain relict grains that were not entirely melted or degassed at the time of impact, suggesting that the actual age of the MIS could be somewhat younger than our preliminary results indicate. The results are consistent with a previously published age estimate of shocked microcline from the MIS central uplift of 65.7 ± 1.0 Ma[1].

The possibility of multiple impacts at the K-T boundary has been suggested by the boundary layer in the Western Interior of North America which consists of a two-part layer that may record two or more bolide impacts[2]. The lower thicker member of this layer is a claystone composed mostly of kaolinite, but it contains spherules that may be the alteration product of impact-produced tektites. This lower layer may be ejecta from the Chixulub crater in Mexico, which has an age indistinguishable from that of the K-T boundary[3,4]. The top surface of the lower claystone layer appears to have supported some plant growth for a period of time before the deposition of the upper member. This upper member, the so-called "magic layer", contains the iridium anomaly and shocked mineral grains that characterize the K-T boundary layer worldwide[5,6], and allowed the recognition of a bolide impact(s) at the K-T boundary. The "magic layer" records an event that is clearly distinct from that of the lower member of the doublet.

If multiple impacts occurred at the K-T boundary, the MIS located in northcentral Iowa is a K-T boundary crater candidate[7] because of its previously published age of 65.7 ± 1.0 Ma[1], and its proximity to K-T boundary sites that have the highest concentrations and largest sizes of shocked mineral grains[6].

The recently drilled M1 core from the MIS apparently penetrates ejecta deposits ("crater fill") that include a unit of probable melt-matrix breccia that contains clasts of apparent basement lithologies that have been intensely shocked. Some clasts have been partially melted. Although petrographic analysis of some of these clasts suggests the growth of new potassium feldspar from a melt, all of the samples studied to date also appear to contain relict potassium feldspar that was not melted by the impact and that may record older pre-impact ages. The matrix of this breccia is cryptocrystalline and also represents material that was incompletely melted because it contains mineral grains (xenocrysts?) with obvious shock features.

$^{40}Ar/^{39}Ar$ DATING OF THE MANSON IMPACT STRUCTURE: Kunk et al.

Samples selected for preliminary $^{40}Ar/^{39}Ar$ dating include feldspar grains from clasts in the melt-matrix breccia that were melted and recrystallized to varying degrees, and the matrix itself from the melt-matrix breccia. Sanidine from the Fish Canyon Tuff (27.79 Ma) and MMhb-I (519.4 Ma) were used as fluence monitors. Tektite glass from the K-T boundary layer in Haiti was irradiated at the same time and was dated at 65.0 ± 0.4 Ma. The results from the Haitian tektites are indistinguishable from previously published results[3].

$^{40}Ar/^{39}Ar$ age spectrum results on feldspar from variably melted and recrystallized clasts from the melt matrix breccia do not develop age plateaux. The overall pattern of these age spectra suggests the presence of incompletely degassed protolith feldspar or the presence of some extraneous argon in the samples. Ages of individual steps increase with temperature of extraction and range from about 68 Ma to 123 Ma. These age spectra are interpreted to represent a maximum age for the MIS of ~68 Ma.

$^{40}Ar/^{39}Ar$ laser probe results from a bulk potassium feldspar sample from the 420.5 foot level of the M1 core are consistent with conventional age spectrum total gas results from the same sample at ~74 Ma. $^{40}Ar/^{39}Ar$ laser probe results of multiple one and two grain aliquots from the same sample range in age from 65.4 ± 0.4 to 97.5 ± 2.6 Ma. Although the 65.4 ± 0.4 Ma result agrees with previously published results from the MIS, it may still represent an overestimate of its age because of the possibility that some portion of the individual grains may be protolith material that has been incompletely degassed. The older ages of some of these analyses are almost certainly due to included incompletely degassed protolith material.

$^{40}Ar/^{39}Ar$ age spectra of melt matrix samples are more complex than those of the feldspars and are interpreted to represent the effects of some combination of the presence of excess ^{40}Ar in the samples, ^{39}Ar recoil during irradiation, and the inclusion of incompletely degassed protolith material. These age spectra suggest that the time of impact is less than ~73 Ma.

Our preliminary $^{40}Ar/^{39}Ar$ results on samples from the MIS M1 core indicate a maximum age for the MIS of 65.4 ± 0.4 Ma. This age taken together with our age results from the Haitian tektite sample of 65.0 ± 0.4 Ma indicates a reasonable probability that the MIS was formed during K-T boundary times. Additional $^{40}Ar/^{39}Ar$ work is required to test for the possibility of yet younger ages, to more precisely date the MIS, and to more tightly compare the age of the MIS with that of the K-T boundary.

[1] Kunk et al.(1989) Science, 244, 1565-1568. [2] Shoemaker and Izett (1992) Lunar and Planerary Science, XXIII, 1293-1294. [3] Swisher et al. (1992) Science, 257, 954-958. [4] Sharpton et al. (1992) Nature, 359, 819-821. [5] Alvarez et al. (1980) Science, 208, 1095-1108. [6] Izett (1987) Geological Society of America Bulletin, 99, 78-86. [7] French (1984) Science, 336, 53. [8] Izett et al (1991) Science, 252, 1539-1542

WAS MARTIAN MANTLE WET? A POSSIBLE CONSEQUENCE OF RAPID CORE FORMATION; Kiyoshi Kuramoto and Takafumi Matsui, Department of Earth and Planetary Physics, University of Tokyo, Bunkyo-ku, Tokyo 113, Japan.

Degassing of H_2O in the planetary interior possibly plays an important role in the evolution of surface environment as well as geologic activity on the terrestrial planets. Mars may be such a planet that well preserves the materials and the geologic features directly related to early evolution of H_2O. In this study, we investigate H_2O content in the interior of proto-Mars during accretion and also core formation.

Geodetic data shows that Mars has a dense core [1]. The existence of iron-rich core on Mars may be also supported by the depletion of siderophile elements in SNC meteorites assuming that these samples came from Mars [2]. Isotope systematics of these meteorites indicate that the core formation occurred very early, probably concurrently with Mars formation [3]. Considering the kinetics of metal segregation from silicate, the melting of silicate is likely to precede the core formation [4]. Once the core formation occurs, substantial amount of gravitational energy is released and thus the planetary interior is heated. This energy may be large enough to keep the silicate material in partially molten state along with the accretional heating. Under such circumstances, the silicate melt probably migrates to the surface. Early crustal formation, therefore, is also likely to be associated with the core formation.

For Mars, the main heat source for the planetary interior is probably accretional heating. Short-lived radio-isotope such as ^{26}Al may not be important as a heat source because the accretion time of the planets probably much longer than the decay time constant of such isotope. An important feature of the accretional heating is that a growing planet is heated stronger with its growth due to the increase in impact velocity of planetesimals. Then the question is whether or not accretional energy of Mars is large enough to result in surface magma ocean. The critical mass of a growing planet at which the melting of silicate and the core formation begin to occur is uncertain mainly because of difficulty in estimating the efficiency of heat deposition due to planetesimal impact [5]. However, the critical size is estimated to be $\sim 0.5\times$ (present Mars mass), assuming that the impact velocity is equal to the escape velocity of a growing planet, 20% of the impact energy is deposited in subsurface layer, and the core formation occurs when the temperature of subsurface layer exceeds 1500K. This estimate is of course crude but strongly suggests a rapid core formation on Mars. This also implies that the substantial size of undifferentiated core is formed in a growing Mars. Such an undifferentiated core probably contains volatiles like H_2O. This is because, although high velocity impact causes the degassing of volatiles such as H_2O contained in accreting materials, Mars is not large enough to experience complete degassing of H_2O during accretion as far as the impact velocity is equal to the escape velocity from the planet [6]. Even if average impact velocity is much higher than the escape velocity due to the perturbation by other planets such as Jupiter, it is unlikely that all the population of planetesimals has the impact velocity high enough to cause the complete degassing. In addition, as inferred from SNC meteorites, the original materials forming Mars is probably volatile rich compared to that for the Earth [7]. Therefore, concurrently with the initiation of the "metallic core" formation, the undifferentiated core may be destroyed and the volatiles may be supplied into the surrounding

proto-mantle.

H_2O buried in the interior may be removed from silicate due to the reaction between metallic iron and H_2O under high pressure which forms FeO and FeH_x [8]. FeH_x may enter into the core. This reaction might make proto-martian mantle dry. The removal of H_2O from silicate by this mechanism, however, is possibly inefficient when the core formation occurs under the presence of silicate melt. This is because substantial amount of H_2O dissolves into silicate melt. We made a preliminary estimate H_2O partition between silicate melt and metallic iron. The result shows that H_2O is likely to be partitioned into silicate melt more than to metallic iron (Fig.1). Thus, a proto-martian mantle is possibly wet after the core formation.

Possible existence of H_2O in the proto-martian mantle may have a profound influence on the formation of proto-crust and surface hydrosphere on Mars. Silicate melt contained H_2O tends to be silica rich [9] and thus the early crust might have such composition although, at present, the composition of the proto-crust on Mars is poorly known. Because recycling of crust into mantle is probably inactive on Mars, extensive degassing associated with early crustal formation may result in dry martian mantle as inferred from the H_2O abundance in SNC meteorites [10]. H_2O extensively degassed from wet proto-mantle may be a prime source of surface H_2O suggested from geologic flow features on early Mars.

References: [1] B. Bills, 1990. *J. Geophys. Res.* **95**: 14,131–14,136; [2] A. Treiman et.al., 1986. *Geochim. Cosmochim. Acta* **50**: 1,071–1,091; [3] J. Chen and G. Wasserburg, 1986. *Geochim. Cosmochim. Acta* **50**: 955–968; [4] D. Stevenson, 1990. In *Origin of the Earth*, eds. H. Newsom and J. Jones (New York: Oxford Univ. Press), pp. 231–249; [5] G. Davies, 1985. *Icarus* **63**: 45–68 [6] M. Lange and T. Ahrens, 1984. *Earth Plant. Sci. Lett.* **71**: 111–119; [7] G. Dreibus and H. Wänke, 1987. *Icarus* **71**: 225–240; [8] Y. Fukai and T. Suzuki, 1986. *J. Geophys. Res.* **91**: 9,222–9,230; [9] Basaltic Volcanism Study Project, 1981. *Basaltic volcanism on the terrestrial planets*, (New York: Pergamonn Press), [10] M. Carr and H. Wänke, 1992. *Icarus* **98**: 61–71; [11] L. Liu, 1987. *Phys. Earth Planet. Inter.* **49**: 142–167

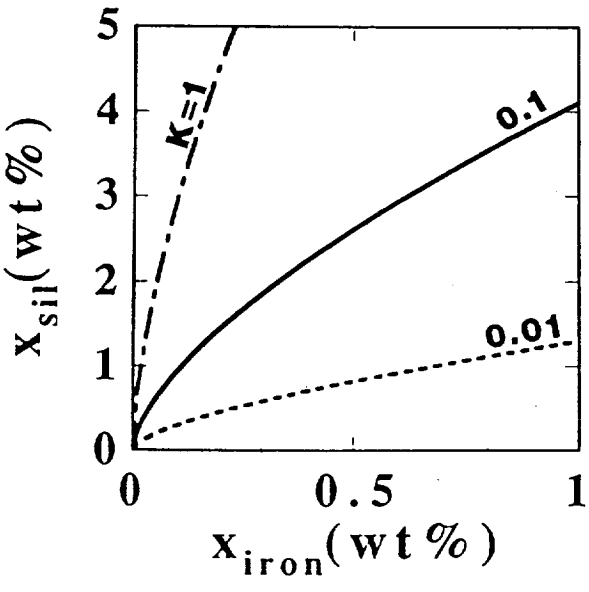

Fig.1. H_2O partition between the silicate melt and liquid metallic iron. On the basis of the data on H_2O solubility in silicate melt [11], H_2O fugacity in the silicate melt is given by $f_{H_2O} = 0.07x_{sil}^2$, where x_{sil} is the concentration of H_2O in silicate melt in wt%. On the basis of estimation of H_2 solubility in liquid metallic iron [8], H_2 fugacity in liquid iron is approximately given by $f_{H_2} = 12x_{iron}^{1.3}$, where x_{iron} is the concentration of H_2 in liquid iron (wt%, but the weight of H_2 in liquid iron is converted into that of H_2O for comparison with the silicate melt). K is f_{H_2O}/f_{H_2} which is a function of the temperature and pressure. When Quartz-Iron-Fayalite buffer is considered, $K \sim 10^{-1}$ at temperature 1000~2000K.

WATER IN EARTH'S MANTLE: HYDROGEN ANALYSIS OF MANTLE OLIVINE, PYROXENES AND GARNET USING THE SIMS.

Masanori Kurosawa, Hisayoshi Yurimoto and Shigeho Sueno, Inst. of Geoscience, The University of Tsukuba, Tsukuba 305, Japan.

Introduction: Hydrogen (or water) in the Earth's interior plays a key role in the evolution and dynamics of the planet [1]. However, the abundance and the existence form of the hydrogen have scarcely been clear in practice. Hydrogen in the mantle was incorporated in the interior during the formation of the Earth [1]. The incorporated hydrogen was hardly possible to concentrate locally inside the Earth considering its high mobility and high reactivity. The hydrogen, preferably, could be distributed homogeneously over the mantle and the core by the subsequent physical and chemical processes. Therefore, hydrogen in the mantle could be present in the form of trace hydrogen in nominally anhydrous mantle minerals [2]. In this study, we have determined the hydrogen and the other trace elements in mantle olivines, orthopyroxenes, clinopyroxenes and garnets using secondary ion mass spectrometry (SIMS) for elucidating (1) the exact hydrogen contents, (2) the correlation between the hydrogen and the other trace elements and (3) the dependence of the hydrogen contents on the depth, (4) the dependence of the whole rock water contents on the depth.

Analytical: We have analyzed hydrogen and the other trace elements in the minerals using the SIMS (Cameca IMS-3F) at the University of Tsukuba. A 100 nA, 14.5 keV $^{16}O^-$ primary beam was focused to a ~ 100 μm diameter spot. Secondary ions ($^1H^+$, $^7Li^+$, $^{28}Si^{2+}$, $^{23}Na^+$, $^{27}Al^+$, $^{30}Si^+$, $^{39}K^+$, $^{40}Ca^+$, $^{47}Ti^+$, $^{52}Cr^+$, $^{56}Fe^+$, $^{59}Co^+$ and $^{60}Ni^+$) were collected from the central region (60 μm in diameter) of the sputtered area using a mechanical aperture. For quantitative hydrogen analysis, H^+-implanted olivines, orthopyroxenes, clinopyroxenes and garnets were prepared as standard materials by an ion-implantation technique with an acceleration energy of 50 keV [3]. For determinations of the other trace elements, fused glass beads of the JB-1a rock powder which is a standard rock reference issued by the Geological Survey of Japan was used as standard material [4]. The elements of Si, Ti, Al, Cr, Fe, Mn, Ni, Mg, Ca, Na and K in the samples were analyzed using EPMA. In addition, the infrared spectra for single crystal part of the samples were measured in the range from 4000 to 2000 cm^{-1} in wavenumbers, in order to check the presence of secondary hydrous minerals. The olivine, orthopyroxene, clinopyroxene and garnet samples were selected from spinel and garnet peridotites (hartzbergite and lherzolite) occurred in island arc, the continental rifts and the craton, and were also selected from mineral inclusions in diamonds.

Results and Disccusion: The hydrogen concentrations range from 10 to 60 ppm wt. H_2O in olivines; 90 to 350 ppm in orthopyroxenes: 90 to 350 ppm in clinopyroxenes; 10 to 70 ppm in garnets and the results are consistent with the previous studies [5]. SIMS and infrared

spectroscopic studies showed that most of the hydrogen contents are not derived from the weathering, secondary alterations and hydrogen reequilibrium with a host magma during the transportation from the mantle to the surface. Olivine, orthopyroxene and pyrope inclusions in diamonds show similar hydrogen contents to peridotitic olivines, othopyroxenes and garnets, so that hydrogen contents in xenolith's minerals can be little affected by the contamination during the transportation.

The hydrogen contents in the minerals showed good positive correlations with Al, Cr, Fe^{3+}, and showed no relationship with cation deficiencies. This suggests that hydrogen in the mantle minerals is incorporated by substitutional mechanisms. In addition, the hydrogen contents in orthopyroxenes and clinopyroxenes increased in proportion to temperature and pressure of the parent peridotite rocks. However, hydrogen contents in olivines decreased with increasing temperature and increased linearly with pressure, and those in garnets reduced with increasing temperature and pressure. These trends are able to explain by the hydrogen partitioning among the minerals and the hydrogen solubilities.

Whole rock water content of peridotites, which was calculated from mineral proportions and hydrogen contents in minerals, ranged from 50 to 140 ppm wt. H_2O. The concentration raised basically as temperature and pressure increased. Pyroxenes contain most abundant hydrogen among peridotite minerals, so that they contribute largely to the total water contents in peridotites. The increase of whole rock water contents with the depth suggests that ascending mantle rocks are capable of providing water which the amount corresponds to difference in the whole rock water contents between the ascending rock and mantle rock of shallower region. The suggestion is important for magma genesis and mantle fluid generation and supports the importance of hydrogen in anhydrous minerals as a water reservoir in the mantle.

References: [1] Matsui T. and Abe Y. (1986) *Nature* **322**, 526-528. [2] Martin R. F. and Donnay G. (1972) *Am. Mineral.* **57**, 554-570. [3] Kurosawa M., Yurimoto H., Matsumoto K. and Sueno S. (1992) In *High-Pressure Research in Mineral Physics* (ed. Syono and M. H. Manghnani), pp. 283-287, Terra Pub/Am. Geophys. Union, Tokyo/Washington D.C. [4] Yurimoto H., Yamashita A., Nishida N., and Sueno S. (1989) *Geochem. J.* **23**, 215-236. [5] Bell D. R. and Rossman D. R. (1992) *Science* **255**, 1391-1397.

N94-16337

Lunar LIGO: A New Concept in Gravitational Wave Astronomy;

Norman LaFave[1] and Thomas L. Wilson[2]; [1]Lockheed Engineering and Sciences Co., Houston, Texas 77058. [2]NASA Johnson Space Center, Houston, Texas 77058.

For three decades, physicists have been in search of an elusive phenomenon predicted by Einstein's general theory of relativity: gravitational radiation. These weak vibrations of spacetime have, thus far, eluded conclusive Earth-based detection due in part to insufficient detector sensitivity and noise isolation. The detection of gravitational waves is crucial for two reasons. It would provide further evidence for the validity of Einstein's theory of relativity, the presently accepted theory of gravitation. Furthermore, the ability to identify the location of a source of a detected gravitational wave event would yield a radical new type of astronomy based on non-electromagnetic emissions. We continue our study of a lunar-based system [1,2] which can provide an important complement to Earth-based analysis because it is completely independent of the geophysical sources of noise on Earth, while providing an Earth-Moon baseline for pin-pointing burst sources in the Universe. We also propose for the first time that a simplified version of the LIGO beam detector optical system, which we will call LLIGO (Lunar LIGO), could be emplaced on the Moon as part of NASA's robotic lander program [3] now under study (Artemis).

The Earth-based investigation has two major programs underway. Both involve large interferometer-type gravitational wave antennas. The incoming waves cause the lengths of the two arms of the interferometer to fluctuate at the same frequency but 180° out of phase. Detection occurs via the resulting motion of the interference fringes at the detector. This type of antenna is more responsive than the bar antennas used in early work because signals propagate at the speed of light rather than the speed of sound. Increasing the length of the arms increases the sensitivity of the interferometer to the waves (as $\sqrt{n}$ where n is the number of waves). These programs are the following:

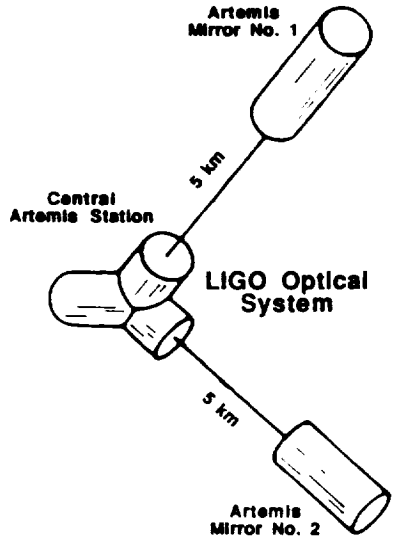

Figure 1. Lunar LIGO using Artemis

(1) The Laser Interferometer Gravitational-Wave Observatory (LIGO) is an MIT/Cal Tech effort to build two interferometers at different sites in the U.S., each one having arms four kilometers in length [4]. This antenna will be sensitive to waves down to around 10 Hz. (2) A similar program to build an antenna with three kilometer arms, and comparable sensitivity range to LIGO, called VIRGO, is headed by a group of French and Italian investigators [5]. A third proposal is the Laser Gravitational Wave Observatory in Space (LAGOS), which is a large LIGO-type interferometer antenna involving three spacecraft in near-circular orbit around the sun [6]. This is a "LIGO in space" with arms roughly 10^6 km in length. This antenna would be sensitive in the range between roughly 10^{-5} to 10^0 Hz. This proposal is in a conceptual stage, is extremely tedious, and appears unrealistic due to its life-cycle operations cost.

It is our contention that a lunar-based LIGO interferometer antenna (**Fig. 1**), in conjunction with these other projects, would provide an important contribution to this effort in both the physics and astronomy arenas. The reasons are as follows:

(a) The lunar antenna will be sensitive down to 0.25 Hz [1]. This covers most of the range for which LIGO, VIRGO, and LAGOS are not sensitive (see **Fig. 2**). This increased sensitivity is due to smaller noise sources, especially seismic noise (100

times greater on Earth in the range between 0.25 and 1.0 Hz), gravity gradient noise (no large moving masses near detector on the Moon), tidal noise, and acoustic noise. Estimates of photon shot noise tend to be a factor of three higher for the lunar antenna above about 30 Hz. Cosmic ray noise, a source unique to the space-based antennas, should not cause significant disruption, except during solar flare events. Thermal noise should be comparable.

(b) The lunar antenna will not be mechanically or geophysically coupled to the terrestrial antennas, thus providing a good method of removing spurious seismic noise via concidence with terrestrial antennas over their common frequencies. It will also provide a significant confidence or voting factor for detected events.

(c) The vacuum of the lunar environment provides significant advantages. It will eliminate the need to maintain a vacuum in the interferometer over the life-cycle of the antenna [1,2]. A minimal antenna could be placed on the Moon using three dedicated Artemis landers, one containing the laser source/beam-splitter/detector, and the other two containing the end mirrors (**Fig. 1:** A 2m Artemis creates a 5.27 km osculating line-of-sight for a lunar radius of 1738 km). The lack of arm enclosures allows the arms to be extremely long, limited only by the Moon's surface curvature. The arms could be easily altered by moving the landers containing the end mirrors.

The extreme distance between the Earth and Moon provides a long parallax baseline with terrestrial antennas for locating the sources of a gravitational wave event. A factor of 50 times better angular resolution may be obtained in the plane of the source, the Earth, and the Moon for short-burst sources. For signals which recur several times during a period of a week or more, and are out of the ecliptic plane, the accuracy of source localization may be improved [1].

These arguments provide compelling support for the development of a lunar-based gravitational wave antenna to complement the programs currently under development on Earth.

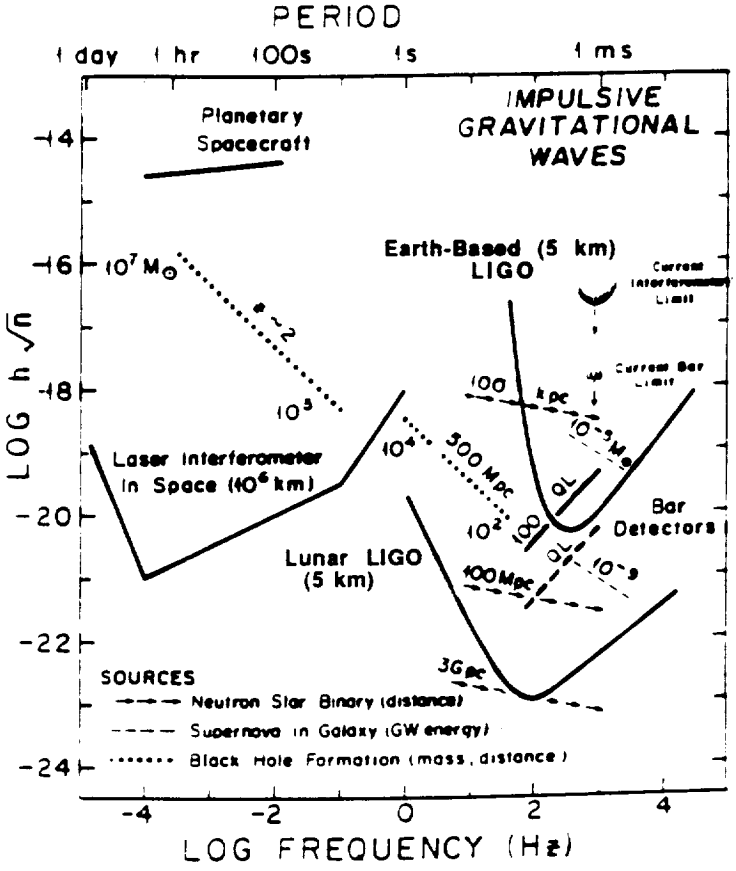

Figure 2. Lunar LIGO & Burst Sources [Adapted from 4 and 6]

References:

[1] LaFave, N., and Wilson, T.L., *23rd LPSC*, Vol 2, 751 (1992). [2] Wilson, T.L., in *Physics and Astrophysics from a Lunar Base*, Potter, A.E., and Wilson, T.L., eds., AIP Conf. Proc. **202**, ix, 53, and program organizer (1990); in *Astrophysics from the Moon*, Mumma, M.J., and Smith, H.J., eds., AIP Conf. Proc. **207**, 608 (1990), Ref. 37. [3] *LPI Workshop on Early Robotic Missions to the Moon* (Lunar & Planetary Institute, Houston, February 4, 1992); *Artemis Phase 2 Study Results* (NASA JSC New Initiatives Office, March 10, 1992). [4] Thorne, K.S., in *300 Years of Gravitation*, Hawking, S., and Israel, W., eds., (Cambridge University Press, 1987), Sect. 9.5.3; Figs. 9.4; 9.6; 9.7. [5] Bradaschia, C., *et al.* Nucl. Instr. & Meth. **A289**, 518 (1990). [6] In: *Physics Through the 1990's: Gravitation, Cosmology, & Cosmic Ray Physics*, Figs. 6 (National Academy Press, Washington, 1986).

SHEET FLOW FIELDS ON VENUS; M. G. Lancaster, J. E. Guest (University of London Observatory, University College London, London, NW7 2QS, U. K.), K. M. Roberts (Brown University, Providence, RI 02912, U. S. A.).

A survey of flow fields with areas greater than 50,000 km^2 has revealed fields with sheet-like morphology[1]. These sheet flow fields are distinguished by their relatively uniform backscatter, lack of internal flow structure such as well defined lava streams or channels, absence of flow lobes, and irregular boundaries. Internal flow boundaries are essentially absent in these fields, and as such they cannot usually be divided into separate stratigraphic units or eruptive episodes. This is unlike other flow fields with more digitate morphologies, which are made up of discrete flow lobes, and can usually be divided into several episodes of flow emplacement. Five sheet flow fields have been studied so far, and other candidates have been found. A flow field associated with Lauma Dorsa is taken as an example and examined in detail here.

The total area of these five fields ranges between 66,000 and 780,000 km^2, the average total area being 380,000 km^2 (Table 1). They are the most areally extensive of all the flow fields on Venus. Overall lengths (from the source to the most distal reach) lie between 450 and 880 km, while the overall widths fall between 230 and 880 km. Average lengths and widths are 640 and 490 km respectively. Widths correspond to the maximum widths of continuous sections of sheet flow normal to the inferred flow direction. The vast extent and irregular non-lobate boundaries suggest a local topographic control rather than cooling limited emplacement. The lack of recognisable flow morphology and structure (lobate boundaries, separate flow units, channels etc.) hinders the determination of flow direction and provenance. Using Magellan topographic data and assuming no post-emplacement topographic adjustment, the flow direction is inferred to be downslope relative to the present topography. Sources may then be inferred from association with upslope tectono-volcanic features, and include possible rift zones (Lauma Dorsa, Kawelu Planitia, and SE of Aino Planitia) and the concentric structures at the flanks of coronae (Hroswitha Patera, and 9.2N, 315.5E). In the case of the rift zones, the sheet flows appear to have been erupted concurrently from extensive fissures along continuous stretches of rift. Some of the larger sheet flow fields may be composed of more than one large flow field, which because of their nearly identical properties, may not be distinguished in the radar imagery. Average radar back scatter cross-sections of the fields range between -3.88 ± 19.54 and 4.20 ± 19.07 dB, with an overall average of 1.03 ± 8.65 dB. Topographically, the flow surfaces have slopes up to 0.32°, averaging 0.09°.

A 304,000 km^2 sheet flow field has flowed up to 540 km west from a 900 km section of the N-S trending ridge belt of Lauma Dorsa in Vinmara Planitia (Figure 1). The spatial association of the flow field with the ridge belt suggests that Lauma Dorsa was the source. However, many N-S trending ridges on the western flank of Lauma Dorsa appear to be post flow emplacement, as the radar back scatter of the ridges and the inter-ridge material is very similar. A compressional origin for this ridge belt has been proposed[2,3], whereas an extensional regime involving open fissures is required to feed the flows. The compressive structures may be largely post-volcanic, with the volcanism occurring during an earlier phase of rifting. Localised sources also exist. At 64N, 183-185E, an ENE-WSW trending fissure appears to have fed the flow field to the west. Short flows emerge from this fissure at 64N, 185.2E and 63.9N, 183.8E, and are isolated from the main part of the field. Similar relations between approximately E-W trending lineaments and the flow field (although less certain), are visible at 62.4N, 181.9E and 61.6N, 182.9E. To the east these E-W structures are superimposed by the ridges of Lauma Dorsa. These observations suggest that some component of the flow field was locally fed by approximately E-W trending fissures, and probably also from fissures within the main N-S trending deformation belt. This volcanism was then followed by a compressional regime which formed the ridge structure of Lauma Dorsa. A region comprising at least 2,000,000 km^2 of sheet flows lies to the east of Lauma Dorsa. These flows are of similar back scatter to the western flow field, and may also originate from the same regional source. However their boundary, particularly in the north, is ill-defined, and local source-flow relations have not been identified.

Name	Location	Total Area/km^2	Length/km	Width/km	Topographic Slope
Lauma Dorsa	52N to 67N 176 to 192E	304,000	540	900	0.32°
Hroswitha Patera	34N to 41N 021 to 037E	197,000	880	410	0.03°
Kawelu Planitia	40N to 52N 253 to 275E	780,000	630	-	0.00°
Corona at 9.2N, 315.5E	8N to 13N 314 to 320E	66,000	450	230	0.05°
SE of Aino Planitia	655S to 52S 123 to 142 E	554,000	720	540	0.05°

Table 1. Surveyed sheet flow fields on Venus

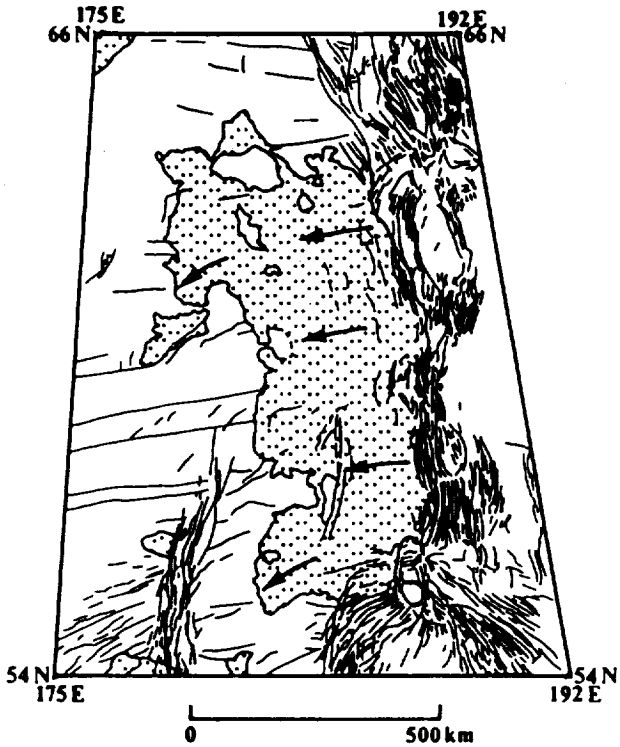

Figure 1. Sketch map of the flow field west of Lauma Dorsa, from C160n180 (arrows show inferred flow direction).

REFERENCES. [1] Lancaster, M. G., et al., (1992), *Papers Presented to the International Colloquium on Venus, Pasadena, California,* 62-64. [2] Sukhanov, A. L. and Pronin, A. A., (1989), *Proc. LPSC 19th,* 335-348. [3] Grosfils, E. B. and Head, J. W. (1992), *Papers Presented to the International Colloquium on Venus, Pasadena, California,* 37-38.

MARS EXOBIOLOGY LANDING SITES FOR FUTURE EXPLORATION;

Ragnhild Landheim[1], Ronald Greeley[1], David Des Marais[2], Jack D. Farmer[2] and Harold Klein[3], *(1)Department of Geology, Arizona State University, Tempe, AZ 85287-1404, (2)NASA-Ames Research Center, Mailstop 239-4, Moffett Field, CA 94035-1000, (3)Department of Biology, Santa Clara University, Santa Clara, CA 95053*

Summary

The selection of landing sites for Exobiology is an important issue for planning for future Mars missions. This report presents results of a recent site selection study which focused on potential landing sites described in the Mars Landing Site Catalog [1]. In addition, we will review basic Exobiology science objectives in Mars exploration, and outline the procedures used in site evaluation and prioritization.

Discussion

The selection of landing sites is based on the assumption that liquid water is a fundamental requirement for life. This is consistent with the assumed importance of a hydrologic cycle in allowing for the development and diversification of life [2]. Geological evidence for abundant water on Mars early in its history is substantial [3]. Depositional environments considered of primary interest include: fluvial-lacustrine, thermal spring, and periglacial. Of these, fluvial-lacustrine sites are considered to be excellent targets for meeting the goals of Exobiology, because 1) fine-grained water-lain sedimentary deposits are good host sediments for fossils and/or organic compounds, and 2) large lacustrine basins that have not received a younger volcanic cover make good landing targets from an engineering standpoint. Potential sites for hydrothermal activity were identified by simple "point source" channels with amphitheater headlands that occurred in close proximity to volcanic areas. Ground-ice may hold the largest reservoir of water on Mars [3]. Frozen soils in periglacial environments are of great interest to Exobiology, because ground-ice may contain a climate record of the past and it may have served to inhibit diffusion of oxidants in the soil, thus favoring preservation of organisms and organic compounds.

The first stage of the evaluation utilized the Viking Mars Chart (MC) prints (scale 1:2M) and the Mars Transverse Mercator (MTM) maps (scale 1:500,000). The subsequent phase applied Viking Orbiter (VO) images to selected sites of relatively high criteria scores from the previous analysis. Based on the latter evaluation, 17 sites were analyzed using the best (~250 m/pixel) resolution Viking Orbiter images obtained from the Image Retrieval and Processing System (IRPS). The final phase consisted of retrieval of Mosaicked Digital Image Models (MDIM's; resolution 231 m/pixel) of the respective sites. Features (landforms and deposits) used to identify each site type were assigned scores based on three subjective weighting factors, including visibility of feature on the image, uniqueness of the feature-process relationship, and importance of the features in relationship to goals of Exobiology.

Of the 83 sites listed in the Mars Landing Site Catalog [1], 13 were assigned a high priority for Exobiology by the methods outlined above. In addition, 5 additional sites not listed in the Mars Landing Site Catalog were identified and proposed as additions to the next edition of the catalog (Table 1).

Two sites that were assigned high priority for Exobiology were also identified by the MESUR Science Definition Team as favorable landing sites for the proposed Pathfinder mission [4]. The sites (Gusev crater: 15 deg S, 185 deg W [5] and Mangala Valles: 6 deg S, 149.5 deg W) are characterized by flat terrain and fine-grained sedimentary cover which meet important engineering constraints for safe landing sites. This illustrates the congruent nature of the criteria used to define high priority sites for Exobiology and other disciplines concerned with landing site identification.

The Gusev crater consists of an ancient 135 km diameter impact crater, filled with sediments derived from an 800 km long channel cut into cratered uplands. The floor of

the crater varies from hummocky crater ejecta to relatively smooth floor at the resolution of available images (50 m/pixel). The Mangala Valles site is on the floor of a 50 km diameter impact crater that has received sediments from channels originating from surrounding highlands. It has a well-developed delta at the mouth of a channel emptying into the crater. Albedo patterns on the floor suggest the presence of sediments reworked by the wind.

In summary, this study identifies a preliminary site list for Mars exploration Exobiology and outlines a conceptual framework for the objective evaluation and prioritization of sites to meet Exobiology science objectives. Exobiology shares important goals in Mars site selection with other planetary science disciplines, illustrating the advantage of a multidisciplinary approach in developing site selection strategies for future Mars missions.

References Cited

1. Greeley, R., Mars Landing Site Catalog, NASA Reference Publication 1238, 1990.
2. Klein. H.P.(ed.), The Search for Life's Origins, National Academy Press, Washington, D.C., 1990.
3. Squyres, S.W., Urey Prize Lecture: Water on Mars, *Icarus 79*, 279-288, 1989.
4. MESUR Science Definition Team, *Proceedings of Sixth Meeting*, Oct. 1992.
5. Goldspiel, J.M. and S.W. Squyres, Ancient Aqueous Sedimentation on Mars, *Icarus 89*, 1991.

POTENTIAL MARS EXOBIOLOGY SITES FOR FUTURE EXPLORATION

LSC site no.	Location of interest area (lat., long.)	Target (lat., long.)	Name of general site area	Relative level of priority	Suggested refr.	Total score (V.O. img.)
1	35°-38°S, 227°-231°W	37°S, 230°W	Eridania NW	High	MC-29NW	72
2	21°-23°S, 9°-14°W	22°S, 11°W	Margaritifer Sinus SE	High	MC-19SE	66
8	22°-23.5°S, 229°-231°W	22.8°S, 230.6°W	Mare Tyrrhenum SE	High	MC-22SE	72
10	24.5°-26.5°S, 264°-266.5°W	24.8°S, 265.8°W	Mare Tyrrhenum SW	High	MC-22SW	72
137	5.6°-6.4°S, 149.1°-149.9°W	6.3°S, 149.5°W	Mangala Valles	High	MTM -05147	54
79	13.5°-15.5°S, 187°-190°W	15.5°S, 188.5°W	Aeolis SE	High	MC-23NE,SE	56
138	13.5°-15.5°S, 183.5°-185.5°W	15.5°S, 184.5°W	Aeolis NE (Gusev)	High	MC-23NE,SE	61
140	6.5°-9°S, 302°-305.5°W	7.3°S, 305°W	Iapygia NW	High	MC-21NW	72
5	10°-11.5°S, 277°-280°W	11°S, 279.5°W	Iapygia NE	Moderate	MC-21NE	75
7	41.5°-43.5°S, 208°-212°W	43.2°S, 208.1°W	Eridania NC	Moderate	MC-29NC	66
22	5.9°-6.2°S, 73.7°-74°W	6.05°S, 73.75°W	Candor Mensa	Moderate	MTM -05072	18
32	33°-35°S, 264°-268°W	33.2°S, 266.4°W	Dao Vallis/Hadriaca Patera	Moderate	MC-28NE	18
4	55°-58°S, 190°-199°W	57°S, 197°W	Eridania SE	Low	MC-29SE	30
21	17.9°-19.2°N, 59.2°-53.8°W	18.95°N, 53.5°W	Maja Valles/ Chryse Planitia	Low	MTM 20052	68
26	17.7°-18.2°N, 55.5°-56.1°W	18.05°N, 55.7°W	Maja Valles	Low	MTM 20057	48
77	2°-4.5°N, 15.2°-17°W	2°N, 16°W	Ares Vallis	Low	MC-11SE	49
139	22°-23.5°N, 34.5°-36.5°W	22.1°N, 36.7°W	Oxia Palus NW	Low	MC-11NW	12
141	0°-2°S, 73.5°-78°W	1.5°S, 76.5°W	Hebes Chasma	Low	MC-18NW	21

Note: Sites 137-141 will be included in the next edition of the Mars Landing Site Catalog

Table 1

FAR-INFRARED SPECTRA OF CO_2 CLATHRATE HYDRATE FROSTS; J. C. Landry and A. W. England, Radiation Laboratory, University of Michigan, Ann Arbor, Michigan, USA.

ABSTRACT: As a product of our interest in remote sensing of planetary ices, we have grown frost samples of CO_2 clathrate hydrate by depositing water vapor on a cooled surface and pressurizing the resulting water frost with CO_2 gas. At pressures above the dissociation pressure of the clathrate, the samples exhibit an absorption peak at 75 cm^{-1}. At pressures below the dissociation pressure, the peak disappears. Since the free CO_2 molecule does not have rotational or vibrational absorption in this region, the absorption is attributed to a CO_2 rattling mode within a clathrate cage.

INTRODUCTION

Clathrate hydrates are believed to exist in many places in the solar system. Uranus, Neptune, Mars, and comets are likely places for the presence of clathrate hydrates, but their natural existence has only been confirmed on earth [1]. The most practical way of detecting clathrate hydrates elsewhere in the solar system is probably through remote sensing experiments. In order to design such experiments, it is necessary to know their dielectric properties.

A clathrate hydrate is made up of a host lattice of water molecules that contains cages which incorporate guest molecules. The guests are free to rotate, vibrate, and translate (rattle) within their cages. Rotational and vibrational absorption bands of the guest are similar to those of the free molecule. Consequently, these bands are unsuitable for the remote detection of a clathrate in the presence of the free gas. Rattling modes, however, are unique to the clathrate and may be useful in a detection experiment.

The long term goal of this research is to determine the dielectric properties of carbon dioxide clathrate hydrate in the region of its rattling modes. The CO_2 hydrate is important because it is believed to be a major constituent of the the northern Martian poles during part of the annual cycle. The present paper describes a preliminary study of the absorption of CO_2 frosts.

SAMPLE PREPARATION AND MEASUREMENT

The sample was prepared inside the polyethylene cell shown in Figure 1. One wall of the cell can be conductively cooled through contact with the cold finger of a liquid nitrogen cooled cryostat. The inner face of this wall is covered with copper foil on which the sample is deposited. The temperature of the foil is measured by a platinum resistance temperature detector (RTD) wrapped several times by the foil. A tube connected through the opposite wall of the cell carries in the wires necessary for the temperature measurement. Two additional tube connections allow gas to be flowed through the cell and allow the cell to be evacuated or pressurized.

The cell was mounted on the cold finger of the cryostat and placed in a Bomem DA8 Fourier transform spectrometer. A mercury vapor lamp source, 12 micron mylar beam splitter, and liquid helium cooled silicon bolometer were used to cover the spectral range of 40-200 cm^{-1}. The spectrometer beam entered the sample cell through its non-cooled wall and reflected off the copper foil. All spectral measurements were at 1.0 cm^{-1} resolution.

To prepare a CO_2 clathrate hydrate frost, a water frost sample must first be formed and its presence verified. The cell was evacuated and cooled to 240K, and a reference spectrum taken. Water vapor from a de-ionized water reservoir was allowed to flow through the sample cell so that it deposited a water frost on the cell's cooled face. A second spectrum was taken and ratioed with the reference spectrum to form a transmission spectrum of the frost. By comparing this spectrum with water ice spectra from other sources [2], the presence of the water frost was confirmed.

The cell was pressurized with 1.7 bars of CO_2 gas, which at 240 K is below the clathrate dissociation pressure. (CO_2 clathrate dissociation pressure curves are given in [1] and [2]). A new spectrum of the sample revealed no significant changes in the water ice. The temperature was then lowered to 210 K. where the dissociation pressure of CO2 clathrate is less than 1 bar, but the CO_2 saturation vapor pressure is above 2 bars. The clathrate hydrate formed and another spectrum was taken and ratioed with the previous water frost spectrum. The resulting transmission spectrum repeatedly exhibited the absorption

at 75 cm^{-1} shown in Figure 2.

To eliminate the possibility that the absorption was due to CO_2 ice, the temperature was lowered to 190 K where the saturation vapor pressure of CO_2 is below 1 bar. At this low temperature, the sample spectrum shows the lattice mode absorptions of CO_2 ice at 68 cm^{-1} and 111 cm^{-1}[3]. These modes were not observed at 210 K, indicating that CO_2 ice was not present.

DISCUSSION

CO_2 has no permanent dipole moment and therefore does not have strong rotational transitions. Furthermore, its vibrational absorptions occur at frequencies above 600 cm^{-1}. Since the free CO_2 molecule has no strong absorption in the region of 75 cm^{-1}, we attribute the observed absorption to a rattling mode. In order to strengthen this conclusion, a future sample will be prepared using CO_2 gas molecules containing the carbon-13 isotope. Spectra obtained from such a sample should show an isotopic frequency shift in the observed absorption.

According to Mariner 7 radiometric measurements of the north polar region of Mars, surface temperatures reach about 148 K, while the CO_2 partial pressure is 6.5 mbar [1]. We intend to examine clathrate films under these conditions and to extract from their spectra dielectric properties that can be used in remote sensing simulations of the Mars ices.

ACKNOWLEDGEMENTS

This work is supported under NASA Center for Space Terahertz Technology Grant NAGW-1334.

REFERENCES

[1] S. L. Miller, "Clathrate Hydrates in the Solar System" in *Ices in the Solar System*, J. Klinger et al Eds., (D. Reidal Co., Dordretcht, Holland), pp. 59-79, 1985.

[2] S. L. Miller, "The Occurrence of Gas Hydrates in the Solar System", *Proceedings of the National Academy of Sciences*, Vol. 47, 1961, pp. 1798-1808.

[3] J. E. Bertie, H. J. Labbe, And E. Whalley, "Absorptivity of Ice I in the Range 4000-30 cm^{-1}", *Journal of Chemical Physics*, 50(10), pp. 4501-4521, 1969.

[4] S. G. Warren, "Optical Constants of Carbon Dioxide Ice," *Applied Optics*, 25(16), pp. 2650-2674, 1986.

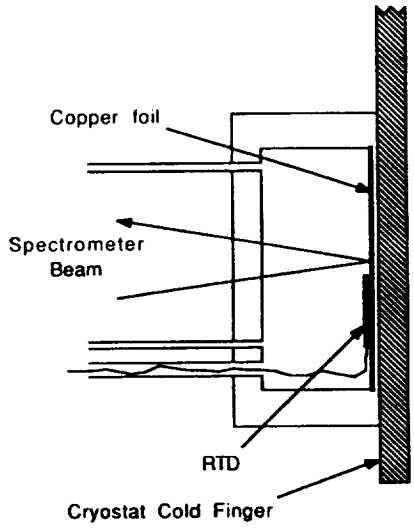

Figure 1: Sample Cell

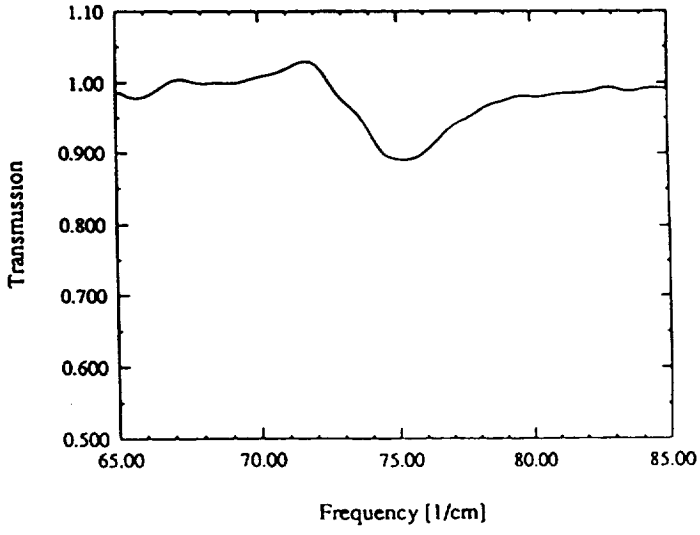

Figure 2: Transmission Spectrum

ORIENTATION OF PLANAR DEFORMATION FEATURES (PDFs) IN QUARTZ; F. Langenhorst and A. Deutsch; Institut für Planetologie, Wilhelm-Klemm-Str. 10, D-4400 Münster, Germany

Differently oriented single crystal quartz was shocked experimentally at pressures of 20 to 32 GPa and pre-shock temperatures up to 630°C. Based on this systematic investigation we can demonstrate that the orientation of planar deformation features in quartz is not only dependent on shock pressure but also on pre-shock temperature and shock direction. Moreover, the orientation of PDFs is strongly influenced by the set-up in recovery experiments.

PDFs in quartz are defined as optically recognizable, planar microstructures diagnostically produced by shock compression [1]. PDFs differ from all kind of microstructures found in volcanic environment [2] and therefore, their presence is a primary criterion for recognizing impact craters and ejecta layers such as the K/T boundary [3]. Because experiments have shown a pressure dependence of the orientation of PDFs (e.g. [4, 5]), this property is used extensively for shock wave barometry in natural impact sites. However, the unreflected application of experimental results neglects that parameters such as pre-shock temperature, shock direction, or the experimental arrangement may influence the spatial distribution of PDFs.

In order to test this assumption we performed in cooperation with Dr. U. Hornemann (Ernst-Mach-Institut, Weil am Rhein) shock experiments on single crystal quartz at pre-shock temperatures of 20°, 275°, 540°, and 630°C [7], and with shock directions [10$\bar{1}$0] and [0001]. Most of the recovery experiments were carried out by using a reverberation technique, whereas in only one experiment a single shock was produced (impedance method). In the former case 0.5 mm thin discs of single crystal quartz were used, in the latter a 15 mm thick cylinder. The orientation of PDFs was measured by means of a conventional universal stage and the results are given in Fig. 1.

Generally, in experimentally shocked quartz the four major orientations of PDFs {10$\bar{1}$3}, {10$\bar{1}$2}, {10$\bar{1}$1}, and {1122} can be indexed unequivocally in a stereoplot while some orientations claimed to occur subordinate in nature have never been detected in experiments (e.g. {11$\bar{2}$2}, [6]). Fig. 1a illustrates the frequency of PDFs in quartz for the pressure range from 20 to 32 GPa. Clear trends are discernible with increasing pressure: *(i)* {10$\bar{1}$3} decreases till it disappears totally at 32 GPa. *(ii)* {10$\bar{1}$2} occuring for the first time at 25 GPa increases distinctly until it is the only orientation at 32 GPa. *(iii)* {10$\bar{1}$1} and {11$\bar{2}$2} are absent above 25 GPa.

Compared to the unheated reference sample shocked at 20 GPa, pre-heating causes a broader distribution of PDFs but {10$\bar{1}$3} and {10$\bar{1}$1} still represent the prevailing orientations up to 540° C (Fig. 1b). In constrast, quartz pre-heated at 630° C and therefore shocked in the ß-structure totally lacks {10$\bar{1}$3} and the forms {10$\bar{1}$2} and {11$\bar{2}$1} occur frequently.

The shock direction affects the development of PDFs quite drastically as visible by comparing Figs. 1a, c, and d. For example, quartz shocked at 26 to 27.5 GPa parallel to the (0001)-face exhibits predominantly the form {10$\bar{1}$3} at all pre-shock temperatures. A shock front travelling parallel to (10$\bar{1}$0) however, results at identical pressures in PDFs with an orientation of {10$\bar{1}$2}.

Effects of the experimentation technique can be derived from Fig. 1d showing the orientation of PDFs in quartz shocked at 27.5 GPa. In comparison to the well defined peaks at {10$\bar{1}$2} found in samples from reverberation experiments, the impedance matching technique causes PDFs with a broad distribution pattern and indistinct maxima.

Our results have serious implications for shock-wave barometry in nature: the existing classification scheme [6] which relates PDF orientation exclusively to shock pressure is no longer applicable. In consequence we need more experimental data!

REFERENCES [1] Grieve R.A.F. et al. (1990) *EOS 71*, 1792. [2] Alexopoulos J.S. et al. (1988) *Geology 16*, 796. [3] Bohor B.F. et al. (1984) *Science 224*, 867. [4] Müller W.F. and Defourneaux W (1968) *Z Geophys* 34, 483. [5] Hörz F. (1968) in French B.M. and Short N.M., Mono Book Corp., 243-254. [6] Grieve R.A.F. and Robertson P.B. (1976) *Contrib Mineral Petrol 58*, 37. [7] Langenhorst F. et al. (1992) *Nature 356*, 507.

PDFs IN QUARTZ: LANGENHORST F. and DEUTSCH A.

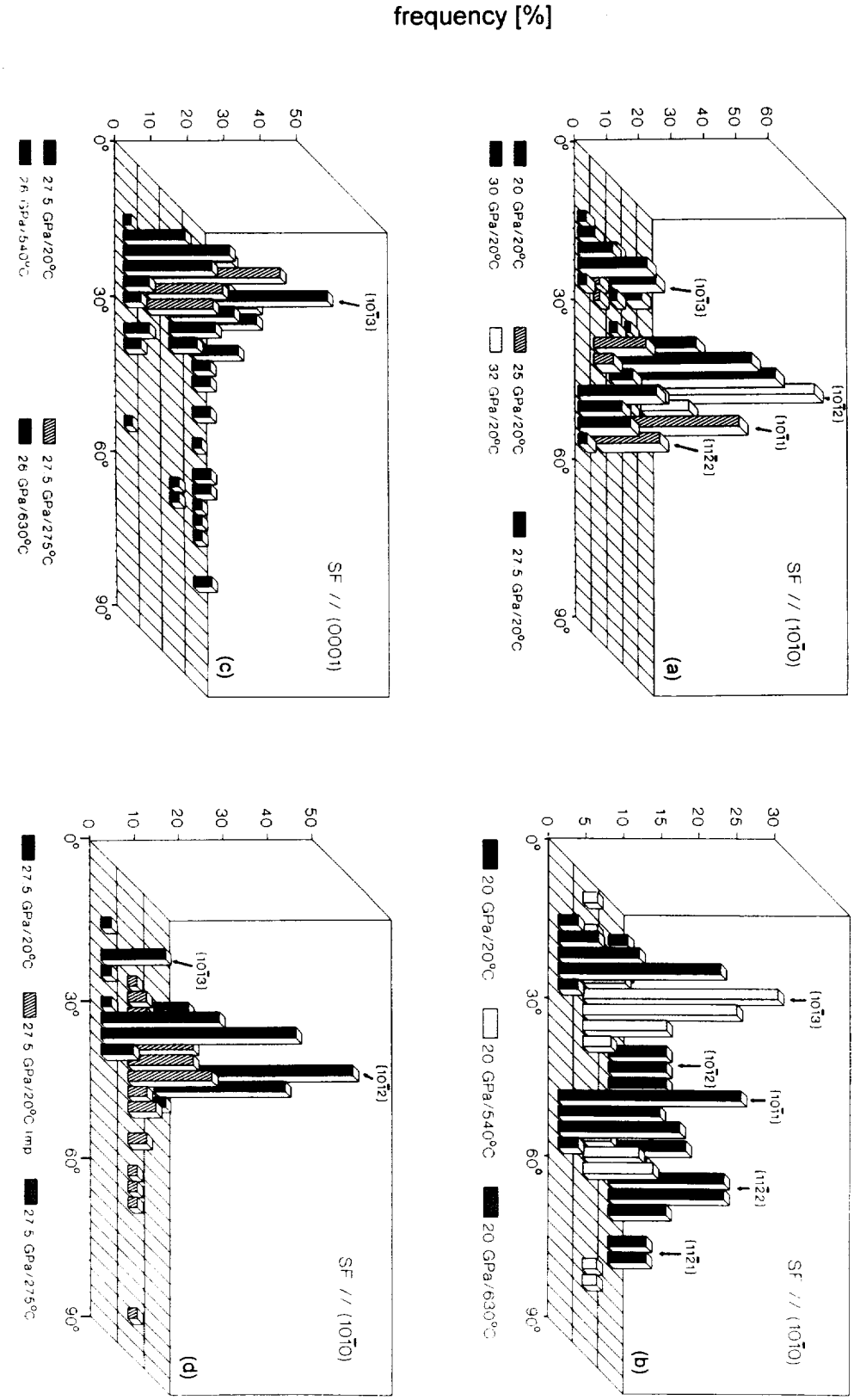

Fig. 1: Frequency distribution of PDFs in experimentally shocked single crystal quartz (a) - (c) reverberation technique (d) comparison reverberation - impedance matching (imp) technique; SF = shockfront

LUNAR PHASE FUNCTION EFFECTS ON SPECTRAL RATIOS USED FOR RESOURCE ASSESSMENT; S.M. Larson, J. Collins, R.B. Singer, J.R. Johnson, and D.E. Melendrez; Lunar and Planetary Laboratory/ Department of Geosciences, University of Arizona, Tucson, AZ 85721

Groundbased telescopic CCD images of 36 selected locations on the moon were obtained in five "standard" bandpasses at 12 phase angles ranging from -78° to +75° to measure phase function effects on the ratio values we have used to quantify the abundance of TiO_2 and qualitatively indicate soil maturity [**1**, **2**]. Consistent with previous studies, we find that the moon is "bluer" at small phase angles, but that the effect on the ratio values for TiO_2 abundance for the phase angles of our data is on the order of the measurement uncertainties throughout the range of abundances found in the mare. The effect is more significant as seen from orbiting spacecraft over a range of selenographic latitude.

Spectral ratio images (400/560 and 400/730 nm) have been used to map the abundance of TiO_2 [**1**, **2**] using the empirical relation found by Charette et al [**3**] from analysis of returned lunar soils. Additionally, the 950/560 and 950/730 nm image ratios have been used to define the regions of mature mare soil in which the relation is valid. Although the phase function dependence on wavelength has been investigated and quantified for small areas and the integrated disc [e.g. **4**, **5**], the effect specifically on TiO_2 mapping has not been rigorously determined. For consistency and convenience in observing the whole lunar front side, our mapping has utilized images taken $-15^{\circ}<\alpha<15^{\circ}$ when the moon was fully illuminated from earth; however, this includes the strong opposition peak.

CCD images with an approximate scale of 440 m per pixel were obtained with the 0.5 m Tumamoc Hill telescope from 11/91 to 2/92 through our usual filters having central wavelengths at 340, 400, 560, 730 and 950 nm. The 5 selected areas contained the full range of TiO_2 abundances, the MS-2 reference, pyroclastic deposits and highlands materials. The flat fielded images were registered, and counts were extracted from 2 by 2 pixel spots from homogenous areas as they appear in the 400/560 nm ratios. Extinction corrections for all filters were applied from nightly standard star observations.

Ratio values for all combinations of filters plotted against phase angle exhibit slightly asymmetric variations on either side of zero phase. The 400/560 nm curves used for TiO_2 mapping showed only the expected shift in ratio values according to TiO_2 abundance. The measurement uncertainties in shape of the curves are much smaller than the inherent uncertainty envelope of the Charette relation, so we conclude that phase corrections for our current maps are not necessary. It is clear, however, that for larger phase angles, such as might be experienced from orbiting spacecraft at high selenographic latitude, phase corrections will be important.

The phase curve at 950 nm was sufficiently different from the others as to

suggest that the optical properties associated with the strong pyroxene absorption play an important role. McCord [4] had pointed out the connection of differential color with phase and the wavelength dependence of polarization of the moon as measured by Gehrels et al [6]. The strong polarization effects in pyroxene measured by Burns [7] is consistent with the pronounced phase effect on the 950 nm band.

This work is supported by the NASA/University of Arizona Space Engineering Research Center, and NASA grant NAGW-247.

[1] Johnson, J.R., Larson, S.M. and Singer, R.B. (1991), *J. Geophys. Res.* **96**, 18861-18882
[2] Melendrez, D.E., Larson, S.M., Johnson, J.R. and Singer, R.B. (1993), *submitted to J. Geophys. Res.*
[3] Charette, M.P., McCord, T.B., Pieters, C., and Adams, J. (1974), *J. Geophys. Res.* **89**, 1605-1613.
[4] McCord, T.B. (1969) *Astron. J.* **74**, No.2 273, 278.
[5] Lane, A.P. and Irvine, W.M. (1973), *Astron. J.* **78**, No. 3 267-277.
[6] Gehrels, T., Coffeen, T., Owings, D. (1964), *Astron. J.* **69**, No. 10 826-852.
[7] Burns, R.G. (1965) Ph. D. thesis, Univ. of Calif., Berkeley.

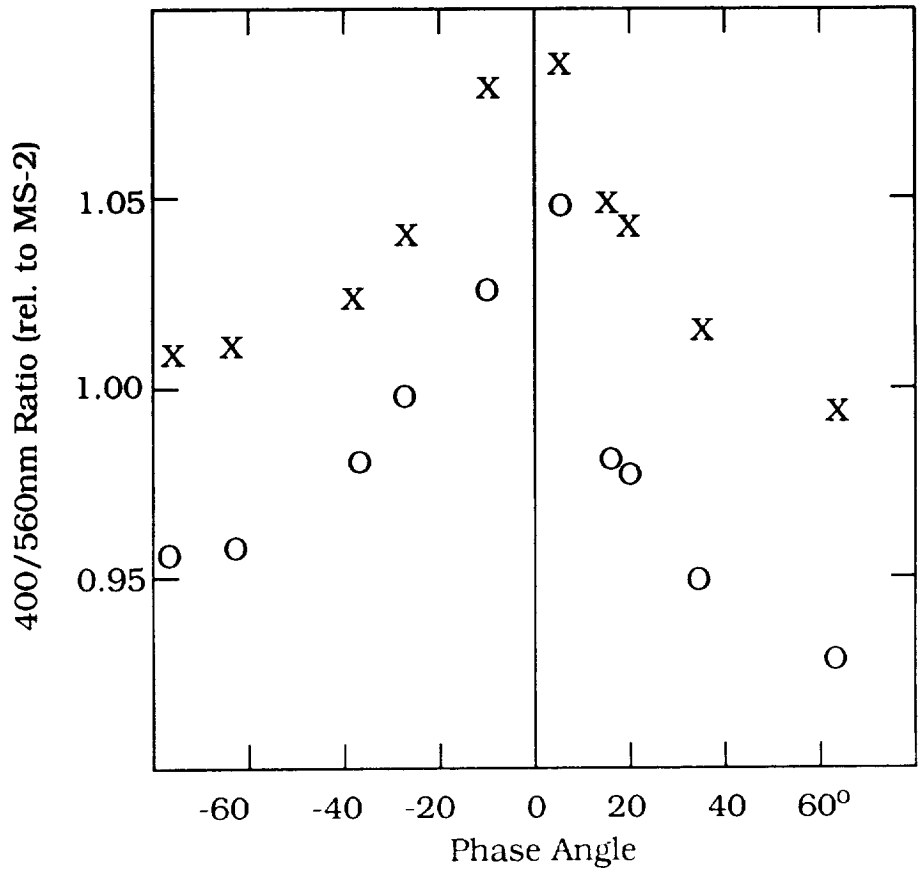

Ratio values for typically high (X) and low (O) TiO_2 areas in Mare Tranquillitatis over the range of observed phase angles.

THE ASTROPHYSICAL INTERPRETATION OF ISOTOPE ANOMALIES IN GRAPHITE AND SiC GRAINS OF CHONDRITES.

A.K.Lavrukhina. V.I.Vernadsky Institute of Geochemistry and Analytical Chemistry, Russian Academy of Sciences, Moscow, Russia

The C, N, Mg isotopic compositions in graphite and SiC grains of carbonaceous chondrites can be explained by nuclear processes in massive O,B stars of second generation passed a stage of WR star with intensive stellar wind, where grain condensation had taken place.

The interstellar graphite and SiC grains with anomalous isotopic compositions of C, N, Ne, Si and other elements of nucleosyntetic origin, found in non-equilibraited chondrites, are most suitable for determination of astrophysical objects, where nucleosynthesis had taken place.We were examined two objects: 1-massive O,B stars of second generation passed a stage of WR star with intensive stellar wind (O,B-WR model) (1) and 2- low-mass stars ($1 \leq M/Mo \leq 3$) during thermally pulsing asymptotic giant branch phase (TP-AGB model)(2). The calculations by means of these models were used for explanation of Ne and Mg isotopic anomalies in graphite and SiC grains of the Murchison CM carbonaceous chondrite (3-6). Graphite grains are carriers of pure Ne-E(L), SiC grains are carriers of Ne-E(H) and ^4He. They have various isotopic compositions of C and N (5,7). The most of SiC grains have $^{12}C/^{13}C=40-90$, but many grains have $^{12}C/^{13}C=4-40$. The unusual grains X have $^{12}C/^{13}C=200-2500$ and grains Y ~ 200. For most of SiC grains and Y grains $^{14}N/^{15}N=275-5000$ and X grains $^{14}N/^{15}N=15-200$. The graphite grains have $^{12}C/^{13}C=4-5000$ and $^{14}N/^{15}N=170-300$. Only four grains have anomalous N($^{14}N/^{15}N=100-700$). According to (1) such isotopic compositions of C and N can be explained by mixing of the products of following nuclear reactions: 1) quasi-equilibrium CNO cycle at H burning stage, explaining high enrichments of graphite and SiC grains in ^{13}C and SiC grains in ^{14}N, 2) reactions on He burning stage: $3^4He \rightarrow {}^{12}C$, $^{12}C(\alpha,\gamma)^{16}O$ and $^{14}N(n,p)^{14}C$. Former leads to high $^{12}C/^{13}C$ rations (up to 5000), the latter leads to moderate impoverishments in ^{12}C and third leads to very high enrichments of SiC X grains in ^{15}N. According to (8) in massive stars CNO cycle happens at O,B star and WN stages, and He burning happens in star core at WR star stage (8,9) with intensive wind, carring out nuclear reaction products into circumstellar envelope.

By laser gas extraction technique high contents of Ne-E(H) in SiC grains (up to $2.74\ 10^{-3}$cc g^{-1}) and Ne-E(L) in graphite grains (up to $16.89\ 10^{-3}$cc g^{-1}) were discovered (6).Only a small fraction ($\sim 4\%$) of SiC grains accounts for $\sim 90\%$ of Ne-E(H) and ^4He, but $\sim 30\%$ of graphite grains appear to carry Ne-E(L). The implantation is incorporation mechanism for Ne-E(H) and ^4He, thus there is no need to invoke in situ decay of ^{22}Na as the source for Ne-E(H) (3). During He burning ^{14}N is transformated into ^{22}Ne through

the chain: $^{14}N(\alpha,\gamma)^{18}F(\beta^+\nu)^{18}O(\alpha,\gamma)^{22}Ne$. This process has taken place in He shell of carbon stars of population I for TP-AGB model and in He core of WR stars for O,B-WR model. ^{22}Na is not formed in He burning.

However ^{22}Na may be a source of pure ^{22}Ne-E(L) in graphite grains (6). ^{22}Na forms in massive stars during Ne-Na cycle of H burning at $T=5\times10^7$K. The calculations (8) for stellar wind of WR stars M=80 Mo at this stage give very low value for $^{22}Ne(^{22}Na/^{20}Na=7\times10^{-4})$. Besides in these conditions C/O < 1, and graphite and SiC grains would not condense. ^{22}Na as sourse of pure ^{22}Ne can be only formed in explosion H burning. But this process should not be lead to explanation of the observed anomalies in isotopic composition of Mg at the expence of decay of ^{26}Al, which in Mg - A cycle of H burning has formed. So at supernova explosion $(^{26}Al/^{27}Al)_o=0.006$ (10), which is lower than maximum values of this ratio for graphite and SiC grains (5,7). Hence ^{22}Na is not source of pure ^{22}Ne-E(L).

The calculations (2) for TP-AGB model give $^{20}Ne/^{22}Ne=0.07-0.085$, which are near to minimum value of this ratio for SiC grains of KJH fraction (0.0973) (3). And they are essentially higher than most of values for graphite (0.015--0.7) (11). According to O,B-WR model this value is equal to 0.0083 (8). It can correspond to end member of mixing line both for Ne-E(H) and for Ne-E(L).

In stellar wind of WN stars ratios of $(^{26}Al/^{27}Al)_o$ are 0.006-0.5 (8). These limits correspond to corresponding values for SiC grains (4.10^{-5}-0.61) (7) and for graphite grains (0.005-0.086) (5).

We propose the following scenario (12). In stellar wind of O,B(WN) star in CNO cycle end has taken place condensation of ultra small grains of Al(^{26}Al)N. According to (13) it happens over wide limits of C/O ratious (lg C/O from -6 to +7). In stellar wind of WR(WC) star at He burning stage, where C/O > 1 (8), AlN grains are condensation embryos of graphite and SiC grains. Graphite grains condense at $T \geqslant 1700$ K and SiC grains at T=1300 K (13). This difference of condensation temperatures has lead to various degree of noble gas retention of graphite and SiC grains. Graphite grains lose implanted ^{4}He and small fraction of SiC grains should trappe its.

References. (1)Lavrukhina A.K.(1991)Geochimia, 1768; (2)Gallino R. et al.(1990)Nature, 348, 298; (3)Lewis R.S. et al.(1990)Nature, 348, 293; (4)Amari S. et al.(1990)LPS XXI, 19; (5)Hoppe P. et al.(1992)LPS XXIII,553; (6)Nichols R.H. et al.(1992)LPS XXIII,989; (7)Amari S. et al.(1992) LPS XXIII,27; (8)Prantzos N.(1985)Preprint; (9)Abbott D. and Conn P.(1987)Ann.Rev.Astron.Astrophys,25,113; (10) Woosley S. and Weaver T.(1986)Nucleosynthesis and its Implications on Nuclear and Particle Physics,145; (11)Amari S. et al.(1990)Nature,345,238; (12)Lavrukhina A.K., in press; (13)Bussoletti E.(1985)Riv. nuovo ciem,8,1.

N94-16344

ON POSSIBLE Mn-53 HETEROGENEITY IN THE EARLY SOLAR SYSTEM;

A.K.Lavrukhina and G.K.Ustinova, Institute of Geochemistry and Analytical Chemistry, Russian Acad.Sci., Moscow 117334, Russia

There are shown the effects of influence of shock wave propagation on the energy spectrum of accelerated particles that lead to different production rates of radionuclides, in particular, Mn-53, on small scales in the early solar system.

Search for evidence for extinct Mn-53 has stimulated investigations of Cr isotope anomalies in meteorites. The linear correlation between the magnitude of the Cr-53* excesses and the Mn/Cr ratio that unambiguously proves the in situ decay of Mn-53 has been detected, really, in different mineral phases of some carbonaceous and enstatite chondrites, primitive achondrites, pallasites and iron meteorites /1-5, etc./. However, the data on the Cr-53* excess rarely define a single linear array on a Mn-53 -Cr-52 evolution diagram even for meteorites of the same chemical group. A clear isochron with Mn-53/Mn-55 = $(4.4\pm1.0)\cdot10^{-5}$ (in range of ~2.4 to $\sim9\cdot10^{-5}$) is observed for CAI of the Allende C3-chondrite /1/ while the data for the Murchison C2- and Orgueil C1-chondrites fall much lower corresponding rather to Mn-53/Mn-55 $< 2\cdot10^{-5}$ /2/. In the case of iron meteorites it ranges from $<5\cdot10^{-8}$ to $<5\cdot10^{-5}$ /3/.

If the initial Cr and Mn distribution in the early solar system was homogeneous, then the different magnitude of the excess of the radiogenic Cr-53* in the mineral phases was conditioned by the different time of their solidification. Thus, using Mn-53 as a chronometer, one could build a time scale for evolution of the matter in the early solar system during, at least, n·10 Myr.

Unfortunately, the high precision investigations of Cr isotope composition in meteorites revealed essential variations of it, the correlation effects for Cr-54 and Cr-53 to be detected too /2,5,6/. It clearly testifies to initial Cr heterogeneity in the early solar system, although, partly, it could be explained by Cr diffusion between different mineral phases /5/, fractionation /2,6/ or even terrestrial weathering /6/.

The authors of practically all the cited works also pointed out possible initial heterogeneity of Mn-53 in the early solar system. This point of view attracts attention in the light of the described earlier possible mechanism of forming isotopic heterogeneities on the primordial stage of evolution of the matter /7,8/. The question is about heterogeneity of the conditions for isotope production during shock wave propagations (e.g., in expanding shells of a supernova or in collisions of strong protosolar winds with matter of the accretion disc) because then the energy spectrum of accelerated particles becomes more rigid /9/; therefore, their fluxes at high energies considerably increase, and the statistically weighted cross sections of many isotopes, whose excitation functions are sensitive to the form of the energy spectrum of particles, change too. Whereas index γ of the solar cosmic ray spectrum can reach 6, and it of the galactic cosmic ray spectrum equals to 2.5, but during the passage of

ON Mn-53 HETEROGENEITY: Lavrukhina A.K. and Ustinova G.K.

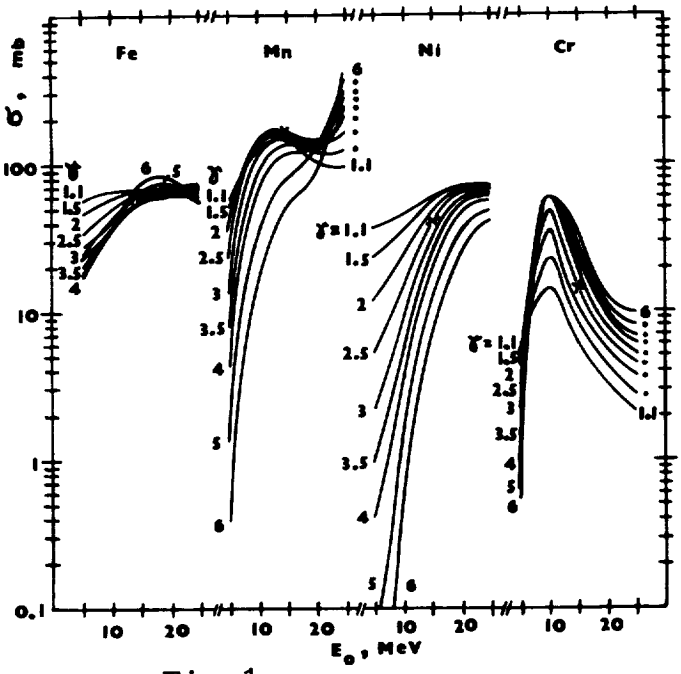

Fig.1

shock waves it can decrease down to 1.5-2 /10/. The observed turbulence of neutral gas in the molecular clouds surrounding supernovas can even form the spectrum of particles with $\gamma \sim 1$ /11/. It is shown in /7/ that with changing γ from 1.1 to 6 the variation of integral flux of protons above the cut-off energy E_o of the spectrum amounts to 6 orders of magnitude. Possible variations of the statistically-weighted (according to the energy spectrum of protons) cross sections of Mn-53 production on Fe, Mn, Ni and Cr in dependence on E_o for different γ (figures on the plot) are demonstrated in Fig.1. The values of the cross sections corresponding to some average irradiation conditions in the early solar system are marked by crosses /7,8/. The ratios Mn-53/Mn-55 and Cr-53*/Cr-52 depending on E_o for different γ are presented in Fig.2. It is seen that these ratios formed in conditions of shock wave propagation can vary by $\sim$7 orders of magnitude that virtually corresponds to the measured range of them in meteorites. In the average irradiation conditions $^{53}Mn/^{55}Mn = 1.00 \cdot 10^{-4}$ is obtained (a cross on the plot) that is in accordance with its maximum measured values in the refractory CAI minerals. In the minerals with much lower solidification time ($\lesssim$1000K) the measured values of this ratio are decreased by 2-3 orders of magnitude. Apparently, those minerals were condenced in calmer (and colder) regions of the early solar system where due to the softness of the particle spectra ($\gamma \gtrsim 4$) smaller amounts of Mn-53 were produced.

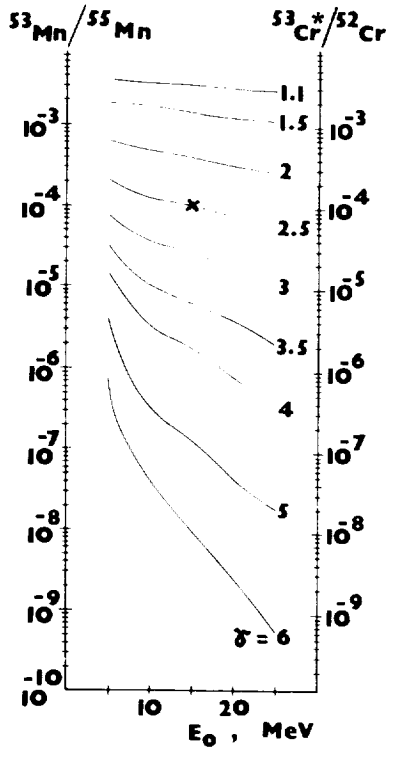

Fig.2

References

[1] Birck J.L.,Allegre C.J. Nature 331(1988) 579. [2] Harper C.L.et al. LPS XXIII (1992) 489,491. [3] Hutcheon I.D.et al.ibid.565. [4] Lugmair G.W.et al.ibid.823. [5] Goresy A.E.et al.ibid.331. [6] Rotaru M.et al. LPS XXI(1990) 1037. [7] Lavrukhina A.,Ustinova G. LPS XXIII (1992)761. [8] Ustinova G.,Lavrukhina A. ibid. 1461. [9] Ellison D.C.,Eichler D. Ap.J. 286 (1984)691. [10] Berézhko E.G.,Krymski G.P. Uspekhi Phys.Nauk (Russian) 154(1988)49. [11] Ginzburg V.L.,Dogiel V.A. ibid. 158(1989)3.

ON ORIGIN OF THE OLIVINE INCLUSIONS FROM THE KAINSAZ CO CARBONACEOUS CHONDRITE. A. K. Lavrukhina, Z. A. Lavrentjeva, A. Yu. Ljul, and K. I. Ignatenko. V. I. Vernadsky Institute of Geochemistry and Analytical Chemistry, Russian Academy of Science, Moscow, Russia.

Olivine inclusions and chondrules of Kainsaz have been formed in a unique process of dust matter melting.

The elemental abundances of four fractions of olivine (Ol) inclusions from Kainsaz were analyzed by INAA. The inclusions of fraction A ($160 < d < 260$ μm) have Fe-Ni grains, the inclusions of fractions B ($100 < d < 160$ μm), C ($160 < d < 260$ μm), and D ($260 < d < 360$ μm) have not theirs. Table shows the everage elemental enrichment factors relative to CI chondrite (1) for each fraction and chondrules of Kainsaz (2). The enrichment factors of siderophile Co, Ni, Ir, Au and non-refractory Na in all fractions are less than 1. The factors of refractory Ca, Sc, La, Sm, Yb are comparative with the corresponding values of Ol aggregates of Allende CV (average 4.76) (3). For chondrules of Kainsaz these values are lower. Fraction A is enriched in Co, Ir, Au relative Ni and CI chondrites: Ir > Au > Co. The values of $(Me/Ni)_{inc}/(Me/Ni)_{CI}$ are equal to 3.25 for Ir, 2.1 for Au and 1.2 for Co. The superabundances in Ir and Au relative to Ni witness to formation of Fe-Ni grains of Ol inclusions by agglomeration of grains enriched in refractory metal with grains enriched in non-refractory metal (Au). The enrichments of fraction A in Ca, Sc, La, Sm, Yb witness about presence of high-temperature phases in Ol inclusions.

Ol inclusions with Fe-Ni grains are like to lithic PO and POP chondrules of Kainsaz in accordance with abundances of various volative elements Ca, Cr, Fe, Au, but differ from them in low abundances of Na, Sc, Co, Ni, Ir (also of various volatilities). Such regularities can not be as result of successive condensation of these elements from solar gas. Hence Ol inclusion with Fe-Ni grains are, lake to lithic chondrules, partial melt agglomerates of different temperature mineral phases.

The elemental enrichment factors of Ol inclusions without Fe-Ni metal (fractions B,C, and D) are less than 1, with exceptions of Sc, Cr, and Eu (in fraction C). Co and Ni are very depleted. The abundances of non-refractory elements Na, Co, Eu, Au are increased and of refractory elements Sc, Sm, Ir are decreased with increasing of grain sizes. The contents of Na, Ca, Co, Ir are essentially less than those in lithic and droplet PO and POP chondrules of Kainsaz (2). The contents of Sc in fraction B, and Cr, Fe in all fractions lie in limits their values of these chondrules. The model of REE in fraction B is flat. The ratios between siderophile elements in Ol inclusions without Fe-Ni grains differ from those of Ol inclusion with Fe-Ni grains. Thus the ratios of $(Co/Ni)_{inc}/(Co/Ni)_{CI}$ are equal to 0.02 for former and 0.01 for the latters. This value corresponds

OLIVINE INCLUSIONS... Lavrukhina A.K. et al.

Table. Average element enrichment factors of olivine inclusions and chondrules of Kainsaz

Element	A	B	C	D	Chondrules (2)
Na	0.66	0.41	0.57	0.67	1.13
Ca	3.1	0.96	<1.10	0.96	3,85
Sc	1.43	1.93	1.68	1.31	2.36
Cr	0.95	1.03	1.17	1.20	1.13
Fe	0.55	0.74	0.75	0.86	0.83
Co	0.31	0.23	0.31	0.35	0.74
Ni	0.25	0.12	0.17	0.16	0.68
La	5.96	0.85	<1.27	0.85	3.67
Sm	5.0	0.80	<1.36	0.54	3.58
Eu	<7.17	0.95	1.53	<1.79	2.51
Yb	5.9	0.98	<1.84	0.98	3.40
Lu	<7.5	0.75	<4.1	<2.5	3.0
Ir	0.80	0.68	0.47	0.23	1.32
Au	0.52	0.24	--	0.81	0.73

to the same of metal condensate from solar gas at $T \leq 1460$ K and $p=10^{-3}$ atm (4). The increasing of Co/Ni ratios in metal condensates had been found by us (5) at vacuum recondensation of metal streams, formed by heating of iron meteorite Sikhote Alin spieces at 1600°C. Obviously Ol unclusions of fractions B,C,D content submicron Fe-Ni grains condensated from gas which in chondrule formation process had formed (6). The decreasing of $(Ir/Ni)_{inc}/(Ir/Ni)_{CI}$ from 5.8 to 1.4 and increasing of $(Au/Ni)_{inc}/(Au/Ni)_{CI}$ from 2.0 to 5.1 and also of non-refractory element contents with grain size increasing of Ol inclusions can be explained by the model (7), according which large Ol inclusions, also as large chondrules, from small ones have been formed. This process are accompanied by capture of fine dispersical matter, enriched in non-refractory and depleted in refractory elements.

Thus the above-mentioned data support an idea what Ol inclusions and chondrules of Kainsaz have been formed in a unique process of dust matter melting. The compositions of these matters were changed at the expence of increasing of low-temperature matter contents in succession: Ol unclusions with Fe-Ni grains < lithic and droplet PO and POP chondrules < Ol inclusions without Fe-Ni grains.

References: (1)Anders E. and Grevesse N.(1989)GCA,53, 197-214. (2)Lavrukhina A.K. et al. (1987)Geochimia, 44-63. (3)Grossman L. et al.(1979) GCA, 43, 817-829. (4)Grossman L. (1985)Cosmochimia of Moon and Planets. M. Nauka, 89-96. (5)Lavrukhina A.K. et al.(1979)Meteoritika,38, 62-64. (6) Lavrukhina A.K.(1989)Geochimia, 1407-1416. (7)Lavrukhina A.K.(1989) Ibid., 665-678.

TEACHING PLANETARY SCIENCES TO ELEMENTARY SCHOOL TEACHERS: PROGRAMS THAT WORK; Larry A. Lebofsky, Lunar and Planetary Laboratory, University of Arizona 85721 and Nancy R. Lebofsky, Steward Observatory, University of Arizona, Tucson, Arizona 85721

Planetary sciences can be used to introduce students to the natural world which is a part of their lives. Even children in an urban environment are aware of such phenomena as day and night, shadows, and the seasons. It is a science that transcends cultures, has been prominent in the news in recent years, and can generate excitement in young minds as no other science can. Planetary sciences also provides a useful tool for understanding other sciences and mathematics, and for developing problem solving skills which are important in our technological world. However, only 15 percent of elementary school teachers feel very well qualified to teach earth/space science, while better than 80% feel well qualified to teach reading; many teachers avoid teaching science; very little time is actually spent teaching science in the elementary school: 19 minutes per day in K–3 and 38 minutes per day in 4–6.

While very little science is taught in elementary and middle school, earth/space science is taught at the elementary level in *less than half* of the states. It has been pointed out that science is not generally given high priority by either teachers or school districts, and is certainly not considered on a par with language arts and mathematics. Therefore in order to teach science to our youth, we must empower our teachers, making them familiar and comfortable with existing materials.

To address these needs we conducted several workshops for elementary school teachers over the last few years. Teachers were introduced to space science concepts and hands-on activities that they could use in their classrooms.

However, Tucson has another, but not unique, problem. Tucson is a culturally-diverse (about 25% Indian/Black/Hispanic) city with a wide variety of public and private schools. The largest public school district, the Tucson Unified School District (TUSD), provides a neighborhood school system enhanced with magnet, bilingual and special needs schools for a school population of 57,000 students that is 4.1% Native American, 6.0% Black, and 36.0% Hispanic (1991). It is predicted that by the year 2050 the minority population in the U.S. will be approximately 40%. However, in TUSD, the "minority" will be the majority by 1993. In Sunnyside, another of Tucson's largest districts, the minority population is over 75% and the Hispanic population is over 72% (1991). This makes TUSD and the other school districts in and around Tucson and the rest of Pima County ideal for a program that reaches students of diverse ethnic backgrounds.

In our earlier workshops, several of our teachers taught in classrooms where the majority of the students were Hispanic (over 90%). However, few space sciences materials existed in Spanish. Therefore, most of our materials could not be used effectively in the classroom.

To address *this* issue, we have translated NASA materials into Spanish and are conducting a series of workshops for bilingual classroom teachers from Tucson and surrounding cities.

We will discuss in detail our space sciences workshops and our bilingual classroom workshops and how they address the needs of elementary school teachers in Arizona.

A SIMULTANEOUS ESTIMATION OF THE MASS OF MARS AND ITS NATURAL SATELLITES, PHOBOS AND DEIMOS, FROM THE ORBITAL PERTURBATIONS ON THE MARINER 9, VIKING 1, AND VIKING 2 ORBITERS; F. G. Lemoine[1,2], D. E. Smith, S. K. Fricke[3], and J. J. McCarthy[4], [1]Laboratory for Terrestrial Physics, NASA/Goddard Space Flight Center, Greenbelt, MD 20771, [2]Dept. of Astronomy, University of Maryland, College Park, MD 20742-2421, [3]RMS Technologies, Inc., Landover, MD 20785, [4]Hughes STX Corporation, Lanham, MD 20706.

The natural satellites of Mars, Phobos and Deimos, caused perturbations on the orbits of the Mariner 9, and the Viking spacecraft that have been used to estimate the satellite masses. The Viking spacecraft were specifically targeted to make close flybys (within a few hundred kilometers) of Phobos in February 1977 and of Deimos in October 1977 [1,2]. These close encounters have been used to estimate the moons' gravitational constant, GM (the universal constant of gravitation multiplied by the satellite mass). However, the Viking and Mariner 9 spacecraft made numerous flybys of Phobos and Deimos at distances of a few thousand kilometers. The tracking data from these more 'distant' encounters have been processed to estimate the masses of Mars, Phobos, and Deimos.

The data include the Mariner 9 Doppler data from November 1971 through March 1972, and the Viking Orbiter Doppler data from orbit insertion in 1976 through January 1979. The data were processed in arcs three to six days in length using the GEODYN orbit determination program, which has been previously used in the analysis of planetary tracking data [3,4]. We processed the spacecraft-based optical observations of Phobos and Deimos [5,6] to produce the satellite ephemerides used in this study. In order to minimize the possibility of ephemeris error contaminating the GM estimates, we have specifically excluded the tracking data from the close flybys (less than 750 km).

During the Mariner 9 mission, the majority of the Phobos flybys were at distances of 3,750 to 4,500 km. In contrast, the flyby distances to the Viking-1 Orbiter ranged mostly from 1,000 to 4,000 km. The Viking-2 arcs while the spacecraft was at 300 km periapse altitude are only weakly sensitive to Phobos since no flybys occur at distances closer than 5,000 km.

In units of km^3/s^2, we find the following estimates for the GM of Mars and Phobos:

Data	Mars GM	Phobos GM
Mariner 9	42828.29 +/- 0.73	0.54 +/- 0.08
Viking 1	42828.32 +/- 0.04	0.54 +/- 0.02
Viking 2	42828.33 +/- 0.13	0.66 +/- 0.05
VO-1 + VO-2 + Mariner 9	42828.32 +/- 0.04	0.55 +/- 0.02

The Phobos GM estimates may be compared with the estimates obtained by Christensen et al. [1] using 14 Viking flybys within 213 km of 0.66 +/- 0.08 km^3/s^2, and by Kolyuka et al. [7] of 0.722 +/- 0.005 km^3/s^2 using the data from Soviet Phobos II Orbiter. Using the Phobos volume estimate of 5680 +/- 250 km^3 from Duxbury [8], our Phobos GM calculations indicate a bulk density of 1.44 to 1.74 g/cm^3. These values may have implications for both the models of the composition of Phobos and its origin since they can be accommodated only by presuming either a high porosity of the regolith or a high concentration of a low density material such as water ice within the moon [9].

Our estimates for the GM of Mars agree quite closely with the values determined from Null [10] using the Mariner 4 hyperbolic flyby tracking data of 42828.32 +/- 0.13 km^3/s^2; and from O'Neil et al. [11] using the Mariner 9 hyperbolic approach data of 42828.35 +/- 0.55 km^3/s^2. We find that the Mariner 9 Orbiter tracking data, and the Viking 2 Orbiter 1500 km periapse tracking data supply the weakest determinations for the Mars GM, whereas the Viking-1 Orbiter 1500 km and Viking-2 Orbiter 300 km periapse data make the strongest contributions.

The mass of Deimos is dependent on analysis of tracking data from only three close flybys of the moon in October 1977 [2]. During the interval from July 23, through October 30, 1977, the Viking-2 Orbiter made ten flybys between 1,000 and 3,500 km. These distant encounters may be used to obtain an independent estimate of the Deimos mass, as with Phobos.

References: [1] Christensen, et al., (1977), *GRL*, Vol. 4, No. 12, pp. 555. [2] Hildebrand et al., (1979), *Natural and Artificial Satellite Motion*, The Univ. of Texas Press. [3] Smith et al., (1992), *EOS Trans. Am. Geophys. Un.*, 73. [4] Nerem et al., 1992, submitted to *GRL*. [5] Duxbury, T. and J. Callahan (1988), *Astron. and Astrophy.*, 201, pp. 169. [6] Duxbury, T. and J. Callahan (1989), *Astron. and Astrophy.*, 216, 1989. [7] Koluyka et al., (1991), *Planet Space Sci.*, 39, pp. 349. [8] Duxbury (1991), *Planet. Space Sci.*, 39, pp. 355. [9] Burns (1992), *Mars*, The Univ. of Arizona Press, pp. 1283. [10] Null (1969), *Bull. Amer. Astron. Soc.*, 1, pp.356. [11] O' Neil et al. (1973), *JPL Technical Report 32-1586.*

MODELS OF THERMAL/CHEMICAL BOUNDARY LAYER CONVECTION: POTENTIAL APPLICATION TO VENUS.

A.Lenardic and W.M.Kaula, UCLA Dept. of Earth and Space Sciences, Los Angeles, CA 90024

Introduction: The upper boundary layer of Venus is comprised of at least two distinct chemical components, mantle and crust. Fluid dynamical models of convection within Venus' mantle have been primarily of the thermal boundary layer type. Models assessing the ability of convective mantle flows to deform the crust have been undertaken, but models exploring the effects of a variable thickness crust on mantle convection have been largely lacking. A Venusian crust of variable thickness could couple back into, and alter, the mantle flow patterns that helped create it, leading to deformation mechanisms not predicted by purely thermal boundary layer convection models. We explore this possibility through a finite element model of thermal/chemical boundary layer convection. Model results suggest that a crust of variable thickness can serve as a mantle flow driver by perturbing lateral temperature gradients in the upper mantle. Resulting mantle flow is driven by the combination of free convection and nonuniform crustal distribution. This combination can lead to a flow instability manifest in the occurrence of episodic mantle lithosphere subduction initiated at the periphery of a crustal plateau. The ability of a light, near surface, chemical layer to potentially alter mantle flow patterns suggests that mantle convection and the creation and/or deformation of such a chemical layer may be highly nonseperable problems on time scales of 10^8 years.

Models and Discussion: We employ a 2-D finite element code [1], modified to treat multi-component flow problems [2]. We model a system comprised of a thin layer of chemically light material, meant to mimic crust, imposed within the upper thermal boundary layer of a deep layer of heavier, thermally convecting material, meant to mimic mantle. Isoviscous and temperature and composition dependent newtonian rheologies are investigated.

For the type of system we model, the crust can potentially thicken above mantle downwellings: zones of near surface convergence [3]. Once a crust of spatially varied thickness has been established it can serve as a driver for flow in the mantle [4,5,6,7,8]. Mantle flow associated with crustal thickness variations results from the modification of horizontal temperature gradients in the upper most mantle by one or more of the following effects: 1) lower thermal conductivity in the crust vs. mantle; 2) higher density of heat producing elements in the crust; 3) crustal thickness approaching the unperturbed thermal boundary layer thickness. For a mantle marginally stable against convective instability due to vertical temperature gradients, horizontal temperature gradients due to crustal thickening can cause an instability characterized by traveling or standing wave solutions for the crust/mantle interface [7]. For an unstable mantle, system evolution can be characterized as the nonlinear superposition of flow due to free convection in the mantle and flow driven by horizontal temperature gradients due to a nonuniform distribution of a light chemical component in the upper thermal boundary layer [5]. When the light component is deformable crust, as in the case of our models, crustal deformation and mantle flow become tightly coupled (i.e., crustal deformation resulting from flow in the mantle leads to spatial and temporal redistribution of crustal thickness, which feeds back into the mantle altering the flow via the introduction of horizontal temperature variations dependent on the shape of the crust/mantle interface, which in turn affects subsequent deformation, etc.). The interconnection of mantle flow drivers in such a system allows for deformation mechanisms unique to thermal/chemical boundary layer convection. A specific mechanism is associated with an upper boundary layer instability that has some similarity to lithospheric subduction [9]. This instability can be episodic in nature; delay intervals are characterized by heating of the mantle and relative stagnation of flow while instability intervals involve bursts in flow velocities and significant increases in surface heat flux.

Conclusion: Thermal/chemical boundary layer convection models show how nonuniform crustal thickness can alter convective flows in the mantle, the strongest alteration involving complete flow reversal. Strong time dependence occurs at Rayleigh numbers for which thermal boundary layer models predict largely steady state flow in the mantle, i.e., relatively fixed convection cells. Model results suggest that, on the time scale of mantle overturn, crustal deformation and mantle convection can not be treated as separable problems (this statement also applies to the interaction of a residuum layer with mantle convection). The models further elucidate various flow and deformation mechanisms unique to thermal/chemical boundary layer systems. The relevance of these mechanisms to the evolution of Venus awaits more thorough comparisons of various model predictions to geophysical observations. What seems certain is that differentiated terrestrial planets possessing thermal/chemical boundary layers will evolve differently from hypothetical planets possessing purely thermal boundary layers. As such, further fully dynamic convection models allowing for thermal/chemical boundary layers are in order.

[1]King, S.D. et al., *Phys. Earth Planet. Inter., 59,* 195-207, 1990. [2]Lenardic, A., and W.M. Kaula, *J. Geophys. Res., 97,* accepted, 1992. [3]Bindschadler, D.L., and E.M. Parmentier, *J. Geophys. Res. 95,* 21,329-21,344, 1990. [4]Pekeris, C.L., *Roy. Astron. Soc. Geophys. Suppl., 3,* 343-367, 1935. [5]Elder, J., *Nature, 214,* 657-660, 1967. [6]Howard, L.N., et al., *Geophys. Fluid Dynamics, 1,* 123-142, 1970. [7]Busse, F.H., *Geophys.J. R. astr. Soc., 52,* 1-12, 1978. [8]Gurnis, M., *Nature, 332,* 695-699, 1991. [9]Lenardic, A., et al., *Geophys. Res. Lett., 18,* 2209-2212, 1991.

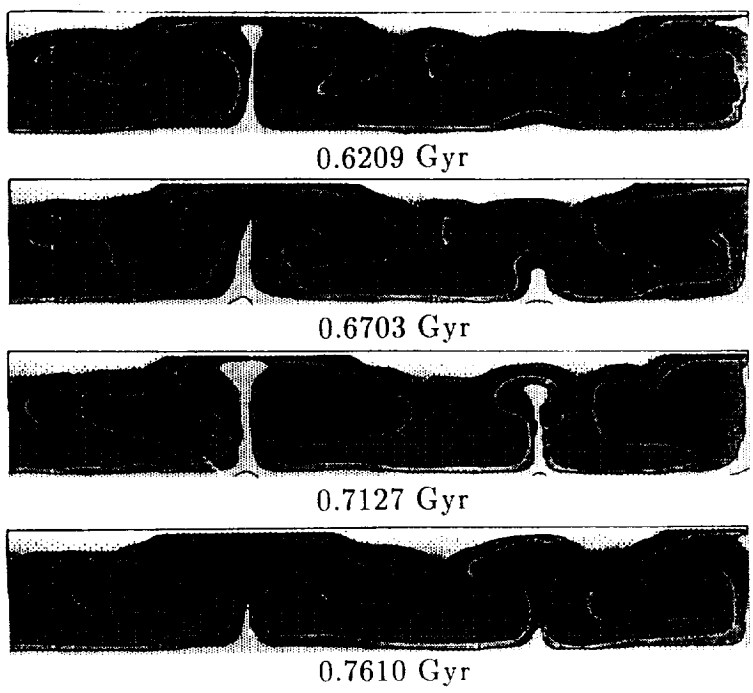

Fig. 1: Density field frames (light indicates lowest density, i.e., crustal material, and dark highest density, i.e., mantle lithosphere) from a 6x1, isoviscous, model, the initial conditions of which had a thin, uniform, crustal layer embedded within the upper thermal boundary layer of the convecting mantle layer. Thermal Rayleigh number, defined for pure bottom heating, is 10^5; reference crust and mantle densities are 2900 and $3300 kg/m^3$; system depth is $700 km$; initial crustal depth is $28 km$, and the thermal conductivity of the crust is one fourth that of the mantle, i.e., results of this model are akin to the crustal thickness instability investigated analytically by Busse [7]. Dimensional time below each frame is from the initial start time of the model. The top portion of the frames is slightly stretched for ease of visualization. Note how the region of thick crust, slightly to the right of center, which formed over a mantle downwelling, alters the convective flow in the mantle by damping heat flux out of the mantle and, as a result, leads to a mantle upwelling below itself. In the absence of a thin, nonuniform, crustal layer, the convective cells in the mantle layer remain fixed in space and in number.

ON THE RELATIONSHIP BETWEEN TECTONIC PLATES AND THERMAL MANTLE PLUME MORPHOLOGY

A.Lenardic and W.M.Kaula, UCLA Dept. of Earth and Space Sciences, Los Angeles, CA 90024

Introduction: Models incorporating plate-like behavior, i.e., near uniform surface velocity and deformation concentrated at plate boundaries, into a convective system, heated by a mix of internal and basal heating and allowing for temperature dependent viscosity, have been constructed and compared to similar models not possessing plate-like behavior. The simplified numerical models are used to explore how plate-like behavior in a convective system can affect the lower boundary layer from which thermal plumes form. A principal conclusion is that plate-like behavior can significantly increase the temperature drop across the lower thermal boundary layer. This temperature drop affects the morphology of plumes by determining the viscosity drop across the boundary layer. Model results suggest that plumes on planets possessing plate-like behavior, e.g., the Earth, may differ in morphologic type from plumes on planets not possessing plate-like behavior, e.g., Venus and Mars.

Models and Discussion: We employ a 2-D finite element code [1] incorporating plate-like behavior through the use of temperature dependent viscosity and narrow zones of, prescribed, low viscosity, used to mimic fixed plate boundaries [2]. Free parameters for the models employed are: the Rayleigh number defined for bottom heating and the viscosity at the base of the system (Ra); ratio of internal to bottom heating Rayleigh number (H), and the aspect ratio (AR). For all parameter combinations, a model with and without plate-like behavior is run. We refer to these as "plate" and "no-plate" runs (no-plate models employ purely temperature dependent rheology, with a three order of magnitude viscosity contrast across the cold upper boundary layer, while plate models also incorporate weak boundaries). The main qualitative conclusions from these runs are: 1) plate-like behavior suppresses secondary upper boundary layer instabilities present in high Rayleigh number or large aspect ratio no-plate runs; 2) the upper boundary layer is thinner in the plate runs; and 3) the temperature drop across the lower thermal boundary layer is greater in plate runs. The principal physical cause leading to these conclusions is that plate-like behavior enhances the mobility of the cold upper boundary layer material and allows it to be injected deep into the interior of the system at a rate comparable to the overturn rate of the weak interior [3]. This is not the case for no-plate runs, for the Rayleigh number range investigated, which show a marked differences in the rate at which the upper boundary layer is overturned vs. the rate of overturn in the weak interior, the latter being much quicker [4].

Applying model results to terrestrial planets is speculative due to simplifications employed, but the models do suggest possible differences between planets with and without plate-like behavior, which can be tested against comparisons of Earth and Venus. One key potential difference is that, as a result of point 3) above, plumes on Venus may differ in morphologic type from those on Earth. Surface feature on Venus believed to be manifestations of mantle plumes appear larger than Earth counterparts and require dynamic support of topography unlike Earth counterparts [5]. These differences may be consistent with different morphologic plume types within the two planets. If the temperature drop across the lower thermal boundary layer from which plumes form is large, then the viscosity drop from plume to host material will also be large and 'cavity plumes' will be favored, while for low temperature, and thus viscosity, drops 'diapir plumes' will be favored [6]. Cavity plumes consist of broad heads, which comprise the majority of plume mass during their lifetime, and very narrow trailing conduits (significantly narrower in radius than the thermal boundary layer thickness [7]), while diapir plumes have heads only slightly larger than their trailing conduits, which comprise the majority of diapir plume mass and have a radius comparable to the boundary layer thickness. Quasi-steady state topographic

features above established plumes (this excludes deformation due to rising plume heads) should be broader for diapir plumes and, since the viscosity of a diapir plume is closer to host mantle viscosity than for cavity plumes, contain a greater component of dynamic support than for cavity plumes. Point 3) suggests that plate-like behavior could establish a larger temperature drop across a hot thermal boundary layer on Earth than exists on Venus. Thus, Venus plumes may be closer to the diapir end-member, while those on Earth are closer to the cavity end-member.

Conclusion: Numerical convection models incorporating plate-like behavior lead to thermal boundary layers quantitatively different from those of models lacking plate-like behavior. A key differences is that the temperature drop across the lower thermal boundary layer is less for models lacking plate-like behavior. This suggests that thermal plumes within the mantles of terrestrial planets may differ in morphologic type due to the presence or absence of plate-like behavior.

[1]King, S.D. et al., *Phys. Earth Planet. Inter., 59,* 195-207, 1990. [2]King, S.D., et al., *Geophys. J. Int., 109,* 481-487, 1992. [3]Gurnis, M., *Geophys. Res. Lett., 16,* 179-182, 1989. [4]Christensen, U.R., *Phys. Earth Planet. Int., 35,* 264-282, 1984. [5]Phillips, R.J., et al., *Science, 252,* 651-658, 1991. [6]Olson, P., and H. Singer, *J. Fluid Mech., 158,* 511-531, 1985. [7]Stacey, F.D., and D.E. Loper, *Phys. Earth Planet. Inter., 33,* 44-55, 1983.

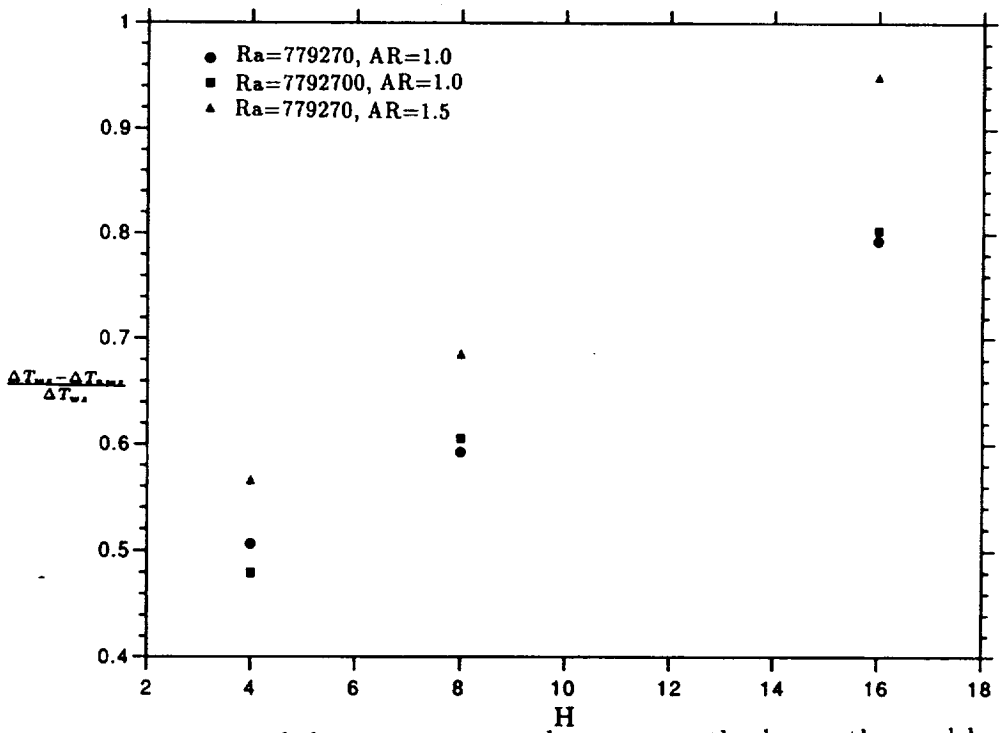

Fig. 1: A scatter plot of the temperature drop across the lower thermal boundary layer for runs with weak zones (ΔTwz), i.e., plate runs, minus the corresponding value of runs without weak zones ($\Delta Tnwz$), i.e., no-plate runs, divided by ΔTwz vs. the H value for run pairs with varied Rayleigh numbers and aspect ratios. The simplified temperature dependent viscosity formulation of these runs achieves a minimum, set by a prescribed cut off value, at a nondimensional temperature of 0.4 and a maximum at the top of the system. Large viscosity variations across the lower thermal boundary layer, which could result after a large temperature drop has been established, are not allowed for due to the numerical expense that would be incurred if a thin velocity layer needed to be resolved (these runs are not intended to study the formation of cavity plumes, rather they are intended to study the conditions that potentially favor their formation).

HELLAS BASIN, MARS: FORMATION BY OBLIQUE IMPACT; **Gregory J. Leonard** and **Kenneth L. Tanaka**, U.S. Geological Survey, 2255 N. Gemini Dr., Flagstaff, AZ, 86001.

Hellas, a 2,000-km-diameter, roughly circular multiring impact basin in the southern highlands of Mars [1-3], has a pronounced southeastern lobe of rim material that extends for some 1,500 km [4]. This lobe and a system of ridges concentric to the southern part of the basin (including part of the lobe) have been interpreted to be formed by an oblique impact that was inclined in the direction of the lobe [5]. Our preliminary geologic mapping of the Hellas region (lat -20° to -65°, long 250° to 320°) at 1:5,000,000 scale gives this hypothesis additional supporting evidence, including a symmetric distribution of basin ejecta and volcanic centers across the inferred trend of the impact. Furthermore, measurements of relief indicate that the downrange ejecta may be about twice as thick as they are elsewhere around the rim.

The generalized geologic map of Hellas (Fig. 1) shows that the basin rim (interpreted to be made up of ejecta [6]) not only varies in width but also is notably discontinuous; basin-ring structures are also discontinuous [1]. We note that major structural and geologic features associated with Hellas, both contemporaneous with and postdating the impact event, appear bilaterally symmetric around a line passing through the center of the basin (at lat -43°, long 291°) and trending about N60°W. The northwest half of the rim is relatively narrow, having an average width of 300 km (in comparison, Argyre basin has about half the diameter and a uniform rim 500 to 600 km wide). The topographic map of Mars [7] and shadow measurements of massif heights (at *1* and *2* in Fig. 1) indicate that the northwestern part of the rim generally does not exceed a kilometer in elevation above surrounding terrain. A few massifs have 2 km of relief, and one has 4 km. Large sections of the rim are buried on the northeast side by volcanic materials of Hadriaca and Tyrrhena Paterae and on the opposite side by degraded volcanic rocks of Amphitrites and Peneus Paterae; these volcanic centers (except Tyrrhena) are approximately equidistant (about 1,350 km) from the basin center. Also, two sets of scarps near the proximal edges of the southeastern lobe of basin-rim material are symmetrically located on either side of the proposed line of impact (Fig. 1). If these scarps formed by normal faulting or ejecta emplacement as a result of the impact event or by excavation due to later impacts, then the adjacent areas of missing rim material may simply have been lower lying and readily buried by the volcanic deposits. Alternatively but perhaps less likely (if we consider the high elevations of the rim massifs), the rim massifs were largely eroded away by fluvial or glacial erosion [8, 9]. Also shown in Fig. 1 are parts of a circumferential ridge system developed on the south side of the basin; these ridges formed sometime after the impact, perhaps controlled by more subtle basin structure. On the Moon, basin-rim and ring-height variations have been interpreted to be caused by pre-impact surface morphology, oblique impact, and post-impact modification [10].

Figure 2 shows a cross section of Hellas basin along the inferred trend of the impact, which suggests that ejecta on the southeast rim rises more than a kilometer above surrounding highlands in some areas and consists of an order of magnitude more cross-sectional area than ejecta on the northwest rim. Experiments have shown that oblique impacts produce bilaterally symmetric ejecta deposits [11], as seen at Hellas. (For trajectories of 45°-60° above the horizon, impacts produce ejecta relatively evenly around their craters, with a preferential concentration downrange [11].) We intend to improve our analysis of Hellas basin structure through further mapping and photoclinometric measurements of massifs.

References cited. [1] Wilhelms, D.E., 1973, *JGR 78*, 4084. [2] Peterson, J.E., 1977, *USGS Map I-910*. [3] Schultz, R.A. and Frey, H.V., 1990, *JGR 95*, 14,175. [4] Greeley, R. and Guest, J.E., 1987, *USGS Map I-1802-B*. [5] Tanaka, K.L. and Scott, D.H., 1987, *USGS Map I-1802-C*. [6] Potter, D.B., 1976, *USGS Map I-941*. [7] U.S. Geological Survey, 1991, *USGS Map I-2160*. [8] Crown, D.A., et al., 1992, *Icarus 100*, 1. [9] Kargel, J.S. and Strom, R.G., 1992, *Geology 20*, 3. [10] Whitford-Stark, J.L., 1981, *in Multi-ring Basins, PLPS 12A*, p. 113. [11] Gault, D.E. and Wedekind, J.A., 1978, *PLPSC 9*, 3843.

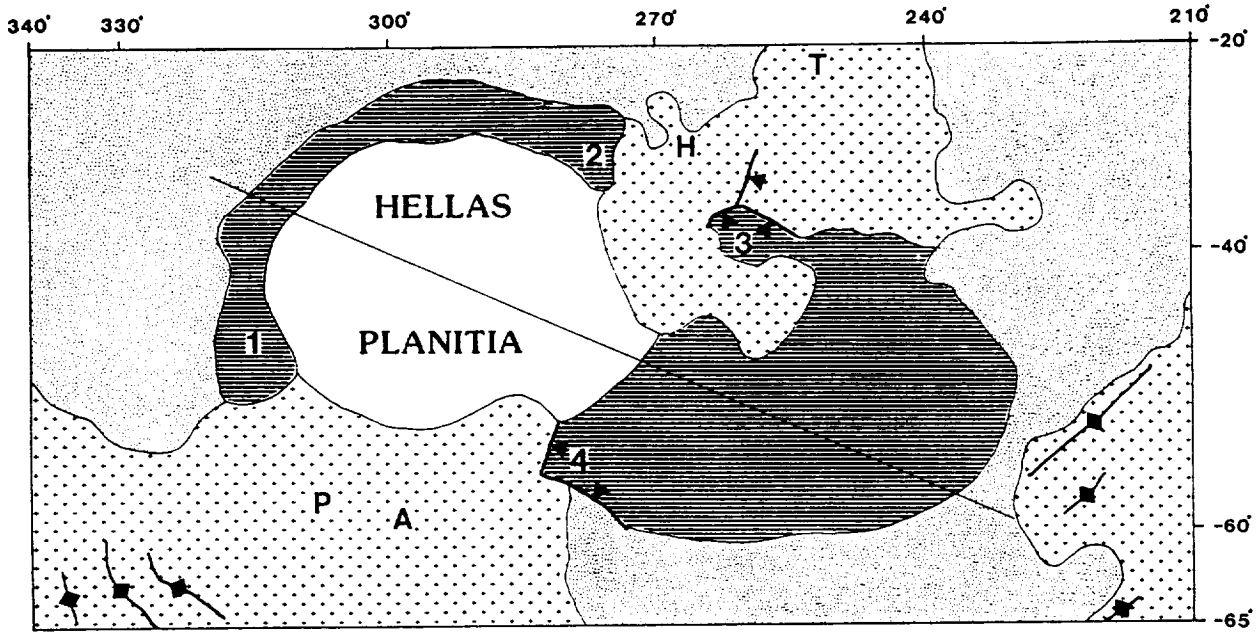

Figure 1. Generalized geologic map of the Hellas region of Mars. Line pattern, basin-rim material (largely made up of ejecta; see text); dotted stipple, highland material; cross stipple, volcanic material; blank, interior basin sedimentary rocks. H=Hadriaca Patera, T=Tyrrhena Patera, P=Peneus Patera, A=Amphitrites Patera; numbers show areas where shadow measurements of rim massifs were obtained. Thin line, line of cross section in Fig. 2, which coincides with inferred trend of impact. Lines with barbs, scarps; lines with diamonds, ridges.

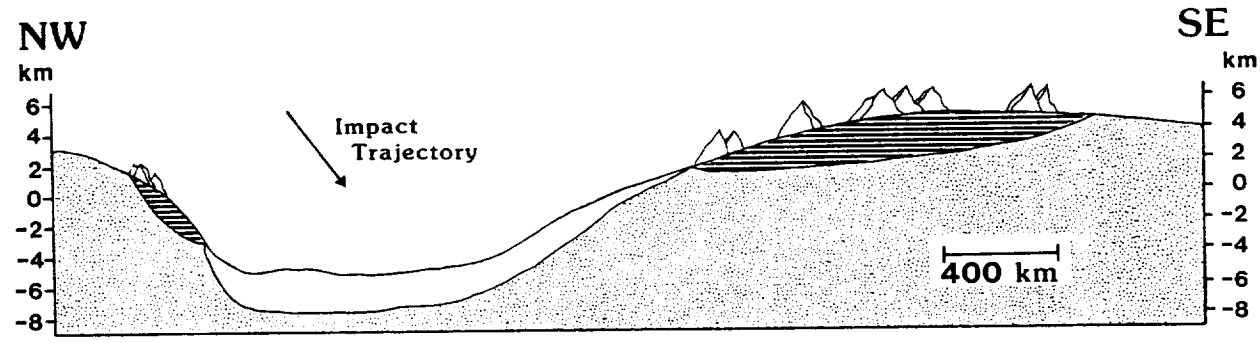

Figure 2. Cross section of Hellas basin along inferred trend of impact (topography from [7]; vertical exaggeration about 55X). Symbols as in Figure 1. Note that uprange (northwest) part of rim is relatively narrow and low, whereas downrange part of rim is broad and high and has larger massifs; much more ejecta were emplaced on downrange side.

MAPPING THE STABILITY REGION OF THE 3:2 NEPTUNE-PLUTO RESONANCE.

H.F. Levison & S.A. Stern (Southwest Research Institute, San Antonio, TX)

Pluto and Charon are most likely the remnants of a large number of objects that existed in the Uranus-Neptune region at early epochs of the solar system [1]. Numerical integrations have shown that, in general, such objects were ejected from the planetary region on timescales of $\approx 10^7$ years (cf. [2]) after Neptune and Uranus reached their current masses. It is thought that the Pluto-Charon system has survived to current times without being dynamically removed in this way because it is trapped in a set of secular and mean motion resonances with Neptune (cf. [3]). The best-known Pluto-Neptune orbit coupling is the 3:2 mean motion resonance discovered almost 30 years ago by C. Cohen and E. Hubbard [4]. These workers showed that the resonance angle, $\delta \equiv 3\lambda_P - 2\lambda_N - \tilde{\omega}_P$, where $\tilde{\omega}_P$ is the longitude of perihelion of the Pluto-Charon system, and λ_N and λ_P are the mean longitude of Neptune and Pluto-Charon respectively, librates about 180° with an amplitude, A_δ, of 76°.

We report here on a numerical simulation project to map out the stability region of the 3:2 resonance. The results of these simulations are important to understanding whether Pluto's long-term heliocentric stability requires only the 3:2 resonance, or whether it instead requires one or more of the other Pluto-Neptune resonances.

Our study also has another important application. By investigating stability timescales as a function of orbital elements, we gain insight into the fraction of orbital phase space which the stable 3:2 resonance occupies. This fraction is directly related the probability that the Pluto-Charon system (and possibly other small bodies) could have been captured into this resonance.

In the simulations we report here, we employed a numerical integrator to evolve the orbits of massless test particles in and around the 3:2 resonance under the direct gravitational influence of Uranus and Neptune. The test particles were followed using the simplectic integration scheme described in [5]. The motions of Uranus and Neptune were calculated analytically from a synthetic secular perturbation theory using the four dominant perihelion precession frequencies discussed in [6]. Thus, although Jupiter and Saturn were not explicitly included in the simulation, their effect on the orbits of Uranus and Neptune are included. This approach has been shown to give good statistical agreement with techniques that include direct integration of the planets for particles in this region [7]. The integrations lasted 2 billion years. The particles were followed until they suffered a close approach to either Neptune or Uranus, at which time they were assumed to be removed from the resonance.

Our goal is to determine whether the orbit of a test particle is stable over a significant fraction of the age of the solar system as a function of A_δ, and its initial inclination and argument of perihelion, i_0 and ω_0 respectively. We plan to study orbits with $A_\delta < 180°$, $i_0 < 180°$, $0 < \omega_0 < 90°$, and an initial eccentricity equal to the current eccentricity of Pluto, 0.248.

We present here a preliminary report on this study. Over 160 test particles have been integrated in order to sample important aspects of the orbital element space. As of this time we have studied the regions of $A_\delta < 180°$, $i_0 \leq 35°$, with ω either 0 or 90°.

First we present the results for our most well studied case, particles with $i_0 = 17.2°$, which is the inclination of Pluto. Figure 1 shows the removal times for these particles as a function of their libration amplitude, A_δ. The open and filled circles represent objects with $\omega_0 = 0$ and 90° respectively. If a symbol is on the dotted line then the particle survived for the length of the integration (2 billion years). The largest A_δ that survived is approximately 80°. Interestingly, the Pluto-Charon system has $A_\delta = 76°$.

An examination of the individual orbits shows that the argument of perihelion circulates rather than librates. Since ω of our particles circulate, there should be no fundamental difference between the $\omega = 0$ and $\omega = 90°$ runs, and this is what is observed. The argument of perihelion of the Pluto-Charon system librates

around 90° so that it is above the orbital plane of Neptune when it is at perihelion ([8]). It has been argued that this aids in the stability of its orbit. Our results show that this may not be necessary. Indeed, we find that objects in the 3:2 resonance with Neptune that have the same A_δ and inclination as the Pluto-Charon system seem to be stable for at least 2 billion years, even if they are not protected by the libration in ω.

Preliminary results for objects with different inclinations are as follows. We find that the maximum libration amplitude that is stable, $A_{\delta,max}$ is not a strong function of either i_0 or ω_0. For most values of i_0 and ω_0, $A_{\delta,max} \approx 90°$. The only exception appears to be for a small region near $\omega_0 = 90°$ for $i_0 \gtrsim 20°$. For this region all orbits appear to be short lived, having lifetimes less than 10^8 years. The explanation for this is being investigated.

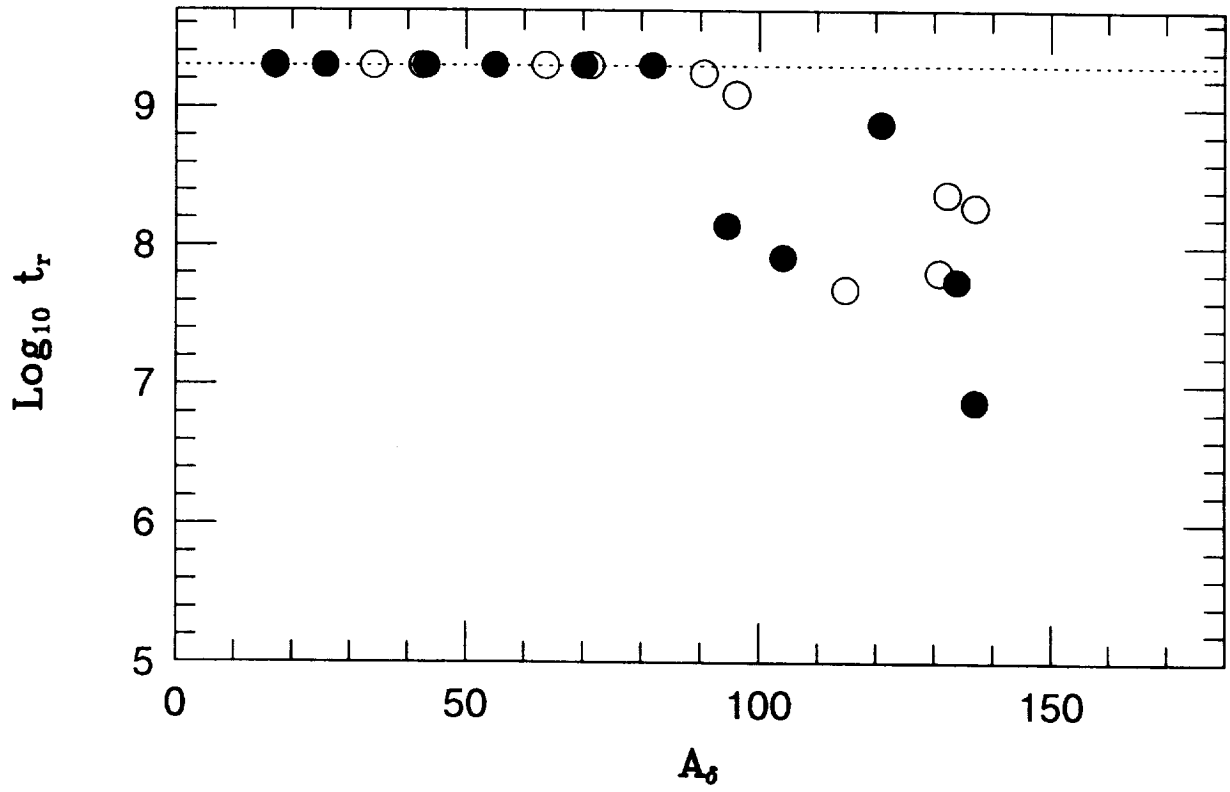

Figure 1 - The removal times of massless test particles in the 3:2 resonance with Neptune. There initial inclination is 17.2°, the initial argument of perihelion is either 0 (open circles) or 90° (filled circles).

References:

[1] Stern, S.A. 1991. *Icarus*, **90**, 271.

[2] Gladman, B., & Duncan, M. J. 1990. *Astron. J.* , 100, 1669.

[3] Milani, A., Nobili, A.M., Carpino, M. 1989. *Icarus*, **82**, 200.

[4] Cohen, C.J., Hubbard, E.C. 1965. *Astron. J.*, **70**, 10.

[5] Wisdom, J., & Holman, M. 1991. *Astron. J.*, **102**, 1528.

[6] Applegate, J. H., Douglas, M. R., Gürsel, Y., Sussman, G. J., & Wisdom, J. 1986. *Astron. J.*, **92**, 176.

[7] Levison, H., & Duncan, M. 1993. *Astphy. J. Lett.*, in press.

[8] Williams, J., & Benson, G. 1971. *Astron. J.*, **76**, 167.

POSSIBLE DUST CONTAMINATION OF THE EARLY SOLAR SYSTEM

E.H. Levy (Lunar and Planetary Laboratory, Department of Planetary Sciences, The University of Arizona, Tucson) and T.V. Ruzmaikina (Lunar and Planetary Laboratory, The University of Arizona, Tucson, and Schmidt Institute of Earth Physics, Moscow)

Measurements carried out over more than twenty years indicate a deficiency of neutrinos emitted from the deep interior of the Sun in comparison with the neutrino flux expected from canonical solar models. The early measurements[1], were sensitive only to high-energy neutrinos emitted from ^{8}B on a minor branch of the energy-producing nuclear reactions in the solar interior. Thus these measurement were not widely considered to be a definitive test of solar physics. However the more recent measurements[2], which are sensitive to lower energy neutrinos, produced primarily by the p-p reaction on the main energy-producing branch of the solar nuclear reactions, pose a far more significant mystery in physics. One possibility is that the Sun's interior opacity is lower than expected due to a paucity of elements. This paper discusses the possibility that the Sun formed from material less abundant in heavy elements than usually believed, and the subsequent contamination due to the settling of surrounding dust brought the abundance of heavy elements—in the protoplanetary nebula, and in the Sun's convective envelope—up to the currently observed value.

Much recent speculation has focused on the possibility that the solar neutrino deficit results from previously unobserved aspects of neutrino physics, specifically the possibility that neutrinos undergo transitions to a form not observable in the the current detectors. This line of speculation has been given additional strength by the fact that the observations—especially the most recently observed p-p–neutrino deficit—now push solar models to extreme departures from standard conceptions about the Sun. However, at least one aspect of the observations is especially provocative, and suggests that serious consideration should be given to the possibility that it is the Sun, rather than the neutrinos, that might not conform to earlier ideas. The measured low-energy neutrino flux—approximately 80 SNU[2]—seems to correspond closely to the minimum neutrino production consistent with the solar luminosity, regardless of the solar model. If the cause of the solar neutrino deficit were a result of neutrino physics alone—having nothing to do with the Sun—then this correspondence would stand as a truly remarkable coincidence.

It has been known that such a low neutrino flux could be explained if the temperature in the Sun's core were substantially lower than the approximately $1.5 \cdot 10^7$ K central temperature given by standard solar models. Such a low central temperature could occur if the solar interior were depleted in the so-called metals—atomic species heavier than helium—resulting in lowered internal opacity. In such a case, the chemical abundances measured in the solar convective zone would be unrepresentative of the deep-interior abundunces. The chemical composition of the Sun is measured spectroscopically using light emitted from the outer layers, and by analyzing solar-wind atoms, which are emitted from the Sun's main-sequence star.

Compositional measurements made at the solar surface must apply to the entire convection zone, i.e. to the outer 30% by radius and 2.5% by mass, which is well mixed. However, it is not equally clear that the composition of the inner, radiative interior matches that of the convection zone, as little material mixing may occur between these two zones. Energy-producing nuclear reactions are concentrated near the center of the Sun, with virtually all of the nuclear reactions and all of the energy production confined within the inner 25%. Assuming that little mixing has occurred between convective-zone and core material over the lifetime of the Sun, the question of radial compositional gradients devolves largely to questions associated with the formation of the Sun—and especially to whether star-formation processes might produce stars with significant radial compositional gradients.

Dust settling from outer regions of a molecular cloud core could result in contamination of the nebula and the outer layers of the Sun. In a quiet (nonturbulent) molecular cloud core with radius 10^{17} cm, the time-scale of settling of grains with radii $r_d = 10^{-4}$ cm, and time scale of the settling $\tau_s \sim 10^7$ yrs. The presence of even weak turbulence, with velocities $v_t > v_{pg}$ results in mixing that overwhelms the

settling of small dust particles. Observations show that molecular clouds, in general, and their cores, particularly, reveal internal chaotic motions with nearly a Kolmogorov spectrum[3]. The characteristic velocities of these turbulent motions are $v_t \sim 10^4$ to 10^3 cm s^{-1}, i.e. the turbulence is subsonic in the scale of core size ($\sim 10^{17}$ cm, $c_s \simeq 3 \cdot 10^4$ cm s^{-1}), but the velocity exceeds the settling speed of small dust particles gas through the gas. We do not expect that such small particles could settle effectively before collapse.

However turbulence causes relative motion of nearby particles, promoting collisions that can be followed by coagulation.[4] A detailed study of the coagulation of grains in the molecular cloud cores is undertaken by Weidenshilling and Ruzmaikina (1993, see abstract for this conference).

$$\delta v_r \simeq \frac{t_k}{t_e} v_t.$$

where t_e is the characteristic time in which a grain changes its motion under the drag force of gas, v_t is the rms turbulent velocity of the gas, and t_k is the eddy time scale for the largest eddies. The equation of coagulation of the particles, assuming that each collision results in coagulation, gives

$$\frac{dm_d}{dt} = \sigma_d v_r n_d m_d,$$

where n_d is the number density of the dust grains in the cloud. Assuming that $n_d m_d = q\rho$ (where q is the mass fraction of the dust in comparison with the gas, and ρ is gas density) and that dust grains are spheres with the density independent of radius, the equation is integrated to give

$$r_d^{1/2} = r_{d0}^{1/2} + 27\, q \left(\frac{\rho}{\rho_d}\right)^{1/2} \left(\frac{v_t^3}{c_s\, l_t}\right)^{1/2} t,$$

where r_{d0} is the initial radius of the grains, l_t is a characteristic length scale of turbulent motions, c_s is the sound speed, and t is a time.

As long as grains grow, they can reach a size where the velocity of settling exceeds the turbulent velocity. After that the turbulence can no longer suppress the precipitation of grains. The ratio of the stationary velocity of settling of growing particles to the typical turbulent velocity is

$$\frac{v_{pg}}{v_t} \simeq \frac{6 \cdot 10^{-2}}{\beta} \left(\frac{q}{2 \cdot 10^{-3}}\right)^2 \left(\frac{t}{10^7 \text{ yrs}}\right)^2 \frac{\rho}{2 \cdot 10^{-19} \text{g cm}^{-3}} \frac{v_t}{c_s},$$

where is $\beta = l_t c_s / v_t R$. For illustration, we take the fraction of the condensible matter in the presolar material q to be 1/10 of the 'solar abundance'; this 1/10 is approximately the abundance of heavy elements in the solar core for the nonstandard solar models calculated by Bahcall and Ulrich[5], which could be consistent with the observed neutrino flux. One can see from this equation that even for $\beta \simeq 1$ the settling of solid particles becomes significant in a time scale $t \sim 3 \cdot 10^7$ yrs, provided the cloud turbulence speed is comparable to the speed of sound.

This paper discusses possible implications—for the formation of the protoplanetary nebula in particular as well as for the formation of stars and protoplanetary nebulae in general—of such preferential dust settling from the surrounding, unaccreted material in protostellar clouds.

REFERENCES [1] Bahcall J.N. and Ulrich R.K. (1988), *Rev.Mod.Phys.*, 60, 297. [2] GALLEX Collaboration, Anselmann P. *et al* (1992), *preprints GX 1-1992, GX 2-1992.* [3] Larson R.B. (1981) *M.N.R.A.S., 194*, 809. [4] Völk H.J., Morfill G.E., Roser S., (1980), *Astron. Ap., 85*, 316. [5] Weidenshilling S.J. and Ruzmaikina T.V. (1993), Coagulation of grains in Static and Collapsing Protostellar Clouds. In *Lunar and Planetary Science XXIV.* [6] Aumann H.H., *et al*, (1984), *Ap.J.*, 278, L23. [7] Artymowicz P., Burrows C., Paresce F. (1989), *Ap.J., 337*, 494. [8] Weidenschilling S.J. (1977), *M.N.R.A.S., 180*, 57.

A search for noble-gas evidence for presolar oxide grains

Roy S. Lewis & B. Srinivasan†
Enrico Fermi Institute, University of Chicago, 5630 S. Ellis Ave, Chicago IL 60637
†Current address: Argonne National Laboratory, Argonne, IL 60439

We present early results from an ongoing search for isotopically distinctive noble gases as evidence for presolar oxide grains. With some qualifications, we do not see such evidence in spinel rich acid residue fractions from the Allende meteorite. We remain hopeful that less abundant mineral separates may yet be fruitful.

Presolar grains, micro-diamonds, silicon carbide, and graphite, have been found in primitive meteorites (1, 2, 3). While the abundances of these three refractory C rich grains are low, a few hundred ppm, a few ppm, &<1ppm respectively in primitive meteorites (4), they are tagged with high concentrations of isotopically anomalous noble gas components, Xe-HL, Kr & Xe-s and Ne-E(H), and Ne-E(L). These tags have served as tracers and allowed the development of techniques for their purification and eventual identification. One might expect similar amounts of refractory presolar oxides to have survived, but so far only three cases exist for their identification. The first two cases are individual corundum oxide grains. Huss *et al.* (5) found one such grain from an Orgueil residue with an $^{26}Al/^{27}Al$ ratio of 8.9 x 10-5, about 18 times higher than the canonical initial solar system value. The second corundum grain, from Murchison, has been found by Nittler *et al.* (6) to have unusual oxygen in addition to a similar $^{26}Al/^{27}Al$ ratio of 8.7 x 10-4 The oxygen was depleted in ^{18}O by 22% and enriched in ^{17}O by a factor of 2. The third case is a measurement by Zinner *et al.* (7) on an aggregate of fine grained spinels from a Murray residue with an ^{17}O enrichment and a possible ^{18}O depletion similar to the second grain, but much subdued. This is consistent with a few such presolar grains diluted by a much larger population of isotopically normal corundum grains and an even larger number of normal spinel grains.

As the three known presolar grains can account for all of the (abundant) anomalous noble gas components found in primitive meteorites, we cannot expect to have the surviving presolar oxides to be so conveniently tagged. What sort of distinguishing compositions can we hope for? Certainly, they are likely to have anomalously high spallation gas concentrations. In addition they may have excess ^{244}Pu fission xenon, or even fission from a shorter lived transuranic element such as ^{248}Cm, although only in grains large enough to trap fission fragments, or in grains occurring in large enough clusters. Such components have already been suggested as possibly detected by Srinivasan *et al.* (8) and by Tang and Anders (9). If one were to concentrate such oxides sufficiently, their trapped noble gas compositions may be distinctive and may serendiptitiosly be abundant enough to stand out. Following the model of the two most abundant known presolar grains, diamond and silicon carbide, refractory and chemically resistant phases are most likely to have survived the formation of the solar system and to be distinctive enough to enable their separation and identification from the bulk of the meteorite. Corundum, as has been found, fits this model. Refractory inclusions have refractory grains in abundance, but appear to have been produced in the early solar system by some high temperature processes, producing partial to nearly complete isotopic homogenization with the average solar system material, as judged by the magnitude of the residual isotopic anomalies found in them (10). However the few presolar silicon carbide grains found in situ in these meteorites were isolated individuals in the matrix, and not found in large aggregates (11). The relatively abundant minerals from the refractory inclusions should therefore just be an (unfortunate) diluent for the presolar grains. The high noble gas concentrations in SiC, which are released in pyrolysis near 1800°C, hinder the detection of noble gases from refractory oxide grains. We have therefore returned to a residue from the Allende C3V meteorite, which has at most very little silicon carbide. Indeed, one goal will be to see if the presence of any silicon carbide can be confirmed.

We have measured He, Ne, Ar, Kr, and Xe, extracted by stepped pyrolysis, on samples prepared from Allende residue BA, a bulk HF-HCl residue. It was treated with perchloric acid twice at 190°C to remove carbon and chromite. Then the presolar diamonds, with their abundant Ne & Xe-HL were depleted >95% six times over (total depletion about 6,000,000) by removal as a colloidal suspension at pH~11. The resulting sample was then divided into 4 size fractions, yielding Allende FF, FG, FH, & FI, nominally >10μm, 3-10μm, 1-3μm & <1μm. Partial data for the last three fractions are given in table 1 and figures 1 and 2. We intend to dissolve the spinel in aliquots of these samples and measure the even more concentrated corundum, hibonite, and possible SiC.

At this stage, and with a couple of caveats, we see no evidence for any presolar grains. First, there is negligible evidence in figure 1 for an isotopic enrichment in ^{22}Ne, as would be carried in SiC. Estimating a conservative upper limit for a ^{22}Ne excess of 10% of the total, table 1, yields an upper limit for SiC of 0.1 ppm, ~60 times less than in Murchison. The spallation Ne, table 1, is more abundant in these fractions than in other Allende samples, but this is expected for nearly pure spinel with its high Mg and Al abundance. Dissolution of this spinel should yield a more sensitive test both for small amounts of SiC and for possible remaining presolar oxide grains carrying excess spallation Ne.

The Xe isotopic composition is consistent with a mixture of trapped Xe, Xe-HL, and ^{244}Pu fission Xe, with no definite evidence for ^{248}Cm fission Xe, though the presence of the He-HL (table 1) in these three samples leaves

Noble gases & presolar oxide grains

Lewis, Roy S. & Srinivasan, B.

some room for argument. The fission rich extraction steps are near 2000°C and should not have Xe-HL remaining. But then these samples should not have any diamonds at all remaining. Yet there is Xe-HL! However, the measured Ne_T/Xe-HL ratio is lower than that of diamonds (table 1.) Hence the Xe-HL cannot be from average presolar diamonds. A distinct carrier leaves open the question of how much contribution Xe-HL makes to the fission rich fractions in figure 2. If those fractions have significant Xe-HL, then the pure fission composition on the abscissa lies to the left of ^{244}Pu, corresponding to a possible contribution from ^{248}Cm.

The concentration of fission Xe in these three fractions lie in the range measured in refractory inclusions (Table 1), consistent with these inclusions being the source of most of these spinels. Any proposed presolar oxides then make negligible contribution to the observed fission Xe. And yet, the high release temperature of the fission Xe, near 2000°C, 500°C above that of the spallation Ne release peak, could be interpreted as an indication that the fission Xe is carried in a minor fraction of the grains, more refractory than the spinel, and at a corresponding higher concentration. If the spallation Ne in each extraction step is used as a measure of the mass sampled (an overestimate of the mass if there are presolar grains with high exposure ages), then the residual spallation Ne in the fission rich steps implies a fission Xe concentration 10 to 20 times higher than found in refractory inclusions. Of course spinel itself melts at >2000°C. If the spinel does not react with the Ta foil container in our extraction furnace, then we may just be seeing diffusive fractionation between the Ne and the Xe.

This work neither finds strong evidence for presolar oxides, nor yet rules out the possibility of their separation.

Table 1		$^{22}Ne_{Spall}$	$^{22}NeE(H)$	$^{22}Ne_T$ /	$^{132}Xe_{Ex}$	$^{132}Xe_{fiss}$
Sample:		E-8 cc/g	E-8cc/g	$^{132}Xe_{Ex}$	E-10 cc/g	E-10 cc/g
Allende:						
bulk	(12)	1.7				
refract. incl.	(13,14)	1.3-1.8				0.10-0.18
diamonds	(15)			400	2500	
FF >10mm		3.20	<0.3	66	0.57	0.13
FG 3-10mm		2.61	<0.3	65	1.57	0.18
FH 1-3 mm		2.76	<0.3	59	3.44	0.17
Murchison:						
SiC average	(16)	23	16,700			

References:(1) Lewis *et al.* (1987) *Nature* **326**, 160-162. (2) Bernatowicz *et al.* (1987) *Nature* **330**, 24-31. (3) Amari *et al* (1990) *Nature* **345**, 238-240. (4) Lewis *et al* (1993) *Geochim. Cosmochim. Acta*, submitted. (5) Huss *et al.*, (1992) *LPSC* **23**, 563-564. (6) Nittler *et al.* (1993) *LPSC* **24**. (7) Zinner *et al.* (1988) *LPSC* **19**, 1323-1324. (8) Srinivasan *et al* (1983) *LPSC* **14**, 741-742. (9) Tang and Anders (1988) *Geochim. Cosmochim. Acta* **52**, 1245-1254. (10) Wasserburg *et al.* (1980) *Early Solar System Processes and the Present Solar System*, 144-191, Soc. Italiana di Fisica, Bologna, Italy. (11) Alexander *et al.* (1992) *LPSC* **23**, 9-10. (12) Lewis *et al* (1975) *Science* **190**, 1251-1262. (13) Drozd *et al* (1977) *Astrophys. J.* **212**, 567-580. (14) Smith *et al* (1977) *Geochim. Cosmochim. Acta* **41**, 627-647. (15) Huss & Lewis (1993) *Meteoritics*, submitted. (16) Lewis *et al* (1993) *Geochim. Cosmochim. Acta*, submitted.

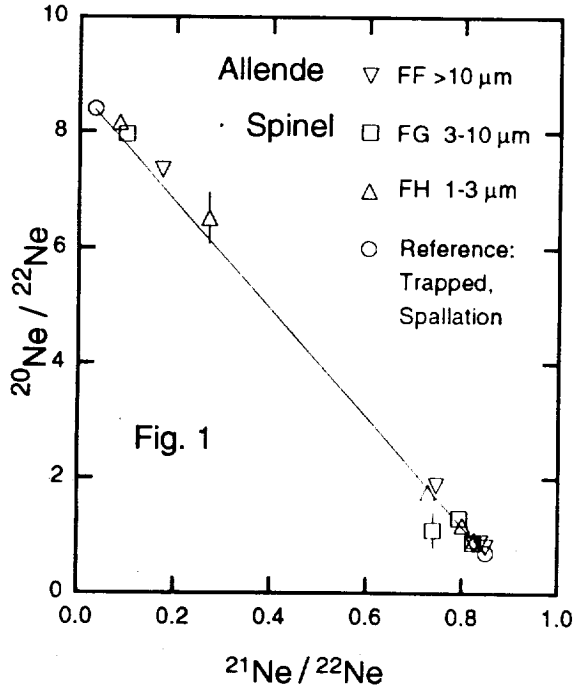

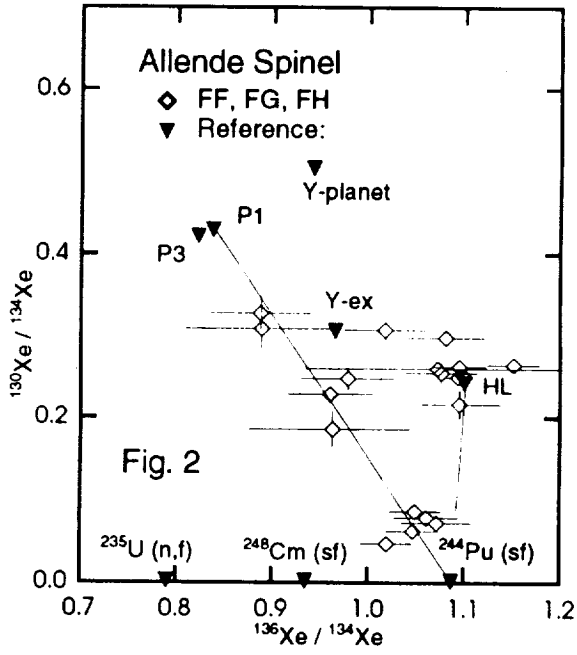

THE SEISMIC RESPONSE OF AN AQUIFER TO THE PROPAGATION OF AN IMPACT GENERATED SHOCK WAVE: A POSSIBLE TRIGGER OF THE MARTIAN OUTFLOW CHANNELS? Ivett A. Leyva[1] and Stephen M. Clifford[2]. [1]California Institute of Technology, Pasadena, California. [2]Lunar and Planetary Institute, Houston, Texas.

Aquifer dilation from shock waves produced by the 8.4 magnitude Alaskan earthquake of 1964 led to water and sediment ejection from the ground up to 400 km away from the earthquake's epicenter [1]. Groundwater disturbances were observed as far away as Perry, Florida (~5500 km), where well water fluctuations with an amplitude of as much as 2.3 m were reported [2]. The martian cratering record provides evidence that the planet has experienced numerous seismic events of a similar, and often much greater, magnitude. Given this fact, and the photogeologic evidence for abundant water in the early crust, we have investigated the response of a basalt aquifer to the propagation of compressional waves (P-waves) produced by impacts in the 33 - 1000 km diameter size range. The resulting one-dimensional changes in effective stress and pore pressure were calculated -- as a function of both distance and time -- based on the following assumptions: (i) that all of the seismic energy radiated by an impact is transmitted as a single compressional wave, (ii) that both the host rock and groundwater are compressible, and (iii) that there is no net flow between the water-filled pores.

After *Croft* [3], an impact producing a crater of final diameter D_f, has a corresponding maximum transient diameter D_{tc}, given by

$$D_{tc} = D_c^{0.15+0.04} D_f^{0.85+0.04} \quad (1)$$

where D_c is the transition diameter between simple and complex crater morphology, which occurs on Mars at a crater diameter of ~ 6 km. According to *Grieve and Cintala* [4], the relation between the kinetic energy of the impactor and D_{tc} is given by

$$E_k = \frac{D_{tc}^{3.85}}{2.91\text{x}10^{-3}\, U^{0.35}\, g^{0.85}} \quad (2)$$

where U is the velocity of the impactor, taken as 10 km s^{-1}, and g is the acceleration of gravity. However, upon impact, only a small fraction of E_k is actually converted into seismic energy, E_s. After *Schultz and Gault* [5,6]

$$E_s = k\, E_k \quad (3)$$

where the seismic efficiency factor, k, is taken to be equal to 10^{-4}.

In this analysis, the propagation of the resultant seismic wave is represented by a sine wave with a period $\tau = 4^* t_o$, where t_o is the time of formation which, after *Schmidt and Housen* [7], is given by

$$t_o = 0.62\, E_k^{0.13}\, U^{-0.04}\, g^{-0.61}. \quad (4)$$

This quantity represents the elapsed time from impact until the wavefront reaches the maximum radius of the transient cavity, r_o (= $D_{tc}/2$). The maximum stress of the P-wave occurs at r_o and is equal to

$$\sigma_o^2 = \frac{3\rho\, c\, E_s}{\pi\, r_o^2 t_o} \quad (5)$$

where ρ is the density of the martian crust and c is the velocity of the P-wave given by

$$c = \left(\frac{E}{\rho}\right)^{1/2}, \quad (6)$$

where E is the Young's modulus (= $\lambda + 2\mu$, where λ and μ are the Lame parameters) [5]. After *Schultz and Gault* [6], the maximum stress associated with the outward propagating shock wave is given by

$$\sigma = \frac{\sigma_o r_o}{x}. \quad (7)$$

The displacement of a particle at this distance, is assumed to oscillate according to the equation

$$u = A_o \sin(k x - \omega t) \quad (8)$$

where ω is the angular frequency (= $2\pi/\tau$), k is the wave number (= ω/c), and where, after *Jaeger and Cook* [8], A_o is the maximum amplitude given by

$$A_O = \frac{\sigma c \tau}{2\pi E} \quad (9)$$

The change in strain, $d\varepsilon$, is then calculated from the derivative of eq. (8), such that

$$d\varepsilon = A_O k \cos(k x - \omega t) \quad (10)$$

After *Pande et al.* [9], the change in pore pressure, dp, is related to the change in strain, $d\varepsilon$, and change in effective stress, $d\sigma'$, by

$$dp = K_f (d\varepsilon - \frac{d\sigma'}{K_S}) \quad (11)$$

where

$$K_f = (\frac{n}{K_W} + \frac{1-n}{K_S})^{-1} \quad (12)$$

and where n is the porosity of the material, K_S is the bulk modulus of the solid matrix, and K_W is the bulk modulus of the water saturating the pores.

The change in strain is related to the changes in total and effective stress ($d\sigma$ and $d\sigma'$ respectively) through the modulus matrix D^* and drained modulus matrix D [9], where

$$d\sigma = D^* d\varepsilon \quad (13)$$

$$d\sigma' = D d\varepsilon \quad (14)$$

and where D^* and D are related to each other by

$$D^* = D + K_f - \frac{K_f D}{3 K_S} \quad (15)$$

For the one-dimension case, D^* reduces to E and D can be solved from eq. (15). Substituting these values in eq. (11), the final equation for the change in pore pressure is found to be

$$dp = d\varepsilon \; K_f (1 - \frac{E - K_f}{3 K_S + K_f}) \quad (16)$$

To place the calculated pore pressure changes in perspective, note that during the Alaskan earthquake of 1964, changes on the order of 1.7 bars were produced in silt and clay sediments at distances up to 400 km away from the earthquake's epicenter (the maximum distance at which water and sediment ejections were observed). On Mars, an impact of equivalent seismic energy (D_f = 33 km [10]) will produce this same change in pressure in basalt at a distance of ~ 100 km, while impacts with diameters >500 km will produce pressure changes in excess of 1.7 bars on a global scale. Impacts with final diameters > 1000 km are capable of generating pore pressures in excess of 10 bars out to distances of over 2000 km. Given a more realistic representation of seismic wave propagation through a planetary body, these pore pressures changes are likely to be amplified enormously as the seismic waves converge at the antipode. These results suggest that seismic disturbances produced by large impacts may have played a role in triggering the martian outflow channels. For example, under conditions where the local hydraulic head in a confined aquifer is already near lithostatic levels, the excess pressure generated by a major impact could conceivably disrupt a several km-thick layer of frozen ground over global distances -- permitting the catastrophic discharge of the accumulated reservoir of groundwater until the local hydraulic head declined to the level of the surrounding topography. Efforts to extend this analysis to include a more realistic representation of seismic wave production and propagation, and to consider the effects of flow in a heterogeneous aquifer possessing both intergranular and fracture porosity, are currently underway.

References: [1] Waller, R.M. (1968). in: The Great Alaska Earthquake of 1964, National Academy of Sciences, 97-116. [2] Cooper, H.H., J.D. Bredehoeft, I.S. Papadopulos, and R.R. Bennet (1968). in: The Great Alaska Earthquake of 1964. National Academy of Sciences, 122-132. [3] Croft, S. K., (1985). *J. Geophys. Res.*, C828-C842. [4] Grieve, R.A.F., and M.J. Cintala. (1992). *Meteoritics*, **27**, *in press*. [5] Schultz, P.H., and D.E. Gault. (1975a). *The Moon*, **12**, 159-177. [6] Schultz, P.H., and D.E. Gault. (1975b). *Proc. Lunar Sci. Conf. 6th.*, 2845-2862. [7] Schmidt, R.M., K.R. Housen (1987). *Int. J. Impact Engng.* **5**, 543-560. [8] Jaeger, C., and G.W. Cook (1976). Fundamentals of Rocks Mechanics, Hapman and Hall., 352-254. [9] Pande, G.N., G. Bear, J.R. Williams. (1990). Numerical methods in rock mechanics. John Wiley & Sons Ltd., 143-145. [10] Clifford, S. (1992). *J. Geophys. Res., in press.*

INAA OF CAIs FROM THE MARALINGA CK4 CHONDRITE: EFFECTS OF PARENT BODY THERMAL METAMORPHISM; D. J. Lindstrom[1], L.P. Keller[1], and R. R. Martinez[2]. [1]SN4, NASA/JSC, Houston TX 77058; [2]C23 LESC, 2400 NASA Road 1, Houston, TX 77058.

Maralinga is an anomalous CK4 carbonaceous chondrite which contains numerous Ca-, Al-rich inclusions (CAIs) unlike the other members of the CK group [1]. These CAIs are characterized by abundant green hercynitic spinel intergrown with plagioclase and high-Ca clinopyroxene, and a total lack of melilite [2]. We have used Instrumental Neutron Activation Analysis (INAA) to further characterize the meteorite, with special focus on the CAIs. High sensitivity INAA [3] was done on eight sample disks about 100-150 μm in diameter obtained from a normal 30 μm thin section with a diamond microcoring device [4]. The CAIs are enriched by 60-70X bulk meteorite values in Zn, suggesting that the substantial exchange of Fe for Mg that made the spinel in the CAIs hercynitic also allowed efficient scavenging of Zn from the rest of the meteorite during parent body thermal metamorphism. Less mobile elements appear to have maintained their initial heterogeneity.

Analytical. Because the samples are too small to weigh accurately (0.1-1.2 μg), their masses have been estimated from the measured amounts of Fe and estimates of FeO content from microprobe work [1,4]. Thus, absolute abundances are uncertain by about ±10%, but elemental ratios for well-determined elements are more accurate. The low abundances of many interesting trace elements in chondritic meteorites make them less than ideal subjects for INAA even when abundant material is available, and the two sigma upper limits for a number of elements under the conditions used here were less than chondritic values. Nonetheless, positive compositional anomalies would have been readily visible even for some unfavorable elements, and the "good" INAA elements offer some interesting insights. This was essentially a feasibility study of a few drilled samples, and would benefit from microprobe analyses of the specific areas sampled.

Results. The disk drilled from one of the two spinel-rich inclusions broke into three pieces (about 0.6, 0.3, and 0.3 μg) which were analyzed separately. Considerable variations in composition are apparent (see Table), with the largest variations observed in Sc (8X), Ir (25X) and Au (about 6X). The sample highest in Ir (about 3 ppm) had the lowest Au value (20 ppb). Refractory metals (including Re and Rh, which were observed but not quantified) show considerable variability at this scale, presumably reflecting trace sulfides, etc. [5]. Sm, the only rare earth element detected in all three aliquots, varied by a factor of 3, as did Na, while Cr, Co, Ni, and Zn varied by about 30% from highest to lowest. The other green spinel inclusion has similar contents of transition metals and somewhat higher contents of rare earths, Ca, and K. The most striking compositional feature of these green inclusions is their very high Zn contents (2930-5510 ppm, averaging about 4000 ppm). Also analyzed were a sample of matrix, a variety of chondrules and other inclusions, a large magnetite grain, and a sample of a hydrated iron oxide weathering vein. The matrix sample resembles previous bulk analyses of Maralinga [6,7], but is slightly lower in Fe, Cr, Co, and Ni (perhaps in part due to normalization to the fairly low matrix FeO value determined by defocused electron beam analysis [1]), and higher in Na. The Sc content of the matrix sample is only about half the bulk value, and may simply represent sampling of matrix in a low-Sc region distant from any high-Sc inclusions. Another curious feature of the matrix analysis is 4.3 ± 0.6 ppm tungsten, presumably due to sampling of a region once containing tungsten-rich minerals. Three textural varieties of olivine-rich chondrules were sampled, and their analyses are unremarkable, except that one has quite high Sc.

Discussion. Variability in Sc (note the vertical trends in the figure) may be simply a problem in sampling the clinopyroxene that is the phase richest in Sc, or may mean that inhomogeneities arising from high-Sc CAIs have not been fully erased during metamorphism. The 4000 ppm average Zn content of the CAIs is 40X the average CK chondrite value [6], and 60-70X the bulk Maralinga value of 65 [7] or 57 ppm [6]. If all the Zn in the meteorite were in the green inclusions, they could comprise no more than ~1.5% of the

sample, a value which is in surprisingly good agreement with the estimated abundance of CAIs obtained using the petrographic microscope [1]. Of course, substantial amounts of Zn are also observed in our matrix and chondrule analyses, and it is quite possible that the aliquots from which the bulk samples were taken were poor in CAIs. Still, the Zn enrichment in spinel is remarkable. Volatile Zn should have been absent from the original CAIs, and must have been transported efficiently from a sizable volume of meteorite in order to attain the levels observed. Homogeneous olivine compositions throughout the meteorite attest to the efficiency of redistribution of divalent Mg, Fe, and Ni. Also, matrix plagioclase grains are strongly zoned, with ~An_{80} rims surrounding cores of ~An_{40}, suggesting that extensive Ca diffusion occurred during thermal metamorphism [8]. Additional petrographic evidence of Ca diffusion is the replacement of perovskite by ilmenite in several of the inclusions. Thus, redistribution of Zn is to be expected. Less mobile species such as Al and Si could not have moved substantially without obliterating much of the texture. Perhaps other more highly charged species such as Sc have also experienced limited mobility, and could help explain the small-scale variability observed in this work.

References: [1] Keller L.P., Clark J. C, Lewis C. F., and Moore C. B. (1992) **Meteoritics** 27, 87-91. [2] Keller L. P. (1992) LPSC XXIII, 671-2. [3] Lindstrom D. J. (1990) **Nucl. Instr. Meth. Phys Res. A299**, 584-588. [4] Ulrike Medenbach, Bruno-Heide Strasse 8, D-5810 Witten 3, Germany. [5] Geiger T. and Bischoff A. (1989) LPSC XX, 335-336. [6] Kallemeyn G. W., Rubin A. E., and Wasson J. T. (1991) GCA 55, 881-892. [7] Geiger T. and Spettel B. (1991) LPSC XXII, 133-4. [8] Keller L.P. (1993), this volume.

	CALCIUM-, ALUMINUM-RICH INCLUSIONS				MATRIX	CHONDRULES			
	A1	A2	A3	B		olivine	fine grained	barred	
	0.60 ug.	0.28 ug.	0.30 ug.	0.76 ug.	0.44 ug.	0.43 ug.	0.16 ug.	1.09 ug.	
Na2O	0.1050 ±0.0018	0.200 ± 0.003	0.442 ± 0.007	0.347 ± 0.005	0.420 ± 0.007	0.0387 ±0.0008	0.0867 ±0.0016	0.258 ± 0.004	Na2O
FeO	15.01 ± 0.18	15.05 ± 0.20	15.01 ± 0.19	15.03 ± 0.18	27.0 ± 0.3	30.1 ± 0.3	29.9 ± 0.4	30.2 ± 0.3	FeO
Sc	6.58 ± 0.09	16.9 ± 0.2	54.0 ± 0.6	23.3 ± 0.3	5.83 ± 0.09	8.40 ± 0.11	8.44 ± 0.13	33.2 ± 0.4	Sc
Cr	2800. ± 40.	1980. ± 30.	2130. ± 30.	2640. ± 40.	2820. ± 40.	1169. ± 16.	1910. ± 30.	2400. ± 30.	Cr
Co	564. ± 7.	689. ± 8.	747. ± 9.	725. ± 9.	332. ± 4.	456. ± 5.	397. ± 5.	457. ± 5.	Co
Ni	3710. ± 70.	4530. ± 130.	5040. ± 130.	4450. ± 90.	3490. ± 90.	4800. ± 100.	3760. ± 140.	4920. ± 90.	Ni
Sm	0.097 ± 0.013	0.178 ± 0.017	0.32 ± 0.03	0.388 ± 0.017	0.132 ± 0.018	0.210 ± 0.011	0.096 ± 0.012	0.485 ± 0.014	Sm
Ir	0.120 ± 0.014	3.2 ± 0.3	0.112 ± 0.015	4.2 ± 0.4	0.137 ± 0.016	0.31 ± 0.03	0.16 ± 0.02	<0.04	Ir
Au	0.047 ± 0.005	0.019 ± 0.009	0.124 ± 0.012	0.013 ± 0.006	0.033 ± 0.007	0.012 ± 0.005	0.020 ± 0.006	<0.019	Au
Zn	2930. ± 50.	3590. ± 80.	3890. ± 70.	5510. ± 80.	50. ± 20.	72. ± 15.	<80.	79. ± 12.	Zn

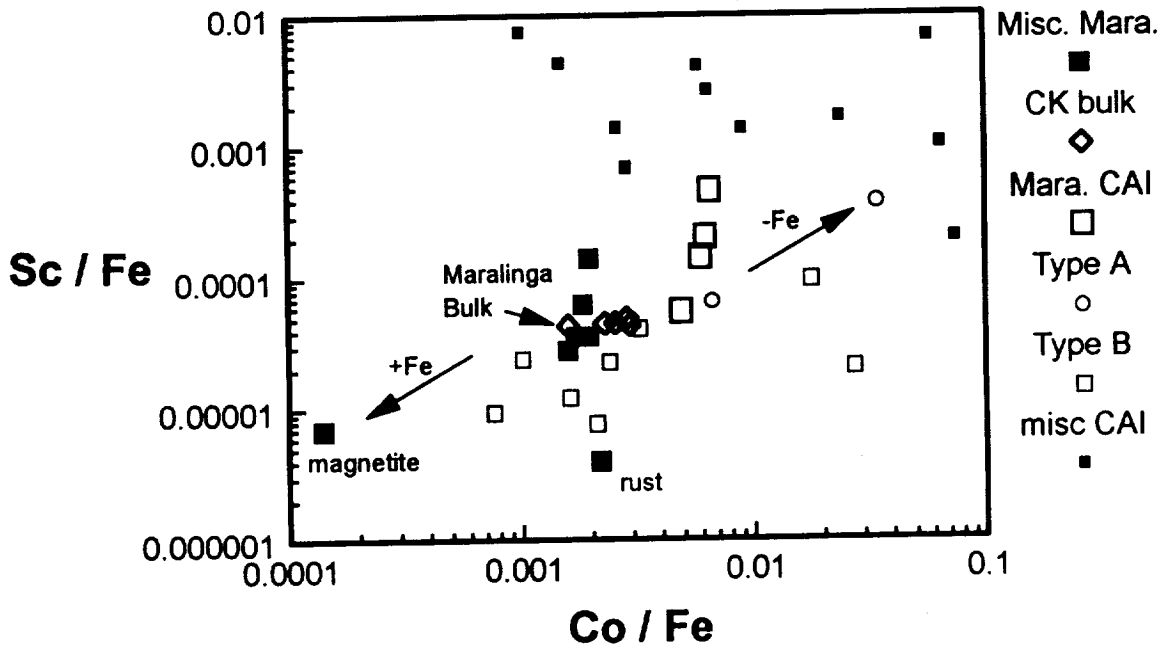

SPACESHIP EARTH: A PARTNERSHIP IN CURRICULUM WRITING.

Marilyn M. Lindstrom and the NASA Partners-In-Space Team*, NASA Johnson Space Center, Houston, TX 77058.

As the Apollo astronauts left Earth to venture onto the surface of another planetary body, they saw their home planet in a new global perspective. Unmanned NASA missions have given us a closer look at all the other planets in our solar system and emphasized the uniqueness of Earth as the only place in our solar system that can sustain life as we know it. Spaceship Earth is a new science curriculum which we developed to help students and teachers to explore the Earth, to see it in the global perspective, and to understand the relationships among life, the planet and the sun. We use astronaut photographs, especially shuttle pictures, as well as groundbased studies to help students to understand global Earth Science and integrate various aspects of physical, life and social science.

The Spaceship Earth curriculum was developed at by a team of JSC scientists working in collaboration with teachers from local school districts. The project was done under the auspices of Partners-In-Space, a local non-profit organization dedicated to improving science education and our general knowledge of space. The team met once a month for a year then assembled the curriculum during the summer. The project is now in the testing stage as the teachers try it out in their classrooms. It has been supported by the Texas Education Agency and will be offered by the State of Texas as a supplemental curriculum for statewide use. Because the curriculum was developed by teachers, it is self contained and the lessons are easy to implement and give students concrete experiences. The three sub-units follow in a logical order, but may be used independently. If they are used separately, they may be tied together by the teacher returning to the basic theme of the global Earth as each unit is completed.

Curriculum Overview

Search for a Habitable Planet. The introductory unit focuses on the uniqueness of Earth in our solar system. The students become extraterrestrial explorers on a mission to search for a new home. They begin by defining the life requirements of different types of creatures. Students are divided into six groups of creatures having different life requirements. After creating models of their creatures, they tour our solar system looking for planets that provide the needs of their creatures. They conclude that different planets are appropriate for different types of creatures, but that Earth is the only one that meets our needs.

Blue Planet. The main unit focuses on Earth and the connections between life, the planet, and the sun. It is divided into three distinct parts:

1. Life Support System - Water and Air. The importance of water and air to the inhabitants of Earth is explored through exercises about water distribution, air composition, the effects of greenhouse gases, ozone depletion and pollution. Students will learn the effects of human intervention on the water and air that sustain life.

2. Dynamic Earth. Earth is active and volatile. Energy from the Sun produces weather from the atmosphere and oceans. Energy from inside the Earth produces new crust while it consumes old crust. Exercises show the effects of these powerful internal and external forces on Earth's surface and its inhabitants.

3. Living in the Environment. Students will learn about the problems of living in extreme environments and plan an expedition to Antarctica to collect meteorites. They will evaluate requirements for clothing, shelter, food, water, transportation, communication and recreation. They will realize that living at Earth's last frontier is challenging, but not out-of-this-world.

Moon, Our Nearest Neighbor. The final unit concludes the Spaceship Earth curriculum by leaving Earth. Students learn about our Moon as they plan to set up a Moon base. Their plans to meet life's needs on this lifeless planetary body contrast strongly with their plans for an Antarctic expedition. This contrast reinforces the uniqueness of Earth and its life support system.

CHONDRITIC RATIOS OF Fe/Cr/Ir IN KERGUELEN PLATEAU (HOLE 738C) K/T CARBONATE-RICH SEDIMENTS SUPPORT ASTEROID-COMETARY IMPACT AT K/T TIME;

Y.G. Liu[1,2] and R.A. Schmitt[1-4], [1]The Radiation Center and Departments of [2]Chemistry and [3]Geosciences, and [4]College of Oceanography, Oregon State University, Corvallis, Oregon 97331

In the study of marine carbonate sediments from Holes 577 and 577B, Shatsky Plateau (Rise), a net extraterrestrial Fe/Ir = C1 chondritic ratio at the K/T boundary was reported [1]. Applying a similar procedure to Hole 738C (Kerguelen Plateau) data reported by [2], we obtain Fe/Cr/Ir ratios similar to C1 or C2 chondritic ratios.

Hole 738C data were normalized to Th. Because Th is very low in seawater, $\sim 3\pm2 \times 10^{-5}$ μg/L [3,4], little if any Th precipitated from seawater onto the detrital clay, and therefore, Th is an excellent diagnostic clay indicator. (Scandium was used as a normalization element by [2], none of which involved Fe/Cr/Ir calculations. Because ~77-86% of the total observed Sc is precipitated from the overlying $\lesssim$300m of seawater, normalization to Sc is invalid as a detritus indicator.) Using Th-normalized data, the net extraterrestrial ratio Fe_{ext}/Ir_{ext} can be calculated by integrating under the total peaks and subtracting the terrestrial ratios.

$$\frac{\sum_i (Fe_{tot} / Th_{tot})_i - (Fe_{ter} / Th_{ter})_i}{\sum_i (Ir_{tot} / Th_{tot})_i - (Ir_{ter} / Th_{ter})_i} = \frac{\sum_i (Fe_{ext} / Th_{ter})_i}{\sum_i (Ir_{ext} / Th_{ter})_i} = \frac{Fe_{ext}}{Ir_{ext}}$$

where $\sum_i$ is the summation of all ith intervals over the total peak. In the above equation, Fe_{tot}, Ir_{tot} and Th_{tot} are total amounts in the sample; Fe_{ext} and Ir_{ext} are extraterrestrial (e.g. cometary or asteroidal ejecta fallout etc.) in the samples. The above equations are valid because $Th_{ter} >> Th_{ext}$; therefore, $Th_{tot} = Th_{ter}$; e.g. Th_{ter} = 12.3 ppm in North American Shale Composite (NASC) [5], and Th_{ext} = 0.03 ppm in C1 chondrites [6]. Also because Th_{ter} values fluctuate, the final equation over the entire peak is valid only if Fe_{ext}/Ir_{ext} = constant in all of the ith intervals. Similar equations are obtained for Fe_{ext}/Cr_{ext}.

We obtain the results that $Fe_{ext}/Ir_{ext} = 4.5\pm1.1 \times 10^5$ and $Fe_{ext}/Cr_{ext} = 85\pm21$, which are the same as found in C1 and C2 chondrites. For C1 chondrites, Fe/Ir = $4.0\pm0.3 \times 10^5$ and Fe/Cr = 72 [6].

The agreement for the net Fe/Cr/Ir ratios between Hole 738C data and C1 chondrites suggests that all three elements were precipitated as their insoluble oxyhydroxides onto clay detritus and carried to the 738 site as well as from direct fallout over the 738 site at K/T time. Now at two very different oceanic K/T sites, one at the Shatsky Plateau (Rise) (~12°N at K/T time) in deep (>1800m) seawater near the west central Pacific and the other on the Kerguelen Plateau (~60°S at K/T time) in seawater at $\leq$ 300m, we have found net $(Fe/Ir)_{ext}$ = C1 chondritic ratio. This strongly supports either the L.W. Alvarez asteroidal [7] or the H.C. Urey cometary [8] impact hypothesis and our previous observation [1] that C1 Fe/Ir in the vaporized impactor ejecta fallout were C1 or C2 as were eight other elements at selected sites (see #5 in [9]). The results are remarkably similar to those obtained by computer simulations [10].

We have used our Shatsky Rise Hole 577 data to calculate the $(Fe/Ir)_{ext}$ and $(Fe/Cr)_{ext}$ at the K/T boundary in the same manner as for Hole 738C data. We found that the $(Fe/Ir)_{ext} = 4.4\pm0.9 \times 10^5$ ratio agrees with the C1 ratio within error. The $(Fe/Cr)_{ext} = 260\pm30$ is ~3.6X higher than the C1 ratio, indicating a lesser amount of Cr was carried along with the Fe from the impactor ejecta fallout. If we follow the same calculational approach, i.e. normalization to Th by using the L.B.L. data [11] for the Shatsky Rise Hole 577B, we obtain $(Fe/Ir)_{ext} = 6.6\times10^5$ and $(Fe/Cr)_{ext}$ = 290. Perhaps the higher $(Fe/Ir)_{ext}$ ratio could be explained by their use of "standard pottery" as the Fe standard. But when we used a relative background subtraction method as outlined in [1] which eliminates possible errors in an analytical standard, we obtain from their Hole 577B data $(Fe/Ir)_{ext} = 3.4\pm0.6 \times 10^5$ and $(Fe/Ir)_{ext} = 4.0\pm0.3 \times 10^5$ for our Hole 577 data. The higher $(Fe/Cr)_{ext}$ ratios at Holes 577 and 577B could be interpreted in terms of the higher Ksp of $Cr(OH)_3$ by nine magnitudes relative to $Fe(OH)_3$, i.e. less coprecipitation of $Cr(OH)_3$ with $Fe(OH)_3$, both of which are assumed to be present in C1 ratio in the vaporized ejecta fallout [10].

We obtained a higher $(Fe/Co)_{ext}$ ratio of 1330 relative to a C1 ratio of 380, which indicates that ~29% of the Co from the impactor C1-like ejecta fallout was carried or deposited directly at the site 738C relative

to Fe/Cr/Ir. We attribute the small fraction of coprecipitated Co from the impactor fallout to the very different seawater chemistry of Co relative to Fe, Cr, and Ir. Using the latest solubility values for Fe and Co in seawater, it is estimated that the residence time of Co is ~200X greater than that of Fe in seawater. Also we found essentially no net impactor signals from Ni and Co at the K/T boundary on the Shatsky Rise (see Table 1 in [1]) because the Ni/Al and Co/Al ratios for K/T boundary samples agreed within errors with the corresponding ratios in the trace elements peaks before and after the K/T trace element peaks. The reason no Co peak was observed in the Shatsky Rise K/T boundary is attributed again to its much longer residence time and to the deep oxic Pacific regime relative to the different regimes in the intermediate seawater depths of ≤ 300m over the Kerguelen Plateau, where we observed ~29% of relative impactor Co.

Iridium in Hole 738C exhibits an asymmetrical peak with a gradual tailing upward. If we assume a Gaussian dispersal because of a little bioturbation (the presence of extensive bioturbation has been ruled out by [2] because of the presence of sedimentary laminations), then a FWHM of ~0.8 cm seems apparent, thereby yielding ~21 ng/cm^2 of Ir. The total Ir found at 738C is ~270 ng/cm^2 according to our calculation. Therefore only ~8% of the total Ir deposited at 738C is direct impact fallout and ~92% originates from fluvial sedimentary input and/or later turbidity currents.

Because the lamination formation probably was derived from local provenance a time interval for deposition of ~10^3-10^5 years after K/T was estimated [2]. The smaller value of ~21 ng/cm^2 of Ir for higher K/T latitudes of ~60°S is now more in line with ~71 ng/cm^2 of Ir found at the Shatsky Rise (~12°N). If the main impact occurred between 30°S to 30°N, one would expect more global impactor ejecta fallout between 30°S-30°N relative to ~60°S or ~60°N.

References: [1] Jin Y.-G. and Schmitt R.A., (1989) L.P.S. XX, 460-461, 462-463. [2] Schmitz B. et al. (1991) Q.D.P. Scientific Results, 119, 719-730. [3] Huh C.-A. et al. (1989) G.C.A. 53, 1357-1366. [4] Lee T. and Chen J.H. (1988) E.A.G. Int'l Conf., Paris. [5] Gromet L.P. et al. (1984) G.C.A. 48, 2469-2482. [6] Anders E. and Ebihara M. (1982) G.C.A. 46, 2363-2380; Anders E. and Grevesse N. (1989) G.C.A. 53, 197-214. [7] Alvarez L.W. (1980) Science 208, 1095-1108; Hut P. et al. (1987) Nature 329, 118-126. [8] Urey H.C. (1957) Nature 179, 556; (1962) Science 137, 746; (1963) Nature 197, 228. [9] Schmitt R.A. (1990) L.P.S. XXI, 1085-1086. [10] Roddy D.J. et al. (1991) L.P.S. XII, 1129-1130. [11] Michel H.V. et al. (1985) Init. Repts. Deep Sea Drilling Project 86, 533-538.

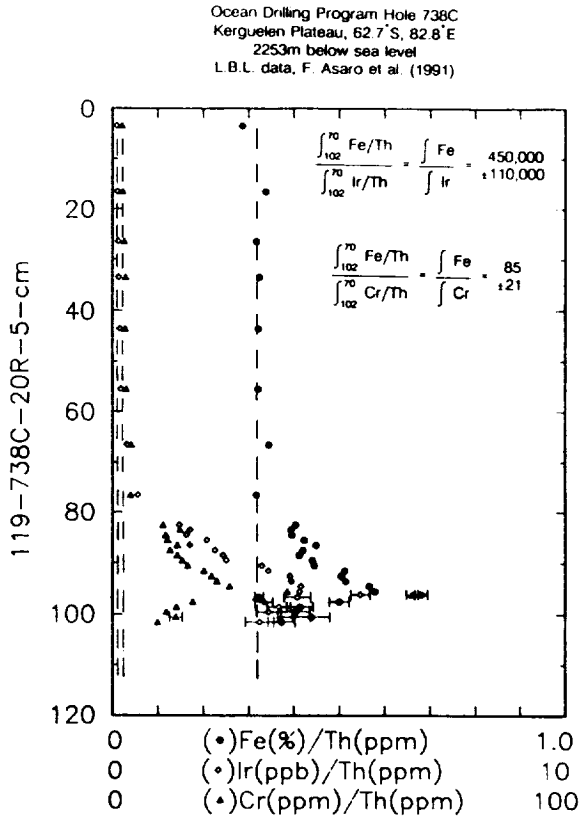

EARTH'S PARTIAL PRESSURE OF CO_2 OVER THE PAST 120 Ma; EVIDENCE FROM Ce ANOMALIES IN THE DEEP (>600 m) PACIFIC OCEAN, I;

Y.-G. Liu[1,2] and R.A. Schmitt[1-4], [1]The Radiation Center and Departments of [2]Chemistry and [3]Geosciences, and [4]College of Oceanography, Oregon State University, Corvallis, Oregon 97331

We [1] have found that Ce serves as a chemical tracer of paleo-oceanic redox conditions. It has been shown [2-6] that the unoxidized and soluble Ce^{3+} in modern seawater exhibits a negative anomaly relative to the other soluble REE^{3+}. We [1] derived an expression of soluble Ce^{3+} in seawater that was ~1900X greater than the average observed Ce in 600-5000 m Pacific seawater [7]. Since $Ce(CO_3)^+$ and $Ce(CO_3)_2^-$ complexes greatly exceed the $Ce(PO_4)^\circ$ complexes in seawater [8], we have followed the formulations of [1] using carbonate complexes and have found that the calculated Ce and observed concentrations in the deep 600-5000 m Pacific Ocean agree within the uncertainties of the thermodynamic data. As expected, the calculated Ce concentrations are a strong function of pH and found to be lesser functions of CO_3^{2-} activities.

Cerium depletion in seawater is expressed in a relative way by a defined anomaly, Ce^{A^*} = observed Ce abundance normalized to N.A.S.C. (North American Shale Composite)/Ce expected abundance interpolated between La and Nd, normalized to REEs in N.A.S.C. [9]. Abundances of the light REE in average fluvial input to the oceans are approximately proportional to N.A.S.C. abundances [10-12]. Because seawater pH is controlled by $P(CO_2) \propto [H^+]^2$, the Ce^{A^*} is in turn governed mainly by $P(CO_2)$.

The seawater REE pattern is preserved in relatively pure $CaCO_3$ sediments [1]. Correcting for the contributions of small amounts of aeolian or other N.A.S.C.-like clay particulates in the whole rock carbonate specimens, we observe that generally 95-98% of the total observed REEs in the carbonate sediments of this study precipitated from seawater onto the Fe-oxyhydroxide coatings of the $CaCO_3$ grains and onto the clay particulate surfaces during the 10^4-10^6 year exposure of the sediment to direct seawater and interstitial seawater. Therefore, the observed Ce^{A^*}s in the carbonates equal the Ce^As of the parental oceans.

If we assume that the REE concentrations in seawater remained constant at times 1 and 2, the following expression is used for estimations of pHs at times 1 and 2.

$$\log (Ce_2^{A^*}/Ce_1^{A^*}) = [0.50 \log (a^3_{CO_3^{2-}}) - 0.50 \log (a_{Ce(CO_3)_2^-}/a_{Ce(CO_3)^+}) - \log (0.33\ pH\text{-}2.0) - 0.25 \log P_{O_2} - 3.0\ pH]_2 - [0.50 \log (a^3_{CO_3^{2-}}) - 0.50 \log (a_{Ce(CO_3)_2^-}/a_{Ce(CO_3)^+}) - \log (0.33\ pH\text{-}2.0) - 0.25 \log P_{O_2} - 3.0\ pH]_1$$

For calculations of pHs at 1 and 2, we will assume that P_{O_2} changes during the Phanerozoic were trivial relative to $P(CO_2)$ changes. Also the buffering effects and formulas [13] were utilized for estimations of $P(CO_2)$. Therefore, from experimentally determined Ce^{A^*} in marine carbonates of different ages and associated paleo-pH values atmospheric $P(CO_2)$ values are calculated relative to present deep sea conditions as a reference.

Using INAA, we have determined 26-32 elements in ~205 carbonate samples. We have also calculated the Ce^{A^*} for 60 carbonates, 63.4-65.1 Ma, L.B.L. Hole 577B data [14]; ~40 samples were mostly under the full K/T Ir peak.

Observations shown in Figs. 1 and 2 are summarized as follows: 1. From 0-14 Ma, the Ce^{A^*}s and $P(CO_2)$ are equal to the present values. 2. Between 15-19 Ma, the Ce^{A^*} peak at ~17 Ma corresponds to a $P(CO_2)$ ~1.6X $P^\circ(CO_2)$. Within age uncertainties, this peak corresponds to the flooding time of Columbia River Basalts (CRBs). 3. From ~20-50 Ma, the Ce^{A^*}s and $P(CO_2)$s appear to increase uniformly. 4. In the 50-57 Ma interval, early Eocene, the data from three Pacific sites indicate an average Ce^{A^*} of 0.13 and $P(CO_2) \approx 1.5 \pm 0.2X$. 5. In Fig. 2, we have expanded the Paleocene and upper-upper Maastrichtian to emphasize relationships to the K/T Ir peak at 64.7 Ma [15] and the floodings of the Deccan Traps that began before the K/T Ir peak [15]. The K/T Ir peak in Shatsky Plateau samples has been defined at 65.0 Ma for calculation of other relative ages. Ce^{A^*}s and $P(CO_2)$ increase uniformly from ~58-62 Ma. From 62.5-64.3 Ma, the Ce^{A^*} and $P(CO_2)$ reached their maxima, with an average $P(CO_2)$ ~1.9X over this interval. 6. At 64.3 Ma, the Ce^{A^*} and $P(CO_2)$ decline abruptly, with a $P(CO_2)$ ~1.3X at 64.5 Ma. 7. At K/T Ir peaking, the Ce^{A^*}s and $P(CO_2)$ are identical to the present Pacific Ocean. Phenomena that caused the celebrated K/T observations did not affect significant changes in the Earth's $P(CO_2)$. 8. The K/T Ir peak is flanked by Ce^{A^*} and $P(CO_2)$ peakings at 64.6 Ma and 65.2 Ma yielding $P(CO_2)$ values of ~1.6X and ~1.5X, respectively. 9. From 65.3-66.2 Ma, the deep Pacific regime was identical to the present. If the Deccan Traps (DTs) began

before the K/T Ir peaking event [15] and flowed over a ~0.5 Ma interval, the voluminous DTs' emissions of CO_2, SO_2, HCl etc. gases were insufficient to change the Pacific Ocean's pH. Because the DTs are considerably more voluminous relative to the CRBs, the tentative conclusion reached in #2 above is questionable. 10. At 95 Ma, the Ce^{A*} and $P(CO_2)$ were identical to present conditions. 11. The four Hole 316 data between 115-119 Ma represent carbonates deposited in shallow to intermediate depths, i.e. <200 m - ~500 m (?) [16]. For such suggested depths, the observed Ce^{A*} and $P(CO_2)$ correspond to the present values. 12. In the interval 69-76 Ma, we have analyzed 24 carbonates, yielding an average Ce^{A*} = 0.16±0.05. Because some or most of these samples may have derived from turbiditic flows from nearby edifices, i.e. carbonates deposited in shallow seawater, we are not able to use a definite seawater reference. For example, the present geometric mean Ce^{A} in shallow Pacific seawater is ~0.22, with a range from 0.10-0.43. If the above 24 carbonates were deposited in shallow seawater, the best estimate of $P(CO_2)$ in the 69-76 Ma would be the present value. 13. Paleosol carbonate data yield estimates of $P(CO_2)$ ~5-10X at ~120 Ma [17] and <2X throughout the Tertiary [18]. These estimates at 120 Ma are clearly at variance with our estimate of ~1.0X. Our $P(CO_2)$ estimate at ~3 Ma agrees with [19]. 14. Our $P(CO_2)$ estimates contrast sharply with the theoretical modeling of [20] who calculated $P(CO_2)$ values of 6^{+6}_{-4}X at ~120 Ma, $4^{+6}_{-2.5}$X at 95 Ma, and $2^{+1.5}_{-0.8}$X at K/T time. At these three times, our Ce^{A}s and $P(CO_2)$s of the Pacific Ocean were identical to the present values.

References: [1] Liu Y.-G. et al. (1988) G.C.A. 52, 1361-1371. [2] Goldberg E.D. et al. (1963) J.G.R. 68, 4209-4217. [3] Høgdahl O.T. et al. (1968) Adv. Chem. Ser. 73, 308-325. [4] Elderfield H. and Greaves M.J. (1982) Nature 296, 214-219. [5] Klinkhammer G. et al. (1993) Nature 305, 185-188. [6] De Baar H.J.W. et al. (1985) G.C.A. 49, 1943-1959. [7] Piepgras D.J. and Jacobsen S.B. (1992) G.C.A. 56, 1851-1862. [8] Lee J.H. and Byrne R.H. (1992) G.C.A. 56, 1127-1137. [9] Gromet L.P. (1984) G.C.A. 48, 2469-2482. [10] Goldstein S.J. and Jacobsen S.B. (1988) E.P.S.L. 88, 241-252; 89, 35-47. [11] McLennan S.M. (1989) Rev. Min. 21, 169-200. [12] Elderfield H. et al. (1990) G.C.A. 54, 971-991. [13] Stumm W. and Morgan J.J. (1981) Aquatic Chem., Chapter 4. [14] Michel H. et al. (1985) Init. Repts. D.S.D.P. 86, 533-538. [15] McWilliams M.O. (1992) EOS 73, No. 14, 363; the K/T Ir age is probably closer to 64.9 Ma, priv. com. from McWilliams. [16] Kauffman E.G. (1973) Init. Repts. D.S.D.P. 33, 503-535. [17] Cerling T.E. (1984) E.P.S.L. 71, 229-240; Am. J. Sci. (1991) 291, 377-400. [18] Cerling T.E. et al. (1992) EOS 73, No. 43, 95. [19] Raymo M.E. and Rau G. (1992) Ibid. [20] Berner R.A. (1990) Science 249, 1406-1409.

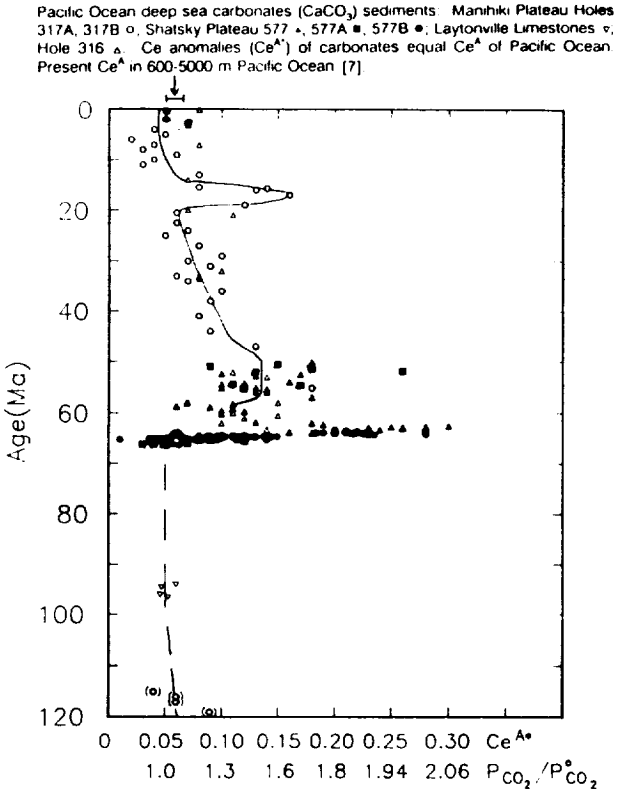

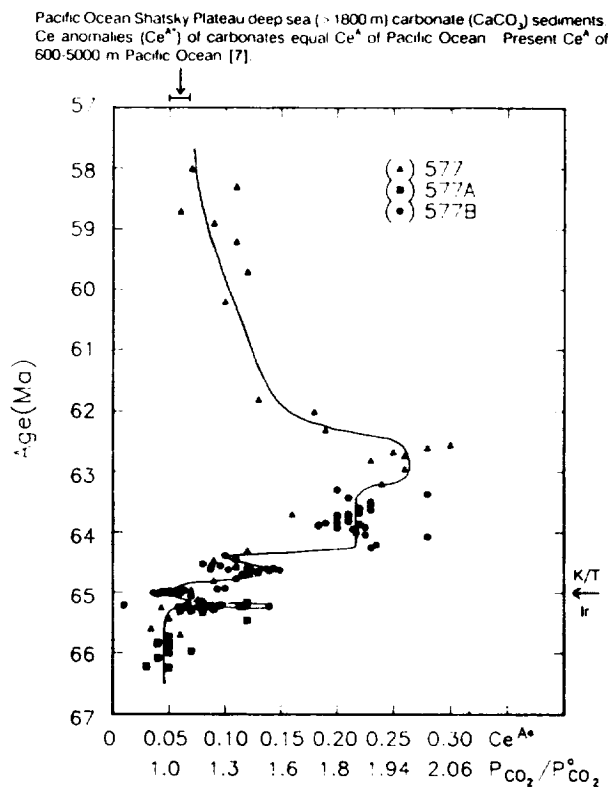

GEOCHEMICAL EVIDENCES FOR TWO CHONDRITIC-LIKE COMETARY OR ASTEROIDAL IMPACTS BEFORE AND AT THE K/T BOUNDARY; **Y.-G. Liu[1,2] and R.A. Schmitt[1-4], [1]The Radiation Center and Departments of [2]Chemistry and [3]Geosciences, and [4]College of Oceanography, Oregon State University, Corvallis, Oregon 97331**

Mass extinctions caused by multiple impacts of cometary showers within a short time period have been proposed by [1-3]. Detailed calculation of temporal profile shows that cometary showers last ~3 Ma, with the bulk of the comets arriving within ~1 Ma. A number of geological and palaeontological evidences support multiple impacts and their connection with mass extinctions. Observations [2] include clustered crater ages, stratigraphic horizons of impact ejecta closely spaced in time, and evidence for stepwise mass extinctions spanning intervals of 1-3 Ma. For the K/T boundary, three candidates, Popigai, Manson, and Yucatan, have been proposed as impact craters [3]. Two distinct strata at the K/T boundary in western North America have been interpreted [4,5] as evidence for two sequential impacts. If multiple impacts occurred within a time span of ~1 Ma then multiple Ir enrichments should be observed.

DSDP Hole 577B on the Shatsky Plateau (Rise) in the northern Pacific at ~12°N at K/T time is the first site. At this site, the K/T boundary was undisturbed and well recovered. Samples contain $\gtrsim$97% $CaCO_3$, which exhibit clear chemical signals associated with asteroidal/cometary impact. Ir, Fe, and Cr data from Hole 577B [6] are plotted in Fig. 1. All data are normalized to Th. In the study of this site [9], we found that the normalized abundances of Al, Hf, Ta, and Th essentially overlap the N.A.S.C. (North American Shale Composite) abundances; i.e. the detrital component in these carbonate sediments resemble the N.A.S.C. composition. Considering the very low Th concentration in seawater, ~3±2 x 10^{-5} μg/L [10], little Th is precipitated from seawater onto the detrital clay; therefore, Th is an excellent diagnostic aeolian clay indicator. From the Th-normalized Ir data, two satellite peaks below the major peak at 78 cm and 81 cm of 577B-1-4 are clearly shown. The major Ir peak (K/T boundary) is at 72 cm. Fe and Cr, from C1-like impactor ejecta fallout [11], also show two peaks at the same positions.

Hole 738C on the southern Kerguelen Plateau has been studied by [7]. A complete K/T boundary sequence was recovered. The Ir values reach a peak concentration of 18 ppb in the clay layer at 96.0-96.2 cm in section 20R-5, and gradually tail off. But in the sample 115 cm above the boundary, Ir concentrations have still not reached background levels. From the Ir peak downward to the lowermost sample analyzed at 102 cm, the Ir concentration is still as high as 1.7 ppb. From the Th-normalized data in Fig. 2, we observed a small Ir/Th peak at 100-101 cm. Though this peak is within the error margin, the trend is clear. Fe and Cr exhibit the same pattern.

The third case is Hole 690C on the Queen Maud Ridge. Trace element studies have been reported by [8]. Applying the same Th normalization procedure to Hole 690C data, we obtained Fig. 3 for Ir and Fe. Cr was not measured at all levels like Ir and Fe by [8], and also the large Cr errors precluded estimates of the Cr/Th pattern. Again, the Ir/Th plot indicates the strong possibility of satellite peaks at ~52 cm. The main peak is at 39-40 cm. It was noted that the Hole 690C K/T boundary was bioturbated [12]. Due to the high clay content, one would expect that only ~2% of the observed total Fe in the Ir peaking samples would be from impactor ejecta fallout. Therefore, use of Fe/Th ratios will not permit accurate estimates of Fe_{net} and also not permit us to define precise Fe/Th satellite peaks.

It seems significant that the background level of Ir/Th at 690C-15X is obtained for samples that contain ~54% detritus (0-21 cm) and ~15% detritus (100-145 cm), which indicates a uniform Ir of ~0.20 ppb in the detrital NASC-like clay component. For example, the background level of Ir in the 15X-5-0-29 interval is equivalent to ~0.24 ppb Ir in NASC-like detrital clay, assuming all Ir is in the clay component. Similarly, for eight background samples before the K/T boundary in the 15X-4-90-145 interval, a value of 0.16 ppb Ir in NASC-like detrital clay is obtained. These levels of Ir are consistent with 0.5±0.3 ppb Ir in 24 pelagic clays [13] and 0.39 ppb Ir in 34 Gubbio "background" shales [14].

Observations by [15,16] indicate that the stratification of trace elements appears threefold with peak concentrations in sublayers A1, A3 and B2 for different element groups, including Ir, in the Stevns Klint K/T boundary layers. C1 ratios for many siderophile elements were found by [17] in combined layers III and IV, corresponding to layers A, B, C and D. These C1 ratios for combined layer samples strongly support the impact hypothesis and also an indication of redistribution between layers. Recent data [15] do not indicate a satellite peak before the main K/T peak at the Stevns Klint. The clay rich K/T boundary plus the bioturbation and excessive organic carbon preclude any attempt to find such evidence.

Multiple Ir anomalies in the K/T section at Lattengebirge, Bavarian Alps are reported [18]. The main peak of 4.4 ppb is precisely at the boundary. A peak of 3.6 ppb was detected at 16 cm below the boundary, corresponding to 14,000-9,000a before KTB. The third peak of 2.8 ppb is 10 cm above the KTB. They suggested an alternative causative agent for the K/T events like prolonged and intense volcanism combined with sea-level and climate changes. But the recent works on Ni-rich spinels and Ir at the K/T boundaries [19,20] clearly establish cometary/asteroidal impactors at the K/T boundary. The pre K/T Ir enriched layer could be ascribed to a cometary impact. The third peak ~10 cm above the KTB has an Ir enrichment of ~6X relative to average pelagic clays. In Hole 577B 0.073±0.009 ppb Ir in carbonate rich sediments ~3 m (~1 Ma) above the K/T boundary was reported [6]. This is equivalent to 1.8 ppb of Ir in the NASC-like detrital clay in the sample. We cannot rule out another cometary impact after the main K/T event.

The Ir contents in Gubbio shales ~2m above and below the K/T boundary (i.e. over ~1 Ma interval and K/T boundary shale values were excluded) were ~5X higher relative to Ir contents in shales 6-219 m below the K/T boundary [14]. Observations by [21] indicate similar Ir enrichments above background over 1-2 m of section with a peaking at the K/T boundary at the Stevns Klint, Carravaca, and Bidart, France, with an estimated enhancement duration of $\sim 10^4$a. Volcanism was favored by [14]; however, the cometary showers [2] explains the enhanced Ir contents over ~1 Ma as well.

In conclusion, the data from three world wide sites such as Shatsky Rise (Holes 577, 577B), Kerguelen Plateau (Hole 738C) and Qeen Maud Ridge (Hole 690C), where K/T sediments were deposited in different chemical regimes from intermediate depth at the K.P. Hole 738C of ≤300m to deep oceanic sites (1800-2400 m) for the S.R. and Q.M.R. sites, strongly indicate a small satellite Ir/Th peak before the main Ir/Th peak at the respective K/T boundaries. From estimates of the sedimentation rates at the three sites, the time intervals between the satellite and the main Ir/Th peaks are ~8000a (S.R.), ~2000a (K.P.), and 13,000a (Q.M.R.), with a most probable value of ~6000a.

References: [1] Davis M. et al. (1984) Nature 308, 715-717. [2] Hut P. et al. (1987) Nature 329, 118-126. [3] Hut P. et al. (1991) L.P.S. XXII, 603-604. [4] Izett G.A. (1991) EOS, 72, No. 44, 278. [5] Shoemaker E.M. and Izett G.A. (1992) L.P.S. XXIII, 1293-1294. [6] Michel H.V. et al. (1985) Init. Repts. DSDP 86, 533-538. [7] Schmitz B. et al. (1991) Proc. ODP. Sci. Results 119, 719-730. [8] Michel H.V. et al. (1990) Proc. O.D.P. Sci. Results 113, 159-168. [9] Schmitt R.A. et al. (1991) L.P.S. XXII, 1187-1188. [10] Huh C.A. et al. (1989) G.C.A. 53, 1357-1366. [11] Liu Y.-G. and Schmitt R.A. (1993) L.P.S. XXIV, this volume. [12] Scott L.D. and Kennett J.P. (1989) Nature 342, 526-529. [13] Kolde M. et al. (1991) G.C.A. 55, 1641-1648. [14] Crocket J.H. et al. (1988) Geol. 16, 77-80. [15] Graup G. and Spettel B. (1992) Met. 27, 228. [16] Graup G. et al. (1992) L.P.S. XXIII, 445-446. [17] Ganapathy R. (1980) Science 209, 921-923. [18] Graup, G. et al. (1989) E.P.S.L. 95, 271-290. [19] Robin E. et al. (1991) E.P.S.L. 107, 715-721. [20] Robin E. et al. (1992) E.P.S.L. 108, 181-190. [21] Rocchia R. et al. (1987) Soc. Geol. de France Mém. 150, 95-103.

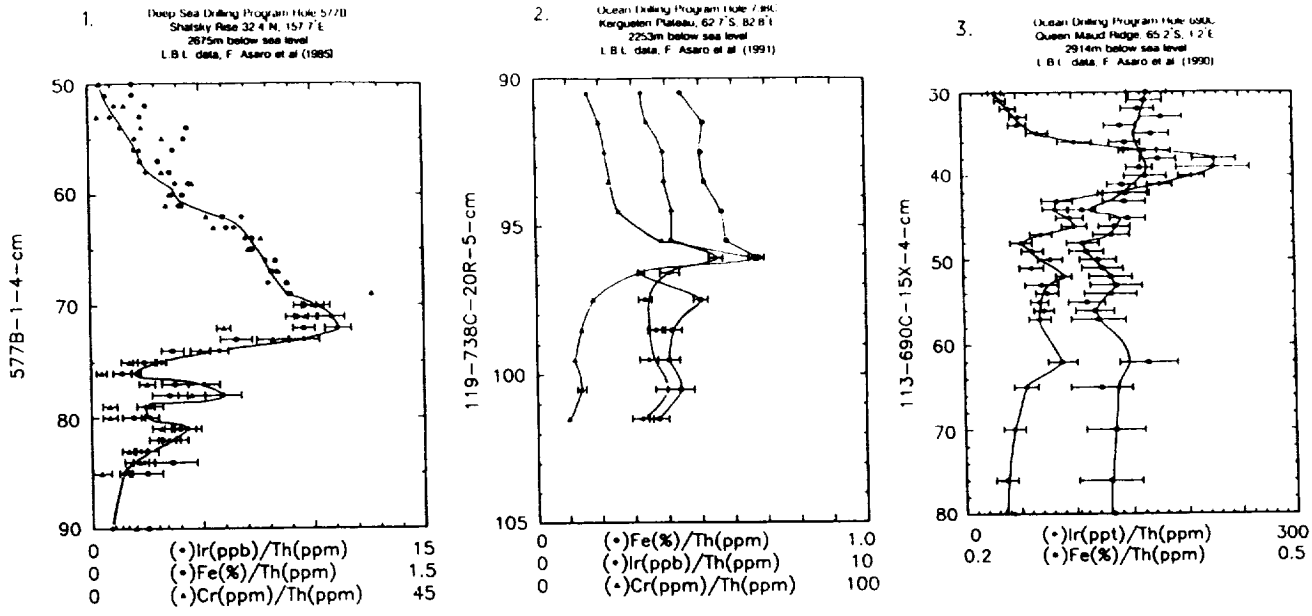

EARTH'S PARTIAL PRESSURE OF CO_2 OVER THE PAST 100-500 Ma; EVIDENCE FROM Ce ANOMALIES IN MOSTLY SHALLOW SEAS (<200m) AS RECORDED IN CARBONATE SEDIMENTS, II;

Y.-G. Liu[1,2], J.W. Reinhardt[5], and R.A. Schmitt[1-4], [1]The Radiation Center and Departments of [2]Chemistry and [3]Geosciences, and [4]College of Oceanography, Oregon State University, Corvallis, Oregon 97331, USA; and [5]Institute for Paleontology, Universität Erlangen, Erlangen, Ger. Present at Myanma Shell-Burma, 2501 An The Hague, The Netherlands.

In a previous abstract in this volume [1] we reported the direct relationship of Ce anomalies, Ce^{A*}, recorded in 0.2-119 Ma $CaCO_3$ sediments to the Ce anomalies, Ce^{A}, in the parental Pacific deep seawater and their relationship to atmospheric $P(CO_2)$ relative to the present $P^{\circ}(CO_2)$. Because carbonate samples from ocean basins, obtained from D.S.D.P. and O.D.P., are restricted to <130 Ma, we have analyzed via INAA [1] continental $CaCO_3$ samples that were deposited in ancient oceans and shallow sea platforms <200 m over central USA, central Europe, China, and Saudi-Arabian/Oman. Shallow sea conditions over continents as well as platforms may have been subjected to more localized variations because of their complex chemical regimes as well as being at higher temperatures relative to the <200 m Pacific Ocean's mixed layer. This has been observed in the spread of trace elements in ~250 Ma China carbonates and in carbonates from the ~150 Ma oil-rich Arab Formation.

Although many dolomites were analyzed, they were excluded from $P(CO_2)$ calculations in order to avoid unknown dolomitization effects. Although we adopted such a conservative approach, examination [2] of REE and Nd geochemistry of regionally dolomitized carbonates indicates dolomitization does not affect their geochemistry during diagenesis. Comparison of our dolomite and limestone data from the same formations support the [2] observations.

It has been noted that carbonates with low U/Th ratios and low U abundances (e.g. 0.16±0.10 ppm in Central Pacific deep sea carbonates) may be utilized as diagnostic indicators for obtaining reliable Ce^{A*} measurements [3]. Because of associated organic debris in shallow sea platforms, considerable reduction of $UO_2^{2+} \rightarrow U^{4+}$ is expected (U/Th > $3x10^4$ in seawater) with adsorption of $U(OH)_4$ onto oxyhydroxide coatings of carbonate minerals; e.g. the average U in 16 Arabian limestones was 1.4±0.9 ppm. Regimes favoring reduction of UO_2^{2+} could also inhibit $Ce^{3+} \rightarrow Ce(OH)_4$ oxidation. However, the absence of significant Ce^{A*} - U correlations at many shallow sea sites indicates that Ce^{A*} values obtained from shallow sea deposited carbonates may be considered reliable for ΔpH and $P(CO_2)$ calculations.

We have plotted the Ce^{A*} values over the 75-470 Ma interval. For $P(CO_2)$ calculations, we assumed as a reference standard, the <200 m mixed Pacific Ocean with a Ce^{A} geometric mean of 0.22 and a range of 0.10-0.43 [4]. Five China carbonates at 250, 261, and 280 Ma that are shown as (♦) were deposited in deeper open platforms, say up to ~1000 m and therefore exhibit quite reliable Ce^{A*} and $P(CO_2)$ values. Their actual Ce^{A*} values were 0.28, 0.19, 0.19, 0.10, and 0.08 which are consistent with the Ce^{A} in Pacific intermediate seawater, 200-600m [4]; we normalized these actual values to the average Ce^{A} in shallow seawater for depiction, i.e. multiply by 0.22/0.10. Another 430 Ma China deeper ocean platform sample was 0.74, which corresponds to a $P(CO_2)$ ~2.7X $P^{\circ}(CO_2)$. This more reliable value of 2.7X relative to an average of $P(CO_2)$ ~1.9X for two USA 430 Ma shallow seawater samples is in line with lower CO_2 solubilities expected from higher temperatures, say $\gtrsim$30°C, in the <100 m shallow sea over the central USA during the early Silurian period.

Observations are summarized below.

1. Because $P(CO_2)$ values obtained from reliable deep Pacific Ocean carbonates [1] in the 67-119 Ma interval were similar to the present $P^{\circ}(CO_2)$ values, we have drawn a 1.0 ratio for that interval. Two of three Saudi-Arabian 75-106 Ma carbonates fall within the Ce^{A} range for the present Pacific Ocean mixed layer. Coincidentally, a 90 Ma Oman carbonate yielded Ce^{A*}=0.18. This Ce^{A*} for a shallow sea platform agrees well with the Ce^{A*}s of the 95 Ma Laytonville Limestones deposited in deep seas [1], both yielding $P(CO_2)$ ~1.0X.

2. Although there is considerable scatter among the ~150 Ma carbonates, the average Ce^{A*} value suggests that $P(CO_2)$ increased during the early Cretaceous, i.e. 1.0X at ~120 Ma to ~1.4X at ~150 Ma.

3. At ~250 Ma, the average Ce^{A*} in 13 shallow sea China carbonates agrees well with the single and more reliable ~250 Ma China carbonate (♦) deposited in deeper open platform. We suggest that $P(CO_2)$ ranged from 1.4-1.7X over the Jurassic and Triassic periods.

4. At ~280 Ma, three China carbonates deposited in deeper open platforms and therefore considered more reliable are consistent with a European carbonate, which indicate Ce^A and $P(CO_2)$ values similar to the present. The minimum at ~280 Ma corresponds to the great Permo-Carboniferous glaciation. Modeling levels of atmospheric CO_2 over the past 570 Ma predicts a $P(CO_2)$ ~1.0±0.2 at 280 Ma [5].

5. From 280 Ma to 470 Ma, the trend favors increasing Ce^{A*} and corresponding $P(CO_2)$ values between 1.9-2.7X, with a more reliable value closer to 2.7X at 430 Ma because of the unknown higher (≳30°C relative to ~20°C in the present Pacific's mixed <200 m layer between ±20° latitude) temperature in the <100 m seawater over continental USA which was located just south, ~15°S, of the equator at ~430 Ma [6].

For comparison, paleosol carbonate data yield considerably higher $P(CO_2)$ estimates of ~5-10X $P^\circ(CO_2)$ at ~120 Ma, ~5-9X at ~140 Ma, ~7-13X at ~200 Ma [7], and ~3-5X at ~370 Ma and ~11-16X at ~410 Ma [8]. Corresponding theoretical models indicate $P(CO_2)$ values of 6^{+6}_{-4}X at ~120 Ma, $4^{+2}_{-2.5}$X at ~140 Ma, $4^{+3}_{-1.5}$X at ~200 Ma, 8^{+5}_{-5}X at ~370 Ma, 11^{+7}_{-7}X at ~410 Ma, and $14^{+?}_{-10}$X at ~470 Ma [5]. During the Cretaceous, a predicted $P(CO_2)$ ~2.3X was reported [9].

The greenhouse effect induced by increasing CO_2 seems to be an important factor contributing to Earth's climatic changes [10,11]. The $P(CO_2)$ trend is in general consistent with climatic changes noted in the past: glaciation during the Carboniferous-Permian periods, warmer climates through the Mesozoic, and a temperature decline during the Paleogene [12]. The $P(CO_2)$ patterns of our work are similar to a "best guess" by [13].

The geochemical cycles that control atmospheric CO_2 have been discussed by [14,15,9]. Plate tectonics, which affects both metamorphic-magmatic decarbonation and changes in continental land area, is one of the major controls of atmospheric CO_2. Climatic changes induced by CO_2 have been limited to the intensity of sea-floor hydrothermal activity induced by tectonic rearrangements of sea-floor spreading center; e.g. in the early Eocene [16]. The estimated $P(CO_2)$ values of ~1.5X [1] for that epoch support their [16] suggestion. During the Mesozoic, similar $P(CO_2)$ values could be related to the breakup of Pangaea starting with the separation of North America and Gondwanaland in the late Triassic (~230 Ma) followed by the breakup of Gondwanaland during the late Jurassic (~150 Ma) and Cretaceous [17,6,18].

We acknowledge the following persons and institutions for supplying carbonate samples: Arabian-American Oil Co. (Aramco), S.D. Bower (and D.G. Hadley and D.L. Schmidt of the U.S.G.S.) for Saudi-Arabian/Oman samples; Illinois State Geol. Survey, R.D. Norby and M.W. Leighton for Illinois and Iowa samples; Ohio Dept. Nat. Res., D.A. Stith for Ohio samples; U.S.G.S., H.E. Cook for Laytonville Limestones; and D.S.D.P. and O.D.P. personnel for Pacific carbonates.

References: [1] Liu Y.-G. and Schmitt R.A. (1993), this volume. [2] Banner J.L. et al. (1988) J. Sed. Pet. 58, 415-432. [3] Liu Y.-G. et al. (1988) G.C.A. 52, 1361-1371. [4] Piepgras D.J. and Jacobsen S.B. (1992) G.C.A. 56, 1851-1862. [5] Berner R.A. (1990) Science 249, 1406-1409. [6] Ziegler A.M. (1981) Paleobot. Paleoecol., and Evol. 2, 231-266. [7] Cerling T.E. (1991) Am. J. of Sci. 291, 377-400. [8] Mora C.I. and Driese S.G. (1992) EOS 73, No. 43, 95; Mora C.I. et al. (1991) Geol. 19, 1017-1020. [9] Walker J.C.G. (1988) Ind. J. Rad. Space Phys. 17, 147-154. [10] Walker J.C.G. et al. (1981) J.C.R. 86, 9776-9782. [11] Marshall H.G. et al. (1988) J.G.R. 93, 791-801. [12] Frakes L.A. (1979) Climates Throughout Geol Time (Elsevier). [13] Kasting J.F. (1987) Precamb. Res. 34, 205-229. [14] Berner R.A. et al. (1983) Am. J. Sci. 283, 64-83. [15] Berner R.A. (1992) G.C.A. 56, 3225-3231. [16] Owen R.M. and Rea D.K. (1985) Science 227, 166-169. [17] Seyfert C.A. and Sirkin L.A. (1973) Earth History and Plate Tectonics (Harper & Row). [18] Ziegler A.M. et al. (1983) Tidal Friction and Earth's Rot. II, 240-252.

Shallow Sea deposited carbonate ($CaCO_3$) sediments: Saudi-Arabian Platform ●, China Platform ♦, Europe ■, USA (Ill., Iowa, Ohio) ▲. Range and geom. mean Ce^A in <200 m Pacific Ocean [4]

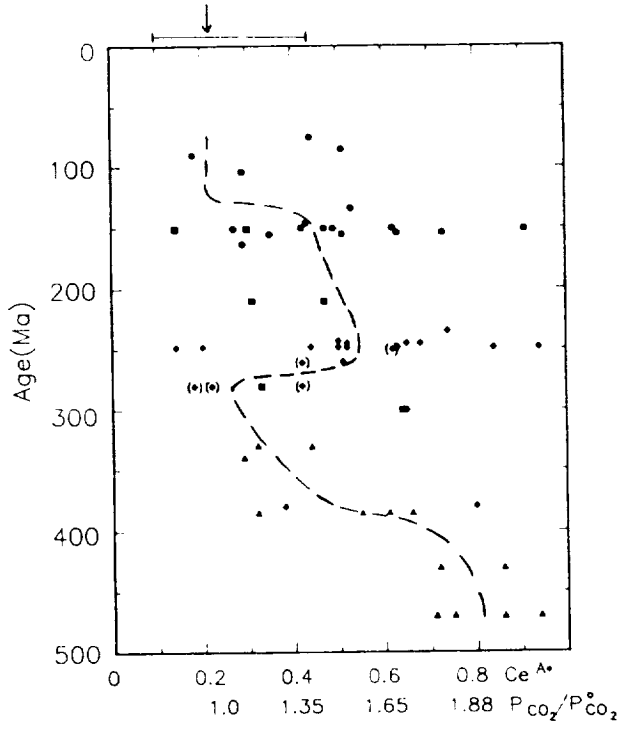

NOBLE GASES IN TWENTY YAMATO H-CHONDRITES: COMPARISON WITH ALLAN HILLS CHONDRITES AND MODERN FALLS

Th. Loeken, P. Scherer, and L. Schultz, Max-Planck-Institut für Chemie, 6500 Mainz (Germany)

Concentration and isotopic composition of noble gases have been measured in 20 H-chondrites found on the Yamato Mountains ice fields in Antarctica. The distribution of exposure ages as well as of radiogenic ^{4}He contents is similar to that of H-chondrites collected at the Allan Hills site. Furthermore, a comparison of the noble gas record of Antarctic H-chondrites and finds or falls from non-Antarctic areas gives no support to the suggestion that Antarctic H-chondrites and modern falls derive from differing interplanetary meteorite populations.

On the basis of statistically significant differences in the concentration of a number of trace elements, it has been suggested that H-chondrites found on blue ice fields of Antarctica and those falling in non-Antarctic areas represent members of different extraterrestrial populations which have had different thermal histories during formation of their parent material [1]. In addition, it was concluded that Antarctic H-chondrites found in Victoria Land (Allan Hills) differ from those found in Queen Maud Land (Yamato Mountains) [2]. Takaoka et al. [3] noted the similarity of exposure age distributions of Yamato L- and H-chondrites with those of non-Antarctic ones and Schultz et al. [4] have shown that the noble gas record of Antarctic Allan Hills H-chondrites and that of modern falls is very similar. Both distributions show a characteristic clustering of cosmic ray exposure ages around 7 Ma. Also the distribution of radiogenic gases yields no evidence that H-chondrites derive not from the same population. In this paper we report noble gas measurements of 20 Yamato chondrites which seem to contain no paired samples. The full data set and the experimental details will be given elsewhere.

Exposure ages are calculated from cosmogenic ^{21}Ne using the production rate and shielding correction procedures as described by Eugster [5]. Fig.1 shows the exposure ages of the Yamato H-chondrites and of all Antarctic H-chondrites (this paper and [3]). For comparison, the exposure ages of non-Antarctic H-chondrites, calculated from literature values [6], are given. To prevent additional uncertainties due to extreme shielding corrections only measurements with cosmogenic ^{22}Ne/^{21}Ne between 1.08 and 1.18 are considered. All three distributions of Fig.1 show the prominent exposure age cluster of H-chondrites at about 7 Ma which indicates that about 40% of the Antarctic and non-Antarctic H-chondrites were excavated from their parent body at the same time.

Also the radiogenic ^{4}He in Yamato H-chondrites and modern falls is very similar (Fig.2). Both groups have a maximum between 1250 and 1500 10^{-8}ccSTP/g indicating that their thermal history is similar. For ^{40}Ar an apparent difference to measurements reported in the literature was noted [4]. This, however, is attributed to an experimental artefact in measurements carried out more than twenty years ago. The Yamato H-chondrites, however, show a very similar distribution to that of Allan Hills chondrites [4] and also to modern falls

measured recently [7]. We conclude from these observations that the noble gas record of chondrites from two Antarctic find locations show no evidence for different interplanetary populations of H-chondrites.

[1] Dennison J.E. et al. (1986) Nature 319, 390-393. [2] Wolf S.F. and Lipschutz M.E. (1992) Lunar Planet Sci. XIII, 1545-1546. [3] Takaoka N. et al. (1981) Mem. Natl. Polar inst. (Tokyo), Spec. Issue No. 20, 264-275. [4] Schultz L. et al.(1991) Geochim.Cosmochim.Acta 55, 59-66. [5] Eugster O. (1988) Geochim.Cosmochim.Acta 52, 1649-1662. [6] Schultz L. and Kruse H. (1989) Meteoritics 24, 155-172. [7] Weber H. et al. (1989) Meteoritics 24, 338.

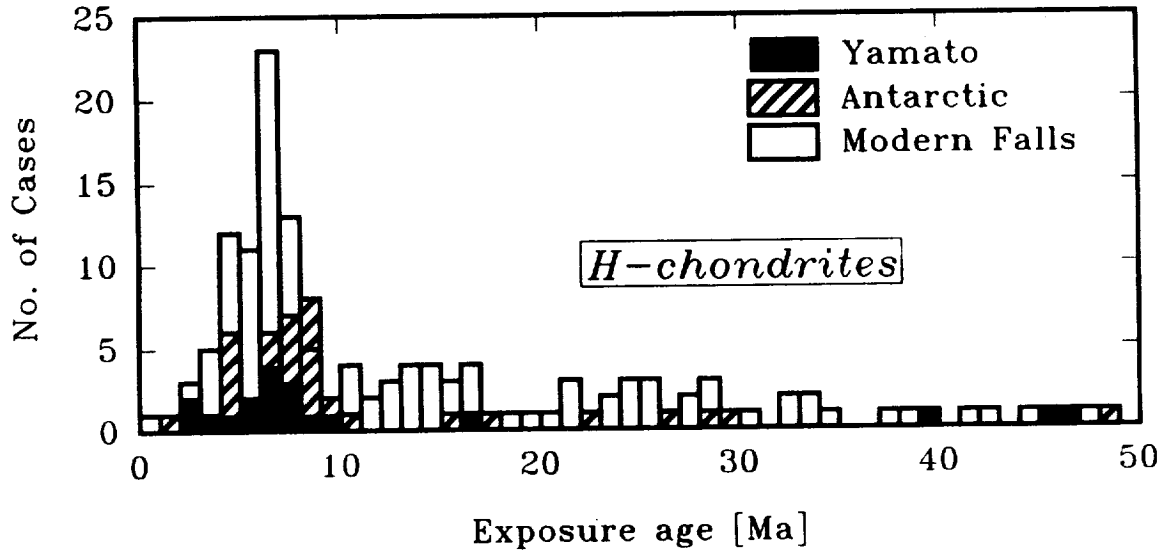

Fig. 1: Distribution of cosmic ray exposure ages.

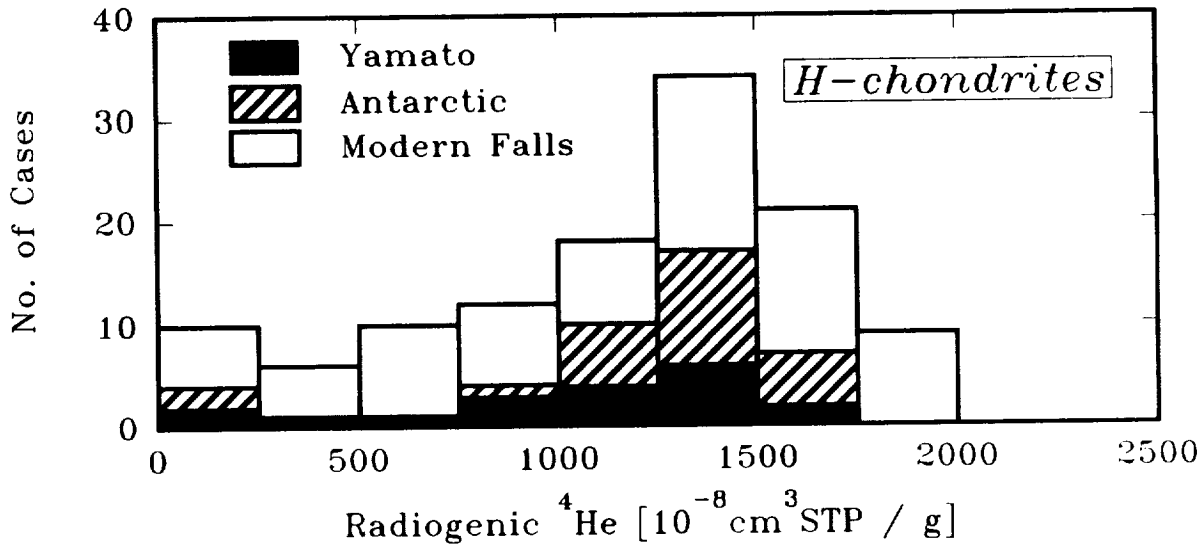

Fig. 2: Concentrations of radiogenic ^{4}He.

THE FIRST LUNAR OUTPOST: THE DESIGN REFERENCE MISSION AND A NEW ERA IN LUNAR SCIENCE; Gary E. Lofgren, Code SN-4, NASA-Johnson Space Center, Houston, TX 77058

The content of the First Lunar Outpost (FLO) Design Reference Mission has been formulated and a "strawman" science program has been established. The mission consists of two independent launches using heavy lift vehicles that land directly on the lunar surface. A habitat module and support systems are flown to the Moon first. After confirmation of a successful deployment of the habitat systems, the crewed lunar lander is launched and piloted to within easy walking distance (2 km) of the habitat. By eliminating the Apollo style lunar orbit rendezvous, landing sites at very high latitudes can be considered. A surface rover and the science experiments will accompany the crew. The planned stay time is 45 days, 2 lunar days and one night. A payload of 3.3 metric tons will support a series of geophysics, geology, astronomy, space physics, resource utilization, and life science experiments. Sample return is 150 to 200 kg. The rover is unpressurized and can carry 4 astronauts or 2 astronauts and 500 kg of payload. The rover can also operate in robotic mode with the addition of a robotics package. The science and engineering experiment strategy is built around a representative set of place holder experiments.

An experiment station similar to ALSEP on Apollo will include instruments to measure heat flow, magnetic fields, seismic activity, micrometeorite and secondary ejecta flux, and the precise distance to Earth. A solar system physics experiment package will be deployed at the same locality and measure particles and fields and the lunar atmosphere and its variations. The stations will be deployed by the crew and operated remotely from Earth.

Astronomy experiments will be deployed in a remote locality (10 km from habitat) after the area has been explored geologically to avoid dust contamination. The experiments currently include a lunar transit telescope, a small research telescope, and a small solar telescope. The lunar transit telescope will take advantage of the lack of an atmosphere to survey the sky in the UV spectral range providing images of stars, galaxies, clusters, and the interstellar medium. The research telescope will be pointable and used to observe various astronomy targets as well as provide engineering and operating data for future telescope design. The solar telescope will provide high resolution images of the sun to examine solar flare tracking and other solar processes. All of the telescopes will be deployed by the crew and will be operated from the earth.

In Situ Resource Utilization (ISRU) experiments will demonstrate and allow testing of possible utilization and engineering concepts that could be used in future lunar outpost design. Three concepts are being considered for early evaluation. Oxygen extraction from lunar materials which uses imported hydrogen will be evaluated to possibly provide oxygen for chemical propulsion systems and to make water. Methods will be studied to optimize brick fabrication from lunar soil. A gas flow unit will test pneumatic transport and pneumatic size sorting methods to be used primarily for preparing feedstocks for other processes.

Life science EVA experiments will consist of monitoring equipment for human performance during EVA. There will specialized testing for such attributes as vision, locomotion, balance, orientation etc. An exobiology experiment might consist of a cosmic dust collector deployed on the lunar surface to be returned on a later mission for analysis.

Extensive geologic traverses are planned. The unpressurized rover is similar to the one used on Apollo but with an increased payload. Rover traverses will be limited to distances with a walk back capability, approximately 20 km. Robotic rover traverses can extend the radius to 100 km. There is a traverse geophysical package which includes an electromagnetic sounder for subsurface data collection, an active seismic experiment to determine the structure of the upper few kilometers, a traverse gravimeter, an electrical properties experiment which will also return data on subsurface structure, and a profiling magnetometer. Geologic field studies will have specific objectives similar to Apollo field studies, but with considerably more latitude to adapt the traverse to targets of opportunity. EVA's will occur nearly every day with alternating crews. The total EVA traverse time in one 45 day mission will more that

double the total Apollo EVA time. EVA's will be a maximum of 8 hours when conditions are favorable and of shorter duration when heating or light conditions are less opportune. The tools available to the astronauts will be patterned on those used on Apollo including the 3 meter drill and drive tubes for sampling the regolith. In addition a drill capable of drilling rock is being considered. The geologic investigation should cover an area about 50 km in diameter around the outpost.

Robotic operations with the rover would allow excursions of up to 100 km from the outpost; beyond the area that can be explored by the crew. Robotic missions could be operated from the habitat or from Earth when the habitat is not occupied. Samples of rocks and soils could be collected and documented. A manipulator arm will be available to dig, scoop, and sample soil and rocks. Many of the geophysical traverse instruments could still be used and some basic analysis instruments might also be included. Samples collected between outpost missions could be returned when the outpost is next occupied. Up to four 200 km round trip traverses could be accomplished per year in remote mode. It would also be possible to do preliminary traverses to help planning the crew explorations.

Science experiments conducted within the habitat may include basic characterization of the lunar samples. The samples can be examined and subsamples taken for return to Earth. A binocular microscope and some kind of spectral analysis device will be available to assist in the characterization. Other IVA experiments may include gravitational biology and physiological experiments. For example the mutagenicity of cosmic radiation and the nature of chloroplast movement could be studied. Physiological experiments on the central nervous system, thermoregulation in the body and body fluid analysis are being considered.

The sortie missions are an important aspect of the FLO exploration. The sortie mission resembles an Apollo mission. It will be a two week mission with 2 crew and a single landing vehicle; the same vehicle used to occupy the outpost. The crew with have an unpressurized rover with similar capabilities to the one mentioned above. They will deploy appropriate instruments with the objective of establishing the desired network science, i.e. seismology.

The FLO mission will have a large scientific return in the form of samples and scientific instrument deployed. This information will provide input to future planning for a Lunar Base and for missions to Mars.

EXPERIMENTALLY REPRODUCED RELICT ENSTATITE IN PORPHYRITIC CHONDRULES OF ENSTATITE CHONDRITE COMPOSITION;

Gary E. Lofgren, John M. DeHart, Code SN4, NASA-Johnson Space Center, Houston, TX 77058; Tammy L. Dickinson, Code SLC, NASA Headquarters, Washington DC, 20546.

We recently proposed a model for the origin of porphyritic pyroxene (PP) chondrules in enstatite chondrites that contain phenocrysts of enstatite with blue cathodoluminescence (CL) set in a matrix of radial, dendritic enstatite with red CL [1]. The model is based upon studies of chondrules in ordinary chondrites [2] which suggest that they form as mechanical aggregates of crystalline and other material that are then partially melted and cooled. When melting is essentially complete so that only submicroscopic nuclei remain, the texture that forms is porphyritic and all the phenocrysts will be newly formed with virtually undetectable relict cores. If melting is significantly less complete, however, relatively large relict crystals will remain. Such relict crystals were first described in chondrules in enstatite chondrites by [3,4] and identified by their distinctly different CL and chemistry compared with the dominant crystals in the chondrule. In this case the pyroxene phenocrysts which we consider relict have distinctive levels of Mn and Cr and Al which produce a characteristic blue CL. We have completed experiments in which previously grown blue CL En (relict) is enclosed in a matrix of red CL En with a coarsely radial texture.

Our proposed history begins with the mechanical aggregation of i) nearly pure enstatite (i.e. low in Mn, Cr, and Al) which typically has blue CL, ii) enstatite with increased levels of these minor elements which typically has red CL, iii) sulfides, iv) Fe-metal, and v) other minor phases. This aggregate is then partially melted so that some of the blue CL enstatite, presumably initially coarser grained, is preserved. The chondrule is then cooled quite rapidly and the remaining melt crystallizes to a radial texture. The radial texture would develop only if the remaining melt in the chondrule is free of nuclei at the beginning of cooling. Nucleation would then occur on embryos which become nuclei during the cooling [5]. The Mn, Cr, and Al in the radial enstatite could come from melted red Cl enstatite in the aggregate or from the sulfides and other minor phases, if no red CL enstatite was aggregated. During the rapid growth necessary to produce the radial texture, the minor elements would be readily incorporated into the newly grown enstatite producing the red CL. If nuclei are preserved in the melt surrounding the relict blue CL enstatite, the matrix will be microporphyritic to even porporphritic.

We have conducted experiments to test this model using established one-atmosphere, gas-mixing techniques [6]. Enstatite crystals that give off blue CL were grown from a very pure melt of enstatite composition. Several large crystals (up to 1 mm in diameter) were added to the standard enstatite chondrule starting material [7] that contained significant quantities of Mn, Cr, and Al. The few enstatite crystals added only a few micrograms to a charge of approximately 100 micrograms. This charge was melted for 20 to 45 minutes at 1537°C, a temperature slightly below the liquidus of the melt so as not to completely melt the pure, blue CL enstatites. The appropriate melt temperataure will vary with the size of the crystals and the liquidus temperature of the specific melt composition. The run was then cooled at 1000°C/hr in attempt to duplicate the typical matrix texture. We were successful in producing relict enstatite phenocrysts with blue CL in a matrix of coarsely radial to dendritic enstatite with red CL.

The relict crystals are preserved in runs with a melt time of 36 minutes or less at 1537°C. The relicts remain angular with smooth crystal/melt interfaces (Fig. 1). There are no embayments as suggested by [8] along the crystal/melt interfaces, and thus melting has occured uniformly. Partial melting does occur along fractures produced when the blue CL enstatite was initially grown and cooled through the proto/ortho enstatite transition with the attendent volume change. There is either reaction with the melt and diffusion of Mn and Cr into the blue CL En, or there is an overgrowth of red CL En along the fractures (Fig. 1). The bulk of the relicts remain blue. The melt enclosing the relicts crystalized to a coarsely radial to

dendritic to microporhyritic texture comprised of enstatite that has a bright red CL with decreasing melt time. The blue CL En has Mn and Cr contents at or below detection limits of the electron probe as described in earlier studies [9] and in natural blue Cl En [1]. In the red CL En in this study, the Mn, Al2O3, and Cr are at levels observed in [9] and the levels change rapidly also as observed in [9].

These experiments show that our model appears feasible. Relict crystals with Blue CL can survive a brief melting period and retain the blue CL with very modest reaction while enstatite with red CL will crystallize from the surrounding melt. The melting textures are not totally reminscent of natural chondrules, as the real relict En appear to have been annealed and do not show the inversion fracturing. Unfortunately we did not have the time to anneal the En crystals to such a condition. No embayments were observed in the relicts in the experiments, a problem raised by [8] to negate the partial melting origin. A similar senario could work for olivine. The variable matrix textures in the experiments correlate well with similar textures observed in natural chondrules. Leitch and Smith [8] studied chondrules with radial matricies, but we have observed many with microporphyritic textures. We can conclude that the physical process that form EC chondrules is basically the same as OC chondrules. The differences are in both the redox conditions and the bulk composition. If metamorphism is an important process in the formation of these EC chondrules, it occurs early before aggregation of materials which are then melted to form chondrules as suggested by [10]. These studies also show that enstatite can grow from igneous melts given the right nucleation conditions.

REFERENCES: [1] Lofgren et al. (1992) Lunar and Planetary Science XXIII, Lunar and Planetary Institute, Houston, 801-802. [2] Hewins (1988) in *Meteorites and the Early Solar System*, Kerridge and Matthews eds, 660-679. [3] Nagahara (1981) Nature **292**, 136. [4] Rambaldi (1981) Nature **293**, 558-561. [5] Lofgren (1983) J. Petrol. **24**, 229-255. [6] Lofgren and Russell (1986) GCA **50**, 1715-1726. Lofgren (1989) GCA **53**,461-470. [7] Lofgren et al. (1991) Meteoritics, **26**, 366-367. [8] Leitch and Smith (1982) GCA **46**, 2083-2097. [9] Lofgren and Dehart (1992) Lunar and Planetary Science XXIII, Lunar and Planetary Institute, Houston, 799-800. [10] McKinley et al. (1984) LPSC 14, JGR **89**, Suppl. B567-B572.

Fig. 1: A black and white photograph of a colar CL image. The light area labeled bl is blue CL enstatite and the dark gray area labeled rd is the red CL enstatite. The dark lines in the light (bl) area are the fractures with red CL. The width of the photograph is 250 micrometers.

LIQUIDUS EQUILIBRIA OF LUNAR ANALOGS AT HIGH PRESSURE.

J. Longhi, Lamont-Doherty Earth Observatory, Palisades, NY 10964

Melting experiments have been performed in the range of 20 to 40 kbar on partially crystallized synthetic glasses in order to test the accuracy of the polybaric fractional fusion model for picritic lunar green glasses (1). Results show that the model predicts the position of the olivine(ol) + orthopyroxene(opx) liquidus boundary within the uncertainty of the measurements, but that details of the calculations are subject to change because of new crystal/liquid partitioning data for olivine and pyroxene.

Volcanic glasses with picritic compositions (2) have posed a thorny problem for petrologists: their compositions are multiply-saturated with olivine and orthopyroxene at pressures of 17.5 to 25 kbar (cf. 3) and traditionally the pressure of multiple saturation is interpreted as the minimum pressure of melt segregation, yet on the Moon these pressures translate to depths of 350 to more than 500 km.. The physics of transporting melt these distances through cracks without altering the melt composition have been modeled (4) and the possibility of such transport seems remote at a time in lunar history when the thickness of the elastic lithosphere was on the order of 50 to 100 km (5). Thus polybaric melting models analogous to those proposed for terrestrial midocean ridge basalts (6) provide attractive alternatives. Because of the paucity of data, algorithms in the polybaric melting model proposed by the author (1) depended upon several extraoplations of phase equilibria and crystal/liquid partitioning from experiments at lower pressures on terrestrial compositions, so a series of melting experiments was initiated to provide data at high pressure with which to test and refine the model.

Partially crystallized glasses were synthesized with compositions designed to produce multiply-saturated liquids at high pressure and run in high purity iron capsules for 1 to 2 days in a piston-cylinder apparatus. The resulting charges contained remarkably homogeneous olivine + pyroxene ± garnet set in fine intergowths of quench crystals. In one charge a comparison of the average of 36 spot analyses (electron microprobe) collected on a grid was compared with the average of 4 rastered-beam analyses (100 μm on a side): all elements agreed within the standard deviations indicating that raster analyses of highly mafic quench intergrowths (no plagioclase) are accurate. Fig. 1 shows the compositions of melts in equilibrium with ol and opx (open squares) together with segments of the ol + opx liquidus boundary calculated for each melt according to the algorithms in (1). In each case except at 25 kbar the melt composition has a slightly higher Qtz component than the predicted liquidus boundary, however, the differences are not significant with respect to the overall uncertainty of the model.

The new experiments also provide relevant data on partitioning and phase equilibria. There is a dramatic increase in the molar partition coefficient (D*) for Al_2O_3 between opx and liquid(liq) from an average value of ~0.1 at low pressure to a value of 0.5 at 30 to 40 kbar. Values of D* for TiO_2 and Cr_2O_3, however, remain constant (~0.15 and ~ 2, respectively) over this pressure range. The different behaviors can be explained in terms of liquid structure: Al is tetrahedrally coordinated in silicate liquids at low pressure, but these tetrahedral sites become increasingly unfavorable with respect to the octahedral sites available in pyroxene as pressure increases; whereas Ti and Cr find no greater advantage in pyroxene with increasing pressure because they are already in octahedral sites in the liquid at low pressure. The previous model (1) employed a single value of D* (0.35) for opx and liq at high pressure that is now obviously too low for pressures in the range of 30 to 40 kbar. A consequence of using a pressure-dependent D* for Al is that now it is more difficult to deplete the source in Al_2O_3 at high pressure and extraction of melt at each pressure must, therefore, be more efficient to produce a polybaric pooled melt with green glass composition.

Fig. 2 shows the approximate location of liquidus boundaries at 25 kbar (dashed curves) in two projections based on multiply-saturated experimental liquid compositions (squares). Crystal compositions are shown as circles. Phase equilibria at 30 kbar are similar albeit displaced slightly farther away from Qtz. It is not clear yet whether in these intermediate Mg' liquids there is a liquidus boundary in the {Ol} projection separating fields of ol + pigeonite(pig) and ol + aluminous augite(aug) or whether there is a single continuous field of ol + clinopyroxene (cpx). In any case because most estimates of lunar mantle compositions have low Wo contents, melting of the interior at P > 25 kbar probably begins in the presence of ol, opx, and pig. Similar behavior has been observed in experiments on martian analogs (7). If there is sufficient Al in the source to stabilize garnet(gar), as there is in most estimates of whole Moon composition (8), then the equilibrium at the solidus will be opx + liq = ol + gar + pig. As in the case of the martian analogs, the initial melt will be nepheline-normative.

Finally, the Fe-Mg exchange coefficient for ol and liq (K_D) has similar values in the high pressure experiments as in previously reported low pressure experiments on lunar basalts (3) at comparable concentrations of TiO_2 (cf. Fig. 3 in ref. 3). However, even though TiO_2 levels are similar, the silica contents of the high pressure liquids are much lower than those of the basalts, so that tendency for increasing pressure to

increase K_D at constant composition (9) is offset by the shift in the ol + opx liquidus boundary to lower silica with increasing pressure.

REFERENCES

(1) Longhi J. (1992) *Proc. Lunar Planet. Sci. 22, 343-353.* (2) Delano J.W. (1986) *J. Geophys. Res. 91,* D201-D213. (3) Longhi J. (1992) *Geochim. Cosmochim. Acta, 56,* 2235-2251. (4) Spera F. J. (1992) *Geochim. Cosmochim. Acta, 56,* 2253-2265. (5) Solomon S.C. and Head J.W. (1979) *J. Geophys. Res. 84,* 1667-1682. (6) Klein E.M. and Langmuir C.H. (1987) *J. Geophys. Res. 92,* 8089-8115. (7) Bertke C. M. and Holloway J. R. (1990) *Lunar Planet. Sci. XXI,* 73-74. (8) BVSP (1981) *Basaltic Volcanism on the Terrestrial Planets,* Pergamon. (9) Ulmer P. (1989) *Contrib. Mineral. Petrol., 101,* 261-273.

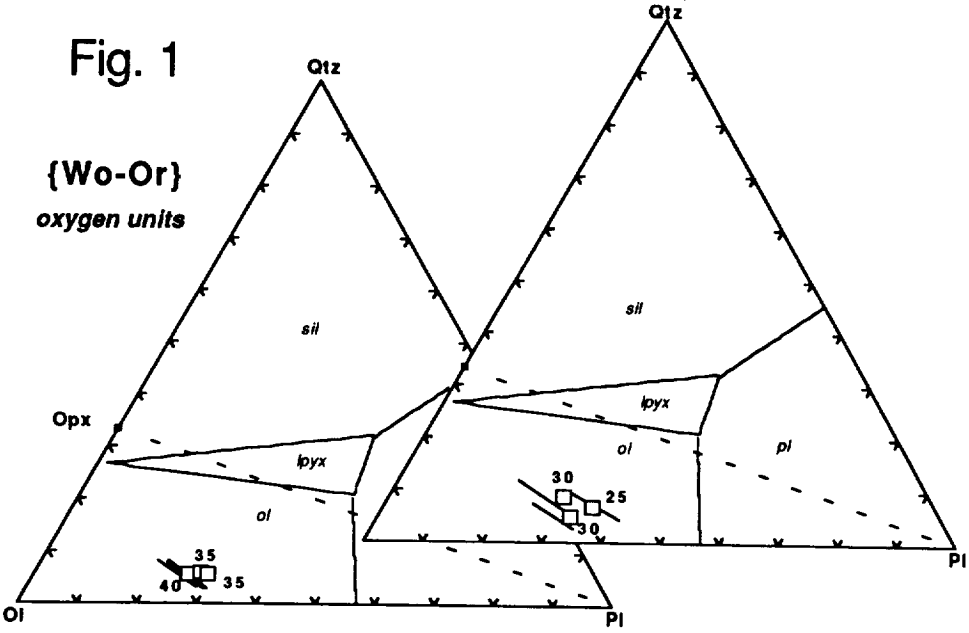

Fig.1. Comparison of positions of the ol + opx liquidus boundary in wollastonite (Wo) projection: squares are experimental determinations (this study); line segments are calculations of the liquidus boundary based on the algorithms of (1) and using the observed liquid compositions as inputs. Low pressure liquidus boundaries are shown for reference.

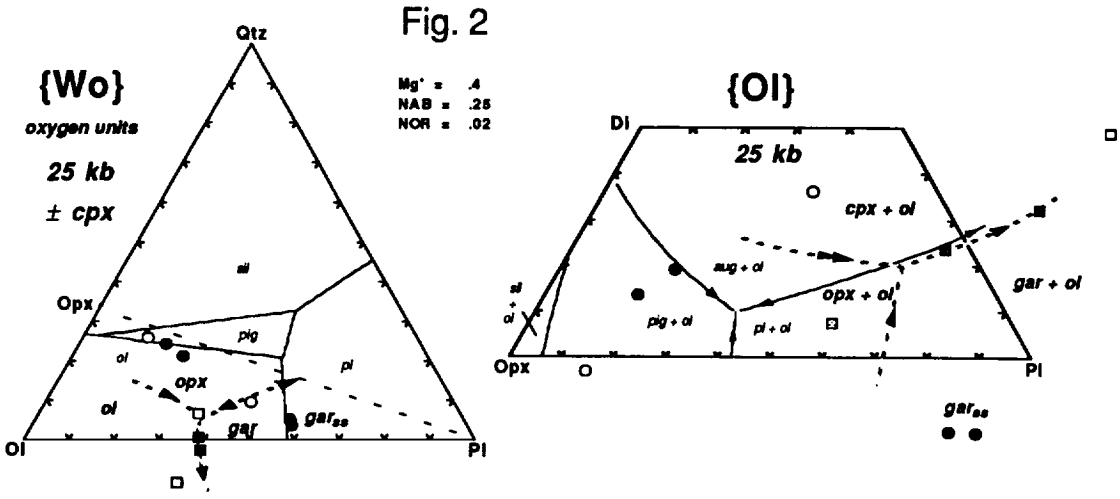

Fig. 2. Schematic liquidus equilbria at 25 kbar in Wo and Ol projections. ol-pig-gar-saturated liquids shown as solid squares; ol-opx- and ol-cpx-saturated liquids shown as open squares. Crystal compositions shown as solid or open circles as appropriate. Dashed curves are inferred 25 kbar liquidus boundaries; solid curves are 1 bar liquidus boundaries.

THE MONZONORITE-ANORTHOSITE CONNECTION: THE PETROGENESIS OF TERRESTRIAL KREEP.

J. Longhi, Lamont-Doherty Earth Observatory, Palisades, NY 10964 and J. Vander Auwera, LA Géologie, Pétrologie, Géochimie, Université de Liege, B-4000 Sart Tilman, Belgium.

There is a suite of rocks typically associated with Proterozoic massif anorthosites that bear some interesting similarities to lunar KREEP. In many cases (e.g., Laramie [1]) these rocks are plutonic and have traditionally been referred to as the jotunite-mangerite- ±charnockite- ±syenite suite. However, in the Rogaland district of southwestern Norway, where they are referred to as "monzonorites", these rocks are also present as fine-grained dikes and as the chill margin of a layered intrusion [2,3], and thus approximate magmatic liquid compositions are readily obtained by chemical analysis. Monzonorites are typically enriched in incompatible lithophile elements such as K (alkali feldspar is present), the rare earths (REE), and P. They have intermediate to low Mg', low-Ca pyroxene, and more evolved types have low Ti/Sm ratios. Much debate has developed over attempts to explain the link between monzonorites and massif anorthosites. One feature seems clear: monzonorites and associated anorthosites have different initial isotopic ratios [3,4], so a simple relation is not possible. However, there is apparently a continuum in major elements between the monzonorites and gabbros believed to represent magmas parental to the anorthosites. This continuum suggests a link via high pressure fractionation coupled with assimilation. Although more complicated, this scenario is similar that evoked for the early Moon: following the formation of ferroan anorthosites, continued fractional crystallization of the residual liquids at the base of the crust led to the formation of KREEP [5]. An attempt is made here to establish a link between monzonorites and high-Al gabbros which are nearly always found as ancillary intrusions associated with anorthosites, and which may record processes in lower crustal magma chambers.

Fig. 1 illustrates some of the evidence for a link by fractionation between monzonorites and gabbros . The upper panels show a continuous variation in TiO_2, P_2O_5, and MgO between gabbros and ferrodiorites of the Harp Lake Complex of Labrador [6] and the monzonoritic dikes of the Rogaland district of Norway [3]. Patterns for other elements (SiO_2, Al_2O_3, FeO, etc.) versus MgO are also continuous. Interpretation of the elemental variations are not straightforward, however. The peaked TiO_2-MgO pattern is as expected for fractional crystallization of a magma that eventually becomes saturated in ilmenite. Except for the subset of analyses with P_2O_5 above 2 wt %, the P_2O_5-MgO pattern is generally similar and indicates crystallization of a phosphate (apatite) between 2 and 3 wt % MgO. The samples with the highest P_2O_5 also have lower SiO_2 (43-45 wt%) and higher FeO (15-20 wt%) than those one the main trend. These samples are from dikes that show large regional variation in composition, and it seems possible that these dikes underwent an internal differentiation caused by differential flow of a crystalline matrix and interstitial liquid. The high-P-Fe, low-Si samples thus may be partial cumulates. If so, then the highest TiO_2 concentrations may be enhanced by accumulation as well. Experimental liquids obtained from gabbroic (HLCA) and monzonoritic (TJ) starting materials tend to mimic the high-MgO portion of the natural trend although it is clear that the specific compositions employed cannot be directly related. The steep trend of increasing TiO_2 with decreasing MgO for the natural samples in Fig. 1 indicates that fractionation must have involved extensive Fe-Mg equilibration.

Trace elements provide evidence of further complications. Several of the monzonoritic dikes lack negative Eu anomalies in their REE patterns and have only weak depletions of chondrite-normalized Sr relative to the light REE [3] — hardly what is expected from liquids residual to the formation of anorthosite. Phase equilibria complicates matters still more. Experiments on one of the most primitive monzonorites (sample TJ, the chill margin of the Bjerkeim-Sokndal intrusion [7]) show that plagioclase(pl) and orthopyroxene(opx) are together on the liquidus from 10 to 13 kbar. This pressure is consistent with experiments that showed aluminous opx megacrysts found in anorthosite plutons to have formed in this pressure range [8]. However, as Fig. 2 illustrates, the TJ composition is close to a thermal divide on the pl-opx(±pigeonite)-augite(aug) liquidus boundary in this pressure range, yet it would be extremely fortuitous for a residual liquid to remain on a thermal divide. One way to generate a liquid on a thermal divide would be in a second stage fusion of the lower crust: the first stage removes a granitic component leaving a pyroxene-plagioclase residuum, which would necessarily produce melts on the thermal divide at these pressures. This residuum would likely be depleted in incompatible elements and have positive Eu and Sr anomalies with respect to the other REE, so it would be necessary to invoke small degrees of melting to produce incompatible element enrichments and flatten out the Eu and Sr anomalies. Such a scenario would not, however, readily explain the continuous variation in major elements evident in Fig. 1 nor the continuous variation in mineral compositions between anorthositic and monzonoritic rocks [1].

A final option is assimilation-fractionation. In this scenario the compositions of the monzonoritic parent magmas (derived by high pressure crystallization of gabbroic liquids) are altered by assimilation of

granitic crust at lower pressures (i.e. ≤ 7 kbar) where the pyroxene-plagioclase thermal divide is no longer present. Thus the present location of the TJ composition near the thermal divide is accidental and the incompatible element patterns are hybrids. Further work is needed to verify this hypothesis.

REFERENCES

[1] Kolker A. and Lindsley D. H. (1989) *Amer. Mineral., 74*, 307-324. [2] Duschene, J.C., Roelandts I., Demaiffe D., and Weiss D. (1985) *Contrib. Mineral. Petrol. 90*, 214-225. [3] Duchesne J.C., Wilmart E., Demaiffe D. and Hertogen J. (1989) *Precambrian Res., 45*, 111-128. [4] Geist D. J., Frost C. D., and Kolker A. (1990) *Amer. Mineral., 75*, 13-20. [5] Warren P. H. and Wasson J. T. (1979) *Rev. Geophys. Space Phys.* 17, 73-88. [6] Emslie, R.F. (1980) *Geol. Surv. Can. Bull. 293*, 1-136. [7] Duchesne J.C. and Hertogen J. (1988) *C. R. Acad. Sci. Ser. II, 306*, 45-48. [8] Fram M.S. and Longhi J. (1992) *Am. Mineral., 77*, 605-616.

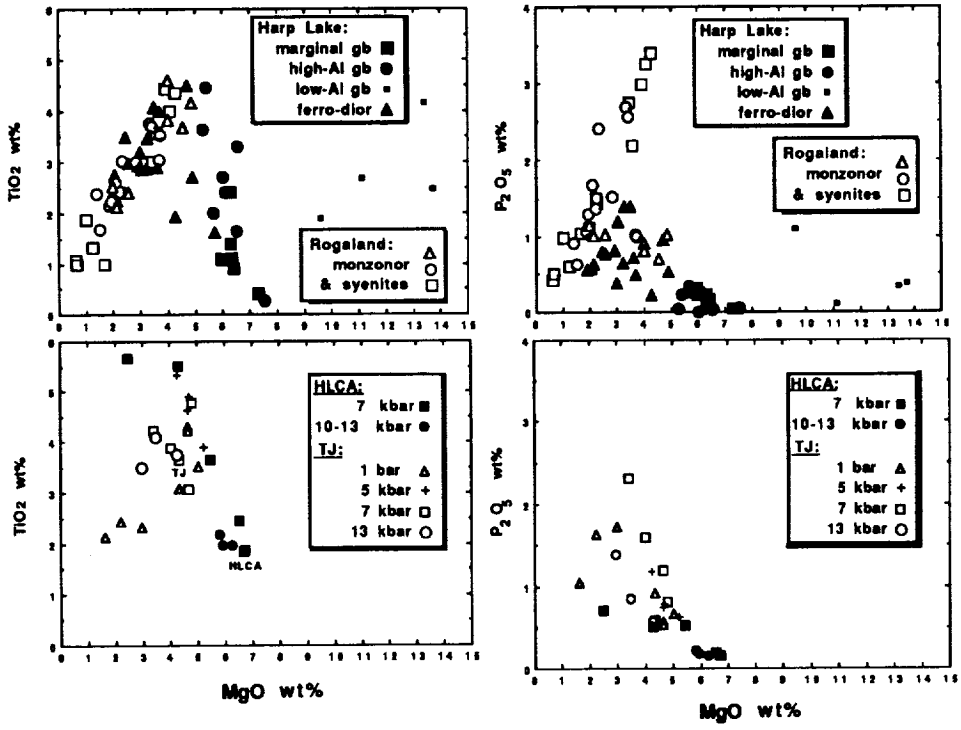

Fig. 1

Fig. 1 Major element variation in gabbros and monzonoritic rocks associated with the Harp Lake (Labrador) [6] and Rogaland (Norway) [3] anorthosites compared with liquid compositions ([8] and this study) obtained from experiments in graphite capsules on natural compositions. Fig. 2 Liquidus equilibria on the plagioclase + ilmenite saturation surface at lower crustal pressures. Liquids shown as filled squares; dashed tie lines connect coexisting pyroxene compositions (small open circles).

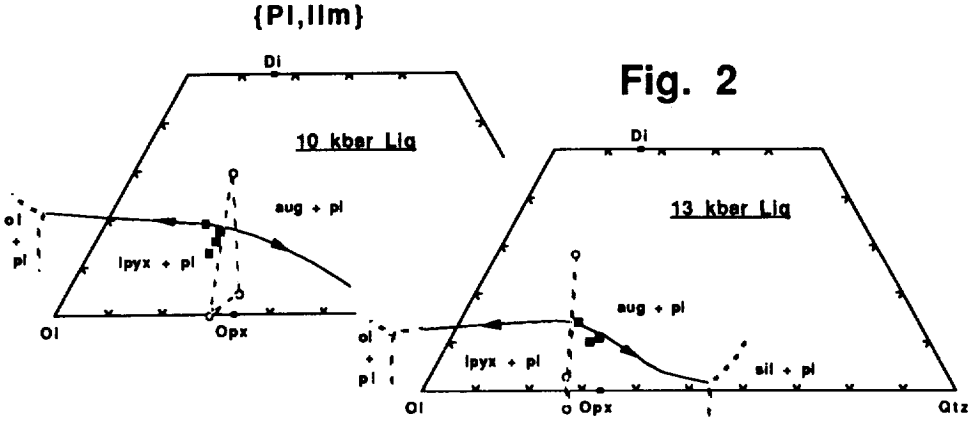

Fig. 2

MARTIAN LAVAS: THREE COMPLEMENTARY REMOTE SENSING TECHNIQUES TO DERIVE FLOW PROPERTIES: R. Lopes-Gautier (Jet Propulsion Laboratory, California Institute of Technology, MS 183-601, Pasadena CA 91109), B. C. Bruno, G. J. Taylor, S. Rowland (Planetary Geosciences, Dept. of Geology and Geophysics, University of Hawaii, Honolulu HI 96822) and C. R. J. Kilburn (Dept. of Environmental Sciences, University of Lancaster, Lancaster, UK)

Several remote sensing techniques have been developed to determine various properties of lava flows. We are currently focusing on three such techniques to interpret Martian lava flows on Alba Patera, which are based on measurements of (i) distal flow lobe widths which can be used to infer silica content (1); (ii) convolution of flow margins which can distinguish between pahoehoe and a'a types of basaltic flows (2); (iii) final flow field dimensions which can be combined with ground slope to derive effusion duration and average effusion rate (3). These methods are extremely complementary and together provide a more significant and complete understanding of extra-terrestrial lava flows. However, each of these techniques have specific and distinct data requirements.

Distal flow lobe widths (1): Distal flow lobes represent the arrest of free-flowing isothermal liquids on a slope. As such, their widths reflect rheological properties, which can, in turn, be related to silica content (Fig. 1). However, this technique cannot be confidently applied to flows on shallow slopes, because in these cases the flow margin tends to follow minor topographic irregularities. Wadge and Lopes (2) defined the lower limit of slope to be at least 0.6 degrees for Martian flows, which tend to have low aspect ratios (e.g.h/w = 0.005 on Olympus Mons).

Flow margin convolution (2): This technique uses the fractal dimension (a parameter which measures flow margin convolution) to distinguish between basaltic a'a and pahoehoe lavas, as the pahoehoe margins are more convoluted (Fig. 2). However, measuring the fractal dimension requires the lava flow margins to be sufficiently long, clearly exposed, and unaffected by large-scale topographic controls.

Flow-field growth characteristics (3): Studies of terrestrial lavas suggest that flow field growth is systematic and that a general, normalized relation can be established linking the final dimensions of a flow field to underlying slope and eruption duration, independent of explicit knowledge of rheological characteristics, lava density, and gravity. Using this relation (Fig. 3), the effusion duration (and average effusion rate and flow velocity) can be calculated from measurements of flow length, maximum width, average thickness, and ground slope on Mars, assuming that flow growth patterns are similar on Earth and Mars. This technique is only applicable to a'a and blocky flows; the growth of pahoehoe lavas is fundamentally different (3). This technique requires a well-exposed flow for which the vent area can be identified.

Ideally, all three techniques should be applied to the same flow. Realistically, it is often difficult to find flows for which the current data meet all the above requirements. However, if we assume that morphologically similar flows in the same area have similar compositions, we can combine measurements of several such flows. In particular, we can use distal flow lobe widths from several flows to determine the most likely composition for lavas of a particular area. If the distal flow lobe widths indicate a basaltic composition, it is then possible to use flow margin convolution measurements to determine whether the flow was emplaced as a'a or pahoehoe. If, in turn, the fractal dimension of the flow margin falls in the a'a range, we can infer flow growth characteristics according to the flow growth model to better understand flow emplacement.

Similarly, if the distal flow lobe width measurements suggest a more silicic composition, the flow growth model can also be applied. Often, however, because of the overlap between compositional ranges as shown in Fig. 1, the distal flow lobe widths are not conclusive. We are currently developing the flow margin convolution technique to distinguish between flows of different compositions (4).

Alba Patera has several well-defined flows which are suitable for these measurements. Distal flow lobe widths measured from morphologically similar flows fall in the ranges of basaltic to basaltic andesitic compositions as defined by Wadge and Lopes (2) shown in Fig. 1. Additional data to support a basaltic composition is provided by the flow margin convolution technique. Measurements of 4 flow margins (2 flows) were made. All four are fractal, indicating a basaltic composition. Furthermore, the fractal dimensions, ranging from 1.054 to 1.066, indicate an a'a morphology. This justifies the use of the flow growth model, which show these flows had durations in the range of 3.7 to 132 days and effusion rates in the range of 0.7-89 x 10^3 m^3 s^{-1} (5).

These results for Alba Patera illustrate how these three techniques can be used in combination to characterize extra-terrestrial lavas. We are continuing our investigation by measuring other extra-terrestrial flows, as well as by improving the techniques themselves.

References: (1) Wadge, G. and R.M.C. Lopes (1991), *Bull. Volcanol.* **54**, 10-24; (2) Bruno, B.C. et. al. (1992), *Geophys. Res. Lett.* **19**, 305-308; (3) Kilburn, C.R.J. and R.M.C. Lopes (1991), *J. Geophys. Res.*, **96**, B12, 19,721-19,732; (4) Bruno, B.C. et. al.(1993), this volume; (5) Lopes, R.M.C. and C.R.J. Kilburn (1990), *J. Geophys. Res.*. **95**, B9, 14,383-14,397.

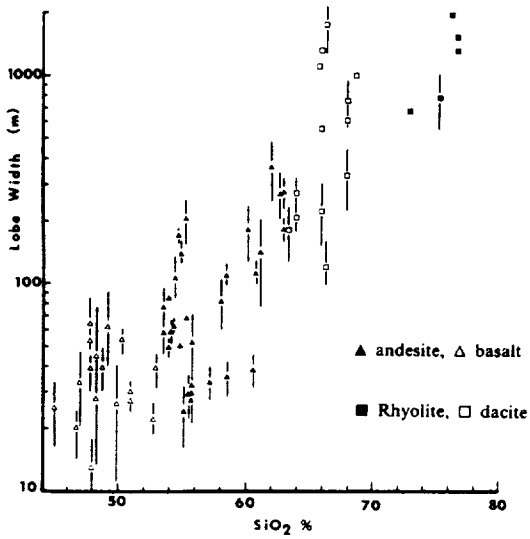

Fig. 1: Plot of average distal flow lobe width (units are log 10 x m) with one standard deviation error bars vs. silica content for terrestrial lava flows. (From 1).

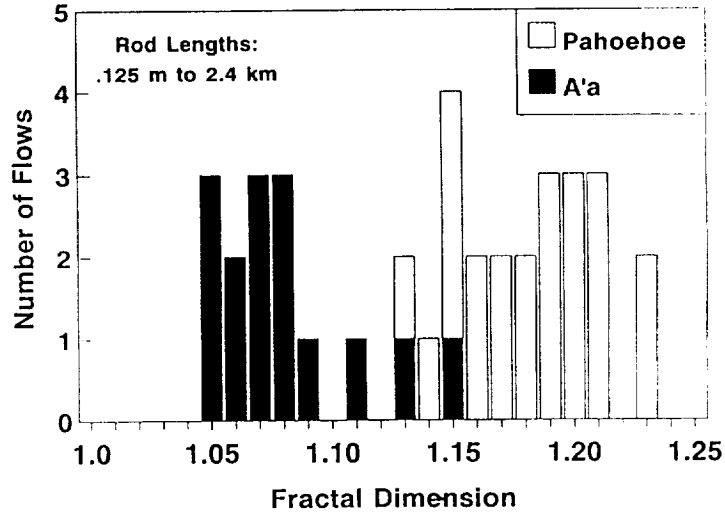

Fig. 2: Histogram of fractal dimension of terrestrial basaltic flows. Alba Patera flows fall in the range 1.054-1.066, characteristic of a'a lavas.

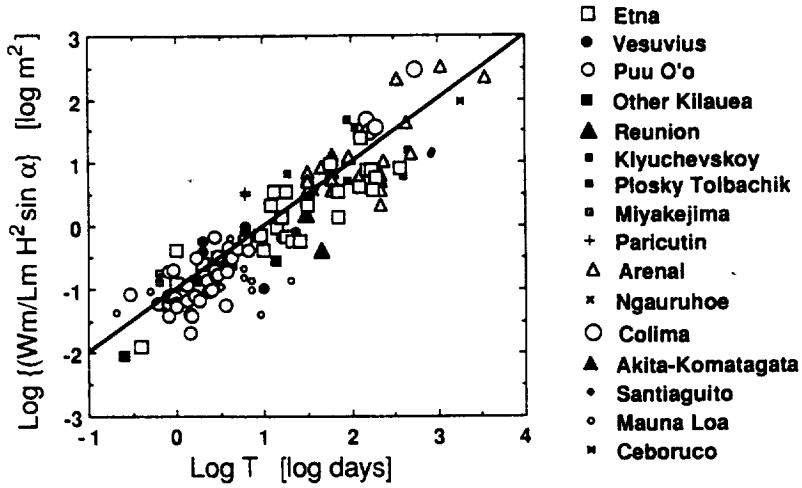

Fig. 3: Relation between final flow field dimensions (max length, Lm; max width, Wm, average thickness, H), underlying slope (alpha) and eruption duration (T). The solid line represents the model trend. (From 3).

DENSITIES OF 5-15 μm INTERPLANETARY DUST PARTICLES; S. G. Love, D. J. Joswiak, and D. E. Brownlee, Department of Astronomy FM-20, University of Washington, Seattle, WA 98195.

We have measured the densities of about 100 5-15 μm stratospheric IDPs. Great care was taken to minimize selection bias in the sample population. Masses were determined using an absolute x-ray analysis technique with a transmission electron microscope, and volumes were found using scanning electron microscope imagery. Unmelted chondritic particles have densities between 0.5 and 6.0 g/cc. Roughly half of the particles have densities below 2 g/cc, indicating appreciable porosity, but porosities greater than about 70% are rare. IDPs with densities above 3.5 g/cc usually contain large sulfide grains. We find no evidence of bimodality in the unmelted particle density distribution. Chondritic spherules (melted particles) have densities near 3.5 g/cc, consistent with previous results for deep sea spherules.

Particle Selection and Compositions: Roughly 200 dark colored 5-15 μm particles were randomly selected from stratospheric cosmic dust collection surfaces U2-30 and U2012. The sample set represents well the extraterrestrial dust population in the stratosphere. To accurately represent the exoatmospheric population, density sorting by atmospheric fall speed (which may be partially offset by the tendency for low-density particles to stay entrained in the ram air stream and miss the collection plate) and atmospheric entry effects (although most IDPs of this size are relatively unaltered during atmospheric entry [1]) must be considered.

The particles were arranged on Nuclepore filters, and quantitatively analyzed for elemental composition in a SEM using a 20 kV beam, following the EDX method described by Schramm *et al.* [2]. The ≈100 particles that proved to be extraterrestrial formed the sample for this work.

Masses: Individual particle masses were found in a manner analogous to the synchrotron x-ray fluorescence technique of Flynn and Sutton [3], except that we used the 120 kV beam of a TEM to excite Fe Kα x-rays in each particle. For these small particles, the 120 kV beam illuminates the entire volume, and x-ray self-absorption is negligible, so the Fe Kα flux from a particle is proportional to the number of Fe atoms it contains. Using controlled beam raster areas and calibrating with stainless steel standard spheres of known size, mass, and iron abundance, we were able to determine the absolute Fe content of each particle from its Fe Kα emission. The inferred mass of iron in each particle, divided by its abundance of iron as found in the elemental analysis described above, yielded its total mass.

The mass determination technique was checked by examining the set of 1-6 μm stainless steel calibration spheres. Figure 1 shows Fe x-ray counts as a function of mass (as computed from density and measured volume) for the spheres. The number of counts is strictly linear with mass, with only one significant exception, which probably contained a void or air bubble. The relation shows no decline at the high end, the expected result if electron beam attenuation or x-ray self-absorption were important at these sizes. The method for finding masses is valid for particles up to at least 20 μm diameter if they have chondritic density and iron content.

An uncertainty in this method is the unknown oxidation state of iron in the particles. For chondritic particles, however, no reasonable oxygen abundance causes a large change in the derived mass. Another uncertainty is the carbon abundance, as carbon is not seen by the x-ray detector. Gross compositional inhomogeneity in a particle can add uncertainty if the 20 kV SEM EDX spectrum does not accurately represent the particle's bulk composition.

Volumes: Particle cross-sectional areas were measured by tracing outlines of their SEM photos into a computer, which measured the shape's area within a few percent. Particle heights were measured with the TEM in SEM mode, using high magnification and a configuration that yields a narrow depth of focus. The height was found using the difference in focus steps between the substrate and a representative point near the top of the particle. Calibration of focus steps to actual distance was performed using the standard spheres, and fell within 5% of the JEOL 1200 TEM factory calibration. The uncertainty in the height measurement was ± 0.5 μm. The heights of the particles were generally less than or nearly equal to their widths.

Volumes were computed using $V=0.7Ah$, where A is the cross-sectional area and h is the height. The leading factor 0.7 is adapted from a general formula for the volumes of regular

solids [4]. The estimated uncertainty is no more than 20 percent for reasonable shapes. The possibility of embayments and shape irregularities out of the line of sight means that we tend to overestimate volume and underestimate density.

Results and Discussion: The distribution of densities for unmelted particles is presented in Fig. 2. The mean density of unmelted chondritic stratospheric IDPs is 2 g/cc, and the range is 0.5 to 6.0 g/cc. The mean density of chondritic spherules in this sample is 3.5 g/cc, comparable to the 3.0 g/cc result of Murrell *et al.* [5] for deep sea spherules.

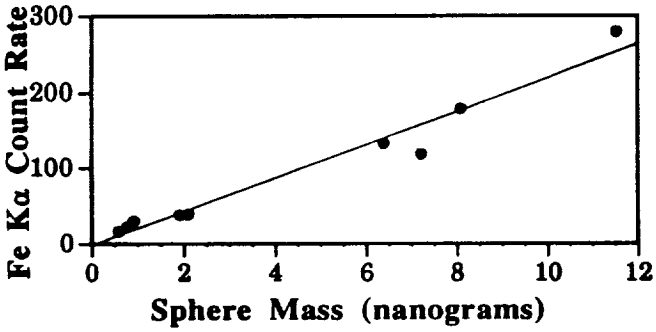

Fig. 1. Steel Sphere Counts vs. Mass

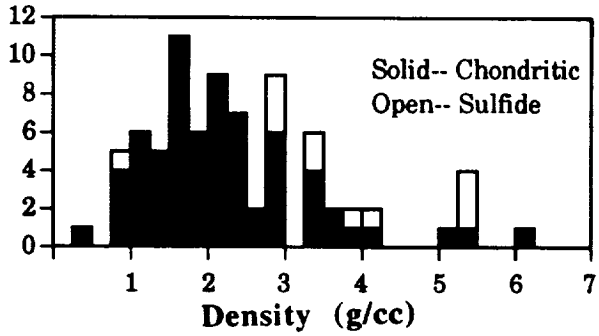

Fig. 2. Unmelted Particle Density Distribution

Flynn and Sutton [3] found a mean density of 1.2 g/cc for unmelted IDPs, a significantly lower value than ours, but consistent with the results of Zolensky *et al.* [6] who used an INAA method. Both studies found a large proportion of particles with densities below 1.0 g/cc. Fraundorf *et al.* [7] found an average IDP density similar to ours, using more direct techniques for measuring mass and volume. A standard NASA micrometeoroid model [8] assumed an average density of 0.5 g/cc based on meteor studies.

In our sample, we find no particles with densities below 0.5 g/cc. This is not an absolute statement, as three very porous and fluffy particles which fragmented during capture or analysis were not measured. They could have had very low densities, but in view of the fact that they comprise only 3% of our sample, we must conclude that particles with very low densities (and porosities in excess of 70%) are rare.

Flynn and Sutton have suggested that the IDP density distribution contains two clearly distinct populations, on the basis of 25 particles' measured densities [3]. We see no indication of a bimodal distribution, finding instead a single broad peak around 2 g/cc with a high density tail. Possible explanations for the discrepancy include the fact that many previous studies' particles were selected from a catalog of SEM photographs, and may thus be more subject to selection biases (based on shape and consistency) than the particles studied here. We also examined smaller particles. In addition, the present study took greater care to measure particle compositions completely.

The results of this work have implications for the assessment of meteoroid collisions with spacecraft and with one another, the effects of Poynting-Robertson orbital decay on interplanetary dust motes, theoretical models of the zodiacal light, and calibration of micrometeoroid detectors. This study also affects the treatment of meteoroid flight in the atmosphere. The difference in mean density between melted and unmelted particles indicates that micrometeoroid densities change upon melting, an effect which has not been treated in atmospheric entry calculations.

References: [1] Love, S. G., and D. E. Brownlee (1991) Icarus **89**, 26-43. [2] Schramm, L. S., *et al.* (1989) Meteoritics **24** 99-112. [3] Flynn, G. J., and S. R. Sutton (1990) LPS XXI, 375-376. [4] Hodgman, C. D., ed. (1957) CRC Mathematical Tables, Chemical Rubber Publishing Co., Cleveland. [5] Murrell, M. T., *et al.* (1980) Geochim. Cosmochim. Acta **44**, 2067-2074. [6] Zolensky, M. E., *et al.* (1989) LPS XX, 1255-1256. [7] Fraundorf, P., *et al.* (1982) LPS XII, 225-226. [8] Cour-Palais, B. G. (1969) NASA SP-8013.

RESOLVING TOPOGRAPHIC DETAIL ON VENUS BY MODELING COMPLEX MAGELLAN ALTIMETRY ECHOES; Amy J. Lovell, F. Peter Schloerb, Department of Physics and Astronomy; George E. McGill, Department of Geology and Geography, University of Massachusetts, Amherst MA 01003, USA.

Magellan's altimeter is providing some of the finest resolution topography of Venus achieved to date. Nevertheless, efforts continue to improve the topographic resolution whenever possible. One effort to this end is stereoscopic imaging, which provides topography at scales similar to that of the SAR. However, this technique requires two SAR images of the same site to be obtained and limits the utility of this method. In this paper, we present another method to resolve topographic features at scales smaller than that of an altimeter footprint, which is more globally applicable than the stereoscopic approach.

Each pulse which is transmitted by Magellan's altimeter scatters from the planet and echoes to the receiver, delayed based on the distance between the spacecraft and each surface element. As resolved in time, each element of an altimetry echo represents the sum of all points on the surface which are equidistant from the spacecraft. Thus, individual returns, as a function of time, create an echo profile which may be used to derive properties of the surface, such as the scattering law or, in this case, the topography within the footprint. The Magellan project has derived some of this information by fitting model templates to radar echo profiles. The templates are calculated based on Hagfors' Law [1], which assumes a smooth, gently undulating surface. In most regions these templates provide a reasonable fit to the observed echo profile; however, in some cases the surface departs from these simple assumptions and more complex profiles are observed. Specifically, we note that sub-footprint topographic relief apparently has a strong effect on the shape of the echo profile.

An echo profile which is misshapen by sub-footprint scale topography contains information about the surface topography at higher resolution than is normally available. Unfortunately, since it is impossible to invert an echo profile directly into a topographic distribution, it is necessary to have some knowledge about the surface which creates the echo in order to utilize this additional information. Investigation of SAR mosaics provides many constraints on the two-dimensional distribution of topography. Such insight into the appearance of the surface at these scales allows parameterization of new topographic models which can be used to derive sub-footprint topography.

To demonstrate the effects of sub-resolution relief on echo profiles, we have calculated the echo shapes from a wide range of simple topographic models. At this point, our topographic models have emphasized surfaces where only two dominant elevations are contained within a footprint, such as graben, ridges, crater rims, and central features in impact craters. Fortunately, these are features for which improved resolution is highly desirable. For example, the depths of grabens can be related directly to total extension if the attitude of the bounding faults are known or can be reasonably inferred. Moreover, crater morphometry provides important constraints on the energy of the impact event and on the rheological properties of the target materials.

Model surfaces are constructed on a Cartesian grid which lies at a given distance from the spacecraft. The heights of the elements in the grid are adjusted to simulate a particular surface feature, and a model echo is constructed by summing the contributions of scattering from each surface element. Assuming that each individual element scatters according to Hagfors' law, echoes which more closely approximate the complex Magellan profiles are constructed. In general, topographic relief below the average value within the footprint will create additional echo features on the trailing edge of the echo profile, while features due to elevated relief will appear on the leading edge. The time difference between the two superposed echoes is directly related to the vertical separation of the two regions in space, and by measuring this value, the relative elevations of features which are smaller than an altimeter footprint can be determined.

An example of a surface feature which illustrates the usefulness of this approach is the crater Duncan (68N, 292E), shown in Figure 1 with overlaid altimetry footprints for orbits 2035 to 2040. Figure 2 shows the successive echo profiles stepping across the crater from the east (orbits 2040 through 2035, footprint -769). The altimetry echoes which incorporate the rim (panels 3 and 4) have two distinct components, one corresponding to the crater floor, the other to the rim. The temporal resolution between the two components is on the order of 4 μs, corresponding to a height difference of 650 meters. Since the origin on the time axis corresponds to the crater floor, the earlier echoes (those at negative time offset) must correspond to higher elevations, *i.e.* the rim and surrounding terrain. In this way, the depth of the crater can be determined even in cases where there is not an entire altimetry footprint on the floor of the crater.

In conclusion, we have demonstrated a method for using Magellan altimetry echoes to improve topographic resolution on Venus. Currently, this method applies only to relatively simple features with two dominant elevations. However, we believe that in the future, the method can be extended to apply to slightly more complex features, such as ridge belts and other topographic distributions containing several distinct elevations.

[1] Hagfors, T. (1970) *Radio Science*, **5**, pp. 189-227.

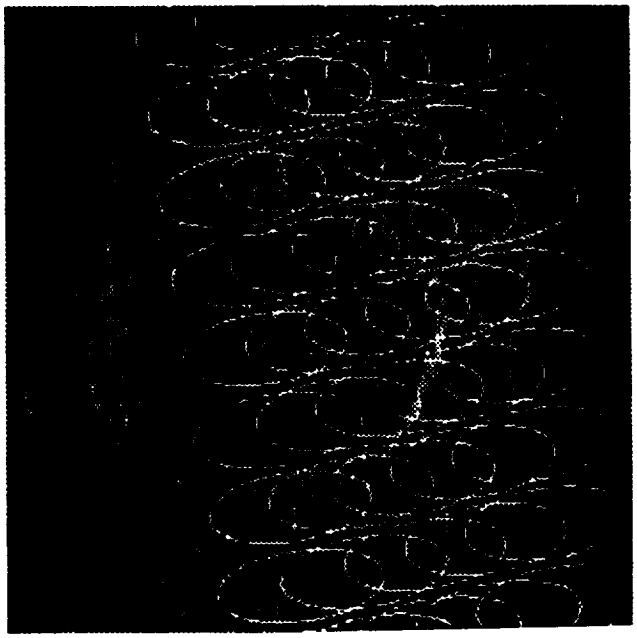

Figure 1: Crater Duncan showing altimetry footprints for orbits 2035 to 2039.

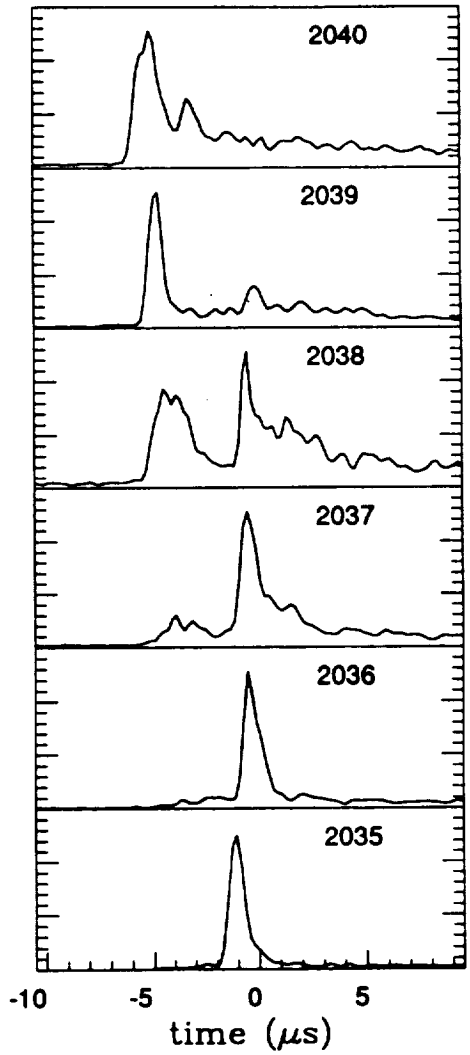

Figure 2: (right) Altimetry echo profiles for footprint -769 in 6 orbits. Top to bottom moves east to west across the lower half of crater Duncan.

SEDIMENTATION, VOLCANISM, AND ANCESTRAL LAKES IN THE VALLES MARINERIS: CLUES FROM TOPOGRAPHY; **B.K. Lucchitta, N.K. Isbell, and A. Howington-Kraus,** U.S. Geological Survey, Flagstaff, AZ 86001.

Abstract. Compilation of a simplified geologic/geomorphic map onto a digital terrain model of Valles Marineris has permitted quantitative evaluations of topographic parameters. The study showed that, if their interior layered deposits are lacustrine, the ancestral Valles Marineris must have consisted of isolated basins. If, on the other hand, the troughs were interconnected as they are today, the deposits are most likely of volcanic origin, and the mesas in the peripheral troughs may be table mountains. The material eroded from the trough walls was probably not sufficient to form all of the interior layered deposits, but it may have contributed significantly to their formation.

Method. We prepared a geologic/geomorphic map of the Valles Marineris, simplified and modified from Witbeck et al. [1], transferred it to existing topographic maps, and digitized and co-registered it with the digital terrain models (DTMs) of the topographic maps. We then calculated areas occupied by the individual map units. We also calculated the depth of troughs and the volume of void spaces above individual units by obtaining the difference between the DTMs and a restored surface linking the adjacent plateaus across the troughs. Finally, we calculated volumes of interior deposits by obtaining the difference between the DTMs and a designated "floor" under the deposits. (Details of the method were given in a previous report [2].) We then analyzed the results of the various topographic and volume relations in regard to erosional and structural implications for the history of the Valles Marineris.

Central troughs. The favored hypothesis for the origin of the interior layered deposits is that they are sediments emplaced in lakes. However, in Ophir and Candor Chasmata, lakes could not have been sustained if all the troughs were interconnected; lake waters in these troughs must have reached a 9-km elevation in order to lay down the uppermost layered deposits. These high-standing lakes would have spilled out of Coprates Chasma onto the surrounding plateaus that have surface elevations of only 4-5 km. If the lakes were interconnected, their levels inside the central troughs could not have been higher than about 4 km. Thus, at least the upper interior layered deposits cannot be lake sediments. A likely alternative is that they are volcanic.

On the other hand, the troughs may not have been interconnected but may have formed isolated basins when the interior layered deposits were emplaced. As also shown by independent structural and stratigraphic evidence, these ancestral basins occupied the southern parts of Ophir, Candor, and Melas Chasmata [3]. The northern parts of these troughs and the entire Coprates/north Melas/Ius graben system may have formed later, after deposition of the interior layered deposits had ceased.

Peripheral troughs. The peripheral troughs Juventae, Gangis, and Capri/Eos Chasmata, reaching depths of 2-5 km, are shallower than the central troughs. Our investigation showed that they most likely formed from a combination of erosional collapse and structural activity. Furthermore, the existence of chaotic material in these troughs at similar elevations (near the 4-km contour on the adjacent plateau surfaces) supports the idea that the chaotic material may have indeed formed from release of confined artesian water [4]. In the peripheral troughs, the interior layered deposits bury chaotic material, indicating that lakes formed after the chaotic collapse of the surface (if the layered deposits are indeed lake sediments). The lakes were apparently breached only later to form the presently observed outflow channels. However, the layered deposits in these troughs may not be lake sediments at all; they may be volcanic materials, as is perhaps true for the central troughs. A volcanic composition is suggested because in Gangis and Juventae Chasmata the layered deposits occur in free-standing mesas that have the shape of table mountains in Iceland [5], a form supporting sub-ice emplacement. The volcanic materials could have been erupted below segregated ice masses postulated to have existed in those areas [6], or they could have formed in shallow, completely frozen

lakes. The main scarps of the mesas rise about 2 km or less above the trough floors, a thickness consistent with the depth of frozen ground in the equatorial area [7].

Redeposition of wall material. The troughs were significantly widened by erosion, but volumetric comparisons and topographic and geomorphic analyses show that material eroded from trough walls may not have been sufficient to be the sole source for interior layered deposits. Even though the total eroded and deposited volumes match approximately, to fill Ophir and Candor Chasmata with eroded wall material from Coprates and Ius Chasmata would have required uphill transport of material into the central troughs, which is an improbable concept. Also, the Coprates/north Melas/Ius system may not yet have existed at the time of layered-deposit emplacement; if it did not, the amount of material eroded from trough walls at that time would have been only about half as much as the estimated total. Because of these considerations, it is likely that other material contributed to the formation of layered deposits. Some may have come from subterranean piping and some from volcanism.

History. A brief history of the Valles Marineris, based on the above observations, can be envisioned as follows. In the region of the central troughs, ancestral deep basins formed partly from collapse, partly from structural adjustment along previous structural alignments. These basins, which may have contained lakes, were filled with material from the eroding walls and perhaps with some materials from subterranean piping and volcanism. Probably at the same time as formation of the deep basins, the peripheral troughs formed, mostly by collapse due to eruption of artesian water. In these troughs, layered deposits were also emplaced in ancestral lakes, which were eventually drained by the outflow channels we see today. Later, the central basins were widened and deepened by the addition of subsidiary northern grabens. The Coprates/north Melas/Ius graben system cut the entire region, including the ancestral Melas Chasma. These new grabens connected the troughs with one another and with the peripheral troughs in the east. When all the troughs merged, a major flood may have emptied the central troughs, but more likely lakes in those troughs had already dried up because they were filled with sediments and volcanic material.

Alternatively, all troughs were already interconnected early in their development. No deep lakes formed, and thus the layered deposits are probably largely of volcanic origin. Volcanic material in the peripheral troughs may have been emplaced as table mountains.

Even though both scenarios are within the constraints of the topographic analysis, a combination of them is probably closer to reality. The troughs likely contain both volcanic and mass-wasted materials emplaced in a series of basins that eventually interconnected. The existence of former lakes is more questionable for the central troughs than for the peripheral troughs.

References

[1] Witbeck, N.E., Tanaka, K.L., and Scott, D.H. (1991) *U.S. Geol. Survey Misc. Inv. Ser. Map I-2010*, scale 1:2,000,000. [2] Lucchitta, B.K., and Isbell, N.K. (1992) In *Lunar and Planetary Science XXIII*, 817-818. Lunar and Planetary Institute, Houston. [3] Lucchitta, B.K., and Bertolini, L.M. (1990) In *Lunar and Planetary Science XX, 2*, 590-591. Lunar and Planetary Institute, Houston. [4] Carr, M.H. (1979) *JGR, 84*, 2995-3007. [5] Van Bemmelen, R.W., and Rutten, M.G. (1955) *Table mountains of northern Iceland*. E.J. Britt, Leiden, Holland, 217 p. [6] Howard, A.D. (1990) In *Reports of Planetary Geology and Geophysics Program-1990: NASA TM-4300*, 120-122. [7] Rossbacher, L.A., and Judson, S. (1981) *Icarus, 45*, 39-59. [8] Lucchitta, B.K. (1990) *Icarus, 86*, 476-509.

THE CLEMENTINE INSTRUMENT COMPLEMENT; Paul G. Lucey, Planetary Geosciences, University of Hawaii at Manoa, Honolulu HI 96822

The recent successes of the Galileo SSI imaging experiment at the Moon and Gaspra show the utility of multispectral imaging of planetary objects. "Clementine" is the planetary community's "code name" for the SDIO (Space Defense Initiative Organization) mission to the Moon and the asteroid Geographos. This mission is designed as a long term stressing test on sensors and space systems developed for SDIO. In the course of this test Clementine will obtain science data using a varied and powerful array of remote sensing instruments which were developed by or for Lawrence Livermore National Laboratory in Livermore, California. Clementine carries five cameras, one for navigation and four for science experiments. In addition, a laser ranger is included which will serve as a laser altimeter. The Clementine cameras cover a wider range of spatial resolutions and wavelength range than did Galileo and are almost ideally suited to mapping of mafic rock types as are present on the Moon and expected at Geographos. The technical characteristics of the Clementine cameras are listed in the following tables.

Table 1. Camera Characteristics

CAMERA NAME	ARRAY TYPE	ARRAY DIMENSIONS	ANGULAR EXTENT OF A PIXEL	RESOLUTION @ 500 KM MAPPING ORBIT
LIDAR	intensified Thompson CCD	288x384	20μrad	20 meters
UV-VIS	Thompson CCD	288x384	255μrad	125 meters
Near-IR	Amber InSb array	256x256	350μrad	175 meters
LWIR	Rockwell HgCdTe	128x128	143μrad	70 meters

Table 2. LIDAR camera filters

Center	415 nm	560 nm	650 nm	750 nm	broadband (400-750 nm)
Bandpass (FWHM)	40 nm	50 nm	50 nm	50 nm	350 nm

Table 3. UV-Vis camera filters *

Center	340 nm	415 nm	750 nm	900 nm	950 nm	1.00 μm	broadband (400-750nm)
Bandpass (FWHM)	60 nm	40 nm	10 nm	20 nm	30 nm	30 nm	350 nm

* If the broadband filter is determined not to be required for navigation, all 6 science filters will fly, else one will be dropped.

Table 4. Near-IR camera filters

Center	1.1 μm	1.25 μm	1.50 μm	2.0 μm	2.6 μm	2.78 μm
Bandpass (FWHM)	60 nm	60 nm	60 nm	60 nm	60 nm	30 nm

The LWIR camera is broadband only, covering 8 to 10.5 μm.

Calibration of the cameras will occur at the sensor calibration laboratory at LLNL. In flight calibrations using standard stars and other standards should improve the stated accuracies. SNR's include the following noise sources: shot noise, calibration error, digitization noise, readout noise, and frame transfer noise (where applicable). The achieved SNR's are a balance between detector saturation and acceptable image smear. The "worst" case uses the longest possible integration times.

Table 5. Camera calibration and design SNR

CAMERA NAME	RELATIVE CALIBRATION	ABSOLUTE CALIBRATION	BEST CASE SNR (70% ALBEDO, 0° PHASE)	WORST CASE SNR (5% ALBEDO, 85° PHASE)
LIDAR	1%	20%	41	13
UV-VIS	1%	15%	87	25
Near-IR	1%	30%	97	11
LWIR	1%	30%	954 (300K, emissivity = 0.3)	

MIXING MODEL ANALYSIS OF TELESCOPIC LUNAR SPECTRA; Paul G. Lucey, Beth C. Clark, and B. Ray Hawke, Planetary Geosciences, University of Hawaii, Honolulu, HI, 96822.

We have analyzed very high quality reflectance spectra of the lunar surface from the University of Hawaii lunar spectral data collection using a spectral mixing model. The spectra analyzed are those of 45 mare sites and 75 highland sites. The spectra were selected on the basis of very high signal to noise ratios based on error bars and point to point scatter, and on quality of removal of telluric water bands. The spectral mixing model used 7 components, not all of which were used in each fit. Four of the components were mineral spectra of an orthopyroxene, a clinopyroxene, an olivine and an anorthite, measured at the Brown University's RELAB . All of the minerals were 45-90 μm splits. Lunar soil contains other components which have the effect of reddening and darkening the soil as well as reducing spectral contrast. In addition, lunar soil contains spectral neutral bright material (likely very fine grained feldspar) which serves to reduce spectral contrast and brighten soils. Early attempts to fit many of the spectra pointed out the need for a component which has a very broad smooth absorption feature centered near 1.1 microns. Glass is a good candidate for this component. For the bright component we used a flat reflectance of 70% to represent fine grained feldspar. For the "glass" component we used a telescopic spectrum of a pyroclastic glass present on the Aristarchus plateau which is characterized by a strong smooth band centered at 1.07 microns (1). This spectrum was converted to albedo using the map of (2). In addition to exhibiting the glass band this spectrum is very red and has a low albedo. On the assumption that the dark component and the red component are agglutinates, which is reasonable but not necessarily true (Pieters, pers. comm, 1992) we sought a dark red component. To derive its properties we modelled the spectrum of an Apollo 16 soil (16xxx) using mineral proportions from (3), and assumed the dark red component to comprise 60% of the soil, appropriate to agglutinate abundance in mature soil. We adjusted the albedo and slope of a straight line representing the dark red component until the contrast and albedo of the model spectrum matched the soil spectrum. The mixing was done after conversion to single scattering albedo using the equations of (4) and average single particle phase functions for silicates measured by (5).

Fit criteria: The intent of this stage of the modelling is principally to match the spectral shape and contrast of the bands present in the telescopic spectra in order to determine relative abundances of crystalline components. These ratios are relatively insensitive to grain size if the grain sizes of the components vary in concert. We also matched the scaled continuum slope with an appropriate mixture of the flat bright component and the dark red component. From this fit of shape and continuum slope we derive a model feldspar abundance from the sum of the crystalline component and the bright component.

Systematic errors in the abundance of the neutral components lie in under or overestimate of the grain size of the crystalline components and incorrect assignment of the albedo and slope of the neutral and glass components. Overestimate of the grain size will increase the proportion of the neutrals (and hence model feldspar). Underestimate of the grain size of the crystalline components will have the opposite effect. Overestimate of the slope of the dark red component or underestimate of the slope of the bright component will result in too much of the amount of model bright component.

Systematic errors in the opx:cpx ratio lie in the choice of Fe-poor ortho- and clinopyroxenes for fitting. More Fe-rich pyroxenes will yield higher opx:cpx ratios as the opx band center shifts to longer wavelengths. The width of the mixture bands changes significantly with Fe content while holding either mixing proportion or composite band minimum constant. This observation may offer a method for determining the Fe/Mg ratio of the pyroxene assemblage remotely.

A subset of the results is shown in the accompanying figures showing crystalline plagioclase over mafics versus opx over total pyroxene, and model plagioclase over mafics versus opx/total pyroxene. The mare locations tightly cluster in the latter plot while the highland areas vary widely in pyroxene chemistry and model plagioclase. It should be noted that crystalline plagioclase was often not required. The best developed plagioclase bands were in the gabbroic highlands areas.

SPECTRAL MIXING MODELS: Lucey et al.

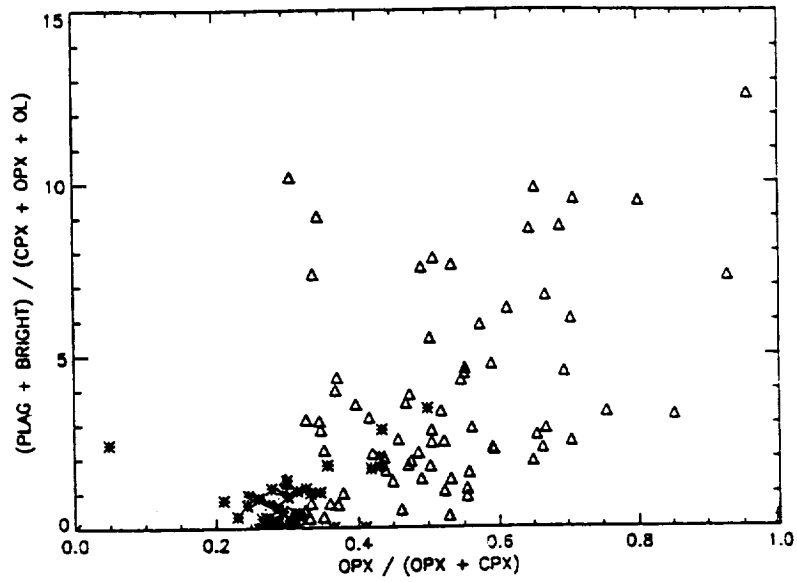

Figure 1. Model plagioclase (abundance of crystalline anorthite plus neutral bright component) over crystalline mafics versus model opx/(opx+cpx). Asterisks are mare locations, triangles are highland locations.

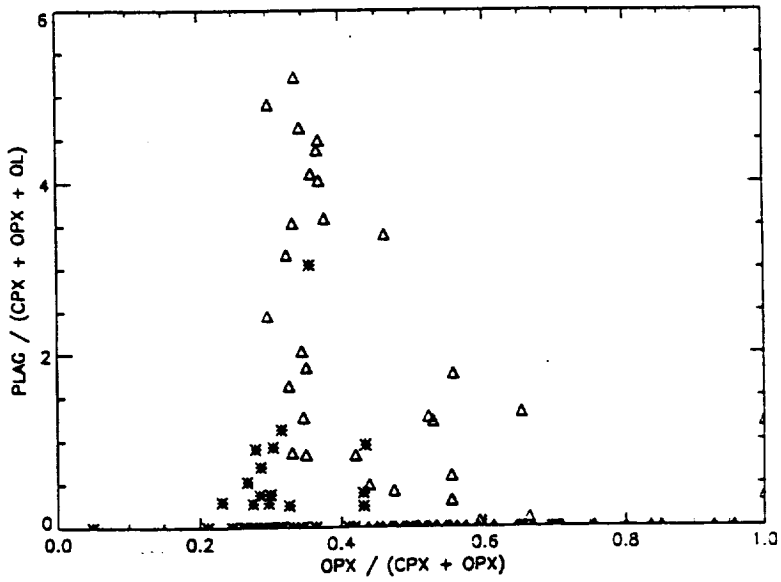

Figure 2. Abundance of crystalline anorthite over crystalline mafics versus model opx/(opx+cpx). Asterisks are mare locations, triangles are highland locations.

References: 1) Lucey, P.G., Hawke, B.R., Pieters, C.M., Head, J.W., and McCord, T.B., *Proc. Lunar Planet. Sci. Conf.* 16th, in *JGR* 91 D344-D354, (1986), 2) Pohn, H.A. and Wildey , R.L.,US Geol. Surv. Prof. Pap. 599-E, Plate 1.;3) The Lunar Source Book, University Cambridge Press,1991; 4)Hapke B. JGR 86, 3039-3054, (1981); 5).Mustard, J.F.and Pieters, C.M.,JGR 94, B10,13619-13634, 1989.

FIRST RESULTS FROM A LABORATORY FACILITY FOR MEASUREMENT OF EMISSION SPECTRA UNDER SIMULATED PLANETARY CONDITIONS. Paul G. Lucey, Natalie Domergue-Schmidt, Planetary Geosciences, Department of Geology and Geophysics, U. of Hawaii at Manoa, Bradley G. Henderson and Bruce Jakosky, LASP, U. Colorado.

We have developed a laboratory spectroscopic facility for the measurement of emission spectra under simulated planetary conditions. Spectral measurements are made from 6 to 13 microns with a scanning grating monochromator equipped with a HgCdTl detector. An environment chamber in in service in Hawaii for several years in which we can control the temperature from 77K to 500K, the pressure from 10^{-5} torr to two atmospheres, has been equipped with a 77K or 273K cold shield. The shield serves to minimize light reflected off the sample and to aid in development of thermal gradients for obtaining spectra under conditions simulating the thermal environment of airless bodies. Samples are placed in small cups on a temperature controlled substrate allowing measurements of emission due to heating from below by the substrate, or from illumination from a solar simulation source. Figure 1 is a sketch of the environment chamber system.

The data presented here show the emission from a fine-grained quartz sample heated from below at 100°C under ambient conditions with no cold shield, the same sample inside the environment chamber filled with 1 atmosphere of nitrogen with the shield cooled to 77K, and under vacuum conditions with 77K cold shield. In the chamber, a reentrant cavity is attached to the bottom of the cooled radiation shield to serve as a cold reference for measurement of instrument background. A second reentrant cavity is attached to the heater substrate to serve as a hot blackbody reference. The temperature of the substrate is measured with a platinum resistance thermometer. For each of the spectra shown in Figure 2, separate cold and hot reference spectra were obtained. The spectra shown were calculated from sample minus cold reference divided by hot reference minus cold reference. The resultant spectra shown in Figure 2 are in terms of relative emission, that is, sample over blackbody reference. Additionally, the spectra were multiplied by a Planck function calculated for the measured hot substrate temperature and divided by an estimate of the temperature of the sample (300K), and offset by .1 units to facilitate comparison. The spectra shown are of the same sample of quartz ground to a mean grain size of 10 microns using a shatterbox and ball grinder, size determined through SEM photography, placed in a glass sample cup and heated from below. The sample thickness was about 5mm, and the diameter of sample cup is near 10 mm. Temperature control was rather poor allowing slow monotonic drifts of several kelvins of the hot substrate during data collection. The upper two spectra were taken under vacuum conditions and are in qualitative agreement. They show a substantial inflection near 9.5 microns and a small emission feature near 11.5 microns. While some systematic error causing these features cannot be ruled out at this time, the sample chamber was flooded with dry nitrogen to eliminate thermal gradients via convective heat transport within the sample, and the spectrum obtained under these conditions, the third from the bottom and labeled A1, does not show these features. The bottom spectrum, shown with error bars, was obtained under ambient conditions without a cold shield with increased integration time. This spectrum is contaminated by about 10-20% reflected room background light as determined by measuring the flux reflected from a 77K diffuse gold standard placed in the sample position. This spectrum shows a very weak quartz doublet and is qualitatively similar to the spectrum obtained in the chamber under 1 atmosphere of nitrogen with a cold shield.

LABORATORY EMISSION SPECTRA: Lucey et al.

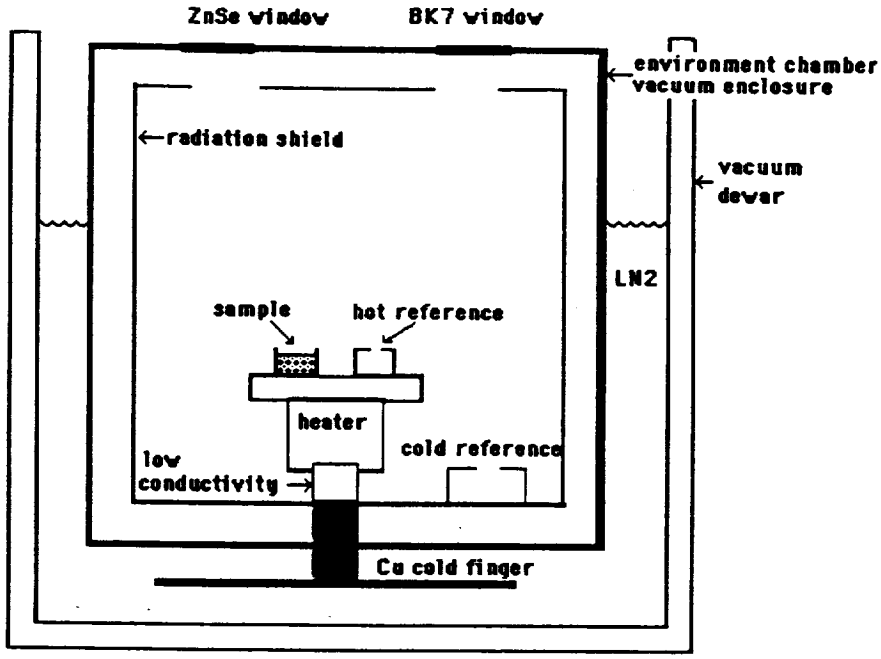

Figure 1. Schematic diagram of the environment chamber.

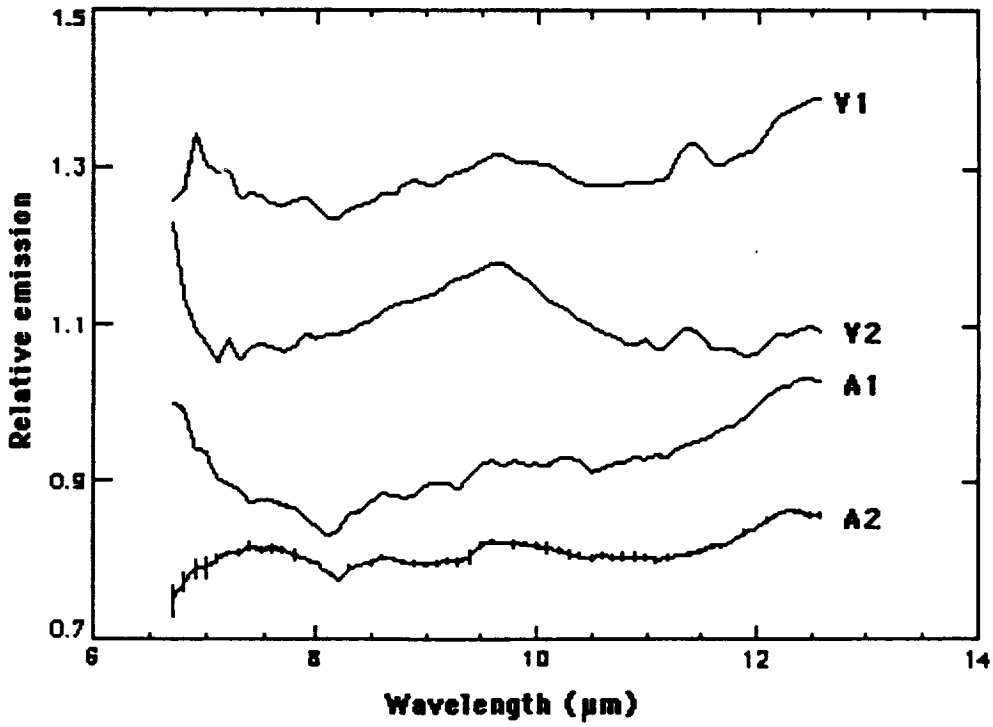

Figure 2. Spectra obtained under vacuum conditions (V1 and V2), 1 atm of nitrogen in the chamber with a 77K cold shield (A1), and in air without cold shield (A2).

EVOLUTION OF TRITON'S VOLATILE BUDGET; J.I. Lunine, University of Arizona, Tucson AZ 85721

Triton's volatile budget provides important links to planetary formation processes in the cold outer solar nebula. However, the budget has been modified by processes subsequent to the accretion of this body. It is of interest to assess whether certain formation environments can be ruled out for Triton on the basis of its current volatile abundances, and also to quantify some of the post-accretional processes by which the abundances have been modified.

Current surface abundances: A combination of Voyager UVS, IRIS and RSS data strongly point to the nitrogen atmosphere being in saturation equilibrium with surface frost on the sunlit hemisphere. Since Triton is approaching southern summer solstice, a minimum surface abundance can be computed based on the continued presence of nitrogen in the southern hemisphere. The energy-limited mass flux of nitrogen northward is ~ 10^{-7} g cm^{-2} s^{-1}; over 50 years a layer 2 meters thick can be sublimated. An upper limit to the nitrogen abundance is obtained by considering limits to the thickness of nitrogen frost deposits. The scale of topography on Triton is limited to of order kilometers in cliffs, ridges, etc. The edges of the polar frost deposits do not seem to exhibit such relief. More significant is that heat flow models of the nitrogen cap yield a thermal gradient of 15K per kilometer [3]; a 2-3 km-thick cap would reach the melting point of nitrogen at its base. Before then, viscous spreading of the cap would decrease its thickness [4], so that 1-2 km is a good upper limit to the cap thickness. Averaged over the surface, an upper limit of 0.5-1 km thickness is obtained for the amount of nitrogen ice; this is converted in the accompanying table to an equivalent mass.

Carbon monoxide has a saturation vapor pressure roughly an order of magnitude below that of nitrogen at 38K. Application of Raoult's law to the atmospheric *upper limit* of 1% mixing ratio CO/N_2 from UVS data [2] yields a ratio in the mixed ice of 15%. Alternatively, one could postulate that carbon monoxide ice is physically separate from the nitrogen ice, but the CO vapor is compelled to move northward in the general nitrogen vapor flow. Then the areal coverage of CO frost in the summer hemisphere can be computed to be <1% to produce an undersaturation of at least 10% in the atmosphere. Thus whether the CO is mixed with the nitrogen or separate, a reasonable upper limit to its abundance range is 1-10% of the surface nitrogen abundance. Recent work [14] suggests that the atmospheric mixing ratio limit might be 3 orders of magnitude smaller than given in [2], leading to a surface abundance commensurately smaller. Methane is present in Triton's atmosphere and is within a factor of 10 of saturation at 38 K. Because it is close to or at saturation the methane abundance is not constrained by the nitrogen abundance in surface frosts. An upper limit to the methane frost abundance can be obtained by similar arguments to those presented above for nitrogen, though the higher melting point of methane allows a thicker layer. A lower limit for methane is obtained by considering the amount of methane photolyzed over the age of the solar system, which is the equivalent of roughly a meter-thickness of products spread over the surface.

The photolysis rate implies that the volatile frosts are underlain by a meter or so of photolysis products. This raises the question as to how carbon dioxide frost has remained exposed to view; perhaps impact stirring has allowed some CO_2 to be present at the optical surface, or perhaps recent internal activity has allowed fresh CO_2 to be outgassed. More intriguing is the idea that the CO_2 seen in the spectra is the product of photolysis of CO and subsequent addition of oxygen through infalling ice particles. Such a photochemistry is predicted for Titan, although the rate is computed to be only 0.1% of the methane photolysis rate [13]. If the same holds on Triton, the photochemically-produced CO_2 could be highly diluted in the detritus of higher hydrocarbons.

Models for initial volatile inventory. The first two models use the computations presented in [12] to compute molecular abundances in the gas phase of a model solar nebula and proto-satellite nebula. The molecules are then assumed to either condense or become trapped in water ice as clathrate hydrate, with abundances determined from the computations of [6]. The gas phase molecular abundances in [12] are determined by equilibration reactions with finite rates which are allowed to proceed for a disk lifetime fixed at 10^{13} seconds, for concreteness. Likewise for concreteness the proto-satellite disk model is that for Jupiter; a detailed temperature-pressure profile for a nebula around Neptune has not been published, but the circum-Jovian disk case illustrates sufficiently well the effect of a more reducing environment. For both nebular models we consider results for two different types of chemistry: A fully gas-phase chemistry with no catalysis by grains, and a much more rapid set of reaction rates appropriate for efficient grain catalysis.

Given the molecular abundances, we assume that ammonia and carbon dioxide condense out directly and mix with the water ice either at the molecular or grain level. This is appropriate for ammonia, but a small amount of the carbon dioxide may instead be incorporated in clathrate hydrate [6]. Nonetheless, even for the small mixing ratios in the proto-satellite nebula, the partial pressure of carbon dioxide is sufficient to allow condensation below 60-70K. At 30 AU from the sun, the environment of Triton was colder than this during planet formation. Methane, carbon monoxide and molecular nitrogen were assumed to be trapped in clathrate hydrate; we use the published results at 80 K [6], though the fractionation effects are likely more severe at lower temperatures.

These cosmochemical models are undoubtedly oversimplified. The gas phase molecular abundances at 30 AU, in the solar nebula, are almost certainly not determined by chemical quenching much closer to the center of the nebula, because radial mixing may be severely limited [15] (but see [11]). Instead, infalling material from the surrounding collapsing cloud core will be partially processed but still retain a strong signature of molecular cloud abundance [7]. Additionally, volatile trapping in water ice was equally complex, may have involved several stages, and probably did

not involve clathrate hydrate formation [1, 7]. Rather than put together a more complicated model here, we include an additional column in the table which assumes a volatile inventory for Triton based on comets [8]. While cometary and proto-Triton material might have undergone modestly different histories, the inventory is instructive in its differences from the first two columns. The methane abundance in Comet Halley could be zero [10]; however, the observation of interstellar methane [5] strongly argues for this molecule being introduced into outer solar system bodies, and we adopt a finite lower value here. Likewise, the amount of formaldehyde in comets is controversial; we use a non-zero lower value here based on [9].

Comparison of initial and present-day (surface) inventories: Sufficient amounts of nitrogen, carbon monoxide and methane exist in the solar nebula and cometary models to account for the surface abundances, but the proto-satellite inventory falls short on nitrogen. The nitrogen abundance is not fatal to the proto-satellite model since the present-day surface amounts could have been derived from ammonia. Because the surface CO abundance is only an upper limit, it is not inconsistent with the proto-satellite model.

What is striking about the solar nebula and cometary models is that the surface *ratio* of carbon monoxide to nitrogen, required by the data to be <0.1, is very poorly matched in either case. Carbon monoxide is much more abundant than nitrogen in either model volatile inventory. Selective outgassing could be invoked to achieve the surface ratio, but the chemical differences between CO and N_2 are not so large as to make this particularly appealing. The surface ratio of CO/CH_4 does not appear to cause problems for either model: One can choose an intermediate amount of grain catalysis in the solar nebula model to yield the right surface ratio, and one is free to choose for the surface ratio CH_4/CO = 0.1 which is consistent with the cometary model.

Perhaps the most profound process modifying Triton's volatile inventory is early escape of gases from an atmosphere raised by tidal heating; [8] presents estimates for the total amount of escape during the lifetime of the atmosphere. If the atmosphere survives for a time of order a gigayear, which is plausible based on the models in [8] and the cratering record, then *most* of the initial volatile budget could be lost through escape. More detailed calculations are required to quantify the relative amounts of each gas which is lost through early, rapid atmospheric escape.

Acknowledgment. This work was supported by NASA grant NAGW-1039.

TRITON'S VOLATILE BUDGET[1]

Molecule	Solar Nebula[2]	Proto-satellite [2]	Cometary model[3]	Present Surface [4]
N_2	10^{-3}, 10^{-8}	10^{-11}, 10^{-17}	10^{-4}	10^{-6}-10^{-3}
NH_3	10^{-6}, 10^{-4}	10^{-1}	10^{-3}-10^{-2}	?
HCN	--	--	10^{-3}	?
CH_4	10^{-7}, 10^{-1}	10^{-1}	10^{-3}-10^{-2}	10^{-6}-10^{-3}
CO	10^{-1}, 10^{-7}	10^{-12}, 10^{-16}	10^{-2}-10^{-1}	< 10^{-7}-10^{-4}
CO_2	10^{-3}, 10^{-6}	10^{-8}, 10^{-12}	10^{-1}	*
H_2CO	--	--	10^{-3}-10^{-1}	?
CH_3OH	--	--	10^{-2}-10^{-1}	?

[1] Masses given, as order of magnitude only, in units of 10^{25} g.
[2] Predictions of solar and proto-satellite nebula models. First number assumes gas phase reactions are not catalyzed by grains; second number assumes efficient grain catalysis. Where only one number is given, results for the two cases are the same. Symbol (--) indicates no prediction available from [12], or too uncertain.
[3] Volatile budget based on abundances in comets. Cometary data from review by [10].
[4] Estimated mass of surface frost deposits. The ranges for CO and N_2 are coupled, that is, $CO/N_2 < 0.1$ in any case. Symbols:? = not yet observed ; * = observed but no abundance constraint available.

REFERENCES: [1] Bar-Nun, A., et al.. 1988. Phys. Rev. B 38:7749. [2] Broadfoot, A.L., et al. 1989. Science 246:1459. [3] Brown, R.H., et al. 1990. Science 250: 431. [4] Kirk, R.L. and Brown, R.H. 1992. BAAS 23:1209. [5] Lacy, J.H., et al. 1991. Astrophys. J. 376:556. [6] Lunine, J.I. and Stevenson, D.J. 1985. Astrophys. J. Suppl. 58:493.[7] Lunine, J.I.,et al. 1991. Icarus 94:333.[8] Lunine, J.I. and Nolan, M. 1992. Icarus 100:221.[9] Mumma, M.J. and Reuter, D.C. 1989. Astrophys. J. 344:940.[10] Mumma, M.J., et al. 1992. In Protostars and Planets III, eds. E.H. Levy, J.I. Lunine (Tucson: UA Press) in press. [11] Prinn, R.G. 1990. Astrophys. J. 348:725. [12] Prinn, R.G. and Fegley, M.B. 1989. In Origin and Evolution of Planetary and Satellite Atmospheres, eds. S.K. Atreya, J.B. Pollack and M.S. Matthews (Tucson: UA Press), p. 78. [13] Samuelson, R.E., et al. 1983. J. Geophys. Res. 88:8707-8715.[14] Stevens, M.H. et al., 1992. GRL 19:669-672. [15]Stevenson, D.J. 1990. Astrophys. J. 348:730.

THE EFFECT OF AN ON-ORBIT NEAR ENCOUNTER ON THE NUMBER FLUX DENSITY OF MICRON SIZED PARTICLES

Carl R. Maag[1], William G. Tanner[2], Tim J. Stevenson[3], Janet Borg[4], Jean-Pierre Bibring[4], W. Merle Alexander[2] and Andrew J. Maag[5]

1. Science Applications International Corporation; Glendora, CA 91740 USA
2. Baylor University Space Science Laboratory Department of Physics, Waco, TX 76798 USA
3. University of Kent at Canterbury, Unit for Space Sciences; Kent CT2 7NR, UK
4. Institut d'Astrophysique Spatiale; 91405 Orsay Cedex, France
5. Stanford University, Palo Alto, CA 94305 USA

Many materials and techniques have been developed by the authors to sample the flux of particles in Low Earth Orbit (LEO), and through regular *insitu* sampling of the flux in LEO, the materials and techniques have produced data which compliment the data now being amassed by the Long Duration Exposure Facility (LDEF) research activities. Several recent flight experiments have been conducted on the Space Shuttle as part of an ongoing program to develop an understanding of the Spatial Density as a function of size (mass) for particle sizes $1 \cdot 10^{-6}$ cm and larger. During the course of one of the missions, the Space Shuttle corrected its altitude to evade an upper stage. The results of this near encounter provided unexpected data.

Extensive research [1] has been conducted to characterize the effects on materials subjected to hypervelocity impacts by large masses. Even though the large mass impactors carry the highest probability of precipitating a catastrophic event, the number of large mass objects which might be encountered by an exposed surface in LEO is believed to be quite small. However, the size distribution of objects that will be encountered in LEO has not been adequately characterized; especially for that portion of the distribution which contains the largest number of objects, i.e., micron and sub-micron size.

Characterization of the orbital debris and micrometeoroid complex which any surface will encounter in LEO implies an implementation of several concurrent processes. Foremost, there should be a means to sample *insitu* , the flux with a frequency which can establish good statistics for multiple samples. There also should be access to that environment for an extended period so that the existence of any temporal fluctuations in that flux can be identified. The experiments flown can be passive sensors if the materials can be easily returned to Earth. In fact, the complete analysis of the LEO environment cannot be adequately conducted without repeated examinations of materials which have been exposed to the extremes of space. Hence, the experimental design which can provide a much needed investigation of small grains would be a passive sensor which could both detect and capture constituents of the orbital debris and micrometeoroid complex.

Recent flight experiments on STS-32, STS-44, STS-46 and STS-52 have been conducted to develop an understanding of the Spatial Density as a function of size (mass) for particle sizes $1 \cdot 10^{-6}$ cm and larger. In addition to the enumeration of particle impacts, it was also the intent of these experiments that hypervelocity particles be captured and returned intact. Measurements were performed post-flight to determine the flux density, diameters, and subsequent effects on various optical, thermal control and structural materials.

During the course of the STS-44 mission, the Space Shuttle corrected its altitude by 26 km to evade a spent upper stage. The results of this near encounter suggests that a cloud of micron sized particles exist in the vicinity of the object. Data also suggests that the flux density is nearly two (2) orders of magnitude higher than background flux. A comparison of the number flux density, along with microphotographs of the captured particles will be presented for the referenced shuttle flights.

REFERENCES. [1] Tanner, W. G. et al. An Examination of Hypervelocity Particle Penetration Parameters for Thin Films Flown in Space. HVIS 1992.

N94-16375

SUGGESTION FOR EXTENDED VIKING MAGNETIC PROPERTIES EXPERIMENT ON FUTURE MARS MISSIONS

M.B. Madsen[1], J.M. Knudsen[1], L. Vistisen[2], R.B. Hargraves[3]
[1]Physics Laboratory, H.C. Ørsted Institute, DK-2100 Copenhagen Ø, Denmark; [2]Niels Bohr Institute, DK-2100 Copenhagen Ø, Denmark; [3]Department of Geological and Geophysical Sciences, Princeton University, Princeton, NJ 08544.

An array of permanent magnets, with the purpose of establishing if the magnetic particles on Mars are present as discrete or as composite particles, has been constructed.

Introduction: A remarkable result from the Viking missions was the discovery that the Martian soil is highly magnetic, in the sense that the soil is attracted by a small magnet [1]. The soil was found to adhere almost equally well to a strong and a weak SmCo magnet in the Viking lander backhoe at both landing sites. The strong magnet had a magnetic field and field gradient of 0.25 T and 100 Tm^{-1}, respectively, whereas the corresponding values for the weak magnet were 0.07 T and 30 Tm^{-1}. Besides the backhoe magnets the Viking landers also carried a strong magnet situated at the Reference Test Chart (RTC). This magnet was exposed solely to the airborne dust. The RTC magnets of both landers attracted a substantial amount of airborne dust. Based on the pictures returned of the soil clinging to the magnets, it was estimated that the particles in the Martian dust contain between 1% and 7% of a strongly magnetic phase, probably a ferrimagnetic oxide intimately dispersed throughout the soil. Chemical analyses by means of the Viking X-ray fluorescence spectrometer indicate a content of about 18% by weight of Fe_2O_3. The limits of the saturation magnetization, σ, of the soil may be given approximately as: 5 $Am^2(kg\ Fe_2O_3)^{-1} < \sigma <$ 38 $Am^2(kg\ Fe_2O_3)^{-1}$. A significant observation was that both the weak and the strong backhoe magnets were essentially saturated with magnetic soil throughout the whole Viking mission. The results were the same for both landing sites. A notable result was that the dust on the RTC magnets, the dust on the backhoe magnets and the dust on the surface of Mars were optically very similar, if not identical. It seems that the attracted airborne dust and the attracted surface dust were of the same composition and probably also in the same grain size range.

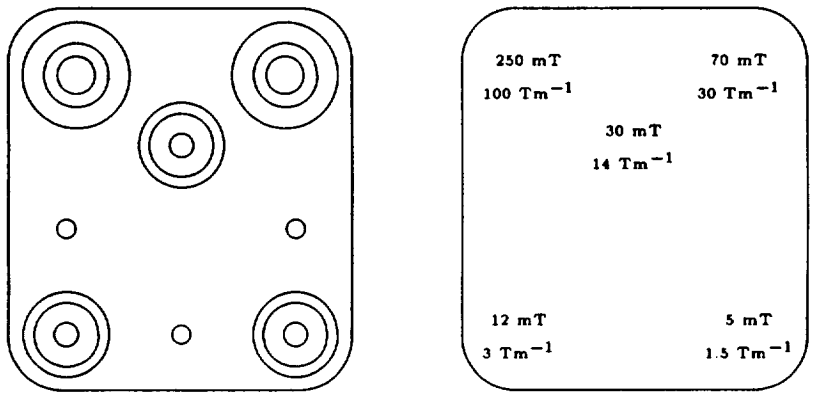

Array of 5 permanent magnets. The three smallest circles represent measurement posts, casting shadows that are used to estimate the amount of material on the array.

EXTENDED MAGNETIC PROPERTIES EXPERIMENT

M.B. Madsen *et al.*

An essential problem that was not definitively solved by the Viking Magnetic Properties Experiment is the following: Is the magnetic phase in the Martian soil present as discrete (single phase) particles or is the magnetic phase part of composite (multiphase) particles? The objective of the experiment suggested here is to contribute to the solution of this and other problems related to the study of the magnetic phase on Mars.

Experimental: We have produced various prototypes of permanent magnet arrays, including weak magnets. As an example we show an array consisting of 5 permanent magnets.

When mounted the magnets are imbedded in a magnesium panel. The mass of the panel is 70 g. The dimensions are 67 × 60 × 9 mm^3. The fields and field gradients on the surface of the panel are given in the figure.

Discussion: Tests with various Mars soil analogues have shown that inclusion of low strength magnets will give additional information about the magnetic properties of the Martian dust. For example: Dust composed of pure maghemite (γ-Fe_2O_3) will stick to all five magnets. Dust composed of thermally altered nontronite, which contains a small amount of maghemite, will stick only to the two (three) strongest magnets. The thermally altered nontronite is an example of composite multiphase particles. By studying the amounts and colour of the dust adhering to the various magnets, and the interaction of the dust on the array with the wind, we may come close to determining the magnetization of the particles adhering to the magnet array. A complete identification of the magnetic phase will probably not be possible.

It is under consideration to include a Mössbauer spectrometer in future missions to Mars [2,3]. It will be demonstrated that the array of magnets will give significant contributions to the interpretation of Mössbauer spectra of the Martian soil.

Conclusion: It is suggested that future missions to Mars carry permanent magnet arrays that include several weaker magnets as well as the types of magnets carried by Viking. If the landers - for other purposes - carry also a magnetometer, the magnet array should consist of 4 (not 5) magnets. The four magnets should be arranged in such a way that the magnetic field far from the magnet array decrease at least as a quadrupole field. In this way the magnet array will not interfere with the measurements of the magnetometer.

Acknowledgement: Financial support from the Danish Natural Science Research Council is gratefully acknowledged.

References [1] R.B. Hargraves, D.W. Collinson, R.E. Arvidson and C.R. Spitzer, *J. Geophys. Res.* 82, no. 28 (1977) 4547; [2] D.G. Agresti, R.V. Morris, E.L. Wills, T.D. Shelfer, M.M. Pimperl, B.C. Clark and B.D. Ramsey, *Hyperfine Interactions* 72 (1992) 285; [3] G. Klingelhöfer, J. Foh, P. Held, H, Jäger, E. Kankeleit and R. Teucher, *Hyperfine Interactions* 71 (1992) 1449;

LARGE-SCALE VOLCANISM ASSOCIATED WITH CORONAE ON VENUS; K. Magee Roberts and J. W. Head, Department of Geological Sciences, Brown University, Providence, RI 02912

The formation and evolution of coronae on Venus are thought to be the result of mantle upwellings against the crust and lithosphere and subsequent gravitational relaxation.[1-6] A variety of other features on Venus have been linked to processes associated with mantle upwelling, including shield volcanoes on large regional rises such as Beta, Atla and Western Eistla Regiones[7] and extensive flow fields such as Mylitta and Kaiwan Fluctus near the Lada Terra/Lavinia Planitia boundary.[8] Of these features, coronae appear to possess the smallest amounts of associated volcanism, although volcanism associated with coronae has only been qualitatively examined. An initial survey of coronae based on recent Magellan data indicated that only 9% of all coronae are associated with substantial amounts of volcanism, including interior calderas or edifices greater than 50 km in diameter and extensive, exterior radial flow fields.[4] Sixty-eight percent of all coronae were found to have lesser amounts of volcanism, including interior flooding and associated volcanic domes and small shields; the remaining coronae were considered deficient in associated volcanism.[4] It is possible that coronae are related to mantle plumes or diapirs that are lower in volume or in partial melt than those associated with the large shields or flow fields. Regional tectonics or variations in local crustal and thermal structure may also be significant in determining the amount of volcanism produced from an upwelling. It is also possible that flow fields associated with some coronae are sheet-like in nature and may not be readily identified. If coronae are associated with volcanic flow fields, then they may be a significant contributor to plains formation on Venus, as they number over 300 and are widely distributed across the planet.[4] As a continuation of our analysis of large-scale volcanism on Venus,[8,9] we have reexamined the known population of coronae and assessed quantitatively the scale of volcanism associated with them. In particular, we have examined the percentage of coronae associated with volcanic flow fields (*i.e.*, a collection of digitate or sheet-like lava flows extending from the corona interior or annulus), the range in scale of these flow fields, the variations in diameter, structure and stratigraphy of coronae with flow fields, and the global distribution of coronae associated with flow fields.

Considered in this analysis are 323 coronae with full or partial annuli.[4,10,11] Volcanic features with strictly radial fractures and structures that lack annuli ("novae"[5,10]) and volcanic edifices with well-developed calderas often resembling coronae are not considered. Of this population, 126 or 39% possess exterior radial flow fields. This is a higher percentage than the 9% reported in the inital survey[4] and is based on a careful reexamination of the image data and mapping criteria developed during our analyses of extensive flow fields on Venus.[8,9] Flow field areas range from 1400 km^2 to 1.5 x 10^5 km^2, with an average area of 1.1 x 10^5 km^2. For comparison, the average area associated with the "great flow fields"[9] or fluctus on Venus is 3.7 x 10^5 km^2.

The average diameter of coronae associated with flow fields is 339 km; that of coronae without flow fields is 249 km. This difference is statistically significant and suggests that coronae with flow fields are generally larger than those without and may be associated with larger mantle upwellings and volumes of partial melt. There is no correlation between flow field size and coronae diameter (Fig. 1); the largest flow fields are not associated with the largest coronae (and, presumably, the largest upwellings). Other factors such as age and state of preservation, local crustal structure and thermal gradients may also influence the presence of flow fields at coronae.

Coronae have been classified into five different categories based primarily on the morphology of the annulus.[4] The "concentric" and "asymmetric" classes are the most common, characterizing over 66% of the entire population.[4] The majority (41%) of coronae with flow fields are in the concentric category, similar to the population of coronae as a whole. In terms of classification, the distribution of coronae with flow fields differs from the general population only in the greater abundance of coronae with radial structural elements (up to 46%). Such features may be due to tectonic uplift[4-6] and/or dike emplacement[12] and are consistent with an association of large amounts of volcanism. There is no correlation between corona type and either flow field area or corona diameter.

The bulk of the flow fields (49%) appear to have been emplaced early in coronae evolution, prior to annulus formation. Approximately 40% were emplaced throughout corona evolution (before and after annulus formation) and only 11% appear to post-date annulus formation. This suggests that flow field emplacement is generally related to the initial stage of corona formation, as might be expected by analogy to flood basalt formation on the earth, which is thought to be linked to the early stages of plume impingement against the lithosphere.[13] Interior flooding generally occurs after the emplacement of extensive radial flow fields.

Coronae are distributed widely, but not randomly, across Venus; they are concentrated near the equator at about 240° east longitude[14] in the Beta-Atla-Themis (BAT) region that is characterized by a major concentration of volcanic features, broad rises and a complex network of rift and deformation zones.[10] A Mercator plot of coronae with and without flow fields (Fig. 2) reveals no significant difference in the distribution of these features. One possible exception is the region including Themis Regio where there is an alignment of coronae with flow fields directly along the deformation zone and another alignment of coronae without flow fields to the SW, away from the

CORONA VOLCANISM: Magee Roberts, K. and Head, J. W.

zone of active rifting. Approximately 58% of coronae with flow fields are associated with zones of extension, including rift zones, coronae chains, and chasmata. This suggests that regional structure has exhibited some control on the formation of flow fields at coronae, although the distribution of the two populations of coronae does not appear to be significantly different.

In summary, volcanism is shown to be associated with a considerably greater number of coronae than found in initial surveys. Flow field volcanism is preferentially associated with larger coronae and in many cases is related to extensional tectonic environments. Volcanism is predominately associated with early stages of corona evolution, although in some cases, late-stage volcanic activity in the central parts of coronae has occurred. We are currently assessing flow lengths, volumes, and distribution to further define the nature and geometry of melting associated with coronae and are developing criteria for distinguishing the relative ages of coronae and associated flow fields to assess any evidence for variations in the preservation of flow fields as a function of time. In addition, we are evaluating the potential contribution volcanism associated with coronae may have on plains formation and reasons for the differences in the scale of volcanism between the range of features on Venus linked to mantle upwelling.

REFERENCES CITED: 1) Stofan, E. R. and Head, J. W. (1990) *Icarus, 83*, 216; 2) Pronin, A. A. and Stofan, E. R. (1990) *Icarus, 87*, 452; 3) Stofan, E. R. et al. (1991) *JGR, 96*, 20,933; 4) Stofan, E. R. et al. (1992) *JGR, 97*, 13,347; 5) Squyres, S. W. et al. (1992) *JGR, 97*, 13,611; 6) Janes, D. M. et al. (1992) *JGR, 97*, 16,055; 7) Senske, D. A. et al. (1992) *JGR, 97*, 13,395; 8) Magee Roberts, K. et al. (1992) *JGR, 97*, 15,991; 9) Lancaster, M. G. et al. (1992) (abstract) LPSC XXIII, 753; 10) Head, J. W. et al. (1992) *JGR, 97*, 13,153; 11) Crumpler, L. C. et al. (1992) manuscript in preparation; 12) Parfitt, E. A. et al. (1992) (abstract) Intl. Colloq. Venus, 83; 13) Richards, M. A. et al. (1989) *Science, 246*, 103; 14) Squyres, S. W. et al. (1992) (abstract) Intl. Colloq. Venus, 119.

Figure 1. Corona diameter vs. flow field area

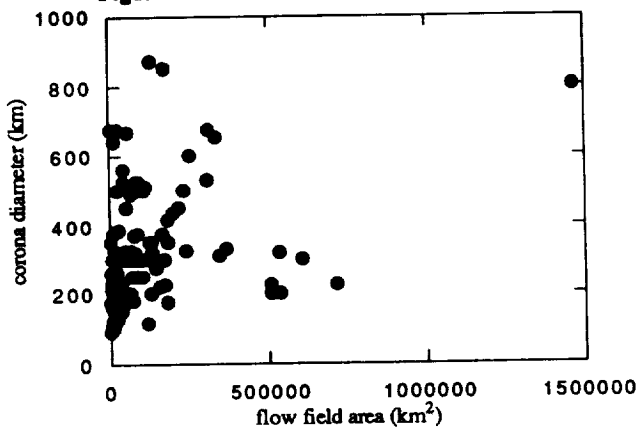

Figure 2. Distribution of coronae with flow fields (x's) and without (triangles)

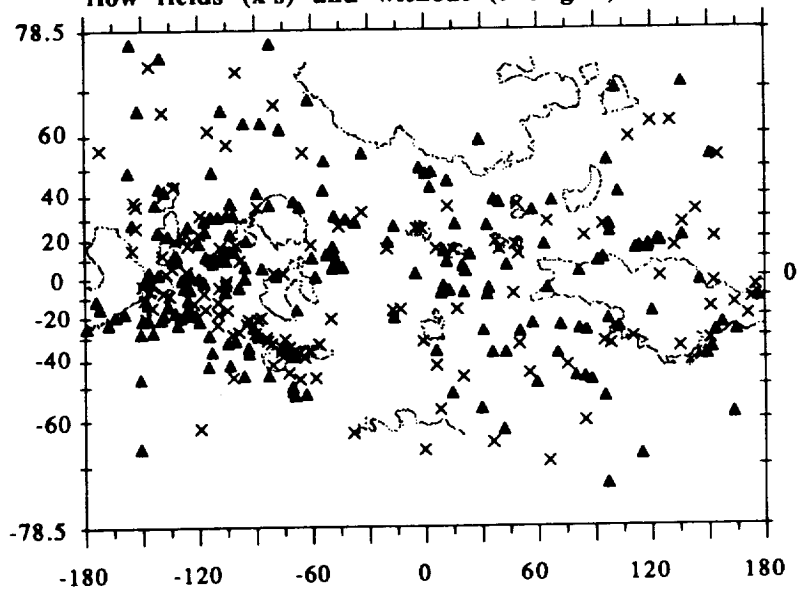

POSSIBLE SOURCES OF [H_2] TO [H_2O] ENRICHMENT AT EVAPORATION OF PARENT CHONDRITIC MATERIAL; A.B. Makalkin[1], V.A. Dorofeyeva[2], and A.V.Vityazev[1], [1]Schmidt Institute of Physics of the Earth, Russian Acad. Sci., B.Gruzinskaya 10, 123810 Moscow; [2]Vernadsky Institute of Geochemistry, Russian Acad. Sci., Kosygin str. 19, 117334 Moscow, Russia

One of the results obtained from thermodynamic simulation of recondensation of the source chondritic material (1,2) is that at 1500-1800 K it's possible to form iron-rich olivine by reaction between enstatite, metallic iron and water vapor in the case of $[H_2O]/[H_2] \approx 0.1$ (Fig. 1 in [2]). This could be reached if the gas depletion in hydrogen is 200-300 times relative to solar abundance. To get this range of depletion one needs some source material more rich in hydrogen than the carbonaceous CI material which is the richest in volatiles among chondrites. In the case of recondensation at impact heating and evaporation of colliding planetesimals composed of CI material (3), we obtain insufficiently high value of $[H_2]/[H_2O]$ ratio. In the present paper we consider some possible source materials and physical conditions necessary to reach gas composition with $[H_2]/[H_2O] \sim 10$ at high temperature.

Carbonaceous chondrites have mass ratio $H_2O/Si \approx 1.0 - 2.5$ at the bulk content of chondritic material $\approx 10 - 11$ mole/mole Si (for example [4]). Therefore, in order to get the gas with $[H_2O]/[H_2] \sim 0.1$ at evaporation of this material, it should be admixed with 10 mole H_2 per 1 mole Si or, equivalently, 1 mole hydrogen per 1 mole of bulk chondritic (CI) material.

The gas in the surrounding solar nebula (if not dissipated by the time of high-energy collisions) could be a source for hydrogen, but only in the case if the nebular pressure was higher than in the explosion cloud (3). The pressure near the central plane of the nebula in the formation region of the carbonaceous and ordinary chondrites ($R \sim 2$ AU) even at the early stage was higher than 10^{-5} bar (according to all current physical models of the solar nebula) and probably was $\sim 10^{-6}$ bar. These values are lower than the average pressures in the explosion cloud (3). Therefore, the necessary pressure relation could be reached only in a boundary layer between the explosion cloud and the surrounding gas of the nebula. But it's possible that the gas had already dissipated from the nebula at the time when high-velocity collisions occurred.

We'll consider another source of H_2 enrichment in the gas phase of the explosion cloud. The source could be related to a source material itself. Two possible mechanisms can be considered.

1) The material of carbonaceous chondrites contains significant amount of carbon and its compounds, including such volatile compounds as lower hydrocarbons, amino acids, carbon acids *et al.* There is evidence on significant loss of the volatile fraction of the organic component of chondrites during their fall onto the Earth and on the Earth's surface (5). It seems reasonable to suggest that the most of the mass of the volatile organic component has been lost from meteorites and their parent bodies at some stages

of evolution or during the lifetime of the solar system. The temperature inside parent bodies of the carbonaceous chondrites could not be higher than 600-700 K in order for hydrosilicates, and in particular chlorite, to survive. But the temperature due to some internal or external heat sources could be well above T ~300-400 K, that is in the range 300-600 *K*. At these temperatures, volatile organic compounds should be more or less gradually destroyed and gaseous products of their decomposition would be lost from the surface of a body.

If the initial abundance of volatile fraction of organics was 2 orders of magnitude higher than observed in C chondrites, this fraction should supply 3-4 times higher content of carbon than in observed CI chondrites and yield $H_2O/C \sim 1$. On heating of such a parent material to $T > 1200$ K during an impact event, organic carbon had enough time to react with water released at decomposition of silicates:

$$C(org) + H_2O \rightarrow CO + H_2 \qquad (1)$$

If the abundance of H_2O was a little higher than that of C, we obtain the ratio $[H_2O]/[H_2]$, necessary for formation of the iron-rich olivine. For example, at $H_2O/C = 1.2$ we obtain from reaction (1) $[H_2O]/[H_2] = 0.2$. Taking into account also some additional hydrogen released at decay of organic compounds with approximate $H/C \approx 2$ ratio, we obtain $[H_2O]/[H_2] \approx 0.1$.

2) There exists another possible source material which can produce $[H_2O]/[H_2] \approx 0.1$. at the impact evaporation process: it is comet-like material, but previously depleted in water. The data on the comet material (6) yield the ratio of carbon in organics to water ice approximately as 0.06/0.5 (by mass). When cometary-type bodies due to gas drag and/or gravitational perturbations appeared in the inner, warmer region of the early solar system, they lost water and other ices. Due to significant size of comet nuclei this loss could be not completed before a high-energy impact event. After release of ~80% of water from the cometary material, we obtain $H_2O/C \gtrsim 1$. This ratio leads to $[H_2O]/[H_2] \sim 0.1$ at high-temperature process according to Eq. 1.

REFERENCES: (1) V.A. Dorofeyeva, A.B. Makalkin, M.V. Mironenko, A.V. Vityazev (1993) This volume. (2) V.A. Dorofeyeva, A.B. Makalkin, A.V. Vityazev (1993) This volume. (3) A.V. Vityazev, V.A. Dorofeyeva, A.B. Makalkin (1993) This volume. (4) S.K. Saxena, G. Eriksson (1983) *Geochim. Cosmochim Acta*, 47, 1865-1874. (5) J.R. Cronin, S. Pizarello, D.P. Cruikshank (1988) In *Meteorites in the Early Solar System*, Eds. J.F. Kerridge, M.S. Matthews (Tucson, Univ. of Arizona Press), 819-860. (6) E.K. Jessberger, J.Kissel, J.Rahe (1989) In *Origin and Evolution of Planetary and Satellite Atmospheres*, Eds. S.K. Atreya, J.B. Pollack, M.S. Matthews (Tucson, Univ. of Arizona Press), 167-191.

TIDAL REGIME OF INTACT PLANETOID CAPTURE MODEL FOR THE EARTH-MOON SYSTEM: DOES IT RELATE TO THE ARCHEAN SEDIMENTARY ROCK RECORD?; Robert J. Malcuit, Dept. of Geology and Geog., Ronald R. Winters, Dept. of Physics and Astron., Denison Univ., Granville, Ohio 43023.

Regardless of one's favorite model for the origin of the earth-moon system (fission, coformation, tidal capture, giant-impact) the early history of lunar orbital evolution would produce significant thermal and earth and ocean tidal effects on the primitive earth. Three of the above lunar origin models (fission, coformation, giant-impact) feature a circular orbit which undergoes a progressive increase in orbital radius from the time of origin to the present time [1,2]. In contrast, a tidal capture model places the moon in an elliptical orbit undergoing progressive circularization from the time of capture (for model purposes about 3.9 billion years ago) for at least a few 10^8 years following the capture event. Once the orbit is circularized, the subsequent tidal history for a tidal capture scenario is similar to that for other models of lunar origin and features a progressive increase in orbital radius to the current state of the lunar orbit. This elliptical orbit phase, if it occurred, should have left a distinctive signature in the terrestrial and lunar rock records. Depositional events would be associated terrestrial shorelines characterized by abnormally high, but progressively decreasing, ocean tidal amplitudes and ranges associated with such an orbital evolution.

In previous work we have demonstrated that gravitational (tidal) capture of a lunar-mass planetoid by an earth-mass planet is physically possible [3,4]. A typical coplanar, three-body stable capture scenario is shown in Figure 1a. Figure 1b shows a semilog plot of Tidal Amplitude vs. Time for this 4-year stable capture sequence. To account for the angular momentum of the earth-moon system the earth rotation rate for such an tidal capture scenario is about 10 hours/day. Using a numerical two-body orbit evolution program and reasonable deformational and dissipative parameters for the interacting bodies, we find that the most realistic time scales for orbit circularization to 10% eccentricity are in the range of 1.0-1.6 billion years. Two such scenarios are shown in Figure 2. Figure 2a depicts a two-body orbit circularization sequence in which all energy is dissipated in the satellite by way of radial tidal action; thus the satellite orbit does not gain angular momentum during the orbit circularization. The scenario in Figure 2b is more realistic and features angular momentum transfer from the rotating planet to the satellite orbit via the tangential tidal mechanism. In this scenario the major axis of the lunar orbit decreases from about 183 R_e to 93 R_e as the rotation rate of the planet decreases from about 10 hours/day to 14.4 hours/day. Using a 3-body orbit program (4th order Runge-Kutta integrator) and a program for plotting the equilibrium tidal amplitudes and ranges directly from the numerical orbital data, we find that the maximum perigean earth tidal ranges at 2, 6, and 10 hundred million years after capture are about 20, 5, and 3 meters, respectively. Although solid rock tides tend not to yield much of a geological record, such action could contribute substantially to the thermal regime of a planet or satellite. The ocean tides, however, can be recorded in the sedimentary rock record. Several rock units in the age range 3.6-2.5 billion years before present are reported to have a major tidal component. Examples are the Warrawoona, Fortescue, and Hamersley Groups of Western Australia [5,6,7] and the Pangola and Witwatersrand Supergroups of South Africa [8,9]. Detailed study of the features of these tidal sequences may be helpful in deciphering the style of lunar orbital evolution during the Archean Eon.

TIDAL REGIME OF CAPTURE MODEL; Malcuit R. J. and Winters R. R.

References: [1] Peale, S. J. and Cassen, P. (1978) Icarus, 36, 245-269; [2] Ross, M. N. and Schubert, G. (1989) Jour. Geophys. Res., 94, 9533-9544; [3] Malcuit, R. J. et al. (1989) Proc. 19th LPSC, Cambridge Univ. Press and Lunar Planet. Inst., 581-591; [4] Malcuit et al. (1992) Proc. Vol., 3rd Int. Archaean Symp., Geol. Dept. & Univ. Ext., Univ. of Western Australia, Pub. #22, 223-235; [5] Lowe, D. R. (1983) Precambrian Res., 19, 239-283; Ho, S. E. et. al. (1990) 3th Int. Archaean Symp. Excur. Guidebook, Geol. Dept. & Univ. Ext., Univ. of Western Australia, Pub. #21, 1-57; [7] Simonson, B. M. et al. (1993) Precambrian Res., in press; [8] Von Brunn, V. and Mason, T. R. (1977) Sedimentary Geol., 18, 245-255; [9] Eriksson, K. A. et al. (1981) Sedimentary Geol., 29, 309-325.

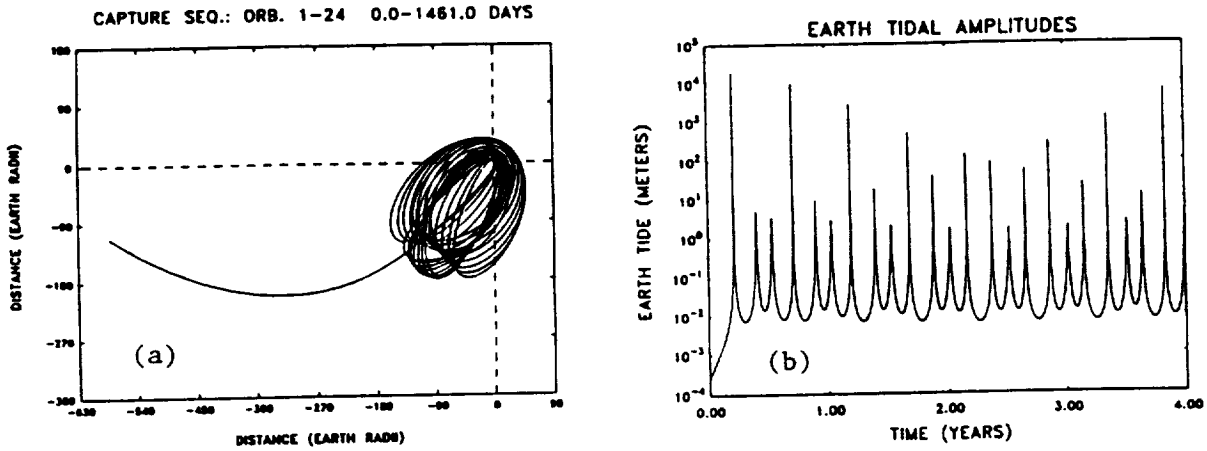

Figure 1. (a) Diagram showing the first 24 orbits (4 years) of a stable prograde capture scenario in a co-planar, non-rotating coordinate system. Some values for this run are r_p = 1.43 R_e, earth anomaly = 320°, planetoid anomaly = 190.392°, planetoid heliocentric eccentricity = 1.25%, h_m = 0.26, Q_m = 1 for the initial encounter and 10 for all subsequent encounters, h_e = 0.7, Q_e = 100. (b) Semilog plot of Earth Tidal Amplitude vs. Time for the four-year orbital sequence shown in Figure 1a. Note the irregular pattern of tidal spikes associated with the close encounters.

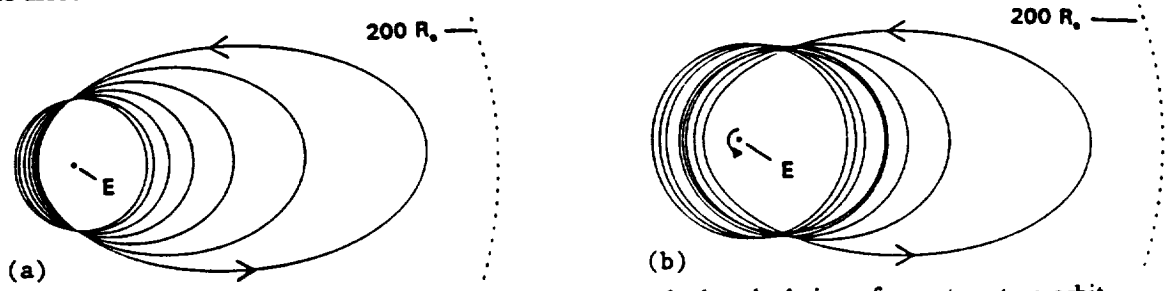

Figure 2. (a) Sequence of seven orbital stages in a two-body calculation of a post-capture orbit circularization seqeunce in which all energy is dissipated within the body of a lunar-like planetoid with h=0.5 and Q=1000. In this case the orbital angular momentum of the planetoid remains the same throughout the orbit circularization sequence. A 30 R_e prograde circular orbit is consistent with a 10 hour/day rotation rate for the pre-capture planet. The largest orbit on the diagram is the maximum size orbit that is stable relative to solar perturbations in a 3-body system for the specified quantity of angular momentum. Each of the orbital stages represent 200 million years of orbital evolution (circularization). The time scale for orbital circularization in this scenario is about 1.1 billion years. (b) Sequence of eight orbital stages in a two-body system calculation of a post-capture orbital circularization sequence in which energy is dissipated in both the lunar-like planetoid (radial tides) and the earth-like planet (radial and tangential tides). For this run h_m=0.5, Q_m=1000, h_e=0.7, Q_e=100. Note that the tangential tides operating on the planet transfer rotational angular momentum from the planet to the satellite's orbit. The timescale for circularization to 10% eccentricity is about 1.4 billion years. The resulting near circular orbit of the satellite has angular momentum equivalent to a circular orbit of about 46 R_e and the planet rotation rate is about 14.4 hours/day.

ON THE DELIVERY OF PLANETESIMALS TO A PROTOPLANET IN THE SOLAR NEBULA

Renu Malhotra, *Lunar and Planetary Institute, 3600 Bay Area Blvd, Houston, TX 77058*

A planetesimal moving in the solar nebula experiences an aerodynamic drag which causes its orbit to circularise and shrink. However resonant perturbations from a protoplanet interior to the planetesimal's orbit can counteract both the orbital decay and the damping of the eccentricity: the planetesimal can be captured into an orbital resonance and its eccentricity pumped up to an equilibrium value. The resonance trapping phenomenon is sensitive to several factors and we elaborate on these below. Orbital resonances form (partial) barriers to the transport of planetesimals into the feeding zone of the protoplanet. Here we report on a systematic study of the idealised system of a single protoplanet of mass much larger than the masses of the planetesimals, comparing relevant analytic estimates with numerical simulations. Our principal conclusion is that in a gas-rich environment, the bulk of the solid material delivered to the feeding zone of the protoplanet is in the form of quite small bodies of radius $s < s_0$,

$$\frac{s_0}{1\,\mathrm{m}} \approx 5.5\left(\frac{3\,\mathrm{g\text{-}cm^{-3}}}{\rho}\right)\left(\frac{\rho_{\mathrm{gas}}}{10^{-10}\mathrm{g\text{-}cm^{-3}}}\right)\left(\frac{\eta}{0.005}\right)\left(\frac{a_P}{1AU}\right)\left(\frac{M_P}{M_\oplus}\right)^{-3/7} \tag{1}$$

where ρ is the bulk density of the planetesimal, ρ_{gas} is the gas density, $\eta = (1 - v_{\mathrm{gas}}/v_{\mathrm{kep}})$ measures the offset of the pressure supported gas velocity from the local keplerian velocity, and M_P and a_P are the mass and orbital radius of the protoplanet, respectively.

Much of the work summarized here is built upon previous work by Weidenschilling & Davis (1985) and Weidenschilling (1987) on the phenomenon of resonance capture; we have also drawn upon the analysis of Adachi etal (1976). The following points can be made regarding the capture of a planetesimal into an exterior $j : j + 1$ orbital resonance with a protoplanet:

(i) Resonance capture occurs with high probability if the planetesimal radius is larger than a minimum value, s_{min},

$$\frac{s_{\mathrm{min}}}{1\mathrm{km}} \simeq \frac{2}{j(j+1)}\left(\frac{3\,\mathrm{g\text{-}cm^{-3}}}{\rho}\right)\left(\frac{\rho_{\mathrm{gas}}}{10^{-10}\mathrm{g\text{-}cm^{-3}}}\right)\left(\frac{\eta}{0.005}\right)\left(\frac{a_P}{1AU}\right)\left(\frac{M_P}{M_\oplus}\right)^{-1}, \tag{2}$$

and its eccentricity is smaller than a value e_{crit} as it approaches the resonance:

$$e_{\mathrm{crit}} \simeq 0.023\left(\frac{M_P}{jM_\oplus}\right)^{1/3}. \tag{3}$$

(ii) Upon capture into resonance, the planetesimal will acquire an equilibrium eccentricity, e_{eq}, that balances the resonant excitation and the damping by gas drag:

$$e_{\mathrm{eq}} \simeq C\sqrt{\frac{\eta}{j+1}}, \tag{4}$$

where the coefficient C is 1.14 for a v^2 drag law and 1 for Stokes' law.

(iii) These estimates do not hold for resonances arbitrarily close to the protoplanet: for $j > j_{\mathrm{crit}} \approx 0.4(M_P/M_\odot)^{-2/7}$ the resonance is unstable (Wisdom 1981), and a planetesimal that approaches this resonance will reach the feeding zone of the protoplanet with high probability.

DELIVERY OF PLANETESIMALS TO A PROTOPLANET : R. Malhotra

Since larger planetesimals are more easily captured into resonance, they may reach the protoplanet only if their orbital eccentricities are sufficiently high to allow a diffusion past the orbital resonances. However, due to the efficacy of eccentricity-damping by gas drag, only a small fraction of the larger planetesimals is likely to fall in this category. Weidenschilling & Davis (1985) have suggested that the resonance capture of the larger planetesimals will enhance their collision rates. If a collision imparts a sufficiently high velocity kick to a planetesimal, the resonance can be unlocked. We estimate the magnitude of this kick to be

$$\frac{\delta v}{v_{\rm kep}} \approx 0.007(\frac{M_P}{jM_\oplus})^{1/2}. \qquad (5)$$

However, unless the particle is comminuted, it is very likely to be trapped into the next orbital resonance as its orbit decays. Thus, only those particles that are comminuted to a size sufficiently small that they can escape being captured into all $j : j+1$ resonances with $j < j_{\rm crit}$ will be easily delivered to the protoplanet. s_0 in equation (1) is our estimate of the maximum particle radius that satisfies this condition.

References

Adachi, I. C.Hayashi and K.Nakazawa (1976) *Prog. Theor. Phys.* **56** 1756-1771.
Weidenschilling, S.J. and Davis, D.R. (1985) *Icarus* **62**, 16-29
Weidenschilling, S.J. (1987) Gerlands Beitrage Zur Geophysik **96** 21-33.
Wisdom, J. (1980) *Astron. J.* **85** 1122-1133.

TECTONIC RESURFACING OF VENUS. Michael C. Malin, Malin Space Science Systems, 3535 General Atomics Court, Suite 250, San Diego CA 92121, Robert E. Grimm, Dept. of Geology, Arizona State University, Tempe AZ 85287-1404, and Robert R. Herrick, Lunar and Planetary Institute, 3600 Bay Area Blvd., Houston TX 77058.

Introduction. Impact crater distributions and morphologies have traditionally played an important role in unraveling the geologic histories of terrestrial objects, and Venus has proved no exception. The key observations are[1,2]: (i) mean crater retention age about 500 Ma, (ii) apparently random spatial distribution, (iii) modest proportion (17%) of modified craters, and (iv) preferential association of modified craters with areas of low crater density. The simplest interpretation of these data alone is that Venus experienced global resurfacing (assumed to be largely volcanic) prior to 500 Ma, after which time resurfacing rates decreased dramatically[1]. This scenario does not totally exclude present geological activity: some resurfacing and crater obliteration is occurring on part of the planet, but at rates much smaller than on Earth.

An alternative endmember model holds that resurfacing is also spatially randomly distributed[2]. Resurfacing of about 1 km^2/yr eliminates craters such that a typical portion of the surface has an age of 500 Ma, but actual ages range from zero to about 1000 Ma. Monte Carlo simulation indicates that the typical resurfacing "patch" cannot exceed about 500 km in diameter without producing a crater distribution more heterogeneous than observed. Volcanic or tectonic processes within these patches must be locally intense to be able to obliterate craters completely and leave few modified.

In this abstract, we describe how global geologic mapping may be used to test resurfacing hypotheses. We present preliminary evidence that the dominant mode of resurfacing on Venus is tectonism, not volcanism, and that this process must be ongoing today. Lastly, we outline a conceptual model in which to understand the relationship between global tectonics and crater distribution and preservation.

Approach. Although craters are randomly distributed around the planet, their distribution with respect to *terrain type* is unknown. Observations of impact crater location, size, modification state, and surrounding terrain[3] may be used as a basis for prediction. For a uniform population of craters that has changed very little since a global resurfacing event, each terrain type should contain a number of craters proportional to its area. To the extent that the actual areal abundances differ, the terrain is younger or older than the global mean and thus provides a first-order measure of the average age of each terrain.

A complete test of this hypothesis first requires a global geologic map from which the areas of each terrain type may be estimated. We are presently compiling a 1:20 million geologic map using data from C2 and C3 MIDRs. For now, we present one preliminary result using an automated mapping procedure. We are interested in testing the specific hypothesis that faulting - whether in the form of tesserae, ridge or mountain belts, coronae, rifts, or plains fractures - dominates crater obliteration on Venus. Faulted units typically have both high radar backscatter and RMS slope. Although use of either quantity alone is problematic, backscatter is more sensitive to variations in local morphology and chemical composition, so we adopt RMS slope as a general indicator of faulting as manifested by meter-scale roughness (e.g., 4). Recognizing that other processes such as blocky lava flows could also contribute to high RMS slopes, a trial-and-error cutoff value was established by visually comparing the RMS slope map to selected tectonic zones visible in backscatter and shaded relief. The adopted contour of 2.5° is shown in Figure 1. These criteria show Venus as a planet dominated by tectonism: approximately 60% of the planet may be characterized as faulted, 45-50% if fractured plains are neglected. Yet only 40% of the craters with D > 30 km are contained within faulted regions. Since there are nearly 200 samples (craters), the probability of this distribution occurring by chance is very small. There are fewer craters in tectonized zones because they are being destroyed.

Further evidence for tectonic obliteration comes from crater preservation states. Within the plains areas defined by Figure 1., none of the craters is tectonically deformed. Within the fractured plains, however, nearly half of the craters are cut by faults. Returning to the existing crater data base, 60% of craters in rift areas and 40% in tesserae are faulted. All tolled, 75% of all craters occur on the 50% of the planet covered by plains (either disturbed or undisturbed), and the vast majority of these craters are undeformed. In contrast, over a third of the remaining 25% of craters are tectonically deformed. Although craters may be uniformly distributed geographically, such variances in crater abundances and modification, scaled as they are to global areas, are clear indications of non-uniform geologic distribution. These results clearly indicate that a substantial portion of the planet is undergoing modification.

Interpretation. If craters are being tectonically obliterated but are spatially randomly distributed, then tectonism must be widespread, recurrent, and operating at a variety of scales. Although the eye is drawn in radar backscatter images to major deformation zones such as the Equatorial Highlands and Ishtar Terra, faulted areas occur across the planet (Fig. 1). Resurfacing models[2] still constrain the size of a typical "patch" to less than about the mean intercrater distance in order to preserve spatial homogeneity.

These requirements are in good agreement with the emerging picture of global tectonics on Venus both from theory and Magellan observations. On Earth, plate decoupling focuses deformation in narrow zones a few hundred km across separated by undeformed regions thousands of km in size. On Venus, direct coupling to mantle convection results in more pervasively distributed deformation, but in patterns coherent over length scales of several hundred kilometers[5]. This is precisely the patch size required by crater resurfacing models (although new simulations incorporating belt-like deformations in addition to equant ones may be necessary). Vigorous mantle convection will ensure that resurfacing patterns are both spatially and temporally variable since the time scale for reorganization of convective patterns is small compared to the crater retention age of 500 Ma.

Conclusion. Tectonic resurfacing of Venus is supported both by the distribution of impact craters with terrain type and by the statistical associations of crater preservation states. Widespread and pervasive tectonic deformation of Venus is a natural consequence of "standard" geophysical models of surface-interior interactions and is geologically straightforward.

References. [1]G. Schaber et al, *JGR. 97*, 13257 (1992). [2]R. Phillips et al., *JGR, 97*, 15923 (1992). [3]R. Herrick, Ph.D. Thesis, SMU (1993). [4]D. Bindschadler et al., *GRL, 17*, 171-174 (1990). [5]S. Solomon et al., *JGR 97*,13199 (1992).

Fig. 1. Cylindrical equal-area map of Venus showing areas above 2.5° RMS slope in gray, roughly corresponding to faulted regions of the planet. Undeformed areas in black; white areas not imaged. Impact crater locations shown as white dots. Tectonized regions comprise 60% of the planet yet contain only 40% of the craters, providing clear evidence for ongoing resurfacing.

VENUSIAN 'PANCAKE' DOMES: INSIGHTS FROM TERRESTRIAL VOLUMINOUS SILICIC LAVAS AND THERMAL MODELING. Curtis R. Manley, Dept. of Geology, Arizona State University, Tempe, AZ 85287-1404; agcrm@asuacad.bitnet.

The so-called 'pancake' domes, and several other volcanoes on Venus, appear to represent large extrusions of silicic lava. Similar voluminous rhyolite lava flows, often associated with mantle plumes, are known on Earth. Venus' high ambient temperature, and insulation by the dome's brecciated carapace, both act to prolong cooling of a dome's interior, allowing for episodic lava input over an extended period of time. Field relations and aspect ratios of terrestrial voluminous rhyolite lavas imply continuous, non-episodic growth, reflecting tapping of a large volume of dry, anatectic silicic magma. Petrogenetically, the venusian domes may be analogous to chains of small domes on Earth, which represent 'leakage' of evolved material from magma bodies fractionating from much more mafic liquids.

Physical volcanology: The volumes, high aspect ratios, and morphologies of certain lava flows on Venus, especially the pancake domes, imply that these are "unusually large" non-explosive eruptions of silicic magma [1-3]. Even on Earth, large volumes of silicic magma do not always erupt explosively, and rhyolite lava flows of great areal extent and large volume are increasingly being recognized. These units have silica contents ranging from 68 to 77 wt. %, long dimensions usually in excess of 10 km, and areas of generally up to 800 km^2 [4-11]. The volumes of these terrestrial lavas range up to about 200 km^3, while the largest Venus pancake domes are an order of magnitude larger [3] (see Fig. 1).

The beautiful circularity of the Venusian pancake domes contrasts with the shapes of large-volume silicic lavas on Earth. The terrestrial lavas are ovoid to irregular in plan shape [4,5,8,9], due in part to sloping topography, but also to the presence of near-vent tephra rings. Dome-forming rhyolitic eruptions on Earth characteristically begin with explosive activity that results in a ring of tephra concentric to the vent [12]. Such tephra deposits can be a serious impediment to the spreading of even large-volume units. The fissure-fed, 15 km^3 rhyolitic Badlands lava flow of SW Idaho, USA, divided into several separate flow lobes of various sizes as it pushed aside and flowed over and around its earlier-erupted tephra [9,10]. If explosions driven by moderate volatile content are suppressed by Venus' high atmospheric pressure [13], tephra rings may form only rarely, and the observed circular dome shapes may be a result of this.

The unnamed 175 by 250 km-wide complex of thick flow units between Artemis Chasma and Imdr Regio [2] is very similar in structure and appearance to the Juniper Mtn. Volcanic Center in SW Idaho, though the latter is smaller by half an order of magnitude. Shield-shaped Juniper Mtn. was originally interpreted as a construct of ignimbrite units [14,15], but further fieldwork has shown it to be a 20 by 30 km-wide stack of overlapping rhyolite lavas, presumably fed from a central vent, sitting atop a broad, 35 by 50 km-wide plateau of thicker lava units [16].

Thermal modeling: Many geologists familiar with small, thick silicic domes such as those of the Mono and Inyo Craters, E California, USA, assume that terrestrial rhyolite lava flows are constrained to be small because of the lava's high viscosity. While a high viscosity is certainly an impediment to flow movement, it must be evaluated in relation to the lava flow's heat budget [11]. Several factors combine to keep a large rhyolite lava hot and able to flow: 1) the pumiceous and brecciated top and base of the lava flow provide extremely efficient insulation; 2) the unit's thickness and release of latent heat helps keep its interior near the extrusion temperature for an extended period of time; and 3) the unit's substantial thickness at the vent provides a large horizontal force for sustaining flow advance.

While Venus' high atmospheric pressure will suppress vesiculation [13] and thus prevent formation of a thick pumiceous layer at the surface of a silicic lava flow, the lava's carapace will nonetheless be a jumble of welded and loose, boulder- to ash-sized debris [10,11] that will also insulate the flow. Under Venus' ambient surface conditions, cooling (from perhaps 950 °C) to solidus temperature (~700 °C) of the interior of an average pancake dome 600 m thick will require on the order of 1000 years [16]. During such a long period of potential activity, these domes could advance appreciable distances even if spreading was very slow, and they could be formed

VOLUMINOUS SILICIC LAVAS ON VENUS AND EARTH: C.R. Manley

by many episodes of endogenous growth -- even decades apart -- once a sufficient lava volume (probably as little as 2-5 km^3) had been extruded.

That individual pancake domes may have been emplaced by such episodic growth is implied by the positive correlation of their aspect ratios (height/diameter) and volumes [17]. This same relation is shown by the Mt. St. Helens dome, emplaced in 16 episodes over six years [18], and by episodically emplaced domes of polyethylene glycol wax extruded under cold water in the laboratory [17]. In contrast, populations of terrestrial large-volume silicic lavas show a negative correlation of aspect ratio and volume -- as lava flow volume increases, aspect ratios decrease (Fig. 1). Few voluminous terrestrial lavas are sufficiently exposed to be studied for evidence of episodic emplacement, but the Badlands lava flow is an exception [9,10]. In the well-exposed vent area of the Badlands flow, long, coherent flow foliations outline the vent and parallel the flow margins, implying that extrusion from the fissure vent was uninterrupted, not episodic [16].

Petrogenesis: Many voluminous rhyolite lavas on Earth are not associated with caldera structures, but seem to be the result of magmatic systems that differ from the crystal fractionation-dominated caldera-type systems to which most small-volume rhyolite domes and flows are related. In SW Idaho, silicic magma bodies were originally formed by melting of dry crustal rock over the Yellowstone Hotspot plume [4,15], but these silicic magmas evolved further by fractional crystallization processes, as indicated by chemical analyses of the lavas [16]. Preliminary melt inclusion data indicate that the SW Idaho lavas had pre-eruptive dissolved water contents of only about 3 wt. % [19], which may explain why they did not erupt as ignimbrites.

Available evidence indicates that terrestrial voluminous rhyolite lavas extruded in a continuous manner from large bodies of 'dry' rhyolitic magma. If the venusian pancake domes are indeed silicic and were formed by episodic growth, they may be the products of huge basaltic magmatic systems from which relatively small volumes of silicic differentiates could repeatedly 'leak out', as quickly as they were generated. At least in terms of magma genesis and eruption, then, the Venus domes might in fact be more analogous to terrestrial small-volume domes than to the voluminous rhyolite lavas that are most nearly their own size.

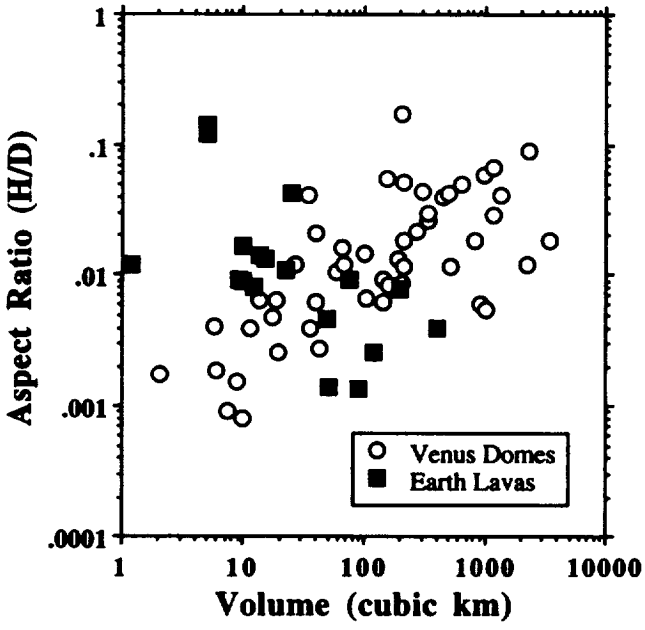

Figure 1. Aspect ratio (height/diameter) as a function of volume for Venus 'pancake' domes with the most accurate height determinations [1,3,17] and for some voluminous rhyolite lava flows on Earth [5-9,16,20]. For the terrestrial data, 'diameter' is that for a circle with an area equal to that of the lava flow.

References: [1] McKenzie D., Ford P.G., Liu F. and Pettengill G.H. (1992) *JGR*, **97**:15967-15976. [2] Moore H.J., Plaut J.J., Schenk P.M. and Head J.W. (1992) *JGR*, **97**:13479-13493. [3] Pavri B., Head J.W. III, Klose K.B. and Wilson L. (1992) *JGR*, **97**: 13445-13478. [4] Bonnichsen B. (1982) In: *Idaho Bur. Mines Geol. Bull.* **26**:283-320. [5] Bonnichsen B. and Kauffman D.F. (1987) In: *GSA Spec. Pap.* **212**:119-145. [6] Cas R. (1978) *GSA Bull.*, **89**:1708-1714. [7] Christiansen R.L. and Hildreth W. (1988) *GSA Abs. Prog., Rocky Mtn. Sec.* **20**:409. [8] Henry C.D. et al. (1988) *Geology*, **16**:509-512. [9] Manley C.R. (1990) *GSA Abs. Prog.*, **22**:A290 [10] Manley C.R. (1992) *Eos - Trans. AGU*, **73**:636. [11] Manley C.R. (1992) *JVGR*, **53** (in press). [12] Williams H. and McBirney A.R. (1979) *Volcanology*, Freeman, Cooper, San Francisco. [13] Head J.W. III and Wilson L. (1986) *JGR*, **91**:9407-9446. [14] Ekren E.B., McIntyre D.H., Bennett E.H. and Malde H.E. (1981) *USGS Map* **I-256**, scale 1:125,000. [15] Ekren E.B., McIntyre D.H. and Bennett E.H. (1984) *USGS Prof. Pap.* **1272**. [16] Manley C.R. - unpublished data. [17] Fink J.H., Bridges N.T. and Grimm R.E. (1993) *GRL* (in press). [18] Swanson D.A. and Holcomb R.T. (1990) In: *IAVCEI Proc. Volcan.*, **2**:1-24. [19] Manley C.R. and Hervig R.L. (1991) *Eos - Trans. AGU*, **72**:567. [20] Guest J.E. and Sanchez J. (1969) *BV*, **33**:778-790.

GEOPHYSICAL MODELS OF WESTERN APHRODITE-NIOBE REGION: VENUS, K.I. Marchenkov, Institute of Physics of the Earth, Moscow, Russia, R.S. Saunders, and W.B. Banerdt, Jet Propulsion Laboratory, Calif. Institute of Technology, Pasadena, CA 91109

In terms of its mechanical parameters (such as mass, mean radius, and mean density) Venus is very similar to the Earth. But the tectonic regimes of Venus and Earth are quite different. Unlike the Earth, where the effects of mantle convection are manifest on the surface in mid-oceanic ridges (spreading zones) and trenches (subduction zones), a global system of ridges rifts and subduction zones is not observed on Venus. There is no evidence of Earth-like plate tectonics and Venus may be a one-plate (or no-plate) planet. Magellan radar data confirm this point of view. One possible consequence of this conclusion is that Venus's convection is confined beneath a thick, buoyant lithosphere. In thermal models of Venus [1] a thick Venusian crust overlies a convecting mantle. The style of convection in Venus is an open issue (e.g. two layer or whole mantle convection. But two layer convection provides high temperature at the crust-mantle boundary. Additionally, the geochemical data show that the upper mantle of Venus is apparently depleted [1].

This could explain why convection is only partly revealed in the long-wave part of the gravitational field. It is reasonable to suppose that at least the long-wavelength part of gravitational field of Venus, for spherical harmonics greater than two (which correlate with corresponding harmonics of the relief), is due to crustal thickness variations [2] or possibly also to variations of crustal density (for example, hot mantle plumes, intruding into the base of the crust).

The new topography and gravitational field data for Venus expressed in spherical harmonics of degree and order up to 50 allow us to analyze the crust-mantle boundary relief and stress state of the Venusian lithosphere. In these models, we consider models in which convection is confined beneath a thick, bouyant lithosphere. We divide the convection regime into an upper mantle and lower mantle component. The lateral scales are smaller than on the Earth. In these models, relative to Earth, convection is reflected in higher order terms of the gravitational field. On Venus geoid height and topography are highly correlated, although the topography appears to be largely compensated. We hypothesize that Venus topography for those wavelengths that correlate well with the geoid is partly compensated at the crust-mantle boundary, while for the others compensation may be distributed over the whole mantle. In turn the strong sensitivity of the stresses to parameters of the models of the external layers of Venus together with geological mapping allow us to begin investigations of the tectonics and geodynamics of the planet. For stress calculations we use a new technique of space-and time-dependent Green's response functions using Venus models with rheologically stratified lithosphere and mantle and a ductile lower crust. In the basic model of Venus the mean crust is 50-70 km thick, the density contrast across the crust-mantle boundary is in the range from 0.3 to 0.4 g/cm-3. The thickness of a weak mantle zone may be from 350 to 1000 km. Strong sensitivity of calculated stress to various parameters of the layered model of Venus together with geological mapping and analysis of surface tectonic patterns allow us to investigate the tectonics and geodynamics of the planet. The results are presented in the form of maps of compression-extension and maximum shear stresses in the lithosphere and maps of crust-mantle boundary relief, which can be presented as a function of time.

The technique of using Green's response functions for the distribution of stresses and

deformation in one-plate planets with elastic mantles including a low viscosity zone was developed earlier [1,2]. In our present Venus model the rheology of the interior layers is more complicated but possibly more realistic. The main features of the rheology are: 1) In the mantle, dislocation climb is the dominant process, although diffusion creep is also included; 2) the rheology of the lithosphere includes a so-called unstable beta-creep and stable gamma-creep. The basic, parametrically simple model of Venus, is constructed using a new geochemical model of Dreibus and Wanke [3], the mean crustal thickness is varied from 50 to 70 km, and the density contrast across the crust-mantle boundary is in the range 0.3 to 0.6 g/cm-3.

It is instructive to calculate the time-history of stresses and deformation in the interior during the formation of major topographic features, Beta Regio, Ishtar Terra, Aphrodite Terra and others. First we model the rheology then find a corresponding transformation of our equations to Laplace transform space. Thus we will have in Laplace space the equivalent elastic problem, which can be solved. The next step is to find the inverse transformation of these solutions back to the time domain. This step is the most difficult. The rheology of the lithosphere and mantle is modeled by a generalized Bingham-Maxwell Body Law, including the brittle-elastic-ductile transition in the crust.

To perform the calculations we need to know the effective viscosity variations with depth and with time, as well as gravity and topography at high resolution.

With this approach it is possible to simultaneously satisfy the observed topography and gravity with spherical harmonic models using reasonable strength and viscosity parameters for the Venusian crust and mantle. We have modeled the region of Western Aphrodite and the Niobe plains to get reasonable depths of compensation. These results are based on Magellan topography and Pioneer Venus gravity fit to spherical harmonic models of order and degree 50. Continuing work uses the higher resolution Magellan data as they become available, both as local spherical harmonic models and the highest resolution line-of-sight gravity data. Crust mantle boundary relief is calculated for Western Aphrodite - Niobe relative to a mean crustal thickness of 50 km. The calculations include the consequences of simple crust models and more complicated models with a weak, ductile lower crust, a strong upper mantle and a weak lower mantle layer. We use a mean crustal thickness of 50 km, of which the upper 20 km is elastic. The mantle between 50 km and 200 km is strong, and the mantle at depths between 200 km and 481 km is weak and acts like an asthenosphere. The calculated crust-mantle boundary relief is similar for simple models and the more realistic layered models, but the stress distributions are markedly different. This can be explained by the role of lithospheric bending in the more complicated model.

References: [1] Solomotov and Zharkov, Icarus, 1990.; [2] Marchenkov,K.I. et al.: 1990. Earth, Moon, and Planets. V.50/51. P.81.; [3] Dreibus, G. and Wanke, H., Adv. Space Res. V. 10, No. 3-4, p (3) 7.

Acknowledgements: This work was performed, in part, at the Jet Propulsion Laboratory, California Institute of Technology, under contract with NASA.

CO_2-PRODUCTION BY IMPACT IN CARBONATES ?: AN ATEM- AND STABLE ISOTOPE (C,O) STUDY; I. Martinez, P. Agrinier, F. Guyot, Ph. Ildefonse, M. Javoy, U. Schärer, Univ. Paris 7, 2 place Jussieu, 75251 Paris cedex 05, France and U. Hornemann, A. Deutsch, Inst. für Planetologie, Univ. Münster, Wilh. Klemm Str. 10, D-4400 Münster, Germany.

Carbonates may have been a common target for large impacts on the Earth and possible related CO_2 outgassing would have important consequences for the composition of the atmosphere. To estimate volatile release during such impacts, isotopic ratios ($^{13}C/^{12}C$ and $^{18}O/^{16}O$) were determined on highly shocked carbonate samples in combination with SEM and analytical transmission electron microscopy (ATEM) investigations. The study was performed on both naturally and experimentally shocked rocks, i.e. 50-60 GPa shocked limestone-dolomite fragments from the Haughton impact crater (Canada), and carbonates shocked in shock recovery experiments such as described in [1]. For the experiments, unshocked carbonates consisting of mixture of dolomite and calcite from the Haughton area were used. Naturally shocked samples were collected in the polymict breccia [2] near the center of the Haughton crater (Anomaly Hill [3]).

Previous shock experiments [4,5] on limestones have suggested that for high pressures of about 60 GPa, roughly 70% of CO_2 should be volatilized. If CO_2 is released to such a large degree, strong isotopic effects should be registred, because CO_2 is enriched in ^{13}C and ^{18}O and consequently, residual carbonates are depleted in these isotopes if classical thermal decarbonation occurs [6]). In addition, this isotopic effect should be correlated with CaO,MgO enrichment in the residual solid. The theoretical Rayleigh model curve for such progressive loss of CO_2 is shown in Fig. 1. In our samples from Haughton, i.e. 30 highly shocked clasts (full squares in Fig. 1), carbonates represent between 0.5 to 10 wt% of the rock. As shown in Fig. 1, ^{13}C is enriched in most of the samples instead of being depleted as to expect from the classical decarbonation model. Values for $\delta^{13}C$ range up to +9‰, relative to about -3‰ in the unshocked references samples (open squares), and relative to values of about -1‰ measured in lacustrian sediments that formed in the crater-lake (open triangles). On the other hand, the very same carbonate fractions are systematically depleted in ^{18}O with $\delta^{18}O$ ranging between +14‰ and +22‰ (Fig. 1). In contrast to these naturally shocked samples, carbonates shocked experimentally to the same pressure conditions reveal largely unchanged isotopic composition ($\delta^{13}C$= -3‰, $\delta^{18}O$ = 25‰, Fig. 1 open circles) compared to the unshocked aliquots. Moreover, the experimentally shocked samples still consist exclusively of calcite and dolomite yielding the same relative volumes of CO_2-gas such as obtained from the unshocked equivalents.

Experimentally shocked samples. X-ray diffraction spectra on the 60 GPa shocked carbonates confirm that only calcite and dolomite are present after the experiment; not the slightest evidence for the existence of CaO or MgO is observed. X-ray diffraction lines of dolomite and calcite are broadened due either to large plastic deformation within the crystals, mosaic textures, or disordering of Mg and Ca in the lattice. SEM documents that after the shock, both calcite and dolomite crystals are highly fracturated relative to individual grains in the unshocked samples but again, no major chemical transformation was observed. Electron diffraction patterns (TEM) substantiate important crystallographic disorientations within single crystals of calcite and dolomite. These results are in good agreement with the stable isotope data from these samples (Fig. 1), which do not yield any evidences for decarbonation.

Naturally shocked samples. SEM studies reveal that carbonate crystals in the 50-60 GPa shocked fragments from Haughton occur essentially along cavity walls (bubbles, cracks). These 10-100 μm-size calcite and dolomite crystals lie adjacent to either a pure SiO_2 phase or a silica-rich phase containing minor amounts of Al, K, Mg, Na, and Ca. Another observation is that the carbonates have reacted with the SiO_2 phases producing domains that have the chemical composition of aegirine-augite (Ca-Mg pyroxene), larnite (Ca_2SiO_4), or domains with a Si-Al-Ca-Mg chemistry which does not correspond to any distinct mineral. In thin-sections, these domains are essentially isotropic, and no individual crystals can be distinguished. An ATEM

study was performed on these samples to obtain a better resolution for images (≈ 4Å) and information on the crystallographic state of the shock produced phases. It shows that carbonates are present either as very small crystals (< 400 nm large) or bigger crystals (> 500 nm) which contain planar defects essentially in dolomite. The ATEM also corroborates the existence of strong shock-metamorphic reactions between silicates and carbonates at high temperatures. Some glasses, in contact with small crystals of calcite, are characterized by a garnet-like chemical composition ($(Ca,Mg)_3Al_2Si_3O_{12}$) representing pyrope-grossular glass. Other types of glass show a Ca-Mg pyroxenitic composition or SiO_2 composition with minor amounts of Mg, Al, and K. In association with calcite and dolomite in the highly shocked Haughton samples, other types of 2000 nm large crystals are produced by these reactions: β-Ca_2SiO_4 (larnite), typical for temperature above 700°C and generally sensitive to alteration, and unreverted pigeonite (Ca-poor monoclinic pyroxene). Such pigeonite is generally reverted to an orthorombic pyroxene by cooling below 1000° C and therefore, the unreverted form is typical for fast cooling conditions. This observation, together with the presence of larnite and glass, are strong evidences in favour of very rapid quenching after the shock.

From our observations, it appears that the classical decarbonation reaction ($CaMg(CO_3)_2 \rightarrow CaO + MgO + 2CO_2$) does not occur on a large scale either in the naturally or experimentally, 50-60 GPa shocked carbonates. Concerning the experiments, holes of different configurations were drilled in the ARMCO-steel container in order to facilitate CO_2 escape through the container however, even these experiments did not yield any evidence for decarbonation reactions either on calcite or dolomite. The absence of this reaction was already suspected by field and petrographic observations in the Haughton crater, where no highly shocked carbonates or CaO-MgO reaction products could be identified. Moreover, the occurence of this type of fragment is limited to the center of the crater, representing a very minor part of the shocked rocks. The ^{13}C and ^{18}O effects observed here are probably related to post-shock temperatures. In consequence, the ^{13}C systematics of these samples can be interpreted as the back-reaction with CaO, MgO or calcium silicates of small amounts of ^{13}C enriched CO_2 previously produced by partial, and very limited decarbonation. On the other hand, the ^{18}O depletion in these carbonates can be ascribed to the observed reactions with liquid SiO_2 phases ($\delta^{18}O \approx +10‰$) which penetrate these fragments (see above).

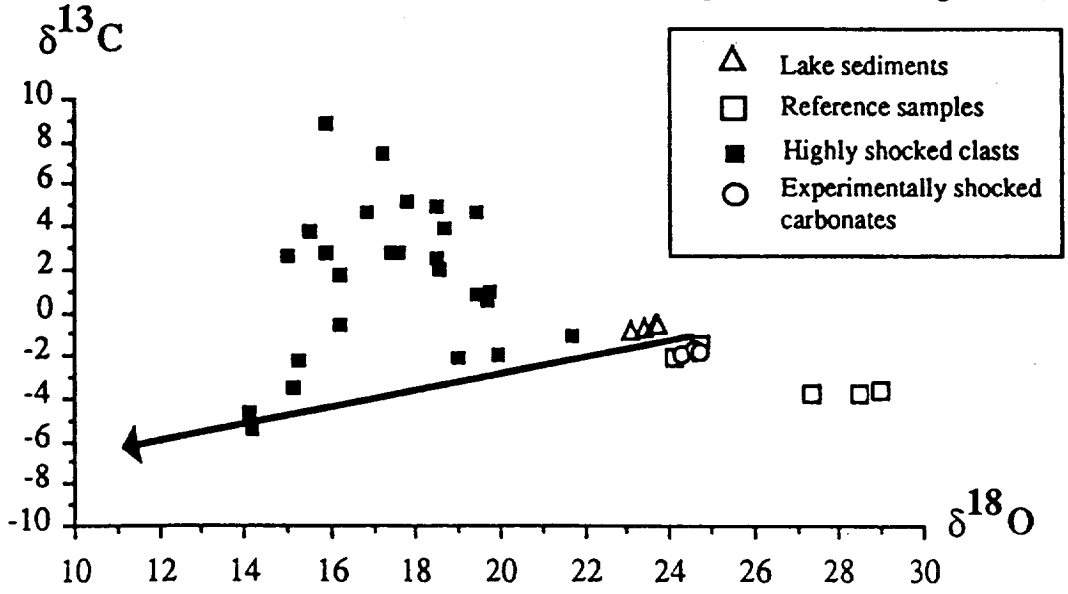

Fig 1: δ13C vs δ18O. The line represents a degassing of CO2 according the Rayleigh law, with α carbon=1.0022 and α oxygen= 1.0060

[1] Redeker H.J. and Stöffler D. (1988) *Meteoritics* 23,185. [2] Müller W.F. and Hornemann U. (1969) *Earth Planet. Sci. Lett.*, 7, 251. [3] Pohl J. et al. (1988) *Meteoritics* 23,185. [4] Lange M.A. and Ahrens T.J. (1986) *Earth Planet. Sci. Lett.*, 77, 409. [5] Tyburczy J.A. and Ahrens T.J. (1986) *JGR*, 91, 4730. [6] Valley J.W. (1986) Rev. in mineralogy, 16, 445.

DUST GRAIN RESONANT CAPTURE: A STATISTICAL STUDY

F. Marzari, V. Vanzani, Dipartimento di Fisica "Galileo Galilei", Università, 35131 Padova, Italy
S.J. Weidenschilling, Planetary Scienze Institute,Tucson, AZ 85719

A statistical approach, based on a large number of simultaneous numerical integrations, is adopted to study the capture in external mean motion resonances with the Earth of micron size dust grains perturbed by solar radiation and wind forces. We explore the dependence of the resonant capture phenomenon on the initial eccentricity e_0 and perihelion argument ω_0 of the dust particle orbit. The intensity of both the resonant and dissipative (Poynting–Robertson and wind drag) perturbations strongly depends on the eccentricity of the particle [1] while the perihelion argument determines, for low inclination, the mutual geometrical configuration of the particle's orbit with respect to the Earth's orbit. We present results for three j:j+1 commensurabilities (2:3, 4:5 and 6:7) and also for particle sizes s=15, 30 μm. This study extends our previous work on the long term orbital evolution of single dust particles trapped into resonances with the Earth [2].

The orbits of about 1000 dust particles are simultaneously integrated with the Everhart method [3] taking into account the gravitational attraction of the five major influencing planets, Venus, Earth, Mars, Jupiter and Saturn (a seven–body problem). The initial positions of the planets are derived from the ephemerides JPL DE200 at the epoch 1993.0. The orbital evolution of all the dust particles initiates at the same semimajor axis a_0, whose value has been chosen close to the resonant value a_R appropriately modified by radiation pressure ($\beta = 0.122/s$, s in μm [4]).

In Fig. 1 we show the trapping regions for the 2:3 resonance (a_R=1.3086 AU) in the (e_0, $\omega_0 - \omega_{0E}$) plane, with ω_{0E} perihelion argument of the Earth's orbit at 1993.0. The initial inclinations of the dust particles, referred to the ecliptic plane, are set to 10°, the longitudes of node to 0° and the mean anomalies to 90°. The filled circles represent particles trapped into resonance while the dots represent particles passing through the resonance without being trapped. We have verified, using a finer sampling interval both in e_0 and ω_0, that these regions are stable against small variations in the two orbital parameters. The maximum probability of capture occurs for eccentricities close to $e_0 \simeq 0.23$ for which the dust grain's and planet's orbits become crossing. This correlation between the location of trapping regions and the particle's eccentricity at almost tangent orbits is confirmed for the 4:5 and 6:7 commensurabilities (see Figs. 2 and 3, respectively). The trapping regions for the latter resonances are shifted downward with respect to Fig. 1 and are centered around the values $e_0 \simeq 0.13$ and $e_0 \simeq 0.95$, respectively, for which the Earth's and particle's orbit begin to cross. As a consequence low eccentricity dust particles are captured more frequently in high–j resonances.

Results for a 15 μm dust–particle size at the 4:5 commensurability are shown in Fig. 4. In this case the capture occurs only in small isolated regions. The marked

difference with respect to the cases of Figs. 1–3, can be regarded as a consequence of the increased decay rate for smaller particles.

REFERENCES: [1] Sicardy B., Beaugè C., Ferraz–Mello S., Lazzaro D., Roques F., *Cel. Mech.*, in press; [2] Marzari F., Weidenschilling S.J., Fabris M. , Vanzani V. (1991) *LPSC XXII*, 861; [3] E. Everhart, in *Dynamics of Comets: Their Origin and Evolution* (Reidel, Dordrecth, 1985), p. 185; [4] See: Mukai T., Schwehm G. (1982), *Astron. Astroph. 107*, 97;

Figs. 1–3. Trapping regions in the (e_0, $\omega_0 - \omega_{0E}$) plane for the 2:3, 4:5 and 6:7 resonances, respectively, for a 30 μm particle size. **Fig. 4**. For a particle size reduced to 15 μm trapping occurs only in small isolated regions (4:5 resonance).

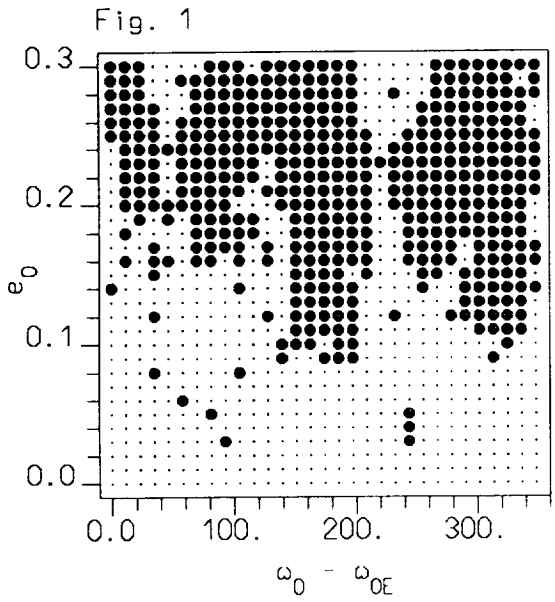

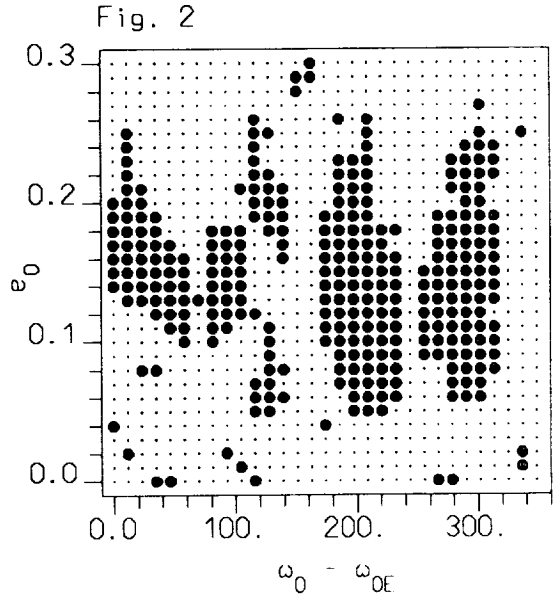

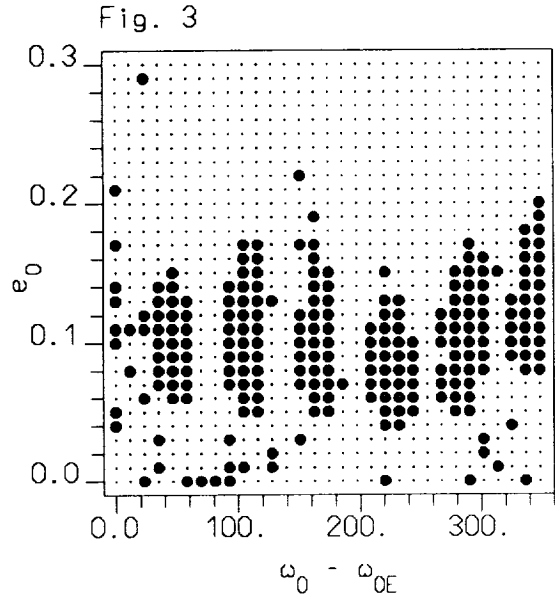

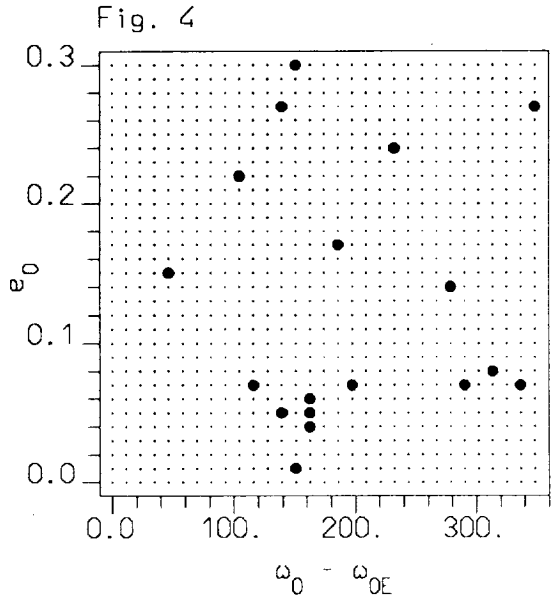

EFFECTS OF BULK COMPOSITION ON PRODUCTION RATES OF COSMOGENIC NUCLIDES IN METEORITES*; Jozef Masarik and Robert C. Reedy, Space Science and Technology Division, Mail Stop D436, Los Alamos National Laboratory, Los Alamos, NM 87545.

The bulk chemical composition of meteorites has been suggested as a main factor influencing the production of cosmogenic nuclides. Numerical simulations with Los Alamos Monte Carlo production and transport codes were done for $^{21}Ne/^{22}Ne$ ratios and ^{38}Ar production rates in meteorites with a wide range of compositions. The calculations show that an enhanced flux of low-energy secondary particles in metal-rich phases is the essential key for the explanation of experimentally observed differences in nuclide production processes in various meteorite classes.

Nuclides produced by the interaction of cosmic-ray particles with meteorites provide valuable information about both the meteorite and the cosmic rays. The accurate modeling of the production processes is necessary for the interpretation of measured concentrations. The bulk composition is one of the factors that influences final production rates by its effects on the shape of differential fluxes of primary and secondary nucleons and their total fluxes. These particle fluxes strongly depend on the multiplicities for production of secondary particles, which are functions of mass number. The transport phenomena are also dependent on the bulk composition. In stony meteorites, the average atomic and mass numbers vary by less than 15%. A substantial difference in inter- and intranuclear cascade development is expected for iron meteorites. The ranges of production rates for neon and argon isotopes in stones, stony-irons, and irons discussed in [1] were attributed to an enhanced flux of low-energy secondary particles, especially neutrons, in metal-rich phases. The bulk-composition problem was also discussed in [2,3]. However, the influence of a meteorite's matrix on the production of nuclides, especially by neutrons, needed more calculations. Our previous results [4] showed the influence of bulk composition on both secondary-particle production and particle transport, with there being higher fluxes of neutrons in irons than in stones.

In this paper, we present the results of the simulations of production rates of cosmogenic nuclides in meteorites with various bulk compositions. Our calculations are based on the Los Alamos LAHET Code System [5], which is a system of coupled Monte Carlo computer codes that treats the relevant physical processes of particle production and transport. A homogenous and isotropic GCR irradiation, corresponding to an averaged GCR primary cosmic-ray spectrum, of spheres with chemical compositions equivalent to average compositions for chondrites, mesosiderites, eucrites, and pallasites was calculated. Particle fluxes for the individual meteorites within a classes are very similar to that for a class average [4]. To avoid effects due to size, the spheres had the same radii of R = 106.5 g/cm^2 (corresponding to R = 30 cm for L-chondrites). Production rate P of cosmogenic nuclide j at depth d in an irradiated meteorite with a radius R was calculated with

$$P_j(R,d) = \sum_i N_i \sum_k \int_0^\infty \sigma_{jik}(E_k)\, J_k(E_k,R,d)\, dE_k$$

where N_i is the number of atoms for target element i per kg of sample, σ_{jik} is the cross section for the production of nuclide j from target element i by particle k, and J_k is flux of primary and secondary particles of type k with energy E_k. For particles, only protons and neutrons are important. Production rates were calculated for concentric shells with thickness 8.875 g/cm^2. Statistical errors for the calculated particle fluxes were less than 5%. The reported composition of each individual meteorite was used in getting production rates. In some cases, these rates were averaged over the whole volume of meteorite for comparison with experimental measurements.

Our simulations confirm the importance of bulk composition on nucleon fluxes inside the meteorite and consequently on production rates of cosmogenic nuclides. Fig. 1 shows experimental [1] and our calculated ratios of the production rates for ^{38}Ar from Ca to that from FeNi. These ratios strongly depend on the FeNi content of the matrix in which the production takes place. The ratio for L-chondrites with 23 % FeNi is about a factor of two lower than for mesosiderites with ~60 % FeNi. This difference can be explained by the influence of bulk composition on production and transport of nucleons that induce nuclear reactions producing ^{38}Ar. The higher yield for the production of secondary, mainly low-energy, particles from heavy elements like Fe and Ni than from light elements like O, Mg, and Si is the main source of the calculated differences. These production differences are further increased with the transport of the produced particles, especially at lower energies. Both production and transport processes cause a higher flux of low-energy secondary particles in materials composed mainly of elements with higher atomic number, like Fe and Ni [4], accounting for the observed differences in the ratio of ^{38}Ar from Ca to that from Fe.

BULK COMPOSITION EFFECTS Masarik J. and Reedy R.C.

A similar effect is observed for the cosmogenic $^{21}Ne/^{22}Ne$ ratio plotted on Fig. 2 as a function of the sample's $Mg/(Mg+Al+Si)$ ratio, the same format used by [1]. In all meteorite classes, the $^{21}Ne/^{22}Ne$ ratio increases with decreasing $Mg/(Mg+Al+Si)$. The $^{21}Ne/^{22}Ne$ ratio for stony-irons is significantly lower than the lower limit found for L-chondrites and eucrites. The $^{21}Ne/^{22}Ne$ ratio is thus sensitive to the bulk composition of the matrix in which the irradiation took place.

From these two sets of trends, we conclude that bulk composition can strongly affect the production rates of nuclides in meteorites. The production of cosmogenic nuclides can also be influenced by size, shape, and probably other effects that can complicate the unfolding of bulk-composition effects in real samples. However, in the two cases presented in [1] and here, the influence of bulk composition on particle fluxes, especially neutrons, is the dominant effect. Absolute production rates vary with the reactions involved. For example, in meteorites of the same mass, ^{53}Mn is ~20% higher in iron meteorites than in CI-chondrites.

References: [1] Begemann F. and Schultz L. (1988) *LPS XIX*, p. 51. [2] Englert P.A.J., Reedy R.C., and Michel R. (1990) *LPI Tech. Rpt. 90-05*, p. 11. [3] Michel R., Dragovitsch P. and Filges D. (1990) *Meteoritics*, **25**, 386. [4] Masarik J. and Reedy R.C. (1992) *Meteoritics*, **27**, 256. [5] Prael R.E. and Lichtenstein H. (1989) *Los Alamos Report LA-UR-89-3014*. * Work supported by NASA and done under the auspices of the US DOE.

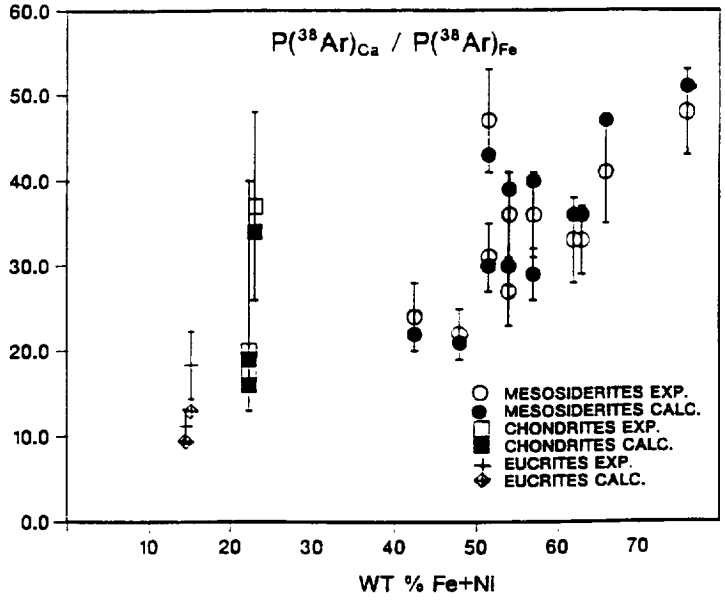

Fig. 1. Measured (with errors) [1] and calculated ratios for the production of cosmogenic ^{38}Ar from Ca to that from metal samples are plotted as a function of the Fe and Ni content of the bulk meteorite. There are some variations due to the composition of each meteorite, but the trend is for this ratio to increase with increasing metal content.

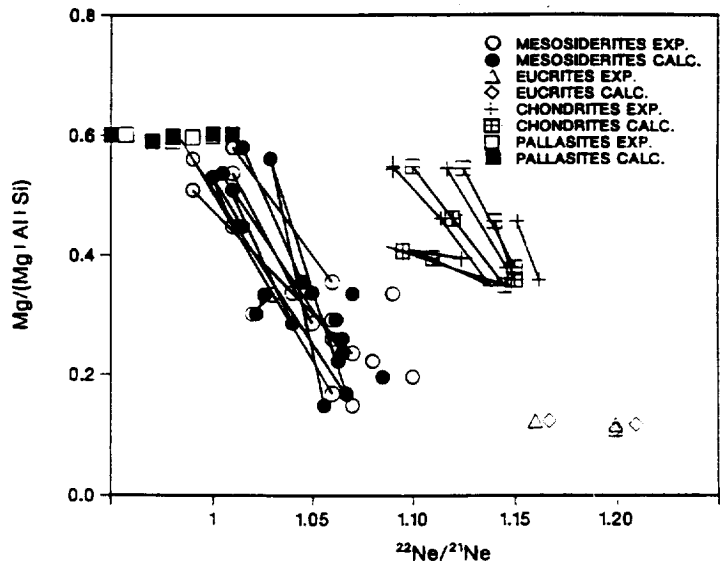

Fig. 2. Measured [1] and calculated $^{22}Ne/^{21}Ne$ ratios are plotted as a function of the fraction Mg for the major elements making cosmogenic neon. The stony-iron meteorites have ratios lower than those for stony meteorites because of more low-energy neutrons in their metal.

A DECADE'S OVERVIEW OF IO'S VOLCANIC ACTIVITY D. L. Matson, G. J. Veeder, T. V. Johnson, D. L. Blaney, and J. D. Goguen, Jet Propulsion Laboratory, California Institute of Technology, Pasadena, CA 91109.

Over the past decade some aspects of Io's volcanic activity have changed greatly, while others have essentially remained constant. This contrast has emerged from our study of multi-wavelength, infrared, observations of Io's thermal emission. From 1983 to 1992 we observed the disk integrated flux density of Io from the NASA Infrared Telescope Facility (IRTF) on Mauna Kea, Hawaii. Our spectral coverage allows us to separate out the emission components due to volcanic thermal anomalies which are warmer than the background emission caused by solar heating. Our temporal coverage allows us to resolve individual eruptions and also to obtain the disk-integrated flux density as a function of longitude (or, equivalently, orbital phase angle). [1]. Characteristics that persisted over the decade involve (1) Loki's location and intensity of emission , (2) the leading hemisphere emission, and (3) the average heat flow. The variable aspects of Io over the decade include (1) Loki's hotter area(s), and (2) the outbursts in the leading hemisphere.

Persistent Characteristics: (1) the location of Loki and its status as the brightest thermal anomaly, (2) the level of activity in the leading hemisphere, and (3) the average heat flow. Loki has consistently been the major thermal anomaly on Io. This is evident in our longitude data, a sample of which is plotted in the Fig. 1. While our data set does not yield latitude, this emission peak has always been found to be associated with Loki whenever its position has been observed by other techniques (e. g., polarimetry [2], occultation photometry [3], infrared imagery from the IRTF [4], and, of course, Voyager [5]).

The leading hemisphere (0-180°W) has consistently shown an excess of thermal emission above that due purely to the absorption of sunlight, although its emission is generally less than that of the trailing hemisphere (180-360°W). On the leading hemisphere there is no source equivalent to Loki and there is no apparent longitudinal concentration of thermal anomalies.

The average heat flow from volcanic regions during the decade is relatively constant, at about 9×10^{13} W (~2 W m^{-2} averaged over Io's surface). This value is a preliminary estimate based upon an assumed distribution of thermal anomalies [6] and a "quick-look" subset of the data. The heat flow value will be refined as we carry out the detailed analysis of the whole data set. The lack of error bars is intentional. While the yearly scatter is typically less than about thirty percent, systematic errors (such as possible unrecognized small thermal anomalies and uncertainties in the latitudinal distribution of sources) will dominate in our assessment of the accuracy of the heat flow determination.

Variable Characteristics: (1) Loki's hotter area(s), and (2) the outbursts in the leading hemisphere. The general level of flux from Loki changes, typically on time scales of months to years. Loki can be modeled using two anomalies with the smaller at a much higher temperature than the other. Variations in the temperature and areal exposure of the higher temperature anomaly are sufficient to explain the bulk of the observed variation, which is more pronounced at the shorter wavelengths. A major "outburst" (significant increase in 4.8 μm flux density over a short time), requiring a temperature in excess of 1,000 K, is shown in Fig. 1. More typically model temperatures in the range of 400 to 700 K can explain the observed flux densities.

The leading hemisphere also has shown changes in general emission level from apparition to apparition. This activity appears to be distributed in longitude and cannot be identified with a single source analogous to Loki. A number of spectacular outbursts have occurred on the leading hemisphere. As with the event in Fig. 1, they tend to be sufficiently hot to require the presence of silicate lava [7]. In the available data for well characterized outbursts (i.e., both temperature and size are known) from our program and other observations (i.e., see tabulation by [8]), there is an indication that longitudes of 70-80° W are preferred. Outbursts are apparently short-lived, lasting hours to days and are interpreted as local eruptive activity. Their sizes, typically in the 5 to 20 km range, are small compared to Io and to the sizes of the other geologic structures on the surface of Io. In our data set, outbursts occurred on ~5 percent of the nights we observed. Outbursts occur infrequently and they contribute only a little to Io's global heat flow due to their small size.

REFERENCES: [1] Johnson, T. V., *et al.* (1984) *Science 226*, 134. [2] Sinton, W. M., *et al.* (1988) *Astron. J. 96*, 1095. [3] Goguen, J. D., *et al.* (1988) *Icarus 76*, 465. [4] Spencer, J. R., *et al.* (1990) *Nature 348*, 618. [5] Pearl, J., and W. M. Sinton (1982) in *Satellites of Jupiter*, D. Morrison, ed., U. of AZ Press, 724. [6] McEwen, A. S., *et al.* (1985) *J. Geophys. Res. 90*, 12345. [7] Johnson, T. V., *et al.* (1988) *Science 242*, 1280. [8] McEwen, A. S., *et al.* (1989) in *Time-Variable Phenomena in the Jovian System*, NASA SP-494, 11-46. This work was carried out under contract to NASA. The authors are visiting astronomers at the IRTF which is operated for NASA by the University of Hawaii.

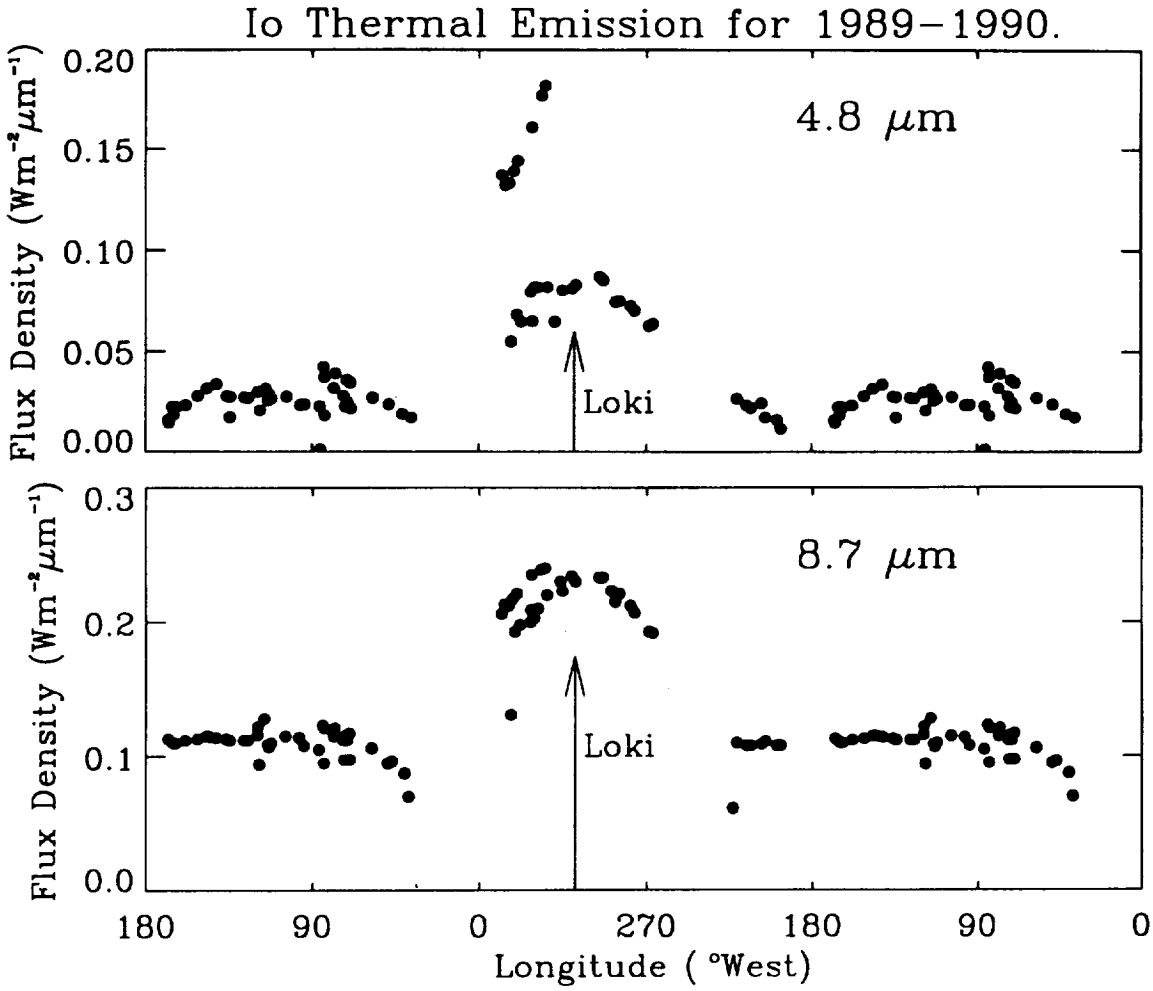

Fig. 1. Io's flux density (W m^{-2} μm^{-1}) versus West Longitude for infrared emission at 4.8 μm (with reflected sunlight subtracted) and 8.7 μm. The longitude scale spans 1.5 revolutions. Thus the observations between 0 and 180° are plotted twice. The longitude of Loki (309° W) is marked near the center of each panel. Hot-spot emission from this feature produces a characteristic peak in the lightcurves for each wavelength as it rotates across the central meridian of Io as viewed from the Earth. Such hot spots contribute their highest flux density near 8.7 μm and also produce most of the total power. During January 9, 1990 (UT) there was increased emission from an outburst while Io was near an orbital phase angle of 330°. Such outbursts briefly dominate the flux at wavelengths as short as 4.8 μm. The non-Loki hemisphere of Io remained quiescent during the intervals of our observations for the 1989/1990 apparition.

A Mission Concept of Phobos/Deimos Exploration

K. Matsushima[1], J. Saito[1], M. Utashima[2] and H. Koshiishi[3]
1: Control Systems Division, National Aerospace Laboratory. Chofu, Tokyo 182, JAPAN
2: Earth Observation Center, National Space Development Agency of Japan. Hatoyama, Saitama, JAPAN
3: Remote Sensing Technology Center of Japan. Roppongi, Tokyo 106, JAPAN

We have been designing the concept of Phobos/Deimos mission using the Japanese H-II rocket as a first step in asteroid exploration. In planning the mission concept, we focused on development of methods to characterize the materials of Phobos/Deimos. The development of such methods will contribute to both scientific and resource explorations of asteroids. Here we report the preliminary concept of the mission.

Introduction

The exploration of space resources will be a part of space developments in the 21st century. Among the extraterrestrial bodies in the solar system, minor bodies, especially asteroids, are very attractive targets not only because of their scientific value, but also because they are promising extraterrestrial resources for future utilization. In considering the exploration of these bodies, the minute characterization of their component materials is the most important instrumental problem.

Phobos and Deimos are selected as the first targets of our exploration strategy of minor bodies. This choice stems from the following four reasons : (1) they are easily accessible compared with other minor bodies; (2) we can use them to study and develop methods to characterize materials of other minor bodies, including approaching and landing (docking) technologies; (3) fairly good information on these bodies, necessary for mission design, has been obtained by previous missions; (4) it is a suitable mission for H-II launching Vehicle, being developed now in Japan. Here we report the preliminary mission concept for Phobos and Deimos exploration.

Mission Outline

The launching windows to Mars and the payloads using H-II launching vehicle are shown in Table 1. The outline of the mission is shown as a schematic sketch in Fig. 1. The mission consists of several exploration phases shown below:

1. Observation of Deimos

After insertion into the capture orbit of Mars, the orbit of the spacecraft is changed to one crossing Deimos' orbit (Fig. 1: a). In this phase, the image data of the whole surface of Deimos are obtained using a CCD camera, and UV-Visible and/or Visible-NIR spectrometer. The imaging spectrometer, using area solid state sensor, is now being developed. Chemical analysis employing X-ray fluorescence (XRF) and γ-ray spectrometry is also performed.

2. Rendezvous with Phobos

The orbit of the spacecraft is again transferred to the rendezvous orbit, which has slightly different a, e, and i from those of Phobos (Fig. 1: b). We have calculated an appropriate rendezvous orbit for global survey of Phobos. The mean distance for

observation is about 50km and the same instruments as those for Deimos are used. In addition, determination of the depth of regolith layer (probably, using underground radar) will be performed to obtain the information for selection of Landing (docking) site(s) on the surface.

3. Hovering and Landing (Docking) on Phobos

In order to obtain more information of selected docking site(s), the observation distance is decreased to about a few hundreds to tens of meters (Fig. 1: c). After that, the spacecraft contacts with the surface, and in-situ experiments to characterize materials are performed (Fig. 1: d).

Since the data derived by remote sensing techniques such as imager, XRF, and reflectance spectroscopy provide information only about surface, we must obtain data under the surface by sampling underground materials, and characterize them using the techniques of material sciences such as mass spectrometry and powder X-ray diffractometry.

One of the serious problems during sampling is to anchor the spacecraft to a surface with a thick regolith layer under microgravity. Solving this problem will be essential in asteroid missions, and its research development is now taking place.

4. Sample return

The possibility of sample return from Phobos, which is our long-cherished desire, has also been examined, but at present, we have to take a pessimistic view of it's materialization, judging from the ability of the booster.

Future Direction of Mission Design

Although the mission design has not been fully established yet, the effort for design of scientific instruments, spacecraft systems and operation systems is going to be made in parallel. The simulational study of the observation of asteroidal materials using meteorites is also planned.

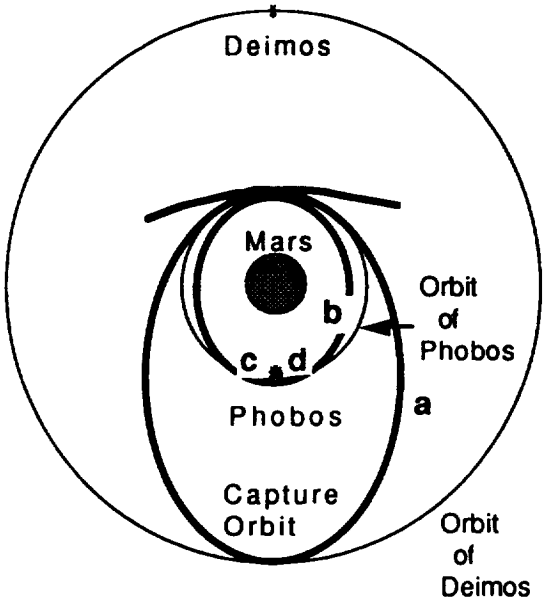

Fig. 1

Launch Date	Injectable payload into transfer orbit	Injectable payload into Mars capture
01-Mar-08	2168	1084
03-June-23	2925	1100
05-Aug-14	2835	1439
07-Sep-18	2855	1409
09-Oct-17	2922	1187
		(kg)

Table 1. Injectable Payload by H-II booster

SIZE DISTRIBUTION OF INTERPLANETARY IRON AND STONY PARTICLES RELATED WITH DEEP-SEA SPHERULES

H. Matsuzaki and K. Yamakoshi
Institute for Cosmic Ray Research, University of Tokyo, Tanashi, Tokyo 188, Japan

To study origin and evolution of the interplanetary dust, it is very important to investigate the size distribution. Here the changes of the size distribution of meteoroid particles due to the ablative effects during atmospheric entry were investigated by numerical computer simulation. Using the results, the pre-atmospheric size distribution of the interplanetary dust particles could be estimated from that of ablated spherules taken from deep-sea sediments. We are now analyzing deep-sea spherules from some aspects and examining if we could get any information about the interplanetary dust.

Fundamental equations of the numerical simulation are followed[1];

$$(1)\ d\mathbf{p}/dt = Md\mathbf{v}/dt = -\rho_{atm} v A \mathbf{v} + M\mathbf{g}, \qquad (2)\ 1/2\,\rho_{atm} A v^3 = \pi s^2 \varepsilon \sigma T^4 - L dM/dt,$$

$$(3)\ A = 1/4\,\pi s^2, \qquad (4)\ M = 1/6\,\pi \rho s^3, \qquad (5)\ -dM/dt = \pi s^2 p_e (\mu m_H / 2\pi k T)^{1/2}.$$

($\mathbf{p}$, M, $\mathbf{v}$, s, ρ: momentum, mass, velocity, diameter, density of the meteoroid particle; ρ_{atm}: atmospheric density; $\mathbf{g}$: gravitational acceleration; ε: emissivity(=1.0); σ: Stephen-Boltzmann constant; L, p_e, μ: latent heat of vaporization, vapor pressure, molecular weight of the meteoroid material; m_H: mass of the hydrogen atom; k: Boltzmann constant)

(1) is the equation of motion, in which the momentum change of the meteoroid particle going through the atmosphere is equal to sum of the momenta of colliding air molecules and gravitational effect. Here, we can set $d\mathbf{p}=Md\mathbf{v}$ if evaporating mass is to dissipate in 4π direction. (2) represents energy balance. Kinetic energy transported to the meteoroid particle by colliding air molecules is to be dissipated through radiation and ablative mass loss. We set (3) and (4) so that the meteoroid particle is spherical. Mass loss rate is determined by (5). p_e is a function of temperature of the meteoroid, T, such that; $p_e(T) = 10^{c1+c2/T}$ (in MKS units). So, in practice, we solve (2) as the equation of T. The value of ρ_{atm} at each altitude is taken from U. S. Standard Atmosphere of 1976. In this study, two kinds of meteoroid particles, iron and stony, were taken. Physical properties of the materials used in this calculation are presented in Table 1[2,3]. The calculation starts at the meteoroid altitude 190km at t=0, then equations (1) to (5) are solved at every 0.02 seconds. The calculation is terminated if the altitude is over 250km or below 50km, or the velocity becomes less than 1km/s.

Parameters in this calculation are the initial size of the meteoroid particle, s_0, atmospheric entry angle, θ (in the case of perpendicular input, θ=90°), and initial velocity, v_0. 7920 atmospheric entry events with various (s_0,θ,v_0) value combinations ranged 10μm < s_0 < 1000μm, 0° < θ < 90°, and 11.2km/s < v_0 < 20.2km/s were calculated. To these 7920 events, pre-atmospheric (initial) size distribution; $dn \propto s_0^{-A} ds_0$, entry angle distribution; $dn \propto -d(\cos 2\theta)$[1], and initial velocity distribution; $dn \propto v_0^{-5.4} dv_0$[4], were taken into account, where dn represents the number of particles (or probability) having initial size between s_0 and s_0+ds_0, entry angle between θ and $\theta+d\theta$, and initial velocity between v_0 and v_0+dv_0, respectively. Index value A in the initial size distribution, we call "the initial index A" here after, was varied from 2 to 7. To each initial index A, the final size distribution was counted out in accordance with these three distributions. For example, the final size distribution was found to be shown as Fig. 1 in the case of iron material and the initial index A=4.5. (In this diagram, relative population before atmospheric entry is to be unity with parameter s_0 between 45μm and 55μm, and parameter v_0 between 13.7km/s and 14.7km/s.) In Fig. 1 we can see that the final size distribution is also expressed nearly as; $dn \propto s^{-B} ds$, and the final index B is found to be 5.9 in this case. Fig. 2 was obtained by calculations in cases of various initial indices A and counting out the correspoding final indices B. The relation between the initial index A and the final index B was found to be formally as; B = 1.20A + 0.40 (Iron). Similarly, about stony material particles, the relation was such that; B = 1.45A - 0.25 (Stony).

Using these relations, we can estimate the pre-atmospheric size distributions of iron and stony meteoroid particles inversely by measuring that of ablated iron and stony spherules taken from deep-sea sediments. Both

SIZE DISTRIBUTION OF INTERPLANETARY IRON AND STONY PARTICLES

H. Matsuzaki and K. Yamakoshi

iron and stony spherules were picked up from the same fraction of sediments which had been taken as a dredged sample : GH79-1, St.1476 (9°49.96'N, 167°17.68'W, 5151m-depth). In this work, iron spherules in size larger than 80μm were counted, whereas many smaller ones exsisted. Stony spherules smaller than 100μm were rarely found, so the almose of all stony spherules could be thought to be picked up from the fraction. The results were showed in Fig. 3 in cumulative numbers with some other studies'[5,6,7]. Iron spherules are found to have the gradient -1.9~-2.5 in Fig. 3, that is, the final index B = 2.9~3.5 (Iron). Using the relation obtined before, we get the initial index A = 2.1~2.6 (Iron). Similarly, in the case of stony spherules, the final index is; B = 4.8~5.0 (Stony), and then the initial index is; A = 3.5~3.6 (Stony).

Dohnanyi (1972)[8] gave the size distribution of the interplanetary meteoroid particles as; $dn \propto s^{-4.5}ds$ (s~100μm). More recently, we can get from the data compilation of Grün et al. (1985)[9]; $dn \propto s^{-4.0\sim-4.6}ds$ (s~100 μm). These size distributions are consistent with that estimated from the stony spherules. However, the iron spherules themselves have smaller index of size distribution (2.9~3.5) so that estimated index of pre-atmospheric size distribution (2.1~2.6) is much smaller than that of the interplanetary meteoroid particles (4.0~4.6). As a consequence, it is suggested that the major components of the interplanetary meteoroid particles are stony particles, and that, in the interplanetary space, iron particles have different size distribution from stony ones in the size range around 100μm.

(References) [1] Love, J. J. and Brownlee, D. E. (1991) Icarus, 89, 26-43; [2] Bronshten, A. E. (1983) "Physics of meteoric phenomena", Geophys. Astrophys. Monographs, D. Reidel; [3] Kornblum, J. J. (1969) JGR,74(8), 1893-1907; [4] Fraundorf, P. (1980) Geophys. Res. Let., 10, 765-768; [5] Brownlow, A. E. et al. (1966) Geophys. J. R. Astro. Soc., 12, 1-12; [6] Murrell, M. T. et al. (1980) GCA, 44, 2067-74; [7] Yamakoshi, K. et al. (1981) JGR, 86(B4), 3129-32; [8] Dohnanyi, J. S. (1972) Icarus, 17, 1-48; [9] Grün, E. et al. (1985) Icarus, 62, 244-272

Table 1. Physical properties used in the calculation

	Iron	Stony
Material Density ρ (g/cm^3)	8.0	3.0
c_1	9.607	9.6
c_2	-16120	-13500
Latent heat of vaporization L (J/kg)	6.4×10^6	6.05×10^6
Molecular weight μ	56	45

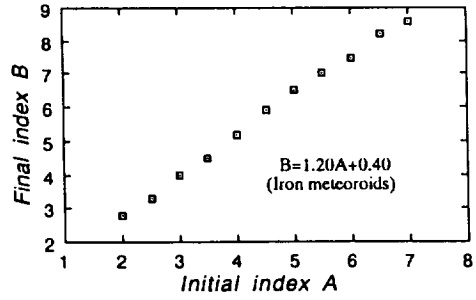

Figure 2. Relation between the initial index A and the final index B

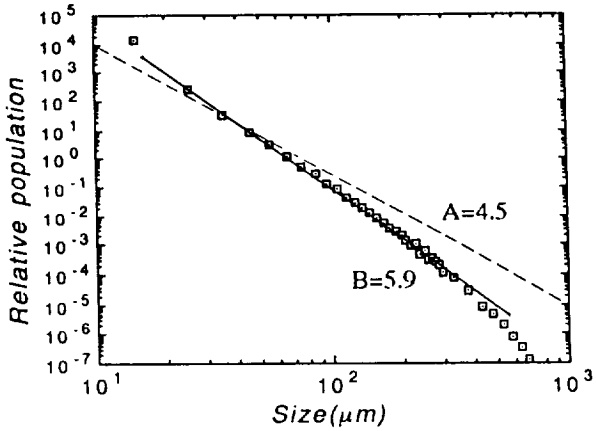

Figure 1. The final size distribution of iron meteoroid particles in the case of the initial index A = 4.5

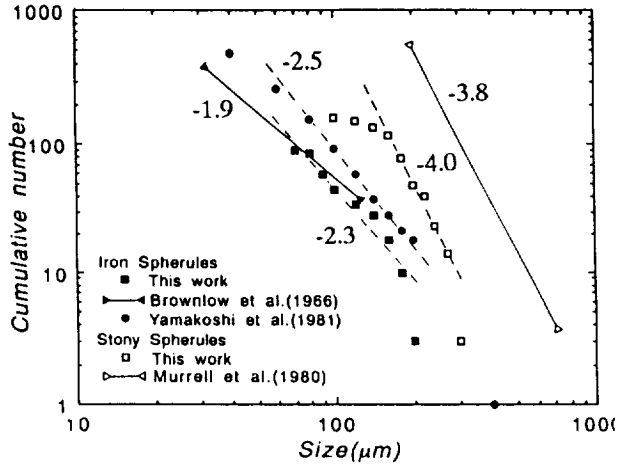

Figure 3. Cumulative size distributions of deep-sea spherules

CLASSIFICATIONAL PARAMETERS FOR ACAPULCOITES AND LODRANITES: THE CASES OF FRO 90011, EET 84302 AND ALH A81187/84190

T.J. McCoy[1], K. Keil[1], R.N. Clayton[2] and T.K. Mayeda[2] [1]Planetary Geosciences, Department of Geology and Geophysics, SOEST, University of Hawaii at Manoa, Honolulu, HI 96822, USA; [2]Enrico Fermi Institute, University of Chicago, Chicago, IL 60637, USA.

Abstract. Acapulcoites and lodranites probably sample a common parent body, which has experienced a range of partial melting [1-3]. We present classificational parameters which allow acapulcoites-lodranites to be distinguished from other groups of meteorites, as well as from each other. Petrography can complement oxygen isotopic compositions [4] in separating these meteorites from other groups of stony-irons and primitive achondrites, while petrographic properties alone distinguish acapulcoites from lodranites. Acapulcoites differ from lodranites in having smaller grain sizes, abundant Fe,Ni-FeS as μm-sized veins and plagioclase which escaped melting. We have applied these criteria to three new members of the group. FRO 90011 is a typical lodranite; EET 84302 is intermediate in many properties between acapulcoites and lodranites; and ALH A81187/84190 are paired meteorites and are the first low-FeO acapulcoites. These meteorites provide a wider spectrum of samples from the acapulcoite-lodranite parent body and suggests that this body may have had a complex structure.

Distinguishing Acapulcoites/Lodranites from Other Groups. Acapulcoites and lodranites are rocks consisting of equigranular aggregates of olivine + pyroxene + metal + troilite ± plagioclase. This distinguishes them from stony-iron meteorites such as pallasites and IAB irons: Acapulcoites and lodranites are not stony-iron meteorites with silicate clasts set in a matrix of Fe,Ni metal. This also distinguishes these meteorites from ureilites which contain ubiquitous carbon. Based on mineralogy and petrology, it is almost impossible to distinguish between winonaites and low-FeO acapulcoites and lodranites [5]. However, they can be readily distinguished on the basis of oxygen isotopic compositions.

Distinguishing Acapulcoites from Lodranites. The most important difference between acapulcoites and lodranites is in their thermal history. Acapulcoites experienced partial melting at the Fe,Ni-FeS eutectic [1], while lodranites were heated to somewhat higher temperatures and have also experienced silicate partial melting [2]. While the temperature differences may only have been 50-100°C, it has resulted in dramatic differences in petrologic and compositional properties of the two groups which can be used as distinguishing parameters. We concentrate on three major parameters. Other features (e.g., relict chondrules, evidence for reduction) can be used for classification in some cases.

Grain Size. Lodranites are coarse-grained, with average mafic mineral grain sizes of 538-702 μm. In contrast, acapulcoites are finer-grained, with average grain sizes of 146-173 μm. This is consistent with differences in their thermal and partial melting histories. In acapulcoites, grain growth of the silicates occurred by lattice diffusion in the solid state and, because of the low diffusion rates in solid silicates, grain growth was limited. In contrast, grain growth in lodranites was aided by the existence of silicate partial melts, in which diffusion rates are high, resulting in coarse-grained rocks. This difference in grain size provides a rapid means of initial classification.

Plagioclase Content and Shape. Plagioclase and pyroxene form the first silicate partial melt in a chondritic system. Acapulcoites have 7-15.6 vol.% plagioclase, occurring as small, isolated grains interstitial to mafic silicates. In contrast, lodranites tend to be depleted in plagioclase, although some have up to 10.3 vol.%; many, including Lodran, contain no plagioclase. When present, plagioclase occurs as large, interstitial grains which have been molten.

Metal/Troilite Abundances. Acapulcoites have roughly chondritic troilite abundances (3.6-8.0%), but lodranites are significantly depleted in FeS (0.2-2.7%). Both types have experienced partial melting at the Fe,Ni-FeS eutectic. In acapulcoites, the Fe,Ni-FeS melt is preserved as μm-sized veins which cross-cut plagioclase, indicating that the plagioclase was never molten. In the lodranites, silicate partial melting opened pathways which allowed segregation of the Fe,Ni-FeS eutectic, resulting in a depletion of troilite.

New Acapulcoites and Lodranites. We examined a number of primitive achondrites and found them to belong to the acapulcoite/lodranite clan.

FRO 90011. This meteorite was initially described as an acapulcoite [6]. It is coarse-grained (538 μm) and is depleted in plagioclase (only trace amounts) and troilite (3.0 vol.%). Olivines ($Fa_{9.4}$) and pyroxenes ($Fs_{12.6}$) show reverse FeO zoning. This meteorite is a lodranite.

EET 84302. This rock was thought to be related to silicate inclusions in IAB irons, based on similarities in olivine compositions (Fa_5) [7]. Our oxygen isotopic data ($\delta^{18}O$=+3.31, $\delta^{17}O$=+0.53) and olivine analyses ($Fa_{8.4}$) suggest classification as an acapulcoite or lodranite. This rock is the closest to a transitional member between acapulcoites and lodranites. It is intermediate in grain size (343 μm). Olivine ($Fa_{8.4}$) and pyroxene ($Fs_{8.3}$) compositions are approximately equal, and reverse FeO zoning in olivines is minor. Although plagioclase content is high (11.4 vol.%), individual grains appear to have been molten. Finally, troilite is very low (0.1 vol.%). We conclude that this meteorite has experienced silicate partial melting and should be classified as a lodranite.

ALH A81187/84190. These meteorites are paired and are moderately weathered. Oxygen isotopic compositions (81187, $\delta^{18}O$=+2.79, $\delta^{17}O$=+0.42; 84190, $\delta^{18}O$=+2.54, $\delta^{17}O$=+0.20) suggest that they are members of the acapulcoite/lodranite clan. They are relatively fine-grained (220 μm). Plagioclase contents are chondritic (10.0 vol.%), and individual grains do not appear to have been molten. While troilite contents are low (2.1 vol.%), weathering products (11.3 vol.%) are abundant. Thus, troilite contents are probably not a reliable indicator of classification. Veins of Fe,Ni-FeS cross-cut plagioclase. Olivines ($Fa_{4.2}$) and pyroxene ($Fs_{6.8}$) do not exhibit reverse FeO zoning. These meteorites are classified as acapulcoites.

Discussion. We have shown that acapulcoites and lodranites can be distinguished from other meteorite groups on the basis of petrography and oxygen and mineral compositions. They can also be distinguished from one another, based on mineralogic-petrologic properties that have resulted from differences in their thermal histories.

Our examination of new acapulcoites/lodranites yields two noteworthy new results. First, a meteorite intermediate in properties between acapulcoites and lodranites exists. This is not unexpected, since previously classified lodranites show a wide range of silicate partial melting [2,3]. EET 84302 represents the lowest degree of silicate partial melting of the known lodranites. Second, we discovered a low-FeO acapulcoite, which had been predicted by [2]. Surprisingly, this rock has roughly the same $\Delta^{17}O$ as the higher-FeO acapulcoites, suggesting that acapulcoites come from a reservoir of homogeneous oxygen isotopic compositions, while oxygen isotopic compositions of lodranites are correlated with their FeO content. Either the acapulcoite-lodranite parent body structure must have been very complex or, possibly, these meteorites sample more than one parent body. Discovery of a breccia containing materials of both types would provide definitive evidence for a common parent body.

References: [1] McCoy *et al.* (1992) *LPSC XXIII*, 871-872. [2] McCoy *et al.* (1992) *Meteoritics* **27**, 258-259. [3] Nagahara (1992) *Proc. NIPR Symp. Antarct. Met.* **5**, 191-223. [4] Clayton *et al.* (1992) *LPSC XXIII*, 231-232. [5] Kimura *et al.* (1992) *Proc. NIPR Symp. Antarct. Met.* **5**, 165-190. [6] Folco (1992) *Meteoritics* **27**, 221-222. [7] Mason (1986) *Antarct. Met. News*. **9** No. 3, 18. Samples provided by EUROMET and MWG. Funding in part by NAG 9-454 (K.Keil, P.I.)

Table 1. List of previously classified acapulcoites and lodranites.

Acapulcoites - Acapulco, Monument Draw, Y-74063, ALH A77081, ALH A78230, ALH 81261, ALH 81315
Lodranites - Lodran, Gibson, Y-791491, Y-791493, Y-74357, Y-75274, Y-8002, MAC 88177, LEW 88280

N94-10390

THE DREGS OF CRYSTALLIZATION IN ZAGAMI T.J. McCoy, K. Keil and G.J. Taylor, Planetary Geosciences, Department of Geology and Geophysics, School of Ocean and Earth Science and Technology, University of Hawaii at Manoa, Honolulu, HI 96822, USA.

Abstract. The Zagami shergottite is a basaltic meteorite [1] which formed when a phenocryst-bearing lava flow was emplaced at or near the surface of Mars [2]. Recently, a cm-sized olivine-rich lithology has been identified in Zagami by Mössbauer spectroscopy [3]. Olivine is extremely rare in shergottites, particularly in Zagami and Shergotty [1], where it occurs only as minute grains. We report petrologic and microprobe studies of this olivine-rich lithology. This material represents the last few percent of melt and is highly enriched in phosphates, opaques and mesostases, all of which are late-stage crystallization products. Phosphates replaced augite as a phenocryst phase when the magma became saturated in P. This late stage melt also includes a fayalite-bearing, multi-phase intergrowth which crystallized after the melt became too rich in iron to crystallize pigeonite. We can now reconstruct the entire crystallization history of the Zagami shergottite from a deep-seated magma chamber to crystallization of the final few percent of melt in a near-surface dike or thick flow. Small pockets (tens of microns) of late-stage melt pockets are ubiquitous but volumetrically minor in Zagami. We do not know the physical relationship between these areas and the cm-sized olivine-rich material described here. It is possible that these small pockets were mobile, forming larger areas. Perhaps inspection of the entire hand specimen of Zagami would clarify this relationship.

Results. The modal mineralogy of the late stage melt, discovered by Mössbauer spectroscopy and called Zagami DN by [3], differs dramatically from the major portions of the Zagami shergottite [2], here called Normal Zagami (NZ). DN contains much less pyroxene (13.6 vol.%) than NZ (77.7 vol.%). Maskelynite abundances are similar in the two. Phases which occur as minor constituents in NZ are highly enriched in DN, including phosphates (11.4 vol.%), mesostases (8.1 vol.%), ilmenite/titanomagnetite (5.9 vol.%) and pyrrhotite (1.6 vol.%). Also found in DN is a fayalite-rich intergrowth (39.9 vol.%), which is unknown from NZ.

DN contains pigeonite, plagioclase and phosphates as phenocryst phases. Although augite occurs as phenocrysts in NZ, it does not in DN. All of these phases in DN are at the compositional extremes of similar phases in NZ: Pigeonite in DN is FeO-rich (Fs_{56-71} vs. Fs_{28-56}), while maskelynite is more sodic (Ab_{56-59} vs. Ab_{42-53}). Whitlockite is the dominant phosphate and contains 5.0 wt.% FeO, comapred to 3.0 wt.% in NZ. Fluorapatite is also present as millimeter long laths. Low sums for microprobe analyses and stoichiometric deficiencies of F and Cl suggest that this apatite may contain significant (~1wt.%) OH, although no direct measurment of the water content has been conducted. Hydroxyapatite has been identified in Shergotty by X-ray studies [4]. The major assemblage in DN is an olivine-bearing intergrowth. Near the pigeonite grains, this intergrowth is dominated by augite, fayalite and a K-rich mesostasis. Augite is more FeO-rich (Fs_{46-54}) than augite in NZ (Fs_{19-39}). Olivine is Fa_{90-96} and makes up 25-30 vol.% of this intergrowth. The K-rich mesostasis is compositionally similar to mesostasis described by [1]. At the edges of the large whitlockite crystals, the intergrowth is coarser-grained and is dominated by olivine (Fa_{96}), which encloses a mixture of mesostases and phosphates. Fayalitic olivine comprises greater than 50 vol.% of this type of intergrowth. DN also contains titanomagnetite with exsolved ilmenite, pyrrhotite and mesostases. Mesostases compositions are similar to those reported by [1]. This material appears to be composed of three phases: maskelynite similar in composition to the maskelynite laths; SiO_2 with about 10% of small maskelynite laths; and K-rich feldspar. The presence or absence of the K-rich feldspar accounts for the difference between K-rich and K-poor mesostases. No baddelyite was identified, despite an extensive search using optical microscopy and X-ray mapping.

Unfortunately, we do not know the original size or shape of this "pocket" of late stage melt. The material we studied has a maximum dimension of 8 mm, suggesting an original size of at least

1 cm in diameter. We do not know the original shape of this "pocket" of melt (e.g., round bleb, layer, vein).

Discussion. One of the most remarkable features of DN is its size. While areas rich in whitlockite, titanomagnetite and mesostases are present in all Zagami samples [1,2], these seldom exceed a few hundred μm in size. We do not know the physical relationship between the micron-sized pockets and the cm-sized olivine-rich late-stage melt. One possibility is that the micron-sized materials were mobile and at times formed cm-sized segregations. In terrestrial basalts, such late-stage melts are often found as dikelets [5,6]. Perhaps examination of the entire material of Zagami in hand specimen could clarify this relationship.

The most exciting aspect of DN is that it allows us to reconstruct the entire crystallization history of Zagami (Fig. 1). The rock experienced a two-stage crystallization history [2], in which homogeneous Mg-rich pyroxene cores crystallized in a deep, slowly-cooling magma chamber, which were then entrained in a lava flow emplaced as a near-surface dike or thick lava flow. This magma crystallized pigeonite, augite and plagioclase for most of its history. Late-stage differentiated melt occurs as interstitial areas hundreds of μm in diameter and as a cm-sized pocket. Because of its relatively large size, the cm-sized pocket of late stage melt continued to differentiate. The presence of phosphates and absence of augite as phenocrysts in DN suggests a change in the crystallization history. The magma became saturated in P, which scavenged Ca from the melt and prevented the crystallization of augite. Instead, phosphates crystallized from the magma. The presence of apatite suggests that the magma contained significant amounts of F, Cl and, possibly, water. The next major change in the crystallization occurred when the melt became too Fe-rich to crystallize pigeonite. Instead, fayalite began to crystallize along with an SiO_2-normative mesostases. In some parts of the intergrowth, whitlockite continued to crystallize, due to the availability of sufficient P, while augite crystallized in other parts. This explains both the presence of the olivine-bearing intergrowth and the heterogeneity of this intergrowth. Finally, mesostases and opaque minerals crystallized.

References. [1] Stolper and McSween (1979) *GCA* **43**, 1475-1498. [2] McCoy *et al.* (1992) *GCA* **56**, 3571-3582. [3] Vistisen *et al.* (1992) *Physica Scripta* **46**, 94-96. [4] Fuchs (1969) In *Meteorite Research* (ed. Millman), 683-695. [5] Walker (1940) *Bull. Geol. Soc. Amer.* **51**, 1059-1106. [6] Bunch and Keil (1971) *Contrib. Min. Petrol.* **31**, 267-274.

We thank L. Vistisen, D. Petersen and M.B. Madsen for supplying this very interesting sample. Funding provided in part by NASA grant NAG 9-454 (K.Keil, P.I.).

Figure 1 Crystallization history of Zagami showing percent crystallization (%Xn), location, and the crystallization interval for each phase.

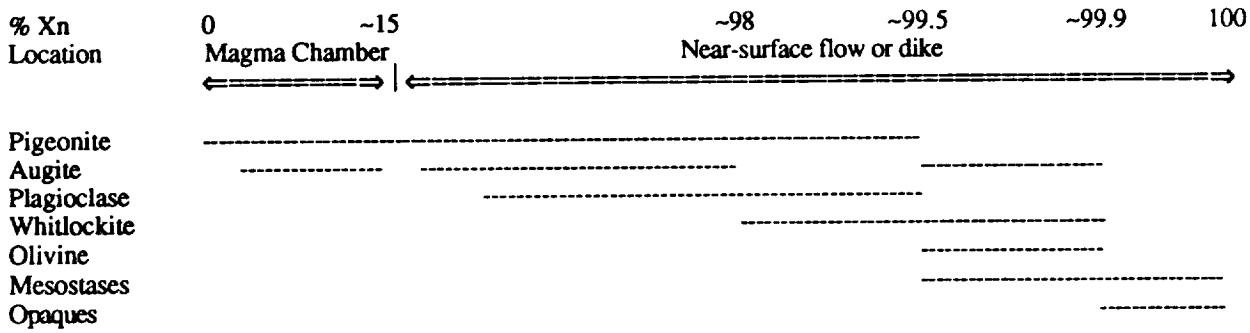

RESOLVING LDEF'S FLUX DISTRIBUTION: ORBITAL (DEBRIS?) AND NATURAL METEOROID POPULATIONS. J.A.M. McDonnell, Unit for Space Sciences, University of Kent at Canterbury, Kent CT2 7NR. UK

A consistent methodology for the collation of data from both *penetration* and *perforation* experiments and from data in the *Meteoroid and Debris Special Investigator Group (M-D SIG) data-base* has led to the derivation of the average impact flux over LDEF's exposure history 1984-1990. Data are first presented for LDEF's N,S,E,W and Space faces ("offset" by 8° and "tilted" by 1° respectively). A model fit is derived for ballistic limits of penetration from 1μm to 1mm of aluminium target, corresponding to impactor masses from 10^{-18}kg (for ρ_p=2g/cm^3) to 10^{-10}kg (for ρ_p=1g/cm^3). A second order harmonic function is fitted to the N,S,E and W fluxes to establish the angular distribution at regular size intervals; this fit is then used to provide "corrected" data corresponding to fluxes applicable to true N,S,E,W and Space directions for a LEO 28.5 degree inclination orbit at a mean altitude of 465 km.

Utilising dynamical modelling techniques [1; 2], the model fluxes are then analysed on the basis of two component flux *orbital* and *meteoroid*, model with several parameters allowed to float (e.g. meteoroid velocity and the ratio of orbital to interplanetary flux). Prior to this modelling, note is taken of a space debris component (of some 15%) on the trailing West face which is identified from chemical residues [3; 4].

Parameters deduced are:

1) The meteoroid impact flux from some 10^{-15}kg to 10^{-7}kg
2) The average meteoroid velocity at LEO altitudes;
3) The orbital flux (space debris ?) incident on the N, S and E directions for impactor masses 10^{-15} to 10^{-12}kg.

It is shown that the meteoroid population is asymmetrical in the mass range 10^{-12}kg to 10^{-9}kg regarding the North - South symmetry. This is discussed in the light of likely interplanetary sources; it may demand a small number of prolific cometary sources, rather than a well mixed population.

The orbital flux, which exceeds the natural component by a factor of 4 for micro particle fluxes, is compared with NASA models, the Solar Max Mission [5] and with the results of recent revisions in the Space Debris flux [6].

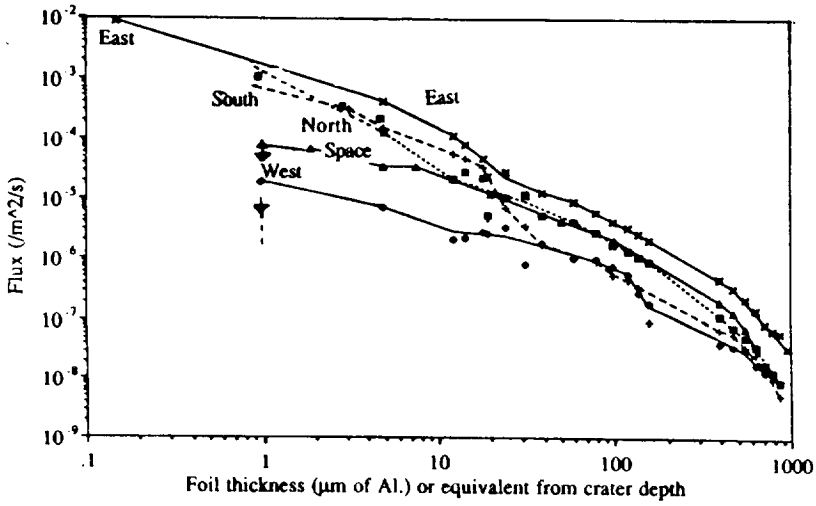

Fig.1. Ballistic limit impact data from LDEF's 4 peripheral and Space faces from the MAP experiment [7] and the M-D SIG database. Thick target data is converted using crater depth times 1.5.

RESOLVING LDEF'S FLUX DISTRIBUTION MCDONNELL J.A.M.

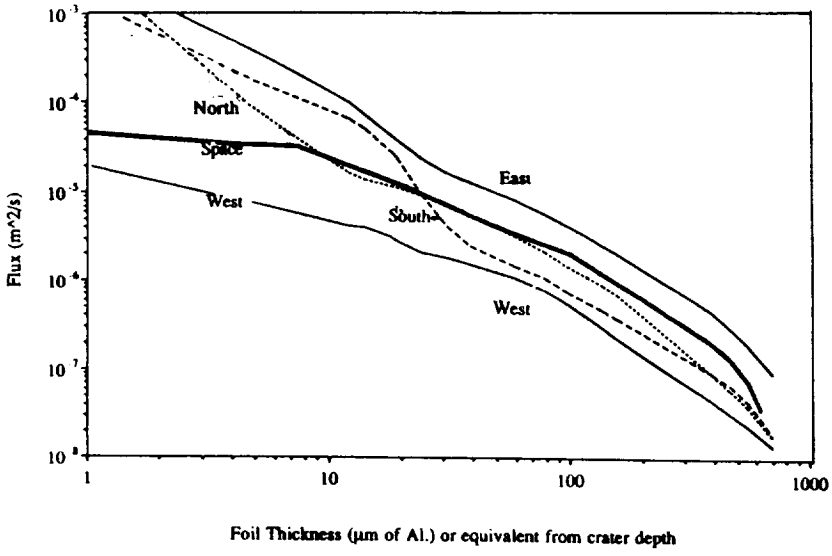

Fig.2. Model fluxes for "true " N,S,E,W directions (and Space un-corrected) relative to the orbit vector; they are derived using angular fits to data in Figure X.

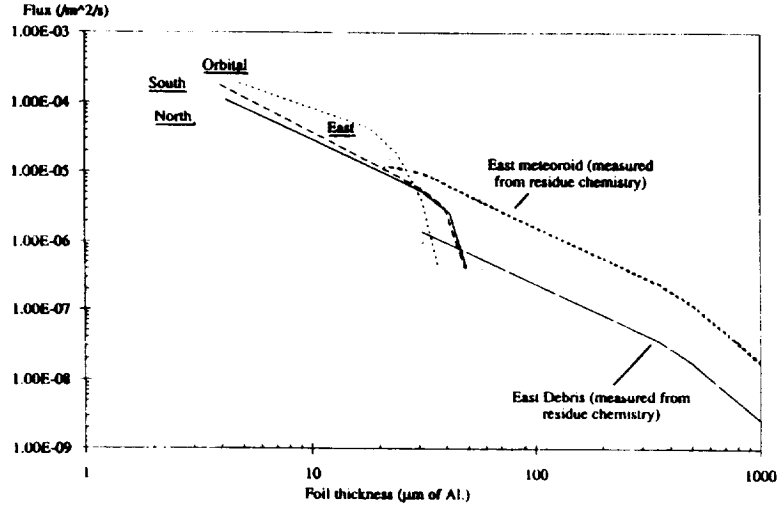

Fig.3. Populations of Orbital and Interplanetary Meteoroids derived from the 2 component modelling [8]. The **microparticle** orbital component (dominant on the East, South and North) exceeds the natural component on the West and Space faces. At larger dimensions, the debris deduced from chemical data [3] is some 15 % of the natural flux.

References

[1] Zook, H.A. (1992) Procs. Second LDEF Post Retrieval Symposium, San Diego, in press.

[2] Sullivan,K. and McDonnell,J.A.M. (1992) Proceedings of Workshop "Hypervelocity Impacts in Space". Publishers USS University of Kent U.K.

[3] Horz,F., Bernhard R.P., Warren, J.L., See, T.H., Brownlee,D.E., Lawrance, M.R., Messenger, S and Peterson, R.B.. (1991), NASA CP 3134 .

[4] Bernhard, R.P., Davidson, W. and Horz, F., (1992), Second LDEF Post Retrieval Symposium.

[5] Lawrance,M.R. and Brownlee, D.E., (1986) Procs. Second LDEF Post Retrieval Symposium, San Diego, in press.

[6] Kessler D.J. (1992).IAU/Cospar World Congress Washington D.C.

[7] McDonnell,J.A.M.(1992) Procs. of Lunar and Planetary Science, Volume 22, 185-193.

[8] Deshpande, S.P.(1993) Space Debris Or Natural Impacts On NASA's Long Duration Exposure Facility. Ph.D Thesis . In submission.

CLEMENTINE: ANTICIPATED SCIENTIFIC DATASETS FROM THE MOON AND GEOGRAPHOS

A. S. McEwen, U.S. Geological Survey, Flagstaff, Arizona

Introduction

The Clementine spacecraft mission is designed to test the performance of new lightweight and low-power detectors developed at the Lawrence Livermore National laboratory (LLNL) for the Strategic Defense Initiative Office (SDIO) [1]. A secondary objective of the mission is to acquire useful scientific data, principally of the Moon and the near-Earth asteroid Geographos. The spacecraft will be in an elliptical polar orbit about the Moon for about 2 months beginning in February of 1994, and it will fly by Geographos on August 31. Clementine will carry seven detectors, each weighing less than about 1 kg: two Star Trackers, wide-angle uv/vis, wide-angle Short Wavelength IR (SWIR), Long-Wavelength IR (LWIR), and LIDAR (Laser Image Detection And Ranging) narrow-angle imaging and ranging (see Table 1). Additional presentations about the mission, detectors, and related science issues are in this volume [1-4].

If fully successful, Clementine will return about 3 million lunar images, a dataset with nearly as many bits of data (uncompressed) as the first cycle of Magellan, and more than 5000 images of Geographos. The complete and efficient analysis of such large datasets requires systematic processing efforts. Described below are concepts for two such efforts for the Clementine mission: global multispectral imaging of the Moon and videos of the Geographos flyby. Other anticipated datasets for which systematic processing might be desirable include (i) multispectral observations of Earth; (ii) LIDAR altimetry of the Moon with high-resolution imaging along each ground track; (iii) high-resolution LIDAR color along each lunar ground track, which could be used to identify potential titanium-rich deposits at scales of a few meters; and (iv) thermal-IR imaging along each lunar ground track (including nighttime observations near the poles).

Global Multispectral Imaging of the Moon

The lunar orbit has been designed to enable global coverage with the uv/vis and SWIR cameras at the highest feasible resolutions and with sufficient overlap between frames to enable automated frame matching. To the extent possible, the uv/vis and SWIR filters were selected to optimize the compositional mapping of the Moon and Geographos [see ref. 3], except for the 2780-nm filter (required by SDIO) and (most likely) a clear filter on the uv/vis camera (for optical navigation to Geographos). The image scales will be about 100 m/pixel (uv/vis) and 150 m/pixel (SWIR) at +30° and -30° latitude (e.g., at periselene, 400 km altitude); 120 m/pixel (uv/vis) and 180 m/pixel (SWIR) at the equator; and 190 m/pixel (uv/vis) and 285 m/pixel (SWIR) at the poles. Global coverage will require 120 wide-angle frames per orbit times 300 orbits times up to 12 filters, for a total of 432,000 image frames. Rather than attempt to analyze nearly half a million small images, most lunar scientists would undoubtedly prefer to do their science analyses on a single global 12-wavelength image cube (separated into "tiles" or map quadrangles), following geometric and radiometric calibrations and photometric normalizations.

The task of processing this dataset into a calibrated global image cube will not be trivial. Processing steps will include (1) decompression of the data, (2) radiometric calibration, (3) removal of camera distortions, (4) co-registration of 12-filter sets of images (see below), (5) replacement of bad or missing data, (6) along-track frame matching, (7) geometric reprojection, (8) photometric function normalization, (9) mosaicking into single-orbit strips, and (10) mosaicking orbit strips into map quadrangles. This processing task must be largely automated if it is to be completed within a reasonable time (preferably within about 2 years from when the data is available).

Pixel-to-pixel misregistration between images acquired through different spectral filters can be a major source of error in the spectral analysis and mapping of lunar soils. Although high frame rates will enable acquisition of images through all 12 filters in about 1 s, the orbit velocity (as high as 1790 m/s) will offset frames by up to 18 pixels/s. A series of new programs have been developed in PICS (Planetary Image Cartography System) that resample highly correlated images for co-registration to an accuracy of 0.2 pixel. These procedures, which are fully automated for filter sets that are initially matched to within about 30 pixels, were applied to the Galileo lunar images [5] with excellent results. Subpixel registration of 90 Galileo frames (800 x 800 pixels) required about 20 hr on a Vax 4000/60. Even with scaling to the size of Clementine frames, 3.4 yr of continuous processing on a single Vax 4000/60 would be needed for subpixel registration of the full wide-angle dataset. Furthermore, this task could be much more difficult than with Galileo images if the camera distortions are not well described. The thin lenses on the Clemen-

tine sensors are likely to cause significant geometric distortions, and the distortions may vary with temperature. The other processing steps will at least double the computer requirements, so several capable workstations (or CPUs) running simultaneously will be needed to complete the systematic processing within 2 years.

Once completed, the global image cube will enable a wealth of scientific studies. A series of global or regional compositional maps can be derived that show the distribution and relative abundances of pyroxenes, olivine, anorthosite, shocked anorthosite, norite, troctolite, glassy materials, and titanium. Maps of soil crystallinity can be derived and used to determine relative ages of Copernican-age geologic units [6]. The compositions of excavated or uplifted crater materials can be used to determine subsurface compositions and stratigraphy. These and other datasets could be the basis for a new lunar geologic mapping program. Lunar Orbiter (LO) images are particularly complementary to Clementine's, because LO provides nearly global coverage at high sun angles, which accentuates topography and morphology at about the same resolution (50-300 m) as the Clementine global multispectral coverage. Clementine's orbit was designed to image at low sun and phase angles (except near the poles), which is best for compositional studies but not for topography and morphology.

Videos of Geographos

Clementine is expected to acquire continuous imaging throughout the closest-approach sequence at Geographos with frame rates of 4.5 frames/s for the SWIR, LWIR, and LIDAR detectors and 9 frames/s for the uv/vis camera. For comparison, the highest frame rate on Galileo is 0.4 frame/s in summation mode (400 x 400 pixels), and there was no imaging near closest approach to Gaspra. The relevant capabilities of Clementine include high electronic readout rates, automated tracking, fast data compression (Matra DCT chip), and 200 Mbytes of on-board storage. The high frame rates and continuous imaging are ideal for production of computer "movies" of the flyby, which can be recorded onto video tapes. These movies will consist entirely of actual image data, except where data dropouts are filled, rather than simulated sequences generated from a shape model, as was the case for the Gaspra rotation movie. The use of actual images enables the viewer to see all of the details of the topography, morphology, and distribution of compositional units as the viewing and illumination geometries change.

Several different Geographos video sequences are anticipated, including separate sequences for each imaging system and for merged datasets. The LIDAR will provide the highest spatial resolutions, in four colors, but it cannot image the night side, and Geographos will more than fill the LIDAR field-of-view within about 75 s of closest approach. (With the automated tracking, the LIDAR is expected to image the central portion of the illuminated area throughout closest approach; high-resolution mosaicking will not be possible unless the pointing errors fortuitously provide the appropriate coverage.) The LWIR will provide nightside imaging, so this dataset could be combined with the LIDAR to provide the best topography/morphology video. The viewing and phase angles change most rapidly near the time of closest approach, so the uv/vis camera will provide the highest resolution of the entire visible and illuminated surface during the 75 s before and after closest approach. Although the LIDAR has four filters with wavelengths of 400 to 750 nm, the 1000- and 2000-nm regions provide the best mineralogic information, so the uv/vis and SWIR datasets could be used to map compositional variations; this color-coded compositional data could then be merged with the high-resolution LIDAR sequence.

References

1. Shoemaker, E.M., and Nozette, S., 1993, this volume.
2. Vorder Bruegge, R., et al., 1993, this volume.
3. Lucey, P., 1993, this volume.
4. Spudis, P., and Lucey, P., 1993, this volume.
5. McEwen, A.S., et al., 1993, this volume.
6. McEwen, A.S., et al., submitted to JGR.

Table 1. Characteristics of Clementine's Sensors

Sensor	Field of View (°)	Frame X	Frame Y	Filters	Wavelengths (nm)
Star Tracker	28 x 43	576	384	1	450-1000
UV/Vis	4.2 x 5.6	288	384	6	340, 415, 750, 900, 950, 1000 *
SWIR	5.6 x 5.6	256	256	6	1100, 1250, 1500 2000, 2600, 2780
LWIR	1.0 x 1.0	128	128	1	8000-10500
LIDAR imager	0.3 x 0.4	288	384	5	400, 560, 650, 750, Clear
LIDAR laser	0.3 circular	--		1	1064

* One of these may be replaced by a clear filter.

GLOBAL AND REGIONAL/SEASONAL COLOR MOSAICS OF MARS; Alfred S. McEwen and Laurence A. Soderblom, U.S. Geological Survey, Flagstaff, Arizona

Four regional mosaics of Mars acquired during different seasons, along with their composite as a single global mosaic, have been completed in two colors (red and violet) at scales of 1/16 and 1/64 degrees/pixel. These mosaics were put together from a set of 51 separate mosaics (Table 1), each acquired from a single Viking Orbiter spacecraft orbital revolution [1,2]. Special techniques were developed and applied to suppress large variations between mosaics introduced by highly variable, optically thin, condensate hazes. The techniques utilize a combination of the spatial characteristics of the hazes (generally broad, low-frequency) along with their modulation of the regional color ratios (strongly enhancing the violet/red ratios). Photometric-function normalization was applied following the haze removal. Most of the single-orbit mosaics consist of red and violet or red, green, and violet filters, but a few mosaics with only red-filter data were included to fill gaps in global coverage at high northern latitudes. Global coverage is ~99% complete in red-filter mosaics and ~95% and ~60% complete in corresponding violet- and green-filter mosaics, respectively. All of the mosaics are geometrically tied to the 1/256° per pixel Mars Digital Image Map (MDIM), which is available on Compact Disk (CD), and which will be used as the base map for Mars Observer data sets. Early in 1993, the single-orbit color mosaics will be distributed to the science community in a six-volume set of CDs.

The global and regional/seasonal mosaics consist of the best color coverage of the surface available from each input data set. Where single-orbit mosaics overlap, we favored those with higher resolutions, more filters, lower observing angles (illumination, emission, and phase), relatively clear atmospheric conditions, and frost-free surface conditions. The four regional/seasonal groupings are not arbitrary categories. The Viking imaging team planned color imaging of broad regions during seasons when viewing conditions for the surface were generally best: the southern hemisphere during late southern summer, equatorial regions during early northern summer, and the north polar region during late northern summer.

Perhaps the most scientifically interesting parts of this dataset are the overlap regions, which show significant temporal variations in surface and atmospheric features [1]. Surface changes can be categorized as (1) changes that probably occurred during the great dust storms of 1977; (2) changes that occurred soon after the 1977 storms due to removal or redistribution of recently deposited dust; (3) changes in the northern lowlands that probably occurred during the dusty southern summer of 1979 (when no great dust storm occurred); and (4) changes associated with strong slope winds in the Tharsis and Elysium regions. We are looking forward to comparison of this dataset with wide-angle color images from the Mars Observer Camera [3].

1. McEwen, A.S., 1992, LPSC XXIII, 877-878.
2. Soderblom, L.A., 1992, in Kieffer et al., Mars, 557-593.
3. Malin, M.C., et al., 1992, JGR 97, 7699-7718.

MARS GLOBAL MOSAICS; McEwen, A.S., and Soderblom, L.A.

Table 1. **Viking Orbiter Color Mosaics,** in Regional/Seasonal Groups

Group 1:
Southern Hemisphere/Late Southern Summer, 1977

REV	L_s	FILTERS	PHASE ANGLE (°)
425A	297	RGV	33
441A	326	RGV	50
447A	329	RGV	47
453A	332	RGV	43
459A	336	RGV	41
463A	338	RGV	36
469A	342	RGV	36
356B	314	RGV	73
358B	315	RGV	66
407B	341	RGV	85

Group 2:
Equatorial/Early Northern Summer, 1978

REV	L_s	FILTERS	PHASE ANGLE (°)
577A	33	RGV	20
583A	36	RGV	19
586A	38	RGV	22
590A	40	RV	24
593A	41	RGV	21
605A	46	RV	26
609A	48	RGV	27
614A	50	RGV	29
663A	72	RGV	46
666A	73	RGV	47
669A	74	RGV	49
672A	76	RGV	50
681A	80	RGV	53
684A	81	RGV	55
687A	82	RGV	55
690A	84	RGV	56
735A	104	RGV	62

Group 3:
North Polar/Late Northern Summer, 1978

REV	L_s	FILTERS	PHASE ANGLE (°)
717A	96	RV	13
747A	109	RV	23
756A	113	RV	26
762A	116	R	25
765A	118	RV	46
768A	119	RV	48
771A	120	RV	49
793A	131	R	70
797A	132	R	72
801A	134	R	74
808A	138	R	77
811A	139	R	79
814A	141	R	79
816A	142	R	80
818A	143	R	81
826A	147	R	85

Group 4:
Survey Mission (Global)/Northern Summer, 1979

REV	L_s	FILTERS	PHASE ANGLE (°)
323S	65	RV	35
333S	69	RV	50
334S	70	RV	35
347S	75	RV	40
353S	78	RV	58
378S	89	RV	55
426S	111	RV	58
483S	140	RGV	81

LUNAR MULTISPECTRAL MOSAICS FROM GALILEO'S SECOND EARTH-MOON FLYBY;

A.S. McEwen, T.L. Becker, U.S. Geological Survey, Flagstaff, Arizona; M.S. Robinson, Planetary Geosciences Division, Univ. of Hawaii, Honolulu, Hawaii; K.P. Klaasen, C. Heffernan, Jet Propulsion Lab, Pasadena, California; J.M. Sunshine, Brown Univ., Providence, Rhode Island; and the Galileo SSI Team.

Introduction

Galileo's Solid-State Imaging (SSI) experiment acquired about 800 images of the Moon from the second Earth-Moon flyby (EM2) in December of 1992. Ten major sequences were acquired (Table 1); each consists of mosaics of the entire or nearly entire visible and illuminated surface from each viewing geometry in at least six spectral filters (effective wavelengths for the Moon of 420, 564, 660, 756, 890, and 990 nm). The geometries of LUNMOS numbers 3, 4, 5, and 6 were designed to provide stereo data at the best possible resolutions. Preliminary science results are described in a series of abstracts in this volume [1-4]. The purpose of this abstract is to describe the sequences, calibration, processing, and mosaicking, and to present a set of color products in a poster session.

Data Quality

The SSI EM2 data are generally superior to those acquired during the first Earth-Moon flyby [5], because (1) the spacecraft passed closer to the Moon, so the spatial resolutions are about 3 times better; (2) the exposure times were better, resulting in about 2 times better signal-to-noise ratios; (3) the cover was removed (prior to the Gaspra flyby), thus eliminating the "ghost" images [6] and enlarging the effective aperture area; and (4) target motion compensation (TMC) was fully implemented, thus enabling acquisition of closely matched filter sets, which minimizes the effects of scattered light on the subtle spectral differences.

Unfortunately, the compression algorithm used on the EM2 images resulted in some truncation of significant digits over "busy" image areas, such as topographically rough highland areas imaged at high sun angles. The effects of this truncation are noticeable in the color ratios. This "compression noise" is less noticeable in data acquired at low sun angles. It may be possible to design a filtering sequence that will remove the patterns.

Calibration

In-flight images of the Photometric Calibration Target (PCT) on the spacecraft were acquired for the first time during the first week of December 1992. The PCT images were processed with the pre-flight calibration files for a check on whether the calibration has changed significantly since the pre-flight calibration; the results revealed changes of up to about 5% in all filters and gain states. Calibration errors greater than about 1% are considered significant for the mapping of subtle spectral variations in mature lunar soils or on Gaspra [7]. The largest errors occur near the corners of the frames, especially the bottom corners, and in a central area of about 70 x 200 pixels. Errors in the central area are due to the emplacement of a series of dust particles on the quartz radiation shield. Effects of these dust particles were not seen in the Venus or EM1 images, and the particles were probably emplaced when the cover was removed. Evidence for calibration problems in the corners has been seen in Venus and EM1 images.

We expect new calibration files for SSI to be completed by February 1993. For preliminary analyses before the new calibration files are available, we derived calibration correction files for each filter from a subset of the PCT images, chosen to minimize possible errors due to shading variations of the PCT, changes in the shutter speed, or changes in the gain state ratios. Comparisons of overlapping lunar images show that the errors were probably reduced to less than 1% with the correction files.

SSI's scattered-light problem has not disappeared with the cover removal. This problem is minimized by using matched filter sets and masking the boundaries so that color ratios are not made with data from neighboring filter sets. Small residual frame-to-frame offsets seen in the mosaics will be normalized by histogram matching, as was done for the EM1 mosaics [8].

Following the flat-field corrections, further refinements on the absolute and relative spectra were carried out as described by Pieters et al. [4].

Subpixel Registration

Pixel-to-pixel misregistration (i.e., between corresponding pixels from images acquired through different spectral filters) is a major source of error in the spectral analysis of highly correlated multispectral datasets. For example, in the EM1 lunar mosaics [8],

subpixel misregistration is probably the largest source of error near high-contrast boundaries when spectra are extracted or spectral units are mapped. A series of new programs have been developed in PICS (Planetary Image Cartography System) that resample highly correlated images for co-registration to an accuracy of 0.2 pixel. We applied these techniques to the EM2 images and the results have been excellent. For the matched color sets acquired with TMC, the subpixel registration turned out to be better than expected in some cases, accurate to about 0.1 pixel.

Geometric Control and Mosaicking

Absolute geometric control was achieved by tying a few points per image in one filter to points in the unified control net [9,10]. Match points on overlapping frames were used to adjust the camera angles to improve the frame-to-frame matches in each mosaic. Following completion of a mosaic in one filter, images from the other five filters were tied directly to the corresponding frame in the controlled filter, to subpixel accuracy.

Mosaics have been completed for LUNMOS numbers 4, 7, and 8 (Table 1). Prior to mosaicking, each frame is reprojected to an Orthographic projection centered at a location within the range of subspacecraft latitudes and longitudes for each sequence. After we have completed LUNMOS numbers 5, 6, and 9, we will apply photometric normalizations and mosaic the "best" coverage (defined as a function of resolution and signal:noise) from all six sequences, as well as from the EM1 mosaics, into a single mosaic covering about 75% of the lunar surface.

Photometric Function

For the EM1 mosaics [8], the Hapke photometric-function parameters derived for disk-integrated lunar observations [11] were applied to normalize the albedo. However, it was obvious in the normalized images that this function over-corrected the brightnesses at high planetary latitudes (which were also high photometric latitudes for these observations). This problem is eliminated by reducing the parameter for mean macroscopic roughness (θ) from 20° to 5°. For a preliminary map of normal albedo, we applied these Hapke parameters (but with θ = 5°) to the images of LUNMOS7, the EM2 sequence with the lowest phase angles (Table 1).

Color-Ratio Composites and Special Products

For press-release images we have generally utilized the color-ratio composite consisting of 756/420 as red, 756/990 as green, and 420/756 as blue. However, we used the 660-nm filter in place of the 756-nm filter in the LUNMOS4 composite because of the loss of a 756-nm frame. For this poster, we expect to present composites with other color-ratio combinations in addition to the press-release versions. The color-ratio composites are presented both alone and merged with albedo and/or topography images.

References

1. Greeley, R., et al., this volume.
2. Head, J.W., et al., this volume.
3. McEwen, A.S., et al., this volume.
4. Pieters, C.M., et al., this volume.
5. Belton, M.J.S., et al., 1992, Science 255, 505-652.
6. Belton, M.J.S., et al., Advances in Space Research, in press.
7. Belton, M.J.S., et al., 1992, Science 257, 1647-1652.
8. McEwen, A.S., et al., submitted to JGR.
9. Davies, M.E., et al., 1987, JGR 92, 14177-14184.
10. Davies, M.E., et al., submitted to JGR.
11. Helfenstein, P., and Veverka, J., 1987, Icarus 72, 342-357.

Table 1. Major EM2 SSI Lunar Sequences

Sequence Name	Resolution (km/pixel)	Sub-Spacecraft Lat, Long (°)		Phase Angle (°)
LUNMOS01	2.0	49	200	119-123
LUNMOS02	1.7	53	206	112-118
LUNMOS03	1.4	62	224	85-111
LUNMOS04	1.1	67	290	74-78
HIRES	1.1	61	311	58-74
LUNMOS05	1.1	54	323	54-58
LUNMOS06	1.3	35	341	26-46
LUNMOS07	1.9	16	353	14-21
LUNMOS08	4.3	4	13	24-25
LUNMOS09	5.3	5	29	37-38

GALILEO SSI LUNAR OBSERVATIONS: COPERNICAN CRATERS AND SOILS; A.S. McEwen, U.S. Geological Survey, Flagstaff, Arizona; R. Greeley, Arizona State University, Tempe, Arizona; J.W. Head, C.M. Pieters, E.M. Fischer, Brown University, Providence, Rhode Island; T.V. Johnson, Jet Propulsion Lab, Pasadena, California; G. Neukum, DLR, Berlin; and the Galileo SSI team.

The Galileo spacecraft completed its first Earth-Moon flyby (EM1) in December 1990 [1] and its second flyby (EM2) in December 1992. Copernican-age craters are among the most prominent features seen in the SSI (Solid-State Imaging) multispectral images of the Moon. The interiors, rays, and continuous ejecta deposits of these youngest craters stand out as the brightest features in images of albedo and visible/1-micron color ratios (except where impact melts are abundant). Crater colors and albedos (away from impact melts) are correlated with their geologic emplacement ages as determined from counts of superposed craters [2-4]; these age-color relations can be used to estimate the emplacement age (time since impact event) for many Copernican-age craters on the near and far sides of the Moon.

Unlike Earth, where erosion and other processes obscure the impact record, the Moon exhibits a complete record of the impact flux over the Earth-Moon region during the past few billion years. Deciphering that record (or just its most recent portion) could resolve current controversies over the magnitude and the periodicity or episodicity of the asteroid and comet flux in the neighborhood of Earth and its effects on the evolution of life and on mass extinctions. In principle, this deciphering could be done through remote sensing combined with radiometric dates for key units, such as impact melts of large Copernican craters with extensive ray systems.

Understanding the stratigraphy of crater deposits is essential for determining the geologic history of the Moon. Preferably, geologic ages are assigned from direct stratigraphic observations, such as superposition of a unit on the rays of Copernicus (or vice versa), but for post-Imbrian units this is possible only over a small percentage of the Moon's surface. The next-best method (in the absence of radiometric dates) is use of the size-frequency counts of superposed craters, but sufficiently high-resolution images are not yet available for much of the Moon, especially on the farside. Thus, the presence or prominence of rays and ejecta deposits, as well as crater morphology, have been the key factors for distinguishing between the Copernican and Eratosthenian time-stratigraphic systems. However, ray visibility depends not only on age, but also on crater size (and ejecta volume), compositional differences between ejecta and substrate, and phase angle. Furthermore, crater morphology can be difficult to interpret, especially where images are poor, and Neukum and Konig [3] have documented a tendency for photogeologists to assign younger relative ages to the larger craters than are indicated by crater counts.

The spectral reflectivities of lunar soils are controlled primarily by (1) soil maturity, resulting from the soil's cumulative age of exposure to the space environment; (2) steady-state horizontal and vertical mixing of fresh crystalline materials [e.g., ref. 5]; and (3) the mineralogy of the underlying bedrock or megaregolith. Improved understanding of items (1) and (2) above will improve our ability to interpret item (3), especially for the use of crater compositions as probes of crustal stratigraphy [6]. We have examined the multispectral and superposed crater

frequencies of large isolated craters, mostly of Eratosthenian and Copernican ages, to avoid complications due to (i) secondaries (as they affect superposed crater counts) and (ii) spatially and temporally nonuniform regolith mixing from younger, large, and nearby impacts. Crater counts are available for 11 mare craters and 9 highlands craters within the region of the Moon imaged during EM1. The EM2 coverage provides multispectral data for 10 additional craters with superposed crater counts. Also, the EM2 data provide improved spatial resolution and signal-to-noise ratios [7] over the western nearside.

Correlations between log N (cumulative crater frequency per km^2 reduced to diameter = 1 km) and both the 0.56/0.99 micron color ratios and 0.56-micron normal albedos of the crater materials are clearly significant for craters younger than Copernicus. These results are used to estimate the emplacement ages of many other nearside and farside Copernican craters and to map their distributions. The apparent deficiency of Copernican craters on the farside compared with those on the nearside on published geologic maps is not present in our Copernican-unit map, confirming the suspicion that this apparent deficiency was due to a paucity of low-phase images of the farside. Our Copernican-unit map provides the first age estimates for hundreds of craters in the diameter range of 1 to 10 km.

The linear trends between N and the 0.56/0.99 micron ratio differ between the maria and the highlands and between the interiors and the continuous ejecta of the craters. Similar trends are established for color and albedo versus soil-maturity indices for the returned lunar samples, again with distinct trends for mare and highlands soils. However, the mare versus highland offsets are reversed in the two comparisons: any particular 0.56/0.99 micron ratio value corresponds to a smaller N (younger emplacement age) but to a larger maturity index (older exposure age) for highland relative to mare trends. These trend offsets may be explained by variations in regolith thicknesses, which influences the rates of mixing with relatively fresh ejecta [5,7]. The maria have thinner regoliths than do most highland areas, so mare soils undergo a higher rate of mixing with fresh ejecta from nearby impacts. A similar explanation may apply to the different trends seen in continuous ejecta blankets and in crater interiors: the interiors undergo a higher rate of mixing with fresh ejecta due to (i) greater near-surface abundances of blocky or massive crystalline rock in the crater interior and in the blocky ejecta concentrated near the crater rim, and (ii) relatively steep slopes on crater walls and central peaks, where regoliths are kept thin by downslope mass movements and preferential downslope movement of ejecta from impacts that are small relative to the slope [8]. Therefore, soil maturity parameters, which are related to a soil's cumulative exposure age, correspond to a range of emplacement ages for the underlying geologic unit, depending on the geology of the surrounding area. Understanding these relations will allow us to make better use of multispectral imaging for relative age dating and reconstruction of the geologic history of the Moon.

1. Belton, M.J.S., et al., 1992, Science 255, 570-576. 2. McEwen, A.S., et al., submitted to JGR. 3. Neukum, G., and B. Konig, 1976, Proc. Lunar Plan. Sci. Conf. 7th, 2867-2881. 4. Charette, M.P., et al., 1976, Proc. Lunar Plan. Sci. Conf. 7th, 2579-2592. 5. Basu, A., 1990, Proc. 20th LPSC, 231-238. 6. Fischer, E.M., and C.M. Pieters, this volume. 7. McEwen, A.S., et al., this volume. 8. Soderblom, L.A., 1970, JGR 75, 2655-2661.

ASPECTS OF MODELLING THE TECTONICS OF LARGE VOLCANOES ON THE TERRESTRIAL PLANETS; Patrick J. McGovern, Dept. of Earth, Atmospheric, and Planetary Sciences, Massachusetts Institute of Technology, Cambridge, MA 02139, and Sean C. Solomon, Dept. of Terrestrial Magnetism, Carnegie Institution of Washington, Washington, D. C. 20015.

Introduction. Analytic solutions for the response of planetary lithospheres to volcanic loads have been used to model faulting and infer elastic plate thicknesses [e.g., 1-4]. Predictions of the distribution of faulting around volcanic loads, based on the application of Anderson's criteria for faulting [5] to the results of the models, do not agree well with observations [6,7]. Such models do not give the stress state in the load itself, but only suggest a state of horizontal compressive stress there. Further, these models have considered only the effect of an instantaneously emplaced load. They do not address the time evolution of stresses, nor do they consider the effect of a load which grows. A finite element approach allows us to assign elements to the load itself, and thus permits calculation of the stress state and stress history within the edifice. The effects of episodic load growth can also be treated. When these effects are included, models give much better agreement with observations.

Method. We use the finite element code TECTON [8,9] to construct axisymmetric models of volcanoes resting on an elastic lithospheric plate overlying a viscoelastic asthenosphere. We have implemented time-dependent material properties in order to simulate incremental volcano growth. The viscoelastic layer was taken to extend to a sufficient depth so that a rigid lower boundary has no significant influence on the results. The code first calculates elastic deformations and stresses and then determines the time-dependent viscous deformations and stresses. Time in the model scales as the Maxwell time τ_m in the asthenosphere.

Results. We consider a volcano 25 km in height and 200 km in radius on an elastic lithosphere 40 km thick (parameters approximately appropriate to Ascraeus Mons). The volcano consists of three load increments applied at intervals of 1000 τ_m. Contours of maximum deviatoric stress in the fully-grown edifice at the conclusion of flexure (t = 3000 τ_m) are shown in Figure 1. Note that the maximum stress occurs in the lower mid-section of the edifice. We adopt the convention that tension is positive.

Discussion. Simple models of plate flexure due to an instantaneous load predict a state of horizontal compressive stress in the plate beneath the load [1,4] with an increasing magnitude of compression from the middle of the plate upward, and a maximum at the surface. Models with a succession of loads emplaced from the bottom up display a different distribution of stress. The maximum horizontal stress occurs in the lowest (first) load increment and decreases upward with each later load increment. Thus, thrust faults (predicted by simpler models) associated with such stresses would be expected to occur only early in the evolution (or not at all) and would be covered by later units which remain unfaulted. Such a distribution of stresses could also affect the locations and dimensions of magma chambers. A zone of horizontal compression within the edifice would inhibit ascending magma from reaching the summit and thus might cause magma to pool beneath it. Since magma will propagate perpendicular to the direction of least compressive stress, radial propagation of magma in sheet dikes or sills might also occur. The effects of adding fault slip along a basal detachment between edifice and lithosphere (as proposed in models of the flank tectonics of Hawaii [10]) was shown to achieve an even greater reduction in horizontal compressive stress in the edifice [11]. Such a structure may control the growth and evolution of tectonic features surrounding volcanoes on both Mars and Earth [11].

Stresses calculated from planetary loading models have been used, in conjunction with Anderson's criteria for faulting [5], to predict types of faulting that should be observed [1,2,4]. Typically, a zone is found surrounding the load with both the least compressive stress σ_1 and the most compressive stress σ_3 horizontal (assuming that near the surface, σ_{zz} is small and compressive). Application of Anderson's criteria yields a prediction of strike-slip faulting. Such a region surrounding a large load has not heretofore been observed [6,7]. Given the complete stress field in an element in this region from the TECTON solutions, we can plot Mohr diagrams, as in Figure 2, and compare them with a Mohr-Coulomb failure envelope. The Mohr circles grow in

size as flexure proceeds, until the failure envelope is exceeded at about 70 τ_m after first loading. The largest circle shows stresses at the conclusion of flexure. This stress state corresponds to that given by analytic plate models (in which flexure occurs instantaneously). Simply interpreting this final stress state is seen to be misleading for two reasons. First, σ_1 (= σ_{rr}) is much larger than the tensional strength of any rock. Use of a shear failure criterion (such as Mohr-Coulomb) for such a stress state is improper [7]. Use of a tensile failure criterion will predict the formation of tension joints which may be precursors of graben [7]. Second, consideration of the stress history indicates that at the time of first failure, the shear failure criterion is satisfied, with principal stress directions that predict circumferential normal faulting. Formation of these faults would relieve stresses and provide planes of low resistance along which further faulting with a similar orientation would be expected to develop. Thus, the "prediction" of a zone of strike-slip faulting surrounding a lithospheric load, based on simple instantaneously-loaded plate flexure models, is in error.

Conclusions. Simple interpretations of the results from instantaneous load models lead to predictions of lithospheric stress fields that do not match observations. Consideration of the history of stresses in the lithosphere and within the load itself helps to resolve these discrepancies.

References. [1] R.P. Comer *et al.*, *Rev. Geophys., 23,* 61, 1985; [2] H.J. Melosh, *Proc. LPS 9,* 3513, 1978; [3] P.J. McGovern and S.C. Solomon, *Inter. Colloq. on Venus,* LPI , p. 68, 1992; [4] R.P. Comer, *GJRAS, 72,* 101, 1983; [5] E.M. Anderson, *The Dynamics of Faulting,* 1951; [6] M.P. Golombek, *JGR, 90,* 3065, 1985; [7] R.A. Schultz and M.T. Zuber, *LPS, 23,* 1247, 1992; [8] H.J. Melosh and A. Rafesky, *GJRAS, 60,* 333, 1980; [9] H.J. Melosh and A. Rafesky, *JGR, 88,* 515, 1983; [10] P.W. Lipman *et al.*, *USGS Prof. Pap. 1276,* 45 pp., 1985; [11] P.J. McGovern and S.C. Solomon, *LPS, 23,* 885, 1992; [12] J. Handin, in *Handbook of Physical Constants,* ed. S.P. Clark, 223, 1966;

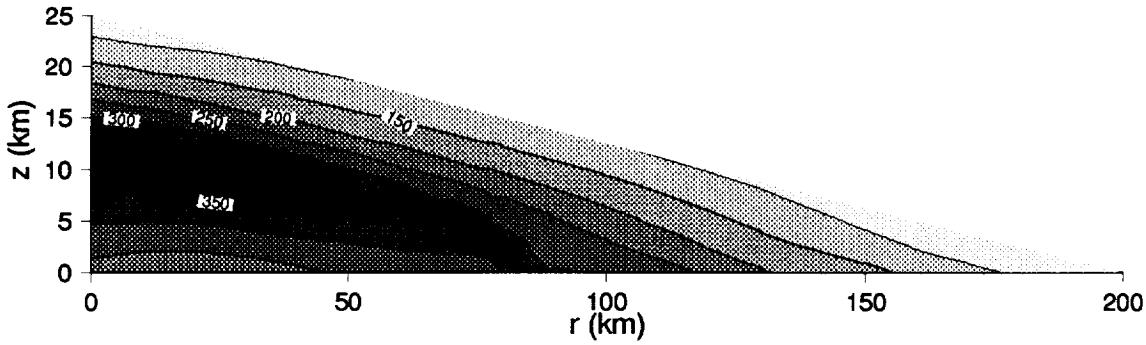

Figure 1. Contours of maximum deviatoric stress (MPa) in the volcanic edifice described above.

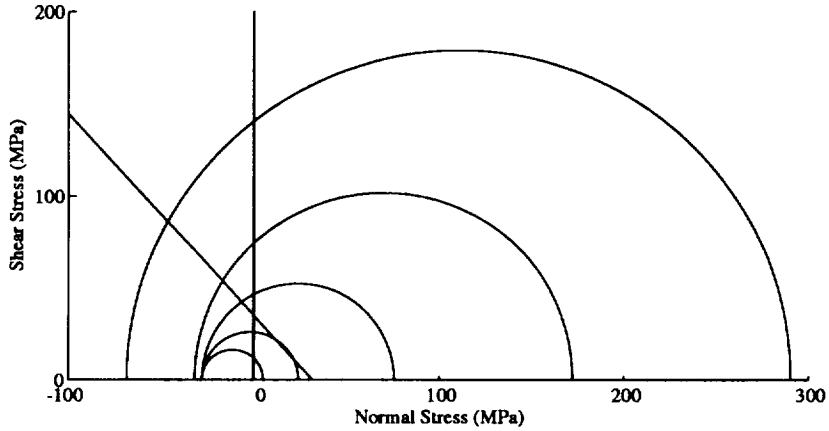

Figure 2. Mohr diagram for element at the top of the lithosphere (stresses calculated at element center: r = 265 km, z = -2.5 km). Diagonal line is Mohr-Coulomb failure envelope for basalt [12] with angle of internal friction ϕ = 49° and cohesion c = 38 MPa. In order of increasing radius, the circles represent stress state at t = 30, 70, 1000, 2000, and 3000 τ_m . When failure envelope is first exceeded (t = 70 τ_m), $\sigma_1 = \sigma_{rr}$ and $\sigma_3 = \sigma_{zz}$. At final time shown, $\sigma_1 = \sigma_{rr}$ and $\sigma_3 = \sigma_{\theta\theta}$.

GRAIN SURFACE FEATURES OF APOLLO 17 ORANGE AND BLACK GLASS. David S. McKay, NASA Johnson Space Center, Houston TX and Sue J. Wentworth, Lockheed, 2400 NASA Rd. 1, Houston TX 77058.

Background: Lunar soil sample 74220 and core samples 74001/2 consist mainly of orange glass droplets, droplet fragments, and their crystallized equivalents. These samples are now generally accepted to be pyroclastic ejecta from early lunar volcanic eruptions (1,2). It has been long known that they contain surface coatings and material rich in volatile condensable phases including S, Zn, F, Cl, and many volatile metals. (3) summarizes the voluminous published chemical data and calculates the volatile enrichment ratios for most of the surface condensates. In an attempt to more completely understand this enrichment of surface volatiles, we have searched for carbon and carbon-bearing phases on droplet surfaces.

Approach: We have reviewed many of our existing photomicrographs and energy dispersive analysis (EDX) of grain surfaces and have reexamined some of our older SEM mounts using an improved EDXA system capable of light element detection and analysis (oxygen, nitrogen, and carbon). In addition, we have made fresh mounts using procedures which should minimize carbon contamination or extraneous carbon x-rays and have analyzed for carbon.

Textures: *Micromounds*: The 74001/2 glasses have micromound coatings which were first described by (1) and appear to be characteristic of other lunar volcanic glasses such as the Apollo 15 green glasses (4). Individual micromounds range in size from ~20-300 Å. (5). The micromound coatings commonly contain scrapes and gouges which suggest that the glasses were abraded while the micromound coatings were still soft, i.e., during fire fountaining. Similar textures can be produced in laboratory vapor deposition processes as thin deposited coatings coalesce into micromounds during deposition. While other forms of condensed material appear to be present, the micromounds are the most pervasive textures and are present on virtually all original droplet surfaces in both 74220 and 74001/2 samples. Such micromounds were also found on all of the green glass droplets (4), and the presence of micromounds may be a definitive characteristic of volcanic glass droplets from anywhere on the moon.

Continuous coatings, Shrinkage cracks, and vesicles: Occasional droplets are covered by relatively thick and continuous coatings of vapor condensates; some of the continuous coatings contain cracks and vesicles which may have resulted from shrinkage during cooling, from desiccation, or by evolution of a volatile species. (5). Thick or continuous coatings of volatiles are quite rare.Such thickly coated droplets may have spent longer times in the plume, or may have been in some particularly vapor-rich zone of the eruption cloud.

Discrete condensate phases. The surfaces of most droplets display many small adhering grains a few micrometers or less in typical dimension. Some of these grains are rounded and appear to be very tiny splash droplets of glass. Other grains are subhedral to euhedral and have chemistries corresponding to volatile condensates of various sorts. The most unambiguous condensates phases are chloride such as NaCl phases and sulfur-rich forms (5). While such discrete grains or crystals of condensate material can be found on many grains, the volume or mass of condensates in these grains appears to be much less than that in the micromound coatings. Other adhering grains are anhedral or fragmental in appearance, and have compositions more typical of the glass or minerals in the glass (mainly olivine and ilmenite). These grains may be fragmental ash material produced in the original eruption or they may be fragmental material produced in the later events which fragmented many of the droplets.

Carbon: Using SEM EDX techniques, we have analyzed original surfaces of many droplets using a relatively low voltage beam (6KV) to enhance x-ray return from the outermost surface materials. Analysis of some droplet surfaces revealed a carbon peak in many of the spectra (Fig. 1). Because the grains were originally mounted on carbon planchettes, we first attributed the carbon signal to stray x-rays from the planchette. However, freshly prepared and mounted grains using Cu planchettes and thin aluminum conductive coatings still showed significant carbon peaks, even though we had taken considerable care to eliminate the possibility of carbon contamination or stray x-rays. Many of the droplets with carbon also show enhanced Zn and S peaks. In most cases, the carbon peak is not present on nearby chipped surfaces (Fig 2). The chipping apparently occurred on the moon, but the absence of micromound coatings on many chipped surfaces indicates that chipping likely occurred late in the eruption sequence after much of the condensate had formed. While it is difficult to quantify the amount of carbon represented by the peaks, under the same analysis conditions, carbon-coated silica glass slides containing about a 300 Å thick layer of carbon produced about the same size peak as typical droplet carbon peaks. This suggests that if the carbon is present as a simple continuous coating on the droplets, it is about the same order of thickness. However, the carbon may be present in forms more complex than a continuous carbon coating. The fact that uncoated

GRAIN SURFACE FEATURES OF APOLLO 17: McKay, D. S. and Wentworth S. J.

droplets exhibit considerable charging in the electron beam argues against the presence of a natural conductive coating of carbon or graphite on these droplets.

Discussion: Sample 74220 does not contain much carbon; (6) measured only 11 ppm total carbon, and noted that about half of it was released as CO2 with a light isotopic composition (-15 $\delta^{13}C_{PDB}$ per mil) which is closer to indigenous lunar carbon than to solar wind carbon. Both (6) and (7) suggested that carbonate-like phases might provide some of the thermally-released carbon.

(8) proposed that the driving gas for the pyroclastic eruption was CO. Normally CO gas would not leave a condensable trace. However, it is possible that during the rapid changes in pressure and temperature associated with the pyroclastic eruptions, a number of chemical reactions may have taken place which produced a condensable carbon phase. Because of rapidly changing conditions, these reactions would not necessarily reflect equilibrium conditions. An example might be a disproportionation reaction $CO \rightarrow C + CO_2$ which could have deposited carbon (graphite) on droplet surfaces during some phase of the eruption and cooling. Another possibility is that a metal carbonyl was formed during some late stage of the eruption or after deposition and that this carbonyl may have decomposed and deposited iron and some carbon on grain surfaces. Yet another possibility is the formation of carbonates at lower temperatures, e. g. $ZnCO_3$, during the late stages of the eruption or after deposition of the ejecta blanket. Such carbonates could form if CO_2 becomes a significant phase in the transient gas environment, produced, for example by the disproportionation reaction described above. Additional studies, including TEM analysis are necessary before the carbon-bearing phase can be fully identified.

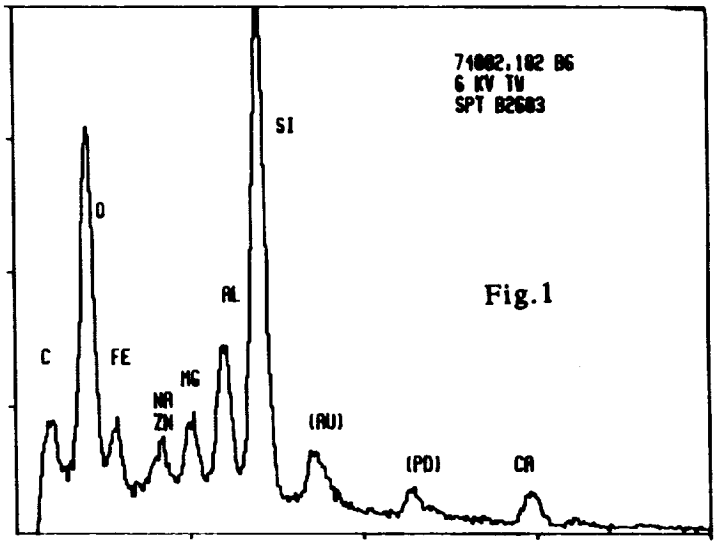

Fig.1

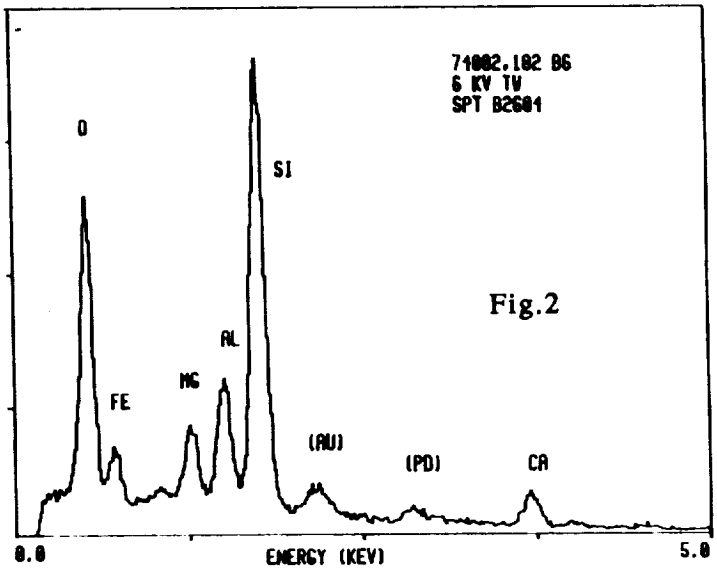

Fig.2

1. Heiken G., et. al. (1974) GCA 38, 1703-1718.
2. Heiken G. and McKay D. (1978) LPSC 9th p.1933-1944.
3. Meyer, C. (1990) LPI Workshop on Lunar Volcanic Glasses. LPI Tech. Rept. 90-02, p. 50-51.
4. McKay et al. (1973) LPSC 4th, p. 225-238.
5. Clanton U., et al. (1978) LPSC 9th, p. 1945-1957.
6. Chang et al. (1974) LPSC 5th, p. 1785-1800.
7. Gibson E. and Moore G. (1973) EPSL 20 p. 404-408.;
8. Sato (1979) LPSC 10th, p. 311-325.

JSC-1: A NEW LUNAR REGOLITH SIMULANT

David S. McKay[1], James L. Carter[2], Walter W. Boles[3], Carlton C. Allen[4], and Judith H. Allton[4]
[1]NASA Johnson Space Center, Houston, TX [2]University of Texas, Dallas, TX [3]Texas A&M University, College Station, TX [4]Lockheed Engineering & Sciences Co., Houston, TX

"Simulants of lunar rocks and soils with appropriate properties, although difficult to produce in some cases, will be essential to meeting the system requirements for lunar exploration" (1). In order to address this need a new lunar regolith simulant, JSC-1, has been developed. JSC-1 is a glass-rich basaltic ash which approximates the bulk chemical composition and mineralogy of some lunar soils. It has been ground to produce a grain size distribution approximating that of lunar regolith samples. The simulant is available in large quantities (> 2000 lb; 907 kg). JSC-1 was produced specifically for large- and medium-scale engineering studies in support of future human activities on the Moon. Such studies include material handling, construction, excavation, and transportation. The simulant is also appropriate for research on dust control and spacesuit durability. JSC-1 can be used as a chemical or mineralogical analog to some lunar soils for resource studies such as oxygen or metal production, sintering, and radiation shielding.

Simulant Preparation. JSC-1 was produced from a basaltic pyroclastic sheet deposit located in the San Francisco volcanic field near Flagstaff, AZ. This pyroclastic deposit was erupted from vents related to Merriam Crater (35°20'N, 111°17' W). One basalt flow from a nearby vent has a K-Ar age of 0.15±0.03 million years. The pyroclastic sheet consists of "airfall ash and lapilli, usually black, locally red, as much as several meters thick . . . (which) forms broad, smooth-surfaced deposits over large areas"(2).

The ash was mined from a commercial cinder quarry near the south flank of Merriam Crater. Following coarse sieving the ash was comminuted in an impact mill. This method broke down the material by means of multiple impacts with other ash particles, resulting in minimal metal contamination. The ash from several grindings was allowed to air dry to an average water content of 2.7 wt% and was then mixed. Finally, it was loaded into plastic bags in 50 lb (22.7 kg) quantities and the bags were heat sealed.

Preliminary Simulant Characterization. The chemical composition of Merriam Crater ash is listed in Table 1. The composition of Apollo 14 soil sample 14163 is included for comparison (3). Normative minerals (CIPW) calculated from the Merrian ash composition include plagioclase, clinopyroxene, orthopyroxene, olivine, magnetite, ilmenite, and apatite (2). Efforts are underway to verify the chemical and mineralogical compositions of JSC-1.

The source quarry is located within an area mapped as "slightly porphyritic basalt" (2). This basalt is described as "containing less that 1 percent phenocrysts of olivine, clinopyroxene, and (or) plagioclase in an intersertal to intergranular groundmass of plagioclase, clinopyroxene, olivine, and opaque oxides, with or without glass." Scanning electron micrographs show broken glass and crystal fragments 300 um across and smaller (Figure 1). Glass particles invariably display broken vesicles with sharp edges. Crystal fragments are angular to sub-rounded, and many display the scars of impacts from the milling process.

The average grain size distribution of four splits of JSC-1 is shown in Figure 2. The upper and lower bounds of grain sizes from the Apollo soil samples are included for comparison (4). Table 2 compares the mean grain size of JSC-1 with median or mean size ranges from lunar soils. Tests to more precisely determine the grain size distribution of JSC-1 are in progress.

Availability. Approximately 30,000 lb (13,600 kg) of JSC-1 simulant is currently available for distribution to qualified investigators. The material is stored at the Texas A&M Lunar Soil Simulant Laboratory. Investigators desiring a portion of this material should address their requests to Dr. Walter Boles, Department of Civil Engineering, Texas A&M University, College Station, TX 77843 (Telephone 409-845-2493, fax 409-862-2800).

References. 1. McKay, D.S. and J.D. Blacic, 1991, Workshop on Production and Uses of Simulated Lunar Materials, *LPI Tech. Rpt. 91-01*, Lunar and Planetary Institute, Houston, TX, 83 pp. 2. Moore, R.B. and E.W. Wolfe, 1987, Geologic Map of the East Part of the San Francisco Volcanic Field, North-Central Arizona, *Map MF-1960*, U.S. Geological Survey, Washington, D.C. 3. Papike, J.J., S.B. Simon, and J.C. Laul (1982) *Rev. Geophys. Space Phys., 20*, pp. 761-826. 4. Carrier, W.D. III, J.K. Mitchell, and A. Mahmood, 1973, *J. Soil Mech. Found. Div.*, Am. Soc. Civil Eng., pp. 813-832. 5. Heiken, G.H., D.T. Vaniman, and B.M. French, 1991, *Lunar Sourcebook*, Cambridge University Press, Cambridge, 736 pp.

Table 1. Chemical Composition

Oxide	Merriam Crater Ash* Wt.%	Lunar Soil 14163** Wt.%
SiO_2	48.77	47.3
TiO_2	1.49	1.6
Al_2O_3	15.65	17.8
Fe_2O_3	1.71	0.0
FeO	8.88	10.5
MgO	8.48	9.6
CaO	10.44	11.4
Na_2O	2.93	0.7
K_2O	0.81	0.6
MnO	0.19	0.1
Cr_2O_3	---	0.2
P_2O_5	0.66	- - -
Total	100.01	99.8

* Sample 2001 of Ref. 2
** Ref. 3

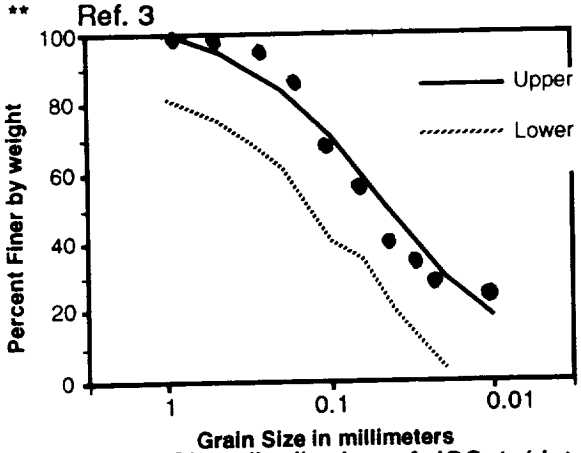

Figure 2. Size distribution of JSC-1 (dots) compared to lunar soil (Ref. 4).

Figure 1. Glass and mineral fragments from JSC-1. SEM image, frame width = 900 um

Table 2. Grain Sizes

Sample	Size Range(um)*
JSC-1 (median)	70
Apollo 11 (median)	48 - 105
Apollo 12 (median)	42 - 94
Apollo 14 (median)	75 - 802
Apollo 15 (median)	51 - 108
Apollo 16 (mean)	101 - 268
Apollo 17 (mean)	42 - 166

* Ref. 5, Table 7.8

THE NAKHLA PARENT MELT: REE PARTITION COEFFICIENTS AND CLUES TO MAJOR ELEMENT COMPOSITION. G. McKay (SN2, NASA-JSC, Houston, TX,77058) L. Le, and J. Wagstaff (Lockheed ESCO, 2400 NASA Rd. 1, Houston, TX 77058)

Introduction. Nakhla is one of the SNC meteorites, generally believed to be of Martian origin. It is a medium-grained augite-olivine cumulate with a variolitic groundmass of sodic plagioclase, alkali feldspar, and Fe-rich pyroxenes and olivine [e.g., 1]. One of the major tasks in deciphering Nakhla's petrogenesis is determining the composition of its parent melt. Gaining an understanding of the composition and petrogenesis of this parent melt may help unravel Nakhla's relationship to the other SNCs, and provide clues to Martian petrogenesis in general. Our experimental partitioning studies provide new information that helps constrain both the major and trace element composition of the Nakhla parent melt.

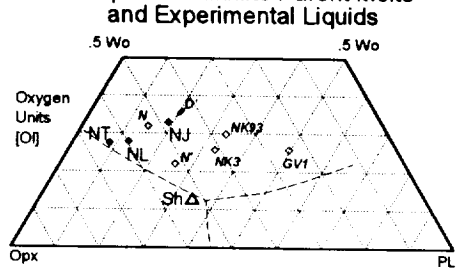

Fig. 1. Projection from Ol showing our quenched melt compositions (NT,NL,NJ), the Shergotty analog melt for which we previously measured DREE (Sh), and proposed nakhlite parent melt compositions N [4], NK3 and GV1 [5], NK93 and N' [6], and D' [1 & pers. comm.]. Multiple saturation curves are after Longhi and Pan [4]. The starting compositions for our experiments are based on Longhi & Pan's composition N (our NL), an abandoned Tennessee composition α (our NT) and a variation of Treiman's now-abandoned composition *D'* (our NJ).

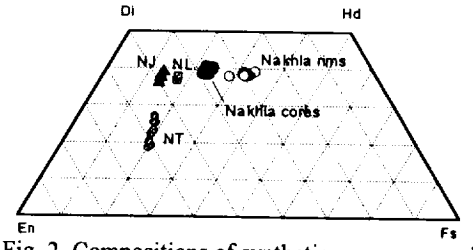

Fig. 2. Compositions of synthetic pyroxenes and Nakhla cores and rims. The same standards and analytical conditions were used for both natural and synthetic samples.

Can we use Shergotty partition coefficients for Nakhla? One approach to determining parent melt composition is to invert the trace element abundances of cumulus minerals. Earlier, we applied this approach to Shergotty pyroxenes [2] with good results. Success depends on accurate partition coefficients. For our Shergotty study, we used REE partition coefficients that we had previously measured for an analog Shergotty parent melt [3]. Because of the similarity in pyroxene compositions, it is tempting to apply those D values to Nakhla. However, partition coefficients depend on many factors, including melt composition. Although pyroxene compositions of Nakhla and Shergotty are similar, the melt compositions may not be.

Proposed Nakhlite parent melts have a wide range of compositions (and have been a real moving target over the last two years). Some recent ones are shown in Fig. 1. Most differ substantially from the Shergotty melt we studied earlier (Sh, Fig. 1). For example, composition N of Longhi and Pan [4] is much lower in Al than Sh, while all compositions are higher in Wo. It is important to determine whether D values for these other melts differ significantly from the Shergotty values.

To address this issue, and to help evaluate whether low- or high-Al parent compositions are more consistent with Nakhla mineral compositions, we are studying partitioning and phase relations for three synthetic compositions, NL, NT, and NJ (Fig. 1). Using these synthetic mixes as starting compositions, we measured REE partition coefficients between liquidus augite and coexisting melt. Charges were doped with 0.5-2% REE oxide, held on Pt wire loops in gas mixing (CO/CO_2) furnaces for four days at 1200°C - 1230°C at QFM. Quenched charges were analyzed with the JSC electron microprobe, along with pyroxenes from Nakhla, to facilitate direct comparison. We reported results for NT last year. This year, we have completed our study of NL and NJ.

Experimental Results. Quenched charges contain glass and a few % augite. Pyroxene compositions are shown in Fig. 2. As in our earlier Shergotty experiments, synthetic NT augite has nearly constant Fe/Mg but is zoned in Wo content. NL and NJ augites are much more homogeneous in major elements, and show a comparable range to Nakhla cores.

Both synthetic pyroxenes and Nakhla cores show significant zoning in minor elements, particularly Al and Ti (Fig. 3) and Cr (not shown). All NL and NT pyroxenes are lower in Al than any Nakhla analyses. However, about half the NJ pyroxenes have Al contents that overlap the low

REE DISTRIBUTION COEFFICIENTS FOR NAKHLA: McKay, G. *et al.*

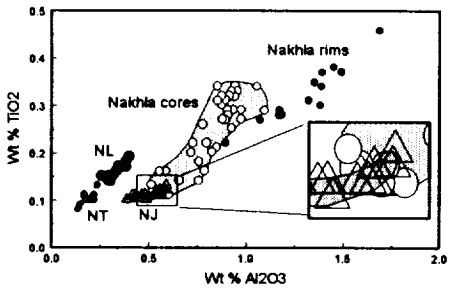

Fig. 3. Al and Ti in synthetic pyroxenes and Nakhla cores and rims. Inset shows enlargement of area in rectangle. NJ pyroxenes (dk gray field) overlap the most Al- and Ti-poor Nakhla cores (lt gray field), but are less Al-rich than majority of Nakhla cores.

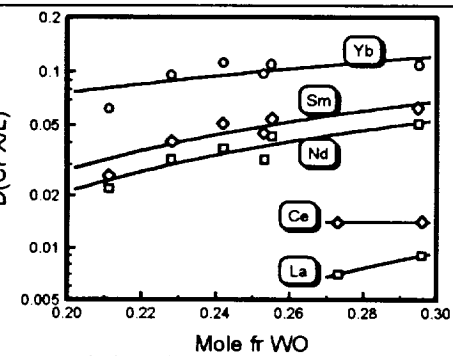

Fig. 4. Variation of D_{REE} with Wo content for NT pyroxenes. We observed a similar correlation with Wo in the Shergotty system [1].

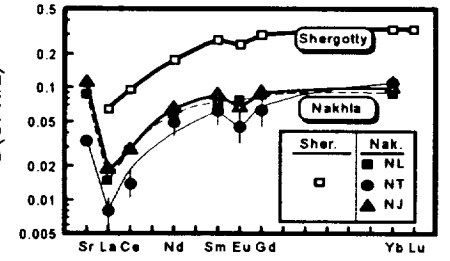

Fig. 5. REE distribution coefficients for clinopyroxenes in the Nakhla system, compared with Ds for pyroxenes of similar Wo in the Shergotty system [3]. Values for Nakhla composition NT are interpolated to Wo_{29} pyroxene, while values for NL and NJ are averages of >30 analyses (Wo_{43}) from several replicate runs. Shergotty patterns were calculated using equations in [3]. Shergotty values are significantly higher than those for Nakhla. Values for NT, NL, and NJ are quite similar, despite large differences in phase composition.

range of the Nakhla cores. This suggests that the Nakhla parent melt may have been similar in Al content to our NJ composition, while the more Al-rich parent melts in Fig. 1 *may* produce pyroxenes that are too Al-rich to match the Nakhla cores. This idea should be tested with further experiments.

As with our Shergotty experiments, we see correlations between D values and Wo content for the NT experiments (Fig. 4). To facilitate comparison with our Shergotty results, we use such correlations to interpolate D values for NT pyroxenes of Wo_{30}, the most Wo-rich NT pyroxenes. Fig. 5 compares D patterns for all our synthetic Nakhla pyroxenes (Wo_{30} NT values plus average values from NL and NJ pyroxenes of $Wo_{\sim 40}$) with a pattern from our Shergotty study extrapolated to Wo_{40} [3].

Discussion. Our new results on the NL and NJ compositions confirm our conclusion from last year based mainly on NT experiments: The Shergotty partition coefficients are higher than those for the Al-poor Nakhla starting compositions by factors of ~5. Thus, if Nakhla cumulus augites formed from a low-Al melt, use of the Shergotty D values to invert the augite REE contents will yield melt abundances that are several times too low. Moreover, the experimental Nakhla values are more than 10x lower than those which Nakamura *et al.* calculated for Nakhla clinopyroxene [8].

Note that D_{Sr} for NL and NJ is significantly higher than D_{Sm} or D_{Gd}, so that there is an apparent positive Sr anomaly, in contrast to the negative Eu anomaly. Although Sr analyses are difficult because of interferences, we have checked our analyses very carefully. Moreover the concentrations in these samples are fairly high, yielding reasonably good peak/bkg. Hence, we believe the positive Sr anomalies are probably not artifacts, but instead reflect real differences in the partitioning behavior of Eu^{2+} and Sr. Note also data are lacking for elements between Gd and Yb. We drew in smooth curves, but have no actual knowledge of how far up those curves might really go.

The major element composition of the Nakhla parent melt remains ambiguous. Our results point towards a composition of moderately low Al (Fig. 3), but experiments should be performed on more Al-rich compositions such as NK3 or NK93 (Fig. 1). Over the limited range of Al in our experiments, there appears to be only minor variation of D_{REE} other than that correlated with pyroxene Wo content. Finally, our synthetic pyroxenes have higher Mg/Fe than Nakhla cores (Fig 2). We have observed no significant effect of Mg/Fe on partition coefficients, although there may be a minor effect. Despite ambiguities in Al and differences in Mg/Fe, we believe that use of the partition coefficients in Fig. 5 will not lead to serious errors in estimating the REE content of the Nakhla parent melt.

References: [1] Treiman (1986) GCA 50, 1061. [2] Lundberg et al. (1983) GCA 52, 2147. [3] McKay et al. (1986) GCA 50, 927. [4] Longhi and Pan (1989) PLPSC 19, 451. [5] Harvey and McSween (1991) EPSL 111, 467. [6] Treiman (1993) GCA (submitted). [7] Treiman (1990) PLPSC 20, 273. [8] Nakamura *et al.* (1982) GCA 46, 1555.

N94-16400

MORE ON THE COOLING HISTORY OF ANGRITE LEW 86010. G. McKay (SN4 NASA-JSC, Houston, TX,77058), T. Ogawa (Dept. of Pure and Applied Sci., Univ. of Tokyo, Komaba, Tokyo 153, Japan), M. Miyamoto and H. Takeda, Mineralogical Inst., Faculty of Sci., Univ. of Tokyo, Hongo, Tokyo 113, Japan)

Introduction. Antarctic angrite LEW 86010 has many chemical and mineralogical characteristics which suggest it is closely related to Angra dos Reis (ADOR) [e.g., 1-5]. However, these meteorites have had very different thermal histories. Olivines and pyroxenes in ADOR are nearly homogeneous [6], suggesting very slow cooling or extensive subsolidus equilibration. In contrast, LEW 86010 pyroxenes are extensively zoned in both major and trace elements [2-4], while olivines are nearly homogeneous, suggesting that cooling of this sample was slow enough to homogenize olivines, but too fast to homogenize pyroxenes.

In an earlier study [7], we used Ca diffusion gradients associated with exsolution lamellae of kirschsteinite in LEW 86010 olivines [1-5] to estimate the cooling rate of this sample. We obtained cooling rates of a few x .01°C/yr, corresponding to a burial depth of ~10^2 m under solid rock (thermal diffusivity = 0.004 cm^2/s), or ~10 m under regolith material (10^{-5} cm^2/s). Unfortunately, this calculation was very sensitive to the assumed temperature of initial exsolution, which we approximated from the estimated initial olivine bulk Ca content, and also to the extrapolated values for the Ca diffusion coefficient (D_{Ca}).

This abstract reports new cooling rate estimates obtained using a refined approach that includes the initial temperature of exsolution as one of the fitted parameters. The purpose of our new calculations is (1) to reduce uncertainties in cooling rate due to uncertainties in bulk olivine Ca content and initial exsolution temperature, (2) to investigate the effects of using different values for D_{Ca}, and (3) to determine how well constrained the cooling rate is for any particular Ca diffusion coefficient.

Method. For kirschsteinite lamellae in olivine in the LEW 86010 angrite, we computed both the width of the lamellae and the compositional gradients between the kirschsteinite and host olivine for various cooling conditions and compared them to profiles measured by electron microprobe. The method is similar to that in our previous studies [7,8], and is analogous to that developed by [9]. As the temperature goes down, olivine begins to exsolve kirschsteinite when the bulk olivine content meets the solvus function. Kirschsteinite lamellae grow as time passes and temperature falls. We used the solvus function reported by [10] to relate the initial exsolution temperature to olivine Ca content. We used D_{Ca} values extrapolated to T<1000°C from experimental values for T>1100°C [11,12]. We assume that the initial Ca concentration is uniform and that cooling is monotonic.

The difference from our earlier calculations [7] is that we now include the initial CaO content as a parameter to be fit. The initial Ca content determines the temperature of onset of exsolution, one of the major sources of cooling rate uncertainty in our previous estimate of the LEW 86010 cooling rate.

An important remaining uncertainty in the calculation is the value of D_{Ca} as a function of temperature over the cooling interval. We used experimentally measured diffusion coefficients for Ca in olivine parallel to the *c* direction from Morioka [11] and Jurewicz and Watson [12]. These measurements were made for temperatures ≥ 1100°C. To extrapolate to lower temperatures, we used two different values for the activation energy (E_a): 25 kcal/mole, based on experimental data for Fe-Mg diffusion in olivine [13] and Ca diffusion in pyroxene [14]; and 42 kcal/mole, the value observed at T>1100°C by Jurewicz and Watson[12].

Results and Discussion. Cooling rates yielding model zoning profiles most closely matching observed profiles for a series of diffusion coefficient values are given in Table 1. Regardless of which diffusion coefficient is used, the best-fit value for initial Ca is ~8 mol %, or ~1.7x higher than the value in our earlier calculations. The earlier value was the concentration measured midway between kirschsteinite lamellae, under the assumption that Ca diffusion had not extended that far into the host olivine. The new calculations suggest that this assumption was not valid. The higher initial Ca concentration obtained by our new fitting procedures yields higher initial exsolution temperatures, and hence higher cooling rates than we estimated in our earlier study (Table 1 and [7]). These cooling rates correspond to burial depths of ~ 15-170 m of rock or ~ 1-10 m of regolith, depending on D_{Ca}.

Table 1. Best-fit cooling rates for various Ca diffusion coefficients (D_{Ca}) and activation energies (E_a).

D_{Ca} @ 1100°C (cm^2/s)	E_a (kcal/mol)	Rate (°C/yr)
1.098×10^{-14} [12]	25[1]	0.35
1.434×10^{-11} [13]	42[2]	10.
"	25[1]	50.

Notes:
1. From pyroxene (see text).
2. Observed at T>1100 [12].

The robustness of our cooling rate solutions is illustrated in Figures 1 and 2. Figure 1 compares the observed Ca profile with model profiles for several cooling rates above and below the best-fit cooling rate. The best-fit rate (0.35°C/yr for D_{Ca} and E_a from line 1, Table 1) gives an obviously better fit to the observed data, particularly the width of the lamella, than rates twice or half as fast.

Figure 2 compares the observed profile with best-fit model profiles for several values of bulk Ca content, and provides an indication of how well our fitting method constrains the initial Ca content, and thus the temperature at the onset of exsolution. Different Ca contents yield different profiles in the host olivine, but no significant difference in lamella width. The observed profile is asymmetrical in the low-Ca phase, and best matches the profile for the 2x faster rate on one side, and for the 2x slower rate on the other. Despite the asymmetry, the observed profile is clearly a better match to the model profile for optimum Ca content than to those for initial Ca contents yielding cooling rates 1/5 and 5 times as high, and a marginally better match than those for rates of 1/2 and 2x. We infer a ~ 2x uncertainty in cooling rate resulting from uncertainty in the Ca fit.

The largest remaining uncertainty in calculating the cooling rate for LEW 86010 is the diffusion rate of Ca in olivine. The discrepancy of > 100x between 1100°C values reported by Morioka [11] and Jurewicz and Watson [12] results in an uncertainty of > 100x in the cooling rate. Further significant refinement of the cooling rate will probably require additional experiments to measure Ca diffusion.

Despite the uncertainties in diffusion rate, we obtain burial depths of a few tens of meters or less, assuming LEW 86010 was covered by material with the thermal diffusivity of solid rock. A physical setting corresponding to this burial depth might be at the bottom of a fairly thick lava flow. Lower limits correspond to about a meter of material with the insulating properties of regolith.

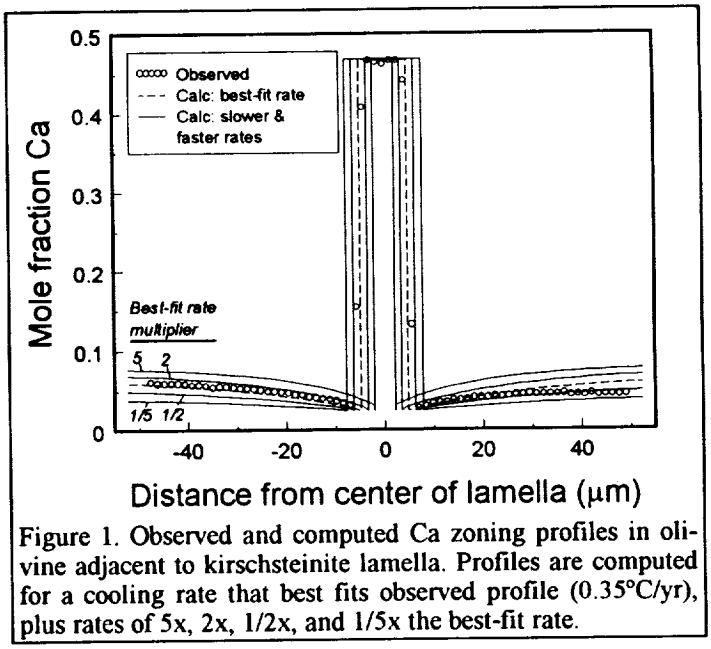

Figure 1. Observed and computed Ca zoning profiles in olivine adjacent to kirschsteinite lamella. Profiles are computed for a cooling rate that best fits observed profile (0.35°C/yr), plus rates of 5x, 2x, 1/2x, and 1/5x the best-fit rate.

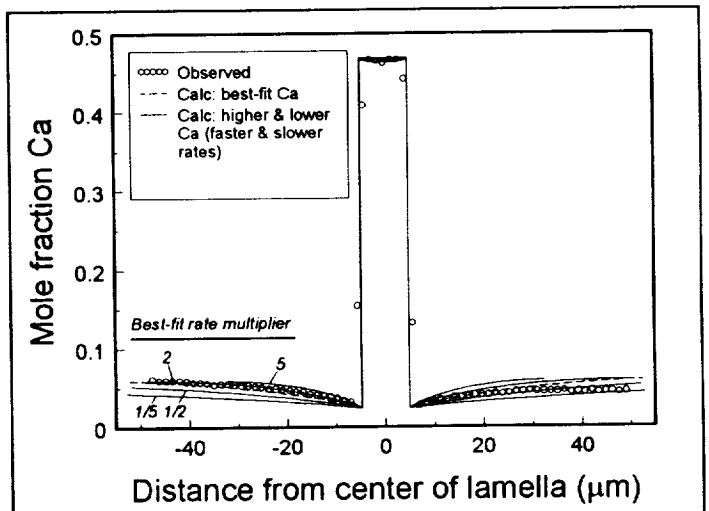

Figure 2. Observed and computed profiles. Profiles are computed for the optimum Ca content (8.0 mol %) and best-fit cooling rate (0.35°C/yr), and for Ca contents (11.4, 9.3, 7.1 and 6.1 mol %) that give best-fit cooling rates of 5x, 2x, 1/2x, and 1/5x the best rate for optimum Ca.

References: [1] Mason (1987) Antarctic Meteorite Newsletter 10, no. 2. [2] McKay et al. (1988) Lunar and Planetary Science XIX, 762. [3] Prinz et al. (1988) Lunar and Planetary Science XIX, 949. [4] Crozaz et al. (1988) Lunar and Planetary Science XIX, 231. [5] Mittlefehldt et al. (1989) Lunar and Planetary Science XX, 701. [6] Prinz et al. (1977) EPSL 35, 317. [7] McKay, Miyamoto, and Takeda (1989) Meteoritics, 24, 302. [8] Miyamoto et al. (1986) J. Geophys. Res. 91, 11804. [9] Goldstein and Short (1967) Geochim. et Cosmochim. Acta 31, 1001. [10] Davidson and Mukhopadhyay (1984) Contr. Min. Pet. 86, 256. [11] Morioka (1981) Geochim. et Cosmochim. Acta 45, 1573. [12] Jurewicz and Watson (1988), Contr. Min. Pet. 99, 186. [13] Buening and Buseck (1973) JGR 78, 6852. [14] Fujino, Naohara, and Momoi (1990) EOS 71, 943.

LIMITED SUBSOLIDUS DIFFUSION IN TYPE B1 CAI; EVIDENCE FROM Ti DISTRIBUTION IN SPINEL; **G.P. Meeker and J.E. Quick**, U.S. Geological Survey, MS 903 Denver Federal Center, Denver CO, 80225 and **Julie M. Paque**, SETI Institute NASA-ARC, MS 244-11 Moffett Field, CA 94035-1000

Most models of calcium aluminum-rich inclusions (CAI) have focused on early stages of formation by equilibrium crystallization of a homogeneous liquid. Less is known about the subsolidus cooling history of CAI. Chemical and isotopic heterogeneities on a scale of tens to hundreds of micrometers [e.g. MacPherson et al. (1989) and Podosek, et al. (1991)] suggest fairly rapid cooling with a minimum of subsolidus diffusion. However, transmission electron microscopy indicates that solid state diffusion may have been an important process at a smaller scale (Barber et al., 1984). If so, chemical evidence for diffusion could provide constraints on cooling times and temperatures. With this in mind, we have begun an investigation of the Ti distribution in spinels from two type B1 CAI from Allende to determined if post-crystallization diffusion was a significant process.

Titanium is an abundant element in type B1 CAI. Most of the Ti in these objects resides in zoned fassaitic pyroxene where concentrations of Ti, expressed as TiO_2, at the cores can be >15 weight percent. Numerous studies indicate that a significant portion of the Ti in the fassaitic pyroxene is in the +3 oxidation state. The only other major phase in type B inclusions that contains Ti in amounts greater than 1000 ppm is spinel. The Ti content of CAI spinel is generally between 0.1 and 0.9 weight percent.

The type B1 CAIs, 3529Z and 5241 have been described by Podosek et al. (1991) and by El Goresy et al. (1985) and MacPherson et al. (1989). We have analyzed spinels in these inclusions using the electron microprobe. These spinels are generally euhedral, range in size from <10 to 50 μm and are poikilitically enclosed by millimeter-sized pyroxene, melilite, and anorthite. Analyses were obtained from both the mantles and cores of the inclusions. Compositions of pyroxene in the vicinity of individual spinel grains were obtained by analyzing at least two points on opposite sides of the spinel and averaging the compositions. The pyroxene analyses were obtained within 15 μm of the spinel-pyroxene interface. No compositional gradients were observed within single spinel crystals.

Ti concentrations in spinels included within pyroxene, melilite, and anorthite are presented in Figure 1. Data include analyses from Meeker et al. (1983). Spinels included within pyroxene show a wide range in Ti concentration that correlates with the Ti concentration of the surrounding pyroxene. These data contrast with analyses from spinels within melilite, and anorthite which have low concentrations of Ti. In 3529Z, the highest concentration of Ti observed in spinel enclosed by anorthite and melilite is 0.22 weight percent TiO_2. A similar situation exists in 5241, although in this inclusion the spinels have an average Ti concentration of 0.25 weight percent TiO_2, which is approximately 25 percent higher than observed in 3529Z. Figure 1 suggests that spinels in the mantle of 5241 have a higher Ti concentration than the spinels in the core. Some of the mantle spinels from 5241 are in contact with small pyroxene blebs containing high (~12 wt.% TiO_2) concentrations of Ti.

Also shown in Figure 1 are spinel compositions from experimental run products produced by Stolper and Paque (1986). These data are for spinels enclosed within pyroxene, melilite, and anorthite. The maximum Ti concentration observed in these spinels is 0.22 weight percent TiO_2. These experiments were quenched at temperatures above 990°C so that no significant subsolidus equilibration occurred.

It is noteworthy that the Ti concentration of spinels in the experimental study are similar to spinels in melilite and anorthite in 3529Z and 5241, but strikingly different from the spinels enclosed by pyroxene. This observation suggests that the concentration of Ti in CAI spinel enclosed within pyroxene is the result of partial subsolidus equilibration rather than primary crystallization from a liquid. Spinels enclosed within melilite and anorthite, which are Ti-free, retain their original composition because they have no opportunity to exchange Ti with the enclosing phase. In contrast, spinels enclosed within pyroxene gain Ti from their host after incorporation. It is possible that the subsolidus cooling history may be constrained by the steep concentration gradients preserved in zoned pyroxene, and by at least partial equilibration of spinel.

REFERENCES: 1] MacPherson, G.J., Crozaz G. and Lundberg L.L (1989) GCA 53, 2413. 2] Podosek, F.A., Zinner E.K., MacPherson G.J., Lundberg L.L., Brannon J.C. and Fahey, A.J., (1991) GCA 55, 1083. 3] Barber D.J., Martin P.M., and Hutcheon I.D. (1984) GCA 48, 769. 4] El Goresy A.H., Armstrong J.T., and Wasserburg G.J., (1985) GCA 49, 2433. 5] Meeker G.P., Wasserburg G.J., and Armstrong J.T., (1983) GCA 47, 707. 6] Stolper E., and Paque J.M., (1986) GCA 50, 1785.

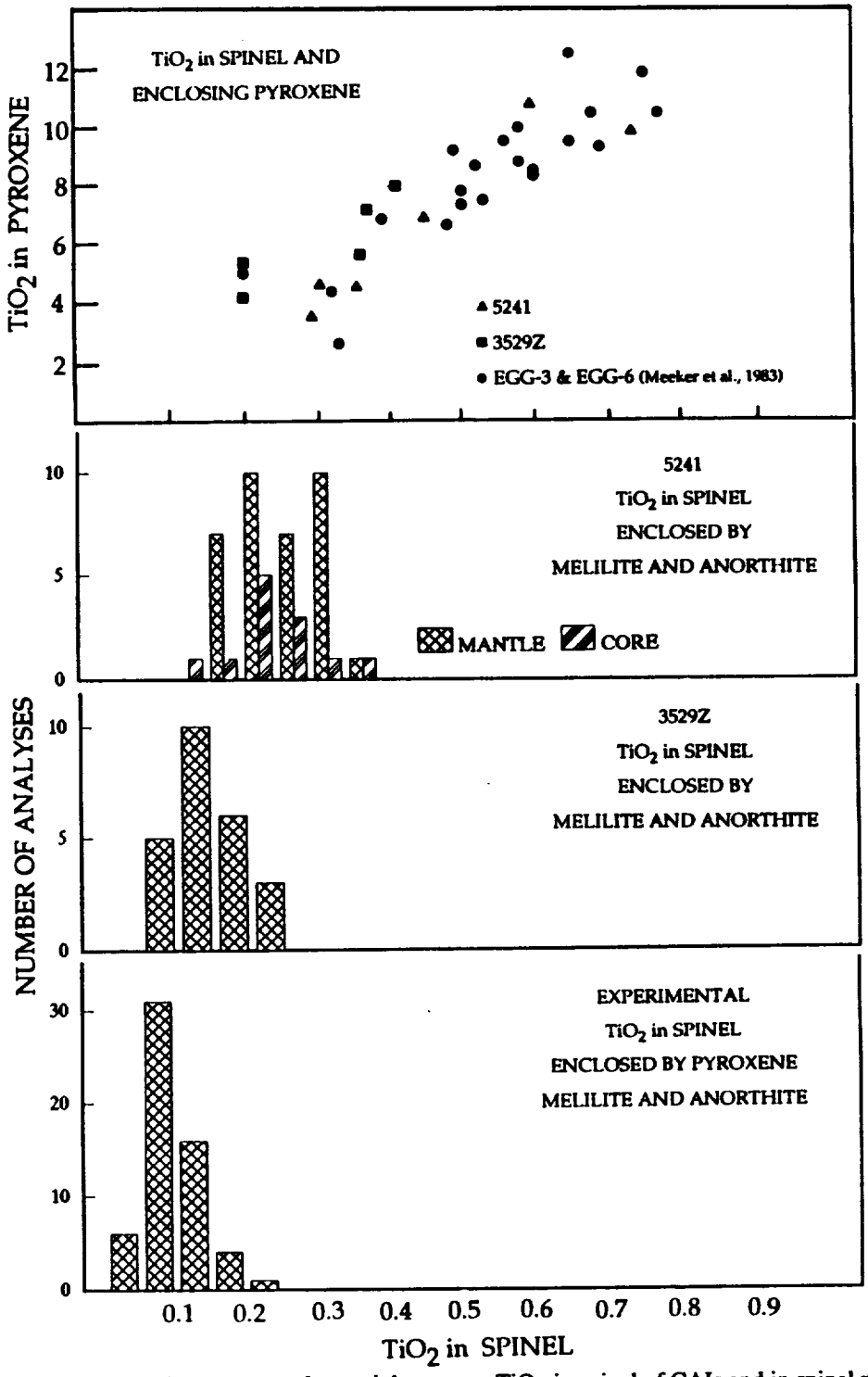

Figure 1. Ti concentrations expressed as weight percent TiO_2 in spinel of CAIs and in spinel produced by crystallization experiments. Data for spinels enclosed by pyroxene (top) plotted against Ti concentration of coexisting pyroxene. Histograms show Ti concentrations in spinel enclosed by melilite and anorthite and in spinel from experimental runs.

The Effects of Orbital and Climatic Variations on Martian Surface Heat Flow; Michael T. Mellon [1,2] and Bruce M. Jakosky [1,3]; [1] Laboratory for Atmospheric and Space Physics, [2] Department of Astrophysical, Planetary, and Atmospheric Sciences, [3] Department of Geological Sciences, University of Colorado, Boulder, CO 80309.

Introduction: Large changes in the orbital elements of Mars on timescales of 10^4 to 10^6 years will cause widely varying climate, specifically surface temperatures, as a result of varying insolation. These surface temperature oscillations will produce subsurface thermal gradients which contribute to the total surface heat flux. We investigate the thermal behavior of the Martian regolith on orbital timescales and show that this climatological surface heat flux is spatially variable and contributes significantly to the total surface heat flux at many locations.

Thermal Behavior: We model the thermal behavior of the Martian regolith by calculating the mean annual surface temperatures for each epoch (spaced 1000 years apart to resolve orbital variations) for the past 200,000 years at a chosen location on the surface. These temperatures are used as a boundary condition for the deeper regolith and subsurface temperature oscillation are then computed. The surface climatological heat flux due to past climate changes can then be found from the temperature gradient between the surface and about 150 m depth (a fraction of the thermal skin depth on these timescales). This method provides a fairly accurate determination of the climatological heat flow component at a point; however, this method is computationally time consuming and cannot be applied to all points on the globe.

To map the spatial variations in the surface heat flow we recognize that the subsurface temperature structure will be largely dominated by the most recent surface temperature oscillations. In fact, the climate component of the surface heat flow will be approximately proportional to the magnitude of the most recent surface temperature change. By calculating surface temperatures at all points globally for the present epoch and an appropriate past epoch, and combining these results with a series of more precise calculations described above, we estimate the global distribution of climatological surface heat flow.

Conclusions: From our calculations we find that orbital oscillations cause oscillations in the annual mean surface temperatures which produce a thermal wave penetrating kilometers in depth. As a result, surface heat flux from residual heat of past orbital epochs can be a significant component of the total surface heat flow at any particular location, in some instances even reversing the direction of, or doubling, the total heat flow.

The magnitude and direction of the climatological component will, of coarse, depend on the thermal history of each location on the surface. In general, the northern hemisphere most recently experienced a warming trend resulting in the subsurface retaining the past cooler temperatures, therefore the climatological heat flow will be into the surface opposing the interior geothermal heat flow. Similarly, the southern hemisphere has experienced a general cooling trend and will have a surface heat flow component which adds to the geothermal flux. The largest magnitude of the climate component of the heat flow was found to coincide with the maximum equatorward extent of the seasonal CO_2 polar caps.

The largest values of the climate component of the surface heat flow were found to be on the order of 30 mW/m^2, which is comparable to theoretical estimates of the geothermal component (ranging from about 20 mW/m^2 to 45 mW/m^2). This result indicates that care should be taken in choosing a location to attempt to measure the geothermal heat flow. In addition, though it has been suggested that a surface penetrator be used to measure the surface heat flow, a penetrator would be unable to separate the climate component from the geothermal component.

We suggest that future measurements of the surface heat flow on Mars be targeted for the equatorial and south polar regions where the climate component to the heat flow is minimal. We also suggest that care be taken in interpreting measurements taken in the north and south mid-latitude regions where the climate component is the largest. It may be possible to separate the climate component by measuring heat flow at geographically close locations (but with different surface thermal histories) or by measuring the latitudinal gradient in the heat flow. Such measurements may provide clues toward the orbital history, the past behavior of atmospheric and surface volatiles, and the history of the thermal properties of the surface.

N94-16403

Equatorial Ground Ice on Mars: Steady-State Stability; Michael T. Mellon [1], Bruce M. Jakosky [1], and Susan E. Postawko [2]; [1] Laboratory for Atmospheric and Space Physics, University of Colorado, Boulder, CO 80309, [2] School of Meteorology, University of Oklahoma, Norman, OK 73019.

Introduction: Current Martian equatorial surface temperatures are too warm for water ice to exist at the surface for any appreciable length of time before subliming into the atmosphere. Subsurface temperatures are generally warmer still and, despite the presence of a diffusive barrier of porous regolith material, it has been shown by Smoluchowski, Clifford and Hillel, and Fanale *et al.* that buried ground ice will also sublime and be lost to the atmosphere in a relatively short time. We investigate the behavior of this subliming subsurface ice and show that it is possible for ice to maintain at a steady-state depth, where sublimation and diffusive loss to the atmosphere is balanced by resupply from beneath by diffusion and recondensation of either a deeper buried ice deposits or ground water.

Steady-State Stability: We examine the behavior of equatorial ground ice with a numerical time-marching molecular diffusion model. In our model we allow for diffusion of water vapor through a porous regolith, variations in diffusivity and porosity with ice content, and recondensation of sublimed water vapor. A regolith containing considerable amounts of ice can still be very porous, allowing water vapor to diffuse up from deeper within the ice layer where temperatures are warmer due to the geothermal gradient. This vapor can then recondense nearer to the surface where ice had previously sublimed and been lost to the atmosphere. As a result we find that ice deposits migrate to find a steady-state depth, which represents a balance between diffusive loss to the atmosphere through the overlying porous regolith and diffusive resupply through a porous icy regolith below. This depth depends primarily on the long-term mean surface temperature and the nature of the geothermal gradient, and is independent of the ice-free porosity and the regolith diffusivity. Only the rate of loss of ground ice depends on diffusive properties.

Figure 1 shows the steady-state depths (calculated from an analytic model) as a function of mean surface temperature and geothermal gradient. For reasonable values of the geothermal gradient within an ice-free regolith (around 10^{-3} K/cm) and equatorial surface temperatures for the current epoch (200 to 220 K) depths range from 50 to 100 m. Figure 2 shows an example of a numerical simulation. The regolith is initially full of ice. Water sublimes from the top of the ice deposit and is lost to the atmosphere. Once a steady-state depth is reached the top of the ice is replenished by diffusion through the ice. When pores open up throughout the deposit overall loss occurs from the bottom.

The precise steady-state depth at a particular location will be complicated by deviations from a simple linear geothermal gradient caused by changes in thermal conductivity with depth above the ice layer and by variations in ice content within the ice layer. Long-term changes in climate due to orbital oscillations will also affect the depth by causing changes in the mean surface temperature, producing subsurface oscillations in temperature and in some cases reversing direction of the geothermal gradient for short periods, and by causing changes in the mean atmospheric water abundance. The atmospheric water abundance will affect the gradient in vapor pressure between the buried ice deposits and the atmosphere and therefore will affect the balance between loss and resupply which controls the steady-state depth.

Conclusions: From the results of our numerical simulations we conclude that, as long as ice exists in the subsurface or can be resupplied from beneath, the steady-state depth will be maintained. The depth at which ice may be found is generally closer to the surface than previously thought (due to recondensation of vapor) and will not increase with time, but may oscillate slightly with climate changes around a mean depth. Ice found closer to the surface will have less regolith to diffuse through to reach the atmosphere. This will result in a larger loss rate and ice will completely disappear sooner unless a deeper subsurface source exists.

Equatorial ground ice may exist close enough to the surface to be detectable by long wavelength ground penetrating radar. If ice is found to currently exist at this steady-state depth, this could either confirm the existence of a deeper source capable of resupplying the ice deposits at least as fast as the loss rate, or the existence of a non-porous cap at the steady-state depth: a cap above this depth would allow ice to migrate along the geothermal gradient toward the underside of this non-porous cap.

The depth of a steady-state ice deposit also has implications toward rampart craters, terrain softening, and channel formation. Rampart craters may have formed from the entrainment of subsurface volatiles during impact. The interpretation of the latitudinal dependence of the minimum rampart crater size is that craters excavate into a ground ice layer, the depth of which varies with location and time. However, the steady-state depths for reasonable geothermal gradients may be much shallower than depths estimated from rampart craters and will not vary in time (until all the ice is gone, if there is no source). Similarly terrain softening may be affected by ground ice closer to the surface than previously suspected providing a thicker zone for creep deformation. Ice could be available closer to the surface for a longer period of time, which could suddenly melt to form outflow channels, rather than steadily becoming deeper and less available as water is lost to the atmosphere.

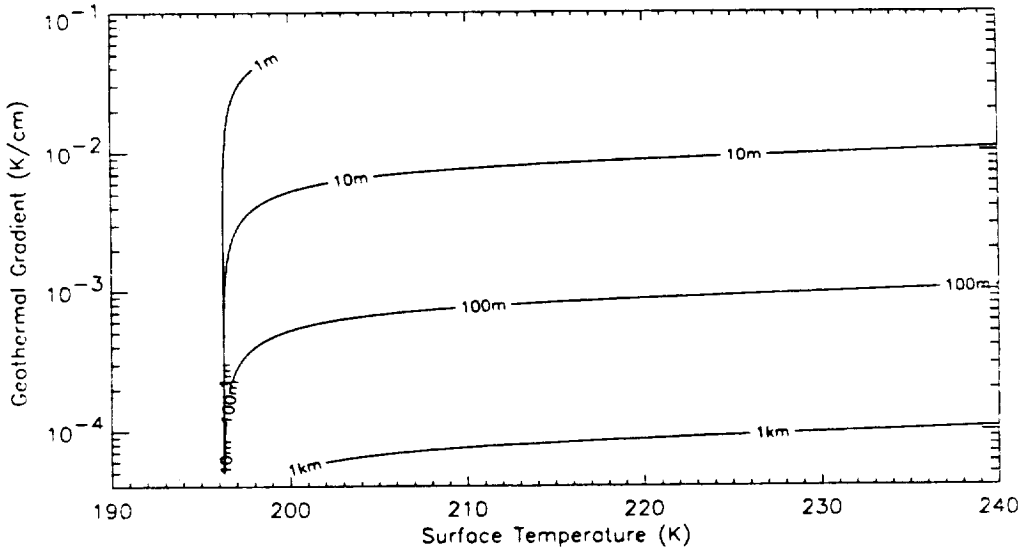

Fig. 1. Depth to the steady-state uppermost-occurrence of ice. These depths represent a balance between loss to the atmosphere and resupply from beneath following the geothermal gradient. Within the ice layer the geothermal gradient drives diffusion via the vapor pressure gradient. This simple model ignores the changes in thermal conductivity with depth as well as climate oscillations. The contours cut off at 196 K because we have chosen this temperature to represent frost stability with respect to the atmosphere.

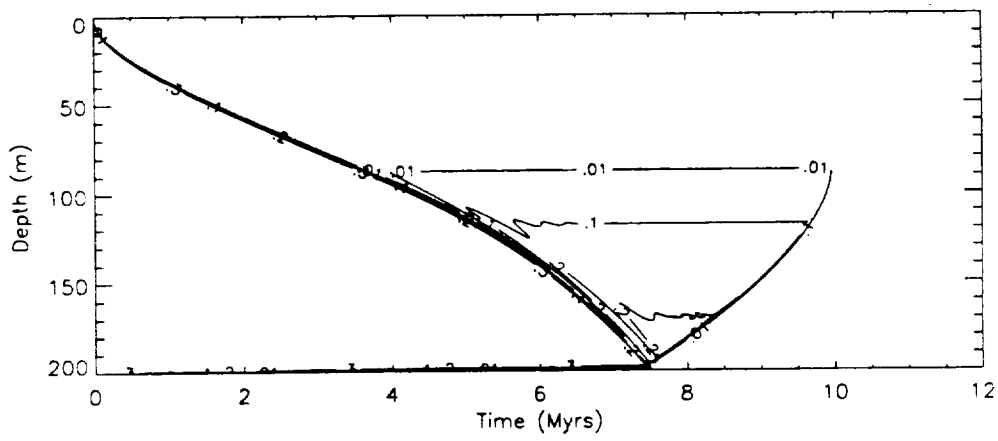

Fig. 2. Ice concentrations (g/cm^3) from a numeric simulation. Here we assume a mean surface temperature of 220 K and a geothermal gradient of 10^{-3} K/cm. 40% porosity is assumed, allowing a maximum of 0.37 g/cm^3 of ice as an initial condition.

REMOTE VISUAL DETECTION OF IMPACTS ON THE LUNAR SURFACE: H. Jay Melosh*, N. A. Artemjeva#, A. P. Golub#, I. V. Nemchinov#, V. V. Shuvalov#, and I. A. Trubetskaya#. *Lunar and Planetary Laboratory, University of Arizona, Tucson, Arizona 85721. #Institute for Dynamics of Geospheres, Russian Academy of Sciences, Moscow 117334, Russia.

Collisions of small meteoroids or comets with the terrestrial planets and their satellites are an important factor in the evolution of the Solar System [1]. Moderate size impacts on the Earth may even present a hazard to human civilization. Further information about the composition and size-velocity distribution of such objects is thus of great interest. We propose a novel method of remotely observing impacts on the airless Moon that may extend the present data base on meteoroids down to 1 m in diameter. Meteorites or comets of radius r_0 ~ 1-100 m are burnt away or dispersed in the atmospheres of the Earth and Venus. However, when such objects strike the Moon they deposit their energy in a small initial volume, forming a plasma plume whose visible and infrared radiation may be visible from the Earth.

We consider impacts of model SiO_2 projectiles on the surface of an SiO_2 model Moon (these compositions are chosen for simplicity, because the equation of state of SiO_2 is well known: more sophisticated analysis may be performed with more realistic compositions). Figure 1 shows the shock hugoniot and release adiabats in temperature-density coordinates for various impact velocities. These curves were computed following [2]. At velocities larger than 20 km/s initial shock temperatures reach 1-10 eV (1eV = 11,640 K). At such temperatures the radiation flux is an important part of the energy balance in the expanding plume.

The electromagnetic flux density from a hot volume is more than σT_*^4 while its temperature is more than T_*, the transparency temperature [3], which is equal to 0.5 eV for SiO_2. Here σ is Stefan-Boltzman constant.

Figure 1 shows that the transparancy temperature is reached when the density of the expanding plume plume declines to $\rho = 10^{-3}$ g/cm^3. The plume achieves this density after its volume has increased by 10^3-10^4 times. In other words, the temperature decreases to T_* when the size of the plume is equal to 10-15 r_0. The radiation flux from the impact can thus be estimated as $Q_{min} \approx 5 \times 10^2 r_0^2 \sigma T_*^4$. This relation gives the minimum value of Q, which is attained when $\rho V^3 < \sigma T^4$, where V is the impact velocity.

Using this estimate, we can evaluate the size r_c of the smallest projectile whose impact can be detected from the Earth. The sensitivity of modern photomultipliers is of the order of $Q_c \approx 10^{-6}$ W. If the radius of the telescope mirror (in the focus of which the detector is placed), R_T, is equal to 1 m, the radiation flux density must be more than $Q_c/\pi R_T^2$. Finally, the value of r_c can be estimated from the relation

$$\frac{Q_c}{\pi R_T^2} = \frac{5 \times 10^2 r_c^2 \sigma T_*^4}{2 \pi R_{ME}^2}$$

where $R_{ME} \approx 3.5 \times 10^8$ m is the distance between the Moon and the Earth. The result is $r_c \approx 1$ m.

This simple estimate shows that the radiation from small impacts on the Moon may be detected from the Earth with a modest telescope. The peak of the blackbody spectrum of this radiation is in the visible, since T_* is comparable to the surface temperature of the Sun. The duration of the resulting "flash" is brief: only a few milliseconds, but recording such flashes is well within the capability of modern instrumentation.

However, to go further and determine the composition of an impactor by such observations one must consider the physics of radiation emission in more detail. We have thus performed numerical simulations of the impact of SiO_2 bodies on the surface of an SiO_2 Moon using one-dimensional and two-dimensional gasdynamic codes. Detailed data on the optical

IMPACTS ON THE LUNAR SURFACE: H.J. Melosh *et al.*

properties of SiO_2 were used to describe the radiative transfer. These data were placed at our disposal by G. S. Romanov and his group (Institute of Heat and Mass Transfer, Minsk, Belarus). Figure 2 shows the time dependence of the radiation flux Q, in GW, within a unit solid angle for the case of $r_0 = 1$ m, velocity V = 50 km/s (cometary debris). The dashed line corresponds to the flux Q_E of radiation that reaches the surface of the earth (photons with energies $\varepsilon < 4$ eV).

Observations by equipment placed on satellites orbiting the Moon would allow detection of impacts of objects much smaller than 1 m. The spectrum and power of the radiation pulse may be used to determine the composition of the body and surface material as well as impactor's size and velocity.

Our investigation also shows that the radiative effects of impacts on the Moon are different from those on planets having atmospheres. In spite of high initial temperatures, the emitted radiative energy in lunar impacts is lower than the kinetic energy of the projectile due to the large initial optical thickness of plasma plume. By the time that the plume it is rarefied enough for the radiation to escape, most of the its thermal energy is converted into kinetic energy. On planets with atmospheres, however, the plume's kinetic energy is converted back into thermal energy of the atmospheric gases.

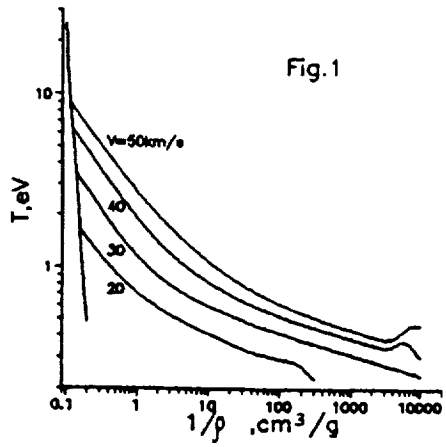

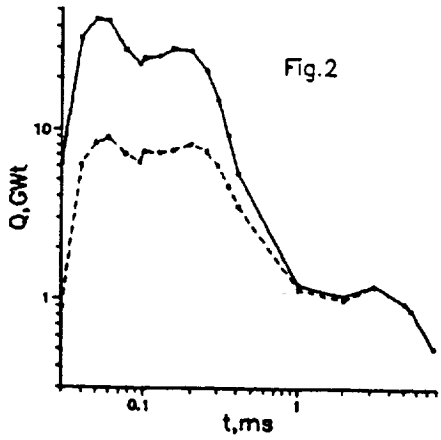

References: [1] Melosh, H. J. (1989) *Impact Cratering: A Geologic Process*, Oxford. [2] Vickery, A. M., J. Geophys. Res. **91**, 14,139-14,160. [3] Zeldovich, Ya. B. and Raizer, Yu. P., (1967) *Physics of shock waves and high temperature hydrodynamic phenomena*, Academic Press.

THERMOGEOLOGIC MAPPING OF THE MOON FROM LUNAR ORBIT

W. W. Mendell, SN4/Planetary Science Branch, NASA Johnson Space Center, Houston, TX 77058; M A. Wieczorek; SUNY at Buffalo, Dept. of Physics and Astronomy, Buffalo, NY 14260.

The Infrared Scanning Radiometer (ISR) onboard the Apollo 17 Command-Service Module (CSM) mapped thermal emission of the lunar surface from orbit. Measured temperature values span the diurnal range of lunar temperatures (85 K to 400 K) and have an accuracy of approximately ±2 K [1]. Surface spatial resolution at nadir is 2.2 km. This Apollo data is being revisited using data presentation software for the Macintosh computer, which was not available 20 years ago, even on mainframes. The new thermal images exhibit subtleties in the delineation of geophysical surface units that were unappreciated in the original survey of the data. Looking first at nighttime thermal emission from the ground tracks over Oceanus Procellarum to Mare Orientale, we have confirmed and expanded on earlier observations of regolith differences between mare and highlands and of a scheme for relative age-dating of larger impact craters of the Copernican age. We see an impact crater near Lenz, just north of Orientale, which exhibits an extraordinarily fresh ejecta blanket. Photography of this area is extremely poor, but we can see the feature in the Galileo data. We plan to derive geophysical surface properties of the overflown region using thermal models of regolith structures.

Thermogeologic mapping of the Moon began with ground-based infrared scans of the eclipsed Moon. Although the lunar disk cooled while in the Earth's shadow, certain features were observed to remain warm relative to the background. These features, called "thermal anomalies", were found subsequently to contain populations of surface rocks, usually excavated by relatively young craters.

Most rocks seen on the lunar surface today have been excavated from beneath mature regolith developed on the lunar highlands and the filled mare basins over the last 2 -3 billion years. Other surface rocks lie on crater rims or mountain tops where they have been exposed by impact-driven mass-wasting processes. All surface rocks are eventually comminuted to soil by the ubiquitous meteorite flux, but the time required to fracture and destroy a rock is a nonlinear function of its size [2]. The most prominent features on thermal maps of the nighttime lunar surface therefore document the most recent lunar depositional and erosional history. In addition, more subtle features in the images relate to regolith maturity, directionality of emissivity, solar albedo, and surface roughness.

Maria-Highland Differences

The data analyzed here are predominantly from within the Procellarum and northern Orientale regions. Most of the thermal anomalies found in this region are associated with features such as primary impact craters and rilles. In general, the highlands are characterized by a low thermal contrasts, while the maria contain a much larger concentration of thermal anomalies on the order of one resolution element in size. Thermal enhancements for resolution-sized features in typical highlands units are approximately 4 K, whereas enhancements in typical maria units are 8 K. Apparently, surface rocks associated with impacts in the highlands are not as numerous, or the rock populations have been comminuted to smaller sizes as a result of exposure to meteorite erosion. The observations suggest that kilometer-sized craters exhibit more excavated bedrock in Procellarum because the regolith there is thinner than in the highlands to the west.

The maria contain abundant medium to large (15-90 km) thermally enhanced impact craters, while such craters with thermal enhancements greater than 10 K are rare in the highlands. Two exceptions are the craters Olbers A and a small unnamed crater located at 259E, 2.56N, approximately 5 km to the southeast of Lenz Crater. The remainder of large anomalies within the highlands come from small craters, ≤ 6 km diameter, having high central temperatures and a slightly thermally enhanced ejecta deposit. Many highland craters classified as Copernican in age, such as Conon, appear relatively featureless and have temperature enhancements much lower than other Copernican craters.

Although a large crater such as Olbers A would be expected to exhume large blocks from beneath the highlands regolith, the smaller craters should not. However, most craters larger than Olbers A do not have significant thermal enhancements. Even if these large craters were unable to expose bedrock or exhume large blocks, impact melt would be expected to form within the crater floor, giving the crater a large thermal enhancement. In order to explain this contradiction, it is proposed that mass wasting processes, such as slumping, avalanching, and the downslope migration of surface materials may operate at much higher rates in the highlands. A highly incoherent regolith would facilitate the movement of materials from the rim crest to crater floor and would essentially cover exposed rock with a layer of fine-grained materials.

Mass Wasting Along Scarps

Several cool anomalies are found. The most noticeable are linear features that lie at the boundary between the Apennines and Mare Imbrium. These cool anomalies correspond to a unit mapped by Hackman [3] as *slope material* which is found at the base of steep slopes. Hackman, however, describes this unit as exposed bedrock and partially sorted talus materials. Since low temperatures are consistent with loose, fine-grained surface materials, this unit may be fine-grained debris. It is possible that these debris deposits are continually accumulated as a metastable regolith forms on a steep slope and sporadically avalanches as minor instabilities arise. Similar deposits are also found along the Carpathians and along the edge of Lacus Veris.

Crater Halos

Within the maria, many of the thermally enhanced craters and their ejecta blankets (if present) are surrounded by an annular region which lacks thermal features and is often cool relative to the surroundings. In general these "halos" span up to one crater radius away from the enhanced ejecta or two crater radii from the crater rim crest. Halos around craters in the highlands such as Olbers A are featureless, but are not noticeably cooler than the surroundings. Typically, crater halos located in the mare have a temperature approximately 2 K lower than the surrounding region,. There appear to be a continuum of states ranging from craters having enhanced ejecta deposits and well defined halos, to craters containing only a well defined halo extending from the rim, to craters containing halos that are barely distinguishable with respect to the surroundings. Mendell [1] has proposed that crater halos could be a result of the blanketing of subresolution (~100 meters) craters with the ejecta from a larger crater. The concentric placement of the halos around the blocky craters suggests that it is a part of the original ejecta blanket which has had its surface rocks comminuted into soil. This scenario could work if the ejecta from a large crater has a gradation of large blocks near the rim crest to smaller blocks at the edge of the ejecta deposit. Since small blocks erode at a faster rate than larger ones, the halo should appear to expand towards the rim crest as the ejecta deposit erodes through time. As smaller craters form within the halo, the region should loose its cool appearance because of the excavation of blocks beneath the thin, fine-grained cover.

Conclusions

The Apollo 17 ISR obtained high resolution thermal maps of the lunar surface that show document the degradation of geologically young lunar features. Evidence of mass wasting processes is found at the base of the Apennine scarp and other high relief slopes. Slumping, avalanching, and the downslope migration of surface materials are also believed to be responsible for the decrease in temperatures of crater floors. Micrometeorite weathering is believed to play a major role in the production of soils on relatively flat surfaces. Models of the lunar surface thermal regime and of the fragmentation of rocks should allow estimation of ages for many Copernican Age features.

References:

[1] Mendell W. W. (1975) *Proc. Lunar. Sci. Conf. 6th*, p. 2711-2719. [2] Horz, F., et al. (1975) *The Moon*, **13**, 235 - 258.. [3] Hackman R. J. (1966) 'Geology of the Moon: Montes Apenninus Region,' *I-463 (LAC-41)*. U.S Geological Survey Geological Atlas of the Moon.

DEUCALIONIS REGIO, MARS: EVIDENCE FOR A UNIQUE MINERALOGIC ENDMEMBER AND A CRUSTED SURFACE; E. Merényi[1], K. S. Edgett[2], R. B. Singer[1]; [1]University of Arizona, LPL, PIRL, Tucson, AZ 85721; [2]Department of Geology, Arizona State University, Tempe, AZ 85287-1404

A small equatorial region south of Sinus Meridiani, Deucalionis Regio, has been found spectrally distinct from other regions as seen in a high spectral resolution telescopic image of the meridian hemisphere of Mars. Analysis of Viking IRTM and other related data suggest that Deucalionis Regio has a crusted surface. The crust-bonding minerals may contribute to the spectral uniqueness of this region.

Deucalionis Regio is a cigar-shaped, moderate-albedo region which runs nearly parallel to the Martian equator, just south of Sinus Meridiani and Sinus Sabaeus. Its main body extends from about 10W to 340W and between 13S and 17S. The western end has a narrow continuation which curves to the northwest at a nearly right-angle toward Oxia, to form the southern and western borders of Sinus Meridiani. Deucalionis Regio was frequently observed throughout the 19th and early 20th centuries, during which time it often appeared to change color, and showed occasional dark streaks [1]. This relatively nondescript region has received little attention in the spacecraft-era Mars literature because, it has not seemed as interesting as the surrounding regions such as Arabia, Sinus Meridiani, or Oxia.

Owing to a near-infrared, multispectral image we found that this region was worth more attention. The spectral image was obtained during the 1988 Mars opposition, 26 September, by the 1.5 m telescope at the University of Arizona's Catalina Station near Tucson, Arizona. It is centered south of Sinus Meridiani, has 280 x 150 km/pixel resolution at sub-earth point, and 300 spectral channels in the 0.44 to 1.04 μm range. The data are described by [2].

Two independent analyses of the above spectral image, linear spectral mixing and supervised classification based on the spectral shapes, showed that in addition to the well-known spectral endmember regions in this image (western Arabia, south Acidalia, and Sinus Meridiani), Deucalionis Regio has spectral properties that are unique enough to make it a principle endmember unit [3] [4]. In those earlier works, Deucalionis Regio was referred to as "Meridiani Border."

Analysis of thermal inertia, rock abundance, and albedo information derived from Viking images and Infrared Thermal Mapper (IRTM) data obtained 1977-80 also indicate that Deucalionis Regio has a surface of distinctly different physical properties when compared to Arabia, Sinus Meridiani, and Acidalia. Deucalionis Regio has a thermal inertia equivalent to the Martian average (5.1-6.9), a low rock abundance (<5%), and an intermediate albedo and color. Considerable effort by previous investigators has revealed a consistent model for the surface (upper few cm) properties of the endmember regions Arabia, Sinus Meridiani, and Acidalia (e.g. [5] [6] [7] [8] [9]). Compared with these regions, we consider that Deucalionis Regio is not a region of either 1) unconsolidated, fine bright dust like Arabia, 2) considerable windblown unconsolidated sand like Sinus Meridiani, or 3) a rocky-and-sandy surface like Acidalia. Thus, we are forced to consider that either the surface of Deucalionis Regio is made of unconsolidated fine to medium sand (about 250 μm) of an unusual and previously unreported color and albedo, or that the surface is crusted, fine-grained weathered soil, and the thermal inertia is an indicator of the degree to which the surface sediments have become indurated. We favor the latter.

Crust, or "duricrust," was observed at the Viking lander sites. It may consist largely of dust- and silt-sized grains bonded by Cl- and S-rich salts, and may be an ubiquitous feature of the Martian surface layer, especially where not currently covered by loose aeolian debris [10]. Deucalionis Regio may indeed be a southern extension of a set of proposed

crust layers of differing degrees of induration that are semi-concentric to Arabia, seen in Oxia (a similar arrangement semi-concentric to Tharsis is seen on Lunae Planum) [11] [12].

Deucalionis Regio, though probably crusted, is not entirely without wind-worked unconsolidated sediment, as evidenced by the occasional dark streaking seen by earlier astronomers [1], and evidenced by small (relative to other medium-thermal inertia regions) amounts of dark, perhaps sandy [13] sediment on a few crater floors. However, for the most part, Deucalionis Regio appears to be devoid of loose material. This is interesting, because wind shear stress patterns derived from General Circulation Model results for present climate conditions [14] [15] suggest that Deucalionis Regio is fairly windy compared to Arabia, Sinus Sabaeus, and Sinus Meridiani. That the surface of Deucalionis Regio is not made up of loose material is bolstered by the observation that none of the localized dust storms catalogued by Peterfreund [16] for the period of 1914-1980 originated in this region, though many formed in the surrounding, lower-albedo regions.

We propose that much of the Deucalionis Regio surface, particularly a region approximately 200 km in diameter near 15S, 350W, has a well-exposed, crusted surface. We speculate that the endmember spectral character of this surface may be an indicator of the crust-bonding minerals (salts), or at least serve as an indicator that the proposed indurated sediments have certain minerals that are not apparent in regions of thick unconsolidated sand or dust cover. It is interesting to note that the "brown" unit in Oxia, also proposed to be an exposure of duricrust [8] covers 50 to 80% of the Oxia surface, and in the mixture model of the 1988 spectral image of Mars, referred above, Oxia has over 50% contribution from the Deucalionis Regio endmember.

The ratio of averaged Deucalionis Regio spectra to averaged spectra of other type regions can provide key information on the mineralogic uniqueness of Deucalionis Regio. In particular, comparision to Arabia might give the best clue if we accept the working hypothesis that these two regions originally consisted of the same material and crust formation added new component(s) to Deucalionis Regio. However, such comparision may be complicated by large-scale areal mixing or non-linear mixing and scattering differences of the pure mineral spectra that constitute the type region spectra. Further analysis concerning possible mineralogy will be forthcoming. In addition, we anticipate that Mars Observer Thermal Emission Spectrometer mid-infrared spectra that will be obtained for this region should be able to provide further constraints on the proposed Deucalionis Regio crust and crust-bonding-agent mineralogy.

REFERENCES:

[1] Antoniadi, E.M. (1930), La Planète Mars, Hermann et Cie, Paris.
[2] Singer, R. B., J. S. Miller, W. K. Wells, E. S. Bus, (1990), *Lunar and Planetary Sci XXI*, 1164-1165
[3] Merényi, E., J. S. Miller, R. B. Singer (1992), *Lunar and Planetary Sci. XXIII*, 897-898
[4] Merényi, E., R. B. Singer, J. S. Miller (1992), *Bull. A.A.S., 24* No. 3 979
[5] Zimbelman, J.R. and H.H. Kieffer (1979) *J. Geophys. Res., 84*, 8239-8251.
[6] Christensen, P.R. (1986) *J. Geophys. Res., 91*, 3533-3546.
[7] Christensen, P.R. (1986) *Icarus, 68*, 217-238.
[8] Presley, M.A. and R.E. Arvidson (1988) *Icarus, 75*, 499-517.
[9] Arvidson, R.E. *et al.* (1989) *J. Geophys. Res., 94*, 1573-1587.
[10] Jakosky, B.M. and P.R. Christensen (1986) *J. Geophys. Res., 91*, 3547-3560.
[11] Christensen, P.R. and M.C. Malin (1988) *Lunar and Planetary Sci. XIX*, 180-181.
[12] Christensen, P.R. and H.J. Moore (1992) In *MARS*, Univ. Arizona Press, 686-729.
[13] Edgett, K.S. and P.R. Christensen (1993) *J. Geophys. Res.* (submitted, in review).
[14] Skypeck, A.P. (1989) M.S. Thesis, Ariz. State Univ., Tempe, 78p.
[15] Pollack, J.B. et al. (1990) *J. Geophys. Res., 95*, 1447-1473.
[16] Peterfreund, A.R. (1985) PhD Thesis, Ariz. State Univ., Tempe, 246p.

DO IT YOURSELF REMOTE SENSING: GENERATING AN INEXPENSIVE, HIGH TECH, REAL SCIENCE LAKE MAPPING PROJECT FOR THE CLASSROOM; Stephen M. Metzger, St. Lawrence University Geography, Canton, NY, 13617.

The utilization of modest equipment and software revealed bottom contours and water column conditions of a dynamic water body. Classroom discussions of field techniques and equipment capabilities followed by exercises with the data sets in cause-and-effect analysis all contributed to participatory education in the process of science. This project is presented as a case study of the value of engaging secondary and collegiate level students in planning, executing and appraising a real world investigation which they can directly relate to.

A 1 km wide bay, experiencing marsh inflow, along an 8 km long lake situated 120 km north of Ottawa, Canada, on the glaciated Canadian Precambrian Shield was mapped in midsummer for submerged topography, bottom composition, temperature profile, turbidity, dissolved oxygen and biota distribution. Low level aerial photographs scanned into image processing software are permitting spatial classification of bottom variations in biology and geology.

Instrumentation consisted of a portable sport fishing SONAR depth finder, an electronic lead line multiprobe with photocell, thermistor and dissolved oxygen sensors, a selective depth water sampler, portable pH meter, an underwater camera mounted on a home-made platform with a bottom-contact trigger and a disposable underwater camera for shallow survey work. Sampling transects were referenced using a Brunton hand transit triangulating several shore markers. SONAR readings and bottom photographs were taken at each sampling station. Unlike most modern digital systems, the analog SONAR's spinning neon display gave different readings depending on the reflectivity characteristics of the lake bottom. Multiprobe readings were also taken throughout the water column at each sampling station, noting the level of the thermocline. The water sampler allowed independent temperature measurements in addition to acidity readings and the occasional bottom material specimen.

Kodachrome 35 mm color slides of the bay taken from a small plane at 300 m have been scanned into a satellite image processing raster GIS package (IDRISI) as a 3 band (RGB) image. This new representation is being referenced to the SONAR, lead line and underwater camera remote sensing that preceded it.

Results indicate that dissolved oxygen and turbidity levels were elevated along the wave-churned shoreline and at the marsh outlet. A distinct thermocline at 6 m depth with visible shear planes dipping lakeward separated the 2'C anoxic hypolimnion from the 18'C epilimnion. Zones of mollusks and grasses were delineated parallel to the beach by the underwater camera and snorkeling forays. Mud, sand, boulder and sunken log distributions were interpreted after correlating SONAR texture readings with snorkeling examinations of type localities.

DO IT YOURSELF REMOTE SENSING: Metzger, S.

Students have performed all aspects of data reduction including plotting sample sites from compass readings, manually estimating topographic contours, using spread sheet software to chart temperature profiles, generating 3-D computer mesh diagram perspective views of the bottom topography (fig. 1) and more elaborate image processing procedures currently underway to derive bottom contours and the geographic distribution of bottom materials from the aerial photographs. Acetate overlays were used to link the observed conditions with their environmental settings and formative causes. They discuss all aspects of the exploration process including:

- the local environment & habitat,
- desirable research goals,
- the equipment available & its capabilities or weaknesses,
- field measuring problems and sources of error,
- plotting & computing decisions,
- whether data & analyses make sense,
- how different environmental aspects interact,
- presentation of results

and when to declare the project finished.

The very real-world flavor of this inquiry is reinforced by photographs, specimens of drift wood & mounted birds or fish, recordings of Loon calls and classroom examination of the equipment with outdoor demonstrations where possible. Every student has been responsible for reporting their results in an orderly manner. Thus the esoteric and practical aspects of science become tangible, especially when THEY propose the quest.

References:

Bartier, P.M., & Keller, C.P., 1992, GIS Capabilities for the Earth Sciences: J Geological Education, v. 40, p. 360-366.

Emery, K.O., 1969, A Coastal Pond Studied by Oceanographic Methods: New York, American Elsevier, 80 p.

Hutchinson, G., 1957, A Treatise On Limnology: New York, Wiley and Sons

Mathews, W.H., 1956, Physical Limnology and Sedimentation in a Glacial Lake: GSA Bull., v. 67, p. 537-552.

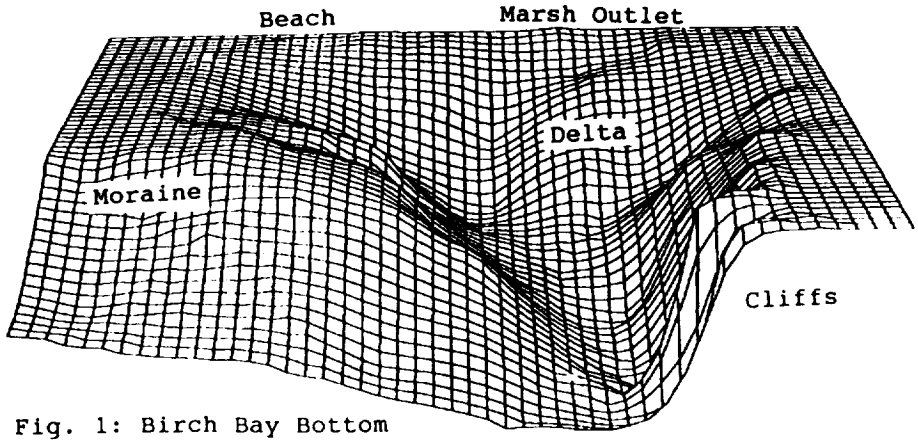

Fig. 1: Birch Bay Bottom

OPPORTUNITY FOR EARLY SCIENCE RETURN BY THE ARTEMIS PROGRAM

Charles Meyer, SN2, NASA Johnson Space Center, Houston TX

The purpose of the Artemis Program is to gather vital scientific and engineering data by conducting robotic exploration missions on the lunar surface both prior to and concurrent with human missions. The Artemis Program includes rapid, near-term development of a variety of small experimental and operational payloads, a low-cost capacity to deliver these payload to any location on the lunar surface, and the analysis of the data returned. The Artemis Program will provide opportunities to improve the understanding of lunar geosciences, to demonstrate the Moon's unique capacity as an astronomical platform to study the universe, to conduct scientific and technology development experiments, and to prepare for and complement human missions.

"Human beings have never yet put their footprints on a new land and then turned back, never to return." [1] However, the return to the lunar surface should include a partnership of robots and humans working together [2]. Robotic missions should explore numerous places on the Moon based on site selection using data collected by lunar polar orbiters and Earth-based telescopic observation. Rovers should be used to reconnoiter the landing area and paths to be followed by human explorers. Once a site for a lunar base is selected, rovers should be used to extend the reach and capability of astronauts. Multi-spectral imaging systems and various analytical instruments on rovers will allow close-up observations of outcrops and preliminary selection of important samples to be returned to Earth. Although, human field geologists may be required to make the final selection of samples to be returned, well-equipped rovers could make an informed preliminary examination of numerous samples collected from a wide area over a long period of time. Astronauts working out of a lunar base would then be able to concentrate their time on the most important outcrops. Rovers could also be used to deploy, align and attend geophysical and astronomical instruments as well as pilot plants for "resource" development. In general, tasks that can be accomplished by robots should not be done alone by humans.

Scientific goals for future robotic lunar geoscience lander missions are; 1) to develop a more complete understanding of the stratigraphy, structure, composition and evolution of the lunar crust by close examination of the geology and geochemistry of multiple, carefully-selected, wide-spaced landing sites on the Moon; 2) to improve the understanding of the lunar regolith and history of solar system events that have affected the lunar surface; 3) to improve the understanding of the lunar interior and set constraints on planetary evolution using geophysical techniques; 4) to identify and characterize potential lunar "resources" that could be utilized by future human missions; and 5) to identify and transport important samples to a (future) sample return vehicle. A high degree of mobility is a primary requirement for lunar geoscience landers. Chemical and mineralogical analyses are required for hundreds of samples, including rock fragments, collected over hundreds of kilometers. Exploration of the Moon using scientific rovers would also provide additional engineering data and confidence for mission planners for the use of similar devices on Mars and provide significant educational and training opportunities for the next generation of space explorers and robotics engineers.

Scientific rovers should be designed as integrated scientific measurement systems. There is currently much enthusiasm for the use of rovers in planetary exploration [3], but scientific goals (above) must remain the focus of this enthusiasm and all of the instruments, cameras and high-fidelity, supporting elements must work together as a system. Scientists experienced with the study of samples returned by Apollo will demand that rocks be studied as well as regolith samples and that certain key elements be measured with precision. The Russian Lunokhod has already demonstrated the engineering feasibility of wide-ranging mobility on the lunar surface, however, future lunar rovers should be able to travel several hundred kilometers and last several lunar nights. One of the current programmatic problems that must be overcome, is that the development of analytical instrumentation for use on planetary surfaces has been sadly neglected for many years. A light-weight alpha and proton backscatter spectrometer is flight-ready and a backscatter Mossbauer spectrometer is under development. However, additional instrument development is essential. Light-weight, CCD-based multi-spectral imaging systems, covering

ARTEMIS PROGRAM: Charles Meyer

the spectrum from 0.3 to 2.5 microns, are the result of an emerging technology that will become available, but auto-focus lenses for these cameras need to be developed for the cold lunar environment. Manipulator arms, close-up cameras and supporting systems would make a true robotic field geologist! With these instruments and tools, a highly mobile rover will be able to measure the chemical and mineralogical composition and texture of samples *in situ* . Each Artemis rover should also deploy a small seismograph, such as designed for the MESUR missions, a short distance from the lander, until there is a global seismic network on the Moon.

Previous study of the Moon has focused on the small area of the Apollo and Luna landings. There is evidence that rock types might be quite different at distant locations on the Moon. The new geochemical data from Galileo [4], and expected from Clementine and Scout, will allow us to target specific geochemical regions that will require "ground truth" from robotic missions and eventual sample return. From Apollo we have learned that the large basins on the front side have covered the northern highlands with thick sheets of "gray ejecta." However, Earth-based telescopic studies now show a number of places in the southern highlands, where there are apparently windows through the basin deposits of gray ejecta [5], that should be investigated by highly-instrumented scientific rovers.

The Moon has several advantages as a potential site for astronomical observations as well as several apparent disadvantages (cold, dusty environment) that need to be explored and overcome. The lack of essentially any lunar atmosphere allows superb viewing conditions in the ultraviolet wavelengths and several proposals have been made for a sky survey in the UV by small robotic lunar telescopes operating around 200 nm. This concept was already proven during Apollo 16, but the azimuth tracking mechanism partially froze in the shade of the LM requiring astronaut intervention. Since experience is the great teacher, numerous other, small precursor telescopes should be attempted before large lunar telescopes are assembled by human missions. The Moon itself has very low seismic activity such that it may serve as an ideal platform for long-baseline interferometry. However, the extreme thermal variations make design of stable telescopes a difficult proposition. Experimentation would seem appropriate. Since the Moon always points towards the Earth, the Moon would be an ideal site for extreme ultraviolet imaging of transitory phenomena associated with the solar wind interaction with the Earth's outer magnetosphere. In this way, long-term, synoptic viewing of the Earth's magnetosphere at various wavelengths in the EUV (30 nm) would allow a study of variations in the corpuscular radiation of the Sun and test models of the Earth's (and other planets) magnetosphere(s).

The extraction of oxygen from lunar rocks has been suggested as a potential "resource" for human missions to the Moon and beyond. Ilmenite-rich soils and/or iron-rich glass deposits have been shown to have the highest yield of H_2O in a hydrogen furnace. Robotic missions should be used to locate these deposits and to test pilot plant operations prior to human missions. Depending on the results achieved by experiments performed on robotic missions, the scenario for the first lunar outpost may be changed.

JSC has designed a Common Lunar Lander for the Artemis Program based on a planned payload weight of 200 kg. This weight was selected to meet the requirements for large scientific rovers, small (0.8 m) telescopes, pilot plants and even for potential sample return in the future. Under present scenarios, the Artemis lander could land 85 kg using a Delta II or 200 kg using an Atlas launch vehicle. In the JSC design, no payload services will be provided by the lander vehicle, but it will be able to safely land a payload anywhere on the lunar surface (within 3 km, 3 sigma). The top of the landed vehicle will be about 60 inches above the lunar surface. This newly-designed spacecraft makes use of several recent technology developments including; graphite-epoxy structure, fiber-overrapped tanks, SDI light-weight, high-performance engines, a new range velocity sensor, a new light-weight Startracker and a central avionics architecture. The Common Lunar Lander could be flight-ready in about 3.5 years from start.

References: [1] Heiken G., Vaniman D. and French B. (1991) The Lunar Sourcebook: a users guide to the moon, Cambridge Univ. Press, p640. [2] U. S. Congress, O.T.A. (1991) Exploring the Moon and Mars: Choices for the Nation, U.S. Gov. Printing Office. [3] see for example, Planetary Report Nov/Dec 1992; Final Frontier Feb 1993. [4] Belton M. et. al. (1992) Lunar Impact Basins and Crustal Heterogeneity, Science **255**, 570. [5] Hawke B et. al. (1992) The Distribution and Modes of Occurrence of Lunar Anorthosite: abs. LPSC XXIII, 505, LPI.

^{26}Al PRODUCTION PROFILE AND MODEL COMPARISONS IN CANYON DIABLO; E. Michlovich[1], D. Elmore[1], S. Vogt[2], M. Lipschutz[2], J. Masarik[3], R.C. Reedy[3]. Departments of Physics[1] and Chemistry[2], Purdue University, West Lafayette, IN 47907; Space Science and Technology Division[3], Los Alamos National Laboratory, Los Alamos, NM 87545.

The large preatmospheric size of the Canyon Diablo meteorite, a radius of about 15 m, makes it especially suitable for systematic studies of cosmogenic nuclide production rates of iron objects in a 2π geometry. To reconstruct the exposure history of the meteoroid, Heymann *et al.* (1) investigated several fragments recovered from known geographic locations around the crater for their shock features and cosmogenic noble gases. They applied the Signer-Nier noble gas production rate model (2) to establish the preatmospheric depth of the specimens in the meteoroid. Cosmic ray exposure ages suggested a multi-episodic irradiation, with 170 or 540 Ma being inferred for most of the samples studied while two anomalous specimens indicated a possible third exposure age at 940 Ma. ^{10}Be and ^{36}Cl have been measured in a number of these same samples (3) by accelerator mass spectrometry (AMS), with use being made of the preatmospheric depths determined in (1) to construct production profiles. The present study extends the cosmogenic radionuclide data to ^{26}Al and compares the results with both the production rate model of Reedy and Arnold (4) and production rates determined from the cross sections used by the Reedy-Arnold model (for the major nuclear reactions making ^{26}Al) in combination with differential fluxes calculated using the Los Alamos High Energy Transport (LAHET) Code System. Model calculations for ^{10}Be and ^{36}Cl have also been obtained and will be presented. All AMS measurements were made at the PRIME Lab facility at Purdue University.

Figure 1 shows the ^{26}Al results. Production rates were calculated by correcting activities to the 50 ka terrestrial age (5,6). The half-attenuation length of the profile is 85 g/cm^2 (10.8 cm). Three samples anomalously low in ^{26}Al are seen around d = 27 cm. These samples are correspondingly low in ^{10}Be and ^{36}Cl: their noble gases are being re-measured. A sample with no measurable noble gas content was analyzed to give an estimate of the lower discrimination level (0.03 dpm/kg). A comparison of data for the 3 measured radioisotopes yields a production rate ratio of P(^{10}Be)/P(^{26}Al) and P(^{36}Cl)/P(^{26}Al) of 1.46±0.06 and 7.5±0.4 dpm/kg respectively, in good agreement with values cited in (7) and references therein from studies of small irons.

The results of the model calculations are also shown in Figure 1. The composition of the Canyon Diablo matrix was taken to include 7.1% Ni, 0.4% Co and 0.2% P. The Reedy-Arnold model curve is very similar in half-attenuation length to the experimental result, but a factor of 3 lower in magnitude. By contrast, production rates calculated from LAHET results yield a profile in relatively good agreement with experiment. This suggests that the build-up of the secondary particle flux in the iron-nickel matrix of Canyon Diablo may be significantly different from that seen in silicate matrices, where the Reedy-Arnold model has heretofore been applied. Such bulk composition dependence on flux development has previously been reported in (8).

We calculated cosmic ray exposure ages using the ratio ^{26}Al/^{21}Ne and the relative production rate of R = 0.51± 0.03 determined in (9) from a calibration of ^{26}Al/^{21}Ne ratios with ^{41}K/^{40}K exposure ages in several meteorites. These age estimates include only one (CD 4337) which seems to belong to the 170 Ma group proposed in (1). The remaining samples have ages which are generally consistent with 540 Ma. The results fail to confirm the existence of the 940 Ma group.

CANYON DIABLO: Michlovich *et al.*

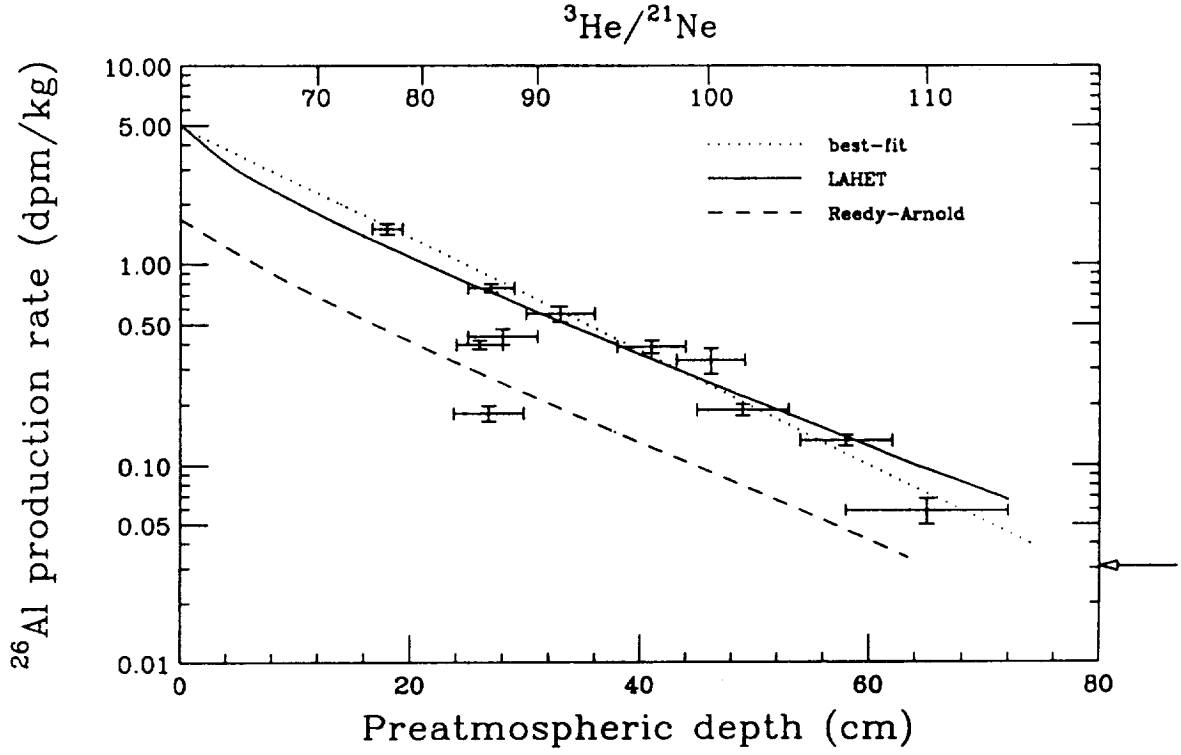

Figure 1 . Production rate of ^{26}Al vs. preatmospheric depth in Canyon Diablo. The arrow indicates the result of the sample with no cosmogenic gases.

(1) Heymann D., Lipschutz M., Nielson B., Anders E. (1966) *J. Geophys. Res.* **71**, 619-641.

(2) Signer P. and Nier A.O. (1960) *J.Geophys.Res.* **65**, 2947-2964.

(3) Michlovich E., Lipschutz M., Shortreed M., Vogt S., Elmore D. (1992) In *Lunar Planet Sci. XXIII*, 907-908.

(4) Reedy R.C. and Arnold J.R. (1972) *J. Geophys.Res.* **77**, 537-555.

(5) Phillips F., Zreda M.G., Smith S.S., Elmore D., Kubik P.W., Dorn R.I., Roddy D.J. (1991) *Geochim. Cosmochim. Acta* **55**, 2695-2698.

(6) Nishiizumi K., Kohl C.P., Shoemaker E.M., Arnold J.R., Klein J., Fink D., Middleton R. (1991) *Geochim. Cosmochim. Acta* **55**, 2699-2703.

(7) Vogt S., Herzog G.F., Reedy R.C. (1990) *Rev.Geophys.* **28**, 253-275.

(8) Masarik J. and Reedy R.C. (1992) *Meteoritics* **27**, 256.

(9) Aylmer D., Bonanno V., Herzog G.F., Weber H., Klein J., Middleton R. (1988) *Earth Planet. Sci. Letters* **88**, 107-118.

EXSOLVED KIRSCHSTEINITE IN ANGRITE LEW86010 OLIVINE:

Takashi Mikouchi[1], Hiroshi Takeda[1], Hiroshi Mori[1], Masamichi Miyamoto[1] and Gordon McKay[2] ; [1]Mineralogical Institute, Faculty of Science, University of Tokyo, Tokyo 113, Japan [2]NASA SN2, Johnson Space Center, Houston, TX77058, USA

Mineralogy of kirschsteinite exsolution in olivine from Antarctic meteorite LEW86010 has been studied by single crystal X-ray diffraction technique. The LEW86010 olivine crystals have exsolution lamellae of kirschsteinite about 15 μm wide[1]. Determination of crystallographic orientation of exsolved kirschsteinite in an olivine grain has been made. Weak reflections of exsolved kirschsteinite share common crystallographic orientation with the host olivine. The cell dimensions of the exsolved phase (*a* 4.87±0.05Å, *b* 11.14±0.10Å, *c* 6.36±0.05Å) and intensities were well accord with those of kirschsteinite previously reported[2]. Oriented section perpendicular to the *a* axis shows exsolution lamellae in two directions parallel to (031) and (0$\bar{3}$1) . The lamellae are up to 10 μm in width and spacings between them were usually 50-100 μm.

INTRODUCTION

Angrite group with only four total meteorites, are classified as a unique achondrite with remarkably high Ca, Al and Ti never seen in any other achondrites[1,3]. They have very small Rb/Sr ratio which is less than BABI (Basaltic Achondrite Best Initial)[4] and show many chemical and mineralogical properties distinct from other groups. They have conspicuously high Ca content. Olivine has 2% CaO bulk composition[1] and kirschsteinite ($CaFeSiO_4$) is exsolved from the host olivine during subsolidus cooling. Spectacular M shaped diffusion profile of the exsolution lamellae of kirschsteinite in the LEW86010 olivine offer a chance to estimate the cooling history[5]. It is reported that the lamellae are commonly parallel to (001), (011) or (031)[6], but no crystallographic study has been performed. They are typically up to 20 μm in width, while the spacings between them are a few hundred μm[1]. We performed determination of crystallographic orientation of LEW86010 olivine by single crystal X-ray diffraction technique and examine the crystallographic relation between olivine host and exsolved kirschsteinite. Then, we will be able to observe real diffusion profile of Ca of the exsolved kirschsteinite perpendicular to the lamellae after slicing parallel to (100).

METHODS

Five LEW86010 olivine grains (up to 0.5mm) were supplied from the consortium leader for this study to estimate its cooling rate. Each of them was yellowish, prismatic single crystal as far as observed through an optical microscope before taking X-ray photographs. For the determination of the crystallographic orientation of olivine host, we employed an X-ray precession camera with CuKα(λ=1.5418Å) and MoKα(λ=0.7107Å) radiations. Exposure time was 50-120 hours with 40kV, 15mA. At first, we obtained X-ray photographs of (*hk*0) and (*h*0*l*) planes by a precession camera. After determining orientation of the host olivine, another reflection that does not belong to the host olivine was searched and ascertained whether it is reflection from kirschsteinite. Then the crystal was mounted in resin and sliced perpendicular to the *a* axis. The direction, width and spacings of exsolved kirschsteinite were examined through an optical microscope and scanning electron microscope(SEM).

RESULTS & DISCUSSION

According to the precession X-ray photographs the cell dimensions of the host olivine were; *a* 4.79±0.03Å, *b* 10.39±0.05Å and *c* 6.06±0.03Å. These data suggest that its Mg/(Mg+Fe) ratio was approximately 0.3 ($Fo_{30}Fa_{70}$) without consideration of Ca content[7].

This ratio agrees with formerly reported value[1].

The faint reflections just inside the host olivine were recognized on the (*hk*0) and (*h*0*l*) planes(Fig.1). If the orientations of kirschsteinite were the same direction as olivine, the cell dimensions are; *a* 4.87±0.05Å, *b* 11.14±0.10Å and *c* 6.36±0.05Å. These values are in accord with the reported cell dimensions of kirschsteinite (*a* 4.875Å, *b* 11.153Å and *c* 6.438Å[2]). The kirschsteinite-like reflections were also detected on the planes parallel and perpendicular to (011). Furthermore, the indices of intense reflections which were found easily on the photographs were as intense as those of the powder diffraction reported for kirschsteinite[2]. It is concluded that these reflections are undoubtedly exsolved kirschsteinite. Olivine and kirschsteinite share common crystallographic orientations.

Then we mounted the crystal in resin and sliced perpendicular to the *a* axis. After grinding and polishing, we examined through an optical microscope and SEM. Ca-rich lamellae in two directions and spherical inclusion of anorthite were observed(Fig.2). The lamellae occur as two symmetrically related sets parallel to (031) and (0$\bar{3}$1). They were typically up to 10 μm in width, while the spacings between them were 50-100 μm. Spherical inclusion of anorthite 70 μm in diameter is also observed.

These results confirm that kirschsteinite was formed by diffusion during the cooling process of olivine. Sharing common crystallographic orientation suggests that diffusion profiles of Ca between olivine host and exsolved kirschsteinite are useful for estimating cooling rate.

REFERENCES

[1]McKay, G. *et al.*, (1988), *LPSC **XIX***, p.762-763 [2]Sahama, T.G. *et al.*, (1958), *The American Mineralogist **43***, p.862-871 [3]Prinz, M. *et al.*, (1977), *EPSL **35***, p.317-330 [4]Papanastassiou D.A. *et al.*, (1969), *EPSL **5***, p.361 [5]McKay, G. *et al.*, (1989), *Meteoritics **24***, p.302 [6]Prinz, M. *et al.*, (1988), *LPSC **XIX***, p.949-950 [7]Akimoto, S. *et al.*, (1976) *The Physics and Chemistry of Minerals and Rocks*, (Ed.,Strens), New York: John Wiley & Sons, p.327-363

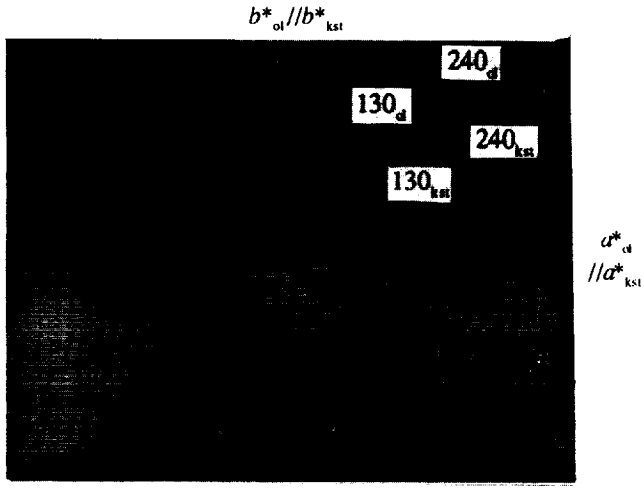

Fig.1 : Precession X-ray(MoKα) photograph (*hk*0)plane including exsolved kirschsteinite reflections

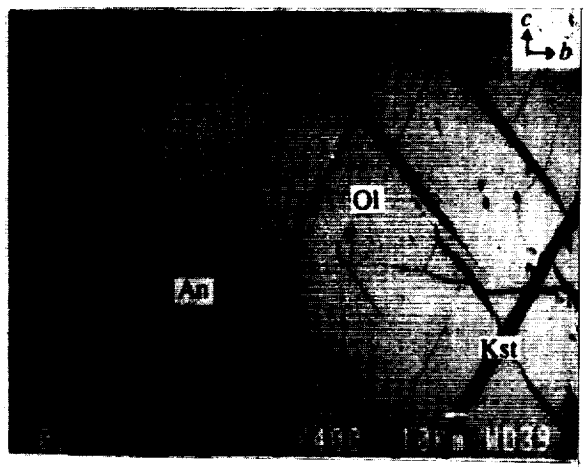

Fig.2 : Backscattered electron image of olivine perpendicular to the *a* axis

ANALYSIS OF PYROXENE ABSORPTIONS OBSERVED IN MARTIAN DARK REGIONS

J.S. Miller *and* R.B. Singer, *Planetary Image Research Laboratory, LPL, Univ. of Arizona, Tucson AZ 85721.*

Introduction. We have investigated the mineralogy of the Martian dark regions by analysis of the pyroxene Fe^{2+} absorption band near 1.0μm in a set of VIS/NIR reflectance spectral images. The data used for these analyses were selected from a larger set, extending from 0.44 to 1.02μm, obtained during the close 1988 opposition [1] and covering substantially all of Mars south of 40°N. This data set is being used in regional mapping of spectral parameters related to surface mineralogy. Martian dark regions are of interest in reconstructing the geologic history because they contain exposures of unaltered or little-altered basaltic crustal material; mapping differences in composition among dark regions could reveal regional or temporal variation in magmatic activity or mantle source composition. Two types of dark regions are seen, with the pyroxene band present and absent; where present, the inferred composition is in the range pigeonite-augite to very high-Fe, low-Ca pyroxene, with a two-pyroxene mixture possible.

Continuum. An important issue in determining the depth and center of spectral absorption bands is the continuum, defining the limits of the band. With our data ending just beyond 1μm, the long-wavelength end of the 1μm band was not well constrained. In order to obtain band parameters from our data, we constructed a continuum based on the brightness/continuum slope relation in other martian telescopic spectral observations [2,3] extending over the full range of the 1-micron band. A variety of continua were tried, yielding similar results.

Derived Band Center and Depth. The band center in the 1μm region was determined by dividing the 0.75μm-1.01μm segment of each spectrum by the linear continuum and fitting a quadratic curve to the divided spectrum. The band center was taken to be the minimum of the quadratic fit. Band depth was computed for all spectra using the same presumed band center of 0.95μm; tests showed that band depth changed little with presumed band center over 0.92-0.97μm. No correlation was seen between computed band center and band depth within the limits of our analysis. When only dark regions having pyroxene bands were considered, the band center ranged 0.92-1.0μm (mean 0.96μm) and the depth 0-10% (clustered near 8% for low-latitude dark regions). Note that pyroxene bands with centers beyond about 1.0μm, if they occur, cannot be determined from these data. The range in band center suggests a variation in pyroxene composition, which will be investigated with regard to regional correlations. Acidalia Planitia (20-40°W, 30-70°N) is a dark region which shows no pyroxene band; this result is consistent with a weaker or longer-wavelength band characteristic of basaltic glass. Oxia Palus, an equatorial dark region showing spectral characteristics similar to Acidalia, has slightly longer band centers (0.99-1.0μm) and lesser band depths than other dark regions.

Band Center and Mineralogy. If we assume that the band is due to one optically dominant pyroxene, following Cloutis and Gaffey's relation [4] the composition associated with a band center near 0.96μm ranges from moderate in calcium and iron to very iron-rich *(Figure 1)*. According to Adams' work [5], this band center suggests a pigeonite-augite composition with >10% Ca, but his data are sparse in this region. A two-pyroxene mixture is not excluded and may be likely for material with the observed band center. High-Mg, low-Ca,Fe pyroxenes are excluded by both systems for our entire range of band centers (0.92-1.0μm). The band center and inferred pyroxene composition are consistent with those reported for other telescopic spectra [3] and Phobos 2 ISM data [6]; the ISM data show notably deeper bands, likely due to less spectral mixing with surrounding regions at the instrument's higher spatial resolution.

References:

[1] Singer, R.B., *et al.* (1990), LPSC XXI, 1164-1165. [2] Singer, R.B., and Roush T.L. **Bull. AAS, 17,** 737. [3] Singer, R.B. and H.Y. McSween, Jr. (1993), in **Resources of Near-Earth Space**, University of Arizona, in press. [4] Cloutis, E.A. and M.J. Gaffey (1991) **J. Geophys. Res. 96,** 22809-22826. [5] Adams, J.B., **J. Geophys. Res. 79,** 4829-4835. [6] Mustard, J.F., *et al.*, **LPSC XXIII,** 955-956. [7] Mustard, J.F., *et al.*, **MSATT proceedings** 1992, LPI Technical Report 92-04 Pt.1, 25-27.

MARTIAN PYROXENE ANALYSIS: Miller J. M. and Singer R. B.

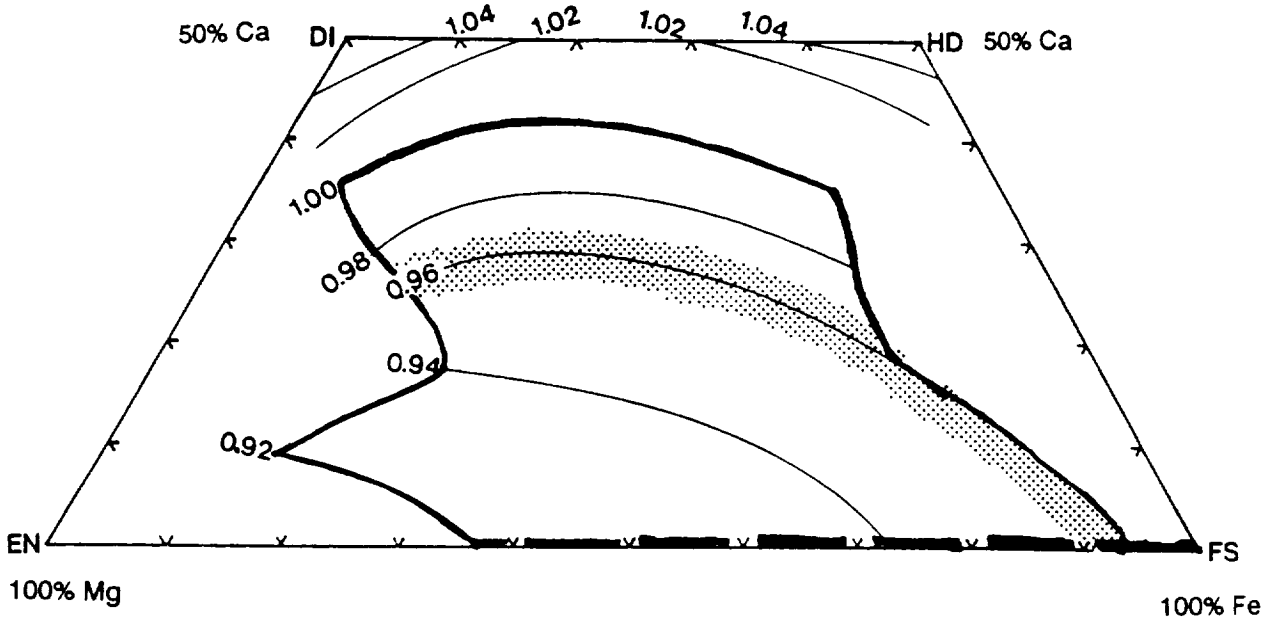

Figure 1. Range of inferred martian pyroxene compositions shown on pyroxene tetralateral. Heavy line outlines compositions based on full range of pyroxene band centers observed in our data (0.92-1.0μm), stippled area is for most commonly occurring band centers (near 0.96μm). These interpretations are based on the assumption of a single optically dominant pyroxene for each spectrum. Based on figure 15 of Cloutis and Gaffey, 1991 [4].

N94-16412

REFRACTORY PRECURSOR COMPONENTS IN AN ALLENDE FERROMAGNESIAN CHONDRULE:
Keiji MISAWA[1], Takashi FUJITA[2], Masao KITAMURA[2], and Noboru NAKAMURA[3] ; [1]Department of Antarctic Meteorites, National Institute of Polar Research, 9-10, Kaga 1-chome, Itabashi-ku, Tokyo 173 JAPAN, [2]Department of Petrology and Mineralogy, Faculty of Science, Kyoto University, Sakyo-ku, 625 Kyoto JAPAN, [3]Department of Earth Sciences, Faculty of Science, Kobe University, Nada-ku, Kobe 657 JAPAN

Chemical and petrological studies of chondrules revealed that they were formed through melting of pre-existing solid precursor materials [1], and that one of the refractory lithophile precursors was a high temperature condensate from the nebular gas and related to Ca, Al-rich inclusions (CAIs) [2,3]. Sheng et al. [4] found relict spinel grains with isotopically fractionated Mg in plagioclase-olivine inclusions from CV chondrites and suggested that the major fractionation processes were common to CAIs and chondrules. We have determined the Mg isotopic composition of five barred olivine chondrules and one coarse-grained rim from the Allende (CV3) meteorite. A reproducibility of instrumental isotope fractionation is ± 2 ‰ per amu. The precision of the $^{26}Mg/^{24}Mg$ data after normalization for mass fractionation can be as good of 0.5 ‰ ($2\sigma_{mean}$). The Mg analytical results are given in Table 1 and indicate that $\Delta^{25}Mg/^{24}Mg$ and $\delta^{26}Mg$ of the chondrules are normal within errors.

Chondrule R-11 mainly consists of olivine (Fa_{10-32}), low-Ca pyroxene ($En_{93}Fs_1Wo_6$), plagioclase (An_{89}), and glass (Na_2O=14 wt %, K_2O=1.8 wt %) with minor amounts of Fe sulfides, and can be assigned to a ferromagnesian type. The most characteristic feature is that a large, unhedral Mg-spinel grain (~ 250 μm in size: Fig. 1) is existed in a central portion of the chondrule. The host chondrule (excluding a spinel grain) shows a fractionated (4.6-7.8 x CI-chondrite), HREE-depleted abundance pattern with a positive Yb anomaly. The REE abundances are hump-shaped functions of elemental volatility (i.e., moderately refractory REE-enriched), suggesting that the precursor component of R-11 host is related to Group II CAIs and could be a condensate from the nebular gas. SEM-EDX analysis reveals that an interior portion of spinel is almost Fe-free but in an outer zone (~ 20-40 μm width), FeO contents increase steeply (Fig. 2). Spinel also contains minor amounts (< 0.75 wt %) of TiO_2, Cr_2O_3, and V_2O_5. On the basis of the abundances of K and Rb in the host chondrule (2.39 x and 2.13 x CI-chondrite, respectively), vaporization loss of moderately volatiles was not so large during melting event of chondrule formation, which in turn strongly suggests that spinel could not be produced as distillation residues [5] of precursor material during chondrule formation. This is consistent with chondrule texture. According to the experiments, barred olivine chondrules were reproduced by melting temperatures of 1400-1600°C and cooling rates of 100-2000°C/hr [6]. The Fe-Mg zoning of spinel may have been generated by diffusional emplacement of Mg and Fe during melting event of chondrule formation.

The spinel crystal contains tiny metallic grains and a 15 μm-sized silicate inclusion. The submicron-sized grains are composed of refractory (Mo, W) Pt-group (Pt, Ir, Os, Ru, Rh) metals with minor amounts of Fe (0.3 wt %) and Ni (5.4 wt %). The silicate inclusion is composed of Al, Ti-rich pyroxene (Al_2O_3=19 wt %, TiO_2=2.6 wt %, CaO=26 wt %) and an Al, Si, Ca-rich phase (Al_2O_3=21 wt %, SiO_2=38 wt %, CaO=38 wt %). This is the first occurrence of refractory Pt-group metal nuggets (RPMNs) in a ferromagnesian chondrule from Allende. In Fig. 3, CI-chondrite normalized elemental abundances for one of the nuggets (RPMN-1) are compared with the data of a RPMN in a Type A Allende CAI [7]. In RPMN-1, W, Os, Ir, Mo, and Ru are uniformly enriched (2-6 x 10^5 x CI-chondrite) and abundances of Pt and Rh decrease (2-10 x 10^4 x CI-chondrite) with increasing volatility. Moreover, abundances of Fe and Ni in the nugget are equal to or less than CI-chondrite level. The elemental abundance patterns of both RPMNs are identical. Precursor components of refractory siderophiles are suggested for Allende chondrules [8]. However, their chemical features have not been well understood yet. It is generally accepted that RPMNs in CAIs were produced during high temperature events at least 1300°C and before 100 % condensation of Fe in the early solar nebula [9-13]. Thus, we suggest that one of the refractory siderophile precursor components of Allende chondrules is a high temperature condensate from the nebular gas and associate with refractory lithophiles. Since RPMNs in R-11 were surrounded by Mg-spinel, they may have been separated from the common siderophiles (Fe, Ni, Co) during early stage of condensation and were not affected by low temperature sulfidization [14].

References: [1] Grossman J. N. et al. (1988) in *Meteorites and the early solar system* (eds. Kerridge J. F. and Matthews M. S.), pp. 619, The Univ. of Arizona Press, Tucson, AZ. [2] Misawa K. and Nakamura N. (1988) *GCA*, **52**, 1669. [3] Misawa K. and Nakamura N. (1988) *Nature*, **334**, 47. [4] Sheng Y. J. et al. (1991) *GCA*, **55**, 581. [5] A.S. Kornachi A. S. and Fegley B. Jr. (1984) *PLPSC*, **14th**, B588. [6] Hewins R. H. (1988) in *Meteorites and the early solar system* (eds. Kerridge J. F. and Matthews M. S.), pp. 660, The Univ. of Arizona Press, Tucson, AZ. [7] Wark D. A. (1979) *Astrophys. Space Sci.*, **65**, 275. [8] Rubin A. E. and Wasson J. T. (1987) *GCA*, **51**, 425. [9] Wark D. A. and Lovering J. F. (1976) *Lunar Sci.*, **VII**, 912. [10] Palme H. and Wlotzka F. (1976) *EPSL*, **33**, 45. [11] El Goresy A. et al. (1978) *PLPSC*, **9th**, 1279. [12] Blander M. and Fuchs L. H. (1980) *PLPSC*, **11th**, 929. [13] Fegley B. Jr. and Palme H. (1985) *EPSL*, **72**, 311. [14] Blum J. D. et al. (1988) *Nature*, **331**, 405. [15] Catanzaro E.J. et al. (1966) *J. Res. N.B.S.* **70A**, 453.

Table 1: Mg Analytical Results.

Sample	$\Delta^{25}Mg/^{24}Mg$ (‰)‡	$\delta^{26}Mg$ (‰)£
R-1	1.9 ± 1.7¶	-0.1 ± 0.4§
R-11†	2.5 ± 1.5	-0.1 ± 0.2
	2.5 ± 0.6	-0.1 ± 0.3
R-13	0.7 ± 0.8	-0.3 ± 0.3
G-2	2.1 ± 1.1	-0.2 ± 0.4
G-3	1.5 ± 0.7	-0.3 ± 0.2
G-2 CGR*	1.8 ± 1.3	0.3 ± 0.3

‡ $\Delta^{25}Mg/^{24}Mg = [(^{25}Mg/^{24}Mg)_m/(^{25}Mg/^{24}Mg)_s - 1]$ x 1000, where 'm' denotes the measured raw $^{25}Mg/^{24}Mg$ ratios, 's' is grand mean value: $^{25}Mg/^{24}Mg = 0.12464$ for raw data determined from standards.

£ $\delta^{26}Mg = [(^{26}Mg/^{24}Mg)_c/0.139813 - 1]$ x 1000, where 'c' is the value corrected for fractionation according to $(^{26}Mg/^{24}Mg)_c = (^{26}Mg/^{24}Mg)_{meas}/\alpha^2$, where $\alpha = (^{25}Mg/^{24}Mg)_{meas}/(^{25}Mg/^{24}Mg)_c$, and $(^{25}Mg/^{24}Mg)_c = 0.12663$ reported by [15], and 0.139813 is the grand mean value for all standards normalized using power law.

† Exculuding a spinel grain.

* Coarse-grained rim.

¶ Errors are 2 σ.

§ Errors are $2\sigma_m$.

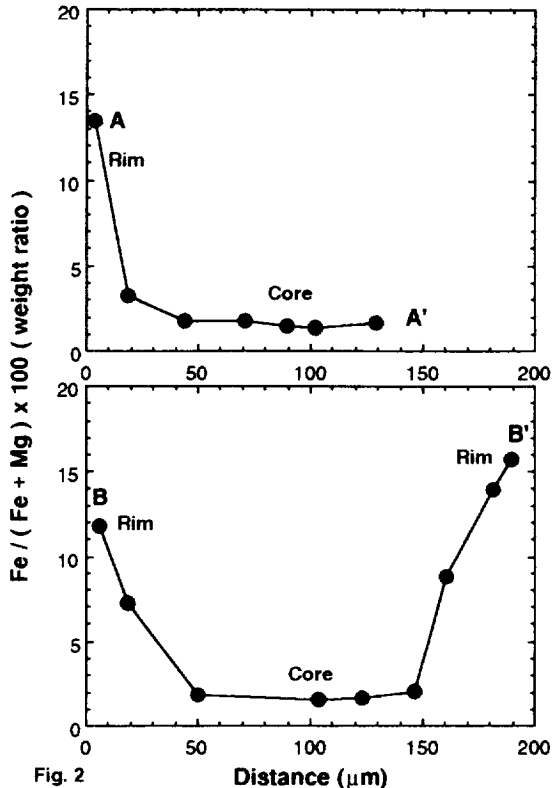

Fig. 2
Variations of Fe /(Fe+Mg) ratios between the Fe-rich rim and the Fe-poor core of spinel in R-11.

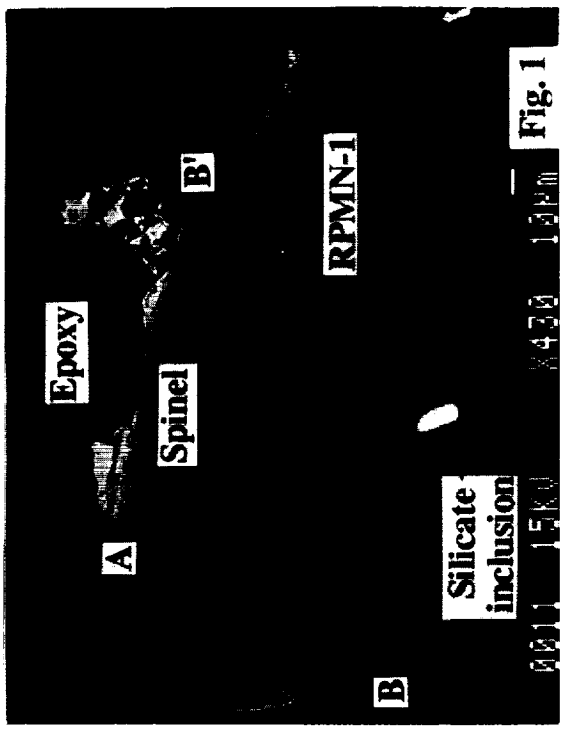

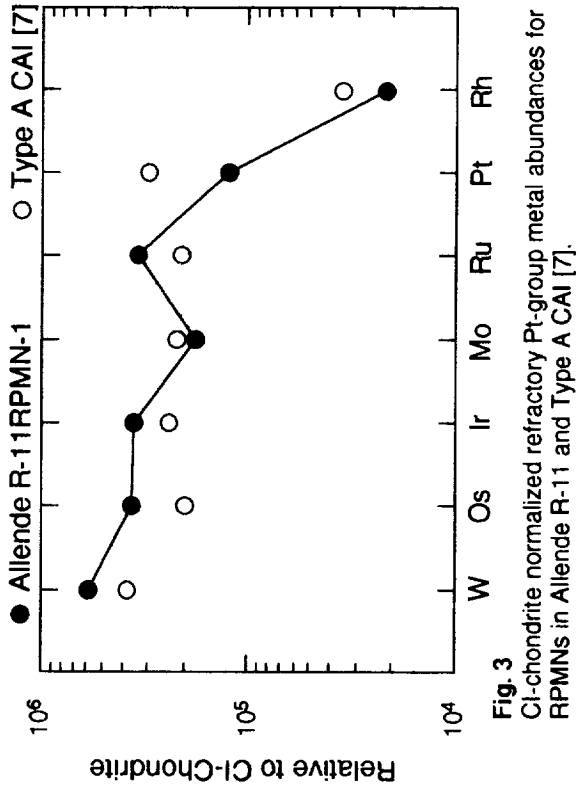

Fig. 3
CI-chondrite normalized refractory Pt-group metal abundances for RPMNs in Allende R-11 and Type A CAI [7].

IGNEOUS FRACTIONATION AND SUBSOLIDUS EQUILIBRATION OF DIOGENITE METEORITES. **David W. Mittlefehldt**, C23, Lockheed Engineering and Sciences Co., 2400 Nasa Rd. 1, Houston, TX 77058.

Diogenites are coarse-grained orthopyroxenite breccias of remarkably uniform major element composition. Most diogenites contain homogeneous pyroxene fragments up to 5 cm across [1] of $Wo_2En_{74}Fs_{24}$ composition. Common minor constituents are chromite, olivine, troilite and metal, while silica, plagioclase, merrillite and diopside are trace phases. Diogenites are generally believed to be cumulates from the eucrite parent body [2], although their relationship with eucrites remains obscure. It has been suggested that some diogenites are residues after partial melting [3]. I have performed EMPA and INAA for major, minor and trace elements on most diogenites, concentrating on coarse-grained mineral and lithic clasts in order to elucidate their igneous formation and subsequent metamorphic history.

Minor and Trace Element Correlations. Although diogenite orthopyroxene grains are very uniform in major element composition, they exhibit a wide range in minor, incompatible element contents. Excluding Yamato Type B diogenites (Y-75032-type), TiO_2 and Al_2O_3 vary by factors of 7 and 4, respectively. Among the majority of diogenites, TiO_2 and Al_2O_3 are strongly correlated (Fig. 1), as would be expected for cumulus orthopyroxene grains formed from an evolving magma. Correlation between minor elements determined by EMPA and trace elements determined by INAA is not as straightforward because a small amount of crystallized trapped liquid may affect bulk analyses. Among the *incompatible* trace elements determined by INAA, Sc and Yb concentrations will be least affected by a trapped liquid component because they have the highest opx/melt partition coefficients [4]. Both TiO_2 and Al_2O_3 are correlated with Sc and Yb for most diogenites (Fig. 1; TiO_2 correlations not shown). Excluding unusual diogenites (labeled in Fig. 1), Sc varies by a factor of 2, and Yb by a factor of 9. These correlations also indicate that diogenites record an extensive igneous fractionation sequence. Individual diogenites can show a wide range of incompatible element contents. However, in EETA79002 most orthopyroxenes have a limited range in minor element content (Fig. 2), suggesting that brecciation may have mixed in pyroxenes from different regions of diogenite lithologic unit(s); *i.e.* EETA79002, and perhaps other diogenites, may be genomict breccias. This is also suggested by major element compositions of EETA79002 orthopyroxenes (see below).

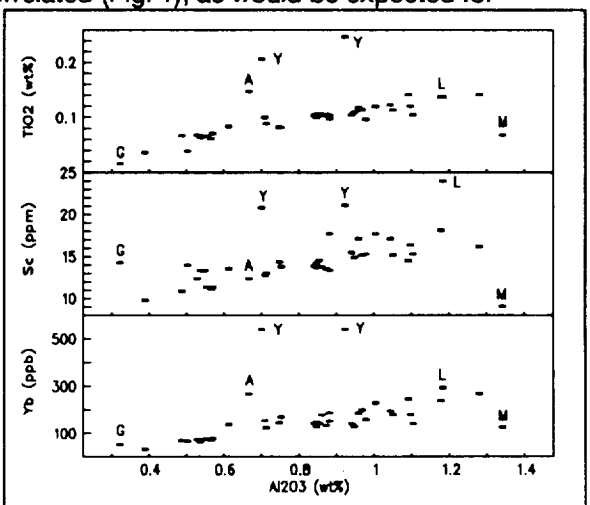

Fig. 1. Trace and minor element compositions of diogenite orthopyroxenes. Labeled diogenites are; A - ALH84001, G - Garland, L - LEW88008, M - Manegaon, Y - Yamato Type B.

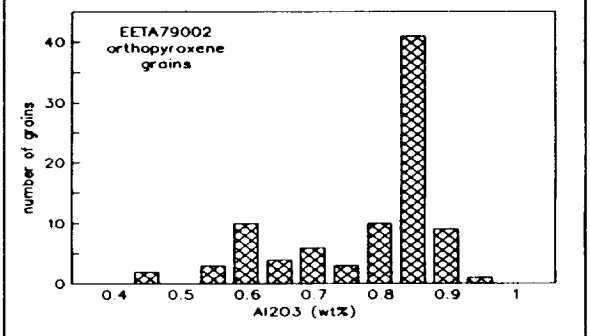

Fig. 2. Histogram of Al_2O_3 contents of individual EETA79002 orthopyroxene grains.

Major Element Uniformity. The igneous fractionation inferred from minor and trace elements is at odds with the general uniformity in molar 100*MgO/(FeO+MgO) (hereafter mg#) in the diogenite suite. The majority of diogenites have mg# of ~75, which implies minimal igneous fractionation (Fig. 3). These same diogenites vary in incompatible trace elements (TiO_2 - 0.03 to 0.14 wt%; Sc - 9.8 to 18.1 μg/g; Yb - 30 to 290 ng/g; Fig. 3), which implies extensive igneous fractionation. Weak positive correlations between Cr_2O_3 and mg# have been shown for some diogenite orthopyroxenes, indicating that evidence for igneous fractionation is partially preserved in diogenite major element compositions [5]. For comparison, cumulus orthopyroxene grains from the Upper Bronzitite Zone of the Stillwater Complex generally show the expected increase in TiO_2 and Yb with decreasing mg# resulting from igneous fractionation [6]. The observed scatter in TiO_2 and Yb relative to mg# for Stillwater cumulus orthopyroxenes (Fig. 3) has been attributed to partial subsolidus equilibration of Fe and Mg [6].

Unusual Diogenites. Several diogenites are distinct from the majority. Manegaon is the most primitive diogenite; it has the highest mg# (78.5) and lowest Sc content (9.1 μg/g) (Fig. 3). However, Manegaon orthopyroxene contains the highest Al_2O_3 content (1.34 wt%) (Fig. 1), which would suggest it originated from the most evolved parent magma. Manegaon is anomalously low in TiO_2, Yb and especially Sc for its

DIOGENITE METEORITES, David W. Mittlefehldt

Al_2O_3 content (Fig. 1). Therefore, Manegaon was probably not formed from the same parent melt as other diogenites. ALH84001, Garland, LEW88008 and Yamato Type B diogenites are more ferroan than typical diogenites (Fig. 3), implying that they were formed from more evolved parent melts. Garland orthopyroxene, however, contains the lowest TiO_2 (0.02 wt%) and Al_2O_3 (0.32 wt%) contents of any diogenite, and the second lowest Yb content (50 ng/g) (Fig. 1). These low incompatible element contents suggest that Garland's parent melt was more primitive than that of the majority of diogenites. Garland also has an anomalously high Sc content for its generally low incompatible element contents and has the highest Sc/Al_2O_3 ratio of any diogenite (Fig. 1). ALH84001 and the Yamato Type B diogenites have unusually high TiO_2/Al_2O_3 and Yb/Al_2O_3 ratios (Fig. 1), and were probably formed from different parent magmas than the majority of diogenites. Chromite grains from ALH84001 and Yamato Type B diogenites contain high TiO_2 contents, about 3 times those of other diogenites, and Yamato Type B diogenites contain ilmenite as well [7]. Hence, these diogenites were likely formed from unusually TiO_2-rich magmas. Yamato Type B diogenites contain a significant amount of crystallized trapped liquid [7,8], and therefore, trace element contents are difficult to evaluate in relation to the EMPA data. LEW88008, in addition to being the second most ferroan diogenite (Fig. 3), is rich in all the incompatible elements (Fig. 1) and is a plausible Fe-rich differentiate of the diogenite parent magma.

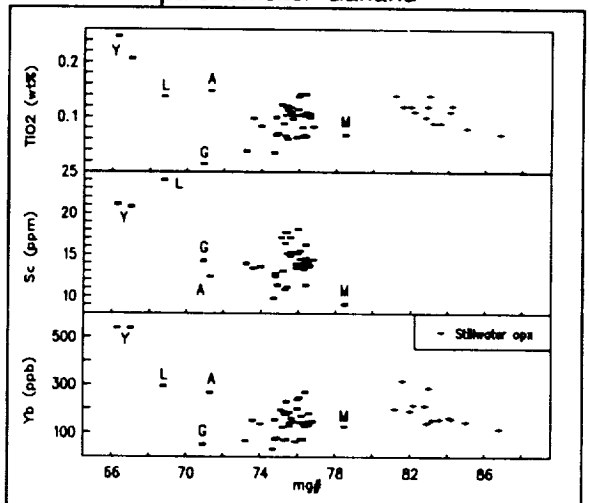

Fig. 3. Minor and trace element variations with mg# in diogenite orthopyroxenes. Labels as in Fig. 1. Cumulus orthopyroxene from the Stillwater Complex Upper Bronzitite Zone [6] are shown for comparison.

Thermometry and Subsolidus Equilibration. Mineral phases in diogenites can be used to calculate equilibration temperatures using two-pyroxene thermometry [9], and orthopyroxene-spinel thermometry [10]. Two-pyroxene thermometry yields temperatures ranging from about 900°C for ALHA77256 to about 620°C for Ibbenbüren (Table 1). Diopside grains are generally small, on the order of 10-20 μm, and were formed by subsolidus exsolution from the orthopyroxene host [11]. Orthopyroxene-spinel temperatures are in the range of 880°C to 640°C (Table 1), except for higher temperatures for Tatahouine, 960°C, and Yamato Type A diogenites (Y-74013-type), 1050°C [7]. Large, mm-sized chromite grains record higher equilibration temperatures than do small, < 100 μm chromite grains (Table 1). The low orthopyroxene-clinopyroxene and orthopyroxene-spinel temperatures indicate subsolidus equilibration of major elements in diogenites. This equilibration predated brecciation; in EETA79002 magnesian orthopyroxene (mg# 81) is in breccia contact with typical orthopyroxene (mg# 76), again suggesting that this is a genomict breccia.

Table 1. Equilibration temperatures (°C) of diogenites.

		opx-sp	opx-cpx
Aïoun el Atrouss			750
ALHA77256	large cm	790	900
	small cm	780	
ALH84001		720	
EETA79002		750	
Garland		880	
Ibbenbüren			620
Johnstown		640	
Manegaon		650	750
Roda			880
Shalka	large cm	850	
	small cm	740	
Tatahouine		960	
TIL82410		680	
Yamato A	large cm	1050	
	small cm	840	
Yamato B		700	860

Summary. Major element compositions of diogenites are decoupled from minor and trace element compositions; the latter record an igneous fractionation sequence that is not preserved in the former. Low equilibration temperatures indicate that major element diffusion continued long after crystallization. Diffusion coefficients for trivalent and tetravalent elements in pyroxene are lower than those of divalent elements [*e.g.* see 6]. Therefore, major element compositions of diogenites may represent means of unknown portions of a cumulate homogenized by diffusion, while minor and trace elements still yield information on their igneous history. The scale of major element equilibration is unknown, but is likely to be on the order of a few cm [*e.g.* see 6]. Therefore, the diogenite precursors may have consisted largely of cm-sized, igneously zoned orthopyroxene grains, which were subsequently annealed during slow cooling, obliterating major element zoning but preserving minor and trace incompatible element zoning.

References. [1] Mason (1963) *Am. Mus. Nov.* **2155,** 13pp. [2] Fukuoka *et al.* (1977) *PLSC 8th*, 187. [3] Sack *et al.* (1991) *GCA* **55,** 1111. [4] Colson *et al.* (1988) *GCA* **52,** 539. [5] Berkley and Boynton (1992) *Meteoritics* **27,** 387. [6] Lambert and Simmons (1987) *AJS* **287,** 1. [7] Mittlefehldt and Lindstrom (1993) *Proc. NIPR Symp. Ant. Met.* **6,** submitted. [8] Takeda and Mori (1985) *PLPSC 15th*, C636. [9] Lindsley and Anderson (1983) *PLSC 13th*, A887. [10] Mukherjee *et al.* (1990) *PLPSC 20th*, 299-308. [11] Mori and Takeda (1981) *EPSL* **53,** 266-274.

SIDEROPHILE ELEMENT FRACTIONATION IN METEOR CRATER IMPACT GLASSES AND METALLIC SPHERULES;

D.W. Mittlefehldt[1], T.H. See[1] and E.R.D. Scott[2], [1]Lockheed-ESC, C23, 2400 NASA Road 1, Houston, TX 77058, [2]Planetary Geosciences Division, Dept. of Geology & Geophysics, SOEST, Univ. of Hawaii, Honolulu, HI 96822

Abstract - Meteor Crater, Arizona provides an opportunity to study, in detail, elemental fractionation processes occurring during impacts through the study of target rocks, meteorite projectile and several types of impact products. We have performed EMPA and INAA on target rocks, two types of impact glass and metallic spherules from Meteor Crater. Using literature data for the well studied Canyon Diablo iron [θ], we can show that different siderophile element fractionations affected the impact glasses than affected the metallic spherules. The impact glasses primarily lost Au, while the metallic spherules lost Fe relative to other siderophile elements.

Stratigraphy / Geologic Setting - Meteor Crater is a small, bowl-shaped impact crater ~1.2 km in diameter and ~180 m deep located in the southern part of the Canyon Diablo Region of the Colorado Plateau in north-central Arizona. Formation of the structure is believed to have occurred ~49,000 years ago [1] when a IA iron meteorite ~30 m across, traveling at ~15 km/s collided with the Earth. The crater rim rises between 30-60 meters above the surrounding, low-relief Plateau. The somewhat squarish shape of the crater is the result of two perpendicular sets of vertical joints within the target strata. These strata consist of sandstones, siltstones and dolomites of Permian to Triassic age [2].

Only the upper portions of the Permian Coconino Sandstone, a crossbedded, clean-quartz sandstone, are exposed. Overlying the Coconino is the ~2.7 meter thick Permian Toroweap Formation composed of calcareous, medium- to coarse-grained sandstone and dolomite. Above the Toroweap lies the ~80 meters thick Permian Kaibab Formation composed of dolomitic limestone with minor amounts of calcareous sandstone. Above the Kaibab is a thin layer (~9-15 meters) of the Triassic Moenkopi Formation consisting of fine-grained sandstone and siltstone [2].

Sample Description - Three varieties of samples from Meteor Crater have been examined in this study. One type, Spherical Impact Glasses (SIG), occurred as dark, generally hollow, spherical glass beads ~0.5 cm in diameter. Small vesicles were visible on exterior surfaces, as were minor amounts of clastic detritus. In thin section the glasses exhibited varying degrees of crystallization (ranging from ~20% to >75% small, aphanitic crystals); vesicles ranged from circular to elliptical. Numerous, small circular Fe-Ni blebs were commonly scattered about the interior. The second sample type was the elongated Irregular Impact Glasses (IIG) which averaged ~1 x 2 cm in size. Macroscopically, these samples were reddish-brown in color, exhibited ropy to irregular exterior morphologies often containing larger spherical to elliptical vesicles in exterior surfaces. Exposed interior surfaces commonly exhibited larger white clasts. In thin section these samples were much more vesicular (≥50% of the surface area in several specimens) than the SIG samples. The IIG samples also exhibited higher degrees of crystallization and contained fewer metallic blebs than the SIG samples. Both sample types were clearly molten when formed. The third sample type was small, metallic spherules (MS) ~0.5-1.5 mm in diameter and weighing 0.7 to 13 mg. The metallic spherules possess an iron-oxide coating. The texture and mineralogy of these metallic spherules were classified in [3].

Analyses - We have performed electron microprobe analysis (EMPA) of the glass in the IIG and SIG samples as in [4]. The EMPA were purposefully targeted to avoid the Fe-Ni blebs contained in the glass. Bulk splits of the IIG and SIG samples were analyzed at JSC by instrumental neutron activation analysis (INAA) as in [4]. The MS samples were analyzed by INAA at UCLA in 1975 following the procedure of [5]. Following [6], we abraded the oxide coatings off of the metallic spherules prior to performing our analysis.

Discussion - In our previous work [4] we analyzed similar samples from Wabar Crater, Saudi Arabia in order to investigate mixing between the target lithologies and the projectile. The target lithology at Wabar is much less complex and is composed of sandstone with possibly some drift sand. Wabar Crater was formed by a IIIA iron meteorite projectile. In addition, Wabar Crater is small (~90 m diameter) compared to Meteor Crater.

At Wabar we found that smaller, aeroballistically dispersed samples, akin to the SIG samples of this study, contained the highest percentage (~11%) of meteoritic materials, while the larger glass samples, similar to the IIG of this effort, possessed ~7% meteoritic component. The black and white melts discussed in [4] have no equivalents in Meteor Crater impactites. However, they contained ~4% and 0.4% meteoritic component, respectively. We concluded that the smaller, more meteorite-rich samples originated from the upper portion of the target near the impact point, while the larger samples originated from deeper within the target.

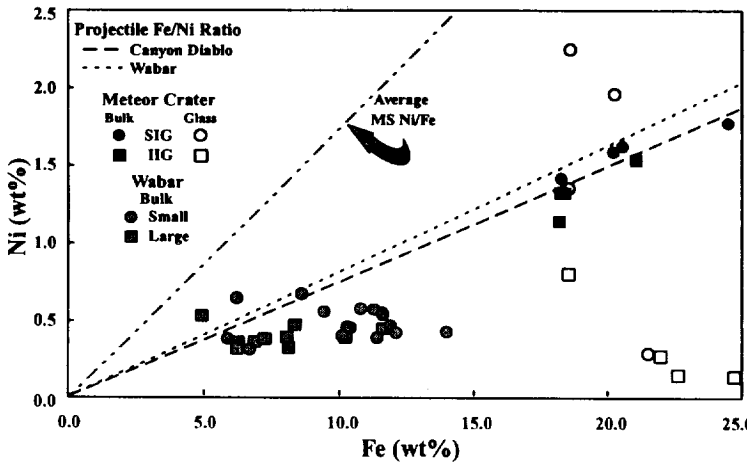

Figure 1 is a Ni vs. Fe diagram showing the bulk INAA analyses and the glass-only analyses collected via EMPA for the Meteor Crater impact glasses. Bulk analyses by INAA for Wabar impact glasses [4] are shown for comparison, as are Wabar and Canyon Diablo projectile Fe/Ni ratios and the average ratio for the Canyon Diablo metallic spherules. A general Ni-depletion, relative to the Wabar/Nejed projectile was observed for most of the Wabar specimens [4].

The microprobe data show that all four of the IIG samples have fractionated Ni/Fe, within the glass, relative to Canyon Diablo projectile. The SIG samples, on the other hand, yield mixed results with one sample having Ni/Fe similar to the most depleted IIG samples, one SIG possessing essentially meteoritic proportions of Fe and Ni, and two samples exhibiting small degrees of Ni-enrichment relative to Fe within the glass. However, bulk Fe-Ni concentrations obtained by INAA analyses exhibit little deviation from the meteoritic ratio and suggest little siderophile element fraction on the scale of the bulk specimen.

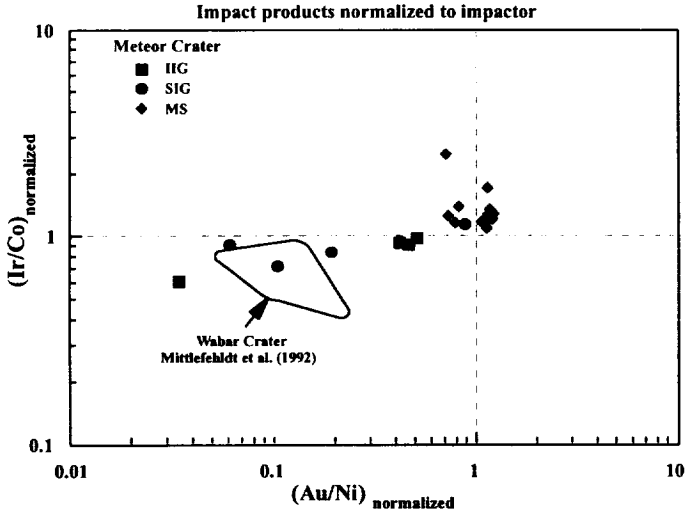

Figure 2 compares the siderophile element fractionations of the IIG, SIG and MS samples. As was the case for Wabar Crater impact glasses [4], Au shows the strongest depletion among the siderophile elements in Meteor Crater impact glasses; Au/Ni ratios vary from ~1 to ~0.03 times that of the Canyon Diablo meteorite. The IIG samples *generally* have higher Au/Ni ratios than the SIG samples, although clearly there is a wide range in ratios for both sample types. Most of the SIG samples have impactor normalized Au/Ni ratios similar to those of Wabar Crater impact glasses.

Previous work on metallic spherules from Meteor Crater has shown that they contain projectile ratios of Co/Ni and Cu/Ni but are depleted in Fe [6]. Our MS samples show little fractionation in Ir/Co or Au/Ni from the projectile ratios (Figure 2). The most extreme Ir/Co ratio is ~2.3 times that of Canyon Diablo, and Au/Ni ratios are within 30% of Canyon Diablo. However, Ni/Fe ratios in MS are strongly fractionated relative to the projectile (Figure 1). Kelly *et al.* [6] concluded that Fe in the metal spherules was selectively oxidized in molten metal droplets in the atmosphere, and that some of the FeO was lost through vaporization. However, our metallic spherule samples have average Ga/Fe, Ge/Fe and As/Fe ratios of 1.6, 2.5 and 4.5 times those of Canyon Diablo meteorite, respectively. These are the most volatile of the siderophile elements we have analyzed, and the boiling point of As is undoubtedly >1000°K lower than that of FeO or Fe_2O_3. Therefore, oxidation and vaporization of Fe is probably too simplistic a model for Fe loss from the metallic spherule. Because oxide coatings were abraded off the metallic spherules by us and [6], it is possible that the Fe fractionation was generated at the time of sample preparation as follows: During impact, mm-sized metal droplets were sprayed out of Meteor Crater. Iron was oxidized during flight, and the iron oxides were concentrated on the outside of the droplets. During residence on the desert surface, some of this oxide coating was spalled off by weathering, and the remainder was removed by careful geochemists trying to avoid what appeared to be terrestrial weathering products. This process would give the *appearance* of Fe fractionation, when in fact, analysis of whole metallic spherules, including the oxide coating, would show that Fe was not fractionated. However, bulk analyses by EMPA [4] show that P is enriched relative to Fe in the metallic spherules. As P should be more susceptible to oxidation than Fe, the above model would predict that P/Fe, and especially P/Ni, ratios should be lower than those of bulk Canyon Diablo, contrary to observation. Clearly, however, the impact glasses and metallic spherules were affected by different fractionation processes; the former primarily lost Au while the latter lost Fe in preference to other siderophile elements.

Presently, we do not have bulk chemical compositions for the various target litholgies. However, we can deduce from the general lithologic descriptions of the target rocks that SiO_2 was a prominent component of the Moenkopi and Coconino, while CaO and MgO are dominant in the Kaibab. Figure 3 illustrates the relationships between SiO_2 and both CaO and MgO within the impact glasses. The increases in CaO and MgO within the SIG samples relative to the IIG suggest that the SIG samples contain larger proportions of the Kaibab limestone and dolomite. Based on the size, shape and petrography of the impact glasses, we expect that the SIG were formed higher in the target stratigraphy than the IIG [*e.g.* 4]. We infer, then, that the higher SiO_2 and lower CaO and MgO contents of the IIG samples reflect a larger component of Coconino sandstone, rather than the Moenkopi sandstone/siltstone. Verification of this awaits bulk chemical analyses of the various target lithologies.

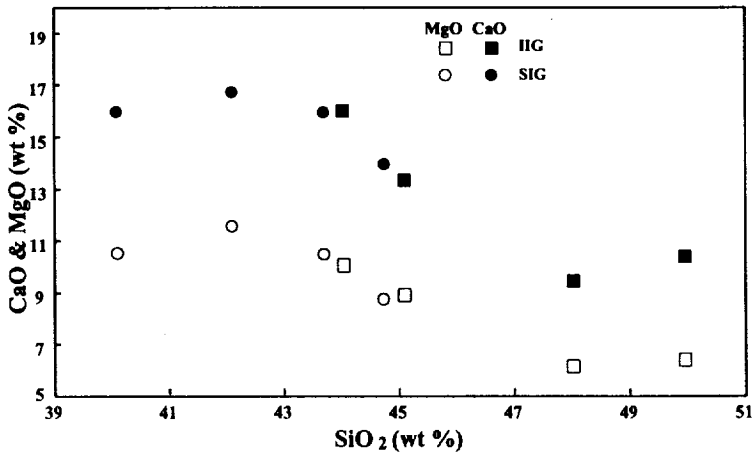

References - [0] Wasson and Ouyang (1990) *CGA, 54*, 3175. [1] Sutton (1985) *JGR, 90*, 3690. [2] Shoemaker and Kieffer (1974) *Guidebook to the Geology of Meteor Crater, Arizona.* [3] Blau *et al.* (1973) *JGR, 78*, 363. [4] Mittlefehldt, *et al.* (1992), *Meteoritics, 27*, 361. [5] Scott (1978) *CGA, 42*, 1243. [6] Kelly *et al.* (1974) *GCA, 38*, 533.

IDENTIFICATION OF NEW METEORITE, MIHONOSEKI (L), FROM BROKEN FRAGMENTS IN JAPAN; Y. Miura and Y. Noma, Faculty of Science, Yamaguchi University, Yamaguchi 753, Japan.

New meteorite of Mihonoseki fallen in Shimane-ken was identified by fine broken spieces by using energy-dispersive scanning electron microprobe analyzer. It shows fusion-crust (i.e. Fe-Si melt), meteoritic minerals (kamacite, taenite, troilite, amorphous plagioclase etc.) and chondrule with clear glassy rim. Mineralogical, and petrological data of several fine grains suggest that broken fragments of Mihonoseki is L3/4 chondritic meteorite which is the first identification in Japanese fallen meteorite. The prompt identification method of meteorite-fragment will be applied to the next lunar, Martian and Asteroid explorations, as well as meteorite fall on the terrestrial surface.

1. Sample

The sample used in this study is several broken speices of Mihonoseki meteorite fallen and found in house of Mr. M. Matsumoto, ca. 22, December 10, 1992. Main mass of about 6.5 kg and 25x15x10 cm was first found almost without fusion-crust, because it passed his roof, two ceiling (two floor) to the basement of his house. Main purpose of the present study is to identify the meteorite from broken speices distributed in his house. Almost main fragments near the roof were completely lost for two days by his repair of the roof for rain-fall, because he thought that it was thunder-storm and did not realize that it was meteorite effect.

We collected several small fragments by magnet on two carpets, by helping with Mr. K. Handa on December 12, 1992. Ten grains of 2mm in width were selected to examine Scanning electron microscopy (SEM) with energy-dispersive device (EDX), JSM-5400 in Yamaguchi University.

2. Identification of meteorite from small fragment

The following three characteristic data suggest that it is really stony meteorites from small broken spieces distributed near fallen site within the house.

1) Fusion-crust (Fig.1): Analytical SEM data show that one big dark fragment is fusion-crust with Fe (69 to 78 wt.% FeO) and Si (7 to 17 wt.SiO_2) including silica grains (99 wt.% SiO_2, ca.10 to 50 μm in width) and irregular holes for gas passage. Fusion-crust with same Fe-Si composition is also found with silicates (Fig.1) but without silica grain. The two types of fusion-crust are due to different fragments of meteorite (i.e. only fusion-crust and fusion-crust close to unmelted silicates).
2) Meteoritc minerals: Kamacite and taenite of Fe-Ni metals are found by coexisting with silicate fragments. Troilite is observed with kamacite and silicates. Plagioclase-compositions (ca.8 to 13 mol.% An-content) are found in glassy matrix outside of olivine-chondrule.
3) Chondrule: Thin section with cross-nicols shows clear olivine chondrule rim, dark glassy matrix and pyroxene fragments, together with Fe-Ni metals.
This prompt identification method of meteorite-fragments will be useful method in the next unmanned exploration project of the Moon and Mars, together with new prompt method of meteorite fall on terrestrial surface.

3. Classification of chondrite

Pyroxene grains show two types of compositions [1]:

1) Orthopyroxene (including fusion-crust grains) shows Wo:0.0-2.0 (average 1.4), En: 68.6-81.2 (av.78.5 mol.%), and Fs:17.2-29.6 (av.20.1) with 14 % M.D. of percent mean deviation (in 14 analytical points).

2) Orthopyroxene (without any fusion-crust) shows less Fe composition of Wo:0.0-1.7 (av.1.4), En:76.3-81.2 (av.80.0), and Fs:17.1-23.8 (av.18.6) with 8 % M.D. (in 7 analytical points). The pyroxene data with larger values of % M.D. (over 5% M.D.) indicate petrologic type 3.

Olivine grains of 14 analytical points (without fusion-crust) are Fo:75.1-79.3 (av. 77.7) and Fa:20.7-24.9(av.22.3) with 5 %.M.D [1]. Chemical group of the Mihonoseki fragments belongs to L-group (Fa:22.3, and Fs: 20.1). But petrological type from percent mean deviation of olivine compositions is 3/4 between 3 and 4. Although the main mass of the Mihonoseki should be examined for classification soon, the fragments near fusion-crust in this study belongs to L3/4. This is mainly because the heterogeneous fragments reveal range from L3 to L4 which will be known from classification of main mass.

4. Evaluation of meteorites

Mihoneseki meteorite is 41st meteorite of Japanese non-Antarctic meteorites, 32nd chondrite in Japan, and 11th chondrite of weight. But L3/4 chondrite of Mihonoseki is 'the first identified chondrite in Japan', though eight Japanese chondrites are not clearly classified.

5. New additional chondrite in Japan

New chondrite of 42nd in Japan was 'found' at December 28, 1992. The unnamed and un classified chondrite was found in Matsue-shi, Shimane-ken after reading news-paper of the Mihonoseki meteorite. The unnamed chondrite of 430 gr (85x65x5mm) with clear half-covered fusion-crust has been stored by Mr. H. Minao who was picked up within their car-transport ship during anchor of 9 km offshore near Tahara-ko, Aichi-ken, two years ago. He said that the deck was broken by 30 cm in diameter and ca. 15 cm in depth. He is now checking the rest of fragments to his crew members.

References:

[1]Dodd R. T. (1981): In Meteoritics (Cambridge Univ. Press), p.24,

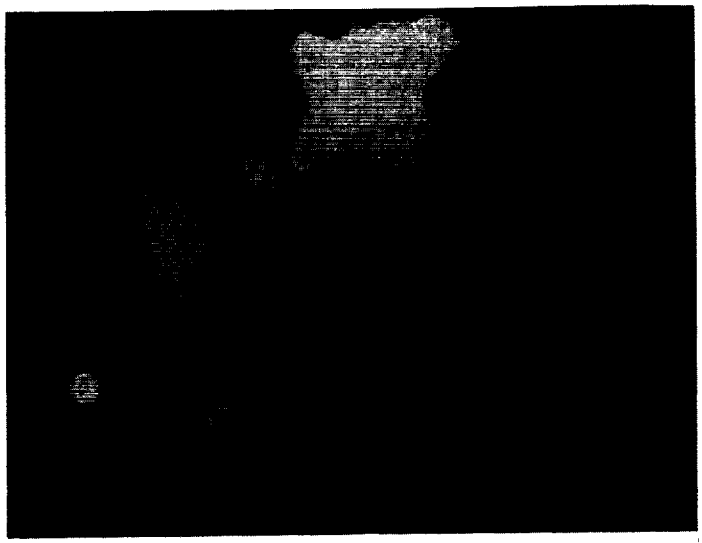

Fig. 1. BEI image of Mihonoseki (L3/4) fragment. Kamacite of Fe-Ni metal (white), Pyroxene $Fs_{18}Wo_{1.5}$ (gray grain of left-below), and fusion-crust Si-Fe melt (spotty gray of middle-below).

THE THICKNESS OF EUCRITIC CRUST IN THE HED PARENT BODY; M. Miyamoto and H. Takeda, Mineralogical Institute, Faculty of Science, University of Tokyo, Hongo, Tokyo 113, Japan.

Because cumulate eucrites are generally thought to be located at the lower part in a eucritic crust on a diogenitic mantle in the HED parent body [e.g., 1], the burial depth of cumulate eucrites gives information on the thickness of the eucritic crust. We estimated the burial depth and cooling rate of cumulate eucrites, Serra de Magé and Moore County on the basis of the width of augite lamellae and compositional gradients of Ca in pyroxenes by numerically solving the diffusion equation [2]. We obtained the burial depth of the eucrites of 7-8 km and cooling rate of 0.00016-0.0002 degrees C/yr.

The cooling rate was obtained by fitting both the calculated width of augite lamella and compositional gradients at the interface between augite and the host pyroxene to the observed ones. We assumed the solvus reported by Lindsley [3] to calculate the chemical compositions of augite and pigeonite at the interface of the lamella and host phase as a function of temperature during a cooling. We used the Ca diffusion coefficient in pyroxene parallel to the c direction which is experimentally determined by Fujino et al. [4], because pyroxenes in these eucrites contain (001) augite lamellae. The method of diffusional calculation is similar to that used in Miyamoto and Takeda [2]. We determined the bulk chemical composition of pyroxene including exsolution lamella by dense spot analyses along lines which traverse several augite lamellae with an electron microprobe.

Pyroxene in the Serra de Magé eucrite contains coarse (001) augite lamellae up to about 35 μm in width in the host orthopyroxene. The host phase of the Serra de Magé pyroxene is inverted to orthopyroxene from initially crystallized pigeonite during slow subsolidus cooling history [5]. The chemical composition of the augite lamellae is $Ca_{41}Mg_{40}Fe_{19}$ and that of the host orthopyroxene is $Ca_2Mg_{54}Fe_{44}$. The bulk chemical composition of the Serra de Magé pyroxene is $Ca_8Mg_{52}Fe_{40}$ and is slightly Mg-rich compared with that of the Moore County pyroxene ($Ca_{10}Mg_{46}Fe_{44}$)[6].

For the Serra de Magé pyroxene, pyroxene having the bulk Ca composition of 8 mol% begins to exsolve at 970 °C when the bulk Ca composition meets the solvus, and cools down to 600 °C at a rate of 0.0002 °C/yr to form a coarse (001) augite lamella of 35 μm in width (Fig. 1). This cooling rate corresponds to a burial depth of about 7 km by assuming a rock-like thermal diffusivity (0.004 cm^2/s). The result of Serra de Magé gives a good agreement between the calculated profile and observed one without the assumption of a reheating event, unlike the Moore County pyroxene [2]. The slow cooling rate of Serra de Magé is in agreement with earlier proposal by Harlow et al. [5]. Table 1 summarizes the results of the burial depth and cooling rate of eucrites obtained by our diffusional calculations.

Table 1 also shows the result of "ordinary eucrite" Juvinas [1] which is different from cumulate eucrite for comparison. The Juvinas pyroxene has thin augite lamellae, suggesting the shallower origin compared with the cumulate eucrites.

The slow cooling yields the wide lamella. Roughly speaking, the width of lamella is inverse to the square root of a cooling rate on the assumption of diffusion-controlled lamella growth. Although the Serra de

THICKNESS OF EUCRITIC CRUST: Miyamoto M. and Takeda H.

Magé pyroxene has augite lamella of 35 μm in width much narrower than the Moore County pyroxene (100 μm), the cooling rate obtained for the Serra de Magé pyroxene (0.0002 °C/yr) is a small value which is similar to that for the Moore County pyroxene (0.00016 °C/yr). This slow cooling of Serra de Magé despite thin augite lamella compared with Moore County is mainly due to the bulk Ca content of the Serra de Magé pyroxene (8 mol%) lower than that of the Moore County pyroxene (10 mol%)[6].

According to the results of our calculations of the Serra de Magé and Moore County eucrites which have relatively wide augite lamellae among eucrites, the thickness of a eucritic crust in the HED parent body is estimated to be about 10 km.

We thank Drs. M. Prinz and G. E. Harlow for the meteorite samples.

References: [1] Takeda H. (1979) Icarus, 40, 455. [2] Miyamoto M. and Takeda H. (1992) Lunar Planet. Sci. XXIII, 921. [3] Lindsley D. H. (1983) Amer. Mineral., 68, 477-493. [4] Fujino K., Naohara H., and Momoi H. (1990) EOS, 71, 943. [5] Harlow G. E., Nehru C. E., Prinz M., Taylor G. J. and Keil K. (1979) Earth Planet. Sci. Lett., 43, 173. [6] Hess H. H. and Henderson E. P. (1949) Amer. Mineral., 34, 494.

Table 1. The burial depth and cooling rate of eucrites obtained by our diffusional calculation.

Sample	Aug. lamella width(μm)	Burial depth(km)	Cooling rate(°C/yr)	Bulk Ca content of pyroxene(mol%)
Serra de Magé*	35	7	0.0002	8
Moore County*	100	8	0.00016	10**
Juvinas+	3	0.5	0.05	12

* Cumulate eucrite; + Ordinary eucrite. ** Hess & Henderson [6]

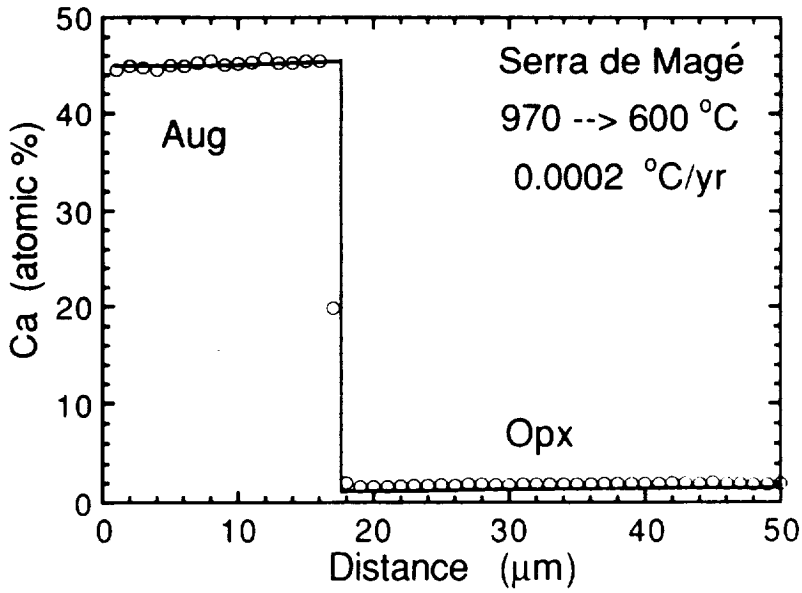

Fig. 1. Ca compositional profiles for augite and orthopyroxene in the Serra de Magé eucrite. Open circles show an observed profile at the interval of 1 μm. The origin is the center of augite lamella. Solid line shows the calculated profile by a cooling from 970 to 600 °C.

ZAOYANG CHONDRITE COOLING HISTORY FROM PYROXENE Fe^{2+}-Mg INTRACRYSTALLINE ORDERING AND EXOLUTIONS: G.M. Molin, Dipartimento di Mineralogia e Petrologia, Università di Padova, Italy; M. Tribaudino. Dipartimento di Scienze Mineralogiche e Petrologiche, Università di Torino Italy and E. Brizi, Dipartimento di Scienze della Terra, Università di Perugia, Italy.

The Zaoyang ordinary chondrite fell as a single 14.15-kg mass in Hubey province (China) in October 1984 and was classified as a non-brecciated H5 chondrite, shock facies b [4]. Cooling rate in pyroxenes can be calculated down to about 1000°C by using fine textures and at still lower temperatures (700 to 200 °C) by intracrystalline ordering processes [1] [2] [3]. The crystal chemistry of clinopyroxene and orthopyroxene from the matrix of the H5 Zaoyang chondrite has been investigated by X-ray structure refinement and detailed microprobe analysis. By comparison with terrestrial pyroxenes cell and polyhedral volumes in clino- and orthopyroxenes show a low crystallization pressure. Fe^{2+} and Mg are rather disordered in M1 and M2 sites of clino- and orthopyroxenes; the closure temperatures of the exchange reaction are 600 and 512°C respectively, which is consistent with a quite fast cooling rate, estimated of the order of one degree per day. The closure temperature for the intercrystalline Ca-Mg exchange reaction for clino- and orthopyroxenes is 900°C, as calculated from a matrix orthopyroxene showing clinopyroxene lamellae about 10μ thick. Kinetic evaluations based on the thickness of exolved lamellae give a cooling rate of not more than a few degrees per 10^4 years.

The different cooling rates obtained from Fe^{2+}-Mg intracrystalline partitioning and exolution lamellae suggest an initial episode of slow cooling at 900°C, followed by faster cooling at temperatures of 600-500°C at low pressure conditions. The most probable scenario of the meteorite history seems that the exolved orthopyroxene entered the parental chondrite body after exolution had taken place at high temperature. Subsequent fast cooling occurred at low temperature after the formation of the body.

REFERENCES

1 Ganguly J. (1982) Me-Fe order-disorder in ferromagnesian silicates. II. Thermodynamics, kinetics and geological applications . Vol. 2. Saxena S. K., (ed). Springer, New York Berlin Heidelberg, 58-99.

2 Molin G.M., Saxena and Brizi E. (1991) Iron-magnesium order-disorder in an orthopyroxene crystal from the Johnstown meteorite. Earth and Pl. Sc. Letters 105,260-265.

3 Molin G. and Zanazzi P.F. (1991) Intracrystalline Fe^{2+}-Mg ordering in augite: Experimental study and geothermometric applications. Eur. J. Mineral. 3,863-875.

4 Wang d. and Rubin A.E. (1987) Petrology of nine ordinary chondrite falls from China. Meteoritics, 22, 97-104.

RELIEF OF SOME SMALL LANDFORMS ON VENUS; H.J. Moore, U.S. Geological Survey, Menlo Park, CA 94025, J.J. Plaut, and T.J. Parker, California Institute of Technology, Jet Propulsion Laboratory, Pasadena, CA 91109.

Three sets of radar images have been acquired under different viewing conditions by the Magellan synthetic aperture radar: (1) left-looking with varied incidence angles (cycle 1); (2) right-looking with nearly constant incidence angles (cycle 2); and (3) left-looking with varied incidence angles, most of which were smaller than those in (1) except for those acquired on passes across Maxwell Montes with incidence angles larger than those in (1) (cycle 3).

Image displacements in the radar images that are caused by the relief of landforms provide several methods of estimating this relief: (1) monoscopic measurements of foreshortening of landforms that are symmetrical in the plane of the look-direction of the radar (includes radial symmetry) [1], (2) stereoscopic measurements of parallax in same-side image pairs [2] (cycles 1 and 3), and (3) measurements of parallax in opposite-side image pairs [3] (cycles 1-2 and/or 2-3). Success in methods 2 and 3 (especially 3) depends on identifying conjugate image points in the two images.

Here, we report our preliminary results for five impact craters, seven small volcanic edifices, and two lava flows (Table 1). The three methods mentioned above lead to the interesting result that Venusian impact craters have depth-diameter ratios like those on Mars rather than those on Earth [4,5,6,7], but some appear partly filled [5]. Our results for de Lalande and Melba also suggest filling, but there may be other causes for their relatively small depth-diameter ratios [8].

A host of small volcanic edifices [9,10] have relief that can be crudely estimated using the above methods (fig. 1). Relief/diameter ratios for our cratered cones (Table 1) are about the same as those of Icelandic lava shields [11,12]; some Venusian cones resemble the Martian shields of Mareotis-Tempe and Ceraunius Fossae, but the Venusian relief/diameter ratios are larger, The smallest cratered dome is similar in size and profile to a Martian dome north of Uranius Patera; the smallest cratered cone resembles one in Chryse Planitia.

Lava flows on Venus that are thick enough to measure are rare, but we have applied methods 1 and 3 to the huge flow of Ovda Regio and flows of an unusual volcano, Mahuea Tholus [3] (Table 1). We know of no terrestrial analogs for the thickest of these flows, but the rhyolite flows of Yellowstone attain thicknesses of 300 m [13].

REFERENCES

[1] Leberl, F. et al., Photog. Engr. Rem. Sens., 57, #12, 1561, 1991.
[2] Leberl, F. et al., JGR, 97, E8, 13,675, 1992.
[3] Moore, H.J. et al., JGR, 97, E8, 13,479, 1992.
[4] Schaber, G.G. et al., JGR, 97, E8, 13,257, 1992.
[5] Sharpton, V.L., AGU, Eos Suppl., Fall Mtg., 331, 1992.
[6] Pike, R.J., Icarus, 43, 1, 1980.
[7] Pike, R.J. and Davis, P.A., LPSC XV, 645-646, 1984.
[8] Schultz, P.H., JGR, 97, E10, 16,183, 1992.
[9] Guest, J.E. et. al., JGR, 97, E10, 1992.
[10] Head, J.W. et al., JGR, 97, E8, 13,153, 1992.
[11] Pike, R.J., Proc. 9th LPSC, 3239-3273, 1978.
[12] Pike, R.J. and Clow, G.D., USGS Open-file Rept. 81-1038, 1981.
[13] Christiansen, R.L. and Hildreth, W., Bull. NM Mines and Miner. Res.,131, 52, 1989.

RELIEF OF SMALL LANDFORMS ON VENUS: H.J. Moore et al.

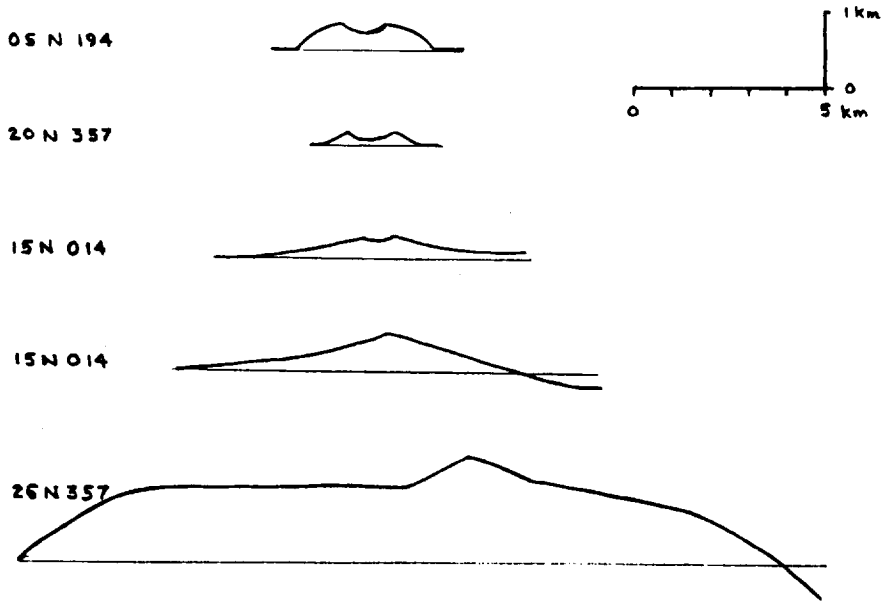

Figure 1. Profiles of small volcanic landforms on Venus. Shapes of flanks of small volcanoes appraised by visual inspection of backscatter. Image numbers shown at left.

TABLE 1. Preliminary estimates of relief of some small landforms on Venus based on relief displacements on monoscopic and paired Magellan images.

Landform	Image Number	Diameter (D) (km)	Relief (R) (km)	Ratio R/D	Method[1]
Impact Craters					
Riley[2]	14N073	24.0	1.3, 1.1, 1.2	0.050 ± 0.004	(1), (1-3), (1-2)
Chloe	06S097	18.5	1.2 - 1.5	0.068 - 0.081	(1-2)
de Lalande[2]	20N357	21.0	0.8 - 0.9	0.038 - 0.043	(1-3)
Melba	05N194	23.5	1.0, 0.9, 0.8, 1.1	0.034 - 0.047	(1), (2), (1-2)
Salika	06S097	15.0	No conjugate images of crater floor		(1-2)
Volcanoes					
cratered dome	05N194	3.5	0.34	0.095	(1-2)
cratered cone	20N357	2.4	0.16 ± 0.07	0.067 ± 0.027	(1-3)
cratered cone	15N014	8.3	0.31	0.037	(1-3)
cone	15N014	10.6	0.48 - 0.68	0.045 - 0.064	(1-3)
dome	25N357	20.9	1.4 - 1.8	0.065 - 0.089	(1-3)
cratered dome	73S101	4.7	0.24 ± 0.05	0.051 ± 0.010	(1-3)
cratered cone	73S101	3.3	0.18 ± 0.03	0.054 ± 0.010	(1-3)
Lava Flows					
Mahuea Tholus	37S165				
lobes			0.06 ± 0.03		(1)
lobes			0.12 ± 0.05		(1-2)
thick flows			0.54 ± 0.20		(1-2)
thick flows			0.09 ± 0.05		(1-2)
Ovda Regio[2]	06S097				
lobes			0.17 - 0.28		(1)
lobes			0.42 ± 0.15		(1-2)

[1] Numbers refer to cycle of image(s); methods are: monoscopic - (1), (2); same-side stereo-parallax - (1-3); opposite-side parallax - (1-2)

[2] Name formally approved by the International Astronomical Union; names of other features are provisional..

MARS BRINE FORMATION EXPERIMENT; Jeffrey M. Moore[1], Mark A. Bullock[2], and Carol R. Stoker[1], (1) Space Sciences Division, NASA Ames Research Center, Moffett Field, CA 94035; (2) Department of Astrophysical, Planetary, and Atmospheric Sciences, University of Colorado, Boulder, CO 80309

The presence of water-soluble cations and anions in the martian regolith has been the subject of speculation for some time (e.g. Malin, 1974). Viking lander data provided evidence for salt-cemented crusts on the martian surface. This evidence is in the form of lander imagery of friable soil layers and planar fragments of disturbed soil (e.g. Moore *et al.*, 1977; Mutch *et al.*, 1977), and the detection of abundant sulfur and some evidence for chlorine in the soil (e.g. Clark *et al.*, 1976). Martian sulfur is very likely to exist in the form of sulfate, and chlorine in the form of chlorides (Clark *et al.*, 1976), chlorates, or perchlorates (Oyama *et al.*, 1977). Following the Viking landings, there was considerable discussion of other salt-forming materials which "should" exist on the martian surface, including carbonates (e.g. Gooding, 1978) and nitrates (e.g. Yung *et al.*, 1977; Yung, 1989). Very recently, earth-based IR spectroscopic evidence has been obtained indicating the presence of carbonates as well as sulfates and other hydrates on the martian surface (Pollack *et al.*, 1989). Carbonates have been detected in the SNC meteorites that are commonly believed to have a martian origin (Gooding *et al.*, 1988). If the crusts observed at the two Viking landing sites are, in fact, cemented by salts, and these crusts are globally widespread, as IRTM-derived thermal inertia studies of the martian surface seem to suggest (e.g. Jakosky and Christensen, 1986), then evaporite deposits, probably at least in part derived from brines, are a major component of the martian regolith. The composition of liquid brines in the subsurface, which not only may be major agents of physical weathering (Malin, 1974), but may also presently constitute a major deep subsurface liquid reservoir (Clifford, 1987), is currently unconstrained by experimental work.

A knowledge of the chemical identity and rate of production of martian brines is a critical first-order step toward understanding the nature of both these fluids and their precipitated evaporites. Laboratory experiments are being conducted to determine the identity and production rate of water-soluble ions that form in initially pure liquid water in contact with Mars-mixture gases and unaltered Mars-analog minerals. The main components of the experiment apparatus consist of ten identical, hermetically sealable sample containers made of Teflon. The interior volume of the containers is 250 ml. The lids of each container have two ports to which are fixed stopcocks to provide gas flow access to the head space when needed. Above one of the stopcocks a stainless steel vacuum/gas line fitting was mounted. Eight of the containers will be kepted within a large (and heavy) bell jar. The bell jar's mouth is sealed to its base plate with vacuum grease. The bell jar base contains two gas ports. Each port has a stainless steel gas line running from the exterior of the base. One line is attached to a cylinder of gas with the same mixture as that of the martian atmosphere. The entire assembly of bell jar and enclosed sample containers set within a large refrigerator whose interior can be maintained at 20±0.5°C. The other two sample containers also reside within the refrigerator.

The experiment pilot run set consists of ten samples. Individual pristine minerals to be used to simulate martian rocks were chosen on the basis of SNC meteorite mineralogy as outlined by McSween (1985). Six of the samples are composed of 50 g of sorted and mixed minerals (57.2% augite, 25.26% forsterite, 13.14% anorthoclase, 3.14% ilmenite, 0.78% pyrite, and 0.48% chloro-apatite) acting as unaltered Mars rock analogs immersed in 100 ml of de-oxygenated, doubly distilled liquid H_2O, and above which the head space is filled with a martian gas mixture (CO_2 95.50%, N_2 2.70%, Ar 1.60%, O_2 0.13%, CO 0.07%). These six containers will be the source of the principle data to be obtained by this pilot run set. Two other sample containers are filled with the same materials as those just discussed but with terrestrial gas in their head space. The results of the analysis of their fluids will provide some ability to compare the "martian" verses terrestrial environmental influence, which in this case is only the difference between the two

MARS BRINE FORMATION EXPERIMENT: Moore, J.M., M.A. Bullock and C.R. Stoker

atmospheric compositions. Two other sample containers hold 100 ml of de-oxygenated, doubly-distilled H_2O and martian gas mixture in the head space (no rock particles). These serve as controls. The rock/gas/water or gas/water mixtures are allowed to interact with one another for specific time durations then the reaction are stopped by the removal of the fluid, which is stored under argon in the transfer containers. The individual run durations were chosen on the basis that most chemical reaction rates (including those that are grain-rind diffusion limited) decay exponentially with time.

Eight Mars gas-containing containers were placed within a bell jar. The bell jar is flushed with Mars gas. The bell jar and the two containers with Earth gas in their head space reside within a refrigerator. The temperature within the refrigerator is maintained at a constant $20 \pm 0.5°$ C. The temperature is periodically monitored with an analog (Hg-containing) thermometer which sets within a depression on the bell jar base (exterior to the bell jar). The gas pressure within the sample containers is 1 bar. When sample interaction is terminated, the container is removed from the bell jar. The fluids of the samples are analyzed for their *p*H and for a number of cations and anions. The cations to be searched for are Fe, Mg, Al, K, Na, Ca, Ti, Mn, and Ba with minimum quantity detection limit of 1 ppm. The anions to be examined are Cl^-, F^-, $SO_4^=$, SO_3^-, $NO_3^=$, NO_2^-, and $CO_3^=$ with minimum detection limits of 10 ppm. **The preliminary results at the end of the sixth month of the experiment are that "martian" aqueous chemistry is dominated by Ca and CO_3, and a CO_2 atmosphere significantly alters dissolution rates and products (in comparison to the terrestrial case).**

The results of the pilot run set will provide the first experimental determination of the rates of formation and relative abundances of the common water-soluble cations and anions that form in liquid water in contact with initially unaltered "martian" rocks and the gases of the present martian atmosphere for up to two years after initial contact. If an equilibrium composition is recognized or can be extrapolated from trends in the production rates, then a model martian brine composition will be established. Such a brine can then be synthesized in any lab. The dehydration of the model brine could be used to create a model martian evaporite. The presence of brines on Mars has been hypothesized, both as a crustal store of H_2O-rich liquid and as an agent of chemical rock weathering. The physical properties of martian brine can be evaluated by making solutions of brine at various concentrations, guided by the results of this experiment, and then measuring such parameters as density and freezing point. The model martian brine can also be used in rock weathering experiments or calculations. An extension of this work would be to investigate the effect of brine/evaporite composition on clay mineral chemistry. The spectral signature of the model evaporite can be compared with spectral data to be obtained from past, present, or forthcoming missions and observations.

REFERENCES

Clark, B.C., *et al.* (1976) Inorganic analyses of martian surface samples at the Viking landing sites, *Science, 194*, 1283-1288. Clifford, S.M. (1987) Polar basal melting on Mars, *J. Geophys. Res., 92*, 9135-9152. Gooding, J.L. (1978) Chemical weathering on Mars: Thermodynamic stabilities of primary minerals (and their alteration products) from mafic igneous rocks, *Icarus, 33*, 483-513. Gooding, *et al.* (1988) Calcium carbonate and sulfate of possible extraterrestrial origin in the EETA79001 meteorite, *Geochim. Cosmochim. Acta, 52*, 909-915. Jakosky, B.M. and P.R. Christensen (1986) Global duricrust on Mars: Analysis of remote sensing data, *J. Geophys. Res., 91*, 3547-3559. Malin, M.C. (1974) Salt weathering on Mars, *J. Geophys. Res., 79*, 3888-3894. Moore, *et al.* (1977) Surface materials of the Viking landing sites, Mars, *J. Geophys. Res., 82*, 4497-4523. Mutch, T.A., *et al.* (1977) The geology of the Viking 2 site, *J. Geophys. Res., 82*, 4452-4467. Oyama, *et al.* (1977) Preliminary findings of the Viking gas exchange experiment and a model for martian surface chemistry, *Nature, 265*, 110-114. Pollack, *et al.* (1989) Thermal emission spectra of Mars (5.4-10.5 mm): Evidence for sulfates, carbonates, and hydrates (abs.), *Bull. Amer. Astron. Soc., 21*, 956-957. Siever, R. and N. Woodford (1979) Dissolution kinetics and the weathering of mafic minerals, *Geochim. Cosmochim. Acta, 43*, 717-724. Yung, Y.L., *et al.* (1977) Photochemistry of nitrogen in the martian atmosphere, *Icarus, 30*, 26-41. Yung, Y.L. (1989) Is the martian atmosphere denitrified by ice clouds? (abs.), *Bull. Amer. Astron. Soc., 21*, 979.

CATALYTIC CRYSTALLIZATION OF ICES BY SMALL SILICATE SMOKES AT TEMPERATURES LESS THAN 20K; M. Moore, R. Ferrante [1], R. Hudson[2], T. Tanabe [3] and J. Nuth, Astrochemistry Branch, Code 691, NASA Goddard Space Flight Center, Greenbelt, MD 20771

Samples of methanol and water ices condensed from the vapor onto aluminum substrates at low temperatures (below ~80 K) form amorphous ices; annealing at temperatures in excess of 140-155K is usually required to convert such amorphous samples to crystalline ices. However, we have found that when either methanol or water vapor is deposited onto aluminum substrates that have been coated with a thin (0.1-0.5 mm) layer of amorphous silicate smoke, the ices condense in crystalline form. We believe that crystalline ice forms as the result of energy liberated at the ice/silicate interface perhaps due to weak bonding of the ice at defect sites on the grains and the very high surface to volume ratio and defect density of these smokes. Annealing of amorphous water ice mixed with more volatile components such as methane, carbon monoxide, etc., has been suggested as an efficient way to produce clatherates in the outer solar nebula and thus explain the volatile content of comets and icy satellites of the outer planets (Lunine et al., 1991). This hypothesis may need to be re-examined if amorphous ice does not form on cold silicate grains.

Silicate smokes were prepared in a bell jar by the evaporation of SiO solid heated in an alumina crucible at T > 1500K followed by vapor phase nucleation and growth in a 100 torr hydrogen atmosphere at the ambient temperatures above the crucible (Nuth and Donn, 1983). Smokes were collected onto aluminum substrates placed from 10-30 cm away from the crucible. This provided considerable variation in the thickness of the smoke layers from relatively thick deposits (> 1mm) to less than a full monolayer of smoke. Smoke-covered substrates were transferred in air from the bell jar to a dessicator where they were stored until needed. Inidividual substrates were attached to a cold finger, evacuated to 10^{-6} torr, cooled to T ~10K then exposed to condensible vapor sprayed onto the surface through a capillary tube from a 5 liter reservoir. The temperature of the substrate was maintained below 15K during deposition of the ice layer (Nuth and Moore, 1989).

Infrared spectra of the ice deposits were obtained using a Mattson Polaris FTIR; the sample beam is reflected from the aluminum substrate resulting in an absorbance spectrum representing two passes through the sample. In studies of the effects of the silicate smoke on the ice, the "background" spectrum used was the initial smoke-covered substrate. In studies of the effect of the ice on the smoke, the reference spectrum used was a polished aluminum substrate free from smoke. Spectra of the ices on the smoke covered substrate were obtained in both the mid-(4000-400 cm^{-1}) and far-(500-100 cm^{-1}) infrared regions in separate experiments due to the need for different beamsplitter/detector combinations to operate in these wavelength ranges. Spectra detailing the changes in the smokes resulting from exposure to the ice were only obtained in the mid-infrared. In both sets of experiments some studies of the effects of irradiating the samples with 1 MeV protons to a total flux of up to 10^{15} protons/cm^2 were undertaken using the GSFC Van der Graaf accelerator.

In general changes in the structure of the silicate smoke due to exposure to water vapor or oxygen, as evidenced by changes in the infrared spectra of the samples, occurred on a relatively long timescale and were usually quite subtle in nature. Larger changes were observed only when water-ice coated samples were annealed at temperatures significantly above 100K or after proton irradiation. More detailed results of these

experiments will be reported elsewhere. Because of the relative stability of the silicate smoke at low temperatures, one smoke-coated subtrate could be used for many volatile-ice studies.

As noted above when either methanol or water vapor was deposited onto a smoke-coated substrate at T <15K, the resultant ice spectra appear to be typical of crystalline ices in both the mid- and far-IR experiments. Ammonia deposited onto the silica coated substrate exhibited a far-IR spectrum intermediate between an amorphous (peak near 417 cm^{-1}) and crystalline (peak near 352 cm^{-1}) ice with maximum absorbance near 388 cm^{-1}. An experiment in which water-vapor was deposited onto a thick (>1 mm) smoke-covered substrate which had remained in the dissicator for ~ 1 month prior to use resulted in an amorphous ice deposit. Because the smoke is a relatively good insulator we might have initially expected this substrate to form a stratified amorphous-crystalline desposit with the amorphous ice near the cold substrate and the more crystalline ice near the outer surface of the smoke. Alternatively we would have expected a crystalline ice deposit. However, production of an amorphous ice can really only be explained if the smoke catalyst had been poisoned by long exposure to air prior to the experiment. This idea leads naturally to the conclusion that the catalytic crystallization occurs via reaction of the vapor with oxygen-defect sites in the solid smoke. In support of this hypothesis we note that deposition of methanol onto silicate smoke results in several bands not observed when methanol is deposited directly onto aluminum. We postulate that these bands represent methanol bonded to oxygen defect sites in the smoke.

Irradiation of crystalline methanol ice on a smoke-covered aluminum substrate results in an amorphous methanol ice and the synthesis of new species such as carbon monoxide and formaldehyde. No substantial changes were noted between irradiation of methanol on silica and similar experiments on an aluminum substrate. Finally, deposition of water or methanol onto silica smoke appears to result in a large decrease in the strength of the far-IR absorbance of the ice. More experiments on the effect of the silica substrate on the far-IR cross-section of water and methanol ices and on the synthesis of new species during the irradiation of methanol ice are needed before firm conclusions can be reached. Experiments to test the hypothesis that active, oxygen-defect sites are responsible for the catalytic production of crystalline ices are also needed. If this hypothesis is correct then follow-up experiments to determine the rate at which such defects are eliminated by exposure to air and water vapor as a function of temperature and partial pressure of the reactive species will also be needed in order to assess the longevity of such catalytic agents in the primordial solar nebula.

1. also: Chemistry Dept., US Naval Academy, Annapolis, MD
2. also: Chemistry Dept., Echerd College, St. Petersburg, FL
3. also: Institute of Astronomy, University of Tokyo, Mitaka, Tokyo, Japan

References

Lunine, J. I., Engel, S., Rizk, B. and Haranyi, M. (1991), Icarus 94, 333-344.

Nuth, J. A. and Donn, B. (1983), J. Geophys. Res. Red Suppl. 88, A847-A852.

Nuth, J. A. and Moore, M. H. (1989), Proc. Lun. Plan. Sci. Conf. 19, 565-569.

EFFECTIVE ELASTIC THICKNESS OF THE VENUSIAN LITHOSPHERE WITH LATERAL VISCOSITY VARIATIONS IN THE MANTLE. Louis Moresi, Seismological Laboratory 252-21, California Institute of Technology, Pasadena, CA 91101.

Both the Earth and Venus have a convecting mantle at the top of which is a relatively strong, mechanical boundary layer. The surface topography and gravity signals which result from the convection within the viscous mantle are modified by the elastic properties of this lithospheric boundary layer. In particular the ability of the of the lithosphere to support loads and transmit stresses from below is a function of the wavelength of the load — the lithosphere is strong to loading at shorter wavelengths [1]. As a consequence it is usual to expect that long wavelength topography cannot be supported by the mechanical strength of the lithosphere and must be compensated — isostatically or dynamically — within the uppermost mantle or the crust [2]. The flexural rigidity of the lithosphere can therefore be determined by estimating the greatest wavelength at which uncompensated surface topography can be supported, usually by measuring the admittance as a function of wavelength [3,4]. In fact this procedure for determining the elastic thickness relies upon being able to distinguish topography with underlying support from that supported by the brittle lithosphere on the basis of their each having a characteristic value of the admittance. However, in the presence of lateral viscosity variations in the mantle, it is possible for topography to be generated which is NOT compensated by density anomalies in the underlying mantle at the same wavelength. Although this effect is not likely to be important for the Earth, on Venus, where the high surface temperatures would be expected to give a weaker lithosphere, lateral viscosity variations in the mantle can give a misleadingly large apparent elastic thickness for the lithosphere.

In the Earth the strength of the oceanic lithosphere is sufficient to mask signals from the mantle with a wavelength greater than about 500 km — the elastic thickness corresponds to the depth to the 300-600°C isotherm [5,6]. On Venus, the higher surface temperature should lead to a smaller lithospheric elastic thickness allowing the surface expression of shorter wavelength topography with origin in mantle convection processes. Flexural models for Venus produce ambiguous results for the elastic thickness of the lithosphere. For mountainous areas a value between 10 and 20 km is obtained [7] whereas subduction models of coronae require a value of 30–40 km [8] which is very similar to that of oceanic lithosphere on the Earth.

Zuber and Nerem recently suggested that a regionally averaged effective elastic thickness could be obtained for Venus in areas where high quality gravity and altimetry data coexist [9]. If, however, the lithosphere of Venus is truly weak and short wavelengths in the topography are derived from underlying viscous flow processes then it is likely that lateral variations in the mantle viscosity will give rise to a falsely large value of the elastic thickness.

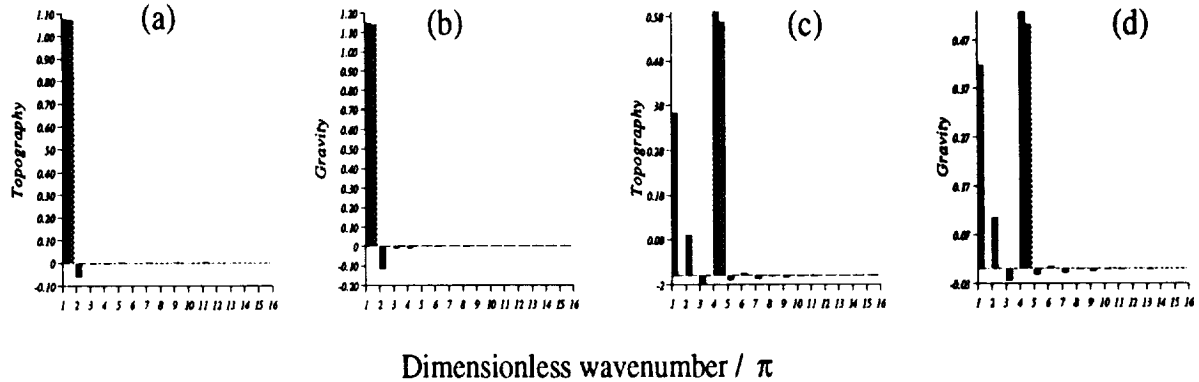

Figure 1: *Fraction of the topography (a,c) and gravity (b,d) signal produced at a wavenumber of π in a,b and at 4π in c,d by each of the wavenumbers in the temperature field along the horizontal axis.*($k = 2\pi D_{\text{layer}}/\lambda$) *At the shorter wavelength approximately half of the each signal at the surface is produced by coupling. The light bar indicates the signal recovered using a horizontally averaged viscosity with the full temperature field. Results are for a convecting layer, Ra* 10^5, *viscosity* = $\exp(-2.7T)$, *free boundaries, fixed temperature top and bottom.*

For constant viscosity convection models, the surface topography and gravity at a given wavelength are produced by density anomalies within the mantle of the same wavelength [10]. However, with temperature dependent viscosity, this relationship is not preserved. Perturbation calculations show that density anomalies with one wavelength can couple through the lateral viscosity variations to produce surface topography at both longer and shorter wavelengths [11].

APPARENT T_e FOR VARIABLE VISCOSITY CONVECTION Moresi, L.

The strongest coupling effects will be *observed* at the shortest wavelengths in the system where the temperature anomalies of the same wavelength are weakest and the surface observables are only sensitive to the structure of the uppermost mantle. This is borne out in numerical calculations of convection with temperature dependent viscosity, summarized in figure 1.

The most important property of short wavelength topography which is generated from long wavelength temperature anomalies within the mantle is that there is no compensating density anomaly of the same wavelength at shallow depth. This gives a value of the admittance at this wavelength which is the same as if the topography was supported on a strong, rigid lithosphere. This observation depends only upon the predominance of long wavelengths in the spectrum of the density anomalies in the mantle. The wavelength at which the topography appears to be uncompensated, though, must depend on the detailed structure of the convection and the strength of the lateral viscosity variation.

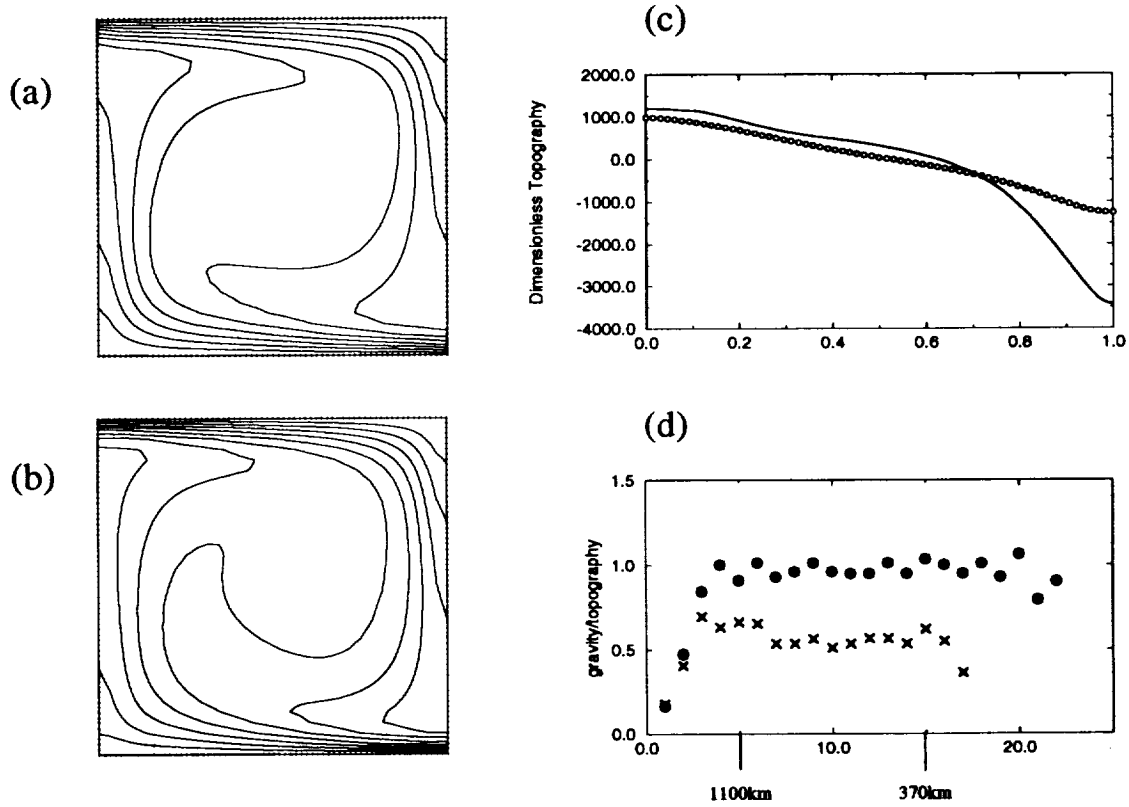

Figure 2: *(a) Constant viscosity convection model with free boundaries at Ra* 3.17×10^4*, 64×64 grid. (b) Viscosity* $= \exp(-2.31T)$*, Ra* 10^4*. (c) Dimensionless topography for (a) shown with circles, (b) solid, thick line. (d) Admittance as a function of dimensionless wavenumber (and wavelength) for (a) shown by crosses and (b) shown by solid circles.*

The two solutions of figure 2 are chosen to have the same Nusselt number [12]. The variable viscosity solution has a richer topography spectrum at short wavelengths much of which is due to coupling from long wavelength temperature anomalies. High (uncompensated) values for the admittance occur for relatively long wavelengths of ~1000 km. At higher, more realistic Rayleigh numbers these effects are more pronounced but limited to shorter wavelengths. Coupling processes in broader boxes also give rise to phase shifts between the topography and gravity at intermediate wavelengths i.e. a genuinely complex admittance.

References [1] Walcott, R.,(1970) JGR 75, 3941–3954; [2] McKenzie, D.,(1967), JGR 72, 6261–6273; [3] McKenzie, D., C. Bowin, (1976), JGR 81, 1903–1915; [4] Watts A., (1978), JGR 83, 5989–6004; [5] Watts, A.,J. Bodine, N. Ribe, (1980), Nature 283, 532–537; [6] Watts, A.,J. Bodine, M. Steckler, (1980), JGR 85, 6369–6376; [7] Solomon, S., J. Head, (1990), GRL 17, 1393–1396; [8] Sandwell, D., G. Schubert, (1992), Science 257, 766-770; [9] Zuber, M., R. Nerem, (1992), EOS 73 suppl., 329; [10] Parsons B., S. Daly, (1983), JGR 88, 1131–1144; [11] Moresi, L., (1992) D.Phil. Thesis, Oxford University, UK; [12] Nataf, H.-C., F. Richer, (1982), Phys. Earth. Plan. Inter. 29, 320–329.

OPTICAL EFFECTS OF REGOLITH PROCESSES ON S ASTEROIDS AS SIMULATED BY LASER IMPULSE ALTERATION OF ORDINARY CHONDRITE; L.V.Moroz (1), A.V.Fisenko (1), L.F.Semjonova (1), and C.M.Pieters (2). 1 - Vernadsky Institute, Russian Academy of Sciences, 117975, Kosygin St.19, Moscow, Russia. 2 - Brown University, Box 1846, Providence, RI 02912.

The spectral properties of some powdered chondrites and minerals altered by laser impulse are studied in order to estimate possible optical effects of regolith processes (micrometeoritic bombardment). Gradual reduction of overall reflectance and spectral contrast, the increase of continuum slope, the increase of spectrally derived olivine/ pyroxene ratio and Fs content of orthopyroxene with increasing alteration degree show that regolith processes could affect optical properties of surface material more heavily than has been previously appreciated.

INTRODUCTION: Ordinary chondrites (OCs) are known to account for 80% of observed meteorite falls, but so far no main belt parent bodies have been identified for these meteorites. S-asteroids resemble OCs spectrally, but are characterized by a steeper red continuum unlike that of OCs and their spectrally derived mineralogies are far outside OC range [1]. Attempts were made to explain the spectral mismatch between OCs and S asteroids by some process, which alters optical properties of uppermost regolith. However, the spectral studies of shocked (black) OCs [2], gas-rich OCs [3], melted OCs [4] and synthetic metal-rich regoliths derived from OCs [5] demonstrate that such altered OC materials darken, but do not redden.

EXPERIMENTAL PROCEDURE: To evaluate possible spectral effects of regolith processes on asteroidal surfaces the powdered specimens of Elenovka (L5), Allende (CV3), pure olivine and clinopyroxene and ol-cpx mixture (50/50) were treated by 1.06 μm laser impulse in vacuum 10^{-4} Torr (spot's focussing diameter 0.1 mm). Initial samples ("unaltered") were ground and sieved to particle size <75 μm and their spectra were measured. The specimens after treatment by laser impulse were sieved. The spectra of finer separates (<75 μm; "partly altered samples") have been recorded. More heavily altered coarser size fractions were ground to a particle size < 75 μm ("altered samples"). Among other effects, the samples after the treatment contain a lot of glass. Reflectance spectra of these samples were also obtained. Bidirectional reflectance spectra in the range of 0.3-2.7 μm at a viewing geometry $i=30^{\circ}$, $e=0^{\circ}$ were recorded with NASA RELAB instrument at Brown University. Straight line continuum removal has been performed in some cases to isolate specific absorption bands. Band centers were calculated by fitting a quadratic equation to 10 data points on either side of visually determined center. The ratios of the areas of 2 μm absorption feature (band II) to 1 μm one (band I) [6] have been calculated for Elenovka series.

RESULTS: The most obvious spectral changes are a drop in overall reflectance (darkening) and a reduction of spectral contrast with increasing alteration degree (Table 1 and Fig.1). Such optical effects are observed for shocked OCs [e.g. 2], gas-rich OCs [3], fused OCs [4]. More striking effects are:

1) A continuum slope reddens noticeably with increasing alteration degree. For example, $R_{2.5}/R_{0.56}$ ratio raises from 1.043 for unaltered Elenovka sample up to 1.49 for altered one (the value similar to that of S-type asteroid 8 Flora, Fig.1). $R_{2.5}/R_{0.56}$ range for Allende samples is 1.159-1.494. $R_{2.5}/R_{1.3}$ ratio for olivine series changes from 1.007 (unaltered) up to 1.086 (altered).

2) Alteration caused by laser impulse results in the shifts of wavelength positions of band I and band II centers (Table 1). Band I moves from 0.94 μm (unaltered) up to 1.05 μm (altered) for Elenovka series. The band I position is a function of relative abundance and composition of olivine and orthopyroxene phases. The band moves toward longer wavelength with increasing olivine abundance as well as increasing ferrous iron content [7]. The lesser shift to longer wavelength with increasing alteration degree are observed for band II (Table 1). Band II position is sensitive to Fs content of pyroxene [8]. Calibration of Adams [8] appears to overestimate Fs content of unaltered Elenovka opx (Table 1). Actual Fs content of Elenovka opx is 22 [9].

3) The 2 μm/1 μm (BI/BII) band area ratio for Elenovka series decreases as the result of alteration. BI/BII area is primarily a function of relative abundance of ol and opx phases [7]. Ol/px ratio by weight increases from 2.8 for "unaltered" Elenovka to ~ 5.4 for "altered one". Similar trend can be observed for olivine-clinopyroxene series (50/50).The data of Cloutis and Gaffey [6] allow to roughly estimate cpx abundance, using the position of tangent intercept. "Tangent intercept" (Table 1) is a position of intersection point of a horizontal straight line tangent to the peak near 0.7 μm with the long wavelength side of band I [6]. Spectrally derived cpx abundance decreases from 50% for "unaltered" sample to 0-18% for "altered" one.

IMPLICATIONS FOR S-TYPE ASTEROIDS: Shown in Fig.1 are the spectra of Elenovka series compared to the spectral reflectance curve of 8 Flora [5]. The spectral slope of "altered" Elenovka sample (curve 3) is comparable with that of 8 Flora, although the Band I and II positions and BII/BI area ratios are different [5]. Fig.2 shows the band I centers plotted relative to the BI/BII area ratios for 23 S-asteroids and Vesta compared to those of chondrites, achondrites (from [5]) and Elenovka series. The point for Elenovka OC shows a shift from "chondritic" field ("unaltered" sample) to the field of olivine rich S-asteroids ("altered" sample). Laser impulse alteration raises spectrally derived ol/px ratio up to 5.4. This value is far outside OC range (~ 0.6-3.5 [10]), but within the ol/px range for S-type asteroids (usually 1.5 - 6 [11]). The results suggest that micrometeoroid impacts simulated by

laser impulse can enhance spectral similarity between S asteroids and OCs in terms of spectral slope and spectrally derived ol/px ratio. Thus, regolith processed OC-like material may be presented on the surfaces of S-type asteroids, if these surfaces contain impact glass. The data obtained in this study demonstrate that reflectance spectra of atmosphereless bodies should be interpreted with great caution, especially if impact glass formation is anticipated.

REFERENCES: 1) Gaffey, M.J. et al. (1990) LPS XXI, 399-400; 2) Britt, D.T. and Pieters, C.M. (1990) LPS XXI, 127-128; 3) Britt, D.T. and Pieters, C.M. (1991), LPS XXII, 129-130; 4) Clark, B.E., Fanale, F.P., and Salisbury, J. (1992) Icarus 97, 288-297; 5) Gaffey, M.J. (1984) Icarus 60, 83-114; 6) Cloutis, E.A. and Gaffey, M.J. (1991) Earth, Moon, and Planets 53, 11-53; 7) Cloutis, E.A. et al. (1986) J.Geophys.Res. 91, 11641-11653; 8) Adams, J.B. (1974) J.Geophys.Res. 79, 4829-4836; 9) Baryshnikova, G.V. and Lavrukhina, A.K. (1979) Meteoritika 38, 37-45; 10) McSween H.Y., Bennett, M.E. and Jarosewich, E. (1991) LPS XXII, 885-886; 11) Gaffey, M.J. et al. (1990) BAAS 22, No.3, 1114; 12) Clark R.N. and Roush T.L. (1984) J.Geophys.Res.89, 6329-6340

Fig.1. Normalized reflectance spectra (scaled to 1 at 0.56 μm) of S asteroid 8 Flora (from [5]) and the series of Elenovka (L5) samples (particle sizes <75 um). 1 - "unaltered" sample; 2 - "partly altered" sample; 3 - "altered" sample. Fig.2. The band I position versus BII/BI area ratio for 23 S-asteroids and Vesta (solid triangles) compared to those for chondrites ("x" symbols) , achondrites ("+" symbols)(All the data are from [1]) and the series of Elenovka (L5) samples (our data). Symbols: closed square - "unaltered" and "partly altered" samples; open square - "altered" sample. The solid line is the approximate trend of ol-opx mixtures [7].

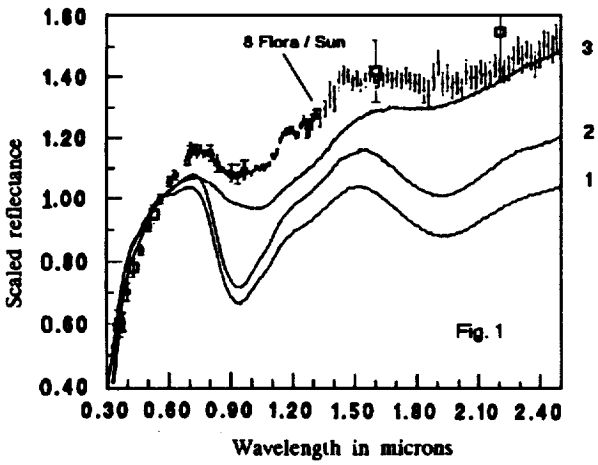

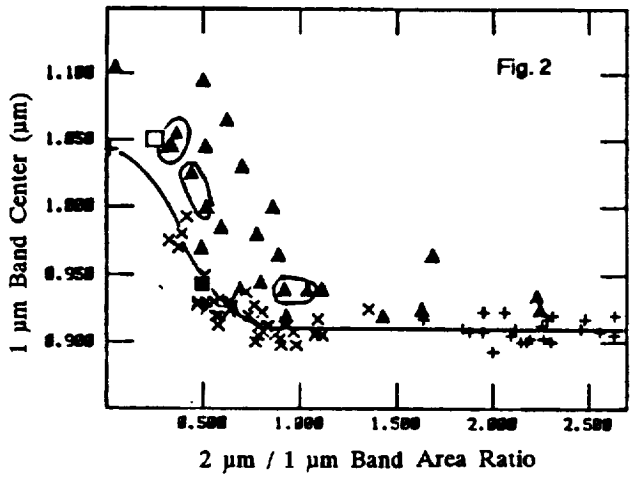

Table 1. Various spectral parameters of some materials used in this study

Sample	Band centers I	Band centers II	Band depth [12]	$R_{0.56}$	Tangent intercept	Peak at 0.7 μm	BI/BII ratio	opx (w%) / opx+ol	ol/px ratio	Fs [8]
ELENOVKA (L5) series:										
unaltered	0.940	1.934	0.363	0.31	1.48	0.71	0.501	26.1	2.8	36
partly altered	0.942	1.936	0.349	0.23	1.37	0.72	0.491	25.7	2.9	36
altered	1.051	1.963	0.160	0.16	1.22	0.75	0.250	15.6	5.4	44
OLIVINE series:										
unaltered	1.055	-	0.452	0.73	1.54	0.57				
partly altered	1.059	-	0.368	0.49	1.38	0.70				
altered	1.072	-	0.174	0.24	2.27	0.75				
OLIVINE-CLINOPYROXENE (50/50) series:										
unaltered	1.047	2.324	0.363	0.55	1.27	0.73				
partly altered	1.048	2.325	0.361	0.44	1.22	0.76				
altered	1.046	1.886	0.296	0.46	1.52	0.60				

ALTITUDE PROFILE OF AEROSOLS ON MARS FROM MEASUREMENTS OF ITS THERMAL RADIATION ON LIMB. V.I.Moroz, D.V.Titov, *Space Research Institute of Russian Academy of Science, Moscow, 117810*, Yu.M.Gektin, M.K.Naraeva, A.S.Selivanov, *Russian Institute of Space Devices Engineering, Moscow, 111024, Russia.*

Measurements of the thermal (range 7 - 13 μm) radiation of Mars with the high space resolution (~2 km) were made by the TERMOSKAN experiment of the Phobos mission (1, 2). Some of results were published earlier but only the surface radiation was analyzed in details (2-4). However some part of these measurements was made near the limb of the planet. The atmosphere gives an important input here in the planetary thermal radiation. Beyond the limb the atmosphere is the only source. The task of this work is to estimate some characteristics of the atmosphere using brightness profiles of the thermal radiation near the limb (Fig.1). An appropriate model of the temperature profile T(h) is necessary for such an analysis. A set of T(h) models (nominal, maximal and minimal) was defined using various sources including MARSGRAM (5), Viking-1 lander data (6), its theoretical considerations (7) and boundary layers models (8). On the next step the possible input of the atmospheric gaseous emissions (wing of CO_2 15 μm band) was estimated. It was found that even for the maximal T(h) this input is no more than a few percents of the measured radiation beyond the limb. Consequently the aerosols are responsible for almost all measured emission. The analysis of the observed profile showed that these aerosols have two components: (1) exponential with the scale height about 10 km and (2) some layered structure (two layers with maxima about 23 and 33 km consisted probably of ice).

Two sorts of aerosols profiles models were builded: grey (all parameters are independent from wavelength) and selective (with some hypotheses about the chemical composition and size distribution of particles). Some of the results are shown on Fig. 1 and in Table 1. Montmorillonite, palagonite, basaltic glasses were tested in selective models for the exponential component. Results are only weakly depend on composition. "Classic" gamma-distribution with $\alpha = \gamma = 1$ by the effective radius 1.6 μm was used for dust (mineral) and also for ice particles. For the dust it was justified by analysis of results of the solar occultation spectrometry (9) and ISM experiment (10) of the Phobos mission. Selective models permit to estimate not only optical depth and scale heights but also mass-loading (5×10^{-5} g/cm^2 for dust and 1×10^{-5} g/cm^2 for high altitude ice layers) and number densities of particles (~2 cm for dust particles near surface).

Selective models admit also the transfer from IR to visible optical depth. It was estimated that the IR (11.25 μm) optical depth 0.06 corresponds to the visible 0.13. This value is in accordance with results of three others remote sensing experiments of the Phobos mission (9-11). However this is 3 times less than measured on Viking landers at the same season (12). Probably a global change of dust content in the Mars atmosphere happened on the time interval about 10 years.

REFERENCES. (1) Selivanov, A.S., et al (1989) Nature, 341, p. 59. (2) Murray, B., et al. (1991) Planet and Space Sci., p. 237. (3) Crumpler, L.S., et al. (1990). Abstracts for the MEVTV bodies on Mars, LPI, p.16. (4) Kuzmin, R.O., et al. (1991) LPSC XXII abstract, p.771. (5) Johnson, D.L., et.al. (1989). The Mars Global Reference atmosphere model. (6) Seiff, a., and Kirk, D.B., (1977) J.Geophys. Res., 82, p. 4363. (7) Pollack, J.B., et al. (1979) J. Geophys. Res. 84, p.2929. (8) Haberle, R., and Houben, H., (1990) COSPAR Simp. on Mars environmental model, Sopron (Hungary), p. 17 (9) Krasnopolsky, V.A., et al. (1991) Icarus, 94, p. 32. (10) Drossart, P., et al. (1991). Ann. Geophis., 9, p.754. (11) Moroz, V.I. et al. (in press), Planet. and Sp. Sci. (12) Colburn, D.S., et al. (1989) Icarus, 79, p.159.

AEROSOLS ON MARS. V.I.Moroz et al.

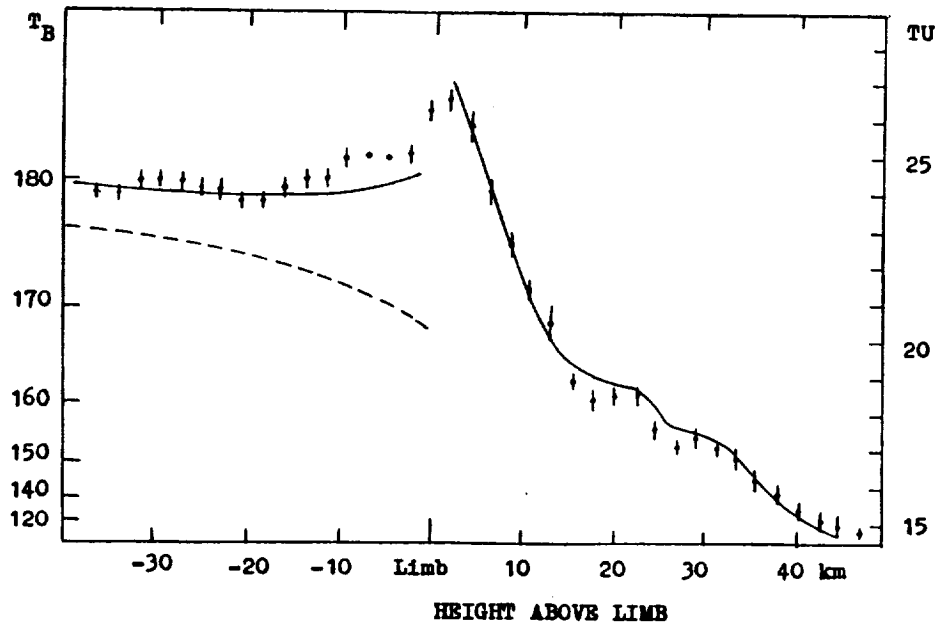

Fig. 1. Results of measurements on morning limb 26 March 1989.
Dots with error bars are measured brightness temperature profile along the limb normal to the limb. This is the average from 8 original profiles. Bars correspond to the r.m.s. errors. Full line is the selective model discribed briefly in the table below. The dashed line is the brightness temperature of the surface "cleaned" from the atmosphere. X-axis is the distance from the geometric limb along the profile. Y-axis on right shows telemetric units (the value 14.5 correspond to zero level of the brightness). The latitude of the observed place was 16°, longitude 148°, solar longitude L_S = 18°, local time $6^h\ 50^m$.

Table 1. Parameters of models of height profile of aerosols.

	Grey	Selective
Single scattering albedo*	0.3	0.3 for dust 0.2 for ice
IR optical depth of exponential component**	$0.060^{+0.040}$	$0.055^{+0.025}$
Scale height	11^{+4}_{-3}	11^{+4}_{-3}
IR optical depth of layers:		
lower (23-24 km)	0.004	0.004
upper (33-34 km)	0.017	0.025

* Averaged (with weights) on the spectral range.

** Here and below for λ = 11.25 μm. Optical constants of palagonite were used by computations for exponential component and water ice for layers.

TERRESTRIAL IMPACT MELTS AS ANALOGUES FOR THE HEMATIZATION OF MARTIAN SURFACE MATERIALS

R. V. Morris[1], H. V. Lauer, Jr.[2], and D. C. Golden[1]. [1]Code SN4, NASA Johnson Space Center, Houston, TX 77058; [2]Lockhheed ESC, Houston, TX 77058.

Abstract. Visible and near-IR reflectivity and Mössbauer data were obtained on powders of hydrothermally-altered impact melt sheets from West Clearwater Lake, Manicouagan, and Ries (Polsingen) impact structures. The data support previous interpretations that Martian bright regions spectra can be interpreted by a ferric-bearing phase that has a relatively featureless absorption edge together with some well-crystalline (bulk) hematite to account for the 860 nm hematite band. The data also show that bands at wavelengths longer than 900 nm, which are characteristic of Martian dark regions, occur when both hematite and pyroxene are present. It thus follows that hematization of Mars can be attributed, at least in part, to hydrothermal alterations of impact melt sheets. Impact heating could also form bulk-Hm from nanophase ferric oxides.

INTRODUCTION. Hydrothermal alteration of impact melt sheets is reported at many terrestrial impact structures, including West Clearwater Lake [1] and Manicouagan [2], both in Quebec, Canada, and the Ries basin [3,4] in Germany. The alteration apparently occurs shortly after the impact by influx of groundwater while the rocks are still hot but below solidus temperatures [1]. The alteration products of glass and mafic minerals at West Clearwater and Manicougan are montmorillonitic clays with hematite and possibly hydrous ferric oxides [1,2]. The reddish, coherent impact melt rock from the Ries basin has been less studied; [3] describe the melts as fine-grained aggregates of predominantly feldspar with minor pyroxene, hematite, and cristobalite. A number of studies [e.g., 5, 6, 7] have advocated that a significant fraction of Martian soil may consist of erosional products of hydrothermally-altered impact melt sheets. This process is consistent with the recent identification of hematite in visible and near-IR spectral data for martian bright regions [e.g., 8, 9, 10].

If erosional products of hydrothermally-altered impact melt sheets are volumetrically important on Mars, their signature may be present in reflectance spectra of Martian bright regions. To investigate this possibility, we have obtained visible and near-IR reflectance spectra for samples from their terrestrial analogues at West Clearwater Lake, Manicouagan, and the Ries Crater (Polsingen). Data were obtained on fine powders (<90 μm) derived from coherent rock samples. To characterize the iron mineralogy and chemistry of the samples, we also obtained Mössbauer and INAA data.

RESULTS AND DISCUSSION. Reflectivity and Mössbauer data (293 K) for five samples are shown in Figure 1. The two samples from West Clearwater Lake (WCW) are red and purple regions from the same rock. The Mössbauer spectra of the samples can be fit by three components: a sextet (IS=0.37 mm/s, QS=-0.21 mm/s, and B_{hf}=51.0 T), a ferric doublet (IS=0.36 mm/s and QS=0.55 mm/s), and a ferrous doublet (IS=1.15 mm/s and QS=2.03 mm/s). The sextet results from well-crystalline hematite (bulk-Hm); the asymmetry of the lines implies impurities (e.g., Ti or Al) are present. The ferrous doublet is reasonably assigned to pyroxene. The assignment of the ferric doublet is uncertain. The Mössbauer parameters imply octahedrally-coordinated ferric iron. The value of QS is significantly smaller than that observed for nanophase ferric oxide particles (np-Ox) in palagonitic soils [e.g., 11, 12]; however, this may result from different formation conditions. It is possible that the doublet results from inherently paramagnetic phases such as lepidocrocite, pseudobrookite, and Fe-bearing clay minerals. Lepidocrocite is not likely, however, because the doublet is not magnetically split at 16 K. The relative contributions of the three components to the individual Mössbauer spectra are highly variable, although bulk-Hm is present in major proportions in all samples. The WCW and Ries samples contain essentially no pyroxene; for the WCW samples, bulk-Hm dominates over the ferric-doublet phase and vice versa for the Ries sample. The two Manicouagan (MAN) samples contain all three phases; MAN-74-125 has the most pyroxene.

The reflectivity spectra of all samples are characterized by an inflection (Ries and MAN) or strong bend (WCW) near 520 nm, an inflection near 620 nm, a relative reflectivity maximum near 750 nm, and, except for MAN-74-217, a band minimum near 860 nm. All off these features are characteristic of bulk-Hm [e.g., 13]. The bend near 520 nm in the WCW samples is stronger because they have the highest relative proportions of bulk-Hm. The band minimum for MAN-74-217 is near 910 nm, which is more characteristic of goethite. However, this assignment is inconsistent with the Mössbauer data. Because Mössbauer data show that this sample has the highest proportion of ferrous iron as pyroxene, the 910 nm minimum is interpreted as a composite feature of ferric and ferrous bands of hematite and pyroxene, respectively.

The spectra of RIES-POL-01 and especially MAN-74-125 are reasonable analogues of Martian bright region spectra. This is additional support for previous interpretations [8, 9, 10] that the Martian bright regions spectra can be interpreted by a ferric-bearing phase that has a relatively featureless absorption edge together with some bulk-Hm to account for the bulk-hematite features. The spectrum for MAN-74-217 is similar to other Martian spectra that have a ferrous-like band minimum longward of 900 nm and a ferric absorption edge [10, 14]. It thus follows that hematization of Mars is, at least in part, a consequence of hydrothermal alterations of impact melt sheets. Impact heating could also form bulk-Hm from nanophase ferric oxides [e.g., 12]. It thus follows that hematization of Mars is, at least in part, a consequence of hydrothermal alterations of impact melt sheets. Impact heating could also form bulk-Hm from nanophase ferric oxides [e.g., 12].

References: [1] Phinney et al., *PLPSC9*, 2659, 1978; [2] Floran et al., *JGR, 83*, 2737, 1978: [3] Pohl et al., *Impact and Explosion Cratering*, 343, 1977; [4] Newsom et al., *PLPSC17, JGR, 91*, E239, 1986; [5] Newsom, *Icarus, 44*, 207, 1980; [6] Kieffer and Simonds, *Rev. Geophys. Space Phys., 18*, 143, 1980; [7] Allen et al., *JGR, 87*, 10083, 1982; [8] Morris et al., *JGR, 94*, 2760, 1989; [9] Morris and Lauer, *JGR, 95*, 5101, 1990; [10] Bell et al., *JGR, 95*, 14447, 1990; [11] Morris et al., *JGR, 95*, 14427, 1990; [12] Bell et al., *JGR*, in press, 1993; [13] Morris et al., *JGR, 90*, 3126, 1985; [14] Murchie et al., *LPS23*, 945, 1992.

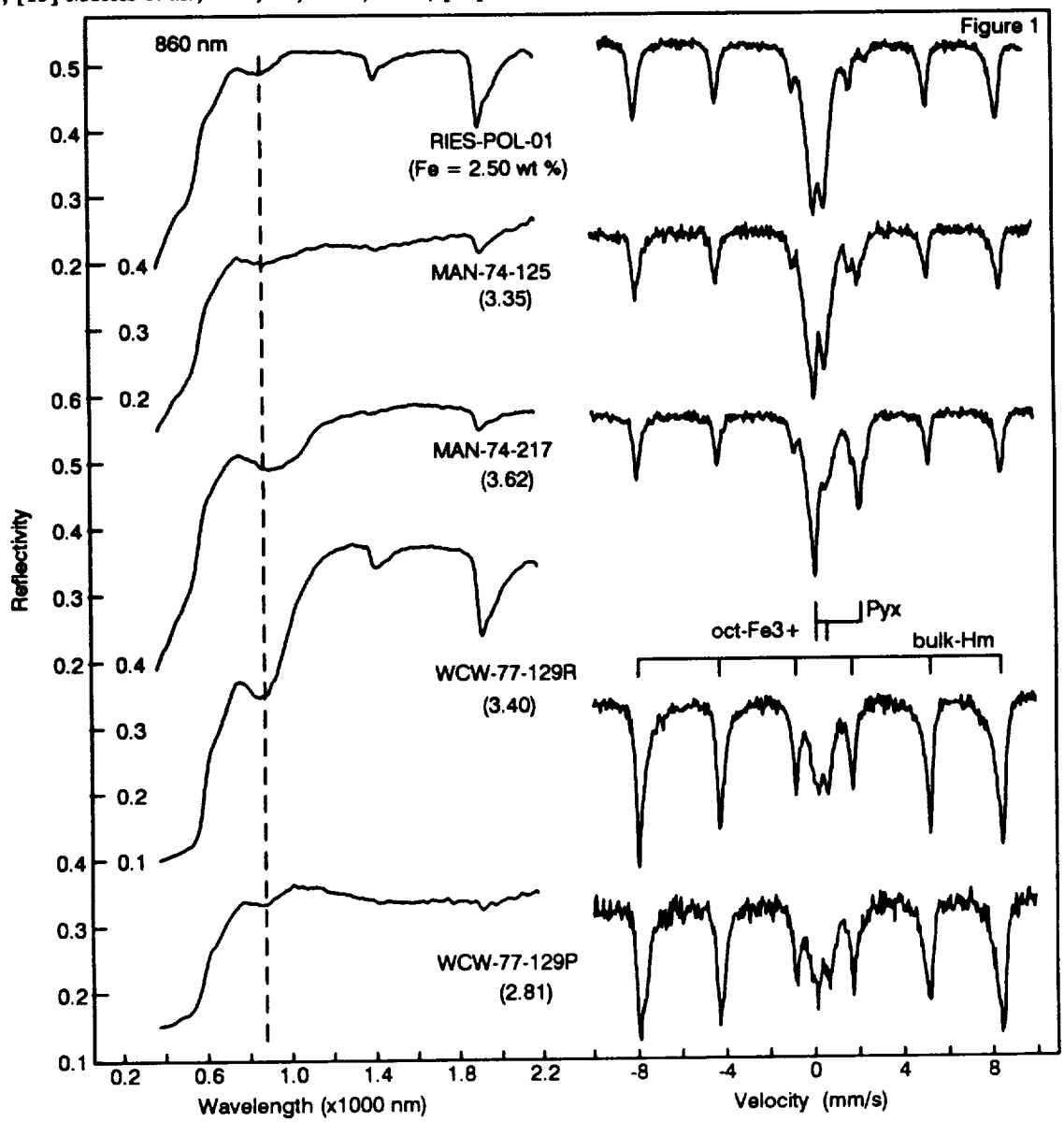

A HYDROGEN ISOTOPE STUDY OF CO3 TYPE CARBONACEOUS CHONDRITES; COMPARISON WITH TYPE 3 ORDINARY CHONDRITES. A.D.Morse, J.Newton and C.T.Pillinger, Planetary Sciences Unit, Department of Earth Sciences, The Open University, Walton Hall, Milton Keynes, MK7 6AA, UK.

Meteorites of the Ornans type 3 carbonaceous chondrites exhibit a range in degree of equilibration, attributed to differing amounts of thermal metamorphism [1,2]. These differences have been used to split the CO3 chondrites into petrologic sub-types from 3.0, least equilibrated, to 3.7, being most equilibrated [2]. This is similar to the system of assigning the type 3 ordinary chondrites into petrologic sub-types 3.0 to 3.9 based upon thermoluminescence (TL) [3] and other properties; however, the actual range of thermal metamorphism experienced by CO3 chondrites is much less than that of the type 3 ordinary chondrites [2]. The least equilibrated ordinary chondrites show evidence of aqueous alteration [4] and have high D/H ratios [5] possibly due to a deuterium-rich organic carrier [6]. The aim of this study was to determine whether the CO3 chondrites, which have experienced similar secondary conditions to the type 3 ordinary chondrites, also contain a similar deuterium-rich carrier. To date a total of 5 CO3 meteorites , out of a set of 11 for which carbon and nitrogen isotopic data are available [7], have been analysed. Ornans has not been analysed yet, because it does not appear to fit in with the metamorphic sequence exhibited by the other CO3 chondrites [1]; it also has an extremely high δD value of +2150‰ [8], unusual for such a comparatively equilibrated meteorite (type 3.4). Initial results indicate that the more equilibrated CO3's tend to have lower δD values, analogous to the higher petrologic type ordinary chondrites. However this is complicated by the effects of terrestrial weathering and the small data-set.

Powdered whole-rock samples, of approximately 50mg, were combusted in two temperature steps. The first low temperature step, from room temperature to 200°C, was an attempt to remove water due to terrestrial contamination whilst the second high temperature step, from 200°C to 1100°C, was assumed to consist of indigenous meteoritic hydrogen. The water obtained from each temperature step was converted to hydrogen by reduction with zinc shot at 450°C, for isotopic analysis by mass spectrometer. The amount of water released was determined by measuring the intensity of the H_2^+ ion beam.

Most of the CO3 chondrites released between 150µg/g to 260µg/g hydrogen, similar to the results of Kerridge [8], with the more equilibrated ones tending to have a lower hydrogen content than the unequilibrated specimens. Two of the CO3's analysed, Colony and Y791717, generated significantly greater amounts of hydrogen, 1560µg/g and 700µg/g respectively. This high hydrogen content is probably an indicator of terrestrial weathering, since both these meteorites are finds and released high amounts of water during the low temperature combustion step which had a δD of *ca.* -150‰ to -100‰. Ash *et al.*[9] found that the effect of weathering on desert CR meteorites was to increase the water content and reduce the high D/H ratios of these meteorites to terrestrial values. The whole-rock carbon

isotopic composition of Colony, $\delta^{13}C$ = -8.8‰, and Y791717, $\delta^{13}C$ = -6.8‰, is another indicator that these two meteorites have experienced terrestrial weathering since most of the CO3 chondrites has $\delta^{13}C$ values in the range of -20 to -13‰[7, 8], apart from the Saharan desert meteorites which have a $\delta^{13}C$ value of approximately -5‰ [7].

The δD values of *ca.* -100‰ of hydrogen released during high temperature steps of the more equilibrated CO3 chondrites is in general in agreement with those of Kerridge [8]. These results suggest that the δD values of the CO3 chondrites decreases with increasing metamorphism, as is the case for the ordinary chondrites[5]. However in this study, the δD of Kainsaz was only -68‰, much lighter than that of δD = +154‰ obtained by Kerridge. This discrepancy could be the result of sample inhomogeneity or incomplete removal of terrestrial contamination during the low temperature step. However we have pointed out previously from carbon and nitrogen studies that Kainsaz petrologic type from that assigned by microscopic studies. A prolonged low temperature combustion at 200°C should be able to resolve the contamination question.

There was no indication of a deuterium-rich component for the least equilibrated CO3, Colony, which had a very light δD value of approximately -150‰. The low δD values obtained for this meteorite, a find, are most likely due to terrestrial contamination; as already reported large quantities of water were released during both low and high temperature steps. Since Colony yields relatively large amounts of hydrogen it will be possible to carry out a stepped combustion with more temperature increments. Longer heating times should ensure that the terrestrial contamination is removed before indigenous hydrogen is released, hence determining whether the least equilibrated CO3's contain a deuterium-rich component, which so far we have been unable to verify.

References

[1] H.Y.McSween Jr., GCA **41**, 477-491 (1977).
[2] E.R.D.Scott and R.H.Jones, GCA **54**, 2485-2502 (1990).
[3] D.W. Sears et al., Nature **287**, 791-795 (1980).
[4] R. Hutchison et al., GCA **51**, 1875-1882 (1987).
[5] N.J. McNaughton et al., J.Geophys.Res **87** A297-A302, (1982).
[6] F.Robert et al., GCA **51**, 1787-1805, (1987).
[7] J.Newton et al., LPSC **XXIII**, 985-986 (1992).
[8] J.F. Kerridge, GCA **49**, 1707-1714, (1985).
[9] R.D.Ash et al., Meteoritics **27**, 199 (1992).

GAMMA-RAY SPECTROMETER FOR LUNAR SCOUT II*; C. E. Moss[1], W. W. Burt[2], B. C. Edwards[1], R. A. Martin[1], G. H. Nakano[3], and R. C. Reedy[1]. [1]Los Alamos National Laboratory, Los Alamos, NM 87545; [2]TRW Space and Technology Group, Los Angeles, CA 90278; [3]Consultant, Los Altos, CA 94022.

We review the current status of the Los Alamos program to develop a high-resolution gamma-ray spectrometer for the Lunar Scout-II mission, which is the second of two Space Exploration Initiative robotic precursor missions to study the Moon. This instrument will measure gamma rays in the energy range of ~0.1–10 MeV to determine the composition of the lunar surface. The instrument is a high-purity germanium crystal surrounded by an CsI anticoincidence shield and cooled by a split Stirling cycle cryocooler. It will provide the abundance of many elements over the entire lunar surface.

Figure 1 shows details of the design. It will contain a ≈ 70% efficient (relative to a 7.62-cm-diameter × 7.62-cm-length NaI(Tl) scintillator) n-type germanium crystal. N-type is used because it is much less susceptible to radiation damage than p-type germanium. Although the radiation damage accumulated in the one-year mission is not expected to degrade the energy resolution if the crystal remains below ~100 K and there are no major solar particle events, we have decided to provide annealing capability to be safe. Because a Stirling cycle cooler will be used, the crystal will be mounted using techniques developed in recent years for operating germanium detectors on vibrating platforms. The inner can, which will be very similar to the Mars Observer one, will be supported by a re-entrant tube design that gives good rigidity and thermal isolation. A CsI(Na) anticoincidence shield on the sides and spacecraft end of the germanium crystal will eliminate most events due to charged particles, gamma rays produced by cosmic rays incident on the spacecraft, and Compton-scattered events in the crystal. This shield will be segmented so that a sector on the side away from the spacecraft can serve as a backup detector with a resolution of about 10%, which is only slightly worse than the 8% value expected with a stand alone CsI(Na) crystal and the resolution for the Apollo NaI(Tl) gamma-ray spectrometers. A plastic scintillator segmented into two pieces surrounds the CsI(Na). The plastic scintillator covering the aperture over the nadir-pointing surface of the germanium crystal rejects charged-particle events without significantly attenuating the lunar gamma-ray flux. Similarly, the plastic scintillator over the backup CsI(Na) segment provides a charged-particle anticoincidence shield in the backup mode. The detector will be on a short pedestal to further reduce the background from the spacecraft.

Because a germanium detector operates at about 80 K, the critical issue for space applications is the method of cooling. For short missions, stored cryogens such as liquid or solid nitrogen, solid methane, or solid argon can be used. For long missions, a passive radiator, as used on the Mars Observer, or an active device, such as a mechanical refrigerator, is required. Because of the complications in shielding a radiator from the Sun, Earth, and Moon when the spacecraft is in a lunar polar orbit, we have chosen to use a split Stirling cycle refrigerator. Such a refrigerator with a germanium detector was successfully flown in 1979 for an extended mission [1]. We selected the British Aerospace (BAe) design [2], which was developed at Oxford University. Designed for a ten-year lifetime, this refrigerator has operated successfully in the laboratory for four years. Two of these units were launched on 12 September 1991 as part of the ISAMS multi-channel infrared radiometer on the Upper Atmosphere Research Satellite, and they are still operating successfully.

Because the germanium detector energy resolution may be degraded by vibration, we will use a pair of these cryocoolers with two compressors and two expanders mounted back to back to minimize vibration. We will also use a flexible vibration decoupler between the expander cold tips and the germanium crystal. Research is being done on these coolers [3] concerning vibration, thermal performance, and reliability, but mainly focused on applications other than germanium detectors. We started tests in 1992 with a single BAe cryocooler coupled via a flexible thermal link to a germanium crystal mounted in a Mars Observer-like can. The compressor and expander were mounted on a 200-pound mass.

The germanium crystal and preamplifier were isolated by suspending them on springs, and the whole system was operated in a vacuum chamber. Preliminary results indicate that the force transmitted to the germanium crystal was only 0.1 N. Based on previous work [1,4] in which known forces were applied to germanium detectors and the resolution was measured, we expect the resolution in a back-to-back configuration to be ~3 keV.

The gamma-ray spectrometer will provide data on many elements over all of the lunar surface. Published estimates of the detection limits for similar detectors range from 0.016 ppm for uranium to 1.3% for calcium [5]. The value for hydrogen is 590 ppm based on the 2.2-MeV hydrogen capture gamma ray. The spatial resolution is about 140-km × 140-km, which is determined by the orbit altitude of 100 km [6]. This instrument senses the elemental composition of the lunar surface to depths of tens of centimeters.

The interpretation of the data will be enhanced by comparisons with data from other instruments. To facilitate this we plan to use software and experience of Mars Observer and to put the data into the Planetary Data System. The neutron spectrometer [7] has a potential sensitivity of 100 ppm hydrogen but needs information from the gamma-ray spectrometer about other elements that can absorb or moderate neutrons. The uncertainties in the elemental abundances from the gamma-ray detector can be reduced if the neutron source intensity in the lunar regolith is provided by the neutron spectrometer because most of the gamma rays are produced by neutron reactions. Comparison of the gamma-ray data with data from instruments having higher spatial resolution and spatial deconvolution of stronger gamma-ray lines will help in understanding lunar features smaller than 140 km.

References: [1] Nakano G. H. *et al.* (1980) *IEEE Trans. Nucl. Sci.*, **NS-27**, 405-410. [2] Werrett S. T. *et al.* (1986) *Adv. Cryo. Engin.*, **31**, 791-799. [3] Ross R. G. *et al.* (1991) *Adv. Cryo. Engin.*, **37**, 1019-1027. [4] Beach L. A. and Phillips G. W. (1986) *Nucl. Instr. Methods*, **A242**, 520-524. [5] Metzger A. E. and Drake D. M. (1991) *J. Geophys. Res.*, **96**, 449-460. [6] Reedy R. C. *et al.* (1973) *J. Geophys. Res.*, **78**, 5847-5866. [7] Auchampaugh G. *et al.* (1993) This Conference. * Work done under the auspices of the US DOE.

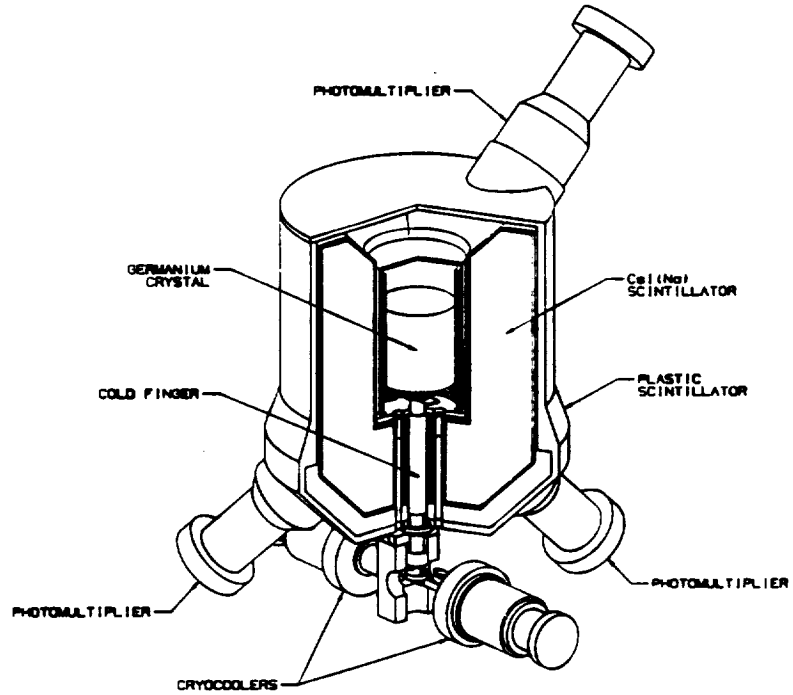

Fig. 1. Gamma-ray spectrometer. The scintillators "shield" the germanium crystal from charged particles and other background radiations. The germanium crystal is cooled via the cold finger from the cryocoolers, which are located on the spacecraft side of the spectrometer.

THE INFLUENCE OF OCEANS ON MARTIAN VOLCANISM Peter Mouginis-Mark, Planetary Geosciences, Geology & Geophysics, SOEST, Univ. Hawaii, Honolulu, HI 96822.

INTRODUCTION: Geomorphological evidence for episodic oceans on Mars has recently been identified (1, 2). This idea of large bodies of water on Mars is innovative and controversial compared to the more generally accepted view of a "dry Mars", but also enables some of the more enigmatic volcanic landforms to be reinterpreted in a self-consistent model. This hypothesis can be used to develop new models for the mode of formation of several volcanic landforms in the W. Tharsis and S.E. Elysium Planitia regions of Mars (Fig. 1).

BASAL ESCARPMENTS: The Olympus Mons escarpment and aureole materials are enigmatic and highly unusual Martian features (3, 4). Early interpretations of the 7 km high escarpment (5) were that it was a wind-eroded cliff (6) or the remnants of a basal layer of heavily cratered materials (7). More recently, a tectonic origin has been proposed (8). However, Olympus Mons is not the only Martian volcano with a basal escarpment; Apollinaris Patera also has such a feature that varies in height from 0.5 - 1.5 km (9). Together with Hecates Tholus (10), these two volcanoes have the lowest base elevations (<2 km above mean Mars datum for each volcano) of any Martian volcano (11). In addition, all three volcanoes are adjacent to the inferred shoreline of the hypothesized Martian seas (2). These relationships may provide a method for eroding the flanks of the volcano, implying that the basal escarpments could be wave-cut cliffs formed in relatively unconsolidated ash deposits.

OLYMPUS MONS AUREOLE DEPOSITS: Considerable debate has also focused on the mode of formation of the Olympus Mons aureole deposits (Fig. 1). A central issue has been the very long run-out distances of the lobes, which evidently originated as slides off of the main edifice of Olympus Mons. Ideas for the formation of the aureole include gravity spreading (12, 13), gravity thrusts and landslides (14 - 16) and ash flows (17). Each mechanism required low shear strength of the materials in order to facilitate sliding, and no equivalent long run-out rock slide has been identified on Earth (18). Surprisingly, one of the closest morphologic examples (13) is that of submarine landslides which, at least in the case of Hawaiian examples (19), commonly achieved large run-out distances compared to their fall height. In the case of the Olympus Mons aureole materials, all of the deposits occur at low elevations (<1 km above Mars datum; ref. 11) and extend in the down-slope direction from the Olympus Mons edifice (16). In the model for the distribution of shallow seas on Mars (2), the entire N.W. side of Olympus Mons would have been submerged, facilitating the formation of submarine landslides. The Olympus Mons aureole materials may therefore be turbidite deposits generated by the submarine collapse of the submerged basal materials of Olympus Mons.

THE AMAZONIS DEPOSITS: The final enigmatic feature that lies on the "southern shore" of the hypothesized Martian sea is the series of smooth, wind-eroded deposits in Amazonis Planitia. Such materials have been described as ignimbrite sheets (20) and paleo-pole deposits (21, 22), but each idea has been vigorously refuted (23, 24). If large bodies of standing water were to have existed on Mars at the times that Olympus Mons and Apollinaris Patera erupted, it is argued here that eruptions similar to phreatomagmatic activity on Earth would have taken place, with the resultant generation of considerable amounts of fine volcanic ash (as has been documented for terrestrial ignimbrites entering the sea; ref. 25). Were this ash to have approximately the same density as ash on Earth, it seems possible that this material could have remained afloat for many months (26). Although the wind and wave circulation patterns at that time on Mars can only be speculated, it may have been possible for wind or wave action to have concentrated this Martian pumice in a few localities along an ancient shoreline. If this were the case, the distribution of the Amazonis materials is consistent with the inferred shoreline at an elevation of 1 - 2 km above mean Mars datum (2, 11).

CONCLUSIONS: Several aspects of volcano morphology and related deposits appear to be consistent with the hypothesis that oceans once existed in the northern plains of Mars. The basal escarpments around Olympus Mons and Apollinaris Patera may have formed as wave-cut cliffs, the Olympus Mons aureole materials may have been submarine landslides, and the enigmatic Amazonis deposits could be pumice layers that accumulated along the shore of ancient seas. Such ideas seem outlandish, but represent the first consistent explanation for these features and the occurrence of explosive (phreatomagmatic) volcanism not only at Apollinaris Patera, but also during the early stages of growth of other Martian volcanoes that are adjacent to the inferred paleo-shoreline. Hecates Tholus and Alba Patera both show morphologic evidence for explosive eruptions (11, 27), and lie within the area believed to have been periodically flooded (2). With the successful launch of the Mars Observer spacecraft and the ability to image landforms at the meter-scale (28), it may be possible to identify morphologic features that support or refute such a model. Observations that would support this model include the identification of desiccation cracks and linear shoreline features on the Amazonis deposits. In order to explain the occurrence of the escarpments, the basal layers of Olympus Mons and Apollinaris Patera must be easy to erode, so that the identification of lava flows in the escarpment cliffs of either volcano would argue against the proposed wave erosion model.

REFERENCES: 1. Parker, T. et al., *Icarus*, 82, 111 - 145 (1989). 2) Baker, V. et al., *Nature*, 352, 589 - 594 (1991). 3) Masursky, H. *J. Geophys. Res.*, 78, 4009 - 4030 (1973). 4) Carr, M. *J. Geophys. Res.*, 78, 4049 - 4062. 5) Wu, S. et al., *Nature*, 309, 432 - 435 (1984). 6) King, J. & J. Riehle, *Icarus*, 23, 300 - 317 (1974). 7) Head, J. et al., *Nature*, 263, 667 - 668 (1976). 8) Borgia, A. et al., *J. Geophys. Res.*, 95, 14357 - 14382 (1990). 9) Robinson, M. *Lunar Planet. Sci.* XXI, 1027-1028. (1990). 10) Mouginis-Mark, P. et al., *J. Geophys. Res.*, 87, 9890 - 9904 (1982). 11) U.S.G.S. *Miscellaneous Map* I-2179 (1991). 12) Francis, P. & G. Wadge, *J. Geophys. Res.*, 88, 8333 - 8344. 13) Tanaka, K. *Icarus*, 62, 191 - 206 (1985). 14) Harris, S. *J. Geophys. Res.*, 82, 3099 - 3107 (1977). 15) Lopes, R. et al., *Moon and Planets*, 22, 221 - 234 (1980). 16) Lopes, R. et al., *J. Geophys. Res.*, 87, 9917 - 9928 (1982). 17) Morris, E. *J. Geophys. Res.*, 87, 1164 - 1178 (1982). 18) Hayashi, J. & P. Mouginis-Mark, *Eos Supp. Fall AGU* , p. 323 (1992). 19) Moore, J. et al., *J. Geophys. Res.*, 94, 17465 - 17484 (1989). 20) Scott, D. & K. Tanaka, *J. Geophys. Res.*, 87, 1179 - 1190 (1982). 21) Schultz, P. & Lutz-Garihan, A., *Lunar Planet. Sci.*, XXI, 946 - 948 (1981). 22) Schultz, P. & A. Lutz, A., *Icarus*, 73, 91 - 141 (1988). 23) Francis, P. & C. Wood, *J. Geophys. Res.*, 87, 9881 - 9889 (1982). 24) Grimm, R. & S. Solomon, *Icarus*, 65, 110 - 121 (1986). 25) Walker, G., *Nature*, 281, 642 - 646 (1979). 26) Whitham, A. & R. Sparks *Bull. Volcanol.*, 48, 209 - 223 (1986). 27) Mouginis-Mark, P. et al., *Bull. Volcanol.*, 50, 361 - 379 (1988). 28) Malin, M. et al., *J. Geophys. Res.*, 97, 7699 - 7718 (1992).

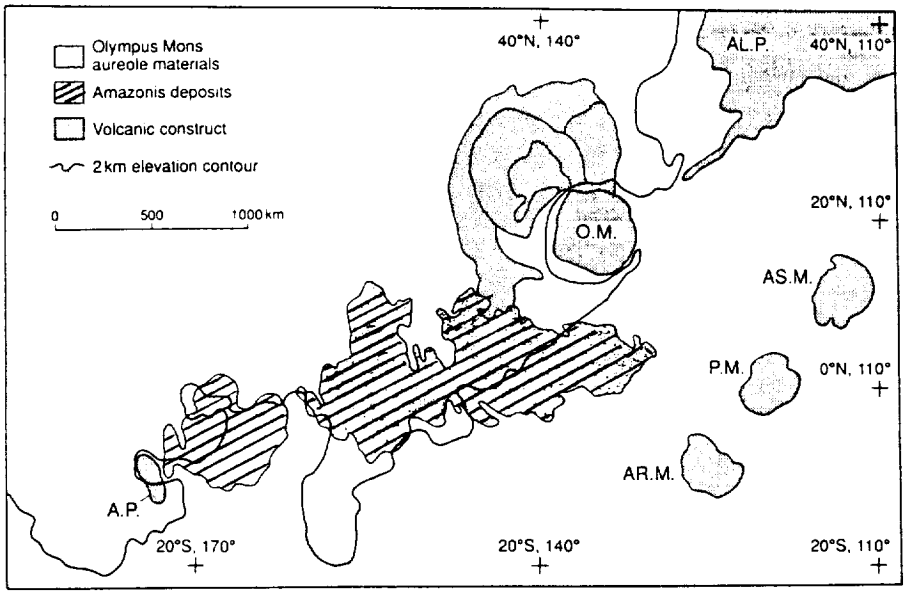

Fig. 1: Distribution of the Olympus Mons aureole materials, the Amazonis deposits, and the major volcanic constructs in Tharsis and Amazonia. Olympus Mons "O.M.", Arsia Mons "AR.M.", Pavonis Mons "P.M.", Ascraeus Mons "AS. M.", Apollinaris Patera "A. P." and the recent lava flows from Alba Patera "AL. P." The 2 km contour, thought to be the edge of the transient ocean (2), is also shown.

HELIUM-3 INVENTORY OF LUNAR SAMPLES: A POTENTIAL FUTURE ENERGY RESOURCE FOR MANKIND? **A. V. Murali and J. L. Jordan,** Earth and Space Resources Laboratory, Department of Geology, Lamar University, Beaumont, TX 77710.

Solar wind is the principal source for the volatile elements (H, C, N, and noble gases) in the lunar samples, which are enriched in the finest fraction of the Moon's comminuted regolith (1, 2). Some of these volatiles (H, N, He, and C) are regarded as potential lunar resources that can support the inhabitants of a lunar base and provide fuels for transportation (3). Various studies indicated that these volatiles may be extracted by heating the lunar soils to approximately 700°C. At this temperature near quantitative release of hydrogen and helium, and approximately 20-30% of the release of nitrogen and carbon and their compounds occurs (4).

It is recognized that the global fossil fuel resources could not provide even half the energy requirement of the world in the 21st century (5). Recent public concern over the safety, cost, and environmental impact of the worldwide fission reactors has focused the attention of scientists and engineers towards perfecting fusion technology because it promises a much more environmentally acceptable "clean" energy supply (6, 7). Among the three fusion reactions considered, namely the $^2D + ^2D$, $^2D + ^3T$, and $^2D + ^3He$, the reaction: $^2D + ^3He \rightarrow p$ (14.7 MeV) + ^4He (3.6 MeV) has long been recognized as an ideal candidate for producing commercially "safer and cleaner" fusion power (5, 6, 7, 8).

Unfortunately, the scarcity of naturally occuring ^3He on earth is the chief impediment to consider this fuel on a commercial scale, aside from plasma physics issues (5, 8). Most of the helium on earth is essentially ^4He produced by the radioactive decay of U and Th, and the ^3He known to be contained in terrestrial natural gas deposits could not power a modest-sized electrical power plant of 500 MW for more than few months. Lunar regolith is a potential ore for ^3He because the high ^3He in solar wind (apparently due to the nuclear reaction ^2D (p,γ) ^3He, which occurs in the high gravitational field of the sun) has been implanted in the lunar regolith for $>4 \times 10^9$ years, along with other volatile species (1, 2). Considering the cost of mining the lunar soil, degassing, isotopic separation, and transportation to earth, the energy payback ratio for ^3He is estimated to be ~250 (5). This payback ratio is highly favorable compared to that for ^{235}U production for nuclear fuel (~20) and coal mining (~16) on earth. More importantly, ^3He from the Moon results in an environmentally "clean" energy to mankind for the next few centuries (5, 8).

We have compiled data on the contents of various volatile elements including ^3He, TiO_2, and the maturity index (I_s/FeO) for all the lunar soils for which measurements have been reported (9). Our study indicates that the helium content of lunar soils varies from 1 to 63 ppm and the helium-3 abundance of these soils ranges from 0.4 to 15 ppb (Table 1). The helium abundance in lunar soils is dependent not only on the maturity of soils (I_s/FeO) but also on their mineralogy (Figs. 1 and 2). The titanium-rich (ilmenite) lunar soils are important repositories for volatiles, which may be released by heating these soils up to ~700°C. We estimate that per tonne of ^3He extracted from the lunar regolith at this temperature, ~6300 tonnes of H, ~700 tonnes of N, and ~1600

tonnes of C (as CO and CO_2) will be released as byproducts that are also essential to sustain a permanent lunar base (2).

This study was performed under Lockheed Engineering Support Contract # NAS9-17900 (subcontract P. O. # 02N0166203).

References: [1] P. Eberhardt *et al.* (1970) *Proc. Apollo 11 Lunar Sci. Conf.*, 1037-1070. [2] L. Haskin and P. Warren (1991) In *Lunar Source Book* (G. Heiken et al., eds.), pp. 357-474, Cambridge Univ. Press. [3] W. W. Mendell (ed.) (1985) *Lunar Bases and Space Activities*, LPI, Houston, 865p. [4] J. L. Jordan (1992) *AIAA Space Technology Conf.*, Huntsville, Al, 1-6. [5] G. L. Kulcinski *et al.* (1986) *1st Lunar Development Symposium.* Atlantic City, 6p. [6] C. K. Choi (ed) (1977) *Proc. of the Review Meeting on Advanced-Fuel Fusion,* ER-536-SR, Electric Power Res. Inst. [7] J. M. Dawson (1981) *Advanced Fusion Reactors, Fusion,* **1** (E. Teller ed.), Academic Press Inc., New York. [8] L. J. Wittenberg et al. (1987) *Fusion Tecnology,* **10**, 167-178. [9] J. L. Jordan (1989) Symposium *Space Mining and Manufacturing*, Univ. Arizona, Tucson, pp. VII-38-VII-50.

Table 1. Lunar Volatile Elements of Significance to Resource Utilization (9)

Element	Measured range (ppm)	Origin
H	0.1-211	Solar wind
He (^{3}He)	1-63 (0.4-15 ppb)	Solar wind
N	13-153	Solar wind
C	10-280	Solar wind
S	20-1330	Indigenous
H_2O	0-20	Terrestrial Contamination (?)

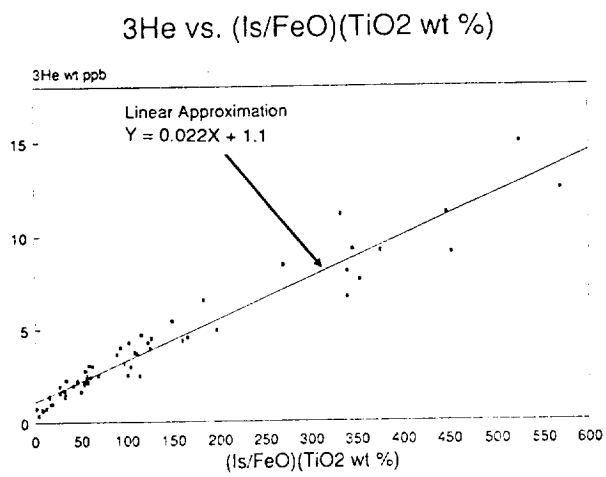

Fig. 1

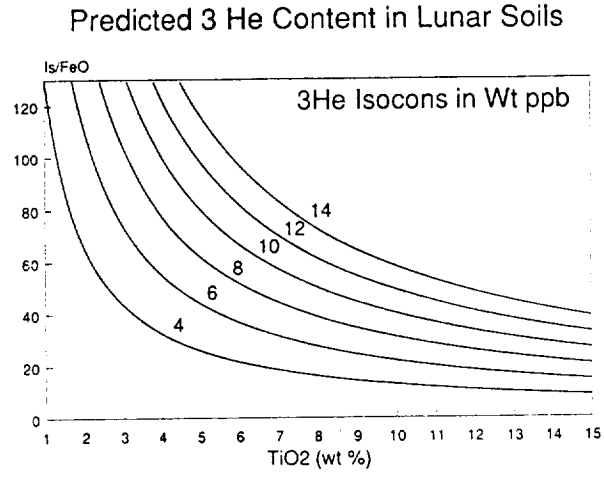

Fig. 2

THE SPECTRUM OF PHOBOS FROM *PHOBOS 2* OBSERVATIONS AT 0.3-2.6 μm: COMPARISON TO PREVIOUS DATA AND METEORITE ANALOGS Scott Murchie[1] and Stephane Erard[2]. [1]*LPI, Houston, TX*; [2]*Instituto di Astrofisica Spaziale, Roma, Italy.*

Introduction. The surface of Phobos has been proposed to consist of carbonaceous chondrite [1,2] or optically darkened ordinary chondrite ("black chondrite") [3]. Measurements of Phobos's spectrum are key evidence for testing these hypotheses. Disk-integrated measurements were obtained by the *Mariner 9* UV spectrometer [1], *Viking Lander* cameras [2], and groundbased observations [4]. In 1989 disk-resolved measurements of Phobos and Mars were obtained by three instruments on *Phobos 2*: the KRFM spectrometer, which covered the wavelength range 0.32-0.6 μm [5,6]; the ISM imaging spectrometer, which covered the wavelength range 0.76-3.16 μm [7]; and the VSK TV cameras, whose wavelength ranges overlap those of KRFM and ISM [6,8]. Here we report analysis of the *Phobos 2* measurements completed since earlier results were reported [3-10]. We validated calibration of the Phobos measurements using observations of Mars for reference, and compared them with pre-1989 measurements. We also combined spectra from the three detectors to produce an integrated spectrum of Phobos from 0.3-2.6 μm. *Phobos 2* results agree well with previous measurements, contrary to some reports [9]. The general shape of the spectrum is consistent with both proposed analogs. However position and depth of the previously unobserved 1-μm absorption are more diagnostic, and indicate the composition of typical surfaces to be more consistent with black chondrite.

Background. The *Mariner 9*, *Viking*, and telescopic observations were combined by Pollack *et al.* [2] and Pang *et al.* [11] to produce disk-integrated spectra of Phobos from 0.2-1.1 μm. Both results indicate a flat spectrum at 0.4-1.1 μm and a falloff in reflectance at wavelengths below about 0.4 μm. However the two studies used different photometric functions to normalize data to 0° phase angle, and yielded slightly different geometric albedos at visible wavelengths, with a value of 0.05±0.01 reported by Pollack *et al.* [2] and 0.046±0.01 by Pang *et al.* [11].

The VSK cameras bracket the wavelength range having a "flat" spectrum, with a "visible" channel at 0.40-0.56 μm and a "NIR" channel at 0.78-1.1 μm. The average disk-resolved vis/NIR ratio was measured as 0.97±0.14 [6]. NIR reflectance is relatively homogeneous, but heterogeneities in the vis/NIR ratio occur due to spatial variations in visible reflectance [6]. These impart visible-wavelength albedo heterogeneities to different parts of Phobos, such that NIR measurements acquired at different times are more comparable than visible-wavelength measurements.

Observations by KRFM and ISM provide higher spectral resolution measurements at a lower spatial resolution than VSK. ISM spectra reveal an absorption near 1 μm consistent with the mafic minerals olivine or pyroxene [7]. Strength of the absorption is up to 5% and largely independent of brightness, but areas with higher vis/NIR ratios measured simultaneously by VSK exhibit stronger absorptions [10]. These relationships support an origin for the 1-μm absorption indigenous to Phobos: an origin due to scattered Mars light measured by the detectors would result in correspondence of stronger absorptions with poorly illuminated regions or lower vis/NIR ratios (because of the "red" color of Mars). KRFM observations also indicate heterogeneities in UV-visible spectral properties, with surfaces having high vis/NIR ratios as measured by VSK also having comparatively flat UV-visible spectra [5,6,10].

Comparison of Viking and VSK Results. VSK imagery is well suited to determination of photometric and color properties of Phobos: the data cover a wide range of phase angles (7°-88° [8]), and the vis/NIR ratio of Phobos was calibrated to telescopic observations of a part of Mars observed simultaneously with Phobos [6,8]. The average vis/NIR ratio near 1.0 agrees with the "flat" disk-integrated spectrum at comparable wavelengths reported by Pollack *et al.* [2] and Pang *et al.* [11]. However geometric albedo calculated from VSK measurements are more compatible with the spectrum of Pollack *et al.* [2]. (A value of 0.062±0.013 is reported for the NIR channel [8]). For this reason, we adopt the Pollack *et al.* disk-integrated spectrum as representative of pre-1989 measurements.

Validation of ISM and KRFM Spectra. ISM and KRFM spectra are critical to defining the 1-μm absorption and the UV falloff, whose positions and magnitudes differ between the proposed compositional analogs. Accurate calibration of these data is therefore crucial. ISM data were calibrated initially using instrumental parameters measured on-ground and in-flight [7,12]. The initial calibration was refined by applying multiplicative coefficients to each channel, based on a spectral model of Phobos. An early version of this procedure was reported by Erard *et al.* [12]. These coefficients have subsequently been refined, and tested by dividing a Mars spectrum calibrated in this way by a telescopic spectrum of the same region. This procedure yielded no absorption-like residuals, assuring that the position and strength of the 1-μm absorption on Phobos are free of calibration artifacts.

Two versions of KRFM spectra have been reported: calibrated to pre-1989 Phobos measurements [6], and calibrated to telescopic spectra of Mars using unobstructed KRFM Mars observations [9]. Surprisingly, these procedures yield different results. To address this dilemma, we rederived the calibration of KRFM using data acquired on 25 March 1989. At that time KRFM observed a groundtrack that covered a portion of Phobos shown by VSK and ISM to be homogeneous, crossed the terminator and entered the nightside, and emerged from occultation over a period of ~25 s into a uniform bright region of Mars. The time series of differing brightnesses of the two uniform regions provide test for inter-channel variations in gain and offset. Regression analysis of the brightnesses in different KRFM channels indicates significant offsets that were previously unrecognized, plus nonlinearity in gains at brightnesses typical of Mars filling the instrumental FOV. This non-linearity and the unremoved offsets explain

the unusual spectrum of Phobos derived by investigators who calibrated Phobos observations using much brighter, unobstructed observations of Mars [9]. Fortunately, gains are linear across the brightness range encompassing both Phobos and Mars *while partly occulted.* With due caution, calibration of Phobos data can be checked against Mars.

Figure 1 shows a rederived KRFM spectrum of a portion of Phobos with an "average" vis/NIR ratio, calibrated using offset-removed data, observations of Mars while partly occulted, and telescopic spectra of Martian "bright regions" [13]. It agrees closely with the disk-integrated spectrum of Pollack *et al.* [2]. This KRFM spectrum differs from previously published KRFM spectra that were calibrated to pre-1989 Phobos measurements [6] only in the 0.4-μm wavelength region, which was undersampled by previous observations. This correspondence occurs despite the formerly unremoved offsets, because the previous spectra [6] were chosen to cover a restricted range of brightnesses.

Integrated spectrum of Phobos. An integrated spectrum of Phobos from 0.3-2.6 μm was derived for a small region where coverages by KRFM, VSK, and ISM overlap (Figure 2). This region corresponds to the "reddish gray" color unit of Murchie *et al.* [6]; the vis/NIR ratio is "redder" than average for Phobos but typical of the trailing hemisphere. The corresponding rederived KRFM spectrum and ISM spectrum were convolved with the response functions of the visible and NIR channels of VSK, respectively, and scaled using the measured vis/NIR ratio.

Discussion. The correspondence between properly calibrated KRFM spectra, VSK measurements, and the spectrum of Pollack *et al.* [2] supports the canonical view of a "flat" average spectrum of Phobos at 0.4-1.1 μm with a falloff in reflectance below 0.4-0.5 μm [1-3,6,10,11]. The general shape of Phobos's spectrum from 0.3-2.6 μm resembles both proposed analogs. However, position and strength of the previously unobserved 1-μm absorption are more diagnostic of proposed compositions. The band minimum for ordinary (including black) chondrites is typically at 0.90-0.95 μm [14]. Low-grade carbonaceous chondrites (CI,CM) exhibit little or no absorption, but in higher metamorphic grades (C3O,C3V) the band minimum is generally at longer wavelengths than in black chondrites (near 1.0 μm) due to more olivine-rich compositions [14]. Figure 2 shows that the band minimum on Phobos is near 0.93 μm, consistent with a relatively pyroxene-rich composition and best matched by black chondrites.

References: [1] K. Pang *et al.*, *Science*, *199*, 64, 1978. [2] J. Pollack *et al.*, *Science*, *199*, 66, 1978. [3] D. Britt and C. Pieters, *Astron. Vestnik*, *22*, 229-239, 1988. [4] B. Zellner and R. Capen, *Icarus*, *23*, 437, 1974. [5] L. Ksanfomality *et al.*, *Planet. Space Sci.*, *39*, 311, 1991. [6] S. Murchie *et al.*, *J. Geophys. Res.*, *95*, 5101, 1991. [7] J.-P. Bibring *et al.*, *Proc. Lunar Planet. Sci. Conf. 20th*, 461, Lunar and Planetary Institute, Houston, 1990. [8] G. Avanesov *et al.*, *Planet. Space Sci.*, *39*, 281, 1991. [9] J.-P. Bibring *et al.*, *Lunar Planet. Sci. XXII*, 99, 1991. [10] S. Murchie *et al.*, *Lunar Planet. Sci. XXII*, 943, 1991. [11] K. Pang et al., Nature, 283, 277, 1980. [12] S. Erard *et al.*, *Proc. Lunar Planet. Sci. Conf. 21st*, 437, 1991. [13] R. Singer and T. McCord, *Proc. Lunar Planet. Sci. Conf. 10th*, 1837, 1979. [14] M. Gaffey, *J. Geophys. Res.*, *81*, 905, 1976.

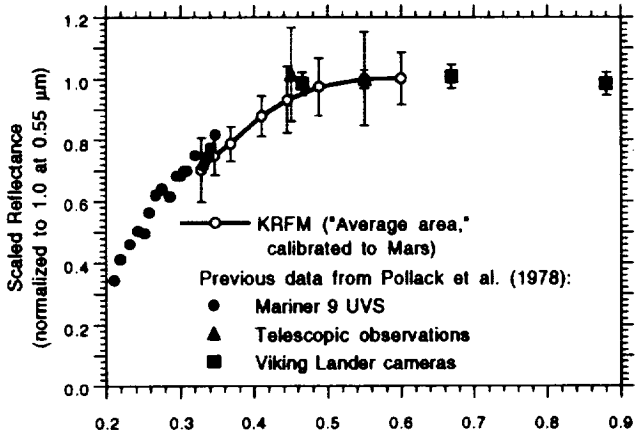

Figure 1. KRFM spectrum of a region of Phobos with an "average" vis/NIR ratio as measured by VSK, compared to previous spectral measurements of Phobos as presented by Pollack *et al.* [12].

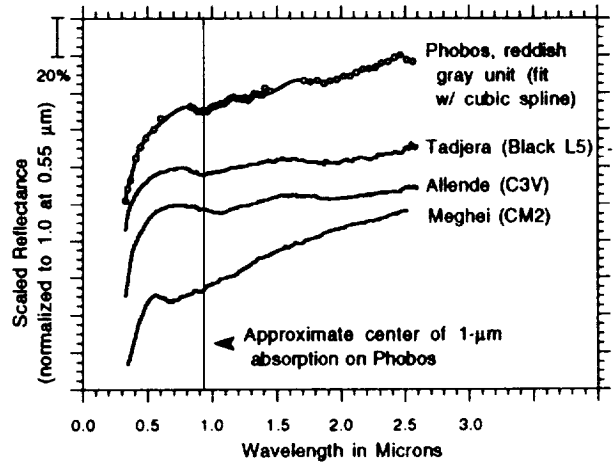

Figure 2. Integrated KRFM-ISM spectrum of Phobos, compared to spectra of proposed meteorite analogs. The verical line shows the approximate center of the 1-μm absorption on Phobos.

BRIGHT SOIL UNITS ON MARS DETERMINED FROM ISM IMAGING SPECTROMETER DATA Scott Murchie[1] and John Mustard[2]. [1]*Lunar and Planetary Institute, Houston, TX;* [2]*Department of Geological Sciences, Brown University, Providence, RI.*

Introduction. The lithology of bright Martian soil provides evidence for chemical and physical processes that have modified the planet's surface. Data from the ISM imaging spectrometer [1], which observed much of the equatorial region at a spatial resolution of ~22 km, cover the NIR wavelength range critical to ascertaining the presence and abundance of Fe-containing phases, hydroxylated silicates, and H_2O in the bright soil. ISM data previously have revealed spatial variations in depth of the 3.0-μm H_2O absorption suggesting differences in water content [2,3], a weak absorption at 2.2 μm indicative of metal-OH in phyllosilicate [3], and variations in the 1-μm Fe absorption indicative of differences in Fe mineralogy [4]. This abstract summarizes first results of a systematic investigation of spectral heterogeneity in bright soils observed by ISM. At least seven "units" with distinctive properties were discriminated. Comparison of their spatial distributions with *Viking* data shows that they generally correspond with previously recognized morphologic, color, and thermal features. These correspondences and the units' spectral attributes provide evidence for lithologic differences between the soils in different geologic settings.

Analysis. We investigated 6 of the 9 data "windows" returned by ISM, covering Tharsis, Arabia, and Isidis. Bright soils in these areas contain examples of most variations in color, reflectance, and thermal inertia that have been recognized in *Viking* data [e.g. 5-8]. Calibration and removal of atmospheric absorptions were performed using previously described methods [2,9]. The data were reduced to a suite of "parameter" images that describe key sources of spectral variability. These include reflectance, strength of the narrow 2.2-μm absorption, depth of the 3.0-μm H_2O absorption, and NIR spectral slope. Spectral slope of Mars analog materials is affected by several variables. Particulate basaltic and ferric materials have flat spectral slopes, but negative spectral slopes occur when the ferric component coats or is intimately mixed with a dark substrate [10-12] or has an extremely fine particle size [13]. Atmospheric scattering may also cause negative spectral slopes in ISM data [2]. Spectral slope was measured as the difference between reflectances at 1.71 and 2.47 μm. If atmospheric scattering makes a nearly constant contribution to reflected light, then *variations* in spectral slope calculated in this way should be related to surface properties.

Preliminary soil groupings were identified using the parameter images, based on systematic, spatially coherent differences in spectral slope and depths of the 2.2- and 3.0-μm absorptions. Representative spectra of the groupings were extracted, and absorption features due to Fe in minerals were identified and analyzed. Where appropriate, the preliminary groupings were subdivided based on differences in these absorptions. Finally, spatial distributions of the resulting "units" were compared to surface morphology, visible color, and thermal properties evident in *Viking* data.

Results. Figure 1 illustrates variations in spectral slope and strengths of the 2.2-μm and 3.0-μm absorptions. Six preliminary "groupings" (Table 1) were identified based on systematic, spatially coherent differences. In a comparison of strengths of the 3.0-μm and 2.2-μm absorptions (Fig. 1a), the geographically largest grouping ("normal bright soil") exhibits a relatively weak 3.0-μm absorption and strong 2.2-μm absorption. This soil covers most "bright red" parts of Tharsis and Arabia. However in soils on Tharsis Montes, especially Ascraeus Mons, both absorptions are weaker. The remaining groupings have stronger 3.0-μm H_2O absorptions, and are loosely termed "hydrated bright soils" [3]. Parts of Lunae Planum and Arabia with "dark red" visible color and the interior of Candor Chasma have stronger 3.0-μm absorptions and weaker 2.2-μm absorptions than normal bright soil. Isidis is unique in having both a strong 3.0-μm absorption and a strong 2.2-μm absorption. Two further groupings are discerned by comparing spectral slope and strength of the 3.0-μm absorption (Fig. 1b). Soil in cratered highlands in Libya Montes is distinguished from normal bright soil by a more negative spectral slope. Soil in Candor Chasma is distinguished from hydrated "dark red" soil by both a negative spectral slope and a stronger 3.0-μm absorption.

Variations in the positions, shapes, and depths of Fe-related absorptions further define and in some cases subdivide these groupings (Table 1). Normal bright soil in Tharsis has a shallow ferric iron absorption centered near 0.85 μm, but normal bright soil in Arabia has a deeper absorption centered near 0.92 μm [4]. Soil at high elevations on Ascraeus Mons exhibits a distinctive ferric absorption centered near 0.88 μm [4], in addition to the differences described above. "Hydrated bright soils" also have Fe-related absorptions different from normal bright soil. These may contain ferric iron phases, glasses, or pyroxene, and are currently being investigated [cf. 4].

Discussion. The soil units generally exhibit spatial correlations with surface units derived by interpretation of surface morphology, *Viking* visible color, and thermal inertia measurements [5-8] (Table 1). These correlations corroborate the compositional heterogeneities of bright soil inferred from ISM data.

"Normal bright soils" correspond almost exactly with low thermal inertia regions interpreted as accumulations of "dust" by airfall [6-8]. The absorptions at ~0.9 and 2.2 μm indicate that the "dust" contains ferric minerals and poorly crystalline phyllosilicate [3,4]. The Fe absorption at 0.85 μm throughout the Tharsis region is indicative of hematite, but the absorption at 0.92 μm throughout Arabia indicates one or more different Fe phases [4]. This difference clearly implies that "dust" is not a single, globally homogeneous lithology, but rather that its lithology varies between regions. In addition, compared to the surrounding Tharsis plains, soil or "dust" at high elevations on Ascraeus Mons exhibits a more negative spectral slope, weaker 2.2-μm and 3.0-μm absorptions, and a ferric

absorption offset to longer wavelengths by ~0.03 μm. The offset in the ferric absorption is similar to that seen in the laboratory in extremely small grain sizes of hematite [14]. Finer-grained "dust" high on the volcanoes than in the surrounding plains may also explain the weaker 2.2-μm and 3.0-μm absorptions and the negative spectral slope.

"Hydrated bright soils" correspond to bright soils outside the low-inertia regions interpreted as airfall deposits. They exhibit greater spectral heterogeneity than "normal bright soil," as well as correlations with independently identified high thermal-inertia features and geologic units. As such, they may be representative of exposures of more indurated soil and/or high-albedo geologic deposits. For example, "dark red" plains in Lunae Planum and Arabia correspond to high thermal inertia surfaces previously interpreted as cemented duricrust [6,15]. Their strong 3.0-μm absorptions suggest enrichment in a water-bearing phase, perhaps hydrated salts acting as the duricrust's "cement."

The Isidis unit also corresponds with material having anomalously high thermal inertia [7,8], as well as with a thick surface deposit mapped by Grizaffi and Schultz [16]. The Isidis deposit's high inertia and strong 3.0-μm absorption would also be consistent with induration of soil by water-bearing cement, but it has a bright red color and strong 2.2-μm absorption which suggest a different compositon of cemented particulates than in "dark red" soils.

The unit in Candor Chasma corresponds with highly eroded layered deposits sculpted by eolian fluting [17]. This unit is distinctive from other bright soils, but it is surrounded by a ~100-km-wide "halo" transitional with normal bright soil (see Figure 1). This gradational contact may imply that eolian processes have transported debris from the layered deposits into surrounding plains, suggesting a discrete source region for some bright airfall deposits.

TABLE 1. Spectral Properties and Geologic Correlations of Bright Soil Units[1]

Unit	3.0-μm band	2.2-μm band	Spectral slope	Center of ferric absorption	Correlations with vis. color, thermal inertia, geology
"Normal Bright" (Tharsis)	Weak	Strong	Flat	0.85 μm	Bright red, low inertia
"Normal Bright" (Arabia)	Weak	Strong	Flat	0.91 μm	Bright red, low inertia
Tharsis Montes	Very weak	Moderate	Negative	0.88 μm	Dark red, low inertia, high-elevation flanks of volcanoes
Libya Montes	Weak-moderate	Strong	Negative		Bright red, heavily cratered highlands
"Hydrated bright soils"					
"Dark red" plains (E Lunae Planum, W Arabia)	Moderate	Moderate	Flat		Dark red, high inertia
Candor Chasma	V. strong	Weak	V. negative		Layered deposits
Isidis	Strong	Strong	Flat		Bright red, high inertia

[1] "Groupings" based on spectral slope and depths of the 2.2-μm and 3.0-μm absorptions are separated by solid lines.

References: [1] J.-P. Bibring *et al., Proc. Lunar Planet. Sci. Conf. 20th*, 461, 1990. [2] S. Erard *et al., Proc Lun. Plan. Sci. Conf. 21st*, 437, 1991. [3] S. Murchie *et al., Lunar Planet. Sci. XXIII*, 941, 1992. [4] S. Murchie *et al.*, this volume, 1993. [5] L. Soderblom *et al., Icarus, 34*,446, 1978. [6] R. Arvidson *et al., J. Geophys. Res., 87*, 10,149, 1982. [7] F. Palluconi and H. Kieffer, *Icarus, 45*, 415, 1978. [8] P. Christensen, *Icarus, 68*, 217, 1986. [9] J. Mustard *et al., J. Geophys. Res.* in press, 1993. [10] E.Fischer and C. Pieters, submitted to *Icarus*, 1993. [11] R. Singer and T. Roush, *Lunar Planet Sci. XIV*, 708, 1983. [12] R. Morris and S. Neely, *Lunar Planet Sci. XIII*, 548, 1982. [13] R. Morris *et al., Geophys. Res. Lett., 9*, 113, 1982. [14] R. Morris *et al., J. Geophys. Res., 90*, 3126, 1985. [15] P. Christensen and H. Moore, in *Mars*, ed. by H. Kieffer et al., p. ,Univ. of Arizona, Tucson, 1982. [16] P. Grizzaffi and P. Schultz, *Icarus, 77*, 358, 1989. [17] N. Witbeck *et al., U.S.G.S. Misc. Inv. Ser. Map I-2010*, 1991.

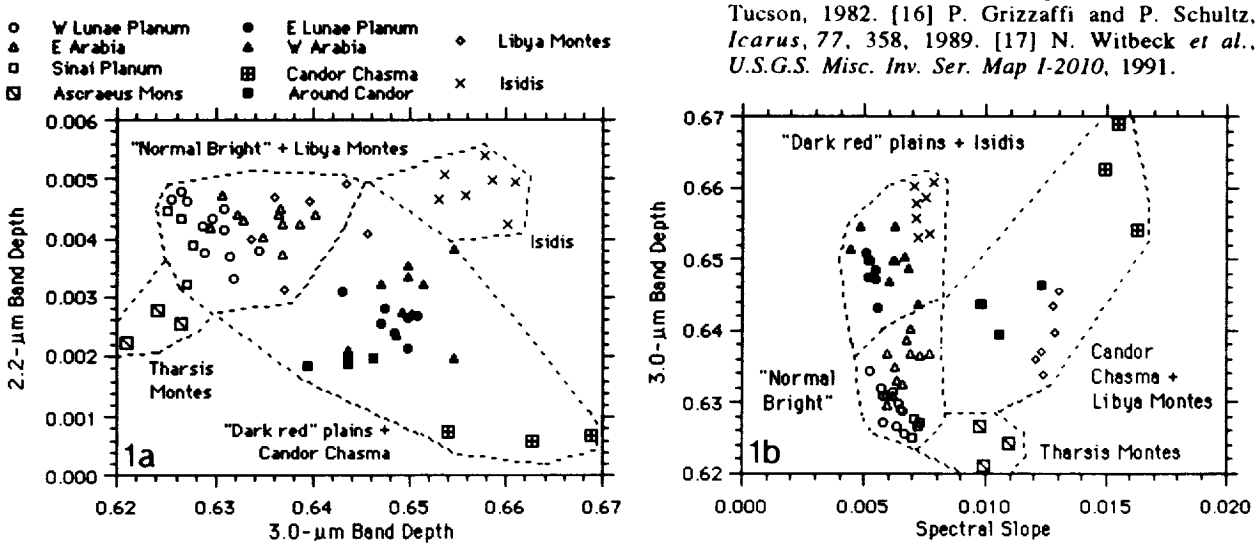

VARIATIONS IN THE Fe MINERALOGY OF BRIGHT MARTIAN SOIL

Scott Murchie[1], John Mustard[2], Stephane Erard[3], Paul Geissler[4], and Robert Singer[4]. [1]*Lunar and Planetary Institute, Houston, TX*; [2]*Department of Geological Sciences, Brown University, Providence, RI*; [3]*Instituto di Astrofisica Spaziale, Roma, Italy*; [4]*Lunar and Planetary Laboratory, University of Arizona, Tucson, AZ.*

Introduction. Bright regions on Mars are interpreted as "soil" derived by chemical alteration of crustal rocks, whose main pigmentary component is ferric oxide or oxyhydroxide [1-3]. The mineralogy and mineralogic variability of ferric iron are important evidence for the evolution of Martian soil: mineralogy of ferric phases is sensitive to chemical conditions in their genetic environments, and the spatial distributions of different ferric phases would record a history of both chemical environments and physical mixing. Reflectance spectroscopic studies provide several types of evidence that discriminate possible pigmentary phases, including the position of a crystal field absorption near 0.9 μm and position and strengths of absorptions in the UV-visible wavelength region [4-6]. Recent telescopic spectra and laboratory measurements of Mars soil analogs [7-9] suggest that spectral features of bright soil can be explained based on a single pigmentary phase, hematite (α-Fe_2O_3), occurring in both "nanophase" and more crystalline forms. Here we report a systematic investigation of Martian bright regions using ISM imaging spectrometer data, in which we examined spatial variations in the position and shape of the ~0.9-μm absorption. We found both local and regional heterogeneities that indicate differences in Fe mineralogy. These results demonstrate that bright soils do not represent a single lithology that has been homogenized by eolian mixing, and suggest that weathering of soils in different geologic settings has followed different physical and chemical pathways.

Data Characteristics and Analysis. ISM data are ideally suited to this analysis because of their high spectral and spatial resolution, broad geographic coverage, and high signal-to-noise ratio. ISM returned 9 images or "windows" covering ~20% of the equatorial region, with a pixel size of 22 km and 128 channels spanning a wavelength range of 0.76-3.16 μm [10]. Data processing has been described by Erard *et al.* [11] and Mustard *et al.* [12]. Spatially averaged ISM spectra for a number of regions have been compared to corresponding telescopic spectra, and found to have a high degree of correlation [13]. Since the signal-to-noise ratio of ISM spectra in the 0.9-μm wavelength region ranges between 600:1 and 1300:1, small variations in shape and position of the 0.9-μm absorption can be recognized and mapped at high spatial resolution over much of the equatorial belt.

A systematic analysis of the shape and position of the ~0.9-μm ferric absorption in bright regions was conducted by surveying bright soils observed by ISM, defining regions with distinctive 0.9-μm absorptions, and measuring representative spectra of these regions. Regions exhibiting evidence for absorptions due to crystalline mafic minerals were avoided, because Fe^{2+} in these minerals would modify the shape and position of the 0.9-μm absorption. Absorption centers were estimated after fitting the spectra with cubic splines, and absorption depths were estimated by dividing reflectances at the absorption centers by reflectances at shorter and longer wavelengths.

Related Studies. We have previously used ISM data to determine the presence, strength, and variability of absorptions related to H_2O and OH in bright Martian soils [14,15]. Bright soils may be loosely grouped into two major classes. "Normal bright soils" represent the majority of bright soils observed by ISM. These have a strong absorption at 3.0 μm due to H_2O, plus a narrow absorption ≤1% in depth centered at 2.20-2.25 μm. The latter is attributed to poorly crystalline phyllosilicate. "Hydrated bright soils" exhibit a consistently stronger 3.0-μm absorption, probably due to greater H_2O content. In most cases the 2.2-μm absorption is weaker or absent, and in some cases the presence of pyroxene is suggested by a broad, shallow absorption centered at 2.0-2.3 μm.

Results. Among "normal bright soils," there are three geographic regions which exhibit distinct absorptions near 0.9 μm (Figure 1). Previous studies have provided some evidence for these differences, but did not fully resolve the distinct absorptions. Bright soils throughout the Tharsis plateau plains and westward into Amazonis exhibit a ferric iron absorption 2-4% deep and centered at 0.84-0.86 μm. Soils at high elevations on the Tharsis Montes volcanoes, particularly Ascraeus Mons, exhibit an absorption shifted longward to 0.88 μm. In earlier analysis of ISM data, Bibring *et al.* [16] recognized that spectral properties near 1 μm distinguish Ascraeus Mons from the surrounding region, though they did not specifically identify position of the ferric absorption as responsible for this difference. The absorption exhibited by bright soils in Arabia is radically different, 5-7% deep and centered near 0.92 μm. The distinctiveness of Arabia had been recognized by McCord *et al.* [17] and attributed to mafic minerals, but ISM spectra do not exhibit evidence for crystalline olivine or pyroxene in this region.

Some "hydrated bright soils" exhibit a broad, shallow absorption at 2.0-2.3 μm, suggesting that their 0.9-μm absorptions are modified by ferrous iron in pyroxene. However at least two regions lack evidence for crystalline mafic minerals but exhibit strong, distinctive features near 0.9 μm (Figure 2). These may be attributable to ferric phases. One region corresponds to a visible-color anomaly within a topographic depression in layered deposits of western Candor Chasma [18]. Here, an absorption 5-6% deep is centered at 0.91 μm. The other region is in eastern Lunae Planum, within the "dark red" visible color unit [2,3]. Here an absorption ~4% deep is centered near 0.89 μm.

Compositional Implications. Variations in the 0.9-μm absorption may be attributable to several factors. Most "normal" bright soils have an absorption centered near 0.85 μm, consistent with hematite (α-Fe_2O_3) being the

dominant ferric phase. Variations in hematite particle size can shift the absorption by as much as 0.03 μm [5], plausibly accounting for small variations such as between the Tharsis plains and Tharsis Montes. However the longer-wavelength absorption centers in "normal bright soil" in Arabia, and in "hydrated bright soil" in Lunae Planum and Candor Chasma, cannot be reconciled with a dominantly hematitic ferric mineralogy. We suggest the presence in these regions of one or more different phases, possibly maghemite (γ-Fe_2O_3), goethite (α-FeOOH), ferrihydrite ($Fe_{10}O_{24}H_{18}$), jarosite ($(K,Na,H_3O)Fe_3(SO_4)_2(OH)_6$), or Fe-containing glass. This heterogeneity in the Fe absorption demonstrates that bright soils are not a single lithology that has been homogenized by eolian mixing [e.g. 2]. These results also suggest that weathering of the bright soils in different settings has followed different pathways, possibly including sorting by particle size and differing contributions of weathering of basaltic glass, precipitation from aqueous solutions, and alteration of the precipitates by heating and desiccation [cf. 4,18,19].

References: [1] R. Singer *et al.*, *J. Geophys. Res.*, *84*, 8415, 1979. [2] R. Arvidson, *et al.*, *J. Geophys. Res.*, *94*, 1573, 1989. [3] L. Soderblom, in *Mars*, ed. by H. Kieffer *et al.*, p. 557, Univ. of Arizona, Tuscon, 1992. [4] D. Sherman *et al.*, *J. Geophys. Res.*, *87*, 10,169, 1982. [5] R. Morris *et al.*, *J. Geophys. Res.*, *90*, 3126, 1985. [6] J. Bishop *et al.*, submitted to *Geochim. Cosmochim. Acta*, 1993. [7] J. Bell *et al.*, *J. Geophys. Res.*, *95*, 14,447, 1990. [8] R. Morris *et al.*, *J. Geophys. Res.*, *94*, 2760, 1989. [9] R. Morris and H. Lauer, *J. Geophys. Res.*, *95*, 5101, 1990. [10] J.-P. Bibring *et al.*, *Proc. Lunar Planet. Sci. Conf. 20th*, 461, Lunar and Planetary Institute, Houston, 1990. [11] S. Erard *et al.*, *Proc Lun. Plan. Sci. Conf. 21st*, 437, 1991. [12] J. Mustard *et al.*, *J. Geophys. Res.* in press, 1993. [13] J. Bell and J. Mustard, this volume, 1993. [14] S. Murchie *et al.*, *Lunar Planet. Sci. XXIII*, 941, 1992. [15] S. Murchie *et al.*, this volume, 1993. [16] J.-P. Bibring *et al.*, *Proc. Lunar Planet. Sci. Conf. 20th*, 461, 1990. [17] T. McCord *et al.*, *J. Geophys. Res.*, *87*, 3021, 1982. [18] P. Geissler and R. Singer, in *Workshop on Chamical Weathering on Mars*, LPI Tech. Rpt. 92-04, p. 12, 1992. [19] J. Gooding *et al.*, in *Mars*, ed. by H. Kieffer *et al.*, p. 626, Univ. of Arizona, Tuscon, 1992.

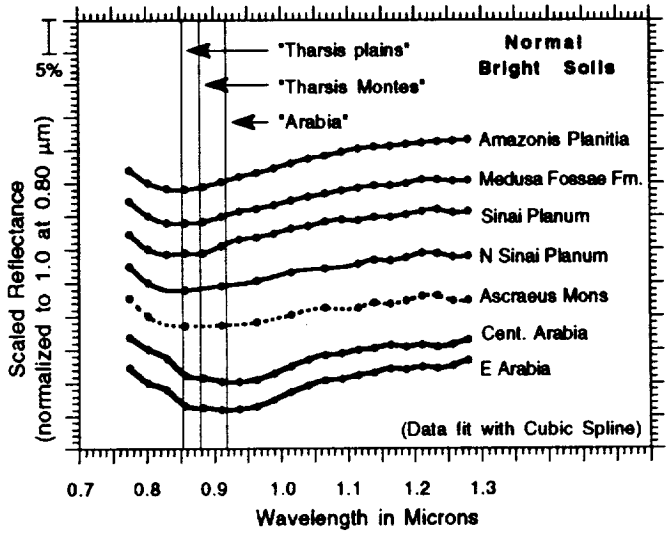

Figure 1. Representative spectra of "normal bright materials" lacking evidence for mafic minerals. Circles indicate ISM channels used in the spectra. Thin solid lines represent bright soils in the Tharsis plains and Amazonis; dashed lines soils at high elevations on the flanks of Tharsis Montes; and heavy solid lines soils in Arabia. Vertical lines are approximate absorption centers in each region.

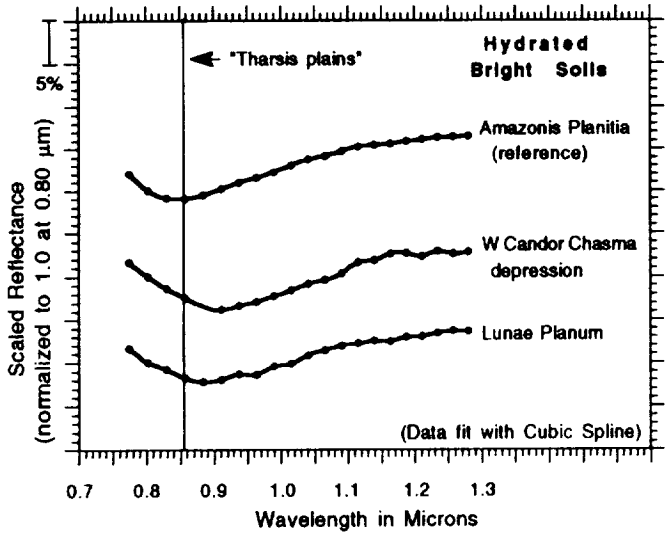

Figure 2. Representative spectra of "hydrated bright materials" lacking evidence for mafic minerals. Circles indicate ISM channels used in the spectra. Amazonis Planitia is included for comparison to "normal bright materials" in the same geographic region from which these spectra were obtained.

SOLAR NOBLE GASES REVEALED BY CLOSED SYSTEM STEPPED ETCHING OF A METAL SEPARATE FROM FAYETTEVILLE. Ch. Murer, H. Baur, P. Signer and R. Wieler, ETH-Zürich, NO C61, CH-8092 Zürich, Switzerland.

Abstract: Solar He, Ne, and Ar in a Fe-Ni separate from the chondrite Fayetteville are analysed by closed system stepped oxidation. We report here data of the first 15 steps comprising 55% of the total solar gases. $^{4}He/^{36}Ar$ and $^{20}Ne/^{36}Ar$ are quite constant at values about 20% below those of present day solar wind (SWC). In this, Fe-Ni differs from lunar ilmenites where $^{4}He/^{36}Ar$ and $^{20}Ne/^{36}Ar$ in the first steps are several times below SWC. Thus, metal retains SW-noble gases even better than ilmenite, almost without element fractionation. Nevertheless, the isotopic composition of SW-He, -Ne, and -Ar in the first steps of the metal sample are identical to those found in a recently irradiated lunar ilmenite, indicating that ilmenites and chondritic metal both contain isotopically unfractionated SW noble gases. A preliminary analysis of a smaller Fayetteville metal separate shows Ne from solar energetic particles (SEP-Ne) with $^{20}Ne/^{22}Ne \leq 11.5$.

Introduction: Diffusion coefficients for He, Ne, and Ar in metallic Fe-Ni are all similar and quite high (1). Therefore, trapped noble gases in Fe-Ni from gas-rich meteorites should reflect element and isotope abundances of the incoming solar corpuscular radiation even better than lunar ilmenites. We have thus extended our studies of solar noble gases by Closed System Stepped Etching (CSSE) to Fe-Ni separates. The CSSE technique is well suited to separate solar wind (SW) noble gases from solar energetic particles (SEP) which are implanted with energies above those of the SW.

Here we report data from a 0.5 g sized metal separate from the dark portion of the Fayetteville (H4-6) chondrite. The separate contained about 10 vol% silicates attached to the Fe-Ni particles. The sample was oxidised with increasingly aggressive $CuCl_2 x n H_2O$-solutions as first proposed by Vilcsek and Wänke (2). This reagent very selectively attacks only metal phases as tests have shown. Average procedural and reagent blanks for a typical step of one hour are (in 10^{-10} cm^3 STP): $^{4}He = 500$; $^{20}Ne = 0.7$; $^{40}Ar = 100$. At the time of this writing, about 55% of the total ^{36}Ar of this sample have been released. We therefore also discuss the Ne isotopic data of a preliminary run on a 0.08 g Fe-Ni separate (3).

Element ratios: Fig. 1 shows $^{4}He/^{36}Ar$ and $^{20}Ne/^{36}Ar$ versus the cumulative fraction of ^{36}Ar. The first 3 steps had very short reaction times and are affected by noble gas element fractionation due to incomplete equilibration between gas- and liquid phase. Element ratios in all other steps are quite constant around the average values of: $^{4}He/^{36}Ar = 18560 \pm 4800$, $^{20}Ne/^{36}Ar = 38 \pm 4$ (standard deviation). These values are only slightly lower than those in the present-day solar wind (SWC: $^{4}He/^{36}Ar = 25650 \pm 5400$, $^{20}Ne/^{36}Ar = 45 \pm 10$, ref. 4). Constant $^{4}He/^{36}Ar$ and $^{20}Ne/^{36}Ar$ ratios close to SWC values were also found by stepped etching of a metal separate from the chondrite Acfer 111 (5). The element abundances in metal of Fayetteville and Acfer 111 thus remarkably differ from those in lunar ilmenite. The latter samples consistently display in the first CSSE steps $^{4}He/^{36}Ar$ and $^{20}Ne/^{36}Ar$ ratios several times below SWC values and approach SWC ratios only towards the end of a run, when mainly SEP gases are released (6,7,8). This indicates that even the most noble gas rententive mineral in lunar soils suffered a fractionating loss of light solar wind noble gases, though the SEP portion is retained with little or no fractionation. In contrast, chondritic metal shows little or no element fractionation even in the first CSSE steps, those which release SW gases.

The average $^{4}He/^{20}Ar$ and $^{20}Ne/^{36}Ar$ ratios of Fayetteville metal both are some 20% below those in Acfer 111 (5,9), the meteorite with the least fractionated solar noble gas composition in bulk samples yet reported. It is not yet clear whether the slight underabundance in Fayetteville metal of He and Ne relative to Ar and SWC ratios indicates a minor loss of He and Ne or some temporal variability in the SW composition. We found no evidence for $(^{4}He/^{36}Ar)_{sw}$ as high as 36000 as postulated by (10) based on a stepped combustion analysis of a metal separate of the chondrite Weston.

He, Ne, Ar isotopes: Because of its quite unfractionated element patterns, the isotopic ratios of the first CSSE steps of the metal sample are of particular interest. Step 1 has a $(^{20}Ne/^{22}Ne)_{sw}$ ratio of 13.9 ± 0.1, followed by 4 steps where this ratio is between 13.65 and 13.85. These values are essentially identical to that of 13.8 for the $^{20}Ne/^{22}Ne$ ratio of SW-Ne retained in recently irradiated (<100 Ma) lunar ilmenite 71501 (6,7) and to the SWC ratio of 13.7 ± 0.3 (4). $(^{20}Ne/^{22}Ne)_{sw}$ in Fayetteville metal and ilmenite from lunar soil 71501 are thus identical, though the ilmenite has lost a large fraction of its SW-Ne, whereas the metal may have retained its SW-Ne quite completely. This supports the conclusion that lunar ilmenites retain isotopically unfractionated SW-Ne (6,7).

The time of exposure of Fayetteville to the solar wind (antiquity) is unknown. Notions that gas-rich meteorites may have acquired their solar noble gases early in solar system history have never been substantiated. In view of high collision rates in the asteroid belt we rather believe that asteroidal regoliths may be young, such that Fayetteville and lunar soil 71501 may be of comparable antiquity.

In both runs here $^{20}Ne/^{22}Ne$ decreases with progressive etching. This pattern is common to all CSSE runs on regolithic samples and indicates the release of SEP-Ne which is isotopically heavier than SW-Ne (e.g.6,7,8,11). Towards the end of the preliminary run $(^{20}Ne/^{22}Ne)_t$ ratios are as low as 11.5, close to the SEP value of 11.3. We thus could isolate rather pure SEP-Ne from Fayetteville metal. Hence, not only does this phase release SW-Ne with an isotopic composition identical to that in lunar ilmenite but it also contains an SEP-Ne component very similar to that found in plagioclase, pyroxene, and ilmenite (6,7,11). To variable degrees, the latter minerals are all more prone to SW noble gas diffusion than Fe-Ni. The data here are thus an additional proof that the more deeply sited, isotopically heavier SEP-Ne component is not the result of diffusive alteration of surficially implanted SW-Ne, but indeed represents a real solar component implanted with higher energies than the solar wind. The complete data set of this ongoing run should also yield an improved ratio of the concentrations of SW- and SEP-gases.

The isotopic composition of Ar and He in the first steps of the 0.5 g sample are in good agreement with values previously deduced for the SW component (e.g.6,7,10). Due to cosmogenic Ar and He, the measured $^{36}Ar/^{38}Ar$ and $^{3}He/^{4}He$ ratios are lower than those of the solar component. A maximun correction for this can be done via cosmogenic ^{21}Ne, assuming that none of the $^{21}Ne_{cos}$ has recoiled from adjacent silicates. In the first 3 steps, the maximum correction ranges between 0.2 and 3% for $(^{36}Ar/^{38}Ar)_{meas}$ and 0.8% for $(^{3}He/^{4}He)_{meas}$. The resulting $(^{36}Ar/^{38}Ar)_{sw}$ ranges between 5.47 and 5.58, the average $(^{3}He/^{4}He)_{sw}$ is $(4.50 \pm 0.07)*10^{-4}$.

Acknowledgments: Work supported by the Swiss National Science Foundation.

References: (1) Nyquist L. E. et al. (1972) *Earth Planet. Sci. Lett.* **14**, 207. (2) Vilcsek E. and Wänke H. (1965) *Z. Naturforsch.* **20a**, 1282. (3) Murer Ch. et al. (1992) *Meteoritics* **27**, 264. (4) Bochsler P. (1987) *Physica Scripta* **T18**, 55. (5) Pedroni A. and Begemann F. (1992) *Meteoritics* **27**, 273. (6) Benkert J.-P. et al. (1993) *J. Geophys. Res.* (Planets), submitted. (7) Wieler R. et al. (1992) *Lun. Planet. Sci. XXIII*, 1525. (8) Wieler R. et al. (1993) *Lun. Planet. Sci. XXIV*, this volume. (9) Pedroni A. and Weber H. W. (1991) *Meteoritics* **26**, 383. (10) Becker R.H. and Pepin R. O. (1991) *Earth Planet. Sci. Lett.* **103**, 55. (11) Wieler R. et al. (1986) *Geochim. Cosmochim. Acta* **50**, 1997.

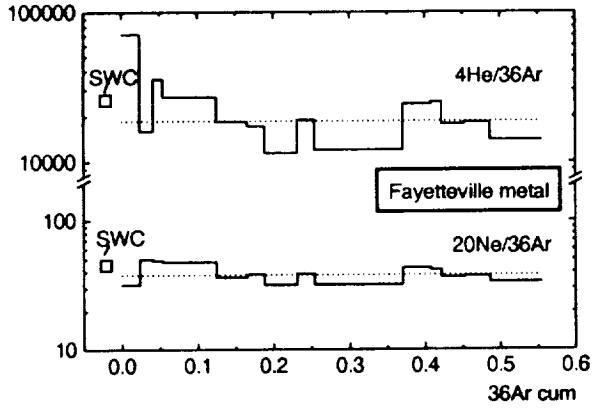

Fig. 1: $^{4}He/^{36}Ar$ and $^{20}Ne/^{36}Ar$ are rather constant and ~20% below the present-day solar wind (SWC, ref. 4). This indicates that Fayetteville metal shows little or no element fractionation even in the outermost, solar wind bearing grain layers.

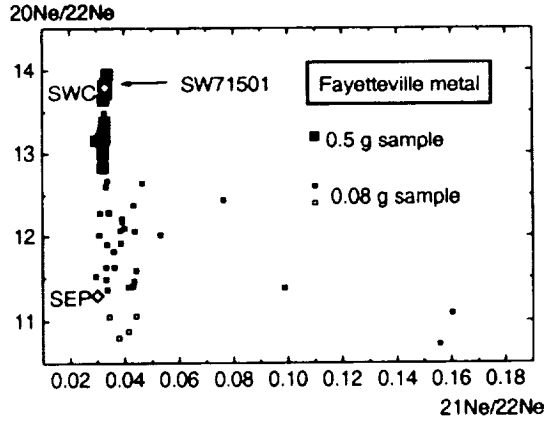

Fig. 2: Ne three-isotope plot. SW-Ne in Fayetteville metal is identical to that in recently irradiated lunar ilmenite 71501 (6,7) and to SWC (4). The SEP-Ne component is very similar to that found in plagioclase, pyroxene and ilmenite (6,7,11). Steps of the small sample shown by open symbols could not be measured accurately (uncertainity > 5%). These data agree within error limits with the SEP composition.

Effects of Levitated Dust on Astronomical Observations from the Lunar Surface

D. L. Murphy and R. R. Vondrak
Lockheed Palo Alto Research Laboratory, Palo Alto, California

It is believed that a substantial population of levitated dust is present in the terminator region of the moon [1]. Stray light scattered by this dust layer may contaminate astronomical observations made from the lunar surface using infrared, visible, and ultraviolet light. The evidence for dust levitation stems from: Surveyor vidicon images of horizon glow [2]; anomalous brightness in photographs of the solar corona taken by Apollo astronauts while the spacecraft was just inside the moon's shadow [3]; and observations by Apollo astronauts of streamers just prior to lunar orbital sunrise or just after lunar orbital sunset [4]. It has been proposed that the differential charging of the lunar surface in the terminator region due to photoemission and the consequent strong local electric fields comprise the mechanism responsible for this levitation [5]. Although quantitative data on the levitated lunar dust distribution are meager, it is possible to estimate column densities and sizes. In this paper we summarize the estimates of particulate sizes and number densities of previous authors, and construct a nominal terminator dust distribution, as a function of particulate radius and altitude above the lunar surface. Using the model we estimate the brightness of scattered sunshine for three wavelength bands. For the results in the visible wavelengths, we compare the estimated brightness with the known brightness of selected astronomical objects and discuss the implications for lunar-based astronomy.

Nominal Terminator Levitated Dust Model

The typical height to which an electrostatically levitated dust grain will be ejected depends on its radius through the charge on the grain at the time of its ejection from the lunar surface. Criswell [5], and Rennilson and Criswell [2], obtain estimates of 5-6 μm radii and levitated altitudes of 10-30 cm. McCoy's Model "0" [3] provides another size, 0.1 μm, and a scale height $\sim$3 km. Assuming the scale height to be a power law function of the grain radius provides the estimate $z_0 = 20a^{-8/3}$ where z_0 is the scale height in meters and a is the particulate radius in μm. Based on the picture provided by McCoy's Model "0", we assume an exponential distribution of dust of radius a with altitude z. We assume a column density, integrated over all particulate radii, of 2×10^5 cm^{-2}. The particulate density for a given size just above the lunar surface is assumed to satisfy a power law. Our model distribution over the terminator is then

$$\rho(a, z) = \frac{n_0}{a^p} \exp[-a^{8/3} z/20]$$

Normalizing the vertical column density, integrated over particulate radii 0.1 μm $\leq a \leq$ 6 μm, gives $n_0 = 8.08 \times 10^{-2}$ cm^{-3} for $p = 1$, $n_0 = 5.88 \times 10^{-3}$ cm^{-3}-μm for $p = 2$, and $n_0 = 4.62 \times 10^{-4}$ cm^{-3}-μm^2 for $p = 3$. The results reported below are calculated for the case $p = 1$.

Results and Conclusions

Assuming a refractive index appropriate to volcanic dust [6], the brightness of scattered sunlight can be calculated using Mie scattering theory. The solar spectrum used was taken from [7]. Plotted in Fig. 1 are results for scattering by the lunar dust layer in the near infrared (1–4 μm), the visible (350–650 nm), and the near ultraviolet (200-350 nm), as functions of solar scattering angle. These results were calculated using Monte Carlo integration; estimated uncertainties are typically a few percent. In Fig. 2 we have plotted the scattered brightness in the visible wavelengths in Rayleighs. In the same plot we have included the brightness of some known astronomical sources, along with the background brightness estimated by the Lunokhod-2 astrophotometer [8].

These results indicate that the lunar sky brightness near the terminator is several orders of magnitude times that of the terrestrial night sky. Lunar-based astronomical observations would be severely impaired one to two days per month at a minimum, due to the presence of the terminator dust layer. Although during the lunar night solar scattering is not present, on the lunar nearside scattered earthshine will enhance the sky brightness. The effects of earthshine and zodiacal light will be included in more detailed calculations.

A major uncertainty in calculating astronomical effects due to dust at locations away from the terminator is the absence of information on dust distributions there. Several strategies for detection of lunar dust altitude distributions using both passive and active lidar techniques have been evaluated and will be described.

Acknowledgments. This paper is supported by the Lockheed Independent Research Program.

References

1. Zook, H. A., and J. E. McCoy, *Geophys. Res. Lett., 18,* 2117, 1991.
2. Rennilson, J. J., and D. R. Criswell, *The Moon, 10,* 121, 1974.
3. McCoy, J. E., *Proc. Lunar Sci. Conf. 7th,* 1087, 1976.
4. McCoy, J. E., and D. R. Criswell, *Proc. Lunar Sci. Conf. 5th,* 2991, 1974.
5. Criswell, D. R., in *Photon and Particle Interactions with Surfaces in Space,* R. J. L. Grard (ed.), Reidel, Dordrecht, 1973, pp. 545-556.
6. Jursa, A. S. (ed.), *Handbook of Geophysics and the Space Environment,* Air Force Geophysics Laboratory, 1985, p. 18-17.
7. Johnson, F. S. (ed.) *Satellite Environment Handbook,* 2nd ed., Stanford University Press, 1965, pp. 97-99.
8. Severny, A. B., E. I. Terez, and A. M. Zvereva, in *Space Research XIV,* Akademie-Verlag, Berlin, 1974, pp. 603-605.

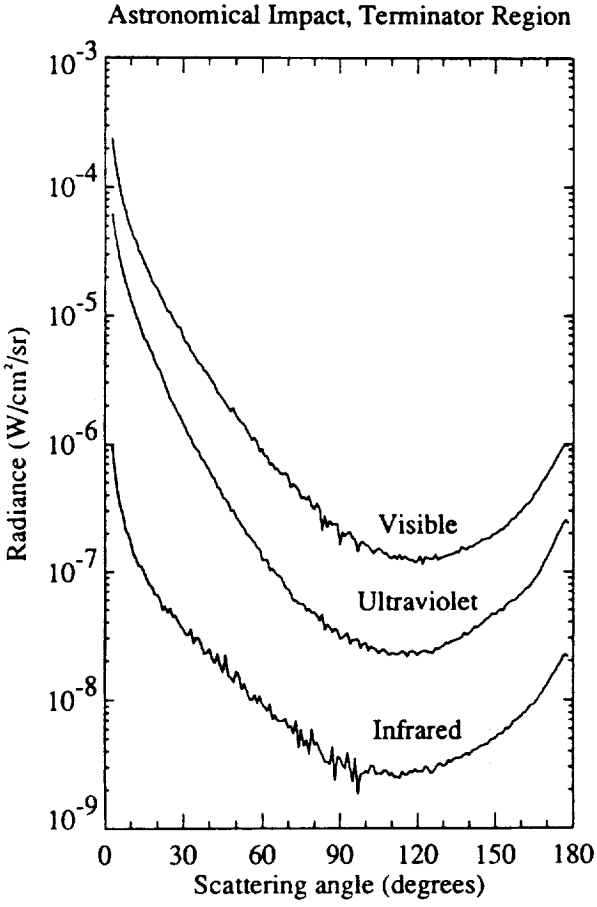

Figure 1

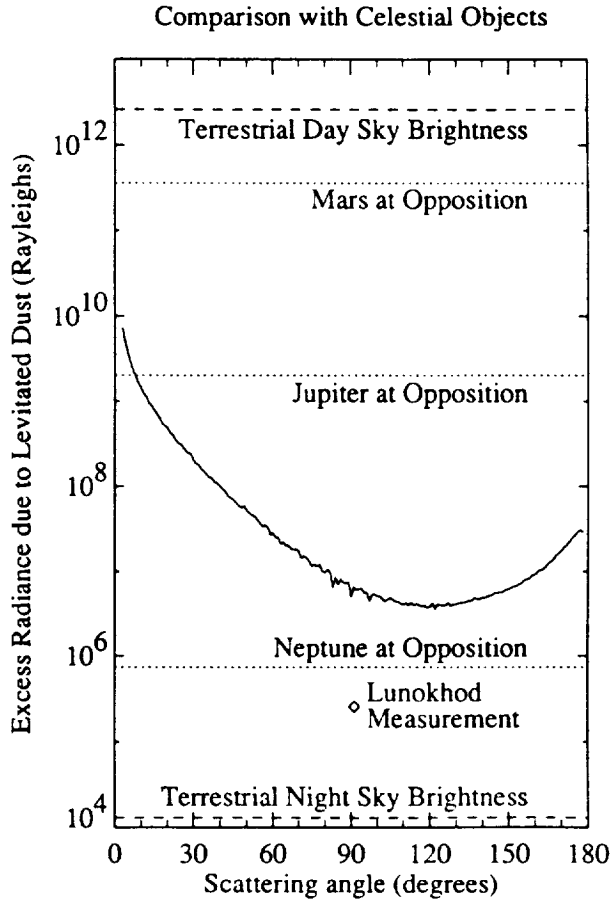

Figure 2

DUST-DYNAMIC FEEDBACKS IN THE MARTIAN ATMOSPHERE: SURFACE DUST LIFTING;
James R. Murphy (NRC, NASA Ames), James B. Pollack (NASA Ames)

The emplacement of dust into the martian atmosphere requires a dynamical interaction between the overlying atmosphere and particles upon the surface. This is the case for both localized lifting events and planetary scale storms. The identification of which specific components of the atmospheric circulation are responsible for dust raising at particular seasons and locations is a fundamental question in regard to understanding the genesis of lifting events and possible feedbacks between lifted dust and continuation or cessation of lifting. We have been developing numerical models [1,2] with which to study a wide range of questions related to suspended dust in the martian atmosphere. Our present model is comprised of interactively coupled 3-D dynamical [3] and aerosol transport/microphysical [4] models. With this model we are investigating the nature of possible feedbacks between surface dust lifting and the amplification/damping of near-surface wind and thermal fields and their implications for additional lifting. These studies allow us to identify preferred locations for dust lifting (*e.g.*, large scale topographic slopes) and the particular circulation component(s) (*e.g.*, overturning circulation, thermal tides, baroclinic waves) responsible for the lifting.

Surface dust lifting is calculated employing model [3] generated surface stress values, which are a measure of the momentum transfer between the atmosphere and ground. Based upon theoretical considerations and wind tunnel studies [5], the static threshold value of the surface stress for the initiation of particle motion under martian surface conditions is ~0.035 N m^{-2}. More appropriately, under conditions of pre-existing particle motion, the threshold value is 80% of the static value, or ~0.028 N m^{-2}. For terrestrial applications, the relationship between surface stress and dust raising has been empirically determined to be proportional to the square of the surface stress [6,7]. We employ this type of prescription to calculate surface dust raising in our model.

Via a sequence of experiments (all carried out at a seasonal date of southern summer solstice, ~L_S=270) we have investigated the impact of the large scale martian topography upon the ability of the atmospheric circulation to lift dust from the surface. This is acconplished by running our model with observed topography (and surface thermal inertia and albedo fields) smoothed to our model

resolution (7.5° latitude-by-9.0° longitude) and also with a flat lower boundary (and spatially invariant thermal inertia and albdeo values). Analogous experiments in which the lifted dust is radiatively inactive (passive tracer) have been conducted to act as a control against which feedbacks are defined.

These simulations, taken in total, indicate the following:

1) the inclusion of topography enhances the amount of dust lifted at northern middle latitudes, apparently via interactions with baroclinic waves present there, though dust-dynamic feedback effects are minimal,

2) the inclusion of topography apparently inhibits (at southern subtropical and middle latitudes) dust-dynamic feedbacks which in the case of a flat lower boundary act to produce a 'dust storm' like occurrence in which minimal dust lifting occurs for several sols after which lifting rapidly increases and then subsequently declines,

3) a dusty-atmosphere (and thus more energetic) initial state results in enhanced dust raising ability and greater positive feedbacks than is the case for an initially dust free atmosphere.

Results from these simulations will be presented including analyses of the various dynamical components to illustrate the nature of the feedbacks and the various circulation components of importance at various locations and times.

[1] Murphy et al. (1990) *JGR*, *95*, 14,629; [2] Murphy et al. (1993), *JGR*, accepted; [3] Pollack et al. (1990) *JGR*, *95*, 1447; [4] Toon et al. (1988) *JAS*, *45*, 2123; [5] Greeley and Iversen (1985) 'Wind as a Geological Process', Cambridge Univ. Press; [6] Gillette, D. (1981) *Spec. Pap. Geol. Soc. Am.*, 186, 11; [7] Westphal et al. (1987) *JGR*, *92*, 3027.

NITROGEN AND LIGHT NOBLE GASES IN PARSA ENSTATITE CHONDRITE. S.V.S. MURTY, Physical Research Laboratory, Navrangpura, Ahmedabad-380009, INDIA.

Nitrogen and light noble gases have been analysed in three bulk samples and an aubritic nodule in Parsa, an EH3 chondrite. While the three bulk samples show varying amounts of trapped He, Ne of solar composition, the nodule is totally devoid of trapped He, Ne. The ^{15}N contents in bulk samples vary from 119 ppm to 197 ppm with $\delta^{15}N$(‰) ranging from -22.6 to -31.2, while for the nodule N=140 ppm with $\delta^{15}N$(‰)= -13.4. The spread in both N and $\delta^{15}N$ in Parsa is due to heterogeneous distribution of N bearing minerals with differing $\delta^{15}N$ signatures. The higher N contents of the nodule as well as its $\delta^{15}N$ signatures, as compared to normal aubrites is suggestive that it may not be genuine aubrite.

Solar gases have been recently reported in Parsa[1]. In an effort to check whether solar gases are uniformly distributed throughout Parsa or they are located in specific phases, we analysed two additional samples of bulk Parsa and one aubritic nodule for N and noble gases. Nitrogen studies are intented for the understanding of the nitrogen components distribution in E-chondrites.

Experimental: The Parsa nodule is very clean, while the bulk Parsa samples are rusty due to weathering. They have all been cleaned to be free of rust. Additionally the sample Parsa-2 has been etched for a short duration in dil. HF to see if the trapped He, Ne can be etched away. Petrological discription of Parsa and the nodule have been given by Nehru et al. [2] and Prinz et al. [3]. In all the four samples N and noble gases have been analysed by stepped pyrolysis, using standard procedures [4]. Here we discuss the results of N and light noble gas.

He, Ne and Ar: The data of the isotopic ratios are given in Table-1. The amounts and elemental ratios of the trapped components of all the samples are given in Table-2. The Ne isotopic composition of the nodule is purely cosmogenic, while the 20/22 values of the bulk Parsa samples clearly show the presence of trapped Ne. The varying values of 20/22 show that the amount of trapped Ne in these three samples is variable. The stepped temperature Ne isotopic data for Parsa-2 and Parsa-3 plot similar to Parsa-1 [1] showing solar wind composition for the trapped Ne. For the nodule, all temperature fractions gave pure cosmogenic Ne ratios. This clearly demonstrates that trapped Ne of solar composition is heterogeneously distributed in Parsa, just like in ALHA 77295 [5] and that the aubritic nodule is not the carrier of solar gases. These conclusions have also been reflected in the trapped amounts of ^{4}He, ^{20}Ne and the ratio (4/20)Trapped (Table-2).

Nitrogen: Both the N contents and $\delta^{15}N$ of the three bulk Parsa samples show variation. The release characteristics are also not identical for the three samples. The maximum N-release for these samples occurred in the 800°C to 1200°C range and the lightest N component has been released at 1200°C and 1400°C fractions. These characteristics are due to the heterogeneous

NITROGEN AND NOBLE GASES IN PARSA: S.V.S. MURTY

distribution of N-bearing minerals with different $\delta^{15}N$ signatures in the Parsa meteorite. Similar N sysematics have been observed in other E-chondrites [6].

The N-systematics of the nodule are entirely different from the bulk samples. The maximum release (~90%) occurred at 1400°C with $\delta^{15}N$(‰)= -10.4, while the low temperature fractions (800 to 1200°C) comprising of ~9% N have $\delta^{15}N$ (‰)= -40.3. The higher N conetnts in this nodule, as well as its complex $\delta^{15}N$ structure, as compared to the normal aubrites [6,7,8], is suggestive that the nodule is not a genuine aubrite, as has also been suggested by Kiel [9].

Table-1: Nitrogen and light noble gases in Parsa samples

Sample	N (ppm)	$\delta^{15}N$ (‰)	$\frac{20}{22}$	$\frac{21}{22}$	$\frac{3}{4}$ ($\times10^4$)	$\frac{38}{36}$	$\frac{40}{36}$
Parsa-1	197.5	-31.16 ± 1.87	3.022 .023	0.7200 .0102	35.79 1.64	0.2330 .0013	242.2 2.0
Parsa-2*	119.2	-26.29 0.69	2.515 .009	0.7470 .0022	62.75 5.27	0.2303 .0005	116.0 .5
Parsa-3	157.5	-22.57 0.55	1.852 .010	0.7717 .0029	117.9 9.4	0.2636 .0006	292.0 1.7
Parsa Nodule	140.5	-13.42 0.57	0.862 .005	0.8907 .0023	227.4 19.0	0.7034 .0030	6925 37

Table-2:Trapped component in Parsa samples

Sample	^4He —10^{-8}cc STP/g—	^{20}Ne	$\frac{4}{20}$
Parsa-1	11186	24.5	456
Prasa-2*	4294	20.8	206
Parsa-3	844	8.8	96
Parsa-Nodule	~0	~0	-

*Etched with dilute HF

References: [1]. Murty, S.V.S. (1992) LPSC XXIII 951-592. [2]. Nahru, C.E. et. al. (1984) LPSC XV, 597-598. [3]. Prinz, M. et al. (1984) LPSC XV, 653-654. [4]. Murty, S.V.S. and Goswami, J.N. (1992) Proc. 22nd LPSC 225-237. [5]. Wieler, R. et al. (1985) LPSC XVI, 902-903. [6]. Grady, M.M. et al. (1986) GCA 50, 2799-2813. [7]. Murty. S.V.S. and Marti, K. (1990) Meteoritics 25, 227-230. [8]. Murty, S.V.S. and Varun Sheel (1991) Meteoritics 26, 375.[9]. Keil, K. (1989) Meteoritics 24, 195-208.

COMPOSITION OF WEAKLY ALTERED MARTIAN CRUST: J. F. Mustard[1], S. L. Murchie[2], and S. Erard[3] (1) Dept. Geol. Sci., Box 1846, Brown University, Providence RI, 02912, (2) LPI, Houston, TX (3) Instituto di Astrofisica Spaziale, Roma, Italy

Introduction: The mineralogic and chemical composition of weakly altered crust remains an unresolved question for Mars. Dark regions hold clues to the composition since they are thought to comprise surface exposures of weakly altered crustal materials (e.g. 1,2). Understanding the in situ composition of relatively pristine crustal rocks in greater detail is important for investigating basic volcanic processes. Also, this will provide additional constaints on the chemical pathways by which pristine rocks are altered to produce the observed ferric iron-bearing assemblages and inferred clay silicate, sulphate, and magnetic oxide phases. Reflectance spectra of dark regions obtained with the ISM instrument are being used to determine the basic mineralogy of weakly altered crust for a variety of regions on Mars. The first results of this analysis are presented here.

Spectral Data: High spatial resolution (22 km/pixel) imaging spectrometer data were acquired in 1989 by the ISM instrument onboard the Phobos 2 spacecraft for 9 different areas near the equatorial regions on Mars (3,4). The data windows are ≈300 km wide and 2000 km long and sample a wide variety of terrain and surface morphologies. The surface in the Tharsis plateau and Valles Marineris regions were well sampled with additional coverage in the Arabia and the Syrtis Major-Isidis regions. A 128 channel reflectance spectrum from 0.76 to 3.16 μm was obtained for each pixel of which 64 channels are used in these analyses. The signal to noise ratio is > 300:1 across most of the detector elements and the absolute radiometric accuracy is ≈10%. Details of data reduction and calibration are presented elsewhere (4,5).

Composition of "Fresh Crustal Materials": Surfaces that are weakly altered, or relatively "fresh", are identified and the basis of several spectral properties (albedo, spectral slope, wavelength of band minimum, band area) that have been discussed previously (5). A relatively fresh surface is typically low in albedo, has a flat to slightly negative continuum slope, large band area, and a band minimum at wavelengths longer than ≈0.9 μm. The entire ISM data set has been transformed into a suite of spectral parameters that characterize these properties . From the parameter maps, many regions have been identified that contain spectra that meet the freshness criteria. A subset of these spectra, with continuua removed, are shown in **Figure 1**.

These spectra sample geologic units of different age and surface morphology. The general geographic region is listed along the left margin of **Fig. 1**. All show a strong, well-defined absorption near 1.0 μm and an absorption of variable strength and definition near 2.1 μm. The shape, position, symmetry, and strength of these absorptions provide unambiguous identification of calcic pyroxene as a mineral phase on the Martian surface (5). However, the spectra also show diversity in the shape, position and relative strengths of these two dominant absorptions suggesting that additional mineral phases are present or that the compositions of the pyroxenes differ. Since pyroxene reflectance spectra exhibit variations in the wavelength position of absorption band minima that are systematic with composition (6,7,8), band minima provide a simple tool for deriving initial estimates of the pyroxene chemistry for these surfaces. The wavelength position of absorption band minima for the 1.0 and 2.0 μm bands of the spectra shown in **Fig. 1** were determined and are presented in **Table 1**. A plot of the wavelength of the 1.0 vs 2.0 μm band minima for these areas (**Figure 2**) illustrates that most conform to the experimentally determined pyroxene trend and these spectra are likely to be dominated by pyroxene of a unique composition. For those that fall off the main trend (e.g. Coprates Chasma) one or both bands is probably modified by other, currently unresolved, mineral components. Using the results of (7), estimates of pyroxene chemistry were derived and are presented in **Figure 3**. The validity of these estimates depend on the completeness of the analysis of (7) and that the band parameters are dominated by the absorption properties of a single pyroxene. Nevertheless, regional variations in pyroxene, and therefore rock composition, are strongly suggested by these results.

Discussion The results obtained thus far show: 1) Relatively unaltered crustal material is well exposed in several areas on the surface over the spatial scale of an ISM pixel (≈500 km^2). They contain well crystalized pyroxenes of augitic composition and are of moderate iron content, consistent with SNC meteorites (9). 2) Surface morphology and pyroxene composition

indicate a volcanic origin and basaltic composition for many of the areas studied. 3) Clearly defined variations in pyroxene absorption bands imply differences in pyroxene composition and/or whole rock mineralogy and composition for different geographic regions on Mars.

Direct evidence of additional mineral phases is not immediately evident from a qualitative examination of **Fig. 1**. Feldspar is certainly an expected phase and may be responsible for the shoulder of variable intensity between 1.1 and 1.3 μm. However clino-pyroxene can have a well defined band in this wavelength region (e.g. 10) and olivine may contribute as well. In order to address the question of complete mineralogy, we are currently pursuing the application of more sophisticated mineralogic modelling approaches (e.g. 11). However, this will require some restructuring of the approaches to include the expected mineral compliments and effects of grain size distributions expected in the natural system (12). In addition to continuing the mineralogic modelling we are examining high resolution images of the surface to better understand surface morphology and possible clues to the differences in composition.

References: (1) Arvidson, R., E., (1989)*J. Geophys. Res., 94*, 1573-1587 (2) Singer, R. B., (1980) *(abstr) Lun. Plan. Sci.* XI, 1048-1050 (3) Bibring, J-P., *et al.*, (1989) *Nature*, 341, 591-592 (4) Erard, S. *et al.*, (1991) *Proc. Lun. Plan. Sci.* 21, 437-456 (5) Mustard, J. F., *et al*, (1992) The surface composition of Syrtis Major: (*in press*) *JGR-Planets* (6) Adams, J. B. (1974) *J. Geophys. Res.*, 79, 4829-4836. (7) Cloutis, E.A. and M. J. Gaffey (1991) *J. Geophys. Res.* 96, 22809-22826. (8) Hazen, *et al.*, (1978) *Proc. Lun. Plan. Sci.* VIII, 2919-2934. (9) McSween, H. Y (1985) *Rev. Geophys. 23*, 391-416. (10) Besancon, J. R. *Am. Mineral. 53*, 965-973. (11) Sunshine *et al.*, (1990) *J. Geophys. Res.*, 95, 6955-6966. (12) Mustard, J. F., *et al.*, (1993) *(abstr) Lun. Plan. Sci.* XXIV (this volume).

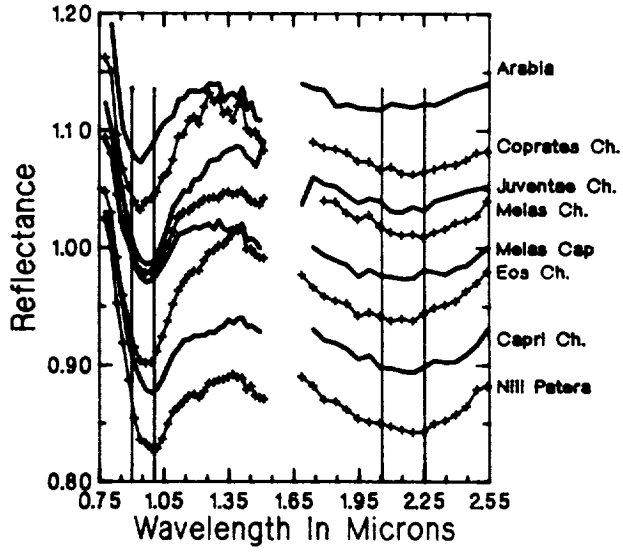

Figure 1

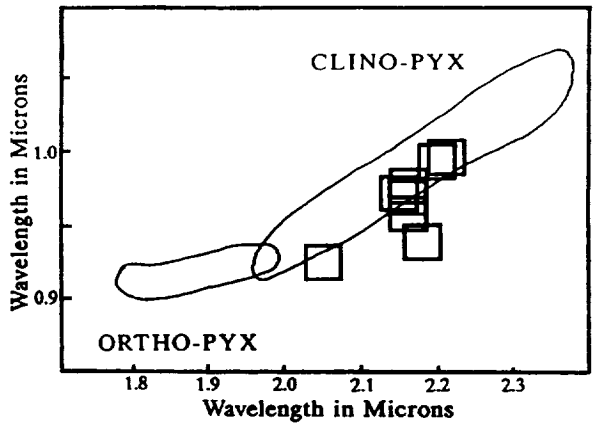

Figure 2
Band minima from Table 1 plotted on the 1.0 vs 2.0 μm band minima plot. Boundaries of pyroxene fields after (7).

Table 1

Location	1.0 μm[1]	2.0 μm[2]
Arabia	0.925	2.05
Coprates	0.938	2.18
Juventae	0.976	2.16
Melas Ch.	0.972	2.20
Melas Cap	0.969	2.14
Eos Ch.	0.964	2.20
Capri Ch.	0.996	2.21
Nili Patera	0.995	2.20

1) ± 28 nm 2) ±50 nm

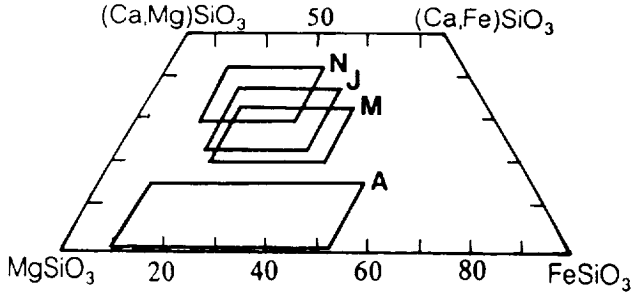

Figure 3
Estimated pyroxene compositions for Arabia (A), Melas Cap (M), Juventae Chasma (J) and Nili Patera (N)

FROM MINERALS TO ROCKS: TOWARD MODELING LITHOLOGIES WITH REMOTE SENSING

John F. Mustard, Jessica M. Sunshine, Carlé M. Pieters, Andrew Hoppin, Stephan F. Pratt, Dept. of Geol. Sci., Brown University, Providence, RI, 02912.

Introduction: High spectral resolution imaging spectroscopy will play an important role in future planetary missions. Sophisticated approaches will be needed to unravel subtle, super-imposed spectral features typically of natural systems, and to maximize the science return of these instruments. Carefully controlled laboratory investigations using homogeneous mineral separates have demonstrated that variations due to solid solution (1), changes in modal abundances (2,3), and the effects of particle size (4,5) are well understood from a physical basis. In many cases, these variations can be modeled quantitatively using photometric models (6), mixing approaches (7), and deconvolution procedures (3). However, relative to the spectra of individual mineral components, reflectance spectra of rocks and natural surfaces exhibit a reduced spectral contrast. In addition, soils or regolith, which are likely to dominate any natural planetary surface, exhibit spectral properties that have some similarities to the parent materials, but due to weathering and alteration, differences remain that cannot yet be fully recreated in the laboratory or through mixture modeling (e.g. 8). A significant challenge is therefore to integrate modeling approaches to derive both lithologic determinations and include the effects of alteration. We are currently conducting laboratory investigations in lithologic modeling to expand upon the basic results of previous analyses with our initial goal to more closely match physical state of natural systems. The effects of alteration are to be considered separately.

Experimental Procedure: We have chosen to begin with an igneous model consisting of five basic igneous rock forming minerals or mineral groups (olivine (OL), clinopyroxene (CPX), orthopyroxene (OPX), plagioclase (PL), and opaques (ilmenite)). These minerals can explain many volcanic and igneous exposures on the terrestrial planets. Each mineral was crushed and wet sieved to three particle sizes (<25 (S) 25-75 (M) 75-250 (L) μm). The particle size separates were combined to form mono-mineralic soils in the following proportions: small soil (SS) (65% S 25% M 10% L), medium soil (MS) (25% S 50% M 25% L), and large soil (LS) (10% S, 25% M, 65% L). Particle size separates and soils were measured in RELAB and these data are presented in **Figure 1**. Mono-mineralic soils of CPX, OPX, and OL were combined with a constant mass fraction ratio of 3:1:1, similar to mafic mineral ratios in gabbroic rocks, but with three different soil combinations: 1) MS:MS:MS 2) SS:SS:LS 3) LS:LS:SS. These data are presented in **Figure 2**. The reflectances of all samples have also been measured at wavelengths out to 25 μm and initial analyses of these data are reported in a companion abstract (9).

Analysis: The spectra of the particle size separates exhibit the well known and characterized particle size variation where the spectra of small particles are brighter and have weaker absorptions than larger particle sizes. The soil spectra show the same systematics where the SS is brightest and has the weaker absorptions than the MS and LS. This generally reflects the relative contributions of the various particles sizes used to construct the soils. However, modeling of these soil mixtures using a simplified intimate mixing model (2) generally shows that the small particles contribute to the measured soil spectra in excess of the known proportions that were used to construct the soil mixtures. This effect is expressed as a weaker absorption for a given brightness and can be seen in the spectra for OPX and OL where the LS has the same general brightness of M, but weaker absorptions. We hypothesize that the finest size fraction does not behave as an independent particle as required by theory, but coats the larger grains and therefore interacts with more photons than expected. In addition, Hapke's (6) treatment of bidirectional reflectance explicitly states that the particle diameters must be greater that the wavelength of light. The particle diameters of the smallest size fraction begin to approach this limit.

Although the endmember compositions and mass fraction ratios used to construct gabbroic soils are the same, the different particle size distributions dramatically affect the measured spectra (**Fig. 2**). Also note that the spectral contrast of the data in **Fig. 2** is much less than in the spectra of individual endmembers. Application of the intimate mixture model for these returns the results shown in **Table 1**. When the appropriate endmember soil spectra are used, good agreement between known and calculated abundances are found and the fitting error is low (1-3 times noise). Some of the discrepancies between known and calculated abundances are attributed to the settling of samples during preparation for measurement. However, even if the correct endmember compositions but inappropriate particle sizes are used, then the mass fraction estimates are in poor agreement, and there is a large fitting error (5-10 times noise). If endmembers of the wrong composition are used, we can expect even greater fitting errors and errors in fractional abundance estimates.

Conclusion: This investigation is the first to systematically study the effects of particle size distributions on the spectra of mineral separates and mineral mixtures. The analyses show that the finest particles dominate the mono-mineralic soil spectra in excess of theoretical expectations. For the mineral mixture spectra, the spectral

contrast of the mixture is less than the endmember spectra. However, one must use the appropriate soil endmembers, rather than size separates, to attain reasonable solutions. We expect natural surfaces to also be dominated by fine particles and photometric mixture modeling approaches must begin to accommodate not only particle size variations, but distributions. Deconvolution procedures, on the other hand, are less sensitive to particle size variations (10). Analyses of these data with deconvolution is being pursued in parallel. We believe that quantitative modeling of lithologies will be best approached with a combination of methods.

References: (1) Cloutis and Gaffey (1991) *JGR 96*, 22809-22826. (2) Mustard and Pieters, *JGR 94*, 13619-13634. (3) Sunshine *et al.*, (1990) *JGR* 95, 6955-6966. (4) Crown and Pieters (1988), *Icarus 72*, 492-506. (5) Hiroi and Pieters (1991), *Proc. Lun. Plan. Sci. XXII*, 313-325. (6) Hapke *JGR 86*, 3039-3054. (7) Johnson *et al.* (1983) *JGR 88*, 2649-2658. 8) Lunar Source Book (1992). (9) Pieters *et al*, (1993), this volume. (10) Sunshine and Pieters (1993) Estimating modal abundance from the spectra of laboratory pyroxene mixtures..., *JGR*, (submitted).

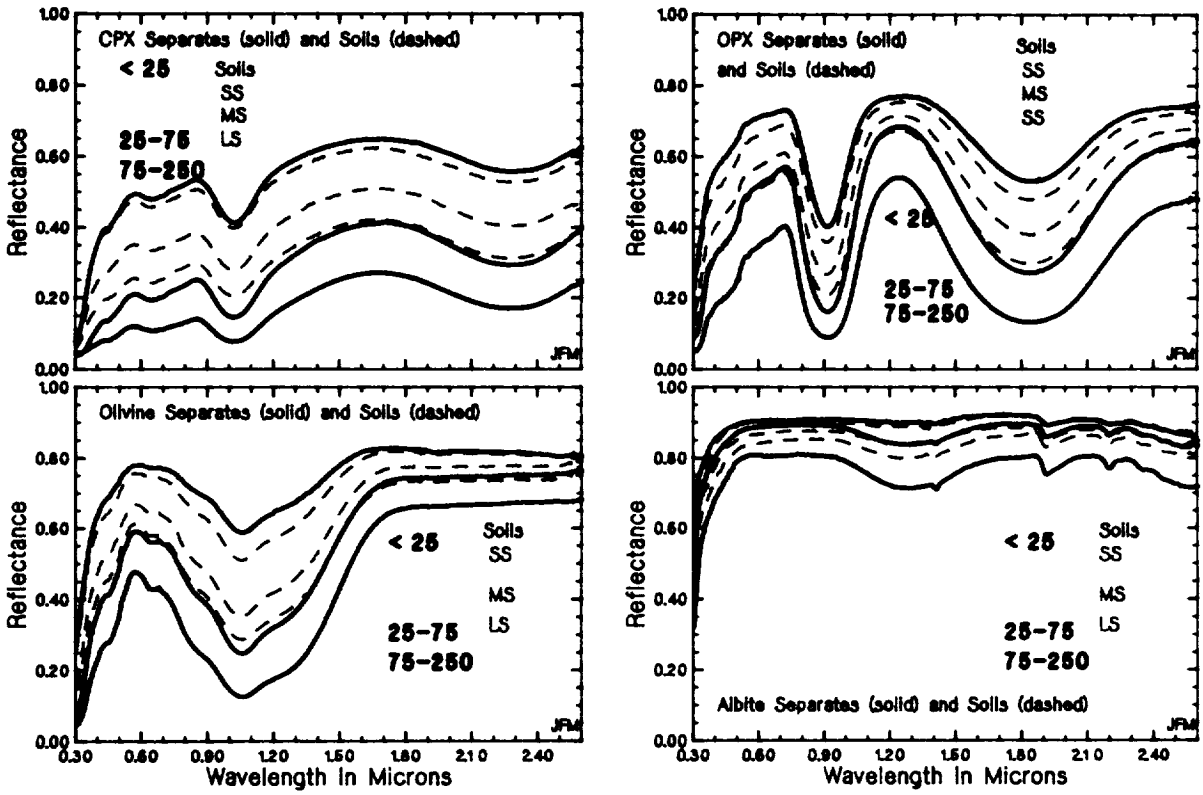

Figure 1

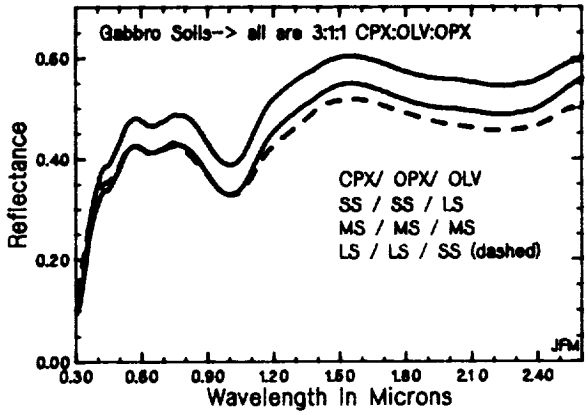

Figure 2

Table 1

	CPX	OPX	OLV	STD
Actual	0.60	0.20	0.20	
MS:MS:MS	0.534	0.203	0.263	0.32
SS:SS:LS	0.725	0.081	0.194	0.47
LS:LS:SS	0.554	0.200	0.246	0.56

AUTHOR INDEX*

*Page numbers refer to the first page of an abstract on which an author appears.

SAMPLE INDEX*

*Page numbers refer to the first page of an abstract in which a sample is mentioned.

METEORITE INDEX*

*Page numbers refer to the first page of an abstract in which a meteorite is mentioned.

KEYWORD INDEX*

*Page numbers refer to the first page of an abstract in which a term is mentioned.